



Application of near infrared sensors to minerals preconcentration

Submitted by

Shekwonyadu Iyakwari

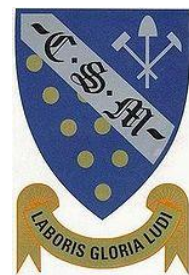
to the University of Exeter as a thesis for the degree of  
Doctor of Philosophy in Mining and Minerals Engineering

In December 2014

This thesis is available for Library use on the understanding that it is copyright material and that no quotation from the thesis may be published without proper acknowledgement.

I certify that all material in this thesis which is not my own work has been identified and that no material has previously been submitted and approved for the award of a degree by this or any other University.

Signature: .....



To the loving memory of Mr. Ezekiel John Iyakwari

1954 - 2001

## **Abstract**

The aim of this project was to investigate the potential and suitability of the application of near Infrared spectroscopy/sensors in automatic preconcentration of complex ores. Two ore types (copper and platinum) were considered for investigation.

The near infrared region of electromagnetic spectrum has been used for mineral mapping in the minerals industries. However, its application as a sensing technology in the sorting of base and precious metals is still minimal. In practice, a near infrared sensor can measure characteristic features of carbonate, hydroxyl and water groups contained in minerals and rocks.

Successful sensor-based sorting requires a good understanding of the minerals and their distribution in an ore. For the copper ores, mineralogical analysis was carried out using QEMSCAN<sup>®</sup> and qualitative XRD analysis. XRF analysis was used to determine the copper concentration in the various particles. In addition to the XRF elemental analysis, copper values were calculated from copper bearing minerals in the ore. XRD analysis was performed on the platinum ore.

Methods of ore sorting based on near infrared readings and near infrared active functional groups (-OH, H<sub>2</sub>O, and CO<sub>3</sub><sup>2-</sup>) were investigated and strategies developed for both ore types. In addition to external environmental influence, most minerals contain water in their chemical structure. Therefore, considering the H<sub>2</sub>O absorption feature(s) for ore sorting was not considered optimal. Strategies were developed which target the discrimination of either or both carbonate and hydroxyl bearing particles as waste. Individual particles spectra were analysed and absorption features assigned to the various chemical species and minerals responsible for the absorptions. Due to individual particle mineralogical variation, particles were classified either as products, waste or middlings.

For copper ore, targeting only the calcite (carbonate) dominated particles for discrimination as waste provided a better option for preconcentration.

Application for the platinum ores targeted the discrimination of chlorite, antigorite, and/or calcite dominated samples as waste. Compared with sample mineralogy, samples could be classified as product or waste using near infrared.

## **Acknowledgements**

I would like to thank Prof. Hylke J. Glass and Dr. Richard Pascoe for their technical support and guidance. I would also like to thank any other staff members at CSM especially Dr. Rob Fitzpatrick who helped me during the course of this work. To Dr. Przemyslaw B. Kowalczyk, words can't explain how indebted I am to you. Thanks should also go to Anglo-American for supplying the samples used during the course of this work and to The Nigerian Tertiary Education Trust Fund (TETFON) through the management of the Nasarawa State University, Keffi and my family for the financial sponsorship.

I would also like to thank my family for their understanding, encouragement and support. To my wife (Maria) and kids (Aweychedu, Adamilo and Yecenu) words can't explain how indebted I am to you guys, three years is a long time away from you. To my mother, Mrs Deborah Kolo, and siblings Doris, Joyce, Patience, Katman, Kemun and Shanyi thanks for your patience.

To Dr. Kelvin F. E. Andersen, Ambo A. Idzi, Billy Dickinson, Abdulqadir Abdulrahman, and Zainab Aliyu thanks for the timely distractions. To Dr. Jurbe J. Mwolwus, Steve Obrike, Ibrahim Adams Mailafia, Olutomi Sodipo, Garry Naman, Dayo Agboola and Femi Odunlami thanks for always giving me memorable summer holiday. To Christy Abubakar you are a sister among sisters.

To Professors J. I. D., Adekeye and Krys Ashano, thank you for making me believe in me.

Finally, to big Daddy, Chief (Barr) Philip J. Iyakwari, only God knows the depth of gratitude in me for you, thank you for your love and believe.

## Table of Contents

Abstract .....	3
Acknowledgements .....	4
Table of Contents .....	5
List of Figures .....	11
List of Tables .....	17
List of accompanying material .....	22
Mineral names and chemical formulae .....	23
Chapter 1: Introduction .....	24
1.1. Introduction .....	24
1.2. Aim of research .....	24
1.3. Thesis structure.....	25
Chapter 2: Background .....	28
2.1. Introduction .....	28
2.2. Sensor-based sorting .....	28
2.2.1. Automated sorters.....	30
2.2.1.1. Particle presentation .....	30
2.2.1.2. Particle examination .....	31
2.2.1.3. Data analysis .....	31
2.2.1.4. Separation .....	31
2.3. Sensors .....	32
2.3.1. Electromagnetic radiation-based sensors .....	32
2.3.1.1. Gamma rays .....	32
2.3.1.2. X-rays .....	33
2.3.1.3. Ultra-Violet.....	34
2.3.1.4. Visible/optical sensors .....	34
2.3.1.5. Infrared .....	35
2.3.1.6. Microwave .....	35
2.3.2. Non-electromagnetic sensors .....	35
2.3.2.1. Magnetic .....	35
2.3.2.2. Conductive.....	36
2.4. The near infrared region of electromagnetic .....	37
2.4.1. Causes of absorption in the NIR region .....	38
2.4.1.1. Electronic processes.....	38
2.4.1.2. Vibrational processes .....	39

2.4.2. Applications of NIR .....	41
2.4.2.1. Recycling industry .....	42
2.4.2.2. Geology and mineral industry .....	43
Chapter 3: Material characterization and methodology .....	46
3.1. Introduction .....	46
3.2. The Mantoverde copper ore .....	46
3.2.1. Sample characterization .....	46
3.3. The Mogalakwena platinum ore .....	49
3.4. Near infrared sensor .....	49
Chapter 4: Mantoverde ore mineralogy and chemistry .....	53
4.1. Introduction .....	53
4.2. Mantoverde ore mineralogy .....	53
4.2.1. QEMSCAN <sup>®</sup> .....	53
4.2.2. X-Ray Diffraction (XRD) analysis .....	61
4.3. Near infrared sensitive minerals .....	63
4.3.1. Mineralogy of near infrared sensitive minerals .....	63
4.3.2. NIR sensitive minerals association .....	67
4.4. Functional groups .....	85
4.4.1. Correlation of functional groups .....	90
4.5. Reconciliation of classification strategy with copper content .....	97
4.6. Mantoverde ore chemistry .....	99
4.6.1. Reconciliation of QEMSCAN <sup>®</sup> and PXRF Cu wt % and Fe wt % concentrations .....	103
Chapter 5: NIR activity and Mantoverde NIR-active minerals .....	107
5.1. Introduction .....	107
5.2. NIR activity and NIR-active minerals .....	107
5.3. Influence of minerals particle grain size on NIR spectra. ....	110
5.3.1. Calcite .....	111
5.3.2. Muscovite .....	113
5.3.3. Hematite .....	116
5.3.4. Malachite .....	117
5.3.5. Chlorite .....	120
5.4. Effect of moisture .....	122
5.5. Implication for ore sorting .....	126
Chapter 6: NIR preconcentration strategy development .....	129

6.1. Introduction .....	129
6.2. Intimate Mixtures .....	130
6.2.1. Mixtures of NIR-active minerals with similar functional groups .....	131
6.2.1.2. Chrysocolla-Kaolinite mixtures .....	132
6.2.1.3. Chrysocolla-Chlorite mixtures .....	134
6.2.1.4. Chlorite-Muscovite mixtures .....	135
6.2.1.5. Kaolinite-Muscovite mixtures .....	136
6.2.1.6. Chrysocolla-Biotite Mixtures .....	138
6.2.1.7. Kaolinite-Chlorite Mixtures .....	138
6.2.1.8. Chlorite-Biotite Mixtures .....	139
6.2.1.9. Biotite- Muscovite Mixtures .....	140
6.2.1.10. Malachite- Calcite Mixtures .....	141
6.2.2. Mixtures of NIR-active minerals with dissimilar functional groups (-OH vs. CO <sub>3</sub> <sup>2-</sup> ) .....	142
6.2.2.1. Chrysocolla- Calcite Mixtures .....	143
6.2.2.2. Muscovite- Calcite Mixtures .....	144
6.2.2.3. Kaolinite- Calcite Mixtures .....	147
6.2.2.4. Chlorite- Calcite Mixtures .....	148
6.2.2.5. Malachite- Chlorite Mixtures .....	149
6.2.2.6. Malachite- Kaolinite Mixtures .....	151
6.2.2.7. Chrysocolla- Malachite Mixtures .....	152
6.2.2.8. Calcite- Biotite Mixture .....	153
6.2.2.9. Malachite- Biotite Mixture .....	154
6.2.2.10. Malachite- Muscovite Mixture .....	155
6.2.3. Influence of hematite on feature(s) displaying NIR-active minerals .....	156
6.2.3.1. Chrysocolla- Hematite Mixtures .....	157
6.2.3.2. Malachite- Hematite Mixtures .....	158
6.2.3.3. Calcite- Hematite Mixtures .....	160
6.2.3.4. Muscovite- Hematite mixtures .....	161
6.2.3.5. Kaolinite- Hematite Mixtures .....	163
6.2.3.6. Chlorite- Hematite Mixtures .....	165
6.2.3.7. Biotite- Hematite Mixtures .....	166
6.2.4. Complex mixtures or mineral associations .....	167
6.2.4.1. Hematite- Chrysocolla- Muscovite Mixture .....	167
6.2.4.2. Hematite- Chrysocolla- Kaolinite Mixture .....	168

6.2.4.3. Hematite-Malachite-Calcite Mixture .....	169
6.2.4.4. Muscovite-Biotite-Chlorite Mixture .....	170
6.2.4.5. Hematite-Malachite-Kaolinite Mixture .....	171
6.2.4.6. Malachite-Muscovite-Hematite Mixture.....	172
6.2.4.7. Chlorite-Biotite-Calcite Mixture .....	173
6.2.4.8. Calcite-Hematite-Muscovite Mixtures .....	174
6.2.4.9. Chrysocolla-Biotite-Hematite Mixture.....	175
6.2.4.10. Biotite-Hematite-Chlorite Mixture .....	176
6.2.4.11. Biotite-Muscovite-Calcite Mixture .....	177
6.2.4.12. Kaolinite-Calcite-Hematite Mixture .....	178
6.2.4.13. Muscovite-Hematite-Kaolinite Mixture .....	179
6.2.4.14. Chlorite-Biotite-Calcite-Hematite Mixtures .....	180
6.2.4.15. Chlorite-Biotite-Calcite-Muscovite Mixtures .....	181
6.2.4.16. Kaolinite-Calcite-Hematite-Muscovite Mixture .....	182
6.2.4.17. Hematite-Biotite-Muscovite-Chlorite-Calcite Mixture.....	183
6.2.4.18. Malachite-Calcite-Hematite-Muscovite-Kaolinite-Chrysocolla Mixture.....	184
6.3. Implications for ore sorting and copper preconcentration strategy development .....	186
Chapter 7: Arrangement of minerals .....	196
7.1. Introduction .....	196
7.2. Linear mixtures.....	196
7.2.1. Vertical alignment .....	196
7.2.2. Horizontal alignment .....	201
7.3. Conclusions.....	207
Chapter 8: Near infrared application on the Mantoverde copper ore.....	208
8.1. Introduction .....	208
8.2. Individual sample NIR spectra mapping.....	208
8.3. Individual sample classification and discussion.....	217
8.4. Classification strategies .....	218
8.4.1. Strategy one .....	218
8.4.1.1. Validation/comparison of splits B1 .....	226
8.4.1.2. Validation/comparison of splits B2 .....	230
8.4.1.3 Validation/comparison of splits A1 .....	232
8.5. Analysis and evaluation of the discrimination results .....	234



8.5.1. Splits B1.....	234
8.5.2. Splits B2.....	236
8.5.2. Splits A1.....	237
8.6. Reconciliation of NIR classification per splits, for strategy one .....	237
8.7. Strategy two .....	240
8.8. Analysis and evaluation of the discrimination results .....	247
8.8.1. Splits B1.....	247
8.8.2. Splits B2.....	248
8.9.3. Splits A1.....	249
8.9. Reconciliation of strategies .....	250
8.10. Economic implication of NIR sorting.....	251
8.11. Conclusions.....	253
Chapter 9: Quality control and data validation.....	255
9.1. Introduction .....	255
9.2. QEMSCAN® .....	255
9.3. NIR-active minerals.....	259
9.3.1. Correlation of NIR-active minerals .....	261
9.3.2. Functional groups .....	264
9.4. Near infrared .....	266
9.5. Effect/influence of resin used on NIR signals .....	270
9.6. Conclusion .....	272
Chapter 10: Applicability of near infrared on the Mogalakwena platinum ore .	273
10.1. The Mogalakwena ore.....	273
10.2. Material characterisation and ore mineralogy.....	274
10.3. NIR-active minerals.....	278
10.4. Functional groups.....	279
10.5. NIR spectra classification and discussion .....	287
10.6. Recommendations .....	293
Chapter 11: Discussion, conclusions and recommendations .....	294
11.1. Discussion.....	294
11.2. Conclusions.....	300
11.3. Key findings.....	302
11.4. Recommendations .....	303
References: .....	305

Appendices..... 315

## List of Figures

Figure 2.1 - Automatic sorter configuration (after De Jong, 2005).....	30
Figure 3.1 - Analysis of Mantoverde samples.....	47
Figure 3.2 - Split B1 and B2 samples marked for directional scanning, used for both the NIR and QEMSCAN <sup>®</sup> analysis.....	48
Figure 3.3 - Image of near infrared setup, at Camborne School of Mines (CSM), (adapted from Gaydon, 2011).....	52
Figure 4.1 - Modal abundance (Wt %), of NIR-active minerals in samples of Mantoverde copper ore.....	66
Figure 4.2 - Segmentation of chrysocolla and hematite grades, for individual particles from NIR-active minerals association mapping.....	85
Figure 4.3 - Proposed model for copper preconcentration, based on ore mineralogy targeted towards eliminating both high-carbonate and high-hydroxyl bearing .....	95
Figure 4.4 - Proposed model for copper preconcentration, based on ore mineralogy targeted towards eliminating only high-carbonate bearing samples.....	96
Figure 4.5 - Copper grades of QEMSCAN <sup>®</sup> mounts (splits B1) inferred from QEMSCAN <sup>®</sup> mineralogical composition with measured PXRF.....	104
Figure 4.6 - Iron grades of QEMSCAN <sup>®</sup> mounts (splits B1) inferred from QEMSCAN <sup>®</sup> mineralogical composition with measured PXRF.....	104
Figure 4.7 - Comparison of Cu wt % determined by PXRF and Cu wt % calculated from the QEMSCAN <sup>®</sup> results.....	105
Figure 4.8 - Comparison of Fe wt % determined by PXRF and Fe wt % calculated from the QEMSCAN <sup>®</sup> results.....	106
Figure 5.1 - Parameters characterising NIR spectrum of calcite: mineral absorption features and overall reflectance (after Iyankwari and Glass, 2014).....	111
Figure 5.2a - NIR reflectance spectra of calcite measured on six different particle size fractions.....	112
Figure 5.2b - NIR spectra of mixture of calcite at four different grain sizes....	112
Figure 5.3a - NIR reflectance spectra of muscovite measured on six different size fractions.....	158
Figure 5.3b - NIR spectra of mixture of muscovite at four different grain sizes.....	115

Figure 5.4a - NIR reflectance spectra of hematite measured on four different size fractions.....	117
Figure 5.4b - NIR spectra of mixtures of hematite at four different grain sizes.....	117
Figure 5.5a - NIR reflectance spectra of malachite measured on six different size fractions.....	118
Figure 5.5b - NIR spectra of mixture of malachite at four different grain sizes.....	119
Figure 5.6a - NIR reflectance spectra of chlorite measured on six different size fractions.....	121
Figure 5.6b - NIR spectra of mixture of chlorite at four different grain sizes...	121
Figure 5.7 - Effects of various conditions on spectrum of sample 2.....	124
Figure 5.8 - Effects of various conditions on spectrum of sample 3.....	125
Figure 5.9 - Effects of various conditions on spectrum of sample 25.....	125
Figure 5.10 - Effects of various conditions on spectrum of sample 27.....	126
Figure 6.1 - NIR spectra of chrysocolla-muscovite mixtures.....	132
Figure 6.2 - NIR spectra of Chrysocolla-kaolinite mixtures.....	134
Figure 6.3 - NIR spectra of Chrysocolla-chlorite mixtures.....	135
Figure 6.4 - NIR spectra of chlorite-muscovite mixtures.....	136
Figure 6.5 - NIR spectra of kaolinite-muscovite mixtures.....	137
Figure 6.6 - NIR spectra of Chrysocolla-biotite mixtures.....	138
Figure 6.7 - NIR spectra of Kaolinite-chlorite mixtures.....	139
Figure 6.8 - NIR spectra of Biotite-chlorite mixtures.....	140
Figure 6.9 - NIR spectra of Biotite-Muscovite mixtures.....	141
Figure 6.10 - NIR spectra of malachite-calcite mixtures.....	142
Figure 6.11 - NIR spectra of chrysocolla-calcite mixtures.....	144
Figure 6.12 - NIR spectra of muscovite-calcite mixtures.....	146
Figure 6.13 - NIR spectra of Kaolinite-Calcite mixtures.....	148
Figure 6.14 - NIR spectra of chlorite-calcite mixtures.....	149
Figure 6.15 - NIR spectra of Chlorite-malachite mixtures.....	150

Figure 6.16 - NIR spectra of malachite–kaolinite mixtures.....	152
Figure 6.17 - NIR spectra of Malachite-chrysocolla mixtures.....	153
Figure 6.18 - NIR spectra of Biotite-calcite mixtures.....	154
Figure 6.19 - NIR spectra of Malachite-biotite mixtures.....	155
Figure 6.20 - NIR spectra of malachite-muscovite mixtures.....	156
Figure 6.21 - NIR spectra of Chrysocolla-hematite mixtures.....	158
Figure 6.22 - NIR spectra of Malachite- hematite mixtures.....	159
Figure 6.23 - NIR spectra of calcite-hematite mixtures.....	161
Figure 6.24 - NIR spectra of muscovite-hematite mixtures.....	163
Figure 6.25 - NIR spectra of kaolinite-hematite mixtures.....	164
Figure 6.26 - NIR spectra of chlorite-hematite mixtures.....	165
Figure 6.27 - NIR spectra of biotite-hematite mixtures.....	166
Figure 6.28 - NIR spectrum of Chrysocolla-hematite-muscovite mixture at ratio of 1:1:1 concentration by mass.....	168
Figure 6.29 - NIR spectrum of Hematite-chrysocolla-kaolinite mixture at ratio of 1:1:1 concentration by mass.....	169
Figure 6.30 - NIR spectrum of hematite-calcite-malachite-mixture at ratio of 1:1:1 concentration by mass.....	170
Figure 6.31 - NIR spectrum of muscovite-biotite-chlorite intimate mixture at ratio of 1:1:1 concentration by mass.....	171
Figure 6.32 - NIR spectrum of Hematite-malachite-kaolinite mixture at ratio of 1:1:1 concentration by mass.....	172
Figure 6.33 - NIR spectrum of Malachite-muscovite-hematite mixture at ratio of 1:1:1 concentration by mass.....	173
Figure 6.34 - NIR spectrum of Chlorite-biotite-calcite mixture at ratio of 1:1:1 concentration by mass.....	174
Figure 6.35 - NIR spectrum of calcite-muscovite-hematite mixture at ratio of 1:1:1 concentration by mass.....	175
Figure 6.36 - NIR spectrum of Chrysocolla-biotite-hematite mixture at ratio of 1:1:1 concentration by mass.....	176
Figure 6.37 - NIR spectrum of biotite-hematite-chlorite mixture at ratio of 1:1:1 concentration by mass.....	177

Figure 6.38 - NIR spectrum of biotite-muscovite-calcite mixture at ratio of 1:1:1 concentration by mass.....	178
Figure 6.39 - NIR spectrum of Kaolinite-calcite-hematite mixture at ratio of 1:1:1 concentration by mass.....	179
Figure 6.40 - NIR spectrum of Muscovite-hematite-kaolinite mixture at ratio of 1:1:1 concentration by mass.....	180
Figure 6.41 - NIR spectrum of Chlorite-biotite-calcite-hematite mixture at ratio of 1:1:1:1 concentration by mass.....	181
Figure 6.42 - NIR spectrum of chlorite-biotite-calcite-muscovite mixture at ratio of 1:1:1:1 concentration by mass.....	182
Figure 6.43 - NIR spectrum of kaolinite-calcite-muscovite-hematite intimate mixture at ratio of 1:1:1:1.....	183
Figure 6.44 - Near infrared spectra of hematite-biotite-muscovite-chlorite-calcite intimate mixture at equal ratio of 1:1:1:1:1.....	184
Figure 6.45 - Near infrared spectrum of calcite-malachite-hematite-kaolinite-muscovite-chrysocolla mixture at ratio of 1:1:1:1:1:1 concentration by mass..	185
Figure 6.46 - Framework for NIR sorting for copper ore, based on characteristics of individual spectrum (modified from Iyakwari et al., 2013)....	195
Figure 7.1 - Vertical alignment of powdered mixtures.....	197
Figure 7.2 - Vertical orientation of solid mixtures.....	197
Figure 7.3 - NIR spectra of linear mixtures of powdered calcite, muscovite and hematite.....	197
Figure 7.4 - NIR spectra of linear mixtures of hematite-chrysocolla.....	198
Figure 7.5 - NIR spectra of linear mixtures of Malachite-hematite.....	198
Figure 7.6 - Near infrared spectra of linear mixtures of calcite-malachite.....	199
Figure 7.7 - Horizontal orientation of mixture of solid minerals. (A) Normal and (B) Transposed.....	202
Figure 7.8 - NIR spectra of Chrysocolla and hematite horizontal mixture (A) chrysocolla-hematite and (B) hematite-chrysocolla.....	203
Figure 7.9 - NIR spectra of Malachite and hematite horizontal mixtures (A) malachite-hematite and (B) hematite-malachite.....	204
Figure 7.10 - NIR spectra of Chrysocolla and calcite horizontal mixture (A) calcite- chrysocolla and (B) chrysocolla-calcite.....	205

Figure 8.1 - Split B1 samples marked for directional scanning and spectra/mineral mapping.....	209
Figure 8.2 - Mantoverde copper samples preconcentration strategy, targeted at discriminating both calcite and muscovite (clay) bearing particles (modified from Iyakwari et al., 2013).....	220
Figure 8.3 - Mantoverde copper samples classification strategy targeted at eliminating only calcite-bearing samples as waste (modified from Iyakwari et al., 2013).....	241
Figure 9.1 - Correlation diagram between chrysocolla in whole sample and cross-section.....	261
Figure 9.2 - Correlation diagram between chlorite in whole sample and cross-section.....	262
Figure 9.3 - Correlation diagram between hematite in whole sample and cross-section.....	262
Figure 9.4 - Correlation diagram between muscovite in whole sample and cross-section.....	263
Figure 9.5 - Correlation diagram between calcite in whole sample and cross-section.....	263
Figure 9.6 - Correlation diagram between biotite in whole sample and cross-section.....	264
Figure 9.7 - Split B1 indicating cross-section.....	266
Figure 9.8 - NIR spectra of sample 3 (A) Whole sample and (B) Cross-section.....	267
Figure 9.9 - NIR spectra of sample 26 (A) Whole sample and (B) Cross-section.....	268
Figure 9.10 - NIR spectra of sample 56 (A) Whole sample and (B) Cross-section.....	269
Figure 9.11 - NIR spectra of Epofix (epoxy resin).....	271
Figure 10.1 Backscattered scanning electron micrographs of a typical association of PGM at the contact between BMS and silicates, and as satellite grains in close proximity to the BMS grain, enclosed within secondary amphiboles (source: Holwell and McDonald, 2007).....	273
Figure 10.2 - Proposed model for Mogalakwena platinum preconcentration, based on ore mineralogy targeted towards eliminating either or both carbonate and high hydroxyl bearing samples.....	284

Figure 10.3 - Model for classification of Mogalakwena platinum ore.....287



## List of Tables

Table 2.1 - The electromagnetic spectrum (Gaydon, 2011).....	32
Table 2.2 - Electrical conductivities of various minerals (Sivamohan and Forssberg, 1991).....	37
Table 2.3 - Absorption features in NIR of molecular bonds between 1300 and 2400 nm (after Iyakwari et al., 2013).....	41
Table 3.1 - Sample number allocation.....	46
Table 4.1- Modal mineralogy of the Mantoverde copper ore samples (mass %) measured by QEMSCAN®.....	56
Table 4.2 - Abundance of copper and iron (mass %) in samples.....	58
Table 4.3 - XRD results of the Mantoverde copper ore samples.....	63
Table 4.4 - NIR-active mineral association mapping of Mantoverde copper ore particles.....	70
Table 4.5 - Calculated modal composition (wt %) of carbonate and hydroxyl functional groups, copper and hematite minerals, with reference to webmineral.com.....	88
Table 4.6 - Classification of samples based on copper-carbonate concentration.....	91
Table 4.7 - Classification of samples based on Copper-Hydroxyl concentration.....	92
Table 4.8 - Classification of samples based on Copper-Hematite concentration.....	93
Table 4.9 - Classification of Mantoverde copper ore samples based on NIR functional groups.....	98
Table 4.10 - PXRF data for splits A1 samples Mantoverde copper ore, values in %.....	100
Table 4.11 - PXRF data for splits B1 samples Mantoverde copper ore, values in %.....	101
Table 4.12 - PXRF data for splits B2 samples Mantoverde copper ore, values in %.....	102
Table 5.1 - Absorption features of minerals (between 1300 nm and 2500 nm) in Mantoverde copper ore.....	109
Table 5.2 - Feature depth at two wavelengths for different size fractions of calcite.....	113

Table 5.3- Reflectance values for different size fractions of calcite.....	113
Table 5.4 - Feature depth at three wavelengths for different size fractions of muscovite.....	116
Table 5.5 - Reflectance values for different size fractions of muscovite.....	116
Table 5.6 - Feature depth at two wavelengths for different size fractions of malachite.....	119
Table 5.7 - Reflectance values for different size fractions of malachite.....	119
Table 5.8 - Feature depth at three wavelengths for different size fractions of chlorite.....	122
Table 5.9 - Reflectance values for different size fractions of chlorite.....	122
Table 5.10 - Description of various conditions of measurement.....	123
Table 6.1 - Features depth at five wavelengths for different ratios of muscovite and calcite.....	146
Table 6.2 - Summary of spectral dominance in intimate mixture of minerals..	190
Table 6.3 - Spectral dominance in intimate mixture of complex mineral associations.....	192
Table 8.1 - Individual particle spectrum and NIR-active mineral map for splits B1.....	210
Table 8.2 - Individual particle spectrum and mineral map for splits B2.....	212
Table 8.3 - Individual sample spectra and mineral map for splits A1.....	214
Table 8.4 - Classification of Mantoverde particles based on analysis of NIR spectra for splits B1, targeted at discriminating both calcite and muscovite as waste.....	221
Table 8.5 - Classification of Mantoverde particles based on analysis of NIR spectra for splits B2, targeted at discriminating both calcite and muscovite as waste.....	223
Table 8.6 - Classification of Mantoverde samples based on analysis of NIR spectra for splits A1, targeted at discriminating both calcite and muscovite as waste.....	225
Table 8.7 - Comparison of classification of splits B1 particles, strategy one...	229
Table 8.8 - Comparison of classification of splits B2 particles, strategy one...	231
Table 8.9 - Comparison of classification of splits A1 samples, strategy one...	233

Table 8.10 - Discrimination results of Mantoverde copper ore particles (splits B1), using copper content calculated from QEMSCAN® .....	234
Table 8.11 - Discrimination results of Mantoverde copper ore particles (splits B1) using copper content measured by PX.....	235
Table 8.12 - Discrimination results of Mantoverde copper ore particles (splits B1) using copper content measured on powdered samples by BPXRF.....	235
Table 8.13 - Discrimination results of Mantoverde copper ore particles (splits B2), copper content measured by PXRF.....	236
Table 8.14 - Discrimination results of Mantoverde copper ore samples (splits B2) using copper content measured on powdered samples by BPXRF.....	236
Table 8.15 - Discrimination results of Mantoverde copper ore samples (splits A1) using copper content measured on powdered samples by BPX.....	237
Table 8.16 - Comparison of splits A1, B1 and B2 NIR classifications.....	239
Table 8.17 - Classification of Mantoverde particles based on analysis of NIR spectra for splits B1. NIR strategy targeted at calcite elimination only as waste.....	242
Table 8.18 - Classification of Mantoverde particles based on analysis of NIR spectra for splits B2. NIR strategy targeted at calcite elimination only as waste.....	244
Table 8.19 - Classification of Mantoverde samples based on analysis of NIR spectra for splits A1. NIR strategy targeted at calcite elimination only as waste.....	246
Table 8.20 - Comparison of discrimination results of splits B1 for strategy one (NIR (1)) and strategy two (NIR (2)), Using copper content calculated from copper-bearing minerals by QEM.....	248
Table 8.21 - Comparison of discrimination results of splits B1 for strategy one (NIR (1)) and strategy two (NIR (2)), Using copper content measured by PX.....	248
Table 8.22 - Comparison of discrimination results of splits B1 for strategy one (NIR (1)) and strategy two (NIR (2)), Using copper content measured on powdered samples by BPXRF.....	248
Table 8.23 - Comparison of discrimination results of splits B2 for strategy one (NIR (1)) and strategy two (NIR (2)), Using copper content measured by PX.....	249

Table 8.24 - Comparison of discrimination results of splits B2 for strategy one (NIR (1)) and strategy two (NIR (2)), Using copper content measured on powdered samples by BPXRF.....	249
Table 8.25 - Comparison of discrimination results of splits A1 for strategy one (NIR (1)) and strategy two (NIR (2)), Using copper content measured on powdered samples by BPXRF.....	250
Table 9.1 - Samples investigated from original 30 mm polished sections (face), polished cross-section, QEMSCAN <sup>®</sup> Fieldscan images of NIR-active minerals and composite minerals.....	257
Table 9.2- Modal mineralogy of Mantoverde copper ore particles cross-sections (mass %) measured by QEMSCAN <sup>®</sup> .....	258
Table 9.3 - Modal mineralogy of the Mantoverde copper ore particles original 30 mm polished sections (mass %) measured by QEMSCAN <sup>®</sup> .....	258
Table 9.4 - NIR-active mineral association mapping of Mantoverde copper ore particles cross-sections.....	260
Table 9.5 - Calculated modal composition (wt %) of carbonate and hydroxyl functional groups, copper and hematite minerals, with reference to webmineral.com.....	265
Table 9.6 - Classification of samples based on copper-carbonate concentration.....	265
Table 9.7 - Classification of samples based on Copper-Hydroxyl concentration.....	265
Table 9.8 - Classification of samples based on Copper-Hematite concentration.....	265
Table 10.1 - Quantitative modal mineralogy of Mogalakwena platinum ore samples (mass %) .....	275
Table 10.2 - Minerals identified by qualitative XRD analysis of the Mogalakwena platinum ore samples.....	277
Table 10.3 - Calculated modal composition (wt. %) of hydroxyl and carbonate functional groups and orthopyroxene mineral.....	281
Table 10.4 - Classification of samples based on orthopyroxene-hydroxyl concentration.....	285
Table 10.5 - Classification of samples based on orthopyroxene-carbonate concentration.....	286
Table 10.6 - NIR classification of the Mogalakwena Platinum samples.....	288

Table 10.7 - Comparison of NIR and Mineralogy classifications.....291

## **List of accompanying material**

**Appendix 4.1** - XRD profiles of Mantoverde copper ore particles

**Appendix 5.1** – Iyakwari, S., Glass, H. J., 2014, 'Influence of mineral particle size and choice of suitable parameters for ore sorting using near infrared sensors'. *Miner Eng*, 69, 102-106.

**Appendix 5.2** – Iyakwari, S., Glass, H. J., Kowalczyk, P. B., 2013, 'Potential for near infrared sensor-based sorting of hydrothermally-formed minerals'. *J Near Infrared Spectrosc*, 21(3), 223-229.

**Appendix 8.1a** - NIR spectra of splits B1 samples

**Appendix 8.1b** - NIR spectra of splits B2 samples

**Appendix 8.1c** - NIR spectra of splits A1 samples

**Appendix 10.1a** - XRD profiles of Mogalakwena Platinum ore samples

**Appendix 10.1b** - NIR spectra of Mogalakwena Platinum samples

### Mineral names and chemical formulae

Chrysocolla –  $(\text{Cu,Al})_2\text{H}_2\text{Si}_2\text{O}_5(\text{OH})_4 \cdot n(\text{H}_2\text{O})$

Malachite –  $\text{Cu}_2(\text{CO}_3)(\text{OH})_2$

Cuprite –  $\text{Cu}_2\text{O}$

Muscovite –  $\text{KAl}_2(\text{Si}_3\text{Al})\text{O}_{10}(\text{OH},\text{F})_2$

Kaolinite –  $\text{Al}_2\text{Si}_2\text{O}_5(\text{OH})_4$

Biotite –  $\text{K}(\text{Mg},\text{Fe}^{3+})_3[\text{AlSi}_3\text{O}_{10}(\text{OH},\text{F})_2]$

Chlorite (clinochore) –  $(\text{Mg},\text{Fe}^{2+})_5\text{Al}(\text{AlSi}_3\text{O}_{10})(\text{OH})_8$

Tourmaline (schorl) –  $\text{NaFe}^{2+}_3\text{Al}_6(\text{BO}_3)_3\text{Si}_6\text{O}_{18}(\text{OH})_4$

Quartz –  $\text{SiO}_2$

K-feldspars –  $\text{KAlSi}_3\text{O}_8$

Plagioclase feldspars –  $(\text{Na,Ca})(\text{Si,Al})_4\text{O}_8$

Hematite –  $\text{Fe}_2\text{O}_3$

Calcite –  $\text{CaCO}_3$

Ankerite –  $\text{Ca}(\text{Fe}^{3+},\text{Mg},\text{Mn})(\text{CO}_3)_2$

Apatite –  $\text{Ca}_5(\text{PO}_4)_3(\text{OH},\text{F},\text{Cl})$

Enstatite –  $\text{Mg}_2\text{Si}_2\text{O}_6$

Augite –  $(\text{Ca,Na})(\text{Mg,Fe,Al,Ti})(\text{Si,Al})_2\text{O}_6$

Labradorite –  $(\text{Ca,Na})(\text{Si,Al})_4\text{O}_8$

Albite –  $\text{NaAlSi}_3\text{O}_8$

Phlogopite –  $\text{KMg}_3(\text{Si}_3\text{Al})\text{O}_{10}(\text{F},\text{OH})_2$

Antigorite –  $(\text{Mg},\text{Fe}^{2+})_3\text{Si}_2\text{O}_5(\text{OH})_4$

Hornblende –  $\text{Ca}_2[\text{Fe}^{2+}_4(\text{Al},\text{Fe}^{3+})]\text{Si}_7\text{AlO}_{22}(\text{OH})_2$

Talc –  $\text{Mg}_3\text{Si}_4\text{O}_{10}(\text{OH})_2$

Chalcopyrite –  $\text{CuFeS}_2$

Andradite –  $\text{Ca}_3\text{Fe}^{3+}_2(\text{SiO}_4)_3$

Brucite –  $\text{Mg}(\text{OH})_2$

Grossular –  $\text{Ca}_3\text{Al}_2(\text{SiO}_4)_3$

## **Chapter 1: Introduction**

### **1.1. Introduction**

Staying ahead of the competition and maintaining profitability is a key challenge in the extractive industry especially during fluctuating economic conditions. It is important to develop novel techniques for mineral processing which can provide enhanced recovery from a low-grade ore, reduce the energy consumption and mitigate environmental impact. A process which shows promise to meet some of these requirements is sensor-based sorting (Iyakwari et al., 2013; Dalm et al., 2014). Sensor-based sorters detect, evaluate and separate every single particle individually. Sensor-based sorting is a technology recognised to hold great potential for increasing productivity in the minerals industry (Cutmore and Eberhardt, 2002).

The objective of application is to separate large chunks of barren ore at an early stage of the processing, reducing the grinding requirements and using a dry process, reducing the requirements for water (treatment) and saving energy. A sensor based technique which shows promise in such application is the Near InfraRed (NIR) spectroscopy (Iyakwari et al., 2013). The NIR region of electromagnetics covers the wavelength range adjacent to the mid infrared and extends up to the visible range. The American Society of Testing and Materials (ASTM) define the electromagnetic near infrared region in the range of 750-2500 nm (Clark and Roush, 1984).

NIR sensor data can be interpreted to distinguish ore from waste particles. The data are measured on small sections or "pixels" of each particle: it contains information on the functional groups present and generates a "fingerprint" for each pixel. These fingerprints are related to the mineralogical composition and are used for subsequent classification and discrimination.

### **1.2. Aim of research**

The aim of this project was to investigate the potential and suitability of application of Near InfraRed (NIR) spectroscopy in preconcentration of complex ores. Two ore types (copper ores from Mantoverde mines in Chile and platinum ore from the Mogalakwena mines in South Africa) were considered for research. Both involved the identification and discrimination of the ore-bearing minerals from associated carbonate and hydroxyl waste minerals. The first part involves



the copper ore bearing minerals chrysocolla and malachite, while the second aspect involved platinum associated minerals (enstatite, chalcopyrite and hornblende). These ores were selected for study based on their availability to the author and also because they were deemed appropriate for research (they contained the NIR-active functional groups).

The overall effect of this research will lead to the upgrading of ores, by improving metal recovery and reducing overall processing cost. Information obtained from near infrared will provide accurate determination of chemical input levels resulting in a higher volume of quality yield while reducing processing time and lowering energy use. Research thus targets the removal of the gangue minerals at early stage. The preconcentration application of the MantoVerde ore was done with acid leaching being the next/final stage of copper extraction.

The project began with spectral and mineralogical analysis of the materials. Mineral processing is always considered in the context of the mineralogy of the ore (Wills and Napier Munn, 2006). Therefore, good knowledge of the mineralogical assemblage of an ore is essential, if efficient processing is to be carried out. For the copper ore, an automated method of quantitative mineral analysis was carried out using QEMSCAN<sup>®</sup>, (the quantitative evaluation of minerals using the scanning electron microscope). X-Ray Diffraction (XRD) analysis was also carried out as a complementary test to the QEMSCAN<sup>®</sup> and results of both analysis compared. X-Ray Fluorescence (XRF) analysis was done to determine the copper concentration in the individual samples. For the platinum ore, samples were accompanied by quantitative XRD data. As a test, qualitative analysis was also carried out by the author. Once an understanding of the nature of material, had been developed, the project moved on to investigate means of discriminating between ore and gangue materials by developing means and strategies that could be used in an automated sorting application.

### **1.3. Thesis structure**

This thesis is divided into eleven chapters and a number of appendices. Chapter two is a review of the literature relating to sensor-based sorting and the NIR region of the electromagnetic spectrum. The initial discussion focuses on the principles of automatic sorting and the sensors that have been used to

separate different materials. The review then moves on to focus on the NIR portion of the electromagnetic spectrum. The origin and causes of absorption features in the NIR region of the electromagnetic spectrum are explained with their applications. Chapter three discusses the origin of the ores, and the various characterization methods employed. While mention of equipment used for mineralogical and chemical analysis is made, more emphasis is laid on the NIR scanner used for data collection.

Chapter four discusses the mineralogy and chemistry of the copper ore used in research. Compositional analysis was carried out on the samples and the results are discussed with respect to implications to NIR preconcentration and economics. This is followed by developing a strategy for classification on the basis of individual sample mineralogy and chemistry. Equipment used in mineralogical and chemical data collection and procedure are also discussed.

Chapter five discusses the individual minerals as analysed by mineralogical methods, classifying them as either NIR-active or non-active. The NIR-active minerals are further classified as absorption feature(s) displaying or non-absorption feature displaying NIR-active minerals. Also considered are factors influencing NIR spectra like particle grain size and moisture. These aspects are considered in order to inform the choice of parameters for selection in identifying individual minerals and developing a method for ore preconcentration.

Chapter six is an extensive study of NIR-active minerals. The chapter is aimed at predicting individual NIR-active minerals influence over one another, when they occur and are scanned along the same NIR spectrum range. Various intimate mineral associations are artificially prepared to stimulate natural ore. Hence, the chapter uses intimate mixtures of minerals with the sole aim of quantitatively and qualitatively defining and or classifying a NIR spectrum by its absorption features, and developing a copper discrimination strategy from associated waste.

Chapter seven is a follow up to chapter six, but unlike chapter six, the individual minerals analysed are optically separated, and arranged to stimulate adjacent natural mineral associations. Hence, the chapter shows single minerals

arranged with the aim of determining spectral dominance and qualitatively defining a spectrum.

Chapter eight discusses the practical application of NIR on the Mantoverde copper ore. Mantoverde samples were classified based on their individual NIR spectrum absorption characteristics, and the possible NIR-active mineral(s) responsible for absorption features based on correlation with mineral data. Two strategies are modified from chapter six and applied for ore preconcentration. The first strategy considers discriminating both muscovite and calcite as waste, while the second strategy targets calcite only for elimination as waste. This is achieved by classifying each sample based on the dominant spectrum group: as product, waste or middling. The chapter is concluded by analysing and comparing both strategies based on calculated ore parameters using quantitative data obtained from XRF and QEMSCAN<sup>®</sup>.

Chapter nine is written to validate the quality of QEMSCAN<sup>®</sup> and NIR data. Also considered in chapter nine is the influence of epoxy resin used for preparing QEMSCAN<sup>®</sup> blocks on the NIR spectra of samples.

Chapter ten explores the possible application of NIR on platinum deposits from the Mogalakwena mine. The chapter is concluded by recommending further analysis to evaluate quantitatively the discrimination strategy proposed.

Chapter eleven summarises the work and presents conclusions, key findings and recommendations for further investigation. A list of references follows. Soft copies of appendices are provided.

## **Chapter 2: Background**

### **2.1. Introduction**

This chapter is an overview of the current knowledge relevant to the research contained within this thesis. The chapter contains three sections: sensor-based sorting, sensors and the near infrared (NIR) region of the electromagnetic spectrum.

The principles of sensor-based sorting, sensors as well as applications are identified and discussed. The origin and causes of absorption features in the NIR region of the electromagnetic spectrum are explained with their applications.

### **2.2. Sensor-based sorting**

Sorting is a selective classification and separation method of a material mixture into two or more products based on different characteristics (Mutz et al., 2003; De Jong and Harbeck, 2005). Sorting has played a major role in mineral processing operations for thousands of years and initially was carried out by hand (De Jong and Harbeck, 2005; Wills and Napier Munn, 2006). In the past, manual sorting or handpicking was considered “a very efficient concentration method” (Salter and Wyatt, 1991; Arvidson, 2002). However, with advancement in technology, mineral processing developed and as ore grades and liberation sizes decreased, hand sorting became impractical and or uneconomic and its application in recent times has been fairly limited (Wills, 1997; Gaydon, 2011).

Sensor based sorting represents all applications where singular particles are individually analysed and mechanically separated based on certain physical properties determined by a sensor (Dalm et al., 2014). However, sensor based sorting is a more recent development. Automated sorters have been used in the food and agriculture industries since the 1930s (Gaydon, 2011). Within the mining industry however, sensor based sorting is still an emerging technology with only a limited number of proven applications (Dalm et al., 2014). It was not until 1946 that the first automated rock sorting machine was developed: “Lapointe picker” (Salter and Wyatt, 1991). Over the last two decades there has been a surge in interest in the use of automated sorting in the minerals industry. According to Iyakwari et al. (2013), sensor-based sorting has the potential to perform dry separation of ore minerals from associated gangue at an early

stage of processing, on relatively coarse particles. The ability of dry processing of coarse ores makes automated sorting an attractive choice in the mining environment especially where water is in short supply. The prospect of cost and energy/water consumption reduction due to downstream crushing encourages the incorporation of a preconcentration step in ore processing operations (Iyakwari et al., 2013; Dalm et al., 2014; Bowman and Bearman, 2014). Cutmore et al. (1998) outlined five advantages of ore sorting to include:

- Reduced capital investment due to the reduction in the tonnage to be processed
- Minimization of waste, leading to reduced environmental harm
- Opportunity to recover previously uneconomic resources at existing mines
- Tailoring products to customers specification, opening up new market for resources
- Maintaining the viability of existing resources through improved recovery.

Arvidson, (2002) and Curtiss, (2012) summed up the benefits of incorporating a preconcentration (sorting) step in mineral processing as “cost saving”. However, just as with any other mineral processing method, sensor based sorting has its own drawbacks. Some of the drawbacks as outlined by Sivamohan and Forssberg (1991) include:

- Cost of preconcentration- whether it be the cost of sizing the feed for the concentrator or the cost of washing and/or drying the feed
- Loss of valuable minerals to waste
- The non-applicability of ores where valuable elements are highly disseminated

Therefore, since preconcentration is to save cost at the same time as improving recovery (Curtiss, 2012), before choosing an application, a rigorous feasibility study should identify if the cost is offset by the potential benefits of an automated sorting set. An important consideration will be the identification of a suitable sensor and appropriate interpretation of the sensor data (Iyakwari et al., 2013).

### 2.2.1. Automated sorters

An automated sorter examines individual particles, compares the measured properties of each particle with a predefined criterion and then classifies and separates the particles using an externally applied force, into different products according to their properties (Salter and Wyatt, 1991). Salter and Wyatt, (1991) and Arvidson, (2002) broke down the stages of an automated sorter into four distinct interactive processes or components to include:

- a. particle presentation (through conveyor belts)
- b. particle examination (by camera or other sensors)
- c. data analysis (by computers linked to the system) and
- d. particle separation (through use of blow bars)

Figure 2.1 presents the principle of an automated sorter with on-belt geometry for conductive and X-ray sensors after De Jong, (2005).

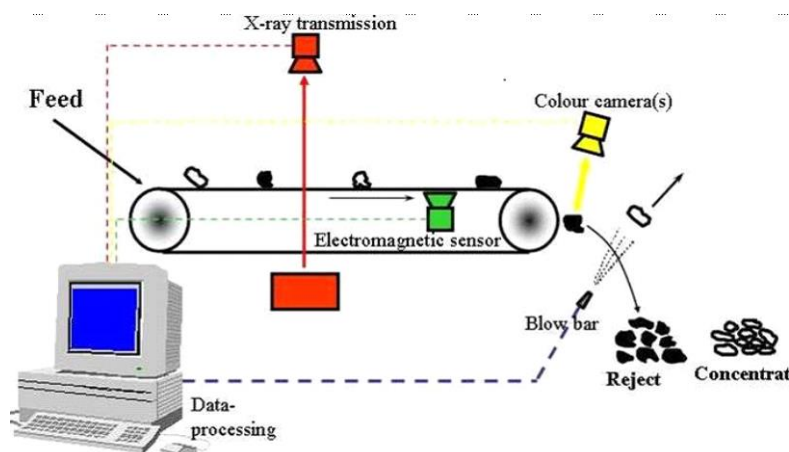


Figure 2.1 - Automatic sorter configuration (after De Jong, 2005)

#### 2.2.1.1. Particle presentation

Feed preparation may consist of a number of steps, such as sizing, washing, controlling the feed rate, particle alignment, wetting, acceleration and stabilisation. All of this will occur before particles pass by the sensor or sensors (Arvidson, 2002).

Vibratory feeders are often used to feed particles on to the belt. A chute may also be used to direct particles onto the belt. For an effective sort, particles fed onto a belt must form a monolayer such that they are observed and scanned

individually. For an accurate sort, it is critical that particles have 'settled' on the belt by the time they reach the sensor area. Any movement (lateral or horizontal relative to the belt) would make it difficult to predict the position of the particle at the point of physical separation and the time elapsed between leaving the sensor area and entering the separation area. This increases the likelihood of misclassification.

#### **2.2.1.2. Particle examination**

For a particle to be sorted, the particle must be examined by some kind of sensors system. The conveyor belt carries the particle through the sensor where data is generated. Data generated by these sensors (which may be cameras) is user defined and may include colour, and metal content among others. Sensor types are discussed in section 2.3.

#### **2.2.1.3. Data analysis**

Once data has been collected from individual particles as a result of sample interaction with the sensors, it must be analysed and the particles classified based on series of instructions defined by the operator. These rules/instructions are arranged so as to emphasis the differences between the product and waste fractions and may be based on characteristics such as colour, shape, texture, size, metal content or chemical composition of the feed.

#### **2.2.1.4. Separation**

Once a particle has been analysed and classified, a means of physical separation is required to divide particles of opposing classes (i.e. product and waste). Typically, one class is allowed to carry on its natural trajectory whereas the other class is redirected. Three methods have been successfully employed to this end: mechanical system, air jets and water jets (Arvidson, 2002).

- a. A mechanical system uses pistons and plungers to separate particles. The main limitation of the mechanical system is speed and system wear.
- b. Water jets are also used to divert particles from their natural trajectories. The limitation of this system is the availability and volume of water consumed, which may offset the economic benefit of system installation.
- c. Air jets are the common systems used for separation in automatic sorting. Here, valves fire a short burst of air at the rejected particle to deflect it from its natural trajectory. The valves respond quickly to

instructions from the system processor. The consumption of compressed air is the major cost of this system of separation. According to Arvidson (2002), the average cost of air used could cost \$0.5 to \$1 per ton of feed.

### 2.3. Sensors

Particles examination or sensing can be undertaken using a number of different sensors depending on the ore mineralogy and the aspect of the ore deemed characteristic for analysis (von Ketelhodt, 2009). The different sensors can be categorised into two, as electromagnetic radiation based and non-electromagnetic radiation based sensors (Gaydon, 2011).

#### 2.3.1. Electromagnetic radiation-based sensors

Many of the automatic sorters available utilize a portion of the electromagnetic spectrum to differentiate between materials. Table 2.1 present a breakdown of the regions of electromagnetic spectrum.

Table 2.1 - The electromagnetic spectrum (Gaydon, 2011)

Region	Wavelength (nm)	Frequency (Hz)
Gamma rays	< 0.01	$>3 \times 10^{19}$
X-Rays	0.01 to 10	$3 \times 10^{17}$ to $3 \times 10^{19}$
Ultraviolet	10 to 400	$7.5 \times 10^{14}$ to $3 \times 10^{17}$
Visible	400 to 700	$4.3 \times 10^{14}$ to $7.5 \times 10^{14}$
Infrared	750 to $1 \times 10^6$	$3 \times 10^{12}$ to $4.3 \times 10^{14}$
Microwave	$1 \times 10^6$ to $1 \times 10^8$	$3 \times 10^9$ to $3 \times 10^{12}$
Radio	$> 1 \times 10^8$	$< 3 \times 10^9$

##### 2.3.1.1. Gamma rays

This method of sorting is also referred to as radiometric sorting. Gamma ( $\gamma$ ) rays are the result of atomic nuclei decaying and, at certain energies, releasing neutrons. Certain minerals emit a characteristic radiation that can be used to distinguish between different minerals.



Lunt et al. (2007) used the radiometric sorting to upgrade uranium ores. At one of the mines recoveries of 90 % were achieved, with mass reduced to 40 % of the total feed.

### **2.3.1.2. X-rays**

X-ray radiation generally occurs between 0.01 and 10 nm in the electromagnetic spectrum and is produced by the transition of high-energy inner shell electrons (Table 2.1). For all but the lightest elements, the transitions available are dependent on the atomic number of a material and not on its composition (as the inner electrons do not play any role in chemical bonding). It is a non-destructive technique.

X-ray radiation can be used in a number of ways to distinguish materials. These include measuring the density (the average atomic number) of a material and to induce fluorescence in a material. The depth of penetration of X-rays into a material is dependent on the density of the material and energy used.

Hence, certain minerals can be detected by measuring their X-ray transparency or transmission. Sivamohan and Forssberg (1991) stated that to distinguish between two materials, they must have a different value of  $\mu t$ , where  $\mu$  is the absorption coefficient of the material with-respect to X-rays and  $t$  is the material thickness.

Fleischer and Bergmann (2004) found that when attempting to discriminate between organic and inorganic waste using X-ray transmission, the varying thicknesses of the materials caused some material to be misidentified. To solve this, a particle sizing step was necessary, so that only material of a similar thickness was analysed. This has been achieved using an X-ray sensor in conjunction with an optical sensor to measure particle size and transmission concurrently.

Dual Energy X-Ray Transmission (DE-XRT) uses two beams to measure the average atomic number and the thickness of an object. It is effective as it has the ability to monitor streams which vary in size as the detection is thickness independent. Mesina et al. (2007) used a DE-XRT sensor to sort scrap metal and found that when used in isolation the sensor could separate light and non-

ferrous metals with good accuracy. When used with an electromagnetic sensor, a much broader range of metals and alloys could be separated.

Another method of sorting materials is to utilise the characteristic fluorescence of certain minerals when exposed to X-ray radiation. This X-ray luminescence can be used to sort materials. In the diamond industry, for example, most diamonds will fluoresce on exposure to X-rays and can be detected by a photomultiplier (Wills, 1997). In many operations this method of sorting is used as an alternative to grease tabling or prior to grease tabling to reduce throughput required on the table. Care must be taken however, as some diamonds do not readily fluoresce and may be missed by an X-ray system.

#### **2.3.1.3. Ultra-Violet**

The Ultra-Violet (UV) region of the electromagnetic spectrum ranges from 10 to 400 nm (Table 2.1). Many minerals, such as fluorite, calcite, quartz and beryl (Sivamohan and Forssberg, 1991) fluoresce under UV lights, making it possible for these to be distinguished from other non-fluorescing minerals.

#### **2.3.1.4. Visible/optical sensors**

The visible region of the electromagnetic spectrum ranges from 400 to 700 nm (Table 2.1). Wavelengths in this range are visible to the human eye and sensors that utilise this region use colour and visible appearance (such as size, shape and texture) to distinguish particles.

There are two types of light source used in optical sorting: continuous (i.e. tungsten bulbs) or discontinuous (i.e. fluorescent tubes or lasers). Two common detectors used are Charged Coupled Devices (CCDs) and photomultipliers (Wills, 1997). CCDs are capable of analysing colours whereas photomultipliers can only measure the amount of light received, hence values are on a monochromatic (grey) scale.

Optical sensors are the most common sensor used in automatic sorting and have been used to classify ferromanganese ores (Singh and Rao, 2005), to improve the product quality of impure marble (Varela et al., 2006), to monitor a nickel-ore with-respect-to its grindability (Tessier et al., 2007), to upgrade lithium minerals (Brandt and Haus, 2010), and to estimate limestone grades (Chatterjee et al., 2010).

### **2.3.1.5. Infrared**

Infrared radiation has a wavelength between 750 nm and  $10^5$  nm (Table 2.1). When a mineral is irradiated by radiation within the infrared range, the mineral produces a characteristic spectrum that yields information concerning its interatomic bonding. The absorption or reflection of infrared radiation by the mineral gives rise to changes in the vibrational energy of the constituent molecules: these changes are specific and can be used to identify the material constituent (Jones, 1987). These changes which are signatures indicating a specific material (mineral) are described as peaks, bands or absorptions features. Infrared is notable for its measurement speed and its ability to discriminate between minerals, as in no case do two minerals show completely identical absorption spectra (Povarennykh, 1978).

This region of the electromagnetic spectrum can be further broken down into a number of regions. The near-infrared ranges from 750 to 2500 nm, the mid-infrared from 2500 nm to  $2.5 \times 10^4$  nm and the far-infrared from  $2.5 \times 10^4$  nm to  $10^5$  nm (Stuart, 2004). Spectra in these regions arise from vibrational and electronic transitions. Spectra measure the variation in the reflectance of a material over a range of wavelengths.

The near-infrared region (750 to 2500 nm) being the region of interest in current research is further discussed extensively in section 2.4.

### **2.3.1.6. Microwave**

Microwaves have wavelengths between 0.01 cm and 10 cm (Table 2.1) and are used to sort rock particles by heating them and measuring their thermal conductivities (Gaydon, 2011). Different materials have different thermal conductivities which makes separation possible. An application of this method was the separation of high value kimberlite from the waste material, gabbro (Nordin and Salter, 1990).

## **2.3.2. Non-electromagnetic sensors**

### **2.3.2.1. Magnetic**

Magnetism can be used in a number of ways to sort material. The simplest separation is the use of a magnet to separate magnetic and non-magnetic material. In this method, the magnetic material adheres to the magnet, which

then deposits it in a processing stream separate from the non-magnetic material. Magnetic separation of this nature is common in iron ore processing. Topkaya et al. (2004) used magnetic separators to remove magnetic material from steel slag. A more uncommon application was reported by Varela et al. (2006), who used it to improve the product quality of marble. Augusto et al. (2002) published a review of magnetic separation, with a focus on magnetic classification, in which, not only are magnetic particles separated from non-magnetic particles, the magnetic particles are further classified based on their magnetic susceptibility.

Magnetic resonance is a quantitative method that can be used to sort/monitor material and is particularly amenable to copper and other transition metal minerals (Bennett et al., 2009). The measurement of magnetic resonance is a form of radio spectroscopy and there are forms where an external static magnetic field is not required. Antiferromagnetic nuclear magnetic resonance arises due to internal magnetic fields in particles and is related to the magnetic ordering imposed by the mineral crystal structure. Bennett et al. (2009) discussed the advantages of this method, in that: results are not influenced by sampling or surface bias (the surface conditions only effect a small proportion of the total particle measured), the method is moisture resistant and if focused on a particular mineral, the resonances are rarely subject to interference from other mineral resonances. This method has been used to measure chalcopyrite levels in particles of a copper ore (Bennett et al., 2009).

#### **2.3.2.2. Conductive**

Every mineral has a specific conductivity value which if measured, may be utilised to sort ores/minerals. Table 2.2 is a list of a number of minerals and their conductivities. Two methods are commonly used for measuring mineral conductivity: the beat frequency method and the induction balance method (Sivamohan and Forssberg, 1991).

The beat frequency uses a detector which is energised with a high frequency alternating current. As particles containing conductive material pass through the sensors, variation in frequency is detected and recorded. The disadvantage of the method is that particles with grain size below 0.6 mm are not easily detected (Sivamohan and Forssberg, 1991).

Table 2.2 - Electrical conductivities of various minerals (Sivamohan and Forssberg, 1991)

Minerals	Electrical conductivity (ohm-m)	
Quartz	$3.8 \times 10^{10}$ to $1.2 \times 10^{12}$	Insulators
Calcite	$5.5 \times 10^{12}$	
Amphiboles	$10^7$	
Mica	$1.5 \times 10^8$ to $9 \times 10^{12}$	
Diamond	$10^{12}$	
Wolframite	$10^2$ to $10^5$	Semiconductors
Siderite	70	
Hematite	$4 \times 10^4$ to $10^7$	
Sphalerite	$10^5$	
Pyrite	$10^{-2}$	Conductors
Chalcopyrite	$1.2 \times 10^{-3}$	
Galena	$10^{-3}$	
Magnetic iron Pyrite	$7 \times 10^{-2}$	
Arsenopyrite	$2 \times 10^{-1}$	
Magnetite	$6 \times 10^{-3}$	

Induction balance uses two planar coils, one for excitation and the other for detection. They are positioned at right angles to one another and adjusted so that a null is produced in the detection coil. When a conductive material (or a magnetic material) passes through, a voltage increase is detected by the detector coil. Particle grain size effect as observed by beat frequency detectors is overcome to some extent by the induction balance. It also responds to other electrically conductive or magnetic minerals such as magnetite, hematite, galena and Cu sulphides (Sivamohan and Forssberg, 1991)

#### 2.4. The near infrared region of electromagnetic

This thesis is focused on developing strategies for the application of Near Infrared (NIR) for sorting of minerals and ore. Therefore, subsequent sections shall provide details on the origin of absorption features in the NIR and application of the NIR.

The NIR region of electromagnetic spectrum extending from approximately 750 nm to 2500 nm contains absorption bands corresponding to C-H, O-H, S-H, and

N-H vibrations (Bokobza, 1998; Pasquini, 2003; Li et al., 2008). The advantages of NIR include: speed (ability to analyse rapidly), simplicity of sample preparation, and its non-destructive, non-invasive nature, among others. Its weak sensitivity to minor constituent is its greatest disadvantage (Bokobza, 1998). According to Hunt (1977) NIR spectra are wavelength-intensity records of interaction of ElectroMagnetic (EM) radiation with matter. For solids particles, a spectrum consists of reflected, transmitted, emitted and elastically and in-elastically scattered components.

#### **2.4.1. Causes of absorption in the NIR region**

Information available in the NIR range results from absorption due to electronic processes involving relatively few constitutional or substitutional ions, and vibrational processes (Hunt, 1977, Clark et al., 1990, Clark, 1995).

##### **2.4.1.1. Electronic processes**

Isolated atoms and ions have discrete electron energy states. Absorption of photons of a specific wavelength causes a change from one energy state to a higher one. When a change to a lower energy state occurs, a photon of a specific wavelength is emitted. The photon emitted when the atom/ion returns to a lower energy state is not usually emitted at the same wavelength as the photon absorbed (Clark, 1995). Four different processes that involve a change in energy of an atom or ion include: charge transfer, crystal-field effects, colour centres and conduction band transitions. These processes are briefly discussed.

Charge transfer processes occur when the absorption of a photon causes an electron to move between two ions (including ions of the same metal in different valence states) or between an ion and ligand. Bands centres usually occur in the UV region of the spectrum with the absorption extending into the visible region and are diagnostic of mineralogy. Colour centres are exhibited in a few materials that show colour as a result of irradiation of an imperfect crystal. The defects have their own energy levels that may correspond to the energy of visible light, into which, excited electrons can fall and become bound to the defect.

Crystal field effects involve the interaction of the outermost electrons of an atom or ion with ligands in a crystal structure. In solids, electrons can be shared between atoms. As a result, the electron energy levels are spread over a range of values – the ‘energy bands’ of the solid. In transition elements, the outermost electrons determine the energy levels. When in a crystal structure, the electron levels are split. The values of these energy levels are determined by the valence state of the atom, the coordination number and the symmetry of the site. As the outermost electrons are not shielded by other electrons, the energy levels are also influenced by the electrostatic fields of the ligands surrounding the ion. The energy levels are affected by the type of ligands, the extent of the distortion of the site by the ligands and the value of metal-ligand interatomic distance. These factors lead to different arrangements of energy levels. As a result, metals in different minerals (i.e. different crystal structures) will have different spectra and can be used to identify minerals. In the case of rare earth ions, however, this is not the case. The unfilled electron shells of rare earth ions involve well-shielded, deep-lying electrons, far removed from the crystal field effects. Absorption bands of rare earth metals are not diagnostic of mineralogy.

In some minerals, there are two energy bands in which electrons are located. The higher band is the conduction band where electrons move freely through the crystal lattice. The lower band is the valence band where electrons are attached to individual atoms. The difference between these two energy levels is the band gap and conduction band transfers occur when an electron moves between these two levels. In semiconductors, the energy of the band gap corresponds to the energy of the visible or near-infrared portion of the electromagnetic spectrum. The resulting spectra of these transitions consist of a step function.

#### **2.4.1.2. Vibrational processes**

Vibrational processes involve the rapid movement of chemically-bonded atoms or group of atoms and their displacement in relation to one another (Gaydon, 2011). The apparently random motion of any vibrating system is made up of a restricted number of simple motions which are also called normal modes or fundamental (Hunt, 1977). For a system of N particles there are  $3N - 6$  normal modes, thus the number and form of normal vibrations and the values of permitted energy levels for any material are determined by the number and type

of its constituent atoms, their spatial geometry and the magnitude of the binding forces between them (Hunt, 1977). The frequency of displacement between bonded atoms is determined by the strength of the bond and the mass of the atoms involved (Clark, 1995). Each vibration can also occur at roughly multiples of the original fundamental frequency. The additional vibrations are called “overtones” when involving multiple of a single fundamental, and “combination” when involving different types of vibrations (Clark, 1995).

The vibrational transitions are significant identification criteria because of bigger influence on the spectra in comparison to electronic transitions processes. The bands which occur to longer wavelengths from 1300 to 2500 nm are from vibrational origin and are overtone or combination tones of either water or carbonate ions (Hunt and Salisbury, 1971). Therefore, particles show more diagnostic absorption features in the region between 1300 and 2500 nm, due to overtone and combination, providing a wealth of information (Clark, 1995).

Due to their diagnostic importance, and significance to this study, these groups are briefly discussed below.

Water (H<sub>2</sub>O) may be trapped in fluid inclusions or embedded in the matrix of minerals (Aines and Rossman, 1984). Whenever water is present, absorption bands are observed around 1400 and 1900 nm (Hunt, 1977). In addition, depending on the mineral type, another feature may be present near 1840 nm (Iyakwari and Glass, 2014). The presence of water in spectra of a mineral may also reduce the overall reflectance of a sample in the NIR region (Gaydon et al., 2009). However, when a hydroxyl group (-OH) is present in the absence of water, the absorption band around 1900 nm vanishes and only the absorption band around 1400 nm remains (Hunt, 1977). In addition, the NIR spectrum of a hydroxyl group contains an absorption band between 2200 and 2350 nm. The exact location of this feature depends on the type of ion the hydroxyl group is attached to and where it is located in the material, hence, diagnostic of mineralogy (Clark, 1995; Hunt, 1977). The location of the more intense features appears to depend upon whether aluminium, magnesium, iron and silicon are present.

Carbonate (CO<sub>3</sub><sup>2-</sup>) has distinct absorption bands around 2100 and 2525 nm. Carbonate-bearing minerals do not normally contain water, so that carbonate



and water absorption features are not observed in the same spectrum. When water features are observed in spectra of carbonate-bearing minerals, this is indicative of impurities (Van der Meer, 1995). Van der Meer, (1995) also noted that the reflectance in NIR spectra of calcite is reduced by the presence of iron and iron-bearing minerals.

The principal absorption bands of these groups are summarised in Table 2.3.

Table 2.3 - Absorption features in NIR of molecular bonds between 1300 and 2400 nm (after Iyakwari et al., 2013).

Molecular bond	Absorption features in NIR (nm)	Source
Water (H <sub>2</sub> O)	1400, 1840, 1900	Aines and Rossman, (1984); Hunt and Salisbury, (1970); Iyakwari and Glass (2014)
Hydroxyl (-OH, overtone)	1400, 1500	Clark et al., (1995); Hunt and Salisbury, (1970)
Combination of metal-OH		
Al-OH	2160-2220	Hunt, (1977); Goetz et al., (2009)
Mg-OH	2300-2360	Hunt, (1977); Goetz et al., (2009)
Fe-OH	2230-2295	Clark, (1995); Hunt, (1977)
Si-OH	2240	Hunt, (1977);
Carbonate (CO <sub>3</sub> <sup>2-</sup> )	2300, 2340, 2360, 1870, 1990, 2155	Hunt and Salisbury, (1971)

Bands due to vibrational processes can be distinguished from those having an electronic origin on the basis of resolution. The vibrational features are much sharper because typically vibrational features occur as multiples whereas electronic features are broad single or double bands (Hunt, 1979).

The NIR sensor used for present research measures NIR reflectance in the wavelength range between 1300 and 2400 nm, hence features observed in range are due to vibrational processes (Hunt and Salisbury, 1971).

#### 2.4.2. Applications of NIR

NIR has been applied with success in recycling, remote sensing for geology, food, agriculture, pharmaceutical, medical, chemical, polymer and petroleum industries (Bokobza, 1998). In the above industries, applications include but are

not limited to: measurement of quality control of pharmaceutical products (Ciurczak, 1987; Lyon et al., 2002). Studying hemodynamic changes during activation of brain function in human adults (Villringer et al., 1993). Determination of quality of oranges by measuring the sugar, acidity, size, shape, colour and defects (Saranwong et al., 2005). The estimation of octane number in gasoline samples, the characterisation of polymers properties such as configurations, conformation, crystallinity, orientation, miscibility or the description of the kinetic and mechanism of cure reactions in different epoxy-amine system (Bokobza, 1998; Li et al., 2008).

Due to their similarities and significance to present study, only applications in recycling and remote sensing are further discussed

#### **2.4.2.1. Recycling industry**

NIR sensors are widely used in the recycling industry. This is due, in part, to the nature of the material processed. Materials, such as plastics, are highly ordered and as a result, absorption features in the NIR are intense and sharp. This means small differences between the chemistries of different plastics can be detected and utilised to separate them (Gaydon, 2011).

Leitner et al. (2003) reported the use of NIR spectral imaging to separate polymers. The method used a dissimilarity-based classifier to distinguish plastic containers and a 93 % success rate was achieved. Of particular interest was its ability to identify paper labels on some of the containers and to remove the relevant data from the classification results. Tachwali et al. (2007) developed a method that could separate plastic bottles of different chemistries and beyond that, of different colours. A NIR sensor was used for the chemistry identification and a second sensor, an optical camera was used to separate the bottles based on their colours. The overall accuracy of this method was 83.48 %.

Beyond plastics, NIR sensors have also been used to separate glass from glass ceramic fragments. Serranti et al. (2006) and later Farcomeni (2008) investigated the potential of and developed methods using the NIR-MIR part of the spectrum (1280 – 4480 nm) to separate glass ceramic from glass. By using the NIR-MIR region, a classification error of only 7.6 % was achieved. This method was found to be independent of the colour, shape, size and dirtiness of the glass samples measured.

#### **2.4.2.2. Geology and mineral industry**

Airborne data acquisition (remote sensing) has enabled or provided opportunity for geologist to gain information on minerals present and discriminate lithologies. This is made possible since common alteration minerals such as phyllosilicates, silicates, carbonates and ammonium minerals have diagnostic signatures within the NIR range. A drawback to application is the fact that features related to H<sub>2</sub>O shown near 1400 and 1900 nm, are often obscured as a result of atmospheric absorption, making their use difficult especially when sun is used as energy source (Hunt, 1979). Other drawbacks of NIR application for remote sensing in geology is vegetation and (relatively) high humidity, as the Earth adds a degree of complexity to the NIR spectra observed. Stettler et al. (2007) discussed techniques to overcome some of the issues and compared spectra of different areas. Other authors have reported methods of estimating and measuring clay and calcium carbonate (Gomez et al., 2008), detecting jarosite and alunite as an indicator for alteration minerals (Bornstein et al., 2007) and mapping acid mine waste (Swayze et al., 2000).

Many of these methods used data from airborne sources (e.g. a sensor on the underside of a plane) but Montero et al. (2005) reported the development of a handheld NIR sensor that can be used in the field to identify minerals. The instrument uses a mineral mapping algorithm to identify peaks within spectra and assign the peaks to particular minerals. The strength of the method was the quick and reliable data analysis, which allowed survey plans to be changed, on the basis of the data collected, whilst still in the field. These portable Infrared Mineral Analysers (PIMA) or point scanners are now common (Augus, 2011; Curtis, 2012). The disadvantage of PIMA is that it measures only a single spectrum of a small surface area of the particle surface, usually within a window of a few micrometres diameter circle (Iyakwari et al., 2013).

In the minerals industry, the NIR has been applied in various aspects to identify different species. Hunt and Salisbury (1970; 1971), Hunt et al. (1971a, 1971b, 1972, 1973) and Hunt (1977) used the NIR to identify the various classes of minerals, ranging from silicate, oxides and hydroxides, carbonates, vanadate and borates, sulphides and sulphate. In his paper titled "Near-infrared (1.3 to 2.4  $\mu\text{m}$ ) spectra of alteration minerals-potential for use in remote sensing" Hunt, (1979) discriminated between hydrothermally altered and unaltered geologic

minerals for exploration purposes. He went further to identify and define a number of wavelength positions diagnostic of the alteration minerals. Hunt (1979) stated that “the fingerprint of a particle in the NIR region is the spectral response of that particle to the NIR sensor”. Clark et al. (1999) published an extensive research on NIR reflectance of rocks and minerals. The USGS (United States Geological Survey) spectral library published by Clark et al. (2007) provides spectra of a wide range of minerals for correlation purposes. Gaffey, (1986) used the NIR to discriminate between carbonate minerals calcite, aragonite and dolomite by determining their mineralogy based on their spectral reflectance. This was achieved by observing changes in spectral properties as they reflect or indicate differences in mineralogy. The paper also investigated the effect of particle size on NIR spectra and observed that spectra parameters that vary with particle grain size include overall brightness, absolute band intensity, while band position and width, and relative band intensities (ratios of intensity of a given band to that of the other bands in the same spectrum) are not affected. This finding was re-echoed by Pasikatan et al., (2001) where he stated that the size of particles and grains or crystals within the particles will influence the NIR reflectance spectrum. Iyakwari and Glass (2014) in determining suitable parameters for selection in ore preconcentration using NIR, also confirmed the above findings and added that H<sub>2</sub>O features in water bearing minerals are not optimal for selection in ore particle classification especially where there is more than one H<sub>2</sub>O bearing mineral in the particle of an ore.

Crowley and Vergo (1998) used NIR to discriminate between minerals in mixture of kaolin group minerals by preparing intimate mixtures to simulate natural clay materials. Of interest to present study is the investigation of intimate mixture by Van Der Meer (1995), Bishop and Dummel (1996) and Iyakwari and Glass (2015). Van Der Meer (1995) investigated the influence of iron bearing minerals in mixtures with carbonate minerals and reported the masking effect of hematite on carbonate minerals. Bishop and Dummel (1996) confirmed the masking effect of hematite in an experiment of mixture of hematite and montmorillonites. As a follow up to further investigate their finding and develop a strategy for present study, chapter six of this research presents an extensive study of minerals mixture at various ratios, aspects of which were published by

Iyakwari and Glass (2015). Given that NIR equipment used for the present research is a line scanner, investigation in chapter seven considers the influence of minerals position when scanned. Hunt and Hall (1981) stated that the longer NIR range of 1300 to 2500 nm is significant for identifying clays and other alteration minerals. This is true since clays show diagnostic absorption features at that range. In the present research, NIR data of coarse particles are used to study alteration mineralogy and discriminate between copper bearing minerals and gangue minerals. Regions which contain important absorption features are the 1400 nm and the 2100 to 2500 nm which is caused by metal-OH and  $\text{CO}_3^{2-}$  (Hunt and Ashley 1979; Clark, 1999). These are regions where several of the alteration minerals in the Mantoverde copper ore as well as the Mogalakwena platinum ore exhibit diagnostic absorption characteristics.

Near infrared sensor-based sorting was described by Gaydon et al. (2009), Iyakwari et al. (2013) and Dalm et al. (2014) as an emerging preconcentration technology which holds promise for many mineral processing applications, such as elimination of calcite and clay waste from ore. Therefore, given that many minerals with distinct mineralogical composition can be classified based on their spectral response in the NIR region (Pasquini, 2003; Iyakwari et al., 2013), present research aims at classifying coarse ore particle based on their values. Iyakwari et al. (2013) in developing a copper preconcentration strategy described NIR as a promising tool and stated that the proper identification of absorption features positions characteristic of individual minerals provided a good route for an efficient strategy development.

However, for this investigation it should be noted that native copper does not display any characteristic diagnostic absorption features in the NIR region being investigated (Iyakwari et al., 2013). Hence, the analysis of NIR spectra focusses on identification and discrimination of copper-bearing minerals from their associated gangue minerals. This is also true for platinum ore. However, for the platinum ore, classification is based on the known association of platinum with orthopyroxenes, Base Metal Sulphides (BMS) and amphiboles (Holwell and McDonald, 2007).

## Chapter 3: Material characterization and methodology

### 3.1. Introduction

This chapter discusses the origin of material and methods of characterization used in this study. The NIR sensor used is further discussed in detail. While mention on equipment used for mineralogical and chemical composition analyses is made, detail discussion is provided in the next chapter.

### 3.2. The Mantoverde copper ore

#### 3.2.1. Sample characterization

Nine bags labelled PTM 5761 to PTM 5769 were received from Anglo American Mantoverde operations in Los Pozos mining district in the Coastal Range of the Atacama Region, Northern Chile. Sixty particles (size between 5 and 10 cm) were systematically selected from the bags and provided with sample numbers (Table 3.1). The choice of particles was informed by visual observation of distinct physical features such as texture, colour, and mineralogy among others. The objective is to comprehensively characterise each of the particles both chemically and with NIR and to develop a strategy for distinguishing ore from waste particles.

Table 3.1 - Sample number allocation

Bag	Bag label	Sample number
1	PTM 5761	6, 21, 52, 53
2	PTM 5762	9, 19, 29, 49
3	PTM 5763	54, 55, 56, 57
4	PTM 5764	1, 2, 3, 4, 10, 11, 12, 15, 16, 18, 24, 28, 31, 33, 41, 45
5	PTM 5765	17, 20, 22, 23, 32, 34, 35, 36, 37, 38, 39
6	PTM 5766	5, 8, 25, 26, 27, 30
7	PTM 5767	40, 42, 43, 44, 46, 47, 50, 51
8	PTM 5768	7, 59, 60
9	PTM 5769	13, 14, 48, 58

Each of the 60 particles was subjected to the characterisation process outlined in Figure 3.1.

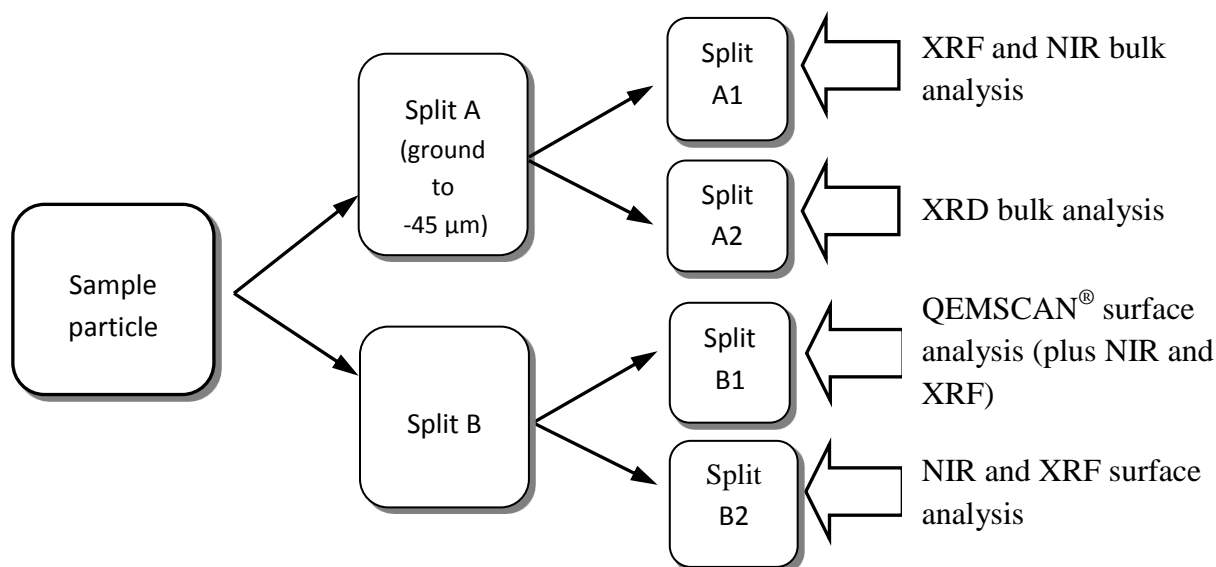


Figure 3.1 - Analysis of Mantoverde samples.

Splits A1 and A2 (Fig. 3.1) were crushed with a Retsch steel jaw crusher and ground to  $-45\ \mu\text{m}$  using a tungsten-carbide mill, homogenised, and prepared prior to analysis with X-Ray Fluorescence (XRF), Near InfraRed (NIR) and X-Ray Diffraction (XRD) analytical methods. Samples of split B1 (Fig. 3.1) were prepared as mounts (width 2 – 2.7 cm) suitable for QEMSCAN<sup>®</sup> (Quantitative Evaluation of Minerals using a Scanning Electron Microscope) analysis (Fieldscan mode) (Pirrie et al. 2000), which were subsequently directly measured on the same face with NIR and XRF. Samples of splits B2 (Fig. 3.1) with an average width of 2 to 10 cm (i.e. the half cuts of split B1) were measured with NIR and XRF. Both splits B1 and B2 were marked prior to analysis with QEMSCAN<sup>®</sup>, XRF, and NIR to keep track of scan locations Figure 3.2. By tracking and maintaining the position of the scan, precise correlation (minerals and spectra mapping) between NIR spectra and data from the QEMSCAN<sup>®</sup> was possible.

Characterisation was performed with standard commercial devices with the notable exception of the NIR (line-scanner) spectrometer, which was developed by CommoDaS (Germany) in a collaborative project with Camborne School of Mines (CSM). XRF analysis was performed with portable desktop thermo-scientific Niton FXL 950 FM-XRF analyser (PXRF) (www.nitonuk.co.uk 2014).

Mineralogical analysis was performed using a QEMSCAN<sup>®</sup> 4300 system and X-Ray Diffraction (XRD) Siemens D5000 instrument (www.bruker.com 2013).

The rationale for analysing (different parts of) a sample particle with a series of techniques is that pooling the results reduces the uncertainty associated with individual analyses of a small volume fraction of the particle with individual techniques. The uncertainty is also influenced by the distribution and proportions of product and waste minerals in the sample particles. By grinding the split A particles, with a largest dimension of about 6.5 cm, to powder of size -45 µm, followed by homogenisation and subsampling prior to analysis, the uncertainty associated with analysis of split A is significantly reduced. NIR and XRF analysis was carried out on the QEMSCAN<sup>®</sup> mount (split B1) and rock face (split B2), which are opposite faces of the rock sample cut into half and the powder (split A1). XRD was only performed on splits A2.

Mineralogical characterisation by QEMSCAN<sup>®</sup> and XRD provided data on the samples that were used to validate and determine NIR-active mineralogy and assess the relations between NIR response and Cu grade. Surface XRF analysis was performed for splits B1 and B2 on the same face as the NIR and QEMSCAN<sup>®</sup> in the case of splits B1. Both XRD and XRF were performed on splits A (1 and 2) are considered to represent the bulk mineralogy and chemistry of the ore.

Ore mineralogy and chemistry based on QEMSCAN<sup>®</sup>, XRD and XRF is discussed in next chapter (sections 4.2.1, 4.2.2 and 4.6 respectively) while NIR is discussed in the next section.

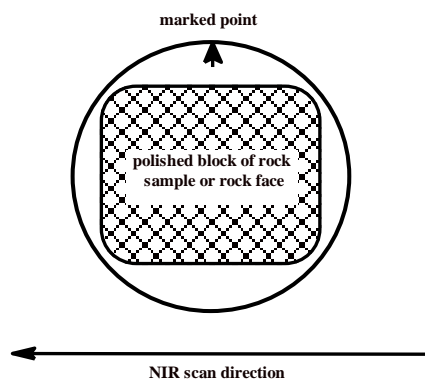


Figure 3.2 - Split B1 and B2 samples marked for directional scanning, used for both the NIR and QEMSCAN<sup>®</sup> analysis.



### **3.3. The Mogalakwena platinum ore**

Fifty one powdered samples were received from the Anglo American platinum operation in Mogalakwena mine, Overysel deposit of the Bushveld Complex, Limpopo province of South Africa. Samples were accompanied by quantitative XRD data. From the data received, most minerals analysed were presented in a group or family name. Therefore, in order to identify specific mineral per group, thirty one samples were taken from the batch of fifty one and qualitative XRD analyses was performed on them, using same XRD equipment as mentioned above.

### **3.4. Near infrared sensor**

Based on the mode of scanning, design and camera type, NIR point scanners and NIR line scanners are distinguished. A point scanner measures a single spectrum of a small surface area of the particle surface, usually within a window of a few micrometres diameter circle. The line scanner measures NIR spectra on a succession of adjacent areas across the mineral surface, (Iyakwari et al., 2013). Results discussed in this research are derived from a line scanner.

The NIR line scanner consists of an enclosed sample chamber with a cooling facility and three basic components: a conveyor belt, a lamp and a camera (Fig. 3.3). The conveyor belt has a width of 45.6 cm and a maximum speed of  $0.5 \text{ ms}^{-1}$ . Data collected for the present research is from stationary samples. The belt is illuminated with two Heraeus Noblelight shortwave-infrared quartz halogen bulbs with gold reflectors (2500 Watt, 480 V each). The lamps were operated at 50 % power to minimize the heating of the conveyor belt while the cooling facility comprising of two fans were also used to reduce the heating of the belt. The camera is positioned 68 cm above the conveyor belt, scanning material from right to left (Fig. 3.2) and data is collected along a single transect of 256 pixels. Individual pixels have dimension of 2.9 by 9 mm. NIR radiation passing through a narrow slit-shaped opening in the roof of the chamber passes through an Acoustic Optical Tuneable Filter (AOTF), an electronically-tuneable spectral band pass filter normally consisting of a birefringent crystal of Tellurium Dioxide ( $\text{TeO}_2$ ). The crystal in the system used for study is composed of Indium-Gallium Arsenide (InGaAs) (Gooch & Housego, Ilminster, UK). The crystal refracts a narrow wavelength band ( $\pm 0.05 \text{ nm}$ ) at 371 wavelengths between 1308 and 2405 nm. The InGaAs detectors are known to have the highest

sensitivity in the NIR region, and can operate at room temperature (Tran, 2000). Spectral sampling interval (the interval in wavelength units, between discrete data points in the measured spectrum) was 1.5 nm at shorter wavelengths and increased to approximately 5.5 nm at longer wavelength. The depth of NIR penetration of the sample depends on the opacity and density of the mineral and can be up to several millimetres (Iyakwari et al., 2013).

NIR radiation measured at each wavelength is acquired using VIEW 2 software (CommoDAS GmbH, Wedel/Hamburg Germany). The VIEW 2 software has two modes of operation: analysis mode and single-colour mode. Single-colour mode involves the use of a single wavelength to collect data on a sample and was not used for this research. The analysis mode of the software collects measurements for the range of the wavelength defined by a lookup table for each pixel in transect of the camera. A lookup table comprises of a comma separated value (csv) file with three columns; the first column being radio frequency applied to the crystal (in MHz), the second column is the power applied (in V) and the third, is the wavelength observed (in nm). The length of time per transect of pixels at one wavelength is termed the line time and values could range from 1500  $\mu\text{m}$  to 8000  $\mu\text{m}$ . 1500  $\mu\text{m}$  was the minimum as the system required time to change the radio frequency applied to the AOTF crystal (Ehlers, 2007; Gaydon, 2011). 3000  $\mu\text{m}$  was considered optimal for present research.

The measured NIR signal is converted to a reflectance by calibrating the signal, by first measuring upper and lower limits. For the upper limit, denoted  $I_{\text{light}}$ , a highly-reflective board made of aluminium is scanned. For the lower limit, denoted  $I_{\text{dark}}$ , a scan is made in the absence of near infrared illumination. The near infrared signal,  $I$ , is now converted into a reflectance,  $R$ , as follows (after Iyakwari et al., 2013):

$$R = \frac{I - I_{\text{dark}}}{I_{\text{light}} - I_{\text{dark}}}.$$

Field data is often accompanied by noise self-generated by the sensor and/or the result of physical fluctuation of the surrounding environment (Stark and Lutcher, 2005; Vaiphasa, 2006). Smoothing algorithms are commonly used as a means of minimizing and removing noise in spectral data, whilst maintaining the

features present in the spectrum (Goetz et al., 2009; Gaydon et al., 2009; Gaydon, 2011). All spectra were smoothed using OriginPro 9.0 software (OriginLab, Northampton, MA, USA. [www.originlab.com](http://www.originlab.com)) with the Savitzky-Golay method (Savitzky and Golay, 1964).

The Savitzky-Golay method uses polynomial least square calculations and fits a curve to spectral data over a number of data points (the number/window size is user defined). The curve chosen is the one that minimizes the square of the differences between the observed spectrum and the computed spectrum. All error is assumed to be in the computed spectrum (the curve). Once a curve has been fitted, the value of the central point of the window on the curve is taken as the new point. The value of this point is the best value of the point based on the least square criterion and the size of the window chosen. With the curve fitted and the new central value calculated, the window moves along one data point and the method repeated until the entire spectrum has been smoothed. This method has two key parameters: the window size and the degree of polynomial order.

The Savitzky-Golay filter was applied using second order polynomial to a frame size of 9 points. The Savitzky-Golay method was chosen for application because it does not distort or disturb original data like other filters and it gives finer details where/when required (Vaiphasa, 2006, Gaydon, 2011).

Camera:  
Unit include  
AOTF Crystal



Illumination:  
Two light boxes

Conveyor Belt:  
45.6 cm wide

Figure 3.3 - Image of near infrared setup, at Camborne School of Mines (CSM), (adapted from Gaydon, 2011).

## **Chapter 4: Mantoverde ore mineralogy and chemistry**

### **4.1. Introduction**

This chapter discusses the mineralogy and chemistry of the Mantoverde samples used in the research. Compositional analysis was carried out on the samples and the results are discussed with respect to implications to Near InfraRed (NIR) preconcentration and economics. This is followed by developing a strategy for classification on the basis of individual sample mineralogy and chemistry.

### **4.2. Mantoverde ore mineralogy**

#### **4.2.1. QEMSCAN<sup>®</sup>**

QEMSCAN<sup>®</sup> is an automated technique for the rapid characterisation of mineral species via combined Scanning Electron Microscopy and Energy Dispersive X-ray Spectrometry (SEM–EDS) (Gottlieb et al., 2000, Pirrie and Rollinson, 2011). The QEMSCAN<sup>®</sup> allows spatial determination of minerals by interpretation of chemical spot analyses with an elemental detection limit of approximately 3 % per analysis point (Andersen et al., 2009). The principle of operation of QEMSCAN<sup>®</sup> is based on a scanning electron microscope, capable of examining mineralogical and textural parameters. Samples were prepared as epoxy mounts with Epofix resin and polished to a 1 µm finish before carbon coating to 25 nm thickness. Each sample had an average size of between 2 and 2.7 cm, and was mapped using the fieldscan measurement mode (this provides a full image of the sample being measured), with a beam stepping interval of 10 µm across the sample surface (i.e. an x-ray was acquired every 10 µm across the sample in a grid). This resulted in the acquisition of typically more than 3,500,000 individual X-ray analysis points per sample (i.e. the total number of analysis points, approximately collected per sample, and is dependent upon the size/area of the sample as resin is ignored).

The mineral mass data (Table 4.1) and approximate abundance of copper and iron (Table 4.2) are based on the assumed average density of each mineral and back-calculated from the QEMSCAN<sup>®</sup> primary list, where chemical data is input

manually (average density and chemistry values from webmineral.com 2013) and as such can only be used as an indicator.

Sixty samples (split B1, Fig. 3.1) were analysed using QEMSCAN<sup>®</sup> and results obtained are presented in Table 4.1. In no particular order, minerals present in the ore include chrysocolla, malachite, cuprite, hematite, biotite, ankerite, calcite, muscovite, kaolinite, chlorite, quartz, k-feldspars, plagioclase feldspars, tourmaline and apatite. Other mineral phases occurring in trace concentration include zircon, rutile and ilmenite.

Mineralogical data show that the main copper bearing mineral is chrysocolla, which is a silicate mineral of secondary origin. Twenty five samples (42 % of total samples) contain 1 wt % and above chrysocolla. Only six samples (samples 13, 15, 27, 33, 41, and 58) i.e. 10 % of total samples, have chrysocolla concentration below detection limit (< 0.01 wt %). Statistically, this therefore means chrysocolla was detected in 90 % of the samples analysed, with 48 % of samples showing concentration below 1 wt % (Table 4.1). With a few exceptions, other minerals containing copper such as cuprite and malachite are either present in trace concentration (below 1 wt %) or their concentration is below a confident detection limit. Of the sixty samples, only sixteen (samples 3, 5, 6, 9, 10, 16, 17, 20, 24, 26, 28, 32, 35, 47, 55 and 57) contain malachite, out of which only five of them (samples 5, 9, 10, 26 and 55) have concentration of 1 wt % and above, with sample 55 showing the highest concentration of 2.21 wt % (Table 4.1). The five high malachite ( $\geq 1$  wt %) bearing samples contain more chrysocolla, than malachite. Comparison between chrysocolla and cuprite show a dominant chrysocolla bearing ore with only three samples (samples 35, 55 and 57) containing cuprite above 0.20 wt %, which also contain about 3 wt %, 5.2 wt % and 6.33 wt % chrysocolla respectively (Table 4.1). All the three cuprite bearing samples are also malachite bearing. Cuprite is a copper oxide. It is therefore true to say that where they occur: all three minerals are present in same samples (Table 4.1).

The percentage composition of copper in each sample is calculated from the copper bearing minerals in the samples, which include: chrysocolla (33.86 % copper), malachite (57.48 % copper) and cuprite (88.82 % copper). On a 1:1 comparison, both malachite and cuprite contain more percentage copper than chrysocolla, but their occurrence in this ore is in trace concentrations. Of these

three minerals, chrysocolla constitutes 93 % by volume while malachite and cuprite constitute 6.4 % and 0.6 % respectively of copper-bearing minerals in the ore. Also, with no exceptions all samples containing either or both malachite and cuprite also contains chrysocolla and in no sample does malachite or cuprite show more concentration than chrysocolla (Table 4.1). Therefore, given the dominance of chrysocolla (both in concentration and occurrence) in the ore, it is considered as the economic mineral of interest for study and preconcentration strategy using NIR shall be developed with reference to chrysocolla.

Note, the chrysocolla tended to be iron-rich: this is not typical but probably as a result of the presence of iron-rich minerals in the ore.

Table 4.1- Modal mineralogy of the Mantoverde copper ore samples (mass %) measured by QEMSCAN®, < 0.01 % = below detection limit.

Sample ID	Silicates										Oxides	Carbonates			Phosphates	Others (Trace phases)	Total
	Cu-bearing		Non-Cu-bearing								Cu-bearing		Non-Cu-bearing				
	Non-Iron-bearing			Iron-bearing				Non-Iron-bearing			Iron-bearing	Non-Iron-bearing		Iron-bearing	Non-Iron-bearing		
	NIR-active						Non-active				NIR-active	Non-active	NIR-active				
	Chrysocolla	Muscovite	Kaolinite	Biotite	Chlorite	Tourmaline	Quartz	K-feldspar	Plag-feldspar	Hematite	Cuprite	Malachite	Calcite	Ankerite	Apatite		
1	8.33	5.95	0.01	15.54	8.87	0.39	17.69	25.54	0.07	16.63	0.01	<0.01	0.01	0.02	0.18	0.75	100
2	19.05	3.79	0.01	8.32	6.68	0.3	14.96	26.21	0.03	19.9	0.02	<0.01	0.01	0.04	0.27	0.41	100
3	21.11	2.96	0.05	4.53	3.08	0.04	18.16	17.87	0.02	31.77	0.01	0.31	<0.01	<0.01	<0.01	0.1	100
4	5.14	3.28	0.68	7.3	5.13	0.72	6.84	15.5	0.06	55.32	0.01	<0.01	<0.01	<0.01	<0.01	0.02	100
5	3.29	5.34	<0.01	8.38	24.87	0.55	37.88	13.11	0.17	3.72	0.01	1	0.02	0.05	0.73	0.9	100
6	1.09	1	<0.01	15.32	6.64	0.13	9.86	32.42	1.16	10.37	0.04	0.01	17.17	2.88	0.13	1.78	100
7	0.15	1.55	<0.01	13.01	8.74	0.48	7.46	38.83	0.03	29.03	<0.01	<0.01	0.01	0.06	0.33	0.33	100
8	5.58	0.22	<0.01	5.96	15.76	0.1	4.91	38.01	<0.01	28.47	0.01	<0.01	0.01	0.02	0.16	0.79	100
9	3.98	0.26	<0.01	6.72	14.12	1.49	18.49	4.45	0.41	11.66	0.15	1.38	31.61	4.06	0.31	0.9	100
10	7.78	1.62	<0.01	5.86	4.47	0.13	15.13	1.32	0.01	62.04	0.03	1.55	<0.01	0.01	0.01	0.03	100
11	9.31	2.67	0.33	5.46	4.66	0.18	13.13	20.65	0.08	43.17	<0.01	<0.01	<0.01	<0.01	<0.01	0.36	100
12	6.92	3.55	0.43	4.9	3.47	0.27	11.19	19.44	0.05	49.74	<0.01	<0.01	<0.01	<0.01	<0.01	0.04	100
13	<0.01	2.31	0.02	3.33	2.99	0.06	18.37	11.74	0.3	53.44	<0.01	<0.01	5.08	2.03	<0.01	0.31	100
14	1.19	3.73	1.16	6.71	13.43	2.4	16.14	11.15	0.82	43.06	<0.01	<0.01	0.1	0.05	<0.01	0.07	100
15	<0.01	8.38	0.04	22.89	10.85	0.07	7.69	33.62	0.21	6.98	<0.01	<0.01	3.77	2.64	0.03	2.84	100
16	0.4	0.12	<0.01	9.42	15.16	0.06	38.98	34.25	<0.01	0.63	<0.01	0.01	0.01	<0.01	0.29	0.69	100
17	3.46	0.02	<0.01	0.51	25.61	0.11	64.6	0.76	0.03	3.41	0.02	0.39	0.02	<0.01	0.17	0.9	100
18	0.27	17.73	<0.01	4.59	2.45	0.03	41.9	30.3	0.06	0.22	<0.01	<0.01	1.08	0.64	0.02	0.71	100
19	0.45	9.9	<0.01	17.7	5.37	0.3	20.54	16.95	1.16	7.13	<0.01	<0.01	16.28	2.45	0.25	1.53	100
20	0.81	1.67	<0.01	10.1	36.47	0.36	38.26	10.07	0.05	0.98	0.01	0.14	0.03	<0.01	0.24	0.79	100
21	0.07	18.82	3.11	4.77	4.2	0.25	31	16.03	2.26	19.18	<0.01	<0.01	<0.01	<0.01	<0.01	0.31	100
22	0.08	0.25	<0.01	6.99	11.25	0.09	46.08	33.64	0.01	0.12	<0.01	<0.01	0.01	0.01	0.66	0.82	100
23	0.05	0.05	<0.01	1.78	33.81	1.13	57.69	3.13	0.2	0.89	<0.01	<0.01	0.03	0.01	0.21	1.02	100
24	1.23	21.55	<0.01	3.46	1.33	0.05	62.89	5.73	0.03	2.92	0.01	0.66	0.01	0.01	0.07	0.05	100
25	0.36	0.1	<0.01	3.36	17.66	0.47	51.9	4.5	0.3	0.51	<0.01	<0.01	18.81	0.45	0.38	1.21	100
26	3.26	4.14	<0.01	8.47	26.35	0.4	36.34	14	0.15	4.13	0.01	1.2	0.02	0.04	0.46	1.04	100
27	<0.01	10.55	0.03	5.08	2.22	0.44	25.81	18.98	3.8	0.18	<0.01	<0.01	28.89	0.27	0.25	3.51	100
28	1.64	<0.01	0.01	0.84	35.08	0.8	57.24	0.1	0.5	1.03	0.01	0.62	0.05	0.01	0.96	1.10	100
29	0.21	14.84	0.02	3.06	1.27	0.51	20.72	11.64	3.51	1.22	<0.01	<0.01	38.82	0.81	0.27	3.10	100



Cont. of Table 4.1- Modal mineralogy of the Mantoverde copper ore samples (mass %) measured by QEMSCAN<sup>®</sup>, < 0.01 % = below detection limit.

Sample ID	Silicates						Oxides				Carbonates			Phosphates		Others (Trace phases)	Total
	Cu-bearing		Non-Cu-bearing				Cu-bearing				Non-Cu-bearing						
	Non-Iron-bearing		Iron-bearing		Non-Iron-bearing		Iron-bearing	Non-Iron-bearing			Iron-bearing	Non-Iron-bearing					
	NIR-active			Non-active			NIR-active	Non-active	NIR-active								
	Chrysocolla	Muscovite	Kaolinite	Biotite	Chlorite	Tourmaline	Quartz	K-feldspar	Plag-feldspar	Hematite	Cuprite	Malachite	Calcite	Ankerite	Apatite		
30	0.08	0.14	0.02	3.54	35.29	2.49	50.49	4.38	1.02	1.16	<0.01	<0.01	0.02	0.01	0.39	0.96	100
31	0.27	1.62	<0.01	5.93	45.02	0.36	30.31	10.25	0.12	4.02	<0.01	<0.01	0.05	0.03	0.86	1.16	100
32	2.05	0.22	<0.01	1.16	34.74	0.1	49.57	2.43	0.13	0.74	0.02	0.91	0.35	0.13	4.99	2.47	100
33	<0.01	11.26	0.14	16.28	5.24	0.17	10.64	40.11	0.98	3.05	<0.01	<0.01	8.01	2.13	0.05	1.94	100
34	0.22	0.04	<0.01	1.69	36.54	0.25	56.91	2.32	0.05	0.26	<0.01	<0.01	0.05	0.01	0.35	1.31	100
35	2.98	1.65	<0.01	7.24	19.1	0.06	21.38	10.43	0.26	3.08	0.23	0.85	27.02	4.1	0.53	1.10	100
36	0.02	0.54	<0.01	12.15	16.3	0.06	30.12	34.5	0.07	0.73	<0.01	<0.01	3.78	0.12	0.18	1.43	100
37	0.82	0.08	<0.01	15.69	43.83	0.02	0.4	35.92	<0.01	1.72	<0.01	<0.01	0.01	<0.01	0.21	1.31	100
38	0.18	1.41	<0.01	40.82	7.89	0.17	21.9	22.92	0.05	3.89	<0.01	<0.01	0.03	0.02	0.42	0.31	100
39	0.98	0.11	<0.01	10.24	45.84	0.02	7.89	32.78	0.01	0.27	<0.01	<0.01	0.02	0.01	0.53	1.33	100
40	0.89	0.06	<0.01	1.59	19.61	0.94	72.21	3.8	0.05	0.02	<0.01	<0.01	0.01	<0.01	0.06	0.76	100
41	<0.01	<0.01	0.01	2.95	23.19	9.41	29.54	<0.01	3.99	3.48	<0.01	<0.01	13.1	6.04	0.17	8.12	100
42	0.27	6.12	<0.01	11.81	4.56	0.34	20.31	11.18	1.79	0.43	<0.01	<0.01	40.52	0.56	0.26	1.86	100
43	0.04	4.96	0.1	8.37	6.28	1.58	30.74	10.56	9.08	1.12	<0.01	<0.01	18.45	0.41	0.32	8.00	100
44	0.15	0.21	<0.01	3.14	40.72	0.06	41.1	1.71	0.05	0.35	<0.01	<0.01	10.11	0.25	0.65	1.50	100
45	0.54	0.16	<0.01	7.00	15.58	0.03	3.19	60.96	0.07	2.38	<0.01	<0.01	8.55	0.38	0.22	0.94	100
46	0.13	8.37	0.06	3.91	4.86	1.82	31.37	8.74	7.32	0.95	<0.01	<0.01	25.81	0.51	0.19	5.96	100
47	1.33	0.1	<0.01	2.74	31.1	0.13	30.81	2.59	0.06	4.46	0.03	0.11	22.64	2.42	0.36	1.13	100
48	4.12	1.68	<0.01	8.79	6.65	0.07	10.39	6.53	0.01	59.78	<0.01	<0.01	1.93	0.04	<0.01	0.02	100
49	0.38	12.95	0.03	3.38	1.63	0.88	19.32	10.07	2.84	1.9	0.01	<0.01	42.12	1.29	0.2	2.99	100
50	34.06	0.25	0.01	2.37	16.85	0.05	34.43	10.86	0.01	0.59	0.01	<0.01	0.01	0.24	0.24	0.02	100
51	2.96	2.11	<0.01	14.26	7.08	0.27	14.04	14.81	1.07	9.84	<0.01	<0.01	29.03	0.15	0.15	4.24	100
52	0.04	9.97	<0.01	9.56	4.82	0.19	24.51	7.97	1.44	12.48	<0.01	<0.01	25.01	2.17	0.13	1.69	100
53	0.04	22.16	0.03	2.24	1.04	0.4	24.42	11.96	3.38	0.27	<0.01	<0.01	29.68	0.17	0.24	4.00	100
54	0.19	2.15	0.02	8.37	26.98	1.07	27.35	5.04	3.4	4.32	<0.01	<0.01	16.56	1.77	0.07	2.71	100
55	5.2	18.87	0.05	12.65	5.42	0.62	22.48	4.18	0.89	7.32	0.27	2.21	12.98	5.3	0.54	0.98	100
56	0.13	12.07	<0.01	13.61	12.14	0.53	19.18	9.42	1.14	0.39	<0.01	<0.01	28.53	0.79	0.11	1.95	100
57	6.33	9.9	0.07	9.97	8.39	1.45	23.09	2.49	2.78	8.77	0.25	0.7	17.08	6.46	0.32	1.94	100
58	<0.01	0.87	0.1	6.38	4.68	0.58	4.02	7.88	0.01	75.44	<0.01	<0.01	<0.01	0.01	<0.01	0.04	100
59	0.1	4.58	0.01	18.22	9.95	0.48	11.28	33.24	0.04	21.03	<0.01	<0.01	0.01	0.05	0.31	0.69	100
60	5.84	1.24	0.04	12.89	8.29	0.4	4.13	24.88	0.04	40	<0.01	<0.01	1.49	0.53	0.01	0.23	100

Table 4.2 - Abundance of copper and iron (mass %), calculated from QEMSCAN<sup>®</sup> modal mineral data of copper-bearing minerals (chrysocolla, cuprite and malachite) and iron-bearing minerals (hematite, biotite, ankerite, chlorite and tourmaline). Note, mineral calculation used the average values of elements per mineral (www.webmineral.com 2013).

Sample ID	Cu	Fe
1	2.83	13.74
2	6.46	15.29
3	7.33	22.88
4	1.75	39.88
5	1.70	6.16
6	0.41	9.51
7	0.05	22.25
8	1.90	22.16
9	2.28	11.14
10	3.55	44.32
11	3.15	31.12
12	2.34	35.55
13	0.00	38.28
14	0.40	32.51
15	0.00	8.07
16	0.14	2.83
17	1.41	5.44
18	0.09	0.85
19	0.15	7.20
20	0.36	5.68
21	0.02	14.25
22	0.03	1.87
23	0.02	4.88
24	0.80	2.43
25	0.12	2.79
26	1.81	6.59
27	0.00	0.82
28	0.92	5.02
29	0.07	1.41
30	0.03	5.57
31	0.09	8.53
32	1.23	4.70
33	0.00	4.17
34	0.07	4.62
35	1.71	5.54
36	0.01	3.23
37	0.28	7.36
38	0.06	6.31
39	0.33	6.23
40	0.30	2.57
41	0.00	7.83
42	0.09	1.74
43	0.01	2.38
44	0.05	5.27
45	0.18	4.01
46	0.04	1.86
47	0.54	7.36
48	1.40	43.18
49	0.14	2.09
50	11.54	2.59
51	1.00	8.69
52	0.01	10.29
53	0.01	0.54
54	0.06	7.18
55	3.28	7.53
56	0.05	2.79
57	2.77	9.04
58	0.00	53.81
59	0.03	17.13
60	1.98	29.93

The main iron-bearing minerals in the ore are hematite, biotite, ankerite, chlorite and tourmaline. Though ilmenite contains 36.81 % on average of iron, it only occurred as traces with no sample having a concentration above 1 wt %. The highest concentration of 0.9 wt % was measured in sample 33. Therefore, ilmenite is not shown on Table 4.1. Hematite, chlorite and biotite are the most abundant iron-bearing minerals, contributing 78 %, 15 % and 5 % respectively of the total iron in the ore (Table 4.1). Hematite is an iron oxide mineral containing on average 69.94 % of iron (webmineral.com 2013). Chlorite, tourmaline and biotite contain on average 11.73 %, 15.91 % and 6.44 % of iron respectively, all of which are silicate minerals. Ankerite is a carbonate mineral containing 16.24 % of iron (webmineral.com 2013). Samples with a high hematite concentration above 20 % (Table 4.1) are: 3 (31.8 wt %), 4 (55.3 wt %), 7 (29 wt %), 8 (28.5 wt %), 10 (62.4 wt %), 11 (43.2 wt %), 12 (49.8 wt. %), 13 (53.4 wt %), 14 (43.1 wt %), 48 (59.8 wt %), 58 (75 wt %), 59 (21 wt %) and 60 (40 wt %). Meaning 22 % of the total samples contain hematite above 20 wt %. The interest in iron and iron-bearing minerals content in the ore is based on the fact that iron and particularly high iron-bearing minerals in an ore especially hematite, suppress NIR spectral features of other minerals (Van Der Meer, 1995; Bishop and Dummel, 1996; Iyakwari and Glass, 2014b).

Almost all the samples contain iron-bearing minerals in appreciable concentrations, with only ten samples (samples 18, 22, 24, 27, 29, 42, 43, 46, 49 and 53) of the sixty analysed samples containing below 20 wt % by concentration. This means that only 17 % of the total samples contain iron-bearing minerals in concentrations below 20 wt %.

The mineral data (Table 4.1) shows that the ore is rich in silicate minerals. The silicate minerals in the ore include: quartz, K-feldspars, plagioclase, chrysocolla, muscovite, chlorite, biotite, tourmaline and kaolinite. This means that the ore is a silicate ore. Silicate composition in the samples varies with abundance from 25 % for sample 58 to above 95 % for samples 16, 17, 18, 20, 22, 23, 24, 28, 30, 32, 34, 37, 38, 39, 40, and 50. Kaolinite is rare, with occurrence of less than 1.2 wt %, with only sample 21, containing high kaolinite (3.11 wt %). Apart from samples 41, 14, 30, 47, 9 and 23 which have tourmaline concentration of 9.4 wt %, 2.4 wt %, 2.50 wt %, 1.8 wt %, 1.49 wt %, and 1.13 wt % respectively, other

samples have concentrations below 1 wt %. Quartz and K-feldspars are the dominant of the silicate minerals.

Apatite is the only phosphate mineral in the ore. Only sample 32 (4.99 wt %) contains apatite above 1 wt %.

Common carbonate minerals in the ore are calcite, ankerite and malachite. About 48 % of the total samples analysed contain below 1 % by concentration of carbonate minerals. Only samples 6, 9, 19, 25, 27, 29, 32, 35, 41, 42, 43, 44, 46, 47, 49, 51, 53, 54, 55, 56 and 57 (i.e. 35 % of total samples) have carbonate minerals concentration of 10 % and above. The dominant carbonate mineral in this ore is calcite (Table 4.1). Samples with high calcite concentration above 20 wt % include: samples 9 (31.6 wt %), 27 (28.9 wt %), 29 (38.8 wt %), 35 (27 wt %), 42 (40.5 wt %), 46 (25.8 wt %), 47 (22.6 wt %), 49 (42 wt %), 51 (29 wt %), 52 (25 wt %), 53 (30 wt %) and 56 (29.5 wt %). Only samples 6, 9, 13, 15, 19, 33, 35, 41, 47, 52, 55 and 57 have ankerite concentration above 2 wt %, with sample 57 having the highest ankerite concentration of 6.5 wt %.

Other minerals present in some samples as analysed by the QEMSCAN<sup>®</sup> but in trace concentrations include: zircon, rutile and ilmenite. None of these minerals singularly have concentration above 1 wt %, in any of the sixty samples analysed.

The texture of the ore varied with individual samples and could best be described as ranging from disseminated, banded to porphyritic. The textures also varied from micro, meso to macro in scale. The majority of the samples appeared finely mixed with disseminated minerals grains, while some samples (e.g. samples 3, 4, 8, 11, 12, 13, 21 and 48) showed clearly large crystallized grains (phenocryst). A few samples, 2, 6, 41, 51, and 57 showed banded or laminated textures. As the samples were already collected it is not possible here for the author to link the texture to a specific location in the mine or deposit.

The QEMSCAN<sup>®</sup> results showed that in all investigated samples only three major mineral groups (silicates, oxides, and carbonates) dominate the ore, with apatite (phosphate) occurring as traces.

#### 4.2.2. X-Ray Diffraction (XRD) analysis

A sub-set of forty four samples (splits A2, Fig. 3.2), of the Mantoverde copper ore were systematically selected from the batch of sixty samples and analysed using the XRD mineralogical analysis method. The selected samples were deemed representative of the ore, thus it was unnecessary to analyse all sixty. Samples were ground to  $-45\ \mu\text{m}$  using a tungsten carbide mill and carefully pressed into an XRD sample holder using a glass plate. The samples were measured at room temperature on a Siemens D5000 XRD from  $2-70^\circ$ , 2 Theta-scale, on a  $0.02^\circ$  step with step time of one second, and rotated during measurement collection. The instrument was set at 40KV, 30mA, using a Cu anode X-Ray tube and V6 anti scatter and divergence slit. The profiles produced by the scan were interpreted to match peaks with known mineral markers using EVA software (www.bruker.com 2013). Profiles of diffraction pattern obtained are presented in Appendix 4.1.

The XRD analysis performed was qualitative and examines samples based on crystallography: therefore, it cannot detect amorphous material that does not have crystal structure. On this basis, with the exception of amorphous minerals like chrysocolla and malachite, most of the minerals detected by the QEMSCAN<sup>®</sup> (Table 4.1) were also identified by the XRD (Table 4.3). XRD mineral identification is also based on a detection limit of 5 % and above. On this basis, only minerals that occurred in concentrations above the XRD detection limit were identified. This means that minerals identified by the XRD were above or approximately 5 % in concentration in the samples. Therefore, XRD only allowed for the determination of the most dominant minerals present in the samples (2 - 5 minerals). For each sample on which XRD was performed, the determined minerals with known NIR activities always showed absorption in the measured NIR spectra, provided it is dominant and accessible to NIR radiation.

Given that amorphous minerals are not identified by XRD, the presence of amorphous minerals is only inferred in samples displaying a significant rise in their XRD baseline pattern as the 2-theta value increases. According to Gaydon (2011), a rise in the baseline of XRD pattern with increase in the 2-theta value is indicative of the presence of amorphous minerals. In this case since chrysocolla is the known dominant amorphous mineral present in the ore based on the

QEMSCAN<sup>®</sup> analysis (Table 4.1), the rise in baseline pattern displayed is assumed to indicate the presence of chrysocolla. Samples that showed this pattern (i.e. rise in baseline) include samples 1, 2, 3, 6, 8, 9, 10, 11, 24 and 35 (Appendix 4.1). The modal mineralogical data obtained by the QEMSCAN<sup>®</sup> (Table 4.1) also show that the ten samples listed above contain considerable concentration of chrysocolla, with samples 9 and 10 containing malachite in addition.

Major minerals identified by XRD analyses include, quartz, hematite, clinochlore (chlorite), orthoclase and microcline (K-feldspars), muscovite, calcite and biotite as the eight dominant crystalline mineral constituents present within the model batch particles (Table 4.3). Quartz is present in all samples, while biotite is the least dominant. Hematite, chlorite, muscovite, calcite and biotite are NIR-active minerals (Hunt, 1979; Iyakwari and Glass, 2015).

The XRD analysis is also in agreement with the QEMSCAN<sup>®</sup> data, confirming that the ore is dominantly of three major minerals groups (oxide, silicate and carbonate).

Table 4.3 - XRD analysis of the Mantoverde copper ore samples, presence of a mineral is marked with +. (Note that the amorphous phase is only inferred from XRD patterns with rising baselines)

Sample ID	Quartz	Hematite	Muscovite	Clinocllore	Calcite	Biotite	Microcline	Orthoclase	Amorphous Phase
1	+	+		+		+		+	+
2	+	+		+				+	+
3	+	+						+	+
4	+	+					+	+	
5	+		+	+			+		
6	+	+		+	+		+		+
7	+	+					+		
8	+	+		+			+		+
9	+			+	+		+		+
10	+	+	+						+
11	+	+					+		+
13	+	+							
14	+	+	+				+		
15	+							+	
16	+			+				+	
17	+			+					
18	+		+	+			+		
19	+	+		+	+	+			
20	+		+	+					
21	+	+	+					+	
22	+							+	
24	+	+	+						+
26	+		+	+			+		
27	+		+		+				
28	+			+					
30	+		+	+			+		
31	+		+	+			+		
32	+			+					
34	+			+					
35	+			+	+				+
36	+			+				+	
37	+			+	+			+	
38	+			+		+			
39	+			+			+		
40	+			+			+		
42	+		+	+	+		+		
43	+		+		+				
45	+			+	+			+	
46	+		+		+				
47	+			+	+		+		
56	+			+	+				
57	+		+		+				
58	+	+		+				+	
59	+		+						

### 4.3. Near infrared sensitive minerals

#### 4.3.1. Mineralogy of near infrared sensitive minerals

The NIR examines minerals based on their functional group(s). The functional groups of interest for present study include -OH and  $\text{CO}_3^{2-}$ . Minerals containing this group(s) in the ore include calcite, ankerite and malachite ( $\text{CO}_3^{2-}$ ),

muscovite, kaolinite, biotite, chrysocolla, malachite, chlorite, tourmaline and apatite (-OH) (Tables 4.1). Though NIR absorption features produced by malachite are largely due to their  $\text{CO}_3^{2-}$  functional group with little contribution of the -OH groups (Clark et al., 2007), malachite appear in both  $\text{CO}_3^{2-}$  and -OH group as it contains both functional groups. Also hematite does not contain any of these groups: it is considered for discussion because of its known high NIR spectral absorption (Iyakwari et al., 2013; Iyakwari and Glass, 2015). More details on minerals NIR activity classification is presented in the next chapter.

Both QEMSCAN<sup>®</sup> and XRD measured mineralogy, but only the QEMSCAN<sup>®</sup> analysis provided a more detailed quantitative and spatial account of composition with a higher detection limit. Therefore, minerals data from QEMSCAN<sup>®</sup> alone will be used for subsequent discussions.

The distribution/concentration of individual NIR-active minerals in each sample is presented in Figure 4.1. Analysis of Figure 4.1 shows that though all minerals contain NIR-active minerals, the NIR-active minerals make up about 50 % and above of the bulk mineral concentrations in forty samples (i.e. 67 % of the total sample). Of all the NIR-active minerals present in the ore, only six (chrysocolla, hematite, muscovite, biotite, chlorite and calcite) occur in appreciable concentration. Malachite, kaolinite, ankerite, tourmaline and apatite only occur as traces in a few samples. Sample 58 has the highest concentration of NIR-active minerals, making up about 88 % of its total mass (Fig. 4.1).

The most abundant NIR-active mineral in the ore is chlorite (clinochlore). It is present in all the samples in appreciable concentration. Twenty nine samples (48 % of total samples) have a chlorite concentration of 10 wt % and above, with sample 39 having the highest concentration of 46 wt %. Sample 53, has the least concentration of 1.04 wt % of chlorite concentration as analysed (Table 4.1 and Fig. 4.1).

Hematite occurs in high concentrations in samples containing chrysocolla (Table 4.1). Ten samples (samples 4, 10, 11, 12, 13, 14, 48, 58, 59 and 60) have 40 wt % and above hematite concentration, with sample 58 having the highest concentration of 75 wt % of hematite (Table 4.1 and Fig. 4.1).



Biotite is second to chlorite amongst NIR-active minerals that occurs in almost all the samples. Sample 38 has the highest biotite concentration of above 40 wt % while the least concentration of 0.5 % is shown by sample 17.

Muscovite also has a fair occurrence in the ore. Twelve samples, (Samples 18, 21, 24, 27, 29, 33, 49, 52, 53, 55, 56, and 57) making 20 % of total samples analysed show significant muscovite concentration of 10 wt % and above. Only sample 41 contains muscovite below detection limit. Sample 53 shows the highest concentration of 22.16 wt % (Table 4.1 and Fig. 4.1).

Calcite is observed to show a rather unique or selective pattern of occurrence, whereby when it occurs in a sample, it occurs in large concentrations. The same can be observed of chrysocolla. In the case of chrysocolla, its occurrence in most samples is observed to be linked or associated with that of hematite though they may not occur in the same proportion or abundance (Table 4.1 and Fig. 4.1).

The occurrence and abundance of these NIR-active minerals (chlorite, chrysocolla, hematite, biotite, muscovite and calcite) which are formed by hydrothermal alteration of primary minerals (Hunt, 1979), is an indication that the Mantoverde deposit experienced hydrothermal alteration activity or activities leading to the deposition of the ore (Benavides et al., 2007, Rieger et al., 2010).

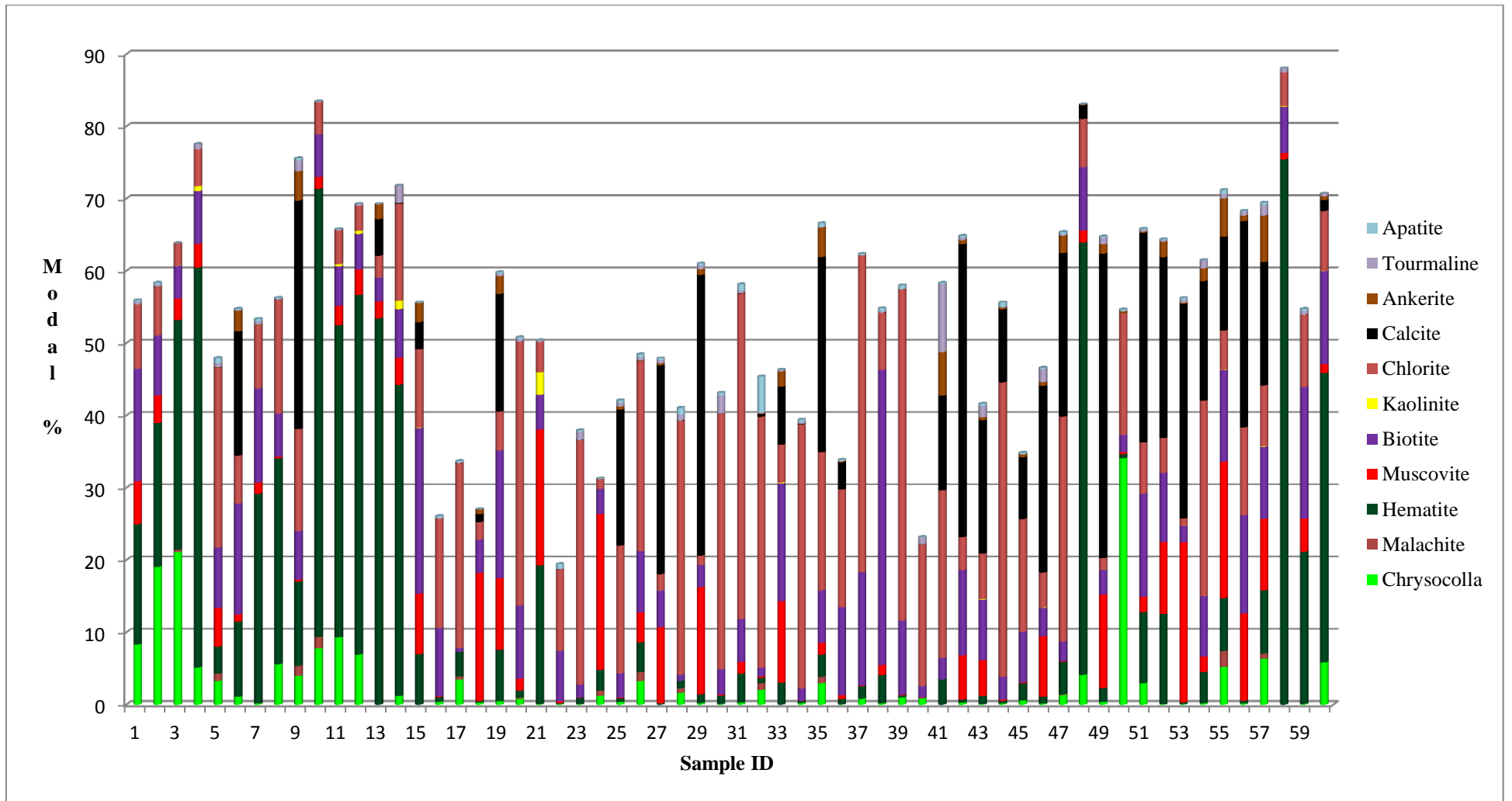


Figure 4.1 - Modal abundance (Wt %), of NIR-active minerals in samples of Mantoverde copper ore.

### 4.3.2. NIR sensitive minerals association

The ore studied is dominated by silicate minerals (quartz, K-feldspars, plagioclase feldspars, muscovite, chlorite, kaolinite, biotite and chrysocolla) with various mixtures of oxides (hematite) and other carbonate minerals (calcite, malachite and ankerite). Amongst all the constituent minerals analysed in the Mantoverde samples, only a few which are all alteration minerals (calcite, malachite, muscovite, ankerite, kaolinite, hematite, biotite, chrysocolla), can produce absorption features or mask absorption features within the range of NIR being investigated (Hunt et al., 1974; Hunt, 1979; Clark et al 1999; Iyakwari et al., 2013; Iyakwari and Glass, 2015). Owing to their lack of absorption feature producing functional group(s), minerals like quartz and feldspars in a complex ore particle do not contribute to its NIR spectrum or spectra (Iyakwari and Glass, 2015). Therefore, only active minerals that occur in appreciable concentration and can contribute to the total rock (ore) spectra are considered for discussion.

NIR-active minerals are therefore selected on the basis of abundance as some occurred in minute concentration in a few samples (e.g. malachite and kaolinite). On this basis, and with reference to Table 4.1, in no particular order, only muscovite, chlorite, chrysocolla, biotite, hematite and calcite are considered.

The QEMSCAN<sup>®</sup> calculates mineral association based on mineral adjacency. Given the disseminated nature of the minerals in the ore studied, mineral association result obtained by QEMSCAN<sup>®</sup> does not correlate well with reality. Therefore, based on the above findings, the QEMSCAN<sup>®</sup> fieldscan images (Table 4.4) are used to discuss the possible mineral associations. The QEMSCAN<sup>®</sup> fieldscan images are surface maps/images of the sample data obtained by the QEMSCAN<sup>®</sup>. These images cover about the same depth as compositional mineralogical data and provide detailed spatial mineralogical information of each sample. Table 4.4 shows fieldscan images of the samples, ranging from individual NIR-active minerals, combined NIR-active minerals and the bulk mineral image in each sample with reference to Table 4.1. All images are presented for ease of minerals identification and comparison. Also, since both QEMSCAN<sup>®</sup> fieldscan images and NIR measures spatial mineral details, it is important to map samples for a 1:1 correlation. The QEMSCAN<sup>®</sup> fieldscan image does not allow user to quantitatively interpret spatial correlation between minerals (textural analysis),

therefore only visual qualitative correlation is made. Importantly the QEMSCAN<sup>®</sup> fieldscan does not measure empty spaces covered only by resin, if a pixel point occurs where there is no sample, then a measurement is not taken there.

Individual NIR sensitive minerals are extracted from the composite image and placed side by side for comparison. From visual examination, results obtained show that most samples display spatial association between chrysocolla and hematite (Table 4.4). In most cases, samples exhibiting such association have their levels of chrysocolla in spatial agreement with that of hematite as observed from the fieldscan images (Table 4.4). With exception of samples 7, 13, 14, 21, 58 and 59 where hematite occurs without chrysocolla, and sample 50 where chrysocolla occurs without hematite, these minerals (hematite and chrysocolla) occur as though they lay on each other, sometimes finely mixed and covering nearly the same space. Therefore, statistically, 88 % of samples analysed show this hematite-chrysocolla spatial association. Also with exception of samples 6, 7, 13, 14, 21, 58 and 59 almost all samples containing hematite above 10 wt % contain appreciable concentration of chrysocolla above 1.5 wt % (1.5 wt % of chrysocolla contain approximately 0.5 % copper content).

Figure 4.2, shows the correlation pattern between hematite and chrysocolla. The correlation reveals that twelve samples (samples 1, 2, 3, 4, 8, 9, 10, 11, 12, 48, 51 and 60) contain hematite above 10 wt % and chrysocolla above 1.5 %. Nine samples (samples 5, 17, 26, 28, 32, 35, 50, 55 and 57) also contain chrysocolla 1.5 % and above, but low hematite (below 10 wt %). With exception of sample 50, fieldscan images (Table 4.4) of these samples reveal an even spatial occurrence of both hematite and chrysocolla in the respective samples. Also from Figure 4.2, eight samples (samples 6, 7, 13, 14, 21, 52, 58 and 59) contain hematite above 10 wt % but only two of these (samples 6 and 14) contain chrysocolla above 1 wt % (i.e. approximately 0.34 % of copper). Thirty two samples classified as low chrysocolla (< 1.5 %) and low hematite (< 10 wt %) with most of them plotting near the origin.

Other spatial mineral associations are also observed, but their occurrence(s) are limited to a few samples. Examples of such associations include chrysocolla-chlorite (sample 50). The chrysocolla-chlorite association is of particular

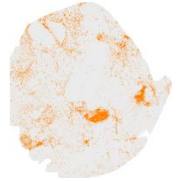
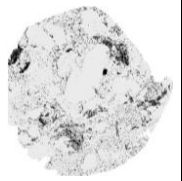
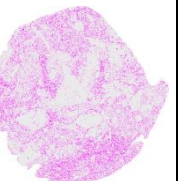
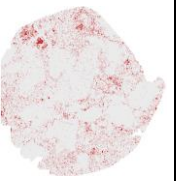
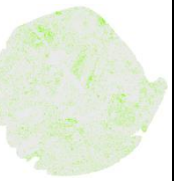


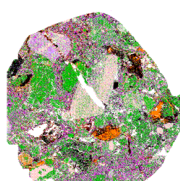
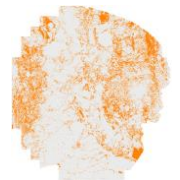
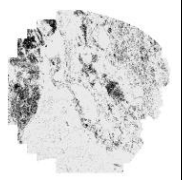
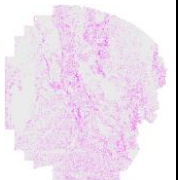
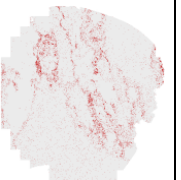



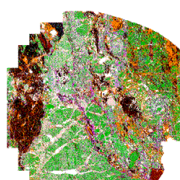
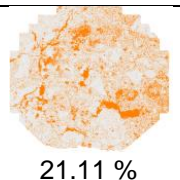
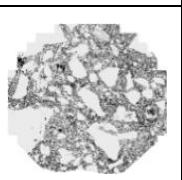
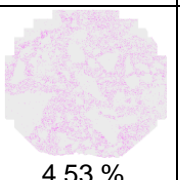
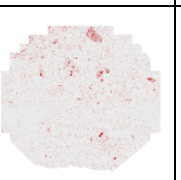
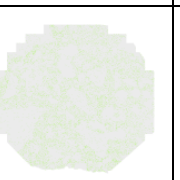
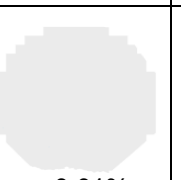

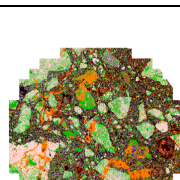
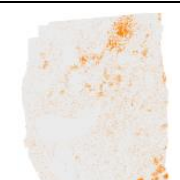
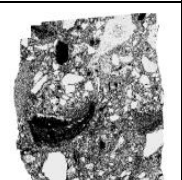

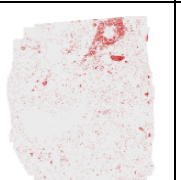


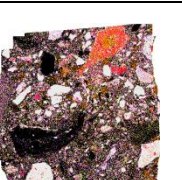
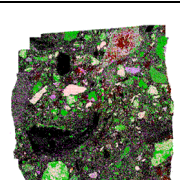
importance, since chlorite is one of the dominant NIR-active minerals occurring in almost all samples (thus chlorite cannot be regarded as waste). Other similarities between these two minerals (chlorite and chrysocolla) will be explored towards developing a preconcentration strategy. Other associations include: biotite-hematite-chrysocolla (sample 1, 4, 7, 10, 11, 13, 48 and 57), biotite-hematite (samples 15, 19, 38, 48, 51, 55, 59 and 60), and biotite-chlorite (samples 4, 5, 7, 8, 10, 14, 15, 16, 22, 36, 37, 39, 45, 54 and 56). Spatial association is also observed for biotite-chlorite-calcite (samples 9 and 15), biotite-calcite (sample 6, 51, 55, 56, and 57), biotite-hematite-chlorite (samples 11 and 21), chlorite-calcite (sample 25 and 54), muscovite-calcite (samples 27, 29, 49, 52 and 56), and muscovite-biotite (samples 20, 33, 35, 52, 55, 56 and 57). Other spatial associations include biotite-muscovite-calcite (samples 19, 42 and 43) and biotite-muscovite-chlorite (samples 5 and 10).

Only few samples display a clear spatial mineral differentiation, where single NIR-active minerals stand out clear above others. Examples of such minerals and samples are chlorite (samples 17, 23, 28, 30, 32, 34, 39 and 40) and muscovite (samples 18, and 24).


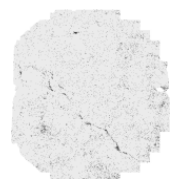
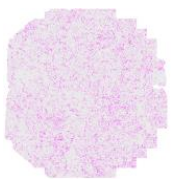
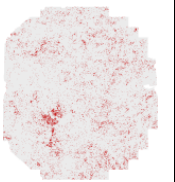


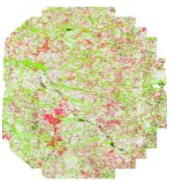
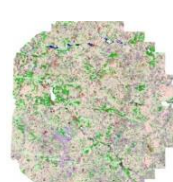

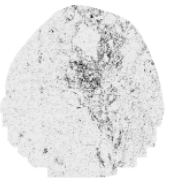



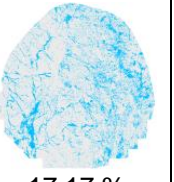
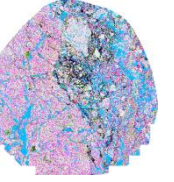


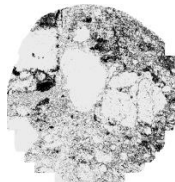
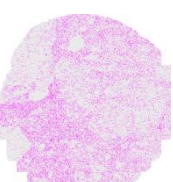
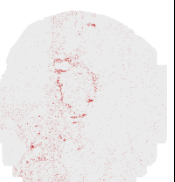


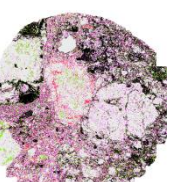
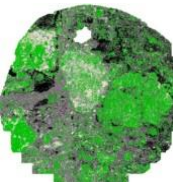
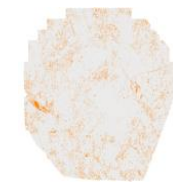
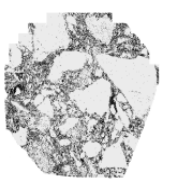





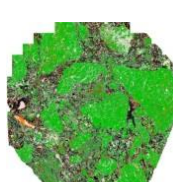
Given the dominant hematite-chrysocolla association, exploring the possible means of preconcentrating these minerals together will lead to economic concentration. Also a strategy that will incorporate chlorite-chrysocolla association may improve recovery since chlorite is not necessarily an acid consuming mineral (Lu et al., 2000). Note that all the samples exhibiting biotite-hematite-chrysocolla associations also fall within the hematite-chrysocolla association.

Though gold was not analysed for, the spatial association between hematite and chrysocolla confirms the origin and classification of the Mantoverde deposit as a hypogene iron oxide-copper-gold deposit (IOCG) (Villa 1996; Benavides et al., 2007; Rieger et al., 2010).

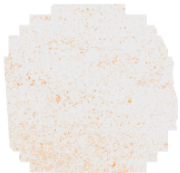
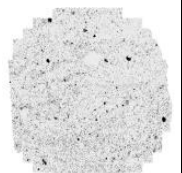

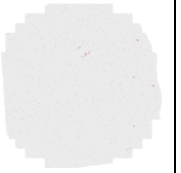
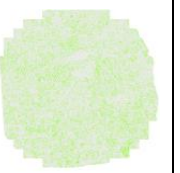
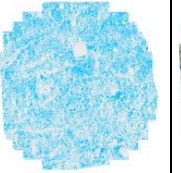
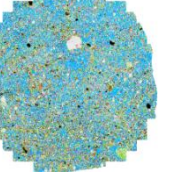

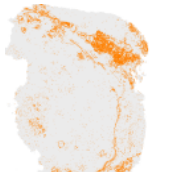
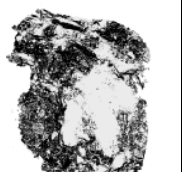
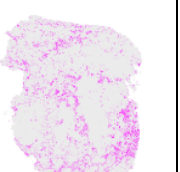
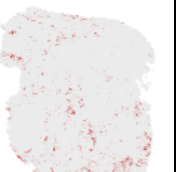


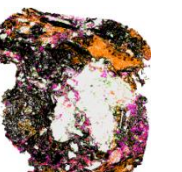


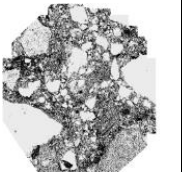
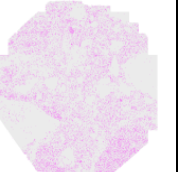
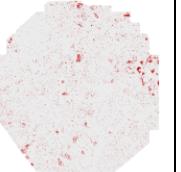
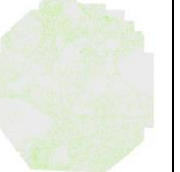


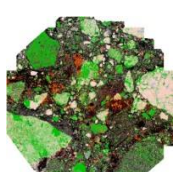
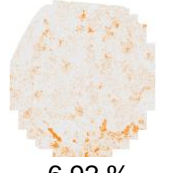
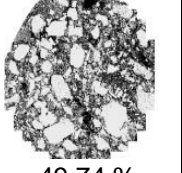
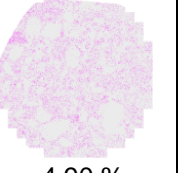
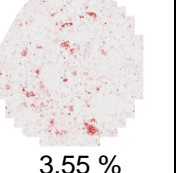
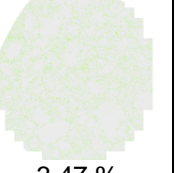
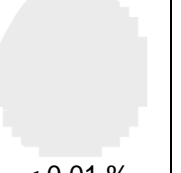

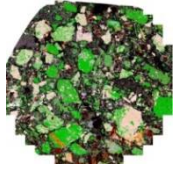
Table 4.4 - NIR-active mineral association mapping of Mantoverde copper ore particles

Sample ID	Chrysocolla	Hematite	Biotite	Muscovite	Chlorite	Calcite	Combined NIR Sensitive minerals	Composite Fieldscan (All Minerals)
1	 8.33 %	 16.63 %	 15.54 %	 5.95 %	 8.87 %	 0.01 %		
2	 19.05 %	 19.90 %	 8.32 %	 3.79 %	 6.68 %	 0.01 %		
3	 21.11 %	 31.77 %	 4.53 %	 2.96 %	 3.08 %	 < 0.01%		
4	 5.14 %	 55.32 %	 7.30 %	 3.28 %	 5.13 %	 < 0.01 %		

Cont. of Table 4.4 - NIR-active mineral association mapping of Mantoverde copper ore particles


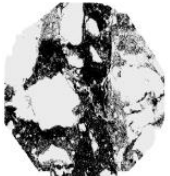
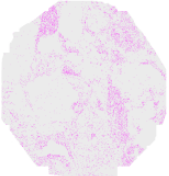
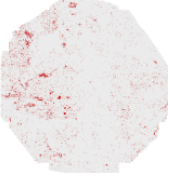

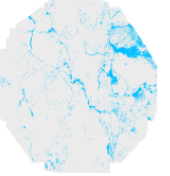
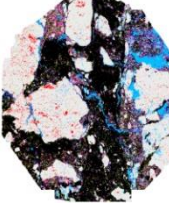
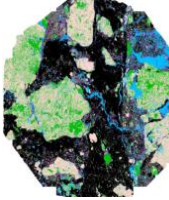

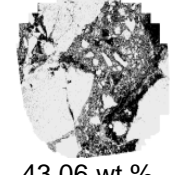

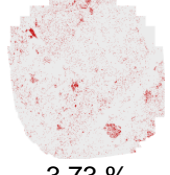

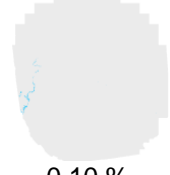
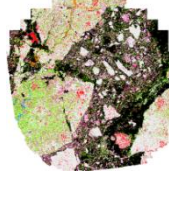
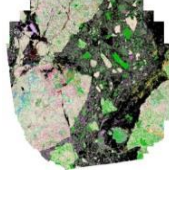

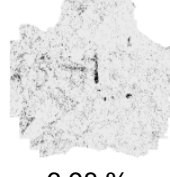
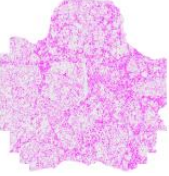




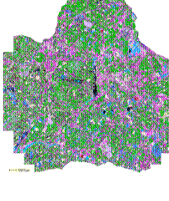
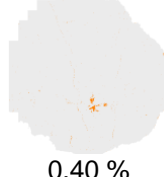
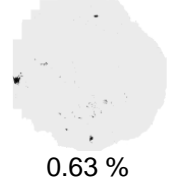
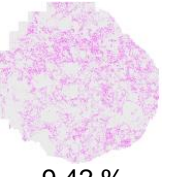
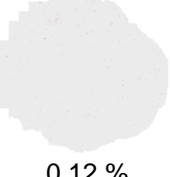
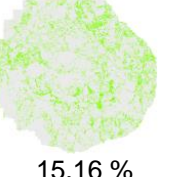
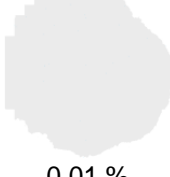
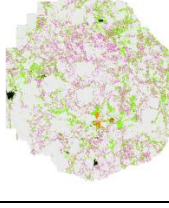
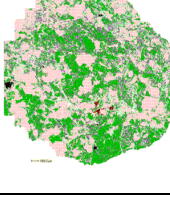
Sample ID	Chrysocolla	Hematite	Biotite	Muscovite	Chlorite	Calcite	Combined NIR Sensitive minerals	Composite Fieldscan (All Minerals)
5	 3.29%	 3.72%	 8.38 %	 5.34 %	 24.87 %	 0.02 %		
6	 1.09 %	 10.37 %	 15.32 %	 1.00 %	 6.64 %	 17.17 %		
7	 0.15 %	 29.03 %	 13.01 %	 1.55 %	 8.74 %	 0.01 %		
8	 5.58 %	 28.47 wt %	 5.96 %	 0.22 %	 15.76 %	 0.01 %		

Cont. of Table 4.4 - NIR-active mineral association mapping of Mantoverde copper ore particles

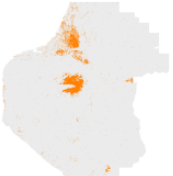
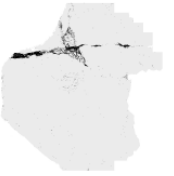


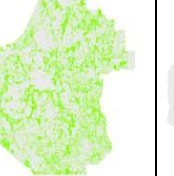

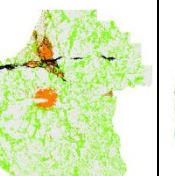
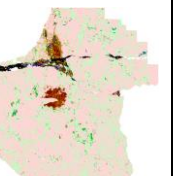
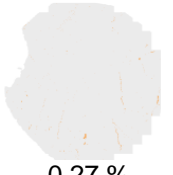
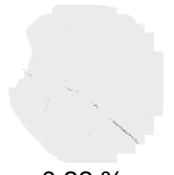
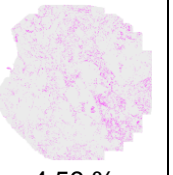
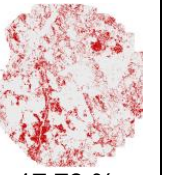

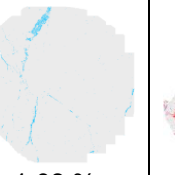
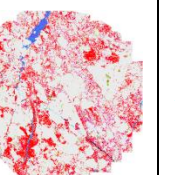
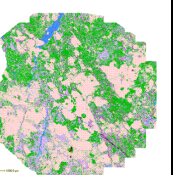

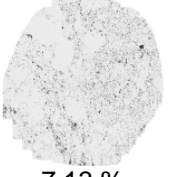
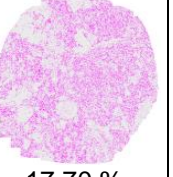
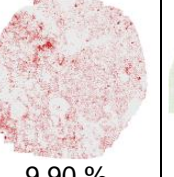
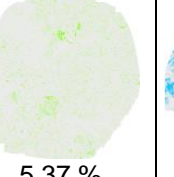
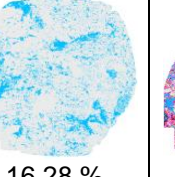
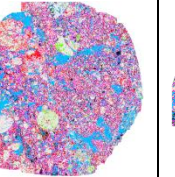
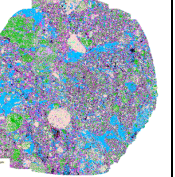
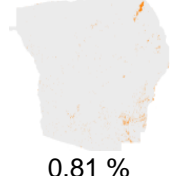
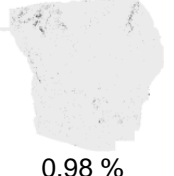
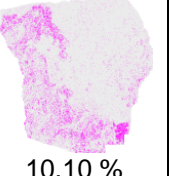
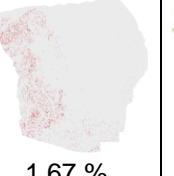
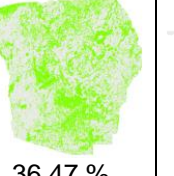
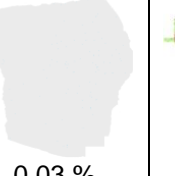
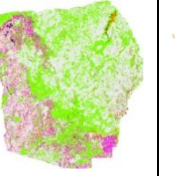
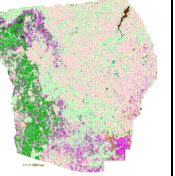
Sample ID	Chrysocolla	Hematite	Biotite	Muscovite	Chlorite	Calcite	Combined NIR Sensitive minerals	Composite Fieldscan (All Minerals)
9	 3.98 %	 11.66 %	 6.72 %	 0.26 %	 14.12 %	 31.61 %		
10	 7.78 %	 62.04 %	 5.86 %	 1.62 %	 4.47 %	 < 0.01 %		
11	 9.31 %	 43.17 %	 5.46 %	 2.67 %	 4.66 %	 < 0.01 %		
12	 6.92 %	 49.74 %	 4.90 %	 3.55 %	 3.47 %	 < 0.01 %		




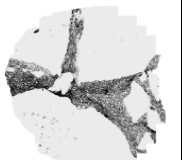




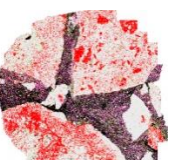



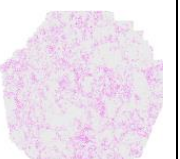









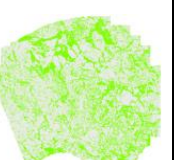

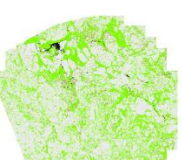



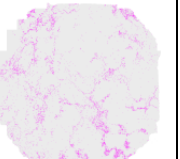
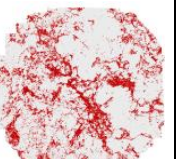


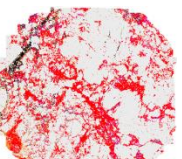
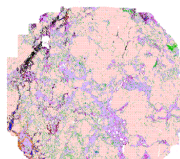
Cont. of Table 4.4 - NIR-active mineral association mapping of Mantoverde copper ore particles

Sample ID	Chrysocolla	Hematite	Biotite	Muscovite	Chlorite	Calcite	Combined NIR Sensitive minerals	Composite Fieldscan (All Minerals)
13	 <0.01 %	 53.44 %	 3.33 %	 2.31 %	 2.99 %	 5.08 %		
14	 1.19 %	 43.06 wt %	 6.71 %	 3.73 %	 13.43	 0.10 %		
15	 < 0.01%	 6.98 %	 22.89 %	 8.38 %	 10.85 %	 3.77 %		
16	 0.40 %	 0.63 %	 9.42 %	 0.12 %	 15.16 %	 0.01 %		


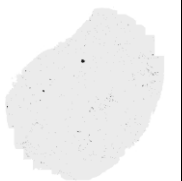
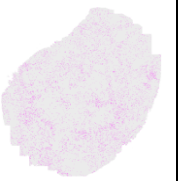


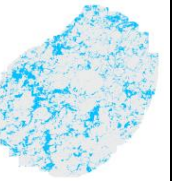
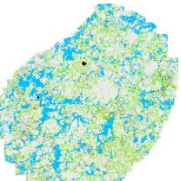

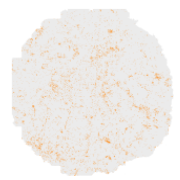
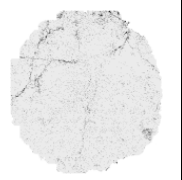
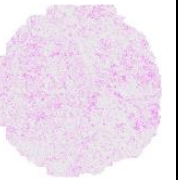
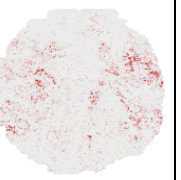
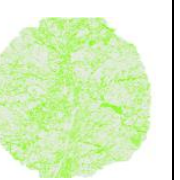

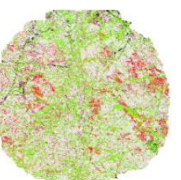
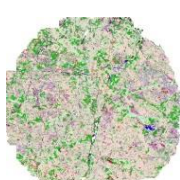


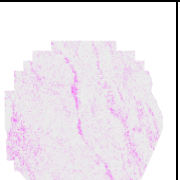
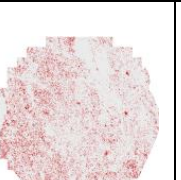

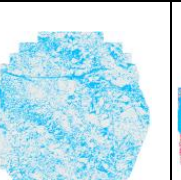
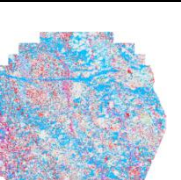

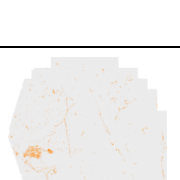
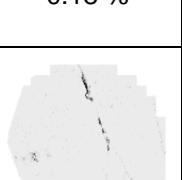

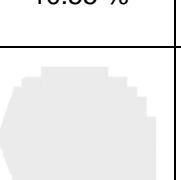
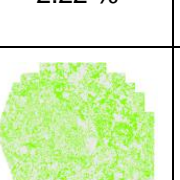
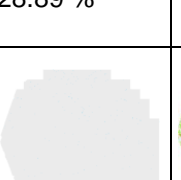
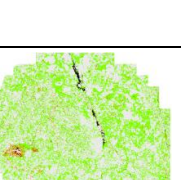

Cont. of Table 4.4 - NIR-active mineral association mapping of Mantoverde copper ore particles

Sample ID	Chrysocolla	Hematite	Biotite	Muscovite	Chlorite	Calcite	Combined NIR Sensitive minerals	Composite Fieldscan (All Minerals)
17	 3.46 %	 3.41 %	 0.51 %	 0.02 %	 25.61 %	 0.02 %		
18	 0.27 %	 0.22 %	 4.59 %	 17.73 %	 2.45 %	 1.08 %		
19	 0.45 %	 7.13 %	 17.70 %	 9.90 %	 5.37 %	 16.28 %		
20	 0.81 %	 0.98 %	 10.10 %	 1.67 %	 36.47 %	 0.03 %		


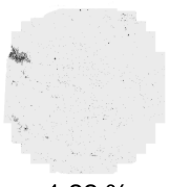
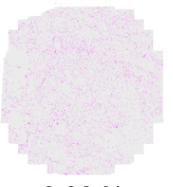
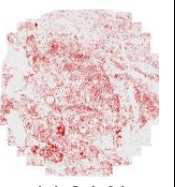

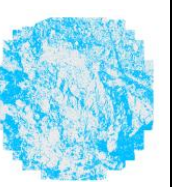
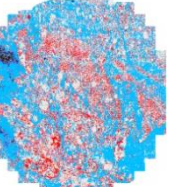
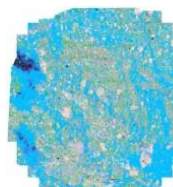


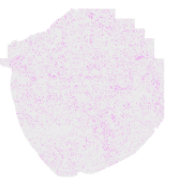

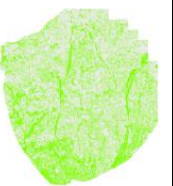



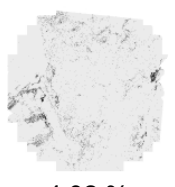

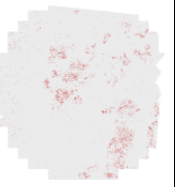
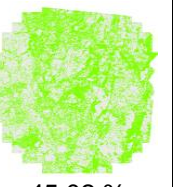


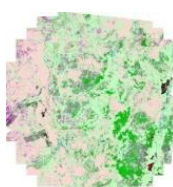






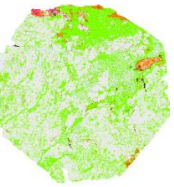
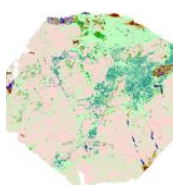
Cont. of Table 4.4 - NIR-active mineral association mapping of Mantoverde copper ore particles

Sample ID	Chrysocolla	Hematite	Biotite	Muscovite	Chlorite	Calcite	Combined NIR Sensitive minerals	Composite Fieldscan (All Minerals)
21	 0.07 %	 19.18 %	 4.77 %	 18.82 %	 4.20 %	 < 0.01 %		
22	 0.08 %	 0.12 %	 6.99 %	 0.25 %	 11.25 %	 0.01 %		
23	 0.05 %	 0.89 %	 1.78 %	 0.05 %	 33.81 %	 0.03 %		
24	 1.23 %	 2.92 %	 3.46 %	 21.55 %	 1.33 %	 0.01 %		


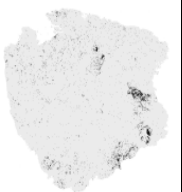
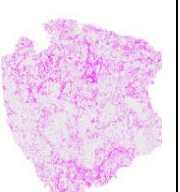
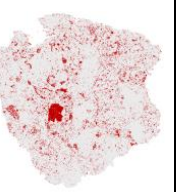
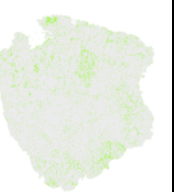
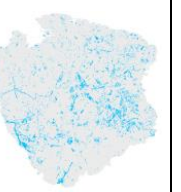
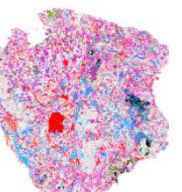

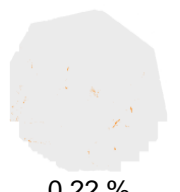

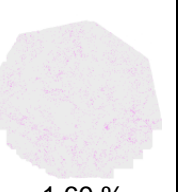

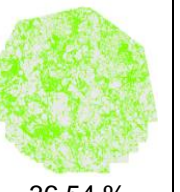

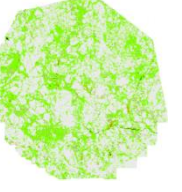
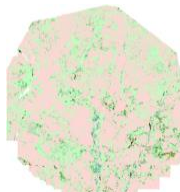
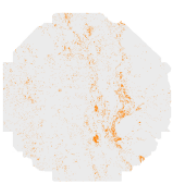
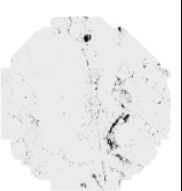
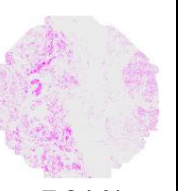
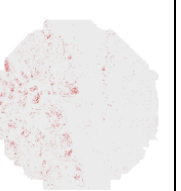
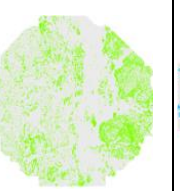
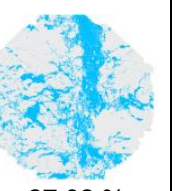
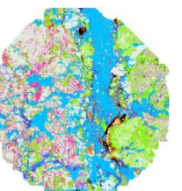
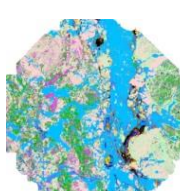






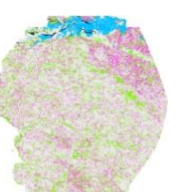

Cont. of Table 4.4 - NIR-active mineral association mapping of Mantoverde copper ore particles

Sample ID	Chrysocolla	Hematite	Biotite	Muscovite	Chlorite	Calcite	Combined NIR Sensitive minerals	Composite Fieldscan (All Minerals)
25	 0.36 %	 0.51 %	 3.36 %	 0.10 %	 17.66 %	 18.81 %		
26	 3.26 %	 4.13 %	 8.47 %	 4.14 %	 26.35 %	 0.02 %		
27	 <0.01 %	 0.18 %	 5.08 %	 10.55 %	 2.22 %	 28.89 %		
28	 1.64 %	 1.03 %	 0.84 %	 <0.01 %	 35.08 %	 0.05 %		



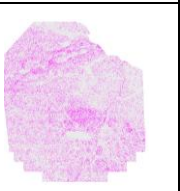

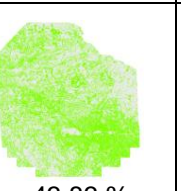

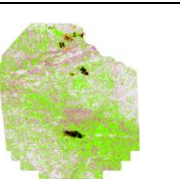

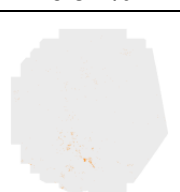

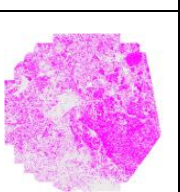

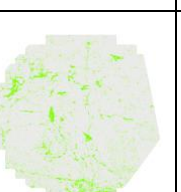
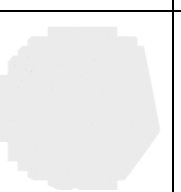
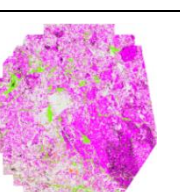
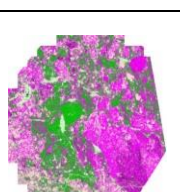
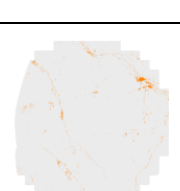
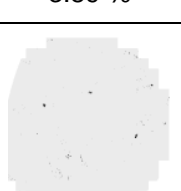
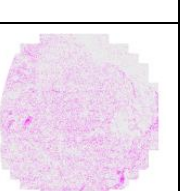
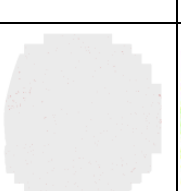
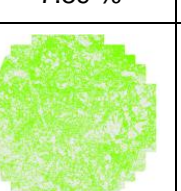
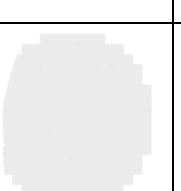
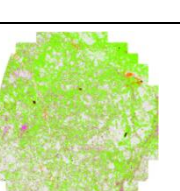
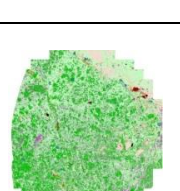

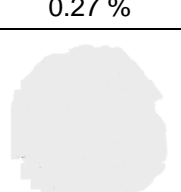

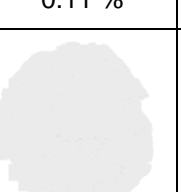
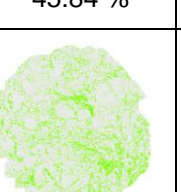
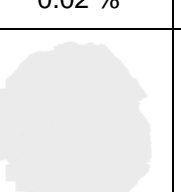
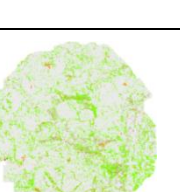
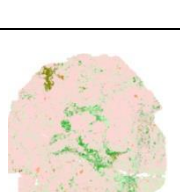
Cont. of Table 4.4 - NIR-active mineral association mapping of Mantoverde copper ore particles

Sample ID	Chrysocolla	Hematite	Biotite	Muscovite	Chlorite	Calcite	Combined NIR Sensitive minerals	Composite Fieldscan (All Minerals)
29	 0.21 %	 1.22 %	 3.06 %	 14.84 %	 1.27 %	 38.82 %		
30	 0.08 %	 1.16 %	 3.54 %	 0.14 %	 35.29 %	 0.02 %		
31	 0.27 %	 4.02 %	 5.93 %	 1.62 %	 45.02 %	 0.05 %		
32	 2.05 %	 0.74 %	 1.16 %	 0.22 %	 34.74 %	 0.35 %		


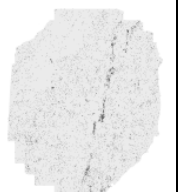


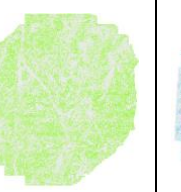
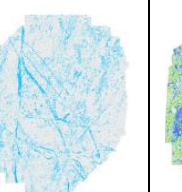
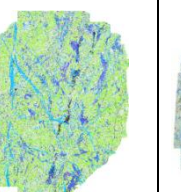
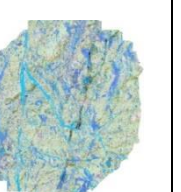
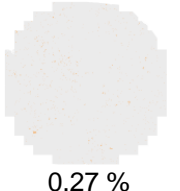
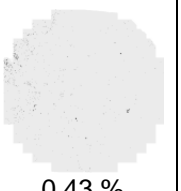
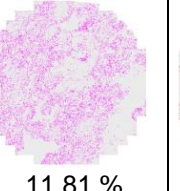
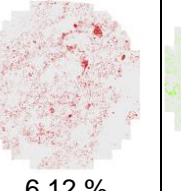
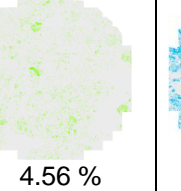
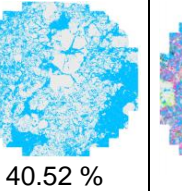
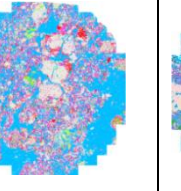
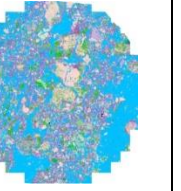
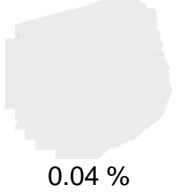
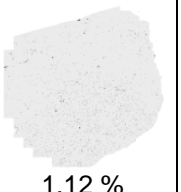
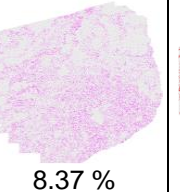
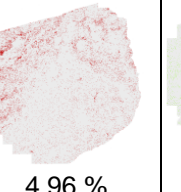
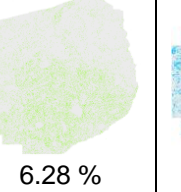
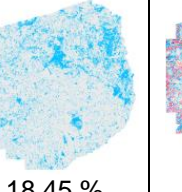
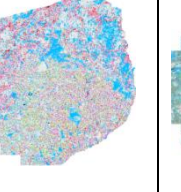
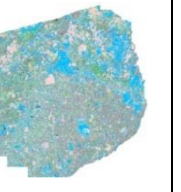
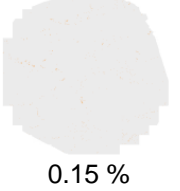
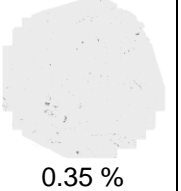
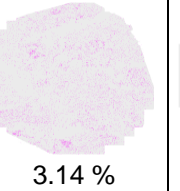
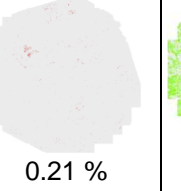
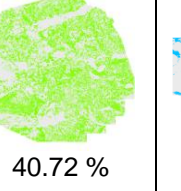
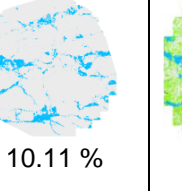
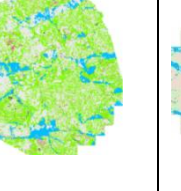
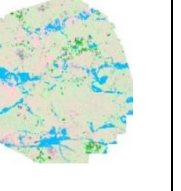
Cont. of Table 4.4 - NIR-active mineral association mapping of Mantoverde copper ore particles

Sample ID	Chrysocolla	Hematite	Biotite	Muscovite	Chlorite	Calcite	Combined NIR Sensitive minerals	Composite Fieldscan (All Minerals)
33	 0.00 %	 3.05 %	 16.28 %	 11.26 %	 5.24 %	 8.01 %		
34	 0.22 %	 0.26 %	 1.69 %	 0.04 %	 36.54 %	 0.05 %		
35	 2.98 %	 3.08 %	 7.24 %	 1.65 %	 19.10 %	 27.02 %		
36	 0.02 %	 0.73 %	 12.15 %	 0.54 %	 16.30 %	 3.78 %		

Cont. of Table 4.4 - NIR-active mineral association mapping of Mantoverde copper ore particles





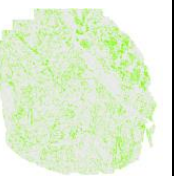
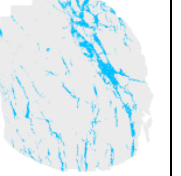





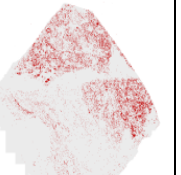

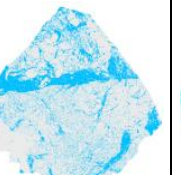
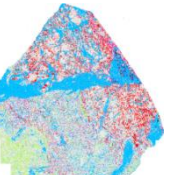



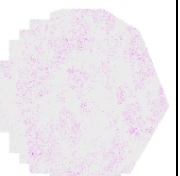


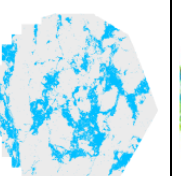


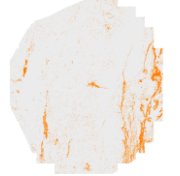

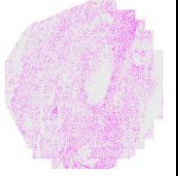
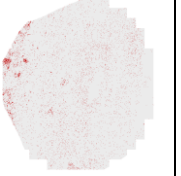
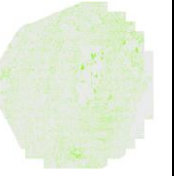
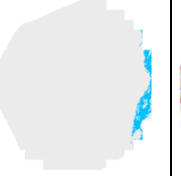

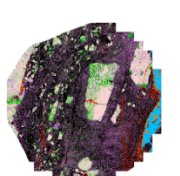
Sample ID	Chrysocolla	Hematite	Biotite	Muscovite	Chlorite	Calcite	Combined NIR Sensitive minerals	Composite Fieldscan (All Minerals)
37	 0.82 %	 1.72 %	 15.69 %	 0.08 %	 43.83 %	 0.01 %		
38	 0.18 %	 3.89 %	 40.82 %	 1.41 %	 7.89 %	 0.03 %		
39	 0.98 %	 0.27 %	 10.24 %	 0.11 %	 45.84 %	 0.02 %		
40	 0.89 %	 0.02 %	 1.59 %	 0.06 %	 19.61 %	 0.01 %		

Cont. of Table 4.4 - NIR-active mineral association mapping of Mantoverde copper ore particles


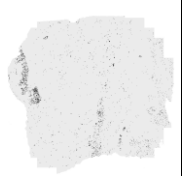

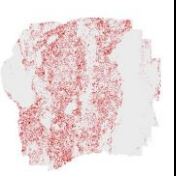

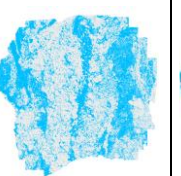
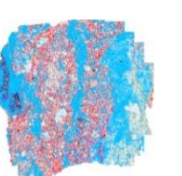

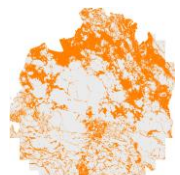


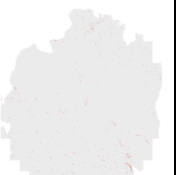
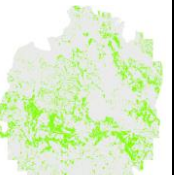
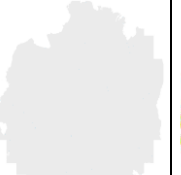

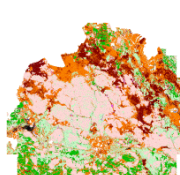
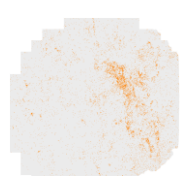
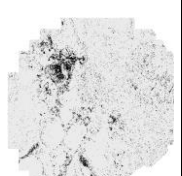
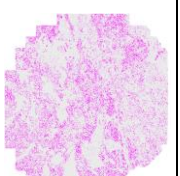
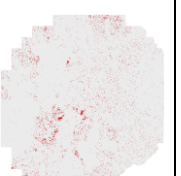
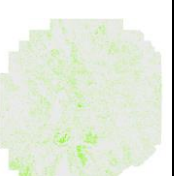
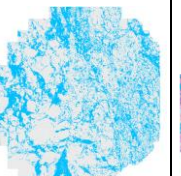
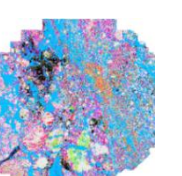
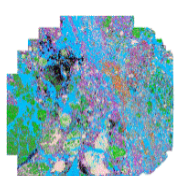

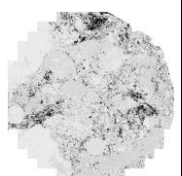
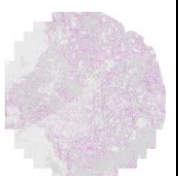
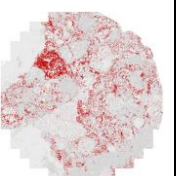
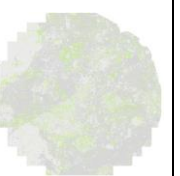
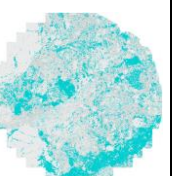
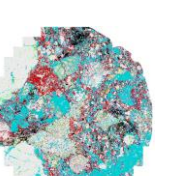
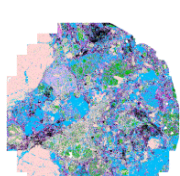
Sample ID	Chrysocolla	Hematite	Biotite	Muscovite	Chlorite	Calcite	Combined NIR Sensitive minerals	Composite Fieldscan (All Minerals)
41	 < 0.0 %	 3.48 %	 2.95 %	 0.00 %	 23.19 %	 13.10 %		
42	 0.27 %	 0.43 %	 11.81 %	 6.12 %	 4.56 %	 40.52 %		
43	 0.04 %	 1.12 %	 8.37 %	 4.96 %	 6.28 %	 18.45 %		
44	 0.15 %	 0.35 %	 3.14 %	 0.21 %	 40.72 %	 10.11 %		



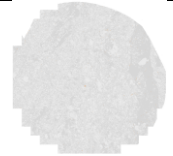
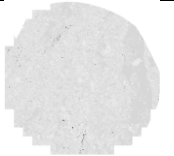

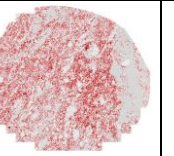

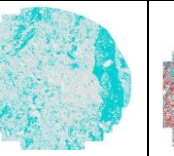
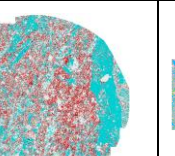
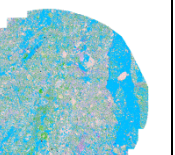
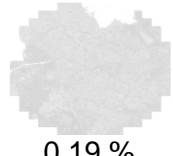
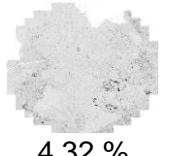
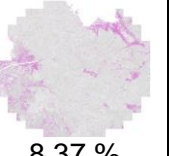
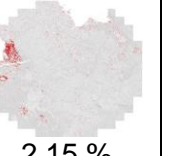
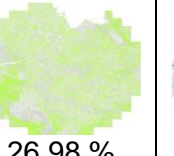
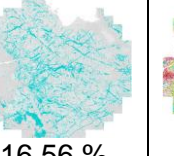
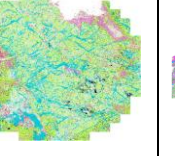
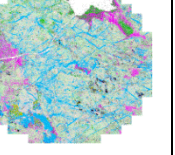

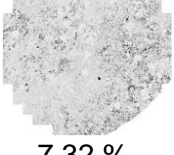
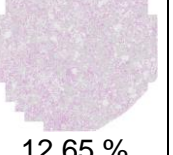
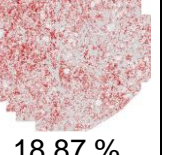
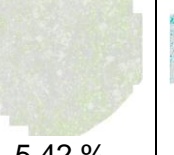
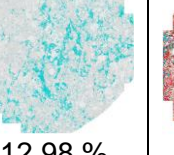
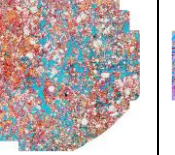
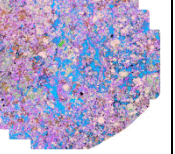
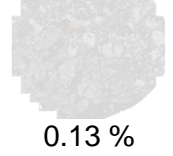
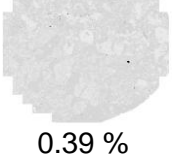
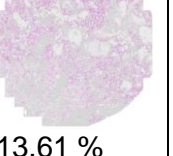
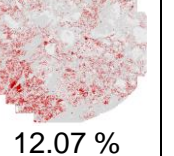
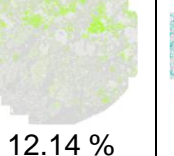
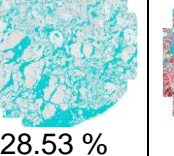
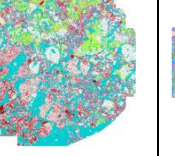
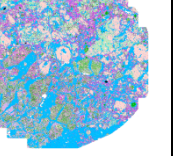
Cont. of Table 4.4 - NIR-active mineral association mapping of Mantoverde copper ore particles

Sample ID	Chrysocolla	Hematite	Biotite	Muscovite	Chlorite	Calcite	Combined NIR Sensitive minerals	Composite Fieldscan (All Minerals)
45	 0.54 %	 2.38 %	 7.00 %	 0.16 %	 15.58 %	 8.55 %		
46	 0.13 %	 0.95 %	 3.91 %	 8.37 %	 4.86 %	 25.81 %		
47	 1.33 %	 4.46 %	 2.74 %	 0.10 %	 31.10 %	 22.64 %		
48	 4.12 %	 59.78 %	 8.79 %	 1.68 %	 6.65 %	 1.93 %		

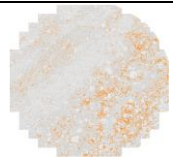
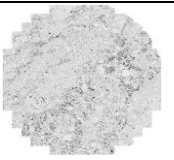
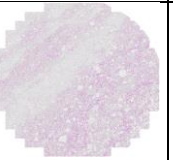
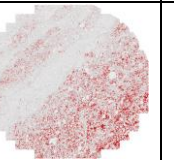
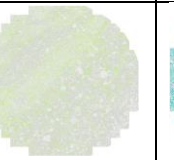
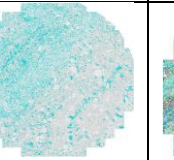
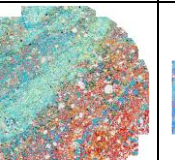


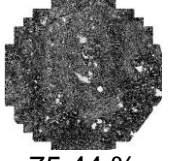

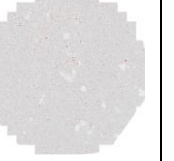
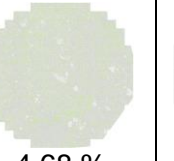
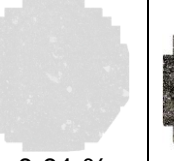

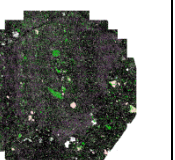

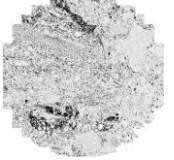
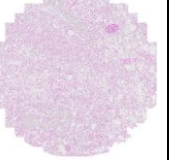
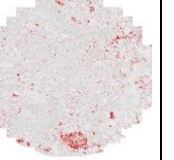

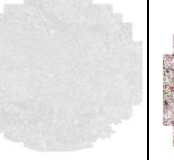
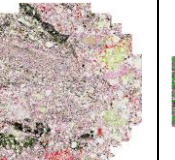
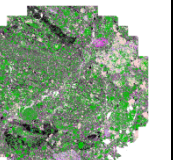

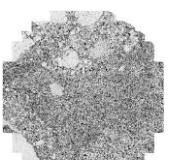

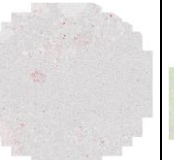

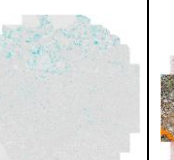


Cont. of Table 4.4 - NIR-active mineral association mapping of Mantoverde copper ore particles

Sample ID	Chrysocolla	Hematite	Biotite	Muscovite	Chlorite	Calcite	Combined NIR Sensitive minerals	Composite Fieldscan (All Minerals)
49	 0.38 %	 1.90 %	 3.38%	 12.95 %	 1.63 %	 42.12 %		
50	 34.06 %	 0.59 %	 2.37 %	 0.25 %	 16.85 %	 0.01 %		
51	 2.96 %	 9.84 %	 14.26 %	 2.11 %	 7.08 %	 29.03 %		
52	 0.04 %	 12.48 %	 9.56 %	 9.97 %	 4.82 %	 25.01 %		

Cont. of Table 4.4 - NIR-active mineral association mapping of Mantoverde copper ore particles

Sample ID	Chrysocolla	Hematite	Biotite	Muscovite	Chlorite	Calcite	Combined NIR Sensitive minerals	Composite Fieldscan (All Minerals)
53	 0.04 %	 0.27 %	 2.24 %	 22.16 %	 1.04 %	 29.68 %		
54	 0.19 %	 4.32 %	 8.37 %	 2.15 %	 26.98 %	 16.56 %		
55	 5.20 %	 7.32 %	 12.65 %	 18.87 %	 5.42 %	 12.98 %		
56	 0.13 %	 0.39 %	 13.61 %	 12.07 %	 12.14 %	 28.53 %		

Cont. of Table 4.4 - NIR-active mineral association mapping of Mantoverde copper ore particles

Sample ID	Chrysocolla	Hematite	Biotite	Muscovite	Chlorite	Calcite	Combined NIR Sensitive minerals	Composite Fieldscan (All Minerals)
57	 6.33 %	 8.77 %	 9.97 %	 9.90 %	 8.39 %	 17.08 %		
58	 <0.01 %	 75.44 %	 6.38 %	 0.87 %	 4.68 %	 <0.01 %		
59	 0.10 %	 21.03 %	 18.22 %	 4.58 %	 9.95 %	 0.01 %		
60	 5.84 %	 40 %	 12.89 %	 1.24 %	 8.29 %	 1.49 %		

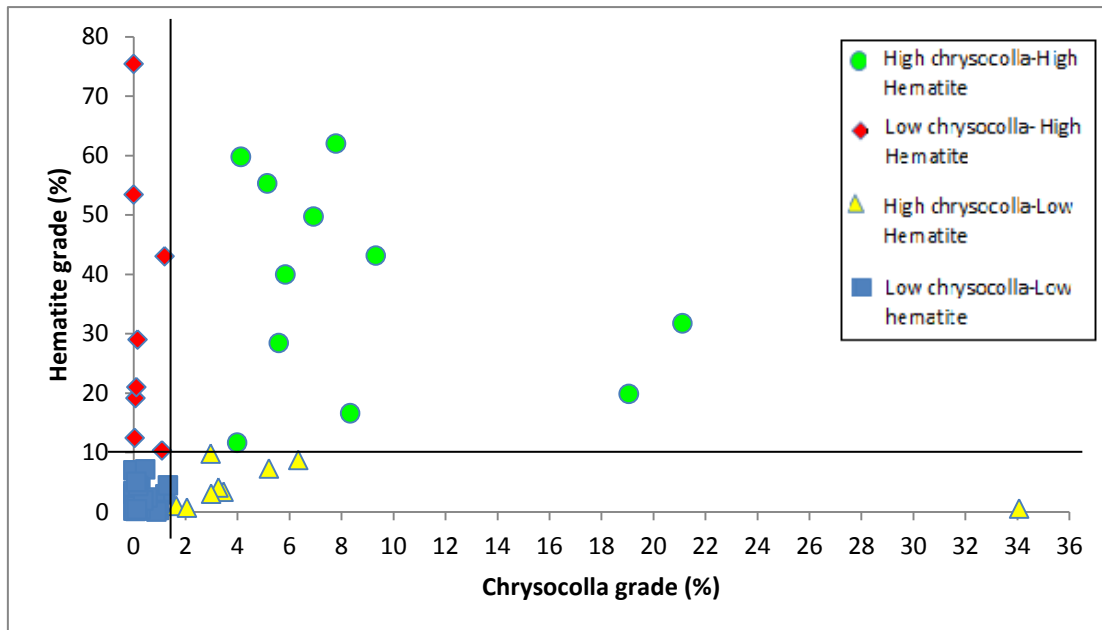


Figure 4.2 - Segmentation of chrysocolla and hematite grades, for individual particles from NIR-active minerals association mapping

#### 4.4. Functional groups

The bulk hydroxyl (-OH) and carbonate ( $\text{CO}_3^{2-}$ ) content are calculated from individual constituent NIR-active minerals in each sample and values are presented in Table 4.5, alongside hematite and bulk copper values. All calculations for functional groups are done with reference to values from webmineral.com (2013). Chrysocolla contain 20.71 % -OH and 33.86 % Cu, malachite contain 15.38 % -OH, 57.48 % Cu, and 27.13 %  $\text{CO}_3^{2-}$ . Muscovite and kaolinite contain 8.53 % and 26.34 % -OH respectively. Biotite and chlorite contain 7.84 and 22.85 % -OH respectively. Tourmaline contains 6.61 % -OH. Apatite contains 3.34 % -OH while calcite contains 59.95 % carbonate. Ankerite contains 58.14 % carbonate

The inclusion of copper and hematite values as stated earlier is due to the fact that copper preconcentration is the subject of investigation using NIR spectroscopy. Since hematite is observed to occur in the ore, though it contains no related NIR absorbing functional groups, studies have shown that hematite absorbs NIR radiation across wavelengths by reducing the overall brightness of spectra without a specific wavelength band centre of its own (Bishop and Dummel 1996, Iyakwari and Glass 2015). Also, investigations of mineral

associations (above) have revealed spatial association between hematite and chrysocolla. On this basis, it is therefore important to study the functional groups in each sample as this will inform the choice of samples to be targeted for acceptance as concentrate or rejected as tailings, in designing a strategy for classification and subsequent separation. This study will inform the economics of the discrimination strategy, since leaching will be the next/final stage of copper extraction. It is worthy to note that functional groups like  $\text{CO}_3^{2-}$  tends to consume acid while groups like -OH especially the clays adsorb acid due to their impermeable nature (Gupta, 2003).

Analysis of the sixty samples, reveal that only twenty nine samples (about 48 % of the total samples) contain the  $\text{CO}_3^{2-}$  group. Out of the twenty nine samples, twenty samples (samples 6, 9, 19, 25, 27, 29, 35, 41, 42, 43, 46, 47, 49, 51, 52, 53, 54, 55, 56 and 57) contain  $\text{CO}_3^{2-}$  group concentration above 10 % with sample 49 having the highest concentration of 26 % (Table 4.5). The remaining nine samples (samples 13, 15, 18, 33, 36, 44, 45, 48 and 60) contain  $\text{CO}_3^{2-}$  concentration below 7 % (Table 4.5). All samples mentioned above to contain high  $\text{CO}_3^{2-}$  concentration also contain high calcite (Table 4.1). Therefore, the  $\text{CO}_3^{2-}$  is dominantly from calcite.

The ore is dominated by silicate minerals and the main copper bearing mineral is chrysocolla which is a phyllosilicate. Therefore, it also contains the -OH functional group. Though only four samples show the -OH concentration above 10 % (samples, 31, 37, 39 and 50), all samples contain the -OH functional group (Table 4.5). With the exception of sample 50 which owes its high -OH concentration to chrysocolla (34 %), contributing about 7 % of its 11 % total -OH, all the other high -OH containing samples are dominantly as a result of their chlorite concentration, with minor contributions from the other -OH bearing minerals (Table 4.1 and 4.5).

Twenty three samples (samples 1, 2, 3, 4, 5, 8, 9, 10, 11, 12, 17, 24, 26, 28, 32, 35, 47, 48, 50, 51, 55, 57 and 60) contain copper above 0.5 %. Only eight samples (samples 9, 35, 47, 48, 51, 55, 57 and 60) out of the twenty three contain  $\text{CO}_3^{2-}$  concentration above 1 % (Table 4.5). All the eight samples with  $\text{CO}_3^{2-}$  above 1 % are also high calcite bearing. Thirteen samples (samples 1, 2, 3, 5, 9, 17, 26, 28, 32, 35, 47, 55 and 57) out of the twenty three copper bearing

samples contain -OH group above 5 % but below 10 % with the highest concentration of 8.80 % for sample 32 (Table 4.5). Only one sample (sample 50) out of the copper bearing samples contains -OH above 10 %. Same sample (sample 50), has the highest copper concentration of 11.54 % (Tables 4.2 and 4.5).

Considering hematite, nineteen samples (samples 1, 2, 3, 4, 6, 7, 8, 9, 10, 11, 12, 13, 14, 21, 48, 52, 58, 59 and 60) contain hematite above 10 wt %. Of all the nineteen hematite-bearing samples, only six samples, i.e. samples 6, 9, 13, 48, 52 and 60 contain  $\text{CO}_3^{2-}$  above 1 %. The remaining eleven samples contain little (i.e. < 0.5 %) or no  $\text{CO}_3^{2-}$  concentration (Table 4.5). With the exception of samples 6, 7, 13, 14, 21, 52, 58 and 59, the remaining eleven hematite bearing samples contain copper above 0.5 %, with concentration ranging from 1.75 % (sample 4) to 7.33 % (sample 3) (Table 4.5).

Table 4.5 - Calculated modal composition (wt %) of carbonate and hydroxyl functional groups, copper and hematite minerals, with reference to webmineral.com (2013).

Sample ID	Hydroxyls							Carbonates				Oxides	Cumulative -OH	Cumulative CO <sub>3</sub> <sup>2-</sup>	Copper
	Percentage functional groups														
	8.53% -OH	7.84% -OH	26.34% -OH	22.85% -OH	6.61% -OH	20.71% -OH	3.34% -OH	15.38% -OH	27.13% CO <sub>3</sub> <sup>2-</sup>	59.95% CO <sub>3</sub> <sup>2-</sup>	58.14% CO <sub>3</sub> <sup>2-</sup>	Hematite			
Muscovite	Biotite	Kaolinite	Chlorite	Tourmaline	Chrysocolla	Apatite	Malachite	Calcite	Ankerite	Hematite	Cumulative -OH	Cumulative CO <sub>3</sub> <sup>2-</sup>	Copper		
1	0.51	1.22	0.00	2.03	0.03	1.73	0.01	0.00	0.00	0.01	0.01	16.63	5.53	0.02	2.83
2	0.32	0.65	0.00	1.53	0.02	3.95	0.01	0.00	0.00	0.00	0.03	19.90	6.48	0.03	6.46
3	0.25	0.35	0.01	0.70	0.00	4.37	0.00	0.05	0.08	0.00	0.00	31.77	5.73	0.08	7.33
4	0.28	0.57	0.18	1.17	0.05	1.06	0.00	0.00	0.00	0.00	0.00	55.32	3.31	0.00	1.75
5	0.46	0.66	0.00	5.68	0.04	0.68	0.02	0.15	0.27	0.01	0.03	3.72	7.69	0.31	1.70
6	0.09	1.20	0.00	1.52	0.01	0.23	0.00	0.00	0.00	10.29	1.67	10.37	3.05	11.96	0.41
7	0.13	1.02	0.00	2.00	0.03	0.03	0.01	0.00	0.00	0.01	0.03	29.03	3.22	0.04	0.05
8	0.02	0.47	0.00	3.60	0.01	1.16	0.01	0.00	0.00	0.00	0.01	28.47	5.27	0.01	1.90
9	0.02	0.53	0.00	3.23	0.10	0.82	0.01	0.21	0.37	18.95	2.36	11.66	4.92	21.68	2.28
10	0.14	0.46	0.00	1.02	0.01	1.61	0.00	0.24	0.42	0.00	0.01	62.04	3.48	0.43	3.55
11	0.23	0.43	0.09	1.06	0.01	1.93	0.00	0.00	0.00	0.00	0.00	43.17	3.75	0.00	3.15
12	0.30	0.38	0.11	0.79	0.02	1.43	0.00	0.00	0.00	0.00	0.00	49.74	3.03	0.00	2.34
13	0.20	0.26	0.01	0.68	0.00	0.00	0.00	0.00	0.00	3.04	1.18	53.44	1.15	4.22	0.00
14	0.32	0.53	0.31	3.07	0.16	0.25	0.00	0.00	0.00	0.06	0.03	43.06	4.64	0.09	0.40
15	0.72	1.79	0.01	2.48	0.00	0.00	0.00	0.00	0.00	2.26	1.53	6.98	5.00	3.79	0.00
16	0.01	0.74	0.00	3.46	0.00	0.08	0.01	0.00	0.00	0.00	0.00	0.63	4.30	0.00	0.14
17	0.00	0.04	0.00	5.85	0.01	0.72	0.01	0.06	0.10	0.01	0.00	3.41	6.69	0.11	1.41
18	1.51	0.36	0.00	0.56	0.00	0.06	0.00	0.00	0.00	0.65	0.37	0.22	2.49	1.02	0.09
19	0.84	1.39	0.00	1.23	0.02	0.09	0.01	0.00	0.00	9.76	1.42	7.13	3.58	11.18	0.15
20	0.14	0.79	0.00	8.33	0.02	0.17	0.01	0.02	0.04	0.02	0.00	0.98	9.48	0.06	0.36
21	1.61	0.37	0.82	0.96	0.02	0.01	0.00	0.00	0.00	0.00	0.00	19.18	3.79	0.00	0.02
22	0.02	0.55	0.00	2.57	0.01	0.02	0.02	0.00	0.00	0.01	0.01	0.12	3.19	0.02	0.03
23	0.00	0.14	0.00	7.72	0.07	0.01	0.01	0.00	0.00	0.02	0.01	0.89	7.95	0.03	0.02
24	1.84	0.27	0.00	0.30	0.00	0.25	0.00	0.10	0.18	0.00	0.01	2.92	2.76	0.19	0.80
25	0.01	0.26	0.00	4.04	0.03	0.07	0.01	0.00	0.00	11.28	0.26	0.51	4.42	11.54	0.12
26	0.35	0.66	0.00	6.02	0.03	0.68	0.02	0.19	0.33	0.01	0.02	4.13	7.95	0.36	1.81
27	0.90	0.40	0.01	0.51	0.03	0.00	0.01	0.00	0.00	17.32	0.16	0.18	1.86	17.48	0.00
28	0.00	0.07	0.00	8.02	0.05	0.34	0.03	0.10	0.17	0.03	0.01	1.03	8.61	0.21	0.92
29	1.27	0.24	0.01	0.29	0.03	0.04	0.01	0.00	0.00	23.27	0.47	1.22	1.89	23.74	0.07
30	0.01	0.28	0.00	8.06	0.16	0.02	0.01	0.00	0.00	0.01	0.01	1.16	8.54	0.02	0.03



Cont. of Table 4.5 - Calculated modal composition (wt %) of carbonate and hydroxyl functional groups, copper and hematite minerals, with reference to webmineral.com (2013)

Sample ID	Hydroxyls							Carbonates				Oxides	Cumulative -OH	Cumulative CO <sub>3</sub> <sup>2-</sup>	Copper
	Percentage functional groups														
	8.53% -OH	7.84% -OH	26.34% -OH	22.85% -OH	6.61% -OH	20.71% -OH	3.34% -OH	15.38% -OH	27.13% CO <sub>3</sub> <sup>2-</sup>	59.95% CO <sub>3</sub> <sup>2-</sup>	58.14% CO <sub>3</sub> <sup>2-</sup>	Hematite			
Muscovite	Biotite	Kaolinite	Chlorite	Tourmaline	Chrysocolla	Apatite	Malachite	Calcite	Ankerite	Hematite	Cumulative -OH	Cumulative CO <sub>3</sub> <sup>2-</sup>	Copper		
31	0.14	0.46	0.00	10.29	0.02	0.06	0.03	0.00	0.00	0.03	0.02	4.02	11.00	0.05	0.09
32	0.02	0.09	0.00	7.94	0.01	0.42	0.17	0.14	0.25	0.21	0.07	0.74	8.79	0.53	1.23
33	0.96	1.28	0.04	1.20	0.01	0.00	0.00	0.00	0.00	4.80	1.24	3.05	3.49	6.04	0.00
34	0.00	0.13	0.00	8.35	0.02	0.05	0.01	0.00	0.00	0.03	0.01	0.26	8.56	0.04	0.07
35	0.14	0.57	0.00	4.36	0.00	0.62	0.02	0.13	0.23	16.20	2.38	3.08	5.84	18.81	1.71
36	0.05	0.95	0.00	3.73	0.00	0.00	0.01	0.00	0.00	2.26	0.07	0.73	4.74	2.33	0.01
37	0.01	1.23	0.00	10.02	0.00	0.17	0.01	0.00	0.00	0.00	0.00	1.72	11.44	0.00	0.28
38	0.12	3.20	0.00	1.80	0.01	0.04	0.01	0.00	0.00	0.02	0.01	3.89	5.18	0.03	0.06
39	0.01	0.80	0.00	10.47	0.00	0.20	0.02	0.00	0.00	0.01	0.00	0.27	11.50	0.01	0.33
40	0.01	0.12	0.00	4.48	0.06	0.18	0.00	0.00	0.00	0.01	0.00	0.02	4.85	0.01	0.30
41	0.00	0.23	0.00	5.30	0.62	0.00	0.01	0.00	0.00	7.85	3.51	3.48	6.16	11.36	0.00
42	0.52	0.93	0.00	1.04	0.02	0.06	0.01	0.00	0.00	24.29	0.33	0.43	2.58	24.62	0.09
43	0.42	0.66	0.03	1.43	0.10	0.01	0.01	0.00	0.00	11.06	0.24	1.12	2.66	11.30	0.01
44	0.02	0.25	0.00	9.30	0.00	0.03	0.02	0.00	0.00	6.06	0.15	0.35	9.62	6.21	0.05
45	0.01	0.55	0.00	3.56	0.00	0.11	0.01	0.00	0.00	5.13	0.22	2.38	4.24	5.35	0.18
46	0.71	0.31	0.02	1.11	0.12	0.03	0.01	0.00	0.00	15.47	0.30	0.95	2.31	15.77	0.04
47	0.01	0.21	0.00	7.11	0.01	0.28	0.01	0.02	0.03	13.57	1.41	4.46	7.65	15.01	0.54
48	0.14	0.69	0.00	1.52	0.00	0.85	0.00	0.00	0.00	1.16	0.02	59.78	3.20	1.18	1.40
49	1.10	0.26	0.01	0.37	0.06	0.08	0.01	0.00	0.00	25.25	0.75	1.90	1.89	26.00	0.14
50	0.02	0.19	0.00	3.85	0.00	7.05	0.01	0.00	0.00	0.00	0.14	0.59	11.12	0.14	11.54
51	0.18	1.12	0.00	1.62	0.02	0.61	0.00	0.00	0.00	17.41	0.08	9.84	3.55	17.49	1.00
52	0.85	0.75	0.00	1.10	0.01	0.01	0.00	0.00	0.00	15.00	1.26	12.48	2.72	16.26	0.01
53	1.89	0.18	0.01	0.24	0.03	0.01	0.01	0.00	0.00	17.79	0.10	0.27	2.37	17.89	0.01
54	0.18	0.66	0.01	6.17	0.07	0.04	0.00	0.00	0.00	9.93	1.03	4.32	7.13	10.96	0.06
55	1.61	0.99	0.01	1.24	0.04	1.08	0.02	0.34	0.60	7.78	3.08	7.32	5.33	11.46	3.28
56	1.03	1.07	0.00	2.77	0.04	0.03	0.00	0.00	0.00	17.10	0.46	0.39	4.94	17.56	0.05
57	0.84	0.78	0.02	1.92	0.10	1.31	0.01	0.11	0.19	10.24	3.75	8.77	5.09	14.18	2.77
58	0.07	0.50	0.03	1.07	0.04	0.00	0.00	0.00	0.00	0.00	0.01	75.44	1.71	0.01	0.00
59	0.39	1.43	0.00	2.27	0.03	0.02	0.01	0.00	0.00	0.01	0.03	21.03	4.15	0.04	0.03
60	0.11	1.01	0.01	1.89	0.03	1.21	0.00	0.00	0.00	0.89	0.31	40.00	4.26	1.20	1.98

#### 4.4.1. Correlation of functional groups

Given that copper is the subject of interest, assuming a copper cut-off grade of 0.5 % and carbonate cut-off of 2 % (note that the low concentration of 2% is assumed for carbonate since even at ratios 9:1 calcite to chrysocolla, calcite features are invisible in NIR spectra (Iyakwari and Glass, 2015)), Table 4.6, shows classification of samples based on their copper-carbonate concentration into four groups. Six samples (samples 9, 35, 47, 51, 55, and 57) are classified as high copper-high carbonate samples, seventeen samples (samples 1, 2, 3, 4, 5, 8, 10, 11, 12, 17, 24, 26, 28, 32, 48, 50 and 60) are classified as high copper-low carbonate. Also, twenty samples (samples 6, 13, 15, 19, 25, 27, 29, 33, 36, 41, 42, 43, 44, 45, 46, 49, 52, 53, 54 and 56) are classified as high carbonate-low copper samples while seventeen samples (samples 7, 14, 16, 18, 20, 21, 22, 23, 30, 31, 34, 37, 38, 39, 40, 58, and 59) are classified as low copper-low carbonate samples (Table 4.6).

Table 4.7, presents correlation and classification of samples on the basis of a copper cut-off grade of 0.5 % and 5 % for -OH (note that the high -OH percentage of 5 % taken is to make allowance for the -OH contributed by both chrysocolla and malachite). On this basis, nine samples (samples 4, 9, 10, 11, 12, 24, 48, 51 and 60), are classified as high copper-low -OH, fourteen samples (samples 1, 2, 3, 5, 8, 17, 26, 28, 32, 35, 47, 50, 55 and 57) as high copper-high -OH, while twelve samples (samples 15, 20, 23, 30, 31, 34, 37, 38, 39, 41, 44 and 54) are classified as low copper-high -OH and twenty five samples (samples 6, 7, 13, 14, 16, 18, 19, 21, 22, 25, 27, 29, 33, 36, 40, 42, 43, 45, 46, 49, 52, 53, 56, 58, and 59) are classified as low copper-low -OH samples (Table 4.7).

Table 4.8, shows that with a cut-off grade of 0.5 % for copper and 10 % for hematite (10 % is taken for hematite since at ratio of chrysocolla to hematite 9:1, chrysocolla features are visible in NIR spectra (Iyakwari and Glass, 2015)), eleven samples (samples 1, 2, 3, 4, 8, 9, 10, 11, 12, 48 and 60) are classified as high copper-high hematite, twelve samples (samples 5, 17, 24, 26, 28, 32, 35, 47, 50, 51, 55 and 57) as high copper-low hematite, eight samples (samples 6, 7, 13, 14, 21, 52, 58 and 59) as high hematite-low copper and twenty nine samples (samples 15, 16, 18, 19, 20, 22, 23, 25, 27, 29, 30, 31, 33,

34, 36, 37, 38, 39, 40, 41, 42, 43, 44, 45, 46, 49, 53, 54, and 56) as low copper–low hematite samples (Table 4.8).

Table 4.6 - Classification of samples based on copper-carbonate concentration. Where HCu = High copper ( $\geq 0.5\%$ ), HC = High carbonate ( $\geq 2\%$ ), LCu = Low copper ( $< 0.5\%$ ) and LC = Low carbonate ( $< 2\%$ ). Class of sample is marked with +

Sample ID	HCu-HC	HCu-LC	LCu-HC	LCu-LC
1		+		
2		+		
3		+		
4		+		
5		+		
6			+	
7				+
8		+		
9	+			
10		+		
11		+		
12		+		
13			+	
14				+
15			+	
16				+
17		+		
18				+
19			+	
20				+
21				+
22				+
23				+
24		+		
25			+	
26		+		
27			+	
28		+		
29			+	
30				+
31				+
32		+		
33			+	
34				+
35	+			
36			+	
37				+
38				+
39				+
40				+
41			+	
42			+	
43			+	
44			+	
45			+	
46			+	
47	+			
48		+		
49			+	
50		+		
51	+			
52			+	
53			+	
54			+	
55	+			
56			+	
57	+			
58				+
59				+
60		+		

Table 4.7 - Classification of samples based on copper-hydroxyl concentration. Where HCu = High copper ( $\geq 0.5\%$ ), HOH = High Hydroxyl ( $\geq 5\%$ ), LCu = Low copper ( $< 0.5\%$ ) and LOH = Low Hydroxyl ( $< 5\%$ ). Class of sample is marked with +

Sample ID	HCu-HOH	HCu-LOH	LCu-HOH	LCu-LOH
1	+			
2	+			
3	+			
4		+		
5	+			
6				+
7				+
8	+			
9		+		
10		+		
11		+		
12		+		
13				+
14				+
15			+	
16				+
17	+			
18				+
19				+
20			+	
21				+
22				+
23			+	
24		+		
25				+
26	+			
27				+
28	+			
29				+
30			+	
31			+	
32	+			
33				+
34			+	
35	+			
36				+
37			+	
38			+	
39			+	
40				+
41			+	
42				+
43				+
44			+	
45				+
46				+
47	+			
48		+		
49				+
50	+			
51		+		
52				+
53				+
54			+	
55	+			
56				+
57	+			
58				+
59				+
60		+		

Table 4.8 - Classification of samples based on copper-hematite concentration. Where HCu = High copper ( $\geq 0.5\%$ ), HH = High Hematite ( $\geq 10\%$ ), LCu = Low copper ( $< 0.5\%$ ) and LH = Low Hematite ( $< 10\%$ ). Class of sample is marked with +

Sample ID	HCu-HH	HCu-LH	LCu-HH	LCu-LH
1	+			
2	+			
3	+			
4	+			
5		+		
6			+	
7			+	
8	+			
9	+			
10	+			
11	+			
12	+			
13			+	
14			+	
15				+
16				+
17		+		
18				+
19				+
20				+
21			+	
22				+
23				+
24		+		
25				+
26		+		
27				+
28		+		
29				+
30				+
31				+
32		+		
33				+
34				+
35		+		
36				+
37				+
38				+
39				+
40				+
41				+
42				+
43				+
44				+
45				+
46				+
47		+		
48	+			
49				+
50		+		
51		+		
52			+	
53				+
54				+
55		+		
56				+
57		+		
58			+	
59			+	
60	+			

On the basis of the above correlation and classification, since copper preconcentration from carbonate and/or hydroxyl group is the subject of research using NIR, and there is spatial association between hematite and chrysocolla (Table 4.4), comparing the various classifications above (Tables 4.6, 4.7 and 4.8), the following groups and samples can be considered for economic preconcentration:

- i. High copper–low carbonate (samples 1, 2, 3, 4, 5, 8, 10, 11, 12, 17, 24, 26, 28 32, 48, 50 and 60),
- ii. High copper–low -OH (samples 4, 9, 10, 11, 12, 24, 48, 51 and 60),
- iii. High copper–high hematite (samples 1, 2, 3, 4, 8, 9, 10, 11, 12, 48 and 60) and
- iv. High copper–low hematite (samples 5, 17, 24, 26, 28, 32, 35, 47, 50, 51, 55 and 57)

Combining all the above groups, ideally on the basis of copper concentration the following samples (samples 1, 2, 3, 4, 5, 8, 9, 10, 11, 12, 17, 24, 26, 28, 32, 35, 47, 48, 50, 51, 55, 57 and 60) should be targeted for preconcentration as they contain valuable concentrates ( $\geq 0.5$  % Cu). However, considering ore processing economics as a key factor, it is noted that some of these samples earlier classified either as high carbonate and/or as high -OH bearing samples. This should be considered during preconcentration using NIR, since NIR range sense the functional groups ( $\text{CO}_3^{2-}$  and -OH) and not copper.

On that basis only samples 4, 8, 10, 11, 12, 24, 48 and 60 can be targeted for economic preconcentration since samples 1, 2, 3, 5, 9, 17, 26, 28, 32, 35, 47, 50, 51, 55 and 57 have either or both high carbonate or hydroxyl concentration. Therefore, only 13 % of the total samples analysed contain economically extractible copper concentration. Preconcentration shall therefore follow as presented in Figure 4.3. Note that this strategy shall produce a high purity concentrate.

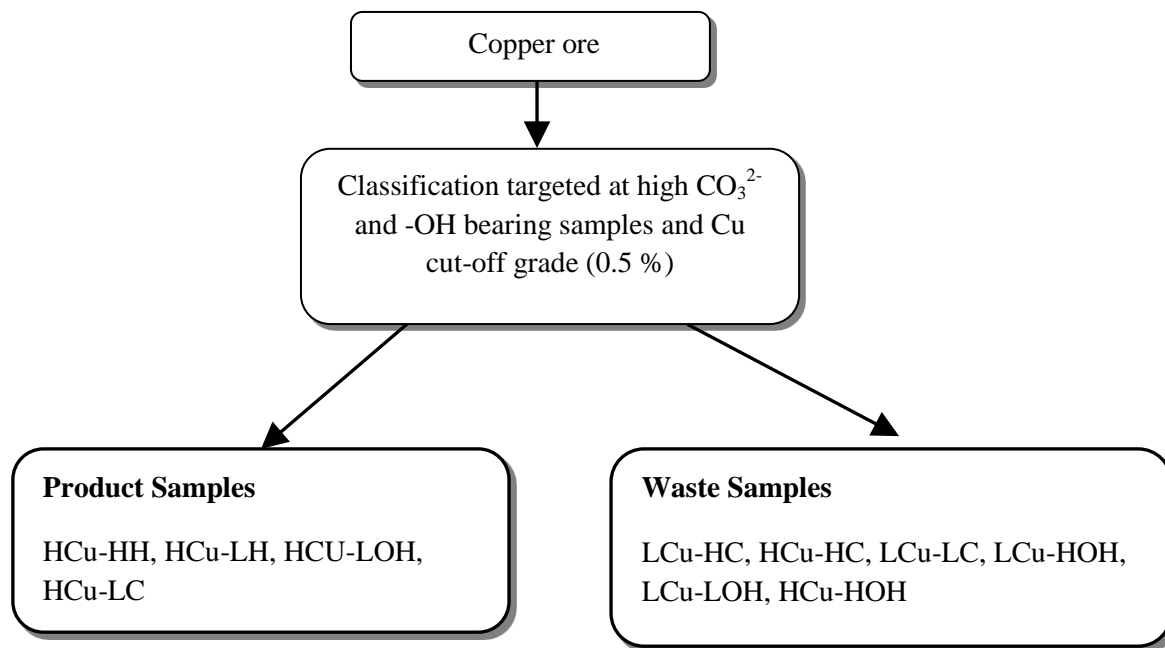


Figure 4.3 - Proposed model for copper preconcentration, based on ore mineralogy and copper cut-off grade of 0.5 % (or chrysocolla grade of 1.5 %) targeted towards eliminating both high-carbonate and high-hydroxyl bearing samples

Where	
<b>HCu-HH</b> = High Copper- High Hematite.	<b>HCu-LH</b> = High Copper-Low Hematite,
<b>LCu-HH</b> = Low Copper-High Hematite.	<b>LCu-LH</b> = Low Copper-Low Hematite
<b>HCu-HOH</b> =High Copper- High -OH.	<b>HCu-LOH</b> =High Copper-Low -OH
<b>LCu-HOH</b> = Low Copper – High –OH.	<b>LCu-LOH</b> = Low Copper – Low –OH
<b>HCu-HC</b> = High Copper- High CO <sub>3</sub> <sup>2-</sup> .	<b>HCu-LC</b> = High Copper –Low CO <sub>3</sub> <sup>2-</sup>
<b>LCu-HC</b> =Low Copper – High CO <sub>3</sub> <sup>2-</sup> .	<b>LCu-LC</b> = Low Copper – Low CO <sub>3</sub> <sup>2-</sup>

Assuming the -OH to be dominantly contributed by chrysocolla as is the case with sample 50, where chrysocolla contributed 7 % of the total -OH, optimising the strategy (Fig. 4.3), by incorporating or increasing the -OH allowance will lead to better or higher copper recovery.

Therefore, samples 1, 2, 3, 5, 17, 26, 28, 32, 50 (High copper-High -OH groups) could be added to the targeted batch. Note that samples 9, 35, 47, 51, 55 and 57 are not targeted because they showed high CO<sub>3</sub><sup>2-</sup> concentration and data from Table 4.1 and 4.5, indicates the CO<sub>3</sub><sup>2-</sup> is largely from calcite. Therefore, this second strategy (Fig. 4.4), only targets CO<sub>3</sub><sup>2-</sup> bearing samples reduction/removal. On this basis, the following samples can now be targeted 1, 2, 3, 4, 5, 8, 10, 11, 12, 17, 24, 26, 28, 32, 48, 50 and 60. This then increases to

28 % the total samples containing economically extractible copper concentration (overall yield). This shows an improvement of 15 % from the earlier 13 % while targeting both carbonate and hydroxyl.

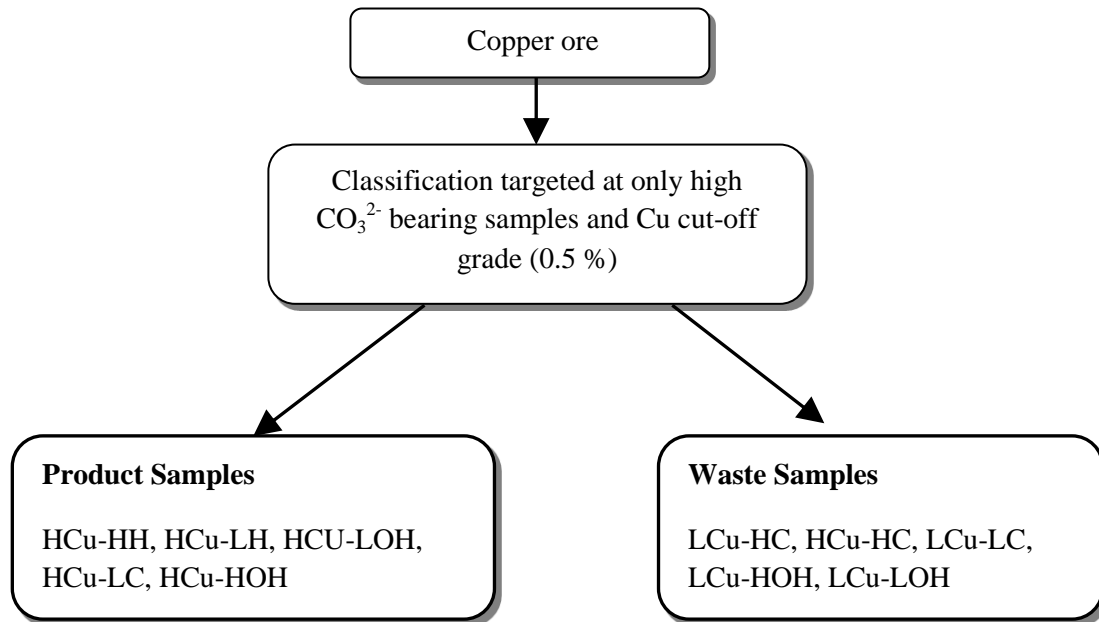


Figure 4.4 - Proposed model for copper preconcentration, based on ore mineralogy and copper cut-off grade of 0.5 % (or chrysocolla grade of 1.5 %) targeted towards eliminating only high-carbonate bearing samples.

Where	
<b>HCu-HH</b> = High Copper- High Hematite.	<b>HCu-LH</b> = High Copper-Low Hematite,
<b>LCu-HH</b> = Low Copper-High Hematite.	<b>LCu-LH</b> = Low Copper-Low Hematite
<b>HCu-HOH</b> =High Copper- High -OH.	<b>HCu-LOH</b> =High Copper-Low -OH
<b>LCu-HOH</b> = Low Copper – High -OH.	<b>LCu-LOH</b> = Low Copper – Low -OH
<b>HCu-HC</b> = High Copper- High CO <sub>3</sub> <sup>2-</sup> .	<b>HCu-LC</b> = High Copper –Low CO <sub>3</sub> <sup>2-</sup>
<b>LCu-HC</b> =Low Copper – High CO <sub>3</sub> <sup>2-</sup> .	<b>LCu-LC</b> = Low Copper – Low CO <sub>3</sub> <sup>2-</sup>

The disadvantage of the second strategy will be the increase in dilution as contributed by the hydroxyl group, but the economics of higher copper recovery provided the acid consuming carbonates are removed or reduced outweighs it.

Generally, the idea of preconcentration here is aimed at eliminating both ore particles with Cu grades that are below cut-off grade (0.5 %) and sub-economic particles (particles containing either or both high CO<sub>3</sub><sup>2-</sup> and -OH) leading to profitable ore processing. Therefore, while strategy one presented by Figure 4.3 targets both high CO<sub>3</sub><sup>2-</sup> and -OH in addition to low Cu bearing samples, Figure



4.4 target only the high  $\text{CO}_3^{2-}$  bearing samples in addition to low Cu bearing samples.

#### **4.5. Reconciliation of classification strategy with copper content**

Using a copper cut-off grade of 0.5 % for classification, with respect to Table 4.3, the following samples (samples 1, 2, 3, 4, 5, 8, 9, 10, 11, 12, 17, 24, 26, 28, 32, 35, 47, 48, 50, 51, 55, 57, and 60) can be targeted for preconcentration. Table 4.9 presents classifications of Mantoverde samples based on both mineralogy and copper content.

Analysis of Table 4.9 shows that seventeen samples are classified based on sample functional groups content (Fig. 4.4) as economic targets while twenty three are classified based on their copper content as economic samples. All the seventeen samples classified based on functional groups are captured in the copper content group as having copper concentrations at 0.5 % and above. Of the twenty three samples having copper above 0.5 %, six samples (sample 9, 35, 47, 51, 55, and 57) are classified as uneconomic. The basis of their classification as uneconomic is due to their high  $\text{CO}_3^{2-}$  (samples 9 and 51) and or -OH (samples 35, 47, 53 and 57) content.

Since NIR range used does not have the ability to sense copper in the samples, copper content classification strategy may not hold true for NIR preconcentration. Therefore, only the mineralogy or functional group classification may achieve a good correlation in comparison with NIR. But a strong 1:1 correlation may not be possible, because the main copper bearing mineral chrysocolla also contains -OH and NIR does not sense bulk -OH but individual mineral's constituent.

Table 4.9 - Classification of Mantoverde copper ore samples based on NIR functional groups with respect to strategy in Figure 4.4 and copper content of samples. Where (+) = economic targets or Cu  $\geq$  0.5 % and (-) = uneconomic samples or Cu < 0.5 %. Copper values calculated from QEMSCAN<sup>®</sup> modal mineral data of Copper-bearing minerals (chrysocolla, cuprite and malachite).

Sample ID	Mineralogy	Cu content
1	+	+
2	+	+
3	+	+
4	+	+
5	+	+
6	-	-
7	-	-
8	+	+
9	-	+
10	+	+
11	+	+
12	+	+
13	-	-
14	-	-
15	-	-
16	-	-
17	+	+
18	-	-
19	-	-
20	-	-
21	-	-
22	-	-
23	-	-
24	+	+
25	-	-
26	+	+
27	-	-
28	+	+
29	-	-
30	-	-
31	-	-
32	+	+
33	-	-
34	-	-
35	-	+
36	-	-
37	-	-
38	-	-
39	-	-
40	-	-
41	-	-
42	-	-
43	-	-
44	-	-
45	-	-
46	-	-
47	-	+
48	+	+
49	-	-
50	+	+
51	-	+
52	-	-
53	-	-
54	-	-
55	-	+
56	-	-
57	-	+
58	-	-
59	-	-
60	+	+

#### **4.6. Mantoverde ore chemistry**

Elemental analysis of samples was carried out using a portable thermo scientific Niton FXL 950 FM-XRF analyser (PXRF) which performs completely non-destructive analyses requiring little or no sample preparation depending on material being analysed. The portable XRF analyser employs Energy Dispersive Spectrometry (EDX) method. X-rays penetrates approximately 1 to 2 mm into the sample. The PXRF analyser have 8 mm diameter scanning window, with integrated camera which shows the surface being scanned. The PXRF consists of a sample mount (stage) which is 360 degrees rotatable and can be set to spin samples when scanning. The equipment also has four testing modes inbuilt (i.e. mining Cu/Zn, mining Ta/Hf, Soil and Test all Geo modes).

Given that the main objective of this research is Cu or rather Cu bearing minerals preconcentration using NIR which on its own does not sense Cu, the use of PXRF here is to determine samples that contain Cu for better scoping of application. For the purpose of this study, the mining Cu/Zn mode was used and equipment was set to scan for 150 seconds per sample for splits A1 and B1, while rotating 360 degrees. The split B2 samples due to their nature and large size were scanned in stationary mode. Results obtained for the three sample types are presented in tables below. Some limitation of the PXRF include, low sensitivity, peak overlap, small area scanned and measurement variability among other.

Analysis of splits A1 (Table 4.10) represents bulk chemistry since it is performed for powdered samples, it is thereby considered to give an average composition of the particles as a whole. NIR is a surface technique. Hence, it will be assumed that the surface mineral(s) is/are responsible for the absorption of NIR radiation observed in spectra per particle. Since three different sample modes (splits A1, B1 and B2) are analysed by both NIR and XRF, discussions and comparison shall be made specifically for like samples only. Measurement by both NIR and XRF were taken on the same face of the particle for splits B1 (Table 4.11) and B2 (Table 4.12). Splits A1 and B2 data will not be discussed here. Data will be used in the application chapter to evaluate strategy by calculating ore parameters. Reconciliation of data of copper and iron for splits B1 samples only, as back calculated from QEMSCAN<sup>®</sup> mineral data (Table 4.1) and the PXRF (Table 4.13) is discussed in the next section.

Table 4.10 - PXRf data for splits A1 samples Mantoverde copper ore, values in % (standardless analysis).

Sample ID	Ba	Zr	Rb	Zn	Cu	Ni	Co	Fe	Mn	Cr	V	Ti	Ca	K
1	0.05	0.01	0.01	0.00	1.30	0.01	0.03	14.73	0.09	0.02	0.03	0.36	0.27	3.25
2	0.05	0.01	0.01	0.01	2.31	0.01	0.04	23.45	0.09	0.03	0.04	0.29	0.26	3.42
3	0.04	0.01	0.01	0.01	3.20	0.01	0.04	22.77	0.00	0.02	0.02	0.09	0.18	2.95
4	0.04	0.00	0.00	0.00	1.40	0.03	0.04	46.82	0.00	0.04	0.04	0.14	0.13	1.95
5	0.03	0.01	0.01	0.00	0.77	0.01	0.00	13.27	0.05	0.03	0.03	0.24	0.32	2.16
6	0.07	0.01	0.01	0.00	1.33	0.01	0.02	18.88	0.07	0.03	0.03	0.23	10.38	3.59
7	0.11	0.01	0.01	0.00	0.14	0.02	0.03	29.27	0.02	0.03	0.05	0.33	0.24	4.90
8	0.09	0.01	0.01	0.00	1.51	0.02	0.06	32.55	0.10	0.03	0.05	0.27	0.20	3.61
9	0.02	0.00	0.00	0.00	2.82	0.01	0.03	17.34	0.11	0.02	0.03	0.14	14.43	0.72
10	0.02	0.00	0.00	0.00	8.66	0.02	0.12	34.11	0.02	0.03	0.04	0.10	0.23	1.15
11	0.02	0.00	0.00	0.00	8.91	0.01	0.03	37.19	0.01	0.03	0.04	0.13	0.43	0.45
12	0.04	0.01	0.00	0.00	1.85	0.02	0.06	40.68	0.00	0.04	0.03	0.13	0.15	2.40
13	0.06	0.01	0.01	0.00	0.18	0.03	0.05	44.05	0.01	0.04	0.03	0.08	1.37	1.69
14	0.05	0.01	0.01	0.00	0.49	0.02	0.04	27.16	0.01	0.03	0.02	0.11	0.46	2.66
15	0.17	0.01	0.01	0.00	0.03	0.01	0.00	11.08	0.36	0.02	0.04	0.51	3.52	5.15
16	0.08	0.02	0.01	0.00	0.35	0.00	0.01	6.18	0.01	0.01	0.02	0.23	0.23	3.63
17	0.01	0.01	0.00	0.00	0.34	0.01	0.00	8.84	0.08	0.01	0.03	0.25	0.32	0.72
18	0.04	0.02	0.01	0.00	0.13	0.00	0.01	4.37	0.00	0.01	0.02	0.35	0.51	4.13
19	0.01	0.01	0.01	0.00	0.25	0.00	0.02	13.35	0.11	0.02	0.03	0.38	7.81	2.94
20	0.01	0.01	0.01	0.00	0.18	0.01	0.02	12.59	0.06	0.03	0.03	0.27	0.27	2.07
21	0.03	0.01	0.01	0.00	0.09	0.01	0.05	28.95	0.00	0.03	0.02	0.10	0.12	2.91
22	0.11	0.02	0.01	0.00	0.08	0.00	0.00	4.71	0.01	0.01	0.01	0.27	0.29	4.17
23	0.01	0.01	0.00	0.00	0.09	0.01	0.00	10.14	0.06	0.02	0.03	0.28	0.21	0.28
24	0.02	0.00	0.01	0.00	3.30	0.02	0.08	38.40	0.02	0.04	0.04	0.17	0.71	2.36
25	0.02	0.01	0.01	0.00	0.74	0.01	0.03	13.30	0.05	0.03	0.03	0.23	0.31	2.05
26	0.02	0.01	0.01	0.00	0.45	0.01	0.01	12.23	0.05	0.03	0.03	0.25	0.36	1.80
27	0.01	0.01	0.01	0.00	0.02	0.00	0.00	2.26	0.11	0.01	0.02	0.29	15.92	2.77
28	0.00	0.01	0.00	0.01	0.73	0.01	0.01	8.67	0.05	0.01	0.03	0.27	0.28	0.21
29	0.00	0.01	0.01	0.00	0.10	0.00	0.00	3.19	0.14	0.02	0.02	0.30	13.97	2.79
30	0.01	0.01	0.00	0.00	0.24	0.01	0.01	8.12	0.03	0.02	0.03	0.25	0.26	1.25
31	0.02	0.01	0.01	0.00	0.22	0.01	0.01	11.53	0.07	0.02	0.02	0.22	0.30	1.63
32	0.00	0.01	0.00	0.01	0.89	0.01	0.01	8.02	0.07	0.01	0.03	0.30	0.48	0.28
33	0.14	0.01	0.01	0.00	0.03	0.01	0.02	10.63	0.23	0.02	0.04	0.53	2.64	5.53
34	0.00	0.01	0.00	0.00	0.21	0.00	0.01	7.08	0.06	0.01	0.02	0.23	0.23	0.39
35	0.01	0.01	0.00	0.00	0.89	0.01	0.00	10.40	0.06	0.02	0.03	0.33	6.18	0.62
36	0.12	0.02	0.01	0.00	0.06	0.01	0.00	7.46	0.04	0.02	0.02	0.45	0.63	4.02
37	0.09	0.01	0.01	0.00	0.12	0.01	0.01	10.01	0.06	0.03	0.03	0.45	0.18	4.27
38	0.00	0.01	0.01	0.00	0.22	0.01	0.02	11.28	0.07	0.02	0.04	0.36	0.26	1.92
39	0.06	0.01	0.01	0.00	0.14	0.01	0.00	9.47	0.06	0.02	0.03	0.41	0.22	3.18
40	0.01	0.02	0.00	0.00	0.44	0.00	0.01	6.40	0.02	0.01	0.02	0.18	0.17	0.78
41	0.06	0.01	0.00	0.00	0.05	0.00	0.00	8.80	0.45	0.02	0.03	0.25	11.33	0.00
42	0.02	0.01	0.01	0.00	0.11	0.00	0.00	4.04	0.16	0.02	0.02	0.28	15.86	2.46
43	0.01	0.01	0.01	0.00	0.13	0.00	0.00	4.06	0.23	0.02	0.02	0.31	13.59	1.66
44	0.01	0.02	0.00	0.00	0.21	0.01	0.00	10.09	0.07	0.02	0.04	0.32	4.07	0.64
45	0.12	0.01	0.01	0.00	0.11	0.01	0.00	8.37	0.05	0.02	0.02	0.34	3.42	4.35
46	0.02	0.01	0.01	0.00	0.16	0.00	0.00	2.99	0.23	0.01	0.02	0.25	11.24	3.18
47	0.03	0.02	0.00	0.00	0.46	0.01	0.02	10.09	0.07	0.02	0.03	0.31	5.96	1.08
48	0.02	0.00	0.00	0.00	0.36	0.01	0.03	16.52	0.02	0.02	0.02	0.10	0.14	0.90
49	0.01	0.01	0.01	0.00	0.13	0.00	0.00	3.20	0.24	0.01	0.02	0.21	19.94	1.93
50	0.02	0.01	0.00	0.01	2.08	0.01	0.01	8.42	0.03	0.01	0.02	0.12	0.26	1.44
51	0.06	0.01	0.01	bdl	1.39	0.01	0.03	20.55	0.06	0.03	0.03	0.23	9.28	3.05
52	0.03	0.01	0.01	0.00	0.14	0.00	0.00	17.02	0.11	0.00	0.00	0.27	6.86	2.16
53	0.02	0.01	0.01	0.00	0.09	0.00	0.00	2.04	0.20	0.02	0.00	0.30	12.10	2.57
54	0.12	0.01	0.00	0.00	0.23	0.00	0.00	7.66	0.16	0.02	0.03	0.44	3.81	2.82
55	0.03	0.01	0.00	0.00	3.03	0.00	0.00	10.71	0.14	0.00	0.00	0.19	6.31	1.70
56	0.04	0.01	0.00	0.00	0.33	0.00	0.00	10.13	0.16	0.02	0.03	0.37	8.89	2.19
57	0.02	0.01	0.00	0.00	2.28	0.00	0.00	8.69	0.19	0.00	0.00	0.19	13.89	1.18
58	0.04	0.01	0.00	0.00	0.07	0.00	0.00	54.36	0.00	0.04	0.00	0.14	0.00	1.15
59	0.10	0.01	0.01	0.00	0.19	0.00	0.00	21.68	0.12	0.02	0.05	0.40	0.21	3.68
60	0.06	0.01	0.00	0.00	4.44	0.00	0.00	30.33	0.00	0.03	0.00	0.18	0.56	1.63

Table 4.11 - PXRF data for splits B1 samples Mantoverde copper ore, values in % (standardless analysis).

Sample ID	Ba	Zr	Rb	Zn	Cu	Ni	Co	Fe	Mn	Cr	V	Ti	Ca	K
1	0.05	0.01	0.01	0.01	1.61	0.01	0.03	16.41	0.31	0.02	0.03	0.31	0.19	2.99
2	0.07	0.01	0.01	0.01	2.59	0.01	0.03	16.52	0.37	0.02	0.03	0.23	0.18	2.99
3	0.05	0.01	0.01	0.00	7.74	0.02	0.03	25.67	0.02	0.02	0.02	0.09	0.17	2.37
4	0.04	0.01	0.01	0.01	1.37	0.02	0.03	44.36	0.00	0.03	0.03	0.14	0.09	2.20
5	0.03	0.01	0.01	0.01	1.77	0.01	0.02	11.14	0.17	0.02	0.03	0.20	0.43	2.21
6	0.11	0.01	0.01	0.00	0.58	0.01	0.01	17.46	0.20	0.03	0.03	0.31	9.99	4.19
7	0.11	0.01	0.01	0.00	0.12	0.01	0.03	21.92	0.06	0.02	0.03	0.25	0.18	5.03
8	0.12	0.01	0.01	0.01	0.61	0.02	0.00	25.15	0.33	0.03	0.03	0.28	0.17	4.41
9	0.02	0.00	0.00	0.01	1.89	0.01	0.01	14.72	0.50	0.02	0.03	0.17	15.22	0.63
10	0.01	0.00	0.00	0.00	1.05	0.01	0.04	25.56	0.05	0.02	0.03	0.06	0.05	0.43
11	0.04	0.01	0.01	0.00	3.93	0.02	0.05	35.24	0.00	0.03	0.02	0.11	0.14	2.28
12	0.04	0.01	0.01	0.01	1.98	0.02	0.05	34.11	0.00	0.03	0.02	0.10	0.11	2.71
13	0.03	0.01	0.01	0.00	0.03	0.02	0.00	31.28	0.00	0.02	0.02	0.05	2.27	1.57
14	0.04	0.01	0.01	0.00	0.97	0.02	0.03	30.00	0.06	0.02	0.02	0.09	0.12	1.64
15	0.19	0.01	0.01	0.01	0.03	0.01	0.02	11.81	0.94	0.02	0.04	0.54	3.27	5.24
16	0.12	0.01	0.00	0.00	0.12	0.01	0.01	5.21	0.07	0.01	0.01	0.20	0.14	4.34
17	0.01	0.01	0.00	0.01	0.72	0.01	0.01	7.76	0.20	0.01	0.02	0.21	0.08	0.15
18	0.05	0.02	0.01	0.00	0.04	0.00	0.00	2.18	0.00	0.01	0.01	0.30	0.65	4.18
19	0.02	0.01	0.01	0.00	0.32	0.01	0.02	12.27	0.58	0.02	0.03	0.37	9.91	2.65
20	0.01	0.01	0.01	0.00	0.12	0.01	0.02	9.88	0.23	0.02	0.03	0.23	0.14	1.20
21	0.02	0.01	0.01	0.00	0.10	0.00	0.01	14.48	0.00	0.01	0.01	0.08	0.05	2.56
22	0.13	0.01	0.00	0.00	0.03	0.00	0.01	3.85	0.08	0.01	0.01	0.22	0.32	4.02
23	0.02	0.01	0.00	0.00	0.04	0.01	0.02	6.50	0.24	0.01	0.02	0.22	0.15	0.37
24	0.01	0.00	0.01	0.00	0.15	0.00	0.01	2.63	0.00	0.00	0.01	0.01	0.08	2.33
25	0.02	0.01	0.00	0.00	0.13	0.00	0.01	4.74	0.20	0.01	0.02	0.17	10.02	0.43
26	0.03	0.01	0.01	0.01	2.02	0.01	0.02	11.02	0.23	0.02	0.03	0.30	0.24	2.01
27	0.02	0.01	0.01	0.00	0.02	0.00	0.00	2.46	0.33	0.01	0.02	0.37	15.81	2.71
28	0.01	0.01	0.00	0.01	0.75	0.01	0.02	7.10	0.25	0.01	0.02	0.22	0.34	0.07
29	0.02	0.01	0.01	0.00	0.06	0.00	0.00	2.58	0.41	0.01	0.03	0.40	16.74	2.43
30	0.02	0.01	0.00	0.00	0.07	0.01	0.02	6.87	0.15	0.01	0.03	0.21	0.20	0.59
31	0.02	0.01	0.00	0.00	0.09	0.01	0.02	13.73	0.33	0.02	0.03	0.21	0.39	1.66
32	0.01	0.01	0.00	0.01	0.34	0.01	0.01	7.41	0.30	0.01	0.02	0.22	2.57	0.30
33	0.10	0.01	0.01	0.00	0.02	0.00	0.00	6.00	0.06	0.01	0.03	0.52	5.58	5.16
34	0.02	0.01	0.00	0.00	0.05	0.01	0.01	6.89	0.29	0.01	0.02	0.28	0.23	0.27
35	0.03	0.01	0.00	0.01	2.16	0.01	0.00	9.20	0.36	0.02	0.02	0.15	18.22	1.17
36	0.14	0.02	0.01	0.00	0.03	0.01	0.01	5.80	0.14	0.01	0.02	0.49	0.34	4.20
37	0.12	0.01	0.01	0.00	0.17	0.02	0.02	12.71	0.34	0.03	0.03	0.53	0.13	3.96
38	0.02	0.01	0.02	0.00	0.22	0.01	0.03	11.13	0.28	0.03	0.03	0.28	0.23	5.04
39	0.11	0.01	0.01	0.00	0.16	0.02	0.02	11.10	0.38	0.02	0.03	0.34	0.15	4.09
40	0.01	0.03	0.00	0.00	0.15	0.00	0.01	4.48	0.11	0.01	0.01	0.22	0.07	0.70
41	0.12	0.01	0.00	0.00	0.04	0.01	0.01	8.35	2.10	0.02	0.03	0.30	8.68	0.00
42	0.03	0.01	0.01	0.00	0.11	0.00	0.00	4.05	0.68	0.02	0.02	0.28	16.87	2.09
43	0.02	0.01	0.01	0.00	0.08	0.00	0.00	4.39	0.55	0.02	0.02	0.35	11.95	1.45
44	0.01	0.02	0.00	0.00	0.08	0.01	0.01	8.97	0.24	0.02	0.03	0.30	4.99	0.28
45	0.22	0.01	0.01	0.00	0.11	0.01	0.00	5.40	0.22	0.02	0.02	0.43	5.89	6.80
46	0.02	0.01	0.01	0.00	0.08	0.00	0.01	3.21	0.67	0.01	0.02	0.26	14.82	1.71
47	0.03	0.01	0.00	0.00	0.27	0.01	0.01	11.09	0.44	0.02	0.03	0.23	16.43	0.29
48	0.00	0.00	0.00	0.00	1.44	0.00	0.00	52.89	0.00	0.03	0.04	0.12	0.00	1.43
49	0.02	0.01	0.01	0.00	0.09	0.00	0.00	2.60	0.13	0.00	0.03	0.40	16.06	2.35
50	0.03	0.01	0.00	0.00	4.08	0.00	0.00	6.63	0.03	0.00	0.00	0.05	0.26	0.23
51	0.04	0.01	0.00	0.00	1.49	0.00	0.00	10.86	0.14	0.00	0.00	0.28	17.67	1.54
52	0.05	0.01	0.00	0.00	0.14	0.00	0.00	12.46	0.16	0.00	0.00	0.29	17.65	2.24
53	0.02	0.01	0.01	0.00	0.05	0.00	0.00	2.29	0.08	0.00	0.02	0.45	7.90	3.20
54	0.11	0.01	0.00	0.00	0.35	0.00	0.00	7.17	0.14	0.00	0.04	0.24	10.60	0.27
55	0.03	0.01	0.00	0.00	7.64	0.00	0.00	7.91	0.16	0.02	0.00	0.18	5.20	2.33
56	0.00	0.02	0.00	0.00	0.05	0.00	0.00	1.99	0.07	0.00	0.00	0.19	7.24	1.01
57	0.04	0.01	0.00	0.00	4.87	0.00	0.00	12.42	0.08	0.02	0.03	0.21	7.52	1.77
58	0.05	0.01	0.00	0.00	0.05	0.00	0.00	52.75	0.00	0.03	0.04	0.19	0.00	1.76
59	0.09	0.01	0.01	0.00	0.20	0.02	0.00	23.19	0.10	0.04	0.04	0.39	0.25	4.73
60	0.06	0.01	0.00	0.00	1.96	0.00	0.00	38.21	0.00	0.03	0.00	0.28	0.66	3.24

Table 4.12 - PXRF data for splits B2 samples Mantoverde copper ore, values in % (standardless analysis).

sample ID	Ba	Zr	Rb	Zn	Cu	Ni	Co	Fe	Mn	Cr	V	Ti	Ca	K
1	0.13	0.01	0.01	0.00	4.40	0.01	0.00	9.72	0.22	0.02	0.02	0.22	0.34	2.37
2	0.06	0.01	0.01	0.00	4.06	0.01	0.04	21.59	0.06	0.02	0.03	0.24	0.24	4.24
3	0.03	0.01	0.01	0.00	5.78	0.01	0.03	23.89	0.00	0.02	0.02	0.09	0.16	2.26
4	0.07	0.01	0.00	0.00	1.87	0.03	0.00	38.90	0.01	0.03	0.03	0.11	0.12	1.25
5	0.03	0.01	0.01	0.01	1.77	0.02	0.00	15.45	0.09	0.02	0.03	0.19	0.35	1.22
6	0.03	0.00	0.00	0.00	0.71	0.01	0.00	21.36	0.15	0.02	0.03	0.21	17.04	1.16
7	0.11	0.01	0.01	0.00	2.93	0.03	0.02	36.14	0.03	0.04	0.06	0.45	0.29	2.31
8	0.06	0.01	0.01	0.00	1.13	0.02	0.00	38.91	0.06	0.03	0.05	0.27	0.14	1.97
9	0.03	0.00	0.00	0.01	2.71	0.02	0.00	21.50	0.14	0.02	0.02	0.15	14.20	0.73
10	0.02	0.00	0.00	0.00	10.95	0.03	0.09	49.63	0.02	0.04	0.06	0.19	0.18	0.78
11	0.06	0.00	0.00	0.00	8.91	0.01	0.03	37.19	0.01	0.03	0.04	0.13	0.43	0.45
12	0.04	0.01	0.00	0.00	0.85	0.03	0.00	43.24	0.01	0.03	0.03	0.13	0.12	1.82
13	0.03	0.01	0.01	0.00	0.03	0.02	0.00	31.28	0.00	0.02	0.02	0.05	2.27	1.57
14	0.04	0.00	0.00	0.00	1.52	0.03	0.04	37.77	0.05	0.03	0.03	0.06	17.56	0.47
15	0.17	0.01	0.01	0.00	0.03	0.01	0.00	10.00	0.21	0.02	0.04	0.50	0.45	4.57
16	0.06	0.01	0.00	0.01	1.31	0.02	0.00	10.33	0.07	0.02	0.03	0.13	0.28	1.10
17	0.02	0.01	0.00	0.00	2.04	0.01	0.00	13.08	0.05	0.02	0.02	0.09	0.16	0.03
18	0.04	0.01	0.00	0.00	4.39	0.00	0.01	1.86	0.36	0.00	0.01	0.04	19.56	0.16
19	0.03	0.01	0.01	0.01	0.61	0.01	0.00	13.75	0.28	0.03	0.04	0.33	12.47	2.43
20	0.02	0.01	0.00	0.00	0.65	0.01	0.00	11.14	0.82	0.02	0.03	0.16	0.25	0.03
21	0.03	0.01	0.01	0.00	0.17	0.01	0.02	17.64	0.01	0.02	0.02	0.12	0.06	3.36
22	0.19	0.01	0.01	0.00	0.62	0.02	0.00	7.42	0.37	0.01	0.02	0.18	0.23	3.00
23	0.02	0.01	0.00	0.01	2.58	0.03	0.00	24.18	0.45	0.02	0.03	0.05	0.27	0.00
24	0.01	0.00	0.01	0.00	0.14	0.00	0.00	2.41	0.00	0.00	0.01	0.01	0.07	2.95
25	0.02	0.02	0.00	0.00	0.33	0.01	0.00	7.64	0.07	0.02	0.02	0.16	10.45	0.40
26	0.06	0.01	0.00	0.00	0.88	0.03	0.00	22.41	0.06	0.04	0.05	0.20	0.14	0.47
27	0.05	0.01	0.01	0.00	0.05	0.00	0.00	2.98	0.42	0.01	0.02	0.41	14.88	2.72
28	0.00	0.01	0.00	0.00	0.30	0.01	0.00	7.95	0.05	0.01	0.03	0.22	1.07	0.10
29	0.02	0.01	0.01	0.00	0.09	0.00	0.00	2.76	0.19	0.01	0.02	0.34	16.68	2.36
30	0.00	0.01	0.00	0.00	0.15	0.03	0.00	13.81	0.10	0.05	0.04	0.28	0.31	0.00
31	0.01	0.01	0.00	0.00	0.46	0.02	0.00	14.88	0.25	0.03	0.03	0.36	0.13	0.10
32	0.02	0.01	0.00	0.00	0.88	0.02	0.00	14.44	0.09	0.02	0.03	0.20	0.95	0.14
33	0.13	0.01	0.01	0.00	0.07	0.01	0.01	7.59	0.20	0.02	0.04	0.56	5.07	5.15
34	0.02	0.01	0.00	0.00	0.21	0.02	0.00	12.62	0.23	0.02	0.03	0.23	0.31	0.00
35	0.04	0.00	0.00	0.01	2.13	0.01	0.00	10.35	0.13	0.02	0.02	0.22	21.15	0.50
36	0.18	0.01	0.01	0.00	0.14	0.01	0.00	9.19	0.20	0.01	0.02	0.43	5.06	2.92
37	0.12	0.01	0.01	0.01	1.42	0.02	0.00	12.88	0.11	0.06	0.07	0.11	0.36	2.36
38	0.02	0.00	0.01	0.00	0.69	0.02	0.00	15.34	0.08	0.02	0.03	0.08	1.49	0.17
39	0.12	0.01	0.01	0.00	0.16	0.02	0.00	10.01	0.08	0.02	0.03	0.30	0.07	2.21
40	0.01	0.03	0.00	0.00	1.78	0.02	0.00	8.31	0.05	0.01	0.02	0.12	2.16	0.00
41	0.03	0.01	0.00	0.00	0.03	0.01	0.00	10.15	0.09	0.02	0.03	0.27	6.71	0.00
42	0.02	0.01	0.01	0.00	0.25	0.00	0.00	3.99	0.32	0.01	0.02	0.25	22.90	1.39
43	0.07	0.00	0.00	0.01	1.31	0.03	0.00	18.29	2.92	0.02	0.03	0.07	11.90	0.32
44	0.03	0.01	0.00	0.00	5.88	0.02	0.00	16.69	0.07	0.01	0.02	0.19	8.43	0.00
45	0.21	0.00	0.00	0.00	2.01	0.04	0.00	38.16	0.23	0.03	0.03	0.05	7.85	0.67
46	0.02	0.00	0.00	0.00	0.11	0.00	0.00	4.02	0.26	0.01	0.02	0.22	23.09	0.79
47	0.03	0.00	0.00	0.00	0.17	0.01	0.00	10.26	0.11	0.02	0.03	0.17	8.82	0.36
48	0.01	0.01	0.01	0.00	0.43	0.02	0.00	23.76	0.01	0.02	0.02	0.06	0.13	1.18
49	0.02	0.01	0.01	0.00	0.31	0.00	0.00	4.67	0.72	0.02	0.03	0.35	9.43	2.60
50	0.03	0.00	0.00	0.00	3.87	0.01	0.00	5.29	0.02	0.01	0.02	0.09	1.56	0.56
51	0.05	0.01	0.01	0.01	0.67	0.01	0.01	11.69	0.09	0.02	0.03	0.42	2.65	3.13
52	0.02	0.01	0.01	0.00	0.11	0.00	0.00	13.67	0.10	0.02	0.00	0.15	7.34	2.33
53	0.06	0.01	0.01	0.00	0.09	0.00	0.00	2.06	0.36	0.00	0.00	0.35	11.96	2.22
54	0.08	0.01	0.00	0.01	0.65	0.00	0.00	7.70	0.78	0.00	0.00	0.37	0.76	1.78
55	0.04	0.01	0.00	0.01	3.93	0.01	0.00	10.05	0.21	0.00	0.03	0.21	9.52	1.38
56	0.04	0.01	0.01	0.00	0.17	0.01	0.00	6.46	0.14	0.02	0.03	0.40	8.91	2.12
57	0.00	0.01	0.00	0.00	1.02	0.01	0.00	9.57	0.31	0.02	0.00	0.20	10.26	0.57
58	0.00	0.01	0.00	0.00	0.09	0.00	0.00	55.90	0.00	0.03	0.00	0.14	0.14	1.00
59	0.08	0.01	0.01	0.00	0.18	0.01	0.00	17.11	0.12	0.02	0.04	0.34	0.45	3.58
60	0.07	0.01	0.00	0.00	1.97	0.00	0.00	26.98	0.00	0.02	0.00	0.20	1.07	2.48

#### **4.6.1. Reconciliation of QEMSCAN<sup>®</sup> and PXRF Cu wt % and Fe wt % concentrations**

Comparison of QEMSCAN<sup>®</sup> calculated Cu and Fe values with PXRF Cu and Fe values are discussed below. Fe and Cu values from QEMSCAN<sup>®</sup> are presented in Table 4.2. Values of Cu and Fe from PXRF are presented in Table 4.11.

Since only splits B1 samples were analysed by QEMSCAN<sup>®</sup>, comparison is only made for data obtained for split B1 sample. Figures 4.5 and 4.6 present correlation plots of Cu and Fe respectively. Analysis show strong positive linear correlation between values obtained from both PXRF and QEMSCAN<sup>®</sup>. The intercept for Figure 4.5 (Cu) is close to zero with slope of 0.87 and  $R^2$  of 0.82. While Figure 4.6 (Fe) has a negative intercept with slope of 0.99 and  $R^2$  of 0.93. Figures 4.7 and 4.8 also confirm the positive relationship in Figures 4.5 and 4.6. Only a few samples have their values under- or over-estimated by either instrument. Figure 4.7 shows that samples 1, 2, 8, 10, 32 and 50 (10 % of total samples) have their Cu content underestimated by PXRF while only samples 11, 55 and 57 (i.e. 5 % of total samples) have their content underestimated by QEMSCAN<sup>®</sup>. Therefore, 85 % of samples have their concentration within range of one another. Figure 4.8 shows uniformity of detection with minor over-estimation of Fe concentration by PXRF. The QEMSCAN<sup>®</sup> only over-estimated values for samples 10 and 13.

The overall correlation reveals a strong positive relationship as there is no sample that either method completely failed to detect the presence of the elements (Cu and Fe) when detected by the other. The explanation for the under or over-estimation by QEMSCAN<sup>®</sup> could be due to the fact that QEMSCAN<sup>®</sup> values are back calculated from minerals suspected to contain these elements, so it is not a direct measurement, but makes the assumptions that the average chemistry and density of a mineral are true which may not hold perfect in some cases.

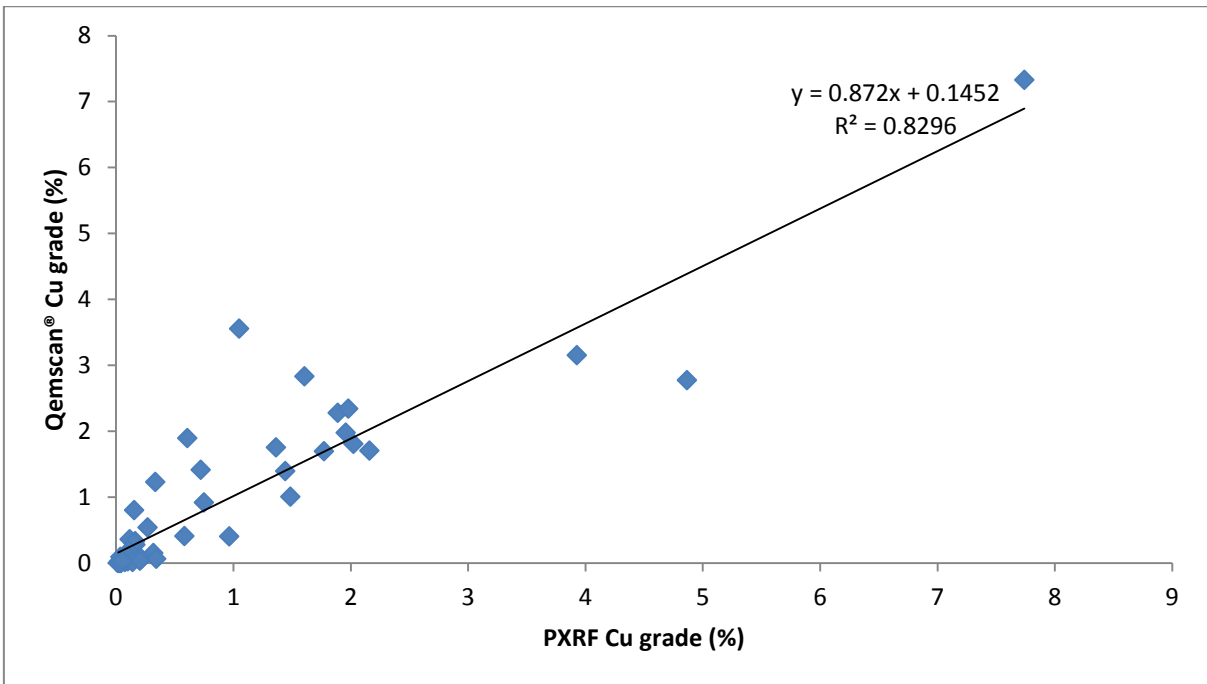


Figure 4.5 - Copper grades of QEMSCAN® mounts (splits B1) inferred from QEMSCAN® mineralogical composition with measured PXRF

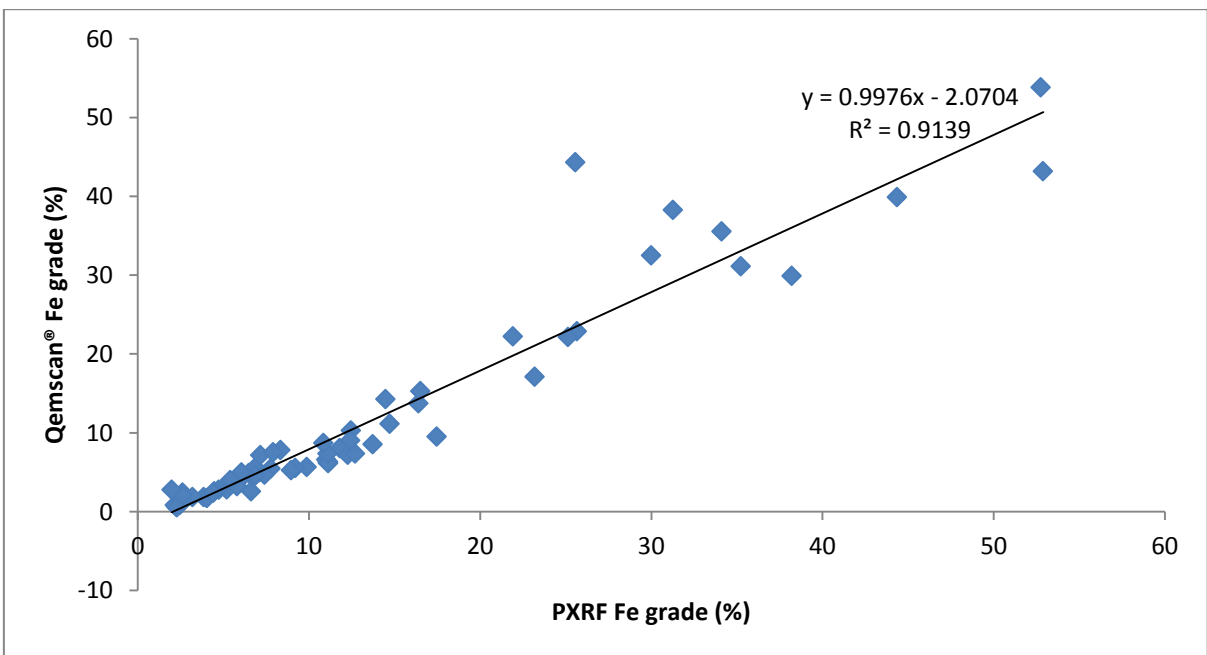


Figure 4.6 - Iron grades of QEMSCAN® mounts (splits B1) inferred from QEMSCAN® mineralogical composition with measured PXRF



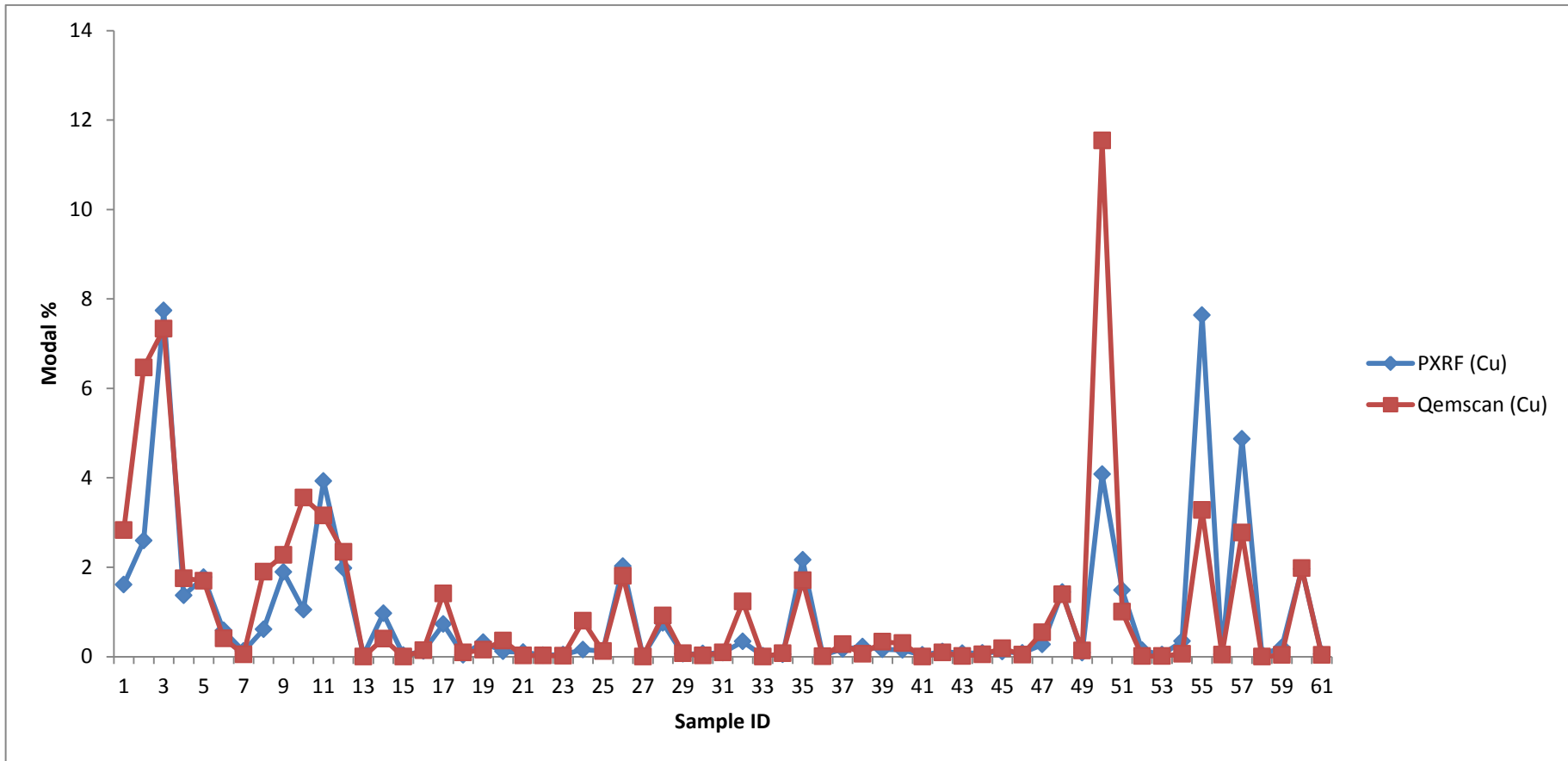


Figure 4.7 - Comparison of Cu wt % determined by PXRF and Cu wt % calculated from the QEMSCAN® results

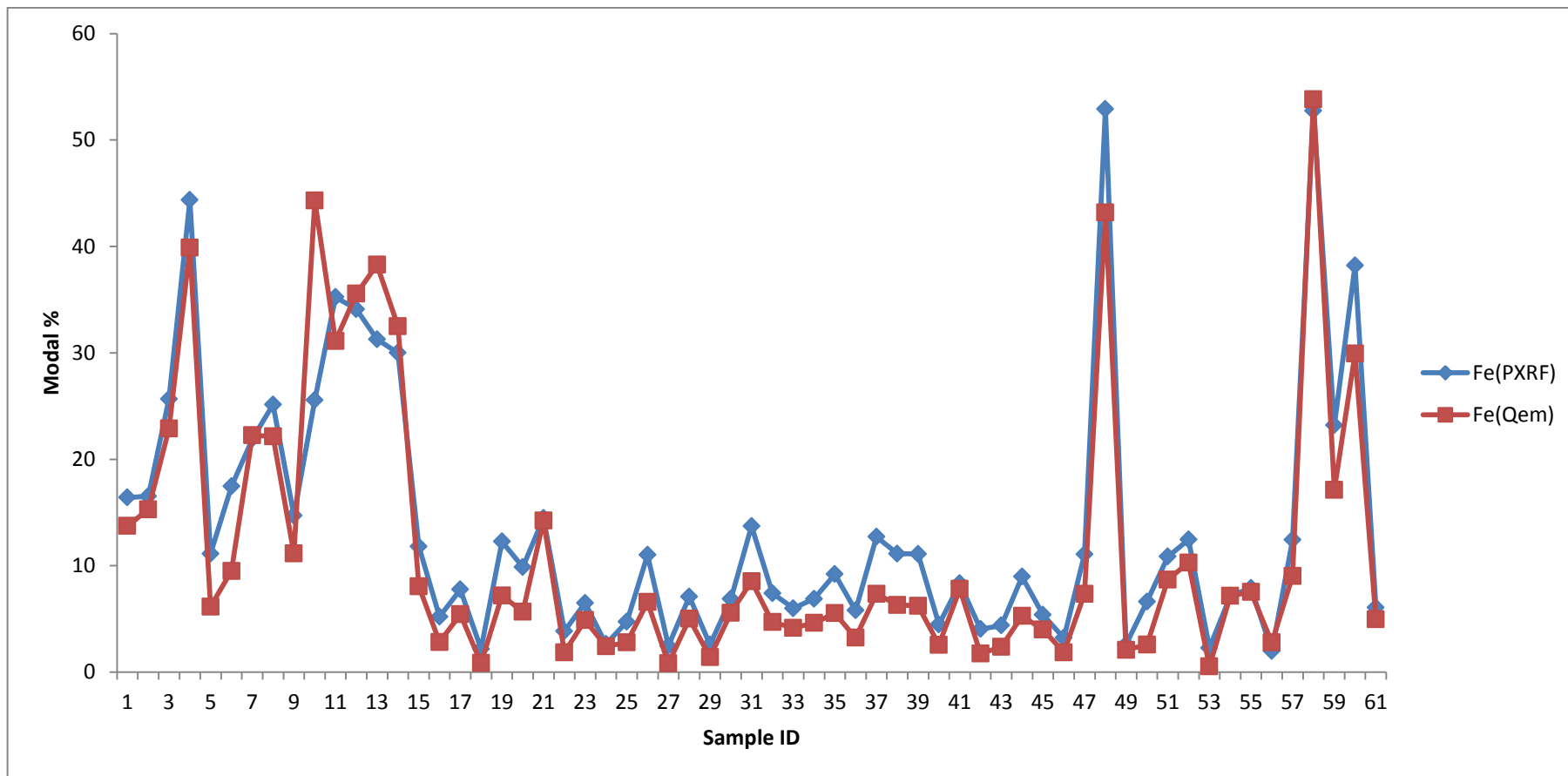


Figure 4.8 - Comparison of Fe wt % determined by PXRF and Fe wt % calculated from the QEMSCAN® results

## **Chapter 5: NIR activity and Mantoverde NIR-active minerals**

### **5.1. Introduction**

This chapter discusses the various analysis and experiments conducted towards identifying individual minerals when developing a strategy for copper preconcentration using Near InfraRed (NIR) spectroscopy. All analyses are carried out with reference to total ore mineralogy as analysed by QEMSCAN<sup>®</sup> and XRD (Tables 4.1 and 4.3 respectively).

The chapter is written in order to achieve desired understanding of application. Initial stage looks at single minerals and classifies them qualitatively as NIR-active or non-active minerals based on absorption of their respective constituent functional groups. Therefore, all the individual minerals as determined by mineralogical analysis were also analysed by NIR. With respect to abundance, classified NIR-active minerals were selected and analysed at different particle grain sizes to investigate the influence of varying particle sizes on NIR. The influence of moisture on spectra was also investigated.

This chapter is concluded by identifying and defining suitable parameters that can be selected in designing NIR preconcentration of hydrothermally formed copper ore bearing minerals from associated waste.

### **5.2. NIR activity and NIR-active minerals**

Ore modal mineralogy Tables 4.1 and 4.3 revealed that the Mantoverde ore is made up of about fifteen different minerals at varying concentration and composition. Individually single minerals display NIR absorption feature(s) as a consequence of their chemistry and structure. Within the longer NIR wavelength region (1300 to 2500 nm), minerals display features as a function of their constituent functional groups ( $\text{CO}_3^{2-}$ ,  $\text{H}_2\text{O}$  and or  $-\text{OH}$ ) (Hunt, 1977; Clark et al, 1990; Aines and Rossman, 1984; Iyakwari et al., 2013).

Individual mineral chemistry indicates that minerals showing absorption feature(s) within the NIR region based on constituent functional groups, in the Mantoverde ore are chrysocolla, malachite, muscovite, biotite, kaolinite, chlorite, calcite, ankerite, tourmaline and apatite. These minerals are therefore referred to here as NIR-active minerals. This group of minerals are mostly alteration or

secondary minerals, produced by hydrothermal alteration processes (Iyakwari et al., 2013).

A second group of minerals do not contain the NIR functional group and as such shows no absorption features within the longer NIR wavelength region (1300 to 2500 nm). But they absorb radiation strongly and have the ability to drown, suppress or mask the NIR-active minerals which display absorption features. This group of minerals are here referred to as NIR-active minerals which do not display absorption features. An example of these minerals in the Mantoverde ore is the Fe-oxide mineral hematite. Other examples include magnetite, and goethite (Van Der Meer, 1995; Bishop and Dummel, 1996). The feature drowning effect of hematite is discussed in details in next the chapter.

A third category of minerals also do not contain NIR-active functional groups. Even when present in combination with other minerals, they go unnoticed, as they do not influence NIR spectra either by absorbing or displaying absorption features. This group of minerals are considered non-active in the NIR. In some instances where these non-active minerals show absorption features, the features are a result of impurities (fluid inclusions) or external environmental interference (moisture) (Aines and Rossman, 1984; Pommerol and Schmitt, 2008; Iyakwari et al., 2013). Water features are common features in most silicate minerals in addition to their diagnostic features, especially the phyllosilicates and occurring in carbonates as traces or impurities from associated clays (Van Der Meer, 1995; Iyakwari et al., 2013). Also the presence and location of the water feature(s) are almost the same in most minerals (Table 5.1), making specific mineral identification using water features difficult and misleading (Iyakwari and Glass, 2014). Examples of non-active minerals in the Mantoverde ore are quartz, plagioclase and potassium feldspars.

Hence, only the NIR-active minerals are considered in designing a strategy for ore preconcentration. Even when spectra contain and display water features, the features are ignored. The influence of external water on NIR feature is discussed in section 5.4.

With reference to Iyakwari et al., (2013), Iyakwari and Glass (2014), Table 5.1 presents minerals in the Mantoverde copper ore, indicating their diagnostic absorption feature(s) wavelength position between 1300 and 2400 nm, the

functional groups responsible for the absorption and classification with respect to their activism. It is assumed here that since quartz, potassium (orthoclase) and plagioclase (anorthite) feldspars samples were dried before taking measurements, the water features observed in their spectra is probably water trapped in their matrix.

Table 5.1 - Absorption features of minerals (between 1300 nm and 2500 nm) in Mantoverde copper ore (after Iyakwari et al., 2013; Iyakwari and Glass, 2014)

Group	Mineral	Molecule absorption feature, nm			Classification
		-OH	H <sub>2</sub> O	CO <sub>3</sub> <sup>2-</sup>	
Silicate	Chrysocolla	1415, 2270	1415, 1915	-	NIR-active
	Muscovite	1415, 2205, 2350	1415, 1840, 1915	-	NIR-active
	Kaolinite	1400, 1415, 2160, 2200	1415, 1840, 1915	-	NIR-active
	Biotite	2255, 2370	1920	-	NIR-active
	Chlorite	1415, 2265, 2360	-	-	NIR-active
	Tourmaline	2210, 2250, 2300, 2370	1950	-	NIR-active
	Quartz	-	1415, 1915	-	Non-active
	Orthoclase	-	1415, 1915	-	Non-active
	Anorthite	-	1415, 1915	-	Non-active
Carbonate	Calcite	-	-	1920, 2000, 2150, 2340	NIR-active
	Malachite	2360	-	2275, 2360	NIR-active
	Ankerite		-	1950, 2320	NIR-active
Phosphate	Apatite	1440, 2000, 2360	-	-	NIR-active
Oxide	Hematite	Does not display absorption feature.			NIR-active

This aspect serves the useful purpose of identifying those spectral absorption features position in the NIR region that are diagnostic of individual minerals in the Mantoverde copper ore. However because natural/geologic materials are rarely, if ever composed of pure, sized, sorted minerals, absorption features collected from an ore may considerably or slightly differ from those collected in single minerals. Ores are commonly composed of assemblages of minerals in a

variety of shapes and sizes with surfaces strained by weathering and alteration (Robb, 2005). Therefore, an ore may or may not show spectrum or spectra displaying complete absorption features of individual NIR-active minerals due to the fact that other NIR-active minerals may also be contributing to the same spectrum. Other factors which may influence individual minerals features in a spectrum are investigated and discussed in subsequent sections.

### **5.3. Influence of minerals particle grain size on NIR spectra.**

To investigate the influence of particle grain size on NIR-active minerals in the Mantoverde copper ore, with exception of malachite, based on mineral abundance, five NIR-active minerals (calcite, muscovite, chlorite, hematite and malachite) were analysed out of the eleven NIR-active minerals in the ore. Pure minerals specimens were crushed and sieved into six (4-2.8 mm, 2.8-2 mm, 2-1.4 mm, 1 mm-710  $\mu\text{m}$ , 710-500  $\mu\text{m}$ , -500  $\mu\text{m}$ ) different size fractions. Of these, hematite is only sieved into four size fractions (4-2.8 mm, 2-1.4 mm, 710-500  $\mu\text{m}$  and -500  $\mu\text{m}$ ). Each sized fraction per mineral were scanned independently, after which four size fractions (4-2.8 mm, 2.8-2 mm, 2-1.4 mm and -500  $\mu\text{m}$ ) of the same mineral were mixed and scanned.

Resultant NIR spectra were analysed in terms of the following parameters considered to be important for mineral identification: a. overall brightness, expressed in terms of the baseline reflectance, b. number of features in the spectrum, c. position, depth, and width of characteristic absorption features. Individual NIR absorption features are characterised in terms of position, depth, and width (Fig. 5.1). The position of the absorption feature is defined by the wavelength where a minimum reflectance is observed (centre), while the feature Depth (D) is defined as the difference between the Maximum Reflectance (Max. R) and the Minimum Reflectance (Min. R). The width of absorption is determined from the difference in wavelengths between the Left shoulder Wavelength (LW) and the Right shoulder Wavelength (RW). The overall Reflectance (R) of a spectrum is defined by the highest reflectance displayed in the NIR wavelength region (Fig. 5.1).

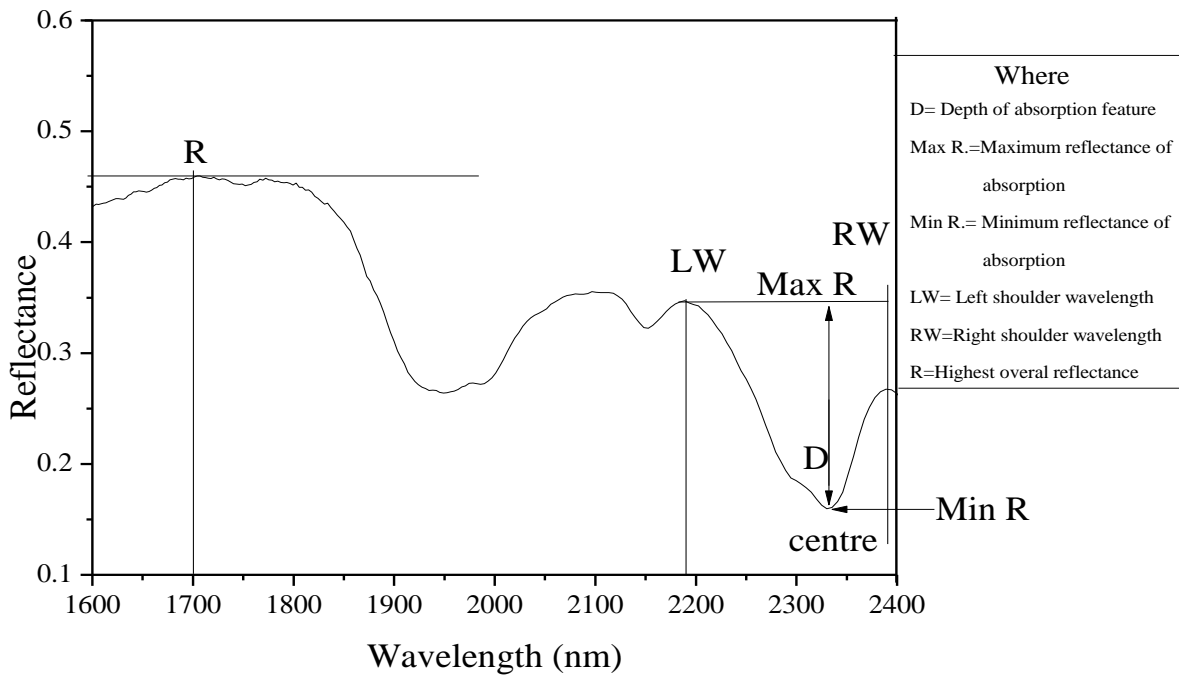


Figure 5.1 - Parameters characterising NIR spectrum of calcite: mineral absorption features and overall reflectance (after Iyakwari and Glass, 2014).

### 5.3.1. Calcite

The calcite sample displays diagnostic absorption features near 1920, 2000, 2150 and 2340 nm (Figure 5.2a). The positions of the absorption features wavelength were consistent across all size fractions. The features near 1920 and 2000 nm were broad and poorly defined and their depth was not measured. The depth of 2150 and 2340 nm features were measured as a function of particle size. The 2150 nm feature revealed an increase in depth of 0.030 for 4-2.8 mm grain size, reaching a maximum of 0.050 for the 1 mm-710  $\mu\text{m}$  size grains class. Below a particle size of 710  $\mu\text{m}$ , the feature depth decreased to 0.03 (Table 5.2). The 2340 nm feature revealed the same pattern from a depth of 0.19 for 4-2.8 mm size fraction, reaching 0.26 for 1 mm-710  $\mu\text{m}$  and decreasing to 0.22 for the finer sizes of -500  $\mu\text{m}$ .

The sample displayed its highest reflectance value around 1700 nm. Therefore, all reflectance measurements were carried out for all size fractions with reference to 1700 nm. Analysis reveals that, with each size reduction, reflectance values increased (Table 5.3). Figure 5.2a shows that the overall brightness of spectra increases with decreasing particle size. Figure 5.2a also confirms that the feature width is constant across all size fractions.

The spectra of the mixtures of the four grain sizes (Fig. 5.2b) reveals absorption positions that are diagnostic of the mineral, as reflectance displayed by spectra cannot be said to be diagnostic of any of the particle grain sizes in the mixture. Hence, given the better visibility of the absorption feature near 2340 nm across all the size fractions and mixture compared to other features, the 2340 nm feature was identified as the best wavelength for identification of calcite.

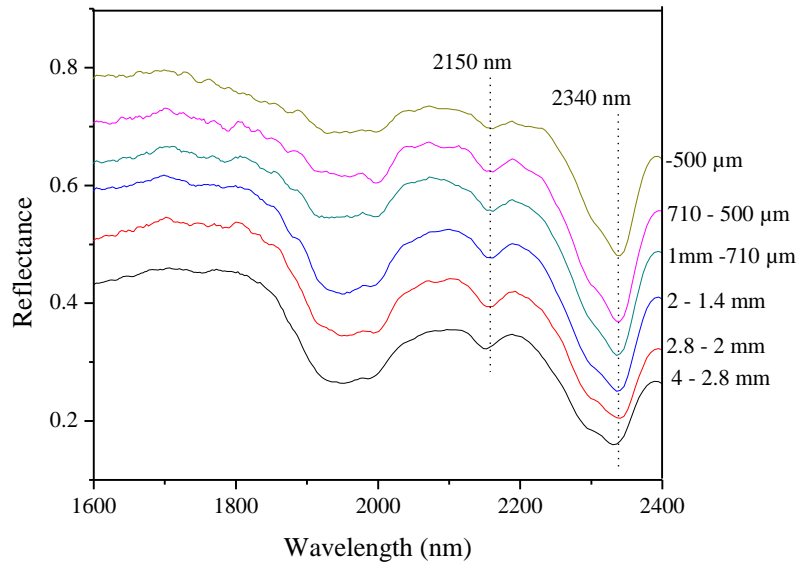


Figure 5.2a - NIR reflectance spectra of calcite measured on six different particle size fractions.

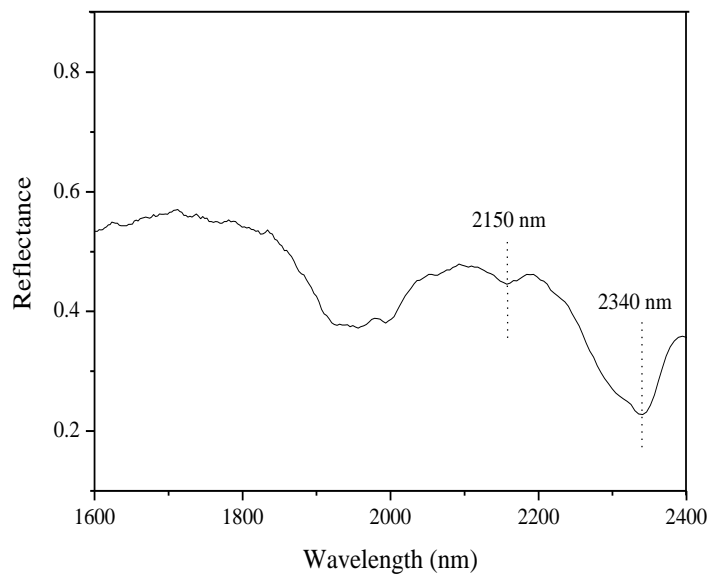


Figure 5.2b - NIR spectra of mixture of calcite at four different grain sizes



Table 5.2 - Feature depth at two wavelengths for different size fractions of calcite.

Size fractions	Feature depth at wavelength	
	2150 nm	2340 nm
4-2.8 mm	0.03	0.19
2.8-2 mm	0.05	0.22
2-1.4 mm	0.05	0.25
1 mm-710 $\mu\text{m}$	0.05	0.26
710-500 $\mu\text{m}$	0.04	0.25
-500 $\mu\text{m}$	0.03	0.22

Table 5.3- Reflectance values for different size fractions of calcite.

Size fractions	Reflectance value measured at 1700 nm
4-2.8 mm	0.46
2.8-2 mm	0.54
2-1.4 mm	0.62
1 mm-710 $\mu\text{m}$	0.67
710-500 $\mu\text{m}$	0.73
-500 $\mu\text{m}$	0.81

### 5.3.2. Muscovite

The muscovite sample displays characteristic absorption features near 1415, 1840, 1915, 2200, and 2350 nm. All characteristic absorption features were consistently observed in spectra across the various size fractions. Features near 1415, 1840 and 2200 nm were distinctly visible for all the various size fractions (Figure 5.3a). The 2350 nm features appeared weak, while the 1915 nm feature was almost invisible in the spectra of some particle size fractions (e.g. 2.8-2 mm, and 1 mm-710  $\mu\text{m}$ ).

The depth of measured features at 1415 and 2200 nm showed a maximum within the 1 mm-710  $\mu\text{m}$  particle size range (Table 5.4). Measurement of

absorption depth at 1415 nm showed an increase from 0.19 at a particle size of 4-2.8 mm to 0.25 for 1 mm-710  $\mu\text{m}$  size particles, before dropping to 0.22 for -500  $\mu\text{m}$  size particles. The 2200 nm feature measured 0.22 for -500  $\mu\text{m}$  size fraction, with the smallest value of 0.13 obtained for 4-2.8 mm size fraction. The depth of the 1840 nm feature, which was a mineral-specific water feature (Aines and Rossman, 1984; Iyakwari and Glass, 2014), varies inconsistently with particle size (Table 5.4), (i.e. -OH bond detection which is indicative of water or -OH minerals in the crystal lattice). This is also true for the other water feature near 1915 nm.

The different size fractions display the highest reflectance values near 1720 nm. Hence, all reflectance measurements for muscovite were made with reference to this wavelength position. Measurement showed that the fine particle sizes have higher reflectance values than the larger particles (Table 5.5). Figure 5.3a shows spectra of all size fractions and their varying overall brightness displaying an increase from larger size fractions to finer size fractions. In addition, the width of the absorption feature revealed no variation across all sizes.

The spectra of mixture (Fig. 5.3b) shows spectra display characteristic absorption features similar to Figure 5.3a. The overall brightness displayed by spectra is not indicative of any of the grain sizes in concentration. The absorption features displayed by spectra are consistent with those of Figure 5.3a.

Due to strong visibility of the 1415 and 2200 nm features, these wavelengths were suitable for identifying muscovite. However, the feature near 1400 nm may also indicate water or -OH bearing minerals when a second feature is observed at 1900 nm (Aines and Rossman, 1984; Iyakwari and Glass, 2014). In the absence of a feature at 1900 nm, interpretation of the feature at 1415 nm was unclear. Hence, the feature at 2200 nm is the best diagnostic for muscovite.

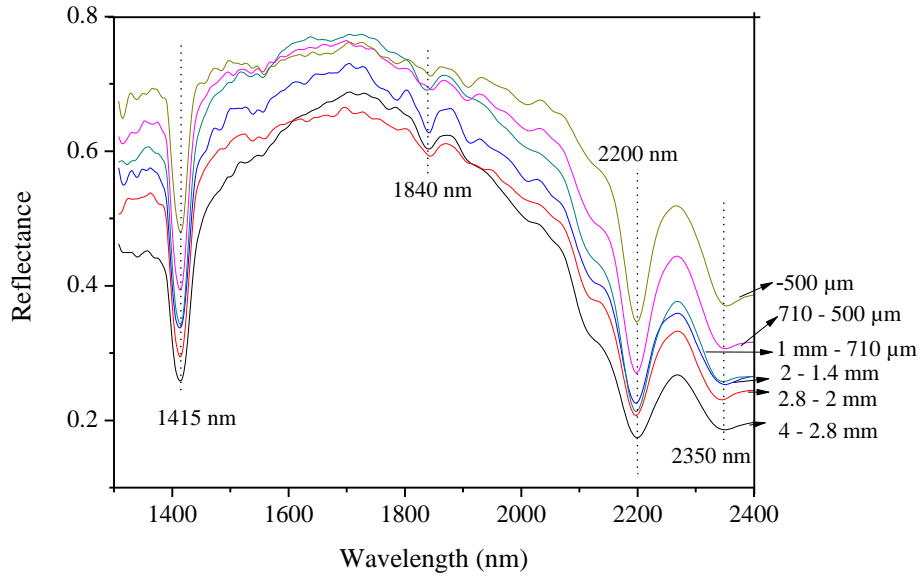


Figure 5.3a - NIR reflectance spectra of muscovite measured on six different size fractions.

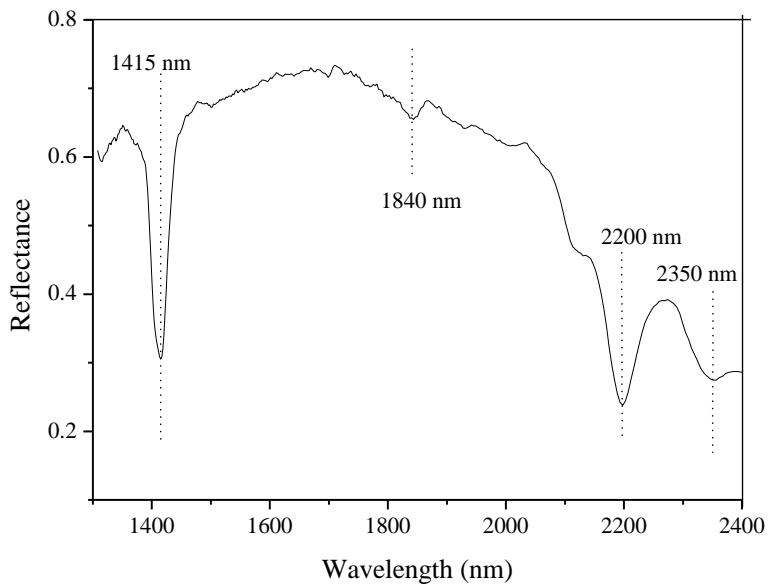


Figure 5.3b - NIR spectra of mixture of muscovite at four different grain sizes

Table 5.4 - Feature depth at three wavelengths for different size fractions of muscovite.

Size fractions	Feature depth at wavelength (nm)		
	1415	1840	2200
4-2.8 mm	0.19	0.07	0.13
2.8-2 mm	0.22	0.05	0.16
2-1.4 mm	0.24	0.06	0.18
1 mm-710 $\mu\text{m}$	0.25	0.04	0.20
710-500 $\mu\text{m}$	0.24	0.02	0.20
-500 $\mu\text{m}$	0.22	-	0.22

Table 5.5 - Reflectance values for different size fractions of muscovite.

Size fractions	Reflectance value measured at 1720 nm.
4-2.8 mm	0.65
2.8-2 mm	0.66
2-1.4 mm	0.73
1 mm-710 $\mu\text{m}$	0.77
710-500 $\mu\text{m}$	0.76
-500 $\mu\text{m}$	0.76

### 5.3.3. Hematite

Hematite is a non-feature displaying NIR-active mineral. Figure 5.4a reveals that the largest particles size (4-2.8 mm) absorbs more strongly and the spectral brightness increased with reduction in particle size. Therefore, it was concluded that, where large hematite crystals were present in a particle, resultant spectra will show low reflectance.

Given hematite's inability to display absorption features, spectrum of mixtures at four size fractions reveals its strong spectra absorption characteristics across wavelength (Fig. 5.4b).

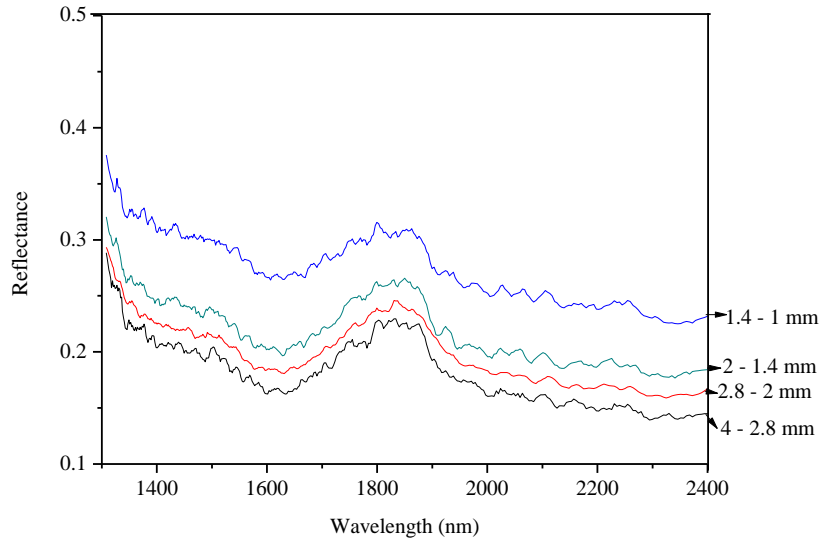


Figure 5.4a - NIR reflectance spectra of hematite measured on four different size fractions.

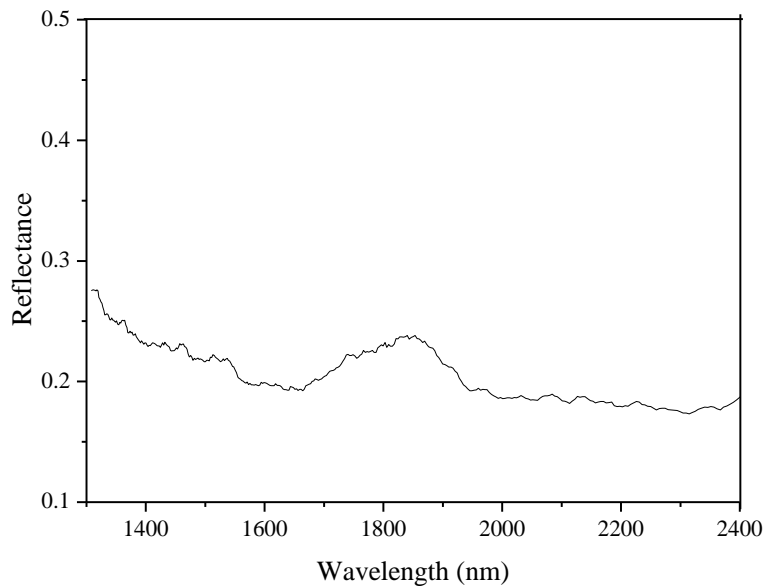


Figure 5.4b - NIR spectra of mixtures of hematite at four different grain sizes

### 5.3.4. Malachite

Malachite displays characteristic absorption features near wavelengths of 2275 nm and 2360 nm. Measurements of the depth of absorption features (Table 5.6) reveal an increase in absorption depth with decreasing particle size. The 2275 nm feature has an initial depth of 0.06 at 4-2.8 mm and increased to 0.13 for -500  $\mu$ m. The 2360 nm feature decreased with particle size from 0.01 for 4-2.8 mm to 0.04 for -500  $\mu$ m size fraction. Given the stronger visibility of 2275 nm

features across the different size fractions, it was the best diagnostic value of malachite within the 1300 to 2400 nm NIR range.

The influence of particle size was also observed in the overall reflectance of the sample as the level of reflectance increased with reducing particle size, from 0.27 for 4-2.8 mm, reaching 0.44 for the -500  $\mu\text{m}$  size fraction (Table 5.7). While the width of the absorption features is approximately constant, the highest reflectance values were observed near 1870 nm.

The spectra of mixture at four size fractions reveal absorption features with maintained wavelength positions and overall brightness not corresponding to any grain size. Thus, indicating that absorption feature position is optimal for malachite identification.

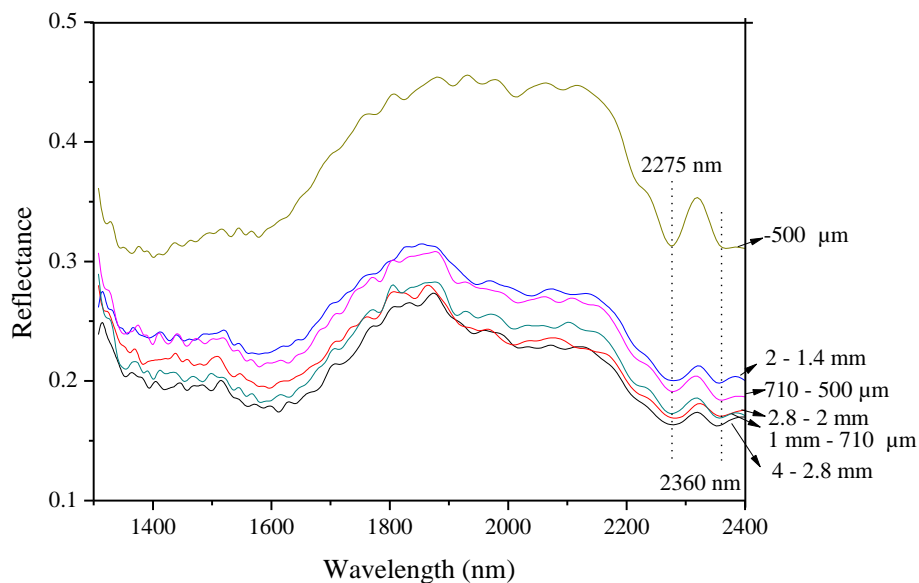


Figure 5.5a - NIR reflectance spectra of malachite measured on six different size fractions

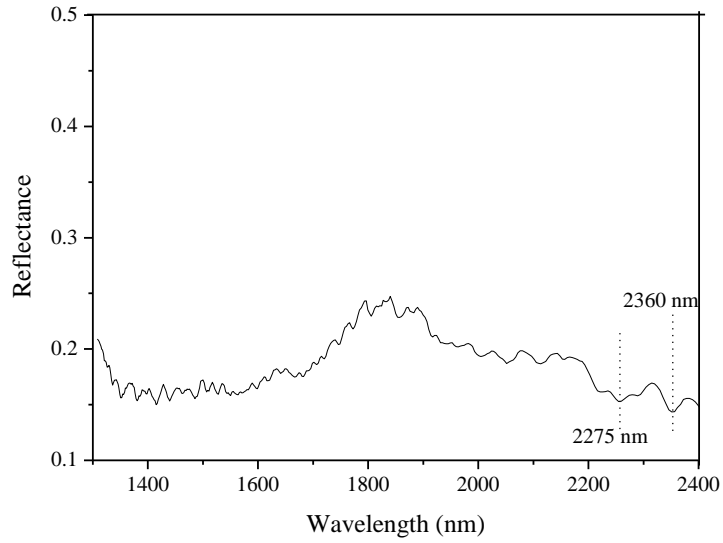


Figure 5.5b - NIR spectra of mixture of malachite at four different grain sizes

Table 5.6 - Feature depth at two wavelengths for different size fractions of malachite.

Size fractions	Absorption depth at wavelength	
	2275 (nm)	2360 (nm)
4-2.8 mm	0.06	0.01
2.8-2 mm	0.06	0.01
2-1.4 mm	0.07	0.02
1 mm-710 $\mu\text{m}$	0.07	0.02
710-500 $\mu\text{m}$	0.08	0.02
-500 $\mu\text{m}$	0.13	0.04

Table 5.7 - Reflectance values for different size fractions of malachite.

Size fractions	Reflectance value measured near 1870 nm.
4-2.8 mm	0.27
2.8-2 mm	0.26
2-1.4 mm	0.30
1 mm-710 $\mu\text{m}$	0.28
710-500 $\mu\text{m}$	0.28
-500 $\mu\text{m}$	0.44

### 5.3.5. Chlorite

Chlorite (clinochlore) displays characteristic features near 1415, 2265 and 2360 nm. Though some absorption features were weak and lacked a clearly defined central absorption wavelength, all absorption feature positions and feature widths are consistent across all size fractions (Fig. 5.6a).

The 2265 nm feature displays its largest depth for <math>-500\ \mu\text{m}</math> sized particles (Table 5.8). The 2360 nm feature was more visible at <math>-500\ \mu\text{m}</math> and <math>710\text{-}500\ \mu\text{m}</math>, with a depth of 0.02 at both size fractions. The 2360 nm feature was invisible at <math>2\text{-}1.4\ \text{mm}</math> size fraction, where the feature lacks absorption centre. The 1415 nm feature was only visible at the smallest (<math>-500\ \mu\text{m}</math>) and largest (<math>4\text{-}2.8\ \text{mm}</math>) particle size (Fig. 5.6a).

The highest reflectance value is measured near 1800 nm (Table 5.9) and the reflectance reduced with increasing particle size. Contrary to the features at 1415 and 2360 nm, the feature at 2265 nm was observed across all particle size ranges and was hence the best diagnostic of chlorite.

The spectra of mixture show all features visible with similar widths, but displaying overall brightness not corresponding to any of the grain size in the mixture (Fig. 5.6b)



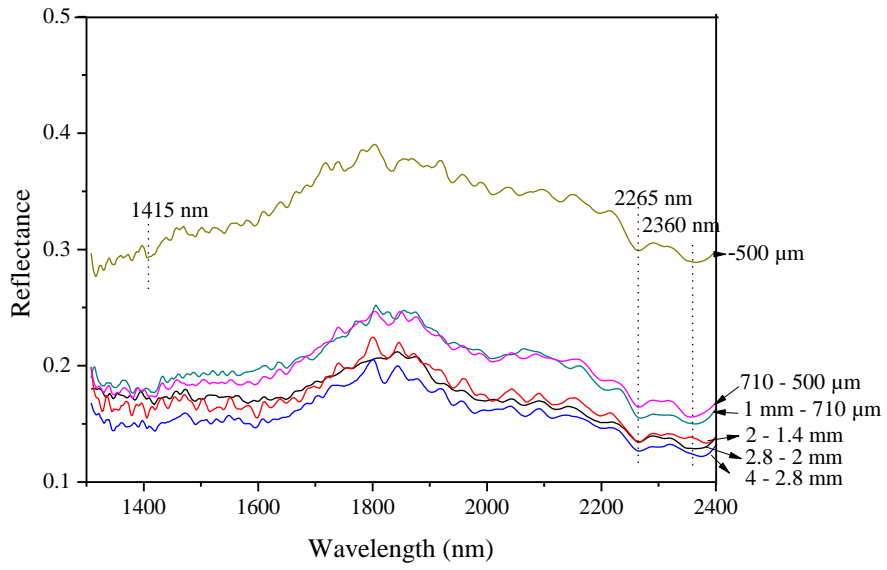


Figure 5.6a - NIR reflectance spectra of chlorite measured on six different size fractions.

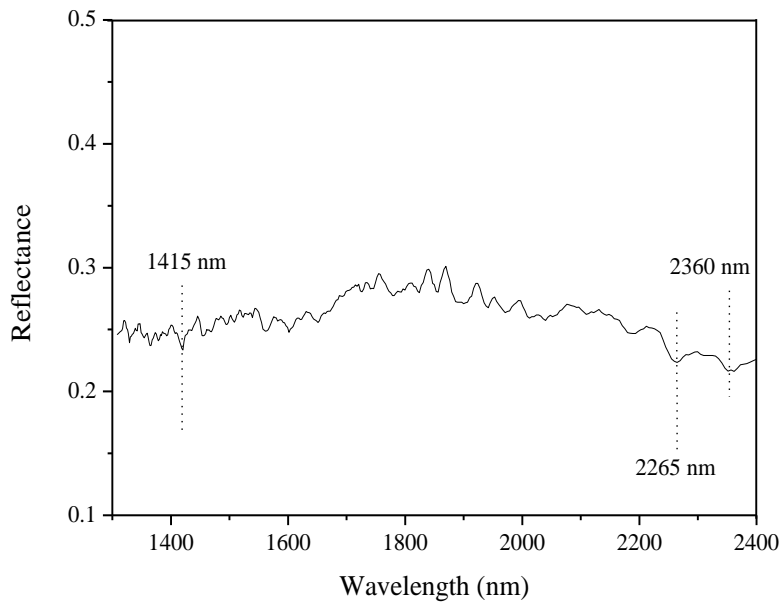


Figure 5.6b - NIR spectra of mixture of chlorite at four different grain sizes

Table 5.8 - Feature depth at three wavelengths for different size fractions of chlorite.

Size fractions	Absorption depth at wavelength		
	1415 (nm)	2265 (nm)	2360 (nm)
4-2.8 mm	0.011	0.02	0.01
2.8-2 mm		0.02	0.01
2-1.4 mm	-	0.02	-
1mm-710 $\mu$ m	-	0.02	0.01
710-500 $\mu$ m	-	0.02	0.02
- 500 $\mu$ m	0.008	0.03	0.02

Table 5.9 - Reflectance values for different size fractions of chlorite.

Size fractions	Reflectance values measured near 1800 nm
4-2.8 mm	0.20
2.8-2 mm	0.20
2-1.4 mm	0.20
1mm-710 $\mu$ m	0.25
710-500 $\mu$ m	0.25
-500 $\mu$ m	0.38

#### 5.4. Effect of moisture

Lawrence (2009) and Gaydon (2011) investigated the effect of moisture on NIR spectra of particles from Mantos Blancos copper ore. Both authors considered the influence of moisture on NIR spectra with little or no consideration on the role played by ore mineralogy. The present investigation on the influence of moisture on the Mantoverde copper samples by the author in addition considers sample mineralogy. Therefore, particles of Mantoverde copper ore were carefully selected to reflect mineralogy of the ore. Four splits B2 particles were selected from a batch of 60 samples (Fig. 3.1). Samples 2 and 3 were selected on the basis of their dominant hematite and chrysocolla content. Samples 25 and 27 were respectively selected on the basis of their chlorite-calcite and muscovite-calcite mineralogy (Table 4.1). Samples were measured separately

under a number of conditions (Table 5.10). Samples were marked, such that individual spectrum was mapped for 1:1 comparison for each condition.

Particles were scanned directly from stock, after which they were soaked in water for six hours. The wet (saturated) samples were subsequently measured with the line NIR scanner. The samples were then dried under the sun, on a dry and sunny summer day with an average atmospheric temperature of 22 °C (www.bbc.co.uk/weather 2013). The dried samples were then measured. Samples wetting was repeated for another six hours, after which they were oven dried at an average temperature of 50 °C. Gaydon (2009) noted that measuring samples directly after oven drying affects spectra due to heat stored in sample. Therefore, the oven dried samples were left to cool before scanning.

Table 5.10 - Description of various conditions of measurement

Measurement Label	Description
Stock	Samples from storage
Wet	Samples soaked and measurement taken while wet.
Sun dried	Measurement taken after sun drying of samples at an atmospheric temperature of 22 °C (www.bbc.co.uk/weather 2013).
Oven dried	Measurement taken after samples dried in oven at temperature of 50 °C and left to cool.

Figures 5.7 to 5.10 are spectra of Mantoverde particles at different conditions. The addition of water to the surface of the particles has significant impact on the NIR spectra. The impact of water is noted by the overall loss of intensity of spectra in the wet specimen. This confirms findings by Lawrence (2009) and Gaydon (2011). Furthermore, samples 25 and 27 which have little or no hematite concentrations (Table 4.1), display a strong absorption near 1900 nm (Fig. 5.9 and 5.10), indicating the presence of water in spectra. NIR spectra of the hematite-rich sample (samples 2 and 3) though displaying low intensity, do not show water absorption features like those observed in samples 25 and 27. Hence, it can be said that the presence of water feature(s) due to external

influence is sample mineral composition dependent. Hence, analysis indicates the hematite feature masking ability on the water feature. Also affected by water were the features originally strong when samples were dry. Features appear weak with some having no absorption centres, while others are displaced from their original position (Fig. 5.10).

Drying the wet samples either under the sun or in oven showed that spectra features quality and visibility can be improved. In term of spectra intensity, compared to sun drying, the oven dried samples show improved spectra intensity. Both drying method achieved almost similar results in terms of feature visibility (Fig. 5.7 to 5.10). Hence, if samples contain moisture, a drying step may be required prior to sorting. This drying step may be important in mines where the as-mine is often saturated with water. While oven drying may be capital intensive, sun drying is environment (weather) dependent.

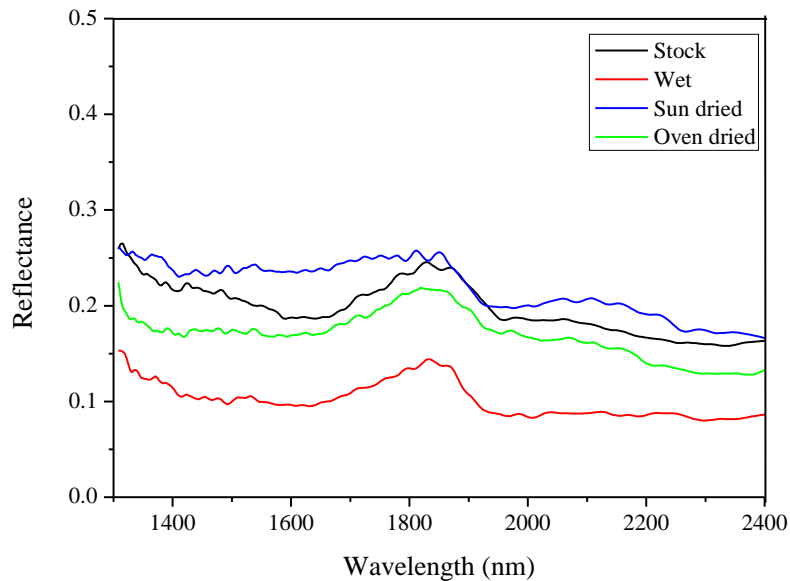


Figure 5.7 - Effects of various conditions on spectrum of sample 2

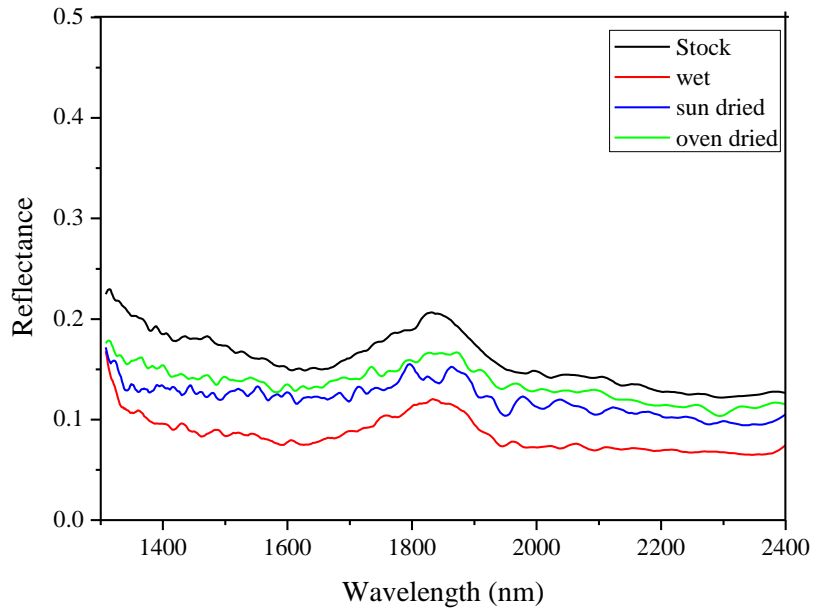


Figure 5.8 - Effects of various conditions on spectrum of sample 3

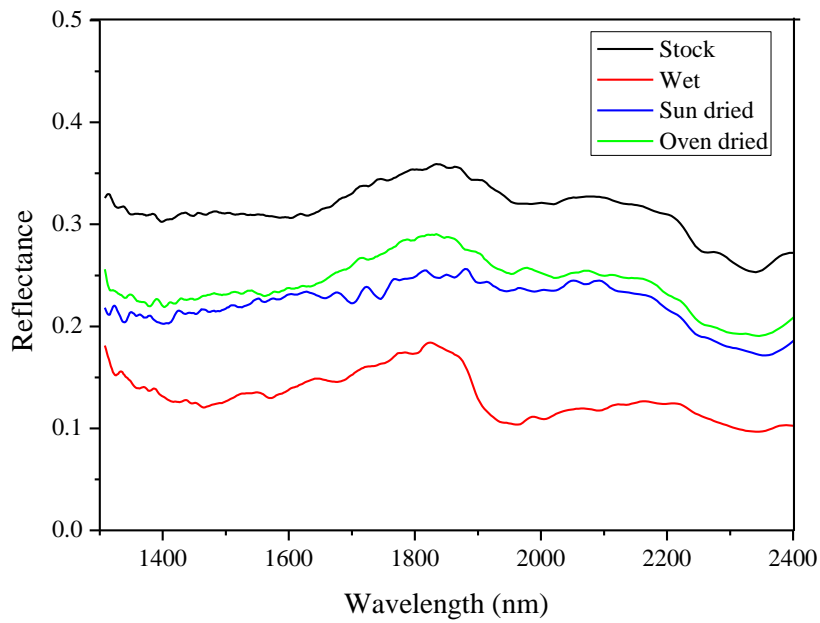


Figure 5.9 - Effects of various conditions on spectrum of sample 25

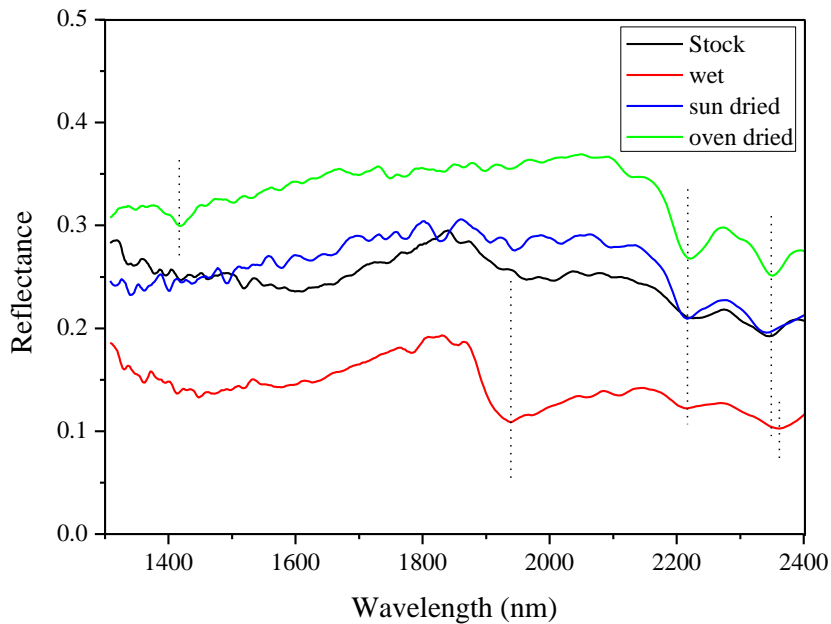


Figure 5.10 - Effects of various conditions on spectrum of sample 27

### 5.5. Implication for ore sorting

Analysis of NIR spectra has shown that secondary copper-bearing minerals (chrysocolla and malachite) can be distinguished from waste minerals (calcite, kaolinite, chlorite, muscovite etc.) based on distinctive characteristic absorption features of their functional groups (-OH and or  $\text{CO}_3^{2-}$ ). Analysis of single minerals also shows that no two minerals display completely identical absorption spectra. Though some features may be common to more than one mineral. For example, muscovite and kaolinite share features in several wavelength regions. However, kaolinite display twin absorption features compared to muscovite's single features. Some mineral spectra may contain features relating to the same functional group at a different wavelength. An example is the spectra of malachite and calcite: while calcite displays strong carbonate features near 2340 nm, carbonates in malachite show absorption features at 2275 and 2360 nm. This also applies to chrysocolla and muscovite, and chlorite and chrysocolla.

Analysis of NIR spectra indicates that, across different particle sizes for all minerals, diagnostic absorption features were observed at similar wavelength

positions and had a similar width. However, feature depth was affected by variation in particle size. The extent to which feature depth was influenced by particle size depends on the type of mineral. This was in agreement with Clark (1999), who states that an increase in particle grain size first increases absorption feature depth before reaching a maximum and then decreasing. Since feature depth was not constant for all particle size fractions of the same mineral, the depth was not a diagnostic of a mineral.

Measurement of reflectance values for each spectrum showed that larger particle sizes display higher spectra absorption across the wavelength range compared to the smaller particle sizes. This was also in agreement with Crowley and Vergo (1988) and Van der Meer (1995). Both authors noted that more light was scattered by fine particles before much absorption can take place, resulting in relatively higher reflectance. Gaffey (1986) observed that a less densely packed-powdered-mineral sample reflects more than the densely packed-solid-sample of the same mineral or rock. Clark (1999) also observed that larger particles have a greater internal path where photons may be absorbed. Hence, due to multiple scattering in the NIR region, overall brightness decreases with increasing particle size. This then means that an ore consisting of individual large crystals (phenocryst) will have a lower overall level of reflectance. This is in agreement with Pasikatan et al. (2001), who state that the NIR reflectance was sensitive to particle size and shape.

When a particle consists of an assembly of minerals, its NIR spectrum was likely to differ from, the spectra of its constituent NIR-active mineral(s). Alternatively, the NIR spectrum may correspond to the spectrum of the dominant NIR-active mineral. The dominant mineral in a spectrum may not be the mineral with the highest concentration. Surfaces of ore particles may consist of a range of grain sizes. In practice, there is no similarity in depth of absorption features and spectral brightness across different grain size fractions of the same mineral. Hence, identification of individual minerals rests on identifying characteristic absorption features at specific wavelengths. With respect to the selected minerals, strong diagnostic features e.g. 2340 nm for calcite, 2200 nm for muscovite, 2275 nm for malachite and 2265 nm for chlorite are promising due to their consistent visibility across different size ranges.

NIR spectra are sensitive to presence of water expressed in features near 1400/1900 nm and 1840 nm (Aines and Rossman, 1984). Water is either adsorbed on the mineral surface or part of the mineral crystal structure (Aines and Rossman, 1984; Dalm et al., 2014). Water/moisture reduces the amount of details observed in a NIR spectrum and as well reduces the spectra intensity. Analysis of muscovite and chlorite suggests that the presence and depth of water features is inconsistent with particle size. In complex mineral assemblies, in addition to external moisture, more than one mineral may be responsible for the water feature in a spectrum. Also samples exposed to water are likely to have the absorption features of their constituent minerals as well as their spectra intensity reduced. Hence, water features are not considered a good diagnostic for particle identification and classification.



## **Chapter 6: NIR preconcentration strategy development**

### **6.1. Introduction**

The objective of most mineral processing operations is to separate minerals into two or more fractions based on their value (Wills and Napier Munn, 2006). Therefore, the main goal of NIR spectral processing in a mineral processing operation is to accurately classify the composition of every spectrum as obtained in a scan relating to a sample composition based on their values into two or more fractions. This is made complicated by the fact that most spectra are a reflection of a complex mixture of minerals. Hence, a number of minerals could exist within the range in varying compositions or arrangements among other modes of occurrence.

This chapter aims to predict individual NIR-active mineral(s) exerting a dominant influence over other mineral(s) response, scanned within the same NIR spectral range. Mineral associations as determined from the Mantoverde copper ore mineralogy is used for this investigation. Since samples provided for studies by Anglo American Mantoverde operations are just a fraction of the entire ore, other possible associations are investigated. Therefore, this is more extensive research.

Chrysocolla, malachite and cuprite are the copper-bearing minerals in the ore as analysed by QEMSCAN<sup>®</sup>. Both chrysocolla and malachite are copper ore minerals that show distinctive absorption features within the NIR region, based on their constituent functional groups. In addition to its trace occurrence, cuprite is non-active in the NIR region. Therefore, chrysocolla and malachite preconcentration is scoped from associated NIR-active waste minerals in the ore. NIR-active waste minerals in the ore include kaolinite, calcite, muscovite, chlorite, biotite, and hematite.

There are four types of complex mixtures or associations of materials at just about any scale: intimate, linear or areal, coating and molecular mixtures (Clark et al., 1999). With respect to current research, intimate and linear mixtures are investigated. This chapter is dedicated to intimate mixtures while the next chapter considers linear mixtures of minerals. The chapter aims to further study intimate mixtures of NIR-active minerals and explore strategies of applications in complex ore preconcentration.

This chapter uses mixtures of minerals with the sole aim of quantitatively and qualitatively defining and or classifying a NIR spectrum by its absorption features (Iyakwari et al., 2013), and developing a copper-bearing mineral discrimination strategy from associated waste.

## **6.2. Intimate Mixtures**

An ore particle may contain minerals with similar or dissimilar functional groups. An attempt is made to investigate the spectral behaviour of individual minerals NIR activity when two or more minerals occur together along the same spectrum range. According to Iyakwari and Glass (2014), NIR feature depth and reflectance are affected by variation in particle size. Hence, to avoid the influence of varying particle size, similar particle sizes were used for study. Individual pure NIR-active minerals were crushed and ground to  $-45\ \mu\text{m}$  particle grain size fraction. Intimate mixtures of NIR-active minerals were prepared, measured and their NIR spectra analysed. Minerals were homogeneously mixed by ratios of mass, such that all minerals appeared together and were scanned within the same spectrum range. Hence, minerals within each prepared association appeared together spatially and homogeneously associated at varying concentrations, such that optical discrimination was not possible.

This study is intended to reveal the degree of sensitivity of these minerals individually in the mixtures. The investigation also aims to see if individual minerals can be singularly identified and classified relative to one another and at what ratio spectra appears mixed, showing absorption features relating to all minerals in concentration or when one mineral relative to the other(s) becomes invisible (masked or replaced) in a spectrum.

In order to achieve these set objectives, the investigation was broken down into four parts:

- i. Minerals with similar functional groups,
- ii. Minerals with dissimilar functional groups,
- iii. Influence of hematite on NIR-active minerals which display absorption feature(s) and
- iv. Complex mixture or associations.

For the purpose of discussion, only one spectrum per mixing ratio or individual mixture is taken and compared with others of different ratios. This is due to spectra similarity.

### **6.2.1. Mixtures of NIR-active minerals with similar functional groups**

Most minerals analysed contain similar functional groups (either -OH, H<sub>2</sub>O or CO<sub>3</sub><sup>2-</sup>), therefore an attempt is made to investigate individual minerals exerting a dominant influence over other mineral responses containing similar functional groups, scanned within the same NIR spectral range.

#### **6.2.1.1. Chrysocolla-Muscovite mixtures**

NIR spectra of mixtures of chrysocolla and muscovite are presented in Figure 6.1. Analysis of the spectra of mixtures across ratios shows the water features near 1415 and 1915 nm are present across all mixing ratios. In addition to the water features in the spectra, from chrysocolla-muscovite ratios of 4:6 to 6:4, two features appear side-by-side near 2200 and 2270 nm, diagnostic of muscovite and chrysocolla respectively. The muscovite feature near 2200 nm disappears from chrysocolla-muscovite ratio of 7:3 to 9:1, where the chrysocolla feature near 2270 nm is the only visible feature at longer wavelengths. Also at longer wavelengths only the muscovite feature near 2200 nm is visible from chrysocolla-muscovite ratio 1:9 to 3:7, signifying muscovite dominance.

Since spectra are mixed between ratios 4:6 and 6:4, and each mineral is only dominant when 70 % and above, spectra dominance by either mineral is therefore concentration dependent. This implies that for either mineral to dominate the spectra it must occur at a higher concentration relative to the other (i.e. 70 % and above).

Therefore, in samples where muscovite and chrysocolla display such behaviours, NIR spectrum showing only chrysocolla features near 2270 nm, with or without water features will indicate high grade chrysocolla (70 % and above). Given that chrysocolla is the mineral sought after, spectrum showing strictly muscovite feature (2200 nm) may not indicate muscovite alone, but high grade muscovite relative to chrysocolla, as muscovite dominates spectra at lower chrysocolla concentrations. Therefore, low grade chrysocolla is easily masked at such a scale. An understanding of the ore grade and nature will be important in dealing with such situations. Where spectrum appears mixed, it

indicates equal concentration. If ore mineralogy confirms that both minerals occur in nearly equal concentration, they are better preconcentrated together, as discriminating between both minerals using NIR applications is not advised, because it may result in incorrect classification.

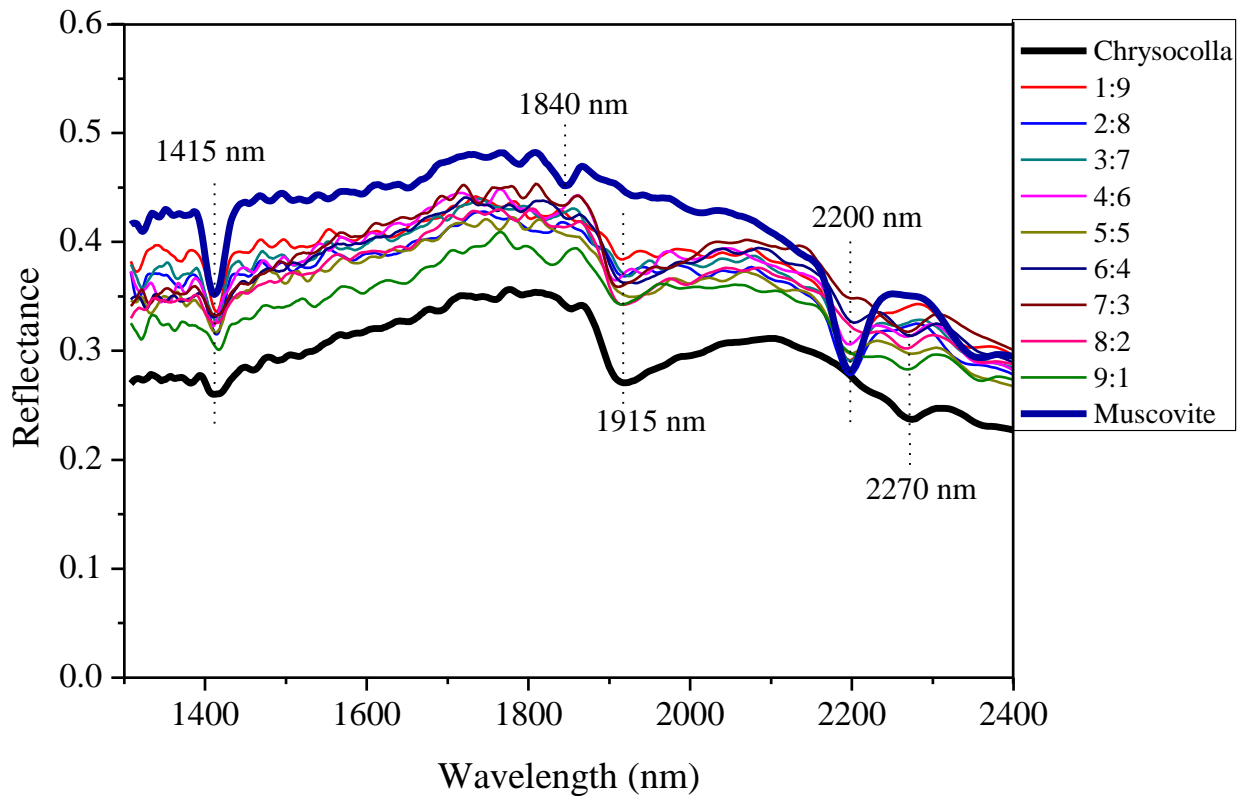


Figure 6.1 - NIR spectra of chrysocolla-muscovite mixtures

Bottom and top spectrum are reference for chrysocolla and muscovite respectively

### 6.2.1.2. Chrysocolla-Kaolinite mixtures

The doubling of features at both shorter (1400 and 1415 nm) and longer (2160 and 2200 nm) wavelengths exhibited by kaolinite differentiates it from other minerals, especially other hydroxyl-bearing minerals. Chrysocolla shares water features near 1415 nm and 1915 nm with kaolinite, but is differentiated from kaolinite by its 2270 nm feature. Kaolinite also shows an additional water feature near 1840 nm.

NIR spectra of mixtures (Fig. 6.2) show kaolinite's double features at shorter wavelengths (1400 and 1415 nm) from chrysocolla-kaolinite ratios 1:9 to 6:4. An indication of the presence of chrysocolla at shorter wavelengths is notable by

the weakening of kaolinite feature near 1400 nm. At longer wavelengths, chrysocolla begins to display its diagnostic features side-by-side to those of kaolinite at ratio 5:5.

Unlike kaolinite, which has features occurring in isolation at higher kaolinite ratios, the chrysocolla feature (2270 nm) is not observed in any of the spectrum to occur in isolation even at higher ratios. The kaolinite feature near 2200 nm is slightly displaced at chrysocolla-kaolinite ratio 9:1, to 2215 nm. Kaolinite is more readily accessible to NIR radiation than chrysocolla and its spectra dominance is not concentration dependent. This is in agreement with Hunt (1979), who noted that the intensity of mineral features does not only reflect its concentration but also its accessibility to radiation.

Hence, in samples where only kaolinite and chrysocolla are the NIR-active minerals, identification of chrysocolla in a spectrum will only be achieved if its concentration is higher than kaolinite (approximately  $\geq 50\%$ ). Discrimination between both minerals will only be achieved if chrysocolla displays its best diagnostic feature (2270 nm) in isolation, not associated with kaolinite. Just like the case of chrysocolla-muscovite (Fig. 6.1), in situations where both minerals occur together and display features as in Figure 6.2, both minerals are better considered together as discrimination will result in a loss of the desired mineral (chrysocolla) to waste.

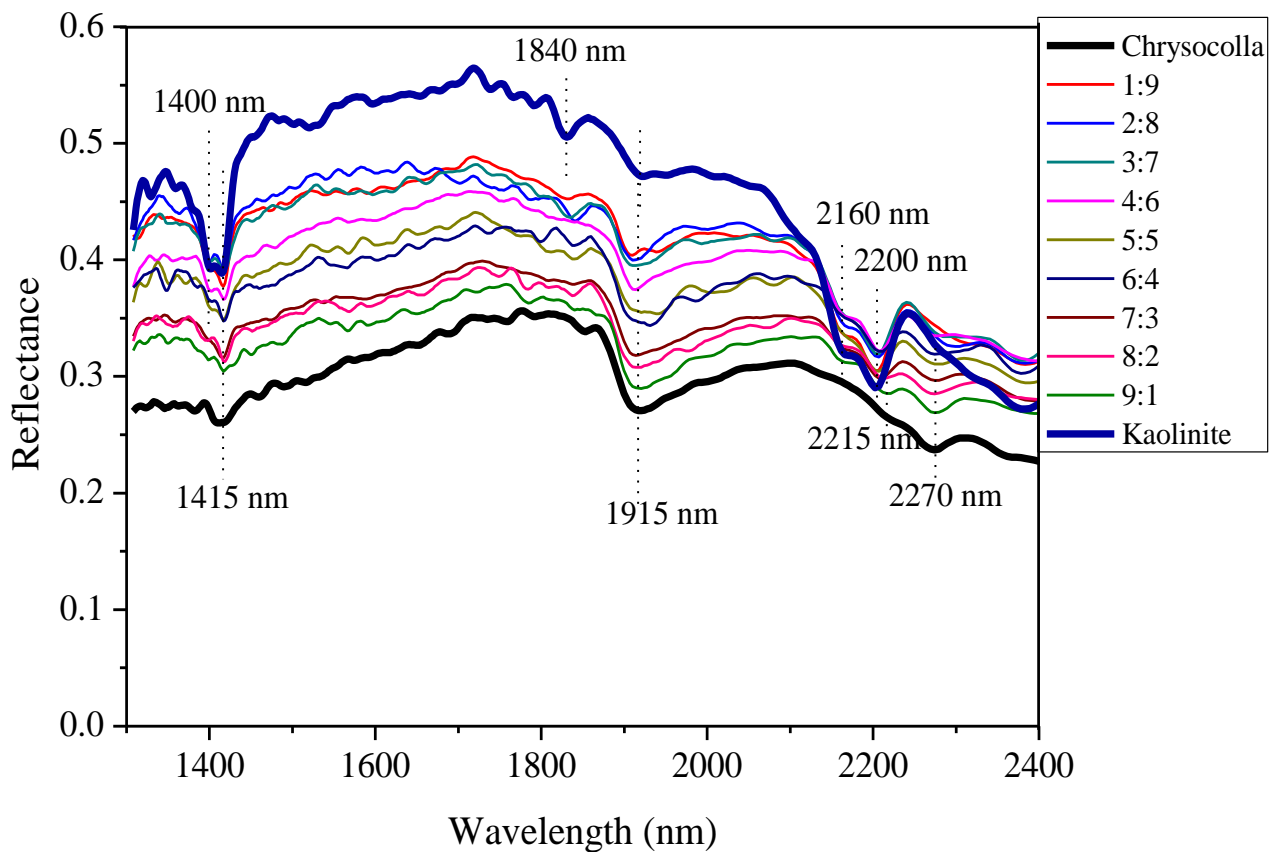


Figure 6.2 - NIR spectra of chrysocolla-kaolinite mixtures

Bottom and top spectrum are reference for chrysocolla and kaolinite respectively

### 6.2.1.3. Chrysocolla-Chlorite mixtures

Both minerals shared feature near 1415nm. As individual minerals, chrysocolla shows additional features near 1915 and 2270 nm while chlorite shows features near 2265 and 2360 nm. NIR spectra of mixtures of chrysocolla-chlorite (Fig. 6.3), displays a typical example of complete spectral mixing. Spectra exhibit features side-by-side corresponding to both minerals across series at all ratios. NIR is not an option for either individual minerals identification or classification of either mineral in this mixture. If there is no prior knowledge of the constituent minerals, interpretation of spectra will favour chlorite, since spectra shows chlorite's additional feature near 2360 nm. The 1915 nm features could as well be interpreted as water in chlorite. The 2270 nm feature could also be interpreted as being displaced from 2265 nm. This will then lead to misclassification and loss of valuable (chrysocolla) as waste.

Where both minerals are present in a sample, as with most of the Mantoverde samples, NIR application must employ an indirect approach. NIR application will involve the selection of chlorite features in addition to chrysocolla features to indicate products (chrysocolla). This implies that at NIR preconcentration stage, discrimination between the two minerals cannot be achieved: therefore, later separation between these minerals will require a different method.

Given the visibility of their individual additional features side-by-side across mixture range, though chlorite's 2265 nm feature is invisible, both minerals dominate spectra at equal strength. This indicates that spectra dominance is neither concentration nor accessibility to radiation dependent.

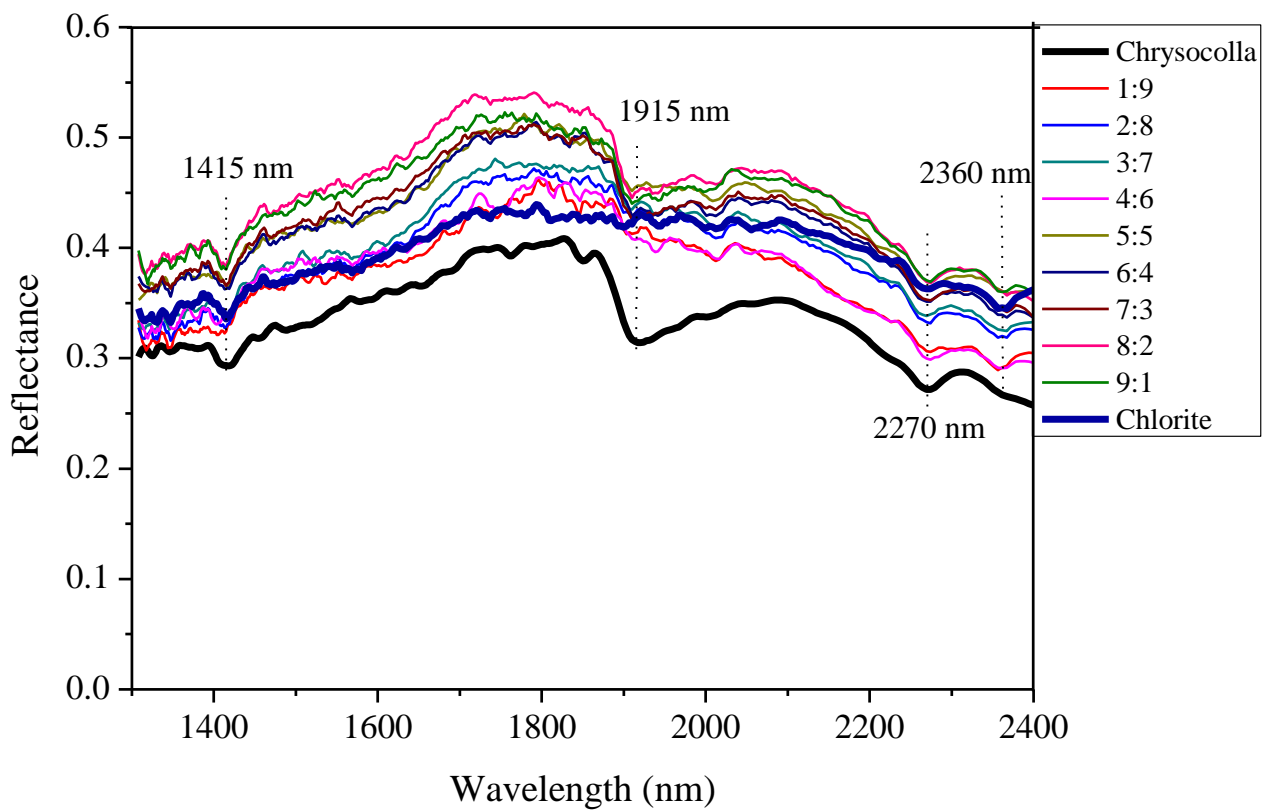


Figure 6.3 - NIR spectra of chrysocolla-chlorite mixtures

Bottom and top spectrum are reference for chrysocolla and chlorite respectively

#### 6.2.1.4. Chlorite-Muscovite mixtures

NIR spectra of mixtures of chlorite-muscovite reveal the dominance of muscovite over chlorite across the spectra at all ratios (Fig. 6.4). As individual

minerals, both chlorite and muscovite share a similar feature near 1415 nm. Muscovite has additional features near 1840/1915, 2200, and 2350 nm, while chlorite shows its additional absorption features near 2265 and 2360 nm. Given the lack of visibility of chlorite features at any range, analysis reveals the spectral dominance of muscovite over chlorite. This indicates that muscovite is more readily accessible to NIR radiation than chlorite. Thus implying that where these two minerals occur together along the same spectrum range as the only NIR-active minerals, spectrum or spectra is likely to display only muscovite features. This explains why at lower muscovite ratios in a sample where both minerals are present as the only and/or dominant NIR-active minerals, only muscovite features are visible (this will be shown later in application).

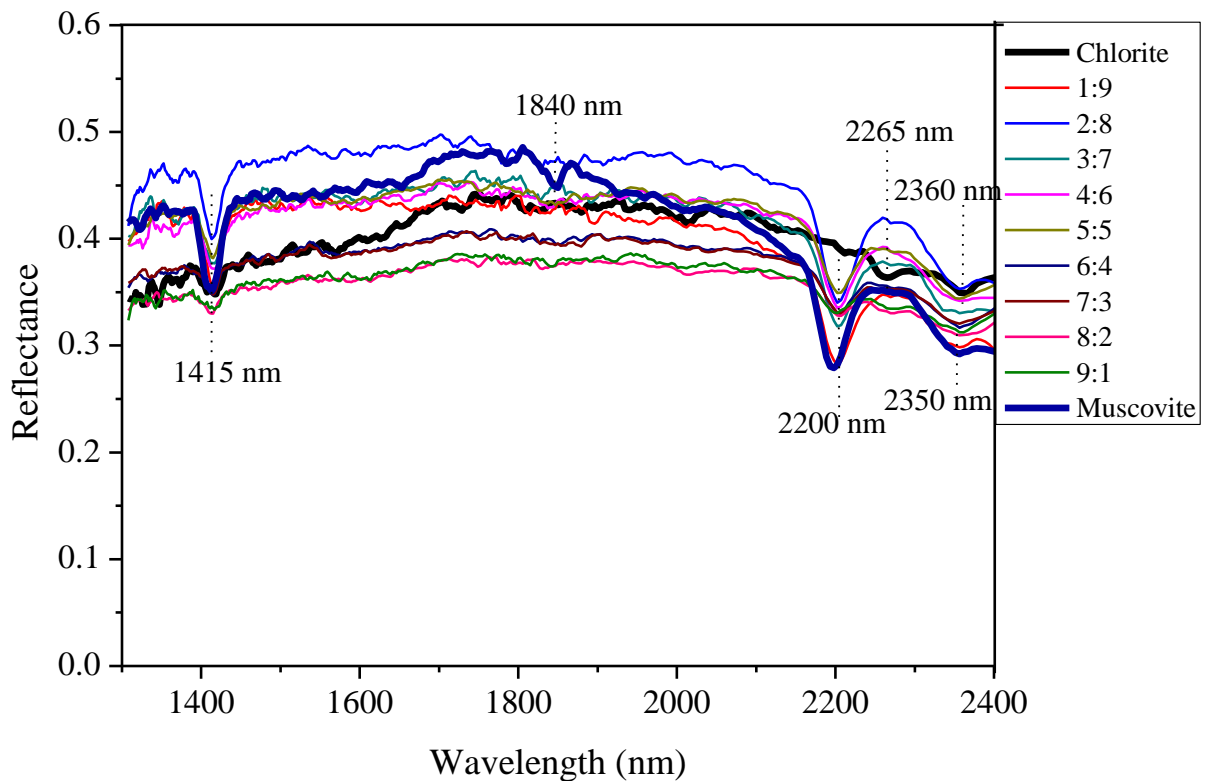


Figure 6.4 - NIR spectra of chlorite-muscovite mixtures

Bottom and top spectrum are reference for chlorite and muscovite respectively

### 6.2.1.5. Kaolinite-Muscovite mixtures

NIR spectra of intimate mixtures of kaolinite-muscovite are presented in Figure 6.5. The distinguishing feature between kaolinite and muscovite is the feature



doubling characteristics of kaolinite compared to the single feature displayed by muscovite (Iyankwari et al., 2013).

Analysis of spectra of the mixture indicates that from kaolinite-muscovite ratios of 1:9 through to 6:4, spectra display only single features near 1415 nm and 2200 nm. Double features at shorter wavelengths near 1410 and 1415 nm and at longer wavelengths near 2160 nm and 2200 nm appear at kaolinite-muscovite ratio 7:3 through to 9:1 (Fig. 6.5). Though features near 1400 and 2200 nm are shared features which are present across spectra at all ranges, the absence of double features which are indicative of kaolinite, even at higher kaolinite ratio (6:4), shows that muscovite is more active in the spectra.

Hence, for preconcentration purpose the choice of either or both the 1415 and 2200 nm features will target both minerals. Spectra with dominant kaolinite features (doubled features near 1400 and 1415 nm and 2160 and 2200 nm) will be indicative of high kaolinite concentration in the sample. However, because of the shared 2200 nm feature, both minerals cannot be separated efficiently.

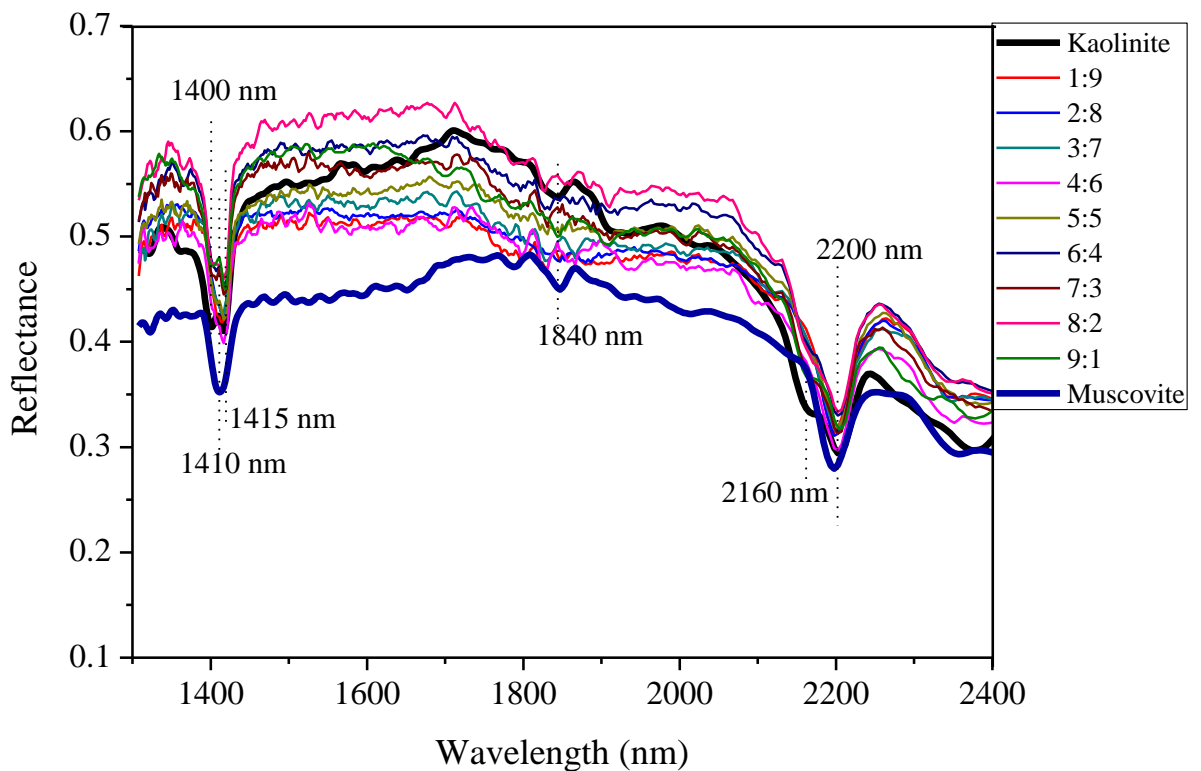


Figure 6.5 - NIR spectra of kaolinite-muscovite mixtures

Bottom and top spectrum are reference for muscovite and kaolinite respectively

### 6.2.1.6. Chrysocolla-Biotite Mixtures

NIR spectra of this mixture (Fig. 6.6), shows no absorption features relating to either mineral. Without knowledge of the minerals present the spectra can easily be misinterpreted to represent that of hematite or any other featureless NIR-active mineral. Hence, where both minerals occur along the same spectra region, identification and subsequent preconcentration of individual mineral is not possible. Therefore, both minerals are better considered together in designing a preconcentration strategy. On that basis, featureless spectra should be considered to also indicate the presence of chrysocolla and hence be classified as product where chrysocolla is known to exist as a constituent mineral. In instances where one mineral displays absorption feature(s) in a spectrum, spectrum indicates the absence of the other mineral in concentration.

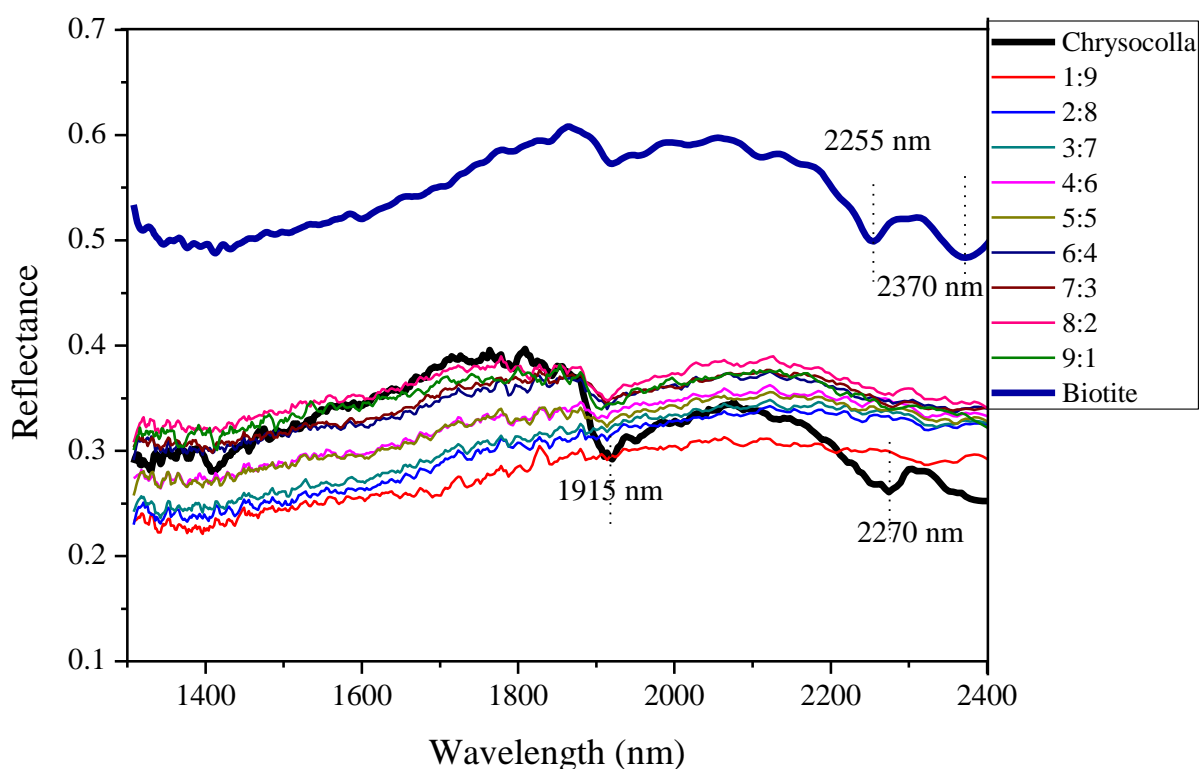


Figure 6.6 - NIR spectra of chrysocolla-biotite mixtures

Bottom and top spectrum are reference for biotite and chrysocolla respectively

### 6.2.1.7. Kaolinite-Chlorite Mixtures

NIR spectra of kaolinite-chlorite mixtures (Fig. 6.7), reveals the total dominance of kaolinite over chlorite across the mixture ranges. Though both minerals are -

OH bearing, kaolinite is more accessible to NIR radiation than chlorite. Hence, NIR activity of kaolinite over chlorite is not concentration dependent. Therefore identification of chlorite when in concentration with kaolinite is not achievable.

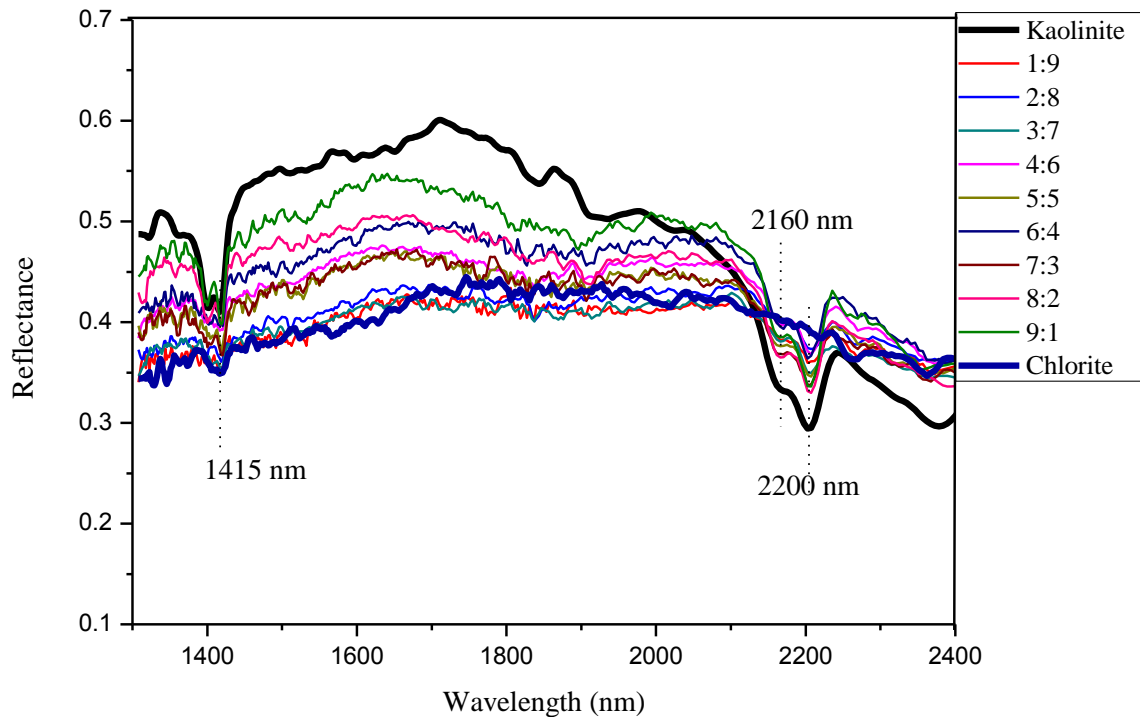


Figure 6.7 - NIR spectra of kaolinite-chlorite mixtures

Bottom and top spectrum are reference for kaolinite and chlorite respectively

#### 6.2.1.8. Chlorite-Biotite Mixtures

NIR spectra of mixtures of chlorite and biotite show no absorption feature(s) indicative of any of the minerals in concentration (Fig. 6.8). Hence, neither mineral can be identified along the same spectra range. Therefore, where spectra show absorption features of one mineral relative to the other, spectra will indicate the absence of the other mineral in concentration. Spectra appear similar to that of mixture of chrysocolla and biotite (Fig. 6.6) and therefore, with no knowledge of mineralogy, spectra can be interpreted to represent that of a non-feature displaying NIR-active minerals.

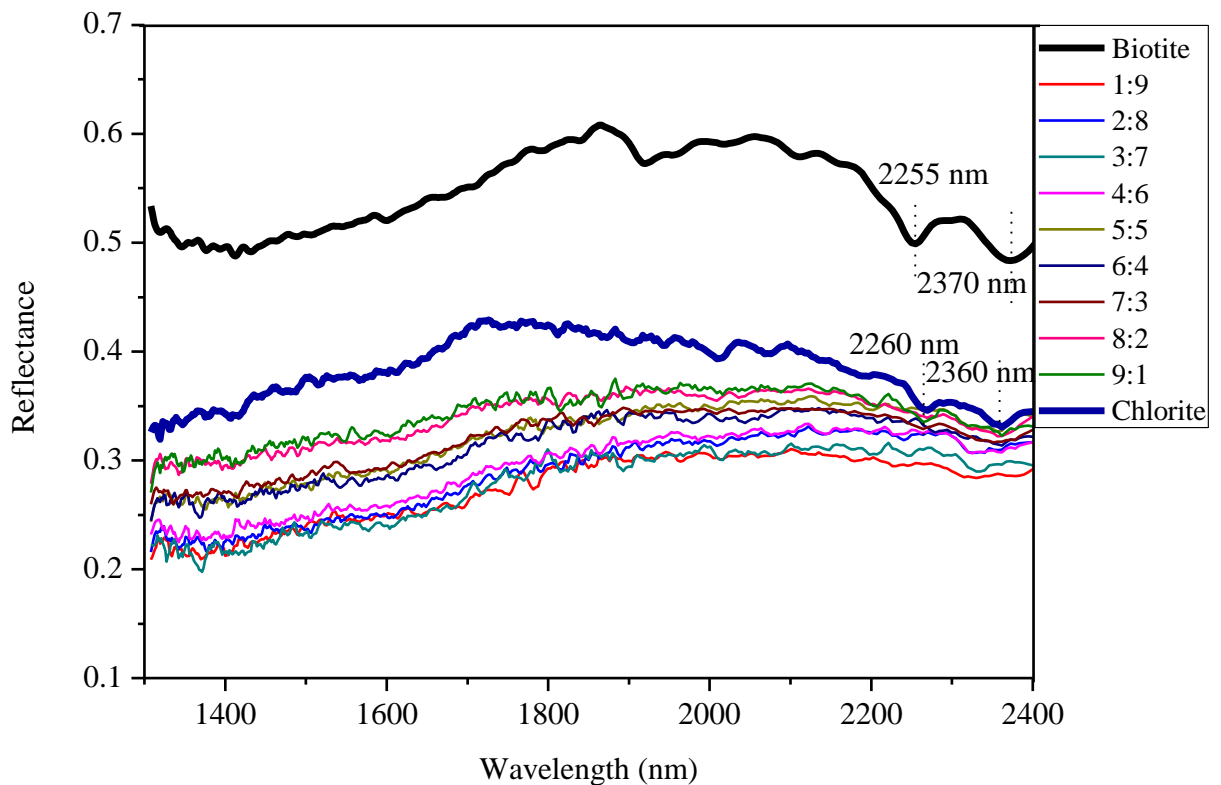


Figure 6.8 - NIR spectra of biotite-chlorite mixtures

Bottom and top spectrum are reference for chlorite and biotite respectively

#### 6.2.1.9. Biotite- Muscovite Mixtures

Analysis of spectra of a muscovite-biotite mixture (Figure 6.9) shows that except at a biotite-muscovite ratio of 9:1 where spectra appear featureless at longer wavelength, muscovite is dominant in the mixture. At shorter wavelengths, spectra appear featureless at higher biotite ratios from biotite-muscovite ratio 6:4 through 9:1, but shows absorption features at longer wavelengths indicative of muscovite. This reveals the dominance of biotite at shorter wavelengths. Given that at ratios where biotite dominates the spectra, muscovite absorption features are only invisible at shorter wavelengths, muscovite is more NIR-active in a spectra of mixture. Hence, the influence of biotite in spectra is only observed at shorter wavelengths and it is concentration dependent, while muscovite is more readily accessible to NIR radiation. The influence of biotite can only be observed in spectra with confidence if mineralogy is known, since biotite absorption features are not visible.

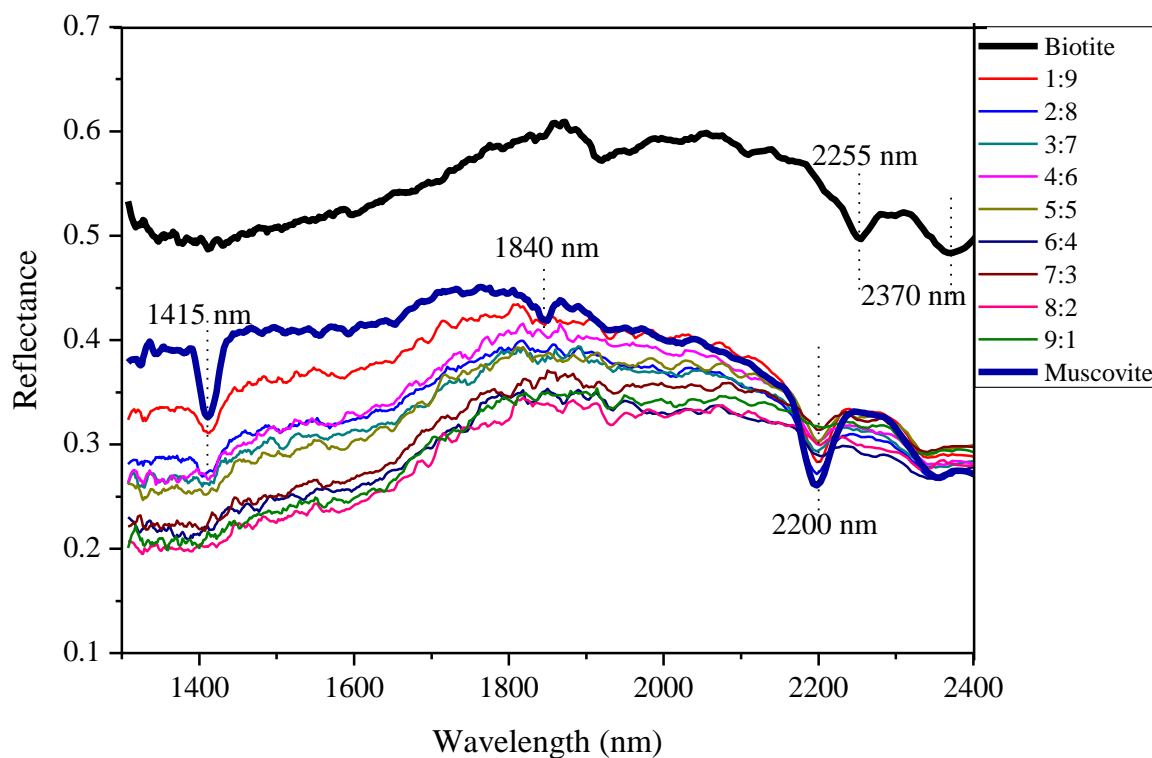


Figure 6.9 - NIR spectra of biotite-muscovite mixtures

Bottom and top spectrum are reference for muscovite and biotite respectively

### 6.2.1.10. Malachite-Calcite Mixtures

Both are carbonate minerals and have their best diagnostic features at longer wavelengths between 1600 and 2400 nm (Iyakwari and Glass, 2014). Hence, spectral analysis of their mixtures is targeted at that range (Fig. 6.10).

In addition to a malachite diagnostic feature near 2275 nm, which is visible across mixture series, NIR spectra of mixtures show absorption feature near 2355 nm at malachite-calcite ratio of 1:9 through 4:6. This feature does not correspond to any of the constituent mineral. Hence, it's a displaced feature, which due to proximity may be of malachite. From ratio 5:5 through 9:1, the feature near 2355 nm is further displaced to 2360 nm, corresponding to the second absorption feature of malachite.

Given the consistent visibility of malachite feature near 2275 nm, preconcentration of malachite from calcite will achieve high recovery but at low copper grade due to dilution by calcite. This is true since malachite is more

readily accessible to NIR radiation than calcite. For ore preconcentration where these minerals occur together, in instances where calcite features are visible (2340 nm) spectra will depict purity of calcite (freely-occurring-calcite). The visibility of malachite features alone in such an ore may not necessarily indicate malachite purity. Therefore, only the removal or reduction of freely occurring calcite samples can be achieved for preconcentration.

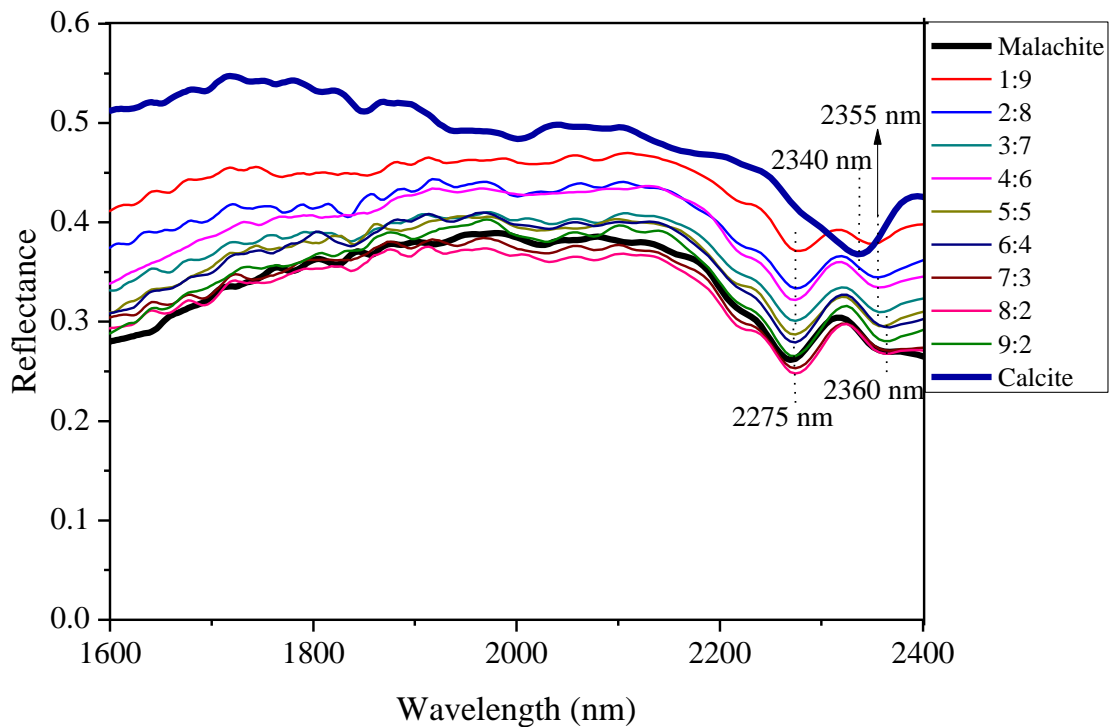


Figure 6.10 - NIR spectra of malachite-calcite mixtures

Bottom and top spectrum are reference for malachite and calcite respectively

### 6.2.2. Mixtures of NIR-active minerals with dissimilar functional groups (-OH vs. $\text{CO}_3^{2-}$ )

The Mantoverde ore consists of a complex mixture of minerals of varying functional groups. To investigate the dominant influence of one mineral's functional group over another in a matrix, intimate mixtures of minerals with dissimilar functional groups were prepared, measured and spectra analysed.

### **6.2.2.1. Chrysocolla-Calcite Mixtures**

Analysis of NIR spectra (Fig. 6.11) indicates that from a chrysocolla-calcite ratio of 1:9 to 4:6, spectra displayed absorption features near 1415 and 1915 nm with broad features between 2260 and 2400 nm. The features near 1415 and 1915 appearing across all the ratios are indicative of water features in chrysocolla, while the broad features lacking absorption centres are those of chrysocolla and calcite at longer wavelengths. Though chrysocolla water features are noticed from ratios 1:9 through 9:1, chrysocolla dominates spectra from ratio 5:5 through to 9:1. In ores where the chrysocolla grade is low relative to calcite, broad spectra or the presence of either -OH features near 1415 or H<sub>2</sub>O features near 1915 and or 1415 nm is indicative of low grade chrysocolla in the spectrum.

Therefore, to minimize the loss of valuable ores to tailings, considering featureless spectra at longer wavelengths or visible features at shorter wavelengths, especially the 1415 nm and 1915 nm, with or without the 2270 nm feature will present an important choice for chrysocolla identification and preconcentration. This will enhance recovery. Where 1415 and 2270 nm features occur together, NIR spectra will indicate high chrysocolla grade. Therefore, only spectrum with strictly calcite features near 2340 nm should be classified as waste, since the visibility of the features defines calcite purity.

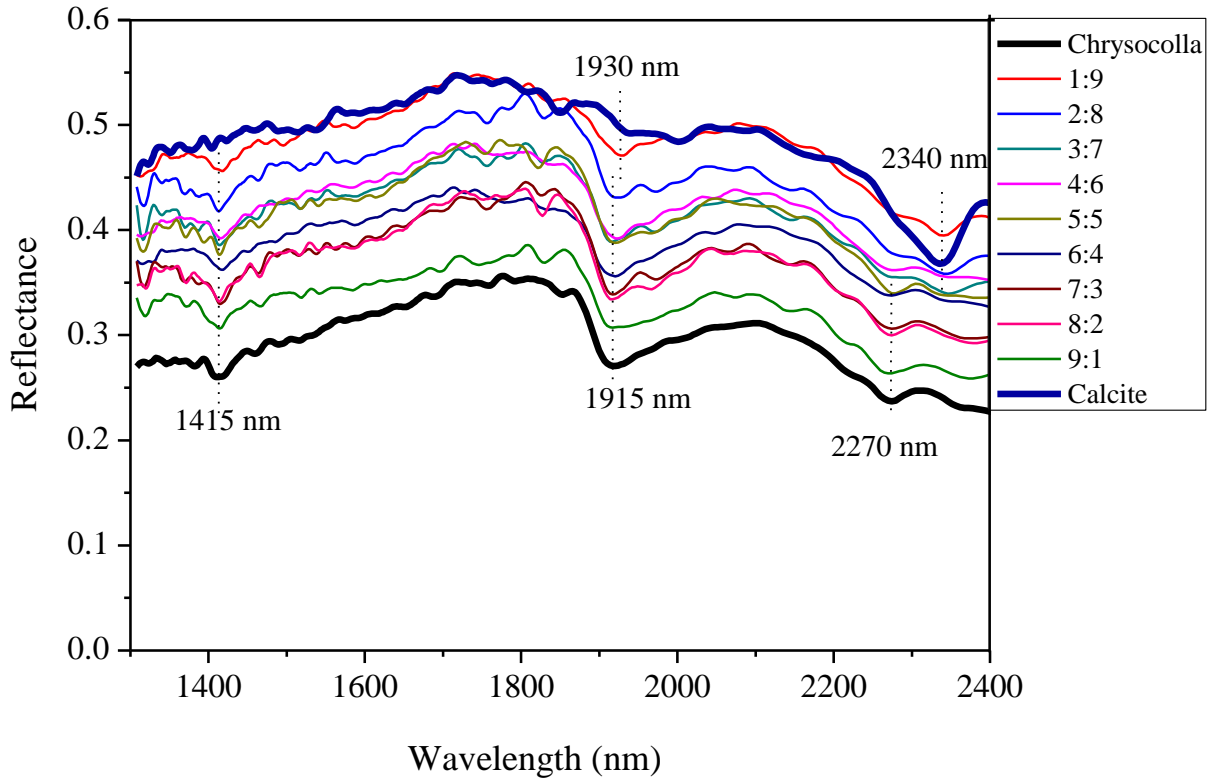


Figure 6.11 - NIR spectra of chrysocolla-calcite mixtures

Bottom and top spectrum are reference for chrysocolla and calcite respectively

### 6.2.2.2. Muscovite-Calcite Mixtures

NIR spectral analysis indicates that on each increase of calcite concentration against muscovite, the individual mineral absorption feature positions and depth of spectra are influenced (Fig. 6.12). To show this, the depth of absorption features is measured (Table 6.1). From a muscovite-calcite ratio of 9:1 to 7:3, the features near 1415 nm and 2200 nm reduces in depth, but their wavelength positions are maintained. The muscovite's weak feature near 2350 nm is the most affected. The depth of absorption of the feature in pure muscovite is measured to be 0.06. The feature position and depth is maintained from ratio 9:1 to 7:3 at 2350 nm and 0.09 depths respectively, but from ratio 6:4 to 5:5, the feature position is displaced to 2345 nm with reduced depth of absorption. With a further increase in calcite concentration from ratios 4:6 to 1:9, the earlier 2345 nm wavelength feature is again displaced but now corresponding to calcite features near 2340 nm. Also observed from ratios 4:6 to 1:9 is an increase in



depth of absorption for the now 2340 nm absorption feature from 0.07 for ratio 4:6 peaking at 0.08 for ratio 1:9. The shift or displacement of the 2350 nm feature position and the reduction in depth of absorption or strength of other features with each addition of calcite is due to substitution of aluminium by calcium (Clark, 1999).

It can be observed that from muscovite-calcite ratios 9:1 to 7:3, calcite is completely invisible, in the spectra. With an increase in calcite concentration to between ratios 6:4 and 5:5 a feature not corresponding to either of the minerals is formed, hence interpreted as a shared feature. Calcite only shows its feature with a visibly maintained wavelength position from muscovite-calcite ratio of 4:6 to 1:9, occurring side-by-side with those of muscovite.

Given that muscovite features near 1415 and 2200 are visible side-by-side with those of calcite even at higher calcite concentrations (muscovite-calcite ratio 1:9), and no calcite feature is observed in spectra of mixture at higher muscovite ratios, on a 1:1 comparison, muscovite is more NIR-active than calcite. Therefore, while muscovite is more readily accessible to NIR radiation, calcite's visibility when in occurrence with muscovite along the same spectrum range is concentration dependent. Therefore where only calcite features are visible, spectra will indicate high calcite purity.

For the purpose of ore preconcentration, where both minerals are considered waste like in the case of the Mantoverde ores, the selection of 2200 nm feature will also eliminate low grade calcite, since the feature is present across all ratios. The selection of 2340 nm in isolation will only target high grade calcite and low grade muscovite bearing material.

Therefore, discrimination will follow that only spectra with calcite features with or without muscovite features can be considered to indicate high calcite, while spectra without calcite features (2340 nm) will indicate muscovite dominance.

Since both malachite and chrysocolla are more NIR-active than calcite (Figs. 6.10 and 6.11, calcite with malachite and chrysocolla respectively), if both muscovite and calcite occurred alongside them as gangue minerals, the choice of only calcite feature near 2340 nm will reduce the loss of the valuable minerals to waste, since muscovite is visible in both copper-bearing minerals when they are low in concentration.

Table 6.1 - Features depth at five wavelengths for different ratios of muscovite and calcite

Ratio (muscovite: calcite)	Feature depth at wavelength (nm)				
	1415	2200	2340	2345	2350
1:0 (Muscovite)	0.09	0.11			0.06
9:1	0.14	0.14			0.09
8:2	0.14	0.14			0.09
7:3	0.13	0.13			0.09
6:4	0.13	0.12		0.08	
5:5	0.07	0.08		0.06	
4:6	0.07	0.08	0.07		
3:7	0.07	0.08	0.05		
2:8	0.08	0.08	0.08		
1:9	0.06	0.07	0.08		
0:1 (Calcite)			0.09		

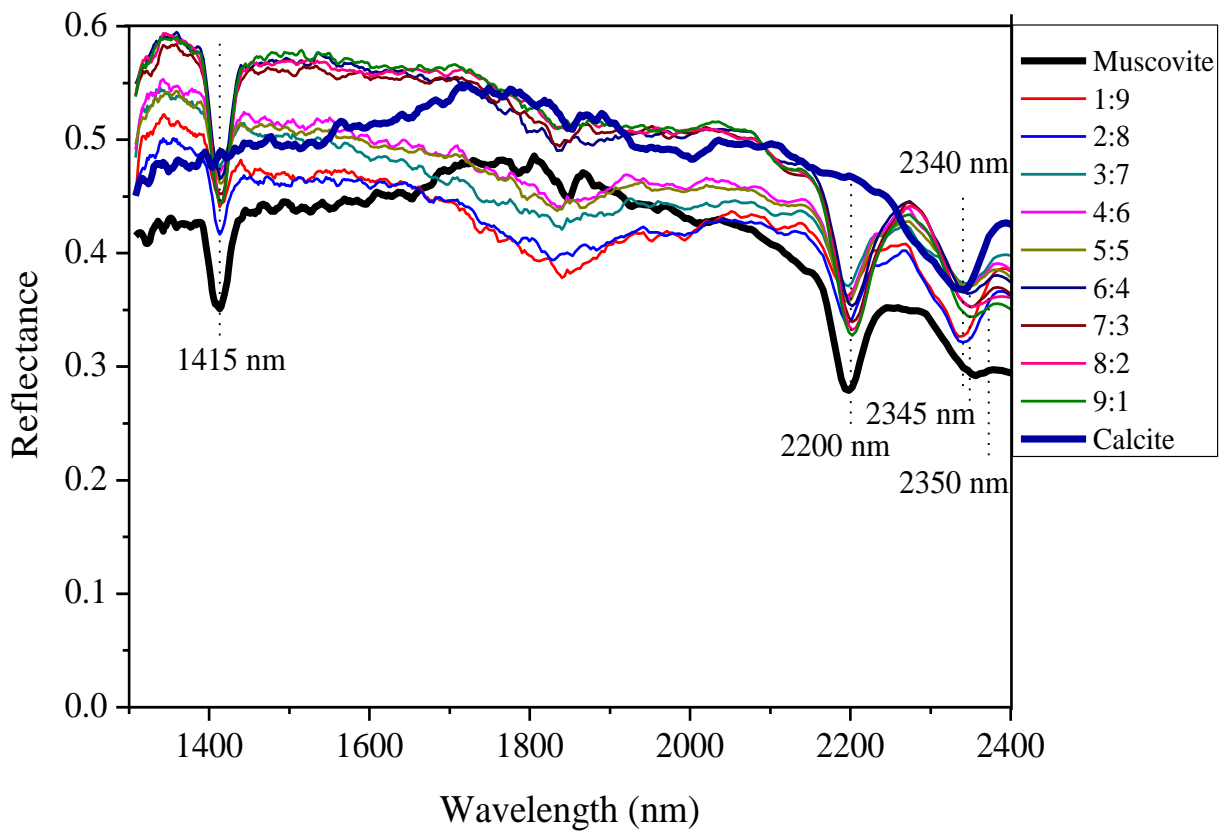


Figure 6.12 - NIR spectra of muscovite-calcite mixtures

Bottom and top spectrum are reference for muscovite and calcite respectively

### 6.2.2.3. Kaolinite-Calcite Mixtures

Figure 6.13 presents spectra of intimate mixtures of kaolinite and calcite. With reference to the spectra of the individual minerals, calcite features are only visible from equal kaolinite-calcite ratio. Here spectra display a weak feature near 2340 nm occurring side-by-side with those of kaolinite. The reduction in absorption intensity of kaolinite's double features near 1400 and 2200 nm is observed at each addition of calcite. Given the fact that calcite is not visible at higher kaolinite ratios, but kaolinite still displays its features at higher calcite ratios, kaolinite is more NIR-active than calcite. Therefore, similar to calcite-muscovite mixtures (Fig. 6.12), calcite features visibility in the spectra is concentration dependent while kaolinite spectra dominance indicates it is more accessible to NIR radiation than calcite.

Where both minerals are targeted as waste, the choice of kaolinite absorption features will also target calcite in concentration since kaolinite features are present across all ratios, especially the 2200 nm features. The appearance of only kaolinite features in such ore may not necessarily indicate purity of kaolinite, but calcite features in isolation will indicate purity of calcite. Similar to calcite-muscovite mixtures (Fig. 6.12), present analysis shows that the choice of the 2200 nm feature which is shared by both kaolinite and muscovite will target calcite, kaolinite and muscovite together when they occur within the same spectrum range. This reduces the number of wavelengths for selection since one wavelength can target three minerals.

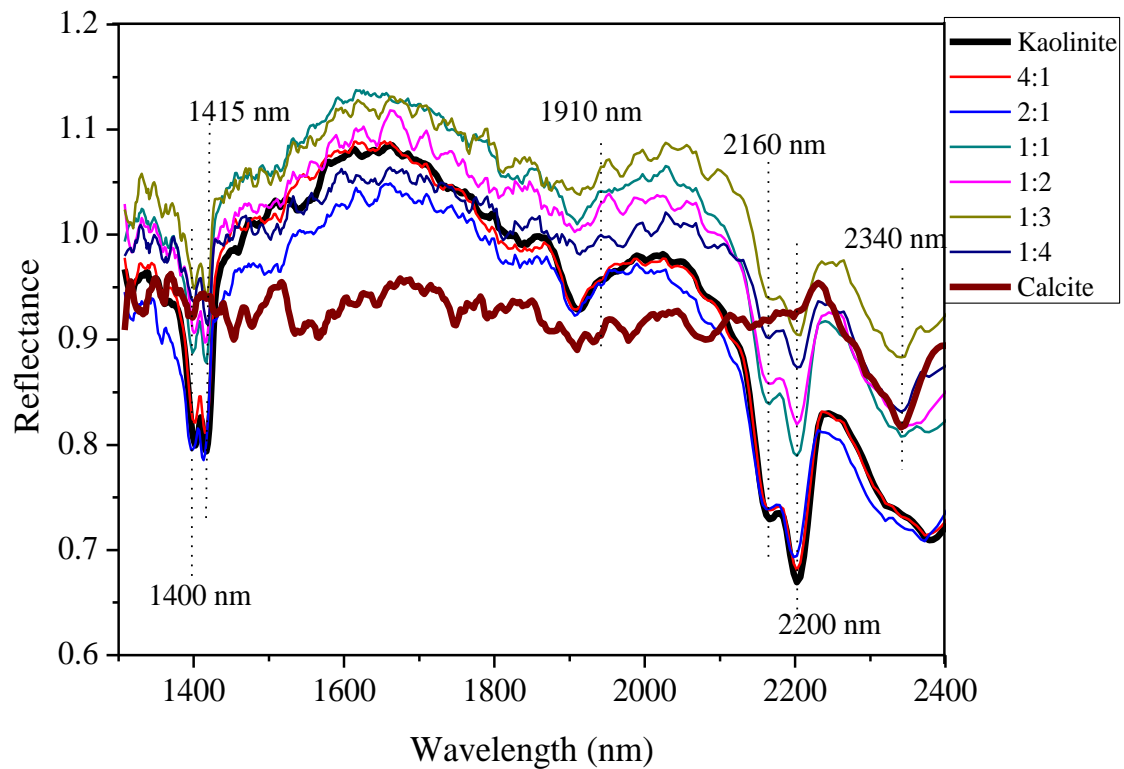


Figure 6.13 - NIR spectra of kaolinite-calcite mixtures

Bottom and top spectrum are reference for kaolinite and calcite respectively

#### 6.2.2.4. Chlorite-Calcite Mixtures

NIR spectra of mixtures of chlorite and calcite at different ratios are presented in Figure 6.14. Spectra from chlorite-calcite ratios of 1:9 to 3:7 reveal broad features between 2260 and 2350 nm. The broad features are displaced features of both chlorite and calcite near 2265 and 2340 nm respectively. From ratios 4:6 to 9:1 spectra show defined features near 2265 and 2360 nm, corresponding to those displayed by chlorite as a single mineral. The chlorite absorption feature at the shorter wavelength near 1415 nm is maintained across all ratios.

Given the complete invisibility of the defined calcite feature near 2340 nm in spectra across all ratios, chlorite is more NIR-active than calcite in the concentration along the spectrum range. Therefore, the occurrence of both minerals in an ore with relatively higher calcite concentration ( $\geq 70\%$  calcite) will show broad or depressions at longer wavelengths having no defined absorption centres. Spectra with defined calcite features in samples will reveal

purity of calcite, since even at higher calcite concentration, features appear broad. At higher calcite-chlorite ratios, which is characterized by broad spectra, individual mineral identification and preconcentration cannot be achieved.

Spectra obtained are a good example of ores from weathered environments where chlorite, which is a product of altered biotite (Veel-er, 1983), dominates spectra when in concentration with calcite. Just like in other calcite mixtures with chrysocolla (Fig. 6.11), muscovite (Fig. 6.12), and kaolinite (Fig. 6.13), analysis reveals the dominance of hydroxyl-bearing minerals over calcite.

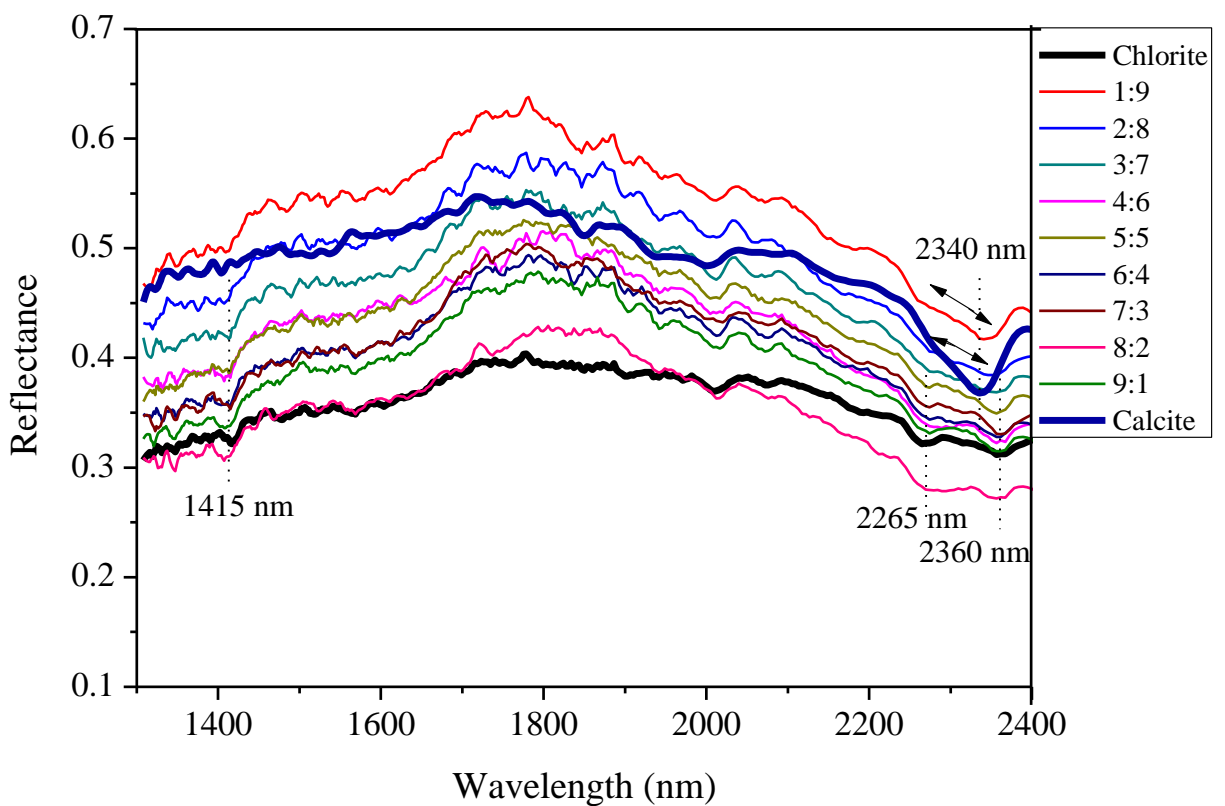


Figure 6.14 - NIR spectra of chlorite-calcite mixtures

Bottom and top spectrum are reference for chlorite and calcite respectively

#### 6.2.2.5. Malachite-Chlorite Mixtures

Both minerals show absorption feature near 2360 nm. Chlorite shows additional features near 1415 nm and 2265 nm, while a malachite additional feature is located near 2275 nm. The NIR spectra of mixtures (Fig. 6.15) reveal features near 2275 nm and 2360 nm across all ratios. While chlorite's 2265 nm feature is invisible across the mixture range, the 1415 nm feature is only visible, but

appearing weak in spectra at a malachite-chlorite ratio 1:9. Spectra of mixtures reveal the dominance of malachite in concentration across all mixing range. The presence or visibility of the shared feature (2360 nm) cannot be used to distinguish between either mineral.

Chlorite identification in malachite-rich ores, where both minerals occur as the only NIR-active minerals along similar spectrum range, will only be achieved if chlorite occurs in very high concentrations ( $\geq 90\%$ ) relative to malachite. High occurrence of chlorite will then be revealed by the presence of the 1415 nm feature which will be indicative of chlorite: otherwise malachite is dominant across the spectra. With the absence of 1415 nm feature in a spectrum, identification without knowledge of the mineralogy will only be indicative of malachite. The spectra dominance of malachite over chlorite as revealed by the invisibility of the 1415 and 2265 nm features show that malachite is more accessible to NIR radiation than chlorite.

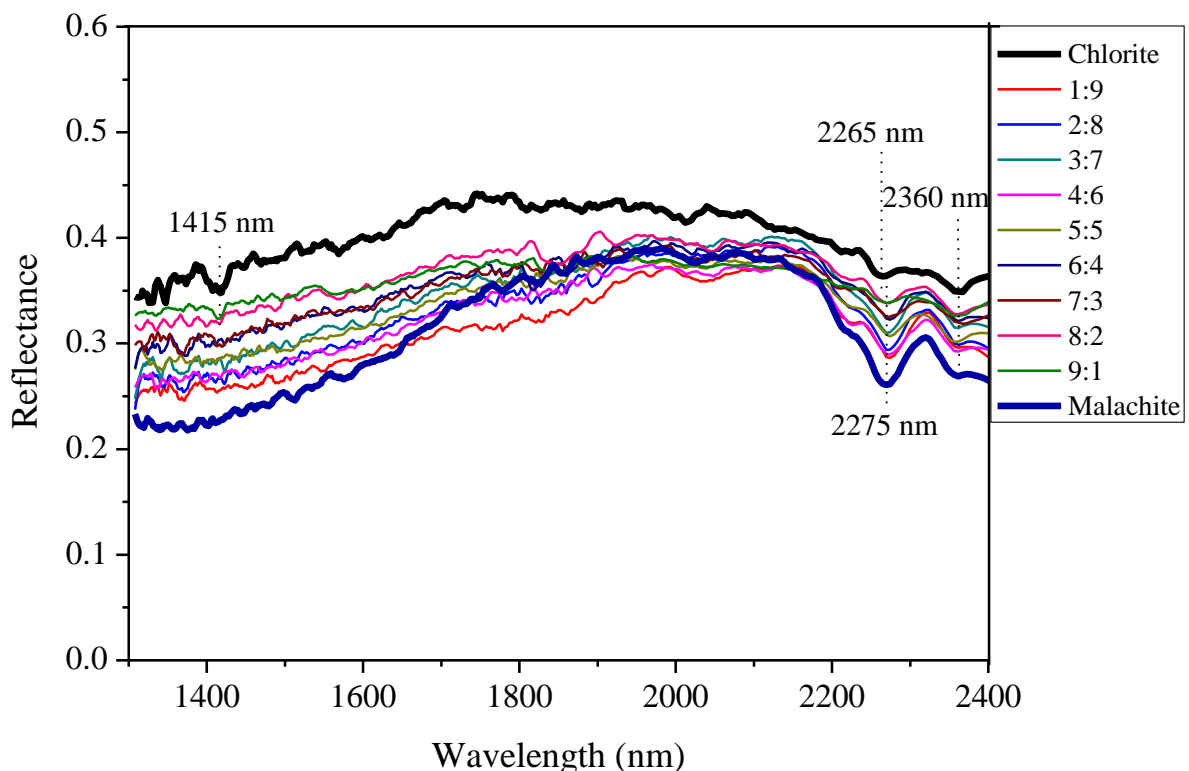


Figure 6.15 - NIR spectra of chlorite-malachite mixtures

Bottom and top spectrum are reference for malachite and chlorite respectively

#### **6.2.2.6. Malachite-Kaolinite Mixtures**

Figure 6.16 presents NIR spectra of a mixture of malachite and kaolinite. Malachite-kaolinite spectral analysis shows that the kaolinite feature near 2200 nm is displaced to 2210 from malachite-kaolinite ratio 9:1 to 2:8, while the 2160 nm feature disappears from malachite-kaolinite ratio of 4:6. Kaolinite's 1840 nm feature is invisible across the spectra of mixtures. The 1400 and 1415 nm kaolinite features appear weak at malachite-kaolinite ratios of 1:9 and 2:8 and disappear from ratios 3:7 through to 9:1. Malachite's 2275 nm feature is present across all ratios with maintained wavelength position, while the 2360 nm feature is not defined in the spectra.

The disappearance and displacement of some kaolinite features by malachite at higher kaolinite ratios indicates the influence of malachite in spectra, but the visibility of both minerals features side-by-side at longer wavelengths shows that individual mineral identification is possible but discrimination is not possible. Therefore, in NIR spectra where both minerals occur together, the presence of the maintained 2200 nm absorption feature will indicate dominance or purity of kaolinite (approximately  $\geq 90$  % kaolinite).

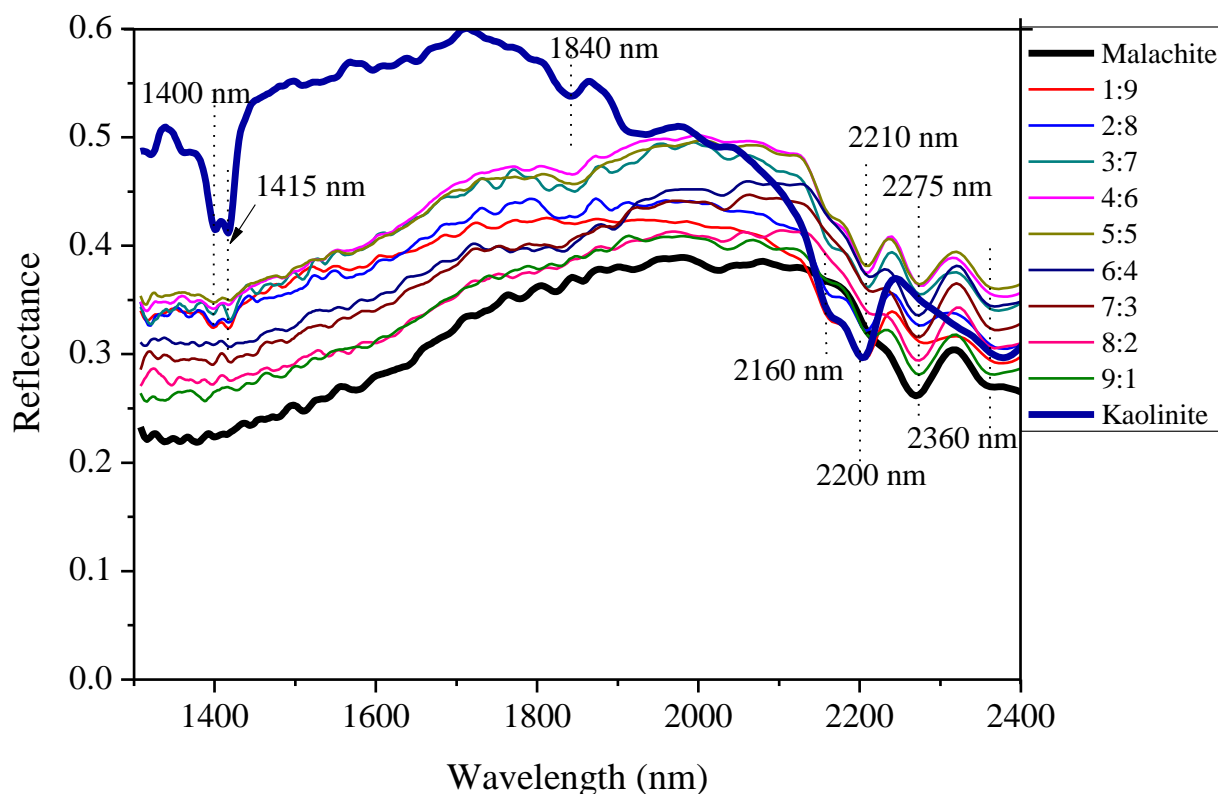


Figure 6.16 - NIR spectra of malachite–kaolinite mixtures

Bottom and top spectrum are reference for malachite and kaolinite respectively

### 6.2.2.7. Chrysocolla-Malachite Mixtures

The NIR spectra of the chrysocolla-malachite mixture are presented in Figure 6.17. Both minerals are secondary copper-bearing minerals. Finding a strategy where both minerals can be efficiently and economically preconcentrated together is the research objective. Individually chrysocolla displays features near 1415, 1915 and 2270 nm, while malachite shows features near 2275 and 2360 nm. Spectra of mixtures from chrysocolla-malachite ratios of 1:9 to 4:6 reveal features near 2270 and 2360 nm only. The feature near 2360 nm disappears from ratio 5:5 leaving behind only the 2270 nm feature, indicating that chrysocolla is gaining dominance over malachite at equal ratios. Additional chrysocolla features near 1415 and 1915 appear weak from ratios 7:3. Hence, spectral analysis indicates that chrysocolla is more NIR-active than malachite in the mixture.



The Mantoverde ore mineralogy (Table 4.1) shows that chrysocolla is the dominant copper bearing mineral in the ore. Also, in samples where malachite occurs, they occur together with chrysocolla and their concentration in such samples is minute compared to that of chrysocolla. The highest concentration of malachite in the ore is shown by sample 55 (Table 4.1) where malachite has a concentration of 2.2 wt. % against chrysocolla 5.2 wt. %, making it ratio 3:7 (malachite to chrysocolla). Hence, the choice of the 2270 nm feature with or without the 1415 nm feature for preconcentration will target both minerals when in concentration together.

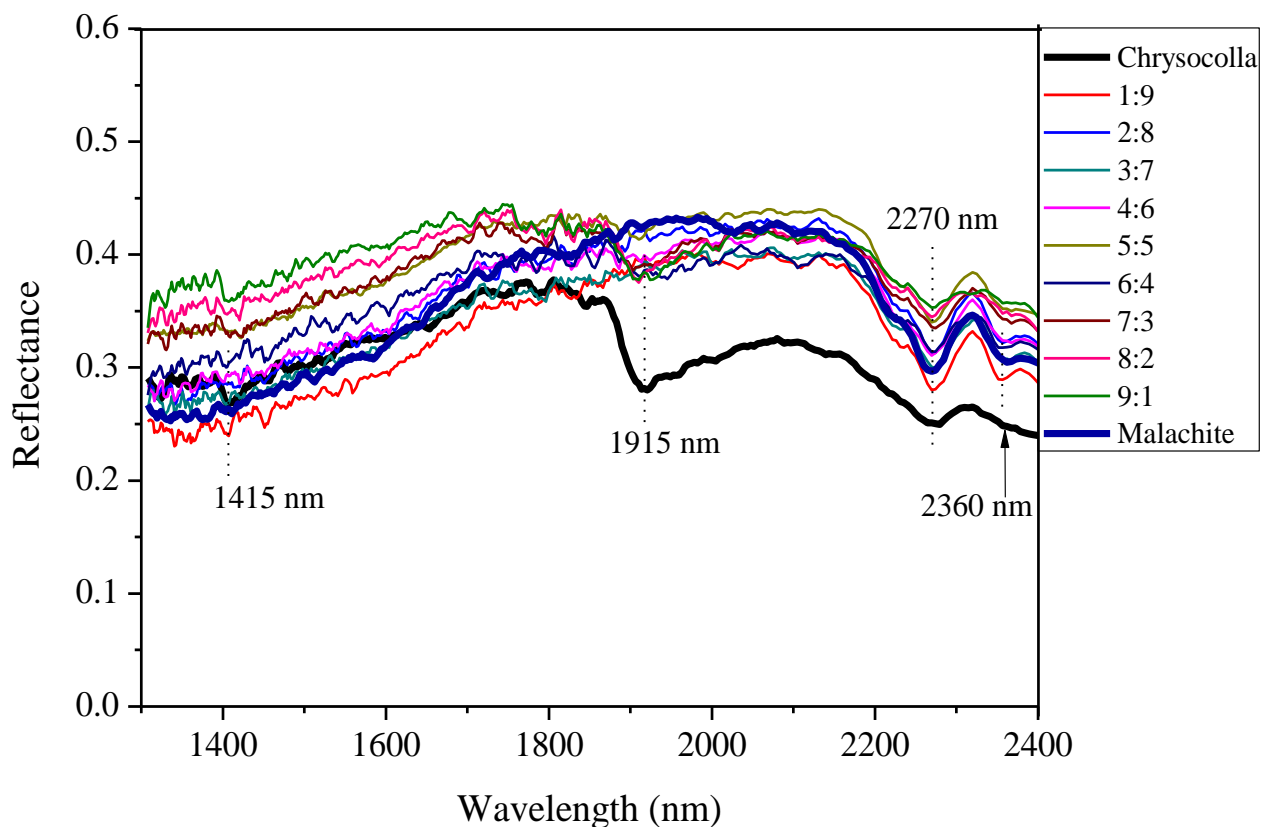


Figure 6.17 - NIR spectra of malachite-chrysocolla mixtures

Bottom and top spectrum are reference for chrysocolla and malachite respectively

#### 6.2.2.8. Calcite-Biotite Mixture

NIR spectra of biotite-calcite mixtures (Fig. 6.18), reveals complete spectra dominance by calcite over biotite across all mixture ranges. Spectra show only an absorption feature near 2340 nm, diagnostic of calcite. Hence, analysis indicates that calcite is more readily accessible to NIR radiation than biotite in

the mixture irrespective of concentration. This therefore means that identification of biotite in calcite-bearing particles is not achievable as even at low concentration of calcite, biotite features are invisible. Hence, where biotite features are present in spectra, spectra will indicate the absence of calcite.

For preconcentration purposes, recovery of calcite in such ores though high will be of low grade due to dilution, since biotite is invisible even at high concentration, while biotite recovery if possible, will be low at high grade.

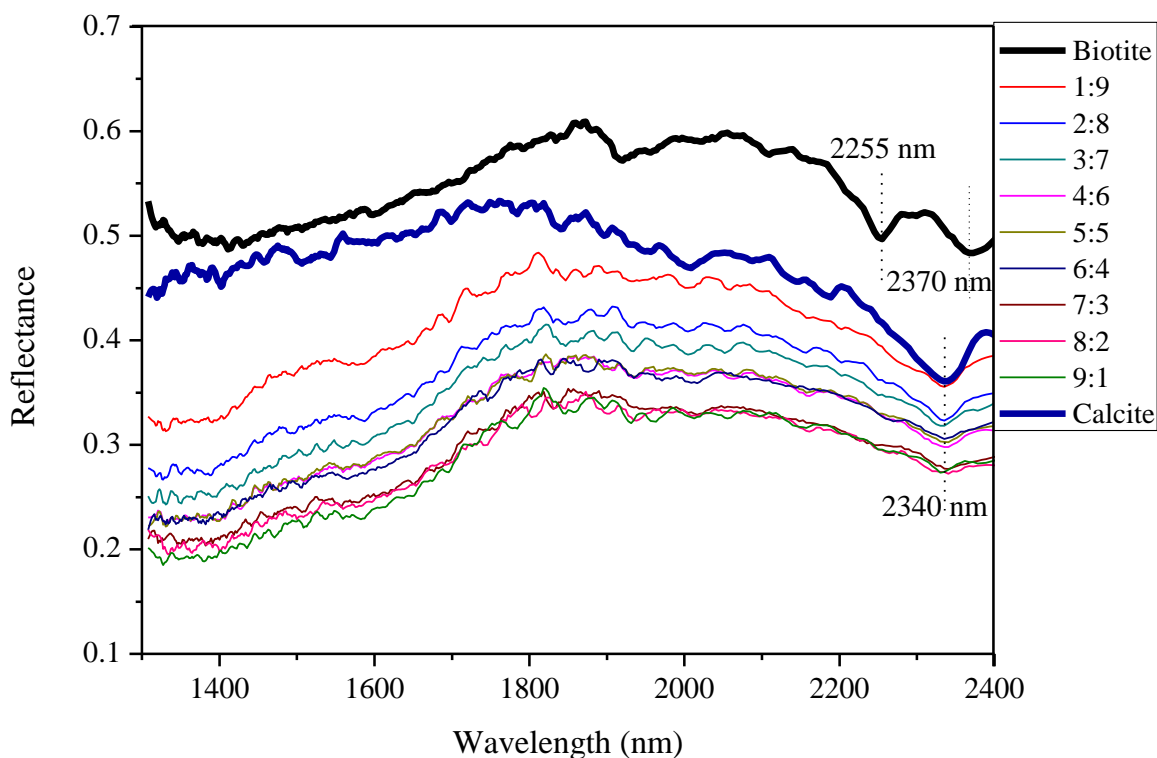


Figure 6.18 - NIR spectra of biotite-calcite mixtures

Bottom and top spectrum are reference for calcite and biotite respectively.

#### 6.2.2.9. Malachite-Biotite Mixture

The NIR spectra of malachite-biotite mixture (Fig. 6.19) reveal spectra dominance of malachite over biotite from malachite-biotite ratio 2:8 through to 9:1. Only the spectrum of malachite-biotite ratio 1:9 appears broad, thereby indicating the influence of biotite. Hence, analysis reveals that malachite is more NIR-active, while the influence of biotite is concentration dependent. Therefore, where biotite absorption features are observed in isolation, spectra will indicate

the absence of malachite in concentration, since even at 90 % biotite, the spectra is featureless.

In ores where both minerals are present, only spectra with visible biotite features can be considered waste, since the presence of malachite makes biotite invisible or spectrally featureless.

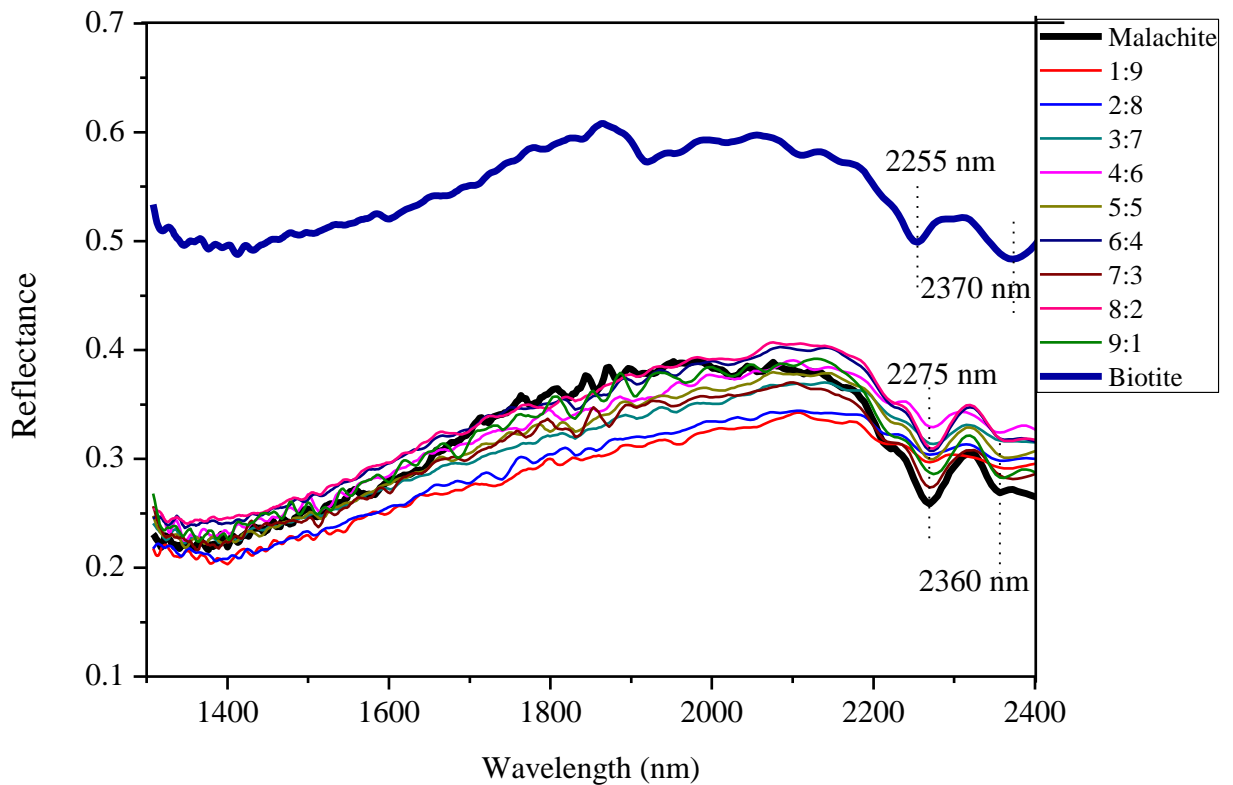


Figure 6.19 - NIR spectra of malachite-biotite mixtures

Bottom and top spectrum are reference for biotite and malachite respectively

#### 6.2.2.10. Malachite-Muscovite Mixture

NIR spectra of mixtures of malachite-muscovite (Fig. 6.20) appear mixed from malachite-muscovite ratios 1:9 to 5:5. From malachite-muscovite ratios 6:4 through to 9:1, only malachite features are visible in spectra at both longer and shorter wavelengths. The visibility of malachite absorption features across the mixing range, reveals that malachite is more NIR-active. Unlike muscovite, the visibility of malachite is not concentration dependent. Hence, since malachite is the economic mineral of interest, the visibility of muscovite absorption features

will indicate the grade of malachite relative to that of muscovite. Therefore, both minerals are better considered together since malachite occurring at low grade shows mixed spectra and only high grade malachite show no muscovite absorption features.

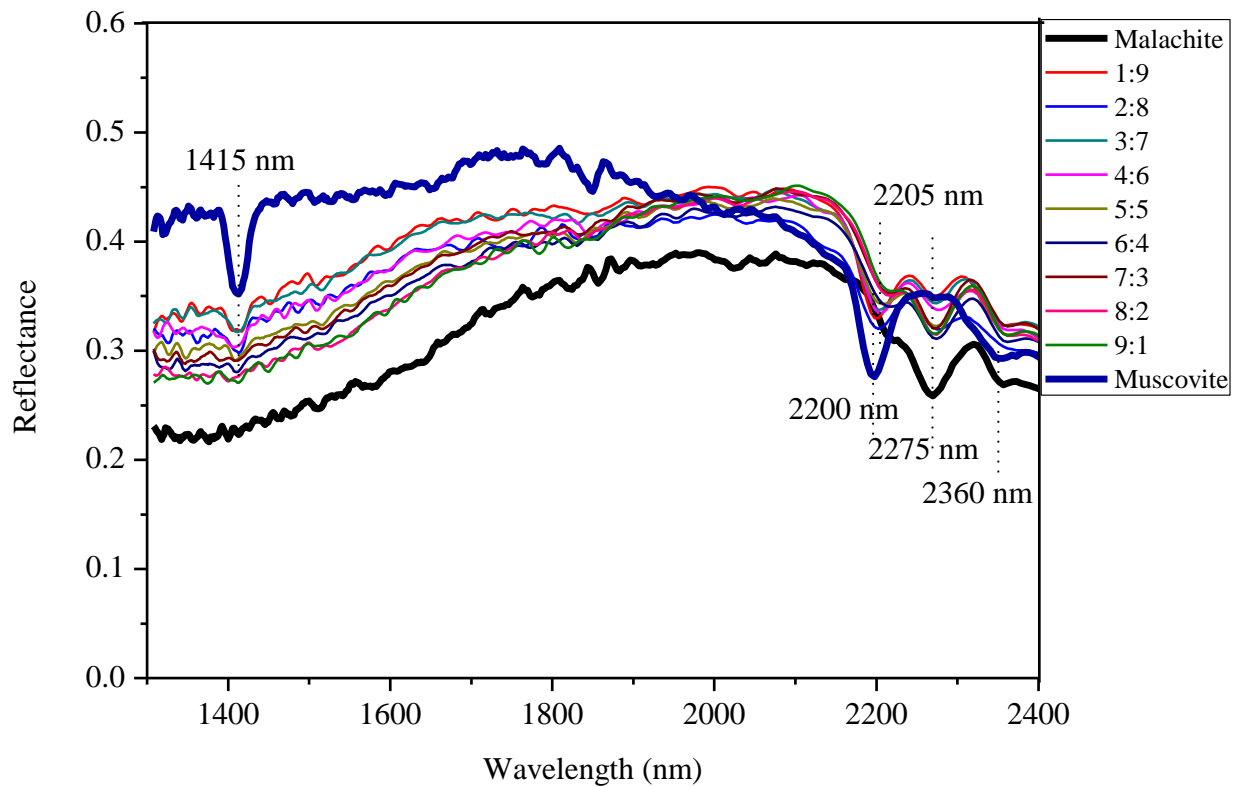


Figure 6.20 - NIR spectra of malachite-muscovite mixtures

Bottom and top spectrum are reference for muscovite and malachite respectively

### 6.2.3. Influence of hematite on feature(s) displaying NIR-active minerals

Hematite is the dominant oxide mineral present in the Mantoverde ore and the only NIR-active mineral which does not display absorption feature(s) (Iyakwari et al., 2013; Iyakwari and Glass, 2014). Bishop and Dummel (1996) in their experiments with mixtures of hematite and montmorillonites noted that hematite decreased the NIR reflectance of montmorillonites by flattening and or reducing their absorption features depth. Van Der Meer (1995) also reported the masking effect of high iron-bearing minerals on carbonate features, displayed by a reduction in the reflectance intensity of calcite in an experiment of mixtures of calcite with siderite, and calcite with goethite. Therefore, to predict the effects of hematite on NIR-active minerals which display absorption features as analysed

in the Mantoverde ores, intimate mixtures of the NIR-active minerals at different ratios of concentration by mass with hematite are analysed.

#### **6.2.3.1. Chrysocolla-Hematite Mixtures**

Analysis of spectra of chrysocolla-hematite mixtures reveals that chrysocolla features appear weak only at a chrysocolla-hematite ratio of 9:1. Spectra appear featureless from ratio 8:2 through to 1:9 (Fig 6.21). This implies hematite is dominant in the spectra. Spectra confirm hematite dominance characteristics when in occurrence with other NIR-active minerals which display absorption features (Van Der Meer, 1995). Hence, where chrysocolla features are visible in the spectra, its concentration must be as high as 90 % and above. Therefore, since hematite almost completely suppresses or cancels out chrysocolla features, an understanding of ore mineralogy is important in scoping NIR application. If a strong association between the two minerals is established like in the case of the Mantoverde ores, it can be taken advantage of and used to design a sorting technique which will not depend entirely on chrysocolla features, since they may not be visible. Therefore, spectra without absorption features will be assumed to be chrysocolla bearing since their features are easily masked by hematite given their low concentration and association. While spectra with visible features not corresponding to chrysocolla will be classed as waste. Though this raises the issue of grade dilution by hematite, this can only be resolved at later stages of separation after the preconcentration of chrysocolla from other waste minerals has been achieved.

Therefore, in chrysocolla bearing copper ores associated with hematite, of which the Mantoverde ore is a good example, the absence of chrysocolla features in spectra is likely due to hematite. For preconcentration of chrysocolla from hematite, NIR is not applicable as chrysocolla will be lost. Given the relatively low grade of chrysocolla in comparison to hematite in the Mantoverde ore, in samples where both minerals occur, spectra is likely to be featureless.

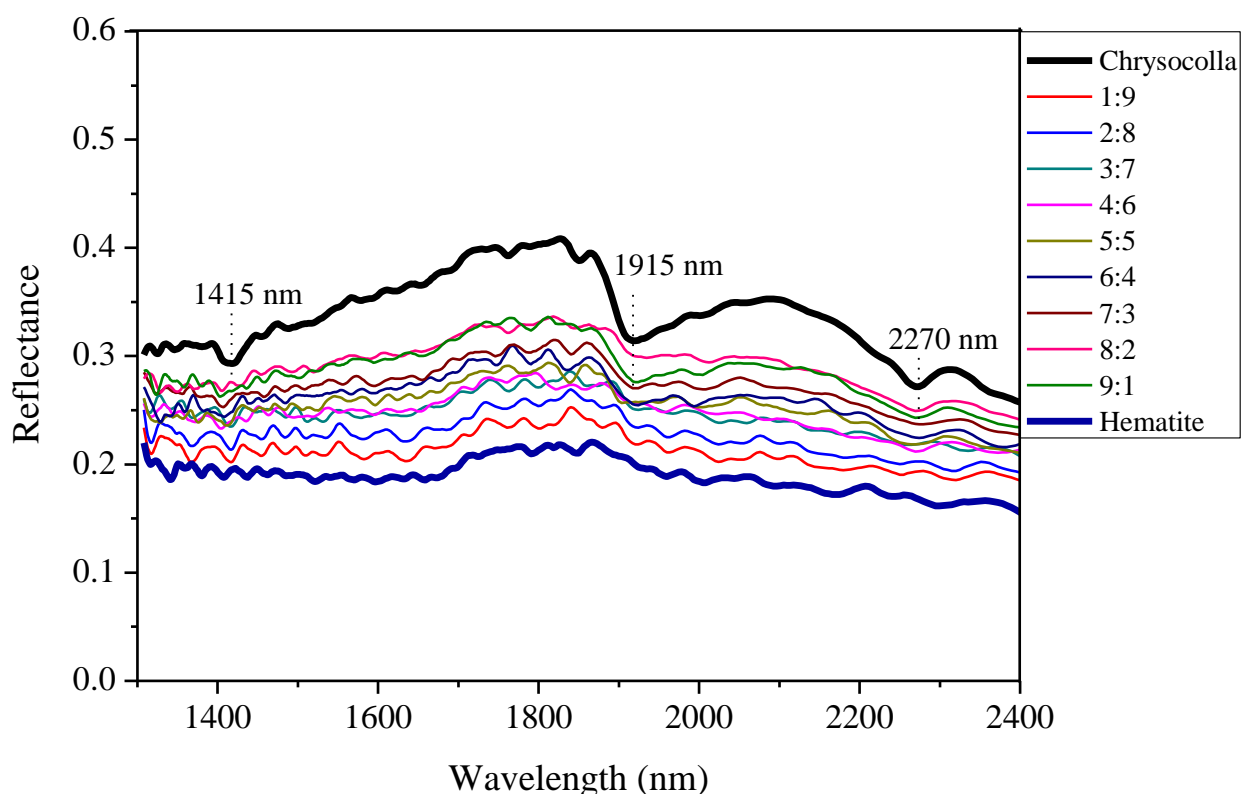


Figure 6.21 - NIR spectra of chrysocolla-hematite mixtures

Bottom and top spectrum are reference for hematite and chrysocolla respectively

### 6.2.3.2. Malachite-Hematite Mixtures

The NIR Spectra of mixtures of malachite-hematite (Fig. 6.22) reveals that at high hematite concentration (i.e. ratio of malachite to hematite 1:9 to 3:7) spectra show no absorption feature(s). Malachite features near 2275 nm are only visible from ratio 4:6. Similar to previous mixing involving malachite, analysis of mixtures of malachite and hematite reveal the relatively strong absorption feature displaying characteristics of malachite, as malachite displays its absorption features even at relatively high hematite concentrations. Malachite's 2360 nm feature is not visible in spectra across the series. This means that hematite has suppressed the feature and only the 2275 nm absorption feature is indicative of malachite when both minerals occur along the same spectrum range. If these are the only two NIR-active minerals in an ore, NIR may not be applicable for preconcentrating low grade malachite particles

from hematite, since at low concentrations (ratio 1:9 to 3:7) malachite features are masked. In low grade ores, the presence of hematite can be exploited if an association between both minerals is established. Just like in chrysocolla-hematite mixtures (Fig. 6.21) since low grade malachite is masked by hematite, spectrum without features and/or features relating to waste minerals will indicate dominance of hematite and also indirectly the presence of malachite.

Though malachite grade is very low in the samples of the Mantoverde ore, this analysis is important as it confirms that together with chrysocolla they can be preconcentrated by indirect means of exploiting the hematite feature masking characteristic. Therefore, given their relatively low concentration in samples compared to hematite, where a spectrum or spectra appears featureless, it or they will be taken to indicate hematite as well as chrysocolla and/or malachite.

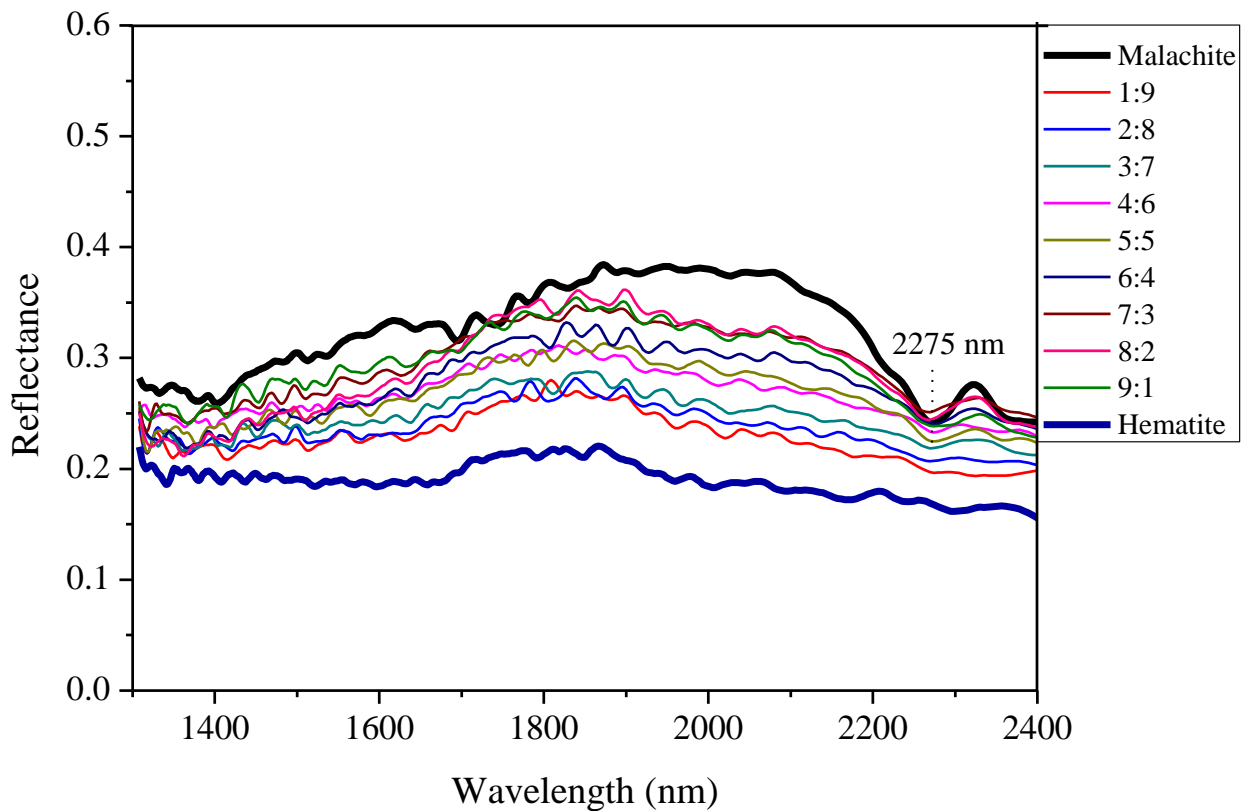


Figure 6.22 - NIR spectra of malachite-hematite mixtures

Bottom and top spectrum are reference for hematite and malachite respectively

### **6.2.3.3. Calcite-Hematite Mixtures**

The effect of hematite on calcite features is that of total dominance even at a lower hematite ratio (Fig. 6.23). All calcite's absorption features are masked in the spectra. This confirms Van Der Meer (1995) conclusions. It therefore means that identification of calcite in a mixture of calcite and hematite is not possible. Therefore, in ores containing both minerals as the only NIR-active minerals associated with each other along individual spectrum range, preconcentration may not achieve the desired objective. Preconcentration can only be possible if calcite features occur in isolation along individual spectrum range. Preconcentration will therefore only aim at removing samples with clear calcite features (freely-occurring-calcite). Visibility of calcite features will indicate high purity of calcite since even at a high calcite concentration, calcite features are masked in the mixture.

In preconcentration of hematite associated with copper-bearing minerals (chrysocolla and malachite) from carbonate (calcite) waste, high recovery will be achieved. However at low grade, only hematite-free calcite samples will be eliminated from such ores. Therefore, spectrum without features will translate to product while those with calcite features indicate high calcite purity (waste). This implies that application will be targeted at reducing high calcite bearing samples from the feed.



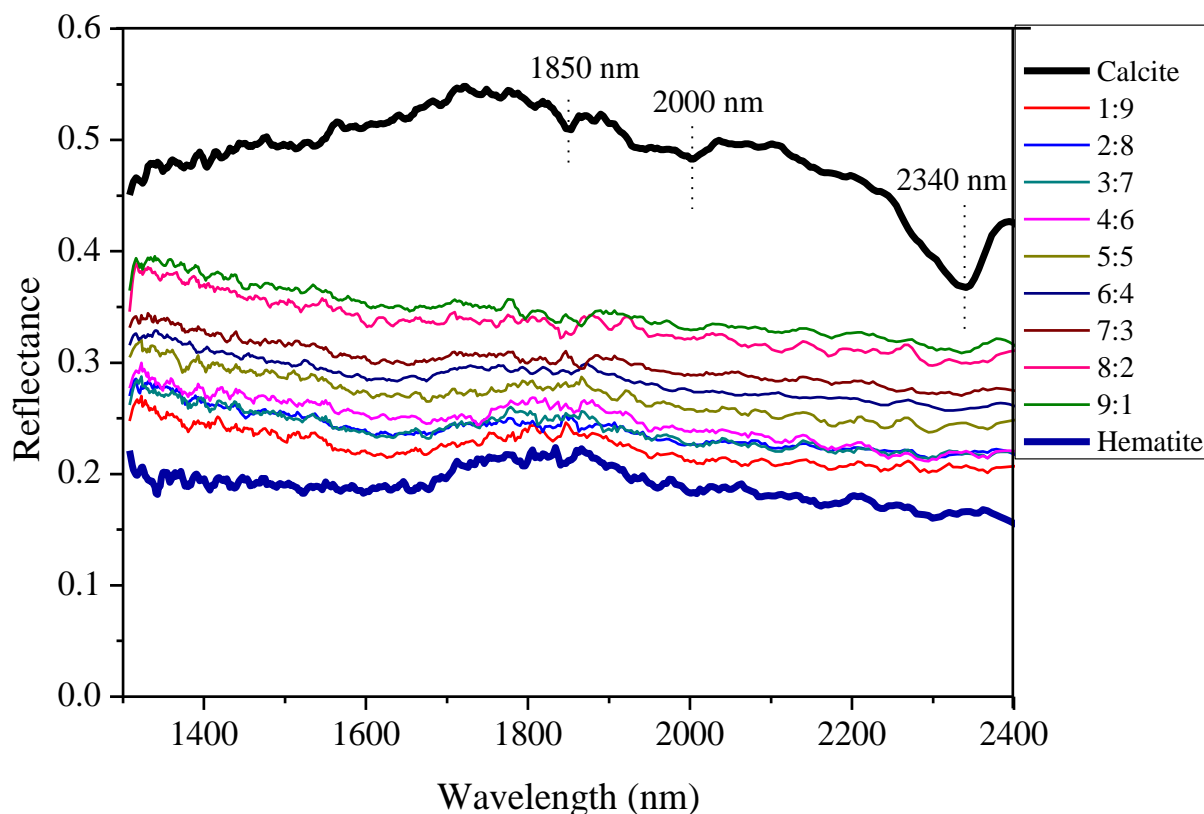


Figure 6.23 - NIR spectra of calcite-hematite mixtures

Bottom and top spectrum are reference for calcite and hematite respectively

#### 6.2.3.4. Muscovite-Hematite mixtures

The NIR spectra of these mixtures and reference minerals are presented in Figure 6.24. The effect of hematite on muscovite features is gradual, compared to calcite-hematite mixtures (Fig. 6.23), but similar to that of malachite (Fig. 6.22). At muscovite-hematite ratios of 1:9 to 3:7, the spectra appear featureless, indicating the dominance of hematite. This means that at these ratios muscovite features are captured by hematite and completely suppressed. With an increase in muscovite concentration from a muscovite-hematite ratio of 4:6 to 5:5 spectra display weak features near 1415 and 2205 nm. Muscovite features appear more visible from ratios 6:4 to 9:1. At these ratios, spectra show features with more defined absorption centres. The 2350 nm feature in muscovite is only visible from ratio 7:3 through to 9:1, appearing with a displaced centre located near 2355 nm. The 1840/1900 nm feature is invisible across the mixture. Therefore,

except for the feature near 1415 nm, both the 2200 and 2350 nm features are slightly displaced (+5 nm).

The maintained wavelength position of the 1415 nm feature in such mixtures and the strong visibility or presence of the 2200 or 2205 nm feature, though with slightly displaced absorption centres, makes these features good options to consider for the purpose of preconcentration of ores in mineral processing operations involving hematite and other suppressive minerals.

In the preconcentration of hematite from aluminium-rich minerals, the absence of absorption features (1415 or 2200 nm) will indicate the dominance of hematite. Hence, preconcentration can be achieved, by upgrading hematite and reducing water consumption during washing. Though the absence of 2200 nm absorption features is indicative of product (hematite), and the presence of the absorption features indicative of presence of muscovite (waste), the waste fraction of this preconcentration strategy shall require washing instead of disposal. Discarding the muscovite bearing material may lead to valuable ore being sent to waste, when absorption features (2200 nm) are present in spectra at equal hematite-muscovite concentration.

For the preconcentration of chrysocolla associated with hematite from muscovite, only the selection of 2200 nm for discrimination of waste (muscovite) will achieve better discrimination, as the 1415 nm feature is also present in chrysocolla.

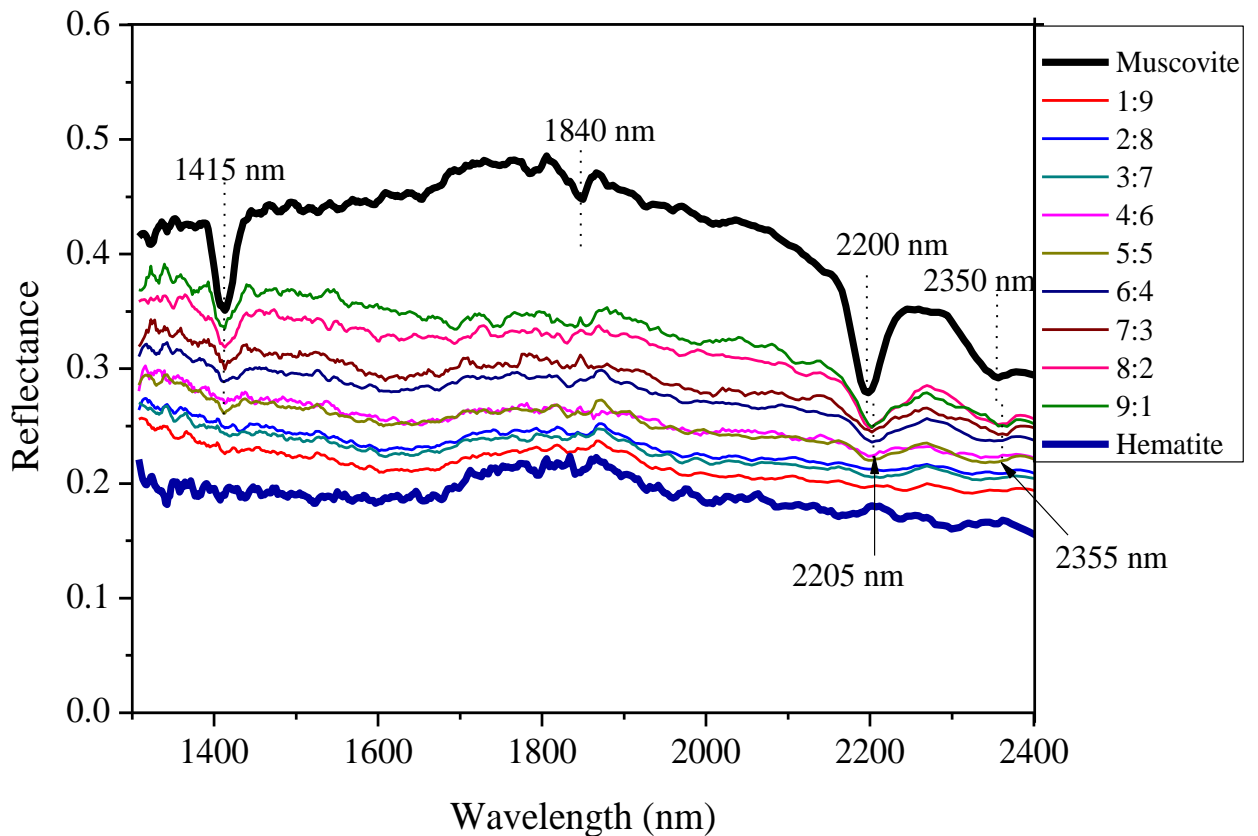


Figure 6.24 - NIR spectra of muscovite-hematite mixtures

Bottom and top spectrum are reference for hematite and muscovite respectively

### 6.2.3.5. Kaolinite-Hematite Mixtures

The NIR spectral analysis of mixtures of kaolinite-hematite (Fig. 6.25) reveals that kaolinite diagnostic doublet features at shorter wavelengths are only visible together at kaolinite-hematite ratios of 9:1. From ratio 8:2 to 5:5 spectra appear broad at shorter wavelengths and flatten at ratio 4:6. The water feature near 1840 nm is completely invisible from ratio 7:3. NIR spectra shows that the 2160 nm feature at longer wavelengths is weaker than the 2200 nm feature, disappearing at ratio 8:2 while the 2200 nm feature disappears at ratio 6:4 (Fig. 6.25).

Given the visibility of the 1415 and 2200 nm features in kaolinite-hematite mixtures, from ratio 9:1 through ratio 7:3, the features are best diagnostic of kaolinite and the choice of either or both for identification and classification in NIR application is possible. It should also be noted that featureless spectra in

such a mixture does not necessarily translate to purity of hematite, rather it indicates hematite spectral dominance.

NIR spectra behaviour is almost a repeat of the muscovite-hematite mixtures (Fig. 6.24), where both the 1415 and 2200 nm features are indicative of the minerals. Though the 2200 nm feature of muscovite experienced a slight displacement, muscovite is more active in hematite compared to kaolinite in hematite mixtures. Muscovite features appeared at ratios 4:6 through ratio 9:1 (muscovite-hematite) while kaolinite appeared at ratios 7:3 through 9:1 (kaolinite-hematite). This indicates that the choice of the 2200 nm feature will target both minerals when in concentration. Spectral analysis also confirms Figure 6.5 where muscovite showed more NIR spectral dominance compared to kaolinite.

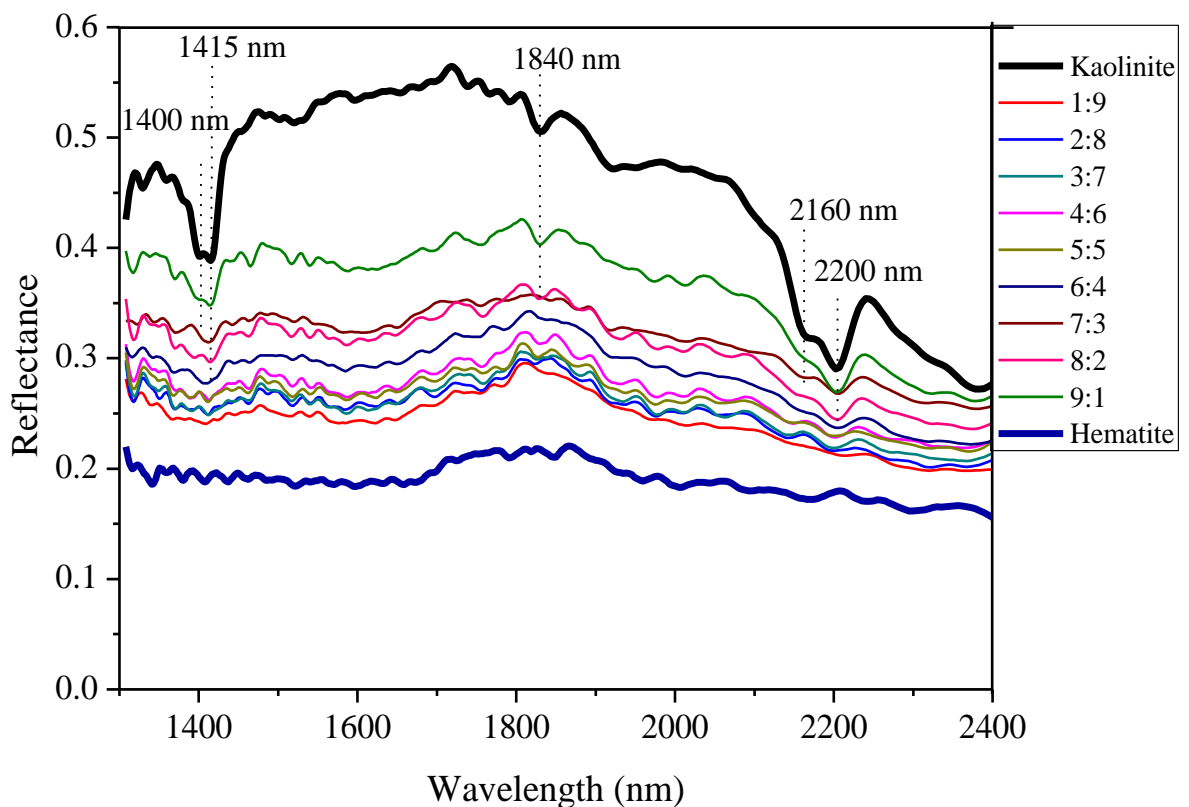


Figure 6.25 - NIR spectra of kaolinite-hematite mixtures

Bottom and top spectrum are reference for hematite and kaolinite respectively

### 6.2.3.6. Chlorite-Hematite Mixtures

A mixture of chlorite and hematite reveal total dominance of chlorite by hematite (Fig. 6.26). NIR Spectra show no feature(s) relating to chlorite at any ratio, as spectra appear featureless. This therefore means that where both minerals occur together as the only or dominant NIR-active minerals along the spectrum range, the spectra will be featureless. In such ore, establishing mineral associations between both minerals will explain the absence of chlorite features. If the mineral constituent of an ore is unknown, spectra could easily be misclassified as only hematite-bearing. Therefore, where a spectrum displays features of chlorite, it reveals that hematite is not in concentration along the spectrum range. Hence, only the freely occurring chlorite spectra can be targeted for removal as waste. Discrimination between both minerals will yield high recovery for hematite but at low grade due to dilution by chlorite.

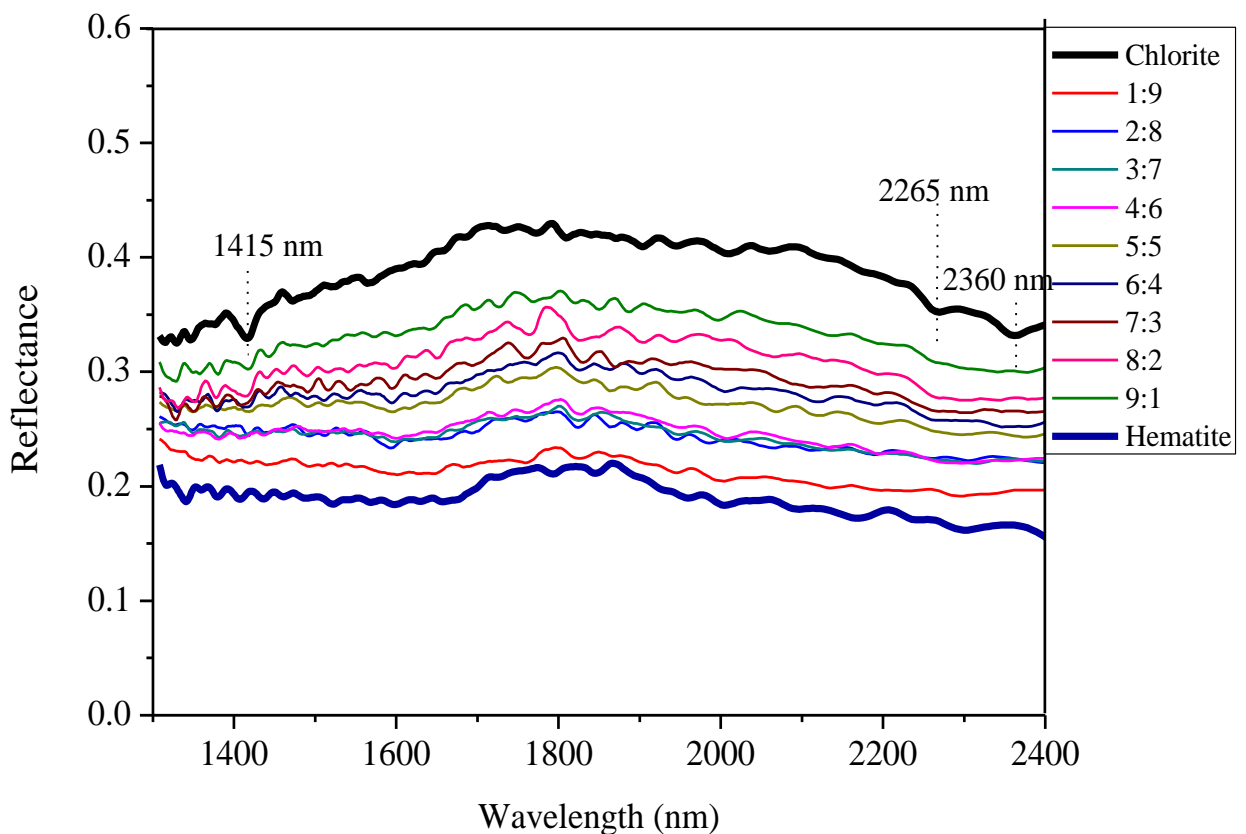


Figure 6.26 - NIR spectra of chlorite-hematite mixtures

Bottom and top spectrum are reference for hematite and chlorite respectively

### 6.2.3.7. Biotite-Hematite Mixtures

The NIR spectra of biotite-hematite mixtures display typical hematite spectra masking characteristics (Fig. 6.27). Spectra across all ratios appear featureless. Biotite though -OH bearing does not display a feature near 1400 nm due to its iron content (Clark, 1995). Therefore, the addition of hematite to biotite will result in an increase in iron content in concentration, thereby readily cancelling out the other biotite features. This is a likely case in hematite-rich copper bearing ore, like the Mantoverde copper ore where biotite features are completely invisible when hematite is present in concentration. Discriminating biotite from hematite is unlikely except when individual minerals occur in isolation. Hence, only the freely occurring biotite spectra can be targeted for removal as waste.

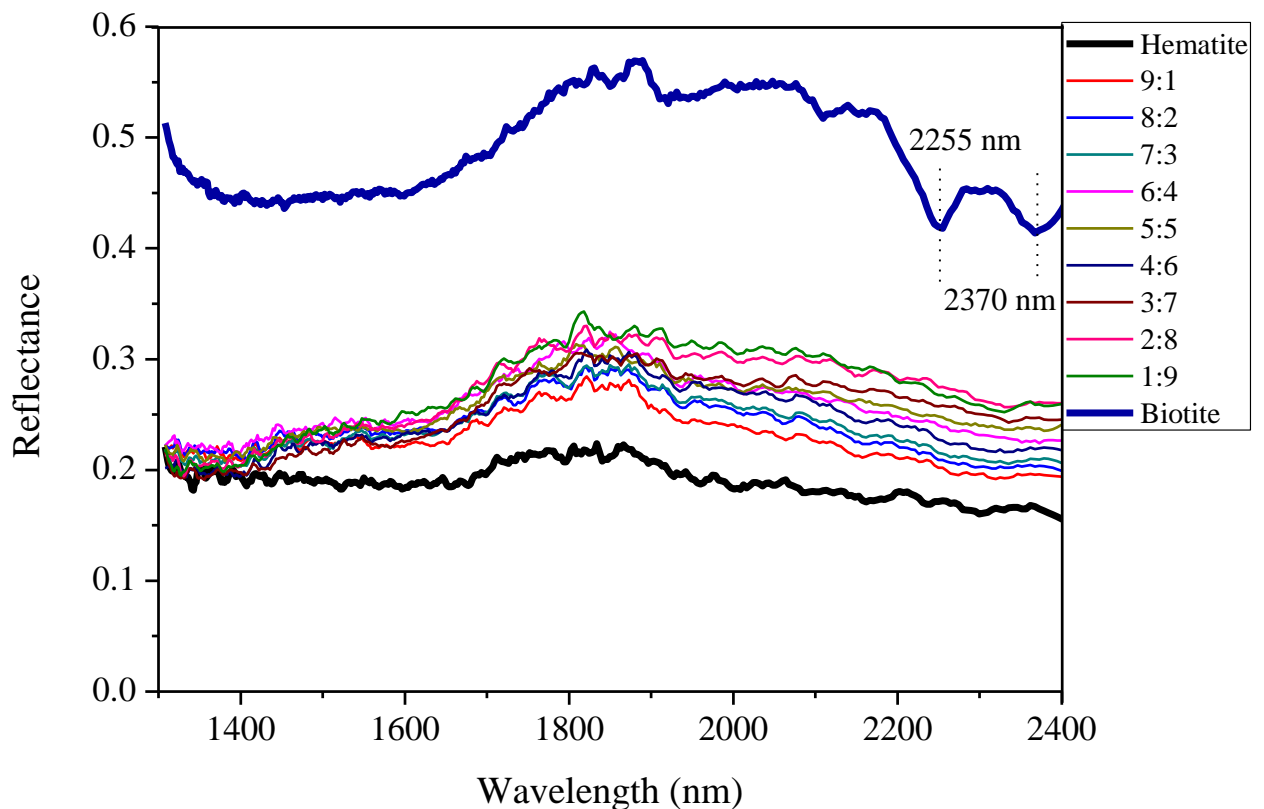


Figure 6.27 - NIR spectra of biotite-hematite mixtures

Bottom and top spectrum are reference for hematite and biotite respectively

#### **6.2.4. Complex mixtures or mineral associations**

The Mantoverde ore consists of complex mixtures of minerals of varying NIR-active functional groups and concentrations. To predict the influence of one mineral over other(s) in NIR spectra, complex intimate mixtures of NIR-active minerals at equal concentration by ratios of mass are analysed and discussed below.

##### **6.2.4.1. Hematite-Chrysocolla-Muscovite Mixture**

The NIR spectrum of hematite-chrysocolla-muscovite mixture is presented in Figure 6.28. Mixtures of chrysocolla with muscovite (Fig. 6.1) showed that both minerals display features side-by-side at relatively equal concentration. A mixture of chrysocolla with hematite only showed chrysocolla features at 90 % chrysocolla concentration (Fig. 6.21), absorption features by either mineral in chrysocolla-muscovite spectra is concentration dependent (Fig. 6.1). While the spectra of muscovite with hematite revealed that muscovite displays features at longer wavelength near 2205 nm in addition to the 1415 nm at equal muscovite-hematite concentration (Fig. 6.24). NIR spectra of complex mixtures of chrysocolla-hematite-muscovite at equal concentration (Fig. 6.28) only show a defined absorption feature near 1415 nm. The 1415 nm absorption feature occurring in the absence of the 1915 nm feature is indicative of -OH (Hunt, 1977; Aines and Rossman, 1984; Clark et al., 1990; Iyakwari et al., 2013) and is characteristic of both chrysocolla and muscovite. At longer wavelengths between 2200 and 2400 nm, spectra shows broad depression without absorption centres.

Spectral analysis therefore reveals the best diagnostic features of both minerals near 2200 and 2270 nm for muscovite and chrysocolla respectively are masked by hematite and only the hydroxyl feature near 1415 nm is visible in the spectra. Since the 1415 nm feature is not considered diagnostic (Iyakwari and Glass, 2014), hematite dominates the spectra. Hence, analysis confirms the dominance of hematite in spectra as it is responsible for the masking of features near 2200 and 2270 nm for muscovite and chrysocolla respectively.

Therefore, the indirect application of hematite to indicate chrysocolla in concentration will yield a good recovery if muscovite was the targeted waste mineral and the 2200 nm is selected for discrimination of waste mineral.

Spectra presented in Figure 6.28 will classify as product. Hence only the spectrum displaying muscovite feature near 2200 nm will classify as waste.

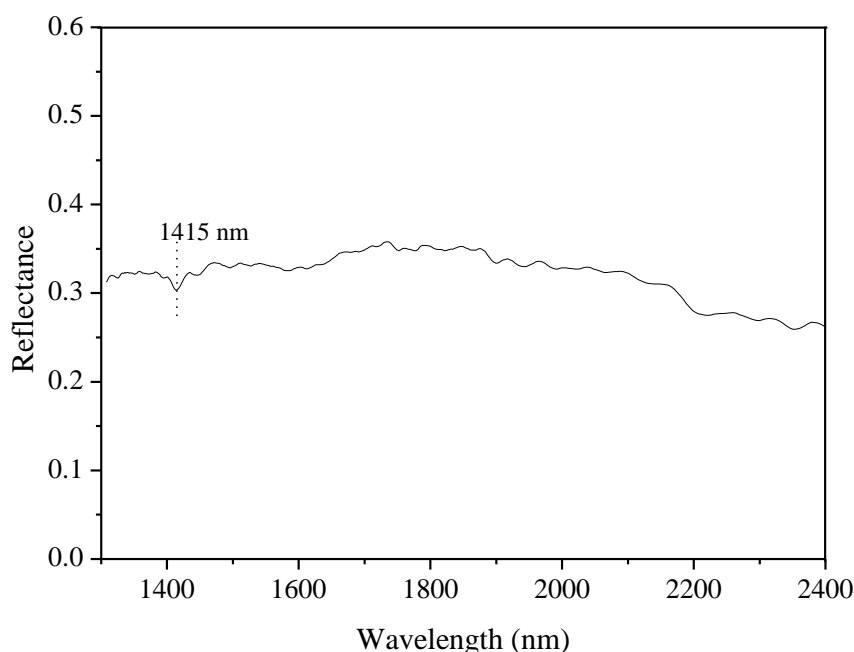


Figure 6.28 - NIR spectrum of chrysocolla-hematite-muscovite mixture at ratio of 1:1:1 concentration by mass

#### 6.2.4.2. Hematite-Chrysocolla-Kaolinite Mixture

The NIR Spectra of mixture of hematite-chrysocolla-kaolinite (Fig. 6.29) shows absorption features near 1415 nm and 2200 nm only. While both kaolinite and chrysocolla show 1415 nm absorption feature, the 2200 nm absorption feature is indicative of kaolinite. Also, given the lack of doubling of features, spectra could as well be interpreted as that of muscovite since muscovite also shows absorption at similar wavelength position. The presence of hematite in concentration is responsible for the invisibility of the kaolinite twin features normally observed at 2160 nm and 1400 nm in addition to the 1415 nm and 2200 nm wavelengths. Chrysocolla' best diagnostic absorption feature near 2270 nm is invisible in the spectra.

Analysis reveals that preconcentration of chrysocolla or hematite from such mixture can only be economic if the 2160 nm feature is chosen for kaolinite discrimination. This is because its visibility is concentration dependent. Hence,



where visible, the 2160 nm absorption features is indicative of the absence of hematite or chrysocolla. The choice of 2200 nm will result in the loss of valuable to waste.

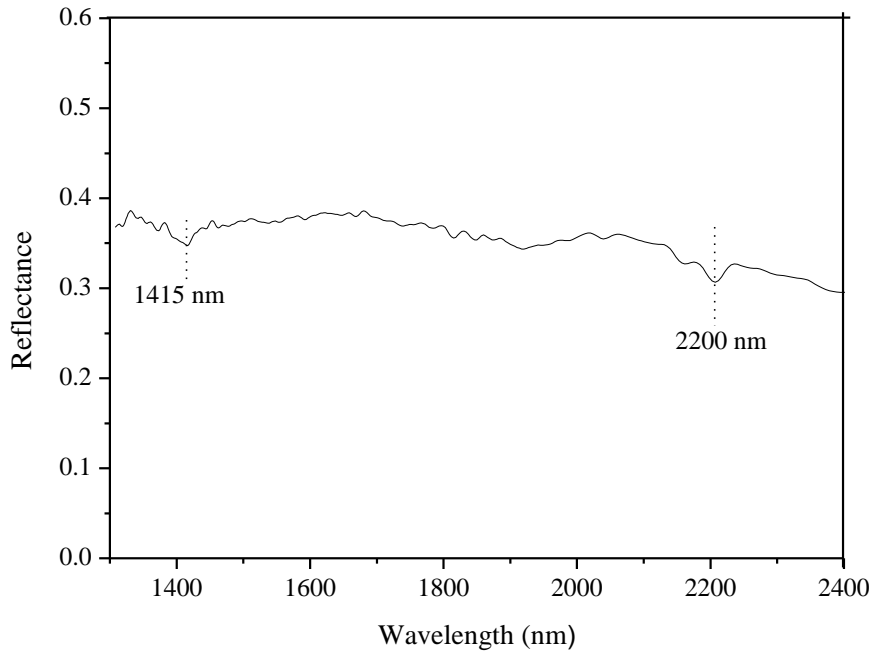


Figure 6.29 - NIR spectrum of hematite-chrysocolla-kaolinite mixture at ratio of 1:1:1 concentration by mass

#### 6.2.4.3. Hematite-Malachite-Calcite Mixture

The NIR Spectrum of complex mixtures of hematite-malachite-calcite (Fig. 6.30) show absorption features near 2275 and 2350 nm. Given the minerals in concentration, the 2275 nm feature is solely assigned to malachite. The 2350 nm feature is either displaced from 2360 nm or 2340 nm for malachite or calcite respectively. Previous analysis indicated that calcite features are completely invisible when in concentration with either minerals (Fig. 6.10 and 6.23), while malachite show features near 2275 nm when mixed with hematite at equal concentration (Fig. 6.22). Hence, both features displayed by the spectra of the complex mixture (Fig. 6.30) can be assigned to malachite. Therefore, displacement of feature (2350 nm) is indicative of the influence of hematite in the spectra.

Spectral analysis confirms that malachite can be economically preconcentrated from calcite (Fig. 6.10). Preconcentration of malachite from hematite using NIR may result in loss of low grade malachite to waste as shown in Figure 6.22. Hence, both featureless spectra, and spectra showing malachite features should be considered as malachite bearing, if hematite is in concentration. Hence where spectra display calcite features, either or both malachite and hematite are not in concentration.

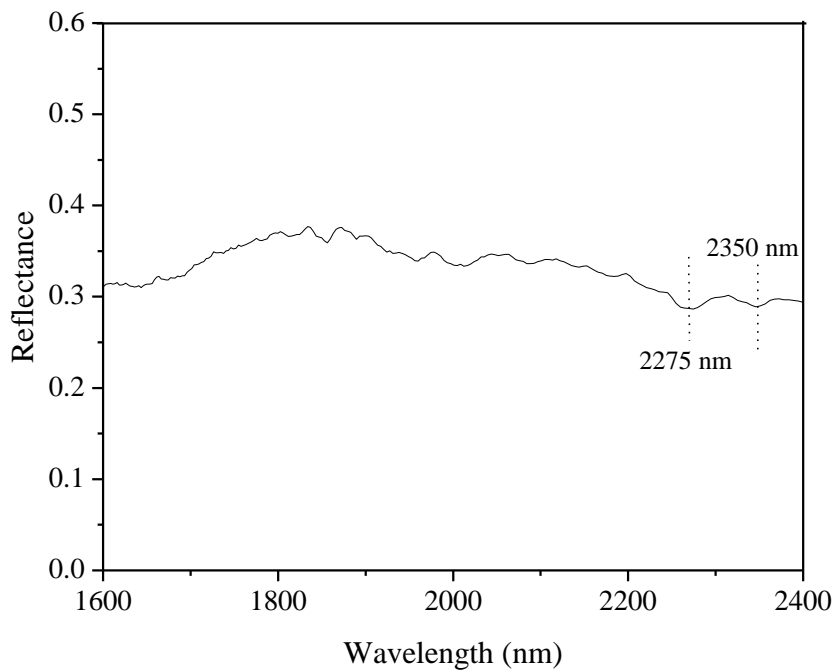


Figure 6.30 - NIR spectrum of hematite-calcite-malachite-mixture at ratio of 1:1:1 concentration by mass.

#### 6.2.4.4. Muscovite-Biotite-Chlorite Mixture

The NIR spectra of complex intimate mixture of muscovite-biotite-chlorite is presented in Figure 6.31. All three minerals contain -OH functional groups and as such display features only characteristic of -OH. With the exception of biotite, both muscovite and chlorite display features near 1415 nm. Muscovite displays additional features near 1840 and/or 1915, 2200 and 2350 nm while chlorite shows additional features near 2265 and 2360 nm. Biotite shows its features near 2355 nm and 2370 nm.

NIR spectrum of the mixture (Fig. 6.31) reveals absorption features near 1415 and 2200 nm with a depression between 2300 and 2400 nm. The 2200 nm feature shows that muscovite is more dominant in the spectra. The depression between 2300 and 2400 nm can be assigned to both biotite and chlorite, as spectra of their mixture appear broad even at equal concentration (Fig.6.8). Muscovite is dominant when in concentration with either mineral (Figs. 6.4 and 6.9). Hence, the 1415 nm feature though individually shown by both chlorite and muscovite minerals, can solely be assigned to muscovite. Therefore, both biotite and chlorite are weak in the spectra. This indicates that in samples where these minerals occur along the same spectrum range, muscovite features will dominate the resultant spectra. Spectral analysis shows muscovite is the most NIR-active mineral of the three minerals analysed.

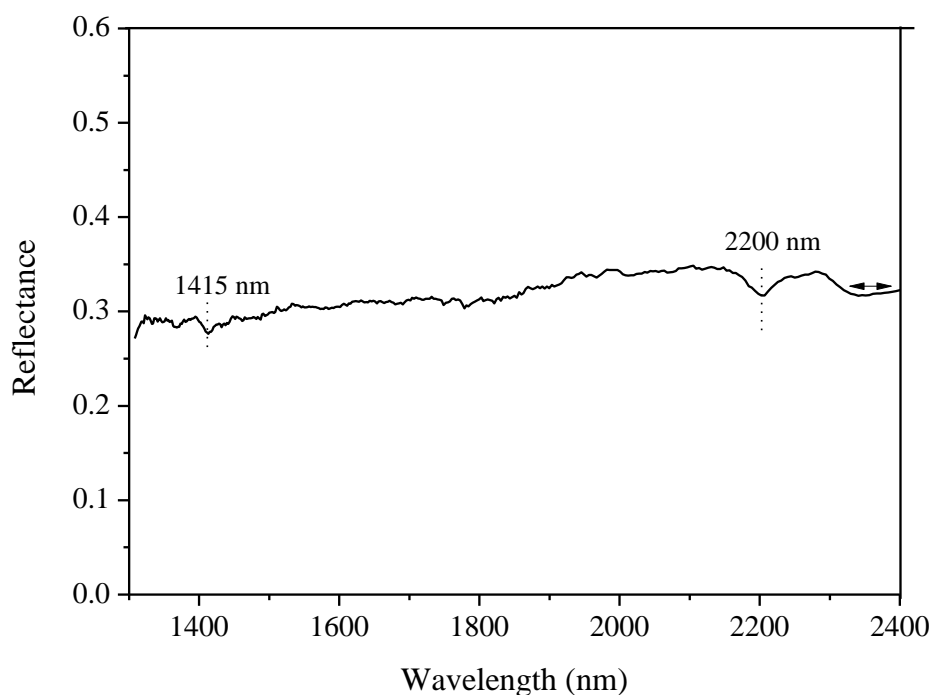


Figure 6.31 - NIR spectrum of muscovite-biotite-chlorite intimate mixture at ratio of 1:1:1 concentration by mass.

#### 6.2.4.5. Hematite-Malachite-Kaolinite Mixture

A NIR spectrum of a mixture of hematite-malachite-kaolinite is presented in Figure 6.32. Unlike the hematite-chrysocolla-kaolinite mixture (Fig. 6.29), spectra of hematite-malachite-kaolinite show absorption features near 2200 and 2275 nm, indicative of kaolinite and malachite respectively. Similar to Figure

6.29, hematite is responsible for the invisibility of the kaolinite double features at longer wavelengths (2160 nm) and the twin features at shorter wavelengths (1400 and 1415 nm). Also, as with the hematite-chrysocolla-kaolinite spectra, discrimination or removal of high grade kaolinite particles in the ore can only be achieved by selecting kaolinite 2160 nm absorption feature as analysis show that where the feature is visible, the concentration of kaolinite is high. Hence complete kaolinite removal is not possible.

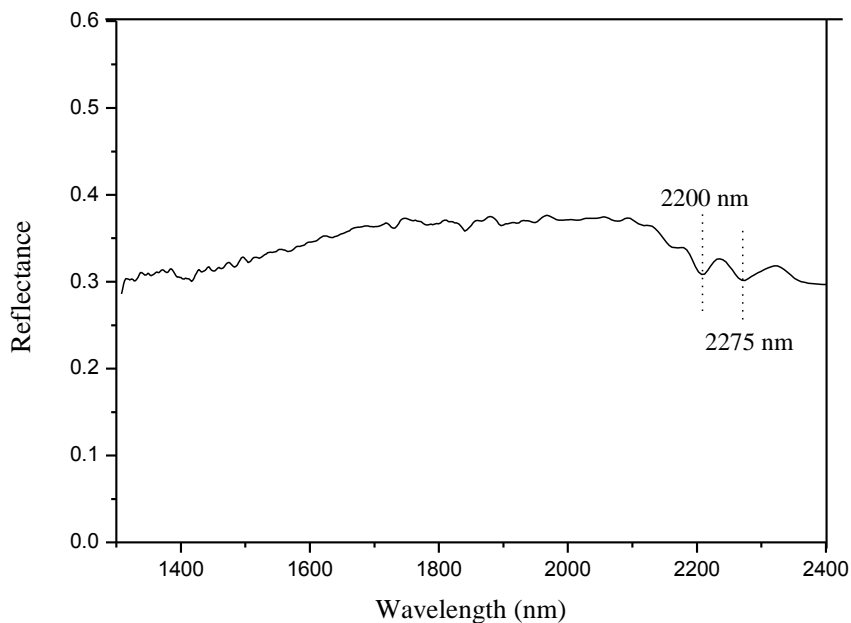


Figure 6.32 - NIR spectrum of hematite-malachite-kaolinite mixture at ratio of 1:1:1 concentration by mass

#### 6.2.4.6. Malachite-Muscovite-Hematite Mixture

Figure 6.33 presents NIR spectrum of a mixture of malachite-muscovite-hematite mixture. Similar to the hematite-malachite-kaolinite spectra (Fig. 6.32), spectra show absorption features near 2200 and 2275 nm, indicative of muscovite and malachite absorption features respectively. The same as Figures 6.31 and 6.32, hematite is responsible for the invisibility of the -OH feature at shorter wavelengths near 1415 nm. As with the malachite-muscovite spectra (Fig. 6.20), identification of individual minerals is achievable, but discrimination will result in the loss of valuable ore (malachite) to waste.

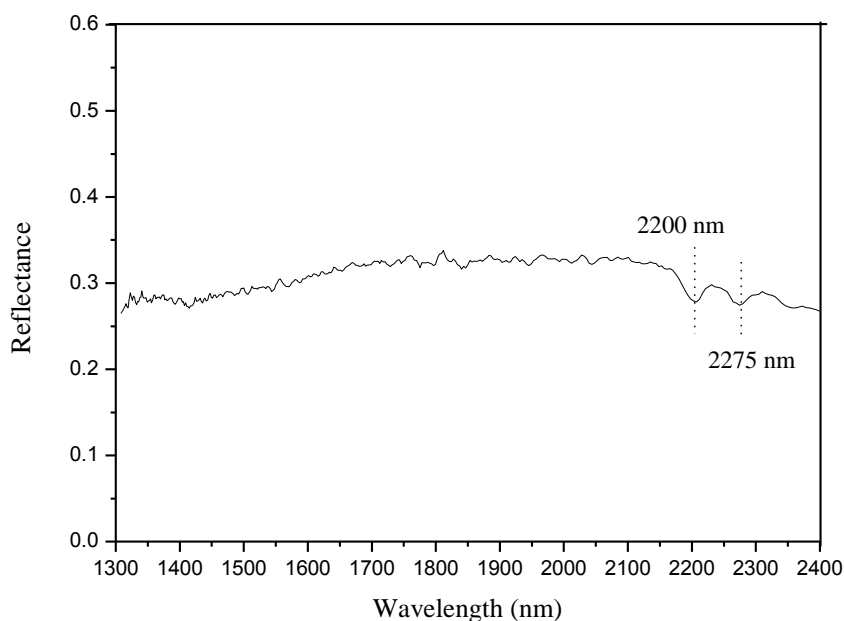


Figure 6.33 - NIR spectrum of malachite-muscovite-hematite mixture at ratio of 1:1:1 concentration by mass

#### 6.2.4.7. Chlorite-Biotite-Calcite Mixture

The NIR spectrum of complex intimate mixtures of chlorite-biotite-calcite is presented in Figure 6.34. Though both biotite and chlorite are -OH bearing minerals, and display featureless spectra when mixed together (Fig. 6.8), as single minerals only chlorite displays a feature near 1415 nm, biotite is featureless at the shorter wavelengths (Clark, 1995; Iyakwari et al., 2013). Therefore, the 1415 nm feature is solely assigned to chlorite. Given the mineralogy of the mixture, the 2350 nm feature is a displaced feature which could be of chlorite or calcite since both minerals show features near 2340 and 2360 nm for calcite and chlorite respectively. A series of intimate mixtures of chlorite and calcite showed that the calcite feature near 2340 nm is invisible when in concentration with chlorite (Fig. 6.14). Though biotite shows features at longer wavelengths near 2370 nm, due to the close proximity of the feature to chlorite's 2360 nm feature and the lack of calcite feature when with chlorite, the feature is interpreted as displaced from chlorite. As such, the feature is assigned to chlorite. Therefore, chlorite is the dominant mineral in this mixture.

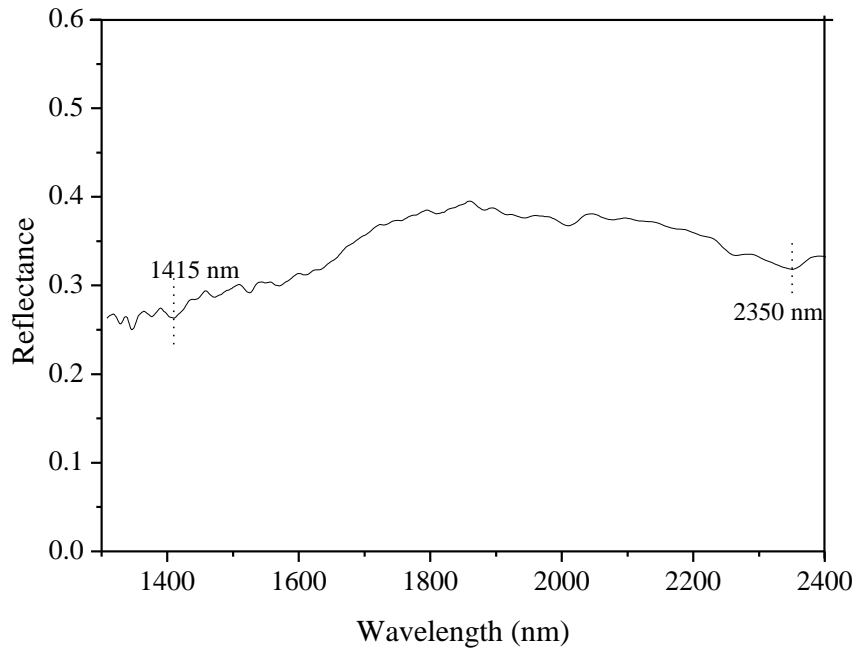


Figure 6.34 - NIR spectrum of chlorite-biotite-calcite mixture at ratio of 1:1:1 concentration by mass.

#### 6.2.4.8. Calcite-Hematite-Muscovite Mixtures

The NIR spectrum of a calcite-hematite-muscovite mixture is presented in Figure 6.35. Spectra display absorption features near 2200 and 2345 nm. Except for the absence of the 1415 nm feature in the spectra, it is a repeat of muscovite-calcite mixture at ratios 6:4 and 5:5 (Fig. 6.12). At equal ratios, while calcite appeared featureless in calcite-hematite mixtures (Fig. 6.23), muscovite displayed its diagnostic features near 1415, 2205, and 2355 nm with the two features at longer wavelengths experiencing displacement (Fig. 6.24). Given the complex nature of the spectra, the feature near 2200 nm is assigned to muscovite while the 2345 nm feature is assigned to calcite as a displaced feature, with muscovite responsible for the displacement.

Though calcite's feature appears displaced, both minerals (calcite and muscovite) are visible in the spectra of complex mixture (Fig. 6.35). Hematite is only responsible for the suppression of the 1415 nm feature of muscovite and the reduction of individual feature absorption intensity (depth). As such all three minerals are active in the mixture as the spectra appear mixed.

In the Mantoverde copper ore preconcentration, samples displaying both -OH and  $\text{CO}_3^{2-}$  features related to muscovite (or kaolinite) and calcite respectively will be classified as waste. Hence, this spectrum is a classic example of a waste sample spectrum. If all the samples in the batch of ore display this characteristic of high spectra mixing, then the material will be considered NIR-un-sortable. NIR will only be useful in identifying the presence of the minerals in the ore.

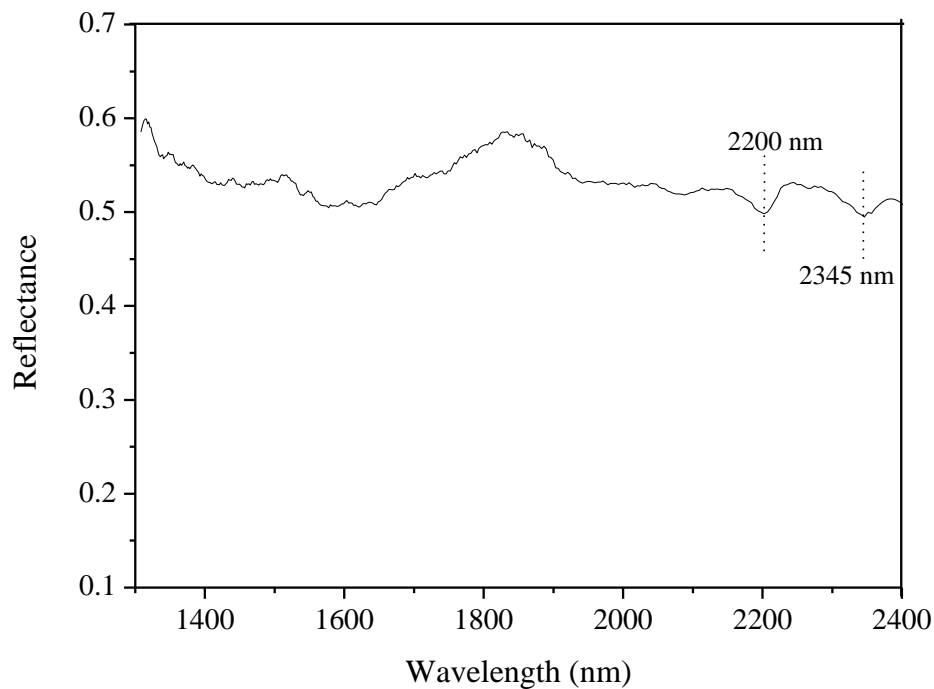


Figure 6.35 - NIR spectrum of calcite-muscovite-hematite mixture at ratio of 1:1:1 concentration by mass.

#### 6.2.4.9. Chrysocolla-Biotite-Hematite Mixture

The NIR spectra of complex mixtures of chrysocolla-biotite-hematite appear featureless across all wavelengths (Fig. 6.36). The lack of absorption features confirms the spectral dominance of hematite over the biotite (Fig. 6.27) and chrysocolla (Fig. 6.21) features. Since none of the NIR-active minerals absorption feature are visible in the spectra, featureless spectra should be considered chrysocolla bearing. Hence, for economic preconcentration of chrysocolla, all three minerals should be considered together. In the absence of detailed mineralogy and mineral association, spectra displaying this characteristic will be classified as hematite spectra.

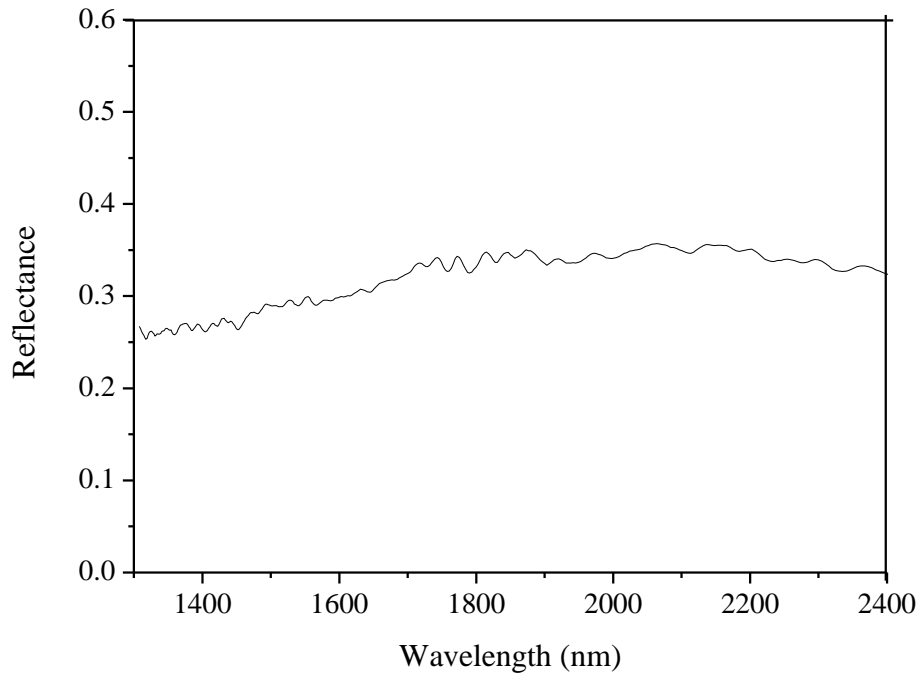


Figure 6.36 - NIR spectrum of chrysocolla-biotite-hematite mixture at ratio of 1:1:1 concentration by mass

#### 6.2.4.10. Biotite-Hematite-Chlorite Mixture

NIR spectra of complex intimate mixtures of biotite-hematite-chlorite appear featureless across all wavelengths (Figure 6.37). The lack of features just like in Figure 6.36 confirms the total spectral dominance of hematite on some absorption feature displaying NIR-active minerals. Spectral analysis indicates that the visibility of features of either or both chlorite and biotite is dependent on the presence of hematite in concentration. The spectrum is similar to that obtained for the chlorite-biotite mixtures as it also appeared featureless (Fig. 6.8). Hence, where either biotite or chlorite show feature(s) in the spectra, this indicates the mineral is occurring free (unmixed).



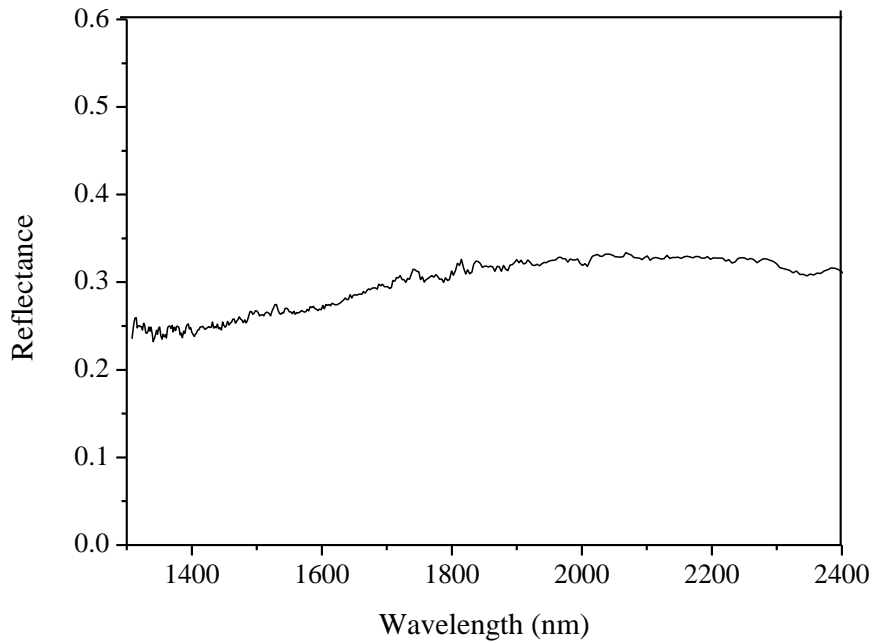


Figure 6.37 - NIR spectrum of biotite-hematite-chlorite mixture at ratio of 1:1:1 concentration by mass

#### 6.2.4.11. Biotite-Muscovite-Calcite Mixture

The NIR spectrum of a biotite-muscovite-calcite mixture presented in Figure 6.38 shows features near 2200 and 2340 nm. Individual features can be assigned to muscovite (2200 nm) and calcite (2340 nm). Hence, biotite is weak and featureless in the spectra. Spectrum confirms the behaviour of muscovite and calcite where they occur along the same spectral range (Fig. 6.12) displaying features side-by-side and therefore making it difficult to preconcentrate between the two minerals. Also confirmed is the spectral dominance of both muscovite and calcite over biotite (Figures 6.9 and 6.18).

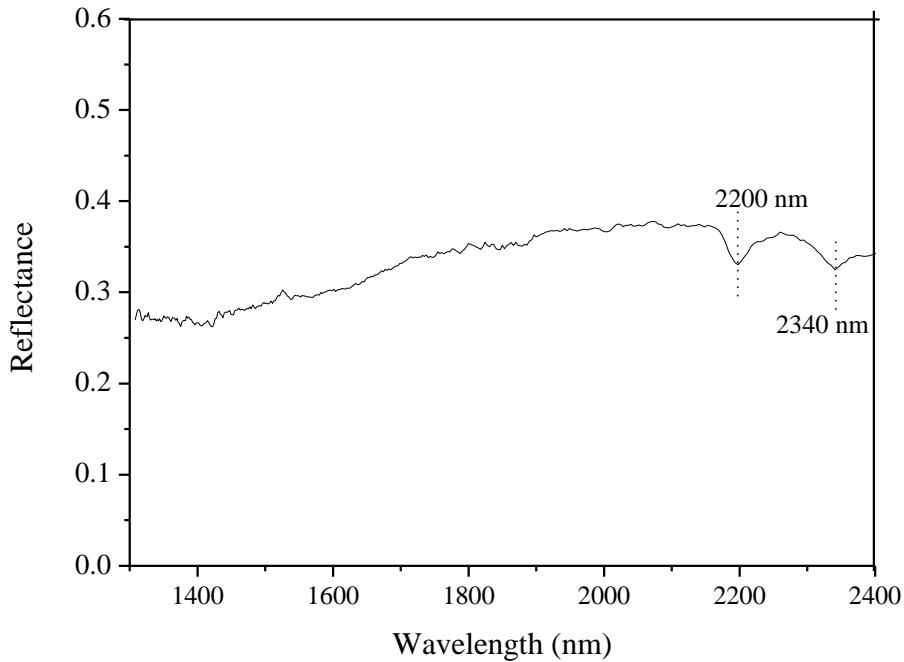


Figure 6.38 - NIR spectrum of biotite-muscovite-calcite mixture at ratio of 1:1:1 concentration by mass.

#### 6.2.4.12. Kaolinite-Calcite-Hematite Mixture

The NIR Spectra of mixtures of kaolinite-calcite-hematite reveal absorption features near 1415 and 2200 nm. Both features correspond to the kaolinite absorption features though appearing without their twin features. Like that observed in Figures 6.29 and 6.32 where the kaolinite twin features are not visible, spectra can be misidentified as muscovite. Similar to Figures 6.29 and 6.32, hematite is responsible for the absence of the kaolinite twin features. Calcite is not visible in the spectra, as its best diagnostic feature near 2340 nm is not observed.

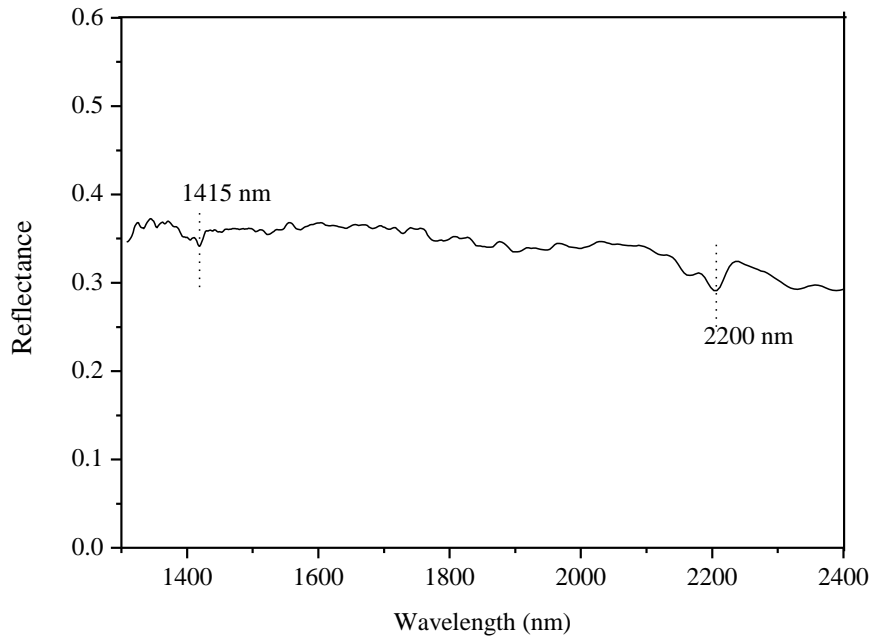


Figure 6.39 - NIR spectrum of kaolinite-calcite-hematite mixture at ratio of 1:1:1 concentration by mass

#### 6.2.4.13. Muscovite-Hematite-Kaolinite Mixture

The spectrum of this mixture shows strong absorption features near 1415 and 2200 nm. Both absorption features correspond to muscovite and kaolinite's best diagnostic features. The spectrum is a repeat of Figure 6.5 where both kaolinite and muscovite are analysed. The influence of hematite in the spectra is minimal, only masking the kaolinite double features near 1400 and 2160 nm.

Where both kaolinite and muscovite are present in a spectrum of complex mixtures, the 2200 and or 1415 nm absorption features appear strong. This is also true for the muscovite-kaolinite simple mixture (Fig. 6.5).

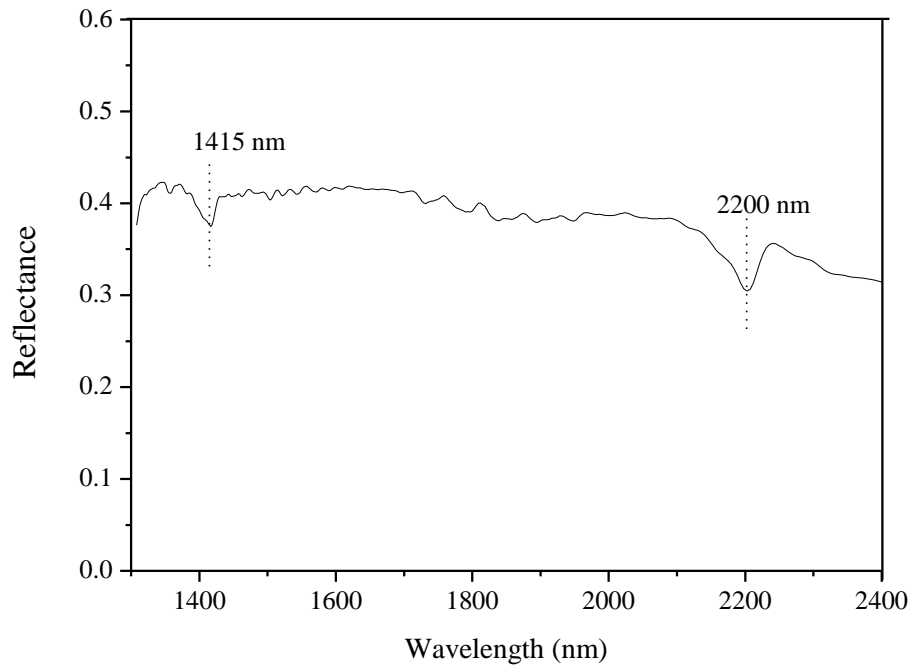


Figure 6.40 - NIR spectrum of muscovite-hematite-kaolinite mixture at ratio of 1:1:1 concentration by mass

#### 6.2.4.14. Chlorite-Biotite-Calcite-Hematite Mixtures

The NIR spectrum of complex intimate mixtures of chlorite-biotite-calcite-hematite is presented in Figure 6.41. The spectrum reveals features near 1415 nm and 2010 nm with a broad depression at longer wavelengths between 2250 and 2400 nm, appearing without defined absorption centres. Though the lack of absorption centres was also observed in the chlorite-calcite mixture at higher calcite concentrations, hematite completely suppressed the features of all three minerals; calcite (Fig. 6.23), chlorite (Fig. 6.26), and biotite (Fig. 6.27) when individually mixed. Analysis of chlorite-biotite-calcite (Fig. 6.34) also showed a feature near 1415 nm in addition to a feature at a longer wavelength near 2350 nm. Since all minerals are at equal concentration, hematite is responsible for the disappearance of the 2350 nm absorption feature present in Figure 6.34. From analysis it can therefore be assumed that an increase in hematite concentration in the mixture will mask the 1415 nm and 2010 nm features.

Since only chlorite shows a feature near 1415 nm, biotite is invisible in the spectra. Therefore, while the 2010 nm feature is a calcite feature, the 1415 nm feature is indicative of chlorite. But where other minerals capable of showing

features near 1415 nm are in concentration, the choice of 1415 nm to indicate chlorite will be misleading (Iyakwari and Glass, 2014).

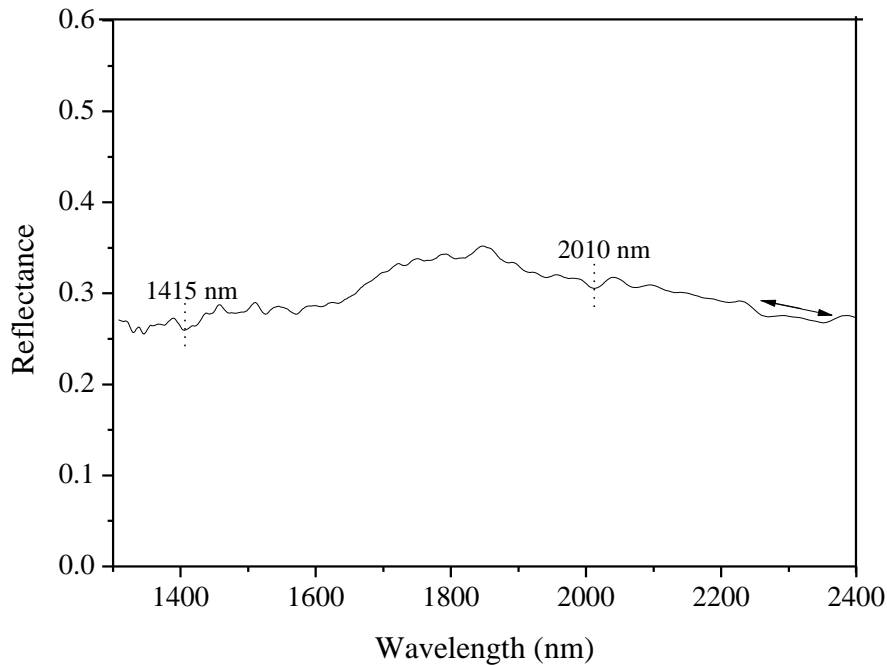


Figure 6.41 - NIR spectrum of chlorite-biotite-calcite-hematite mixture at ratio of 1:1:1:1 concentration by mass.

#### 6.2.4.15. Chlorite-Biotite-Calcite-Muscovite Mixtures

The NIR spectrum of a chlorite-biotite-calcite-muscovite complex intimate mixtures show features near 1415, 1915, 2010, and 2200 (Fig. 6.42). The spectrum also shows depression near 2350 appearing without a defined centre. Though chlorite's 1415 nm feature is visible in chlorite-calcite mixtures (Fig. 6.14), the 1415 nm feature displayed by spectra is assigned to muscovite, as muscovite dominates spectra of mixtures of chlorite and muscovite, (Fig. 6.4). Just like in other mixtures involving biotite, its features are invisible in the spectra. Hence, features displayed by the spectrum are indicative of two minerals (muscovite and calcite); muscovite is indicated by the 1415, 1915 and 2200 nm while calcite is indicated by 2010 nm features.

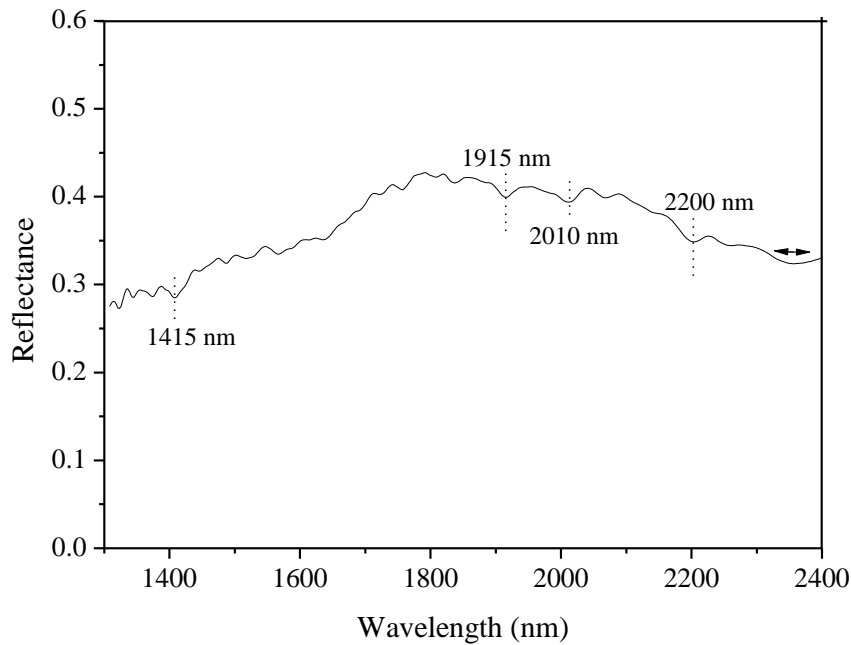


Figure 6.42 - NIR spectrum of chlorite-biotite-calcite-muscovite mixture at ratio of 1:1:1:1 concentration by mass

#### 6.2.4.16. Kaolinite-Calcite-Hematite-Muscovite Mixture

The NIR spectrum of intimate mixtures of kaolinite-calcite-hematite-muscovite is presented in Figure 6.43. Spectrum shows the presence of the muscovite and or kaolinite indicated by an absorption feature located near 2200 nm. The -OH feature at shorter wavelengths (near 1400 nm) is not defined. The disappearance of other features could be assigned to the effect of iron substituting for aluminium in the muscovite and or kaolinite crystal structure (Clark et al., 2007). Analysis of the spectrum reveals that discriminating between the two hydroxyl-bearing minerals in this mixture is not achievable within the NIR region since both minerals share the same feature position (2200 nm). This is a confirmation of the kaolinite-muscovite mixtures (Fig. 6.5). Calcite is completely invisible in the spectra, as the spectrum only shows depression between 2300 and 2400 nm.

Analysis also shows that the aluminium bearing minerals (muscovite and kaolinite) are the most NIR-active minerals in the mixture, based on the visibility of the 2200 nm feature displayed by the spectra. The dominant presence of the 2200 nm features shows that it will take higher concentrations of hematite in such mixtures to suppress or mask it. It can also be observed that the feature

near 1400 nm and water feature near 1900 nm may not be good features for selection in preconcentration of ores containing iron minerals. Hunt (1979) noted that these features are not good for remote sensing purposes as they are always easily influenced by atmospheric conditions (moisture).

For the purpose of determination of the moisture content in kaolinitic clays containing hematite minerals or other NIR-active minerals without absorption features, the presence of hematite is likely to mask the water feature(s) (1915 or 1840 nm and or 1415 nm) and gives an impression that the clay samples are completely moisture free (dry). As an indirect way of determining the moisture content in kaolinitic clay samples, the presence of hematite or any high spectra absorbing mineral in concentration could also indicate the likelihood of presence of moisture, as the absence of water or moisture features does not necessarily imply a dry sample.

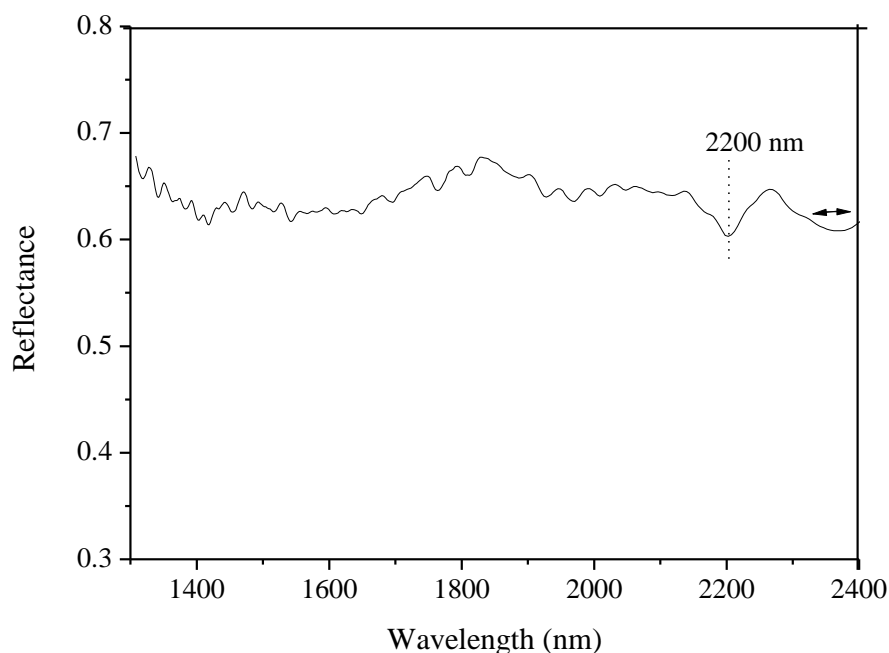


Figure 6.43 - NIR spectrum of kaolinite-calcite-muscovite-hematite intimate mixture at ratio of 1:1:1:1.

#### 6.2.4.17. Hematite-Biotite-Muscovite-Chlorite-Calcite Mixture

The NIR spectrum of the mixture of hematite-biotite-muscovite-chlorite-calcite shows depressions near 2200 nm and between 2300 and 2400 nm (Fig. 6.44). The NIR spectrum of intimate mixtures of muscovite-chlorite-biotite showed

features near 1415 nm and 2200 nm (Fig. 6.31), while mixtures of biotite-muscovite-calcite (Fig. 6.38) and muscovite-calcite (Fig. 6.12) revealed absorption features of both muscovite and calcite appearing side-by-side at equal ratios. In relation to the present mixture it can be seen that the inclusion of hematite is responsible for the broadening of features in the resultant spectra.

Given the nature of the spectrum, which almost compares with that of hematite, as a featureless NIR-active mineral, hematite is more active in the mixture as its presence in concentration is responsible for the suppressed and broad features.

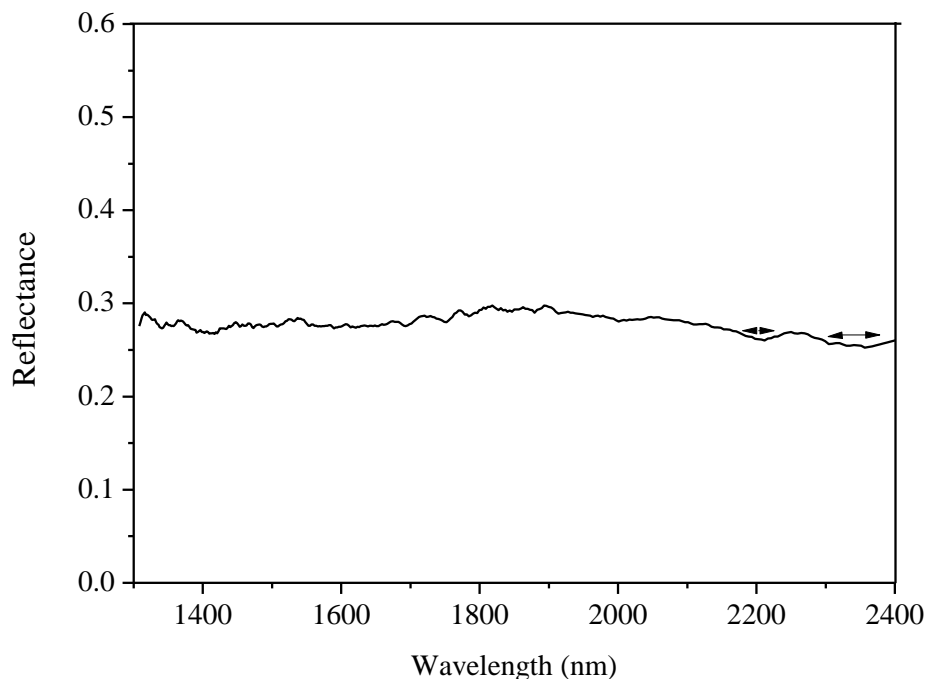


Figure 6.44 - Near infrared spectra of hematite-biotite-muscovite-chlorite-calcite intimate mixture at equal ratio of 1:1:1:1:1

#### **6.2.4.18. Malachite-Calcite-Hematite-Muscovite-Kaolinite-Chrysocolla Mixture**

The NIR spectrum of complex intimate mixtures of malachite-calcite-hematite-muscovite-kaolinite-chrysocolla is presented in Figure 6.45. The NIR spectrum reveals the complex nature of the mixture, as it appears featureless across the wavelength range. The wavelength regions where features of individual minerals are expected only show depressions lacking absorption centres. At this scale, preconcentration of any mineral from hematite which is the only non-



feature displaying NIR-active mineral will be difficult as the spectrum is featureless and could be easily interpreted as a hematite spectrum.

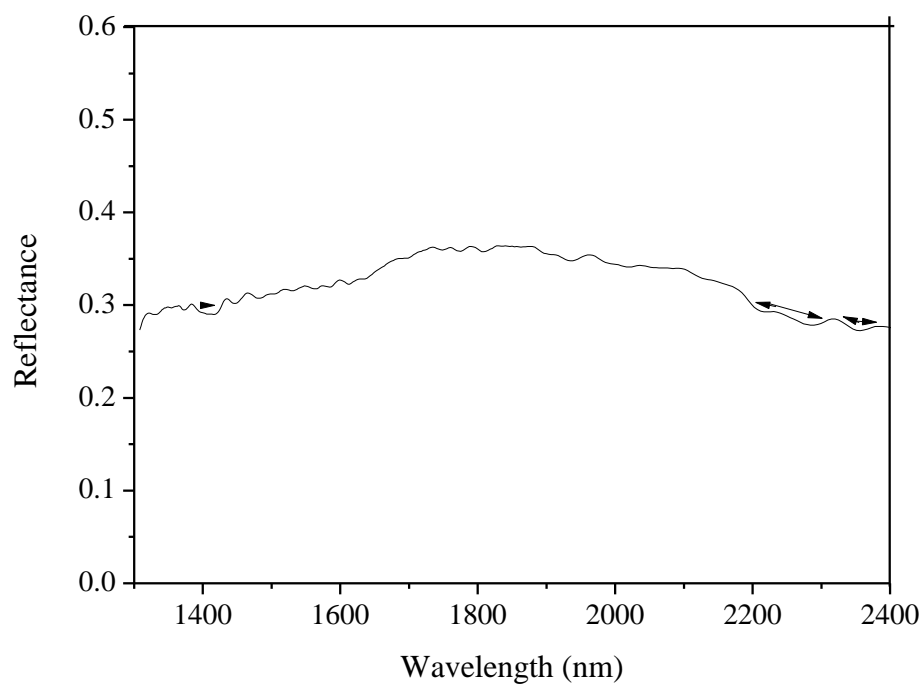


Figure 6.45 - Near infrared spectrum of calcite-malachite-hematite-kaolinite-muscovite-chrysocolla mixture at ratio of 1:1:1:1:1 concentration by mass.

### **6.3. Implications for ore sorting and copper preconcentration strategy development**

NIR spectral analyses of intimate mixtures (Tables 6.2 and 6.3) revealed that when a particle contains intimate mixtures of minerals, the visibility of absorption features of individual minerals in its NIR spectrum or spectra may depend on any or the combination of these mineralogical factors:

- 1) NIR-active mineralogical composition,
- 2) Relative proportion or concentration, or
- 3) Relative mineral accessibility or sensitivity to NIR radiation

Other factors may include instrumental parameters, such as the spatial and spectral resolution (also known as optical resolution) of the sensor, as well as the sensor sensitivity.

For some intimate mixtures, spectra dominance depends on the concentration and mineral accessibility to NIR radiation. An example of a concentration-dependent mixture (association) is chrysocolla and muscovite (Fig. 6.1 and Table 6.2). The mineral with the higher concentration will dominate the spectrum of the mixture. A mixture of muscovite and chlorite is a good example of mineral accessibility-dependent association. Here, muscovite dominates the spectra even at lower concentration relative to chlorite, implying that muscovite is more readily accessible to NIR radiation than chlorite.

In other instances, spectral dominance depends on the NIR-active mineral composition, with minerals behaving differently in different mixtures. For example, a weak mineral in one mixture may be strong when mixed with another mineral. An example is chlorite: when mixed with chrysocolla, both minerals show features side-by-side, with the spectra appearing mixed (Fig. 6.3). The visibility of features of either mineral is not concentration-dependent as both minerals are readily accessible with equal sensitivity. In chrysocolla-malachite mixtures (Fig. 6.17), chrysocolla shows more spectral dominance. This is not true for chlorite in malachite (Fig. 6.15). When mixed with malachite, chlorite features are captured meaning malachite is more readily accessible to NIR than chlorite. Also, though malachite is weak in chrysocolla, it is stronger in hematite than chrysocolla (Figures 6.21 and 6.22).

Except for the weakness of malachite in chrysocolla mixtures, and the complete spectral mixing of malachite and kaolinite, only malachite and hematite are fairly consistent across a range of mixtures. The consistency of both minerals may be due to their colour (Clark et al., 1999). Malachite may also have additional influence due to its -OH and  $\text{CO}_3^{2-}$  combination chemical structure, making it strong enough to display its absorption feature (2275 nm) even at higher hematite concentrations when both are mixed together.

Twelve individual spatial mineral associations were observed based on mineralogy from QEMSCAN<sup>®</sup> (Table 4.4). Observed associations include: chrysocolla-hematite, chrysocolla-hematite-biotite, biotite-hematite, biotite-chlorite, biotite-chlorite-calcite, biotite-calcite, biotite-hematite-chlorite, chlorite-calcite, muscovite-calcite, muscovite-biotite, biotite-muscovite-calcite and biotite-muscovite-chlorite.

The main objectives of this research are to understand whether individual minerals can be identified when they occur together and are scanned within the same spectral range, and if their preconcentration is feasible. From the analysis of spectra of various mixtures, the following observations were made: hematite drowns out chlorite, biotite and calcite features for all realistic proportions of these minerals. Hence, where absorption feature(s) of any of these minerals is visible, the spectra indicate an almost complete absence of hematite. Chrysocolla is only visible in hematite at 90 % concentration relative to hematite. At equal concentration, malachite and muscovite dominate hematite by showing their best diagnostic absorption feature near 2275 nm (malachite) and 2200 nm (muscovite).

Both chrysocolla and malachite which are the copper-bearing NIR-active minerals can be targeted together by selecting the best diagnostic absorption feature of chrysocolla near 2270 nm. This is true since the feature is common at any given ratio of their mixture. Chrysocolla is more NIR-active than calcite, while muscovite spectral dominance over chrysocolla and vice versa is concentration dependent. Kaolinite is more readily accessible to NIR radiation than chrysocolla across all mixing ranges, with spectra appearing mixed at higher chrysocolla concentration. Chrysocolla, chlorite, hematite, and or biotite are better preconcentrated together. While chrysocolla and chlorite show

absorption features side-by-side in a spectrum, chrysocolla in concentration with biotite display featureless spectra across a mixing range. This is similar to the spectra of chlorite and biotite mixtures.

Malachite dominates both chlorite and calcite features at any given ratio. Malachite is relatively more NIR-active than hematite, as it shows one of its features at relatively higher hematite concentration (from ratio 4:6, malachite-hematite), while malachite features appear mixed with kaolinite. For malachite and biotite, at higher biotite concentration (90 %), spectra appear featureless. Malachite dominates muscovite at higher concentration relative to muscovite, while spectra appear mixed at higher muscovite concentration.

Spectral analysis of calcite mixed with malachite, chrysocolla, chlorite, or hematite suggest that identification of calcite in such mixtures is only feasible for freely occurring calcite. Calcite dominates biotite across all mixing ranges. At higher calcite concentration, calcite shows features side-by-side those of kaolinite and muscovite but calcite is completely masked in the spectra from equal ratios. Hence, all three minerals can be preconcentrated together by either selecting the 2200 nm feature to discriminate high -OH -low calcite, or 2340 nm to discriminate high calcite -low -OH.

Though kaolinite is differentiated from muscovite by its double absorption features compared to a muscovite single feature (Hunt, 1979; Hunt and Hall, 1981), complete discrimination between both minerals cannot be achieved. This is because both minerals share the same wavelength position (2200 nm) as their best diagnostic absorption feature position (Iyakwari et al., 2013). The visibility of the double kaolinite features in mixtures with muscovite is concentration dependent. Both muscovite and kaolinite dominate chlorite and biotite.

Chlorite, apart from showing features side-by-side with chrysocolla and dominating calcite, is weak in mixtures with other NIR-active minerals. NIR spectra of mixtures of chlorite and biotite are featureless and hence display a combined sensitivity. Where mineralogy is unknown, spectra can be misinterpreted to represent a strongly absorbing NIR-active mineral without features. This is also true for chrysocolla-biotite mixtures. Therefore, except in biotite mixtures with chrysocolla and chlorite, biotite does not show its

absorption features or any spectral influence in any mixture. Hence, of all minerals and mixtures investigated, spectral analysis indicates that biotite is the weakest of all the NIR-active minerals. According to Clark (1995), the iron content in biotite is responsible for masking the -OH absorption feature at shorter wavelengths near 1400 nm. Therefore, the weakness or absence of biotite features in spectra of biotite mixed with other iron bearing minerals is ascribed to an increasing iron concentration.

With few exceptions, in complex mixtures involving three or more minerals (e.g. calcite-muscovite-hematite mixtures, Table 6.3), calcite features are also invisible where hematite, malachite or chrysocolla are present in concentration. Mixtures of strongly absorbing hematite and strongly reflecting muscovite or kaolinite indicate that at equal proportions or ratio the highly reflective hydroxyl minerals show their best diagnostic absorption feature near 2200 nm. Spectral analysis also confirms strong hematite absorption at longer NIR wavelengths (1300 to 2500 nm), reducing the overall level of reflectance and possibly masking or drowning features of other NIR-active feature displaying minerals (Bishop and Dummel, 1996; Iyakwari and Glass, 2014).

Table 6.2 - Summary of spectral dominance in intimate mixture of minerals

Mineral 1	Mineral 2	Mass ratios of minerals								
		1:9	2:8	3:7	4:6	5:5	6:4	7:3	8:2	9:1
Mixed		1:9	2:8	3:7	4:6	5:5	6:4	7:3	8:2	9:1
<b>Minerals with similar functional groups</b>										
Chrysocolla	Muscovite	Muscovite			Mixed spectra			Chrysocolla		
Chrysocolla	Kaolinite	Kaolinite				Mixed spectra				
Chrysocolla	Chlorite	Mixed spectra								
Chlorite	Muscovite	Muscovite								
Kaolinite	Muscovite	Muscovite						Kaolinite		
Chrysocolla	Biotite	Featureless spectra								
Kaolinite	Chlorite	Kaolinite								
Chlorite	Biotite	Featureless spectra								
Biotite	Muscovite	Muscovite								Featureless spectra
Malachite	Calcite	Malachite								
<b>Minerals with dissimilar functional groups</b>										
Chrysocolla	Calcite	Broad spectra				Chrysocolla				
Muscovite	Calcite	Mixed spectra				Displaced muscovite (2350 nm) features		Muscovite		
Kaolinite	Calcite	Mixed spectra				Kaolinite				
Chlorite	Calcite	Broad spectra			Chlorite					
Malachite	Chlorite	Malachite								
Malachite	Kaolinite	Mixed spectra								
Chrysocolla	Malachite	Mixed spectra				Chrysocolla				
Biotite	Calcite	Calcite								
Malachite	Biotite	Broad spectra	Malachite							
Malachite	Muscovite	Mixed spectra					Malachite			
<b>Influence of hematite on NIR-active features displaying minerals</b>										
Chrysocolla	Hematite	Hematite (Featureless spectra)								Chrysocolla
Malachite	Hematite	Hematite (Featureless spectra)			Malachite					
Calcite	Hematite	Hematite (Featureless spectra)								
Muscovite	Hematite	Hematite (Featureless spectra)			Muscovite					
Kaolinite	Hematite	Hematite (Featureless spectra)						Kaolinite		
Chlorite	Hematite	Hematite (Featureless spectra)								
Biotite	Hematite	Hematite (Featureless spectra)								



Table 6.3 - Spectral dominance in intimate mixture of complex mineral associations

Complex mixture or associations											
Mineral 1	Mineral 2	Mineral 3	Mineral 4	Mineral 5	Mineral 6	Mass ratios of minerals					
						1	1	1	1	1	1
Hematite	Chrysocolla	Muscovite	-	-	-	Hematite (Featureless spectra)					
Hematite	Chrysocolla	Kaolinite	-	-	-	Kaolinite					
Hematite	Malachite	Calcite	-	-	-	Malachite					
Muscovite	Biotite	Chlorite	-	-	-	Muscovite					
Hematite	Malachite	Kaolinite	-	-	-	Malachite/kaolinite					
Malachite	Muscovite	Hematite	-	-	-	Malachite/Muscovite					
Chlorite	Biotite	Calcite	-	-	-	Chlorite					
Calcite	Hematite	Muscovite	-	-	-	Muscovite/Calcite					
Chrysocolla	Biotite	Hematite	-	-	-	Hematite (Featureless spectra)					
Biotite	Hematite	Chlorite	-	-	-	Hematite (Featureless spectra)					
Biotite	Muscovite	Calcite	-	-	-	Muscovite/Calcite					
Kaolinite	Calcite	Hematite	-	-	-	Kaolinite					
Muscovite	Hematite	Kaolinite	-	-	-	Muscovite/Kaolinite					
Chlorite	Biotite	Calcite	Hematite	-	-	Chlorite/Calcite					
Chlorite	Biotite	Calcite	Muscovite	-	-	Muscovite/Calcite					
Kaolinite	Calcite	Hematite	Muscovite	-	-	Muscovite/Kaolinite					
Hematite	Biotite	Muscovite	Chlorite	Calcite	-	Hematite (Featureless spectra)					
Malachite	Calcite	Hematite	Muscovite	Kaolinite	Chrysocolla	Hematite (Featureless spectra)					



For copper-bearing minerals (malachite and chrysocolla) preconcentration, given the fact that spectra appear mixed and in some instance featureless, only freely occurring calcite, muscovite and or kaolinite spectrum can be targeted for removal/reduction as waste. Therefore, four options based on associations of the copper-bearing minerals with or without high iron bearing minerals (non-feature displaying NIR-active minerals) using NIR are developed in Figure 6.46.

The first option considers silicate copper bearing minerals (chrysocolla) occurring without high iron-rich minerals (hematite). Because chrysocolla shows features side-by-side to those of kaolinite and muscovite, when they occur in isolation of hematite, spectrum displaying features diagnostic of chrysocolla (2270 nm) with or without kaolinite (2160 and 2200 nm) or muscovite (2200 nm) features is considered product, in addition to this are featureless spectra. Hence, spectrum showing the calcite feature (2340 nm) is classified as waste, since calcite displaying spectrum in chrysocolla particles indicates high grade calcite (approximately 100 %). Where a spectrum appears showing features of calcite in addition to kaolinite or muscovite, given that chrysocolla has more feature drowning ability on calcite even at higher calcite concentration, the spectrum shall be classified as waste.

The second option considers copper carbonate-bearing minerals (malachite) when occurring without iron-rich minerals. Since malachite show features side-by-side those of kaolinite and muscovite, NIR spectrum showing features near 2275 nm with or without 1415, 2200 and 2360 nm will be classified as product. While spectrum showing exclusively features near 2340 nm diagnostic of calcite are targeted as waste. This is so since calcite (2340 nm) is completely masked or displaced by malachite. Therefore, similar to chrysocolla only freely occurring  $\text{CO}_3^{2-}$  features near 2340 nm shall be considered waste, as any spectrum showing calcite features indicate absence of malachite. In addition to calcite features as waste, are featureless spectra as this may be indicative of biotite and chlorite as malachite dominates both minerals. This addition will only be true in the absence of hematite or other highly NIR absorbing minerals in the mineralogy, as they may also be responsible for the lack of features.

The third option considers both copper-bearing minerals (chrysocolla and or malachite) occurring in association with high iron-bearing minerals (hematite).

Because high iron-rich minerals with either chrysocolla or malachite may result in a featureless spectrum, featureless spectra may indicate product for relatively high concentrations of hematite. This also applies to biotite occurring with chrysocolla and or chlorite. Therefore, in addition to featureless spectra, spectra showing features diagnostic of either or both chrysocolla or malachite near 2270 nm and 2275 nm respectively, with or without 1415, 1915 or 2360 nm shall also be considered product. Hence, only spectra showing features near 2200 nm (muscovite and kaolinite) or 2160 nm (kaolinite only) and 2340 nm (calcite) shall be classified as waste. This option is targeted at removing or reducing both calcite and clay waste. Note that the choice of only the 2340 nm feature may also target low grade clays (kaolinite and muscovite), selecting both features (2200 and 2340 nm) will target both low and high grade calcite and clay minerals. This option should only be chosen if high purity is more important than high recovery: the low grade valuable minerals (malachite and or chrysocolla) are likely to be locked in muscovite or kaolinite.

Finally, when spectra appear to be similar, being featureless or showing diagnostic features of all NIR-active minerals, the ore will not be sortable using a NIR sensor.

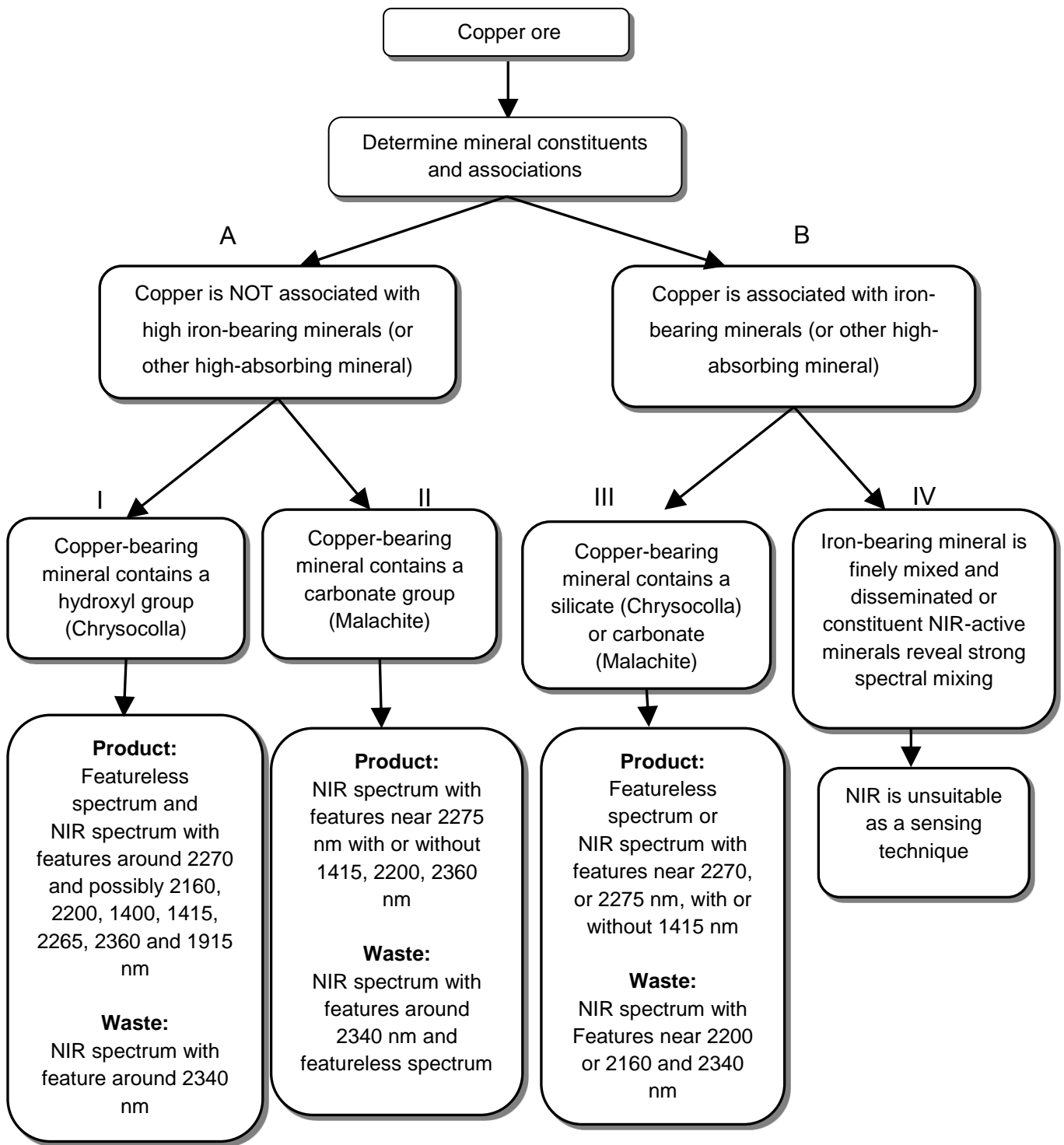


Figure 6.46 - Framework for NIR sorting for copper ore, based on characteristics of individual spectrum (modified from Iyakwari et al., 2013; Iyakwari and Glass, 2015).

## **Chapter 7: Arrangement of minerals**

### **7.1. Introduction**

In a particle of an ore composed of two or more minerals, minerals may occur in various forms of arrangement in relation to each other and may be optically separated in the field of view (have clear boundaries). This chapter is a follow up to the previous chapter where two or more minerals were intimately mixed together at ratios to determine both qualitatively and quantitatively the dominance of minerals in a spectrum. In this chapter, the materials analysed are optically separated, and arranged to stimulate adjacent natural mineral associations. Hence, this chapter uses single minerals with the aim of determining spectral dominance and qualitatively defining a spectrum.

Two forms of optically separated mineral arrangement or associations are investigated: vertical and horizontal arrangement.

### **7.2. Linear mixtures**

The purpose of this investigation is to predict the influence of NIR-active minerals arrangement in an ore, where minerals occur either with vertical or horizontal linear association with one another. To achieve this, linear mixtures were prepared. The prepared mixtures were positioned for scanning in such a way that individual minerals in the field of view were optically separated. Analysis involved the use of both solid and powdered samples. Solid mineral samples were cut into size and shaped to fit in close contact with one another. All minerals had an average thickness of 0.7 cm. The powdered samples were carefully poured into a 3.3 cm container demarcated into 1.1 cm each, in such a way that they made contact with each other at their boundaries. NIR scanning was performed along vertical alignment for powdered samples. Solid samples were scanned along both vertical and horizontal directions. Therefore, discussion of results below is divided into two sections, based on scanning direction (i.e. vertical and horizontal).

#### **7.2.1. Vertical alignment**

To investigate the influence of vertical minerals alignment in an ore where minerals occur in contact side-by-side with vertical adjacent association, both powdered and solid samples were prepared and scanned. Powdered samples consisted of three minerals (calcite-hematite-muscovite), arranged side-by-side

(Fig. 7.1). The NIR spectra generated are presented in Figure 7.3. Solid samples consisted of two minerals per analysis. Samples were also arranged side-by-side (Fig. 7.2). Solid mineral mixtures analysed include: hematite-chrysocolla (Fig. 7.4), malachite-hematite (Fig. 7.5) and calcite-malachite (Fig. 7.6).

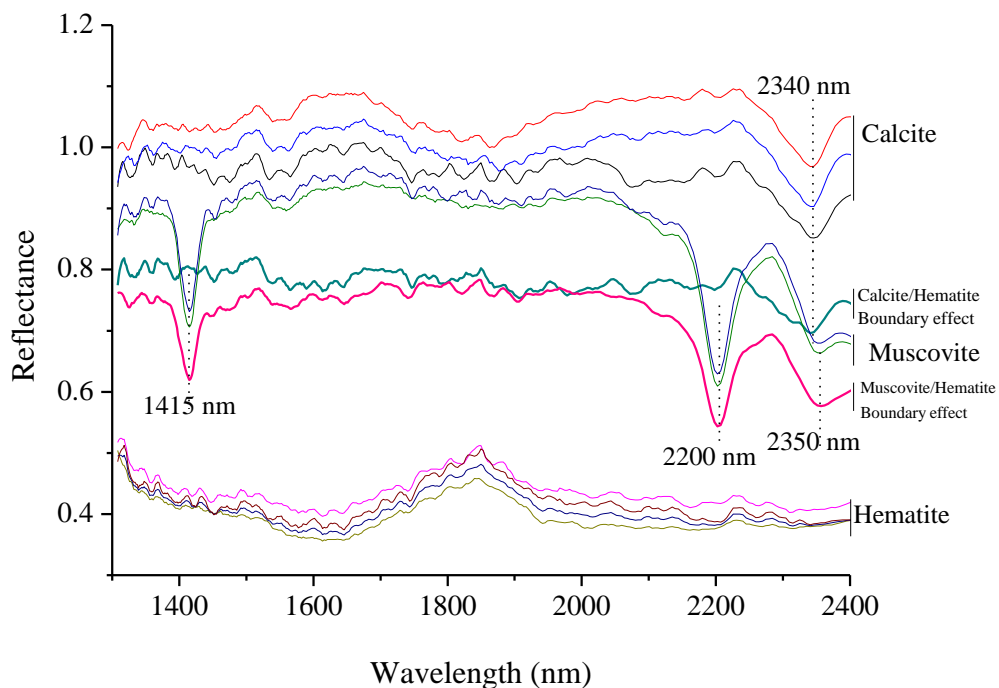
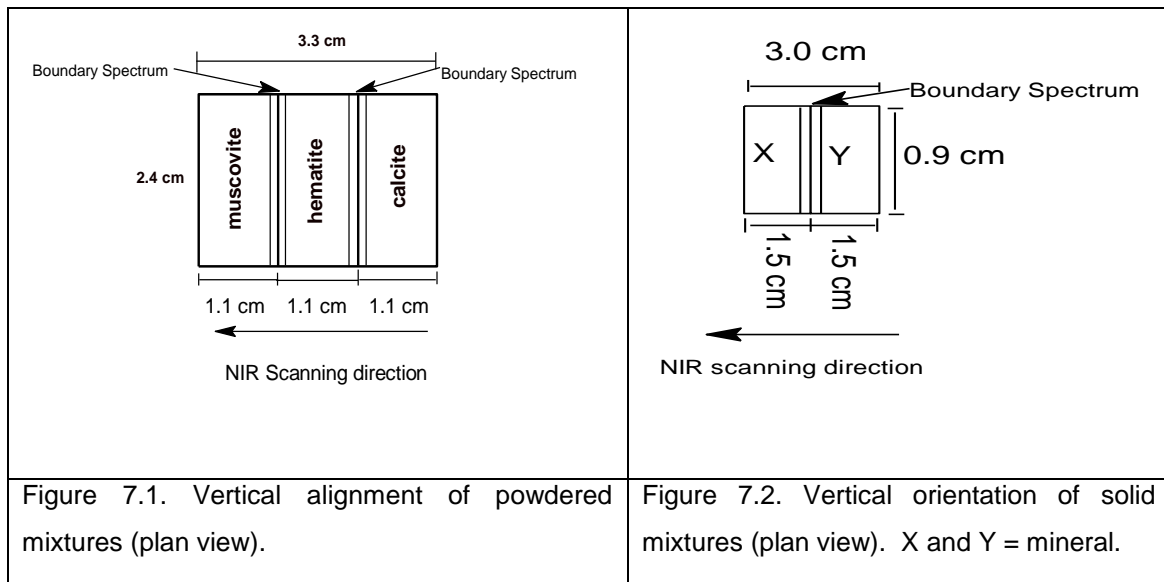


Figure 7.3 - NIR spectra of linear mixtures of powdered calcite, muscovite and hematite.

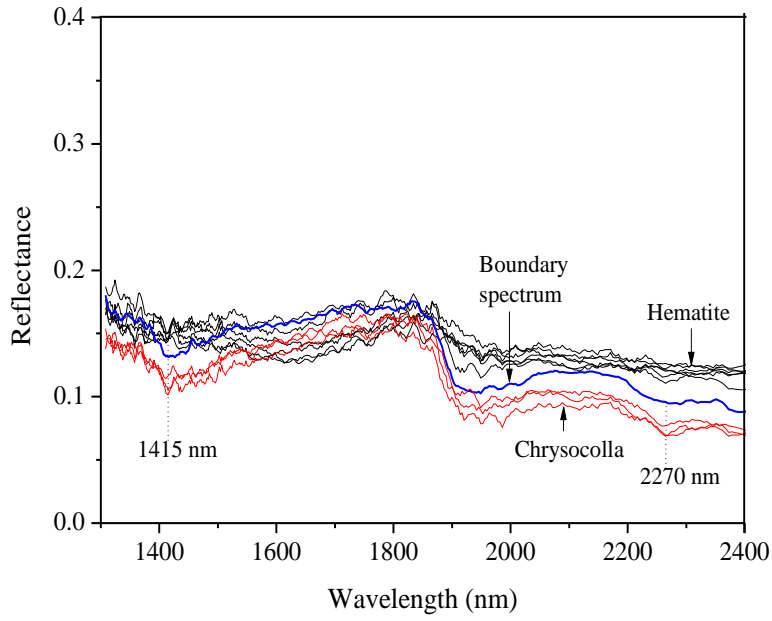


Figure 7.4. NIR spectra of linear mixtures of hematite-chrysocolla

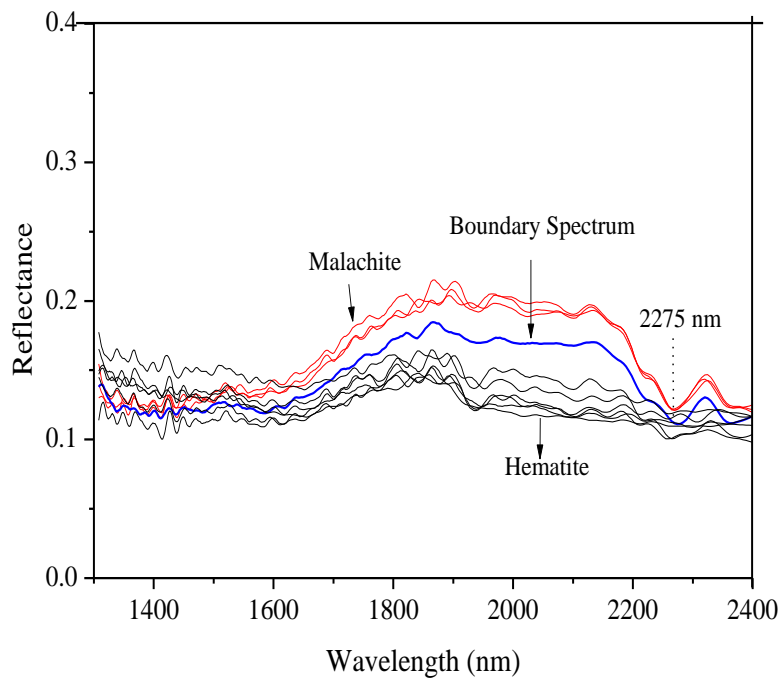


Figure 7.5. NIR spectra of linear mixtures of Malachite-hematite

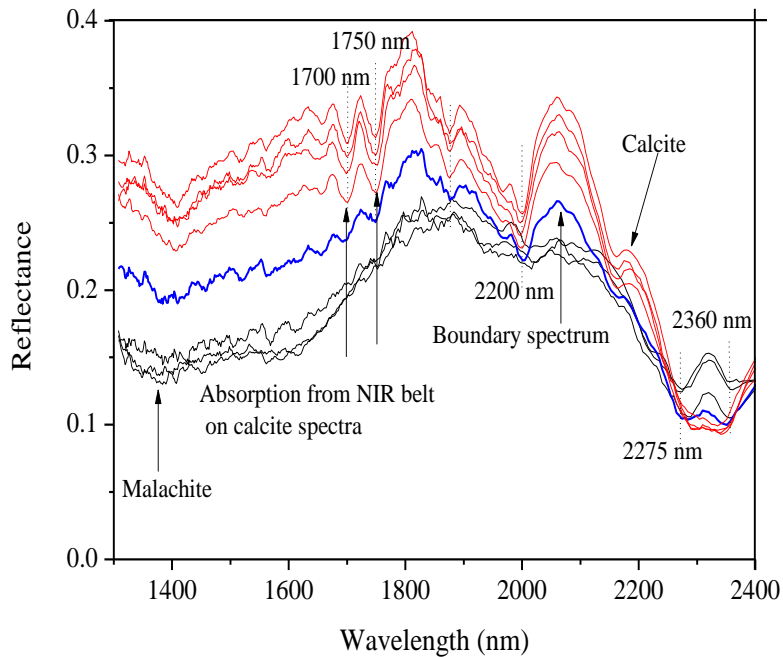


Figure. 7.6. NIR spectra of linear mixtures of calcite-malachite

It is important to note that each spectrum has a dimension (foot print/analysis area) of 2.9 by 9 mm, and given the dimensions of Figures 7.1 and 7.2, each mixture produced between 11 and 9 spectra.

For the powdered mixtures (Fig. 7.3), analysis revealed that hematite and calcite produced four spectra, while three spectra were produced by muscovite. Two spectra, one each of calcite and muscovite are affected as a result of contact with hematite. The two affected spectra have a reduced reflectance or overall brightness relative to other spectra of the same original composition. This phenomenon is here referred to as a “boundary effect”. The affected spectra display absorption features corresponding to the dominant minerals constituent functional group, while the unaffected spectra display diagnostic features corresponding to the constituent functional group(s) of each mineral, all appearing with maintained wavelength position.

The spectrum of the solid mixtures that appear along contact zones also show the mineral boundary effect (Fig. 7.4, 7.5 and 7.6). This means that their proximity (contact) to one another influences the resultant boundary spectrum, producing spectrum with reflectance levels which do not correspond to either of

the contributing minerals. This is similar to EDS analysis on SEM and QEMSCAN<sup>®</sup> (G. Rollinson, personal communication, 2015). Therefore, the boundary spectrum can be said to have the composition of both minerals, but the absorption features retained depicts the dominant mineral. In the case of Figure 7.3, muscovite and calcite are the dominant minerals in those spectra, since their absorption features are visible. Given the lack of absorption features by hematite as a NIR-active mineral, the boundary spectrum though stretched by hematite, still show features of the other minerals (Fig. 7.3 and 7.5).

Figure 7.4 shows boundary spectrum lacking absorption features. Though overall reflectance differs from that displayed by both chrysocolla and hematite, the spectrum shows that hematite is dominant, since chrysocolla features are not visible. In the mixture involving calcite and malachite (Fig. 7.6), the boundary spectrum shows features of both minerals. The features of malachite though weak can be observed at longer wavelengths (2275 and 2360 nm), while calcite's 2340 nm features appear broad lacking a well-defined centre. Calcite showed additional features near 2000 nm. This therefore means that the lack of features corresponding to hematite in Figures 7.3 and 7.5 is due to its non-absorption feature displaying characteristics and the high NIR activity of muscovite/calcite and malachite. Hence when two minerals that have absorption features in the NIR region, occur along the same spectrum with vertical association, the spectrum will or is likely to display absorption features corresponding to both minerals. This means that the boundary spectrum is likely to be mixed depending on individual mineral NIR activity.

Figure 7.6 also shows calcite spectra displaying features corresponding to the NIR line scanner belt. The penetration of NIR radiation beyond 0.7 cm of calcite indicated by the presence of NIR belt absorption features (1700 and 1750 nm) reveals that the depth of NIR penetration of a sample is mineral density or opacity dependent. This confirms findings in Iyakwari et al., (2013).

Hence, when processing ores with spectra displaying boundary effect characteristics further crushing will be required to liberate the individual minerals, if both minerals show absorption features. This is needed so that individual mineral can produce their absorption features independent of the other. The degree of liberation will depend on the mineral particle size of the ore

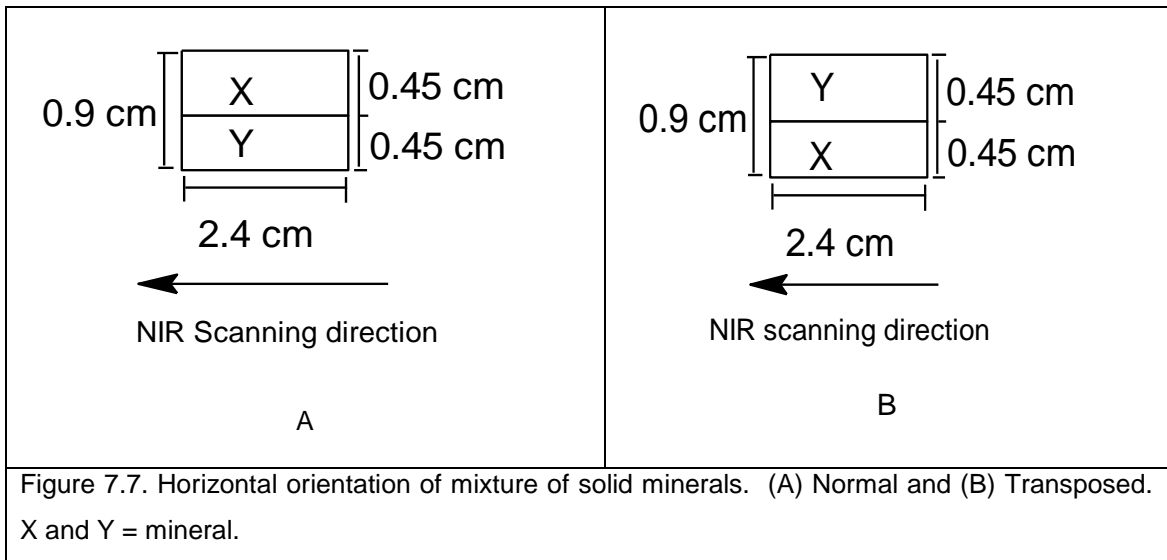


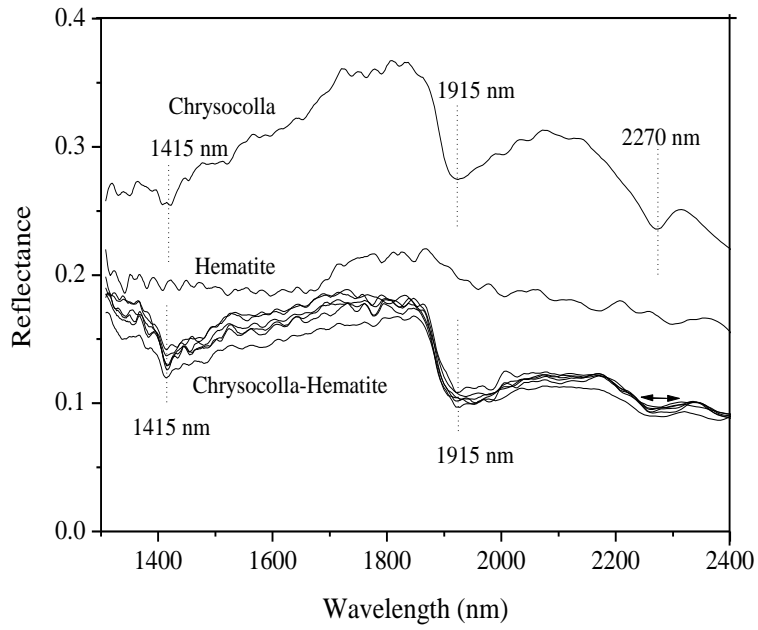
and NIR spectrum dimension. This may apply to an ore consisting of large mineral grains i.e. phenocryst. Though crushing may achieve liberation, total liberation involving the boundary spectrum will depend on the friability of one mineral relative to the other. Therefore, for classification purposes, if the boundary spectrum reveals features of one mineral relative to the other, classification can be achieved. This assertion is true for mixtures with hematite (Fig. 7.3, 7.4, and 7.5), since the absorption features of the other minerals in the boundary spectrum are not visible. The boundary spectrum can be assigned to the minerals showing features or dominance in concentration (i.e. calcite and muscovite (Fig. 7.3), hematite (Fig. 7.4), and malachite (Fig. 7.5) respectively). For mixtures of calcite and malachite (Fig. 7.6), the boundary spectrum can only be used to identify the minerals in concentration, since both minerals show their features side-by-side (spectrally mixed). Therefore, classification or discrimination cannot be achieved, unless the sample is further crushed to liberate the individual minerals. Where the degree of spectra mixing is high, across all spectra of a particle, liberation may not achieve better resolution, hence NIR may not be applicable for preconcentrating such ores as valuable materials are likely to be lost as waste. This confirms option four of Figure 6.46.

For spectra showing the NIR belt absorption features, when making decisions for mineral identification and or ore preconcentration, feature positions relating to the NIR belt should be avoided.

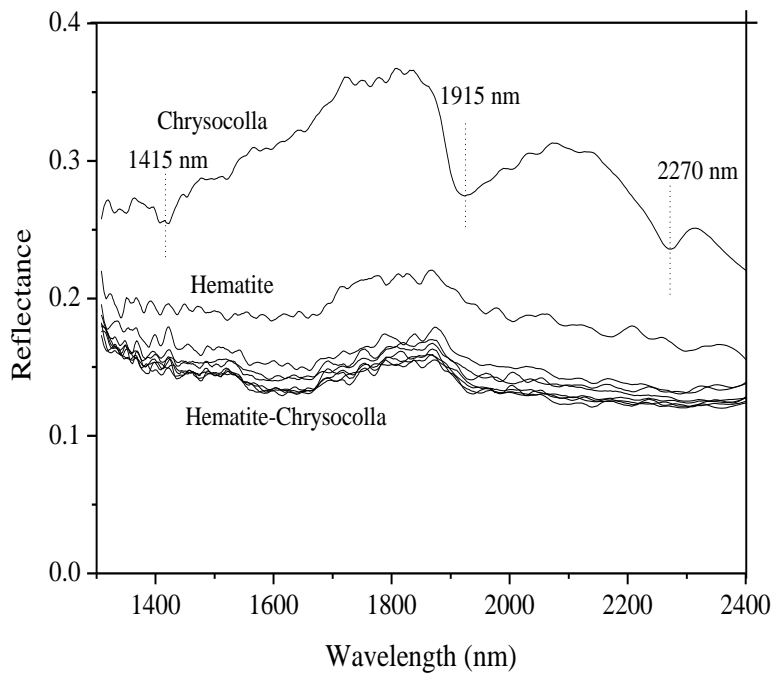
### **7.2.2. Horizontal alignment**

To investigate the influence of horizontal minerals alignment when scanned by the NIR line scanner, where minerals appear in contact side-by-side with horizontal adjacent alignment, solid samples were prepared (Fig. 7.7a and 7.7b) and scanned. Given a spectrum height of 0.9 cm, each mineral was cut to fit into half the spectrum height (i.e. 0.45 cm). Analysis consists of two minerals per scan. Individual minerals were arranged side-by-side and then scanned with their position switched (transposed). Mixtures analysed include: hematite and chrysocolla (Fig. 7.8a and 7.8b), malachite and hematite (Fig. 7.9a and 7.9b) and calcite and chrysocolla (Fig. 7.10a and 7.10b).



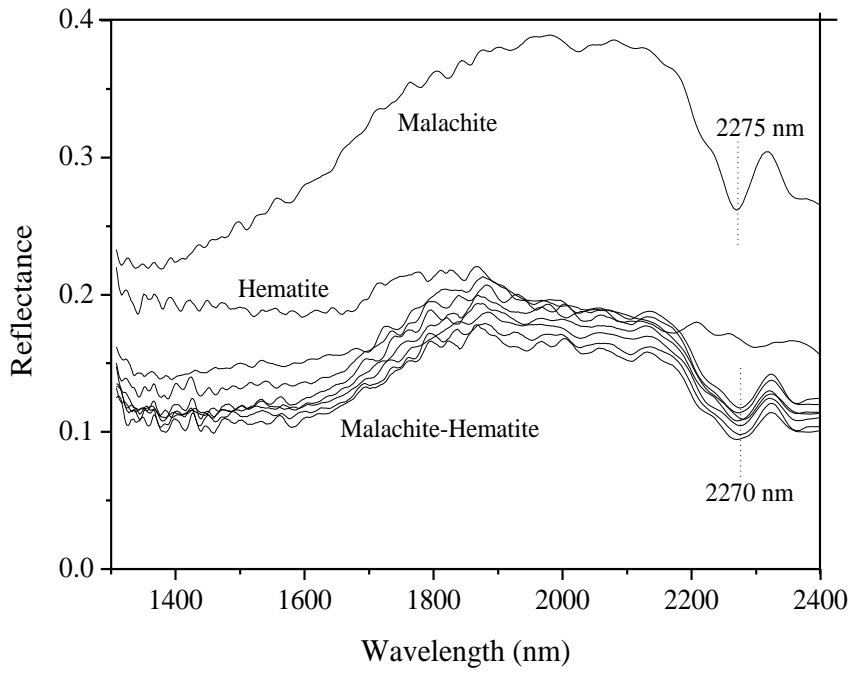


A

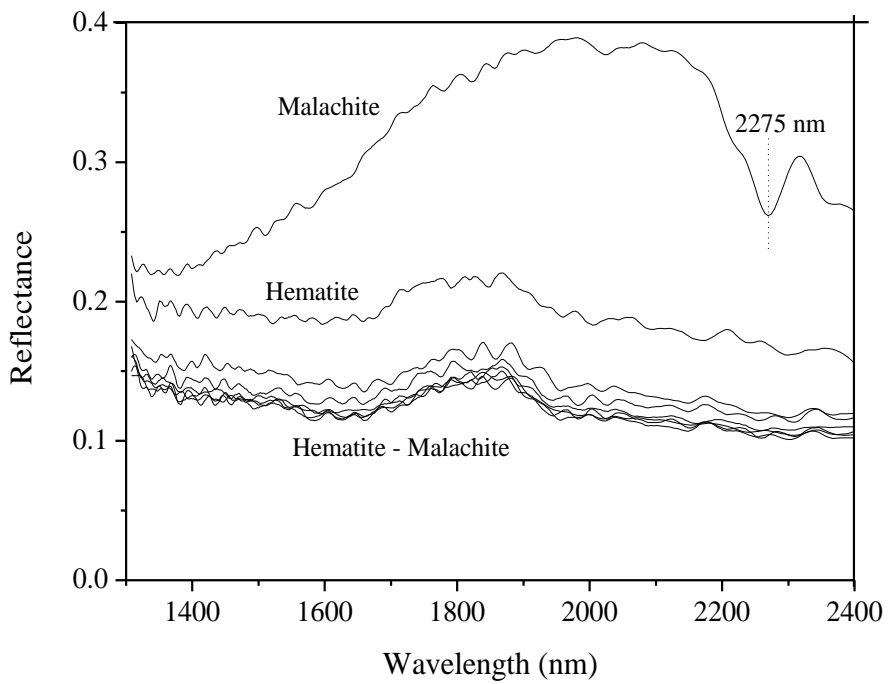


B

Figure 7.8 - NIR spectra of chrysocolla and hematite horizontal mixture (A) chrysocolla-hematite and (B) hematite-chrysocolla: Where top spectra are reference spectra.

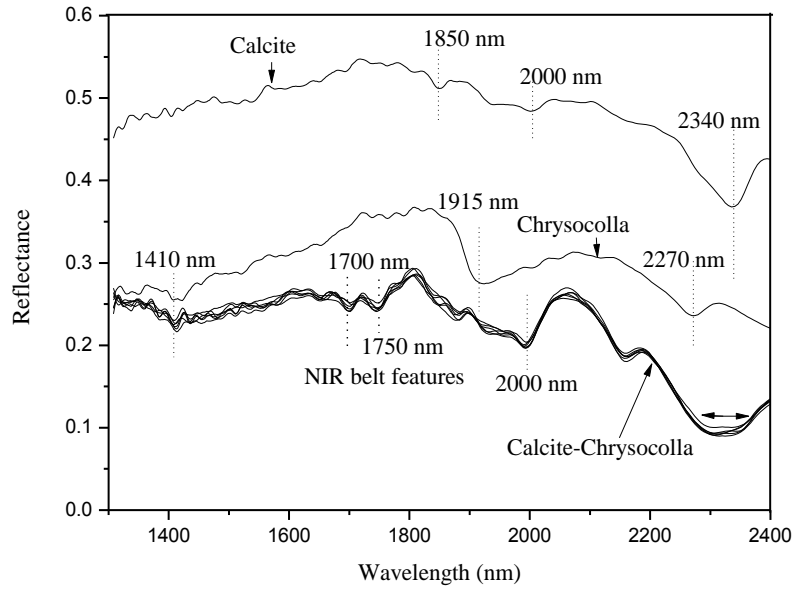


A

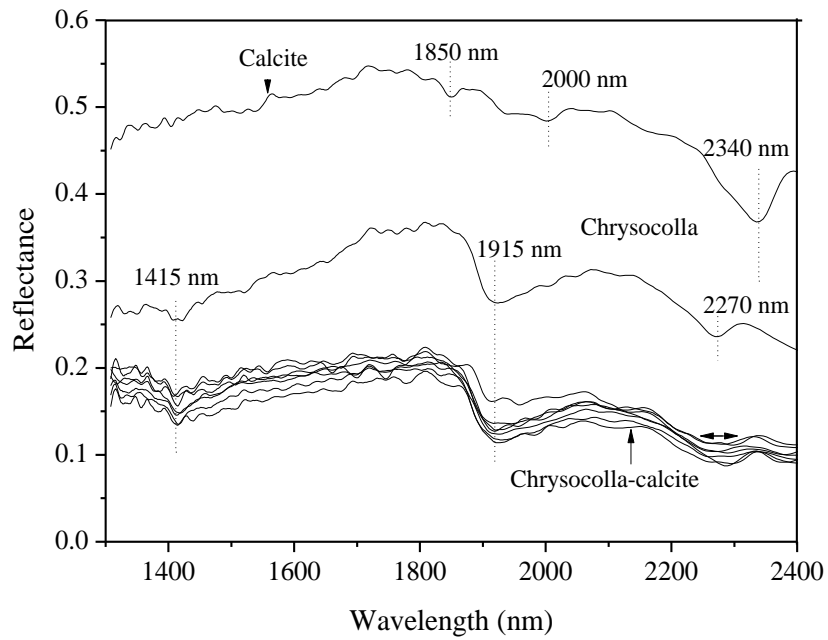


B

Figure 7.9 - NIR spectra of malachite and hematite horizontal mixtures (A) malachite-hematite and (B) hematite-malachite: Where top spectra are reference spectra



A



B

Figure 7.10 - NIR spectra of chrysocolla and calcite horizontal mixture (A) calcite- chrysocolla and (B) chrysocolla-calcite: Where top spectra are reference spectra.

Analysis of scanned results (Fig. 7.8 to 7.10) reveals that for each mixture, spectra dominance is dependent on the constituent minerals. Spectral analysis of the mixture involving chrysocolla (Fig. 7.8 and 7.10) shows that the chrysocolla feature near 2270 nm becomes broad and lacks a defined absorption centre. The broadening of the 2270 nm feature is not mineral position dependant. Other chrysocolla features dominate the spectra when chrysocolla is positioned above the other mineral (Fig. 7.8a and 7.10b). For mixtures involving hematite (Fig. 7.8 and 7.9), hematite dominates the spectra when placed above the other mineral, i.e. when first encountered by NIR. The same can be said of malachite, which dominates the spectra when positioned above hematite. For mixtures of calcite and chrysocolla where calcite is positioned above chrysocolla, spectra appear mixed and also revealing features relating to the NIR belt (Fig. 7.10).

Therefore, with the exception of calcite-chrysocolla mixtures, minerals positioned above the other will dominate the spectra, with little or no trace of the second mineral's absorption features in the resultant spectra. This means that though both minerals appear along the same spectrum width, the first (top) mineral is more in contact and accessible to the NIR radiation, thereby dominating the spectra, while the mineral underneath it is more or less invisible. Hence, dominance in such situations is position or exposure based. With respect to the above analysis, the samples although optically separated do not experience boundary effect as was observed in the vertical linear arrangement. Also, the behaviour observed here is a departure from the intimate mixtures where spectra dominance is a function of the presence of the most active NIR-active mineral across spectrum or spectra. Rather, the effect experienced in horizontal alignment is that of mineral positioning. Also it is important to note that horizontal mixing is more of a spectrum height influence as it does not necessarily take into account spectrum width.

This issue (mineral position dominance) may only be reduced by regulating the speed of a conveyor belt, so the camera can capture the particle as much as possible. The minerals beneath shall be unaccounted for if a fast conveyor belt is used.

### **7.3. Conclusions**

NIR-active minerals were mixed in such a way that they appeared optically separated. Depending on the NIR-active minerals in concentration and type of arrangement, spectra dominance in linear mixtures may depend on: a) mineral NIR sensitivity and or b) mineral position (arrangement) or exposure.

A mixture of chrysocolla or malachite and hematite indicates that both minerals cannot be economically preconcentrated from hematite using NIR. Chrysocolla features are visible when calcite is above it, with spectra appearing mixed, while calcite is completely invisible where chrysocolla occurs above calcite. Hence, mixtures confirm the weakness of calcite when in occurrence with other NIR-active minerals along similar spectrum.

Also confirmed is the depth of NIR penetration being mineral opacity dependent. This is observed by NIR radiation penetration of calcite particle.

## **Chapter 8: Near infrared application on the Mantoverde copper ore**

### **8.1. Introduction**

This chapter discusses the practical application of NIR on the Mantoverde copper ore. Mantoverde samples were classified based on their individual NIR spectrum absorption characteristics, and the possible NIR-active mineral(s) responsible for absorption features, based on correlation with mineral data and fieldscan images (Tables 4.1 and 4.4). With respect to Figure 6.46, two strategies are modified and applied for ore preconcentration. The first strategy considers discriminating both muscovite and calcite as waste, while the second strategy targets calcite only for elimination as waste. This is achieved by classifying each particle based on the dominant spectrum group: as product, waste or middling.

The chapter is concluded by analysing and comparing both strategies based on calculated ore parameters using data obtained from XRF (both surface (PX) and bulk (BPX)) and QEMSCAN<sup>®</sup> (both Cu values and mineralogy) for all splits (A1, B1 and B2).

### **8.2. Individual sample NIR spectra mapping**

The NIR line scanner at Camborne School of Mines (CSM) measures each spectrum at a dimension of 0.29 by 0.9 cm. For splits B1, each sample (60 samples in total) was an average size of between 2 and 2.7 cm. In order to properly map each sample, individual mounts were divided into three sectors measuring 0.9 cm each corresponding to NIR spectrum height, with width measuring 0.29 cm (Fig. 8.1). Therefore, the number of spectra produced by individual samples per sector ranged from 4 to 9 depending on particle size and shape (Table 8.1 and Appendix 8.1a).



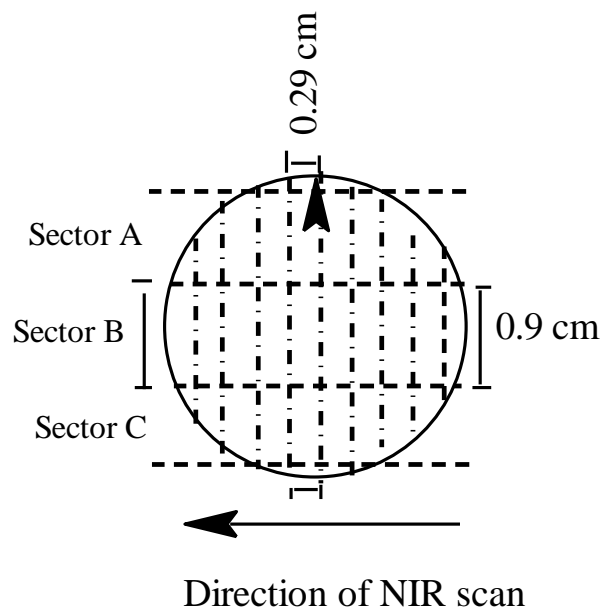


Figure 8.1 - Split B1 samples marked for directional scanning and spectra/mineral mapping

The size of splits B2 samples was variable, ranging from 2 to 10 cm. During NIR measurement, the longest axis was aligned perpendicular to the direction of NIR conveyor belt motion. A single line-scan was made for each particle, ensuring that each particle was characterised by 7 to 30 spectra, depending on sample size (Table 8.2 and Appendix 8.1b).

Splits A1 which are powdered samples were placed on a sample container (petri dish) and measured (Table 8.3 and Appendix 8.1c).

Tables 8.1, 8.2 and 8.3 present individual spectrum maps per particle based on spectrum characteristic absorption feature(s) and the mineral responsible for the absorption in the spectrum.

Table 8.1 - Individual particle spectrum and NIR-active mineral map for splits B1, where (+) = spectrum without feature, (-) = spectrum with feature, Mus. = Muscovite, Cl. = Chlorite, Cr. = Chrysocolla, Cal. = Calcite, Bi. = Biotite and Shared = OH feature common to two or more minerals.

Sample ID	Sector A									Sector B									Sector C									Feature position (nm)					
	1	2	3	4	5	6	7	8	9	1	2	3	4	5	6	7	8	9	1	2	3	4	5	6	7	8	9	Shared	Mus.	Cl./Cr/Bi.	Cal	Mus.	Cl.
1	+	+	+	+	+	+	+	+	+	+	+	+	+	+	+	+	+	+	+	+	+	+	+	+	+	+							
2	+	+	+	+	+	+	+	+	+	+	+	+	+	+	+	+	+	+	+	+	+	+	+	+	+	+							
3	+	+	+	+	+	+	+	+	+	+	+	+	+	+	+	+	+	+	+	-	-	-	-	-	-	-			2270				
4	+	+	+	+	+	+	+	+	+	+	+	+	+	+	+	+	+	+	+	+	+	+	+	+	+								
5	+	+	+	+	+	+	+	+	+	+	+	+	+	+	+	+	+	+	+	+	+	+	+	+	+								
6	+	+	+	+	+	+	+	+	+	+	+	+	+	+	+	+	+	+	+	+	+	+	+	+	+								
7	+	+	+	+	+	+	+	+	+	+	+	+	+	+	+	+	+	+	+	+	+	+	+	+	+								
8	+	+	+	+	+	+	+	+	+	+	+	+	+	+	+	+	+	+	+	+	+	+	+	+	+								
9	+	+	+	+	+	+	+	+	+	+	+	+	+	+	+	+	+	+	+	+	+	+	+	+	+								
10	+	+	+	+	+	+	+	+	+	-	+	+	-	+	+	+	+	+	+	+	+	+	+	+	+			2200					
11	+	+	+	+	+	+	+	+	+	+	+	+	+	+	+	+	+	+	+	+	+	-	-	-	-		1420	2210					
12	+	+	+	+	+	+	+	+	+	+	+	+	+	+	+	+	+	+	+	+	+	+	+	+	+								
13	+	+	+	+	+	+	+	+	+	+	+	+	+	+	+	+	+	+	+	+	+	+	+	+	+		1420	2220				2360	
14	+	+	-	-	-	+	+	+	+	+	+	+	-	-	-	-	-	-	-	+	+	+	+	+		1420	2210						
15	+	+	-	-	-	+	+	+	+	-	-	-	-	-	-	-	-	-	-	-	-	-	-	-			2200						
16	-	-	-	-	-	-	-	-	-	+	-	-	+	+	-	-	+	+	+	+	+	+	-	-	+			2260	2340				
17	+	+	+	+	+	+	+	+	+	+	+	+	+	+	+	+	+	+	+	+	+	+	+	+	+								
18	-	-	-	-	-	-	-	-	+	-	-	-	-	-	-	-	-	-	-	-	-	-	-	-		1410	2200			2350			
19	-	+	+	-	-	-	-	-	+	+	-	-	+	+	-	-	-	-	+	+	+	+	+	+	-			2210					
20	-	-	-	-	-	-	-	-	-	-	-	-	-	-	-	-	-	-	-	-	-	-	-	-				2260			2360		
21	-	-	-	-	-	-	-	-	+	+	+	+	+	+	+	+	+	+	+	+	+	+	+	+		1410	2210						
22	-	-	-	-	-	-	-	-	-	-	-	-	-	-	-	-	-	-	-	-	-	-	-	-				2260			2360		
23	+	+	+	+	+	+	+	+	+	+	+	+	+	+	+	+	+	+	+	+	+	+	+	+									
24	-	-	-	-	-	-	-	-	-	-	-	-	-	-	-	-	-	-	-	-	-	-	-	-		1420	2220				2360		
25	+	+	+	+	+	+	+	+	+	+	+	+	+	+	+	+	+	+	+	+	+	+	+	+									
26	+	+	+	+	+	+	+	+	+	+	+	+	+	+	+	+	+	+	+	+	+	+	+	+									
27	-	-	-	-	-	-	-	-	-	-	-	-	-	-	-	-	-	-	-	-	-	-	-	-			2215			2350			
28	+	+	+	+	+	+	+	+	+	+	+	+	+	+	+	+	+	+	+	+	+	+	+	+									
29	-	-	-	-	-	-	-	-	-	-	-	-	-	-	-	-	-	-	-	-	-	-	-	+			2215			2350			
30	-	-	-	-	+	+	+	+	+	+	+	+	+	+	+	+	+	+	+	+	+	+	+	+				2250					
31	-	-	-	-	-	-	-	-	-	-	-	-	-	-	-	-	-	-	-	-	-	-	-	-						2350			
32	+	+	+	+	+	+	+	+	+	-	-	-	-	-	-	-	+	+	+	+	+	+	+	+				2270					
33	+	+	-	-	+	+	+	+	+	-	-	-	-	-	-	-	-	-	-	-	-	-	-	-			2210						
34	+	-	+	-	-	-	-	+	-	+	+	+	+	+	+	+	+	+	+	+	+	+	+	+				2250					
35	+	+	-	-	+	-	-	+	+	+	-	-	-	-	-	-	-	-	-	-	-	-	-	+					2340				
36	-	+	-	-	-	+	-	-	-	-	-	-	-	-	-	-	-	-	-	-	-	-	-	-				2260		2350			
37	-	-	+	+	-	-	+	+	+	+	+	+	+	+	+	+	+	+	+	+	+	+	+	+				2260					
38	+	+	-	-	+	+	+	+	+	+	+	-	-	-	-	-	+	+	+	+	+	+	+	+				2240					
39	+	+	-	-	+	+	+	+	+	+	+	+	+	+	+	+	+	+	+	+	+	+	+	+				2260					
40	-	-	-	-	-	+	+	+	+	-	+	-	-	-	+	-	-	-	-	-	-	-	+	-				2260					

Cont. of Table 8.1 - Individual particle spectrum and NIR-active mineral map for splits B1, where (+) = spectrum without feature, (-) = spectrum with feature, Mus. = Muscovite, Cl. = Chlorite, Cr. = Chrysocolla, Cal. = Calcite, Bi. = Biotite and Shared = OH feature common to two or more minerals.

Sample ID	Sector A									Sector B									Sector C									Feature position (nm)					
	1	2	3	4	5	6	7	8	9	1	2	3	4	5	6	7	8	9	1	2	3	4	5	6	7	8	9	Shared	Mus.	Cl./Cr/Bi.	Cal	Mus.	Cl.
41	+	+	+	+	+	+	+			+	+	+	+	+	+			+	+	+	+	+											
42	-	-	-	-	-	-	-	+		-	-	-	-	-	-	-	-	-	-	-	-	-	-	-	-	-	-	-	-				
43	+	-	-	-	-	-	-	-		+	-	-	-	-	-	-	-	-	+	+	-	-	+	+									
44	+	+	+	+	+	+	+			+	+	+	-	+	+	+	+	+	+	+	+	+	+										
45	-	-	+	-	-	-	+			+	+	-	-	-	-	+	+	+	-	-	-	-	-	-	-	-	-	-	+				
46	-	-	-	-	-	-				-	-	+	+	+	+	+	+	-	-	-	-	+	-	-	-	-	-	-	-				
47	+	+	+	+	+	+	+			-	-	-	-	-	-	-	-	-	-	-	-	-	-	-	-	-	-	-	+				
48	+	+	+	+	+	+	+	+		+	+	+	+	+	+	+	+	+	+	+	+	+	+	+	+	+	+	+	+				
49	-	-	-	-	-	-	-			-	-	-	-	-	-	-	-	-	-	-	-	-	-	-	-	-	-	-	-				
50	+	+	+	+	+	+	+	+		+	-	+	+	-	-	+	+	+	+	+	+	+	+	+	+	+	+	+	+				
51	+	+	+	+	+	+	+	+		+	+	+	+	+	+	+	+	+	+	+	+	+	+	+	+	+	+	+	+				
52	+	+	+	+	+	+	-			+	+	+	+	+	+	+	+	+	+	+	+	+	+	+	+	+	+	+	+				
53	-	-	-	-	-	-	-			-	-	-	-	-	-	-	-	-	-	-	-	-	-	-	-	-	-	-	-				
54	-	+	+	+						-	+	-	-	-	+	-	-	-	+	-	+	+	+	+	+	+	+	+	+				
55	-	-	-	-	-	-	-			-	-	-	-	-	-	-	-	-	-	-	-	-	-	-	-	-	-	-	-				
56	-	-	-	-	-	-	-			-	-	-	-	-	-	-	-	-	-	-	-	-	-	-	-	-	-	-	-				
57	-	-	-	-	-	-	-			-	-	-	-	-	-	-	-	-	-	-	-	-	-	-	-	-	-	-	-				
58	+	+	+	+	+	+	+			+	+	+	+	+	+	+	+	+	+	+	+	+	+	+	+	+	+	+	+				
59	+	+	+	+	+	+	+			+	+	+	+	+	+	+	+	+	+	+	+	+	+	+	+	-	-	-	-				
60	+	+	+	+	+	+	+			+	+	+	+	+	+	+	+	+	+	+	+	+	+	+	+	+	+	+	+				

Table 8.2 - Individual particle spectrum and mineral map for splits B2, where (+) = spectrum without feature, (-) = spectrum with feature, Mus. = Muscovite, Cl. = Chlorite, Cr. = Chrysocolla, Cal. = Calcite, Bi. = Biotite, and Shared = OH feature common to two or more minerals.

Sample ID																															Feature Position (nm)									
	1	2	3	4	5	6	7	8	9	10	11	12	13	14	15	16	17	18	19	20	21	22	23	24	25	26	27	28	29	30	Shared	Mus.	Cl./Cr/Bi	Cal.	Mus.	Cl.				
1	+	+	+	+	+	+	+	+	+	+	+																													
2	+	+	+	+	+	+	+	-	-	+	+	+	+																											
3	+	+	+	+	+	+	+	+	+	+	+	+	+	+	+	+	+	+	-	+																				
4	+	+	+	+	+	+	+	+	+	+	+	+	-	-	-	-	-	-	-	+																				
5	+	+	+	+	+	+	+	+	+	+	+	+	+	+	+	+	+																							
6	+	+	+	+	+	+	+	+	+	+	+	+	+	+	+	+	+																							
7	+	+	+	+	+	+	+	+	+	+	+	+	+	+	+	+	+	+	+																					
8	+	+	+	+	+	+	+	+	+	+	+	+	+	+	+	+	+																							
9	-	-	-	-	-	-	-	-	-	-	-	-	-	-	-	-	-	-	-	-	-	-	-	-	-	-	-	-	-	-	-	-	-	-	-	-	-			
10	+	+	+	+	+	+	+	+	+	+	+	+	+																											
11	+	+	+	+	+	+	+	+	+	+	+	+	+	+	+	+	+	+	+	+																				
12	+	+	+	+	+	+	+	+	+	+	+	+	+	+	+	+	+																							
13	-	-	-	-	-	-	-	-	-	-	-	-	-	+	+	+	+																							
14	-	-	-	+	+	+	+	+	+	+	+	+	+	+	+																									
15	-	-	-	-	-	-	-	-	-	-	-	-	-	-	-	-	-	-	-	-	+																			
16	-	-	+	-	-	-	-	-	-	-	-	-	-	-	-	-	-	-	-	-	+																			
17	+	+	+	+	+	+	+	+	+	+	+	+	+	+	+	+	+	+	+	+																				
18	-	-	-	-	-	-	-	-	+	+	+	-	+	-																										
19	+	+	+	+	+	+	+	+	+	+	+	+	+	+	+	+	+																							
20	-	-	-	-	+	+	+	+	+	+	+	-	+	+	-	+	-																							
21	+	+	+	+	+	+	+	-	-	+	+	-	+	+	+	-	+																							
22	+	+	+	+	+	+	+	+	+	+	+	+	+	+	+	+	+																							
23	+	+	-	-	-	-	-	-	+	+	+	+	+	-	-	-	-	-	-	+	+																			
24	+	+	+	-	-	-	-	-	+	+	-	-	+																											
25	-	-	-	-	-	-	-	-	+	+																														
26	-	-	-	-	-	-	-	-	-	-	+	-	-	+	-	+	-	-	-	-																				
27	-	-	-	-	-	-	-	-	-	-	-	-	-	-	-	-	-	-	-	-	-	-	-	-	-	-	-	-	-	-	-	-	-	-	-	-	-	-		
28	+	+	+	+	+	+	+	+	+	+	+	+	+	+	+	+	+																							
29	-	-	-	-	-	-	-	-	-	-	-	-	-	-	-	-	-	-	-	-	-	-	-	-	-	-	-	-	-	-	-	-	-	-	-	-	-	-		
30	+	+	+	+	+	+	+	+	+	+	+	+	+	+	+	+	+	+	+	+	+	+	+	+	+	+	+	+	+	+	+	+	+	+	+	+	+	+	+	
31	+	+	+	+	+	+	+	+	+	+	+	+	+	+	+	+	+	+	+	+	+	+	+	+	+	+	+	+	+	+	+	+	+	+	+	+	+	+	+	
32	+	+	+	+	+	+	+	+	+	+	+	+	+	+	+	+	+																							
33	-	-	-	-	-	-	-	-	-	-	-	-	-	-	-	-	-	-	-	-	-	-	-	-	-	-	-	-	-	-	-	-	-	-	-	-	-	-		
34	+	+	+	+	+	+	+	+	+	+	+	+	+	+	+	+																								
35	-	-	-	-	-	-	-	-	-	-	-	-	-	-	-	-	-	-	-	-	-	-	-	-	-	-	-	-	-	-	-	-	-	-	-	-	-	-		
36	-	-	-	-	-	-	-	-	-	-	-	-	-	-	-	-	-	-	-	-	-	-	-	-	-	-	-	-	-	-	-	-	-	-	-	-	-	-	-	
37	+	+	+	+	+	+	+	+	+	+	+	+	+	+	+	+	+																							
38	-	-	-	-	-	-	-	-	-	-	-	-	-	-	-	-	-	-	-	-	-	-	-	-	-	-	-	-	-	-	-	-	-	-	-	-	-	-	-	
39	-	-	-	+	+	+	+	+	+	+	+	+	+	+	+	+																								
40	+	+	+	+	+	+	+	+	+	+	+	+	+	+	+	+																								

Cont. of Table 8.2 - Individual particle spectrum and mineral map for splits B2, where (+) = spectrum without feature, (-) = spectrum with feature, Mus. = Muscovite, Cl. = Chlorite, Cr. = Chrysocolla, Cal. = Calcite, Bi. = Biotite, and Shared = OH feature common to two or more minerals.

Sample ID																															Feature Position (nm)													
	1	2	3	4	5	6	7	8	9	10	11	12	13	14	15	16	17	18	19	20	21	22	23	24	25	26	27	28	29	30	Shared	Mus.	Cl./Cr/Bi	Cal.	Mus.	Cl.								
41	+	+	+	+	+	+	+	+	+	+	+	+	+																															
42	-	-	-	-	-	-	-	-	-	-	-	-	-	-	-	-	-	-																								2340/ 2355		
43	+	+	-	-	-	-	+	+	+	+	+	+	+	+	+	+	+	+	+																				1420	2210		2340		
44	+	+	+	+	+	+	+	+	+	+	+	+	+	+	+	+	+	+	+	+	+	+	+	+																				
45	+	+	+	+	+	+	+	+	+	+	+	+																																
46	-	-	-	-	-	-	-	-	-	-	-	-	-																												2340/ 2345			
47	-	-	-	-	-	-	-	-	-	-	-	-	-	-	-																											2340		
48	-	-	-	-	-	+	+	+	+	+	+	+	-																										1415	2210		2340		
49	-	-	+	-	-	-	-	-	-	-	-	-	-																										1415	2220			2350	
50	-	-	-	-	-	-	-	-	-	-	-	-	-	-	+	+	+	+	+	+																			1410		2255		2350	
51	+	+	+	+	+	+	+	+	+	+	+	+	+	+																														
52	-	-	-	-	-	-	-	-	-	-	-	-	-	-	-	-	-	-	-	-	-	-	-	-	-	-	-	-	-	-	-	-	-	-	-	-	-				2340			
53	-	-	-	-	-	-	-	-	-	-	-	-	-	-	-	-	-	-	-	-	-	-	-	-	-	-	-	-	-	-	-	-	-	-	-	-	-		2220		2345			
54	-	-	-	-	-	-	-	-	-	-	-	-	-	-	-	-	-	-	-	-	-	-	-	-	-	-	-	-	-	-	-	-	-	-	-	-	-	1415	2220					
55	-	-	-	-	-	-	-	-	-	-	-	-	-	-	-	-	-	-	-	-	-	-	-	-	-	-	-	-	-	-	-	-	-	-	-	-	-	1420	2205			2350		
56	-	-	-	-	-	-	-	-	-	-	-	-	-	-	-	-	-	-	-	-	-	-	-	-	-	-	-	-	-	-	-	-	-	-	-	-	-	1415	2215		2345			
57	-	-	-	-	-	-	-	-	-	-	-	-	-	-	-	-	-	-	-	-	-	-	-	-	-	-	-	-	-	-	-	-	-	-	-	-	-	1415	2210		2355			
58	+	+	+	+	+	+	+	+	+	+	+	+	+	+	+	+	+	+	+	+	+	+	+	+	+	+	+	+	+	+	+	+	+	+	+	+	+							
59	+	+	+	+	+	+	+	+	+	+	+	+	+	+	+	+	+	+	+	+	+	+	+	+	+	+	+	+	+	+	+	+	+	+	+	+	+	+						
60	+	+	+	+	+	+	+	+	+	+	+	+	+	+	+	+	+	+	+	+	+	+	+	+	+	+	+	+	+	+	+	+	+	+	+	+	+	+						

Table 8.3 - Individual sample spectra and mineral map for splits A1, where Mus. = Muscovite, Cl. = Chlorite, Cr. = Chrysocolla, Cal. = Calcite, Bi. =Biotite, and Shared = OH feature common to two or more minerals.

Sample ID	Number of spectra	Minerals and feature position (nm)					
		Shared	Mus.	Cl./Cr./Bi	Cal.	Mus.	Cl.
1	24						
2	24						
3	27						
4	29						
5	26						
6	21						
7	28						
8	25						
9	30						
10	26						
11	20						
12	27						
13	25						
14	25						
15	26		2220				
16	25			2260	2340		
17	28			2260	2340		
18	25	1415	2210		2345		
19	26						
20	20			2260	2340		
21	20						
22	29			2260	2340		
23	22			2260	2340		
24	24						
25	26			2250			
26	24						
27	32		2215			2350	
28	37			2250	2340		
29	24		2215			2350	
30	24			2255	2345		
31	28			2255	2340		
32	25			2260	2340		
33	21		2210				
34	20			2260	2340		
35	30			2255	2345		
36	25			2255	2345		
37	20			2255	2340		
38	24			2255	2345		
39	21			2260	2340		
40	30			2260	2345		
41	21		2210		2345		
42	28						
43	38						
44	22			2260	2340		
45	31			2260	2345		
46	18		2210			2350	
47	30			2260	2345		
48	24						
49	24						
50	26			2260	2345		
51	25						
52	24						
53	26	1415	2215			2350	
54	27						
55	29		2200				
56	28						
57	29		2210				
58	17						
59	24						
60	27						

From the NIR spectrum classification scheme (Tables 8.1, 8.2 and 8.3), it is possible that ore samples fall outside the classification ranges due to feature displacement or presence of feature(s) not corresponding to any mineral in concentration. According to Coates (2000), that could be caused by the influence of other functional groups within the particle, the impact of preferred spatial orientations and environmental effects (chemical and intimate interactions) on the particle. This was also confirmed by intimate mixtures. Hence, to check against misclassification, results of intimate mixtures were used to assign absorption features to the appropriate mineral(s). For example, in order to distinguish between calcite and muscovite in the spectra of samples, features near 2345 nm, were assigned to calcite. In addition, features near 2205, 2210, 2215 and 2220 nm were assigned to muscovite as displaced features. Where applicable, these assignments corresponded with the particles mineralogical composition. Samples with high calcite concentration displayed strong absorption features near 2335, 2340 or 2345 nm.

On the basis of NIR activity or sensitivity of individual minerals in the Mantoverde ore, minerals can be listed in order of decreasing response as muscovite, hematite, calcite, chlorite, chrysocolla, and biotite. Though NIR-active, kaolinite features are absent, even for sample 21, which is the only sample containing high kaolinite at about 3 wt. % (Table 4.1). Intimate mixtures of kaolinite and muscovite (Fig. 6.5) indicated muscovite as more NIR-active. The activity of muscovite over kaolinite is not only concentration dependent. This explains the absence of kaolinite features in sample 21 (Table 8.1). Muscovite is a strongly active mineral in the NIR region with the ability to be visible or readily accessible even when in low concentrations. This implies that muscovite is readily visible within the NIR region and that its visibility is not in most cases concentration dependent. Experiments of mineral mixtures showed that it takes hematite in a ratio of muscovite to hematite of 3:7 to out-stretch muscovite features. While at a ratio of 1:9 for muscovite to calcite, muscovite still displays its characteristic diagnostic features side-by-side to those of calcite even at higher calcite concentration. Calcite is invisible at higher muscovite ratios. The sensitivity of muscovite over calcite has been confirmed in this research (e.g. at muscovite to calcite ratio of 3:7, for samples 27 and 29, and ratio 1:9 for sample 42) (Tables 4.1 and 8.1).

Hematite though featureless within the 1300 to 2400 nm region, has the ability of masking and suppressing the features of other minerals in a matrix (Van Der Meer, 1995; Bishop and Dummel 1996). The influence of hematite was also confirmed by intimate mixtures. With respect to present study, chrysocolla is invisible when in concentrations with hematite, even at a ratio of approximately 1:1 as in sample 26 (Tables 4.1 and 8.1). This is also observed when other NIR-active minerals which display features, like calcite, chlorite and biotite occur with hematite.

Calcite with chlorite when they occur together at a higher calcite ratio, both minerals are indistinguishable at longer wavelengths, as spectrum appears broad between 2250 and 2340 nm (e.g. samples 25 and 35, Table 8.1). Intimate mixtures revealed that even at a ratio of 9:1 calcite to hematite, calcite features are out-stretched (Fig. 6.23). When chlorite occurs with muscovite, chlorite features are invisible as only those of muscovite are observed (e.g. samples 15 and 19, Table 8.1). Calcite in concentration with muscovite retains a strong feature near 2340 or 2345 nm (e.g. samples 46 and 56, Table 8.1, samples 9, 13, 53, 56, Table 8.2).

The presence of biotite with other NIR-active minerals tends to influence absorption by reducing the reflectance of the spectra. Without hematite in concentration biotite displays features along longer wavelengths (e.g. sample 38, Table 8.1). When biotite occurs with chlorite and calcite, together they display broad absorption along longer wavelengths (e.g. samples 25 and 41, Table 8.1). When the three minerals (biotite, chlorite and calcite) are in association with muscovite, only muscovite features are observed in the spectra (e.g. sample 33, Table 8.1). Occurrence of both muscovite and calcite features side-by-side in such association is only observed at higher calcite concentrations (e.g. sample 46, Table 8.1)

Chrysocolla and chlorite are treated together because from their intimate mixture, they showed absorption features side-by-side. When they occur with hematite in concentration, no feature is visible to indicate either mineral, as the spectrum appears featureless. Hence, features of both minerals are believed to be masked by hematite. The same is true for biotite. Therefore, the indirect method is used because of the known masking influence of hematite and or



biotite on their features. Based on the correlation of NIR spectra with the QEMSCAN<sup>®</sup> mineralogical data (Table 4.1), almost all hematite-rich particles contain chrysocolla in economic quantity. Hence, featureless spectra are considered chrysocolla-, chlorite- and or biotite-bearing (Tables 8.1, 8.2 and 8.3).

Ankerite occurred in fourteen samples, but in minute concentrations. Though a feature displaying NIR-active carbonate mineral, no particles showed features indicative of ankerite, even those with concentration above 5 wt % (samples 41, 55 and 57). While sample 41 is featureless, samples 55 and 57 are dominated by muscovite features (Table 8.1).

The characteristic spectral behaviour of samples of the Mantoverde copper ore confirmed results obtained from the intimate mixtures (see chapter six).

### **8.3. Individual sample classification and discussion**

The Mantoverde ore sorting method shall depend on the main NIR-active minerals in the ore, as detected by the NIR sensor, such as hematite, chrysocolla, muscovite (and or kaolinite), calcite, biotite and chlorite. The objective of NIR application on the Mantoverde copper ore is to upgrade the ore at coarse state. This shall be achieved by discriminating the copper-bearing minerals from the waste minerals. Chrysocolla, chlorite, biotite and hematite are considered together since discriminating between them may result in the loss of valuable (chrysocolla) as waste. Hence, the waste minerals in the ore targeted are carbonate gangues (calcite) and hydroxyl minerals (muscovite and kaolinite). Both gangue groups are typified by high acid consumption. While calcite is highly reactive in acids, the clays minerals are high acid consuming due to their ability to agglomerate, thereby reducing solvent percolation, as they can be non-permeable (Gupta, 2003; Curtis, 2012). Hence, samples containing both or either carbonates and hydroxyl bearing minerals (calcite and muscovite/kaolinite) which are not copper bearing are considered waste. The discrimination of calcite from ore product minerals is concentration dependent (Iyakwari and Glass, 2015). Hence, calcite features are only present in the spectrum when chrysocolla, chlorite and or hematite are little or below detection limit in concentration.

#### **8.4. Classification strategies**

From Figure 6.46, four classification options (strategies) are proposed for individual spectrum classification based on intimate mixtures, with the aim of identifying spectrum as either product or waste. Given the economic minerals (chrysocolla with minor malachite), nature of spatial associations of minerals in the Mantoverde ore, and the behaviour of the waste minerals calcite and or muscovite with the ore minerals, two options can be applied to the Mantoverde ore. These options are:

- i. Copper-bearing mineral contains a hydroxyl group (chrysocolla) or carbonate (malachite) associated with high iron bearing minerals (hematite).  
And or
- ii. Copper-bearing mineral contains a hydroxyl group (chrysocolla) not associated with high iron bearing minerals. Given the nature of the ore, where some samples are associated with hematite, the strategy shall be modified to read “copper bearing mineral contain a hydroxyl group (chrysocolla) with or without hematite association”.

##### **8.4.1. Strategy one**

Considering the first option above, which represents option three in Figure 6.46, individual spectrum can be defined as below:

- a. Product - spectrum showing exclusively diagnostic features or characteristics of chrysocolla, chlorite, biotite and or hematite. In addition, any spectrum without absorption feature(s) or defined absorption features centre is considered product.
- b. Waste - spectrum displaying features of calcite and/or muscovite. This spectrum may in addition contain little or no chrysocolla pattern. This group is defined by features near 2200, 2210, 2215 and 2220 nm for muscovite (or clays) and 2335, 2340 and 2345 nm for calcite.

Therefore, the strategy is aimed at targeting both freely occurring calcite and or muscovite occurring particles as waste.

On the basis of above spectrum definition, individual Mantoverde samples shall be classified into three groups as:

- i. Products - samples with all spectra showing chrysocolla and/or hematite, chlorite, biotite pattern. This group includes featureless spectra.
- ii. Waste - samples with all spectra showing calcite and or muscovite spectra characteristics.
- iii. Middlings – samples with spectra containing individual spectrum of both waste and product groups. This is likely since individual spectrum have a dimension of 0.29 by 0.9 mm, and each particle as scanned is large, containing two or more spectra. This group may require further liberation to a size not less than the NIR spectrum dimension and rescanned to achieve preconcentration using NIR.

A diagrammatical chart showing the preconcentration strategy as outlined above is presented in Figure 8.2.

For the sake of this research, any sample containing above 50 % either product or waste spectra, in addition to classification as middling will be classified on the basis of the dominant or majority spectra group as either product or waste. But where a sample contains 50 - 50 % waste and product spectra, the sample shall be classified as waste. This is not dependent on copper cut-off grade since NIR does not sense copper.

Individual particle classification per splits is presented in Tables 8.4, 8.5 and 8.6.

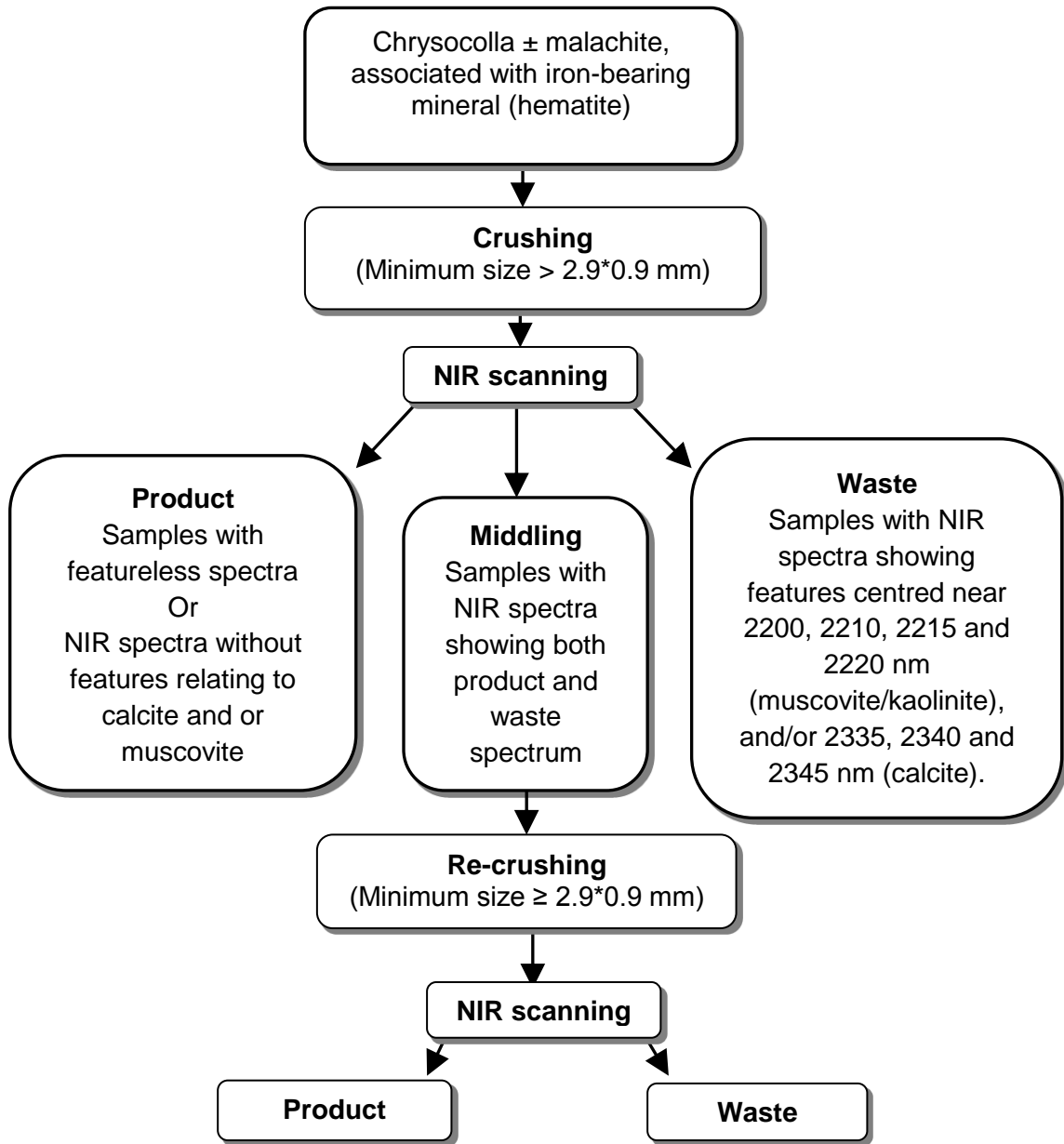


Figure 8.2 - Mantoverde copper samples preconcentration strategy, targeted at discriminating both calcite and muscovite (clay) bearing particles (modified from Iyakwari et al., 2013; Iyakwari and Glass, 2015)

Table 8.4 - Classification of Mantoverde particles based on analysis of NIR spectra for splits B1, targeted at discriminating both calcite and muscovite as waste. Where P = Product and W = Waste, M- = Middling with ≤ 50 % waste spectrums and M\* = Middling with > 50 % product spectrums.

Sample ID	Sector A									Sector B									Sector C									NIR Classification
	1	2	3	4	5	6	7	8	9	1	2	3	4	5	6	7	8	9	1	2	3	4	5	6	7	8	9	
1	P	P	P	P	P	P	P	P		P	P	P	P	P	P	P		P	P	P	P	P	P				P	
2	P	P	P	P	P	P	P	P		P	P	P	P	P	P	P		P	P	P	P	P	P	P				P
3	P	P	P	P	P	P	P			P	P	P	P	P	P	P		P	P	P	P	P	P	P	P			P
4	P	P	P	P	P	P	P			P	P	P	P	P	P	P		P	P	P	P	P	P	P				P
5	P	P	P	P	P	P	P			P	P	P	P	P	P	P		P	P	P	P	P	P	P	P			P
6	P	P	P	P	P	P	P			P	P	P	P	P	P	P		P	P	P	P	P	P	P	P			P
7	P	P	P	P	P	P	P			P	P	P	P	P	P	P		P	P	P	P	P	P	P	P			P
8	P	P	P	P	P	P	P			P	P	P	P	P	P	P		P	P	P	P	P	P	P	P			P
9	P	P	P	P	P	P	P	P		P	P	P	P	P	P	P		P	P	P	P	P	P	P	P			P
10	P	P	P	P	P	P	P			W	P	P	W	P	P		P	P	P	P								M*(P)
11	P	P	P	P	P	P	P	P		P	P	P	P	P	P	P	P	P	P	P	P	W	W	W	W			M*(P)
12	P	P	P	P	P	P	P			P	P	P	P	P	P	P		P	P	P	P	P	P	P	P			P
13	P	P	P	P	P	P	P			P	W	P	P	W	W	W		P	P	P	P	P	P	P				M*(P)
14	P	P	W	W	W	W	P			P	P	P	P	W	W	W		W	P	P	W	W	W	W				M-(W)
15	P	P	W	W	W	P				W	W	W	W	W	W	W	W	W	W	W	W	W	W	W	W	W	W	M-(W)
16	W	W	W	W	W					P	W	W	P	P	W	W	P	P	W	P	W	W	W	W	P	P		M-(W)
17	P	P	P	P	P	P				P	P	P	P	P	P	P		P	P	P	P	P						P
18	W	W	W	W	W	W	W	P		W	W	W	W	W	W	W		W	W	W	W	W	W	W				M-(W)
19	W	P	P	W	W	W	W			P	P	W	W	P	P	W		P	W	P	P	P	P	P	P			M*(P)
20	P	P	P	P	P	P	P	P		P	P	P	P	P	P	P		P	P	P	P	P	P	P	P			P
21	W	W	W	W	W	W	W	W		P	P	P	P	P	P	W	W	W	W	W	W	W	W	W				M-(W)
22	P	P	P	P	P	P	P			P	P	P	P	P	P	P		P	P	P	P	P	P	P				P
23	P	P	P	P	P	P	P	P		P	P	P	P	P	P	P		P	P	P	P	P	P	P	P			P
24	W	W	W	W	W	W	W	W		W	W	W	W	W	W	W	W	W	W	W	W	W	W	W				W
25	P	P	P	P	P	P				P	P	P	P	P	P	P		P	P	P	P	P	P					P
26	P	P	P	P	P	P	P			P	P	P	P	P	P	P		P	P	P	P	P	P	P				P
27	W	W	W	W	W	W	W			W	W	W	W	W	W	W		W	W	W	W	W	W	W				W
28	P	P	P	P	P	P				P	P	P	P	P	P	P		P	P	P	P	P	P	P				P
29	W	W	W	W	W	W	W			W	W	W	W	W	W	W		W	W	W	W	W	W	W				W
30	P	P	P	P	P	P	P			P	P	P	P	P	P	P		P	P	P	P	P	P					P
31	P	P	P	P	P	P	P	P		P	P	P	P	P	P	P		P	P	P	P	P	P	P	P			P
32	P	P	P	P	P	P	P			P	P	P	P	P	P	P		P	P	P	P	P	P					P
33	P	P	W	W	P	P	P			W	W	W	W	W														M-(W)
34	P	P	P	P	P	P	P	P	P	P	P	P	P	P	P	P		P	P	P	P	P	P	P	P			P
35	P	P	W	W	P	W	W	P		P	W	W	W	W	W	W	P	P	P	W	W	W	W	W	P			M-(W)
36	W	P	W	W	P	W	W			W	W	W	W	W	W	W		W	W	W	W	W	W	W				M-(W)
37	P	P	P	P	P	P	P			P	P	P	P	P	P	P		P	P	P	P	P	P	P				P
38	P	P	P	P	P	P				P	P	P	P	P	P	P		P	P	P	P	P	P	P				P
39	P	P	P	P	P	P				P	P	P	P	P	P	P		P	P	P	P	P	P	P				P
40	P	P	P	P	P	P	P	P		P	P	P	P	P	P	P		P	P	P	P	P	P	P	P			P

Cont. of Table 8.4 - Classification of Mantoverde particles based on analysis of NIR spectra for splits B1, targeted at discriminating both calcite and muscovite as waste. Where P = Product and W = Waste, M- = Middling with  $\leq 50\%$  waste spectrums and M\* = Middling with  $> 50\%$  product spectrums.

Sample ID	Sector A									Sector B									Sector C									NIR Classification	
	1	2	3	4	5	6	7	8	9	1	2	3	4	5	6	7	8	9	1	2	3	4	5	6	7	8	9		
41	P	P	P	P	P	P	P			P	P	P	P	P	P	P	P	P	P	P	P	P	P					P	
42	W	W	W	W	W	W	W	P		W	W	W	W	W	W	W	W	W	W	W	W	W	W	W	W	W	W	M-(W)	
43	P	W	W	W	W	W	W	W	W	P	W	W	W	W	W	P	W	W	W	P	P	W	W	P	P			W	
44	P	P	P	P	P	P	P			P	P	P	P	P	P	P	P	P	P	P	P	P	P	P				P	
45	P	P	P	P	P	P	P			P	P	P	P	P	P	P	P	P	P	P	P	P	P	P	P			P	
46	W	W	W	W	W					W	W	P	P	P	P	P	P	W	W	W	W	P	W	W	W			M-(W)	
47	P	P	P	P	P	P	P			W	W	W	W	W	W	W	W		W	W	W	W	W	W	P			M-(W)	
48	P	P	P	P	P	P	P	P		P	P	P	P	P	P	P	P		P	P	P	P	P	P	P			P	
49	W	W	W	W	W	W	W			W	W	W	W	W	W	W		W	W	W	W	W	W	W	W			W	
50	P	P	P	P	P	P	P	P		P	P	P	P	P	P	P	P		P	P	P	P	P	P	P	P		P	
51	P	P	P	P	P	P	P	P		P	P	P	P	P	P	P	P		P	P	P	P	P	P	P			P	
52	P	P	P	P	P	P	W			P	P	P	P	P	P	P	P	P		P	P	P	P	P	P			M*(P)	
53	W	W	W	W	W	W	W			W	W	W	W	W	W	W	W	W		W	W	W	W	W	W	W		W	
54	W	P	P	P						W	P	W	W	W	P	W		W	W	P	W	P	W	P				M-(W)	
55	W	W	W	W	W	W	W	W		W	W	W	W	W	W	W	W		W	W	W	W	W	W	W			W	
56	W	W	W	W	W	W	W	W		W	W	W	W	W	W	W	W		W	W	W	W	W	W	W	W		W	
57	W	W	W	W	W	W	W			W	W	W	W	W	W	W	W		W	W	W	W	W	W	W	W		W	
58	P	P	P	P	P	P	P			P	P	P	P	P	P	P	P	P		P	P	P	P	P	P	P		P	
59	P	P	P	P	P	P	P			P	P	P	P	P	P	P	P	P		P	P	P	P	P	P	P	P		P
60	P	P	P	P	P	P	P			P	P	P	P	P	P	P	P	P		P	P	P	P	P	P	P		P	

Table 8.5 - Classification of Mantoverde particles based on analysis of NIR spectra for splits B2, targeted at discriminating both calcite and muscovite as waste. Where P = Product and W = Waste, M- = Middling with ≤ 50 % waste spectra and M\* = Middling with > 50 % product spectra.

Sample ID	1	2	3	4	5	6	7	8	9	10	11	12	13	14	15	16	17	18	19	20	21	22	23	24	25	26	27	28	29	30	NIR Classification			
1	P	P	P	P	P	P	P	P	P	P	P																				P			
2	P	P	P	P	P	P	P	P	P	P	P	P	P	P																	P			
3	P	P	P	P	P	P	P	P	P	P	P	P	P	P	P	P	P	P	P	P	P	P										P		
4	P	P	P	P	P	P	P	P	P	P	P	P	W	W	W	W	W	W	W	P											M*(P)			
5	P	P	P	P	P	P	P	P	P	P	P	P	P	P																	P			
6	P	P	P	P	P	P	P	P	P	P	P	P	P	P	P	P	P														P			
7	P	P	P	P	P	P	P	P	P	P	P	P	P	P	P	P	P	P	P	P	P	P									P			
8	P	P	P	P	P	P	P	P	P	P	P	P	P	P	P	P	P														P			
9	W	W	W	W	W	W	W	W	W	W	W	W																			W			
10	P	P	P	P	P	P	P	P	P	P	P	P	P	P	P	P	P	P	P	P	P										P			
11	P	P	P	P	P	P	P	P	P	P	P	P	P	P	P	P	P	P	P	P	P	P										P		
12	P	P	P	P	P	P	P	P	P	P	P	P	P	P	P	P	P															P		
13	W	W	W	W	W	W	W	W	W	W	W	W	W	P	P																	M-(W)		
14	W	W	W	P	P	P	P	P	P	P	P	P	P	P	P																	M*(P)		
15	W	W	W	W	W	W	W	W	W	W	W	W	W	W	W	W	W	W	W	W	P											M-(W)		
16	P	P	P	P	P	P	P	P	P	P	P	P	P	P																		P		
17	P	P	P	P	P	P	P	P	P	P	P	P	P	P	P	P	P	P	P													P		
18	W	W	W	W	W	W	W	P	P	P	W	P	W																			M-(W)		
19	P	P	P	P	P	P	P	P	P	P	P	P	P	P	P	P	P	P	P	P	P	P										P		
20	P	P	P	P	P	P	P	P	P	P	P	P	P	P	P	P	P	P	P														P	
21	P	P	P	P	P	P	P	W	W	P	P	W	P	P	P	W	P																M*(P)	
22	P	P	P	P	P	P	P	P	P	P	P	P	P	P	P	P	P	P	P	P	P	P											P	
23	P	W	W	W	W	W	W	W	W	P	P	P	W	W	W	W	W	W	W	W	P	P											P	
24	P	P	P	W	W	W	W	W	W	P	P	W	W	P																			M-(W)	
25	W	W	W	W	W	W	W	W	W	P	P																						M-(W)	
26	P	P	P	P	P	P	P	P	P	P	P	P	P	P	P	P	P	P	P	P	P	P											P	
27	W	W	W	W	W	W	W	W	W	W	W	W	W	W	W	W	W	W	W	W	W	W											W	
28	P	P	P	P	P	P	P	P	P	P	P	P	P	P	P	P	P	P	P	P	P	P											P	
29	W	W	W	W	W	W	W	W	W	W	W	W	W	W	W	W	W	W	W	W	W	W											W	
30	P	P	P	P	P	P	P	P	P	P	P	P	P	P	P	P	P	P	P	P	P	P											P	
31	P	P	P	P	P	P	P	P	P	P	P	P	P	P	P	P	P	P	P	P	P	P											P	
32	P	P	P	P	P	P	P	P	P	P	P	P	P	P	P	P	P	P	P	P	P	P											P	
33	P	P	P	P	P	P	P	P	P	P	P	P	P	P	P	P	P	P	P	P	P	P											P	
34	P	P	P	P	P	P	P	P	P	P	P	P	P	P																			P	
35	W	W	W	W	W	W	W	W	W	W	W	W	W	W																			W	
36	P	P	P	P	P	P	P	P	P	P	P	P	P	P	P	P	P	P	P	P	P	P											P	
37	P	P	P	P	P	P	P	P	P	P	P	P	P	P	P	P	P	P	P	P	P	P												P
38	P	P	P	P	P	P	P	P	P	P	P	P	P	P	P	P	P	P	P	P	P	P												P
39	W	W	W	P	P	P	P	P	P	P	P	P	P	P	P	P	P	P	P	P	P	P												M*(P)
40	P	P	P	P	P	P	P	P	P	P	P	P	P	P	P	P	P	P	P	P	P	P												P

Cont. of Table 8.5 - Classification of Mantoverde particles based on analysis of NIR spectra for splits B2, targeted at discriminating both calcite and muscovite as waste. Where P = Product and W = Waste, M- = Middling with  $\leq 50\%$  waste spectra and M\* = Middling with  $> 50\%$  product spectra.

Sample ID	1	2	3	4	5	6	7	8	9	10	11	12	13	14	15	16	17	18	19	20	21	22	23	24	25	26	27	28	29	30	NIR Classification		
41	P	P	P	P	P	P	P	P	P	P	P	P	P																		P		
42	W	W	W	W	W	W	W	W	W	W	W	W	W	W	W	W	W	W														W	
43	P	P	W	W	W	W	P	P	P	P	P	P	P	P	P	P	P	P	P													M*(P)	
44	P	P	P	P	P	P	P	P	P	P	P	P	P	P	P	P	P	P	P	P	P	P										P	
45	P	P	P	P	P	P	P	P	P	P	P	P	P																			P	
46	W	W	W	W	W	W	W	W	W	W	W	W	W	W	W																	W	
47	W	W	W	W	W	W	W	W	W	W	W	W	W	W	W																	W	
48	W	W	W	W	W	P	P	P	P	P	P	P	W																			M*(P)	
49	W	W	P	W	W	W	W	W	W	W	W	W	W																			M-(W)	
50	P	P	P	P	P	P	P	P	P	P	P	P	P	P	P	P	P	P	P	P												P	
51	P	P	P	P	P	P	P	P	P	P	P	P	P	P																		P	
52	W	W	W	W	W	W	W	W	W	W	W	W	W	W	W	W	W	W	W	W	W	W	W	W	W	W	W	W	W	W	W	W	
53	W	W	W	W	W	W	W	W	W	W	W	W	W	W	W	W	W	W	W	W	W	W	W	W	W	W	W	W	W	W	W	W	W
54	W	W	W	W	W	W	W	W	W	W	W	W	W	W	W	W	W	W	W	W	W	W	W	W	W	W	W	W	W	W	W	W	W
55	W	W	W	W	W	W	W	W	W	W	W	W	W	W	W	W	W	W	W	W	W	W	W	W	W	W	W	W	W	W	W	W	W
56	W	W	W	W	W	W	W	W	W	W	W	W	W	W	W	W	W	W	W	W	W	W	W	W	W	W	W	W	W	W	W	W	W
57	W	W	W	W	W	W	W	W	W	W	W	W	W	W	W	W	W	W	W	W	W	W	W	W	W	W	W	W	W	W	W	W	W
58	P	P	P	P	P	P	P	P	P	P	P	P	P	P	P	P	P	P	P	P	P	P											P
59	P	P	P	P	P	P	P	P	P	P	P	P	P	P	P	P	P	P	P	P	P	P											P
60	P	P	P	P	P	P	P	P	P	P	P	P	P	P	P	P	P	P	P	P	P	P											P



Table 8.6 - Classification of Mantoverde samples based on analysis of NIR spectra for splits A1, targeted at discriminating both calcite and muscovite as waste. Where P = Product and W = Waste.

Sample ID	Number of spectra	Classification
1	24	P
2	24	P
3	27	P
4	29	P
5	26	P
6	21	P
7	28	P
8	25	P
9	30	P
10	26	P
11	20	P
12	27	P
13	25	P
14	25	P
15	26	W
16	25	W
17	28	W
18	25	W
19	26	P
20	20	W
21	20	P
22	29	W
23	22	W
24	24	P
25	26	P
26	24	P
27	32	W
28	37	W
29	24	W
30	24	W
31	28	W
32	25	W
33	21	W
34	20	W
35	30	W
36	25	W
37	20	W
38	24	W
39	21	W
40	30	W
41	21	W
42	28	P
43	38	P
44	22	W
45	31	W
46	18	W
47	30	W
48	24	P
49	24	P
50	26	W
51	25	P
52	24	P
53	26	W
54	27	P
55	29	W
56	28	P
57	29	W
58	17	P
59	24	P
60	27	P

Since copper by itself does not exhibit any absorption feature(s) within the NIR region used (Iyakwari et al., 2013), NIR is used here as a qualitative tool for determining the presence or absence of  $\text{CO}_3^{2-}$  and -OH bearing minerals. Quantitative data are provided by PXRF and QEMSCAN<sup>®</sup> for better discussion and correlation.

#### **8.4.1.1. Validation/comparison of splits B1**

A comparison of the NIR (Table 8.4), mineralogical based classification (MIN) (Fig. 4.4 and Table 4.9), QEMSCAN<sup>®</sup> back calculated Cu values (QEM) (Tables 4.2 and 4.9) and PXRF (PX) (Table 4.11) is presented in Table 8.7. Thirty nine samples (including the five middlings samples (samples 10, 11, 13, 19 and 52) requiring further liberation) (65 % of total samples) were classified as product particles with the NIR.

Based on a copper concentration cut-off grade of 0.5 % and above, using the QEMSCAN<sup>®</sup> back calculated Cu values (QEM), twenty three samples (38 % of total samples) were classified as product. Using the PX, based on copper concentration of 0.5 % and above, twenty two samples (37 % of total samples) are classified as product. While based on mineralogy (functional groups) (MIN), seventeen samples were classified as product (28 % of total samples) (Table 8.7).

On a 1:1 comparison of NIR and QEM classifications, only five samples (24, 35, 47, 55 and 57) that are classified as waste by the NIR but product by QEM have copper concentration above 0.5 %. Also, nineteen samples (6, 7, 13, 22, 23, 25, 30, 31, 34, 37, 38, 39, 40, 41, 44, 45, 52, 58, and 59) classified as product by the NIR but wastes by QEM have copper concentration below 0.5 %. Samples 6, 7, 13, 52, 58 and 59 are classified as products by NIR because of their high hematite content resulting in their featureless spectra. Samples 22, 30, 34, 37, 38, 39, 40, 44 and 45 are classified as products because their spectra showed features corresponding to either chlorite/chrysocolla or biotite. While spectra of samples 23, 25, 31, and 41, appeared featureless across wavelengths with a broad depression at longer wavelength lacking absorption centres. This is due to their complex mineral associations: biotite-chlorite (sample 23), biotite-chlorite-calcite (samples 25, 41) and biotite-chlorite-hematite (sample 31).

Given the lack of any absorption feature(s) to indicate any mineral(s) the samples were classified as product.

The five samples classified as waste by NIR but products by QEM strategy show absorption features diagnostic of either or both calcite and muscovite. Samples 24, 55 and 57 showed muscovite features near 2210 nm while samples 35 and 47 showed calcite features near 2340 nm (Table 8.1). Mineralogically samples 24, 55 and 57 have muscovite concentration at 21.55 wt %, 18.87 wt % and 9.90 wt % respectively, with samples 55 and 57 also containing calcite at 12.98 wt % and 17.08 wt %. Samples 35 and 47 have calcite concentrations at 27.02 wt % and 22.64 wt % respectively (Table 4.1). Hence they were classified as waste by NIR since their waste mineral content showed stronger absorption features than their product minerals concentration.

NIR and PX classification also provided good results. Eighteen out of the twenty two samples classified as product by PX are also classified as product by NIR, (i.e. 82 % of total PX products samples). Hence, only four (samples 14, 35, 55, and 57) of the samples classified as product by PX were classified as waste by NIR (i.e. 18 % of the total PX product). Three of the four NIR waste samples (samples 35, 55 and 57) are classified by both PX and QEM as products because they are calibrated to classify sample based on copper content. The QEM is not in agreement with the PX on sample 14 as it classified the sample as waste just like NIR. This is because both techniques (QEM and PX) differ in the sample's copper content, with the PX overestimating the Cu content in the particle (Table 8.7). NIR classified sample 14 as waste because it shows muscovite features.

Comparison of NIR and mineralogy classification (MIN) indicates that of the seventeen samples classified as product by MIN strategy, sixteen are also classified product by NIR. Hence, only one sample (sample 24) is classified as waste by NIR. This classification indicates a 1:1 correlation for both techniques except for sample 24. This is true since both strategies are based on sample NIR-active minerals functional group(s) content. But while the MIN strategy considered bulk functional group(s) per sample not taking into account specific or individual minerals responsible, NIR considers individual spectrum on the basis of the mineral(s) responsible for the absorption feature(s) they display.

Hence, sample 24 is classified as waste by NIR because its spectra showed muscovite features (Table 8.1). The NIR classified twenty three extra samples as products either due to their individual features indicating chlorite/chrysocolla or biotite which are all -OH bearing or spectra appeared featureless.

Of all the NIR-active -OH bearing minerals in the Mantoverde copper ore, biotite contains the least -OH content (7.84 %) closely followed by muscovite (8.53 %). Muscovite displays strong absorption features in comparison to minerals like chrysocolla and chlorite that contain 20.71 % and 22.85 % -OH respectively. Therefore, while sample 24 only contains a total of 2.77 % of -OH as bulk, which is within the accepted -OH cut-off grade used in developing mineralogy strategy (section 4.4.2), the bulk of the -OH is contributed by muscovite which has a concentration of 21.55 wt. % (contributing approximately 1.8 % -OH) occurring as the dominant NIR-active mineral in the particle.

Note that though kaolinite is not high in concentration in samples of the Mantoverde ore, the NIR classification strategy is developed to accommodate for kaolinite and other clay minerals since they share similar features position especially the 2200, 2210, 2215 or 2220 nm features selected for waste discrimination.

Also from NIR classification all samples with hematite concentration ( $\geq 10$  wt. %) classified either as product or middlings. With the exception of samples 14 and 21, which are further classified as waste due to their dominant waste spectra, all hematite-rich middling are classified as product (Tables 4.1 and 8.4).

Detailed comparison of mineralogical strategy and QEMSCAN<sup>®</sup> copper content is provided in chapter four (section 4.6).

Table 8.7 - Comparison of classification of splits B1 particles. Strategy one, based on the NIR, QEMSCAN® (QEM), PXRF (PX) and Mineralogy (MIN). The copper content (QEM) calculated from Cu-bearing minerals as analysed by QEMSCAN® and obtained from XRF analysis (PX). P and W indicate product and waste, respectively.

Sample ID	Cu Content (QEM) %	Cu Content (PX) %	Classification			
			NIR	Qem	PX	MIN
1	2.83	1.61	P	P	P	P
2	6.46	2.59	P	P	P	P
3	7.33	7.74	P	P	P	P
4	1.75	1.37	P	P	P	P
5	1.70	1.77	P	P	P	P
6	0.41	0.58	P	W	P	W
7	0.05	0.12	P	W	W	W
8	1.90	0.61	P	P	P	P
9	2.28	1.89	P	P	P	W
10	3.55	1.05	P	P	P	P
11	3.15	3.93	P	P	P	P
12	2.34	1.98	P	P	P	P
13	0.00	0.03	P	W	W	W
14	0.40	0.97	W	W	P	W
15	0.00	0.03	W	W	W	W
16	0.14	0.12	W	W	W	W
17	1.41	0.72	P	P	P	P
18	0.09	0.04	W	W	W	W
19	0.15	0.32	P	W	W	W
20	0.36	0.12	P	W	W	W
21	0.02	0.10	W	W	W	W
22	0.03	0.03	P	W	W	W
23	0.02	0.04	P	W	W	W
24	0.80	0.15	W	P	W	P
25	0.12	0.13	P	W	W	W
26	1.81	2.02	P	P	P	P
27	0.00	0.02	W	W	W	W
28	0.92	0.75	P	P	P	P
29	0.07	0.06	W	W	W	W
30	0.03	0.07	P	W	W	W
31	0.09	0.09	P	W	W	W
32	1.23	0.34	P	P	W	P
33	0.00	0.02	W	W	W	W
34	0.07	0.05	P	W	W	W
35	1.71	2.16	W	P	P	W
36	0.01	0.03	W	W	W	W
37	0.28	0.17	P	W	W	W
38	0.06	0.22	P	W	W	W
39	0.33	0.16	P	W	W	W
40	0.30	0.15	P	W	W	W
41	0.00	0.04	P	W	W	W
42	0.09	0.11	W	W	W	W
43	0.01	0.08	W	W	W	W
44	0.05	0.08	P	W	W	W
45	0.18	0.11	P	W	W	W
46	0.04	0.08	W	W	W	W
47	0.54	0.27	W	P	W	W
48	1.40	1.44	P	P	P	P
49	0.14	0.09	W	W	W	W
50	11.54	4.08	P	P	P	P
51	1.00	1.49	P	P	P	W
52	0.01	0.14	P	W	W	W
53	0.01	0.05	W	W	W	W
54	0.06	0.35	W	W	W	W
55	3.28	7.64	W	P	P	W
56	0.05	0.05	W	W	W	W
57	2.77	4.87	W	P	P	W
58	0.00	0.05	P	W	W	W
59	0.03	0.20	P	W	W	W
60	1.98	1.96	P	P	P	P

#### **8.4.1.2. Validation/comparison of splits B2**

As earlier stated, the NIR range used for the study does not sense samples on elemental basis. Therefore, to calibrate the applicability of classification strategy, particles of splits B2 (Fig. 3.1) were scanned with the NIR (Tables 8.2). The classification strategy as shown in Figure 8.2 was used to classify samples (Table 8.5). The PX data (Table 4.12) was used to compare the classification (Table 8.8).

Forty one samples were classified by NIR as product, while PX classified thirty five samples as products using a Cu cut-off grade of 0.5 %. Using the MIN strategy (Fig. 4.4), seventeen samples were classified as product (Table 4.9).

Twenty nine of the thirty five PX product samples were also classified as product by NIR (i.e. 83 % of total PX product samples). Therefore only six samples (samples 9, 18, 35, 54, 55 and 57) classified as product by PX are classified as waste by NIR. The NIR spectra of samples 18, 54 and 55 shows only muscovite features, sample 35 shows only calcite features while sample 9, and 57 shows both muscovite and calcite features (Table 8.2).

On a 1:1 comparison between NIR and MIN classifications strategy, Table 8.8 shows that of the seventeen samples classified by mineralogical strategy as product, only one sample (sample 24) is classified by NIR as waste. This classification is a repeat of splits B1 (Table 8.7), and spectra of sample also shows muscovite features.

Only two of the seventeen product samples (samples 24 and 48) as classified based on mineralogy are shown by PX to contain Cu grade below 0.5 %, indicating that fifteen samples have their Cu grade within or above the cut-off grade (Table 8.8). NIR initially classified sample 48 as middling, as six (46 % of spectra) out of its thirteen spectra show features diagnostic of both calcite and muscovite (Table 8.2). Final classification indicates the sample contains more product spectra which means it is classified as product but requires further liberation (Table 8.5).

Table 8.8 - Comparison of classification of splits B2 particles. Strategy one, based on the NIR, Mineralogy (MIN), and PXRF (PX). The copper content obtained from XRF analysis (PX). P and W indicate product, and waste, respectively.

Sample ID	Cu Content (PX) %	Classification		
		PX	NIR	MIN
1	4.40	P	P	P
2	4.06	P	P	P
3	5.78	P	P	P
4	1.87	P	P	P
5	1.77	P	P	P
6	0.71	P	P	W
7	2.93	P	P	W
8	1.13	P	P	P
9	2.71	P	W	W
10	10.95	P	P	P
11	8.91	P	P	P
12	0.85	P	P	P
13	0.03	W	W	W
14	1.52	P	P	W
15	0.03	W	W	W
16	1.31	P	P	W
17	2.04	P	P	P
18	4.39	P	W	W
19	0.61	P	P	W
20	0.65	P	P	W
21	0.17	W	P	W
22	0.62	P	P	W
23	2.58	P	P	W
24	0.14	W	W	P
25	0.33	W	W	W
26	0.88	P	P	P
27	0.05	W	W	W
28	0.30	W	P	P
29	0.09	W	W	W
30	0.15	W	P	W
31	0.46	W	P	W
32	0.88	P	P	P
33	0.07	W	P	W
34	0.21	W	P	W
35	2.13	P	W	W
36	0.14	W	P	W
37	1.42	P	P	W
38	0.69	P	P	W
39	0.16	W	P	W
40	1.78	P	P	W
41	0.03	W	P	W
42	0.25	W	W	W
43	1.31	P	P	W
44	5.88	P	P	W
45	2.01	P	P	W
46	0.11	W	W	W
47	0.17	W	W	W
48	0.43	W	P	P
49	0.31	W	W	W
50	3.87	P	P	P
51	0.67	P	P	W
52	0.11	W	W	W
53	0.09	W	W	W
54	0.65	P	W	W
55	3.93	P	W	W
56	0.17	W	W	W
57	1.02	P	W	W
58	0.09	W	P	W
59	0.18	W	P	W
60	1.97	P	P	P

#### **8.4.1.3 Validation/comparison of splits A1**

Splits A1 samples are powdered samples ground to  $-45\ \mu\text{m}$  and homogeneously mixed together before scanning. Therefore, the NIR spectra produced appeared similar, showing absorption features at similar locations per sample. So, NIR spectra are only classified as either product or waste based on the minerals responsible for the feature (Table 8.3). NIR classification is compared with Bulk PXRF (BPX) data (Table 4.10) and classification based on mineralogical strategy (MIN) (Fig. 4.4 and Table 4.9).

Comparison of classification indicates that the NIR classified thirty samples as products. The BPX classified twenty one samples as products while only seventeen samples are classified based MIN as products (Table 8.9). Of the twenty one BPX product samples, fifteen are also classified by NIR as product (71 % of the total BPX product samples) while only six samples (samples 28, 32, 35, 50, 55 and 57) are classified by NIR as waste. Spectra of samples 28, 32, 50 and 35 show calcite features while samples 55 and 57 showed muscovite features (Table 8.3).

Fourteen of the seventeen samples classified based on MIN as products contain Cu above 0.5 % as indicated by BPX, while only three samples (samples 17, 26 and 48) contain Cu below the BPX cut-off grade. Also only four of the seventeen MIN product samples (samples 17, 28, 32, and 50) were classified by NIR as waste. NIR spectra of samples 17, 28, 32 and 50 show calcite features near 2340 or 2345, hence classified as waste (Table 8.6).



Table 8.9 - Comparison of classification of splits A1 samples. NIR strategy targeted at discriminating both calcite and muscovite as waste. Where NIR = Near InfraRed, MIN = Mineralogy, and PX = PXRF. The copper content obtained from Bulk XRF analysis (BPX). P and W indicate product, and waste, respectively.

Sample ID	Cu Content (PX) %	Classification		
		NIR	BPX	MIN
1	1.30	P	P	P
2	2.31	P	P	P
3	3.20	P	P	P
4	1.40	P	P	P
5	0.77	P	P	P
6	1.33	P	P	W
7	0.14	P	W	W
8	1.51	P	P	P
9	2.82	P	P	W
10	8.66	P	P	P
11	8.91	P	P	P
12	1.85	P	P	P
13	0.18	P	W	W
14	0.49	P	W	W
15	0.03	W	W	W
16	0.35	W	W	W
17	0.34	W	W	P
18	0.13	W	W	W
19	0.25	P	W	W
20	0.18	W	W	W
21	0.09	P	W	W
22	0.08	W	W	W
23	0.09	W	W	W
24	3.30	P	P	P
25	0.74	P	P	W
26	0.45	P	W	P
27	0.02	W	W	W
28	0.73	W	P	P
29	0.10	W	W	W
30	0.24	W	W	W
31	0.22	W	W	W
32	0.89	W	P	P
33	0.03	W	W	W
34	0.21	W	W	W
35	0.89	W	P	W
36	0.06	W	W	W
37	0.12	W	W	W
38	0.22	W	W	W
39	0.14	W	W	W
40	0.44	W	W	W
41	0.05	W	W	W
42	0.11	P	W	W
43	0.13	P	W	W
44	0.21	W	W	W
45	0.11	W	W	W
46	0.16	W	W	W
47	0.46	W	W	W
48	0.36	P	W	P
49	0.13	P	W	W
50	2.08	W	P	P
51	1.39	P	P	W
52	0.14	P	W	W
53	0.09	W	W	W
54	0.23	P	W	W
55	3.03	W	P	W
56	0.33	P	W	W
57	2.28	W	P	W
58	0.07	P	W	W
59	0.19	P	W	W
60	4.44	P	P	P

## 8.5. Analysis and evaluation of the discrimination results

Ore parameters for each split are calculated based on assumptions that their total mass is 100 % and the mass of each sample is same (1/60).

### 8.5.1. Splits B1

Near Infrared (NIR), QEMSCAN<sup>®</sup> (QEM), Mineralogy (MIN) and PXRF (PX) classification of sixty samples is presented in Tables 8.4 and 8.7. The product concentrate consists of thirty nine samples for the NIR, twenty three for the QEM, seventeen based on MIN and twenty two for PX. Hence, the yield of NIR product is  $\gamma_{\text{NIR}}$  65 %,  $\gamma_{\text{Qem}}$  38 % for QEM,  $\gamma_{\text{MIN}}$  28 % based on MIN and  $\gamma_{\text{PX}}$  37 % for PX (Tables 8.10 and 8.11).

Using QEMSCAN<sup>®</sup> data (Tables 4.1 and 8.7), the calculated recoveries of copper in the product are: 85 % for NIR, 94 % for QEM and 77 % for MIN. The feed grade of copper in sixty samples is 1.12 %. The copper concentrate in the product fraction is 1.47 %, 2.77 % and 3.06 % for NIR, QEM and MIN respectively. The content of copper in waste is higher for NIR at 0.49 % and 0.36 % for MIN, while QEM has the least at 0.1 %, (Table 8.10).

Table 8.10 - Discrimination results of Mantoverde copper ore particles (splits B1) for NIR, MIN, and QEM. Using copper content calculated from QEMSCAN<sup>®</sup>

	NIR	QEM	MIN
Content of copper in feed, %	1.12	1.12	1.12
Content of copper in product, %	1.47	2.77	3.06
Content of copper in waste, %	0.49	0.10	0.36
Recovery of Cu in product, %	85	94	77
Yield of product, %	65	38	28

Using the PX data, the calculated recoveries of copper in the products are 70 % for NIR and 93 % for PX and 59 % for MIN. The feed grade in the sixty samples is 0.96 %. The content of copper in product fraction for NIR is 1.03 %, 2.42 % for PX and 2 % for MIN. Also similar to using the QEMSCAN<sup>®</sup> calculated Cu values (Table 8.10) both NIR and MIN have the highest values of copper in waste material at 0.82 % and 0.54 % respectively, which is above cut-off grade, while the PXRF has 0.11 % (Table 8.11).

Table 8.11 - Discrimination results of Mantoverde copper ore particles (splits B1) for NIR, MIN and PX classifications. Using copper content measured by PX

	NIR	PX	MIN
Content of copper in feed, %	0.96	0.96	0.96
Content of copper in product, %	1.03	2.42	2.00
Content of copper in waste, %	0.82	0.11	0.54
Recovery of Cu in product, %	70	93	59
Yield of product, %	65	37	28

Using data from Bulk XRF (BPX) (Table 8.12), the calculated feed grade is 1.02 %. Recovery of copper is 80 % for NIR, 88 % for BPX and 69 % for MIN, at copper grade of 1.25, 2.56 and 2.50 % respectively. Using BPX data gives better recovery for NIR and MIN than the comparison with surface PX, with an improvement of 10 %. This is a sample liberation and depth of penetration issue. While BPX was measured on liberated powdered samples, the PX data was obtained on solid unliberated samples.

Table 8.12 - Discrimination results of Mantoverde copper ore particles (splits B1) for NIR, MIN and Bulk PXRF (BPX) classifications. Using copper content measured on powdered samples by BPXRF

	NIR	BPX	MIN
Content of copper in feed, %	1.02	1.02	1.02
Content of copper in product, %	1.25	2.56	2.50
Content of copper in waste, %	0.59	0.19	0.43
Recovery of Cu in product, %	80	88	69
Yield of product, %	65	35	28

The calculated results indicate that copper recovery is higher for QEM, PX and BPX products than NIR and MIN products. This is true because QEM, PX and BPX are calibrated to sense copper ( $\geq 0.5$  % as products), while NIR and MIN are calibrated to sense copper-bearing minerals and upgrade the ore by eliminating particles containing waste material (both calcite and muscovite). Therefore, the copper lost to waste by NIR is contained (locked) in particles rich in calcite and or muscovite (clays).

### 8.5.2. Splits B2

The NIR, Mineralogical based (MIN), and PXRF (PX) classification of the sixty splits B2 particles is presented in Table 8.8. Product concentrates consist of 41 samples for NIR, 17 for MIN, and 35 for PX. Hence, the yield of NIR products is  $\gamma_{\text{NIR}}$  68 %, MIN is  $\gamma_{\text{MIN}}$  28 %, while yield for PX is  $\gamma_{\text{PX}}$  58 % (Table 8.13).

The calculated recoveries of copper in the products are: 68 % for NIR, 54 % for MIN, and 95 % for PX. The content of copper in the feed in the sixty samples is 1.55 %. The copper content in the product is 1.87 % for NIR, 2.95 % for MIN, and 2.54 % for PX. All strategies contain Cu grade above the feed grade. But the copper lost to waste for both NIR and MIN strategy is above the cut-off grade, meaning copper is locked in samples containing muscovite and or calcite.

Table 8.13 - Discrimination results of Mantoverde copper ore particles (splits B2) for NIR, MIN, and PX classifications. Copper content measured by PXRF

	NIR	PX	MIN
Content of copper in feed, %	1.55	1.55	1.55
Content of copper in product, %	1.87	2.54	2.95
Content of copper in waste, %	0.88	0.17	0.99
Recovery of Cu in product, %	82	95	54
Yield of product, %	68	58	28

Using data from Bulk XRF (BPX) (Table 8.14), the calculated feed grade is 1.02 %. Recovery for copper is 80 % for NIR, 88 % for BPX and 69 % for MIN, at copper grade of 1.12, 2.56 and 2.50 % respectively. Using BPX gives better recovery for MIN than the comparison with surface XRF (PX) with an improvement from 54 % to 69 %, while there is a 2 % drop for NIR. Unlike Table 8.13, where both NIR and MIN had copper reporting to waste above cut-off grade, only NIR shows copper above cut-off grade reporting to waste.

Table 8.14 - Discrimination results of Mantoverde copper ore samples (splits B2) for NIR, MIN and BPX classifications. Using copper content measured on powdered samples by BPXRF

	NIR	BPX	MIN
Content of copper in feed, %	1.02	1.02	1.02
Content of copper in product, %	1.12	2.56	2.50
Content of copper in waste, %	0.80	0.19	0.43
Recovery of Cu in product, %	80	88	69
Yield of product, %	68	35	28

### 8.5.2. Splits A1

The NIR, MIN, and BPX classification of the sixty splits A1 samples is presented in Table 8.9. Product concentrates consist of 30 samples for NIR, 17 for MIN, and 21 for BPX. The yield of NIR products is  $\gamma_{\text{NIR}}$  50 %, MIN is  $\gamma_{\text{MIN}}$  28 %, while BPX is  $\gamma_{\text{BPX}}$  35 %.

The calculated recoveries of copper in the products are: 77 % for NIR, 69 % for MIN, and 85 % for BPX. The content copper in the feed in the sixty samples is 1.02 %. The copper content in the product is 1.57 % for NIR, 2.46 % for MIN, and 2.50 % for BPX. All strategies have copper content reporting to waste below the cut-off grade of 0.5 %.

Table 8.15 - Discrimination results of Mantoverde copper ore samples (splits A1) for NIR, MIN, and bulk BPX classifications. Using copper content measured on powdered samples by BPX

	NIR	BPX	MIN
Content of copper in feed, %	1.02	1.02	1.02
Content of copper in product, %	1.57	2.46	2.50
Content of copper in waste, %	0.47	0.24	0.43
Recovery of Cu in product, %	77	85	69
Yield of product, %	50	35	28

### 8.6. Reconciliation of NIR classification per splits, for strategy one

NIR classifications of the various splits differ from one another, despite the fact that the individual splits (splits A1, B1 and B2) are of the same particles. Splits B1 consist of thirty nine product and twenty one waste samples, splits B2 has forty one product and nineteen waste while splits A1 classified thirty product and thirty waste (Table 8.16).

Of the thirty nine splits B1 product samples, only four samples (samples 9, 13, 25 and 52) are classified as waste by splits B2. Six of the forty one splits B2 product samples (samples 14, 16, 21, 33, 36 and 43) are waste for splits B1. Seventeen of the splits B1 product samples (samples 17, 20, 22, 23, 28, 30, 31, 32, 34, 37, 38, 39, 40, 41, 44, 45, and 50) are classified as waste in splits A1. However, only eight splits A1 samples (samples 14, 21, 24, 42, 43, 49, 54 and 56) are waste by splits B1 (Table 8.16).

Twenty of the forty one split B2 product samples (sample 16, 17, 20, 22, 23, 28, 30, 31, 32, 33, 34, 36, 37, 38, 39, 40, 41, 44, 45 and 50) are classified waste by splits A1. This is a repeat of the comparison of splits A1 against B1, except for the additional three samples (samples 16, 33 and 36). Analysis indicates that only nine of splits A1 product samples (samples 9, 12, 24, 25, 42, 49, 52, 54 and 56) are waste by splits B2 (Table 8.16).

Therefore, while there is less variation in classification between the solid samples (splits B1 and B2): almost fifty percent of samples classified product by either splits B1 or B2 are wastes for splits A1. Classification variation between the individual splits is a result of sample variation since measurement is made on different sub-samples, therefore the variation is expected. In addition, for the powdered samples, classification variation is also due to the sample nature/mode, as the powdered samples were made homogenous by mixing the samples and the spectra reflect this complex mixture.

Table 8.16 - Comparison of splits A1, B1 and B2 NIR classifications,  
 Where: P and W indicate product, and waste, respectively.

Sample ID	NIR Classification		
	Splits B1	Splits B2	Splits A1
1	P	P	P
2	P	P	P
3	P	P	P
4	P	P	P
5	P	P	P
6	P	P	P
7	P	P	P
8	P	P	P
9	P	W	P
10	P	P	P
11	P	P	P
12	P	P	P
13	P	W	P
14	W	P	P
15	W	W	W
16	W	P	W
17	P	P	W
18	W	W	W
19	P	P	P
20	P	P	W
21	W	P	P
22	P	P	W
23	P	P	W
24	W	W	P
25	P	W	P
26	P	P	P
27	W	W	W
28	P	P	W
29	W	W	W
30	P	P	W
31	P	P	W
32	P	P	W
33	W	P	W
34	P	P	W
35	W	W	W
36	W	P	W
37	P	P	W
38	P	P	W
39	P	P	W
40	P	P	W
41	P	P	W
42	W	W	P
43	W	P	P
44	P	P	W
45	P	P	W
46	W	W	W
47	W	W	W
48	P	P	P
49	W	W	P
50	P	P	W
51	P	P	P
52	P	W	P
53	W	W	W
54	W	W	P
55	W	W	W
56	W	W	P
57	W	W	W
58	P	P	P
59	P	P	P
60	P	P	P

## 8.7. Strategy two

The second strategy assumes chrysocolla is the only copper bearing mineral in the ore and it is associated with muscovite, with little or no hematite. This assumption is made based on the fact that chrysocolla is more NIR-active than malachite when they occur together, while muscovite and chrysocolla spectral dominance is concentration dependent. Hence, where muscovite is higher in concentration than chrysocolla, chrysocolla absorption features may not be visible in spectra.

Therefore, a product spectrum will be differentiated from a waste spectrum by an absorption feature near 2335, and/or 2340 and/or 2345 nm diagnostic of calcite. On this basis individual spectrum shall be classified as:

- a. Waste - spectrum displaying features of calcite. This spectrum may in addition contain little or no chrysocolla and muscovite. This group is defined by features near 2335, 2340 and 2345 nm for calcite. This is, since the visibility of calcite features defines calcite concentration relative to other NIR-active minerals in a spectrum.
- b. Product - spectrum not showing calcite features. In addition to this group is a featureless spectrum.

Therefore, individual Mantoverde ore particles shall be classified into three groups as:

- i. Waste - samples with all spectra showing calcite characteristics absorption features.
- ii. Products - samples with all spectra not displaying calcite absorption features.
- iii. Middlings - samples with spectra containing individual spectrum of both waste and product groups.

Figure 8.3 presents a diagrammatical chart showing the modified preconcentration strategy as outlined above, and henceforth referred to as the second strategy.

As earlier stated, for the sake of this research, any sample containing above 50 % either product or waste spectra, in addition to classification as middling will be classified on the basis of the dominant or majority spectra group as either



product or waste. But where a sample contains 50-50 % waste and product spectra, the sample shall be classified as waste. This is not dependent on Cu cut-off grade since NIR does not sense Cu.

Applying the second strategy (Fig. 8.3) to the various splits with respect to Tables 8.1, 8.2 and 8.3, individual particle classifications are presented in Tables 8.17, 8.18 and 8.19.

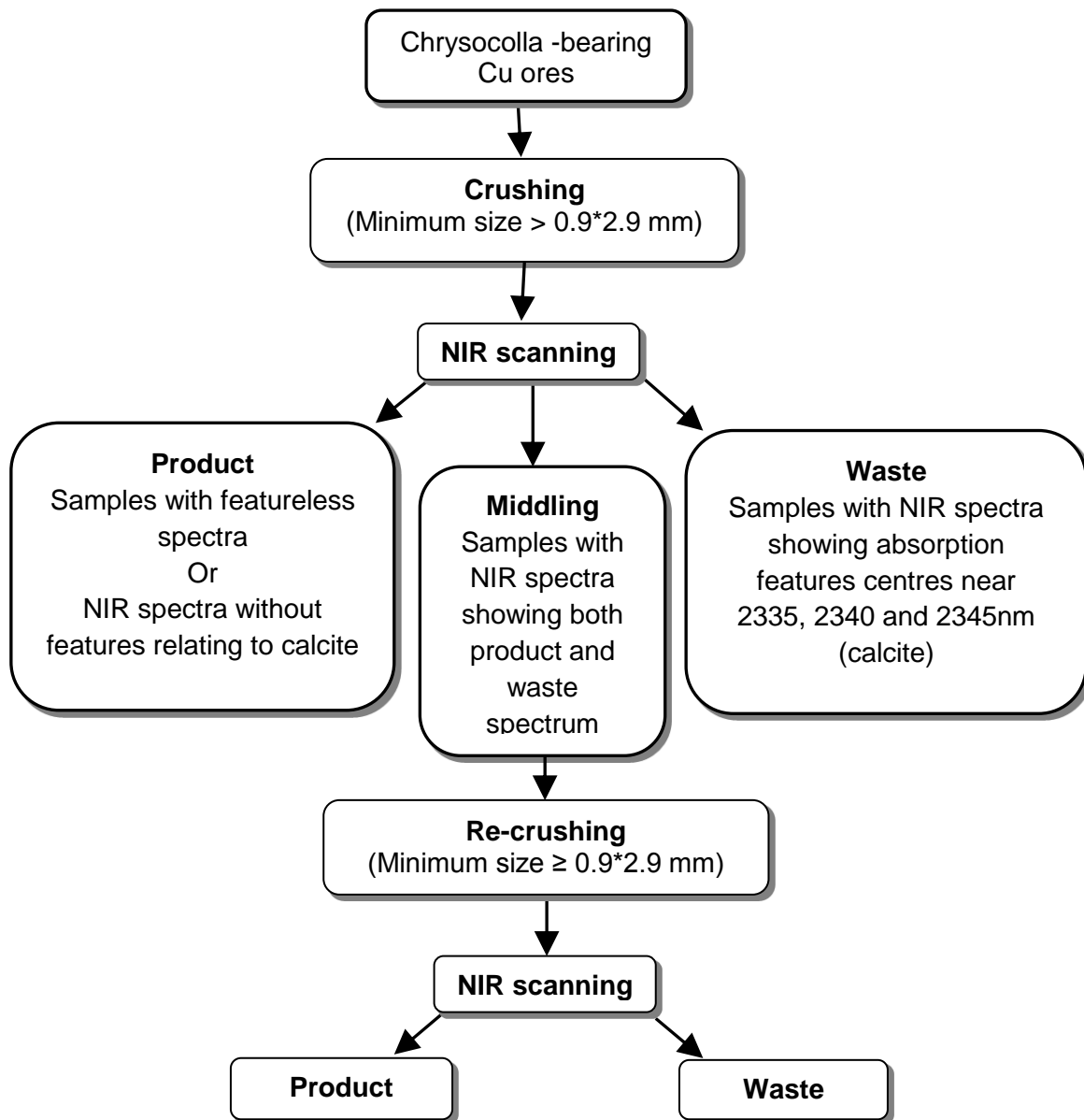


Figure 8.3 - Mantoverde copper samples classification strategy targeted at eliminating only calcite-bearing samples as waste (modified from Iyakwari et al., 2013, Iyakwari and Glass, 2015)

Table 8.17 - Classification of Mantoverde particles based on analysis of NIR spectra for splits B1. NIR strategy targeted at calcite elimination only as waste. Where P = Product and W = Waste, M- = Middling with ≤ 50 % waste spectrums and M\* = Middling with > 50 % product spectrums.

Sample ID	Sector A									Sector B									Sector C									NIR Classification		
	1	2	3	4	5	6	7	8	9	1	2	3	4	5	6	7	8	9	1	2	3	4	5	6	7	8	9			
1	P	P	P	P	P	P	P	P		P	P	P	P	P	P	P	P		P	P	P	P	P	P	P	P	P	P		P
2	P	P	P	P	P	P	P	P		P	P	P	P	P	P	P	P		P	P	P	P	P	P	P	P	P	P		P
3	P	P	P	P	P	P	P	P		P	P	P	P	P	P	P	P	P		P	P	P	P	P	P	P	P	P		P
4	P	P	P	P	P	P	P	P		P	P	P	P	P	P	P	P		P	P	P	P	P	P	P	P	P	P		P
5	P	P	P	P	P	P	P	P		P	P	P	P	P	P	P	P		P	P	P	P	P	P	P	P	P	P		P
6	P	P	P	P	P	P	P	P		P	P	P	P	P	P	P	P		P	P	P	P	P	P	P	P	P	P		P
7	P	P	P	P	P	P	P	P		P	P	P	P	P	P	P	P		P	P	P	P	P	P	P	P	P	P		P
8	P	P	P	P	P	P	P	P		P	P	P	P	P	P	P	P		P	P	P	P	P	P	P	P	P	P		P
9	P	P	P	P	P	P	P	P		P	P	P	P	P	P	P	P		P	P	P	P	P	P	P	P	P	P		P
10	P	P	P	P	P	P	P	P		P	P	P	P	P	P	P	P		P	P	P	P	P	P	P	P	P	P		P
11	P	P	P	P	P	P	P	P		P	P	P	P	P	P	P	P	P		P	P	P	P	P	P	P	P	P		P
12	P	P	P	P	P	P	P	P		P	P	P	P	P	P	P	P	P		P	P	P	P	P	P	P	P	P		P
13	P	P	P	P	P	P	P	P		P	P	P	P	P	P	P	P		P	P	P	P	P	P	P	P	P	P		P
14	P	P	P	P	P	P	P	P		P	P	P	P	P	P	P	P		P	P	P	P	P	P	P	P	P	P		P
15	P	P	P	P	P	P	P	P		P	P	P	P	P	P	P	P		P	P	P	P	P	P	P	P	P	P		P
16	W	W	W	W	W					P	W	W	P	P	W	W	P	P		P	W	P	P	W	W	W	P	P		M-(W)
17	P	P	P	P	P	P				P	P	P	P	P	P	P	P		P	P	P	P	P	P	P	P	P	P		P
18	P	P	P	P	P	P	P	P		P	P	P	P	P	P	P	P		P	P	P	P	P	P	P	P	P	P		P
19	P	P	P	P	P	P	P	P		P	P	P	P	P	P	P	P		P	P	P	P	P	P	P	P	P	P		P
20	P	P	P	P	P	P	P	P		P	P	P	P	P	P	P	P		P	P	P	P	P	P	P	P	P	P		P
21	P	P	P	P	P	P	P	P		P	P	P	P	P	P	P	P		P	P	P	P	P	P	P	P	P	P		P
22	P	P	P	P	P	P	P	P		P	P	P	P	P	P	P	P		P	P	P	P	P	P	P	P	P	P		P
23	P	P	P	P	P	P	P	P		P	P	P	P	P	P	P	P		P	P	P	P	P	P	P	P	P	P		P
24	P	P	P	P	P	P	P	P		P	P	P	P	P	P	P	P		P	P	P	P	P	P	P	P	P	P		P
25	P	P	P	P	P	P	P	P		P	P	P	P	P	P	P	P		P	P	P	P	P	P	P	P	P	P		P
26	P	P	P	P	P	P	P	P		P	P	P	P	P	P	P	P		P	P	P	P	P	P	P	P	P	P		P
27	P	P	P	P	P	P	P	P		P	P	P	P	P	P	P	P		P	P	P	P	P	P	P	P	P	P		P
28	P	P	P	P	P	P	P	P		P	P	P	P	P	P	P	P		P	P	P	P	P	P	P	P	P	P		P
29	P	P	P	P	P	P	P	P		P	P	P	P	P	P	P	P		P	P	P	P	P	P	P	P	P	P		P
30	P	P	P	P	P	P	P	P		P	P	P	P	P	P	P	P		P	P	P	P	P	P	P	P	P	P		P
31	P	P	P	P	P	P	P	P		P	P	P	P	P	P	P	P		P	P	P	P	P	P	P	P	P	P		P
32	P	P	P	P	P	P	P	P		P	P	P	P	P	P	P	P		P	P	P	P	P	P	P	P	P	P		P
33	P	P	P	P	P	P	P	P		P	P	P	P	P	P	P	P		P	P	P	P	P	P	P	P	P	P		P
34	P	P	P	P	P	P	P	P	P		P	P	P	P	P	P	P		P	P	P	P	P	P	P	P	P	P		P
35	P	P	W	W	P	W	W	P		P	W	W	W	W	W	W	P		P	P	W	W	W	W	W	W	P		M-(W)	
36	P	P	P	P	P	P	P	P		P	P	P	P	P	P	P	P		P	P	P	P	P	P	P	P	P		P	
37	P	P	P	P	P	P	P	P		P	P	P	P	P	P	P	P		P	P	P	P	P	P	P	P	P		P	
38	P	P	P	P	P	P	P	P		P	P	P	P	P	P	P	P		P	P	P	P	P	P	P	P	P		P	
39	P	P	P	P	P	P	P	P		P	P	P	P	P	P	P	P		P	P	P	P	P	P	P	P	P		P	
40	P	P	P	P	P	P	P	P		P	P	P	P	P	P	P	P		P	P	P	P	P	P	P	P	P		P	



Table 8.18 - Classification of Mantoverde particles based on analysis of NIR spectra for splits B2. NIR strategy targeted at calcite elimination only as waste. Where P = Product and W = Waste, M- = Middling with  $\leq 50\%$  waste spectra and M\* = Middling with  $> 50\%$  product spectra.

Sample ID	1	2	3	4	5	6	7	8	9	10	11	12	13	14	15	16	17	18	19	20	21	22	23	24	25	26	27	28	29	30	NIR Classification		
1	P	P	P	P	P	P	P	P	P	P	P																				P		
2	P	P	P	P	P	P	P	P	P	P	P	P	P	P																	P		
3	P	P	P	P	P	P	P	P	P	P	P	P	P	P	P	P	P	P	P	P	P										P		
4	P	P	P	P	P	P	P	P	P	P	P	P	P	P	P	P	P	P	P	P	P										P		
5	P	P	P	P	P	P	P	P	P	P	P	P	P	P																	P		
6	P	P	P	P	P	P	P	P	P	P	P	P	P	P	P	P	P	P	P	P	P										P		
7	P	P	P	P	P	P	P	P	P	P	P	P	P	P	P	P	P	P	P	P	P										P		
8	P	P	P	P	P	P	P	P	P	P	P	P	P	P	P	P	P	P	P	P	P										P		
9	W	W	W	W	W	W	W	W	W	W	W																				W		
10	P	P	P	P	P	P	P	P	P	P	P																				P		
11	P	P	P	P	P	P	P	P	P	P	P	P	P	P	P	P	P	P	P	P	P										P		
12	P	P	P	P	P	P	P	P	P	P	P	P	P	P	P	P															P		
13	W	W	W	W	W	W	W	W	W	W	W	W	W	W	W	W	W	W	W	W	W										M-(W)		
14	P	P	P	P	P	P	P	P	P	P	P	P	P	P	P	P	P	P	P	P	P										P		
15	P	P	P	P	P	P	P	P	P	P	P	P	P	P	P	P	P	P	P	P	P										P		
16	P	P	P	P	P	P	P	P	P	P	P																				P		
17	P	P	P	P	P	P	P	P	P	P	P	P	P	P	P	P	P	P	P	P	P										P		
18	P	P	P	P	P	P	P	P	P	P	P	P	P	P																	P		
19	P	P	P	P	P	P	P	P	P	P	P	P	P	P																	P		
20	P	P	P	P	P	P	P	P	P	P	P	P	P	P	P	P	P	P	P	P	P										P		
21	P	P	P	P	P	P	P	P	P	P	P	P	P	P	P	P	P	P	P	P	P										P		
22	P	P	P	P	P	P	P	P	P	P	P	P	P	P	P	P	P	P	P	P	P											P	
23	P	P	P	P	P	P	P	P	P	P	P	P	P	P	P	P	P	P	P	P	P											P	
24	P	P	P	P	P	P	P	P	P	P	P	P	P	P																		P	
25	W	W	W	W	W	W	W	W	W	W	W																				M-(W)		
26	P	P	P	P	P	P	P	P	P	P	P	P	P	P	P	P	P	P	P	P	P										P		
27	W	W	W	W	W	W	W	W	W	W	W	W	W	W	W	W	W	W	W	W	W											W	
28	P	P	P	P	P	P	P	P	P	P	P	P	P	P	P	P	P	P	P	P	P											P	
29	P	P	P	P	P	P	P	P	P	P	P	P	P	P	P	P	P	P	P	P	P											P	
30	P	P	P	P	P	P	P	P	P	P	P	P	P	P	P	P	P	P	P	P	P											P	
31	P	P	P	P	P	P	P	P	P	P	P	P	P	P	P	P	P	P	P	P	P											P	
32	P	P	P	P	P	P	P	P	P	P	P	P	P	P																		P	
33	P	P	P	P	P	P	P	P	P	P	P	P	P	P																		P	
34	P	P	P	P	P	P	P	P	P	P	P	P	P	P																		P	
35	W	W	W	W	W	W	W	W	W	W	W	W	W	W																		W	
36	P	P	P	P	P	P	P	P	P	P	P	P	P	P	P	P	P	P	P	P	P											P	
37	P	P	P	P	P	P	P	P	P	P	P	P	P	P	P	P	P	P	P	P	P											P	
38	P	P	P	P	P	P	P	P	P	P	P	P	P	P	P	P	P	P	P	P	P												P
39	W	W	W	P	P	P	P	P	P	P	P	P	P	P	P	P	P	P	P	P	P											M*(P)	
40	P	P	P	P	P	P	P	P	P	P	P	P	P	P	P	P	P	P	P	P	P											P	

Cont. of Table 8.18 - Classification of Mantoverde particles based on analysis of NIR spectra for splits B2. NIR strategy targeted at calcite elimination only as waste. Where P = Product and W = Waste, M- = Middling with ≤ 50 % waste spectra and M\* = Middling with > 50 % product spectra.

Sample ID	1	2	3	4	5	6	7	8	9	10	11	12	13	14	15	16	17	18	19	20	21	22	23	24	25	26	27	28	29	30	NIR Classification			
41	P	P	P	P	P	P	P	P	P	P	P	P	P																		P			
42	W	W	W	W	W	W	W	W	W	W	W	W	W	W	W	W	W	W													W			
43	P	P	W	W	W	W	P	P	P	P	P	P	P	P	P	P	P	P	P												M*(P)			
44	P	P	P	P	P	P	P	P	P	P	P	P	P	P	P	P	P	P	P	P	P	P									P			
45	P	P	P	P	P	P	P	P	P	P	P	P	P																		P			
46	W	W	W	W	W	W	W	W	W	W	W	W	W																		W			
47	W	W	W	W	W	W	W	W	W	W	W	W	W	W	W																W			
48	W	W	W	W	W	P	P	P	P	P	P	P	W																		M*(P)			
49	P	P	P	P	P	P	P	P	P	P	P	P	P																		P			
50	P	P	P	P	P	P	P	P	P	P	P	P	P	P	P	P	P	P	P	P											P			
51	P	P	P	P	P	P	P	P	P	P	P	P	P	P	P	P	P	P	P	P	P	P	P	P	P	P	P	P	P	P	P			
52	W	W	W	W	W	W	W	W	W	W	W	W	W	W	W	W	W	W	W	W	W	W	W	W	W	W	W	W	W	W	W	W		
53	W	W	W	W	W	W	W	W	W	W	W	W	W	W	W	W	W	W	W	W	W	W	W	W	W	W	W	W	W	W	W	W	W	
54	P	P	P	P	P	P	P	P	P	P	P	P	P	P	P	P	P	P	P	P	P	P	P	P	P	P	P	P	P	P	P	P	P	
55	P	P	P	P	P	P	P	P	P	P	P	P	P	P	P	P	P	P	P	P	P	P	P	P	P	P	P	P	P	P	P	P	P	
56	W	W	W	W	W	W	W	W	W	W	W	W	W	W	W	W	W	W	W	W	W	W	W	W	W	W	W	W	W	W	W	W	W	
57	W	W	W	W	W	W	W	W	W	W	W	W	W	W	W	W	W	W	W	W	W	W	W	W	W	W	W	W	W	W	W	W	W	W
58	P	P	P	P	P	P	P	P	P	P	P	P	P	P	P	P	P	P	P	P	P	P	P	P	P	P	P	P	P	P	P	P	P	P
59	P	P	P	P	P	P	P	P	P	P	P	P	P	P	P	P	P	P	P	P	P	P	P	P	P	P	P	P	P	P	P	P	P	P
60	P	P	P	P	P	P	P	P	P	P	P	P	P	P	P	P	P	P	P	P	P	P	P	P	P	P	P	P	P	P	P	P	P	P

Table 8.19 - Classification of Mantoverde samples based on analysis of NIR spectra for splits A1. NIR strategy targeted at calcite elimination only as waste. Where P = Product and W = Waste.

Sample ID	Number of spectra	Classification
1	24	P
2	24	P
3	27	P
4	29	P
5	26	P
6	21	P
7	28	P
8	25	P
9	30	P
10	26	P
11	20	P
12	27	P
13	25	P
14	25	P
15	26	P
16	25	W
17	28	W
18	25	W
19	26	P
20	20	W
21	20	P
22	29	W
23	22	W
24	24	P
25	26	P
26	24	P
27	32	P
28	37	W
29	24	W
30	24	W
31	28	W
32	25	W
33	21	P
34	20	W
35	30	W
36	25	W
37	20	W
38	24	W
39	21	W
40	30	W
41	21	W
42	28	P
43	38	P
44	22	W
45	31	W
46	18	P
47	30	W
48	24	P
49	24	P
50	26	W
51	25	P
52	24	P
53	26	P
54	27	P
55	29	P
56	28	P
57	29	P
58	17	P
59	24	P
60	27	P

## **8.8. Analysis and evaluation of the discrimination results**

Discussions in this section shall be comparatively done with respect to the earlier strategy (Fig. 8.2), aimed at discriminating both calcite and muscovite since the same data from QEM, MIN, BPX and PX are used to calculate the parameters for both strategies.

### **8.8.1. Splits B1**

Only seven samples are classified by the second strategy (Figure 8.3) as waste (Table 8.16) compared to twenty one samples classified by strategy one (Figure 8.2) as waste (Table 8.4). Hence, the product concentrate by the second strategy consists of fifty three samples. Assuming total mass of the sample is 100 % and the mass of each sample is same (1/60), Tables 8.20, 8.21 and 8.22 presents calculated ore parameters for splits B1 using copper values from QEM<sup>®</sup>, PX and BPX respectively. Also included in the tables are values calculated for the first strategy (NIR (1)) where both calcite and muscovite were targeted.

Comparatively, the second strategy shows improvement in copper recovery and overall yield. An improvement of 11 % and 23 % is achieved using copper values from QEM (Table 8.20). Also achieved is a reduction in copper content reporting to waste from 0.49 % for first strategy to 0.38 for the second strategy. The same is true for values calculated by PX and BPX. The PX shows a reduction of 50 % of the total copper reporting to waste for strategy one, with an improvement in copper recovery of 25 % (Table 8.21). The BPX values indicate 16 % improvement in recovery when compared with results of strategy one. A reduction from 0.59 % to 0.35 % in copper reporting to waste is also achieved by second strategy (Table 8.22).

Values of recovery when compared with the QEM calculated parameter (Table 8.20), PX (Table 8.21) and BPX (Table 8.22) shows the second NIR strategy has better copper recovery.

Table 8.20 - Comparison of discrimination results of splits B1 for strategy one (NIR (1)) and strategy two (NIR (2)), Using copper content calculated from copper-bearing minerals by QEM. Where MIN = Mineralogy, and QEM = QEMSCAN<sup>®</sup> calculated Cu values

	NIR (1)	NIR (2)	QEM	MIN
Content of copper in feed, %	1.12	1.12	1.12	1.12
Content of copper in product, %	1.47	1.22	2.77	3.06
Content of copper in waste, %	0.49	0.38	0.10	0.36
Recovery of Cu in product, %	85	96	94	77
Yield of product, %	65	88	38	28

Table 8.21 - Comparison of discrimination results of splits B1 for strategy one (NIR (1)) and strategy two (NIR (2)), Using copper content measured by PX. Where MIN = Mineralogy, and PX = Portable XRF.

	NIR (1)	NIR (2)	PX	MIN
Content of copper in feed, %	0.96	0.96	0.96	0.96
Content of copper in product, %	1.03	1.03	2.42	2.00
Content of copper in waste, %	0.82	0.41	0.11	0.54
Recovery of Cu in product, %	70	95	93	59
Yield of product, %	65	88	37	28

Table 8.22 - Comparison of discrimination results of splits B1 for strategy one (NIR (1)) and strategy two (NIR (2)), Using copper content measured on powdered samples by BPXRF. Where MIN = Mineralogy, and BPX = Bulk Portable XRF.

	NIR (1)	NIR (2)	BPX	MIN
Content of copper in feed, %	1.02	1.02	1.02	1.02
Content of copper in product, %	1.25	1.11	2.56	2.50
Content of copper in waste, %	0.59	0.35	0.19	0.43
Recovery of Cu in product, %	80	96	88	69
Yield of product, %	65	88	35	28

### 8.8.2. Splits B2

The classification indicates strategy two classified only twelve samples as waste (Table 8.18) as against nineteen samples classified as waste by the first strategy (Table 8.5). Hence, the product concentrate by the second strategy consists of forty eight samples. Assuming that the total mass is 100 % and the mass is the same for each sample (1/60), the calculated parameters are presented in Tables 8.23 and 8.24 using data from PX and BPX respectively.



Table 8.23 - Comparison of discrimination results of splits B2 for strategy one (NIR (1)) and strategy two (NIR (2)), Using copper content measured by PX. Where MIN = Mineralogy, and PX = Portable XRF.

	NIR (1)	NIR (2)	PX	MIN
Content of copper in feed, %	1.55	1.55	1.55	1.55
Content of copper in product, %	1.87	1.79	2.54	2.95
Content of copper in waste, %	0.88	0.60	0.17	0.99
Recovery of Cu in product, %	82	92	95	54
Yield of product, %	68	80	58	28

Table 8.24 - Comparison of discrimination results of splits B2 for strategy one (NIR (1)) and strategy two (NIR (2)), Using copper content measured on powdered samples by BPXRF. Where MIN = Mineralogy, and BPX = Bulk Portable XRF

	NIR (1)	NIR (2)	BPX	MIN
Content of copper in feed, %	1.02	1.02	1.02	1.02
Content of copper in product, %	1.12	1.10	2.56	2.50
Content of copper in waste, %	0.80	0.68	0.19	0.43
Recovery of Cu in product, %	80	87	88	69
Yield of product, %	68	80	35	28

Comparison of calculated parameters indicates improvements in both yields and recovery by 12 % and 10 % respectively for the second strategy, as when using PX values with a reduction of 0.28 % of copper reporting to waste from 0.88 % to 0.60 % (Table 8.23). The same is true using values from BPX (Table 8.24), showing an improvement of 7% in recovery.

### 8.9.3. Splits A1

Only twenty two samples are classified by the second strategy as waste (Table 8.19) as against the thirty samples classified by the first strategy (Table 8.6). Therefore, thirty eight samples are classified as product. Hence, assuming the total mass of a sample is 100 % and the mass of each sample is same (1/60), Table 8.25 presents calculated parameters using copper values measured by BPX.

Similar to splits B1 and B2, is the observed improvement in calculated parameters (recovery, yield and reduction in amount of Cu reporting to waste) using the second strategy as against the first strategy (Table 8.25). In

comparison with calculated BPX parameters, NIR achieved better recovery of 87 % against the 85 % achieved by BPX.

Table 8.25 - Comparison of discrimination results of splits A1 for strategy one (NIR (1)) and strategy two (NIR (2)), Using copper content measured on powdered samples by BPXRF. Where MIN = Mineralogy, and BPX = Bulk Portable XRF

	NIR (1)	NIR (2)	BPX	MIN
Content of copper in feed, %	1.02	1.02	1.02	1.02
Content of copper in product, %	1.57	1.39	2.46	2.50
Content of copper in waste, %	0.47	0.37	0.24	0.43
Recovery of Cu in product, %	77	87	85	69
Yield of product, %	50	63	35	28

### 8.9. Reconciliation of strategies

Comparison of the two strategies shows that targeting only calcite for discrimination achieved better results in terms of copper recovery and also the reduction in the amount of copper reporting to waste than targeting elimination of both calcite and muscovite. This confirms results of intimate mixtures where low grade chrysocolla features are masked (locked) by muscovite or kaolinite. It can therefore be concluded that for the first strategy, chrysocolla features were masked by those of muscovite, thereby leading to misclassification of spectra as not containing chrysocolla. With respect to the first strategy, (Fig. 8.2) samples 14, 15, 18, 21, 24, 27, 29, 33, 42, 53, 54, 55 and 57 of splits B1 (i.e. 61 % of total waste for strategy one) (Table 8.4), while for splits B2 samples 15, 18, 24, 29, 49, 54 and 55 (i.e. 37 % of total waste for strategy one) (Table 8.5) were classified as waste because of their muscovite absorption features. The same is true for samples 15, 27, 29, 33, 46, 53, 55 and 57 of splits A1 (i.e. 27 % of total waste for strategy one) (Table 8.6).

On the basis of copper content, except for samples 14, 24, 55 and 57 (i.e. 31 % of muscovite bearing strategy one waste) of splits B1, the remaining samples (samples 15, 18, 21, 27, 29, 33, 42, 53, 54) (i.e. 69 % of muscovite bearing strategy one waste) have their copper content below the cut-off grade set for classification based on copper content (Table 8.7). Only samples 18, 54 and 55 (i.e. 43 % of muscovite bearing strategy one waste) of the seven additional splits B2 product samples have their copper values above the cut-off grade

(Table 8.8). The same is true for sample 55 and 57 (i.e. 25 % of muscovite bearing strategy one waste) of splits A1. Hence, while the second strategy (Fig. 8.3) shows improvement in copper recovery and reduction in amount of copper reporting as waste, with findings agreeing with results of intimate mixtures (Fig. 6.1), the strategy allows dilution of copper grade by muscovite and probably other clay minerals if present in the ore since their best diagnostic features are not selected for discrimination as waste.

Hence, while the first strategy reduces dilution by producing fairly pure copper concentrate at a lower recovery rate due to loss of valuable to waste, the second strategy has a better recovery rate but with higher dilution from clays. Therefore, the choice of strategy will depend on present economic of processing and demand.

Note that all high malachite bearing ( $\geq 1$  wt %) samples (samples 5, 9, 10, 26, and 55) are also classified as products by strategy two. Except for sample 55 which showed muscovite features, the other four samples were also classified as product by strategy one, for splits B1 samples. Samples 9 and 55 were waste for splits B2 with strategy one, due to calcite and muscovite features (sample 9) and only muscovite features (sample 55). While only sample 9 was classified as waste by strategy two. For splits A1, samples 5, 9, 10 and 26 classified as product while sample 55 was waste due to muscovite features, using strategy one.

### **8.10. Economic implication of NIR sorting**

The economics of any processing method or strategy must be considered prior to its application, since the purpose of mineral processing is to increase the economic value of an ore (Wills and Napier-Munn, 2006). Improvement of the economic value or upgrade of an ore is only economical when it is achieved using the cheapest and most efficient available method and or strategy. Minimizing the amount of ore mineral that reports to gangue is a major consideration. Hence recovery is the key aim.

The aim of using NIR as a preconcentration method is to upgrade the ore by reducing the quantity of overall waste material reporting to the next processing stage. This is achieved by eliminating/reducing the waste fraction, in this ore the calcite and or clay (muscovite/kaolinite) rich particles. These are the only

groups of waste minerals that can be targeted by NIR since other non-copper-bearing minerals like chlorite, biotite and hematite cannot be effectively discriminated from chrysocolla (Iyakwari and Glass, 2015). Since the NIR does not sense the copper signature, the NIR classification was correlated with data from portable XRF and Cu values calculated from Cu-bearing minerals (chrysocolla, malachite and cuprite) as analysed by QEMSCAN<sup>®</sup>. The elemental/mineralogical data is then used to determine the economic/metallurgical implication of NIR application and the individual sample classifications based on NIR, PX, mineralogy (MIN) and QEMSCAN<sup>®</sup> Cu values (QEM) are compared.

Two strategies were employed. The first strategy considered the elimination of both calcite and muscovite as wastes, while the second strategy was aimed at eliminating only calcite as waste. From the first strategy, the calculated data of product fractions for split B1 (Tables 8.10, 8.11 and 8.12), split B2 (Table 8.13 and 8.4) and splits A1 (Table 8.15) showed that calculated recovery of copper is higher in PX and QEM than NIR and MIN. This is because copper content was considered with no consideration for their carbonate and hydroxyl content. Therefore, while the NIR and MIN classified sample material based on only quality of the ore, PX and QEM classification was so designed based on quantity of copper in sample. Also observed from strategy one was the high percentage of copper lost to waste, in most cases with values higher than the assumed cut-off grade.

Copper recoveries from the second strategy revealed a marked improvement from those obtained from strategy one. The strategy achieved higher copper recovery (Tables 8.20 to 8.25) in comparison to the first strategy as well as when compared to QEM, PX and MIN strategies. Results of the second strategy revealed that copper in the form of chrysocolla are locked in muscovite dominated spectra or spectrum. Hence eliminating both calcite and muscovite will amount to the loss of valuable ore as waste. Therefore, in terms of the economics of copper recovery, the second strategy provides a better option for consideration and application in preconcentrating the Mantoverde ore as samples reporting to waste are only samples with known calcite concentration, containing little or no chrysocolla. Hence though the first strategy provides fairly

pure concentrate, the second strategy minimizes the loss of valuable ore as waste.

Given the fact that the total amount of material (dominant waste bearing samples) is reduced as a result of the NIR preconcentration (using either strategies), the amount of money spent on acid and comminution (especially grinding) which takes about 50 % of the total energy used in mineral processing operation (Wills and Napier-Munn, 2006) is thus reduced and the reduction in the total cost is directly proportional to the total volume of the waste fraction.

Therefore the choice of strategies discussed above will depend on factors such as the value of the metal being targeted, whether tonnage (recovery) or purity (grade) is important and also how susceptible the ore is to preconcentration.

### **8.11. Conclusions**

In this study, a 1:1 correlation of the NIR, PX, BPX, and QEMSCAN<sup>®</sup> data (mineralogy (MIN) and calculated Cu values (QEM)) was achieved. Only a few samples were misclassified and this is either due to sample spectrum or spectra showing features of both product and waste mineral. Other factors include high concentration of hematite or complex associations of minerals in a sample (textures), resulting in spectra appearing featureless or spectra lacking absorption centres.

Two strategies were developed for classification and used to calculate ore parameters. The calculated NIR copper recoveries indicate that NIR preconcentration is suitable for the Mantoverde supergene copper ore. While the first strategy targeted both calcite and muscovite as waste the second strategy targets only calcite. Recovery is better achieved by targeting only calcite: hence, the second strategy gave a better result.

Also, NIR sensor allows the discrimination of a significant amount of material at a Cu grade that is less than half the economic cut-off-grade. This indicates that there is potential that the NIR sensor based sorting can provide economic benefits for processing ore.

However, the methods outlined are dependent upon the ore type and character, and may need to be calibrated for other ores to achieve optimal results. Therefore, in order to scope an application, a good understanding of the

constituent minerals and their diagnostic features locations is essential. The latter may also depend on the NIR equipment used.

## **Chapter 9: Quality control and data validation**

### **9.1. Introduction**

Both QEMSCAN<sup>®</sup> and the Near InfraRed (NIR) line scanner are surface techniques. It is therefore assumed that the surface NIR-active mineral(s) as detected by QEMSCAN<sup>®</sup> are responsible for the NIR absorption features observed in the spectra of the samples. This statement may not be entirely true for all the surface NIR-active minerals, as it may also depend on the depth of particle penetration, which in NIR is defined by the opacity and density of the first NIR-active mineral encountered (Iyakwari et al., 2013). Other factors include the thickness and arrangement of minerals in a particle, as observed in linear mixtures.

In order to determine the depth of particle penetration representativity, spatial variation and data quality, three particles or samples (Samples 3, 26, and 56) from splits B1 (Fig. 3.1) were studied. Samples were cut laterally into two halves (Table 9.1) and scanned with both QEMSCAN<sup>®</sup> and the NIR line scanner. Data of the whole samples and cross-section samples were then compared.

Note that the issue of particles settling during sample preparation is not considered here, since samples are cut-slabs and not powdered.

### **9.2. QEMSCAN<sup>®</sup>**

From the 30 mm diameter polished blocks (split B1, Fig. 3.1): three samples were randomly selected and cut into half along their vertical axis (Table 9.1). Samples were measured using fieldscan mode to allow for a 1:1 correlation with NIR spectra and visual assessment of spatial mineral association as well as provide modal mineralogy. Since the new particles are smaller than the original particles (as they are cross sections), this resulted in the acquisition of about 1,100,000 individual X-ray analysis points per sample, almost one third of the X-ray points obtained from the original particle (35,000,000) (section 4.2.1).

Fieldscan images and modal mineral data are presented in Tables 9.1, 9.2 and 9.3. Table 9.1 shows sample images ranging from the original 30 mm diameter polished sections (face), polished cross-section (New), fieldscan images of NIR-active minerals and composite minerals for both sections. Analysis of the

images shows a high degree of mineralogical representativity of the 30 mm diameter sample in the cross-sections.



Table 9.1 - Samples investigated from the original 30 mm polished sections (face), polished cross-section, QEMSCAN® Fieldscan images of NIR-active minerals and composite minerals.

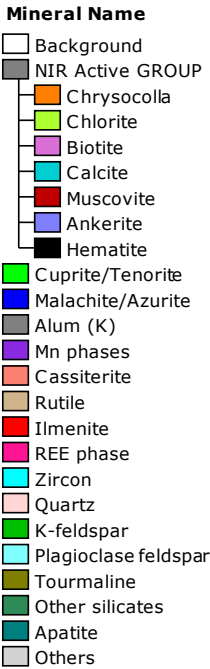
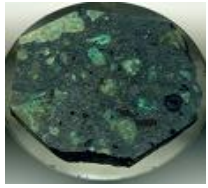
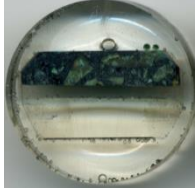


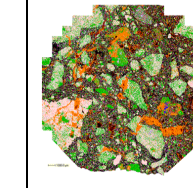


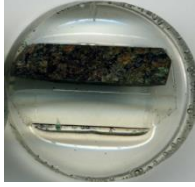

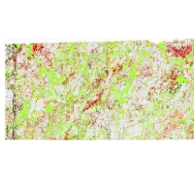
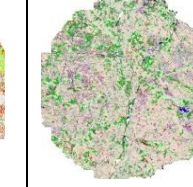
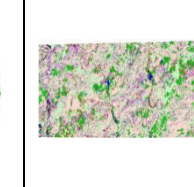

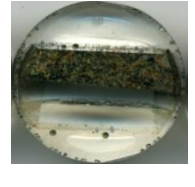
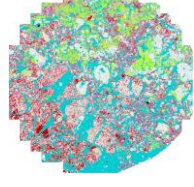

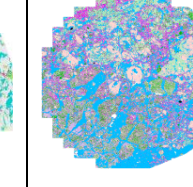
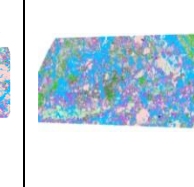
Sample ID	Original Face	New (Cross-section)	Combined NIR-active minerals (original face)	Combined NIR-active minerals (Cross-section)	Composite Fieldscan (original face)	Composite Fieldscan (Cross-section)	<b>Mineral Name</b> 
3							
26							
56							

Table 9.2 - Modal mineralogy of Mantoverde copper ore particles cross-sections (mass %) measured by QEMSCAN<sup>®</sup>, <0.01 % = not detected or below detection limit

Sample ID	Silicates									Oxides	Carbonates			Phosphates	Total	
	Cu-bearing	Non-Cu-bearing									Cu-bearing		Non-Cu-bearing			
	Non-Iron-bearing			Iron-bearing			Non-Iron-bearing			Iron-bearing	Non-Iron-bearing		Iron-bearing	Non-Iron-bearing		
	NIR-active						Non-active			NIR-active	Non-active	NIR-active				
Chrysocolla	Muscovite	Kaolinite	Biotite	Chlorite	Tourmaline	Quartz	K-feldspar	Plag-feldspar	Hematite	Cuprite	Malachite	Calcite	Ankerite	Apatite		
3	17.16	2.67	0.04	4.07	2.13	0.05	25.34	19.71	0.02	28.76	0.01	0.02	<0.01	<0.01	<0.01	99.98
26	3.6	5.76	<0.01	9.61	26.22	0.52	32.94	14.53	0.12	3.78	0.01	1.45	0.02	0.03	0.46	99.05
56	0.11	10.5	<0.01	12.86	9.51	0.37	23.07	10.7	1.06	0.29	<0.01	<0.01	28.91	0.63	0.14	98.15

Table 9.3 - Modal mineralogy of the Mantoverde copper ore particles original 30 mm polished sections (mass %) measured by QEMSCAN<sup>®</sup>, <0.01 % = not detected or below detection limit

Sample ID	Silicates									Oxides	Carbonates			Phosphates	Total	
	Cu-bearing	Non-Cu-bearing									Cu-bearing		Non-Cu-bearing			
	Non-Iron-bearing			Iron-bearing			Non-Iron-bearing			Iron-bearing	Non-Iron-bearing		Iron-bearing	Non-Iron-bearing		
	NIR-active						Non-active			NIR-active	Non-active	NIR-active				
Chrysocolla	Muscovite	Kaolinite	Biotite	Chlorite	Tourmaline	Quartz	K-feldspar	Plag-feldspar	Hematite	Cuprite	Malachite	Calcite	Ankerite	Apatite		
3	21.11	2.96	0.05	4.53	3.08	0.04	18.16	17.87	0.02	31.77	0.01	0.31	<0.01	<0.01	<0.01	99.91
26	3.26	4.14	<0.01	8.47	26.35	0.4	36.34	14	0.15	4.13	0.01	1.2	0.02	0.04	0.46	98.97
56	0.13	12.07	<0.01	13.61	12.14	0.53	19.18	9.42	1.14	0.39	<0.01	<0.01	28.53	0.79	0.11	98.04


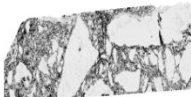

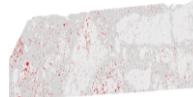






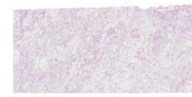
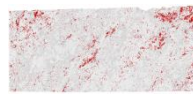
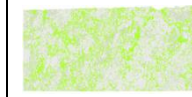

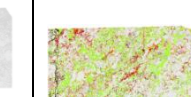
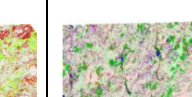


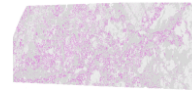
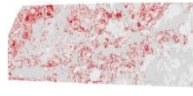
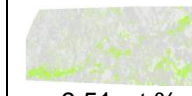


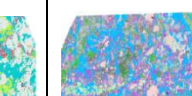
### 9.3. NIR-active minerals

Chrysocolla, hematite, chlorite, muscovite, calcite and biotite are the dominant NIR-active minerals in the Mantoverde samples. Hence their features were those targeted in the scoping application for NIR preconcentration. Therefore mineral data is compared using these dominant NIR-active minerals. Table 9.4 presents QEMSCAN<sup>®</sup> fieldscan images of NIR-active minerals in each sample.

Analysis of the fieldscan images (Table 9.4) revealed spatial association between chrysocolla and hematite in sample 3. Muscovite, chlorite and biotite occur as traces with each having concentrations below 5 wt %. Both chrysocolla and hematite have concentrations above 10 wt %. Sample 26 contains chrysocolla at 3.6 wt %. The sample is low in hematite, with a concentration of 3.8 wt %. Fieldscan images (Table 9.4) reveal an even spatial occurrence of both chrysocolla and hematite across the sample area. Sample 56 contains both chrysocolla and hematite below 1 wt %. Calcite is the dominant NIR-active mineral in the sample. The sample's fieldscan images (Table 9.4) reveal calcite, muscovite and biotite occurring with spatial association as though one mineral lay directly on the other.

While samples 3 and 26 contain chrysocolla above 1.5 wt % (approximately 0.5 % copper), sample 56 is chrysocolla deficient, with a concentration below 0.2 wt %. Only sample 56 contains calcite with a concentration of 29 wt %. Both samples 3 and 26 have calcite concentrations below 0.5 wt %. From the three samples, it can be observed that hematite and chrysocolla displays spatial association, though their modal concentration may not be in 1:1 agreement (Table 9.4).

Table 9.4 - NIR-active mineral association mapping of Mantoverde copper ore particles cross-sections

Sample ID	Chrysocolla	Hematite	Biotite	Muscovite	Chlorite	Calcite	NIR-active	Composite
3	 17.16 wt %	 28.76 wt %	 4.07 wt %	 2.67 wt %	 2.13 wt %	 <0.01 wt %		
26	 3.60 wt %	 3.78 wt %	 9.61 wt %	 5.76 wt %	 26.22 wt %	 0.02 wt %		
56	 0.11 wt %	 0.29 wt %	 12.86 wt %	 10.50 wt %	 9.51 wt %	 28.91 wt %		

### 9.3.1. Correlation of NIR-active minerals

NIR-active minerals in the selected samples are correlated. Figures 9.1 to 9.6 present correlation plots of each NIR-active mineral in the samples.

Correlation plots (Fig. 9.1 to 9.6) revealed strong positive linear correlation between values obtained for both sample types (whole sample and cross-sections).  $R^2$  values range from 0.86 for muscovite to 1 for both hematite and calcite. The Figures have slopes ranging from 0.7 for muscovite and chrysocolla to above 1 for calcite and chlorite. Apart from muscovite which has an intercept above 1, other minerals show intercepts close to zero.

Though only a few samples are used here (three out of sixty), it is expected that the  $R^2$  values and other parameters would be comparable if more samples were measured. Thus the current study is a check rather than a comprehensive study of the samples in cross section, and limitations of plots with three points is acknowledged..

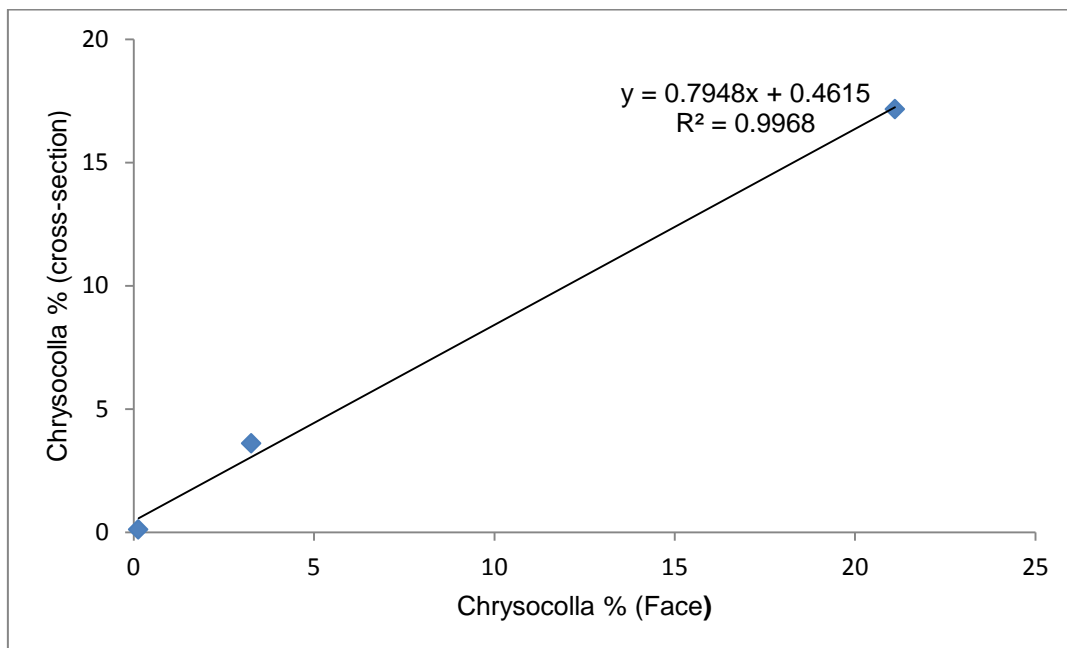


Figure 9.1 - Correlation diagram between chrysocolla in whole sample and cross-section

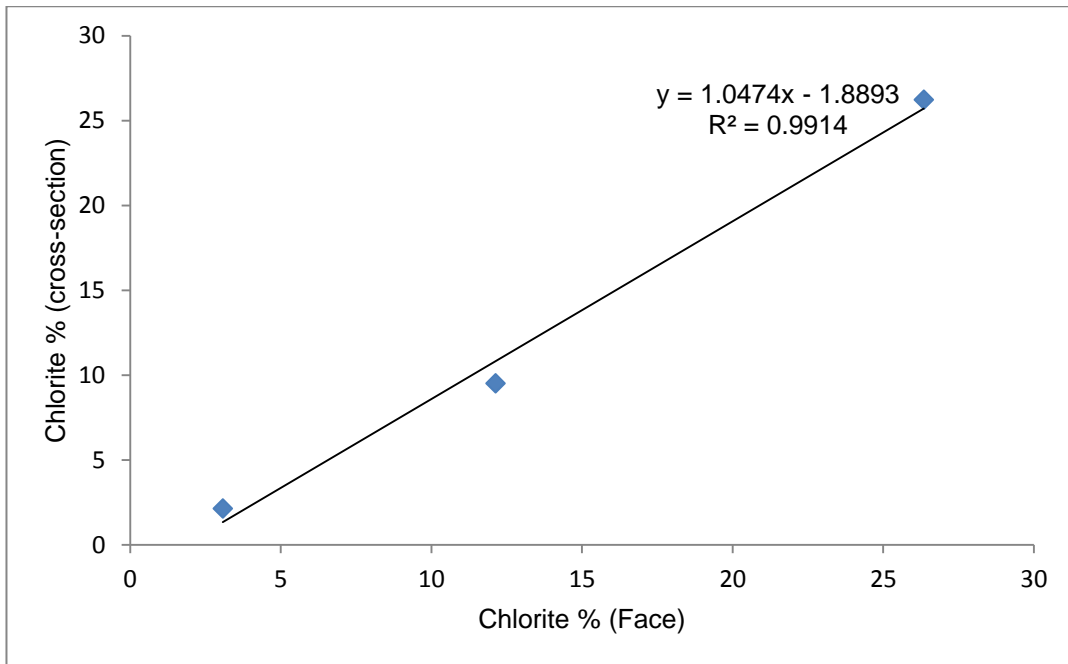


Figure 9.2 - Correlation diagram between chlorite in whole sample and cross-section

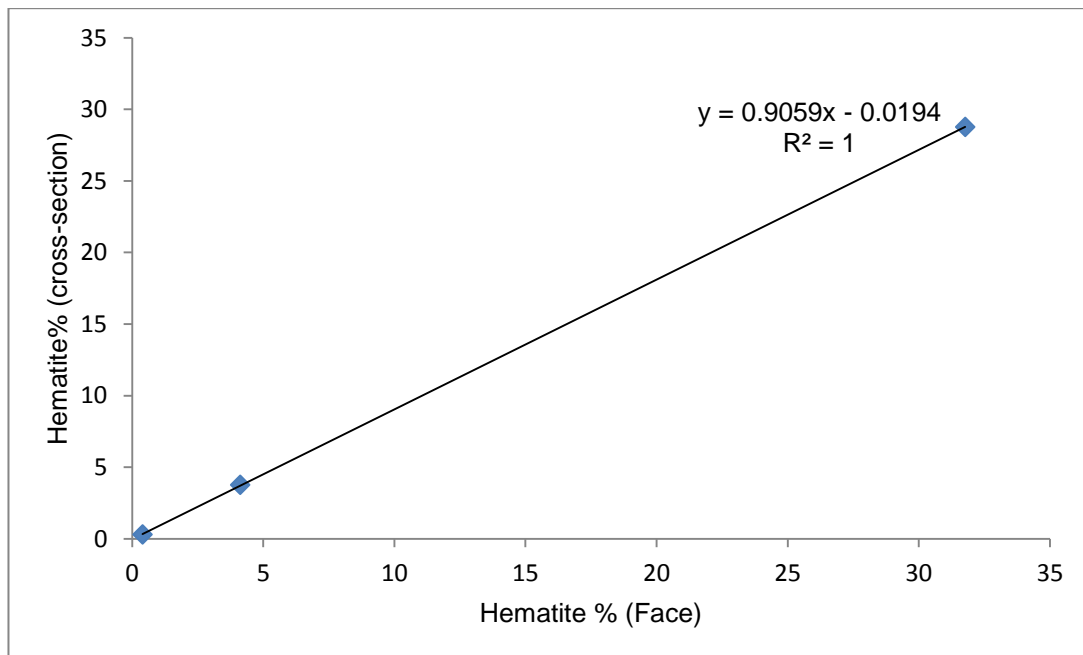


Figure 9.3 - Correlation diagram between hematite in whole sample and cross-section

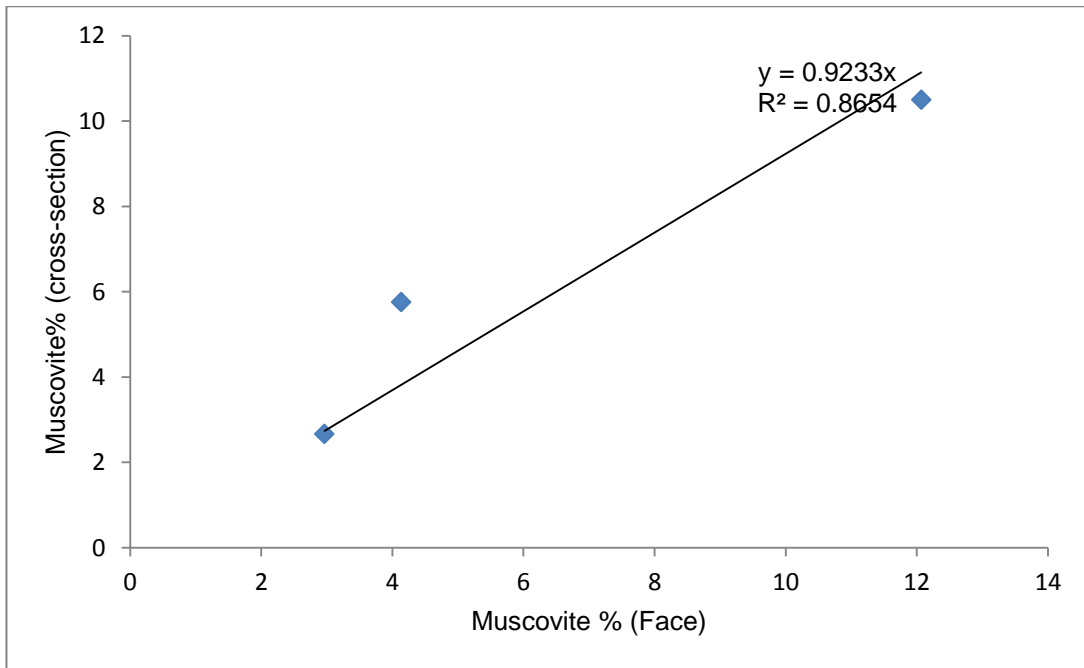


Figure 9.4 - Correlation diagram between muscovite in whole sample and cross-section

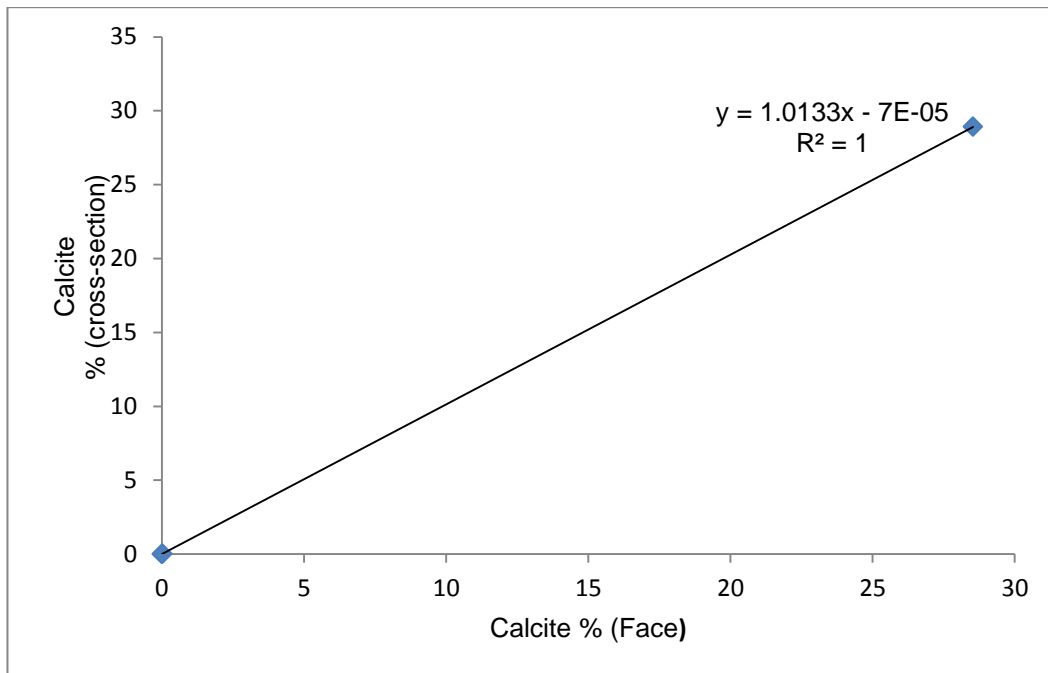


Figure.9.5 - Correlation diagram between calcite in whole sample and cross-section

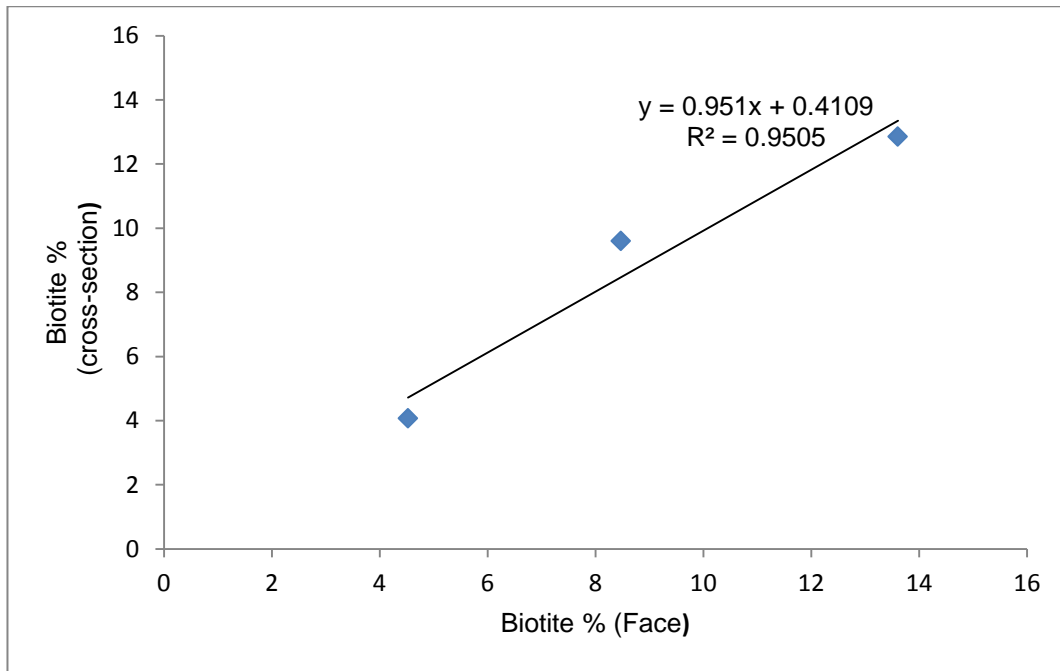


Figure 9.6 - Correlation diagram between biotite in whole sample and cross-section

### 9.3.2. Functional groups

Based on the classification strategy in chapter four, with reference to Fig. 4.4, where cut-off grade of copper is at 0.5 %, -OH at 5 %,  $\text{CO}_3^{2-}$  at 2 %, and 10 % for hematite, using the calculated functional groups composition (Table 9.5), the following classification can be achieved (Table 9.6, 9.7, and 9.8). Sample 3 can be classified as high Cu - low -OH, high Cu-low  $\text{CO}_3^{2-}$  and high Cu - high hematite. Sample 26 is a good example of high Cu - high -OH, high Cu - low  $\text{CO}_3^{2-}$  and high Cu - low hematite. Sample 56 can be classified as low Cu - low -OH, low Cu - high  $\text{CO}_3^{2-}$  and low Cu - low hematite. Hence, with respect to Fig. 4.4, only samples 3 and 26 are economically targetable while sample 56 is uneconomic. This is due to its high  $\text{CO}_3^{2-}$  concentration which is chiefly as a result of its high calcite concentration. Note that though sample 26 contains high -OH concentration, it is considered economic since chrysocolla is also an -OH contributing mineral. Both hematite and Fe are considered here because they are capable of masking features of other minerals functional groups (Bishop and Dummel 1996).



Table 9.5 - Calculated modal composition (wt %) of carbonate and hydroxyl functional groups, copper and hematite minerals, with reference to webmineral.com (2013)

Sample ID	-OH	CO <sub>3</sub> <sup>2-</sup>	Cu	Fe	Hematite
3	4.69	0.01	5.82	20.63	28.76
26	8.44	0.42	1.45	6.42	3.78
56	4.46	17.70	0.04	2.31	0.29

Table 9.6 - Classification of samples based on copper-carbonate concentration. Where HCu = High copper, HC = High carbonate, LCu = Low copper and LC = Low carbonate. Class of sample is marked with +

Sample ID	HCu-HC	HCu-LC	LCu- HC	LCu-LC
3		+		
26		+		
56			+	

Table 9.7 - Classification of samples based on copper-hydroxyl concentration. Where HCu = High copper, HOH = High Hydroxyl, LCu = Low copper and LOH = Low Hydroxyl. Class of sample is marked with +

Sample ID	HCu-HOH	HCu-LOH	LCu- HOH	LCu-LOH
3		+		
26	+			
56				+

Table 9.8 - Classification of samples based on copper-hematite concentration. Where HCu = High copper, HH = High Hematite, LCu = Low copper and LH = Low Hematite. Class of sample is marked with +

Sample ID	HCu-HH	HCu-LH	LCu- HH	LCu-LH
3	+			
26		+		
56				+

The above classification is a repeat of the classification of samples achieved on whole samples (splits B1) in section 4.4.2. Therefore data analysis confirms that classification is repeatable and reproducible.

#### 9.4. Near infrared

Samples were cut into half, each along the line of the middle spectra (Fig. 9.7). Therefore, cross-section spectra are compared with spectra of the whole sample obtained along the face of cut. Due to the shape and smaller size of the cross section of samples 3 and 26 (Table 9.1), only 8, and 7 spectra were obtained compared to 9 and 8 obtained in the original whole samples (splits B1).

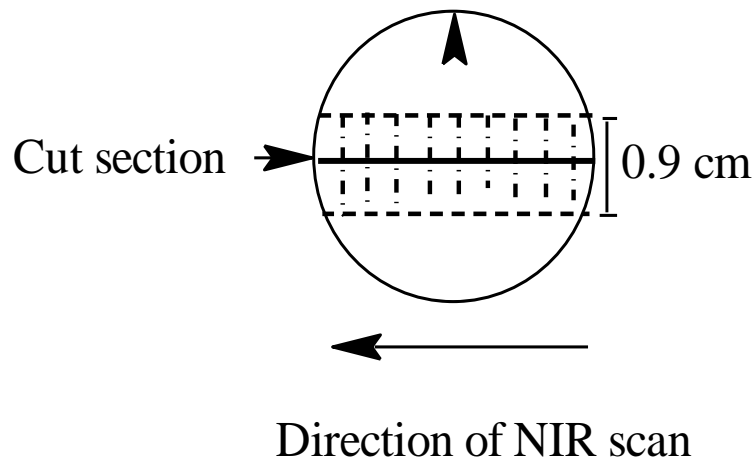
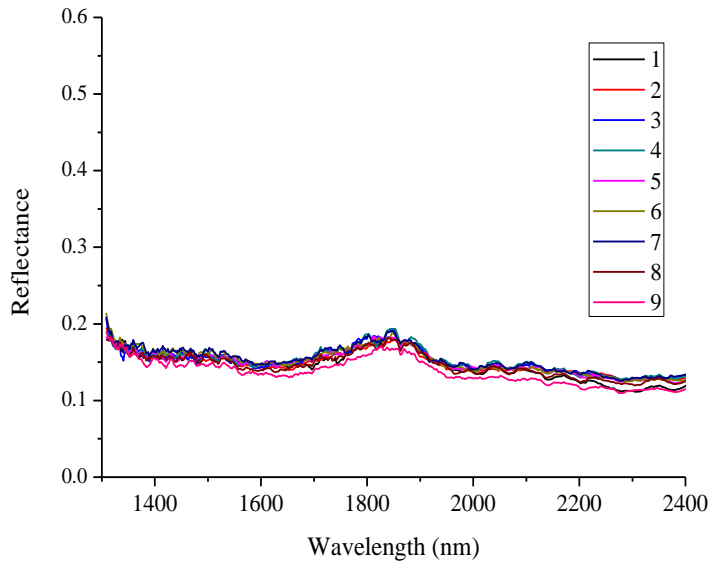
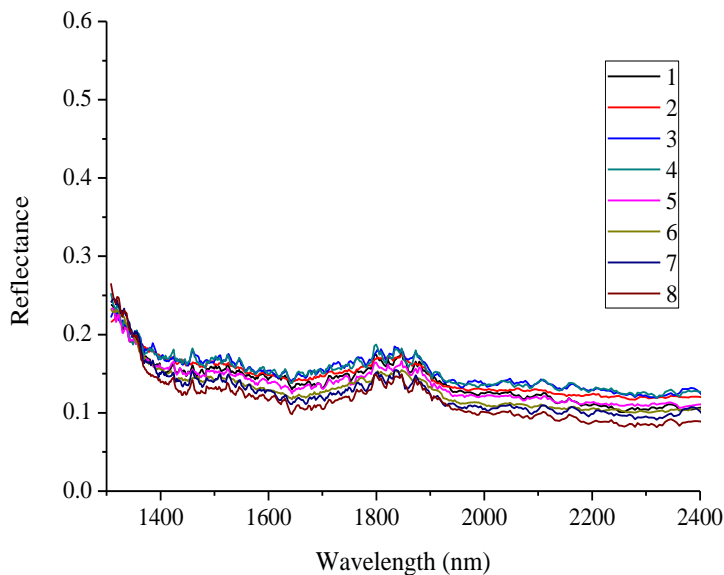


Figure 9.7 - Split B1 indicating cross-section of the sample block

The spectra of sample 3 appear featureless as observed in the original whole sample (Fig. 9.8). The appearance of the spectra corresponds to the mineral content as revealed by sample modal mineralogy, having dominant hematite and chrysocolla (Table 9.3). Chrysocolla and hematite occur at ratios 4:6 with both showing spatial association (Table 9.4). Due to the dominant hematite concentration, the features of chrysocolla are invisible in the spectra.



A

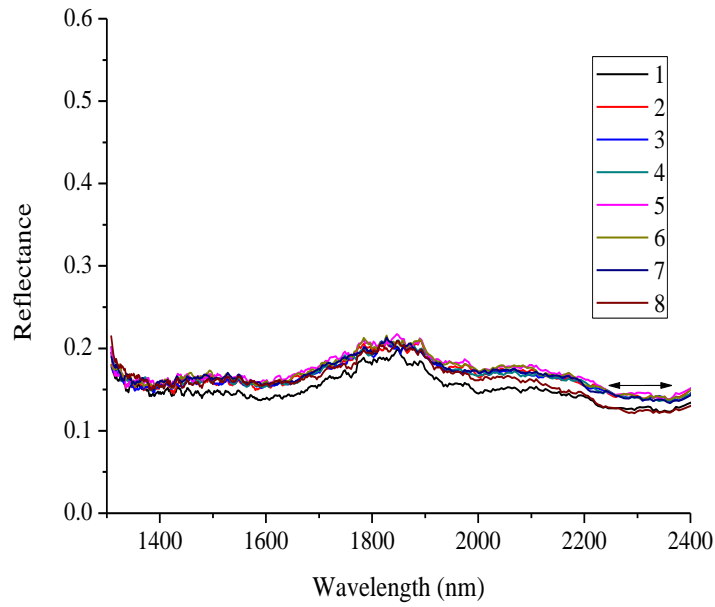


B

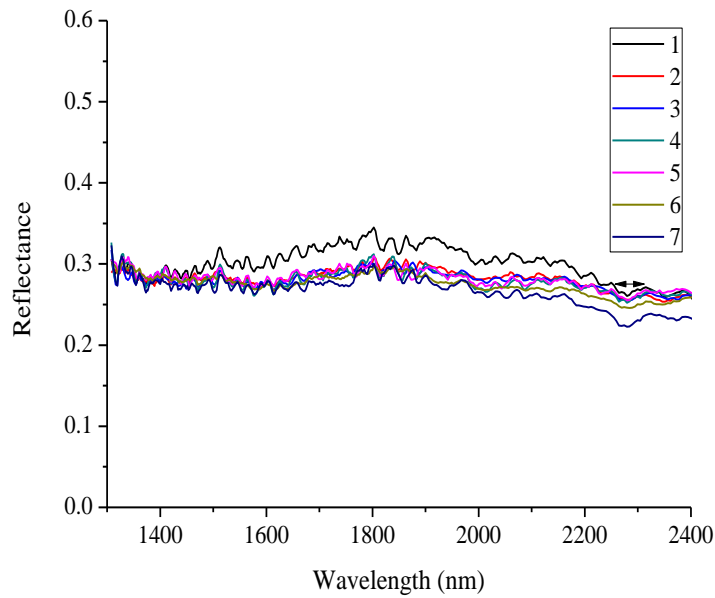
Figure 9.8 - NIR spectra of sample 3 (A) Whole sample and (B) Cross-section.

The spectra of sample 26 shows a depression along the longer wavelengths, with the depression lacking absorption centre (Fig. 9.9). The samples modal composition shows chlorite (26 wt. %) as the dominant NIR-active mineral. Other NIR-active minerals include chrysocolla (3.60 wt. %), malachite (1.5 wt. %), hematite (3.78 wt. %), muscovite (5.76 wt. %) and biotite (9.61 wt. %). Calcite occurs below detection limit in the sample. At the given concentration,

hematite is capable of masking the chlorite features normally observed near 1415, 2265 and 2360 nm. The same is true for hematite with muscovite, chrysocolla and biotite, and biotite and chlorite, at given concentration (Iyakwari and Glass, 2015).



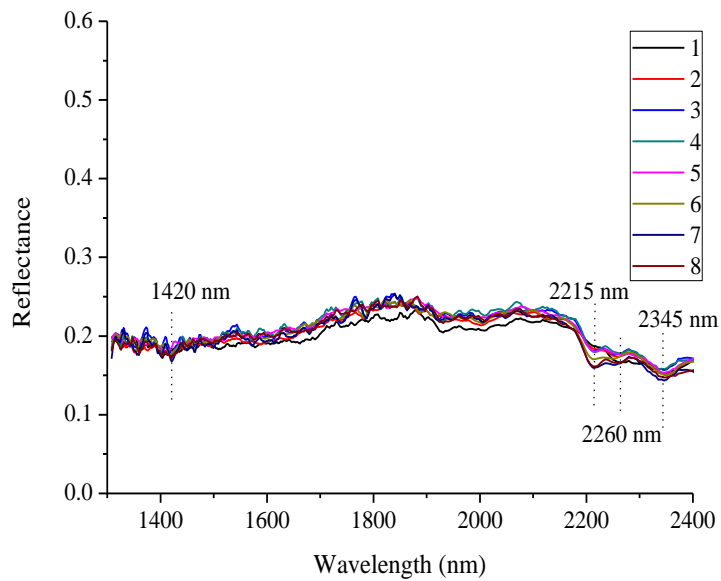
A



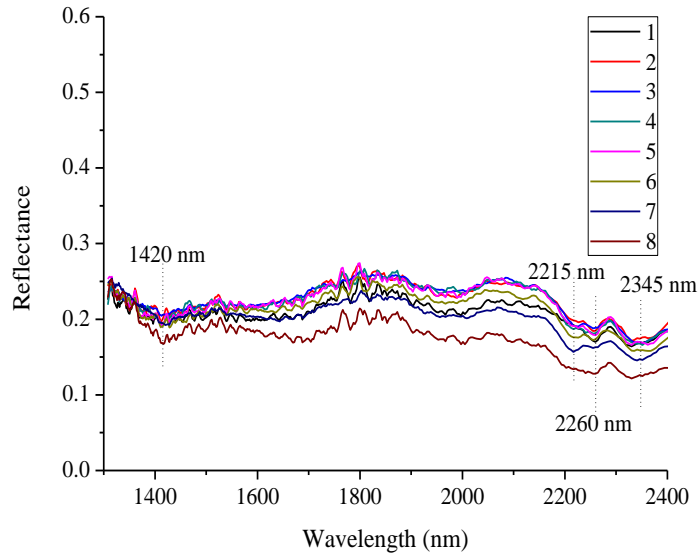
B

Figure 9.9 - NIR spectra of sample 26 (A) Whole sample and (B) Cross-section.

The spectra of sample 56 show features near 1420, 2215, 2260 and 2345 nm. These features can be assigned to muscovite (2215 nm), chlorite (2260 nm) and calcite (2345 nm). Therefore the sample displays a complex spectra mixture. Modal mineral data (Table 9.4) show muscovite (10.50 wt %), chlorite (9.51 wt %), and calcite (28.91 wt %) as the dominant NIR-active minerals in the sample. Though biotite as one of the NIR-active minerals has a concentration of 12.86 wt % in the sample, it does not show features in the spectra. The 1420 nm feature is displayed by both chlorite and muscovite. Hence the feature is assigned to both of the minerals. Furthermore, the presence of the 1420 nm feature indicates that biotite is not strong in the spectra of the sample, as biotite usually occurs with a masked feature near 1400 nm (Clark et al., 2003; Iyakwari et al., 2013). This thus confirms biotite as the weakest NIR-active mineral in the Mantoverde ore.



A



B

Figure 9.10 - NIR spectra of sample 56 (A) Whole sample and (B) Cross-section.

With respect to the first NIR classification strategy where both calcite and muscovite are considered waste (Fig. 8.2), sample spectra can be classified as follows:

Samples 3 and 26 are products while sample 56 is waste. This is also a repeat of sample classification in Table 8.4. Since sample 56 contains and displays calcite features, similar classification is achieved using the second NIR strategy, where only calcite is considered as waste (Fig. 8.3 and Table 8.17).

### 9.5. Effect/influence of resin used on NIR signals

To check the influence and/or effect of the Epoxy resin used in preparing the samples into mounts for the QEMSCAN<sup>®</sup> on NIR spectra of the particles, a pure resin mount was produced and scanned. Spectra obtained were treated with the same method as the rock samples and is presented in Figure 9.11.

Due to the C-H, O-H and N-H absorption in the NIR region, the pure epofix block displays absorption features. The resin exhibits high reflectance at short wavelength between 1308 and 1394 nm. The pure resin block also displays an -OH absorption feature near 1430 nm, NH<sub>2</sub> features near 1470 and 1550 nm and epoxy terminal CH<sub>2</sub> band near 1645 nm. All absorption features corresponds to Li et al., (2008). On comparison with the individual particle

spectra, there is a strong contrast between the NIR signals of pure resin and ore particles. Therefore, identification and discrimination of minerals signal from resin signals was possible. Also, none of these wavelength bands associated with the resin was selected for preconcentration of the ore.

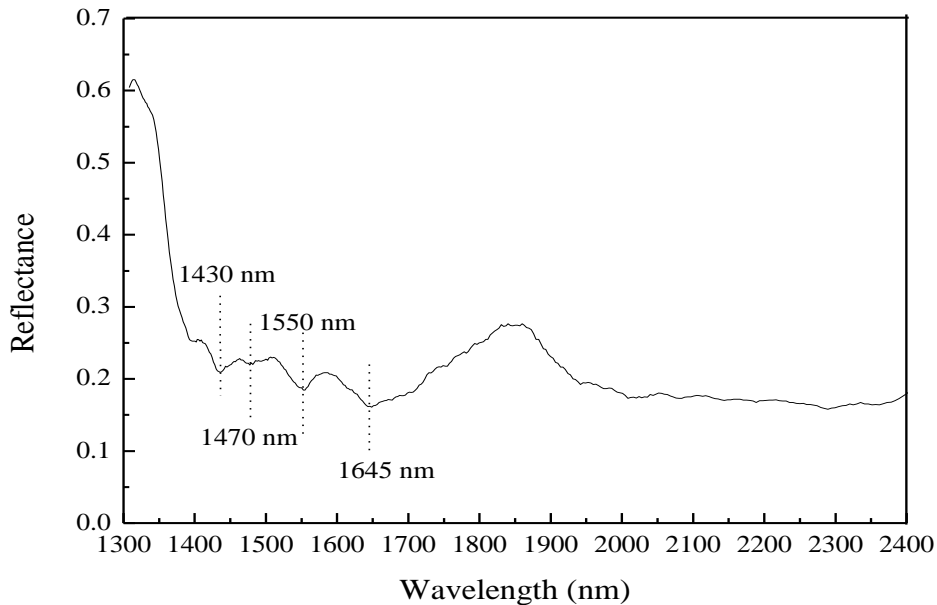


Figure 9.11 - NIR spectra of Epofix (epoxy resin)

The average particle size for all the samples is from 2.0 to 2.7 cm in width. Therefore, given the pixel size of 0.29 by 0.9 cm for the NIR, each sample generated between 7 and 9 spectra per sector (Table 8.1). Due to the uneven nature of some of the particles edges, there was sample edge effect contributed by the resin. Samples with uneven edges were observed to be affected by the influence of the resin and as such those edge pixels were removed from the particles during spectral pre-treatment, e.g. removed two edge pixels leaving only six from the original 8. This does not affect the interpretation as the affected pixels are edge pixels and thus not optimal for analysis.

## 9.6. Conclusion

1. Spectra of all the samples compared well with those obtained from their whole samples. This is also a confirmation that analysis is representative and reproducible.
2. The depth attained by scanning (both with NIR and QEMSCAN<sup>®</sup>) of splits B1 is representative of each sample scanned and sufficient for preconcentration.
3. Overall, results show that analysis of the sixty samples (splits B1) and their classification is representative of the samples. The NIR-active minerals in each particle are also representative and reproducible, and comparison is almost 1:1, only for the size of each particle.



## Chapter 10: Applicability of near infrared on the Mogalakwena platinum ore

### 10.1. The Mogalakwena ore

Fifty one powdered samples were received from the Anglo American platinum operation from the Mogalakwena mine, Overysel deposit of the Bushveld Complex, Limpopo province of South Africa. The Mogalakwena mine is divided into subsections and Overysel deposits, which is located in the Northern section, and is known to have the highest platinum grade in the various subsections of the Mogalakwena mine (Naldrett et al., 2008). According to Holwell and McDonald, (2006); Cawthorn and Boerst, (2006), the deposit is a pyroxenitic reef, where Base Metal Sulphides (BMS) are interstitial to cumulus orthopyroxenes, with the Platinum Group Metal (PGM) commonly located around the margins of the BMS grains or intergrown with secondary silicates. Furthermore, Holwell and McDonalds, (2007), in their detailed mineralogical studies using laser ablation-inductively coupled plasma-mass spectrometry studies, showed that there exists particularly a strong PGM-BMS relationship in the Overysel deposit. Most PGM grains are associated with BMS grains and most occur either as grains at the contact between BMS and silicate or within silicate phases (orthopyroxenes and amphiboles) as satellite grains around BMS (Fig. 10.1).

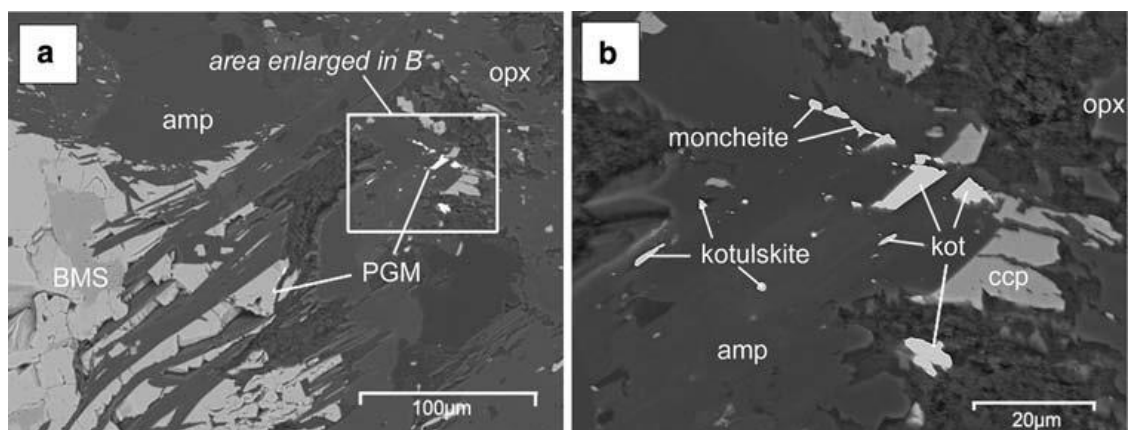


Figure 10.1 - Backscattered scanning electron micrographs of a typical association of PGM at the contact between BMS and silicates, and as satellite grains in close proximity to the BMS grain, enclosed within secondary amphiboles (amp) between the BMS and primary silicates such as orthopyroxene (opx.). (b) Enlarged area from (a), showing grains of moncheite (mon) and kotulskite (kot) and remnant chalcopyrite (ccp) enclosed in secondary amphibole (source: Holwell and McDonald, 2007).

Samples were accompanied by their XRD results. NIR application is intended for the classification of concentrates particles from sericite, serpentinite and carbonate rich samples. Though data indicating platinum concentration is not available (probably due to the very low abundances of PGM, or commercial sensitivity), an indirect approach is targeted since the literature suggests association of PGM with orthopyroxene, BMS and amphiboles.

## **10.2. Material characterisation and ore mineralogy**

Quantitative XRD data of the samples was received from the Anglo America Mogalakwena operations (Table 10.1). Mineral concentration is presented in mass percentages for each sample. In no particular order, the minerals present in the ore include: orthopyroxene, clinopyroxene, feldspars, quartz, mica, serpentine, chlorite, amphibole, talc, andradite, grossular, calcite, chalcopyrite and brucite. From the data received, most minerals analysed are presented in their mineral group or family name. Therefore, in order to identify specific mineral(s) per group, thirty one samples, deemed representative of the entire batch of fifty one samples were systematically selected and qualitative XRD analysis was performed. Results are presented in Table 10.2. The XRD analysis performed was qualitative and examines samples based on crystallography: therefore, it could not detect amorphous material that does not have crystal structure. The qualitative XRD mineral identification was also based on a detection limit of 5 %. This means that minerals identified by the XRD were above or approximately 5 % in concentration in the samples. Therefore, the XRD method only allowed for the determination of the most dominant minerals present in the samples (2 - 5 minerals).

Table 10.1 - Quantitative modal mineralogy of Mogalakwena platinum ore samples (mass %) measured by XRD as received from Anglo America Mogalakwena operations. where bdl = below detection limit.

Sample ID	Allocated ID	Silicates											Hydroxide	Carbonate	Sulfide	Total
		Non-NIR-active					NIR-active									
		Clinopyroxene	Feldspar	Quartz	Andradite	Grossular	Orthopyroxene	Serpentine	Mica	Chlorite	Amphibole	Talc	Brucite	Calcite	Chalcopyrite	
MSGC10076961	1	6	10	3	bdl	Bdl	52	10	6	5	5	3	bdl	bdl	bdl	100
MSGC10035880	2	34	9	Bdl	6	Bdl	13	6	4	8	14	1	bdl	5	bdl	100
MSGC10484545	3	13	5	10	bdl	Bdl	20	7	3	15	13	5	bdl	9	bdl	100
MSGC10484178	4	31	7	Bdl	2	Bdl	26	4	2	18	5	3	bdl	2	bdl	100
MSGC10484297	5	6	12	3	bdl	Bdl	59	4	4	8	2	2	bdl	bdl	bdl	100
MSGC10484104	6	11	3	9	bdl	Bdl	10	11	7	20	9	5	bdl	15	bdl	100
MSGC10483164	7	5	4	Bdl	bdl	Bdl	41	18	4	10	7	10	bdl	bdl	1	100
MSGC10484108	8	12	7	11	bdl	Bdl	16	12	7	18	10	5	bdl	bdl	2	100
MSGC10484164	9	8	16	3	bdl	Bdl	51	3	3	6	5	4	bdl	bdl	1	100
MSGC10483077	10	6	20	4	bdl	Bdl	59	4	4	1	1	1	bdl	bdl	bdl	100
MSGC10483256	11	19	12	11	3	Bdl	15	12	6	10	4	4	bdl	4	bdl	100
MSGC10035039	12	8	12	3	bdl	Bdl	28	13	4	11	15	6	bdl	bdl	bdl	100
MSGC10035411	13	15	27	6	bdl	Bdl	43	bdl	1	1	1	5	bdl	bdl	bdl	100
MSGC10035682	14	21	7	Bdl	bdl	Bdl	37	8	8	5	8	6	bdl	bdl	bdl	100
MSGC10483071	15	15	13	6	bdl	Bdl	27	10	5	10	7	2	bdl	5	bdl	100
MSGC10483074	16	6	21	3	bdl	Bdl	59	3	5	2	1		bdl	bdl	bdl	100
MSGC10483137	17	5	14	5	bdl	Bdl	55	8	3	4	2	4	bdl	bdl	bdl	100
MSGC10483161	18	9	4	1	bdl	Bdl	40	13	4	10	11	8	bdl	bdl	bdl	100
MSGC10483263	19	25	6	1	bdl	Bdl	21	14	5	13	11	3	bdl	1	bdl	100
MSGC10484275	20	10	19	2	bdl	Bdl	59	1	5	1	2	1	bdl	bdl	bdl	100
MSGC10484478	21	46	3	Bdl	12	Bdl	7	9	bdl	10	2	7	bdl	4	bdl	100
MSGC10484502	22	0	Bdl	Bdl	bdl	Bdl	40	24	6	18	3	9	bdl	bdl	bdl	100
MSGC10035875	23	9	44	4	bdl	Bdl	28	5	3	4	2	1	bdl	bdl	bdl	100
MSGC10483055	24	13	3	1	bdl	Bdl	41	16	3	12	5	3	bdl	3	bdl	100
MSGC10483083	25	6	18	2	bdl	Bdl	61	3	5	1	2	2	bdl	bdl	bdl	100
MSGC10483133	26	5	9	1	bdl	Bdl	59	10	4	7	2	3	bdl	bdl	bdl	100
MSGC10483172	27	7	11	2	bdl	Bdl	53	8	4	7	5	2	bdl	bdl	1	100
MSGC10035838	28	34	3	4	13	Bdl	7	12	4	11	6	6	bdl	bdl	bdl	100
MSGC10074904	29	36	8	Bdl	8	Bdl	13	12	4	5	6	6	bdl	2	bdl	100
MSGC10076956	30	12	13	6	bdl	Bdl	52	3	5	5	2	2	bdl	bdl	bdl	100
MSGC10483479	31	34	Bdl	Bdl	20	Bdl	5	13	4	16	2	6	bdl	bdl	bdl	100
MSGC10483567	32	23	6	3	9	Bdl	17	16	6	8	2	4	3	3	bdl	100
MSGC10484107	33	12	14	4	bdl	Bdl	49	6	3	6	3	2	bdl	bdl	1	100

Cont. of Table 10.1 - Quantitative modal mineralogy of Mogalakwena platinum ore samples (mass %) measured by XRD as received from Anglo America Mogalakwena operations. where bdl = below detection limit.

Sample ID	Allocated ID	Silicates										Hydroxide	Carbonate	Sulfide	Total	
		Non-NIR-active					NIR-active									
		Clinopyroxene	Feldspar	Quartz	Andradite	Grossular	Orthopyroxene	Serpentine	Mica	Chlorite	Amphibole	Talc	Brucite	Calcite	Chalcopyrite	
MSGC10484281	34	7	10	4	bdl	Bdl	53	7	6	4	4	4	bdl	bdl	1	100
MSGC10483402	35	32	Bdl	4	19	Bdl	3	21	4	8	2	4	bdl	3	bdl	100
MSGC10483502	36	37	6	Bdl	22	Bdl	8	9	3	9	bdl	3	bdl	3	bdl	100
MSGC10484147	37	0	70	23	bdl	Bdl	2	bdl	2	1	2	bdl	bdl	bdl	bdl	100
MSGC10483789	38	17	9	1	bdl	Bdl	26	13	6	11	13	4	bdl	bdl	bdl	100
MSGC10484219	39	9	17	2	bdl	Bdl	58	5	3	4	bdl	2	bdl	bdl	bdl	100
MSGC10035065	40	6	3	Bdl	bdl	Bdl	30	12	7	13	23	6	bdl	bdl	bdl	100
MSGC10483181	41	4	Bdl	2	bdl	Bdl	28	28	10	18	1	9	bdl	bdl	bdl	100
MSGC10035487	42	21	8	1	bdl	Bdl	41	10	4	5	6	4	bdl	bdl	bdl	100
MSGC10035420	43	16	21	4	bdl	Bdl	49	bdl	2	1	2	5	bdl	bdl	bdl	100
MSGC10035599	44	14	4	Bdl	bdl	Bdl	54	13	3	4	6	2	bdl	bdl	bdl	100
MSGC10483406	45	43	7	3	3	3	18	5	2	7	8	1	bdl	bdl	bdl	100
MSGC10483490	46	29	7	Bdl	7	Bdl	22	12	7	7	5	4	bdl	bdl	bdl	100
MSGC10484179	47	20	8	3	bdl	Bdl	28	3	2	22	5	4	bdl	5	bdl	100
MSGC10484198	48	0	46	46	bdl	Bdl	Bdl	bdl	1	4	3	bdl	bdl	bdl	bdl	100
MSGC10484221	49	10	14	2	bdl	Bdl	62	4	3	2	2	1	bdl	bdl	bdl	100
MSGC10484280	50	7	15	5	bdl	Bdl	49	6	4	5	5	4	bdl	bdl	bdl	100
MSGC10484312	51	5	6	Bdl	bdl	Bdl	47	13	2	11	13	3	bdl	bdl	bdl	100

Table 10.2 - Minerals identified by qualitative XRD analysis of the Mogalakwena platinum ore samples analysed at the Camborne School Mines (CSM).

<b>Minerals Identified</b>
Enstatite
Augite
Labradorite
Albite
Quartz
Phlogopite
Antigorite
Clinochlore
Hornblende
Talc
Calcite
Chalcopyrite
Andradite

Combining the results, the orthopyroxene (Enstatite), clinopyroxene (Augite), feldspar (Labradorite and albite), quartz, serpentine (antigorite), chlorite (clinochlore), mica (phlogopite), and amphiboles (hornblende) are singularly the dominant minerals in the ore. Minerals occurring in minor concentration or as traces include grossular, calcite, talc, chalcopyrite and brucite. Occurrence of brucite and grossular is only restricted to one sample each, sample 32 and sample 45 respectively.

Though chalcopyrite and calcite only occurred in a few samples with low concentration, data indicates that three major mineral groups (silicates, sulphides and carbonates) dominate the ore, with brucite (Hydroxide) occurring as traces.

### 10.3. NIR-active minerals

Due to the nature of the minerals under the influence of NIR radiation, it is important to outline categories of minerals in an ore which are responsive to NIR radiation from others which are not. XRD data (Tables 9.1 and 9.2) reveal that most minerals in the ore are alteration minerals and therefore susceptible to NIR activism. The functional groups in the Mogalakwena ore of interest and susceptible to NIR activism are hydroxyl (-OH) and carbonate ( $\text{CO}_3^{2-}$ ). Therefore, on the basis of occurrence/abundance, the NIR-active minerals in the ore are antigorite, chlorite, hornblende, phlogopite, talc, and calcite. While minerals like antigorite, chlorite, hornblende, phlogopite, and talc, are hydroxyl (-OH) bearing group minerals, calcite is a carbonate ( $\text{CO}_3^{2-}$ ) group bearing mineral. Though brucite shows absorption features in the NIR region, it is not selected here because of its trace occurrence and abundance as it may have little or no influence on spectra, since it occurred in minute concentration and in only one sample (sample 32).

Data analysis revealed that the NIR-active minerals (alteration minerals) make up about 50 % of the bulk mineralogy of only six samples (i.e. 12 % of the total samples). The dominant NIR-active minerals in the ore in terms of abundance and consistency of occurrence are chlorite, antigorite and phlogopite. Only samples 3 and 6 have high calcite concentrations of 9 wt % and 15 wt % respectively, the remaining calcite bearing samples have concentration of  $\leq 5$  wt %. Samples 6 and 41 have the highest concentration of NIR-active minerals, making up 67 % and 66 % respectively of their total composition.

Chlorite is present in all samples: eight samples have concentration of 15 wt % and above. Sample 47 has the highest concentration of 22 wt % while six samples (samples 10, 13, 20, 25, 37 and 43) have the least concentration of 1 wt %.

Though the bulk concentration of antigorite in the ore is more than that of chlorite, it cannot be considered the most dominant as its occurrence is below detection limits in four samples (samples 13, 37, 43 and 48). Sample 41 has the highest antigorite concentration with concentration of 28 wt %.

Only one sample, sample 41 has a concentration of phlogopite at 10 wt %. Phlogopite is also below detection limit for sample 21. The same is true for talc

where only sample 7 has a concentration of 10 wt %, while samples 16, 37 and 48 are below the detection limit.

Sample 40 reveals the highest concentration of hornblende with a concentration of 23 wt %, while the remaining fifty samples have concentrations of 15 wt % and below. Analysis show two samples (samples 36 and 39) having hornblende concentrations below the detection limit.

Unlike the hydroxyl-bearing minerals, the carbonates (calcites) only occur in fourteen out of fifty one samples, as analysed by the quantitative XRD. Therefore, thirty seven samples were measured to have calcite occurring below detection limit.

#### **10.4. Functional groups**

The -OH and  $\text{CO}_3^{2-}$  are the NIR-active functional groups targeted for removal from the ore. With the exception of amphiboles (hornblende) which contain 3.6 % of -OH (www.webmineral.com 2013), no other platinum associated minerals contain them. Table 10.3 presents the concentration of functional groups in the ore as calculated from individual minerals in each sample. Note, NIR activity is not only on the basis of the presence of absorption features: activity may also be based on the ability of a mineral to mask the features of other minerals in a complex mineral assemblage (Bishop and Dummel, 1996; Iyakwari et al., 2013; Iyakwari and Glass, 2015). Therefore, since the literature suggests platinum association with orthopyroxene (enstatite), base metal sulphide (chalcopyrite) and amphiboles (hornblende), NIR spectra of these minerals were examined with reference to Clark et al. (2003). Analysis revealed the ability of both enstatite and hornblende to show features near 2300 nm and 2320 nm respectively with an additional feature near 1400 nm showed by both minerals. Chalcopyrite on the other hand does not display feature(s) within the 1300 to 2400 nm range used. The inability of chalcopyrite to display features is largely due to it not being a NIR functional group bearing mineral and also due to it being iron bearing, as iron suppresses features of some minerals (Clark, 1995; Bishop and Dummel, 1996). Note that the features displayed by enstatite are as a single mineral, it is unknown here whether or not it can show feature(s) when it occurs in intimate or complex mixtures, especially since it does not contain a NIR functional group. Therefore, when scoping NIR application in the next

section, it'll be assumed that spectra without features are enstatite or chalcopyrite dominant.

The study of functional groups will inform the economics of NIR preconcentration strategy or technique, since NIR response is influenced by individual mineral functional group(s). Since chalcopyrite occurrence is not consistent (Tables 10.1), only enstatite and hornblende are considered in the scoping application.

Analysis of the fifty one samples reveals only fourteen samples (25 % of total samples) contain  $\text{CO}_3^{2-}$ , with concentration ranging from 0.6 % (sample 19) to 8.99 % (sample 6). All  $\text{CO}_3^{2-}$  in the samples is from calcite. A calcite mineral contain on average 59.95 % of  $\text{CO}_3^{2-}$  (www.webmineral.com 2013). Almost all samples contain -OH groups. This is due to the fact that the ore is dominated by -OH bearing silicate minerals (chlorite, hornblende, antigorite, and talc). Chlorite contains 22.85 %, hornblende 3.6 %, antigorite 22.61 %, talc 8.96 % and brucite 58.2 % -OH (www.webmineral.com 2013). Sample 37 has the least -OH concentration of 0.46 % while sample 41 has the highest concentration of 12.10 %.



Table 10.3 - Calculated modal composition (wt. %) of hydroxyl and carbonate functional groups and orthopyroxene mineral, with reference to [www.webmineral.com](http://www.webmineral.com) (2013). Where: bdl = below detection limit

Allocated ID	Hydroxyls						Carbonate	Orthopyroxene (enstatite)	Cumulative -OH	Cumulative CO <sub>3</sub> <sup>2-</sup>
	Percentage functional groups									
	8.11% -OH	22.61% -OH	22.85% -OH	3.60% -OH	8.96% -OH	58.20% -OH	59.95% CO <sub>3</sub> <sup>2-</sup>			
Phlogopite	Antigorite	Chlorite	Hornblende	Talc	Brucite	Calcite				
1	0.49	2.26	1.14	0.18	0.27	bdl	bdl	52	4.34	bdl
2	0.32	1.36	1.83	0.5	0.09	bdl	3	13	4.1	3
3	0.24	1.58	3.43	0.47	0.45	bdl	5.4	20	6.17	5.4
4	0.16	0.9	4.11	0.18	0.27	bdl	1.2	26	5.63	1.2
5	0.32	0.9	1.83	0.07	0.18	bdl	bdl	59	3.31	bdl
6	0.57	2.49	4.57	0.32	0.45	bdl	8.99	10	8.4	8.99
7	0.32	4.07	2.29	0.25	0.9	bdl	bdl	41	7.83	bdl
8	0.57	2.71	4.11	0.36	0.45	bdl	bdl	16	8.2	bdl
9	0.24	0.68	1.37	0.18	0.36	bdl	bdl	51	2.83	bdl
10	0.32	0.9	0.23	0.04	0.09	bdl	bdl	59	1.58	bdl
11	0.49	2.71	2.29	0.14	0.36	bdl	2.4	15	5.99	2.4
12	0.32	2.94	2.51	0.54	0.54	bdl	bdl	28	6.85	bdl
13	0.08	bdl	0.23	0.04	0.45	bdl	bdl	43	0.79	bdl
14	0.65	1.81	1.14	0.29	0.54	bdl	bdl	37	4.43	bdl
15	0.41	2.26	2.29	0.25	0.18	bdl	3	27	5.38	3
16	0.41	0.68	0.46	0.04	bdl	bdl	bdl	59	1.58	bdl
17	0.24	1.81	0.91	0.07	0.36	bdl	bdl	55	3.4	bdl
18	0.32	2.94	2.29	0.4	0.72	bdl	bdl	40	6.66	bdl
19	0.41	3.17	2.97	0.4	0.27	bdl	0.6	21	7.21	0.6
20	0.41	0.23	0.23	0.07	0.09	bdl	bdl	59	1.02	bdl
21	bdl	2.03	2.29	0.07	0.63	bdl	2.4	7	5.02	2.4
22	0.49	5.43	4.11	0.11	0.81	bdl	bdl	40	10.94	bdl
23	0.24	1.13	0.91	0.07	0.09	bdl	bdl	28	2.45	bdl
24	0.24	3.62	2.74	0.18	0.27	bdl	1.8	41	7.05	1.8
25	0.41	0.68	0.23	0.07	0.18	bdl	bdl	61	1.56	bdl
26	0.32	2.26	1.6	0.07	0.27	bdl	bdl	59	4.53	bdl
27	0.32	1.81	1.6	0.18	0.18	bdl	bdl	53	4.09	bdl
28	0.32	2.71	2.51	0.22	0.54	bdl	bdl	7	6.3	bdl
29	0.32	2.71	1.14	0.22	0.54	bdl	1.2	13	4.93	1.2
30	0.41	0.68	1.14	0.07	0.18	bdl	bdl	52	2.48	bdl
31	0.32	2.94	3.66	0.07	0.54	bdl	bdl	5	7.53	bdl
32	0.49	3.62	1.83	0.07	0.36	1.75	1.8	17	6.36	1.8
33	0.24	1.36	1.37	0.11	0.18	bdl	bdl	49	3.26	bdl
34	0.49	1.58	0.91	0.14	0.36	bdl	bdl	53	3.49	bdl

Cont. of Table 10.3 - Calculated modal composition (wt. %) of hydroxyl and carbonate functional groups and orthopyroxene mineral, with reference to [www.webmineral.com](http://www.webmineral.com) (2013). Where: bdl = below detection limit

Allocated ID	Hydroxyls							Carbonate	Orthopyroxene (enstatite)	Cumulative -OH	Cumulative CO <sub>3</sub> <sup>2-</sup>
	Percentage functional groups							CO <sub>3</sub> <sup>2-</sup>			
	8.11% -OH	22.61% -OH	22.85% -OH	3.60% -OH	8.96% -OH	58.20% -OH	59.95%				
Phlogopite	Antigorite	Chlorite	Hornblende	Talc	Brucite	Calcite					
35	0.32	4.75	1.83	0.07	0.36	bdl	1.8	3	7.33	1.8	
36	0.24	2.03	2.06	bdl	0.27	bdl	1.8	8	4.6	1.8	
37	0.16	bdl	0.23	0.07	bdl	bdl	bdl	2	0.46	bdl	
38	0.49	2.94	2.51	0.47	0.36	bdl	bdl	26	6.77	bdl	
39	0.24	1.13	0.91	bdl	0.18	bdl	bdl	58	2.47	bdl	
40	0.57	2.71	2.97	0.83	0.54	bdl	bdl	30	7.62	bdl	
41	0.81	6.33	4.11	0.04	0.81	bdl	bdl	28	12.1	bdl	
42	0.32	2.26	1.14	0.22	0.36	bdl	bdl	41	4.3	bdl	
43	0.16	bdl	0.23	0.07	0.45	bdl	bdl	49	0.91	bdl	
44	0.24	2.94	0.91	0.22	0.18	bdl	bdl	54	4.49	bdl	
45	0.16	1.13	1.6	0.29	0.09	bdl	bdl	18	3.27	bdl	
46	0.57	2.71	1.6	0.18	0.36	bdl	bdl	22	5.42	bdl	
47	0.16	0.68	5.03	0.18	0.36	bdl	3	28	6.41	3	
48	0.08	bdl	0.91	0.11	bdl	bdl	bdl	bdl	1.1	bdl	
49	0.24	0.9	0.46	0.07	0.09	bdl	bdl	62	1.77	bdl	
50	0.32	1.36	1.14	0.18	0.36	bdl	bdl	49	3.36	bdl	
51	0.16	2.94	2.51	0.47	0.27	bdl	bdl	47	6.35	bdl	

The ore is dominated by silicates and the dominant silicate is enstatite (Table 10.1). Since enstatite is considered here to be associated with platinum, using an enstatite cut-off grade of 25 % and hydroxyl grade of 5 % (to accommodate for hornblende's 3.6 % -OH content), Table 10.4 presents a correlation between enstatite and hydroxyl. Note that the enstatite grade used does not in any way reflect the percentage of platinum in the ore, it is only assumed. Hence it is suggested that NIR application (intimate mixtures) be sought on precise concentration and conditions at which enstatite can cancel out or dominate any -OH bearing mineral's features.

Table 10.4 reveals that twenty two samples (1, 5, 9, 10, 13, 14, 16, 17, 20, 23, 25, 26, 27, 30, 33, 34, 39, 42, 43, 44, 49 and 50) classified as high enstatite-low hydroxyl bearing. Twelve samples (4, 7, 12, 15, 18, 22, 24, 38, 40, 41, 47 and 51) classified as high enstatite-high hydroxyl samples. Eleven samples (3, 6, 8, 11, 19, 21, 28, 31, 32, 35 and 46) classified as low enstatite–high hydroxyl bearing and only six samples (2, 29, 36, 37, 45 and 48) classified as low enstatite –low hydroxyl.

The near absence of calcite and other carbonate bearing minerals in the ore results in only sample 6 having the highest calcite concentration of 15 % and  $\text{CO}_3^{2-}$  of 8.95 %, Table 10.5 presents enstatite-carbonate correlation, taking an enstatite cut-off grade of 10 % and  $\text{CO}_3^{2-}$  grade of 3 % (note, these are only assumed cut-off-grades). Analysis shows samples classified into three categories. Five samples (2, 3, 6, 15 and 47) classified as high enstatite–high carbonate, seven samples (21, 28, 31, 35, 36, 37 and 48) as low enstatite–low carbonate while thirty nine samples classified as high enstatite–low carbonate.

Since enstatite and hornblende are indirectly the targeted product and preconcentration from -OH and or  $\text{CO}_3^{2-}$  bearing samples is the aim, the following classes are considered to produce economic concentrate.

1. High enstatite-low hydroxyl samples (1, 5, 9, 10, 13, 14, 16, 17, 20, 23, 25, 26, 27, 30, 33, 34, 39, 42, 43, 44, 49 and 50)

and/or

2. High enstatite-low carbonate samples (1, 4, 5, 7, 8, 9, 10, 11, 12, 13, 14, 16, 17, 18, 20, 22, 23, 24, 25, 26, 27, 29, 30, 32, 33, 34, 38, 39, 40, 41, 42, 43, 44, 45, 46, 49, 50 and 51).

When comparing the two groups, note that some samples classified earlier as either high  $\text{-OH}$  or high  $\text{CO}_3^{2-}$ , therefore, combining them, the following samples can be targeted for economic concentration (samples 1, 5, 9, 10, 13, 14, 16, 17, 20, 23, 25, 26, 27, 30, 33, 34, 39, 42, 43, 44 and 50). This is because they contain low  $\text{-OH}$  and  $\text{CO}_3^{2-}$ . Note that this is a repeat of all samples in the high enstatite –low hydroxyl group. Hence, on the basis of above, the preconcentration strategy can follow Figure 10.2.

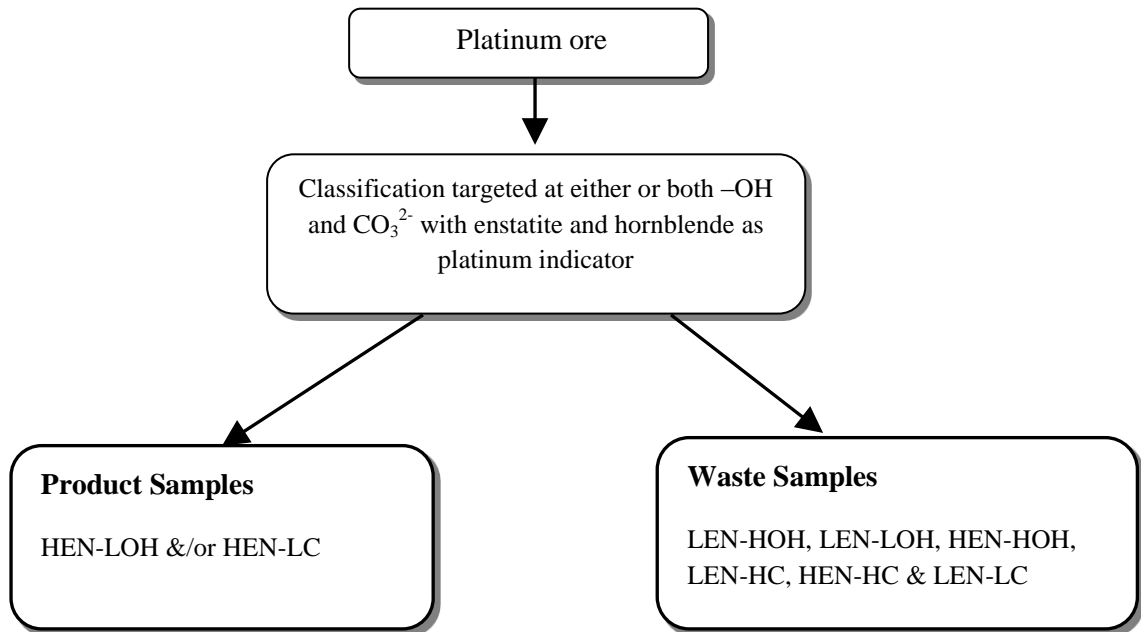


Figure 10.2 - Proposed model for the Mogalakwena platinum preconcentration, based on ore mineralogy targeted towards eliminating either or both carbonate and high hydroxyl bearing samples.

This strategy may not hold perfect for NIR, because hornblende is an amphibole that also contains  $\text{-OH}$  and NIR does not sense bulk  $\text{-OH}$  but individual mineral's constituent.

Table 10.4 - Classification of samples based on orthopyroxene-hydroxyl concentration. Where HEN = High Enstatite, HOH = high hydroxyl, LEN = low Enstatite, and LOH = low hydroxyl. Class of sample is marked with +

Allocated ID	HEN-HOH	HEN-LOH	LEN-HOH	LEN-LOH
1		+		
2				+
3			+	
4	+			
5		+		
6			+	
7	+			
8			+	
9		+		
10		+		
11			+	
12	+			
13		+		
14		+		
15	+			
16		+		
17		+		
18	+			
19			+	
20		+		
21			+	
22	+			
23		+		
24	+			
25		+		
26		+		
27		+		
28			+	
29				+
30		+		
31			+	
32			+	
33		+		
34		+		
35			+	
36				+
37				+
38	+			
39		+		
40	+			
41	+			
42		+		
43		+		
44		+		
45				+
46			+	
47	+			
48				+
49		+		
50		+		
51	+			

Table 10.5 - Classification of samples based on orthopyroxene-carbonate concentration. Where HEN = High orthopyroxene, HC = high carbonate, LEN = low orthopyroxene, and LC= low carbonate. Class of sample is marked with +

Sample ID	HEN-HC	HEN-LC	LEN-HC	LEN-LC
1		+		
2	+			
3	+			
4		+		
5		+		
6	+			
7		+		
8		+		
9		+		
10		+		
11		+		
12		+		
13		+		
14		+		
15	+			
16		+		
17		+		
18		+		
19		+		
20		+		
21				+
22		+		
23		+		
24		+		
25		+		
26		+		
27		+		
28				+
29		+		
30		+		
31				+
32		+		
33		+		
34		+		
35				+
36				+
37				+
38		+		
39		+		
40		+		
41		+		
42		+		
43		+		
44		+		
45		+		
46		+		
47	+			
48				+
49		+		
50		+		
51		+		

## 10.5. NIR spectra classification and discussion

Spectra of the samples are presented in Appendix 10.1b. Almost all the alteration minerals show a feature near 1400 nm, with additional features at longer wavelengths, with positions dependent on individual mineral constituent functional group(s). Therefore, the strategy for ore classification shall follow:

- A. Product - these are samples with features near 2300 nm (enstatite), 2320 nm (phlogopite and hornblende), and or featureless spectra.
- B. Waste - this are samples with spectra showing features near 2260 or 2265 and/or 2360 (chlorite), 2330 nm (antigorite) and 2340 and/or 2335 nm (calcite).

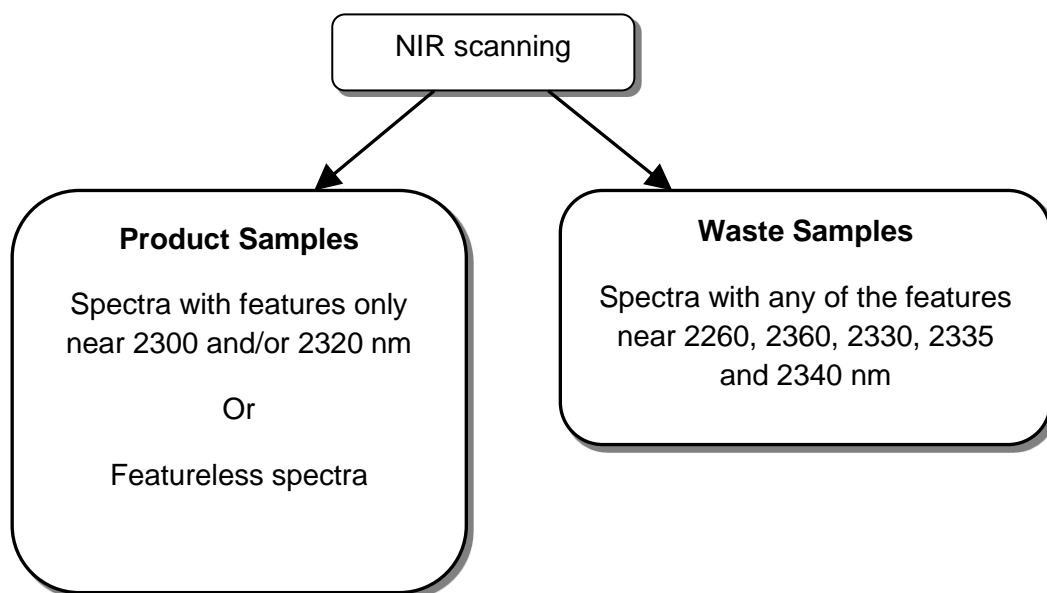


Figure 10.3 - Model for classification of the Mogalakwena platinum ore

From the fifty one samples analysed, seven absorption features are observed in most spectra at the longer wavelength range near 2260, 2315, 2320, 2325, 2330, 2335 and 2360. These features when compared with the spectra library (Clark et al., 2003) are characteristic of chlorite (2260 and 2360 nm), phlogopite and hornblende (2320 nm), antigorite (2325 and 2330 nm) and calcite (2335 and 2340 nm). Since these minerals, with the exception of hornblende, are not of economic interest, classification of the spectra will depend on the presence or absence of absorption features related to them. Therefore, spectra with features

relating to these minerals are thereby considered waste (gangue) while those without the features or having features relating to hornblende or phlogopite are considered product. Hornblende and phlogopite are considered together since they share a feature near 2320 nm and discrimination cannot be achieved when they occur together. Therefore, only calcite, antigorite and chlorite are targeted by NIR for discrimination.

This strategy is true even if chromite and other sulphides were to be present in concentration as they show no absorption features within the 1300 to 2400 nm NIR range.

Given that the samples are powdered the number of features and probably some features position may vary from those obtained from solid samples of the same deposit. This is because powdered samples are complex mixtures while solids are likely to show spatial variation of minerals.

For economic correlation, it is recommended that a PGM analysis be performed so as to be sure samples are properly classified. This should include ICP-MS and mineralogy as discussed by Holwell and McDonald, (2007).

The NIR classification of fifty one samples is presented below (Table 10.6).



Table 10.6 - NIR classification of the Mogalakwena platinum samples. Where Shared = OH shared feature, Ch. = chlorite, Ho. = Hornblende, Pl. = Phlogopite, Ant. = Antigorite, Cal. = Calcite, W = Waste and P = Product

Allocated ID	NIR absorption feature wavelength (nm)							NIR classification
	1400	2260	2320	2325	2330	2335	2360	
	Shared	Ch.	Ho./Pl	Ant	Ant	Cal	Ch.	
1	+				+			W
2	+							W
3	+		+			+		P
4								P
5								P
6	+		+					P
7								P
8	+		+					P
9	+		+					P
10								P
11	+		+					P
12								P
13								P
14					+			W
15								P
16								P
17	+							P
18	+							P
19	+				+			W
20								P
21	+				+			W
22	+		+					P
23								P
24								P
25								P
26								P
27								P
28	+				+			W
29	+				+			W
30	+		+					P
31					+			W
32	+				+			W
33								P
34				+				W
35					+			W
36					+			W
37								P
38	+				+			W
39								P
40					+			W
41	+							P
42					+			W
43								P
44								P
45								P
46				+				W
47			+					P
48		+					+	W
49								P
50								P
51			+					P

No sample showed a feature near 2300 nm to indicate the presence of enstatite in the spectra, therefore it can be said that enstatite only produces absorption feature(s) as a single mineral and the feature disappears when in mixtures with other minerals. But feature masking is noticed in the spectra of some samples with high enstatite concentration (e.g. samples 7, 15, 18, and 24). While sample 41, contains a complex mixture of four NIR-active minerals at relatively high concentration, making the sample's spectra broad and featureless. For the purpose of the present research and ore, enstatite can be categorised as an NIR-active mineral which does not display absorption feature(s).

On the basis of the NIR activity of individual minerals with respect to the ore, minerals can be listed in order of decreasing activism as antigorite, phlogopite and hornblende, chlorite and calcite. This can be observed from the dominant presence of antigorite features in spectra of samples even when its concentration relative to that of other NIR-active minerals is relatively low.

Mineralogical analysis based on functional groups classified twenty one samples as economic while the NIR classified thirty four samples (as product (Table 10.7).

Of the twenty one samples classified as economic by the mineralogical strategy, only four samples (samples 1, 14, 34, and 42) are misclassified by NIR as waste, while seventeen samples are correctly classified. It should be noted that the NIR senses the constituent functional group in individual mineral rather than the bulk functional composition that is used for mineralogical classification. Therefore, absorption features displayed in spectra are characteristic of individual minerals functional groups and not a combination of various minerals functional group, even if the constituent minerals in a sample contain the same functional group. For example, chlorite and antigorite are all -OH bearing but this does not mean they will show a single feature depicting both of them in a spectrum, rather the mineral with the strongest NIR absorbing ability may dominate the spectra and in some cases both minerals may show their individual features in the same spectrum. When two or more minerals show features in the same spectra, the spectra is considered to be mixed (Iyakwari and Glass, 2015).

Table 10.7 - Comparison of NIR and Mineralogy classifications.

Where MIN = Mineralogy, P and W indicate product, and waste, respectively

Allocated ID	Classification	
	NIR	MIN
1	W	P
2	W	W
3	P	W
4	P	W
5	P	P
6	P	W
7	P	W
8	P	W
9	P	P
10	P	P
11	P	W
12	P	W
13	P	P
14	W	P
15	P	W
16	P	P
17	P	P
18	P	W
19	W	W
20	P	P
21	W	W
22	p	W
23	P	P
24	P	W
25	P	P
26	P	P
27	P	P
28	W	W
29	W	W
30	P	P
31	W	W
32	W	W
33	P	P
34	W	P
35	W	W
36	W	W
37	P	W
38	W	W
39	P	P
40	W	W
41	P	W
42	W	P
43	P	P
44	P	P
45	P	W
46	W	W
47	P	W
48	W	W
49	P	W
50	P	P
51	P	W

Examination of the four NIR misclassified samples show that the samples contained individually one or more NIR-active minerals in the excess of 5 wt %. Samples 1 contain 10 wt % antigorite, 6 wt % phlogopite and 5 wt % chlorite and hornblende respectively. Its spectra shows an antigorite feature near 2330 nm indicating the dominant influence of antigorite relative to other NIR-active minerals in sample and 52 wt % enstatite.

Mineral data shows sample 14 containing all NIR-active minerals in the ore with compositions ranging from 5 wt % for chlorite to 8 wt % for hornblende, antigorite and phlogopite, while spectra the shows absorption features near 2330 nm indicative of antigorite spectra dominance.

Sample 34 shows features near 2325 nm and mineral data indicates antigorite (7 wt %) and phlogopite (6 wt %) as the dominant NIR-active minerals. The feature near 2325 nm indicates a shift from either 2330 nm for antigorite or 2320 nm for phlogopite. As the analysis of a minerals dominance in the ore has not been done to scope at what ratio one mineral is dominant in a spectrum, the feature is assigned to both minerals and the samples is thus classified as waste.

Spectra of sample 42 showed an absorption feature near 2330 nm indicative of an antigorite dominated spectra. Mineral data (Table 10.1) show the sample contains antigorite (10 wt %) as the dominant NIR-active mineral. Chlorite and hornblende occur at 5 wt % and 6 wt respectively.

Seventeen samples were classified as products by NIR but were noted as uneconomic by mineralogical classification. They are so classified by NIR because their spectra are either featureless or in some cases the spectra appeared broad. Examination of the mineral data indicates high enstatite concentration in samples 4, 7, 15, 18, 22, 24, 41, 45, 47, 49, and 51 and this may be responsible for masking the features of NIR-active minerals in concentration. In most of these samples the NIR-active mineral is chlorite and this suggests that enstatite may have a strong masking influence on the chlorite features. Samples 3, 6, 8, 11, and 12 contain two or more NIR-active minerals in high concentrations, resulting in a complex mixture where the spectra appears to show a depression at longer wavelengths and lacks an absorption

centre. In rare cases the samples does not contain either enstatite or the NIR-active minerals in concentration (e.g. sample 37).

#### **10.6. Recommendations**

Based on the above discussion, the following recommendations are made.

1. Application be sought to determine precisely and quantitatively the cut-off grade at which one mineral dominates spectra over the other.
2. ICP-MS analysis should be carried out on the samples to test whether or not the NIR assumptions hold true. The aim would be for the Products to contain PGE and the waste not to contain PGE, or, very low PGE. ICP-MS analysis allows the concentrations of PGE to be accurately known.

## Chapter 11: Discussion, conclusions and recommendations

### 11.1. Discussion

The aim of this project was to investigate the potential and suitability of applying NIR to the preconcentration of complex ores. Two ore types (copper ore from Mantoverde mine in Chile and platinum ore from Mogalekwena mine in South Africa) were tested. Both ore types were analysed for the removal of carbonate and or clay rich particles, as waste from concentrate copper and platinum ores. The main research objective was to upgrade the ores, by improving metal recovery and reducing overall processing cost. Though powdered samples were received from the Mogalekwena mine, this research is intended at preconcentrating larger chunks/fragments. Hence, reducing the cost of grinding crushed particles to fine particle sizes is a major target, since gangue dominated particles are removed at the early stage of operation.

Individual Mantoverde samples were divided into four fractions by cutting them. Each fraction was subjected to various characterization processes for mineralogical, chemical and spectral analysis. Mineralogical analysis was performed by QEMSCAN<sup>®</sup> and XRD equipment, while the chemical analysis was done by portable XRF equipment. About fifteen minerals phases from four major mineral groups: silicates (chrysocolla, muscovite, kaolinite, biotite, chlorite, tourmaline, quartz, K-feldspars, and plagioclase feldspars), carbonates (malachite, calcite, and ankerite), oxides (hematite and cuprite) and phosphate (apatite) were identified to occur in appreciable concentration. Of the fifteen minerals phases, only chrysocolla, malachite and cuprite are copper bearing. While malachite and cuprite occurred in minute concentrations in a few samples, chrysocolla is the major copper bearing mineral in the ore.

The range of the NIR wavelength used for the research (1300 to 2400 nm) only sensed or identified particles based on their individual constituent mineral functional groups (-OH, H<sub>2</sub>O, and CO<sub>3</sub><sup>2-</sup>) and does not identify elemental composition. Consequently, NIR application was sought for the preconcentration of copper bearing minerals from associated non-copper bearing minerals.

Of the three copper bearing minerals, only chrysocolla and malachite show absorption feature(s) within the NIR range (1300 to 2400 nm). Hence, their preconcentration was sought from other constituent associated gangue minerals. Mineral data was used to develop two preconcentration strategies by assuming cut-off grade for copper (0.5 %), -OH (5 %) and  $\text{CO}_3^{2-}$  (2 %). The first strategy targeted the removal of both -OH and  $\text{CO}_3^{2-}$  dominated particles, while the second strategy targeted only the elimination of  $\text{CO}_3^{2-}$  bearing particles as waste. Observations from both strategies showed that either or both -OH and  $\text{CO}_3^{2-}$  dominant waste particles can be reduced from feed. But given the fact that chrysocolla which is the dominant copper bearing mineral contains -OH, and some samples had their -OH concentration above the assumed cut-off grade, it was discovered that copper in the form of chrysocolla was lost to waste. Therefore, preconcentrating copper bearing particles from dominant  $\text{CO}_3^{2-}$  waste is more economical.

Copper content was calculated from copper bearing minerals as analysed by QEMSCAN<sup>®</sup>. Calculated values were reconciled and compared with measured values obtained from XRF. Correlation results indicated only a few samples were over- or under-estimated by either instrument. Of the sixty samples, 85 % had their copper concentration within range of one another with only 15 % of samples showing variation. Variation in values could be due to the fact that values from QEMSCAN<sup>®</sup> were “back calculated” from copper bearing minerals. Hence, it is not a direct method as it makes assumptions about the average chemistry and density of a mineral, which may not hold perfect in some cases.

Of the fifteen mineral phases detected from mineralogical analysis, only ten minerals (chrysocolla, malachite, muscovite, kaolinite, biotite, chlorite, tourmaline, calcite, ankerite and apatite) contain NIR-active functional groups (-OH,  $\text{H}_2\text{O}$ , and  $\text{CO}_3^{2-}$ ) in their chemical structure. Although hematite does not contain any of the NIR-active functional groups or display any absorption feature, it absorbs strongly across the wavelength range (1300 to 2400 nm). Also where hematite occurs with other NIR-active minerals, depending on the mineral and concentration, hematite has the ability to suppress the absorption feature(s) of the other mineral. Hence, hematite is also considered to be NIR-active. Mineral such as quartz, K-feldspars and plagioclase feldspars do not

contain NIR-active functional groups and as such do not influence spectra either by absorbing or displaying absorption features within the 1300 to 2400 nm NIR region. As a result, minerals were classified into two groups as NIR-active and non-active, with the NIR-active group further divided into absorption feature displaying and the non-feature displaying minerals.

Since individual particles of an ore contain a variable number of NIR-active minerals, and within a NIR spectrum range a number of minerals could exist in various forms of arrangement and associations, about twelve spatial mineral associations were identified. Individual NIR spectra (scan area) had a dimension of 2.9 by 9 mm. To predict the behaviour of NIR-active minerals within the same spectrum range, pure NIR-active minerals were studied individually, after which mineral mixtures were prepared and analysed. Specimens were prepared to simulate natural ore mineral associations. Two types of mixture (intimate and linear) were studied. Intimate mixtures involved the mixing and homogenization of two or more NIR-active minerals at equal or varying ratios of concentration by mass, such that all minerals in concentration appeared together within same spectrum range when scanned. Minerals analysed for linear mixtures were optically separated and arranged to stimulate adjacent natural mineral associations.

While only twelve spatial mineral associations were identified in the Mantoverde particles, to accommodate for more possible associations, other associations were assumed and investigated. On that basis, extensive research was carried out on intimate mixtures, the outcome of which lead to the development of strategies for copper ore (chrysocolla and or malachite bearing) preconcentration using NIR. With respect to chrysocolla preconcentration, similar to the mineralogical strategies, two options were proposed. The first option considered targeting the removal of both muscovite (-OH bearing) and calcite ( $\text{CO}_3^{2-}$  bearing) particles as waste, while the second option only targeted the removal of calcite bearing particles from feed concentrate as waste. The first option depends on the association of chrysocolla and hematite. This option assumes that all chrysocolla features are masked by hematite, with resultant spectra appearing flat and featureless. While the second option considers the fact that muscovite (and other -OH bearing minerals) with chrysocolla show



mixed features at equal concentrations and dominate spectra when either mineral is higher in concentration in the absence of hematite. Hence, the first option is only to be considered for ores with known hematite-chrysocolla association. In addition to both options, flat or featureless spectra are also considered chrysocolla bearing. This is true since biotite-chrysocolla association also produced featureless spectra across intimate mixture ranges. Note that targeting muscovite for elimination also targets kaolinite and other clay minerals that share similar Al-OH absorption feature near 2200 nm (which is beneficial for upgrading the ore).

The overall results of intimate mixtures revealed that chrysocolla, biotite, chlorite and hematite are better considered together for the purpose of chrysocolla preconcentration. Also, calcite visibility in the spectra of mixtures is concentration dependent, except with biotite. Hence, where calcite features are visible in a spectrum, the spectrum indicates nearly a pure calcite specimen. Interestingly, chrysocolla absorption features can also be used to concentrate malachite where both minerals occur together.

From intimate mixtures, strategies for the preconcentration of hematite from clay and carbonate waste were proposed.

While intimate mixtures were optically inseparable, with spectra revealing dominance of one NIR-active mineral over the other mineral response, the linear mixtures revealed the influence of boundary and mineral positioning. Two types of linear mixtures (mineral arrangement) were investigated: a) vertical and b) horizontal arrangements. The vertical arrangement revealed that where two NIR-active minerals have contact with each other along a similar NIR spectrum range, depending on the constituent minerals, the spectrum is likely to show features of both minerals. While horizontal arrangement showed that where one NIR-active mineral appeared above the other, absorption features of the first mineral appeared stronger and in some cases those of the mineral below are absent. Hence, the first mineral encountered exerts more spectral dominance.

Of interest in linear mixtures is the observation that the depth of NIR penetration is mineral opacity dependent. This was observed in the penetration of a 0.7 cm

thick calcite sample by NIR, with resultant spectra showing absorption features of NIR belt.

The analysis of both linear and intimate mixtures revealed that spectra dominance and absorption feature(s) visibility in particles containing a mixture of NIR-active minerals may depend on any or a combination of a) NIR-active mineralogical composition, b) relative proportion or concentration, c) relative mineral accessibility to NIR radiation and d) minerals position or exposure.

The NIR strategies scoped from the various analysis of single and mixtures of NIR-active minerals were applied to ore particles. Given the dominant copper bearing mineral is chrysocolla, options relating to chrysocolla were applied to the Mantoverde ore. To properly map individual Mantoverde particles for a 1:1 correlation of spectra with mineralogy (mineral data and fieldscan images), splits B1(see chapters three and eight) were partitioned into individual spectrum range based on spectrum dimension, with each portion measuring a height of 0.9 cm and a width of 0.29 cm. The splits B2 samples were scanned along their longest axis, while the powdered splits A1 samples were placed on a petri dish and measured.

Spectrum maps per particle based on the spectrum characteristic absorption feature and mineral(s) responsible for the absorption were produced per split. Using the developed NIR strategies, two options were modified and applied for ore preconcentration. The first strategy considered discriminating both muscovite and calcite as waste, while the second strategy targeted calcite only for elimination as waste. This was achieved by classifying each particle based on the dominant spectrum group: as product, waste or middling, with the middling particles further re-classified based on the percentage of dominant spectrum group. Ore parameters were calculated per strategy. Parameters revealed a higher copper recovery for the second option where only calcite was targeted. Thus agreeing with the findings of the second mineralogical strategy where only the  $\text{CO}_3^{2-}$  bearing particles were targeted as waste. Comparison of results revealed that copper as chrysocolla is locked in muscovite bearing particles in the first option. This also confirmed findings of intimate mixtures of chrysocolla and muscovite, and chrysocolla and kaolinite, where features of low

grade chrysocolla are dominated by both clay minerals. Hence, while the first option produced muscovite and calcite free particles as product with reduced dilution but at low recovery, the second option produced higher recovery with additional dilution from muscovite.

Since recovery is the determinant factor in mineral processing operations, the second option is more economic since less copper is lost as waste. Therefore the removal of calcite from chrysocolla rich copper ores is more promising than targeting both calcite and muscovite as low grade copper, in the form of chrysocolla may be locked in muscovite. This is true since the calcite feature visibility is only concentration dependent.

To determine the representativity and repeatability of NIR and QEMSCAN<sup>®</sup> data, spatial variation and data quality analysis was carried out on a few particles by cutting particles laterally into two halves and scanning them with both NIR and QEMSCAN<sup>®</sup>. Data obtained compared favourably with those of their whole samples. Hence, the investigation indicated that the data is representative and reproducible.

The Mogalekwena platinum ore samples were accompanied by their quantitative XRD data, but most minerals analysed were presented in group or family name. Therefore, qualitative XRD was performed by the author and data compared and corrected to reflect specific mineral(s) within each group. A literature review revealed that platinum in the Mogalekwena mine is associated with base metal sulphide (chalcopyrite), orthopyroxene (enstatite) and amphiboles (hornblende). As a result, an indirect approach where the presence of any or all of the associated minerals will indicate platinum occurrence was employed. Similar to the Mantoverde ore, the cut-off grade was assumed and mineralogical preconcentration strategy was scoped. Using NIR, individual samples were only classified into product and waste. This is because the samples were powdered and homogenized, and thus the spectra produced appeared similar showing absorption features at similar wavelength positions.

A product sample was defined by features near 2320 nm (phlogopite and hornblende), and or featureless spectra. While a waste sample was defined by spectra showing features near 2260 or 2265 and/or 2360 (chlorite), 2330 nm

(antigorite) and 2340 and/or 2335 nm (calcite). The NIR preconcentration of platinum targeted only the removal of chlorite, antigorite and calcite dominant samples from the feed. This was because absorption features of both hornblende (which is assumed to reflect platinum occurrence) and phlogopite could not be discriminated from each other. None of the spectra generated from the samples showed absorption features characteristic of enstatite. Yet where enstatite occurred at high concentration relative to other NIR-active minerals, spectra appeared featureless, especially where chlorite is the other NIR-active mineral in concentration. Hence, enstatite was considered a NIR-active mineral which does not show features of its own, but has the ability to mask features of other minerals.

Comparison of mineralogical and NIR classifications showed that only four out of twenty one samples (19 %) classified by the mineralogical strategy as economic were classified as waste by NIR. NIR classified them as waste because they all showed antigorite absorption features which in the NIR strategy is considered waste.

## **11.2. Conclusions**

Importantly, NIR spectroscopy is used in this research as a method of qualitative analysis for preconcentrating complex ores, since it does not measure elemental concentration. NIR techniques or strategies enabled particles with variation in mineralogy to be classified as middling and recommended for further liberation where applicable before re-scanning.

For these mineral preconcentration operations, only absorption features at longer wavelengths (between 2000 and 2400 nm) were considered suitable for separation as carbonates and hydroxyl bearing gangue minerals exhibit their best distinctive characteristics features along that region. These features also have better resistance to NIR-active non-feature displaying minerals masking effects and other environmental influence, such as moisture.

Water on the surface of a particle affects its resultant spectrum, and causes a decrease in reflectance and increases the depth of features near 1400 and 1900 nm. The degree of influence is dependent on the particle's mineral composition. Consequently, the methods developed used NIR regions with

minimal effect by water. In mines where water is a major influence, a drying step prior to sorting is proposed. Also, the use of NIR sensors to determine the moisture content in kaolinitic clays containing hematite is not recommended. The reason is that the absence of water features in such ores does not imply that the moisture content in the sample is zero.

QEMSCAN<sup>®</sup> fieldscan images were provided to show how individual mineral crystals or grains appear in a particle and are sensed by NIR. The comparison was possible because both the NIR and the QEMSCAN<sup>®</sup> have nearly a similar depth of particle penetration. The difference between these methods is that while the NIR sees only NIR-active minerals, QEMSCAN<sup>®</sup> identifies all minerals present in a sample, with an elemental detection limit of about 3 % per analysis point (Andersen et al. 2009). The advantage NIR has over QEMSCAN<sup>®</sup> is its ability to detect active minerals (H<sub>2</sub>O, -OH and CO<sub>3</sub><sup>2-</sup> bearing minerals) without rigorous sample preparation and at a lower detection limit. NIR is also faster than QEMSCAN<sup>®</sup>.

Comparison of XRD and NIR spectroscopy showed that NIR spectroscopy has a better detection limit compared to XRD and as such NIR detects minerals structure at a smaller scale than XRD, making measurement of low-crystallinity minerals possible. Furthermore, for the qualitative XRD, only the dominant NIR-active minerals based on concentration were detected. Hence, some samples showed NIR features of minerals not detected by qualitative XRD.

The combined use of NIR, QEMSCAN<sup>®</sup> (mineralogy and back calculated Cu values), PXRF and XRD (both qualitative and quantitative) has given a system of calibration that is favourable in optimizing mine operations, as the results are precise. The information provided here can be used for both mineralogical and metallurgical purposes aimed towards improving metal recovery, reducing acid consumption, and overall reduction in operational cost, as samples need not be prepared (except when wet and dusty) and the quantity of waste that report to grinding stage is minimized.

Ultimately, this work has indicated that a NIR sensor is suitable for preconcentrating both the Mantoverde and the Mogalekwena ores.

### 11.3. Key findings

Understanding the NIR-active constituent minerals in an ore and their best diagnostic features is an important initial stage in scoping the application of NIR sensing to mineral identification and ore preconcentration. This is true as NIR spectra of a particle is likely to differ from the spectra of its constituent individual NIR-active mineral(s).

- On the basis of minerals constituent functional groups ( $\text{H}_2\text{O}$ ,  $-\text{OH}$  and  $\text{CO}_3^{2-}$ ), and influence on spectra, minerals can be classified into two groups as NIR-active and non-active, with the NIR-active group further divided into absorption feature displaying and the non-feature displaying NIR-active minerals.
- NIR spectra dominance and absorption feature(s) visibility in a particle containing a mixture of NIR-active minerals may depend on any or a combination of:
  - ✓ a. NIR-active mineralogical composition,
  - ✓ b. relative proportion or concentration,
  - ✓ c. relative mineral accessibility to NIR radiation and
  - ✓ d. minerals position or exposure.
- No two minerals display completely identical absorption spectra. Though some features may be common to more than one mineral.
- On the basis of economics, the removal of calcite from chrysocolla-rich copper ores is a more promising option than targeting both calcite and muscovite, as low grade copper in the form of chrysocolla may be locked in muscovite.
- The absence of water or moisture features in spectra of a particle where hematite is present does not imply that its moisture content is zero.
- Near infrared as a preconcentration tool can achieve reduction in quantity of waste material reporting to the next processing stage. Thus reducing the cost of grinding crushed particles to fine particle sizes is a major target, since gangue dominated particles are removed at the early stage of operation.
- Targeting the muscovite absorption feature near 2200 nm for muscovite discrimination also targets kaolinite and other clay minerals. Where

calcite is present in concentration, the feature can also be used to target both low and high grade calcite. Hence, all three minerals can be preconcentrated together.

- The depth of NIR penetration is mineral opacity dependent. Hence, where opaque minerals overlie other NIR-active minerals, they dominate the spectra.
- The presence of water feature(s) in NIR spectra due to external influence is sample mineral composition dependent.
- Sample condition such as external moisture, dust and particle size of feed may necessitate some form of sample preparation (drying and/or crushing to size) in order to achieve good preconcentration.

#### **11.4. Recommendations**

Near infrared analysis was performed on a stationary belt. Therefore, the outcome of this research may differ if carried out on a moving belt in an industrial setting. To overcome the challenges of practical industrial implementation, further research is required. It is recommended that strategies outlined be tried and calibrated on a moving belt. Therefore, further work should concentrate on developing a program for inline ore preconcentration. Important areas worth considering are the speed of the conveyor belt, optimal number of diagnostic wavelengths required for selection and the optimal camera line time (length of time per transect of pixels at one wavelength). These parameters will require calibration and synchronization so that the camera can have enough time to identify a particle on the belt based on the selected wavelengths. For a stationary belt, 3000  $\mu\text{m}$  was deemed optimal for research given that 371 wavelengths were used for the research, while this line time is too slow, the number of wavelength is too much for a moving belt at a speed of  $0.5 \text{ ms}^{-1}$ . The optimal number of wavelengths may also depend on the research requirement, for example if calcite was the only targeted waste mineral, less wavelength will be required for selection, hence faster preconcentration. Therefore, these parameters are interdependent.

A significant observation is that the methods outlined are dependent upon the ore type and character, and may need to be calibrated for other ores to achieve optimal results. Therefore, to scope for application of this technique, a good

understanding of the constituent NIR-active minerals in an ore and their diagnostic features locations is essential.

More detailed investigation is recommended for the Mogalekwena platinum ore samples. Future investigation should analyse for platinum content in samples and compare values with the proposed strategies. Another recommendation is the qualitative and quantitative determination of cut-off grade at which one mineral dominates spectra over the other. Also for future research, chunks/fragments instead of powdered samples should be used to try NIR application on the Mogalekwena ore.



## References:

Andersen, J.C.O., Rollinson, G. K., Snook, B., Herrington, R., Fairhurst, J.R., 2009. Use of QEMSCAN<sup>®</sup> for the characterization of Ni-rich and Ni-poor goethite in laterite ores. *Miner Eng*, 22: 1119 -1129.

Aines, R.D., & Rossman, G.R., 1984. Water in minerals? a peak in the infrared *J Geophys Res*, 89 (B6) 4059-4071.

Arvidson, B., 2002. Photometric ore sorting *In: Mular, A. L., Halbe, D. N. & Barratt, D. J. (eds.) Mineral Processing Plant Design, Practice, and Control*. Littleton, Colorado: Society for Mining, Metallurgy, and Exploration, Inc. (SME).

Augus, A. J. L., 2011. Mapping white mica in milled porphyry copper pebbles using hyperspectral imagery: An exploratory study. MSc. Dissertation University of Twente.

Augusto, P. A., Augusto, P., & Castelo-Grande, T., 2002. Magnetic classification. *Miner Eng*, 15, 35-43.

[bbc.co.uk/weather](http://bbc.co.uk/weather) 2013. Website accessed for Falmouth (Cornwall) weather.

Benavides, J., Kyser, T. K., Clark, A. H., Oates, C. J., Zamora, R., Tarnovschi, R., & Castillo, B., 2007. The Mantoverde iron oxide-copper-gold District, III Región, Chile: The role of regionally derived, nonmagmatic fluids in chalcopyrite mineralization. *Econ Geol*, 102(3), 415-440.

Bennett, D., Miljak, D., & Khachan, J., 2007. The measurement of chalcopyrite content in rocks and slurries using magnetic resonance. *Miner Eng*, 22, 821-825.

Bishop, J. L., & Dummel, A., 1996. The influence of fine-grained hematite powder on the spectral properties of Mars soil analogs; VIS-NIR bi-directional reflectance spectroscopy of mixtures. Lunar and Planetary Institute Science Conference Abstracts, Vol. 27.

Bokobza, L., 1998. Near Infrared Spectroscopy. *J Near Spectrosc*, 6, 3-7.

- Bornstein, B., Gilmore, M., Castano, R., & Greenwood, J., 2007. Automated mineral detection in visible/near-infrared spectra for focus-of-attention. *LPS XXXVIII*.
- Bowman, D. J., & Bearman, R. A., 2014. Coarse waste rejection through size based separation. *Miner Eng*, 62, 102-110.
- Brandt, F., & Haus, R., 2010. New concepts for lithium minerals processing. *Miner Eng*, 23, 659-661.
- Bruker.com\_2013. Website accessed for X-Ray Diffraction (XRD) equipment.
- Cawthorn, G. R., & Boerst, K., 2006. Origin of the pegmatitic pyroxenite in the Merensky unit, Bushveld Complex, South Africa. *J Petrol*, 47(8), 1509-1530.doi:10.1093/petrology/eg1017.
- Chatterjee, S., Bhattacharjee, A., Samanta, B., & Pal, S. K., 2010. Image-based quality monitoring system of limestone ore grades. *Comput Ind*, 61, 391-408.
- Ciurczak, E., 1987. Uses of near-infrared spectroscopy in pharmaceutical analysis. *Appl Spectrosc Rev*, 23, 147-163.
- Clark, R. N., & Roush, T. L., 1984. Reflectance spectroscopy quantitative-analysis techniques for remote-sensing applications. *J Geophys Res*, 89, 6329-6340.
- Clark, R. N., King, T. V. V., Klejwa, M., Swayze, G. A., & Vergo, N., 1990. High spectral resolution reflectance spectroscopy of minerals. *J Geophys Res*, 95(B8) 12653–12680.
- Clark, R. N., Swayze, G. A. Gallagher, A. J. King, T. V. V., & Calvin, W. M., 1993. The U. S. Geological Survey, Digital Spectral Library: Version 1: 0.2 to 3.0 microns, U.S. Geological Survey Open File Report 93-592, 1340 pages.
- Clark, R. N., 1995. Reflectance spectra In: Ahrens, T.J. (Ed.), *Rock Physics and Phase: A Handbook of Physical Constants*, Washington, American Geophysical Union, 178–188.

- Clark, R. N., 1999. Spectroscopy of rocks and minerals and principles of spectroscopy, p3–52. *In N Rencz (ed.)*. Remote sensing for the earth sciences: Manual of remote sensing. Vol. 3. John Wiley & Sons, New York.
- Clark, R. N., Swayze, G. A., Wise, R., Livo, K. E., Hoefen, T. M., Kokaly, R. F., & Sutley, S.J., 2003. USGS Digital Spectral Library splib05a, U.S. Geological Survey, Open File Report 03-395.
- Clark, R. N., Swayze, G. A., Wise, R., Livo, E., Hoefen, T., Kokaly, R., & Sutley, S.J., 2007. USGS digital spectral library splib06a: U.S. Geological Survey, Digital Data Series 231, <http://speclab.cr.usgs.gov/spectral.lib06>.
- Coates, J., 2000. Interpretation of infrared spectra, a practical approach. In: *Encyclopaedia of Analytical Chemistry*, R. A Meyers (Ed), 10815–10837, Wiley & Sons Ltd, Chichester
- Crowley, J. K., & Vergo, N., 1988. Near-infrared reflectance spectra of mixtures of kaolin-group minerals: use in clay mineral studies. *Clay Miner* 36 (4), 310-316.
- Cutmore, N. G., & Eberhardt J. E., 2002. The future of ore sorting in sustainable processing. Green processing conference. Cairn, Qld, 29-31 May 2002.
- Cutmore, N. G., Liu, Y., & Middleton, A. G., 1998. On-line ore characterisation and sorting. *Miner Eng*, 11, 843-847.
- Curtis, B., 2012. Developing automated copper ore processing using NIR analysis and XRD. *Adv Mater Process*, 170 (2): 24–26.
- Dalm, M., Buxton, M. W., van Ruitenbeek, F. J., & Voncken, J. H., 2014. Application of near-infrared spectroscopy to sensor based sorting of a porphyry copper ore. *Miner Eng*, 58, 7-16.
- De Jong, T. P. R., & Harbeck, H., 2005. Automatic sorting of minerals: current status and future outlook. Proceedings of 37th Annual Meeting of the Canadian Mineral Processors, 629-648.

De Jong, T. P. R., 2005. Automatic rock sorting [Online]. Available: <http://www.citg.tudelft.nl/live/pagina.jsp?id=dd1900a4-acbc-4662-a267-c48181275fcd&lang=en> [Accessed 31/07/2013].

Ehlers, A., 2007. Viewing Program 2 User Guide. CommoDaS GmbH

Farcomeni, A., Serranti, S., & Bonifazi, G., 2008. Non-parametric analysis of infrared spectra for recognition of glass and glass ceramic fragments in recycling plants. *Waste Manage*, 28, 557-564.

Fleischer, U., & Bergmann, J., 2004. Waste Separation with the Mogenson AR 1200 X-Ray Sorter. *Aufbereitungs Technik*, 45, 5 - 10.

Gaffey, J. S., 1986. Spectra reflectance of carbonate minerals in the visible and near infrared (0.35-2.55 microns): calcite, aragonite and dolomite. *Am Mineral*, 71, 151-162.

Gavyn Rollinson, 2015, personal communication, discussion on boundary effects issues on QEMSCAN<sup>®</sup> and SEM analytical methods.

Gaydon, J. W., Glass, H. J., & Pascoe, R. D., 2009. Method for near infrared sensor-based sorting of a copper ore. *J Near Infrared Spectrosc* 17, 177-194.

Gaydon J. W., 2011. The application of a near-infrared sensor to the sorting of minerals. Ph.D. Thesis Camborne School of Mines, University of Exeter, Penryn Campus.

Goetz, A. F. H., Curtiss, B., & Shiley, D. A., 2009. Rapid gangue mineral concentration measurement over conveyors by NIR reflectance spectroscopy, *Miner Eng* 22(5), 490–499.

Gomez, C., Lagacherie, P., & Coulouma, G., 2008. Continuum removal versus PLSR method for clay and calcium carbonate content estimation from laboratory and airborne hyperspectral measurements. *Geoderma*, 148, 141-148.

Gottlieb, P., Wilkie, G., Sutherland, D., Ho-Tun, E., Suthers, S., Perera, K., Jenkins, B., Spencer, S., Butcher, A., & Rayner, J., 2000. Using quantitative electron microscopy for process mineralogy applications. *JOM*, 52(4): 24-25.

- Gupta, K. C., 2003. Chemical metallurgy: Principles and practice. WILEY-VCH Verlag GmbH & Co, Weinheim, ISBN: 3-527-30376-6.
- Hunt, G. R., 1977. Spectral signatures of particulate minerals in the visible and near-infrared. *Geophys*, 42(3), 501–513.
- Hunt, G. R., 1979. Near-infrared (1.3-2.4  $\mu\text{m}$ ) spectra of alteration minerals; potential for use in remote-sensing, *Geophys*, 44 (12) 1974-1986.
- Hunt, G. R., & Hall, R. B., 1981. Identification of Kaolins and associated minerals in altered volcanic rocks by infrared spectroscopy. *Clay clay miner*, 29(1) 76-78.
- Hunt, G. R. & Ashley, R. P., 1979. Spectra of altered rocks in the visible and near-infrared. *Econ Geol*, 74, 1613-1629.
- Hunt, G. R., & Salisbury, J.W., 1970, Visible and near-infrared spectra of minerals and rocks: I Silicate minerals. *Mod Geol*, 1, 283-300.
- Hunt, G. R., & Salisbury, J. W., 1971, Visible and near-infrared spectra of minerals and rocks: II. Carbonates. *Mod Geol*, 2, 23-39.
- Hunt, G. R., Salisbury, J. W., & Lenhoff, J. C., 1971a. Visible and near-infrared spectra of minerals and rock: III. Oxides and hydroxides. *Mod Geol*, 2, 195-205.
- Hunt, G. R., Salisbury, J. W., & Lenhoff, C. J., 1971b. Visible and near-infrared spectra of minerals and rocks: IV. Sulphides and sulphates. *Mod Geol*, 3, 1-14.
- Hunt, G. R., Salisbury, J. W., & Lenhoff, C. J., 1972. Visible and near-infrared spectra of minerals and rocks. V. Halides, phosphates, arsenates, vanadates, and borates. *Mod Geol* 3, 121-132.
- Hunt, G. R., Salisbury, J. W., & Lenhoff, C. J., 1973. Visible and near infrared spectra of minerals and rocks. VI. Additional silicates. *Mod Geol*, 4, 85-106.
- Holwell D. A., & McDonald, I., 2006. Petrology, geochemistry and mechanisms determining the distribution of platinum-group element and base metal sulphide mineralization in the Platreef at Overysel, northern Bushveld Complex, South Africa. *Miner Deposita*, 41, 575-598.

Holwell, D. A., & McDonald, I., 2007. Distribution of platinum- group elements in the Platreef at Overysel, northern Bushveld Complex: a combined PGM and LA-ICP-MS study. *Contrib Miner Petr*, 154, 171-190.

Iyakwari, S., & Glass, H. J., 2015. Mineral preconcentration using near infrared sensor-based sorting. *Physicochemical Problems of Mineral Processing* 51(2), in press.

Iyakwari, S., & Glass, H.J., 2014b. Strategy for copper preconcentration using near infrared sensor-based sorting. *Proceedings of the Mineral Engineering Conference (MEC 2014)*, eds. M. Lutynski, T. Suponik, Istebna (2014) 288 – 296.

Iyakwari, S., & Glass, H. J., 2014. Influence of mineral particle size and choice of suitable parameters for ore sorting using near infrared sensors. *Miner Eng*, 69, 102-106.

Iyakwari, S., Glass, H. J., & Kowalczyk, P. B., 2013. Potential for near infrared sensor-based sorting of hydrothermally-formed minerals. *J Near Infrared Spectrosc*, 21(3), 223-229.

Jones, M. P., 1987. Applied mineralogy: a quantitative approach *Graham & Trotman*, p43-131.

Lawrence, D., 2009. An investigation into the effect of conditions of the NIR spectra of Mantos Blancos material. European MSc in Minerals Engineering, University of Exeter.

Leitner, R., Mairer, H., & Kercek, A., 2003. Real-time classification of polymers with NIR spectral imaging and blob analysis. *Real-Time Imaging*, 9, 245-251.

Li, L., Wu, Q., Li, S., & Wu, P., 2008. Study of the infrared spectral features of an epoxy curing mechanism. *Appl Spectrosc* 62(10), 1129-1136.

Lu, Z. Y., Jeffrey, M. I., & Lawson, F., 2000. The effect of chloride ions on the dissolution of chalcopyrite in acidic solutions. *Hydrometallurgy*, 56, 189-202.

- Lunt, D., Boshoff, P., Boylett, M., & El-Ansary, Z., 2007. Uranium extraction: the key process drivers. *Journal of the South African Institute of Mining and Metallurgy*, 107, 419-426.
- Lyon, R. C., Lester, D. S., Lewis, E. N., Lee, E., Lawrence, X. Y., Jefferson, E. H., & Hussain, A. S., 2002. Near-infrared spectral imaging for quality assurance of pharmaceutical products: analysis of tablets to assess powder blend homogeneity. *AAPS PharmSciTech*, 3, 1-15.
- Mesina, M. B., De Jong, T. P. R., & Dalmijn, W. L., 2007. Automatic sorting of scrap metals with a combined electromagnetic and dual energy X-ray transmission sensor. *Int J Miner Process*, 82, 222-232.
- Montero, I. C., Brimhall, G. H., Alpers, C. N., & Swayze, G. A., 2005. Characterization of waste rock associated with acid drainage at the Penn Mine, California, by ground-based visible to short-wave infrared reflectance spectroscopy assisted by digital mapping. *Chem Geol* 215, 453-472.
- Mutz, S., Pretz, Z., & van Looy, E., 2003. An "Old" process for separation of non-ferrous metals. EPD Congress 2003 (Ed) by M.E Schlesinger TMS (The Minerals, Metals and Material Society).
- Naldrett, T., Kinnaird, J., Wilson, A., & Chunnett, G., 2008. Concentration of PGE in the Earth's crust with special reference to the Bushveld Complex. *Earth science frontiers*, 15, 264-297.
- nitonuk.co.uk 2014. Website accessed from 2014 to 2015 for Portable XRF analyser.
- Nordin, L., & Salter, J. D., 1990. Sorting method and apparatus using microwave phaseshift detection. US/07/209846
- Pasikatan, M. C., Steele, J. L., Spillman, C. K., & Haque, E., 2001. Near infrared reflectance spectroscopy for online particle size analysis of powders and ground materials. *J Near Infrared Spectrosc*, 9, 153-164.
- Pasquini, C., 2003. Near infrared spectroscopy: fundamentals, practical aspects and analytical applications. *J Braz Chem Soc*, 14(2), 198–219.

- Pirrie, D., & Rollinson, G. K., 2011. Unlocking the applications of automated mineral analysis. *Geology Today* 27(6), 226-235.
- Pommerol, A., and Schmitt, B., (2008), "Strength of H<sub>2</sub>O near infrared absorption bands in hydrated minerals: Effects of particle size and correlation with albedo", *J. Geophys. Res.*, 113, E100009, doi10.1029/2007JE003069.
- Povarennykh, A. S., 1978. The use of infrared spectra for the determination of minerals. *Am mineral*, 63, 956-959.
- Rieger, A. A., Marschik, R., Diaz, M., Hölzl, S., Chiaradia, M., Akker, B., & Spangenberg, J.E., 2010. The hypogene IOCG mineralization in the Mantoverde district, northern Chile: *Econ Geol*, 105, 1271-1299.
- Robb, L., 2005. Introduction to ore-forming processes. Wiley-Blackwell.
- Salter, J. D., & Wyatt, N. P. G., 1991. Sorting in the minerals industry: past, present and future. *Miner Eng*, 4, 779–796.
- Saranwong, S., Kawano, S., & Davies, T., 2005. Automated NIR sorting of Oranges. *NIR news*, 16(2) 9-10.
- Savitzky, A., & Golay, M. J., 1964. Smoothing and differentiation of data by simplified least squares procedures. *Anal che*, 36(8), 1627-1639.
- Serranti, S., Bonifazi, G., & Pohl, R., 2006. Spectral cullet classification in the mid-infrared field for ceramic glass contaminants detection. *Waste Manage Res*, 24, 48-59.
- Singh, V., & Rao, S. M., 2005. Application of image processing and radial basis neural network techniques for ore sorting and ore classification. *Miner Eng*, 18, 1412-1420.
- Sivamohan, R., & Forsberg, E., 1991. Electronic sorting and other preconcentration methods. *Miner Eng*, 4(7-11), 797-814.
- Stark. E., and Luchter, K., 2005. NIR instrumentation technology. *NIR news*, 16(7) 13-16.



Stettler, E. H., Cole, P., & Eberle, D. G., 2007. Near Infrared Spectra from Low Flying Survey Aircraft to Identify Rock Type. *EGM 2007 International Workshop – Innovation in EM, Grav and Mag methods: a new Perspective for Exploration*. Capri, Italy.

Stuart, B. H., 2004. *Infrared spectroscopy: fundamentals and applications*, Chichester, UK, John Wiley & Sons Ltd.

Swayze, G. A., Smith, K. S., Clark, R. N., Sutley, S. J., Pearson, R. M., Vance, J. S., Hageman, P. L., Briggs, P. H., Meier, A. L., Singleton, M. J., & Roth, S., 2000. Using imaging spectroscopy to map acidic mine waste. *Environ Sci Technol*, 34, 47-54.

Tachwali, Y., Al-Assaf, Y., & Al-Ali, A. R., 2007. Automatic multistage classification system for plastic bottles recycling. *Resour Conserv Recy*, 52, 266-285.

Tessier, J., Duchesne, C., & Bartolacci, G., 2007. A machine vision approach to online estimation of run-of-mine ore composition on conveyor belts. *Miner Eng*, 20, 1129-1144.

Topkaya, Y., Sevinc, N., & Gunaydin, A., 2004. Slag treatment at Kardemir integrated iron and steel works. *Int J Miner Process*, 74, 31-39.

Tran, C. D., 2000. Visualising chemical composition and reaction kinetics by the near infrared multispectral imaging technique. *J Near Infrared Spectrosc*, 8, 87-100.

Vaiphasa, C., 2006. Consideration of smoothing techniques for hyperspectral remote sensing. *Isprs Journal of Photogrammetry and Remote Sensing*, 60, 91-99.

Van der Meer, F., 1995. Spectral reflectance of carbonate mineral mixtures and bidirectional reflectance theory: Quantitative analysis techniques for application in remote sensing, *Remote Sens Rev*, 13, 67-94.

Varela, J. J., Petter, C. O., & Wotruba, H., 2006. Product quality improvement of Brazilian impure marble. *Miner Eng*, 19, 355-363.

Veel-er, D. R., 1983. TEM study of the biotite chlorite reaction and comparison with petrologic observations. *Am Mineral*, 6, 1160-1168.

Vila, T. 1996. Geology of the Mantoverde copper deposit, northern Chile: a specularite-rich, hydrothermal-tectonic breccia related to the Atacama fault zone. *Andean Copper Deposits: New Discoveries, Mineralization Styles and Metallogeny, Soc Econ Geol Spec Publ*, 5, 157-169.

Villringer, A., Planck, J., Hock, C., Schleinkofer, L., & Dirnagl, U., 1993. Near infrared spectroscopy (NIRS): A new tool to study hemodynamic changes during activation of brain function in human adults, *Neurosci Lett*, 154(1–2), 101-104.

Von Ketelhodt, L. 2009. Viability of optical sorting of gold waste rock dumps *World Gold Conference*, 271-277.

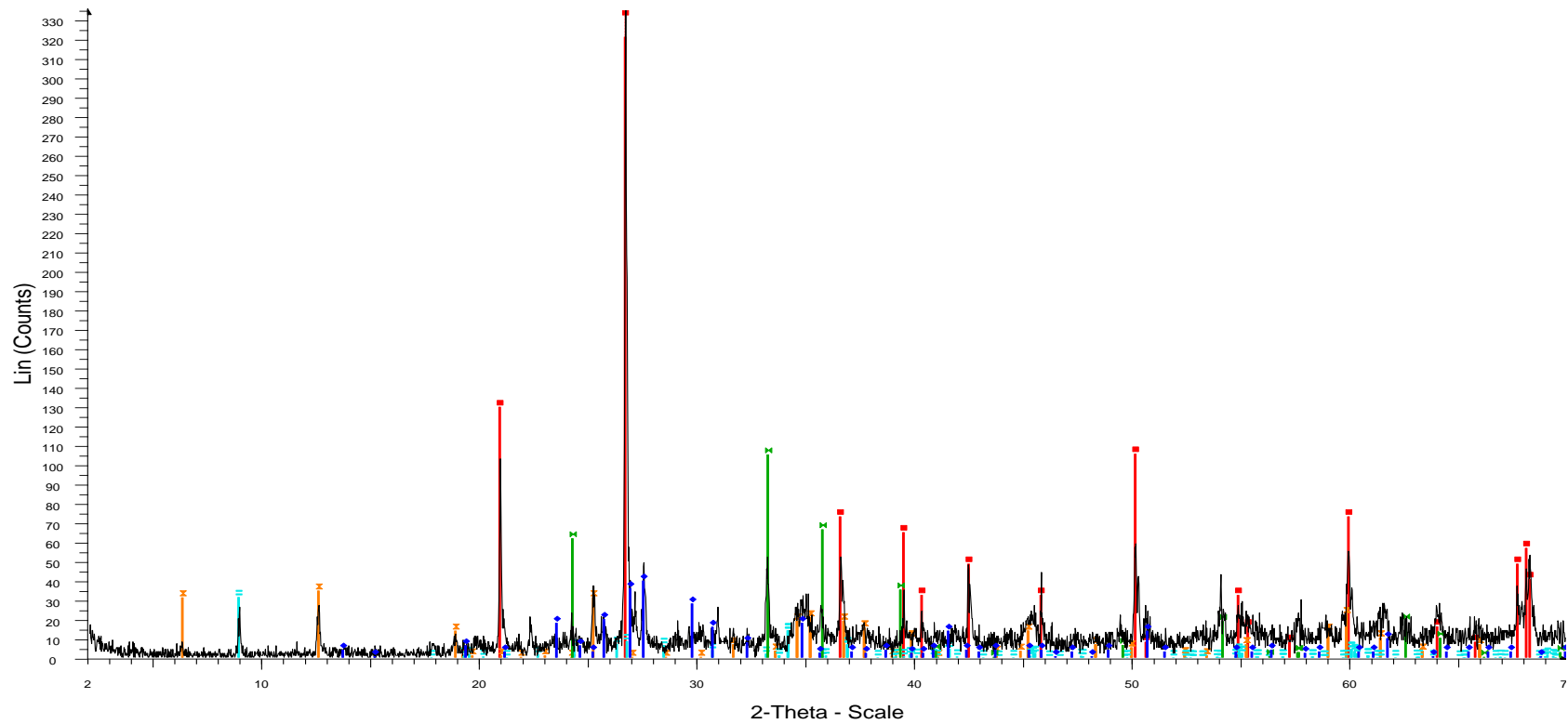
webmineral.com. 2013. Website accessed from 2013 to 2015 for mineralogy data.

Wills, B. A., 1997. *Mineral Processing Technology*, Burlington MA, Butterworth-Heinemann.

Wills, B. A., & Napier-Munn, T., 2006. *Mineral processing technology. An introduction to the practical; aspects of ore treatment and mineral*. 7<sup>th</sup> edition Elsevier Sci. & Tech. Book. ISBN: 0750644508.

## Appendices

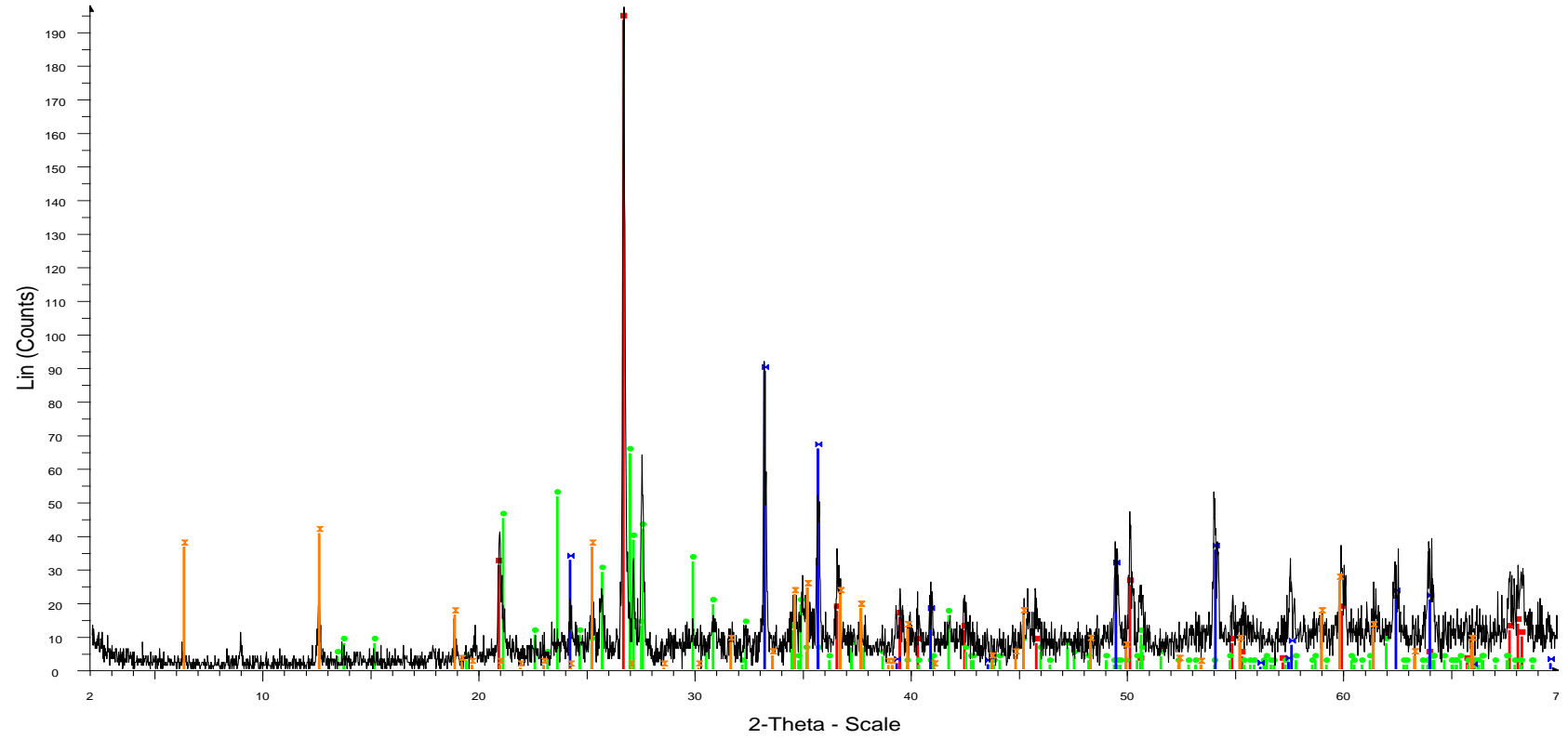
Appendix 4.1 - X-ray diffraction profiles of Mantoverde copper ore particles



3801 - File: C05120059.raw - Type: 2Th/Th locked - Start: 2.000 ° - End: 70.000 ° - Step: 0.020 ° - Step time: 1. s - Temp.: 25 °C (Room) - Time Started: 16 s - 2-Theta: 2.000 ° - Theta: 1.000 ° - Chi: 0.00 ° - Phi: 0.00 ° - X: 0.0 mm - Y: 0.0 mm - Z: Operations: Import

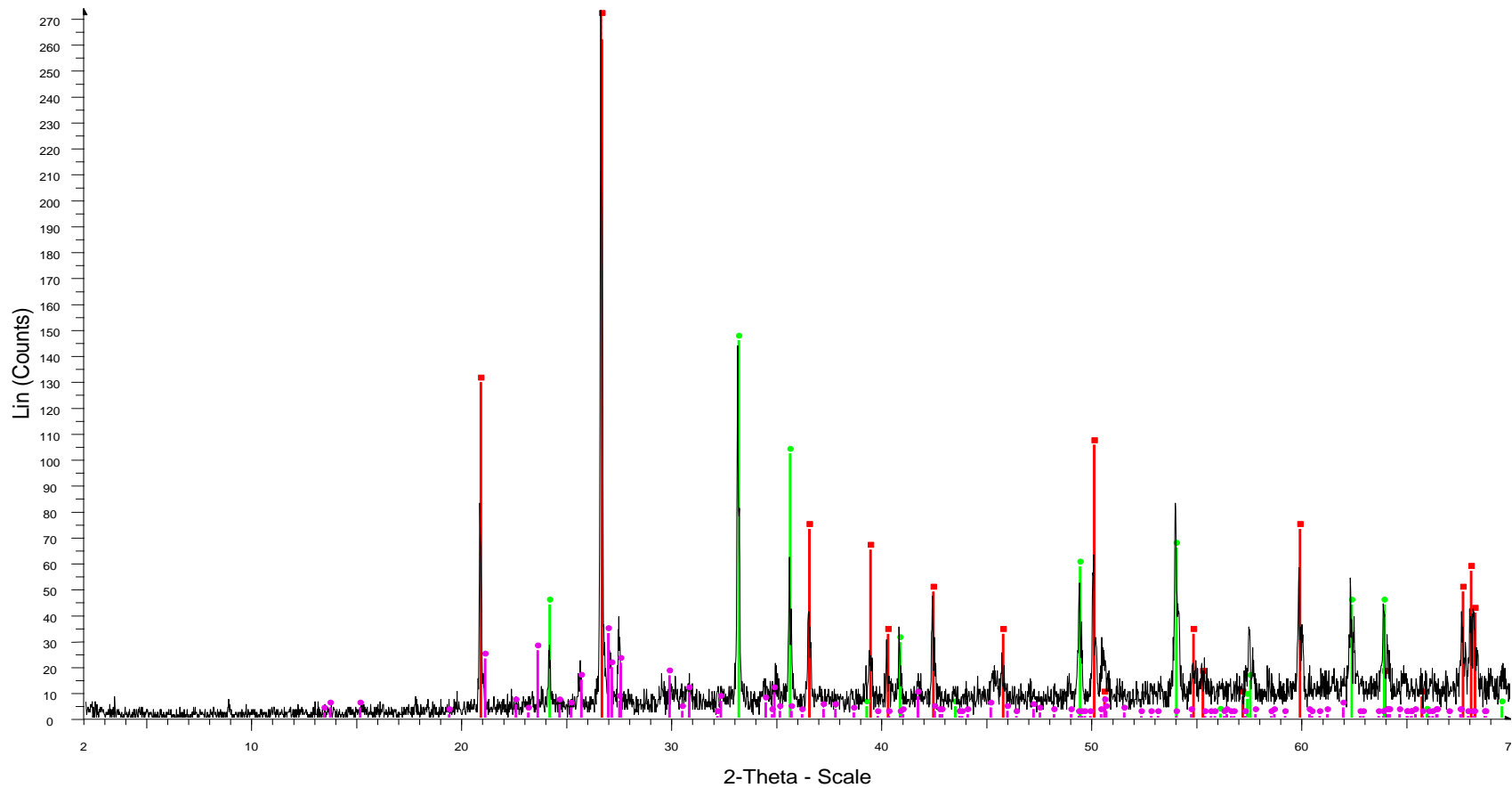
- 00-046-1045 (\*) - Quartz, syn - SiO<sub>2</sub> - Y: 242.01 % - d x by: 1. - WL: 1.5406 - Hexagonal - a 4.91344 - b 4.91344 - c 5.40524 - alpha 90.000 - beta 90.000 - gamma 120.000 - Primitive - P321 (154) - 3 - 113.010 - I/c PDF 3.4 - F30=558(0.0017,
- 00-046-1323 (I) - Clinocllore-1M1b - (Mg,Al,Fe)<sub>6</sub>(Si,Al)<sub>4</sub>O<sub>10</sub>(OH)<sub>8</sub> - Y: 10.34 % - d x by: 1. - WL: 1.5406 - Monoclinic - a 5.34700 - b 9.26300 - c 14.25000 - alpha 90.000 - beta 97.200 - gamma 90.000 - Base-centered - C2/m (12) - 2 - 700.227 -
- 01-088-2192 (C) - Biotite 1M, titanoc barian - (K<sub>1.8</sub>Na<sub>0.15</sub>Ba<sub>0.05</sub>)(Mg<sub>3.26</sub>Fe<sub>2</sub>Ti<sub>0.74</sub>)(Al<sub>2.5</sub>Si<sub>5.5</sub>O<sub>20</sub>)O<sub>1.85</sub>(OH)<sub>2.15</sub> - Y: 9.38 % - d x by: 1. - WL: 1.5406 - Monoclinic - a 5.33100 - b 9.23000 - c 10.16000 - alpha 90.000 - beta 100.190 - gamm
- 01-085-0987 (A) - Hematite - Fe<sub>2</sub>O<sub>3</sub> - Y: 31.40 % - d x by: 1. - WL: 1.5406 - Rhombo.R.axes - a 5.42000 - b 5.42000 - c 5.42000 - alpha 55.200 - beta 55.200 - gamma 55.200 - Primitive - R-3c (167) - 2 - 100.022 - I/c PDF 4. - F26=170(0.0039,3
- 00-019-0002 (I) - Orthoclase, barian - (K,Ba,Na)(Si,Al)<sub>4</sub>O<sub>8</sub> - Y: 11.92 % - d x by: 1. - WL: 1.5406 - Monoclinic - a 8.55200 - b 13.04000 - c 7.20000 - alpha 90.000 - beta 115.700 - gamma 90.000 - Base-centered - C2/m (12) - 4 - 723.502 - F30= 1

Sample 1



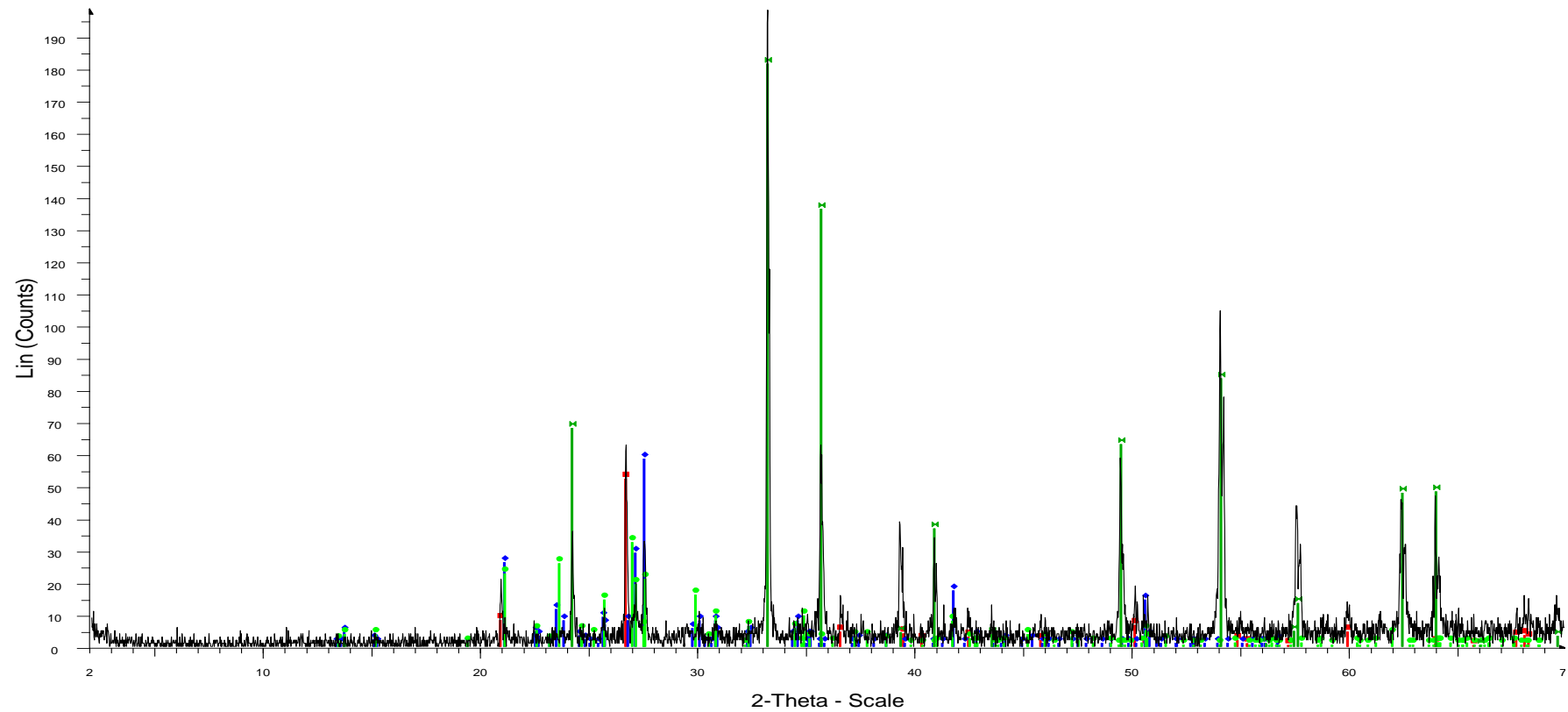
3802 - File: C05120432.raw - Type: 2Th/Th locked - Start: 2.000 ° - End: 70.000 ° - Step: 0.020 ° - Step time: 1. s - Temp.: 25 °C (Room) - Time Started: 20 s - 2-Theta: 2.000 ° - Theta: 1.000 ° - Chi: 0.00 ° - Phi: 0.00 ° - X: 0.0 mm - Y: 0.0 mm - Z: 0.0 mm  
 Operations: Import  
 00-046-1045 (\*) - Quartz, syn - SiO<sub>2</sub> - Y: 98.13 % - d x by: 1. - WL: 1.5406 - Hexagonal - a 4.91344 - b 4.91344 - c 5.40524 - alpha 90.000 - beta 90.000 - gamma 120.000 - Primitive - P3221 (154) - 3 - 113.010 - V/c PDF 3.4 - F30=558(0.0017,3)  
 00-046-1323 (I) - Clinocllore-1Mllb - (Mg,Al,Fe)6(Si,Al)4O10(OH)8 - Y: 20.57 % - d x by: 1. - WL: 1.5406 - Monoclinic - a 5.34700 - b 9.26300 - c 14.25000 - alpha 90.000 - beta 97.200 - gamma 90.000 - Base-centered - C2/m (12) - 2 - 700.227 - F30=55(0.0148,37)  
 00-031-0966 (\*) - Orthoclase - KAISi3O8 - Y: 32.61 % - d x by: 1. - WL: 1.5406 - Monoclinic - a 8.55600 - b 12.98000 - c 7.20500 - alpha 90.000 - beta 116.010 - gamma 90.000 - Base-centered - C2/m (12) - 4 - 719.122 - F30=55(0.0148,37)  
 01-073-2234 (A) - Hematite, syn - alpha-Fe2O3 - Y: 45.07 % - d x by: 1. - WL: 1.5406 - Rhombo.H.axes - a 5.03255 - b 5.03255 - c 13.74039 - alpha 90.000 - beta 90.000 - gamma 120.000 - Primitive - R-3c (167) - 6 - 301.374 - V/c PDF 3. - F28=

Sample 2



6601 - File: C05120062.raw - Type: 2Th/Th locked - Start: 2.000 ° - End: 70.000 ° - Step: 0.020 ° - Step time: 1. s - Temp.: 25 °C (Room) - Time Started: 16 s - 2-Theta: 2.000 ° - Theta: 1.000 ° - Chi: 0.00 ° - Phi: 0.00 ° - X: 0.0 mm - Y: 0.0 mm - Z: 0.0 mm  
 Operations: Import  
 ■ 00-046-1045 (\*) - Quartz, syn - SiO<sub>2</sub> - Y: 296.77 % - d x by: 1. - WL: 1.5406 - Hexagonal - a 4.91344 - b 4.91344 - c 5.40524 - alpha 90.000 - beta 90.000 - gamma 120.000 - Primitive - P3221 (154) - 3 - 113.010 - I/c PDF 3.4 - F30=558(0.0017,  
 ● 00-031-0966 (\*) - Orthoclase - KAlSi<sub>3</sub>O<sub>8</sub> - Y: 11.94 % - d x by: 1. - WL: 1.5406 - Monoclinic - a 8.55600 - b 12.98000 - c 7.20500 - alpha 90.000 - beta 116.010 - gamma 90.000 - Base-centered - C2/m (12) - 4 - 719.122 - F30= 55(0.0148,37)  
 ● 00-033-0664 (\*) - Hematite, syn - Fe<sub>2</sub>O<sub>3</sub> - Y: 53.39 % - d x by: 1. - WL: 1.5406 - Rhombo.H.axes - a 5.03560 - b 5.03560 - c 13.74890 - alpha 90.000 - beta 90.000 - gamma 120.000 - Primitive - R-3c (167) - 6 - 301.926 - I/c PDF 2.4 - F30= 69(0

Sample 3



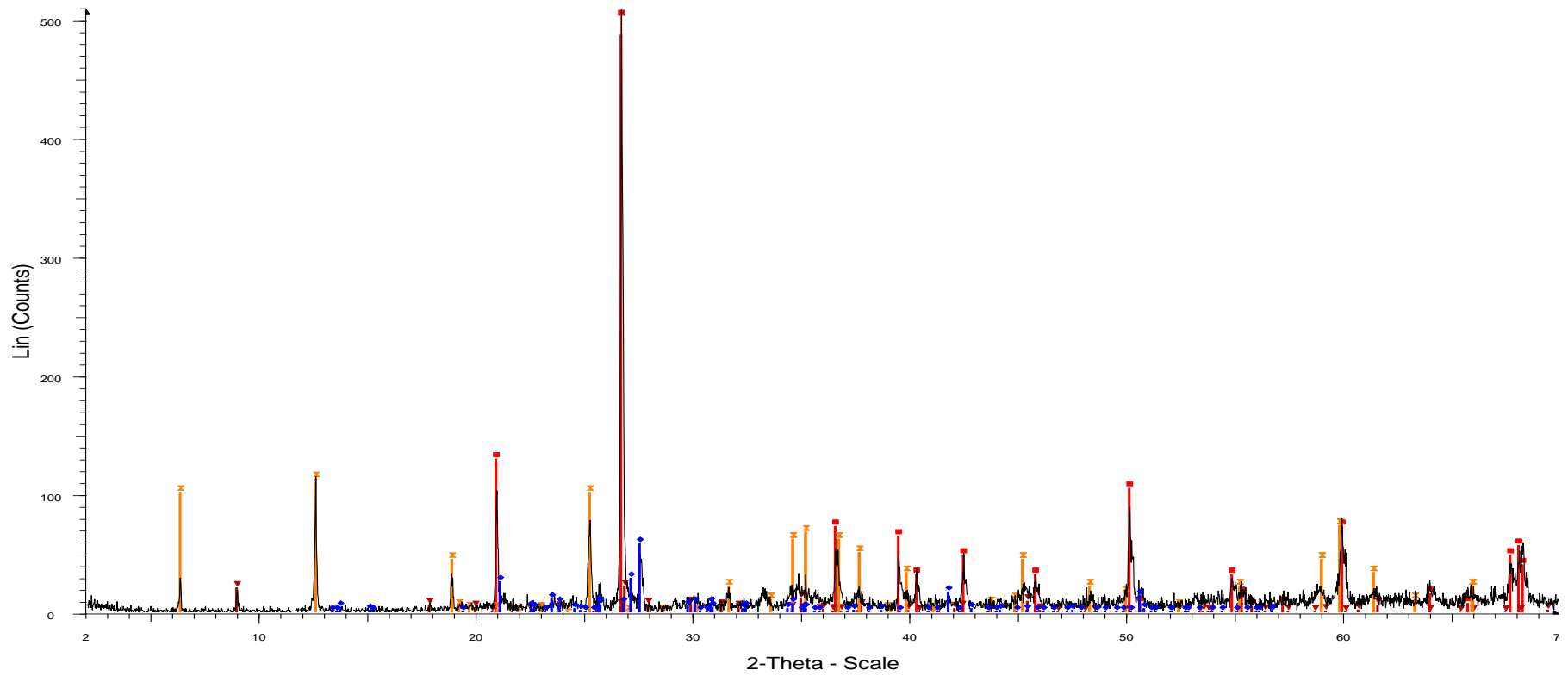
5901 - File: C05120437.raw - Type: 2Th/Th locked - Start: 2.000 ° - End: 70.000 ° - Step: 0.020 ° - Step time: 1. s - Temp.: 25 °C (Room) - Time Started: 17 s - 2-Theta: 2.000 ° - Theta: 1.000 ° - Chi: 0.00 ° - Phi: 0.00 ° - X: 0.0 mm - Y: 0.0 mm - Z:

Operations: Import

- 00-046-1045 (\*) - Quartz, syn - SiO<sub>2</sub> - Y: 26.44 % - d x by: 1. - WL: 1.5406 - Hexagonal - a 4.91344 - b 4.91344 - c 5.40524 - alpha 90.000 - beta 90.000 - gamma 120.000 - Primitive - P3221 (154) - 3 - 113.010 - I/c PDF 3.4 - F30=558(0.0017,3)
- ◆ 00-019-0932 (I) - Microcline, intermediate - KAlSi<sub>3</sub>O<sub>8</sub> - Y: 29.58 % - d x by: 1. - WL: 1.5406 - Triclinic - a 8.56000 - b 12.97000 - c 7.21000 - alpha 90.300 - beta 116.100 - gamma 89.000 - Base-centered - C-1 (0) - 4 - 718.739 - F30= 46(0.0165,
- 00-031-0966 (\*) - Orthoclase - KAlSi<sub>3</sub>O<sub>8</sub> - Y: 16.43 % - d x by: 1. - WL: 1.5406 - Monoclinic - a 8.55600 - b 12.98000 - c 7.20500 - alpha 90.000 - beta 116.010 - gamma 90.000 - Base-centered - C2/m (12) - 4 - 719.122 - F30= 55(0.0148,37)
- 01-089-0599 (C) - Hematite, syn - alpha-Fe<sub>2</sub>O<sub>3</sub> - Y: 91.65 % - d x by: 1. - WL: 1.5406 - Rhombo.H.axes - a 5.03200 - b 5.03200 - c 13.73300 - alpha 90.000 - beta 90.000 - gamma 120.000 - Primitive - R-3c (167) - 6 - 301.146 - I/c PDF 3.1 - F28

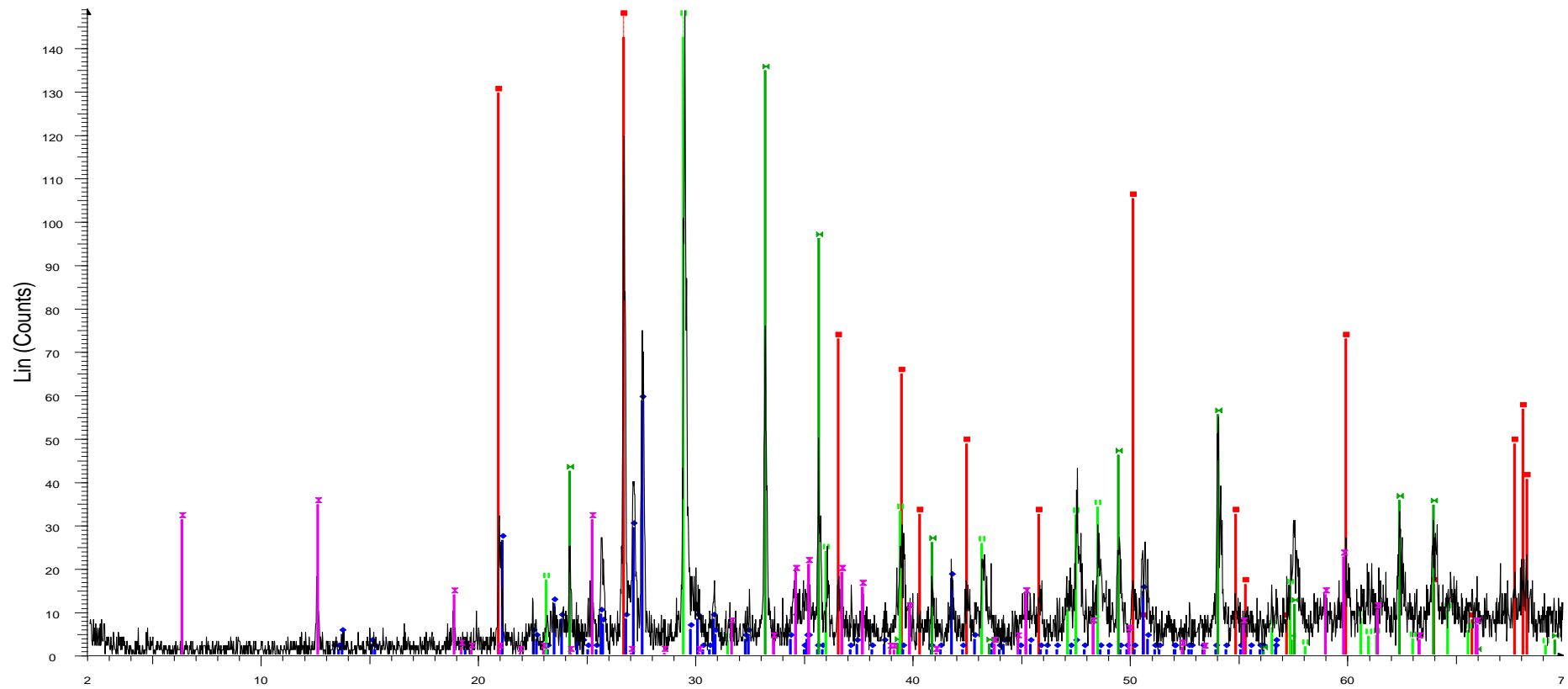
Sample 4





13 - File: C5120105.raw - Type: 2Th/Th locked - Start: 2.000 ° - End: 70.000 ° - Step: 0.020 ° - Step time: 1. s - Temp.: 25 °C (Room) - Time Started: 16 s - 2-Theta: 2.000 ° - Theta: 1.000 ° - Chi: 0.00 ° - Phi: 0.00 ° - X: 0.0 mm - Y: 0.0 mm - Z: 0.0  
 Operations: Import  
 00-046-1045 (\*) - Quartz, syn - SiO<sub>2</sub> - Y: 159.44 % - d x by: 1. - WL: 1.5406 - Hexagonal - a 4.91344 - b 4.91344 - c 5.40524 - alpha 90.000 - beta 90.000 - gamma 120.000 - Primitive - P3221 (154) - 3 - 113.010 - I/c PDF 3.4 - F30=558(0.0017,  
 00-006-0263 (l) - Muscovite-2M1 - KAl<sub>2</sub>(Si<sub>3</sub>Al)O<sub>10</sub>(OH,F)<sub>2</sub> - Y: 4.36 % - d x by: 1. - WL: 1.5406 - Monoclinic - a 5.19000 - b 9.03000 - c 20.05000 - alpha 90.000 - beta 95.770 - gamma 90.000 - Base-centered - C2/c (15) - 4 - 934.896 - F30= 12(  
 00-046-1323 (l) - Clinocllore-1Mlb - (Mg,Al,Fe)6(Si,Al)4O<sub>10</sub>(OH)<sub>8</sub> - Y: 22.29 % - d x by: 1. - WL: 1.5406 - Monoclinic - a 5.34700 - b 9.26300 - c 14.25000 - alpha 90.000 - beta 97.200 - gamma 90.000 - Base-centered - C2/m (12) - 2 - 700.227 -  
 00-019-0932 (l) - Microcline, intermediate - KAISi<sub>3</sub>O<sub>8</sub> - Y: 11.54 % - d x by: 1. - WL: 1.5406 - Triclinic - a 8.56000 - b 12.97000 - c 7.21000 - alpha 90.300 - beta 116.100 - gamma 89.000 - Base-centered - C-1 (0) - 4 - 718.739 - F30= 46(0.0165,

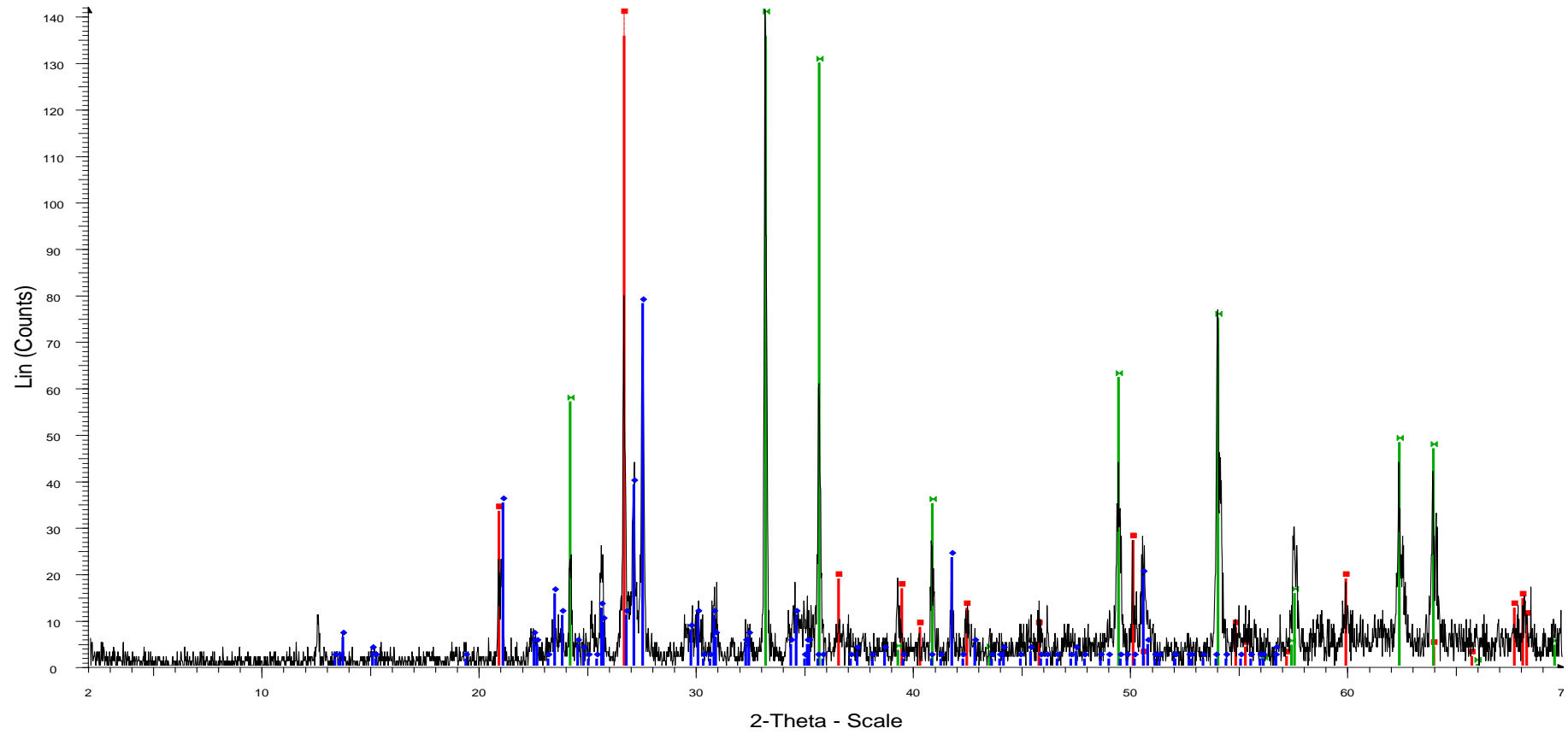
Sample 5



3201 - File: C5120471.raw - Type: 2Th/Th locked - Start: 2.000 ° - End: 70.000 ° - Step: 0.020 ° - Step time: 1. s - Temp.: 25 °C (Room) - Time Started: 17 s - 2-Theta: 2.000 ° - Theta: 1.000 ° - Chi: 0.00 ° - Phi: 0.00 ° - X: 0.0 mm - Y: 0.0 mm - Z: Operations: Import

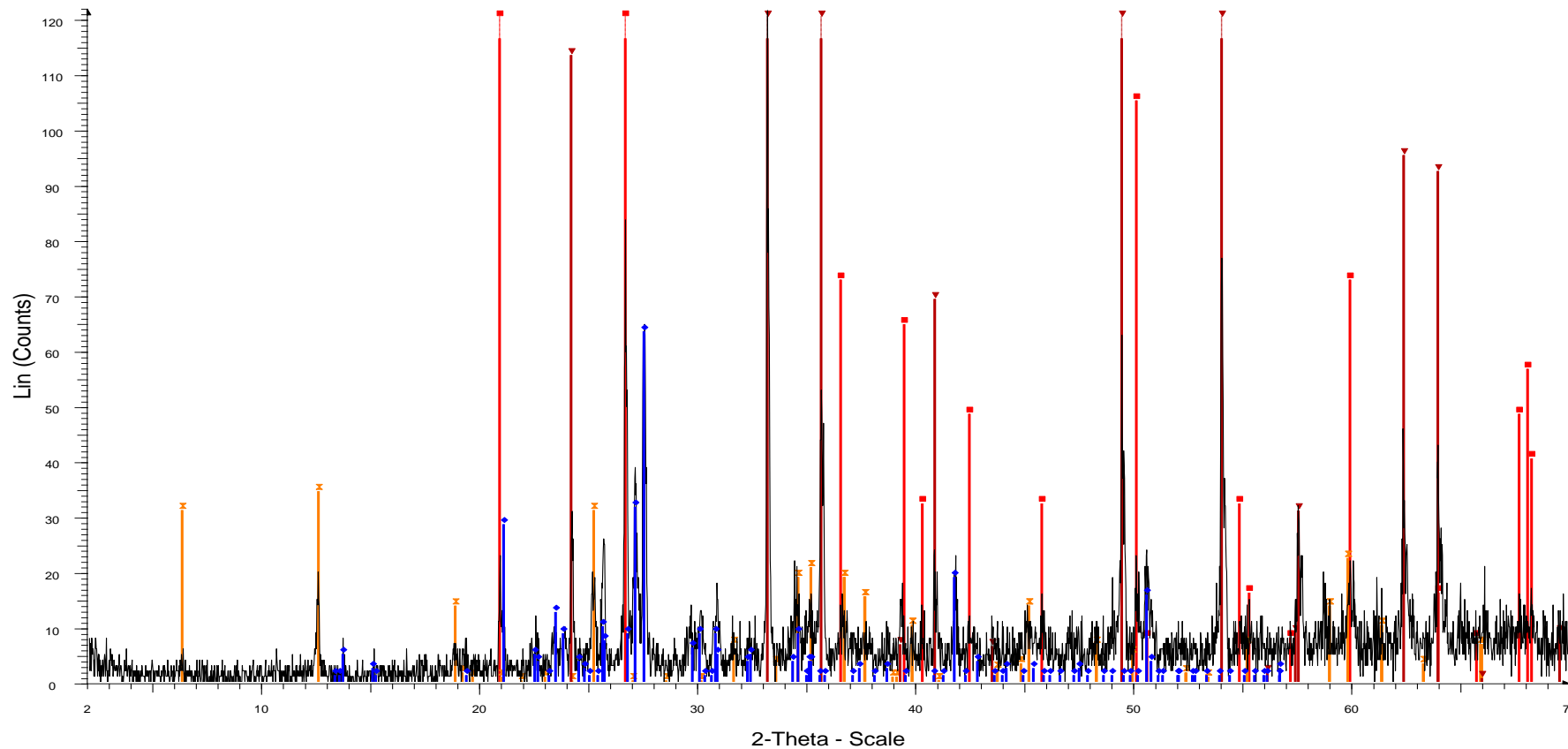
- 00-046-1045 (\*) - Quartz, syn - SiO<sub>2</sub> - Y: 545.73 % - d x by: 1. - WL: 1.5406 - Hexagonal - a 4.91344 - b 4.91344 - c 5.40524 - alpha 90.000 - beta 90.000 - gamma 120.000 - Primitive - P3221 (154) - 3 - 113.010 - I/c PDF 3.4 - F30=558(0.0017,
- 00-046-1323 (I) - Clinocllore-1MIIb - (Mg,Al,Fe)(Si,Al)4O10(OH)8 - Y: 23.32 % - d x by: 1. - WL: 1.5406 - Monoclinic - a 5.34700 - b 9.26300 - c 14.25000 - alpha 90.000 - beta 97.200 - gamma 90.000 - Base-centered - C2/m (12) - 2 - 700.227 -
- 00-019-0932 (I) - Microcline, intermediate - KAlSi3O8 - Y: 39.51 % - d x by: 1. - WL: 1.5406 - Triclinic - a 8.56000 - b 12.97000 - c 7.21000 - alpha 90.300 - beta 116.100 - gamma 89.000 - Base-centered - C-1 (0) - 4 - 718.739 - F30= 46(0.0165,
- 01-087-1164 (C) - Hematite - alpha-Fe2O3 - Y: 90.83 % - d x by: 1. - WL: 1.5406 - Rhombo.H.axes - a 5.03530 - b 5.03530 - c 13.74950 - alpha 90.000 - beta 90.000 - gamma 120.000 - Primitive - R-3c (167) - 6 - 301.904 - I/c PDF 3.3 - F28=10
- 01-083-1762 (A) - Calcite - Ca(CO3) - Y: 120.61 % - d x by: 1. - WL: 1.5406 - Rhombo.H.axes - a 4.98960 - b 4.98960 - c 17.06100 - alpha 90.000 - beta 90.000 - gamma 120.000 - Primitive - R-3c (167) - 6 - 367.847 - I/c PDF 3.3 - F30=1000(0.

Sample 6



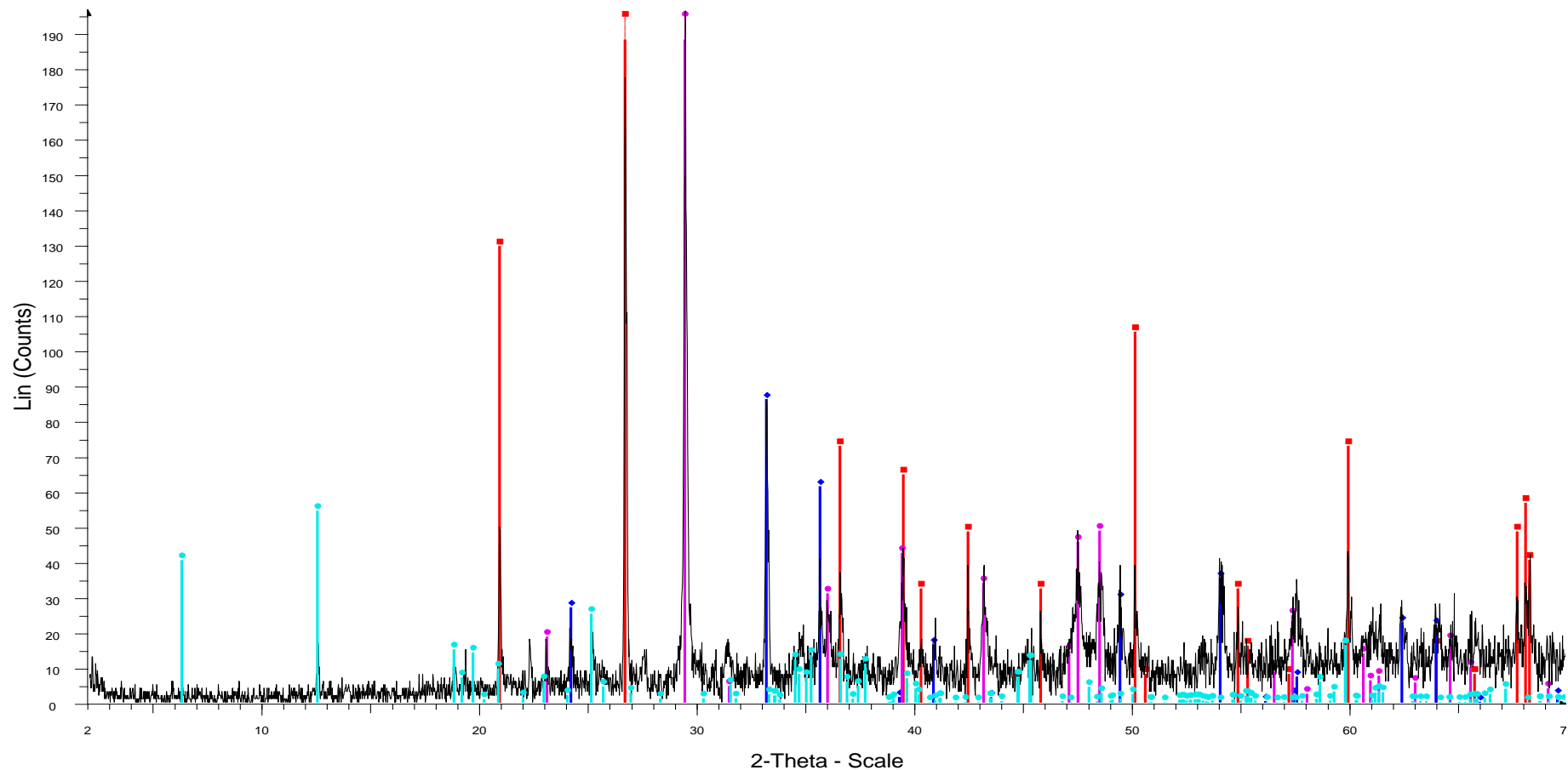
03 - File: C5120470.raw - Type: 2Th/Th locked - Start: 2.000 ° - End: 70.000 ° - Step: 0.020 ° - Step time: 1. s - Temp.: 25 °C (Room) - Time Started: 17 s - 2-Theta: 2.000 ° - Theta: 1.000 ° - Chi: 0.00 ° - Phi: 0.00 ° - X: 0.0 mm - Y: 0.0 mm - Z: 0.0  
 Operations: Import  
 00-046-1045 (\*) - Quartz, syn - SiO<sub>2</sub> - Y: 147.63 % - d x by: 1. - WL: 1.5406 - Hexagonal - a 4.91344 - b 4.91344 - c 5.40524 - alpha 90.000 - beta 90.000 - gamma 120.000 - Primitive - P3221 (154) - 3 - 113.010 - I/c PDF 3.4 - F30=558(0.0017,  
 00-019-0932 (I) - Microcline, intermediate - KAlSi<sub>3</sub>O<sub>8</sub> - Y: 55.27 % - d x by: 1. - WL: 1.5406 - Triclinic - a 8.56000 - b 12.97000 - c 7.21000 - alpha 90.300 - beta 116.100 - gamma 89.000 - Base-centered - C-1 (0) - 4 - 718.739 - F30= 46(0.0165,  
 01-087-1166 (A) - Hematite - alpha-Fe<sub>2</sub>O<sub>3</sub> - Y: 128.93 % - d x by: 1. - WL: 1.5406 - Rhombo.H.axes - a 5.03530 - b 5.03530 - c 13.74950 - alpha 90.000 - beta 90.000 - gamma 120.000 - Primitive - R-3c (167) - 6 - 301.904 - I/c PDF 3.3 - F28=1

Sample 7



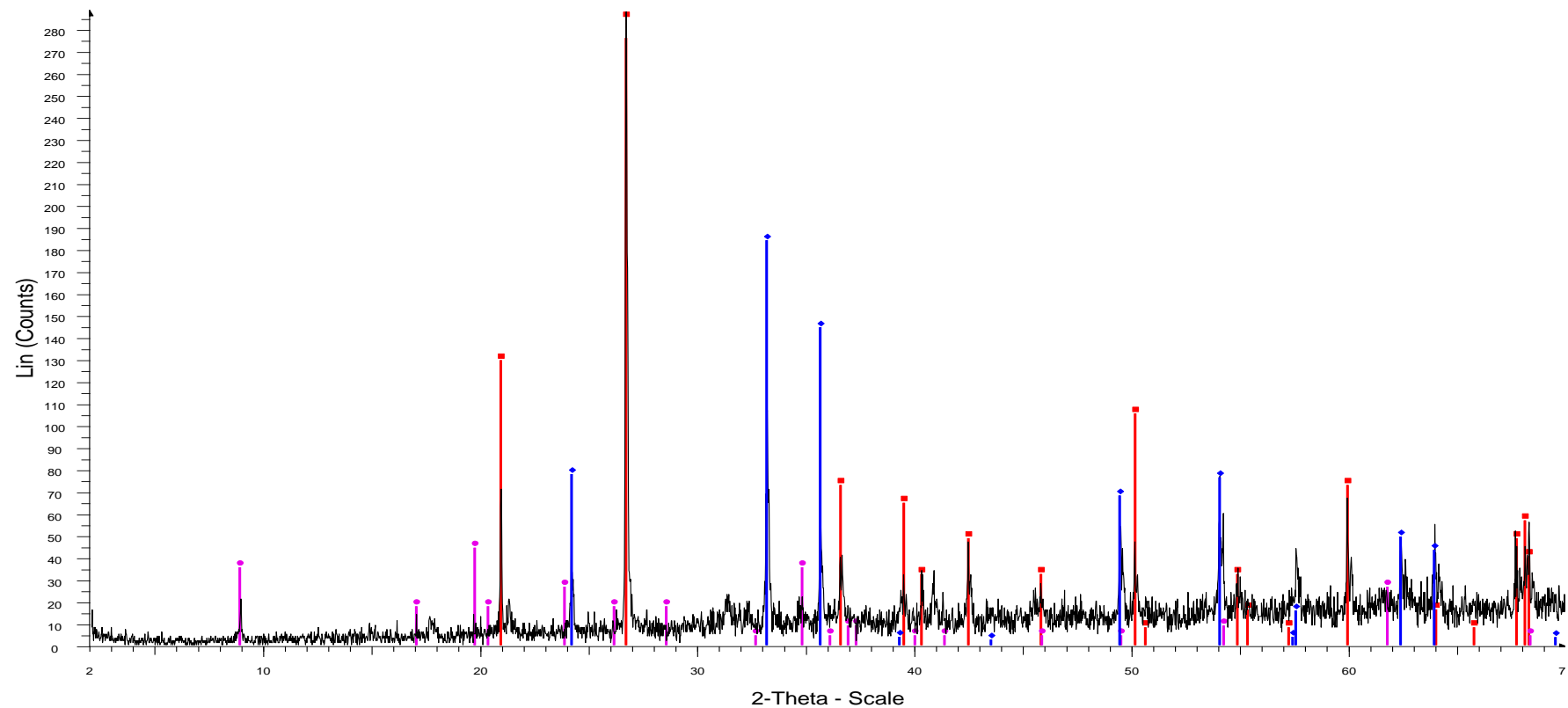
18 - File: C05120080.raw - Type: 2Th/Th locked - Start: 2.000 ° - End: 70.000 ° - Step: 0.020 ° - Step time: 1. s - Temp.: 25 °C (Room) - Time Started: 16 s - 2-Theta: 2.000 ° - Theta: 1.000 ° - Chi: 0.00 ° - Phi: 0.00 ° - X: 0.0 mm - Y: 0.0 mm - Z: 0.  
 Operations: Import  
 00-046-1045 (\*) - Quartz, syn - SiO<sub>2</sub> - Y: 666.51 % - d x by: 1. - WL: 1.5406 - Hexagonal - a 4.91344 - b 4.91344 - c 5.40524 - alpha 90.000 - beta 90.000 - gamma 120.000 - Primitive - P3221 (154) - 3 - 113.010 - I/c PDF 3.4 - F30=558(0.0017,  
 00-046-1323 (I) - Clinocllore-1MIIb - (Mg,Al,Fe)6(Si,Al)4O10(OH)8 - Y: 28.48 % - d x by: 1. - WL: 1.5406 - Monoclinic - a 5.34700 - b 9.26300 - c 14.25000 - alpha 90.000 - beta 97.200 - gamma 90.000 - Base-centered - C2/m (12) - 2 - 700.227 -  
 00-019-0932 (I) - Microcline, intermediate - KAlSi3O8 - Y: 52.27 % - d x by: 1. - WL: 1.5406 - Triclinic - a 8.56000 - b 12.97000 - c 7.21000 - alpha 90.300 - beta 116.100 - gamma 89.000 - Base-centered - C-1 (0) - 4 - 718.739 - F30= 46(0.0165,  
 01-087-1164 (C) - Hematite - alpha-Fe2O3 - Y: 297.14 % - d x by: 1. - WL: 1.5406 - Rhombo.H.axes - a 5.03530 - b 5.03530 - c 13.74950 - alpha 90.000 - beta 90.000 - gamma 120.000 - Primitive - R-3c (167) - 6 - 301.904 - I/c PDF 3.3 - F28=1

Sample 8



27 - File: C5120465.raw - Type: 2Th/Th locked - Start: 2.000 ° - End: 70.000 ° - Step: 0.020 ° - Step time: 1. s - Temp.: 25 °C (Room) - Time Started: 16 s - 2-Theta: 2.000 ° - Theta: 1.000 ° - Chi: 0.00 ° - Phi: 0.00 ° - X: 0.0 mm - Y: 0.0 mm - Z: 0.0  
 Operations: Import  
 ■ 00-046-1045 (\*) - Quartz, syn - SiO<sub>2</sub> - Y: 412.76 % - d x by: 1. - WL: 1.5406 - Hexagonal - a 4.91344 - b 4.91344 - c 5.40524 - alpha 90.000 - beta 90.000 - gamma 120.000 - Primitive - P3221 (154) - 3 - 113.010 - I/c PDF 3.4 - F30=558(0.0017,  
 ● 01-087-1164 (C) - Hematite - alpha-Fe<sub>2</sub>O<sub>3</sub> - Y: 43.93 % - d x by: 1. - WL: 1.5406 - Rhombo.H.axes - a 5.03530 - b 5.03530 - c 13.74950 - alpha 90.000 - beta 90.000 - gamma 120.000 - Primitive - R-3c (167) - 6 - 301.904 - I/c PDF 3.3 - F28=10  
 ● 00-047-1743 (C) - Calcite - CaCO<sub>3</sub> - Y: 107.07 % - d x by: 1. - WL: 1.5406 - Rhombo.H.axes - a 4.98960 - b 4.98960 - c 17.06100 - alpha 90.000 - beta 90.000 - gamma 120.000 - Primitive - R-3c (167) - 6 - 367.847 - F30=1000(0.0002,33)  
 ● 01-079-1270 (C) - Clinocllore - (Mg<sub>2.96</sub>Fe<sub>1.55</sub>Fe<sub>1.136</sub>Al<sub>1.275</sub>)(Si<sub>2.622</sub>Al<sub>1.376</sub>O<sub>10</sub>)(OH)<sub>8</sub> - Y: 27.75 % - d x by: 1. - WL: 1.5406 - Monoclinic - a 5.35000 - b 9.26700 - c 14.27000 - alpha 90.000 - beta 96.350 - gamma 90.000 - Base-centered - C

Sample 9



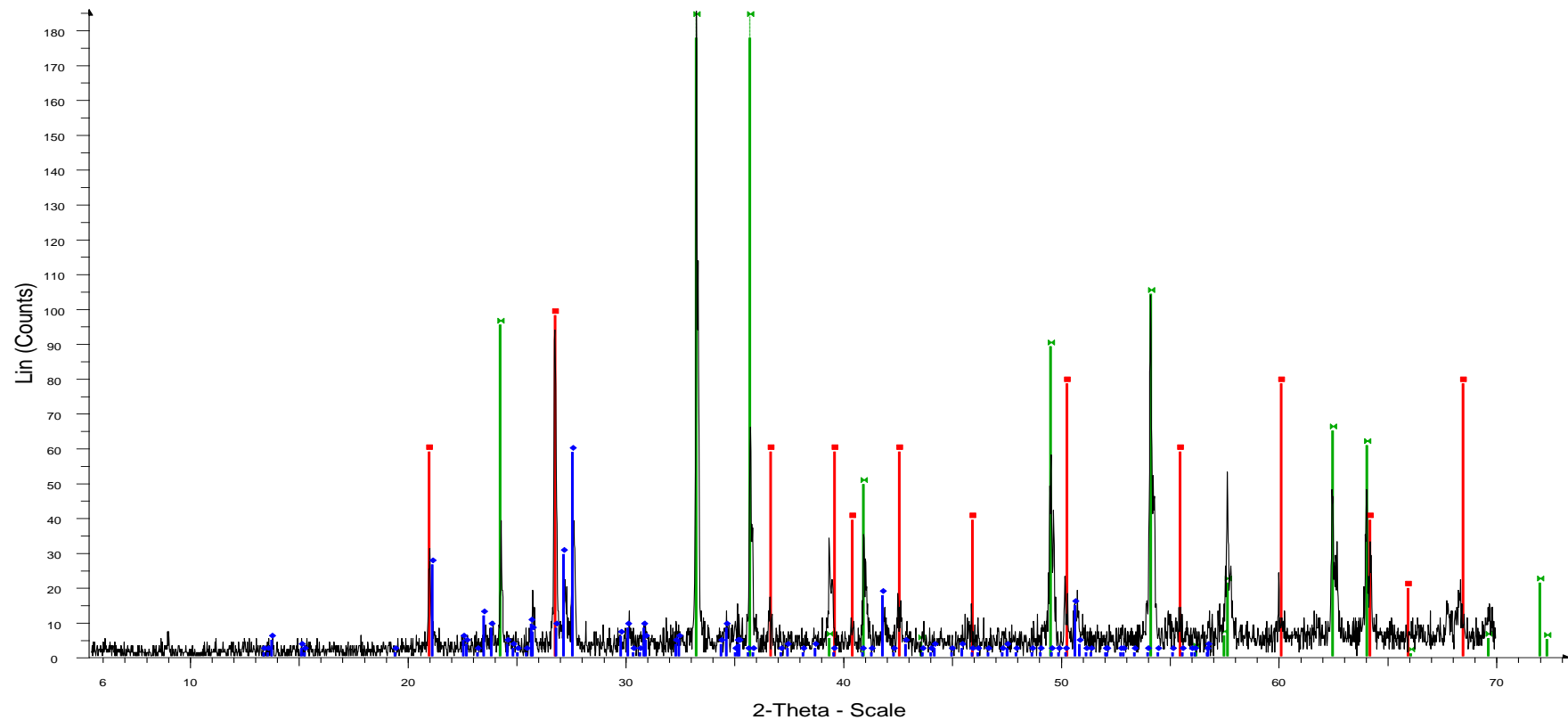
7101 - File: C5120108.raw - Type: 2Th/Th locked - Start: 2.000 ° - End: 70.000 ° - Step: 0.020 ° - Step time: 1. s - Temp.: 25 °C (Room) - Time Started: 16 s - 2-Theta: 2.000 ° - Theta: 1.000 ° - Chi: 0.00 ° - Phi: 0.00 ° - X: 0.0 mm - Y: 0.0 mm - Z: Operations: Import

■ 00-046-1045 (\*) - Quartz, syn - SiO<sub>2</sub> - Y: 281.36 % - d x by: 1. - WL: 1.5406 - Hexagonal - a 4.91344 - b 4.91344 - c 5.40524 - alpha 90.000 - beta 90.000 - gamma 120.000 - Primitive - P3221 (154) - 3 - 113.010 - I/c PDF 3.4 - F30=558(0.0017,

● 01-085-0599 (A) - Hematite - Fe<sub>2</sub>O<sub>3</sub> - Y: 63.98 % - d x by: 1. - WL: 1.5406 - Rhombo.H.axes - a 5.03811 - b 5.03811 - c 13.75559 - alpha 90.000 - beta 90.000 - gamma 120.000 - Primitive - R-3c (167) - 6 - 302.375 - I/c PDF 2.9 - F21=1000(0.0

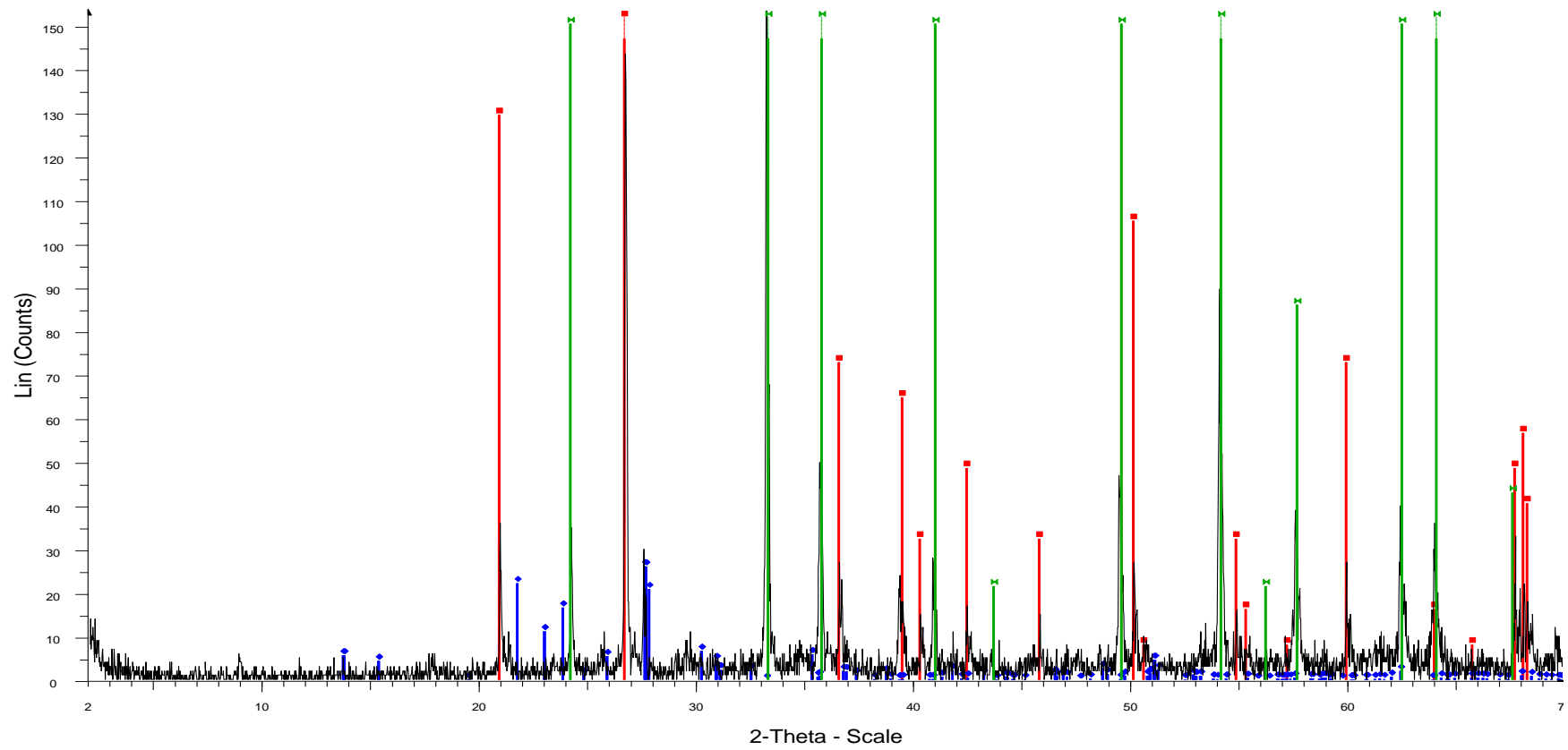
◆ 00-013-0573 (D) - Muscovite - 0.33(NH<sub>4</sub>)<sub>2</sub>O·Al<sub>2</sub>O<sub>3</sub>·2SiO<sub>2</sub>·0.66H<sub>2</sub>O - Y: 15.38 % - d x by: 1. - WL: 1.5406 - Monoclinic - a 5.22000 - b 9.02000 - c 20.02000 - alpha 90.000 - beta 90.220 - gamma 90.000 - 942.623 - F21= 0(0.1080,587)

Sample 10



69 - File: C5120464.raw - Type: 2Th/Th locked - Start: 2.000 ° - End: 70.000 ° - Step: 0.020 ° - Step time: 1. s - Temp.: 25 °C (Room) - Time Started: 16 s - 2-Theta: 2.000 ° - Theta: 1.000 ° - Chi: 0.00 ° - Phi: 0.00 ° - X: 0.0 mm - Y: 0.0 mm - Z: 0.0  
 Operations: Import  
 00-019-0932 (I) - Microcline, intermediate -  $\text{KAlSi}_3\text{O}_8$  - Y: 31.65 % - d x by: 1. - WL: 1.5406 - Triclinic - a 8.56000 - b 12.97000 - c 7.21000 - alpha 90.300 - beta 116.100 - gamma 89.000 - Base-centered - C-1 (0) - 4 - 718.739 - F30= 46(0.0165,  
 01-073-2234 (A) - Hematite, syn -  $\alpha\text{-Fe}_2\text{O}_3$  - Y: 140.41 % - d x by: 1. - WL: 1.5406 - Rhombo.H.axes - a 5.03255 - b 5.03255 - c 13.74039 - alpha 90.000 - beta 90.000 - gamma 120.000 - Primitive - R-3c (167) - 6 - 301.374 - I/c PDF 3. - F28  
 00-002-0458 (D) - Quartz -  $\text{SiO}_2$  - Y: 52.86 % - d x by: 1. - WL: 1.5406 - Hexagonal - a 4.90300 - b 4.90300 - c 5.39300 - alpha 90.000 - beta 90.000 - gamma 120.000 - Primitive - P3221 (154) - 3 - 112.275 - F24= 8(0.0920,34)

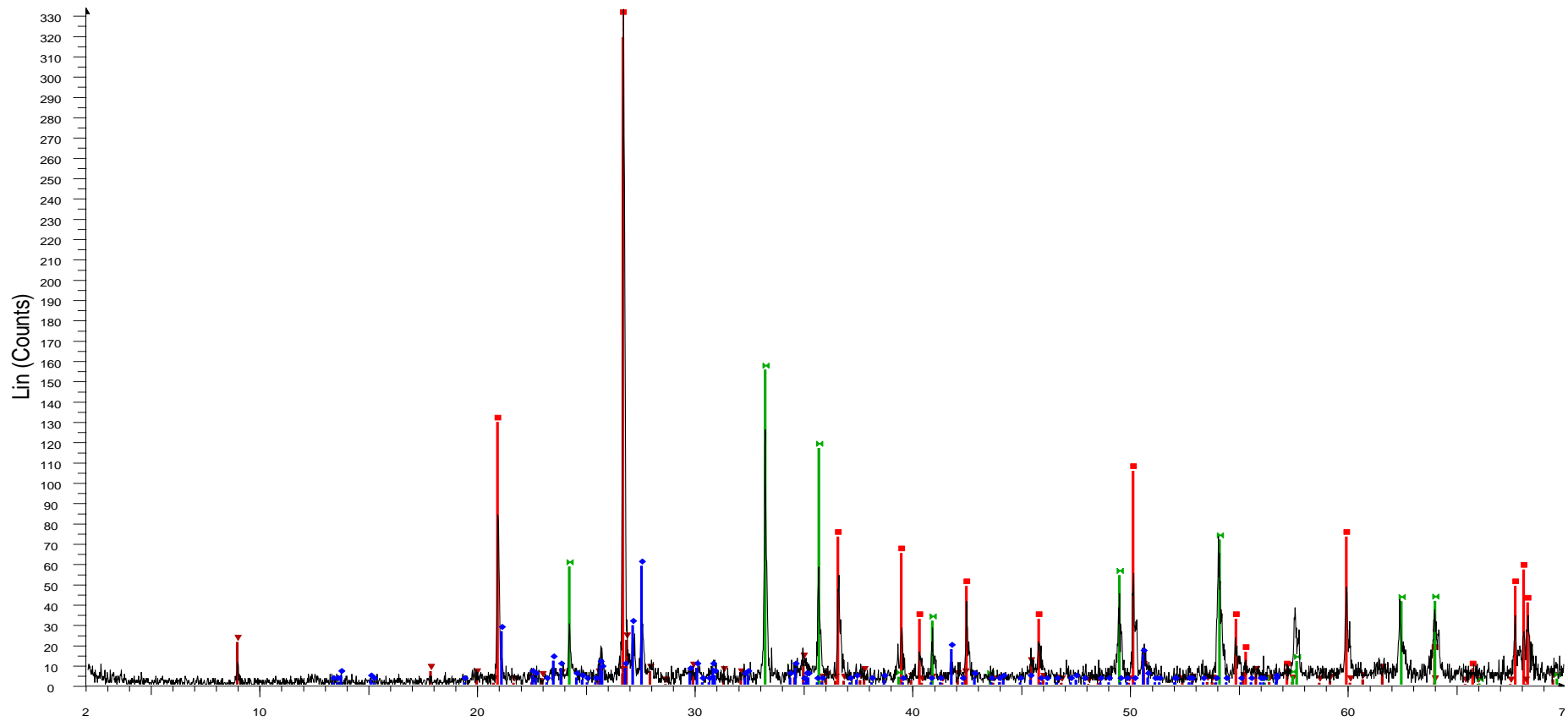
Sample 11



16 - File: C5120100.raw - Type: 2Th/Th locked - Start: 2.000 ° - End: 70.000 ° - Step: 0.020 ° - Step time: 1. s - Temp.: 25 °C (Room) - Time Started: 17 s - 2-Theta: 2.000 ° - Theta: 1.000 ° - Chi: 0.00 ° - Phi: 0.00 ° - X: 0.0 mm - Y: 0.0 mm - Z: 0.0  
 Operations: Import  
 00-046-1045 (\*) - Quartz, syn - SiO<sub>2</sub> - Y: 528.01 % - d x by: 1. - WL: 1.5406 - Hexagonal - a 4.91344 - b 4.91344 - c 5.40524 - alpha 90.000 - beta 90.000 - gamma 120.000 - Primitive - P3221 (154) - 3 - 113.010 - I/c PDF 3.4 - F30=558(0.0017,  
 00-006-0502 (D) - Hematite - alpha-Fe<sub>2</sub>O<sub>3</sub> - Y: 140.17 % - d x by: 1. - WL: 1.5406 -  
 01-071-1156 (C) - Albite high - Na(AlSi<sub>3</sub>O<sub>8</sub>) - Y: 17.02 % - d x by: 1. - WL: 1.5406 - Triclinic - a 8.27830 - b 12.95920 - c 7.14520 - alpha 90.056 - beta 116.087 - gamma 89.997 - Base-centered - C-1 (0) - 4 - 688.448 - I/c PDF 0.6 - F30= 47(0.0

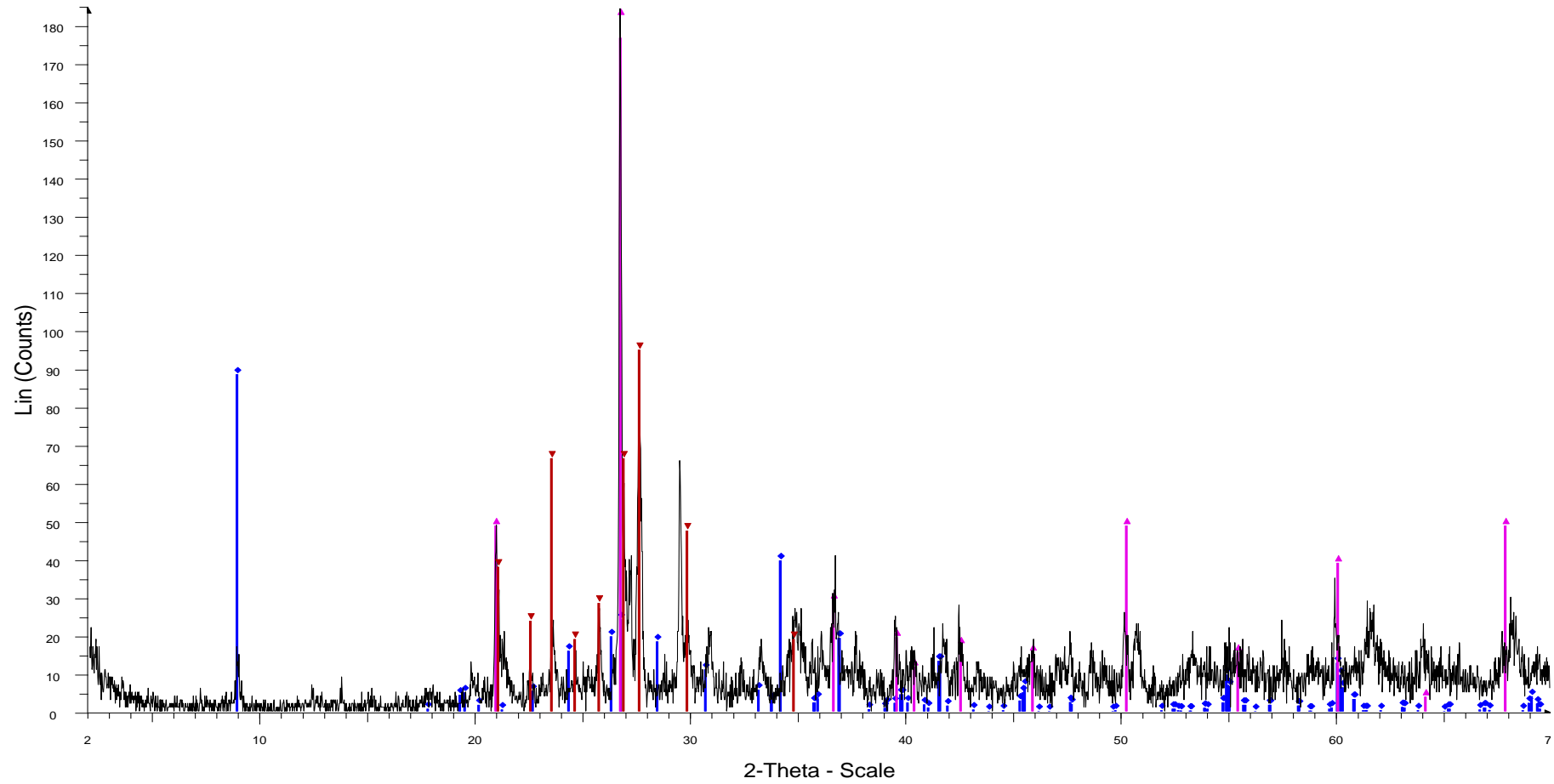
Sample 13





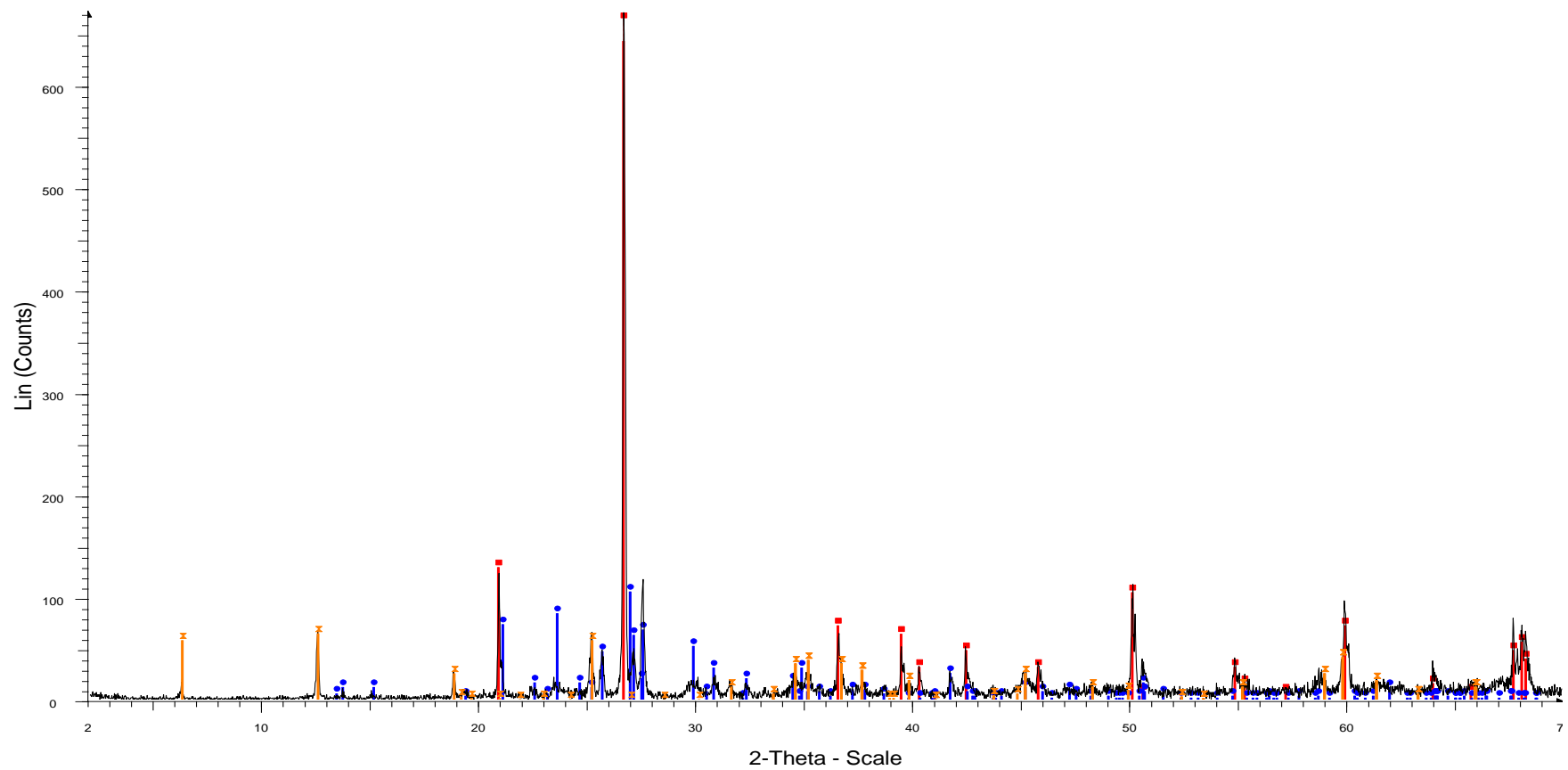
1602 - File: C5120479.raw - Type: 2Th/Th locked - Start: 2.000 ° - End: 70.000 ° - Step: 0.020 ° - Step time: 1. s - Temp.: 25 °C (Room) - Time Started: 16 s - 2-Theta: 2.000 ° - Theta: 1.000 ° - Chi: 0.00 ° - Phi: 0.00 ° - X: 0.0 mm - Y: 0.0 mm - Z: Operations: Import  
 00-046-1045 (\*) - Quartz, syn - SiO<sub>2</sub> - Y: 243.45 % - d x by: 1. - WL: 1.5406 - Hexagonal - a 4.91344 - b 4.91344 - c 5.40524 - alpha 90.000 - beta 90.000 - gamma 120.000 - Primitive - P3221 (154) - 3 - 113.010 - I/c PDF 3.4 - F30=558(0.0017,  
 00-006-0263 (I) - Muscovite-2M1 - KAl<sub>2</sub>(Si<sub>3</sub>Al)O<sub>10</sub>(OH,F)<sub>2</sub> - Y: 6.65 % - d x by: 1. - WL: 1.5406 - Monoclinic - a 5.19000 - b 9.03000 - c 20.05000 - alpha 90.000 - beta 95.770 - gamma 90.000 - Base-centered - C2/c (15) - 4 - 934.896 - F30= 12(  
 00-019-0932 (I) - Microcline, intermediate - KAlSi<sub>3</sub>O<sub>8</sub> - Y: 17.62 % - d x by: 1. - WL: 1.5406 - Triclinic - a 8.56000 - b 12.97000 - c 7.21000 - alpha 90.300 - beta 116.100 - gamma 89.000 - Base-centered - C-1 (0) - 4 - 718.739 - F30= 46(0.0165,  
 01-089-0599 (C) - Hematite, syn - alpha-Fe<sub>2</sub>O<sub>3</sub> - Y: 46.68 % - d x by: 1. - WL: 1.5406 - Rhombo.H.axes - a 5.03200 - b 5.03200 - c 13.73300 - alpha 90.000 - beta 90.000 - gamma 120.000 - Primitive - R-3c (167) - 6 - 301.146 - I/c PDF 3.1 - F28

Sample 14



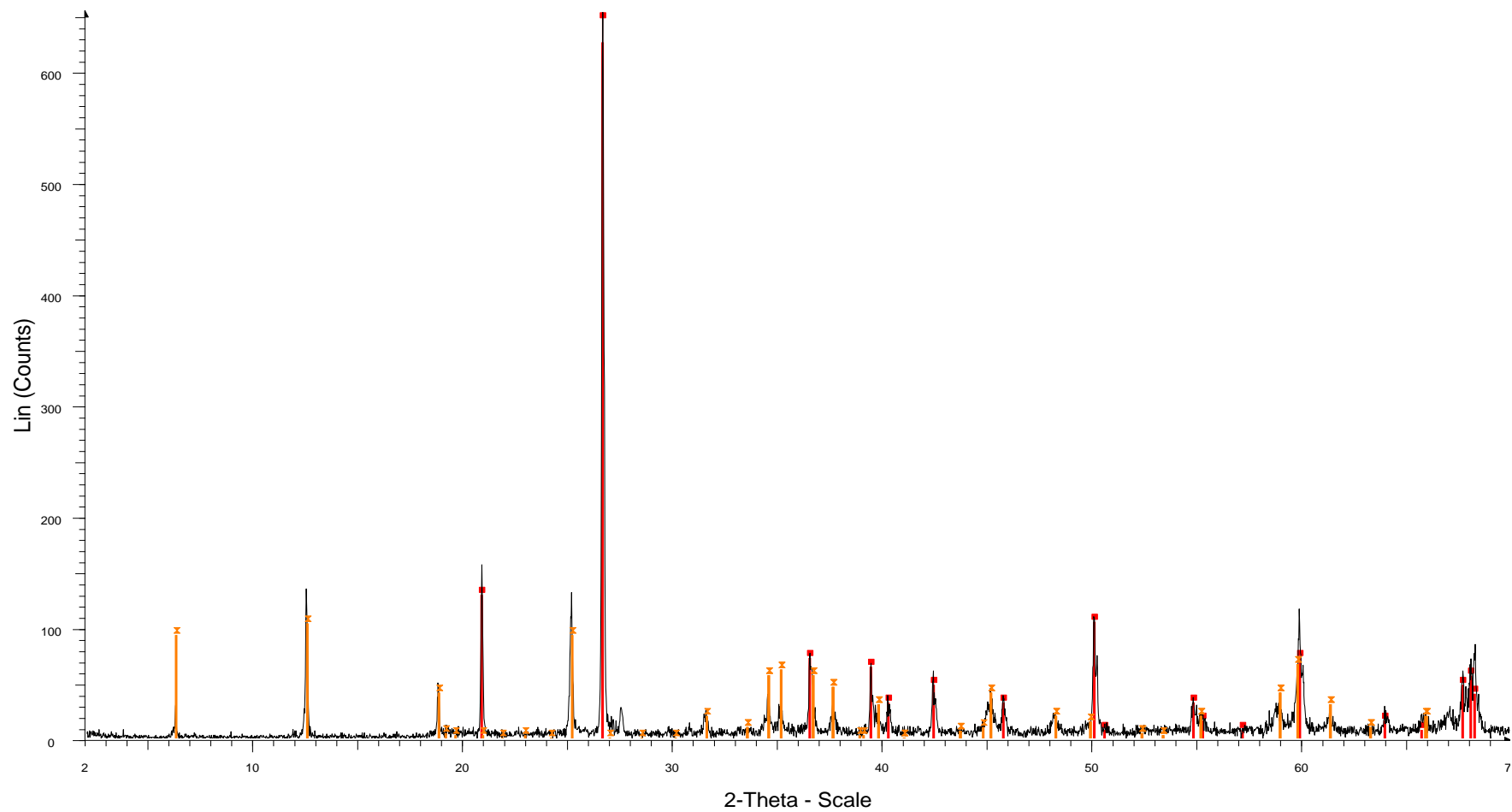
5402 - File: C05120434.raw - Type: 2Th/Th locked - Start: 2.000 ° - End: 70.000 ° - Step: 0.020 ° - Step time: 1. s - Temp.: 25 °C (Room) - Time Started: 16 s - 2-Theta: 2.000 ° - Theta: 1.000 ° - Chi: 0.00 ° - Phi: 0.00 ° - X: 0.0 mm - Y: 0.0 mm - Z: 0.0 mm  
 Operations: Import  
 01-088-2192 (C) - Biotite 1M, titanovanadate - (K1.8Na0.15Ba0.05)(Mg3.26Fe2Ti0.74)(Al2.5Si5.5O20)O1.85(OH)2.15 - Y: 48.00 % - d x by: 1. - WL: 1.5406 - Monoclinic - a 5.33100 - b 9.23000 - c 10.16000 - alpha 90.000 - beta 100.190 - gamma 90.000  
 00-001-0649 (D) - Quartz - SiO2 - Y: 105.83 % - d x by: 1. - WL: 1.5406 - Hexagonal - a 4.90300 - b 4.90300 - c 5.39300 - alpha 90.000 - beta 90.000 - gamma 120.000 - Primitive - P312 (149) - 3 - 112.275 - F22= 6(0.0980,38)  
 00-008-0048 (D) - Orthoclase - K(Al,Fe)Si2O8 - Y: 51.51 % - d x by: 1. - WL: 1.5406 - Monoclinic - a 8.58600 - b 13.02000 - c 7.18900 - alpha 90.000 - beta 115.980 - gamma 90.000 - Base-centered - C2/m (12) - 4 - 722.444 - F9= 13(0.0260,26)

Sample 15



65 - File: C05120430.raw - Type: 2Th/Th locked - Start: 2.000 ° - End: 70.000 ° - Step: 0.020 ° - Step time: 1. s - Temp.: 25 °C (Room) - Time Started: 17 s - 2-Theta: 2.000 ° - Theta: 1.000 ° - Chi: 0.00 ° - Phi: 0.00 ° - X: 0.0 mm - Y: 0.0 mm - Z: 0.  
 Operations: Import  
 00-046-1045 (\*) - Quartz, syn - SiO<sub>2</sub> - Y: 120.64 % - d x by: 1. - WL: 1.5406 - Hexagonal - a 4.91344 - b 4.91344 - c 5.40524 - alpha 90.000 - beta 90.000 - gamma 120.000 - Primitive - P3221 (154) - 3 - 113.010 - I/c PDF 3.4 - F30=558(0.0017,  
 00-046-1323 (I) - Clinocllore-1Mllb - (Mg,Al,Fe)6(Si,Al)4O10(OH)8 - Y: 9.67 % - d x by: 1. - WL: 1.5406 - Monoclinic - a 5.34700 - b 9.26300 - c 14.25000 - alpha 90.000 - beta 97.200 - gamma 90.000 - Base-centered - C2/m (12) - 2 - 700.227 -  
 00-031-0966 (\*) - Orthoclase - KAlSi3O8 - Y: 15.76 % - d x by: 1. - WL: 1.5406 - Monoclinic - a 8.55600 - b 12.98000 - c 7.20500 - alpha 90.000 - beta 116.010 - gamma 90.000 - Base-centered - C2/m (12) - 4 - 719.122 - F30= 55(0.0148,37)

Sample 16

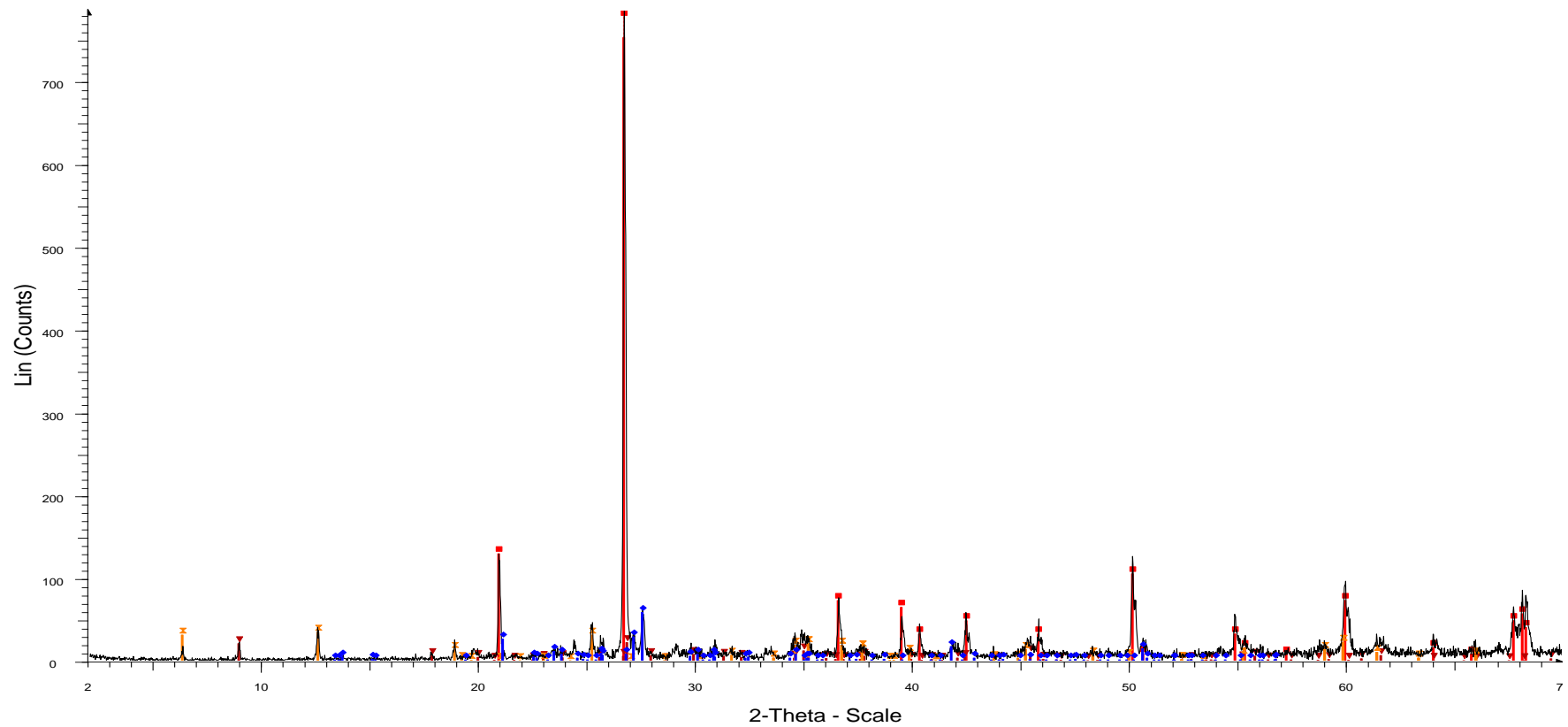


4502 - File: C05120083.raw - Type: 2Th/Th locked - Start: 2.000 ° - End: 70.000 ° - Step: 0.020 ° - Step time: 1. s - Temp.: 25 °C (Room) - Time Started: 17 s - 2-Theta: 2.000 ° - Theta: 1.000 ° - Chi: 0.00 ° - Phi: 0.00 ° - X: 0.0 mm - Y: 0.0 mm - Z: Operations: Import

00-046-1045 (\*) - Quartz, syn - SiO<sub>2</sub> - Y: 123.95 % - d x by: 1. - WL: 1.5406 - Hexagonal - a 4.91344 - b 4.91344 - c 5.40524 - alpha 90.000 - beta 90.000 - gamma 120.000 - Primitive - P3221 (154) - 3 - 113.010 - I/lc PDF 3.4 - F30=558(0.0017,

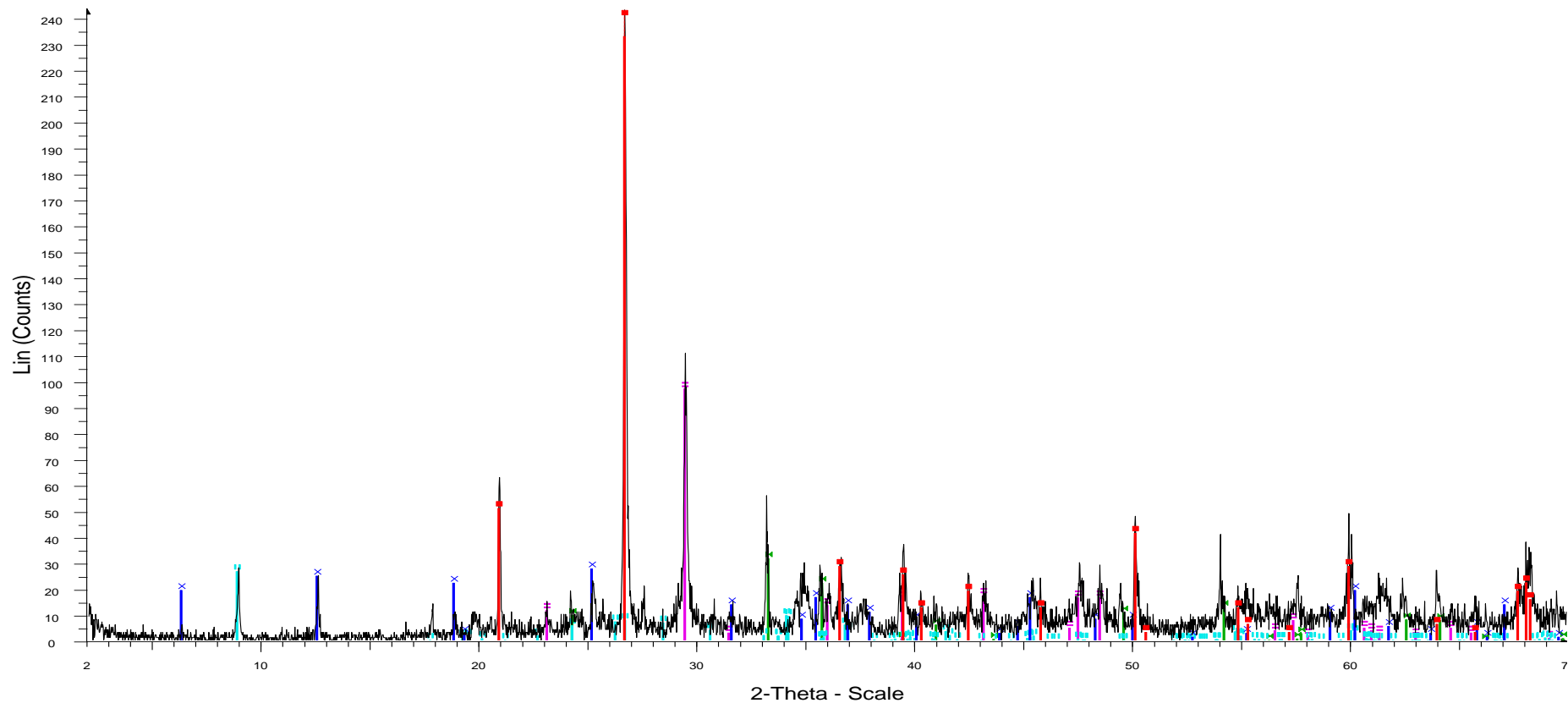
00-046-1323 (I) - Clinocllore-1Mllb - (Mg,Al,Fe)<sub>6</sub>(Si,Al)<sub>4</sub>O<sub>10</sub>(OH)<sub>8</sub> - Y: 15.87 % - d x by: 1. - WL: 1.5406 - Monoclinic - a 5.34700 - b 9.26300 - c 14.25000 - alpha 90.000 - beta 97.200 - gamma 90.000 - Base-centered - C2/m (12) - 2 - 700.227 -

Sample 17



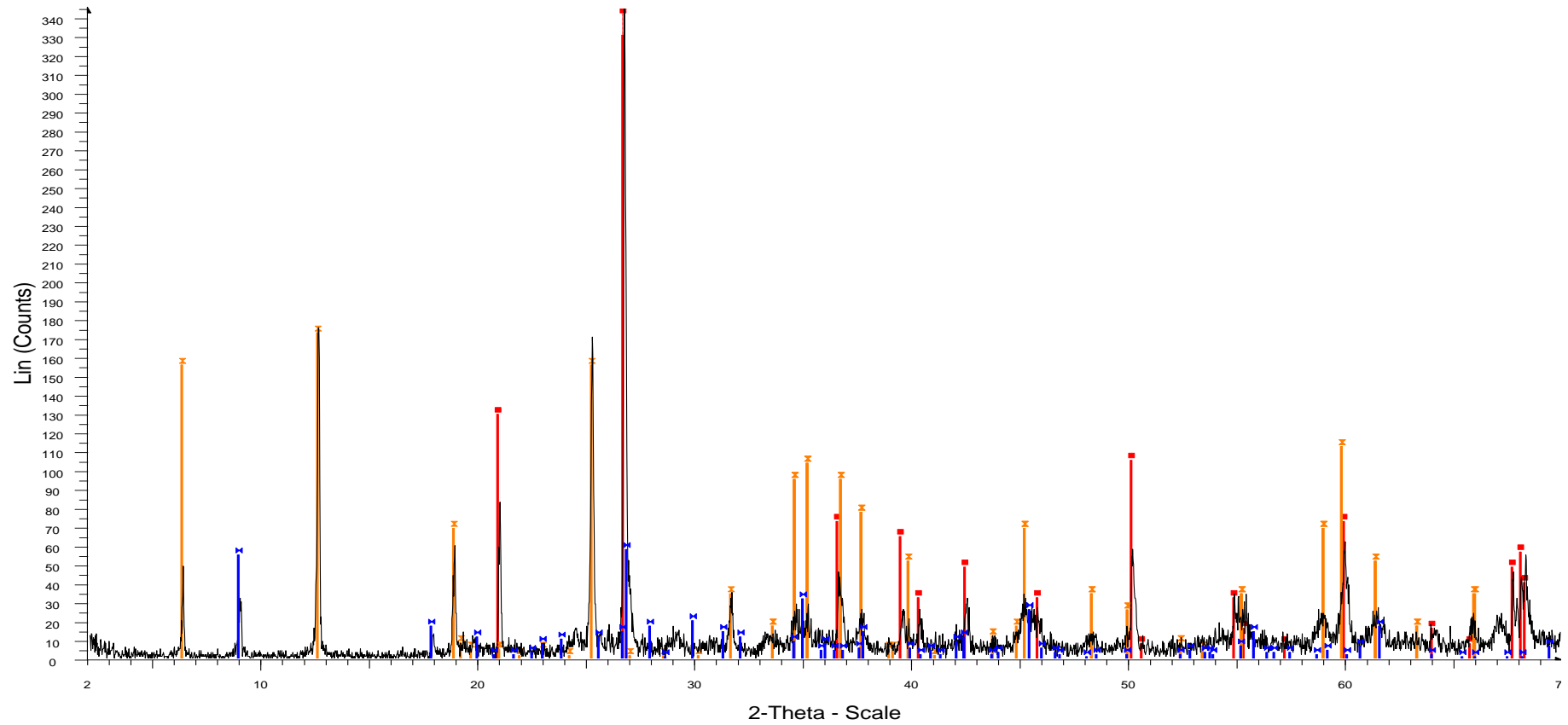
72 - File: C05120071.raw - Type: 2Th/Th locked - Start: 2.000 ° - End: 70.000 ° - Step: 0.020 ° - Step time: 1. s - Temp.: 25 °C (Room) - Time Started: 34 s - 2-Theta: 2.000 ° - Theta: 1.000 ° - Chi: 0.00 ° - Phi: 0.00 ° - X: 0.0 mm - Y: 0.0 mm - Z: 0.  
 Operations: Import  
 ■ 00-046-1045 (\*) - Quartz, syn - SiO<sub>2</sub> - Y: 103.19 % - d x by: 1. - WL: 1.5406 - Hexagonal - a 4.91344 - b 4.91344 - c 5.40524 - alpha 90.000 - beta 90.000 - gamma 120.000 - Primitive - P3221 (154) - 3 - 113.010 - I/c PDF 3.4 - F30=558(0.0017,  
 ▼ 00-006-0263 (I) - Muscovite-2M1 - KAl<sub>2</sub>(Si<sub>3</sub>Al)O<sub>10</sub>(OH,F)<sub>2</sub> - Y: 2.82 % - d x by: 1. - WL: 1.5406 - Monoclinic - a 5.19000 - b 9.03000 - c 20.05000 - alpha 90.000 - beta 95.770 - gamma 90.000 - Base-centered - C2/c (15) - 4 - 934.896 - F30= 12(  
 ✕ 00-046-1323 (I) - Clinocllore-1M1b - (Mg,Al,Fe)6(Si,Al)4O<sub>10</sub>(OH)8 - Y: 4.41 % - d x by: 1. - WL: 1.5406 - Monoclinic - a 5.34700 - b 9.26300 - c 14.25000 - alpha 90.000 - beta 97.200 - gamma 90.000 - Base-centered - C2/m (12) - 2 - 700.227 -  
 ◆ 00-019-0932 (I) - Microcline, intermediate - KAlSi<sub>3</sub>O<sub>8</sub> - Y: 7.47 % - d x by: 1. - WL: 1.5406 - Triclinic - a 8.56000 - b 12.97000 - c 7.21000 - alpha 90.300 - beta 116.100 - gamma 89.000 - Base-centered - C-1 (0) - 4 - 718.739 - F30= 46(0.0165,3

Sample 18



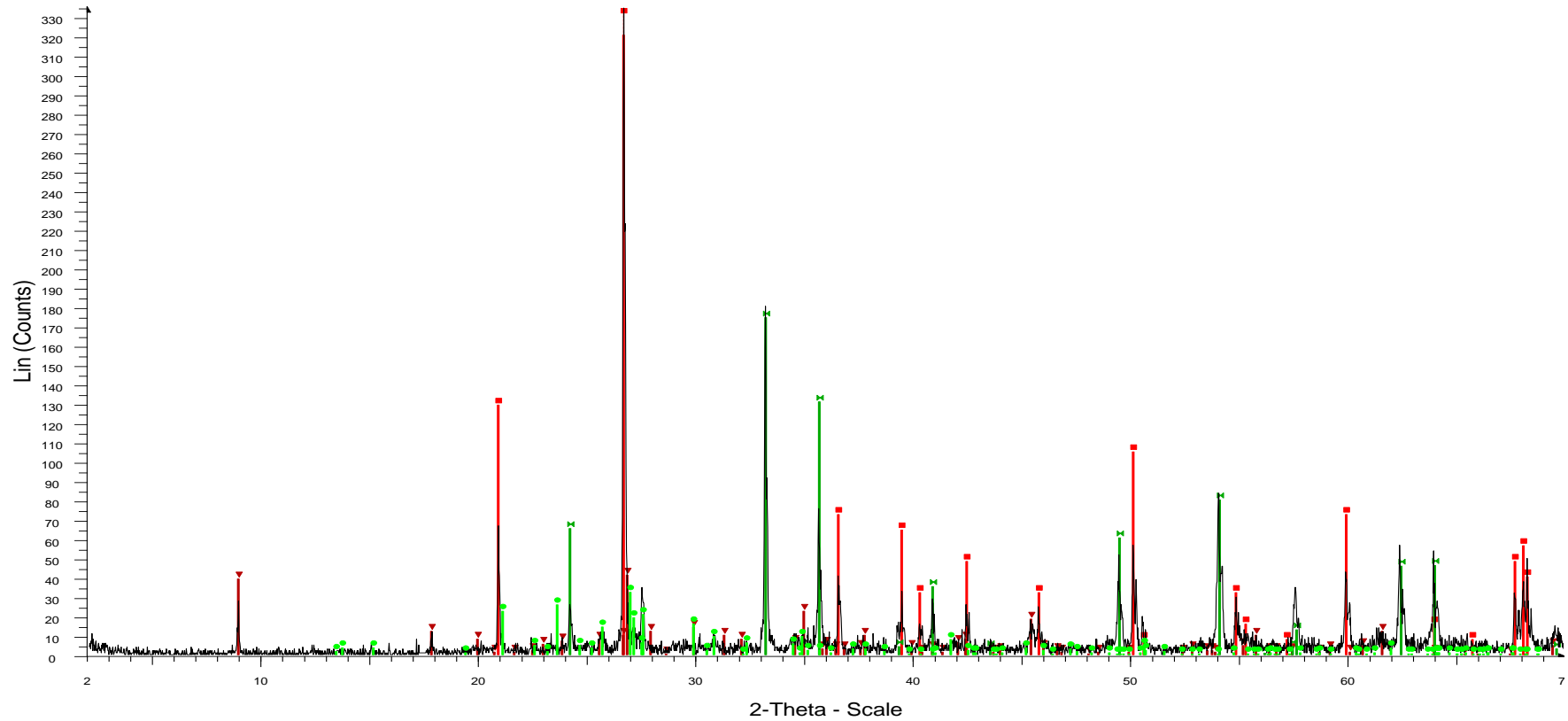
29 01 - File: C05120429.raw - Type: 2Th/Th locked - Start: 2.000 ° - End: 70.000 ° - Step: 0.020 ° - Step time: 1. s - Temp.: 25 °C (Room) - Time Started: 16 s - 2-Theta: 2.000 ° - Theta: 1.000 ° - Chi: 0.00 ° - Phi: 0.00 ° - X: 0.0 mm - Y: 0.0 mm - Z  
 Operations: Import  
 00-046-1045 (\*) - Quartz, syn - SiO<sub>2</sub> - Y: 131.05 % - d x by: 1. - WL: 1.5406 - Hexagonal - a 4.91344 - b 4.91344 - c 5.40524 - alpha 90.000 - beta 90.000 - gamma 120.000 - Primitive - P3221 (154) - 3 - 113.010 - I/c PDF 3.4 - F30=558(0.0017,  
 01-089-8104 (C) - Hematite, syn - Fe<sub>2</sub>O<sub>3</sub> - Y: 12.99 % - d x by: 1. - WL: 1.5406 - Rhombo.H.axes - a 5.02300 - b 5.02300 - c 13.70800 - alpha 90.000 - beta 90.000 - gamma 120.000 - Primitive - R-3c (167) - 6 - 299.524 - I/c PDF 3.3 - F28=100  
 00-005-0586 (\*) - Calcite, syn - CaCO<sub>3</sub> - Y: 39.98 % - d x by: 1. - WL: 1.5406 - Rhombo.H.axes - a 4.98900 - b 4.98900 - c 17.06200 - alpha 90.000 - beta 90.000 - gamma 120.000 - Primitive - R-3c (167) - 6 - 367.780 - I/c PDF 2. - F30= 57(0.0  
 01-088-2195 (C) - Biotite 1M, titanioan barian - (K1.71Na0.22Ba0.07)(Mg3.4Fe1.5Ti0.98)(Al1.52Si6.48O20)O2.28(OH) - Y: 10.94 % - d x by: 1. - WL: 1.5406 - Monoclinic - a 5.33000 - b 9.24500 - c 10.19200 - alpha 90.000 - beta 100.350 - gam  
 00-012-0242 (I) - Clinocllore-1Mlib - (Mg,Al)6(Si,Al)4O10(OH)8 - Y: 11.40 % - d x by: 1. - WL: 1.5406 - Monoclinic - a 5.30800 - b 9.20800 - c 14.28100 - alpha 90.000 - beta 97.250 - gamma 90.000 - Base-centered - C2/m (12) - 2 - 692.419 - F3

Sample 19.



4401 - File: C05120067.raw - Type: 2Th/Th locked - Start: 2.000 ° - End: 70.000 ° - Step: 0.020 ° - Step time: 1. s - Temp.: 25 °C (Room) - Time Started: 33 s - 2-Theta: 2.000 ° - Theta: 1.000 ° - Chi: 0.00 ° - Phi: 0.00 ° - X: 0.0 mm - Y: 0.0 mm - Z: 0.0 mm  
 Operations: Import  
 ■ 00-046-1045 (\*) - Quartz, syn - SiO<sub>2</sub> - Y: 235.01 % - d x by: 1. - WL: 1.5406 - Hexagonal - a 4.91344 - b 4.91344 - c 5.40524 - alpha 90.000 - beta 90.000 - gamma 120.000 - Primitive - P3221 (154) - 3 - 113.010 - I/c PDF 3.4 - F30=558(0.0017,  
 × 00-046-1323 (I) - Clinocllore-1M11b - (Mg,Al,Fe)6(Si,Al)4O10(OH)8 - Y: 50.20 % - d x by: 1. - WL: 1.5406 - Monoclinic - a 5.34700 - b 9.26300 - c 14.25000 - alpha 90.000 - beta 97.200 - gamma 90.000 - Base-centered - C2/m (12) - 2 - 700.227 -  
 □ 00-006-0263 (I) - Muscovite-2M1 - KAl<sub>2</sub>(Si<sub>3</sub>Al)O<sub>10</sub>(OH,F)<sub>2</sub> - Y: 16.82 % - d x by: 1. - WL: 1.5406 - Monoclinic - a 5.19000 - b 9.03000 - c 20.05000 - alpha 90.000 - beta 95.770 - gamma 90.000 - Base-centered - C2/c (15) - 4 - 934.896 - F30= 1

Sample 20.



3202 - File: C05120436.raw - Type: 2Th/Th locked - Start: 2.000 ° - End: 70.000 ° - Step: 0.020 ° - Step time: 1. s - Temp.: 25 °C (Room) - Time Started: 17 s - 2-Theta: 2.000 ° - Theta: 1.000 ° - Chi: 0.00 ° - Phi: 0.00 ° - X: 0.0 mm - Y: 0.0 mm - Z:

Operations: Import

■ 00-046-1045 (\*) - Quartz, syn - SiO<sub>2</sub> - Y: 242.01 % - d x by: 1. - WL: 1.5406 - Hexagonal - a 4.91344 - b 4.91344 - c 5.40524 - alpha 90.000 - beta 90.000 - gamma 120.000 - Primitive - P321 (154) - 3 - 113.010 - *I*/c PDF 3.4 - F30=558(0.0017,

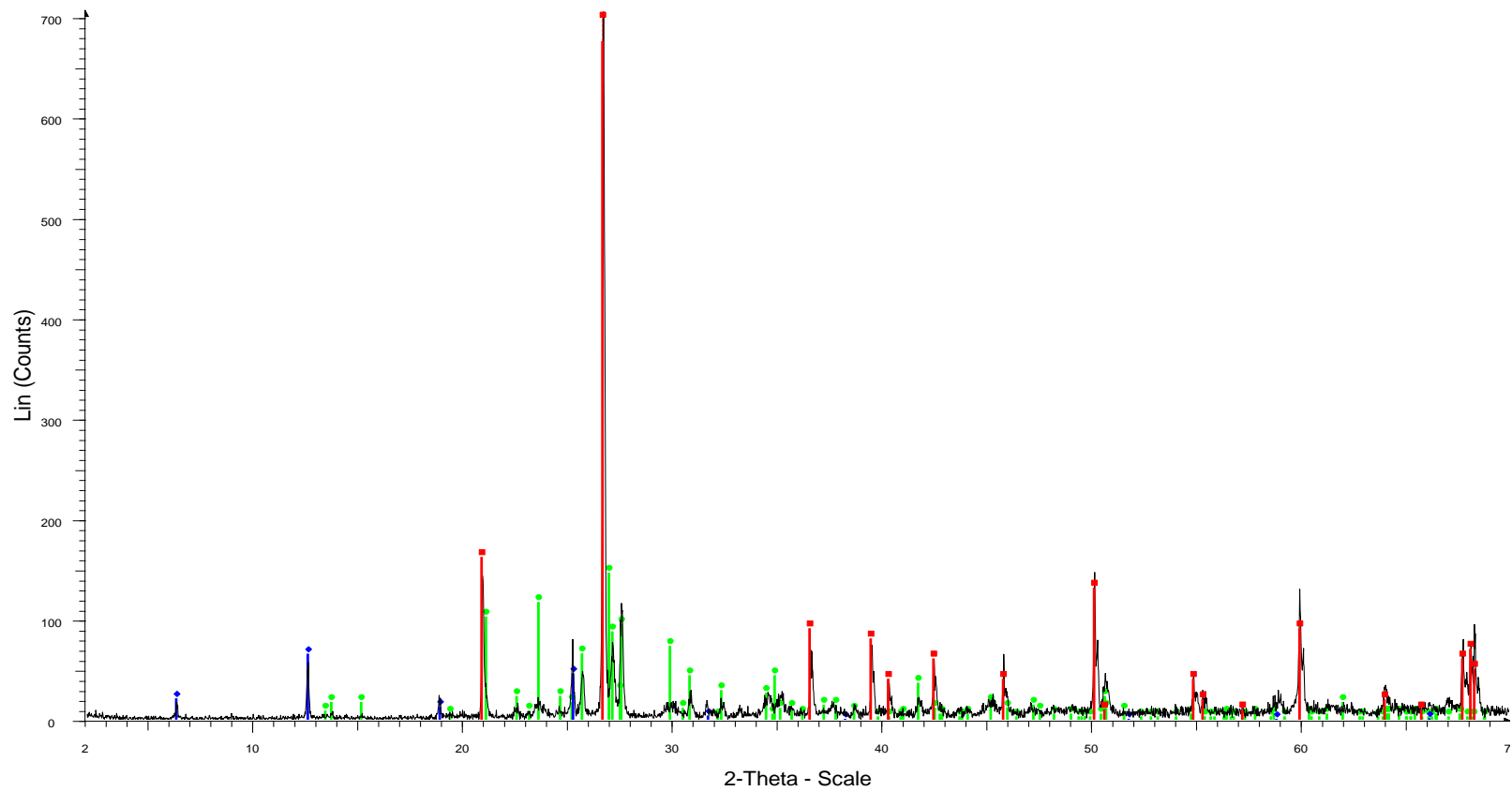
▲ 00-006-0263 (I) - Muscovite-2M1 - KAl<sub>2</sub>(Si<sub>3</sub>Al)O<sub>10</sub>(OH,F)<sub>2</sub> - Y: 12.39 % - d x by: 1. - WL: 1.5406 - Monoclinic - a 5.19000 - b 9.03000 - c 20.05000 - alpha 90.000 - beta 95.770 - gamma 90.000 - Base-centered - C2/c (15) - 4 - 934.896 - F30= 1

× 00-031-0966 (\*) - Orthoclase - KAlSi<sub>3</sub>O<sub>8</sub> - Y: 9.73 % - d x by: 1. - WL: 1.5406 - Monoclinic - a 8.55600 - b 12.98000 - c 7.20500 - alpha 90.000 - beta 116.010 - gamma 90.000 - Base-centered - C2/m (12) - 4 - 719.122 - F30= 55(0.0148,37)

■ 01-089-0599 (C) - Hematite, syn - alpha-Fe<sub>2</sub>O<sub>3</sub> - Y: 52.23 % - d x by: 1. - WL: 1.5406 - Rhombo.H.axes - a 5.03200 - b 5.03200 - c 13.73300 - alpha 90.000 - beta 90.000 - gamma 120.000 - Primitive - R-3c (167) - 6 - 301.146 - *I*/c PDF 3.1 - F28

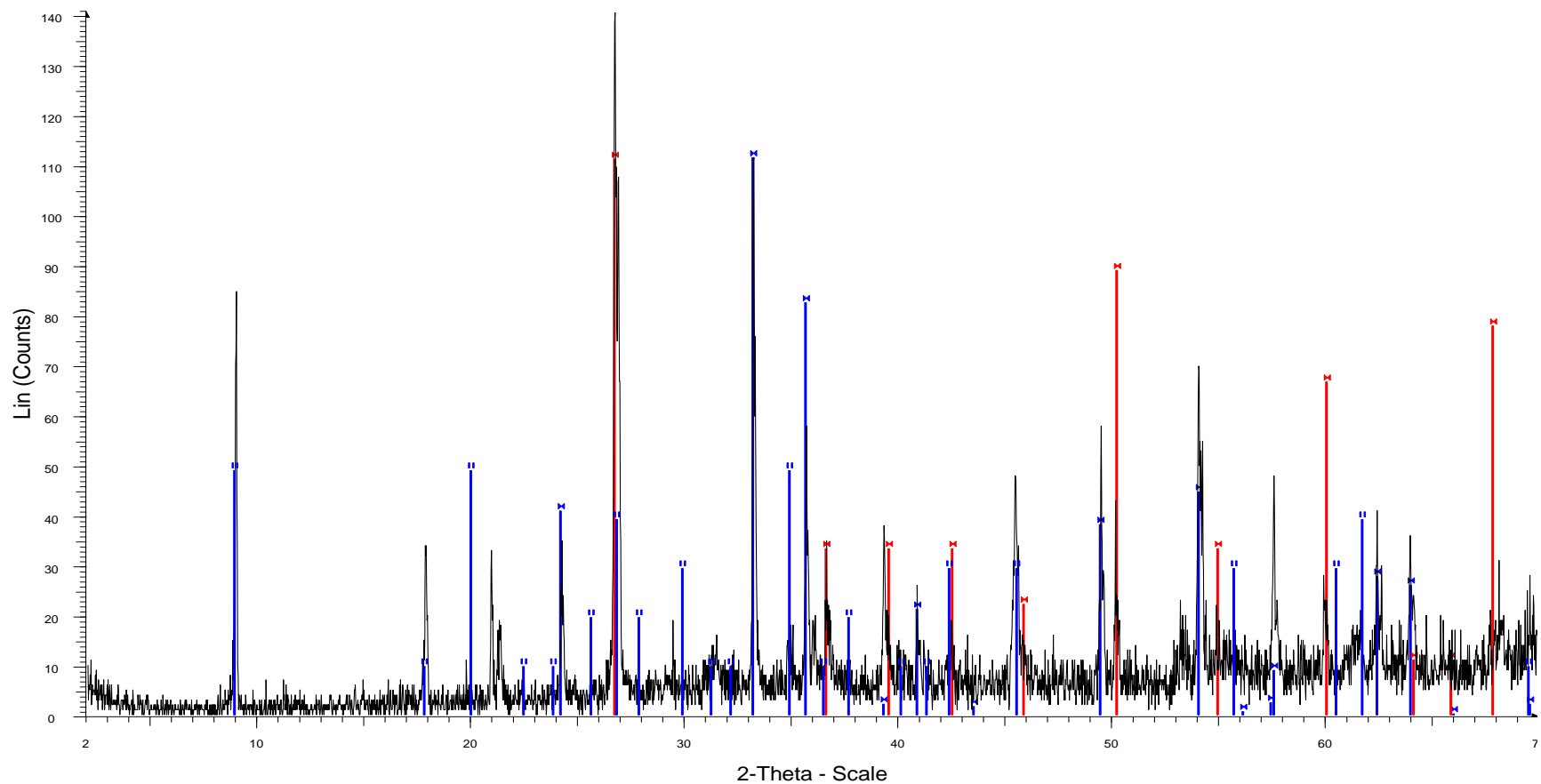
Sample 21.





24 - File: C05120435.raw - Type: 2Th/Th locked - Start: 2.000 ° - End: 70.000 ° - Step: 0.020 ° - Step time: 1. s - Temp.: 25 °C (Room) - Time Started: 16 s - 2-Theta: 2.000 ° - Theta: 1.000 ° - Chi: 0.00 ° - Phi: 0.00 ° - X: 0.0 mm - Y: 0.0 mm - Z: 0.  
 Operations: Import  
 00-046-1045 (\*) - Quartz, syn - SiO<sub>2</sub> - Y: 143.56 % - d x by: 1. - WL: 1.5406 - Hexagonal - a 4.91344 - b 4.91344 - c 5.40524 - alpha 90.000 - beta 90.000 - gamma 120.000 - Primitive - P3221 (154) - 3 - 113.010 - *I*/c PDF 3.4 - F30=558(0.0017,  
 00-031-0966 (\*) - Orthoclase - KAlSi<sub>3</sub>O<sub>8</sub> - Y: 20.79 % - d x by: 1. - WL: 1.5406 - Monoclinic - a 8.55600 - b 12.98000 - c 7.20500 - alpha 90.000 - beta 116.010 - gamma 90.000 - Base-centered - C2/m (12) - 4 - 719.122 - F30= 55(0.0148,37)  
 00-052-1044 (I) - Chlorite-serpentine - (Mg,Al)<sub>6</sub>(Si,Al)<sub>4</sub>O<sub>10</sub>(OH)<sub>8</sub> - Y: 9.32 % - d x by: 1. - WL: 1.5406 - Hexagonal - a 5.34000 - b 5.34000 - c 14.10900 - alpha 90.000 - beta 90.000 - gamma 120.000 - Primitive - P (0) - 1 - 348.425 - F12= 2(0.0

Sample 22.



7102 - File: C05120433.raw - Type: 2Th/Th locked - Start: 2.000 ° - End: 70.000 ° - Step: 0.020 ° - Step time: 1. s - Temp.: 25 °C (Room) - Time Started: 16 s - 2-Theta: 2.000 ° - Theta: 1.000 ° - Chi: 0.00 ° - Phi: 0.00 ° - X: 0.0 mm - Y: 0.0 mm - Z:

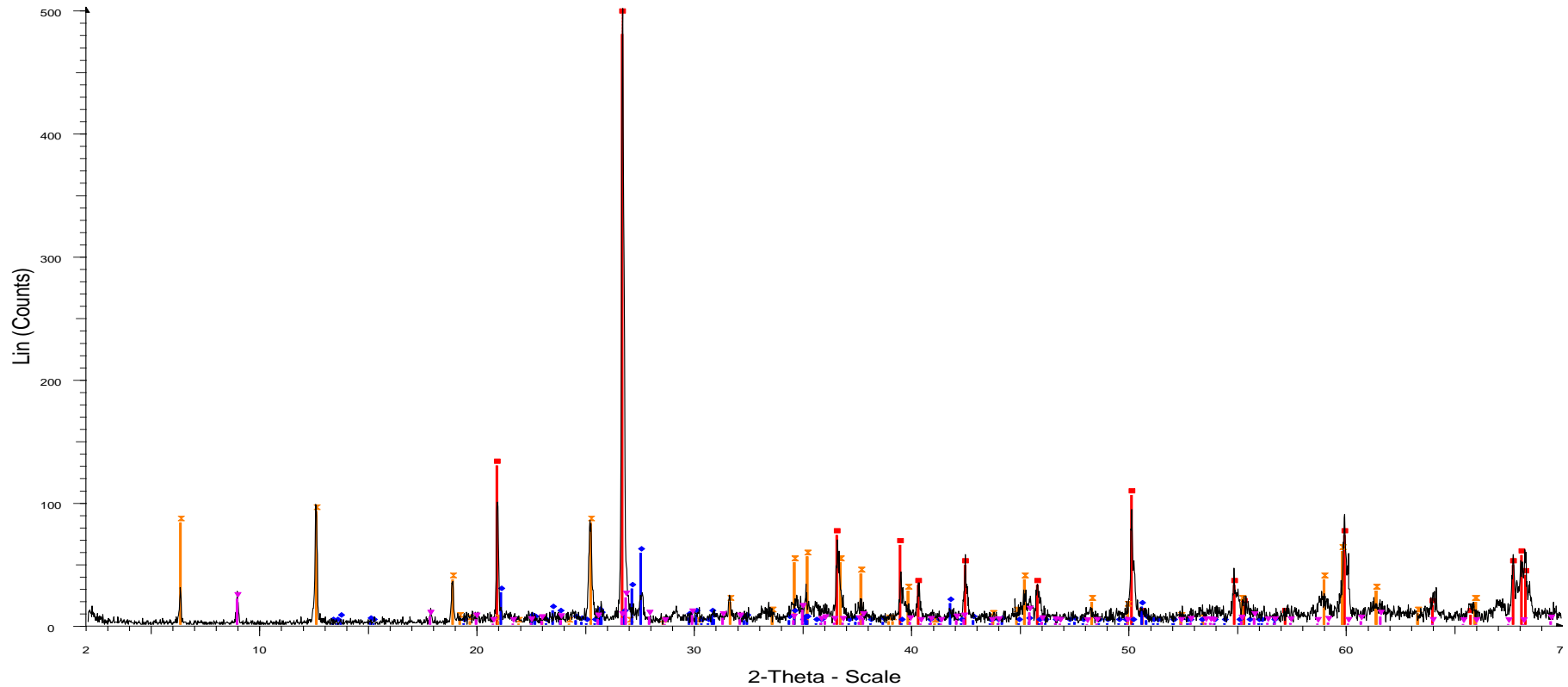
Operations: Import

■ 01-073-2234 (A) - Hematite, syn -  $\alpha$ -Fe<sub>2</sub>O<sub>3</sub> - Y: 79.47 % - d x by: 1. - WL: 1.5406 - Rhombo.H.axes - a 5.03255 - b 5.03255 - c 13.74039 - alpha 90.000 - beta 90.000 - gamma 120.000 - Primitive - R-3c (167) - 6 - 301.374 - I/c PDF 3. - F28=

■ 00-002-0471 (D) - Quartz - SiO<sub>2</sub> - Y: 79.23 % - d x by: 1. - WL: 1.5406 - Hexagonal - a 4.90300 - b 4.90300 - c 5.39300 - alpha 90.000 - beta 90.000 - gamma 120.000 - Primitive - P3221 (154) - 3 - 112.275 - F26= 5(0.0720,67)

■ 00-002-0058 (D) - Muscovite - H<sub>2</sub>KAl<sub>3</sub>Si<sub>3</sub>O<sub>12</sub> - Y: 34.88 % - d x by: 1. - WL: 1.5406 - Monoclinic - a 5.18000 - b 9.02000 - c 20.04000 - alpha 90.000 - beta 95.500 - gamma 90.000 - Base-centered - C2/c (15) - 4 - 932.030 - F25= 4(0.0270,243)

Sample 24.

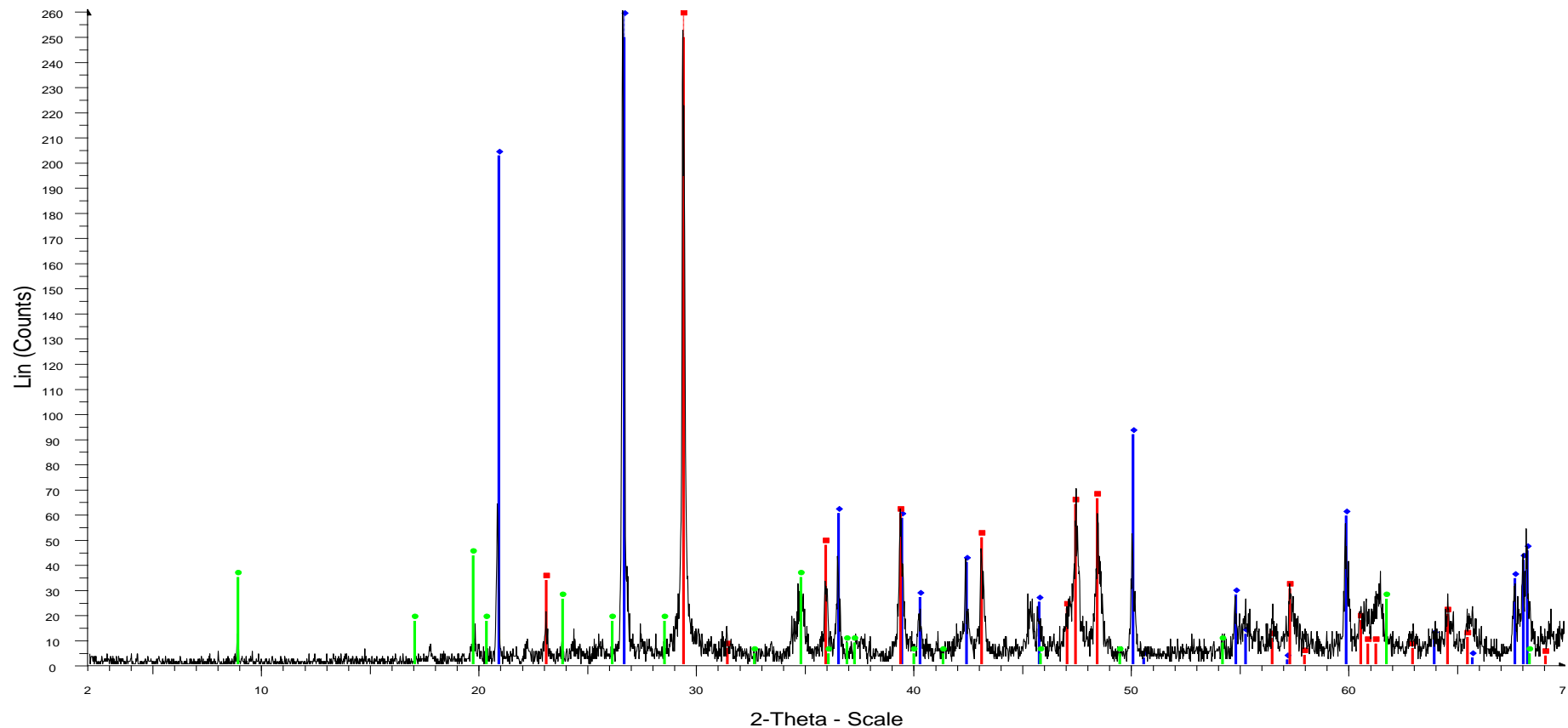


1302 - File: C5120477.raw - Type: 2Th/Th locked - Start: 2.000 ° - End: 70.000 ° - Step: 0.020 ° - Step time: 1. s - Temp.: 25 °C (Room) - Time Started: 16 s - 2-Theta: 2.000 ° - Theta: 1.000 ° - Chi: 0.00 ° - Phi: 0.00 ° - X: 0.0 mm - Y: 0.0 mm - Z:

Operations: Import

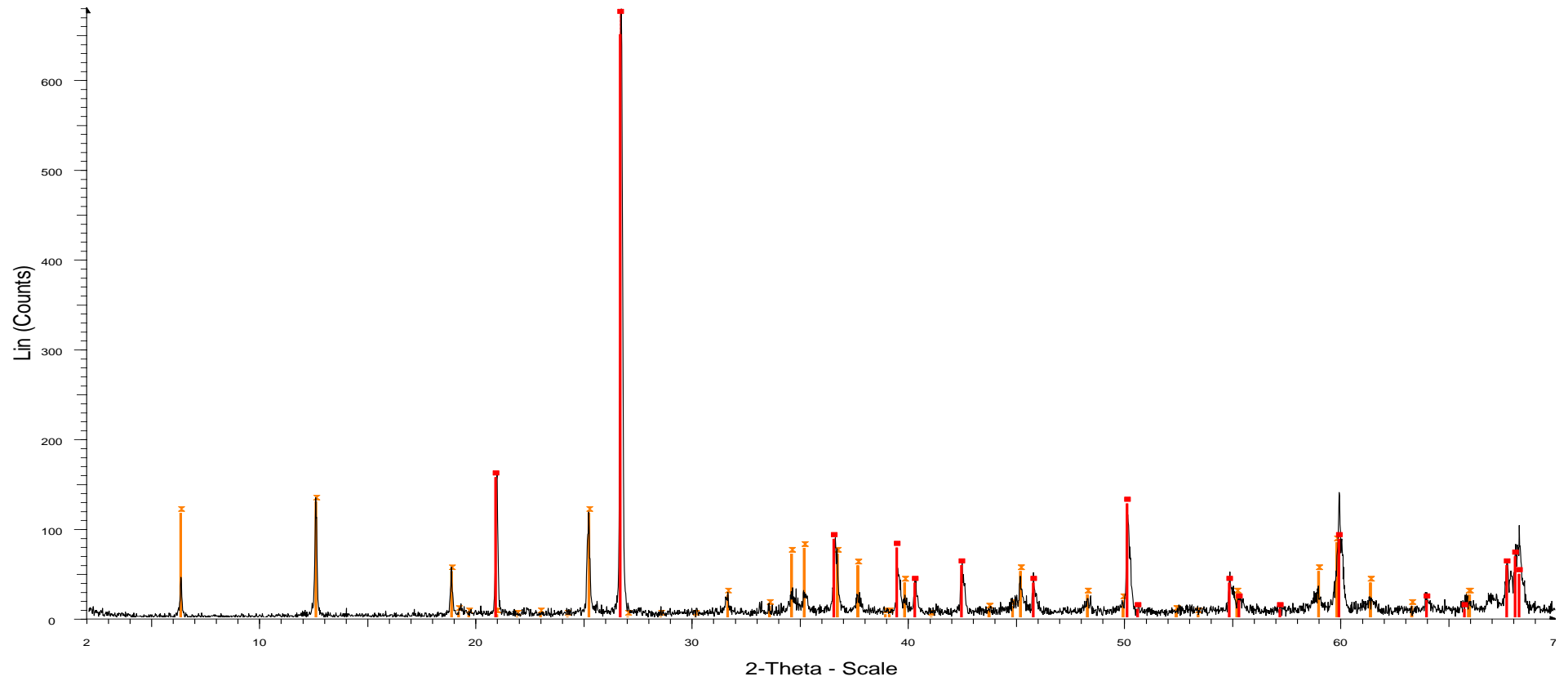
- 00-046-1045 (\*) - Quartz, syn - SiO<sub>2</sub> - Y: 161.66 % - d x by: 1. - WL: 1.5406 - Hexagonal - a 4.91344 - b 4.91344 - c 5.40524 - alpha 90.000 - beta 90.000 - gamma 120.000 - Primitive - P3221 (154) - 3 - 113.010 - I/c PDF 3.4 - F30=558(0.0017,
- 00-006-0263 (l) - Muscovite-2M1 - KAl<sub>2</sub>(Si<sub>3</sub>Al)O<sub>10</sub>(OH,F)<sub>2</sub> - Y: 4.42 % - d x by: 1. - WL: 1.5406 - Monoclinic - a 5.19000 - b 9.03000 - c 20.05000 - alpha 90.000 - beta 95.770 - gamma 90.000 - Base-centered - C2/c (15) - 4 - 934.896 - F30= 12(
- 00-046-1323 (l) - Clinocllore-1M1lb - (Mg,Al,Fe)6(Si,Al)4O10(OH)8 - Y: 18.43 % - d x by: 1. - WL: 1.5406 - Monoclinic - a 5.34700 - b 9.26300 - c 14.25000 - alpha 90.000 - beta 97.200 - gamma 90.000 - Base-centered - C2/m (12) - 2 - 700.227 -
- 00-019-0932 (l) - Microcline, intermediate - KAISi3O8 - Y: 11.70 % - d x by: 1. - WL: 1.5406 - Triclinic - a 8.56000 - b 12.97000 - c 7.21000 - alpha 90.300 - beta 116.100 - gamma 89.000 - Base-centered - C-1 (0) - 4 - 718.739 - F30= 46(0.0165,

Sample 26.



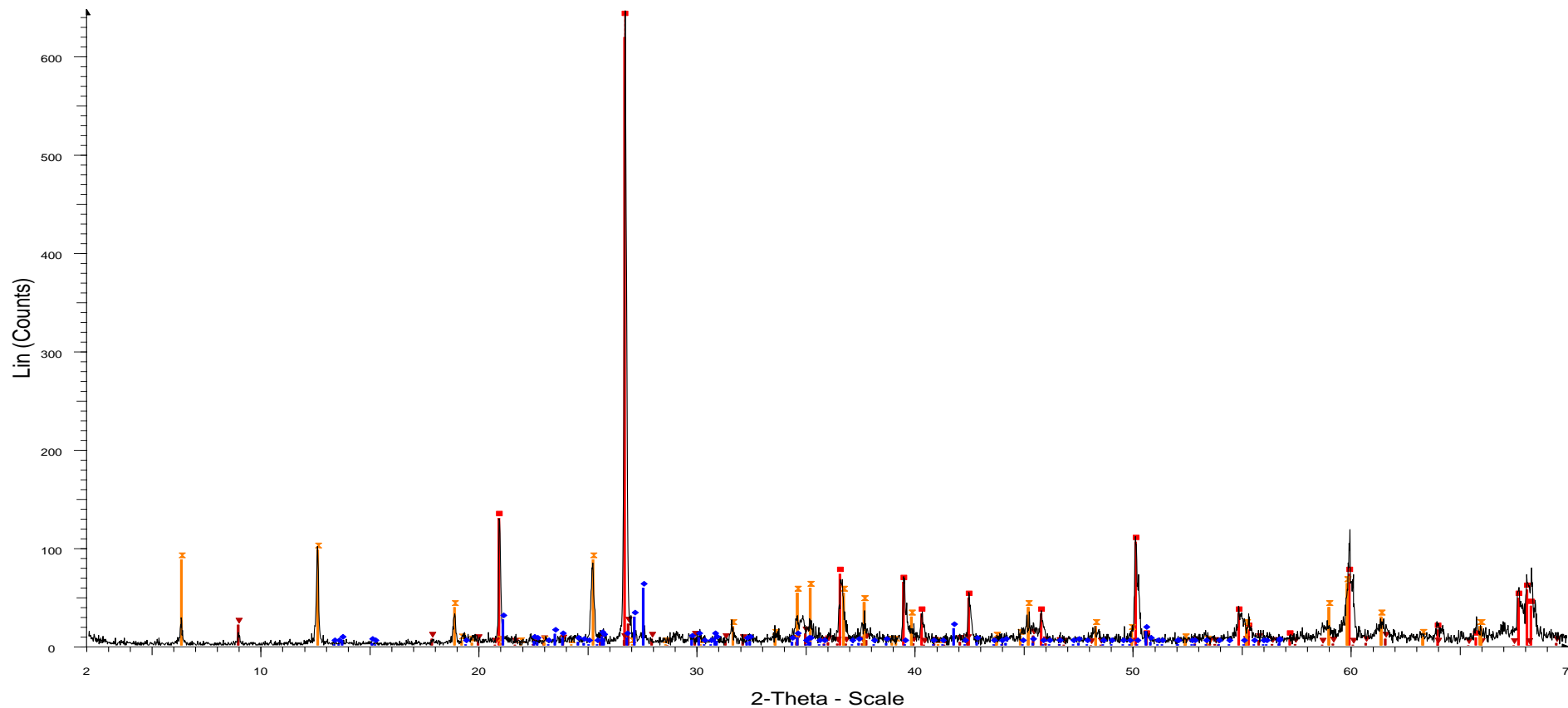
17 - File: C5120096.raw - Type: 2Th/Th locked - Start: 2.000 ° - End: 70.000 ° - Step: 0.020 ° - Step time: 1. s - Temp.: 25 °C (Room) - Time Started: 16 s - 2-Theta: 2.000 ° - Theta: 1.000 ° - Chi: 0.00 ° - Phi: 0.00 ° - X: 0.0 mm - Y: 0.0 mm - Z: 0.0  
 Operations: Import  
 01-070-3755 (C) - Quartz - SiO<sub>2</sub> - Y: 355.11 % - d x by: 1. - WL: 1.5406 - Hexagonal - a 4.91600 - b 4.91600 - c 5.40900 - alpha 90.000 - beta 90.000 - gamma 120.000 - Primitive - P3121 (152) - 3 - 113.206 - I/c PDF 2.9 - F29=1000(0.0000,29)  
 01-072-1937 (C) - Calcite - CaCO<sub>3</sub> - Y: 130.16 % - d x by: 1. - WL: 1.5406 - Rhombo.H.axes - a 4.99400 - b 4.99400 - c 17.08100 - alpha 90.000 - beta 90.000 - gamma 120.000 - Primitive - R-3c (167) - 6 - 368.927 - I/c PDF 3.2 - F30=1000(0.0  
 00-013-0573 (D) - Muscovite - 0.33(NH<sub>4</sub>)<sub>2</sub>O·Al<sub>2</sub>O<sub>3</sub>·2SiO<sub>2</sub>·0.66H<sub>2</sub>O - Y: 16.65 % - d x by: 1. - WL: 1.5406 - Monoclinic - a 5.22000 - b 9.02000 - c 20.02000 - alpha 90.000 - beta 90.220 - gamma 90.000 - 942.623 - F21= 0(0.1080,587)

Sample 27.

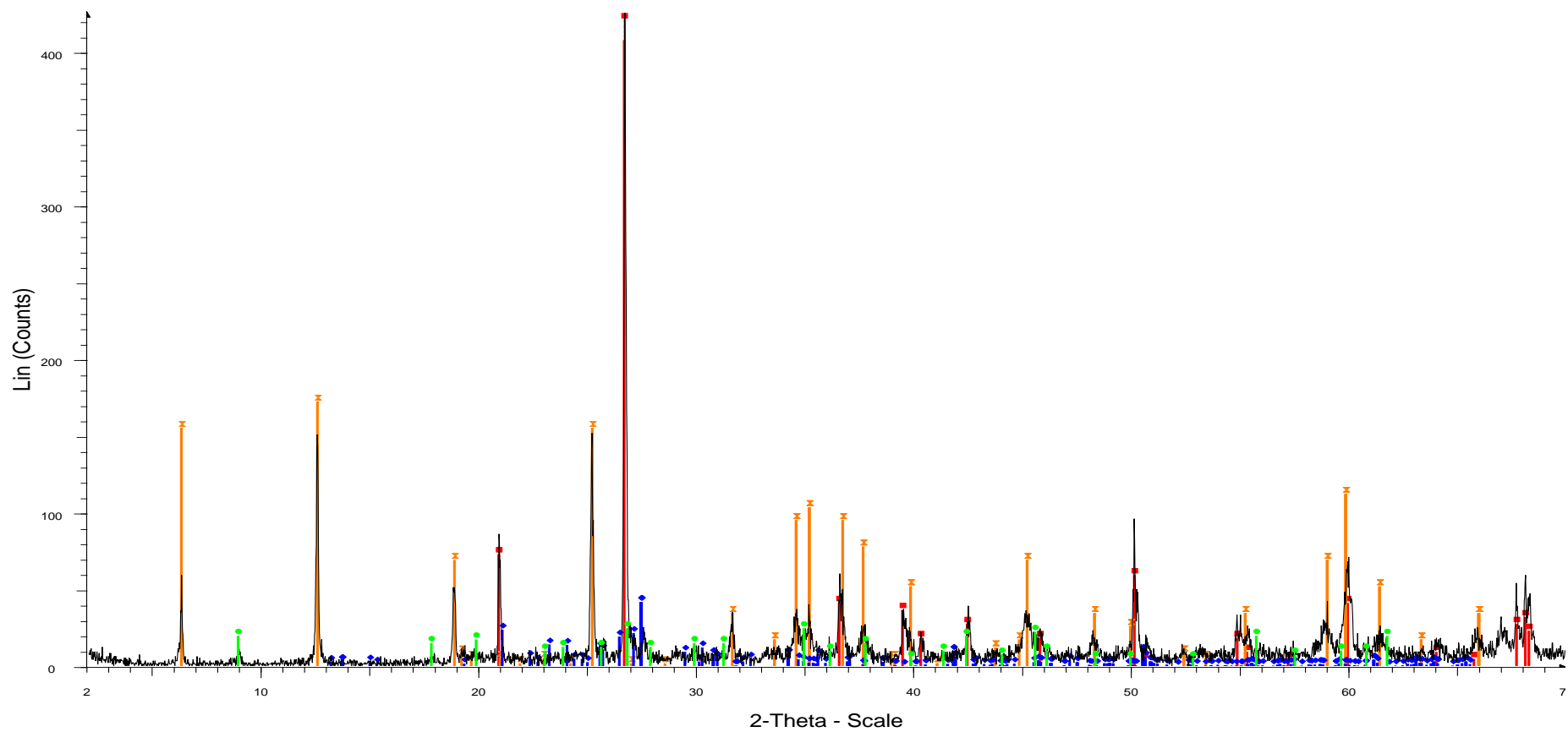


41 1 2 - File: C05120097.raw - Type: 2Th/Th locked - Start: 2.000 ° - End: 70.000 ° - Step: 0.020 ° - Step time: 1. s - Temp.: 25 °C (Room) - Time Started: 17 s - 2-Theta: 2.000 ° - Theta: 1.000 ° - Chi: 0.00 ° - Phi: 0.00 ° - X: 0.0 mm - Y: 0.0 mm -  
 Operations: Import  
 ■ 00-046-1045 (\*) - Quartz, syn - SiO<sub>2</sub> - Y: 144.27 % - d x by: 1. - WL: 1.5406 - Hexagonal - a 4.91344 - b 4.91344 - c 5.40524 - alpha 90.000 - beta 90.000 - gamma 120.000 - Primitive - P3221 (154) - 3 - 113.010 - *I*/c PDF 3.4 - F30=558(0.0017,  
 ☒ 00-046-1323 (I) - Clinocllore-1Mllb - (Mg,Al,Fe)<sub>6</sub>(Si,Al)<sub>4</sub>O<sub>10</sub>(OH)<sub>8</sub> - Y: 19.12 % - d x by: 1. - WL: 1.5406 - Monoclinic - a 5.34700 - b 9.26300 - c 14.25000 - alpha 90.000 - beta 97.200 - gamma 90.000 - Base-centered - C2/m (12) - 2 - 700.227 -

Sample 28.

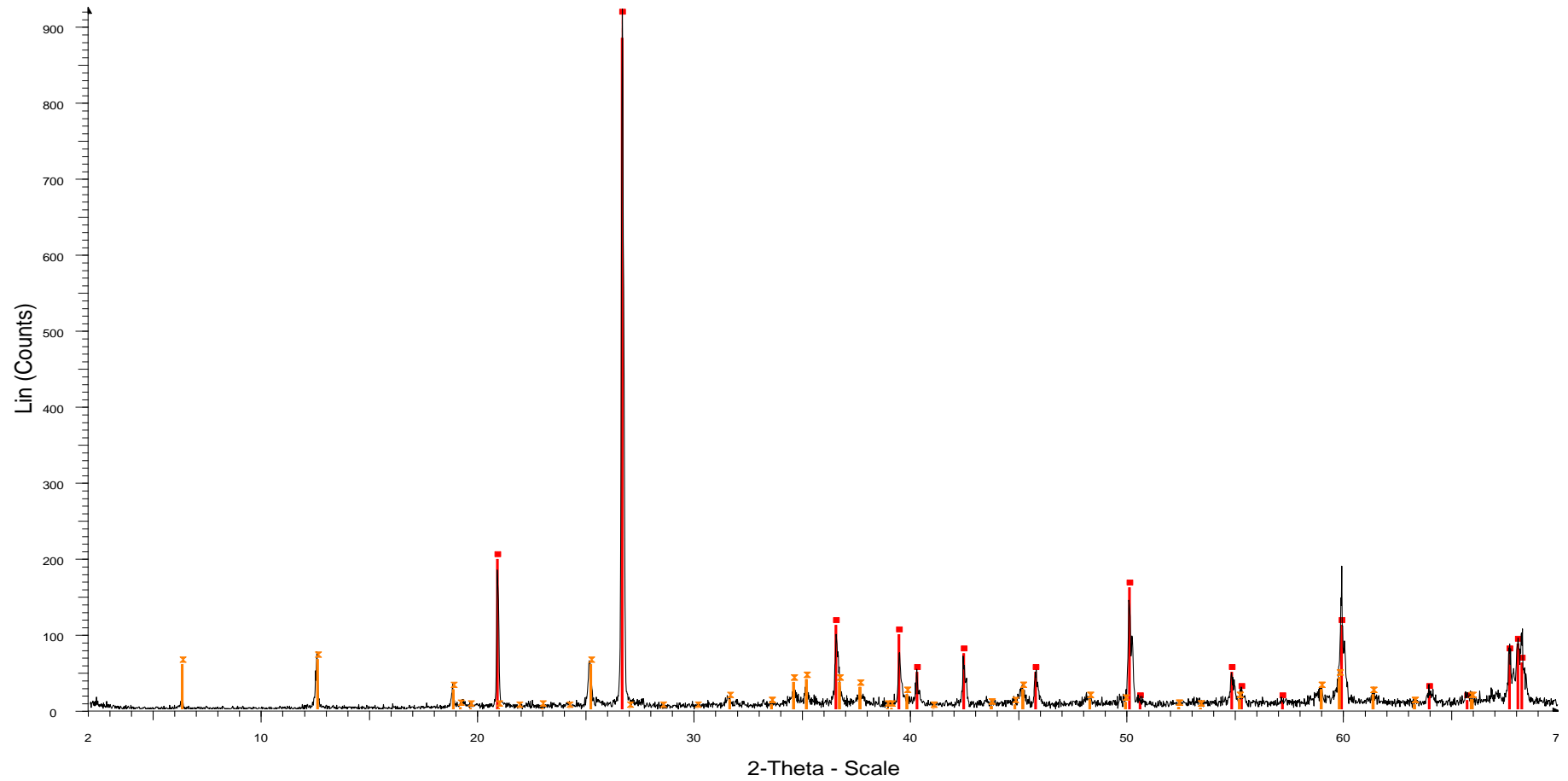


Sample 30.



39 - File: C05120063.raw - Type: 2Th/Th locked - Start: 2.000 ° - End: 70.000 ° - Step: 0.020 ° - Step time: 1. s - Temp.: 25 °C (Room) - Time Started: 17 s - 2-Theta: 2.000 ° - Theta: 1.000 ° - Chi: 0.00 ° - Phi: 0.00 ° - X: 0.0 mm - Y: 0.0 mm - Z: 0.  
 Operations: Import  
 ■ 00-046-1045 (\*) - Quartz, syn - SiO<sub>2</sub> - Y: 107.11 % - d x by: 1. - WL: 1.5406 - Hexagonal - a 4.91344 - b 4.91344 - c 5.40524 - alpha 90.000 - beta 90.000 - gamma 120.000 - Primitive - P3221 (154) - 3 - 113.010 - I/c PDF 3.4 - F30=558(0.0017,  
 ■ 00-046-1323 (I) - Clinocllore-1Mllb - (Mg,Al,Fe)6(Si,Al)4O10(OH)8 - Y: 40.56 % - d x by: 1. - WL: 1.5406 - Monoclinic - a 5.34700 - b 9.26300 - c 14.25000 - alpha 90.000 - beta 97.200 - gamma 90.000 - Base-centered - C2/m (12) - 2 - 700.227 -  
 ■ 01-084-0709 (A) - Microcline maximum - KAlSi3O8 - Y: 9.79 % - d x by: 1. - WL: 1.5406 - Triclinic - a 8.57240 - b 12.96420 - c 7.22310 - alpha 90.647 - beta 115.946 - gamma 87.641 - Base-centered - C-1 (0) - 4 - 721.192 - I/c PDF 0.6 - F30=12  
 ■ 00-002-0467 (D) - Muscovite - KAl2(Si3Al)O10(OH,F)2/H2KAl3Si3O12 - Y: 5.77 % - d x by: 1. - WL: 1.5406 - Monoclinic - a 5.18000 - b 9.02000 - c 20.04000 - alpha 90.000 - beta 95.500 - gamma 90.000 - Base-centered - C2/c (15) - 4 - 932.03

Sample 31.



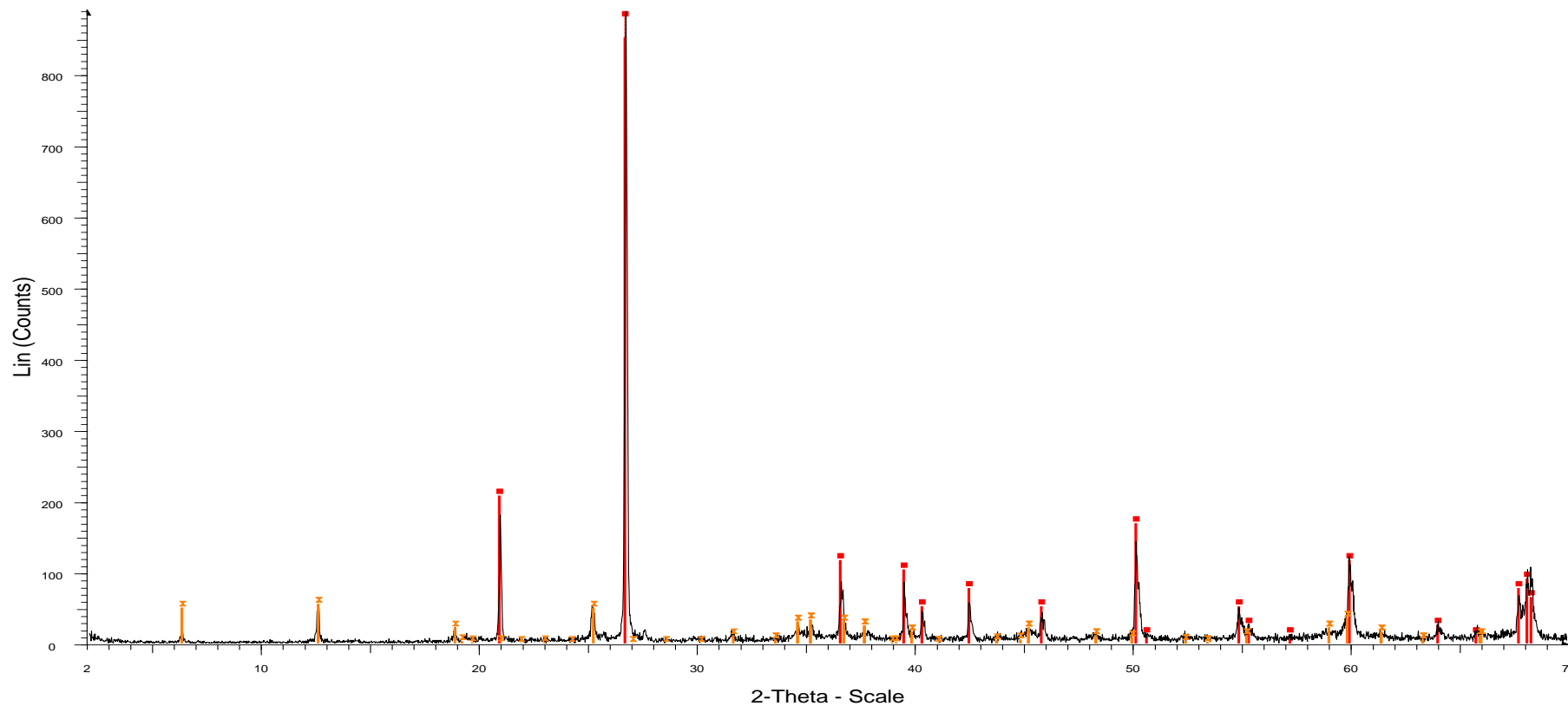
4501 - File: C5120092.raw - Type: 2Th/Th locked - Start: 2.000 ° - End: 70.000 ° - Step: 0.020 ° - Step time: 1. s - Temp.: 25 °C (Room) - Time Started: 16 s - 2-Theta: 2.000 ° - Theta: 1.000 ° - Chi: 0.00 ° - Phi: 0.00 ° - X: 0.0 mm - Y: 0.0 mm - Z: Operations: Import

00-046-1045 (\*) - Quartz, syn - SiO<sub>2</sub> - Y: 134.16 % - d x by: 1. - WL: 1.5406 - Hexagonal - a 4.91344 - b 4.91344 - c 5.40524 - alpha 90.000 - beta 90.000 - gamma 120.000 - Primitive - P3221 (154) - 3 - 113.010 - I/c PDF 3.4 - F30=558(0.0017,

00-046-1323 (I) - Clinocllore-1Mllb - (Mg,Al,Fe)6(Si,Al)4O10(OH)8 - Y: 7.19 % - d x by: 1. - WL: 1.5406 - Monoclinic - a 5.34700 - b 9.26300 - c 14.25000 - alpha 90.000 - beta 97.200 - gamma 90.000 - Base-centered - C2/m (12) - 2 - 700.227 -

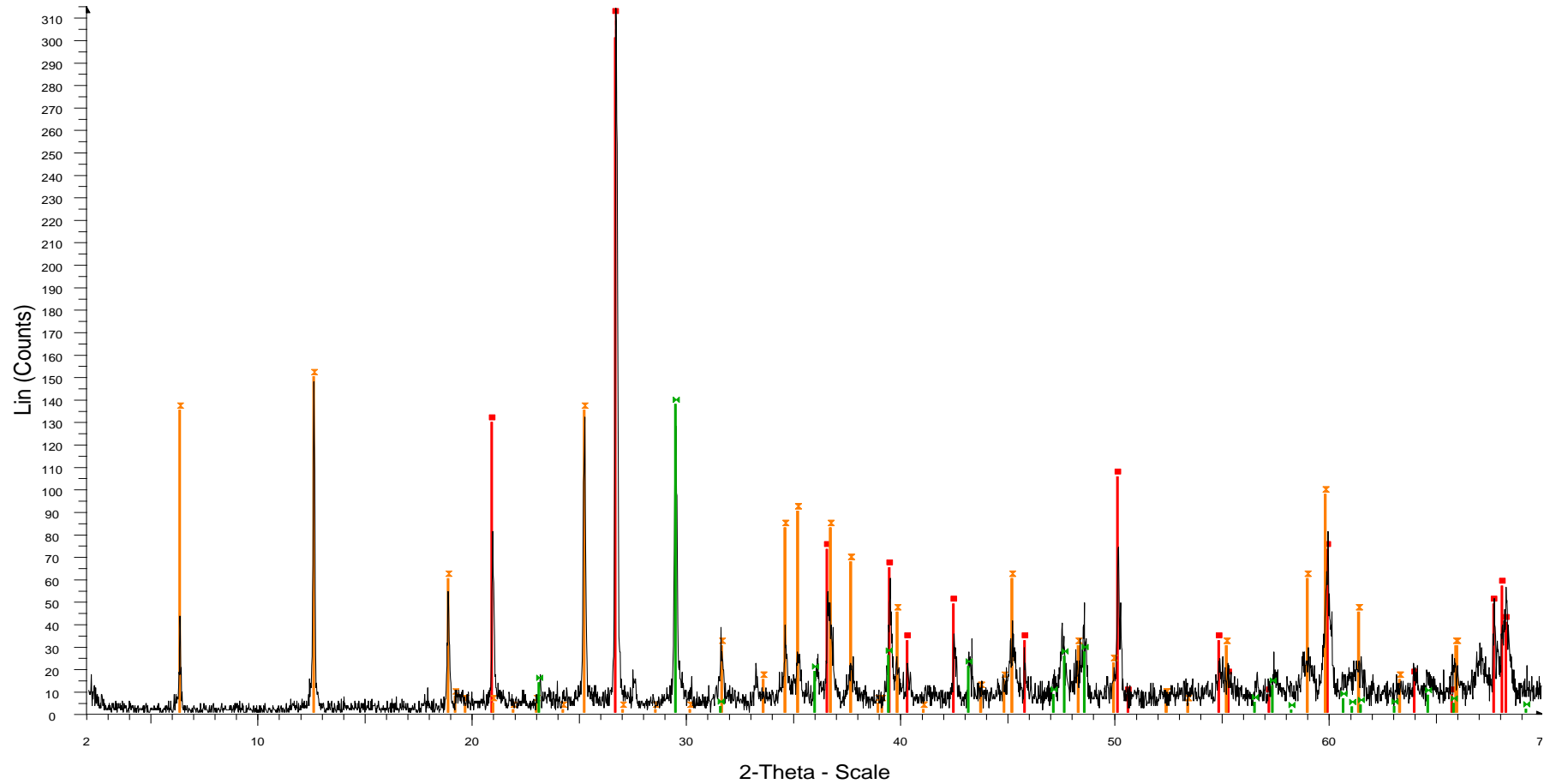
Sample 32.





4201 - File: C5120102.raw - Type: 2Th/Th locked - Start: 2.000 ° - End: 70.000 ° - Step: 0.020 ° - Step time: 1. s - Temp.: 25 °C (Room) - Time Started: 17 s - 2-Theta: 2.000 ° - Theta: 1.000 ° - Chi: 0.00 ° - Phi: 0.00 ° - X: 0.0 mm - Y: 0.0 mm - Z: 0.0 mm  
 Operations: Import  
 00-046-1045 (\*) - Quartz, syn - SiO<sub>2</sub> - Y: 146.23 % - d x by: 1. - WL: 1.5406 - Hexagonal - a 4.91344 - b 4.91344 - c 5.40524 - alpha 90.000 - beta 90.000 - gamma 120.000 - Primitive - P3221 (154) - 3 - 113.010 - I/c PDF 3.4 - F30=558(0.0017, 0.0017)  
 00-046-1323 (l) - Clinocllore-1Mllb - (Mg,Al,Fe)6(Si,Al)4O10(OH)8 - Y: 6.26 % - d x by: 1. - WL: 1.5406 - Monoclinic - a 5.34700 - b 9.26300 - c 14.25000 - alpha 90.000 - beta 97.200 - gamma 90.000 - Base-centered - C2/m (12) - 2 - 700.227 -

Sample 34.



4801 - File: C05120475.raw - Type: 2Th/Th locked - Start: 2.000 ° - End: 70.000 ° - Step: 0.020 ° - Step time: 1. s - Temp.: 25 °C (Room) - Time Started: 17 s - 2-Theta: 2.000 ° - Theta: 1.000 ° - Chi: 0.00 ° - Phi: 0.00 ° - X: 0.0 mm - Y: 0.0 mm - Z:

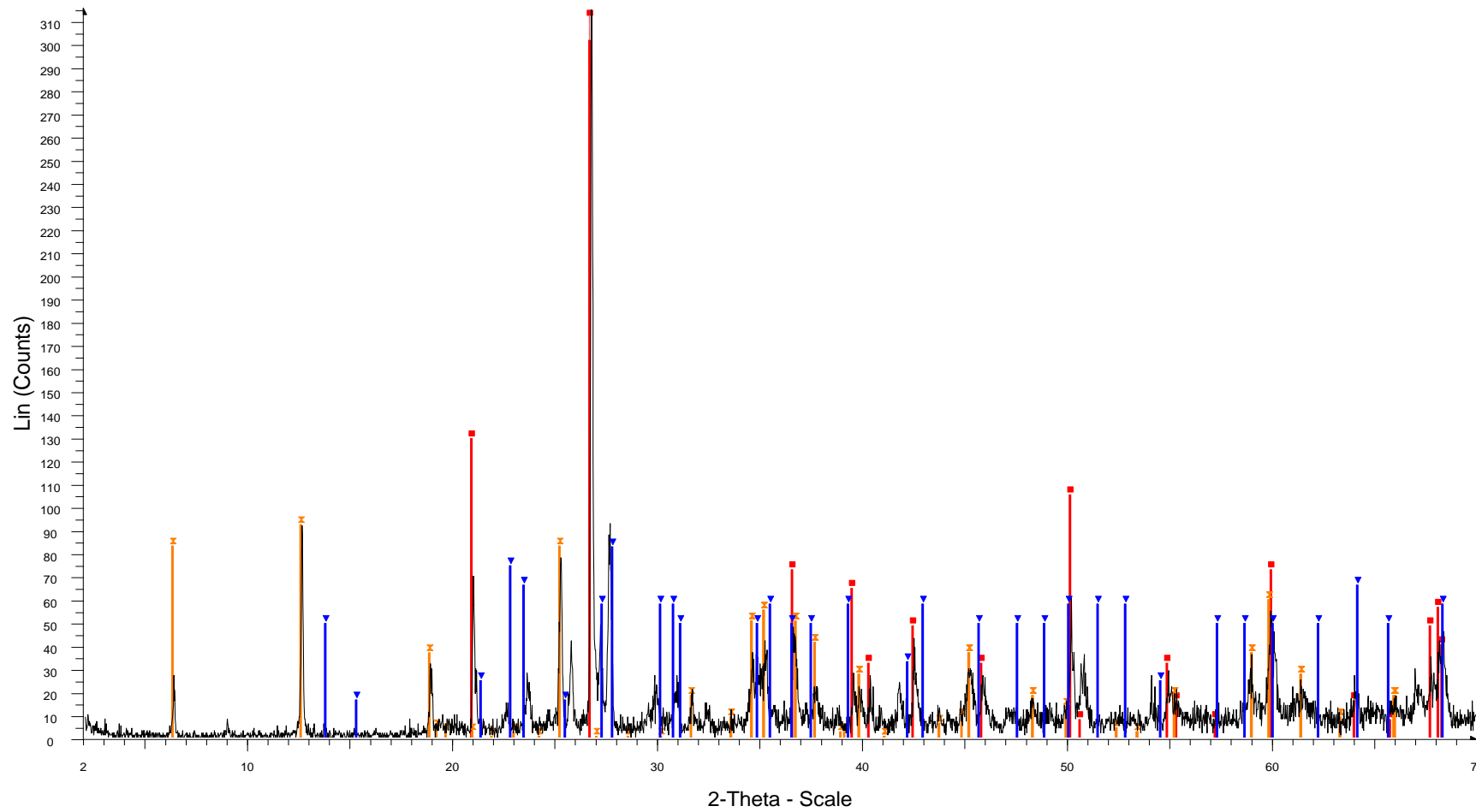
Operations: Import

■ 00-046-1045 (\*) - Quartz, syn - SiO<sub>2</sub> - Y: 258.14 % - d x by: 1. - WL: 1.5406 - Hexagonal - a 4.91344 - b 4.91344 - c 5.40524 - alpha 90.000 - beta 90.000 - gamma 120.000 - Primitive - P321 (154) - 3 - 113.010 - I/c PDF 3.4 - F30=558(0.0017,

× 00-046-1323 (I) - Clinocllore-1MIlb - (Mg,Al,Fe)6(Si,Al)4O10(OH)8 - Y: 47.80 % - d x by: 1. - WL: 1.5406 - Monoclinic - a 5.34700 - b 9.26300 - c 14.25000 - alpha 90.000 - beta 97.200 - gamma 90.000 - Base-centered - C2/m (12) - 2 - 700.227 -

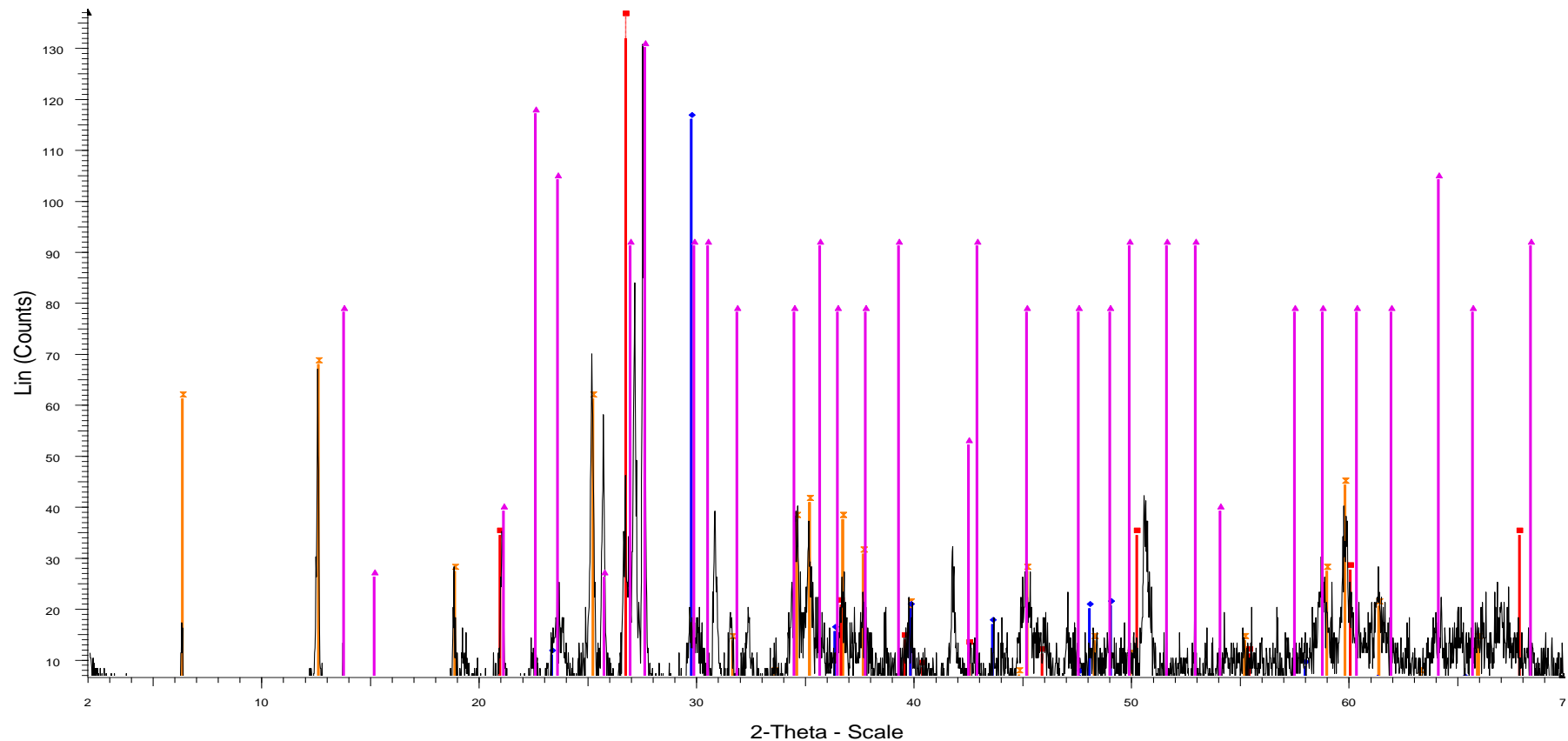
\* 01-072-1652 (A) - Calcite - CaCO<sub>3</sub> - Y: 43.85 % - d x by: 1. - WL: 1.5406 - Rhombo.H.axes - a 4.99000 - b 4.99000 - c 17.00200 - alpha 90.000 - beta 90.000 - gamma 120.000 - Primitive - R-3c (167) - 6 - 366.633 - I/c PDF 3.2 - F30=1000(0.00

Sample 35.



50 - File: C5120463.raw - Type: 2Th/Th locked - Start: 2.000 ° - End: 70.000 ° - Step: 0.020 ° - Step time: 1. s - Temp.: 25 °C (Room) - Time Started: 16 s - 2-Theta: 2.000 ° - Theta: 1.000 ° - Chi: 0.00 ° - Phi: 0.00 ° - X: 0.0 mm - Y: 0.0 mm - Z: 0.0  
 Operations: Import  
 00-046-1045 (\*) - Quartz, syn - SiO<sub>2</sub> - Y: 257.32 % - d x by: 1. - WL: 1.5406 - Hexagonal - a 4.91344 - b 4.91344 - c 5.40524 - alpha 90.000 - beta 90.000 - gamma 120.000 - Primitive - P3221 (154) - 3 - 113.010 - I/c PDF 3.4 - F30=558(0.0017,  
 00-046-1323 (l) - Clinocllore-1Mlib - (Mg,Al,Fe)6(Si,Al)4O10(OH)8 - Y: 29.33 % - d x by: 1. - WL: 1.5406 - Monoclinic - a 5.34700 - b 9.26300 - c 14.25000 - alpha 90.000 - beta 97.200 - gamma 90.000 - Base-centered - C2/m (12) - 2 - 700.227 -  
 00-002-0534 (D) - Orthoclase - Al<sub>2</sub>O<sub>3</sub>-K<sub>2</sub>O-6SiO<sub>2</sub> - Y: 26.32 % - d x by: 1. - WL: 1.5406 - Monoclinic - a 8.45000 - b 12.90000 - c 7.15000 - alpha 90.000 - beta 116.050 - gamma 90.000 - Base-centered - C2/m (12) - 700.209 - F30= 2(0.0930,1

Sample 36.

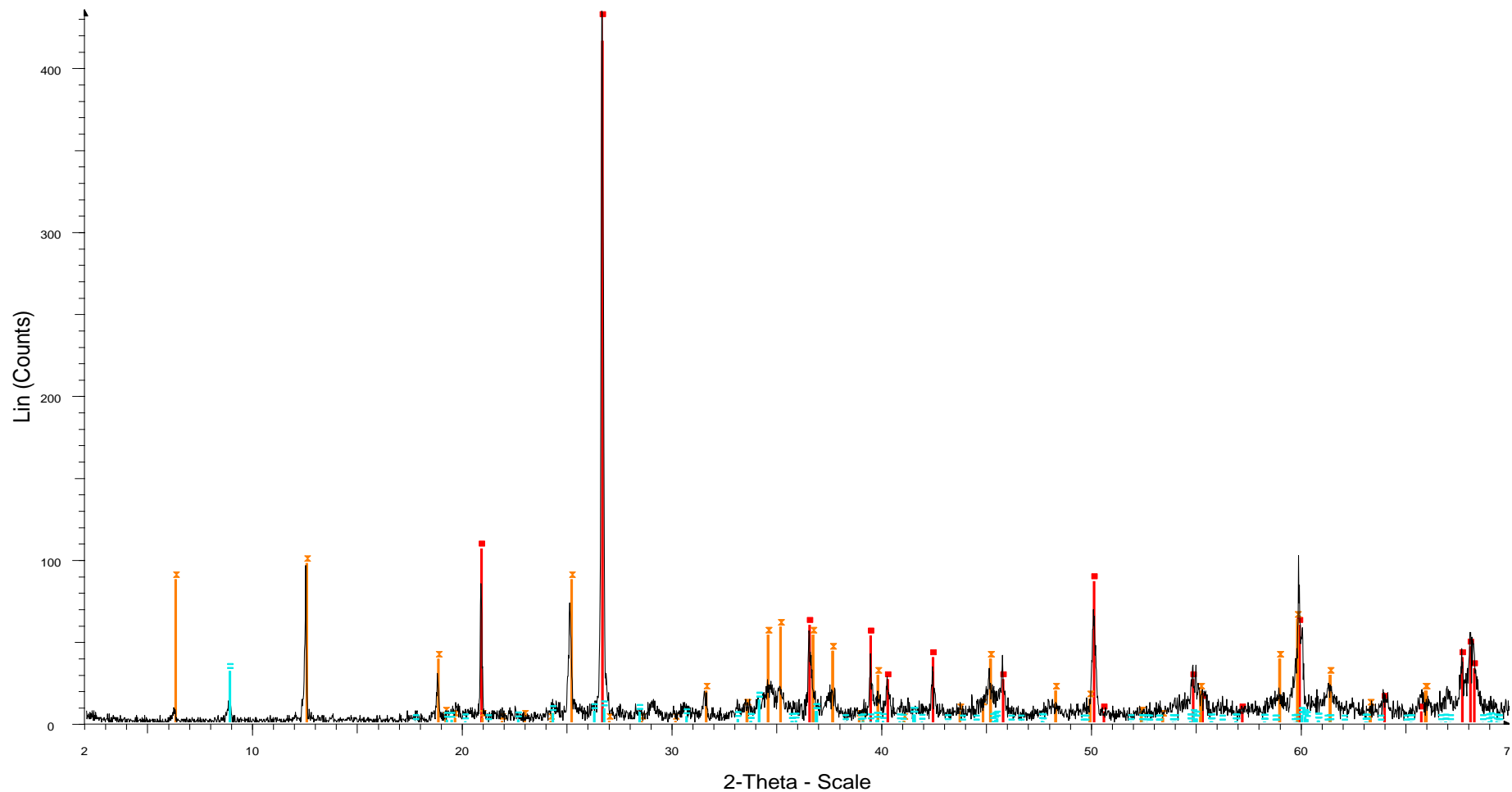


5601 - File: C5120082.raw - Type: 2Th/Th locked - Start: 2.000 ° - End: 70.000 ° - Step: 0.020 ° - Step time: 1. s - Temp.: 25 °C (Room) - Time Started: 17 s - 2-Theta: 2.000 ° - Theta: 1.000 ° - Chi: 0.00 ° - Phi: 0.00 ° - X: 0.0 mm - Y: 0.0 mm - Z:

Operations: Import

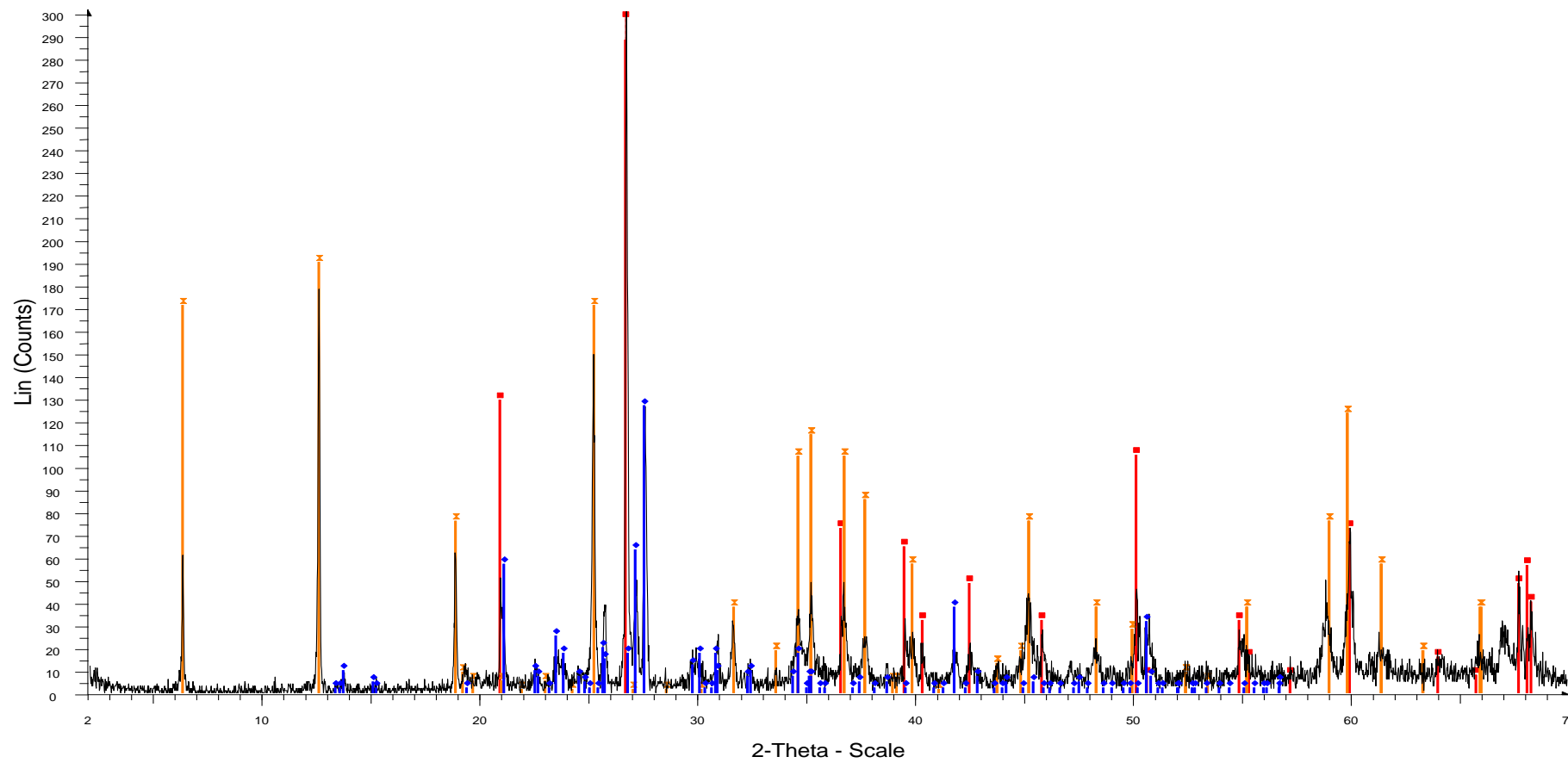
- x 00-046-1323 (I) - Clinocllore-1Mlb - (Mg,Al,Fe)6(Si,Al)4O10(OH)8 - Y: 51.95 % - d x by: 1. - WL: 1.5406 - Monoclinic - a 5.34700 - b 9.26300 - c 14.25000 - alpha 90.000 - beta 97.200 - gamma 90.000 - Base-centered - C2/m (12) - 2 - 700.227 -
- 00-001-0649 (D) - Quartz - SiO2 - Y: 104.92 % - d x by: 1. - WL: 1.5406 - Hexagonal - a 4.90300 - b 4.90300 - c 5.39300 - alpha 90.000 - beta 90.000 - gamma 120.000 - Primitive - P312 (149) - 3 - 112.275 - F22= 6(0.0980,38)
- ◆ 01-071-1663 (C) - Calcite, magnesian - Mg0.1Ca0.9CO3 - Y: 88.85 % - d x by: 1. - WL: 1.5406 - Rhombo.H.axes - a 4.94100 - b 4.94100 - c 16.86400 - alpha 90.000 - beta 90.000 - gamma 120.000 - Primitive - R-3c (167) - 6 - 356.550 - I/c PDF
- ▲ 00-009-0462 (D) - Orthoclase - KAlSi3O8 - Y: 99.65 % - d x by: 1. - WL: 1.5406 - Monoclinic - a 8.56160 - b 12.99600 - c 7.19340 - alpha 90.000 - beta 116.000 - gamma 90.000 - Base-centered - C2/m (12) - 4 - 719.381 - F30= 3(0.0680,136)

Sample 37.



4402 - File: C5120469.raw - Type: 2Th/Th locked - Start: 2.000 ° - End: 70.000 ° - Step: 0.020 ° - Step time: 1. s - Temp.: 25 °C (Room) - Time Started: 17 s - 2-Theta: 2.000 ° - Theta: 1.000 ° - Chi: 0.00 ° - Phi: 0.00 ° - X: 0.0 mm - Y: 0.0 mm - Z: 0.0 mm  
 Operations: Import  
 00-046-1045 (\*) - Quartz, syn - SiO<sub>2</sub> - Y: 152.73 % - d x by: 1. - WL: 1.5406 - Hexagonal - a 4.91344 - b 4.91344 - c 5.40524 - alpha 90.000 - beta 90.000 - gamma 120.000 - Primitive - P3221 (154) - 3 - 113.010 - I/c PDF 3.4 - F30=558(0.0017,  
 00-046-1323 (I) - Clinocllore-1Mllb - (Mg,Al,Fe)<sub>6</sub>(Si,Al)<sub>4</sub>O<sub>10</sub>(OH)<sub>8</sub> - Y: 22.40 % - d x by: 1. - WL: 1.5406 - Monoclinic - a 5.34700 - b 9.26300 - c 14.25000 - alpha 90.000 - beta 97.200 - gamma 90.000 - Base-centered - C2/m (12) - 2 - 700.227 -  
 01-088-2192 (C) - Biotite 1M, titanocan barian - (K<sub>1.8</sub>Na<sub>0.15</sub>Ba<sub>0.05</sub>)(Mg<sub>3.26</sub>Fe<sub>2</sub>Ti<sub>0.74</sub>)(Al<sub>2.5</sub>Si<sub>5.5</sub>O<sub>20</sub>)O<sub>1.85</sub>(OH)<sub>2.15</sub> - Y: 7.23 % - d x by: 1. - WL: 1.5406 - Monoclinic - a 5.33100 - b 9.23000 - c 10.16000 - alpha 90.000 - beta 100.190 - gamm

Sample 38.



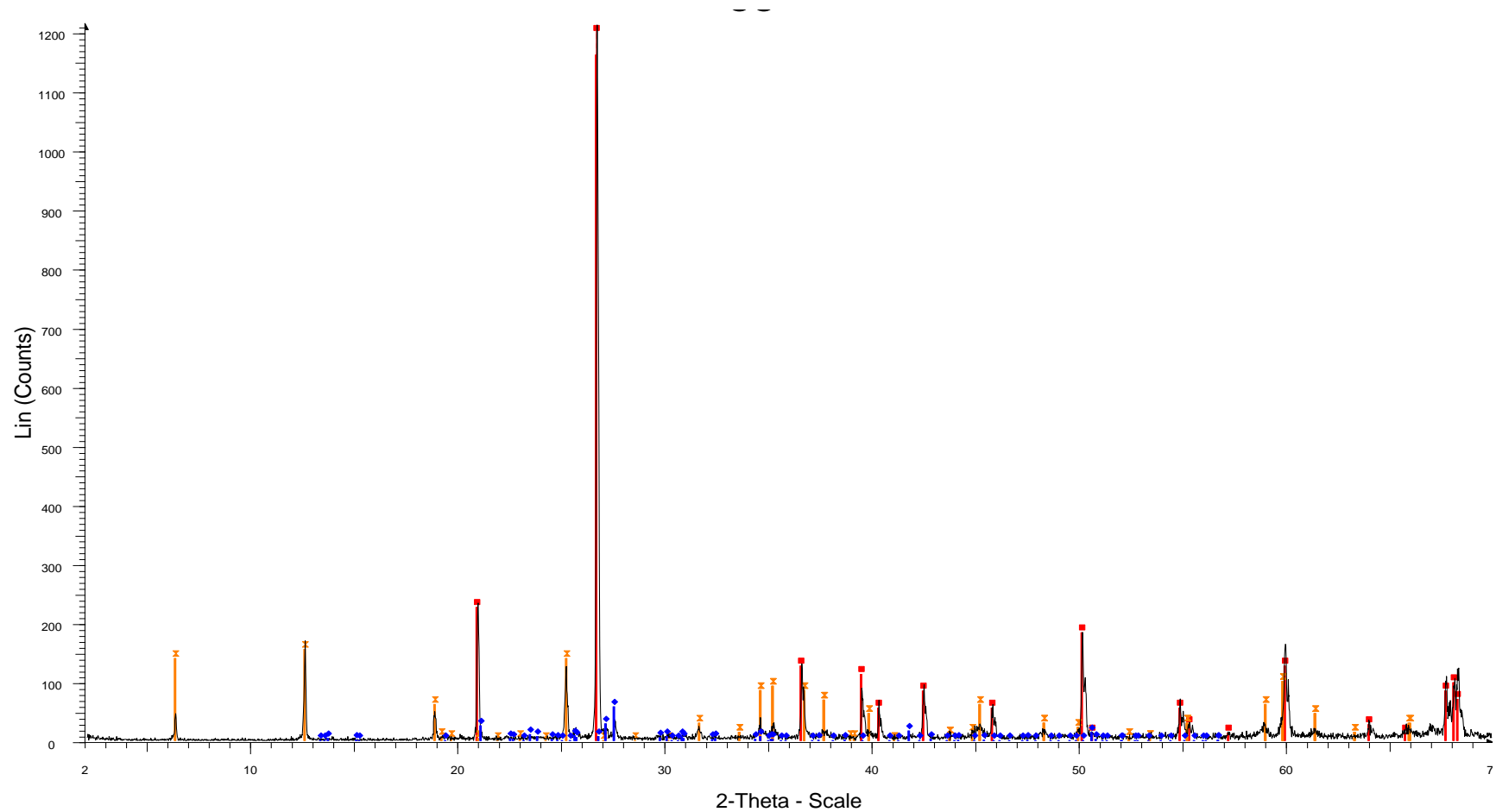
5602 - File: C5120090.raw - Type: 2Th/Th locked - Start: 2.000 ° - End: 70.000 ° - Step: 0.020 ° - Step time: 1. s - Temp.: 25 °C (Room) - Time Started: 17 s - 2-Theta: 2.000 ° - Theta: 1.000 ° - Chi: 0.00 ° - Phi: 0.00 ° - X: 0.0 mm - Y: 0.0 mm - Z: Operations: Import

00-046-1045 (\*) - Quartz, syn - SiO<sub>2</sub> - Y: 269.25 % - d x by: 1. - WL: 1.5406 - Hexagonal - a 4.91344 - b 4.91344 - c 5.40524 - alpha 90.000 - beta 90.000 - gamma 120.000 - Primitive - P3221 (154) - 3 - 113.010 - I/c PDF 3.4 - F30=558(0.0017,

00-046-1323 (l) - Clinocllore-1Mllb - (Mg,Al,Fe)6(Si,Al)4O10(OH)8 - Y: 63.30 % - d x by: 1. - WL: 1.5406 - Monoclinic - a 5.34700 - b 9.26300 - c 14.25000 - alpha 90.000 - beta 97.200 - gamma 90.000 - Base-centered - C2/m (12) - 2 - 700.227 -

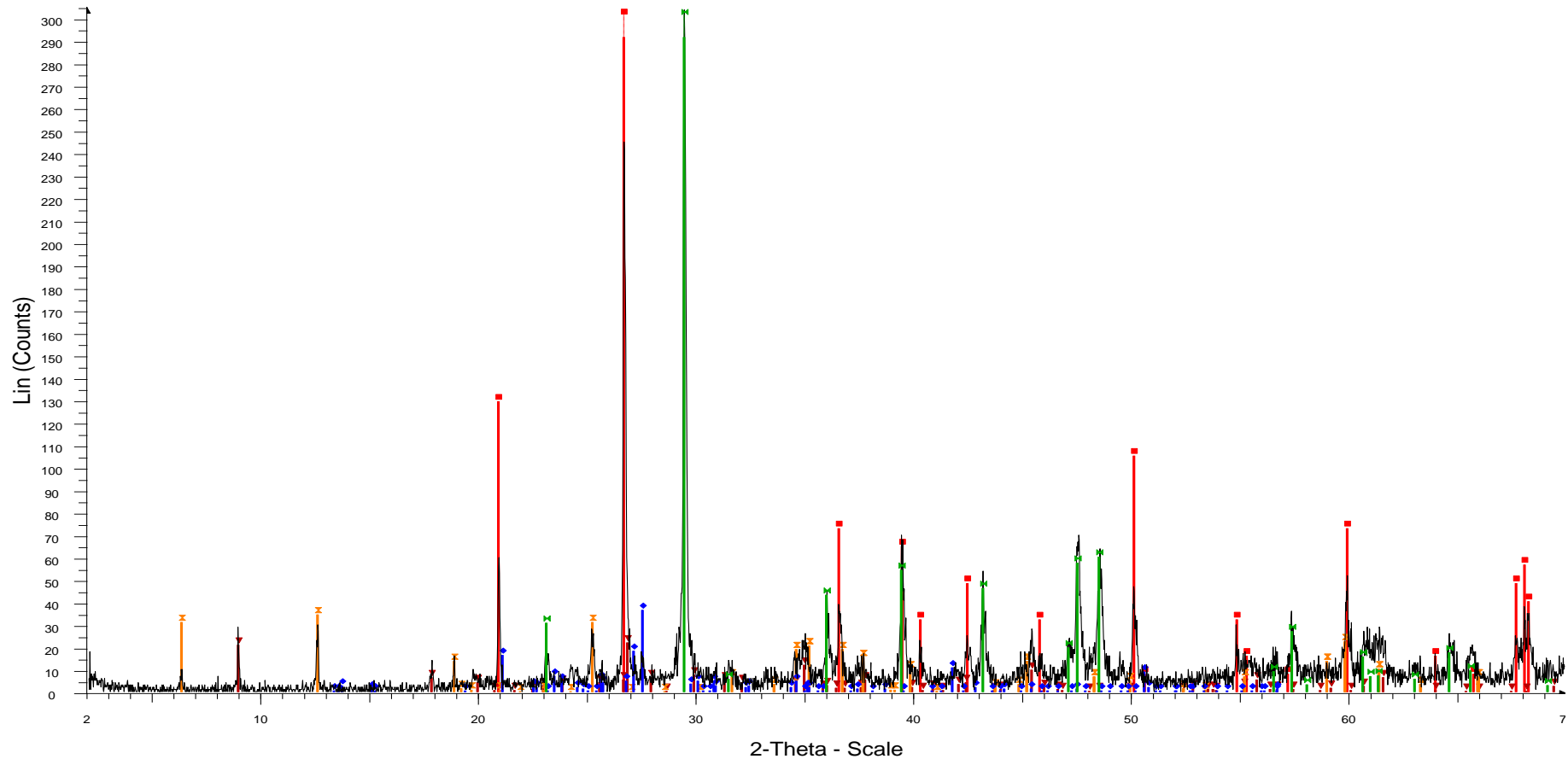
00-019-0932 (l) - Microcline, intermediate - KAlSi3O8 - Y: 42.23 % - d x by: 1. - WL: 1.5406 - Triclinic - a 8.56000 - b 12.97000 - c 7.21000 - alpha 90.300 - beta 116.100 - gamma 89.000 - Base-centered - C-1 (0) - 4 - 718.739 - F30= 46(0.0165,

Sample 39.



55 - File: C5120467.raw - Type: 2Th/Th locked - Start: 2.000 ° - End: 70.000 ° - Step: 0.020 ° - Step time: 1. s - Temp.: 25 °C (Room) - Time Started: 16 s - 2-Theta: 2.000 ° - Theta: 1.000 ° - Chi: 0.00 ° - Phi: 0.00 ° - X: 0.0 mm - Y: 0.0 mm - Z: 0.0  
 Operations: Import  
 ■ 00-046-1045 (\*) - Quartz, syn - SiO<sub>2</sub> - Y: 116.92 % - d x by: 1. - WL: 1.5406 - Hexagonal - a 4.91344 - b 4.91344 - c 5.40524 - alpha 90.000 - beta 90.000 - gamma 120.000 - Primitive - P3221 (154) - 3 - 113.010 - *I*-lc PDF 3.4 - F30=558(0.0017,  
 × 00-046-1323 (l) - Clinoclchlore-1Mllb - (Mg,Al,Fe)(Si,Al)<sub>4</sub>O<sub>10</sub>(OH)<sub>8</sub> - Y: 12.85 % - d x by: 1. - WL: 1.5406 - Monoclinic - a 5.34700 - b 9.26300 - c 14.25000 - alpha 90.000 - beta 97.200 - gamma 90.000 - Base-centered - C2/m (12) - 2 - 700.227 -  
 ◆ 00-019-0932 (l) - Microcline, intermediate - KAISi<sub>3</sub>O<sub>8</sub> - Y: 4.84 % - d x by: 1. - WL: 1.5406 - Triclinic - a 8.56000 - b 12.97000 - c 7.21000 - alpha 90.300 - beta 116.100 - gamma 89.000 - Base-centered - C-1 (0) - 4 - 718.739 - F30= 46(0.0165,3

Sample 40.

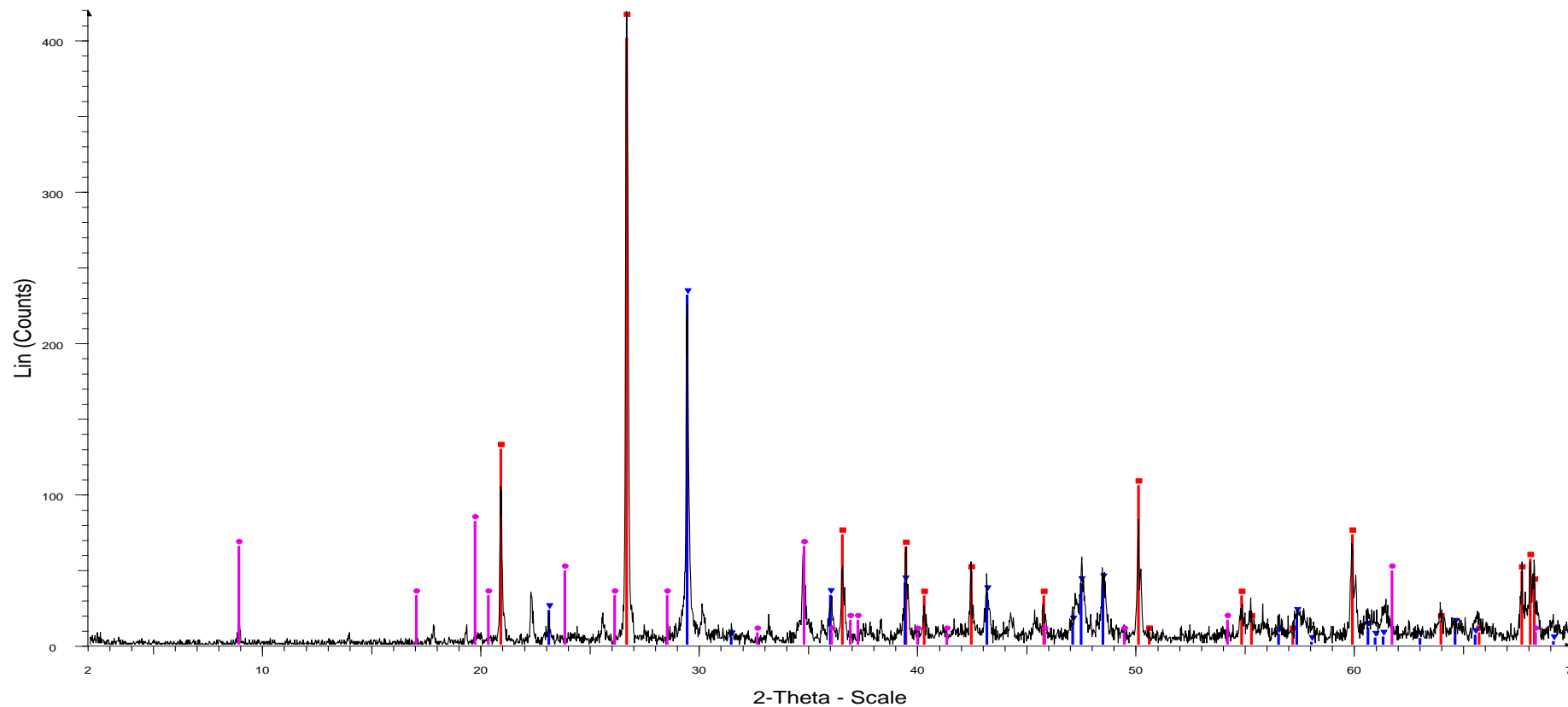


7801 - File: C5120476.raw - Type: 2Th/Th locked - Start: 2.000 ° - End: 70.000 ° - Step: 0.020 ° - Step time: 1. s - Temp.: 25 °C (Room) - Time Started: 17 s - 2-Theta: 2.000 ° - Theta: 1.000 ° - Chi: 0.00 ° - Phi: 0.00 ° - X: 0.0 mm - Y: 0.0 mm - Z: 0.0 mm  
 Operations: Import

- 00-046-1045 (\*) - Quartz, syn - SiO<sub>2</sub> - Y: 266.60 % - d x by: 1. - WL: 1.5406 - Hexagonal - a 4.91344 - b 4.91344 - c 5.40524 - alpha 90.000 - beta 90.000 - gamma 120.000 - Primitive - P3221 (154) - 3 - 113.010 - I/lc PDF 3.4 - F30=558(0.0017,
- ▼ 00-006-0263 (I) - Muscovite-2M1 - KAl<sub>2</sub>(Si<sub>3</sub>Al)O<sub>10</sub>(OH,F)<sub>2</sub> - Y: 7.29 % - d x by: 1. - WL: 1.5406 - Monoclinic - a 5.19000 - b 9.03000 - c 20.05000 - alpha 90.000 - beta 95.770 - gamma 90.000 - Base-centered - C2/c (15) - 4 - 934.896 - F30= 12(
- ⊠ 00-046-1323 (I) - Clinocllore-1Mllb - (Mg,Al,Fe)6(Si,Al)4O10(OH)8 - Y: 11.39 % - d x by: 1. - WL: 1.5406 - Monoclinic - a 5.34700 - b 9.26300 - c 14.25000 - alpha 90.000 - beta 97.200 - gamma 90.000 - Base-centered - C2/m (12) - 2 - 700.227 -
- ◆ 00-019-0932 (I) - Microcline, intermediate - KAlSi<sub>3</sub>O<sub>8</sub> - Y: 12.06 % - d x by: 1. - WL: 1.5406 - Triclinic - a 8.56000 - b 12.97000 - c 7.21000 - alpha 90.300 - beta 116.100 - gamma 89.000 - Base-centered - C-1 (0) - 4 - 718.739 - F30= 46(0.0165,
- ▣ 01-083-0578 (A) - Calcite - Ca(CO<sub>3</sub>) - Y: 102.31 % - d x by: 1. - WL: 1.5406 - Rhombo.H.axes - a 4.98870 - b 4.98870 - c 17.05290 - alpha 90.000 - beta 90.000 - gamma 120.000 - Primitive - R-3c (167) - 6 - 367.539 - I/lc PDF 3.2 - F30=1000(0.

Sample 42.





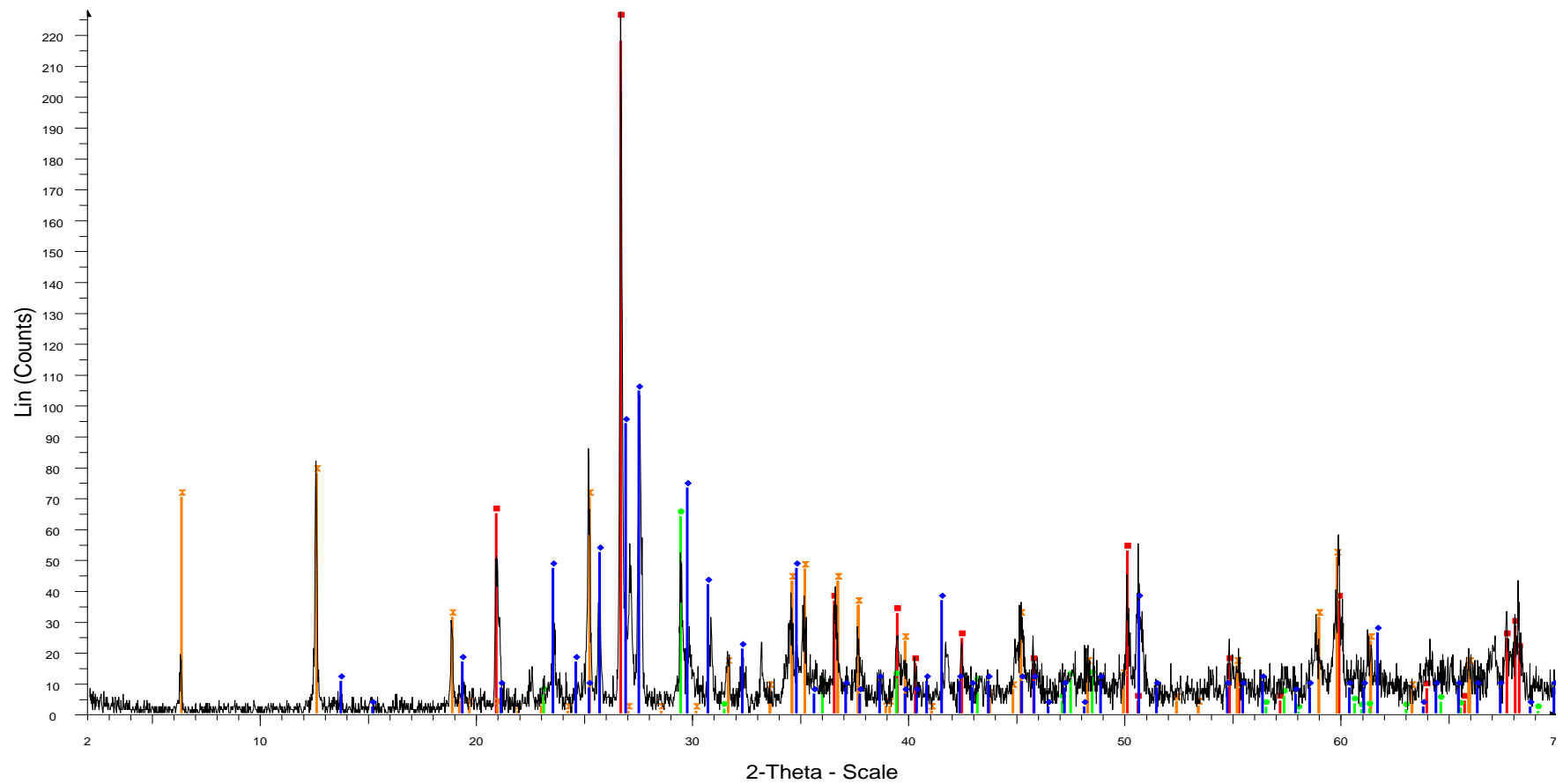
8101 - File: C05120101.raw - Type: 2Th/Th locked - Start: 2.000 ° - End: 70.000 ° - Step: 0.020 ° - Step time: 1. s - Temp.: 25 °C (Room) - Time Started: 17 s - 2-Theta: 2.000 ° - Theta: 1.000 ° - Chi: 0.00 ° - Phi: 0.00 ° - X: 0.0 mm - Y: 0.0 mm - Z: Operations: Import

■ 00-046-1045 (\*) - Quartz, syn - SiO<sub>2</sub> - Y: 193.60 % - d x by: 1. - WL: 1.5406 - Hexagonal - a 4.91344 - b 4.91344 - c 5.40524 - alpha 90.000 - beta 90.000 - gamma 120.000 - Primitive - P3221 (154) - 3 - 113.010 - I/c PDF 3.4 - F30=558(0.0017,

▼ 01-086-2334 (A) - Calcite - Ca(CO<sub>3</sub>) - Y: 55.33 % - d x by: 1. - WL: 1.5406 - Rhombo.H.axes - a 4.98800 - b 4.98800 - c 17.06099 - alpha 90.000 - beta 90.000 - gamma 120.000 - Primitive - R-3c (167) - 6 - 367.610 - I/c PDF 3.2 - F30=1000(0.0

● 00-013-0573 (D) - Muscovite - 0.33(NH<sub>4</sub>)<sub>2</sub>O·Al<sub>2</sub>O<sub>3</sub>·2SiO<sub>2</sub>·0.66H<sub>2</sub>O - Y: 19.54 % - d x by: 1. - WL: 1.5406 - Monoclinic - a 5.22000 - b 9.02000 - c 20.02000 - alpha 90.000 - beta 90.220 - gamma 90.000 - 942.623 - F21= 0(0.1080,587)

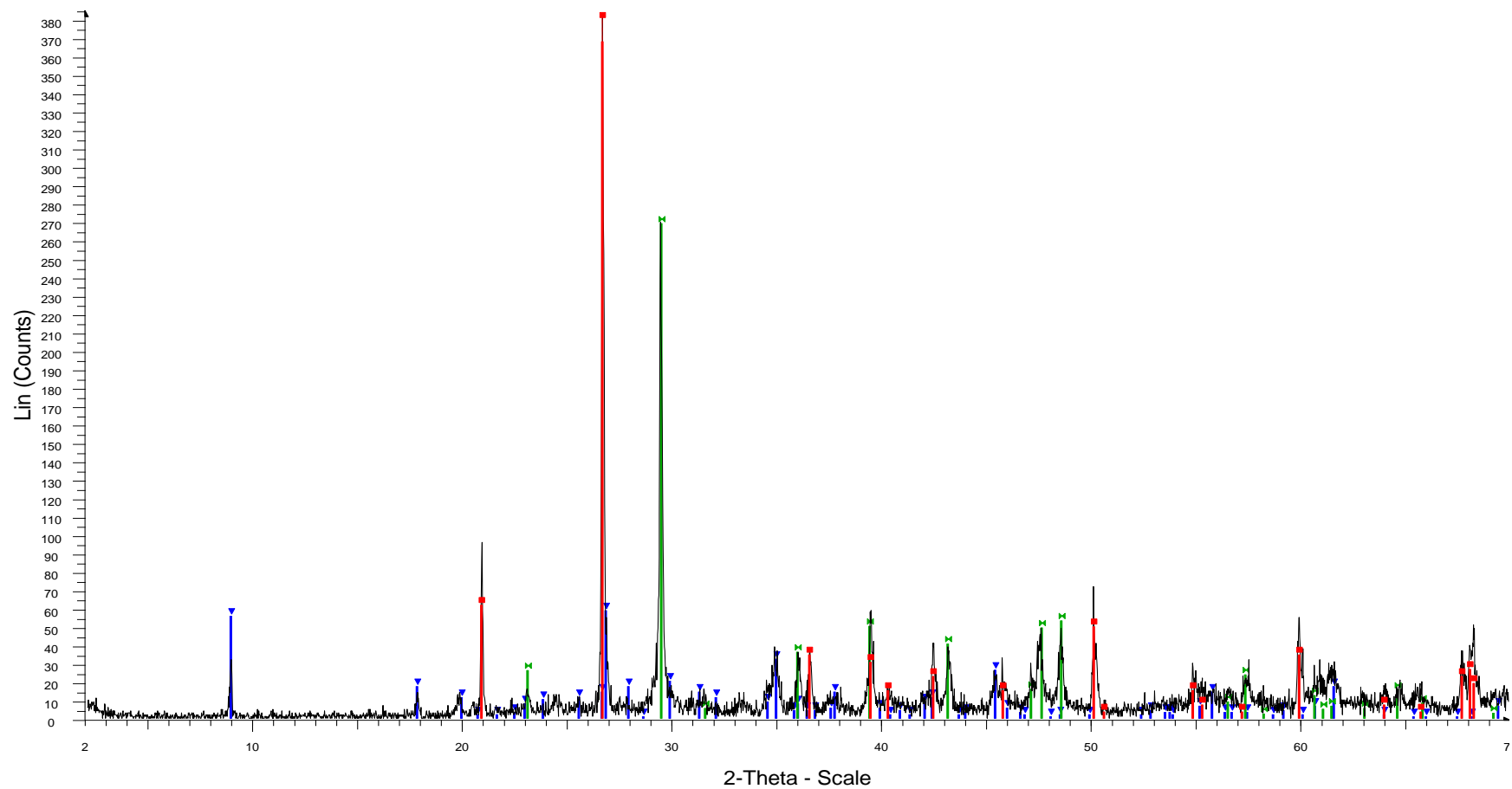
Sample 43.



73 - File: C05120065.raw - Type: 2Th/Th locked - Start: 2.000 ° - End: 70.000 ° - Step: 0.020 ° - Step time: 1. s - Temp.: 25 °C (Room) - Time Started: 17 s - 2-Theta: 2.000 ° - Theta: 1.000 ° - Chi: 0.00 ° - Phi: 0.00 ° - X: 0.0 mm - Y: 0.0 mm - Z: 0.  
 Operations: Import

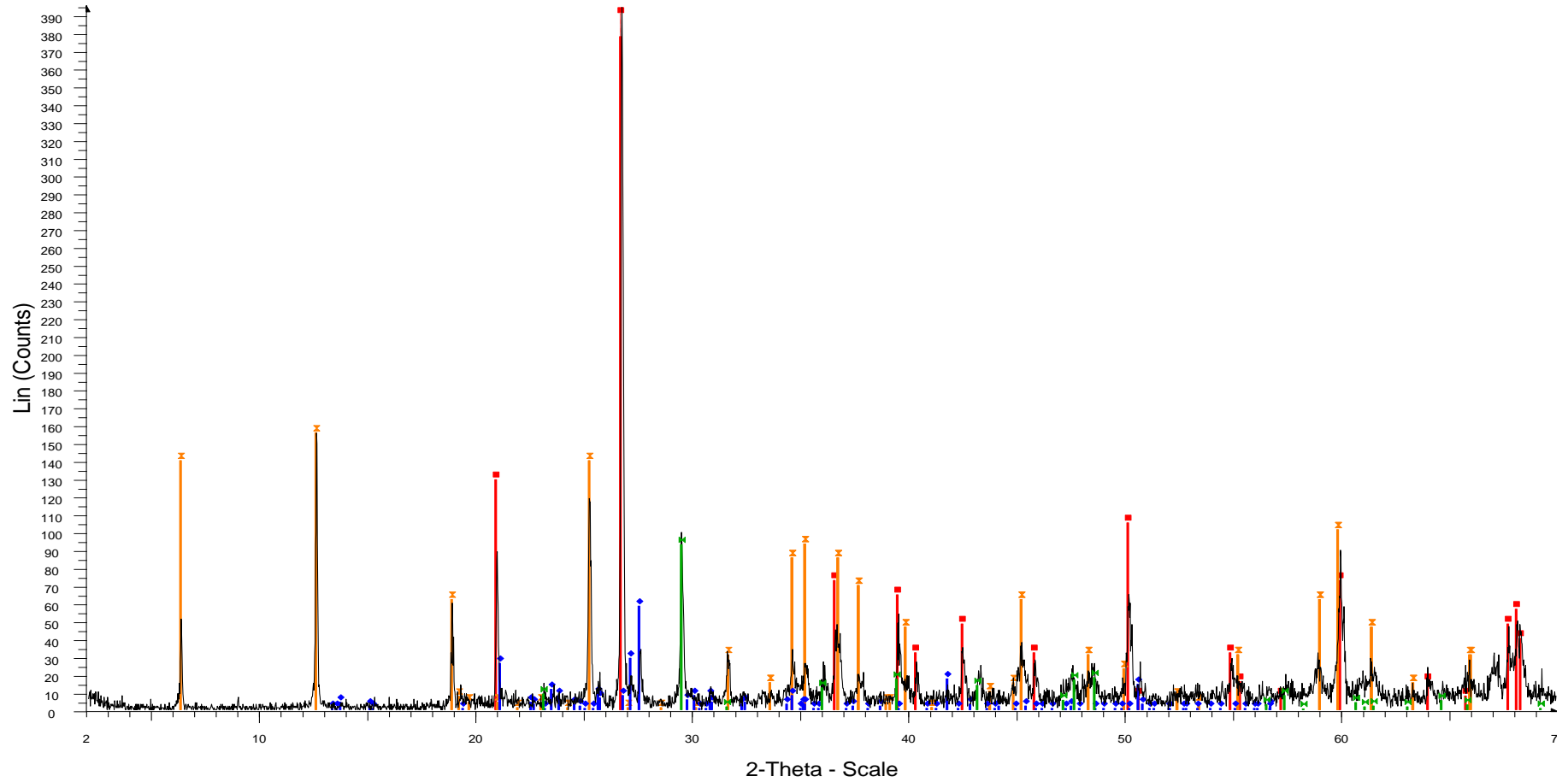
- 00-046-1045 (\*) - Quartz, syn - SiO<sub>2</sub> - Y: 178.32 % - d x by: 1. - WL: 1.5406 - Hexagonal - a 4.91344 - b 4.91344 - c 5.40524 - alpha 90.000 - beta 90.000 - gamma 120.000 - Primitive - P3221 (154) - 3 - 113.010 - I/c PDF 3.4 - F30=558(0.0017,
- 00-046-1323 (I) - Clinocllore-1Mllb - (Mg,Al,Fe)6(Si,Al)4O10(OH)8 - Y: 34.29 % - d x by: 1. - WL: 1.5406 - Monoclinic - a 5.34700 - b 9.26300 - c 14.25000 - alpha 90.000 - beta 97.200 - gamma 90.000 - Base-centered - C2/m (12) - 2 - 700.227 -
- 00-019-0002 (I) - Orthoclase, barian - (K,Ba,Na)(Si,Al)4O8 - Y: 45.99 % - d x by: 1. - WL: 1.5406 - Monoclinic - a 8.55200 - b 13.04000 - c 7.20000 - alpha 90.000 - beta 115.700 - gamma 90.000 - Base-centered - C2/m (12) - 4 - 723.502 - F30=1
- 01-086-2334 (A) - Calcite - Ca(CO<sub>3</sub>) - Y: 28.07 % - d x by: 1. - WL: 1.5406 - Rhombo.H.axes - a 4.98800 - b 4.98800 - c 17.06099 - alpha 90.000 - beta 90.000 - gamma 120.000 - Primitive - R-3c (167) - 6 - 367.610 - I/c PDF 3.2 - F30=1000(0.0

Sample 45.



8102 - File: C05120474.raw - Type: 2Th/Th locked - Start: 2.000 ° - End: 70.000 ° - Step: 0.020 ° - Step time: 1. s - Temp.: 25 °C (Room) - Time Started: 33 s - 2-Theta: 2.000 ° - Theta: 1.000 ° - Chi: 0.00 ° - Phi: 0.00 ° - X: 0.0 mm - Y: 0.0 mm - Z: 0.0 mm  
 Operations: Import  
 ■ 00-046-1045 (\*) - Quartz, syn - SiO<sub>2</sub> - Y: 100.83 % - d x by: 1. - WL: 1.5406 - Hexagonal - a 4.91344 - b 4.91344 - c 5.40524 - alpha 90.000 - beta 90.000 - gamma 120.000 - Primitive - P3221 (154) - 3 - 113.010 - I/lc PDF 3.4 - F30=558(0.0017,  
 ▼ 00-006-0263 (l) - Muscovite-2M1 - KAl<sub>2</sub>(Si<sub>3</sub>Al)O<sub>10</sub>(OH,F)<sub>2</sub> - Y: 15.38 % - d x by: 1. - WL: 1.5406 - Monoclinic - a 5.19000 - b 9.03000 - c 20.05000 - alpha 90.000 - beta 95.770 - gamma 90.000 - Base-centered - C2/c (15) - 4 - 934.896 - F30= 1  
 ■ 01-072-1652 (A) - Calcite - CaCO<sub>3</sub> - Y: 70.26 % - d x by: 1. - WL: 1.5406 - Rhombo.H.axes - a 4.99000 - b 4.99000 - c 17.00200 - alpha 90.000 - beta 90.000 - gamma 120.000 - Primitive - R-3c (167) - 6 - 366.633 - I/lc PDF 3.2 - F30=1000(0.00

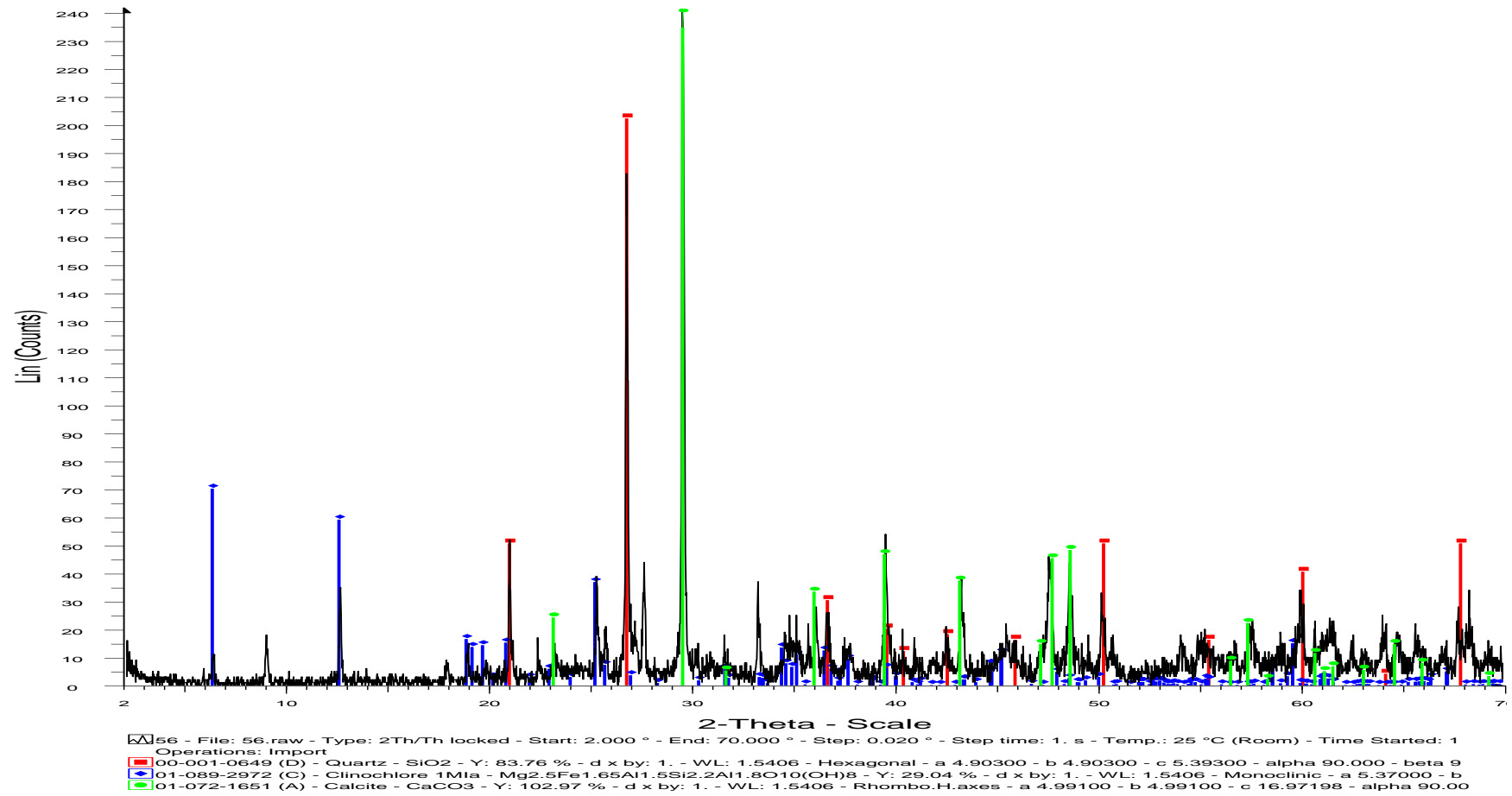
Sample 46.



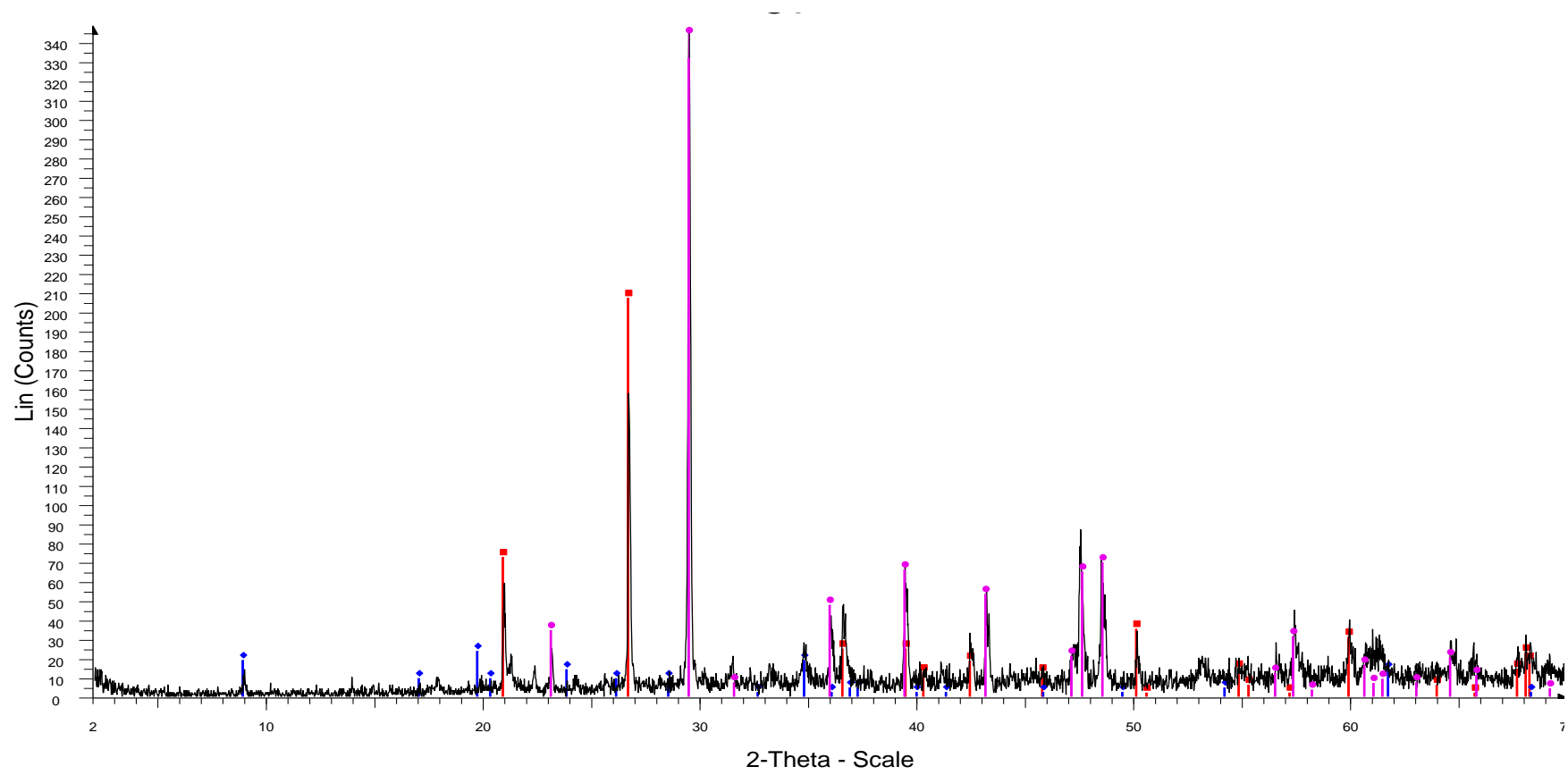
80 - File: C5120472.raw - Type: 2Th/Th locked - Start: 2.000 ° - End: 70.000 ° - Step: 0.020 ° - Step time: 1. s - Temp.: 25 °C (Room) - Time Started: 17 s - 2-Theta: 2.000 ° - Theta: 1.000 ° - Chi: 0.00 ° - Phi: 0.00 ° - X: 0.0 mm - Y: 0.0 mm - Z: 0.0  
 Operations: Import

- 00-046-1045 (\*) - Quartz, syn - SiO<sub>2</sub> - Y: 205.34 % - d x by: 1. - WL: 1.5406 - Hexagonal - a 4.91344 - b 4.91344 - c 5.40524 - alpha 90.000 - beta 90.000 - gamma 120.000 - Primitive - P3221 (154) - 3 - 113.010 - I/lc PDF 3.4 - F30=558(0.0017,
- 00-046-1323 (l) - Clinocllore-1Mllb - (Mg,Al,Fe)6(Si,Al)4O10(OH)8 - Y: 39.51 % - d x by: 1. - WL: 1.5406 - Monoclinic - a 5.34700 - b 9.26300 - c 14.25000 - alpha 90.000 - beta 97.200 - gamma 90.000 - Base-centered - C2/m (12) - 2 - 700.227 -
- 00-019-0932 (l) - Microcline, intermediate - KAlSi3O8 - Y: 14.86 % - d x by: 1. - WL: 1.5406 - Triclinic - a 8.56000 - b 12.97000 - c 7.21000 - alpha 90.300 - beta 116.100 - gamma 89.000 - Base-centered - C-1 (0) - 4 - 718.739 - F30= 46(0.0165,
- 01-072-1652 (A) - Calcite - CaCO<sub>3</sub> - Y: 23.57 % - d x by: 1. - WL: 1.5406 - Rhombo.H.axes - a 4.99000 - b 4.99000 - c 17.00200 - alpha 90.000 - beta 90.000 - gamma 120.000 - Primitive - R-3c (167) - 6 - 366.633 - I/lc PDF 3.2 - F30=1000(0.00

Sample 47.

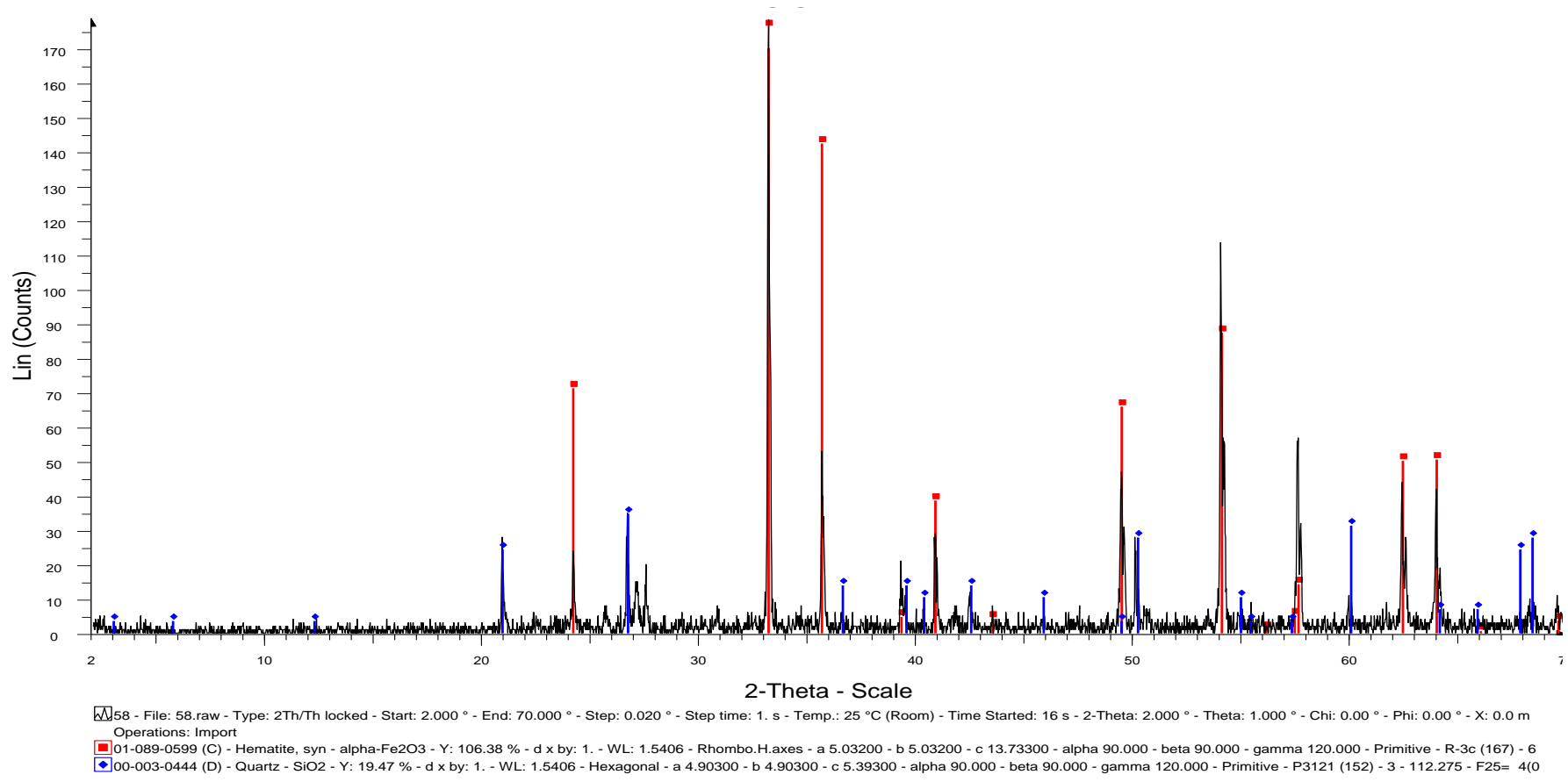


Sample 56.

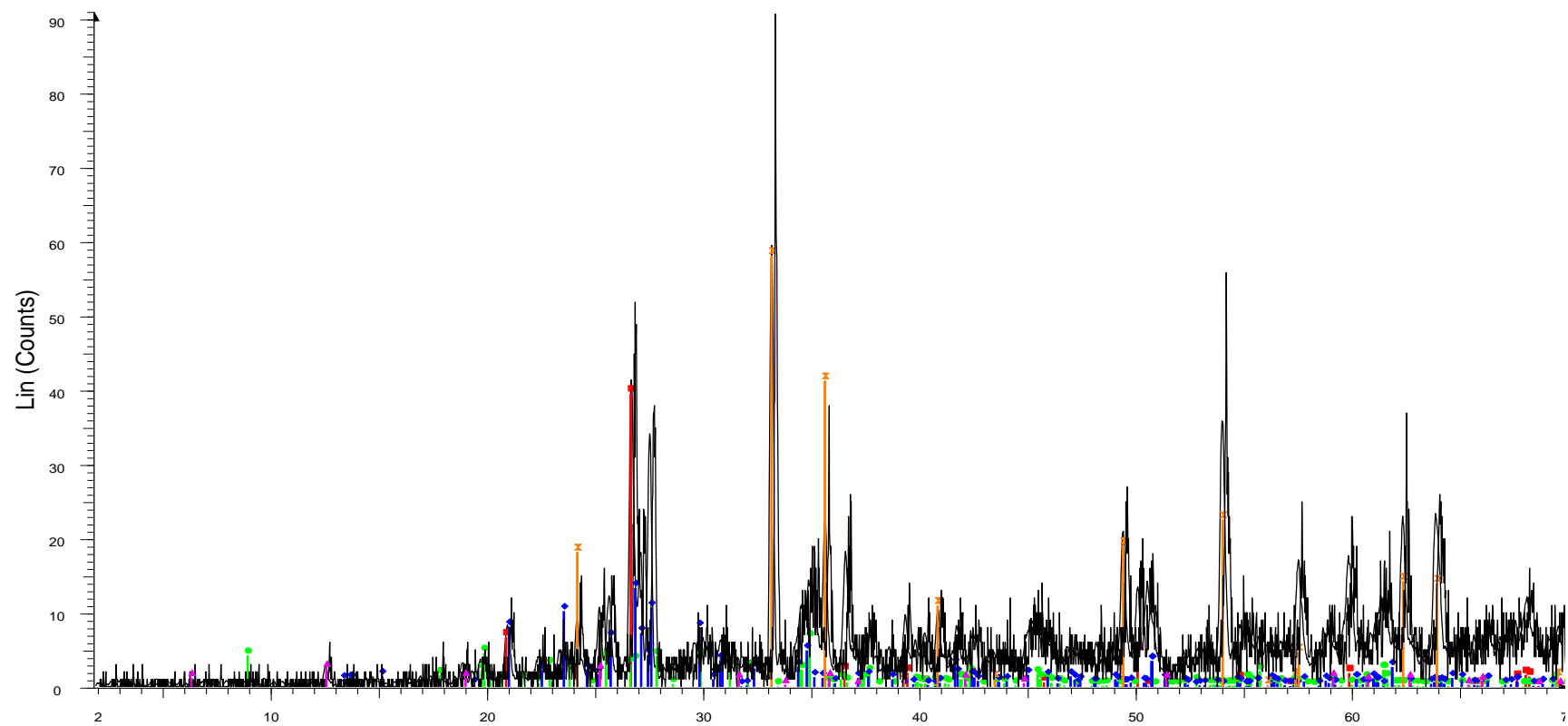


57 - File: 57.raw - Type: 2Th/Th locked - Start: 2.000 ° - End: 70.000 ° - Step: 0.020 ° - Step time: 1. s - Temp.: 25 °C (Room) - Time Started: 16 s - 2-Theta: 2.000 ° - Theta: 1.000 ° - Chi: 0.00 ° - Phi: 0.00 ° - X: 0.0 m  
 Operations: Import  
 00-005-0490 (D) - Quartz, low - alpha-SiO<sub>2</sub> - Y: 59.58 % - d x by: 1. - WL: 1.5406 - Hexagonal - a 4.91300 - b 4.91300 - c 5.40500 - alpha 90.000 - beta 90.000 - gamma 120.000 - Primitive - P3121 (152) - 3 - 112.985  
 00-013-0573 (D) - Muscovite - 0.33(NH<sub>4</sub>)<sub>2</sub>O·Al<sub>2</sub>O<sub>3</sub>·2SiO<sub>2</sub>·0.66H<sub>2</sub>O - Y: 6.81 % - d x by: 1. - WL: 1.5406 - Monoclinic - a 5.22000 - b 9.02000 - c 20.02000 - alpha 90.000 - beta 90.220 - gamma 90.000 - 942.623 - F21  
 01-072-1652 (A) - Calcite - CaCO<sub>3</sub> - Y: 101.34 % - d x by: 1. - WL: 1.5406 - Rhombo.H.axes - a 4.99000 - b 4.99000 - c 17.00200 - alpha 90.000 - beta 90.000 - gamma 120.000 - Primitive - R-3c (167) - 6 - 366.633 - I

Sample 57.



Sample 58.

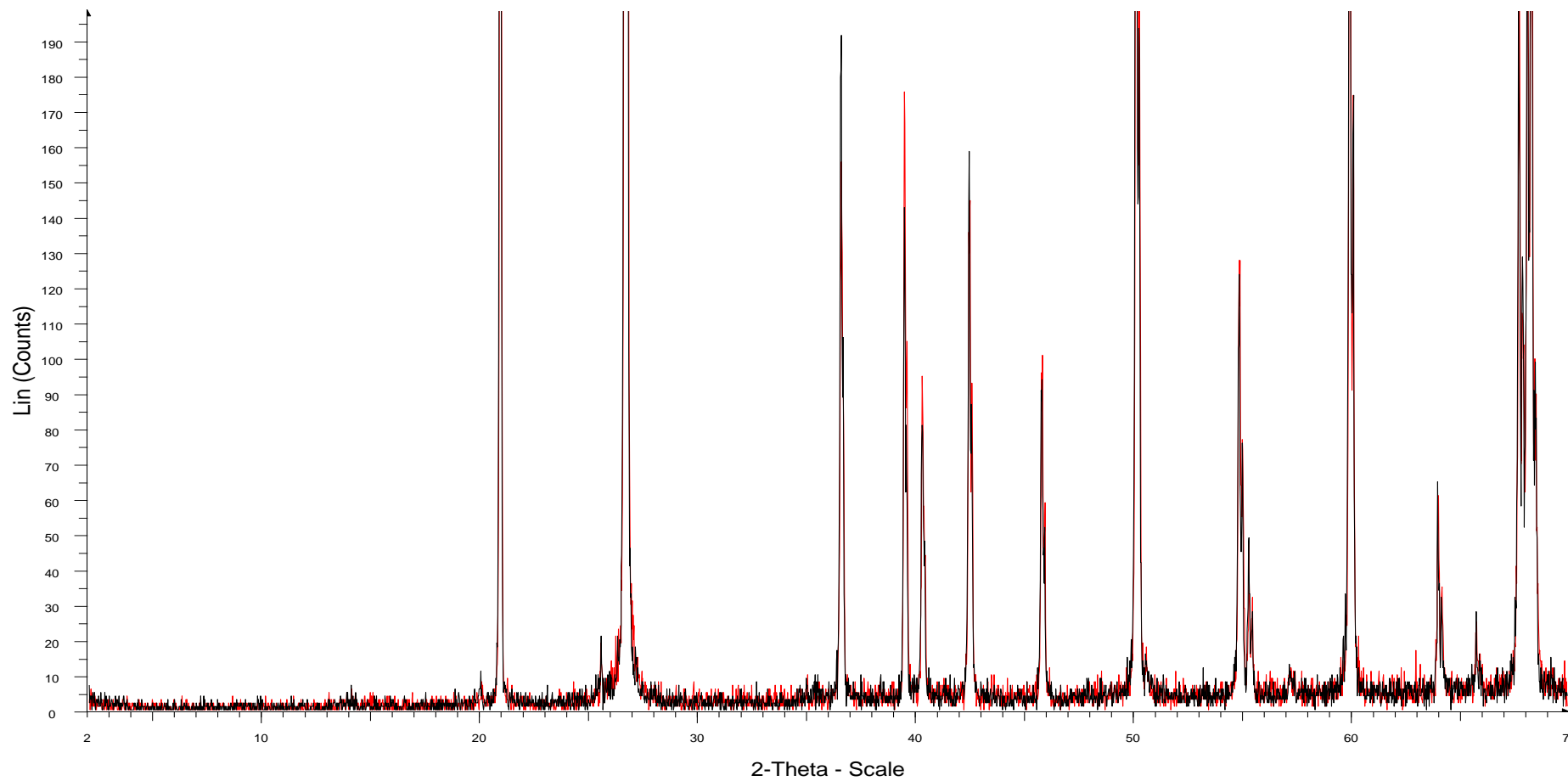


2-Theta - Scale

- ▲ 59 - File: 59.raw - Type: 2Th/Th locked - Start: 2.000 ° - End: 70.000 ° - Step: 0.020 ° - Step time: 1. s - T  
 Operations: Import
- ▲ 01-079-1741 (A) - Hematite, syn - alpha-Fe2O3 - Y: 64.12 % - d x by: 1. - WL: 1.5406 - Rhombo.H.axes -
- ▲ 59 - File: 59.raw - Type: 2Th/Th locked - Start: 2.000 ° - End: 70.000 ° - Step: 0.020 ° - Step time: 1. s - T  
 Operations: X Offset -0.200 | Smooth 0.150 | Import
- 03-065-0466 (C) - Quartz low, syn - SiO2 - Y: 43.63 % - d x by: 1. - WL: 1.5406 - Hexagonal - a 4.91410 -
- 01-082-0576 (C) - Muscovite 2M1 - KAl2(AlSi3O10)(OH)2 - Y: 7.18 % - d x by: 1. - WL: 1.5406 - Monocli
- ◆ 01-086-0439 (C) - Orthoclase - K(AlSi3O8) - Y: 14.67 % - d x by: 1. - WL: 1.5406 - Monoclinic - a 8.5904
- ▲ 00-012-0243 (D) - Clinocllore - Mg-Fe-Fe-Al-Si-O-OH - Y: 2.69 % - d x by: 1. - WL: 1.5406 - Orthorhombi

Sample 59.

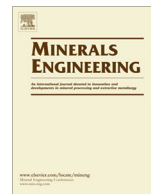




516si - File: 516SI.raw - Type: 2Th/Th locked - Start: 2.000 ° - End: 70.000 ° - Step: 0.020 ° - Step time: 1. s - Temp.: 25 °C (Room) - Time Started: 16 s - 2-Theta: 2.000 ° - Theta: 1.000 ° - Chi: 0.00 ° - Phi: 0.00 ° - X: 0.0 mm - Y: 0.0 mm - Z: 0.0  
Operations: Import

516 - File: 516 Control sample.raw - Type: 2Th/Th locked - Start: 2.000 ° - End: 70.000 ° - Step: 0.020 ° - Step time: 1. s - Temp.: 25 °C (Room) - Time Started: 16 s - 2-Theta: 2.000 ° - Theta: 1.000 ° - Chi: 0.00 ° - Phi: 0.00 ° - X: 0.0 mm - Y: 0.0  
Operations: Import

**Appendix 5.1** – Iyakwari, S., Glass, H. J., 2014, 'Influence of mineral particle size and choice of suitable parameters for ore sorting using near infrared sensors'. *Miner Eng*, 69, 102-106.



# Influence of mineral particle size and choice of suitable parameters for ore sorting using near infrared sensors



Shekwonyadu Iyakwari\*, Hylke J. Glass

Camborne School of Mines, University of Exeter, Penryn Campus, Cornwall, TR10 9EZ, UK

## ARTICLE INFO

### Article history:

Received 22 April 2014

Accepted 22 July 2014

Available online xxxx

### Keywords:

Near infrared  
Absorption  
Preconcentration  
Parameters  
Particle size  
Minerals

## ABSTRACT

Near infrared sensor-based sorting is an emerging preconcentration technology which holds promise for many mineral processing applications, such as elimination of calcite and clay waste from ore. Preconcentration serves to increase the processing efficiency as well as to reduce the total processing cost through the rejection of unwanted gangue. Given small-scale heterogeneity in complex ores, i.e. assorted minerals occurring side-by-side inside an area of measurement, the total mineral composition may not be easily discerned from a near infrared spectrum. Hence, mineral identification and subsequent classification involves the analysis of absorption features in terms of feature depth, width, position, and level of spectral reflectance. This research investigates the near infrared spectral characteristics of minerals as a function of particle size fraction, specifically for individual minerals commonly found in malachite-rich copper ores. Samples of pure minerals are crushed and sieved into different size fractions and scanned with a near infrared line scanner. It was found that the presence of characteristic absorption features and their wavelength position were a better identification parameter than the reflectance level. The implication for preconcentrating a typical malachite-rich copper ore through near-infrared based sorting is discussed.

© 2014 Elsevier Ltd. All rights reserved.

## 1. Introduction

The application of automated sensor-based sorting can help to reduce costs of processing coarse ores through the rejection of gangue minerals (Dalm et al., 2014; Bowman and Bearman, 2014). However, sensor-based sorting of minerals is still an emerging technology with a limited number of proven applications (Dalm et al., 2014). A major consideration in developing ore sorting applications is the identification of a suitable sensor and appropriate interpretation of sensor data (Iyakwari et al., 2013).

Near InfraRed (NIR) sensing consists of measurement of the reflectance when a particle surface is illuminated with NIR light. Vibrational properties of functional chemical groups create absorption features while particle accessibility to radiation determines the level of reflectance (Hunt, 1979; Pasikatan et al., 2001). Measurement of reflectance across a range of NIR wavelengths from a defined area on the particle surface allows detection of the presence or absence of functional chemical groups. Hence, NIR sensing harbours significant potential for classification of minerals contained in particles of broken ore. However, the size of particles

and grains or crystals within the particles will influence the NIR reflectance spectrum (Pasikatan et al., 2001).

In order to scope the application of NIR for preconcentration of ore, the effect of the size of mineral particles on NIR reflectance was investigated for alteration minerals which are characteristic for a hydrothermally-formed supergene-enriched copper ore. Good examples of such deposits are found in the Atacama district in Northern Chile (Daroch and Barton, 2011). Typical alteration minerals present in this copper ore are calcite, muscovite, malachite, chlorite, and hematite (Robb, 2005). The first four minerals are known to be sensitive to NIR with high reflectance and characteristic absorption features (Clark et al., 1990; Hunt et al., 1971; Hunt and Salisbury, 1971). The fifth mineral, hematite, is included in the study because it is a common alteration mineral. Previous experiments and literature show that hematite displays no characteristic absorption feature along any wavelength position in the range considered (1300–2400 nm) (Hunt et al., 1971; Iyakwari et al., 2013). However, hematite is known to lower the level of reflectance and effectively masks features of other minerals which have a higher reflectance (Bishop and Dummel, 1996).

NIR spectra are analysed in terms of the following properties considered to be important for mineral identification (Gaffey, 1986): a. overall brightness, expressed in terms of the baseline reflectance; b. number of features in the spectrum; c. position,

\* Corresponding author.

E-mail addresses: [si233@exeter.ac.uk](mailto:si233@exeter.ac.uk) (S. Iyakwari), [H.J.Glass@exeter.ac.uk](mailto:H.J.Glass@exeter.ac.uk) (H.J. Glass).

depth, and width of characteristic absorption features (Van der Meer, 1995).

## 2. Material and methods

Samples of pure calcite, muscovite, malachite, chlorite (clinochore), and hematite were analysed with X-ray Diffraction (XRD, Siemens/Bruker D5000, [www.bruker.com](http://www.bruker.com)). XRD measurements were matched with known mineral signatures using EVA software. Results of XRD indicate that the samples were of high purity.

Samples of each mineral were crushed using a Retsch steel jaw crusher ([www.retsch.com](http://www.retsch.com)) and sieved into six (4–2.8 mm, 2.8–2 mm, 2–1.4 mm, 1 mm–710  $\mu\text{m}$ , 710–500  $\mu\text{m}$ , –500  $\mu\text{m}$ ) size fractions. Of these, hematite was only sieved into four size fractions (4–2.8 mm, 2–1.4 mm, 710–500  $\mu\text{m}$  and –500  $\mu\text{m}$ ). Each sample was scanned with a NIR line scanner (Tomra, [www.tomra.com](http://www.tomra.com)) to acquire NIR spectra on a succession of adjacent areas. Each area covers 2.9 mm by 9 mm of the particle surface(s). The sizes of the mineral particles were smaller than the dimensions of the pixels measured by the NIR scanner. Samples containing particles with a given size range were placed on a petri dish, illuminated and measured. Details on NIR instrumentation, procedure, data acquisition and treatment, are described in Iyakwari et al. (2013). It was noted that multiple NIR spectra from individual samples were very similar, so only a single, representative spectrum per size fraction was chosen for interpretation.

Individual NIR absorption features were characterised in terms of position, depth, and width. The position of the absorption feature was defined by the wavelength where a minimum reflectance was observed (centre), while the feature Depth ( $D$ ) was defined as the difference between the Maximum Reflectance (Max.  $R$ ) and the Minimum Reflectance (Min.  $R$ ). The width of absorption was determined from the difference in wavelengths between the Left shoulder Wavelength ( $LW$ ) and the Right shoulder Wavelength ( $RW$ ). The overall Reflectance ( $R$ ) of a spectrum was defined by the highest reflectance displayed in the NIR wavelength region (Fig. 1).

## 3. Results

Interpretation of the NIR spectra of each of the 5 pure minerals is described in the following sections.

### 3.1. Calcite

The calcite sample displays diagnostic absorption features near 1920, 2000, 2150 and 2340 nm (Fig. 2). The positions of the

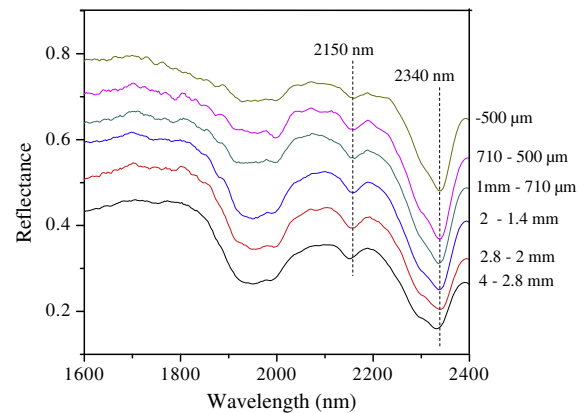


Fig. 2. NIR reflectance spectra of calcite measured on six different particle size fractions.

absorption features wavelength positions were consistent across all size fractions. The features near 1920 and 2000 nm were broad and poorly defined and their depth was not measured. The depth of 2150 and 2340 nm features were measured as a function of particle size. The 2150 nm feature revealed an increase in depth of 0.030 for 4–2.8 mm grain size, reaching a maximum of 0.050 for the 1 mm–710  $\mu\text{m}$  size class. Below a particle size of 710  $\mu\text{m}$ , the feature depth decreased to 0.03 (Table 1). The 2340 nm feature revealed same pattern from a depth of 0.19 for 4–2.8 mm size fraction, reaching 0.26 for 1 mm–710  $\mu\text{m}$  and decreasing to 0.22 for the finer sizes of –500  $\mu\text{m}$  (Table 1).

The sample displayed its highest reflectance value around 1700 nm. Therefore, all reflectance measurements were carried out for all size fractions with reference to 1700 nm. Analysis reveals that, with each size reduction, reflectance values increased (Table 2). Fig. 2 shows that the overall brightness of spectra increase with decreasing particle size. Fig. 2 also confirms that the feature width is constant across all size fractions.

Given better visibility of absorption feature near 2340 nm across all size fractions compared to other features, the 2340 nm feature was identified as the best wavelength for identification of calcite.

### 3.2. Muscovite

The muscovite sample displays characteristic absorption features near 1415, 1840, 1915, 2200, and 2350 nm. All characteristic

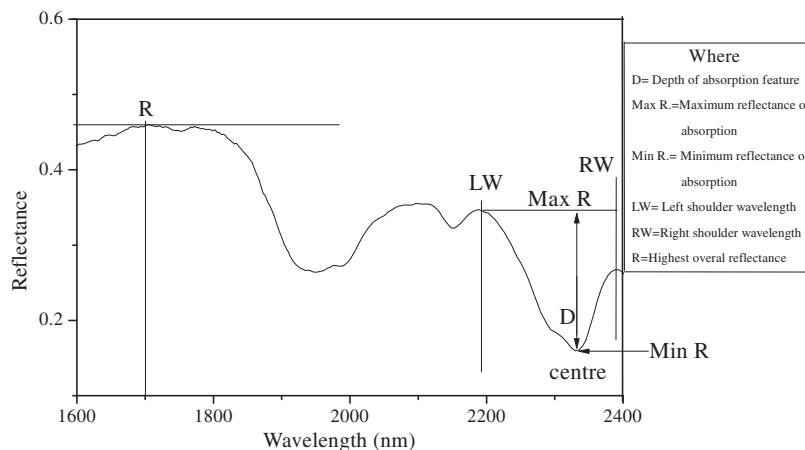


Fig. 1. Parameters characterising NIR spectrum of calcite: mineral absorption features and overall reflectance.

**Table 1**  
Feature depth at two wavelengths for different size fractions of calcite.

Size fractions	Feature depth at wavelength	
	2150 nm	2340 nm
4–2.8 mm	0.03	0.19
2.8–2 mm	0.05	0.22
2–1.4 mm	0.05	0.25
1 mm–710 $\mu\text{m}$	0.05	0.26
710–500 $\mu\text{m}$	0.04	0.25
–500 $\mu\text{m}$	0.03	0.22

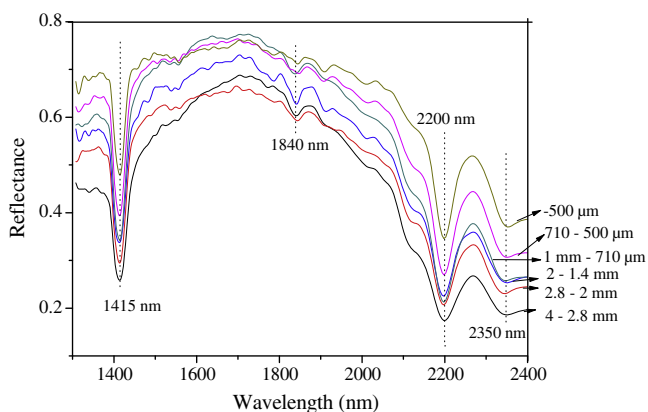
**Table 2**  
Reflectance values for different size fractions of calcite.

Size fractions	Reflectance value measured at 1700 nm
4–2.8 mm	0.46
2.8–2 mm	0.54
2–1.4 mm	0.62
1 mm–710 $\mu\text{m}$	0.67
710–500 $\mu\text{m}$	0.73
–500 $\mu\text{m}$	0.81

absorption features were consistently observed in spectra across the various size fractions. Features near 1415, 1840 and 2200 nm were distinctly visible for all the various size fractions (Fig. 3). The 2350 nm features appeared weak, while the 1915 nm feature was almost invisible in the spectra of some particle size fractions (e.g. 2.8–2 mm, and 1 mm–710  $\mu\text{m}$ ).

The depth of measured features at 1415 and 2200 nm showed a maximum within the 1 mm–710  $\mu\text{m}$  particle size range (Table 3). Measurement of absorption depth at 1415 nm showed an increase from 0.19 at a particle size of 4–2.8 mm to 0.25 for 1 mm–710  $\mu\text{m}$  size particles, before dropping to 0.22 for –500  $\mu\text{m}$  size particles. The 2200 nm feature measured 0.22 for –500  $\mu\text{m}$  size fraction, with the smallest value of 0.13 obtained for 4–2.8 mm size fraction. The depth of the 1840 nm feature, which was a mineral-specific water feature (Aines and Rossman, 1984), varies inconsistently with particle size (Table 3), (i.e. –OH bond detection which is indicative of water or –OH minerals in the crystal lattice). This is also true for the other water feature near 1915 nm.

The different size fractions display the highest reflectance values near 1720 nm. Hence, all reflectance measurements for muscovite were made with reference to this wavelength position. Measurement showed that the fine particle sizes have higher reflectance values than the larger particles (Table 4). Fig. 3 shows spectra of all size fractions and their varying overall brightness displaying an increase from larger size fractions to finer size fractions.



**Fig. 3.** NIR reflectance spectra of muscovite measured on six different size fractions.

**Table 3**  
Feature depth at three wavelengths for different size fractions of muscovite.

Size fractions	Feature depth at wavelength (nm)		
	1415	1840	2200
4–2.8 mm	0.19	0.07	0.13
2.8–2 mm	0.22	0.05	0.16
2–1.4 mm	0.24	0.06	0.18
1 mm–710 $\mu\text{m}$	0.25	0.04	0.20
710–500 $\mu\text{m}$	0.24	0.02	0.20
–500 $\mu\text{m}$	0.22	–	0.22

**Table 4**  
Reflectance values for different size fractions of muscovite.

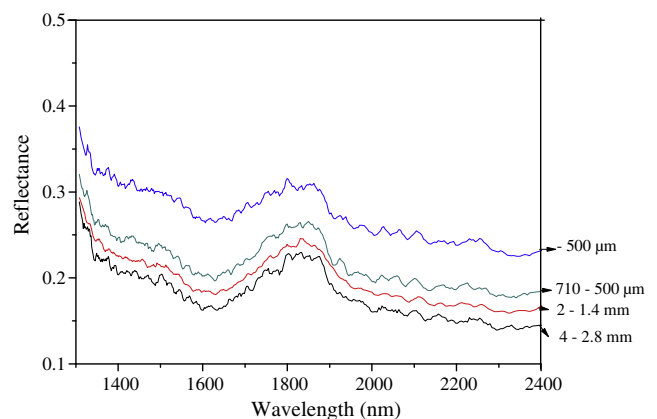
Size fractions	Reflectance value measured at 1720 nm.
4–2.8 mm	0.65
2.8–2 mm	0.66
2–1.4 mm	0.73
1 mm–710 $\mu\text{m}$	0.77
710–500 $\mu\text{m}$	0.76
–500 $\mu\text{m}$	0.76

In addition, the width of the absorption feature revealed no variation across all sizes.

Due to strong visibility of the 1415 and 2200 nm features, these wavelengths were suitable for identifying muscovite. However, the feature near 1400 nm may also indicate water or –OH bearing minerals when a second feature is observed at 1900 nm (Aines and Rossman, 1984). In the absence of a feature at 1900 nm, interpretation of the feature at 1415 nm was unclear. Hence, the feature at 2200 nm is the best diagnostic for muscovite.

### 3.3. Hematite

The NIR spectrum of hematite shows a low reflectance with no distinct characteristic absorption features (Iyakwari et al., 2013). Van Der Meer (1995) investigated the influence of iron bearing minerals in mixtures with carbonate minerals and reported the masking effect of hematite on carbonate minerals. Bishop and Dummel (1996) confirmed the masking effect of hematite in an experiment of mixture of hematite and montmorillonites. Fig. 4 reveals that the largest particles size (4–2.8 mm) absorbs more strongly and the spectral brightness increased with reduction in particle size. Therefore, it was concluded that, where large hematite crystals were present in a particle, resultant spectra will show low reflectance.



**Fig. 4.** NIR reflectance spectra of hematite measured on four different size fractions.

**Table 5**  
Feature depth at two wavelengths for different size fractions of malachite.

Size fractions	Absorption depth at wavelength	
	2275 (nm)	2360 (nm)
4–2.8 mm	0.06	0.01
2.8–2 mm	0.06	0.01
2–1.4 mm	0.07	0.02
1 mm–710 $\mu$ m	0.07	0.02
710–500 $\mu$ m	0.08	0.02
–500 $\mu$ m	0.13	0.04

### 3.4. Malachite

Malachite displays characteristic absorption features near wavelengths of 2275 nm and 2360 nm. Measurements of depth of absorption features (Table 5) reveal an increase in absorption depth with decreasing particle size. The 2275 nm feature has an initial depth of 0.06 at 4–2.8 mm and increased to 0.13 for –500  $\mu$ m. The 2360 nm feature decreased with particle size from 0.01 for 4–2.8 mm to 0.04 for –500  $\mu$ m size fraction. Given the stronger visibility of 2275 nm features across the different size fractions, it was the best diagnostic of malachite within the 1300–2400 nm NIR range.

The influence of particle size was also observed in the overall reflectance of sample as the level of reflectance increased with reducing particle size, from 0.27 for 4–2.8 mm, reaching 0.44 for the –500  $\mu$ m size fraction (Table 6). While the width of absorption features is approximately constant, the highest reflectance values were observed near 1870 nm (Fig. 5).

### 3.5. Chlorite

Chlorite (clinochore) displays characteristic features near 1415, 2265 and 2360 nm. Though some absorption features were weak and lacked a clearly defined central absorption wavelength, all absorption feature positions and feature widths are consistent across all size fractions (Table 7 and Fig. 6).

The 2265 nm feature displays its largest depth for –500  $\mu$ m sized particles (Table 7). The 2360 nm feature was more visible at –500  $\mu$ m and 710–500  $\mu$ m, with a depth of 0.02 at both size fractions. The 2360 nm feature was invisible at 2–1.4 mm size fraction, where the feature lacks absorption centre. The 1415 nm feature was only visible at the smallest (–500  $\mu$ m) and largest (4–2.8 mm) particle size (Fig. 6).

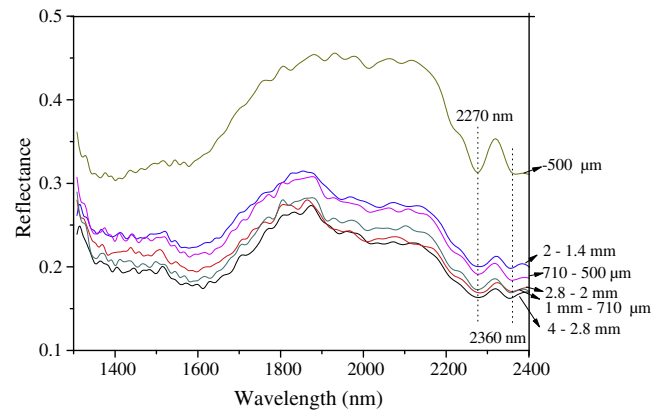
The highest reflectance value is measured near 1800 nm (Table 8) and the reflectance reduced with increasing particle size. Contrary to the features at 1415 and 2360 nm, the feature at 2265 nm was observed across all particle size ranges and was hence the best diagnostic of chlorite.

## 4. Implication to ore sorting

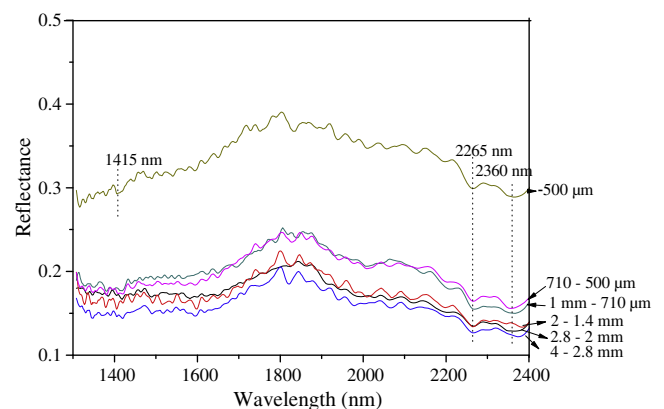
Analysis of NIR spectra indicates that, across different particle sizes for all minerals, absorption features were observed at similar wavelength positions and had a similar width. However, feature depth was affected by variation in particle size. The extent to which feature depth was influenced by particle size depends on the type of mineral. This was in agreement with Clark (1999), who states that an increase in particle grain size first increases absorption feature depth before reaching a maximum and then decreasing. Since feature depth was not constant for all particle size fractions of the same mineral, the depth was not a diagnostic of a mineral.

**Table 6**  
Reflectance values for different size fractions of malachite.

Size fractions	Reflectance value measured near 1870 nm
4–2.8 mm	0.27
2.8–2 mm	0.26
2–1.4 mm	0.30
1 mm–710 $\mu$ m	0.28
710–500 $\mu$ m	0.28
–500 $\mu$ m	0.44

**Fig. 5.** NIR reflectance spectra of malachite measured on six different size fractions.**Table 7**  
Feature depth at three wavelengths for different size fractions of chlorite.

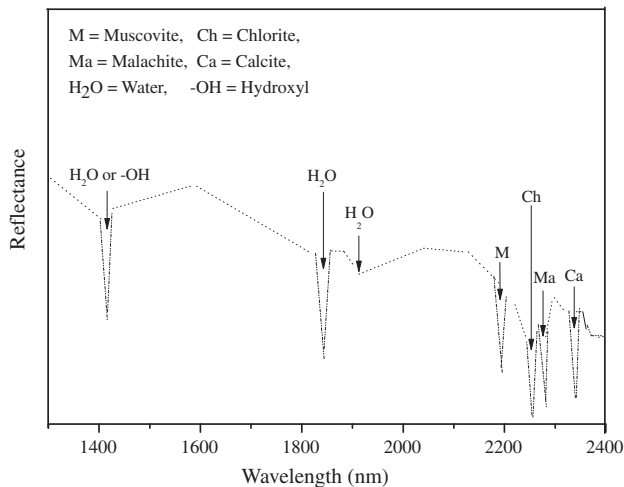
Size fractions	Absorption depth at wavelength		
	1415 (nm)	2265 (nm)	2360 (nm)
4–2.8 mm	0.011	0.02	0.01
2.8–2 mm	–	0.02	0.01
2–1.4 mm	–	0.02	–
1 mm–710 $\mu$ m	–	0.02	0.01
710–500 $\mu$ m	–	0.02	0.02
–500 $\mu$ m	0.008	0.03	0.02

**Fig. 6.** NIR reflectance spectra of chlorite (clinochore) measured on six different size fractions.

Measurement of reflectance values for each spectrum showed that larger particle sizes display higher spectra absorption across the wavelength range compared to the smaller particle sizes. This was also in agreement with Crowley and Vergo (1988) and Van der Meer (1995). Both authors noted that more light was scattered by fine particles before much absorption can take place, resulting in

**Table 8**  
Reflectance values for different size fractions of chlorite.

Size fractions	Reflectance values measured near 1800 nm
4–2.8 mm	0.20
2.8–2 mm	0.20
2–1.4 mm	0.20
1 mm–710 $\mu\text{m}$	0.25
710–500 $\mu\text{m}$	0.25
–500 $\mu\text{m}$	0.38



**Fig. 7.** Characteristic position of muscovite, chlorite, malachite, calcite and water features in a NIR spectrum.

relatively higher reflectance. Gaffey (1986) observed that a less densely packed – powdered-mineral sample reflects more than the densely packed – solid-sample of the same mineral or rock. Clark (1999) also observed that larger particles have a greater internal path where photons may be absorbed. Hence, due to multiple scattering in the NIR region, overall brightness decreases with increasing particle size. This then means that an ore consisting of individual large crystals (phenocryst) will have a lower overall level of reflectance. This is in agreement with Pasikatan et al. (2001), who state that the NIR reflectance was sensitive to particle size and shape.

When a particle consists of an assembly of minerals, its NIR spectrum was likely to differ from, the spectra of its constituent NIR-active mineral(s). Alternatively, the NIR spectrum may correspond to the spectrum of the dominant NIR-active mineral. The dominant mineral in a spectrum may not be the mineral with the highest concentration. Surfaces of ore particles may consist of a range of grain sizes. In practice, there is no similarity in depth of absorption features and spectral brightness across different grain size fractions of the same mineral. Hence, identification of individual minerals rests on identifying characteristic absorption features at specific wavelengths. With malachite-rich ore particles, strong diagnostic features (e.g. 2340 nm for calcite, 2200 nm for muscovite, 2275 nm for malachite and 2265 nm for chlorite) are promising due to their consistent visibility across different size ranges. Fig. 7 presents a schematic summary of the best diagnostic features and their specific wavelength positions, as recreated from the analysis of individual minerals at different particle sizes.

NIR spectra are sensitive to presence of water expressed in features near 1400/1900 nm and 1840 nm (Aines and Rossman, 1984). Water is either adsorbed on the mineral surface or part of the mineral crystal structure (Aines and Rossman, 1984; Dalm et al., 2014). Analysis of muscovite and chlorite suggests that the presence and depth of water features is inconsistent with particle size. Also, in complex mineral assemblies, more than one mineral may be responsible for the water feature. Hence, water features were not considered a good diagnostic for particle classification.

## 5. Conclusion

For the selected minerals, the best diagnostic features of the selected minerals were observed at different wavelengths positions. Establishing the presence of diagnostic features at specific wavelengths in individual particles was a promising route for particle classification. Understanding the NIR-active constituent minerals in an ore and their best diagnostic features is an important initial stage in scoping the application of NIR sensing to mineral identification and preconcentration.

## Acknowledgments

The Nigerian Government, through the academic staff support scheme of the Tertiary Education Trust Fund of Nigeria (TETFON), and the Management of Nasarawa State University, Keffi, are acknowledged for providing financial support for this research.

## References

- Aines, R.D., Rossman, G.R., 1984. Water in minerals? a peak in the infrared. *J. Geophys. Res.* 89 (B6), 4059–4071.
- Bishop, J.L., Dummel, A., 1996. The influence of fine-grained hematite powder on the spectral properties of Mars soil analogs; VIS-NIR bi-directional reflectance spectroscopy of mixtures. *Lunar Planet. Inst. Sci. Conf. Abstr.* 27.
- Bowman, D.J., Bearman, R.A., 2014. Coarse waste rejection through size based separation. *Miner. Eng.* 62, 102–110.
- Clark, R.N., King, T.V.V., Klejwa, M., Swayze, G.A., Vergo, N., 1990. High spectral resolution reflectance spectroscopy of minerals. *J. Geophys. Res.* 95 (B8), 12653–12680.
- Clark, R.N., 1999. Spectroscopy of rocks and minerals, and principles of spectroscopy. In: Rencz, N. (Ed.), *Remote Sensing for the Earth Sciences: Manual of Remote Sensing*, vol. 3. John Wiley & Sons, New York, pp. 3–52.
- Crowley, J.K., Vergo, N., 1988. Near-infrared reflectance spectra of mixtures of kaolin-group minerals: use in clay mineral studies. *Clay Miner.* 36 (4), 310–316.
- Dalm, M., Buxton, M.W., van Ruitenbeek, F.J., Voncken, J.H., 2014. Application of near-infrared spectroscopy to sensor based sorting of a porphyry copper ore. *Miner. Eng.* 58, 7–16.
- Daroch, G.A., Barton, M.D., 2011. Hydrothermal alteration and mineralization in Santo Domingo Sur iron oxide (–Cu–Au) (IOCG) deposit, Atacama Region, Chile. In: 11th SGA Biennial meeting “Let talk ore deposits”.
- Gaffey, J.S., 1986. Spectra reflectance of carbonate minerals in the visible and near infrared (0.35–2.55 microns): calcite, aragonite and dolomite. *Am. Mineral.* 71, 153–162.
- Hunt, G.R., Salisbury, J.W., 1971. Visible and near-infrared spectra of minerals and rocks: II. Carbonates. *Model. Geol.* 2, 23–39.
- Hunt, G.R., Salisbury, J.W., Lenhoff, J.C., 1971. Visible and near-infrared spectra of minerals and rock: III. Oxides and hydroxides. *Model. Geol.* 2, 195–205.
- Hunt, G.R., 1979. Near-infrared (1.3–2.4  $\mu\text{m}$ ) spectra of alteration minerals; potential for use in remote-sensing. *Geophysics* 44 (12), 1974–1986.
- Iyakwari, S., Glass, H.J., Kowalczyk, P.B., 2013. Potential for near infrared sensor-based sorting of hydrothermally-formed minerals. *J. Near Infrared Spec.* 21 (3), 223–229.
- Pasikatan, M.C., Steele, J.L., Spillman, C.K., Haque, E., 2001. Near infrared reflectance spectroscopy for online particle size analysis of powders and ground materials. *J. Near Infrared Spec.* 9, 153–164.
- Robb, L., 2005. *Introduction to Ore-Forming Processes*. Wiley-Blackwell.
- Van der Meer, F., 1995. Spectral reflectance of carbonate mineral mixtures and bidirectional reflectance theory: quantitative analysis techniques for application in remote sensing. *Remote Sens. Rev.* 13, 67–94.

**Appendix 5.2** – Iyakwari, S., Glass, H. J., Kowalczyk, P. B., 2013, 'Potential for near infrared sensor-based sorting of hydrothermally-formed minerals'. *J Near Infrared Spectrosc*, 21(3), 223-229





# Potential for near infrared sensor-based sorting of hydrothermally-formed minerals

Shekwonyadu Iyakwari,<sup>a,\*</sup> Hylke J. Glass<sup>a</sup> and Przemyslaw B. Kowalczyk<sup>b</sup>

<sup>a</sup>Camborne School of Mines, University of Exeter, Tremough Campus, Penryn, Cornwall, TR10 9EZ, UK.  
E-mail: si233@exeter.ac.uk (S. Iyakwari), h.j.glass@exeter.ac.uk (H.J. Glass)

<sup>b</sup>Wroclaw University of Technology, Wybrzeze Wyspianskiego 27, 50-370 Wroclaw, Poland. E-mail: przemyslaw.kowalczyk@pwr.wroc.pl

Dry processing of minerals is increasingly attractive in a mining environment where water is a scarce commodity. Sensor-based sorting has the potential to perform dry separation of ore from gangue at an early stage of the processing, also helping to reduce energy consumption due to downstream crushing. In order to develop a sensor-based sorting process, selection of a suitable sensor is of critical importance. In practice, a near infrared sensor can measure characteristic features of carbonate, hydroxyl and water groups contained in minerals and rocks. This paper examines the process of establishing the suitability of a near infrared sensor for distinguishing hydrothermally-formed minerals. It is concluded that characteristic absorption features in near infrared spectra offer a more robust route to separating out minerals than the level of absorption.

**Keywords:** near infrared, sensor, sorting, hydroxyl, carbonate, water, hydrothermal, minerals, absorption, rocks

## Introduction

Dry processing of minerals is an attractive choice in a mining environment where process water is in short supply. Sensor-based sorting has the potential to perform dry separation of ore from gangue at an early stage of the processing,<sup>1</sup> also helping to reduce energy consumption due to downstream crushing. In order to develop a sensor-based sorting process, selection of a suitable sensor is of critical importance. In practice, a near infrared (NIR) sensor can detect characteristic absorbance features on the mineral surface due to the presence of hydroxyl-, carbonate- and water-bearing minerals, while certain minerals absorb NIR across ranges of wavelengths. A NIR spectrum is some combination of the true spectra of its constituents<sup>2</sup> which may reveal information about the functional groups present. Given small-scale heterogeneity, i.e. assorted minerals side-by-side inside an area of measurement, the total mineral composition may not be discernible from a spectrum. To understand the extent of this confounding on the application of NIR, it is instructive

to compare NIR spectra of pure minerals associated with mining applications. Potential applications could entail the classification of economically important hydrothermally-formed minerals. These are formed near the Earth's surface by alteration of primary ores by low temperature oxidising meteoric waters.<sup>3</sup> Compared to primary ores, the grade of valuable heavy metals in hydrothermal deposits is relatively low. However, with increasing demand for commodities such as iron, copper etc., development of these deposits is becoming viable.<sup>4</sup> This paper analyses the NIR spectra of individual minerals present in a supergene copper deposit in Chile. This analysis provides a basis for developing a sorting process for copper-bearing secondary minerals.

## Background

In the NIR wavelength range, from 780 nm to 2525 nm, electronic processes, such as crystal-field effects, charge transfer,

colour centres and conduction band transitions and vibrational processes may lead to absorption of NIR for a limited number of functional groups,<sup>5,6,7</sup> specifically H<sub>2</sub>O, -OH, and CO<sub>3</sub><sup>2-</sup>.

Water (H<sub>2</sub>O) may be trapped in fluid inclusions or embedded in the matrix of minerals.<sup>8</sup> Whenever water is present, absorption bands are observed around 1400 nm and 1900 nm<sup>6</sup> or may reduce the overall reflectance of a sample in the NIR region.<sup>1</sup> However, when a hydroxyl group (-OH) is present in the absence of water, the absorption band around 1900 nm vanishes and only the absorption band around 1400 nm remains.<sup>6</sup> In addition, the NIR spectrum of a hydroxyl group contains an absorption band between 2200 nm and 2350 nm. The exact location of this feature depends on the type of ion the hydroxyl group is attached to and where it is located in the material.<sup>5,6</sup> Carbonate (CO<sub>3</sub><sup>2-</sup>) has two distinct absorption bands around 2325 nm and 2525 nm. Carbonate-bearing minerals do not normally contain water, so that carbonate and water absorption features are not observed in the same spectrum. When water features are observed in spectra of carbonate-bearing minerals, this is indicative of impurities.<sup>9</sup> Van der Meer<sup>9</sup> notes that the reflectance in NIR spectra of calcite is reduced by the presence of iron. The principal absorption bands of these groups are summarised in Table 1.

We will measure NIR reflectance in the wavelength range between 1300 nm and 2400 nm, where copper by itself does not exhibit absorption features. Hence, targeting secondary copper with a NIR sensor hinges on the distribution of functional groups or on iron oxides, which show absorption across the quoted wavelength range. In addition, detecting the presence of -OH and CO<sub>3</sub><sup>2-</sup> in run-of-mine copper ore could inform a pre-processing step when the downstream recovery of copper from supergene ore requires acid leaching. When either hydroxyl- and/or carbonate-bearing minerals which do not contain copper are separated prior to leaching, acid consumption can be reduced. In practice, kaolinite, chlorite, muscovite and calcite rich particles could be separated from copper ore particles.<sup>12</sup> However, copper in supergene deposits can occur in hydroxyl and carbonate-bearing mineral forms. This may complicate the application of NIR for upgrading supergene copper ore and is the subject of this study.

## Experiments

### Samples

After identification of typical hydrothermally formed minerals, specimens of six silicate, three carbonate and three oxide group minerals were obtained from the Camborne School of Mines (CSM) Museum (Table 2). The elemental composition of the sample surface was analysed with X-ray fluorescence (XRF, Olympus, [www.olympus-ims.com/en/xrf-xrd/delta-handheld](http://www.olympus-ims.com/en/xrf-xrd/delta-handheld)). The measuring window covered a circle with diameter of 1 cm. X-rays penetrate approximately 1–2 mm into the particle surface. Individual samples were also analysed with X-ray diffraction (XRD, Siemens/Bruker D5000, [www.bruker.com](http://www.bruker.com)). XRD measurements were matched with known mineral signatures using EVA software. Results from XRF and XRD indicated that the samples are of high purity. NIR spectra of the minerals were recorded with a NIR sensor described in the next section.

### NIR instrumentation and data acquisition

Based on the mode of scanning, NIR point scanners and NIR line scanners are distinguished. The point scanner measured a single spectrum of a small surface area of the particle surface, usually within a window of a few micrometers diameter circle. The line scanner measured NIR spectra on a succession of adjacent areas across the mineral surface, each with a size of 2.9 mm by 2.4 cm. In this investigation, spectra generated by the NIR line scanner were calibrated with data from the NIR point scanner. Results discussed in the remainder of this paper are derived from a line scanner.

The NIR line scanner consisted of an enclosed sample chamber with a cooling facility and illumination with two shortwave-infrared quartz halogen bulbs (Heraeus Noblelight, [www.heraeusnoblelight.com](http://www.heraeusnoblelight.com)) with gold reflectors (2500 watt, 480V each). NIR radiation emerging through a narrow slit-shaped opening in the roof of the chamber passed through an imaging spectrometer developed by Tomra Sorting Solutions ([www.tomrasorting.com/mining](http://www.tomrasorting.com/mining)) and Spectra-Map ([www.spectra-map.co.uk](http://www.spectra-map.co.uk)). The spectrometer allowed selection of wavelength bands ( $\pm 0.05$  nm) at 371 wavelengths between 1308 nm and 2405 nm. At each wavelength, measured NIR radiation is acquired using VIEW 2 software (Tomra Sorting Solutions, [www.tomrasorting.com/mining](http://www.tomrasorting.com/mining)). Note that the

**Table 1. Absorption features in NIR of molecular bonds.**

Molecular bond	Absorption features in NIR (nm)	Source
Hydroxyl (-OH, overtone)	1400, 1500	7, 10
Combination of metal-OH		
Al-OH	2160–2220	6,16
Mg-OH	2300–2360	6,16
Fe-OH	2230–2295	5,6
Si-OH	2240	6
Water (H <sub>2</sub> O)	1400, 1900	8, 10
Carbonate (CO <sub>3</sub> <sup>2-</sup> )	2300, 2340, 2360, 1870, 1990, 2155	11

Table 2. Selected silicate, carbonate and oxide group minerals studied in this paper.

Mineral group	Mineral	Formula (mineralweb.com)	Image
	Biotite	$K(Mg,Fe)_3(AlSi_3O_{10})(OH,F)_2$	
	Chrysocolla	$(Cu,Al)_2H_2Si_2O_5(OH)_4 \cdot n(H_2O)$	
	Kaolinite (powdered)	$Al_2Si_2O_5(OH)_4$	
	Muscovite	$KAl_2(Si_3Al)O_{10}(OH,F)_2$	
	Chlorite (clinochore)	$(Mg, Fe)_3Al(Si_3Al)O_{10}(OH)_8$	
	Quartz	$SiO_2$	
Carbonates	Azurite	$Cu_3(CO_3)_2(OH)_2$	
	Calcite	$CaCO_3$	
	Malachite	$Cu_2(CO_3)(OH)_2$	
Oxides	Cuprite	$Cu_2O$	
	Hematite	$Fe_2O_3$	
	Tenorite	$CuO$	

depth of NIR penetration of the sample depends on the opacity of the mineral and can range up to several millimetres.

The measured NIR signal was converted to a reflectance by calibrating the signal by first measuring upper and lower

limits. For the upper limit, denoted  $I_{\text{light}}$ , a highly-reflective board made of aluminium, was scanned. For the lower limit, denoted  $I_{\text{dark}}$ , a scan was made in the absence of near infrared illumination. The near infrared signal,  $I$ , was then converted into a reflectance,  $R$ , as follows:

$$R = \frac{I - I_{\text{dark}}}{I_{\text{light}} - I_{\text{dark}}} \quad (1)$$

Field data are often accompanied by noise self-generated by the sensor and/or the result of physical fluctuation of the surrounding environment.<sup>13</sup> All spectra were smoothed using OriginPro 9.0 software (OriginLab, [www.originlab.com](http://www.originlab.com)) with the Savitzky-Golay<sup>14</sup> method, applying a polynomial of order 2 to a frame size of 10 points.

## Results

The NIR line scanner measured between 8 and 10 pixels across each sample particle. To verify the signals for consistency, multiple scans were compared with each other (for reproducibility) and with relevant library spectra (for accuracy). It was found that NIR spectra of individual mineral particles were highly reproducible. Consequently, only a single spectrum of each mineral is presented and discussed in the next section.

### Oxide group minerals (Figure 1)

Haematite [ $\text{Fe}_2\text{O}_3$ ] absorbs strongly across the 1300–2400 nm NIR wavelength region, displaying low reflectance with no distinctive characteristic absorption features. Cuprite [ $\text{Cu}_2\text{O}$ ] and tenorite [ $\text{CuO}$ ] are secondary copper minerals which display several features above 2150 nm.

### Silicate group minerals (Figure 2)

Chrysocolla [ $(\text{Cu},\text{Al})_2\text{H}_2\text{Si}_2\text{O}_5(\text{OH})_4 \cdot n(\text{H}_2\text{O})$ ] displays absorption features at 1400 nm, 1900 nm and 2240 nm. According

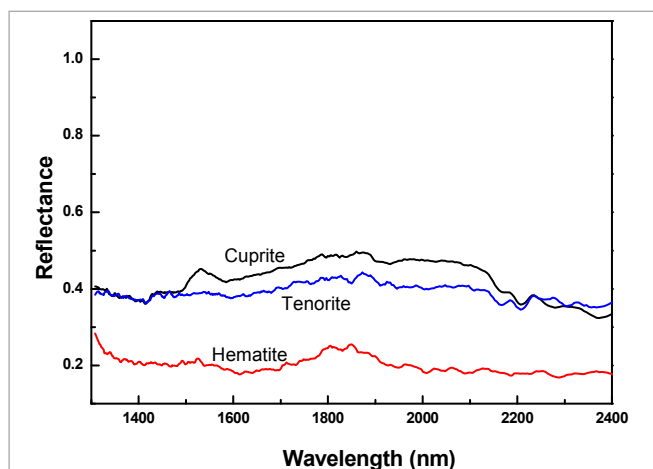


Figure 1. Near InfraRed (NIR) spectra for selected oxide group minerals.

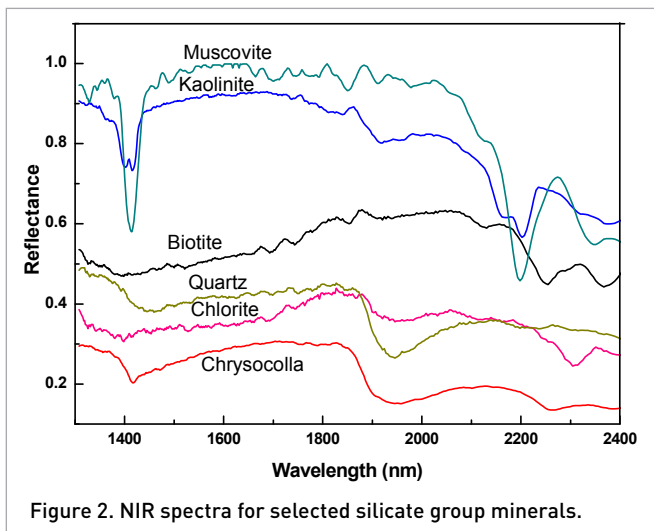


Figure 2. NIR spectra for selected silicate group minerals.

to Clark *et al.*,<sup>15</sup> the intense absorption bands at 1400 nm, 1900 nm and 2240 nm are due to compositional water in chrysocolla.

The NIR spectrum of biotite [ $\text{K}(\text{Mg}, \text{Fe})_3\text{AlSi}_3\text{O}_{10}(\text{OH})_2$ ] shows two bands centred at 2260 nm and 2370 nm, which could be assigned to Fe–OH, and Mg–OH, respectively. The absence of an –OH band around 1400 nm could be due to the presence of iron in the sample as analysed by XRF. Clark<sup>5</sup> also observed that iron has masking effects on the 1400 nm –OH band of the biotite NIR spectrum.

Muscovite [ $\text{KAl}_3\text{Si}_3\text{O}_{10}(\text{OH})_3$ ] has an overall high reflectance which makes the –OH band near 1400 nm and an Al–OH band around 2200-nm stand out. This was also observed by Goetz *et al.*<sup>16</sup> The sample also displays a weak water and hydroxyl band near 1900 nm and 2350 nm, respectively.

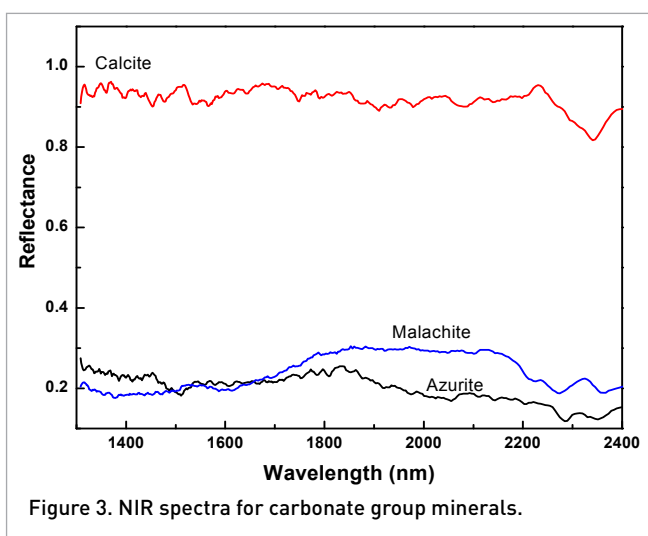
Kaolinite [ $\text{Al}_2\text{Si}_2\text{O}_5(\text{OH})_4$ ] has a similar spectrum to muscovite, with the main absorption features observed as doublets. According to Goetz *et al.*<sup>16</sup> the doublets are caused by differences in the location of –OH in the mineral. The 2150 nm feature can be assigned to Si–OH while the feature near 2190 nm is due to Al–OH.<sup>6</sup> The doubling of features is the main distinguishing characteristic between kaolinite and muscovite.

Contrary to the Al–OH bands in muscovite and kaolinite, chlorite [ $(\text{Mg}, \text{Fe})_5\text{Al}(\text{Si}_3\text{Al})\text{O}_{10}(\text{OH})_8$ ] displays distinct Mg–OH features near 2300 nm, with –OH and water bands near 1400 nm and 1950 nm. The presence of water in quartz [ $\text{SiO}_2$ ] absorbs some NIR. Quartz water bands are pronounced at 1400 nm and 1950 nm.

### Carbonate group minerals (Figure 3)

Calcite [ $\text{CaCO}_3$ ] has a NIR spectrum which trends towards lower reflectance at higher wavelengths. In addition, distinct features are visible above 1600 nm. The most distinct feature is observed near 2340 nm.

According to Clark *et al.*,<sup>15</sup> all the absorption bands (2360 nm and 2270 nm) observed in malachite are as a result of a  $\text{CO}_3^{2-}$



radical, with some  $-OH$  contribution to the 2360 nm feature. At lower wavelengths, a comparison with the calcite spectrum suggests that the reflectance is attenuated.

Azurite  $[Cu_3(CO_3)_2(OH)_2]$  retains a little of the downward trend observed in the spectrum of calcite but lacks the distinct features of the latter.

## Towards a sorting strategy

In view of the limited crustal abundance of copper and the high demand for copper,<sup>4</sup> processing of low grade ore is increasingly common. A complication is the disseminated nature of copper, with many secondary minerals, for example, cuprite, chrysocolla, azurite, malachite, only containing small quantities of copper.<sup>17</sup> This adds cost to the recovery of copper and

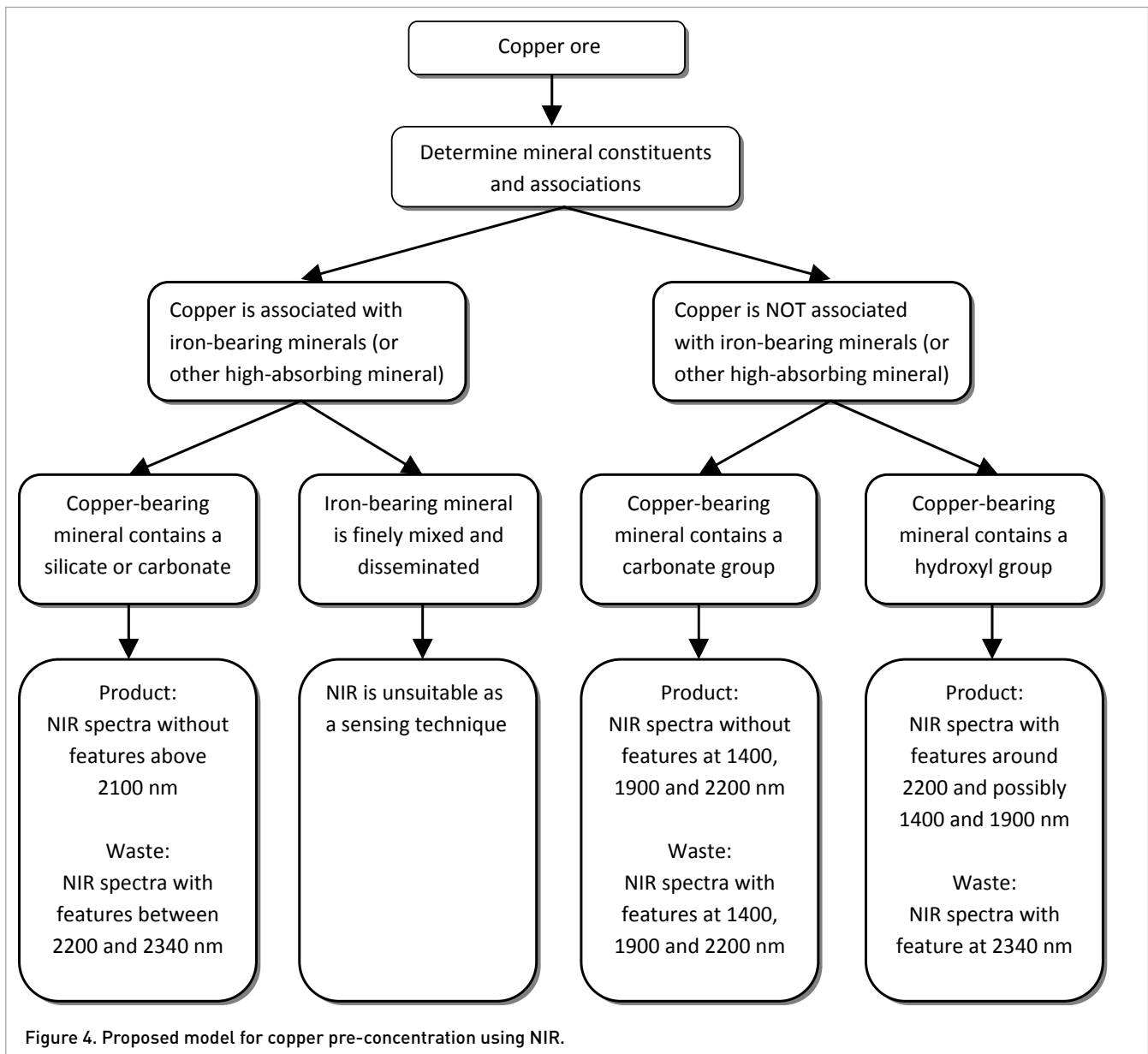
makes early separation of waste from run-of-mine material imperative.

Analysis of NIR spectra has shown that secondary copper-bearing minerals can be distinguished from waste minerals (calcite, kaolinite, chlorite, muscovite etc.) based on distinctive characteristic absorption features of their functional groups ( $-OH$ ,  $CO_3^{2-}$ ). The above analysis also shows that no two minerals display completely identical absorption spectra. In practice, some features may be common to more than one mineral. For example, muscovite and kaolinite share features in several wavelength regions. However, kaolinite exhibits double peaks to muscovite's single peak. Some mineral spectra may contain features relating to the same functional group at a different wavelength. An example is the spectra of malachite and calcite: while calcite displays strong carbonate features near 2340 nm, carbonates in malachite show absorption at 2270 nm and 2360 nm. This also applies to chrysocolla and muscovite and chlorite and chrysocolla. In the case of chlorite and chrysocolla, the difference in location of the  $Mg-OH$  band in chlorite can be used to separate chlorite-dominant minerals from chrysocolla-rich copper ore.

Ores are often heterogeneous, with multiple minerals occurring side-by-side in run-of-mine rocks. The selectivity improves if the rocks are crushed prior to sorting, with the minimum particle size being determined by the mechanism used to separate the ore from waste after sensor-based classification. In practice, this lower limit to the particle size, roughly 5 mm, could imply that crushed ore particles will still contain a combination of minerals. As a result, the NIR spectrum may not correspond to any of the minerals or just to the spectrum of the dominant mineral in terms of absorption. This implies that sorting requires focusses on the reflectance in specific ranges of the NIR spectrum. The options for pre-concentration of copper-bearing minerals are developed in Figure 4.

Table 3. Absorption features of selected minerals (between 1300 nm and 2500 nm).

Group	Mineral	Molecule absorption feature, nm		
		$-OH$	$H_2O$	$CO_3^{2-}$
Silicate	Biotite	2260, 2370	1900	—
	Chrysocolla	1400, 2240	1900	—
	Kaolinite	1400, 2150, 2190	1900	—
	Muscovite	1400, 2200, 2350	1900	—
	Chlorite	1400, 2300	1900	—
	Quartz	1400	1900	—
Carbonate	Azurite	1500	—	2040, 2270, 2340
	Calcite	—	—	2340
	Malachite	2360	—	2270, 2360
Oxide	Cuprite	1400, 2200, 2370	1900	—
	Hematite	Does not display absorption feature.		
	Tenorite	1400, 2150, 2210	—	—



## Conclusions

This paper describes an approach to analysing potential applications of NIR in sensor-based sorting of minerals. Analysis of selected typical minerals found in hydrothermally-formed ores shows that NIR-active functional groups ( $-OH$ ,  $H_2O$ , and  $CO_3^{2-}$ ) present in these minerals display characteristic diagnostic absorption features. Copper-bearing minerals such as chrysocolla (phyllosilicates), azurite and malachite (carbonates), cuprite and tenorite (oxides) display distinctive characteristic absorption features which make separation of hydroxyl ( $-OH$ ) and carbonate ( $CO_3^{2-}$ ) minerals feasible from the ore minerals. This can form the basis for definition of a sorting process using a NIR sensor.

## Acknowledgement

The Nigerian Government, through the academic staff support scheme of the Tertiary Education Trust Fund (TETF) and the Management of Nasarawa State University, Keffi, are acknowledged for providing financial support for this research.

## References

1. J.W. Gaydon, H.J. Glass and R.D. Pascoe, "Method for near infrared sensor-based sorting of a copper ore", *J. Near Infrared Spectrosc.* **17**, 177 (2009). doi: [10.1255/jnirs.849](https://doi.org/10.1255/jnirs.849)

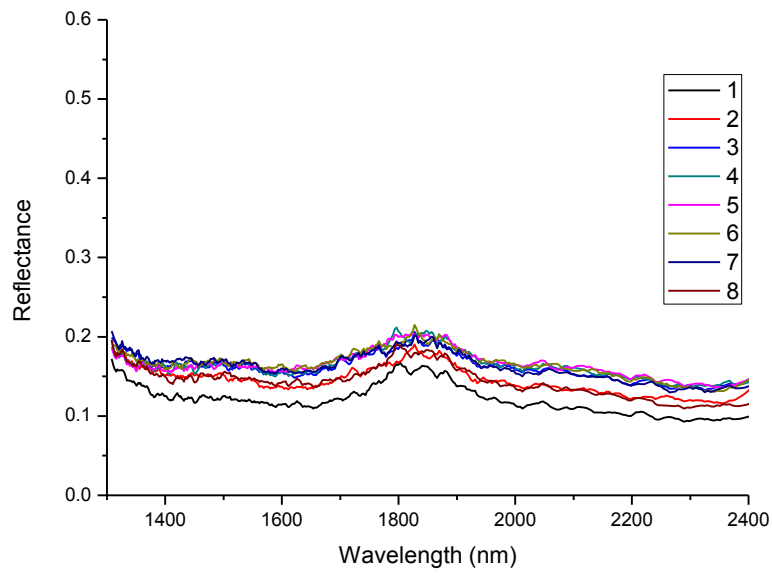
2. G.R. Hunt, "Near-infrared (1.3–2.4  $\mu\text{m}$ ) spectra of alteration minerals; potential for use in remote-sensing", *Geophysics* **44**(12), 1974 (1979). doi: [10.1190/1.1440951](https://doi.org/10.1190/1.1440951)
3. J. Rakovan, "A word to the wise: hypogene and supergene", *Rocks Miner.* **78**(6), 419 (2003). doi: [10.1080/00357529.2003.9926759](https://doi.org/10.1080/00357529.2003.9926759)
4. R.B. Gordon, M. Bertram and T.E. Graedel, "Metal stocks and sustainability", *Proc. Natl. Acad. Sci. USA* **103**(5), 1209 (2006). doi: [10.1073/pnas.0509498103](https://doi.org/10.1073/pnas.0509498103)
5. R.N. Clark, "Reflectance spectra", in *Rock Physics and Phase Relations: A Handbook of Physical Constants*, Ed by T.J. Ahrens. American Geophysical Union, Washington, USA, pp. 178–188 (1995).
6. G.R. Hunt, "Spectral signatures of particulate minerals in the visible and near-infrared", *Geophysics* **42**(3), 501 (1977). doi: [10.1190/1.1440721](https://doi.org/10.1190/1.1440721)
7. R.N. Clark, T.V.V. King, M. Klejwa, G.A. Swayze and N. Vergo, "High spectral resolution reflectance spectroscopy of minerals", *J. Geophys. Res.* **95**(B8), 12653 (1990). doi: [10.1029/JB095iB08p12653](https://doi.org/10.1029/JB095iB08p12653)
8. R.D. Aines and G.R. Rossman, "Water in minerals? A peak in the infrared", *J. Geophys. Res.* **89**(B6), 4059 (1984). doi: [10.1029/JB089iB06p04059](https://doi.org/10.1029/JB089iB06p04059)
9. F. Van der Meer, "Spectral reflectance of carbonate mineral mixtures and bidirectional reflectance theory: Quantitative analysis techniques for application in remote sensing", *Rem. Sens. Rev.* **13**, 67 (1995).
10. G.R. Hunt and J.W. Salisbury, "Visible and near infrared spectra of minerals and rocks, I. Silicates minerals", *Mod. Geol.* **1**, 283 (1970).
11. G.R. Hunt and J.W. Salisbury, "Visible and near-infrared spectra of minerals and rocks: II. Carbonates", *Mod. Geol.* **2**, 23 (1971).
12. B. Curtis, "Developing automated copper ore processing using NIR analysis and XRD", *Adv. Mater. Proc.* **170**(2), 24 (2012).
13. E. Stark and K. Luchter, "NIR instrumentation technology", *NIR news* **16**(7), 13–16 (2005).
14. A. Savitzky and M.J.E. Golay, "Smoothing and differentiation of data by simplified least squares procedures", *Anal. Chem.* **36**, 1627 (1964). doi: [10.1021/ac60214a047](https://doi.org/10.1021/ac60214a047)
15. R.N. Clark, G.A. Swayze, R. Wise, K.E. Livo, T.M. Hoefen, R.F. Kokaly and S.J. Sutley, "USGS Digital Spectral Library splib06a", *US Geological Survey, Data Series*, 231 (2007).
16. A.F.H. Goetz, B. Curtiss and D.A. Shiley, "Rapid gangue mineral concentration measurement over conveyors by NIR reflectance spectroscopy", *Miner. Eng.* **22**(5), 490 (2009). doi: [10.1016/j.mineng.2008.12.013](https://doi.org/10.1016/j.mineng.2008.12.013)
17. F. Habashi, *Handbook of Extractive Metallurgy*, Vol. II: *Primary Metals, Secondary Metals, Light Metals*. Wiley-VCH Verlag, Weinheim, Germany.



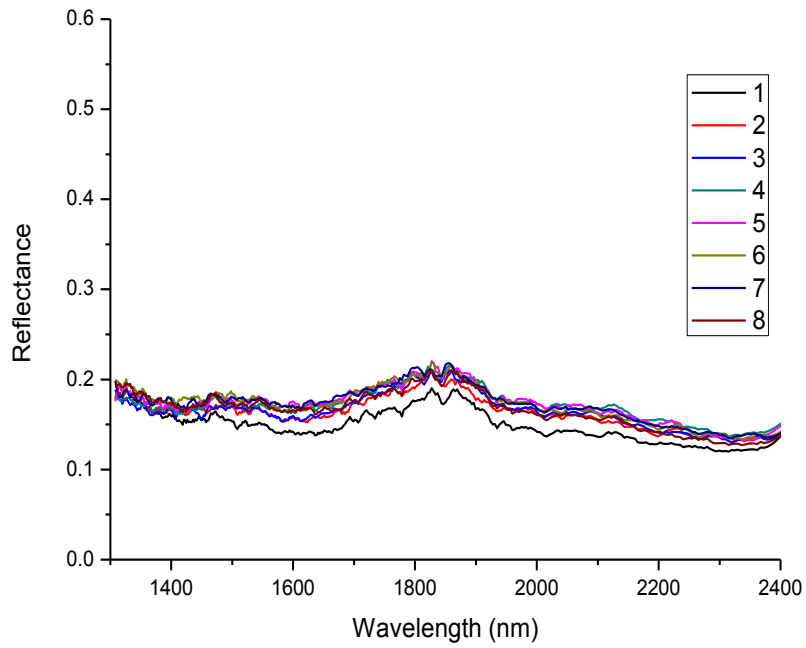


## Appendix 8.1 a. NIR spectra of splits B1 samples

### Sample 1

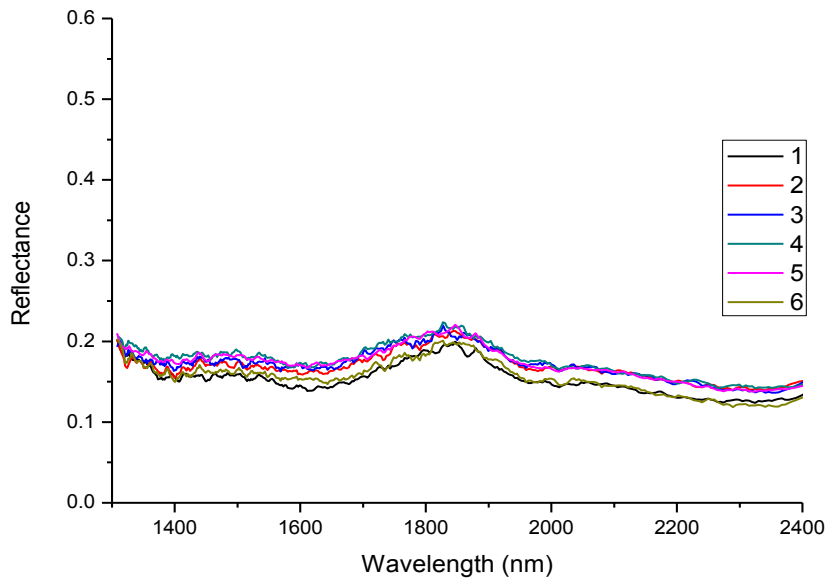


### Sample 1 sector A

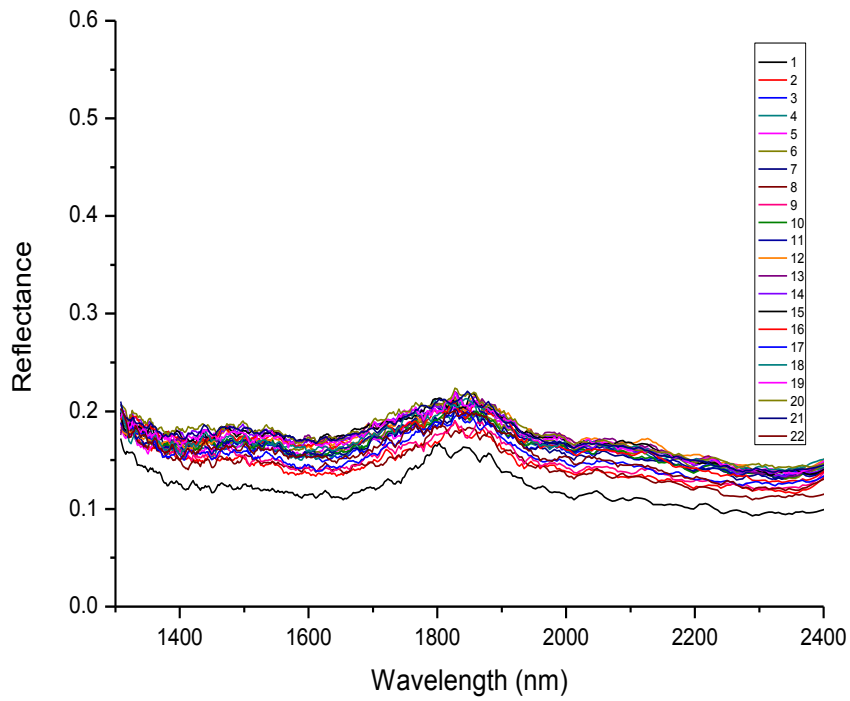


### Sample 1 sector B

### Sample 1

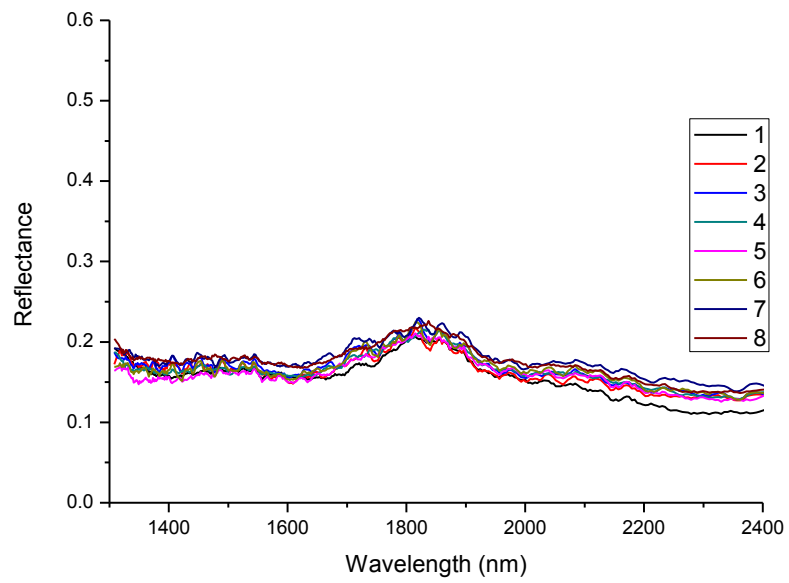


### Sample 1 sector C

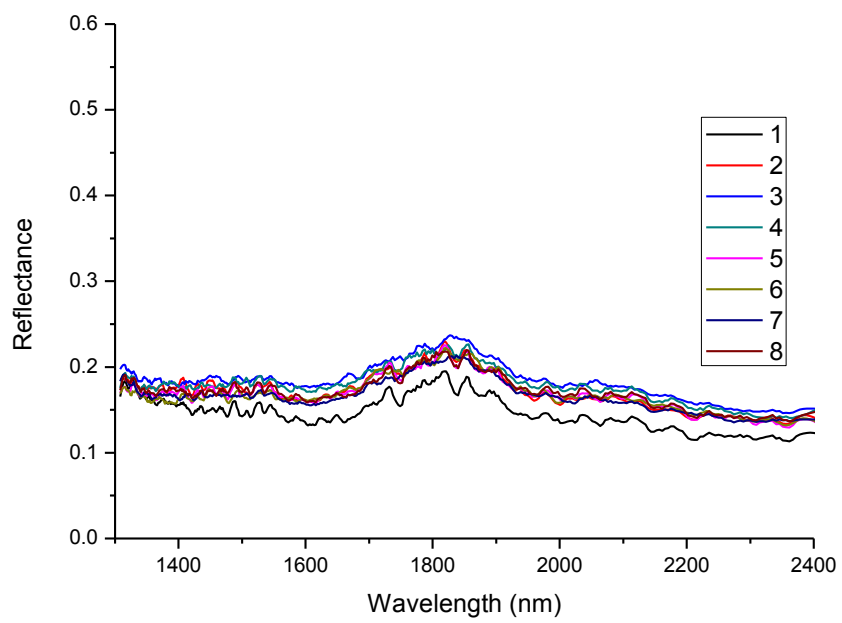


### Sample 1 COMBINED

## Sample 2

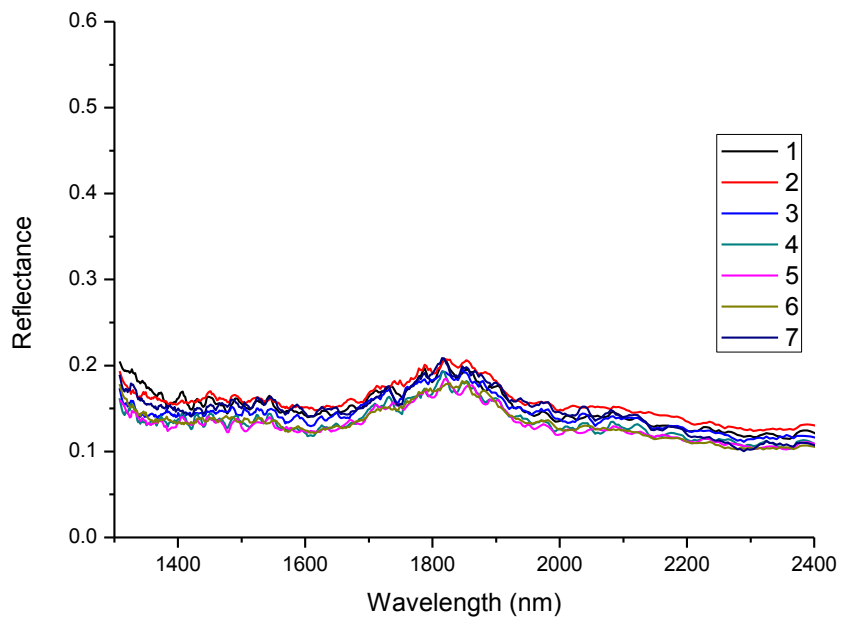


## Sample 2 sector A

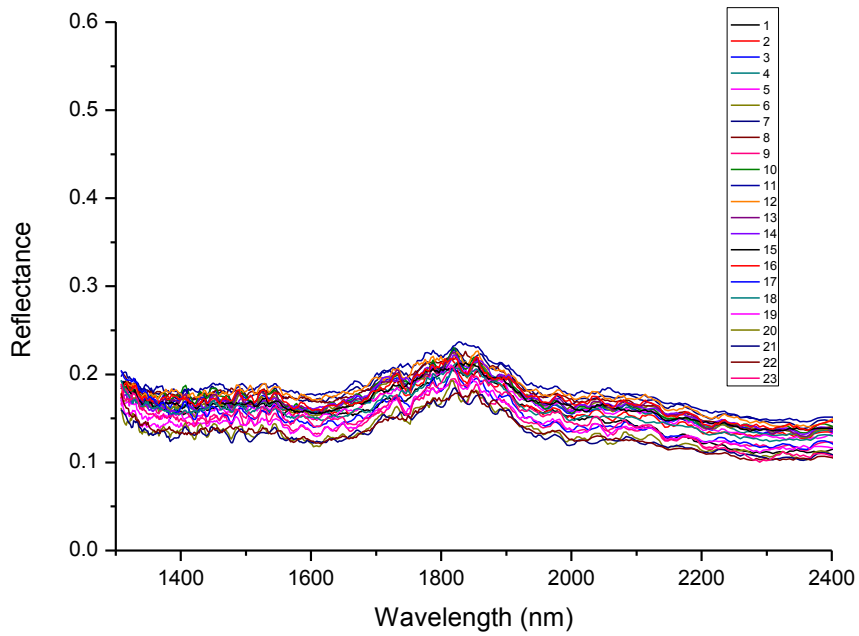


## Sample 2 sector B

## Sample 2

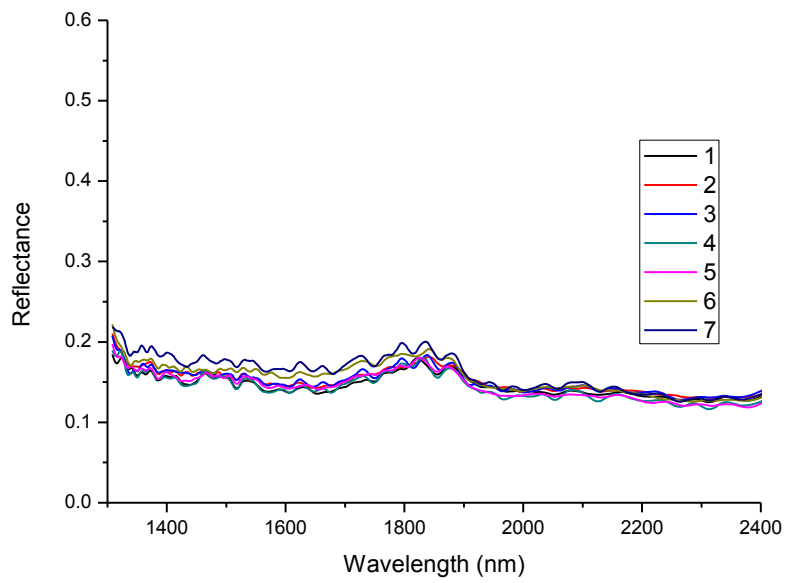


## Sample 2 sector C

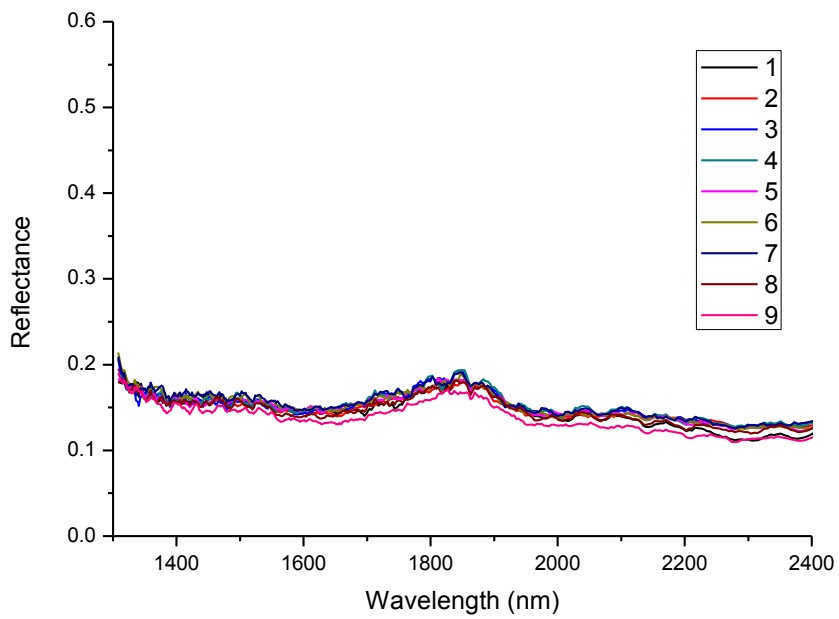


## Sample 2 COMBINED

### Sample 3

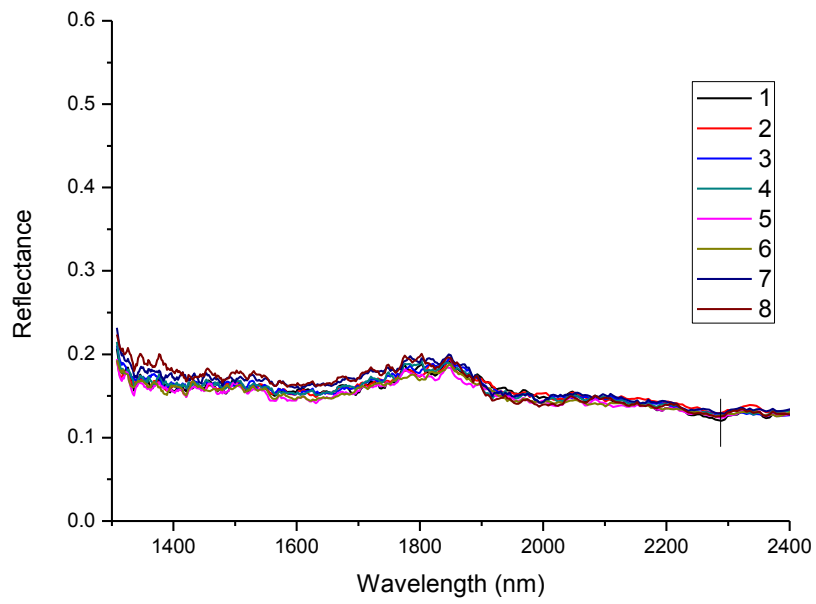


### Sample 3 sector A

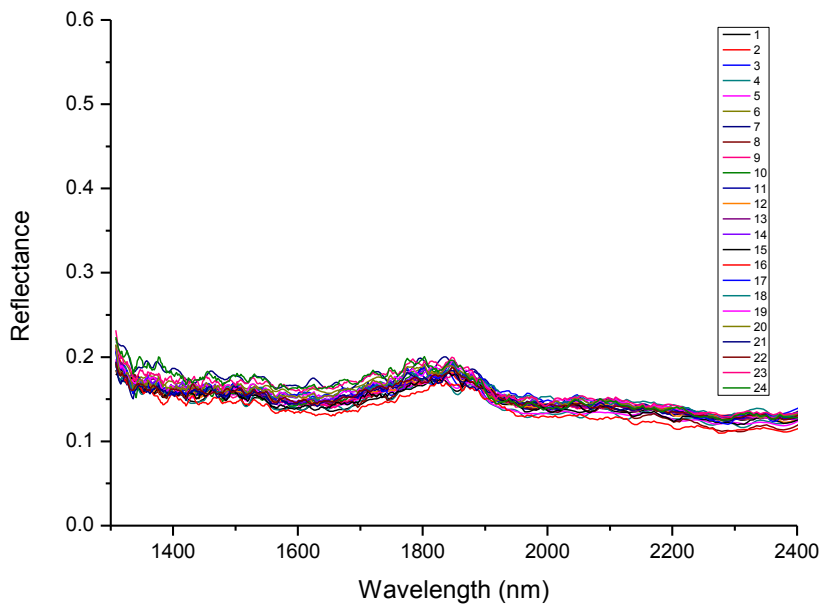


### Sample 3 sector B

### Sample 3

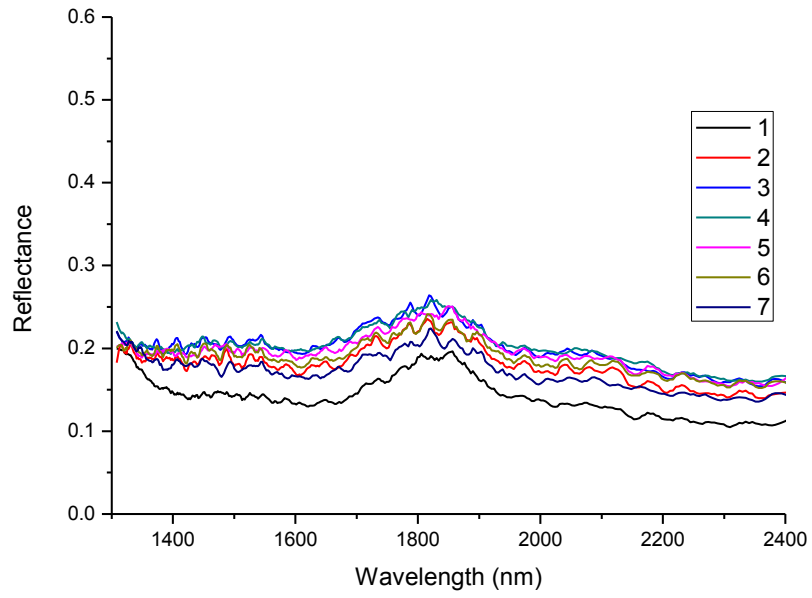


### Sample 3 sector C

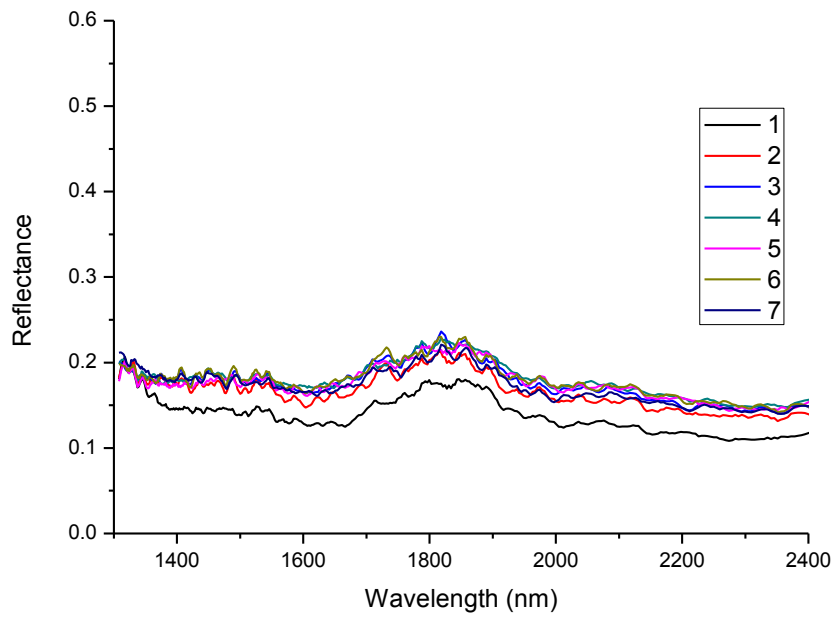


### Sample 3 combined

### Sample 4



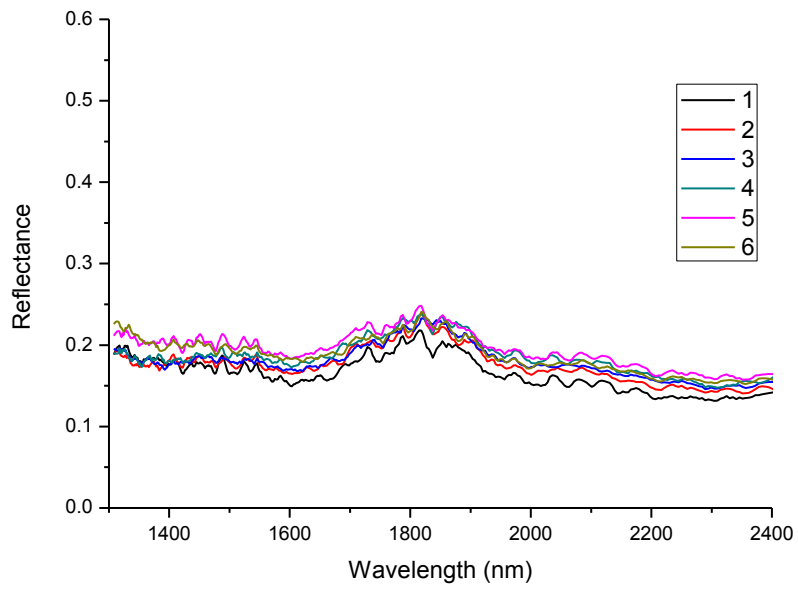
### Sample 4 sector A



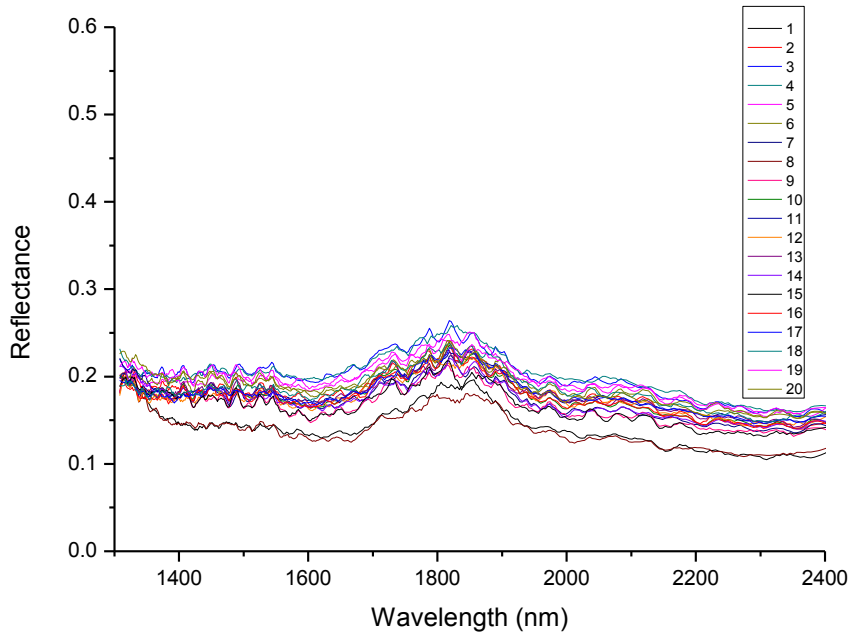
### Sample 4 sector B



### Sample 4

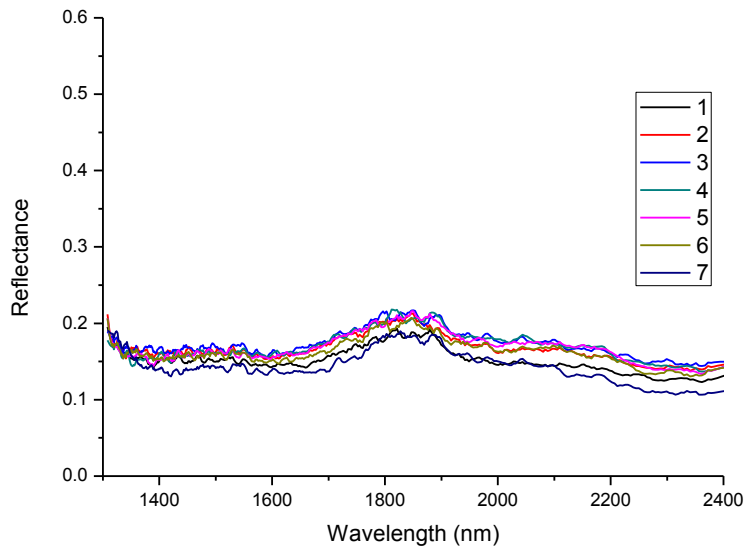


### Sample 4 sector C

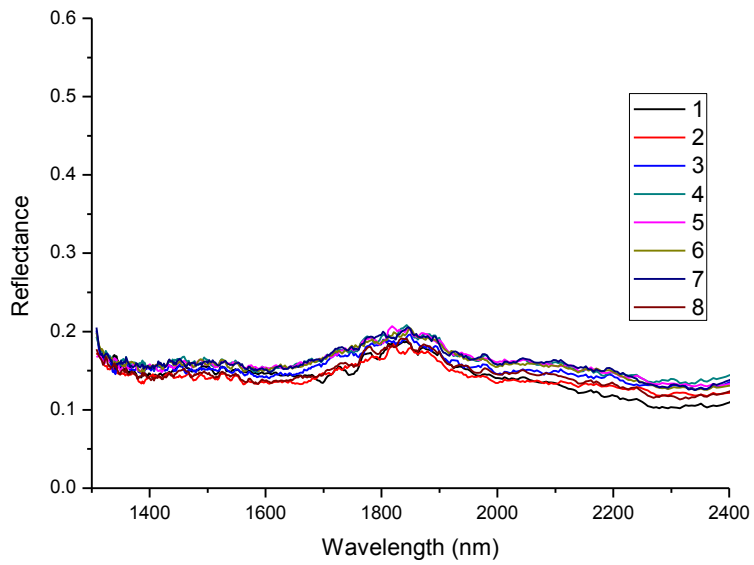


### Sample 4 combined

### Sample 5

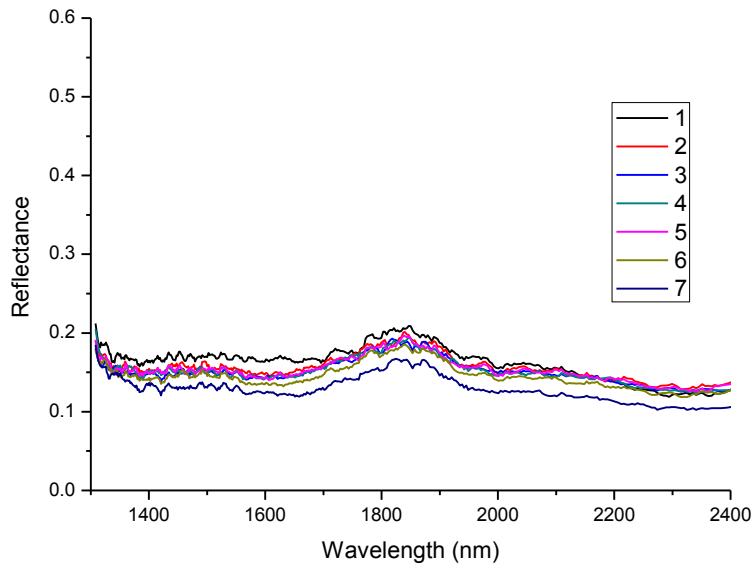


### Sample 5 sector A

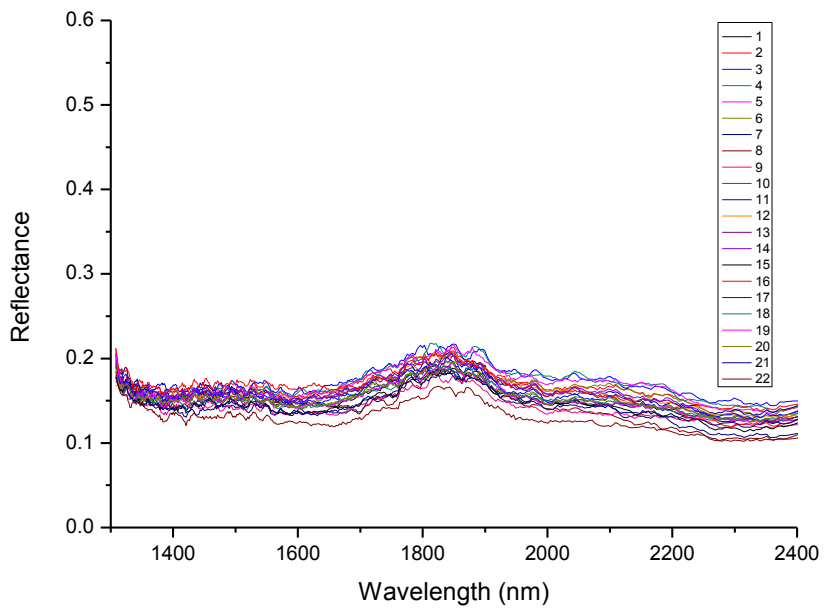


### Sample 5 sector B

### Sample 5

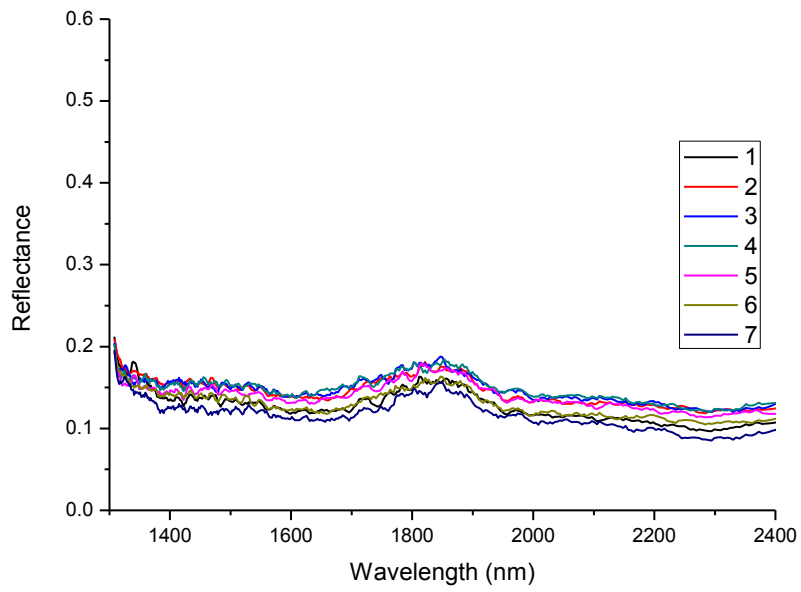


### Sample 5 sector C

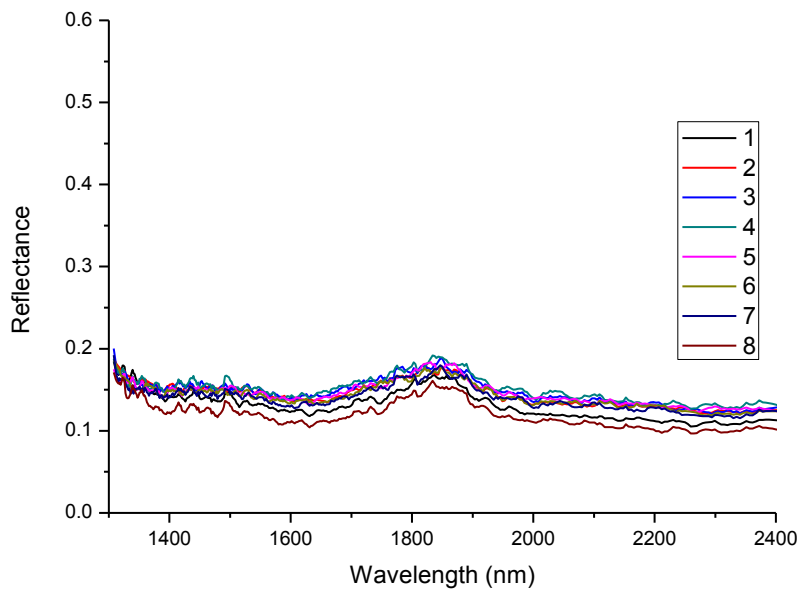


### Sample 5 combined

### Sample 6

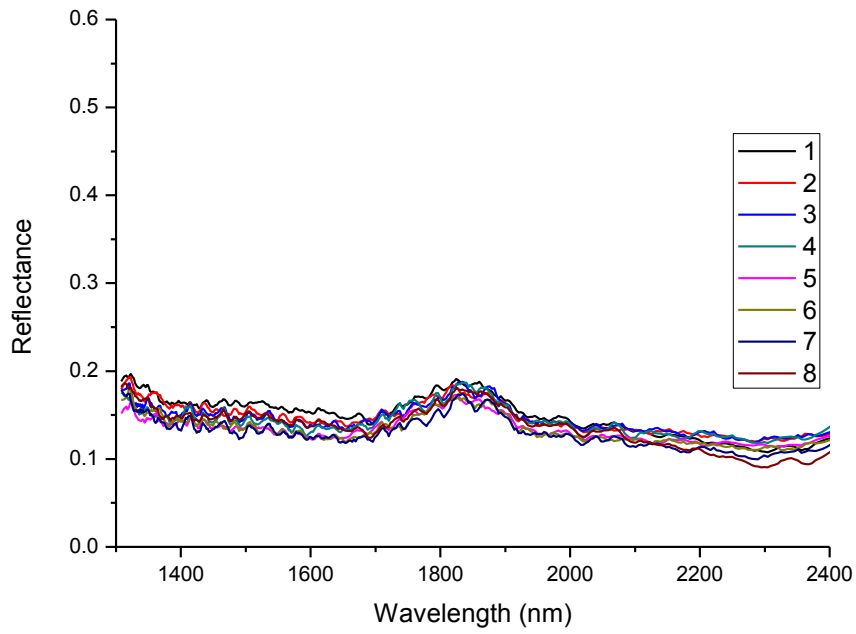


### Sample 6 sector A

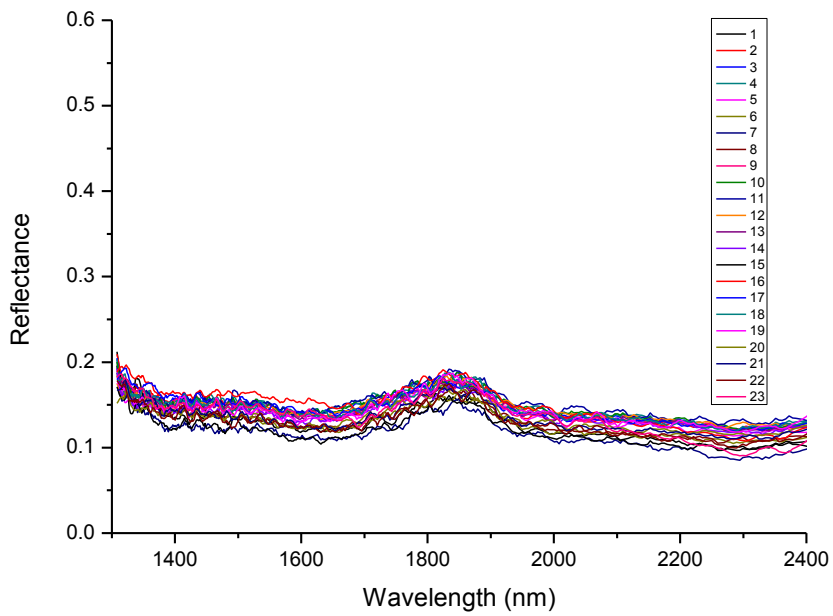


### Sample 6 sector B

### Sample 6

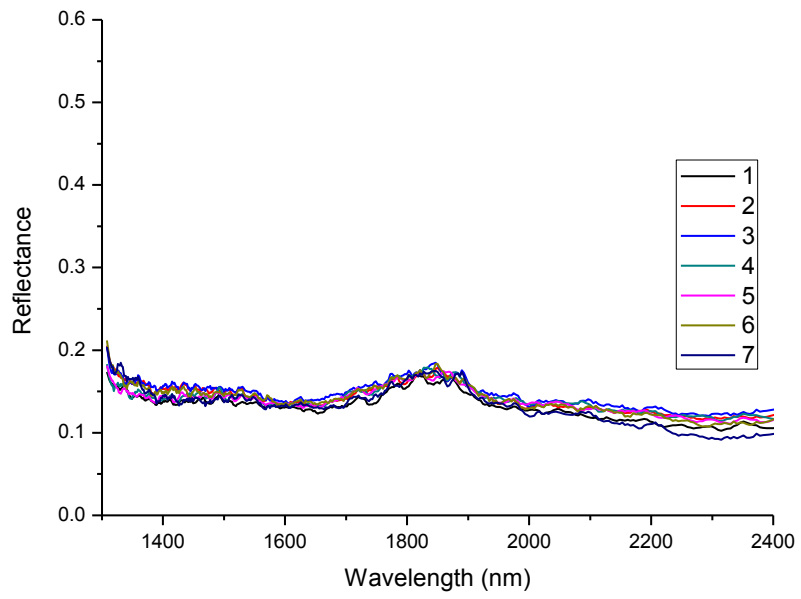


### Sample 6 sector C

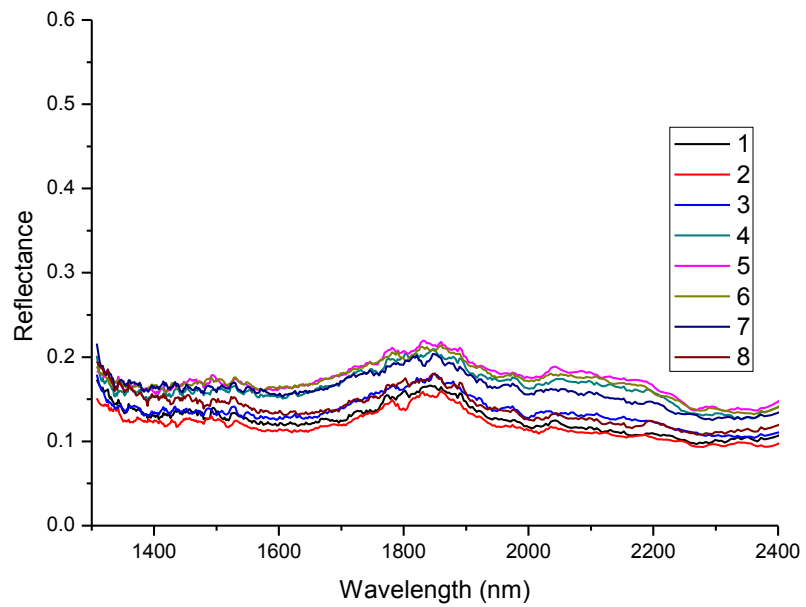


### Sample 6 combined

### Sample 7

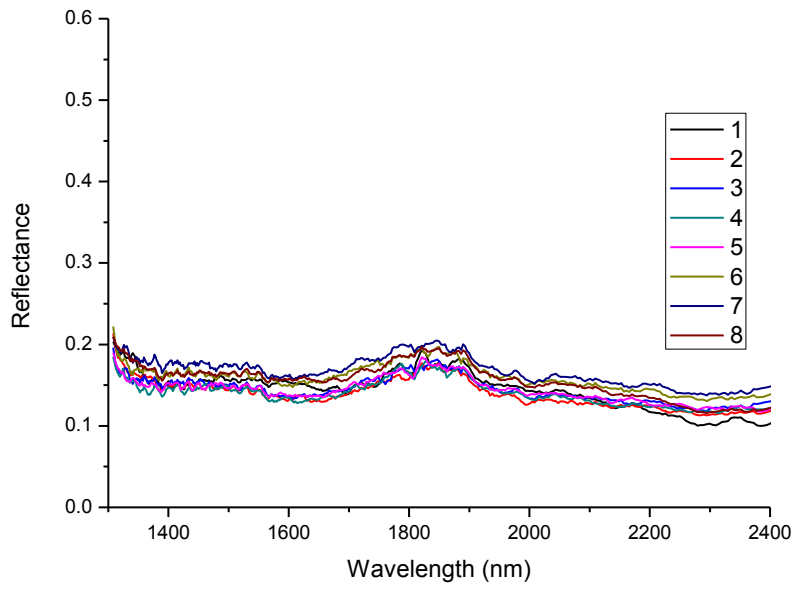


### Sample 7 sector A

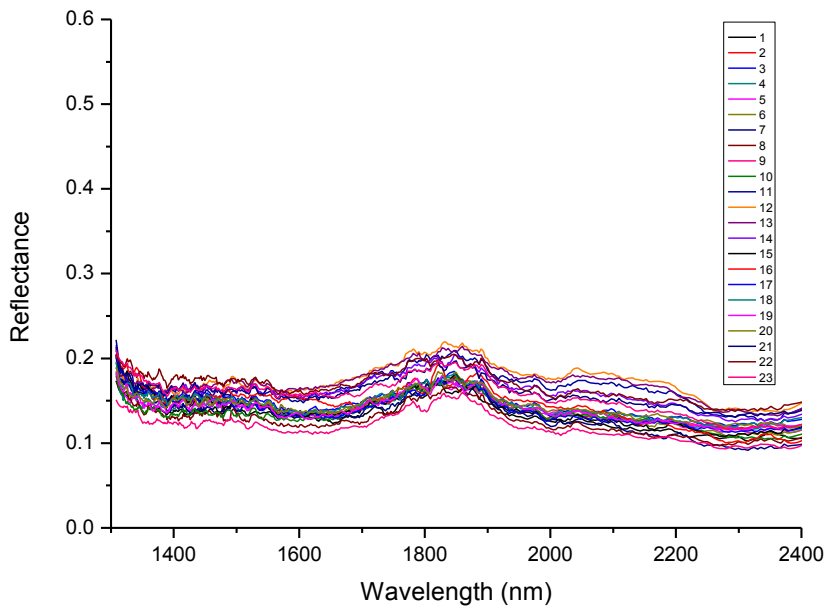


### Sample 7 sector B

### Sample 7

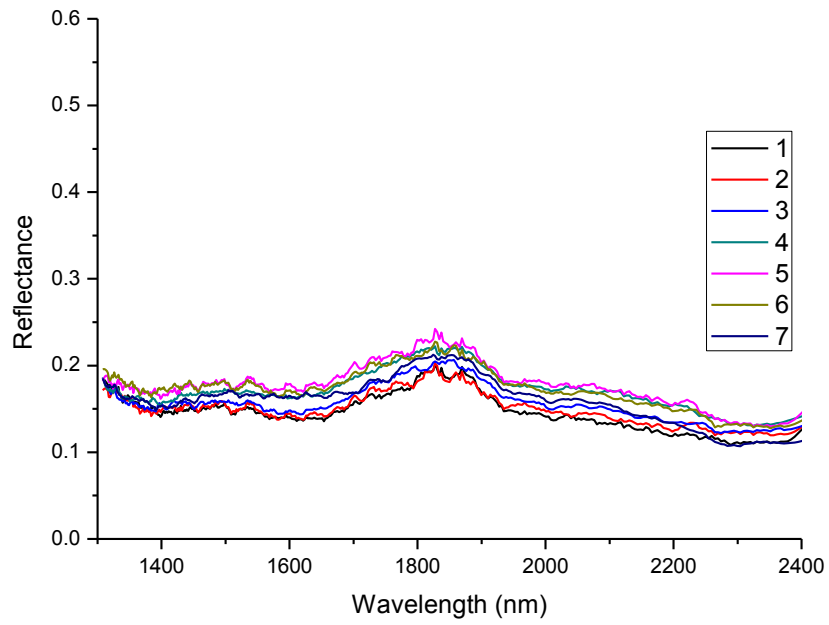


### Sample 7 sector C

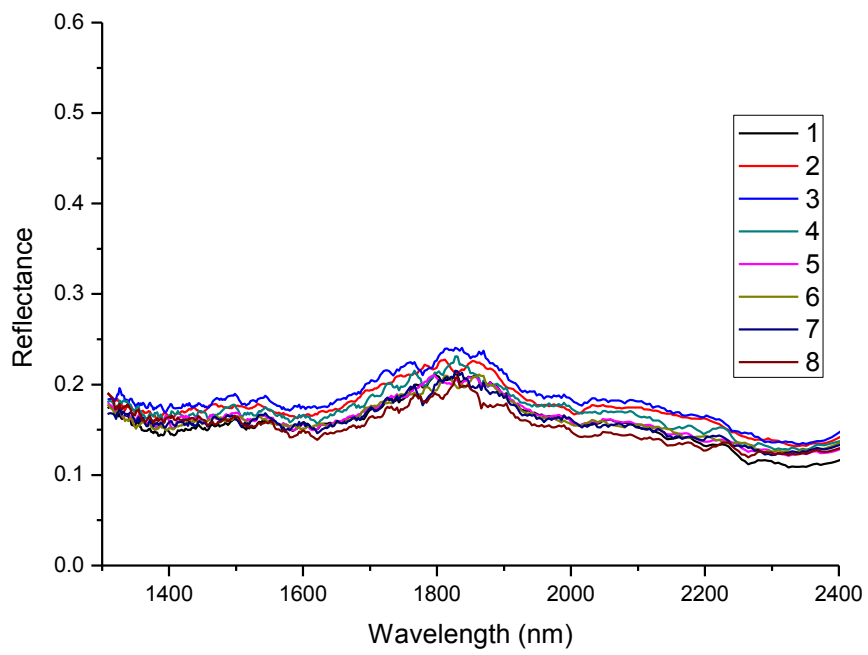


### Sample 7 combined

### Sample 8



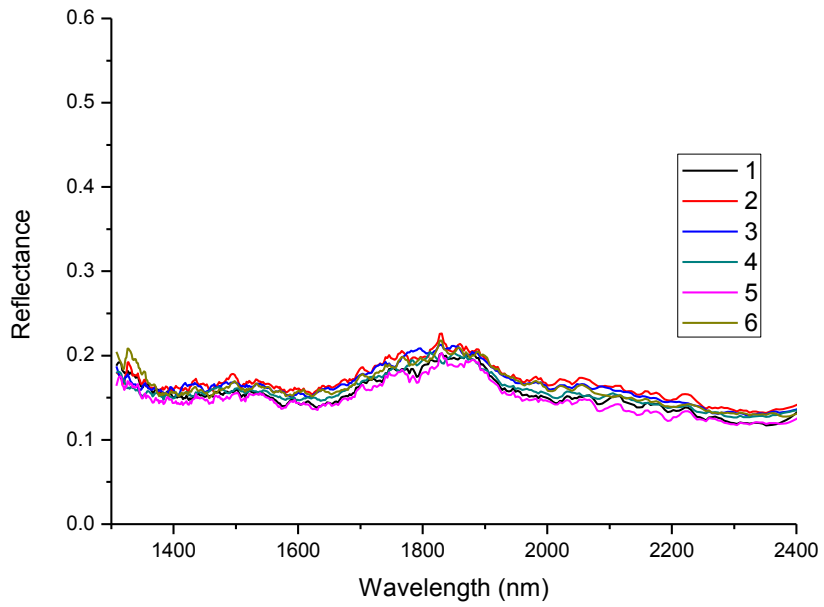
### Sample 8 sector A



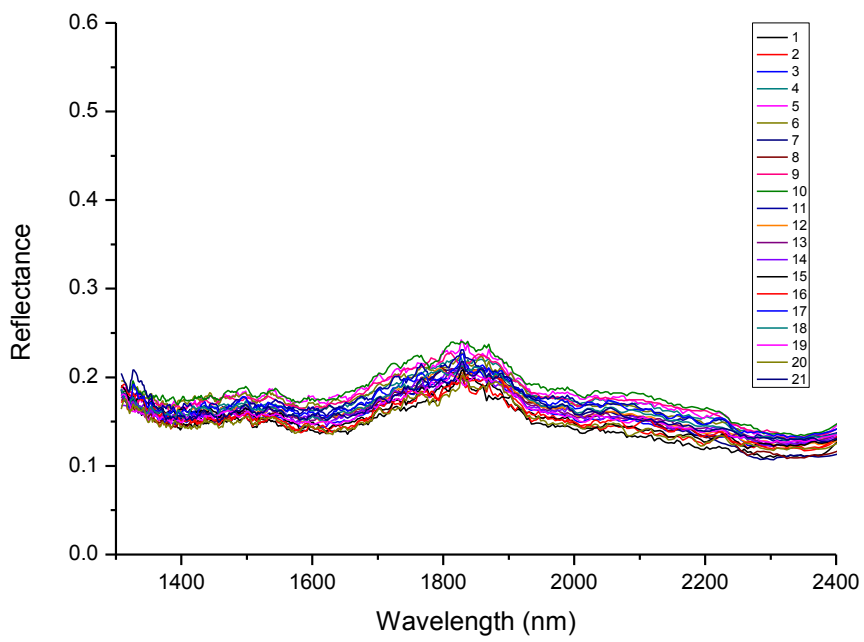
### Sample 8 sector B



### Sample 8

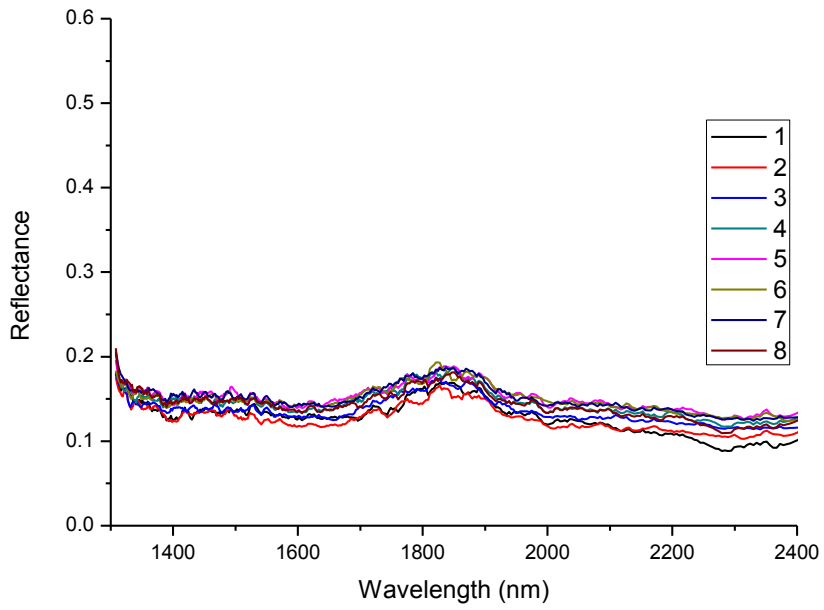


### Sample 8 sector C

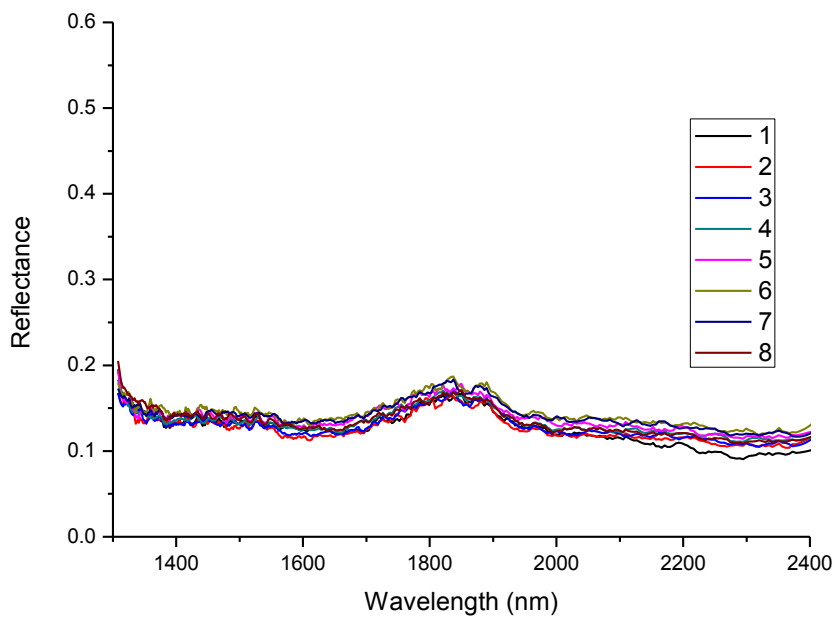


### Sample 8 combined

### Sample 9

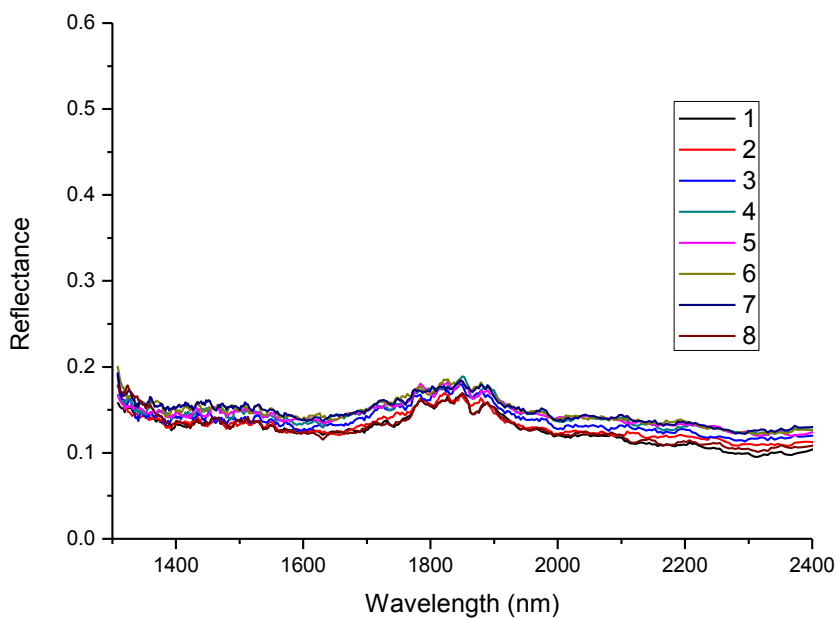


### Sample 9 sector A

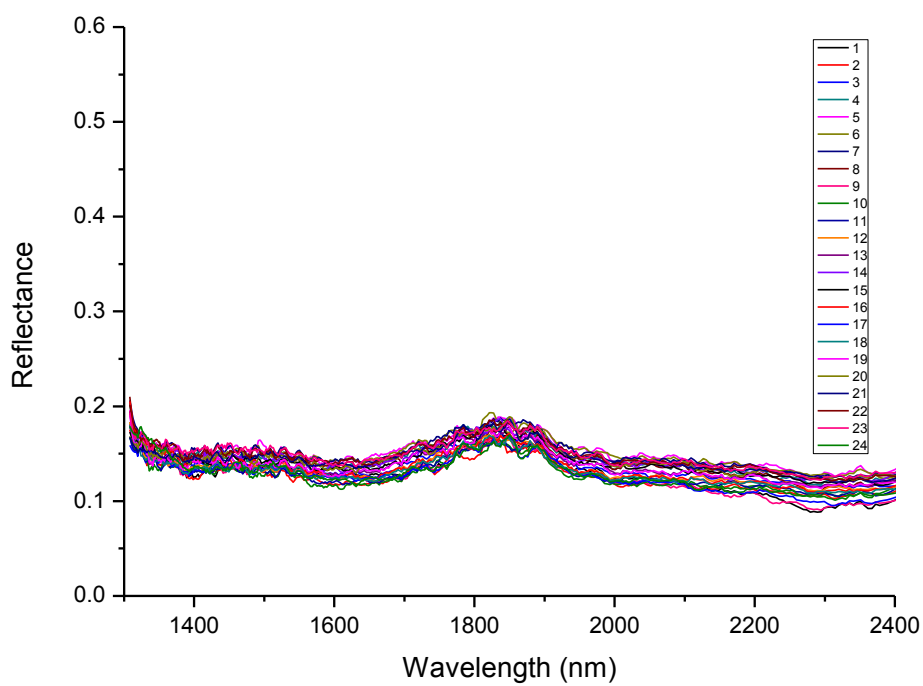


### Sample 9 sector B

### Sample 9

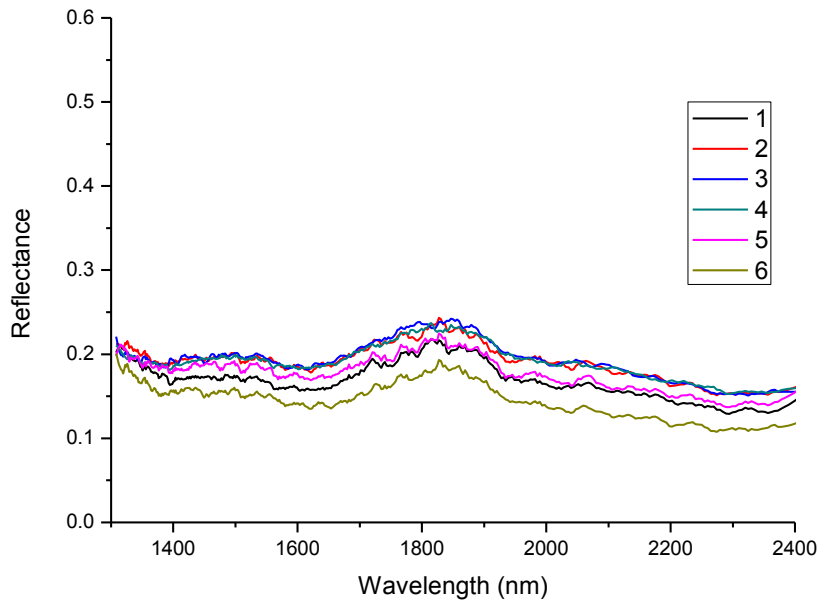


### Sample 9 sector C

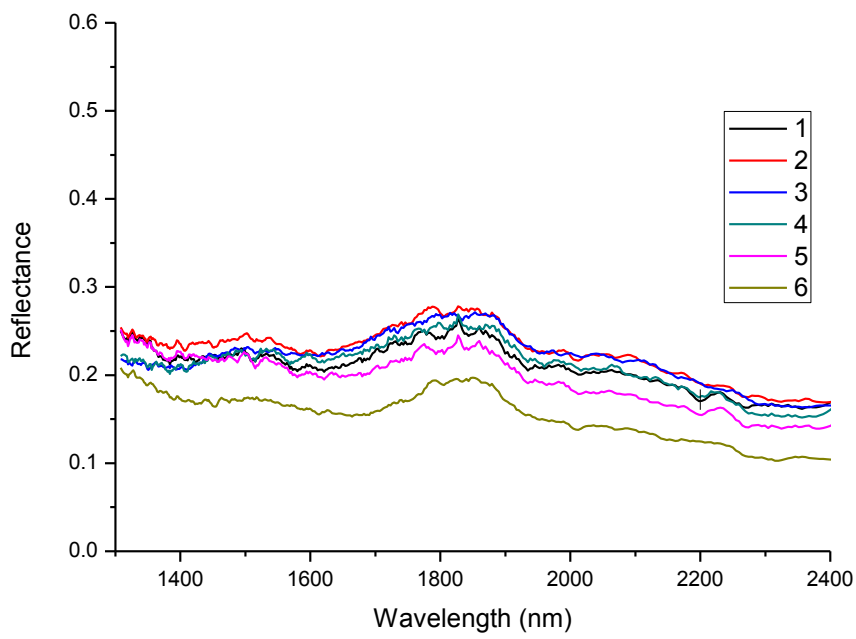


### Sample 9 combined

### Sample 10

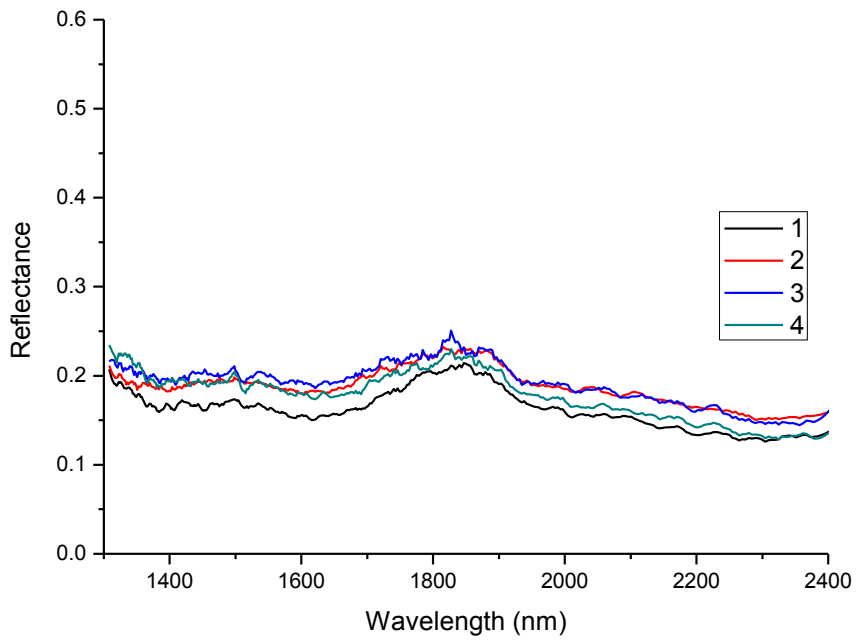


### Sample 10 sector A

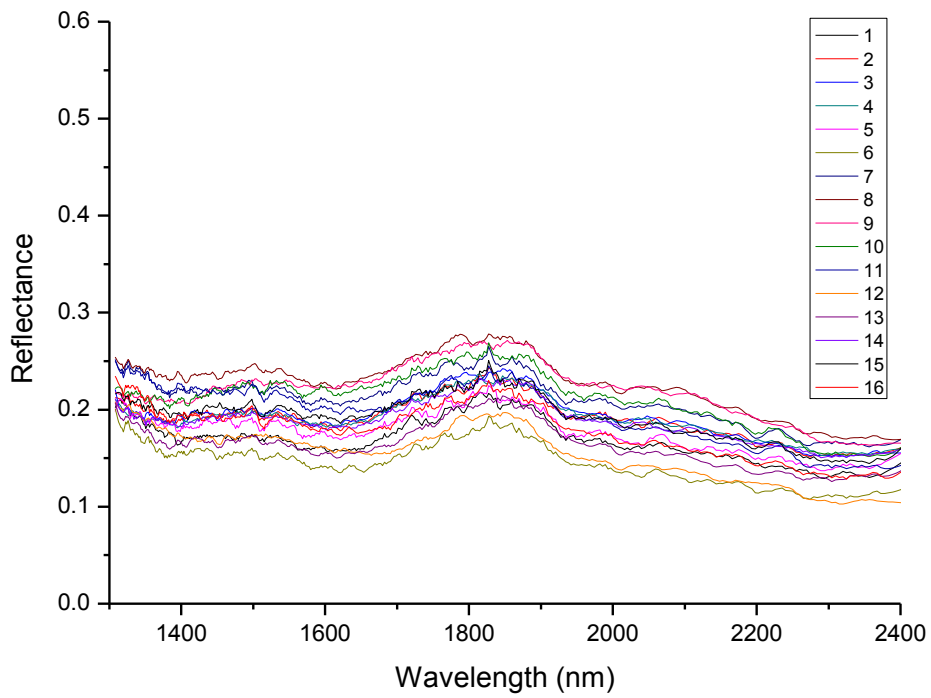


### Sample 10 sector B

### Sample 10

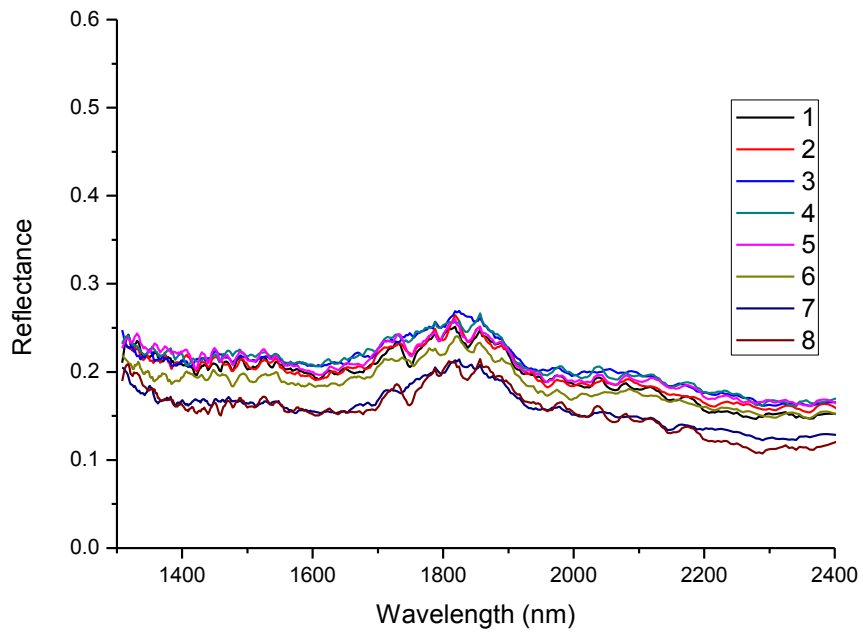


### Sample 10 sector C

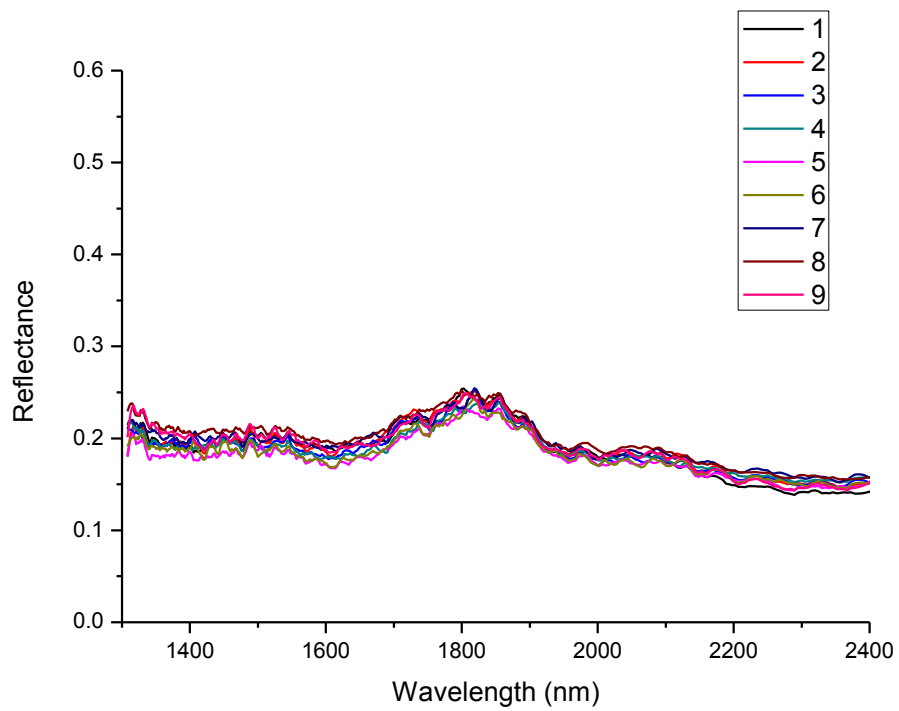


### Sample 10 combined

### Sample 11

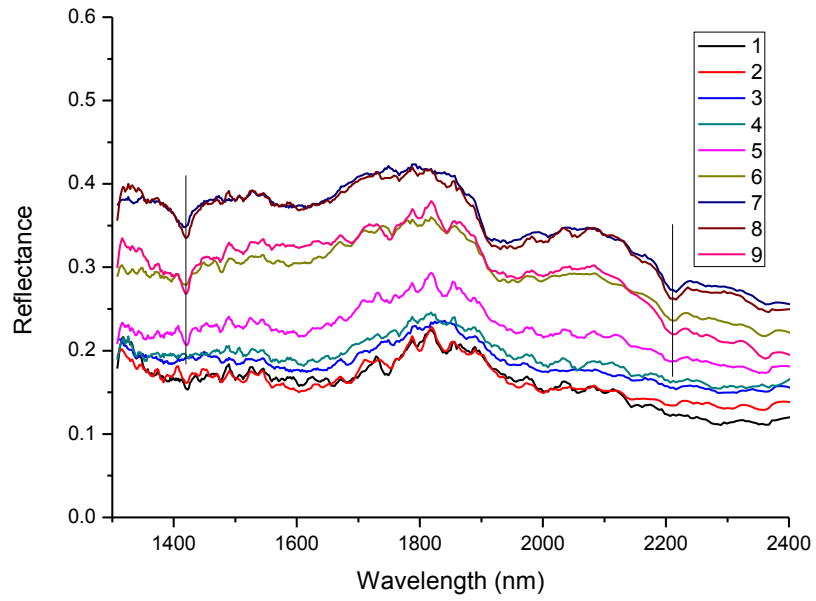


### Sample 11 sector A

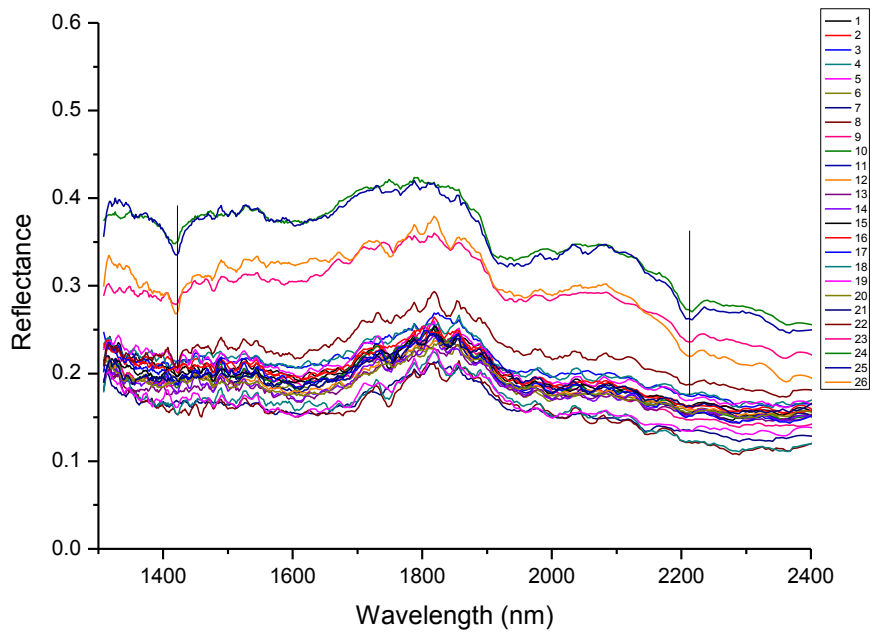


### Sample 11 sector B

### Sample 11

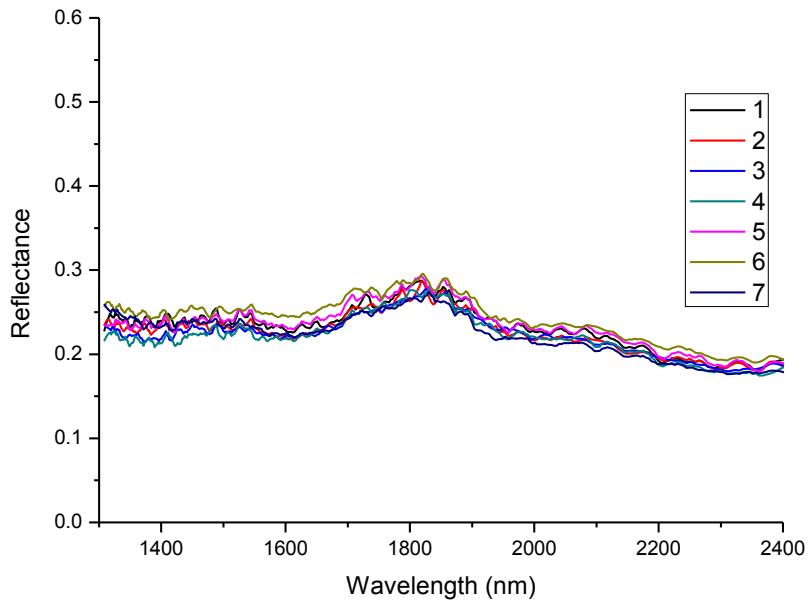


### Sample 11 sector C

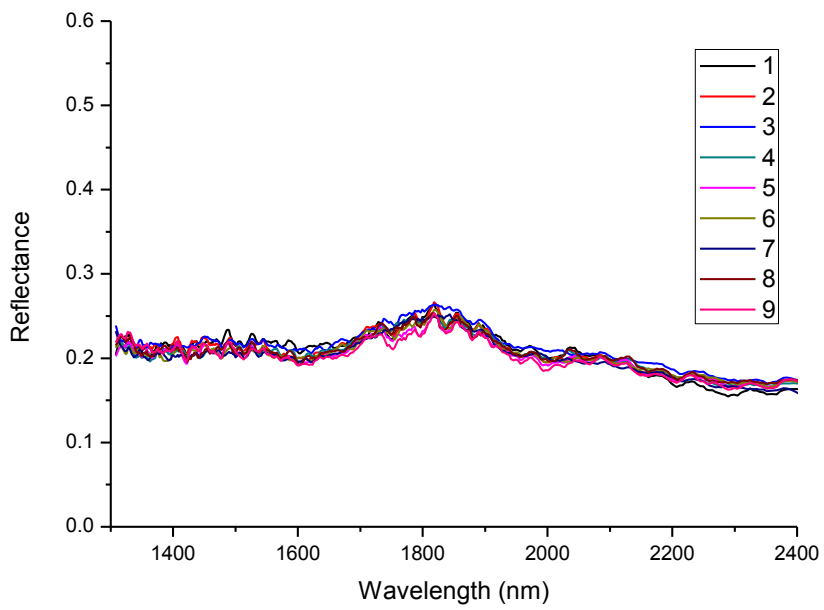


### Sample 11 combined

### Sample 12



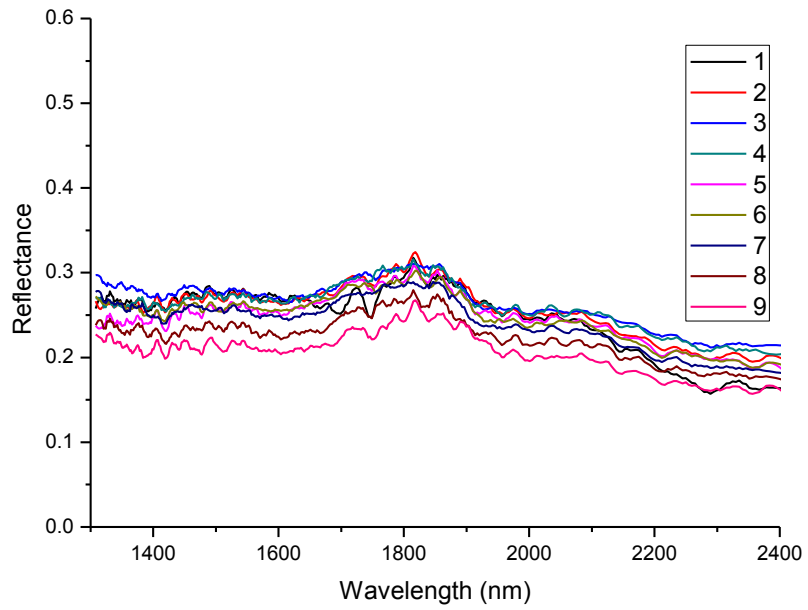
### Sample 12 sector A



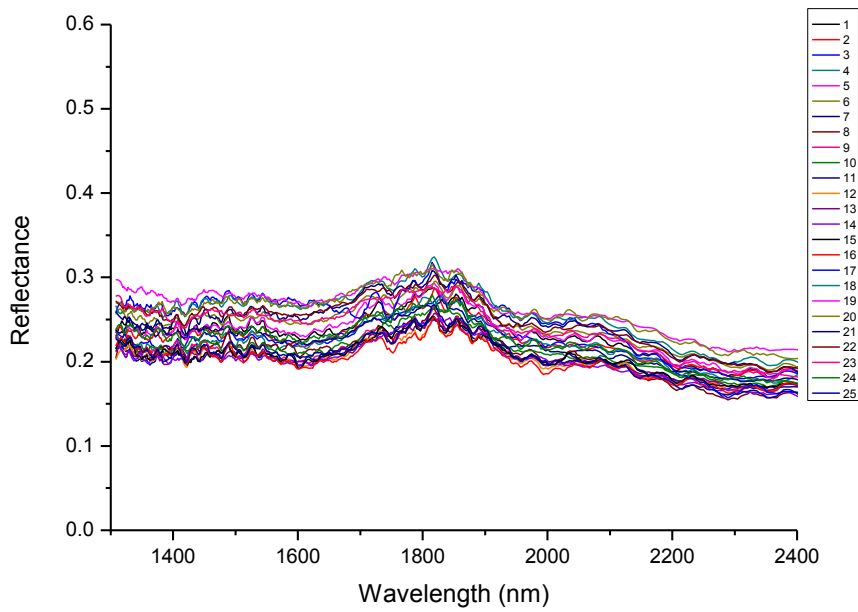
### Sample 12 sector B



### Sample 12

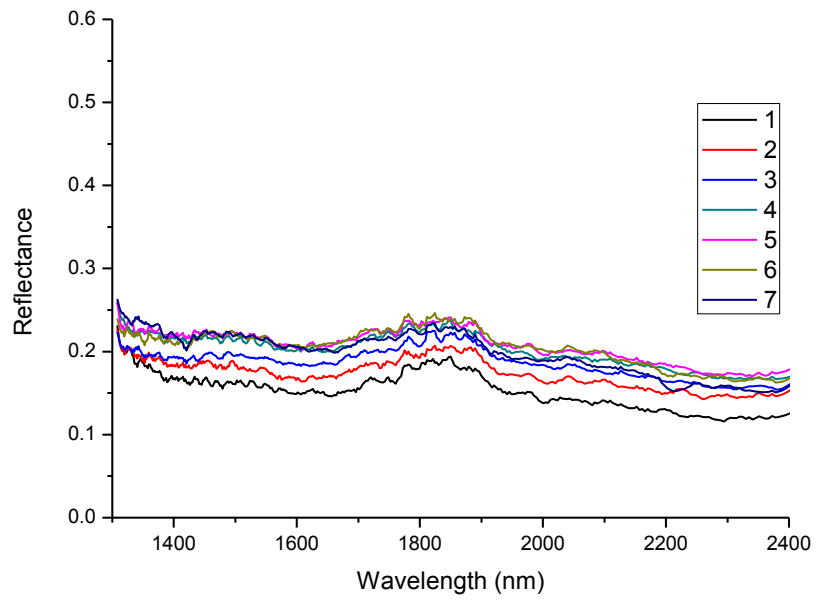


### Sample 12 sector C

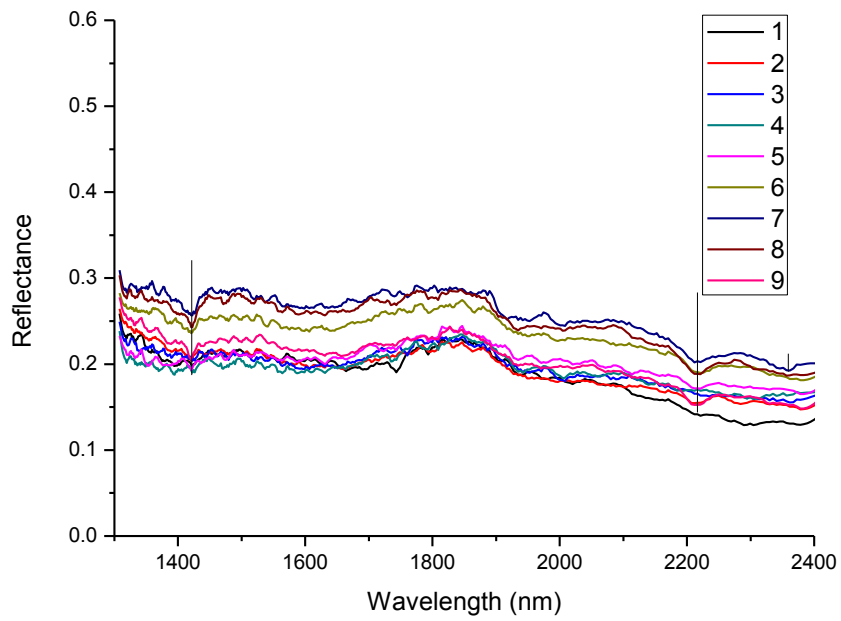


### Sample 12 combined

### Sample 13

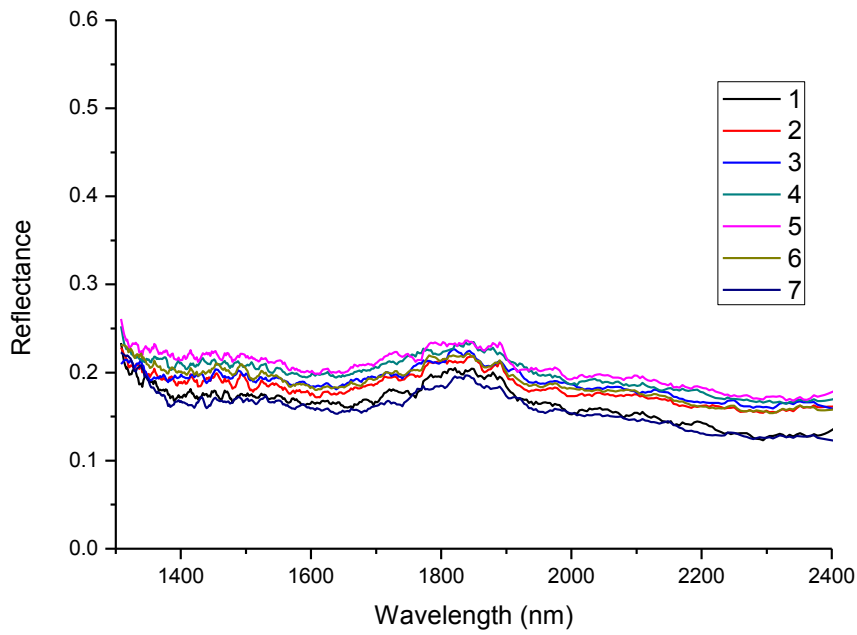


### Sample 13 sector A

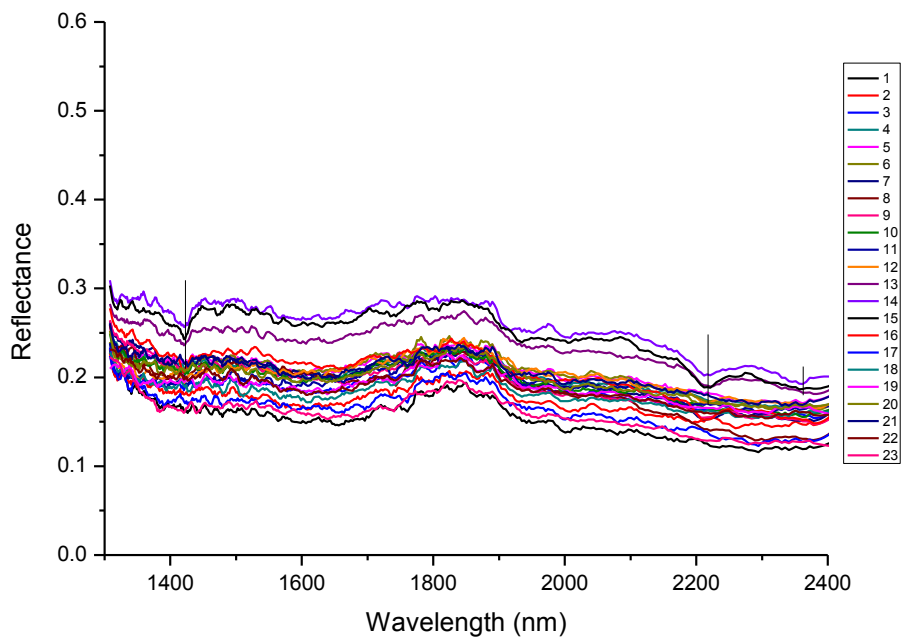


### Sample 13 sector B

### Sample 13

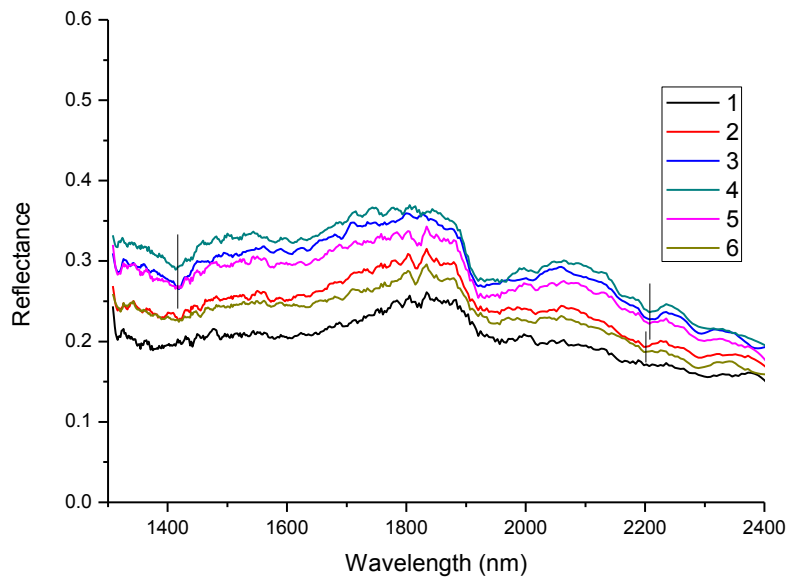


### Sample 13 sector C

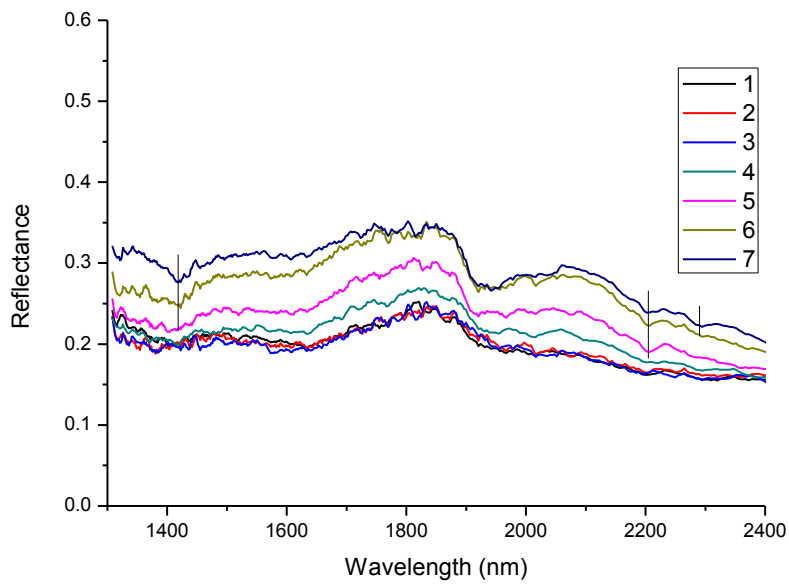


### Sample 13 combined

## Sample 14

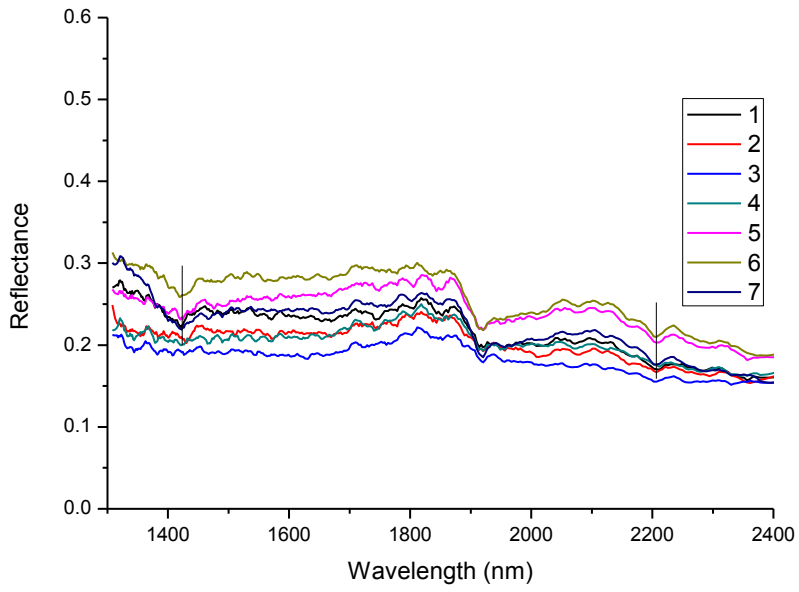


## Sample 14 sector A

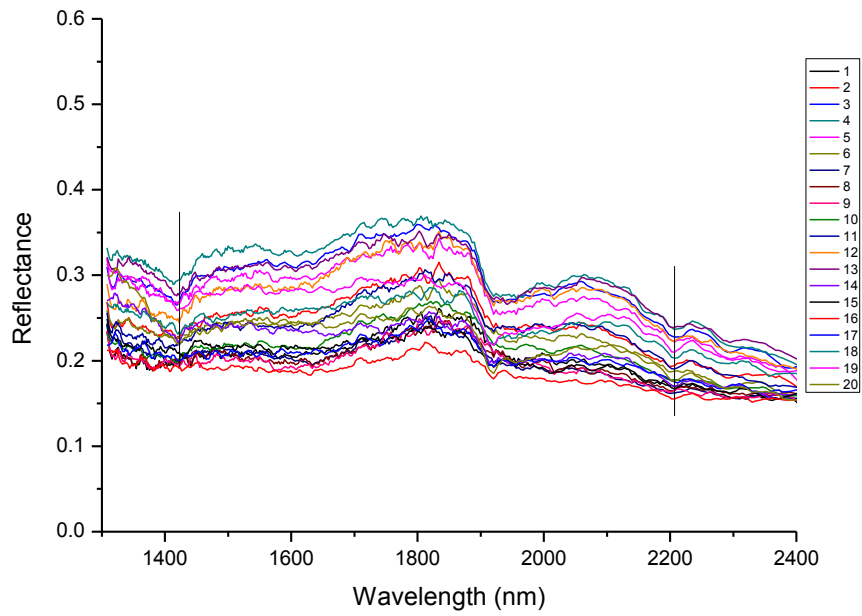


## Sample 14 sector B

### Sample 14

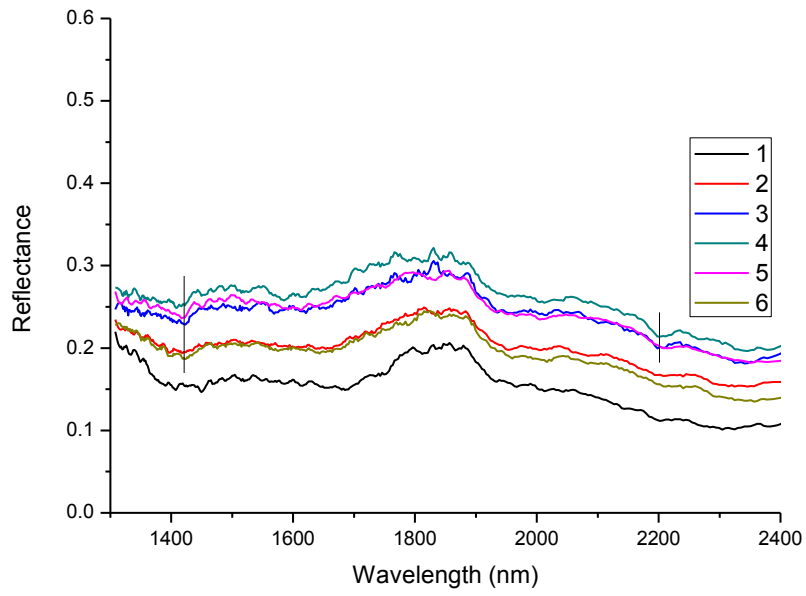


### Sample 14 sector C

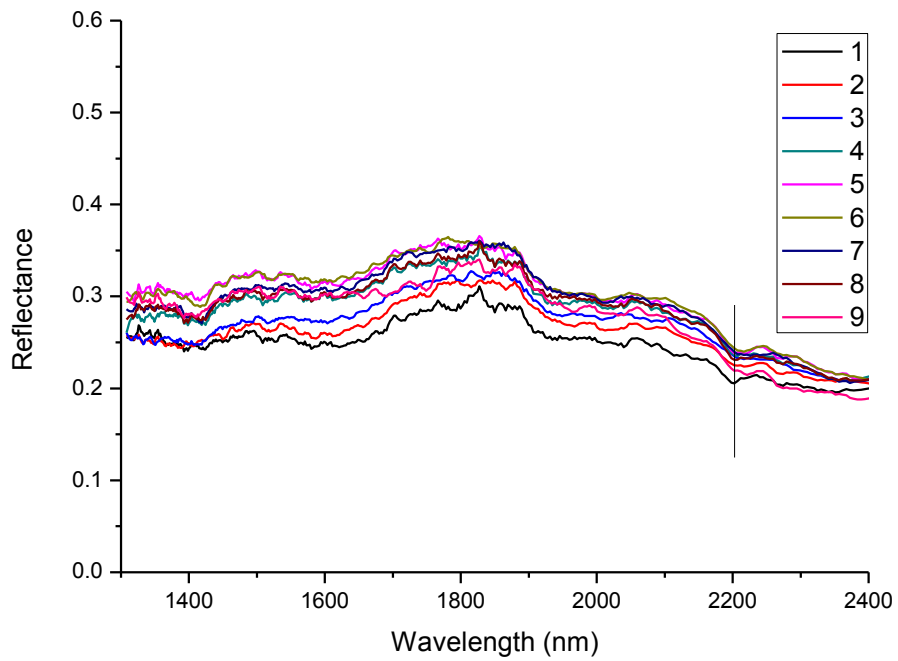


### Sample 14 COMBINED

### Sample 15

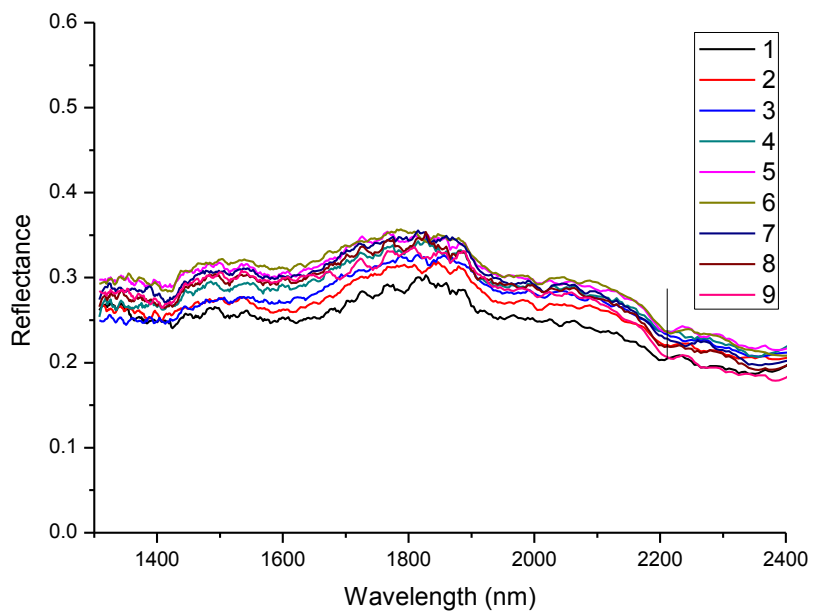


### Sample 15 sector A

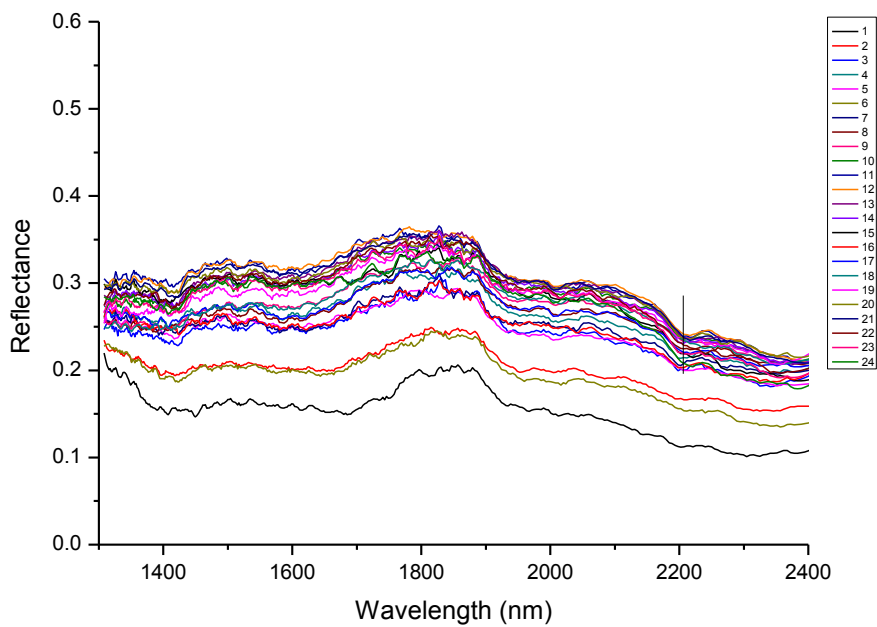


### Sample 15 sector B

### Sample 15

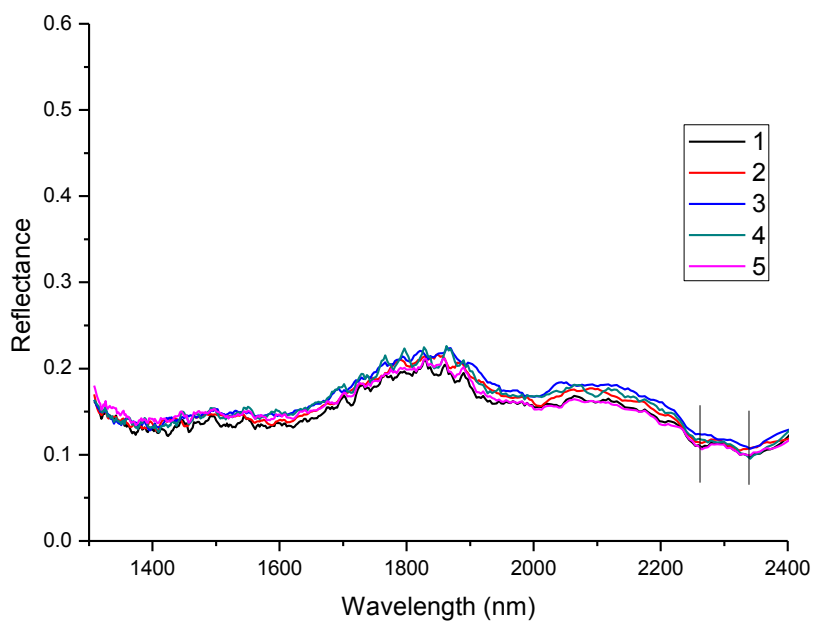


### Sample 15 sector C

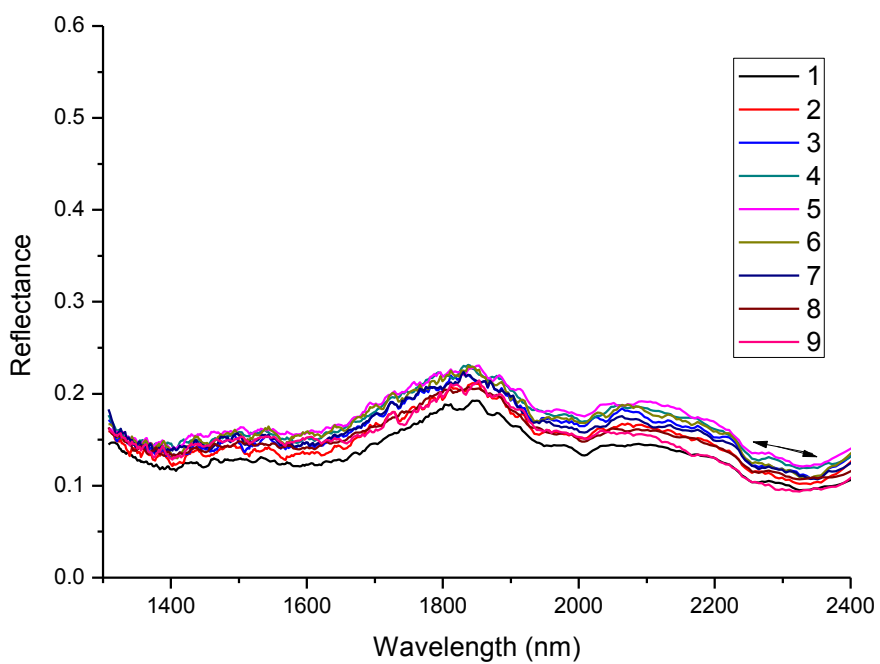


### Sample 15 COMBINED

### Sample 16



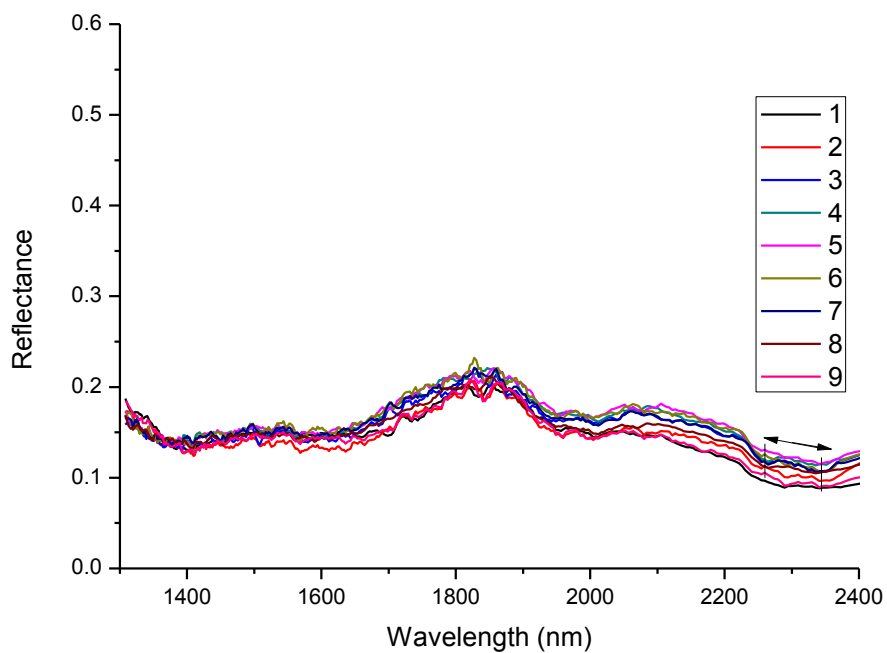
### Sample 16 sector A



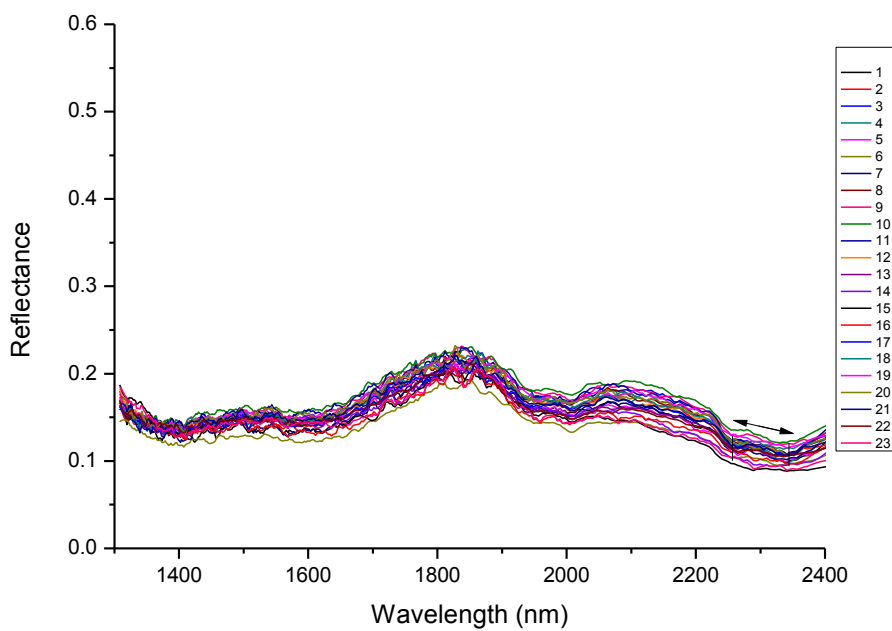
### Sample 16 sector B



### Sample 16

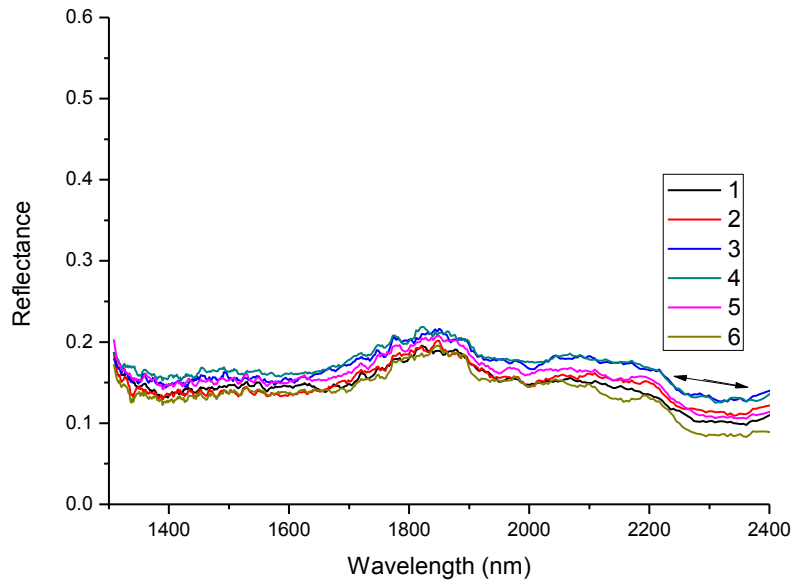


### Sample 16 sector C

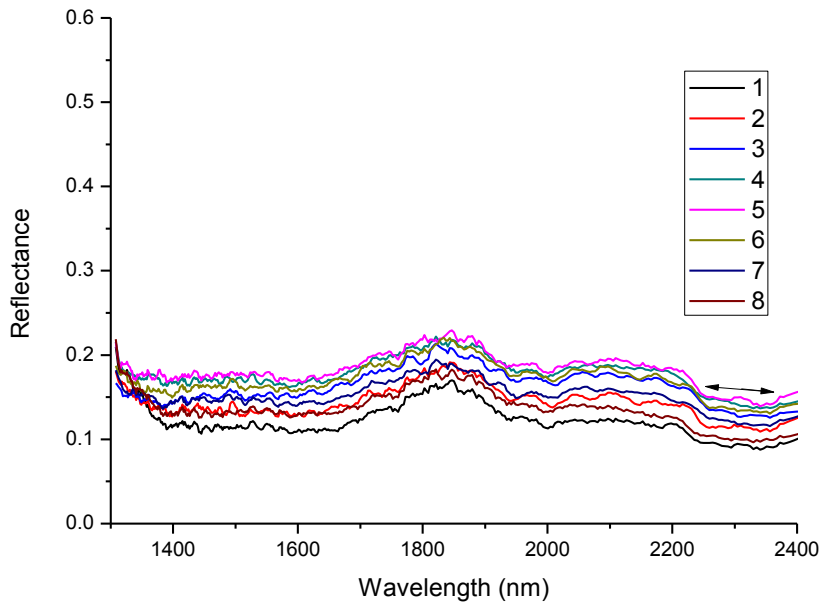


### Sample 16 COMBINED

### Sample 17

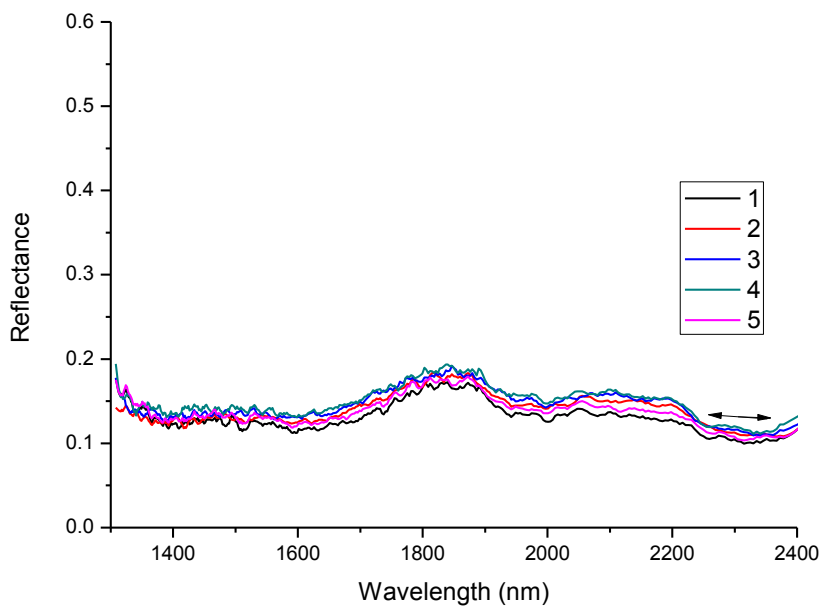


### Sample 17 sector A

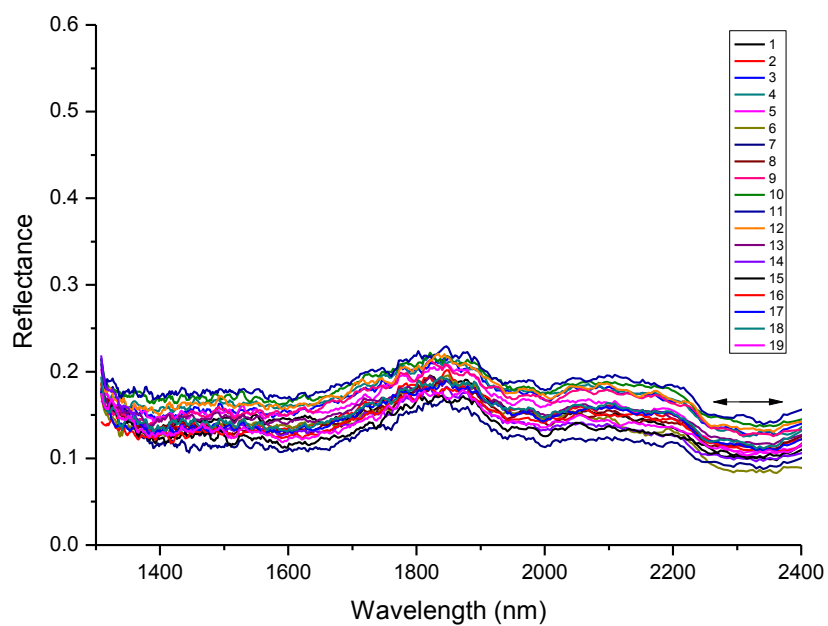


### Sample 17 sector B

### Sample 17

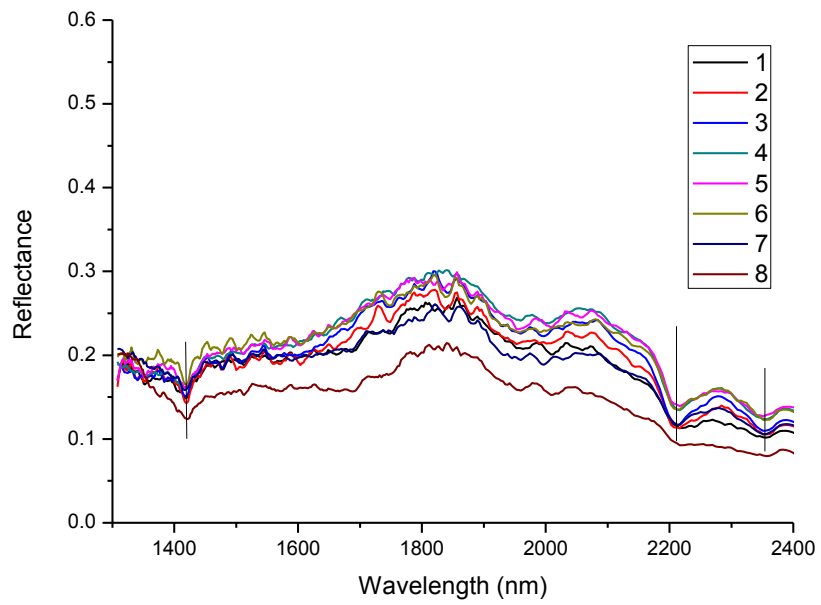


### Sample 17 sector C

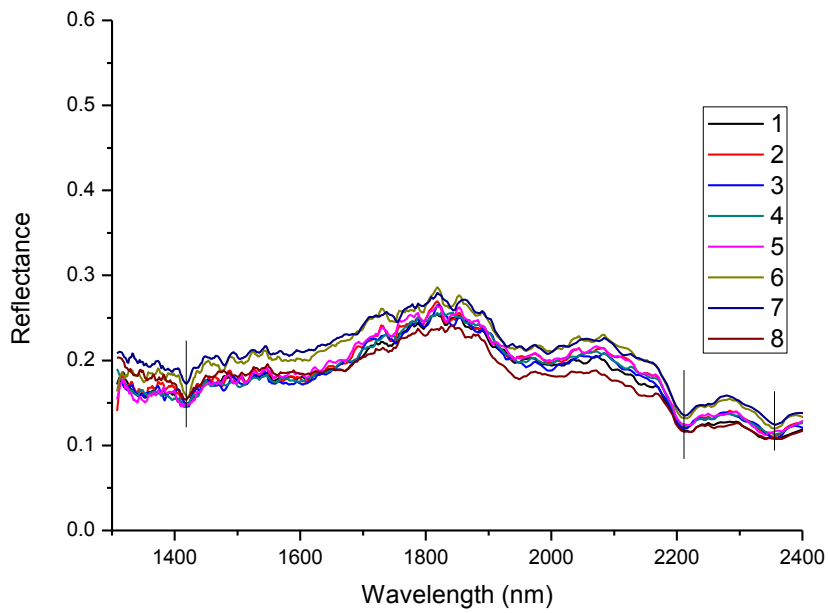


### Sample 17 COMBINED

### Sample 18

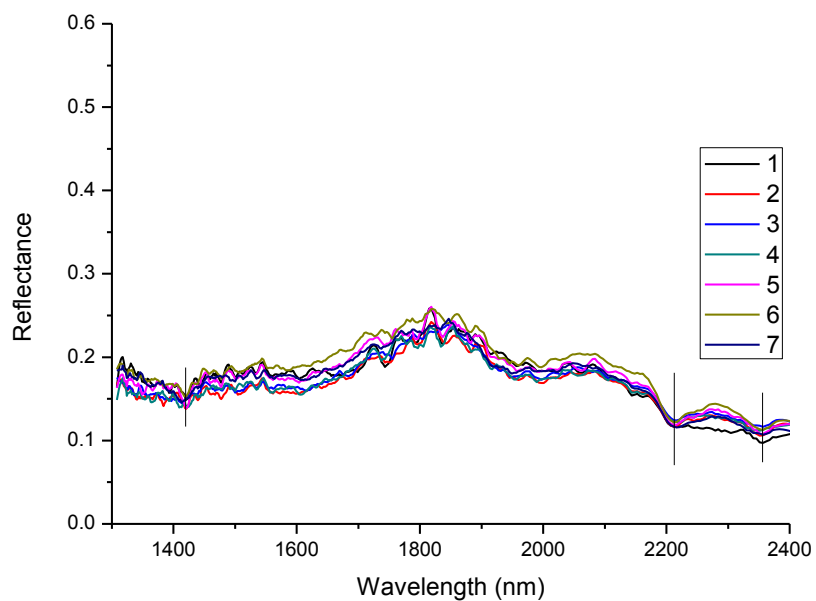


### Sample 18 sector A

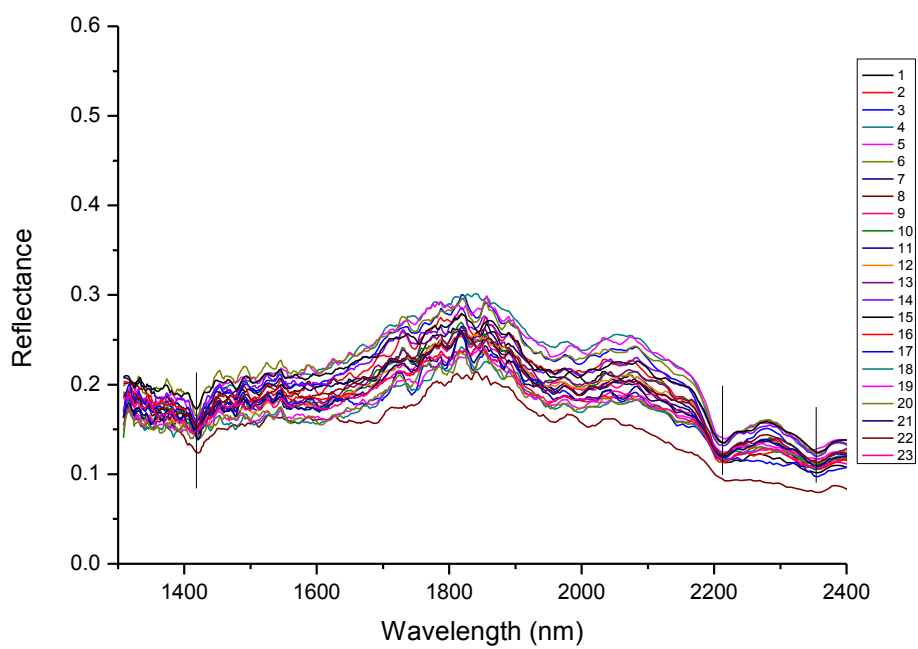


### Sample 18 sector B

### Sample 18

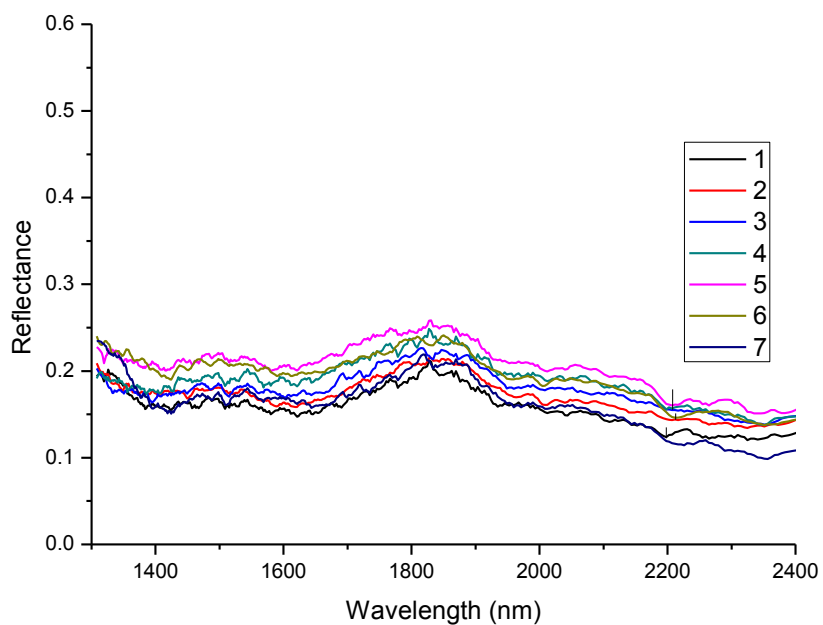


### Sample 18 sector C

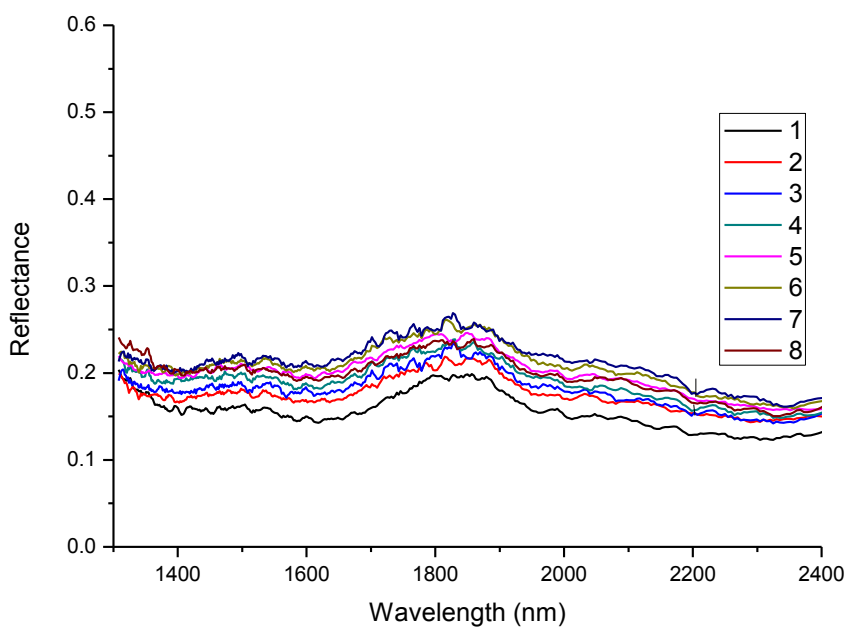


### Sample 18 COMBINED

### Sample 19

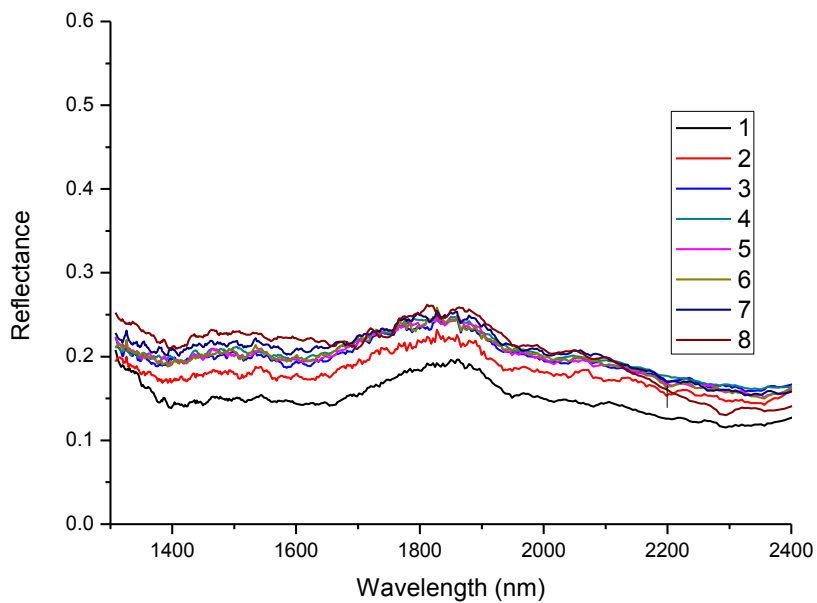


### Sample 19 sector A

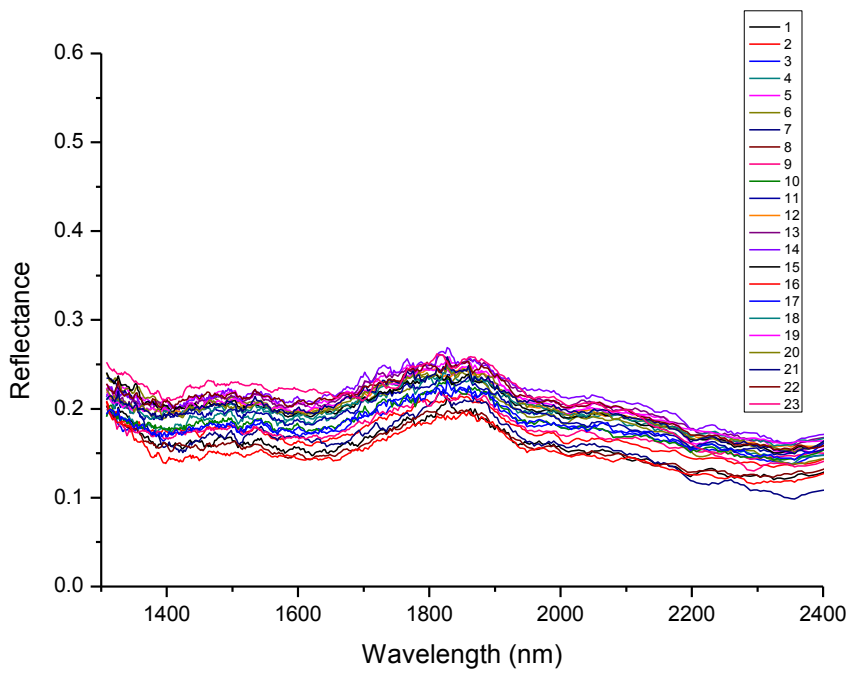


### Sample 19 sector B

### Sample 19

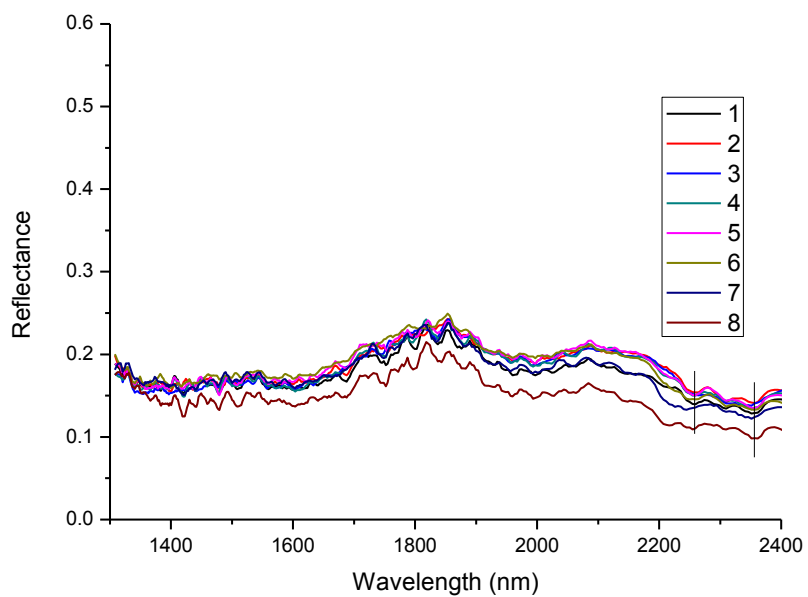


### Sample 19 sector C

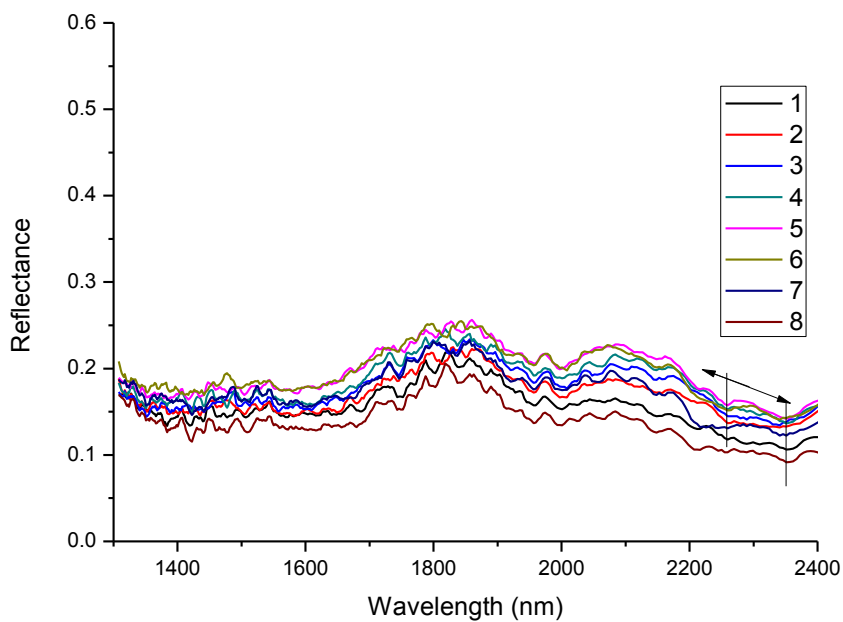


### Sample 19 COMBINED

### Sample 20



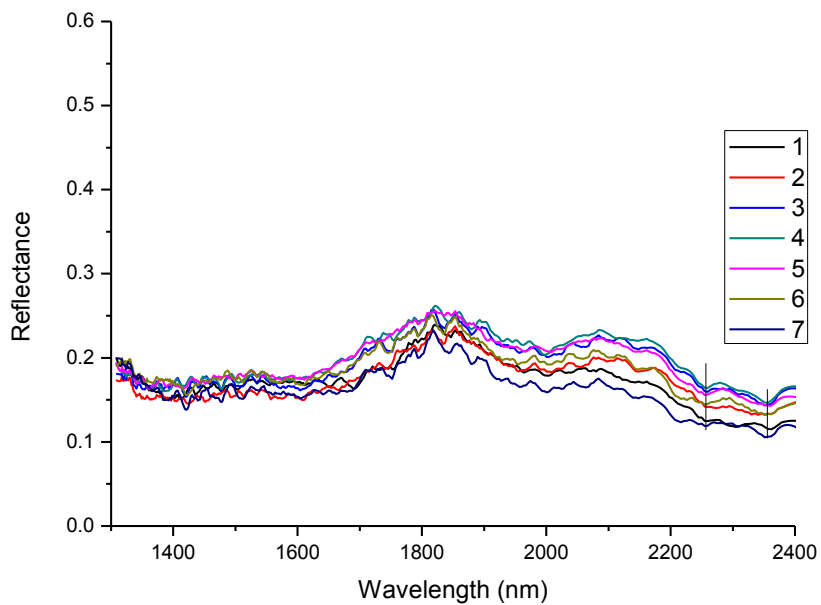
### Sample 20 sector A



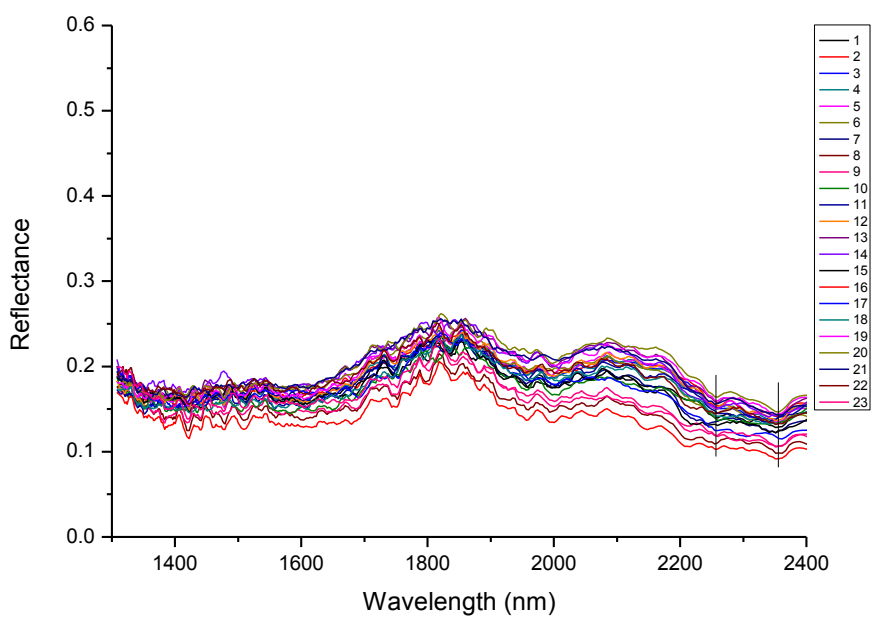
### Sample 20 sector B



### Sample 20

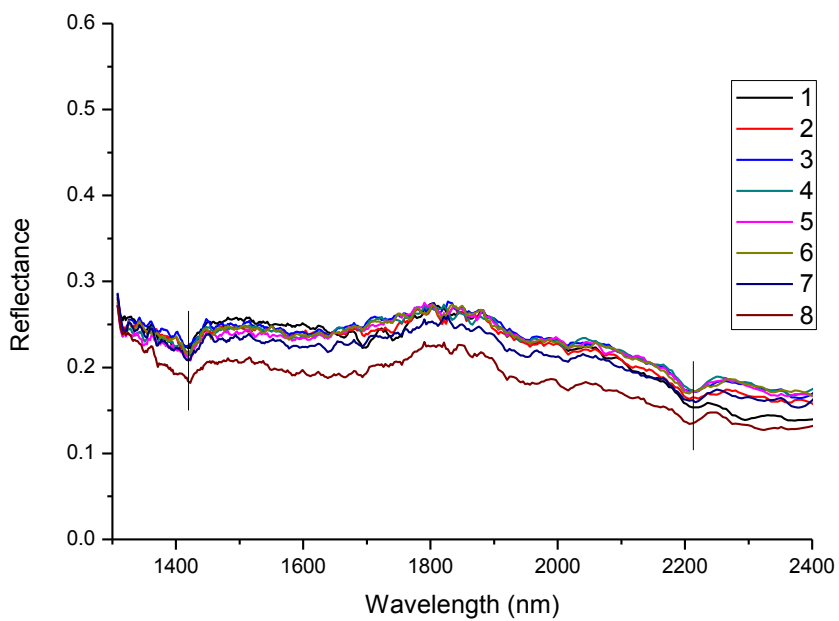


### Sample 20 sector C

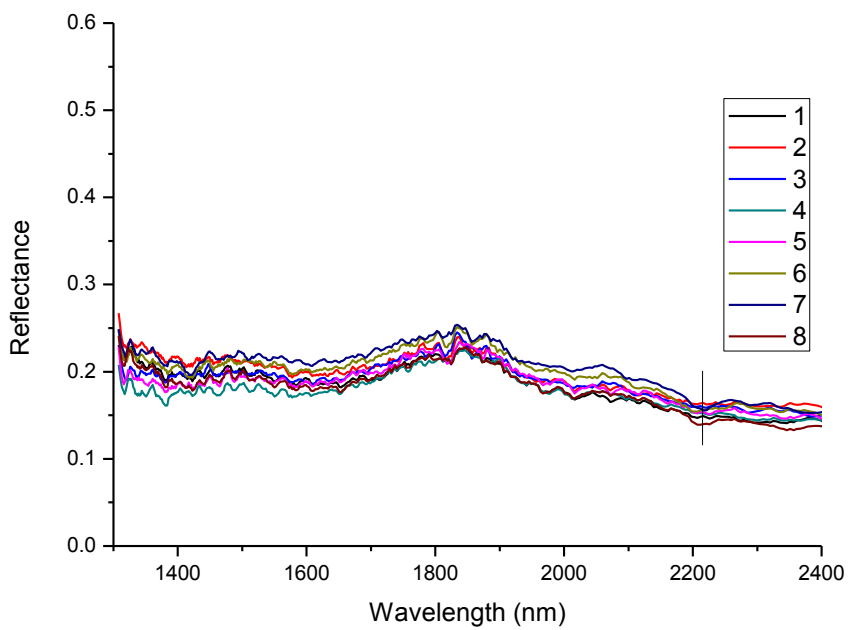


### Sample 20 COMBINED

### Sample 21

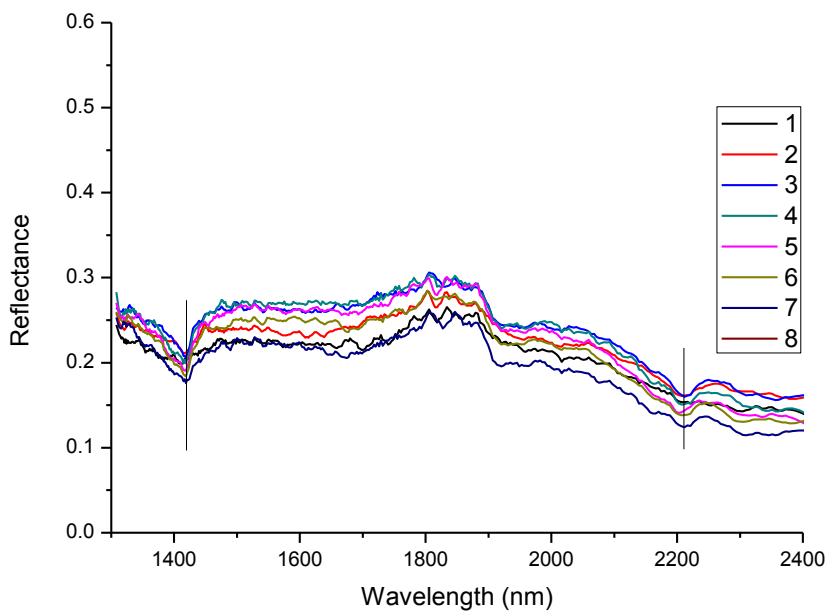


### Sample 21 sector A

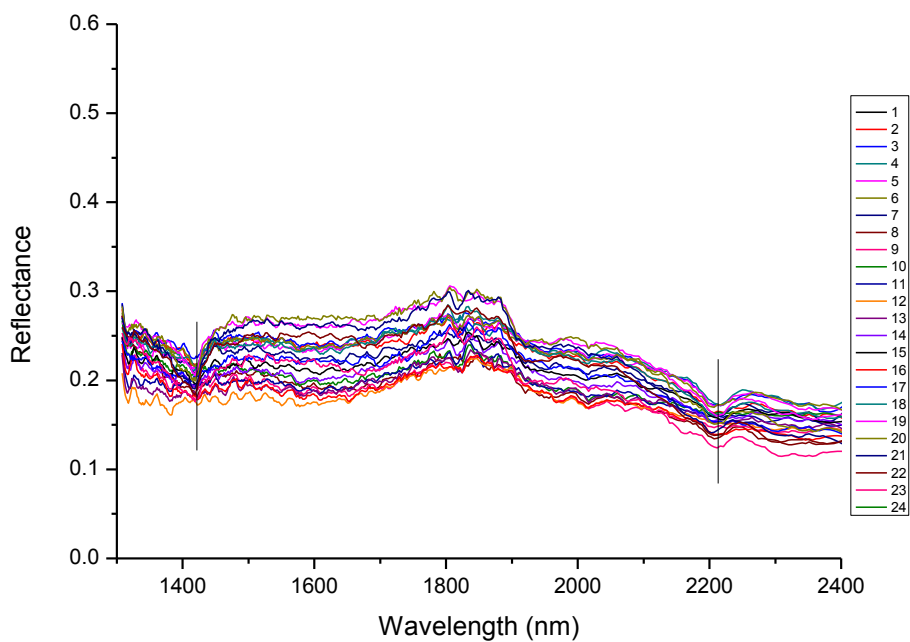


### Sample 21 sector B

### Sample 21

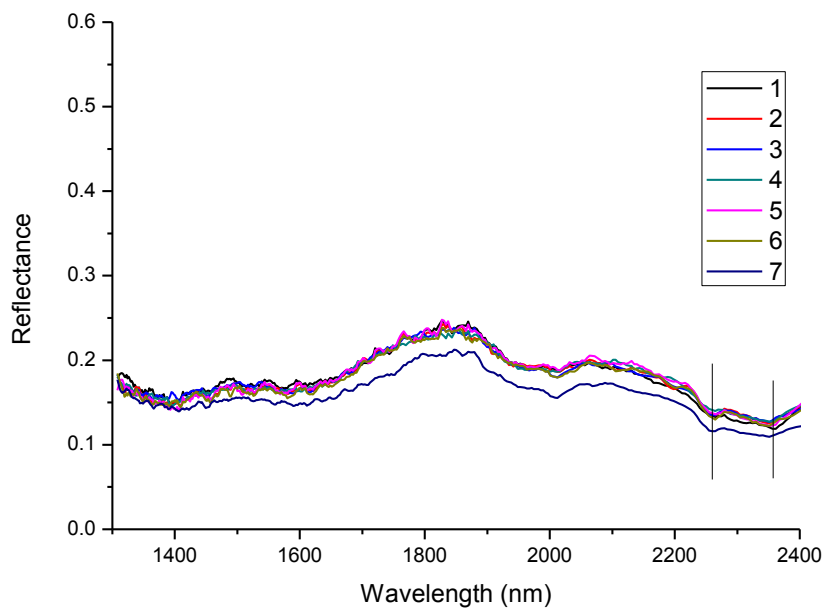


### Sample 21 sector C

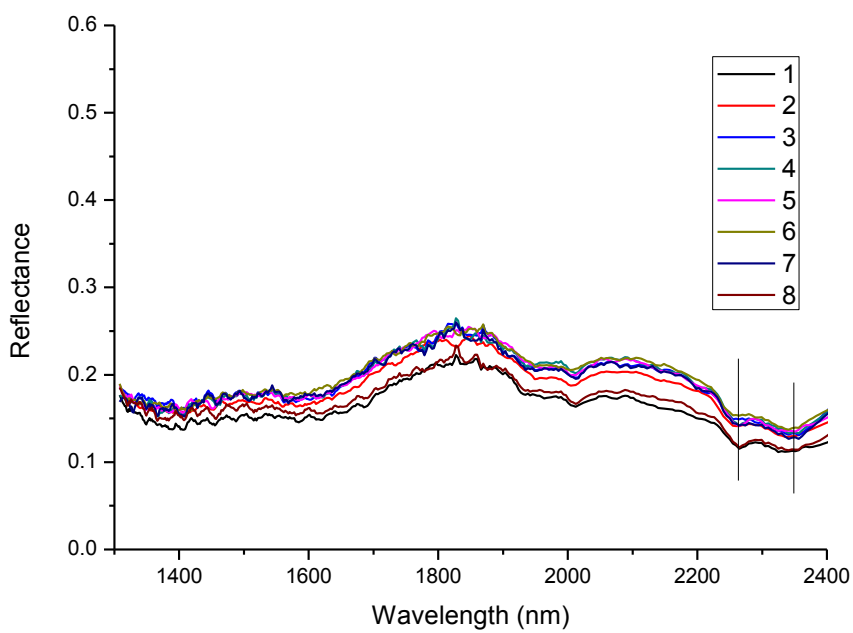


### Sample 21 COMBINED

### Sample 22

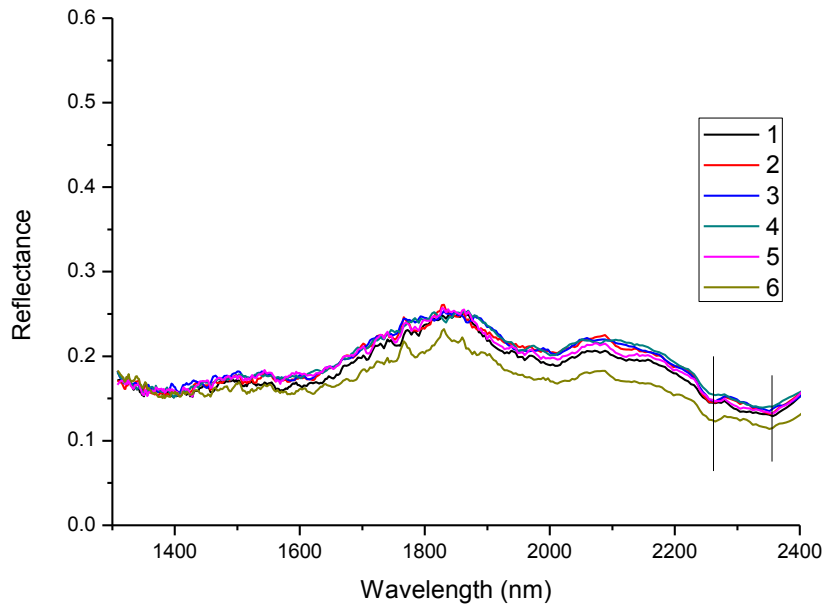


### Sample 22 sector A

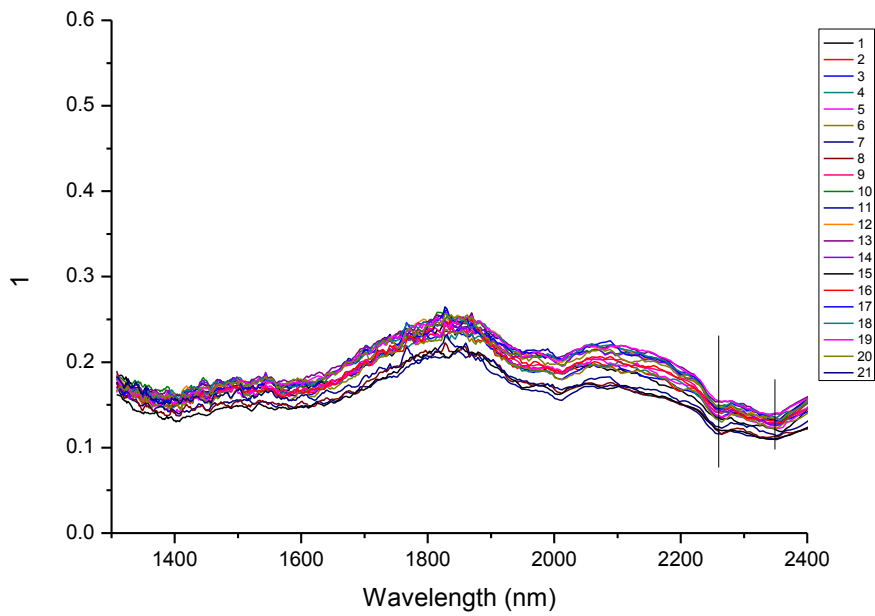


### Sample 22 sector B

### Sample 22

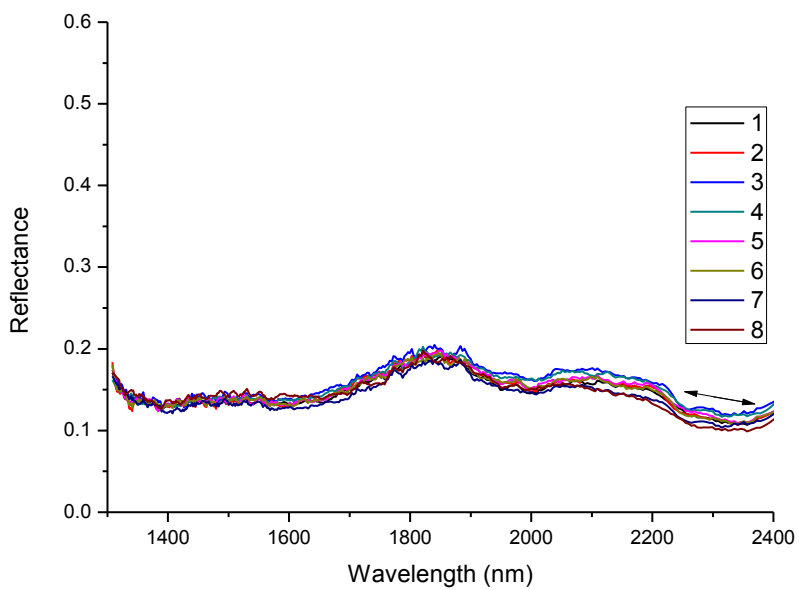


### Sample 22 sector C

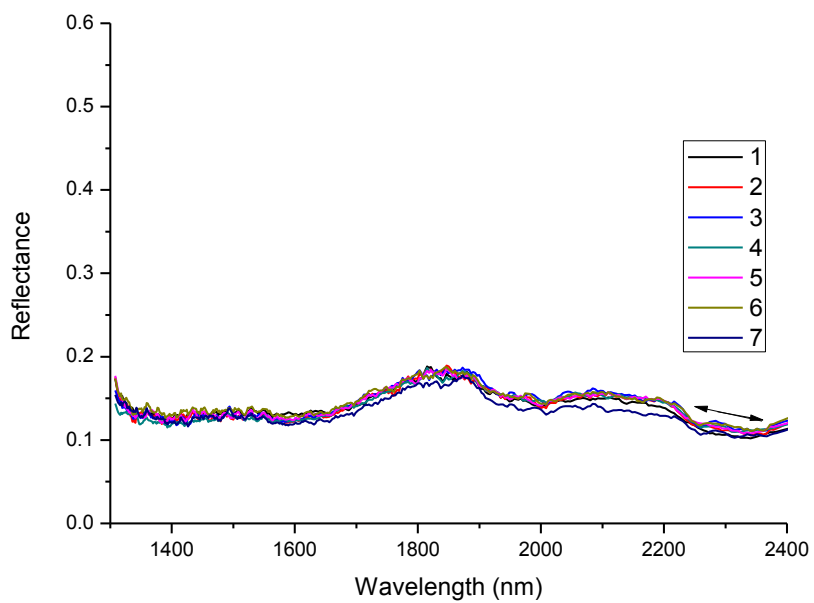


### Sample 22 COMBINED

### Sample 23

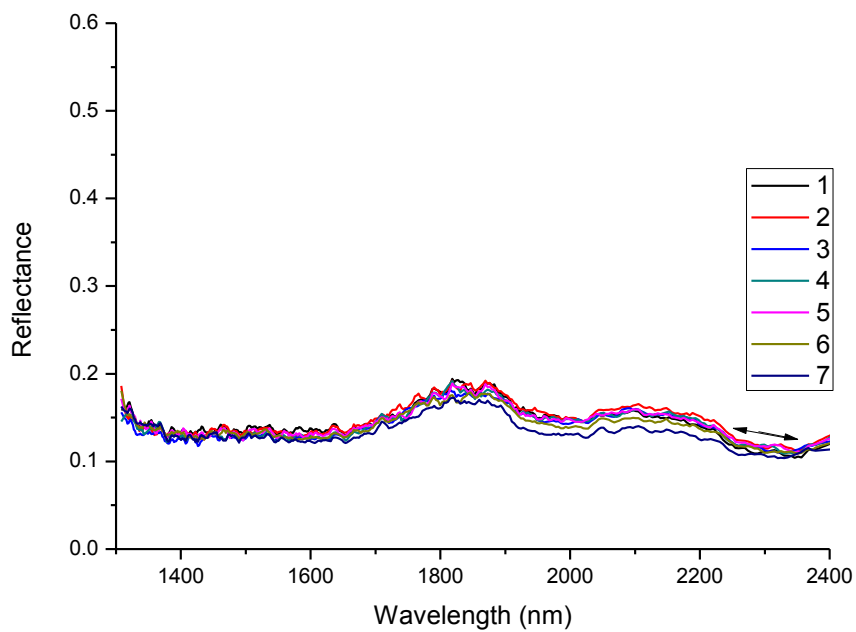


### Sample 23 sector A

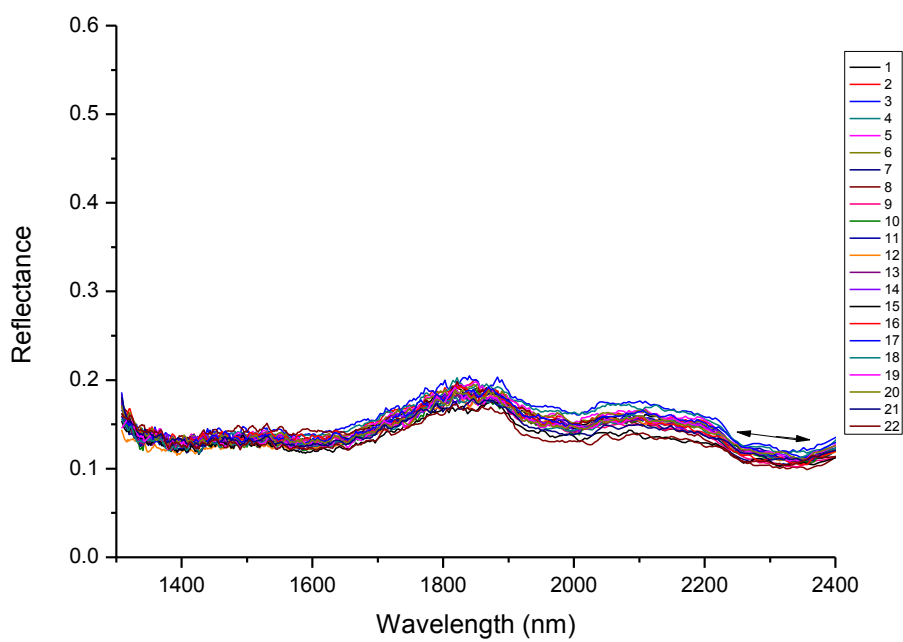


### Sample 23 sector B

### Sample 23

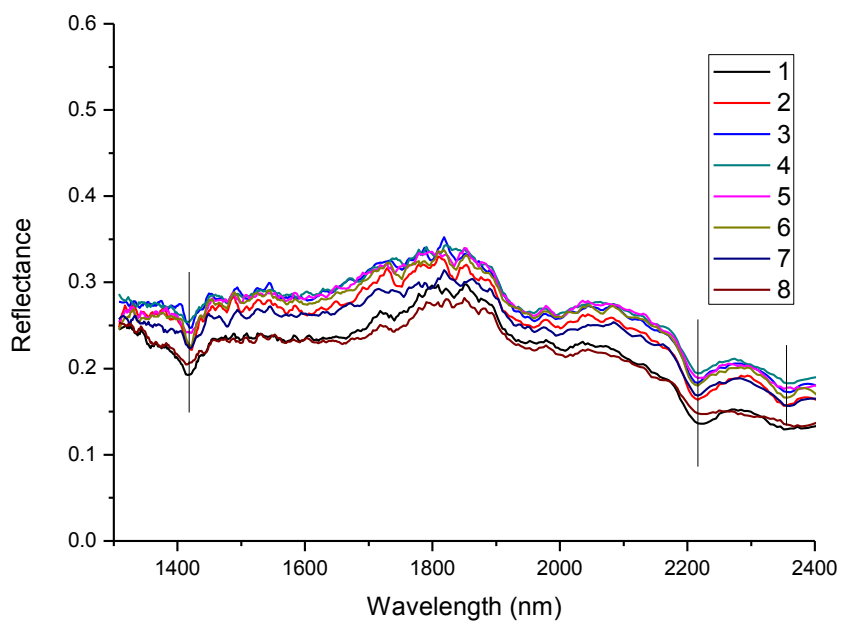


### Sample 23 sector C

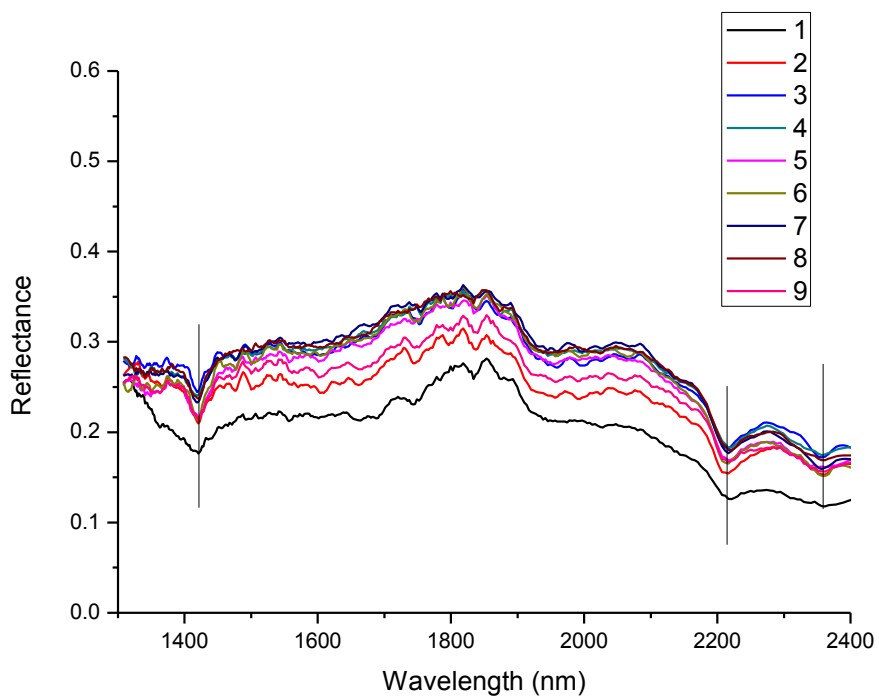


### Sample 20 COMBINED

### Sample 24



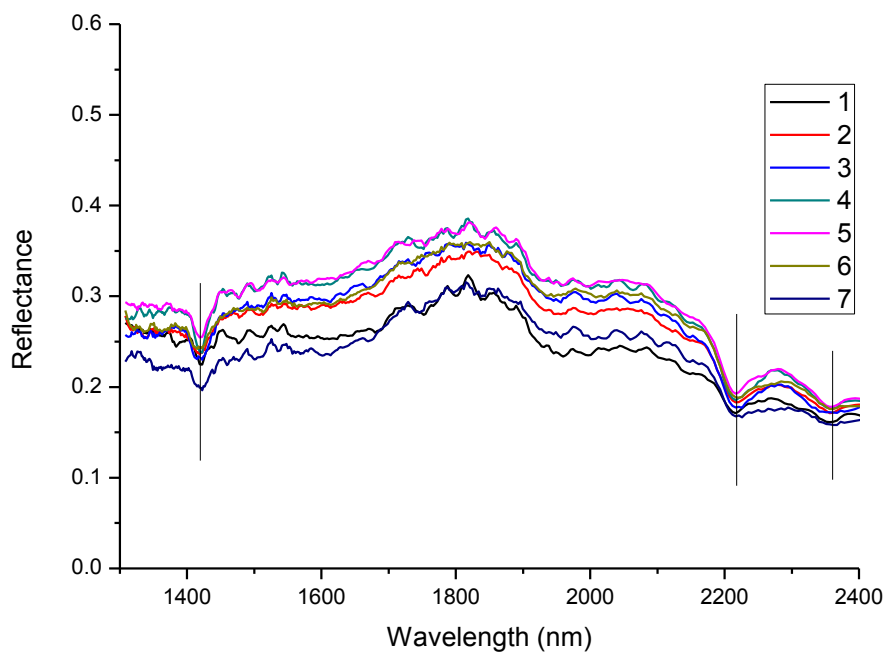
### Sample 24 sector A



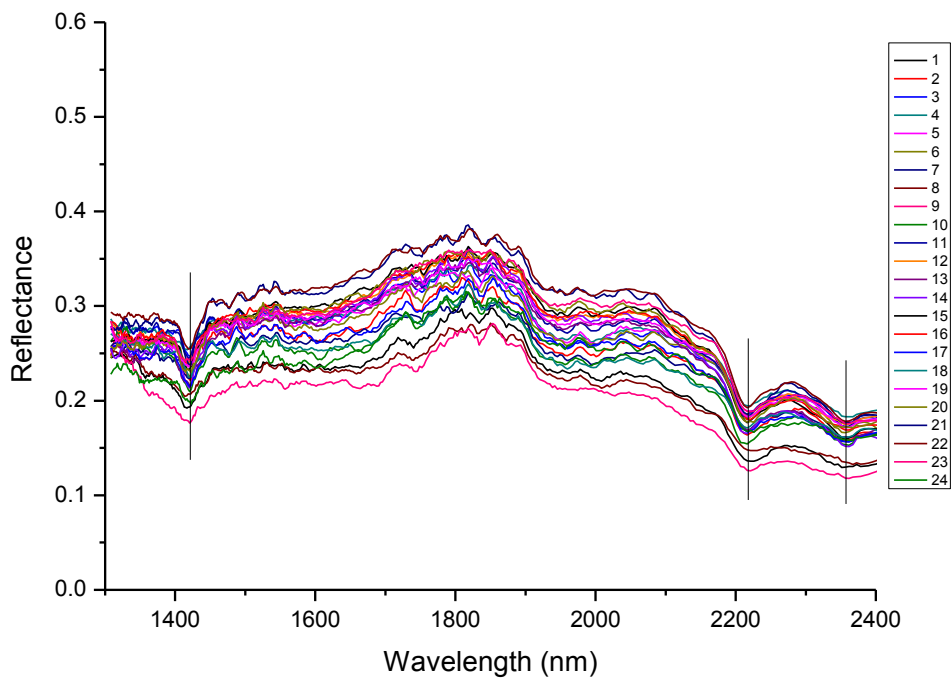
### Sample 24 sector B



### Sample 24

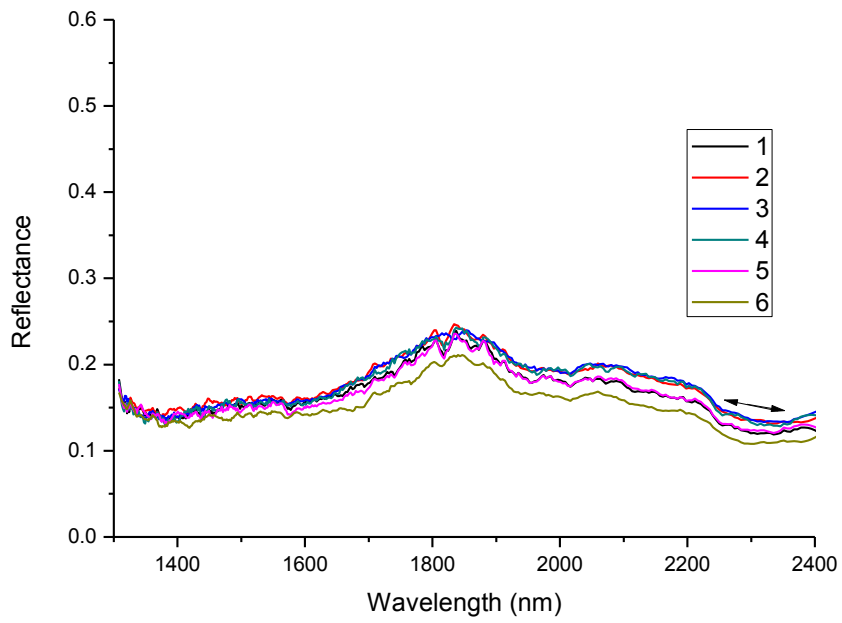


### Sample 24 sector C

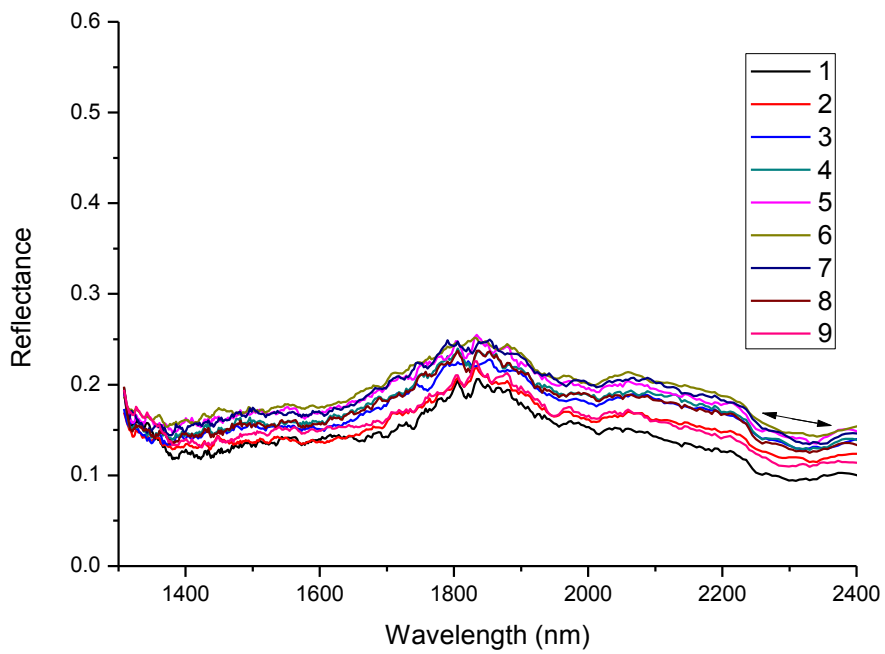


### Sample 24 COMBINED

### Sample 25

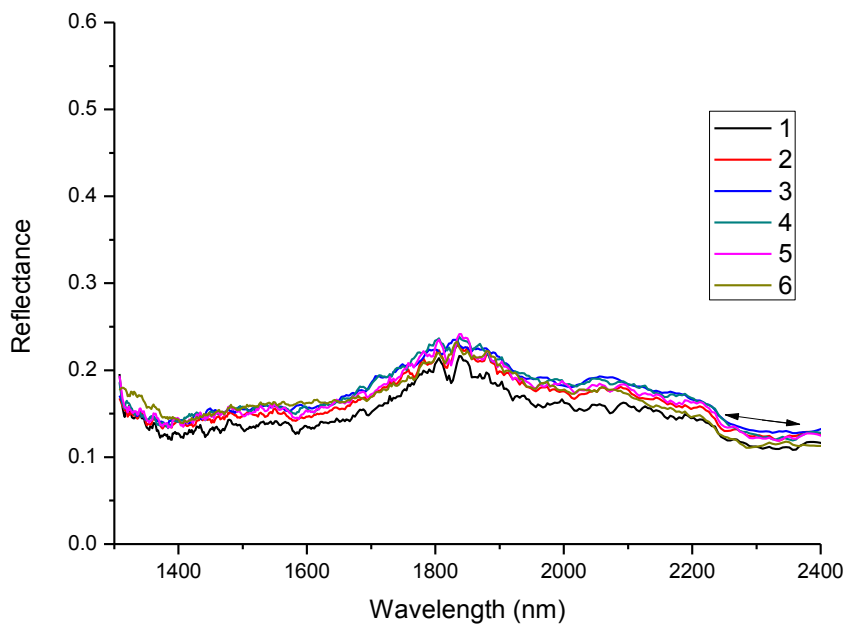


### Sample 25 sector A

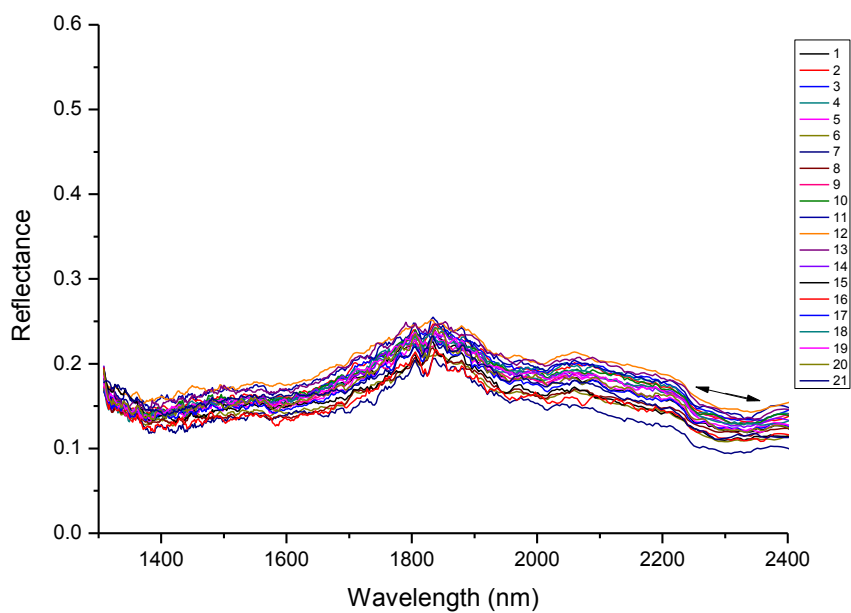


### Sample 25 sector B

### Sample 25

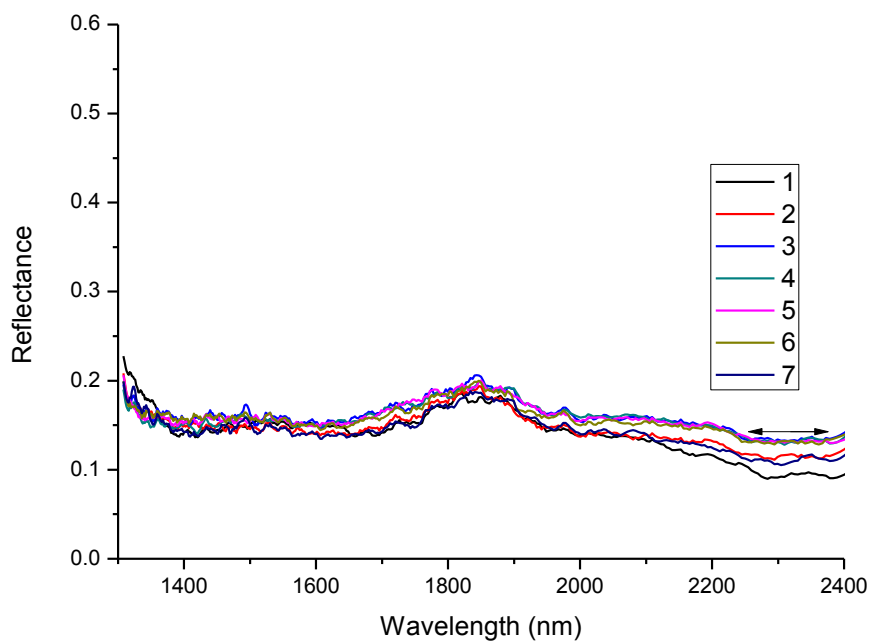


### Sample 25 sector C

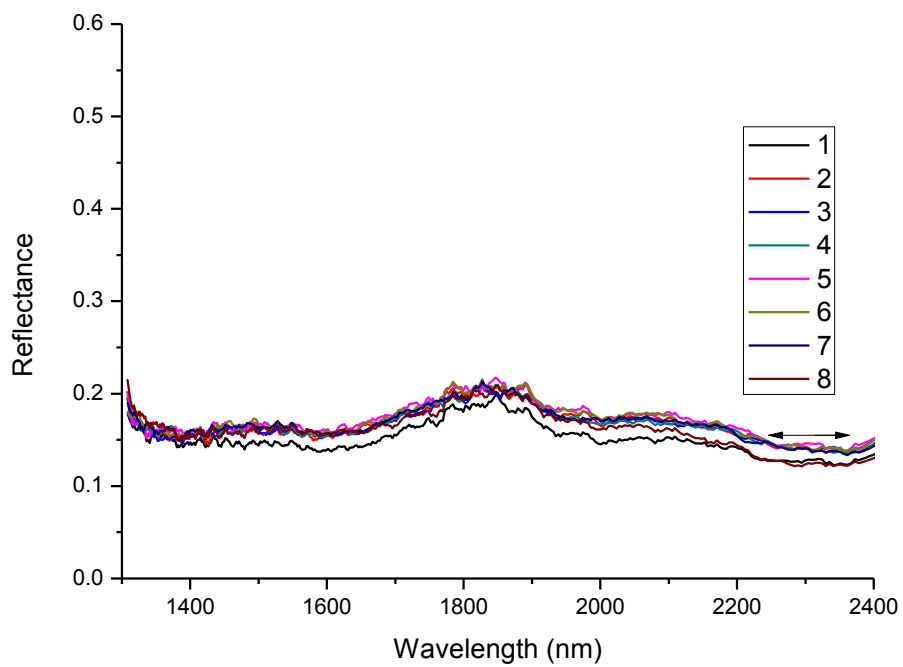


### Sample 25 COMBINED

### Sample 26

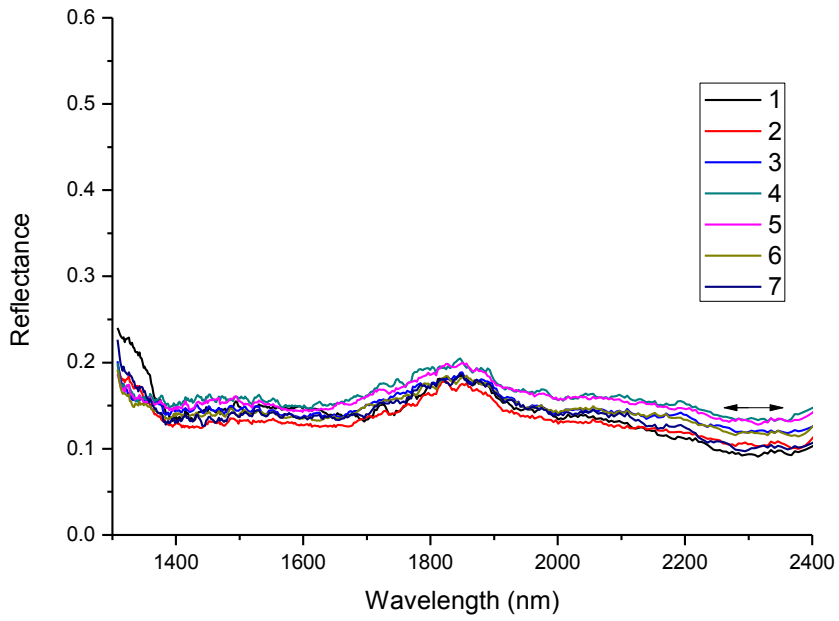


### Sample 26 sector A

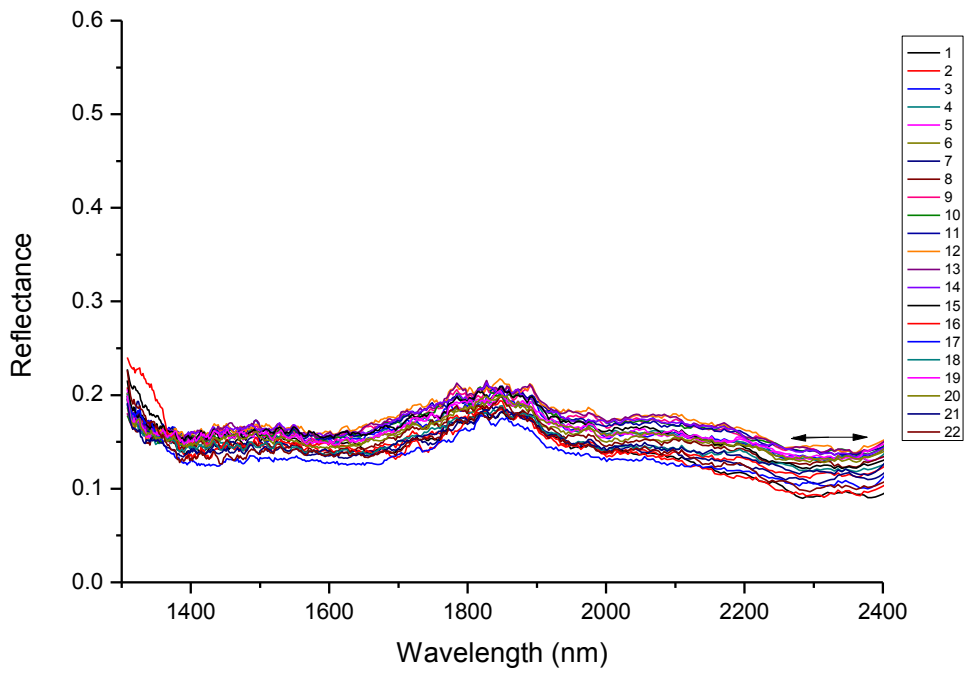


### Sample 26 sector B

### Sample 26

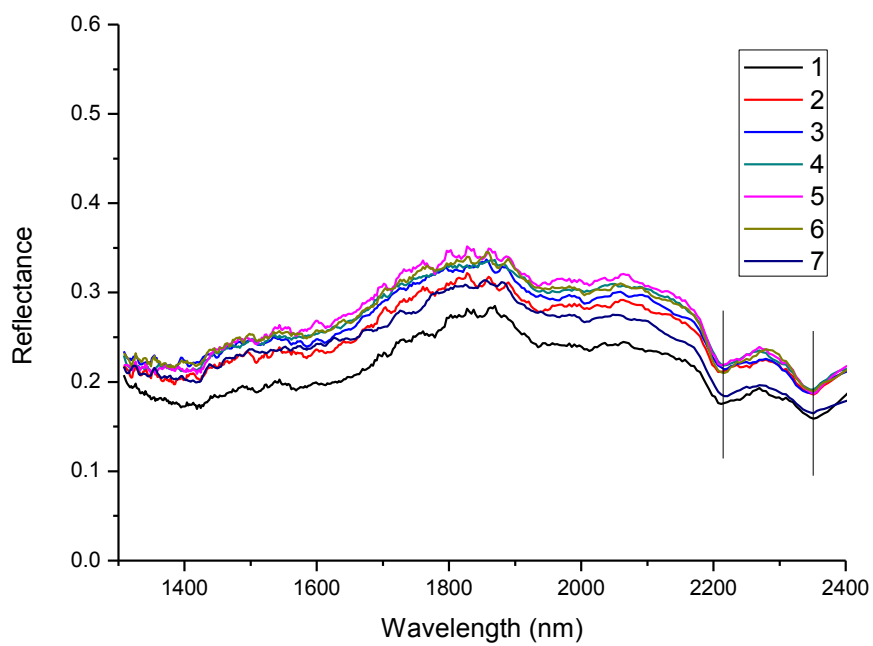


### Sample 26 sector C

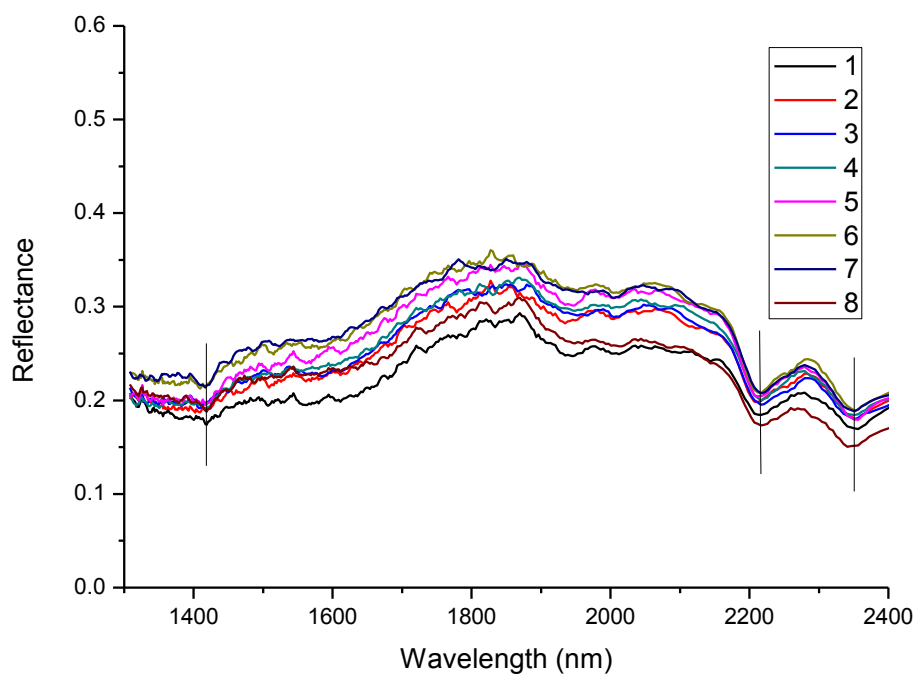


### Sample 26 COMBINED

### Sample 27

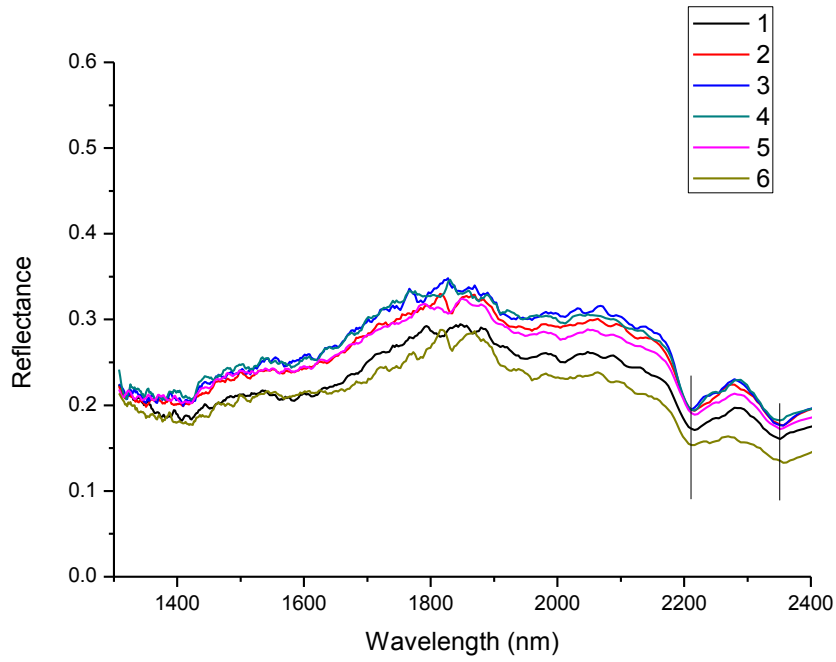


### Sample 27 sector A

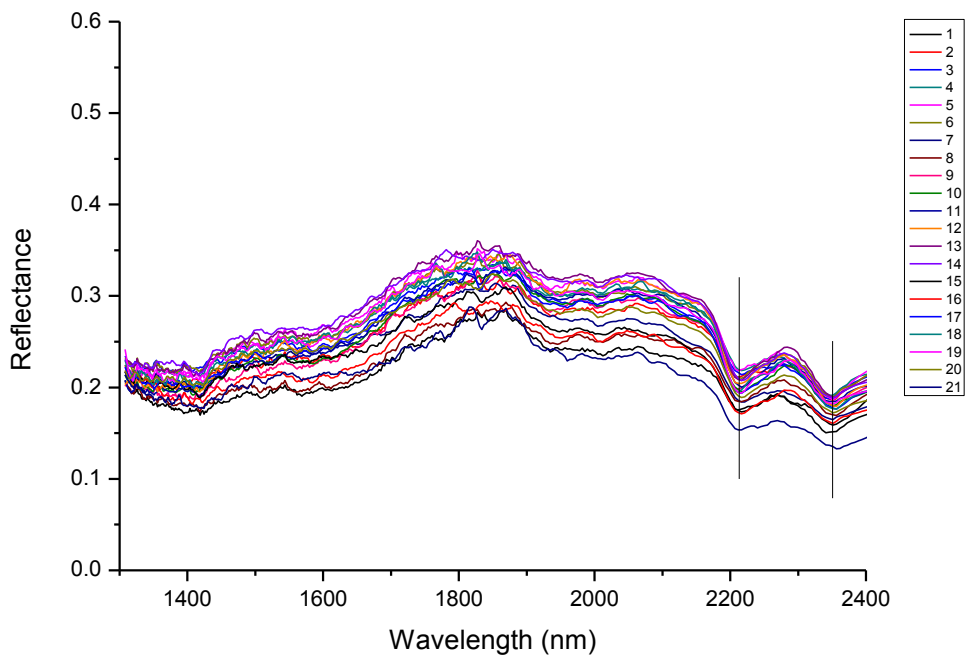


### Sample 27 sector B

### Sample 27

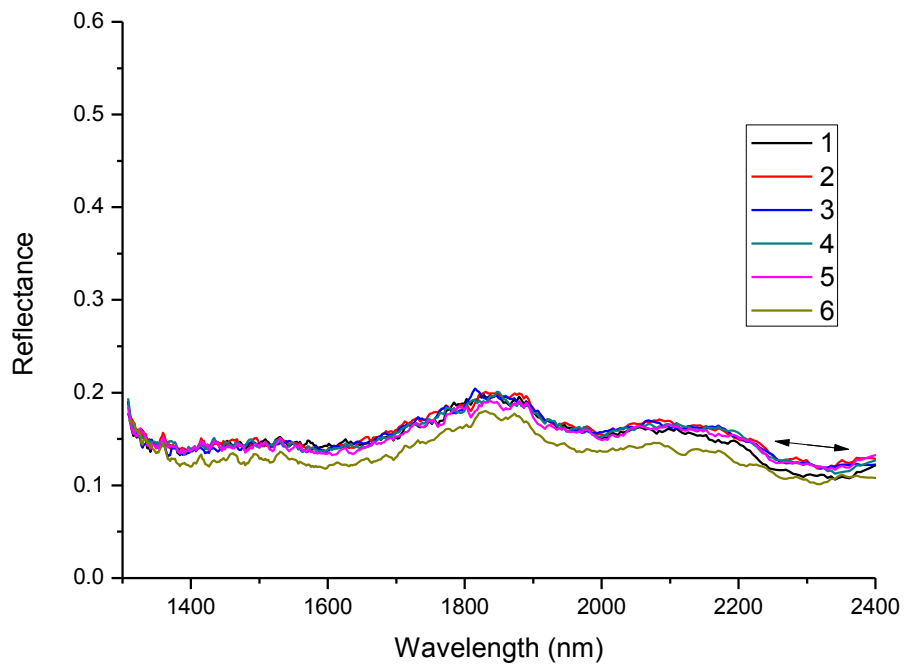


### Sample 27 sector C

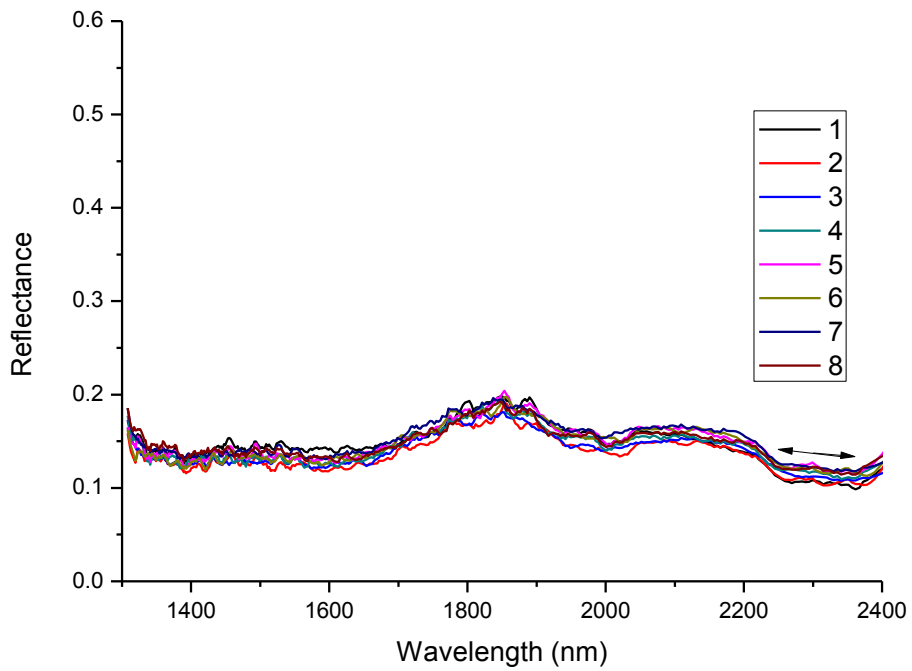


### Sample 27 COMBINED

### Sample 28



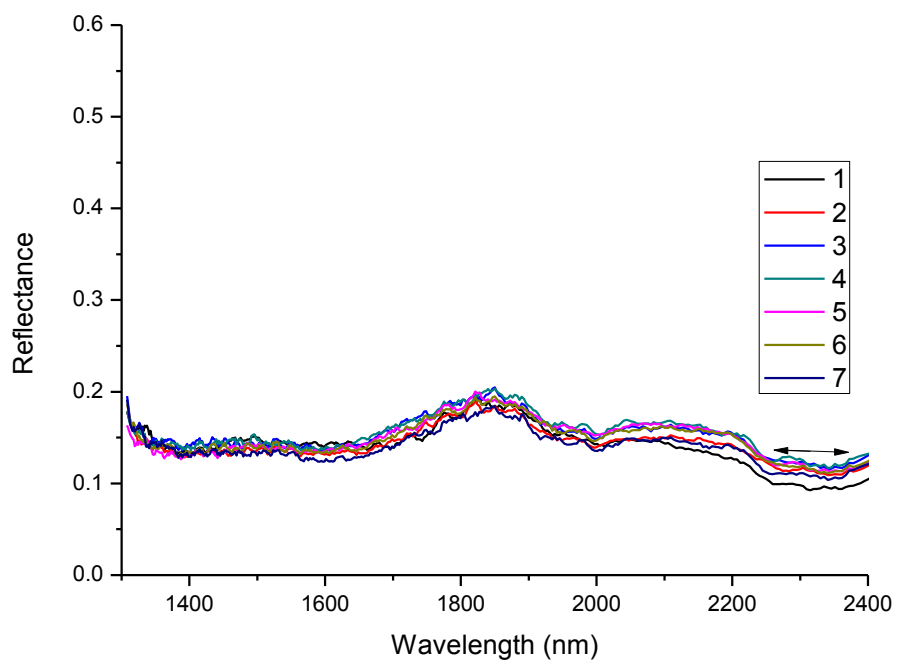
### Sample 28 sector A



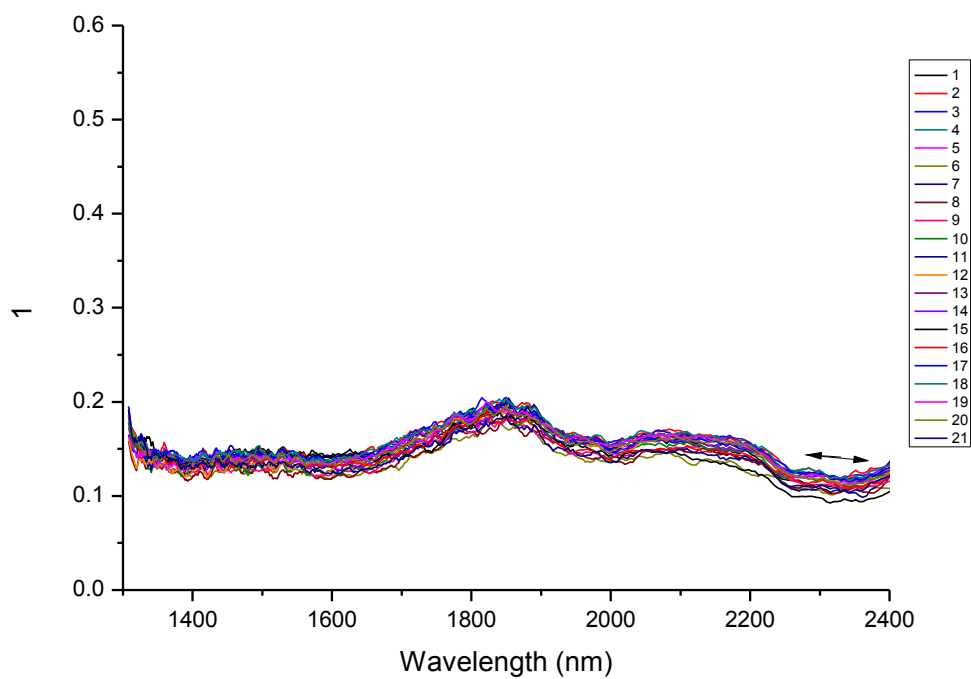
### Sample 28 sector B



### Sample 28

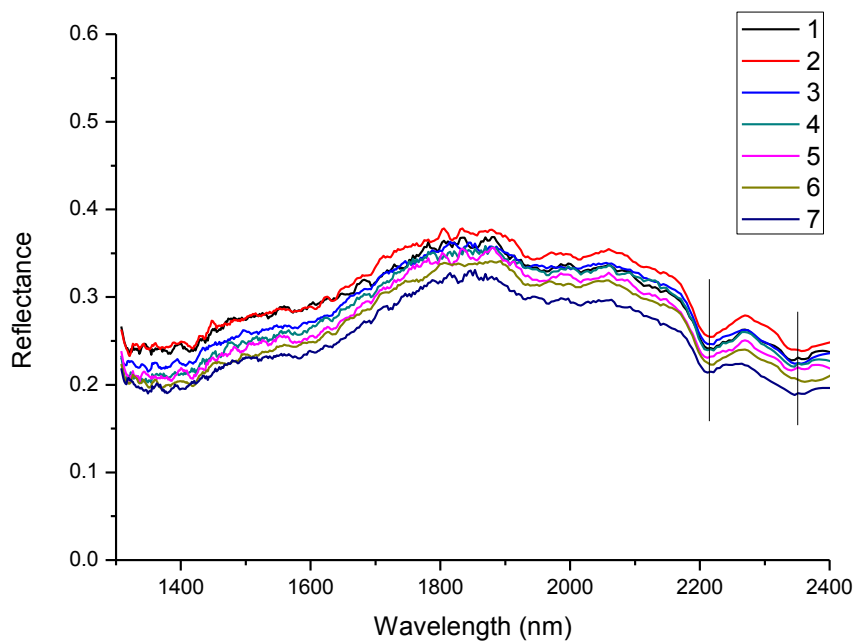


### Sample 28 sector C

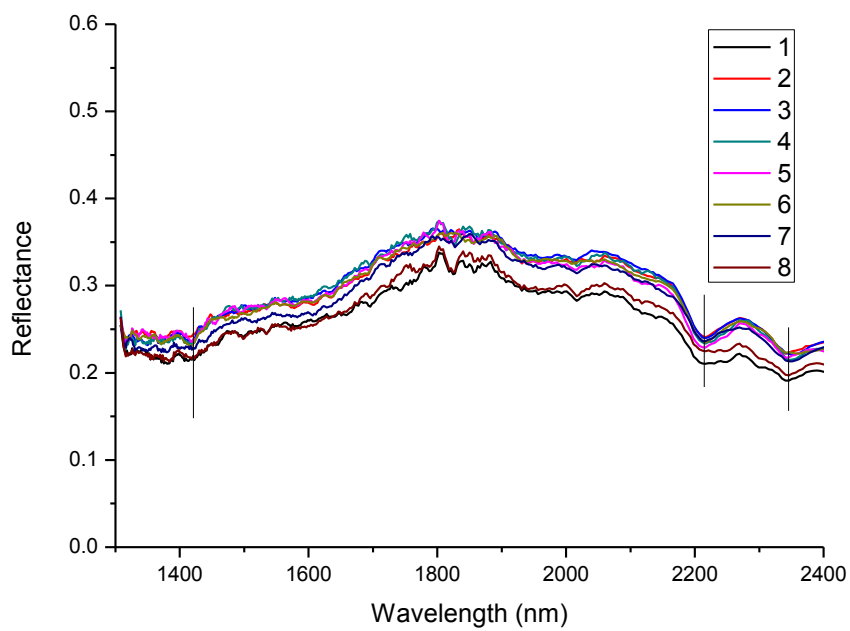


### Sample 28 COMBINED

### Sample 29

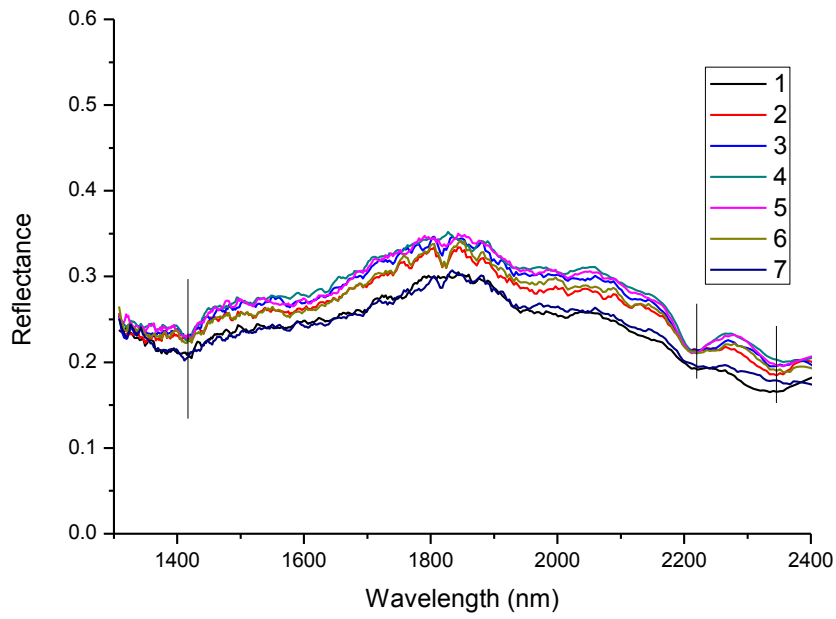


### Sample 29 sector A

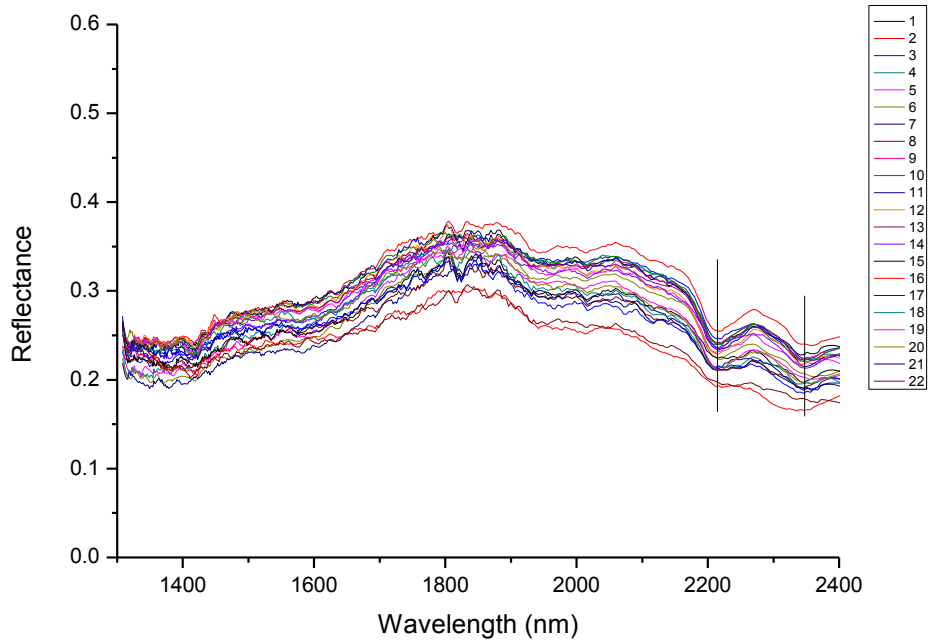


### Sample 29 sector B

### Sample 29

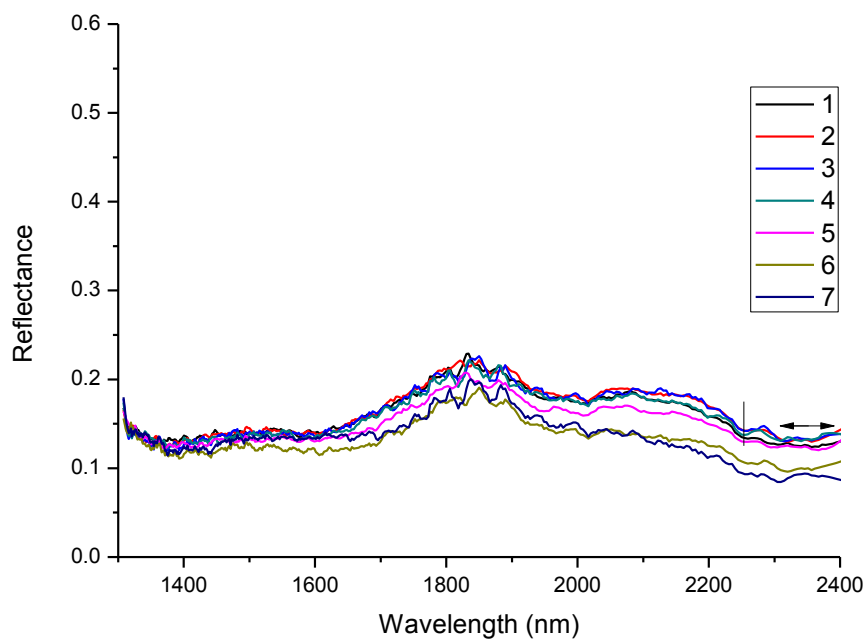


### Sample 29 sector C

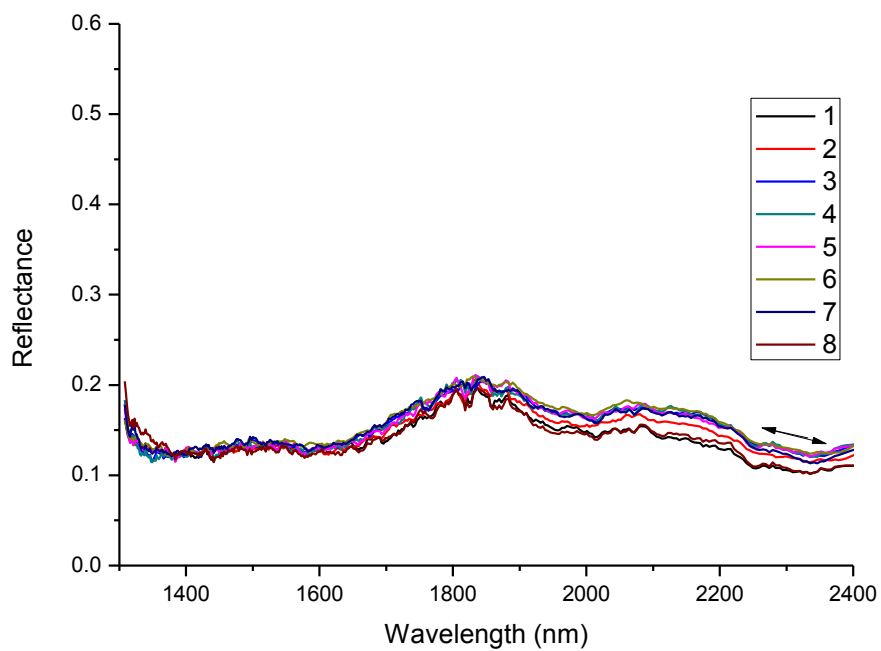


### Sample 29 COMBINED

### Sample 30

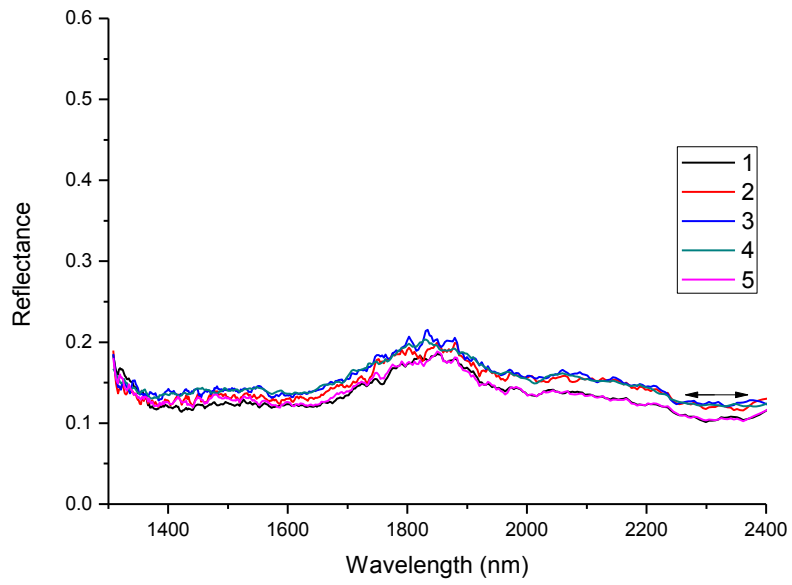


### Sample 30 sector A

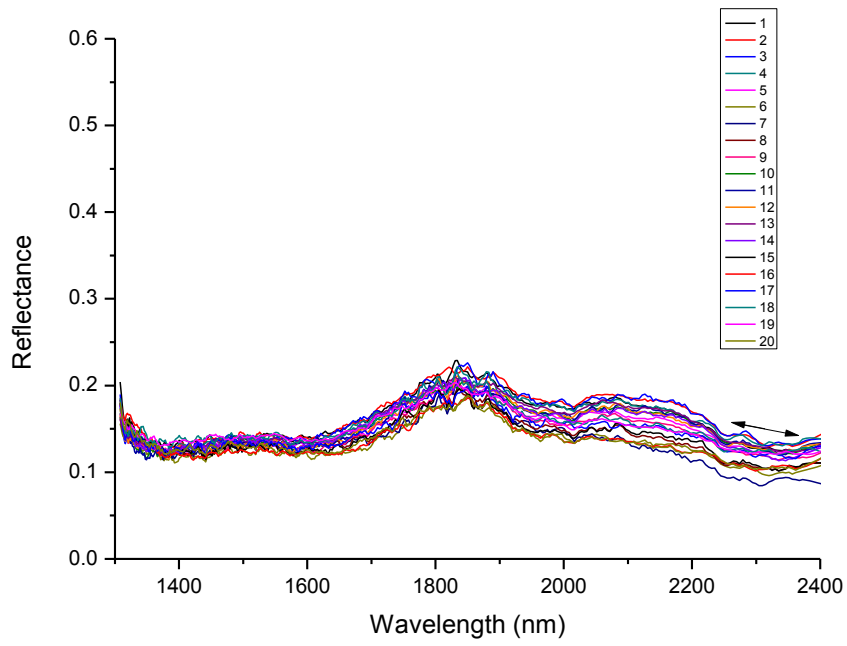


### Sample 30 sector B

### Sample 30

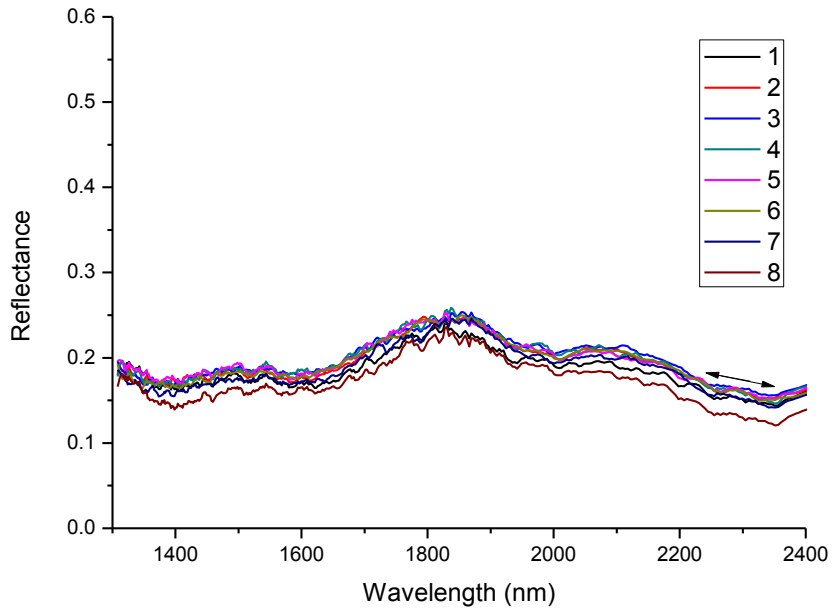


### Sample 30 sector C

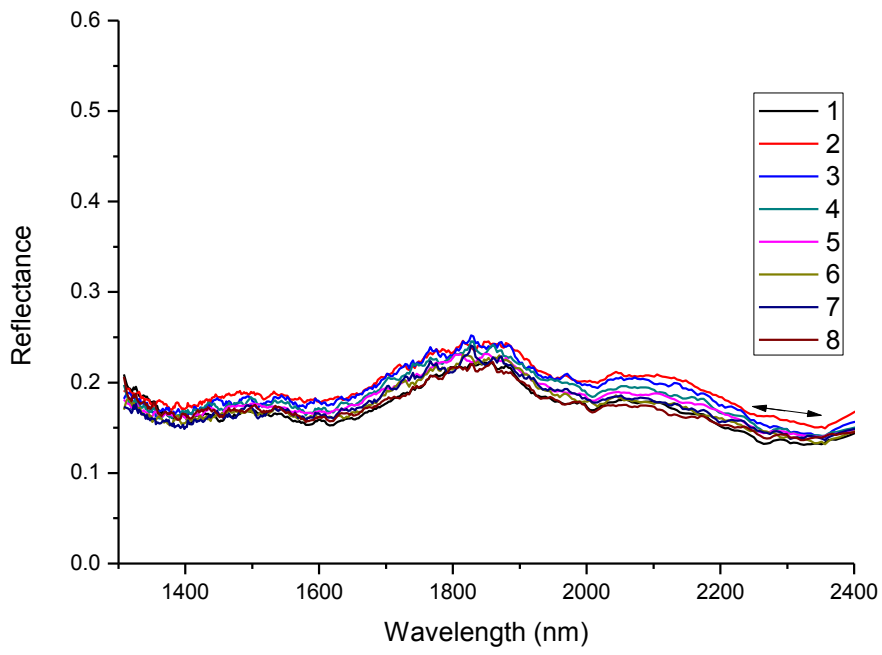


### Sample 30 COMBINED

### Sample 31

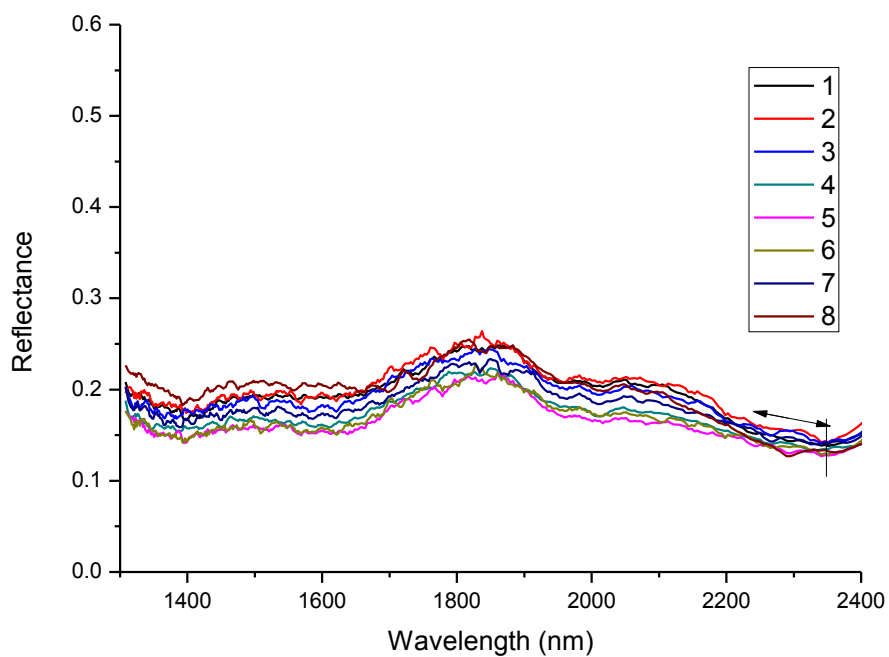


### Sample 31 sector A

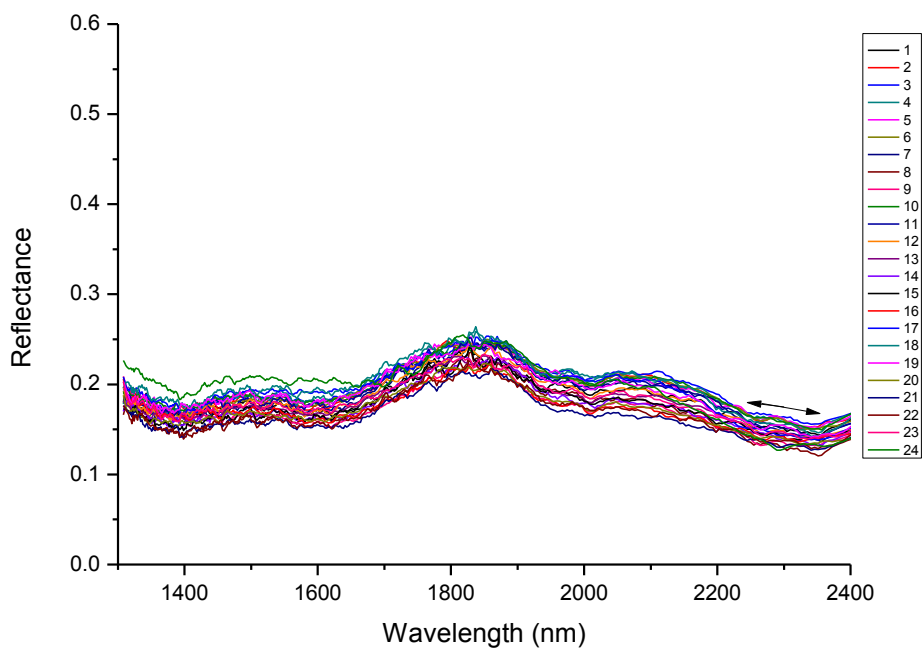


### Sample 31 sector B

### Sample 31

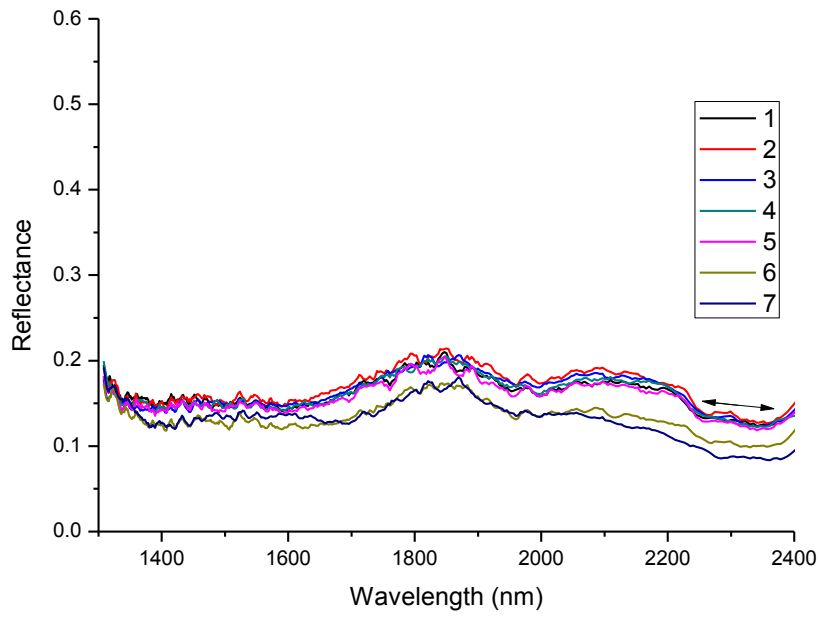


### Sample 31 sector C

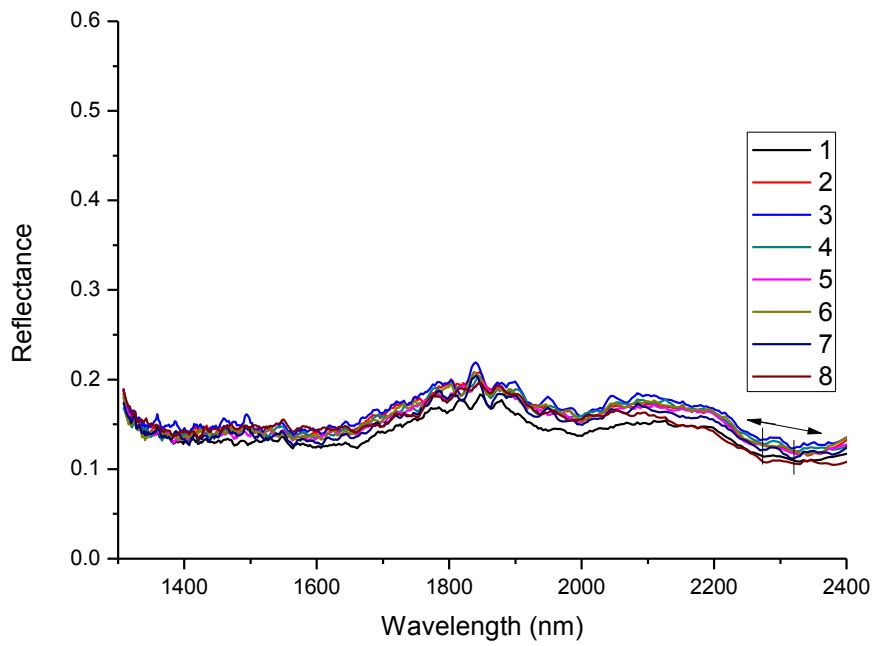


### Sample 31 COMBINED

### Sample 32



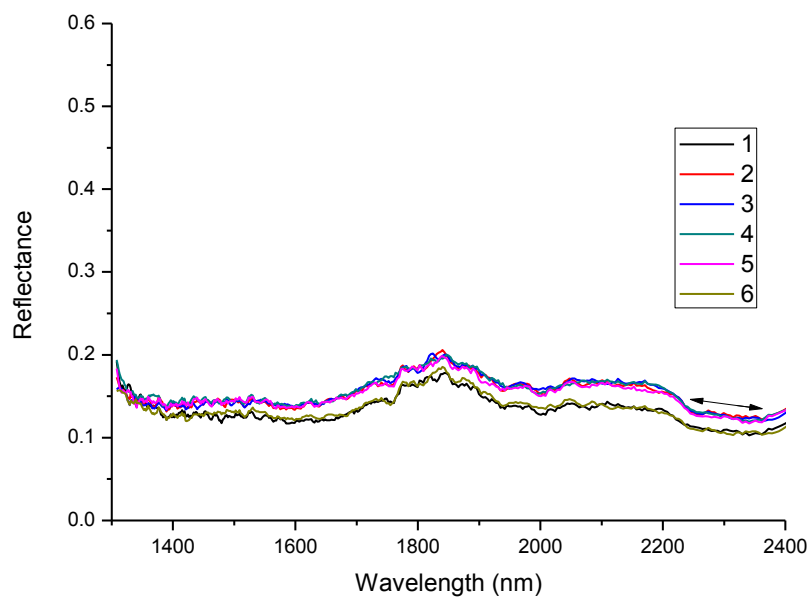
### Sample 32 sector A



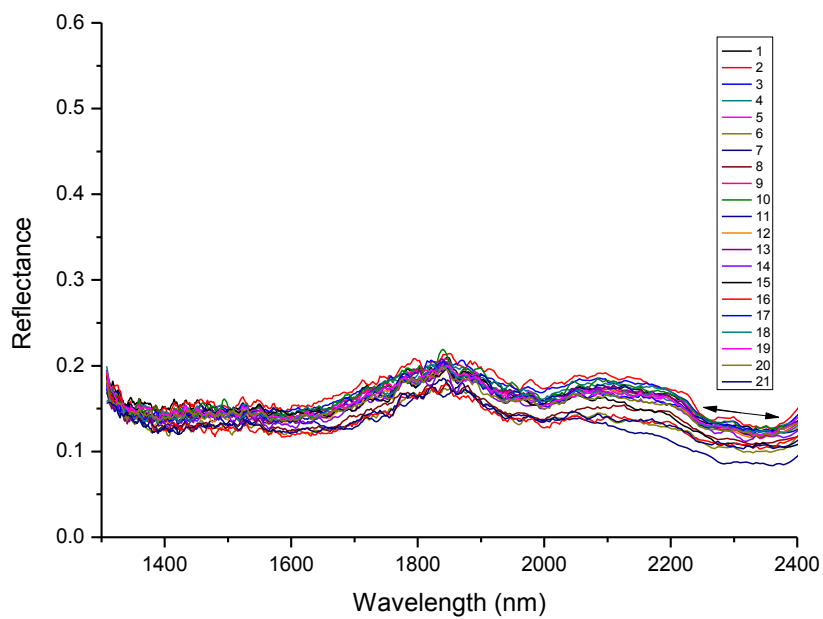
### Sample 32 sector B



### Sample 32

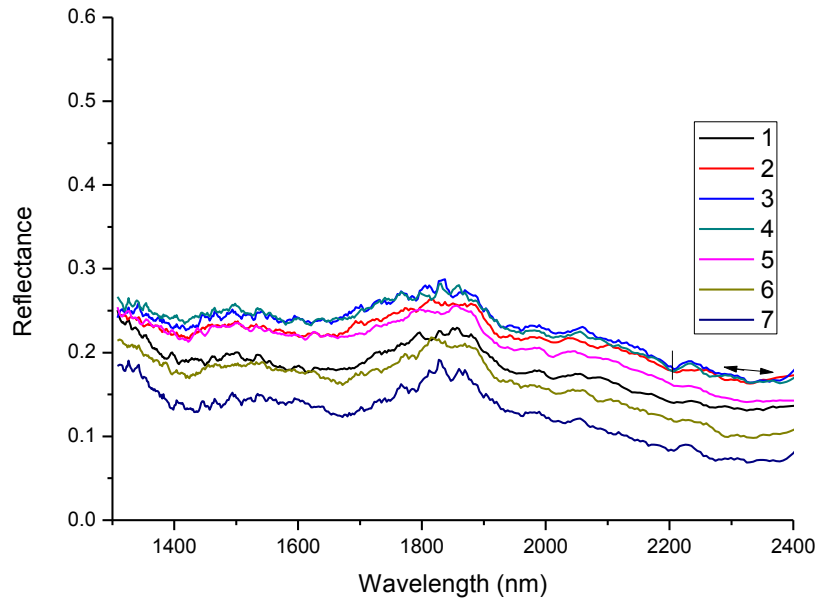


### Sample 32 sector C

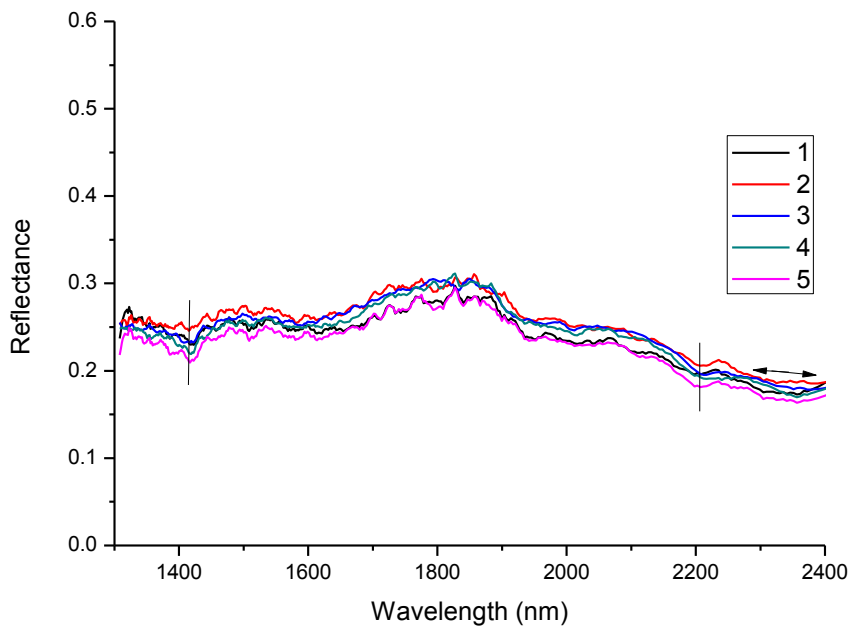


### Sample 32 COMBINED

### Sample 33

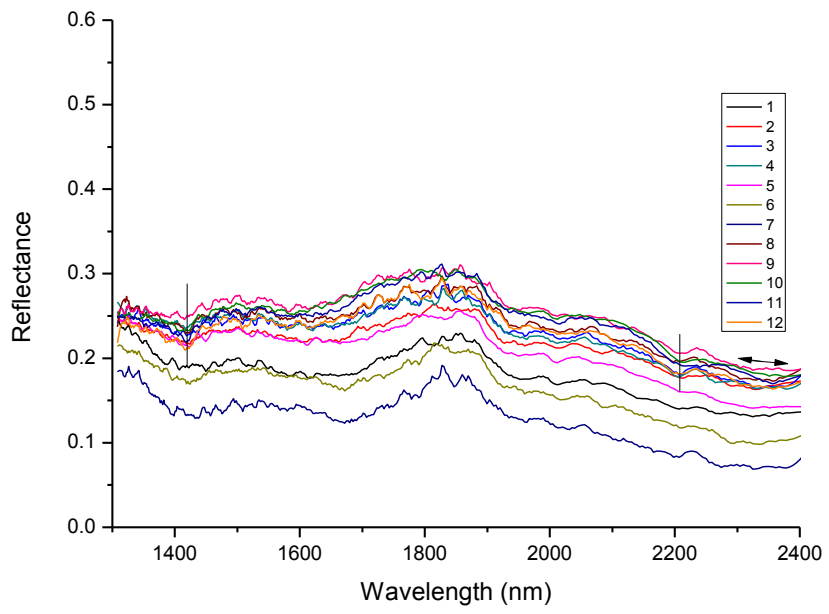


### Sample 33 sector A



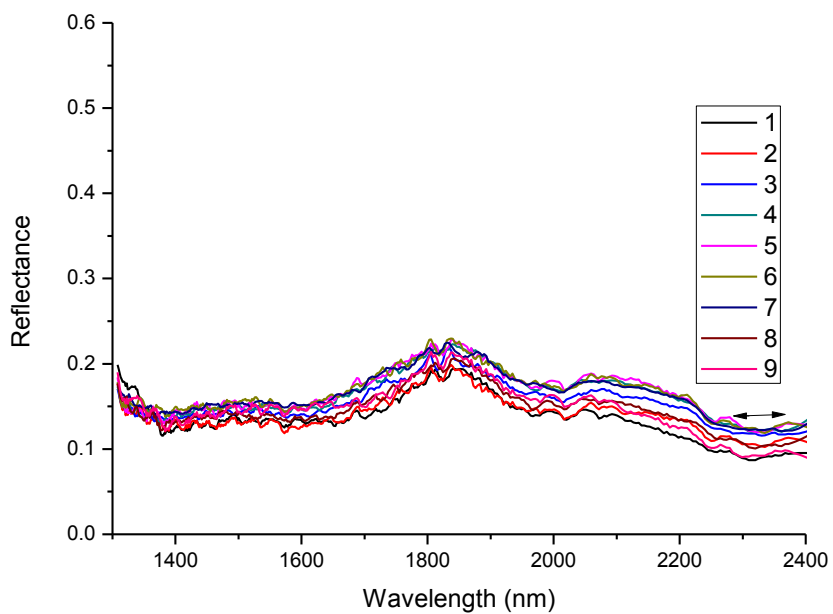
### Sample 33 sector B

### Sample 33

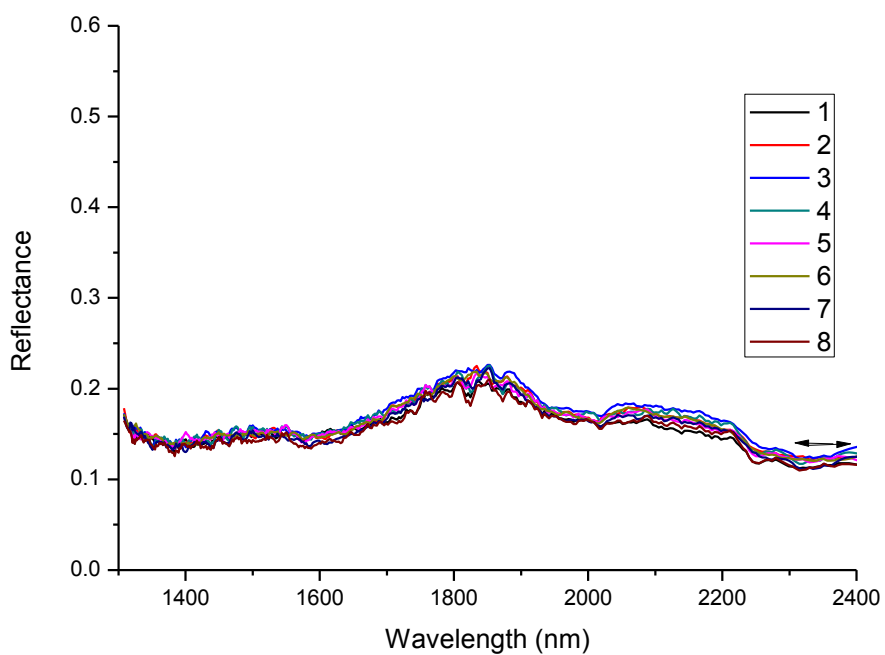


Sample 33 COMBINED

### Sample 34

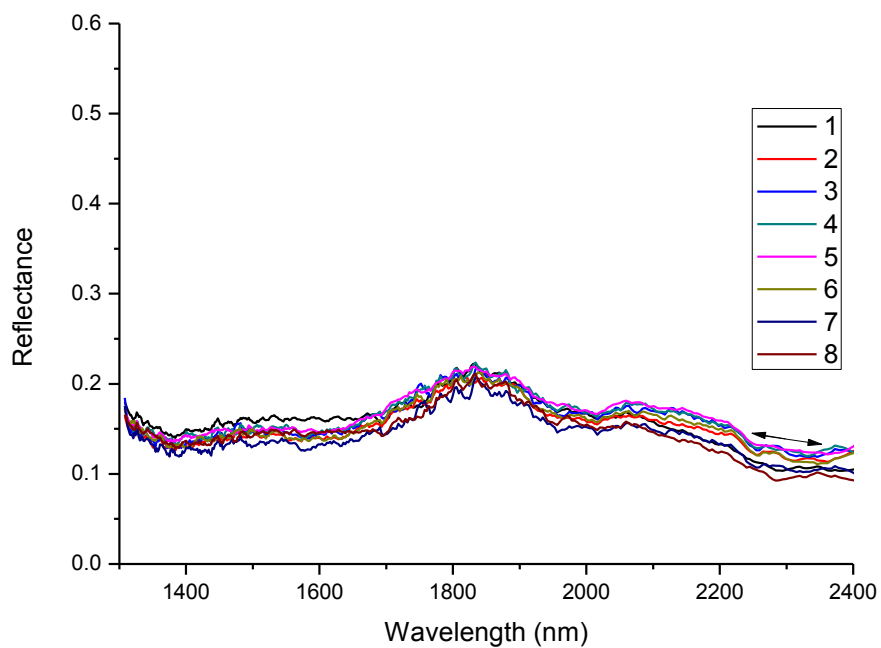


### Sample 34 sector A

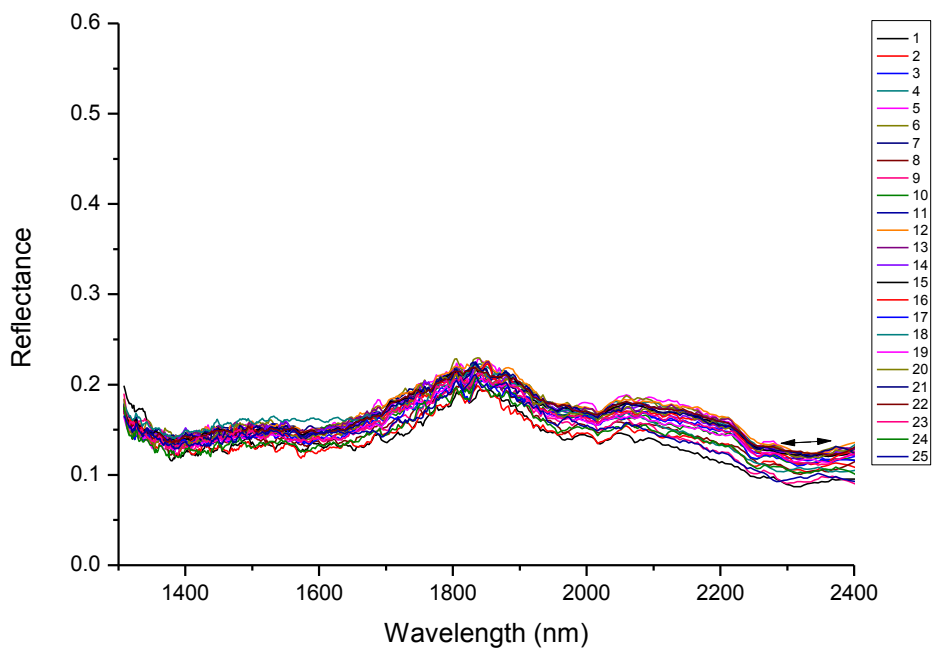


### Sample 34 sector B

### Sample 34

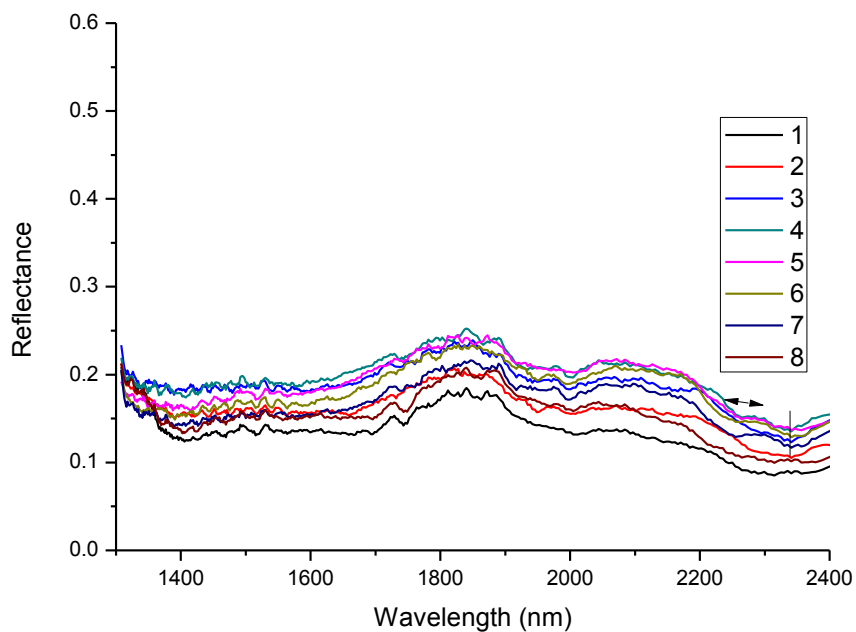


### Sample 34 sector C

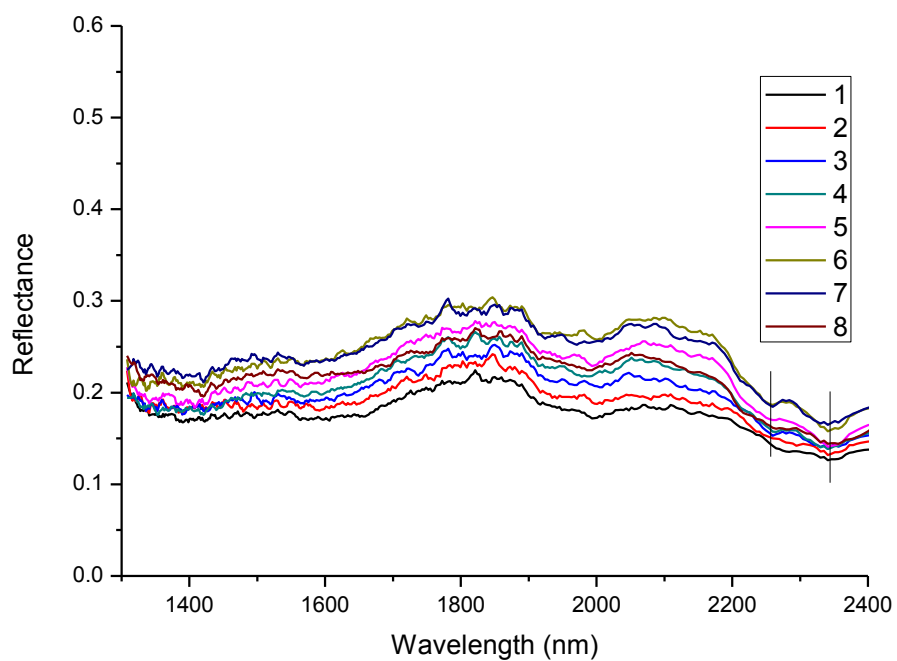


### Sample 34 COMBINED

### Sample 35

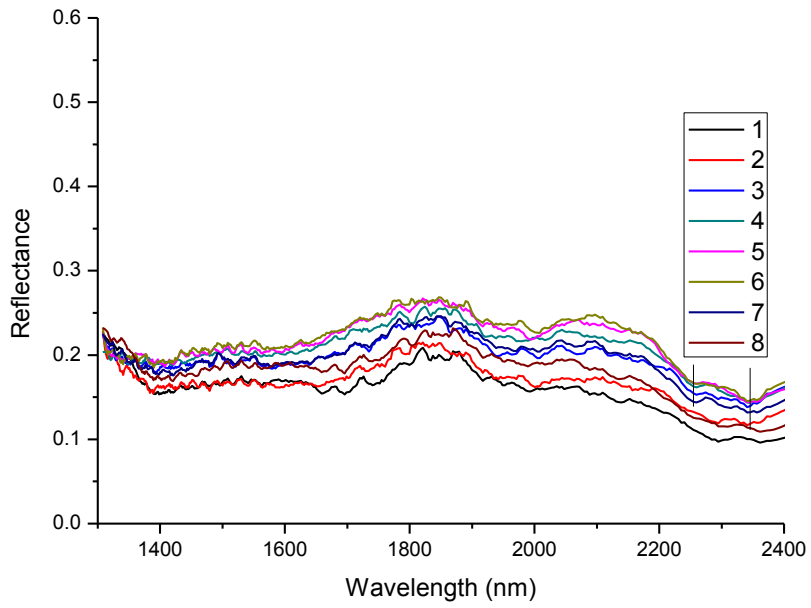


### Sample 35 sector A

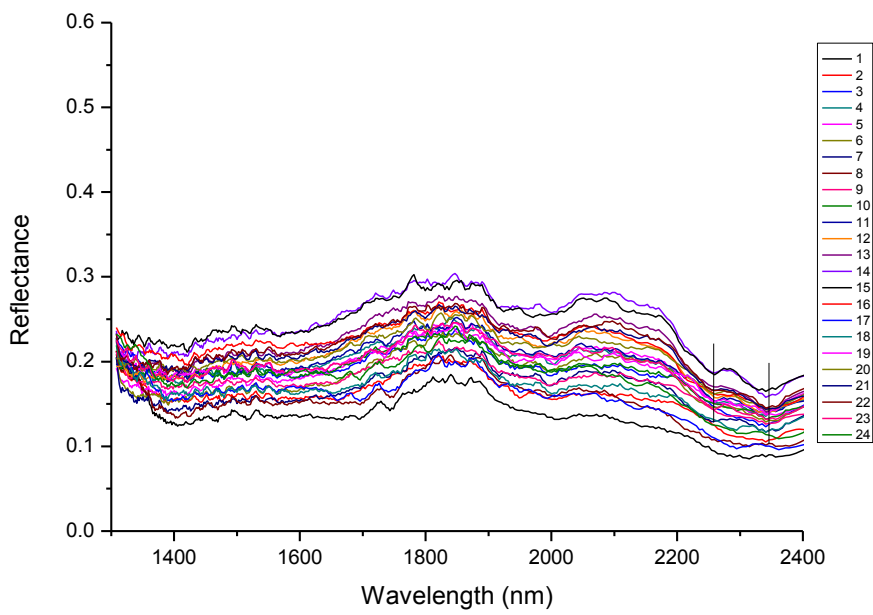


### Sample 35 sector B

### Sample 35

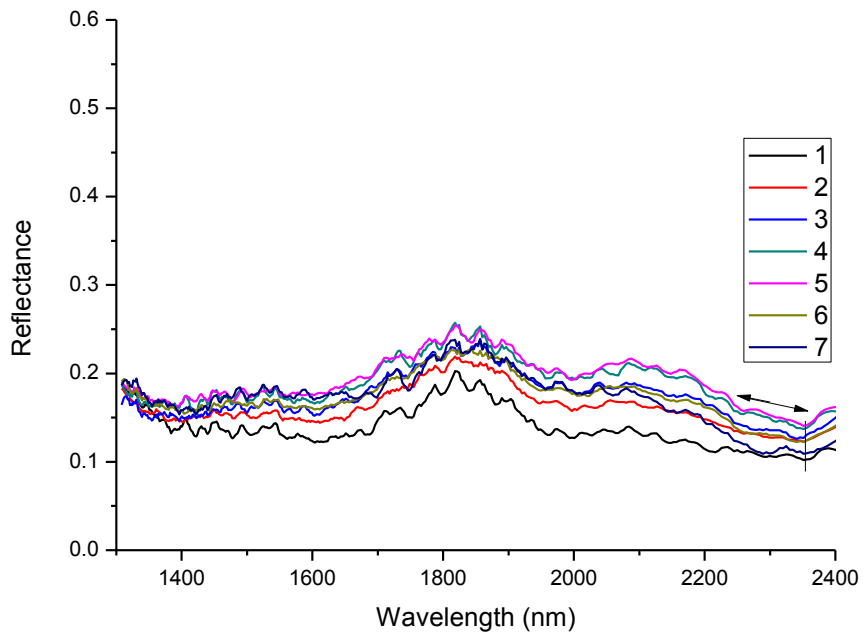


### Sample 35 sector C

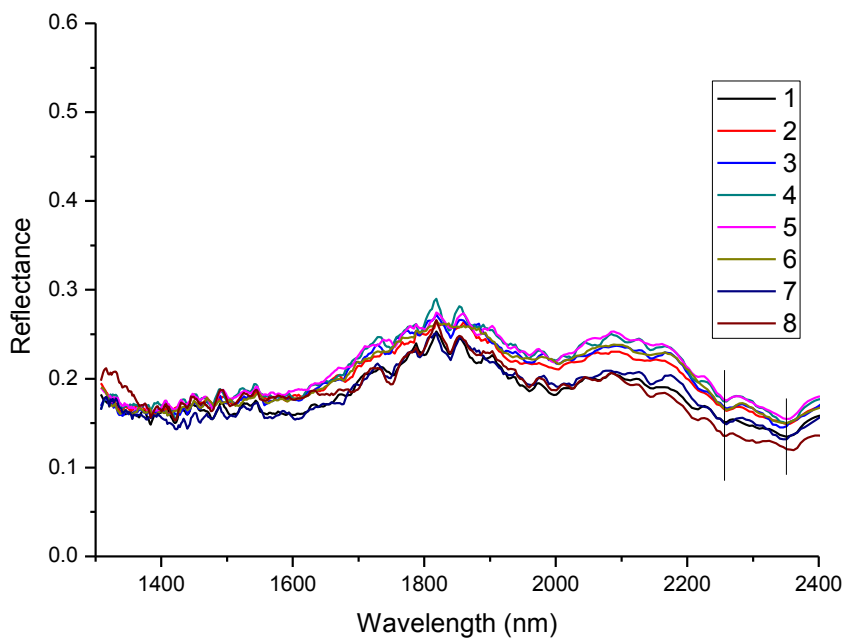


### Sample 35 COMBINED

### Sample 36



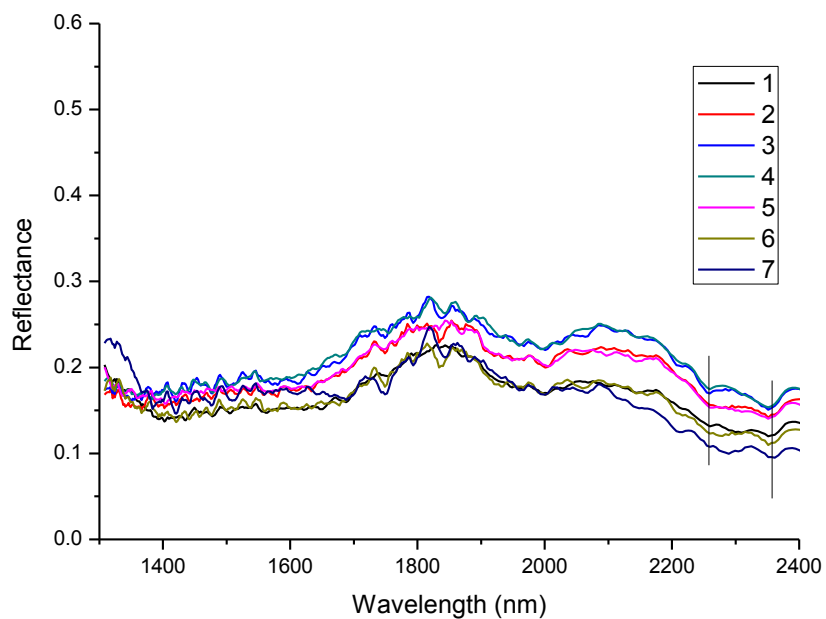
### Sample 36 sector A



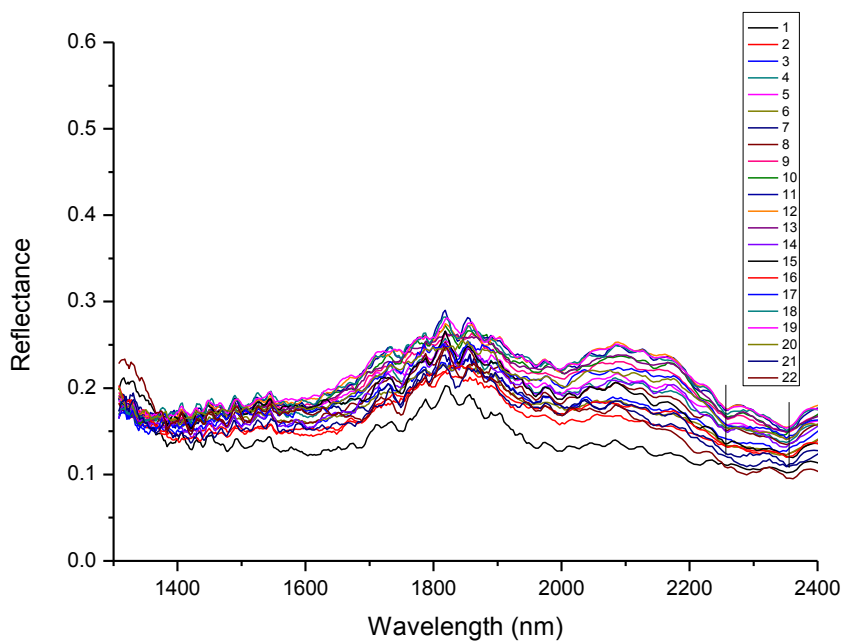
### Sample 36 sector B



### Sample 36

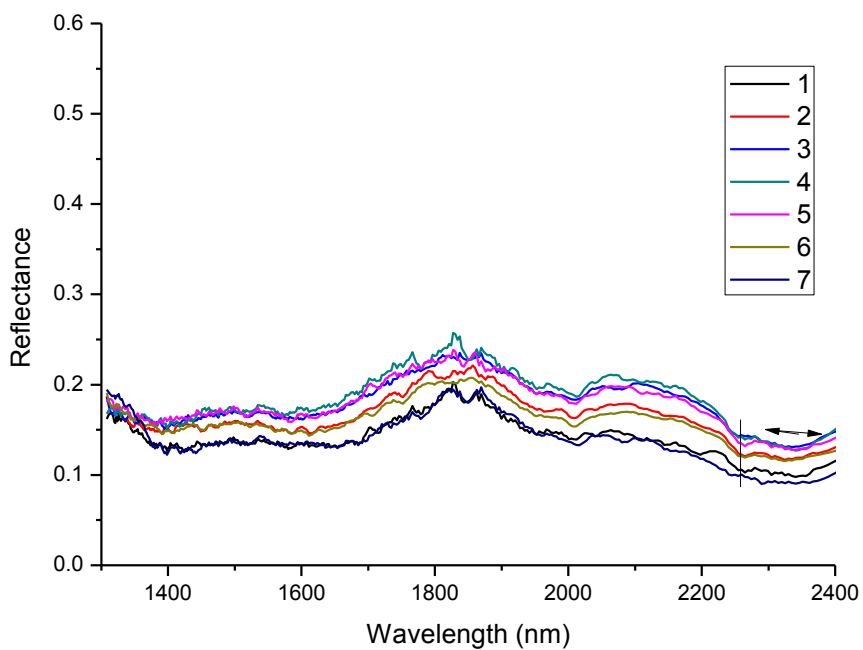


### Sample 36 sector C

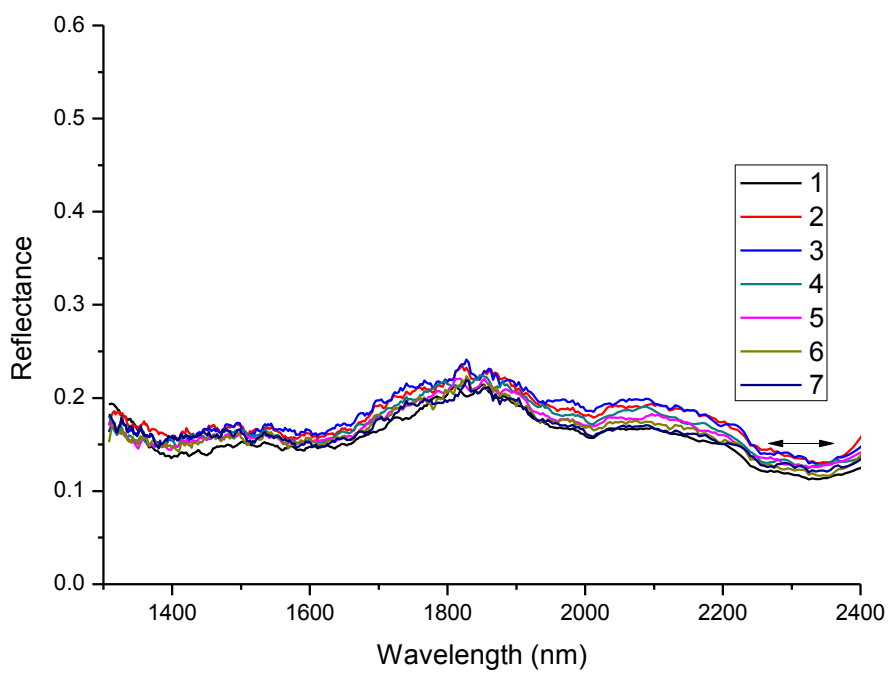


### Sample 36 COMBINED

### Sample 37

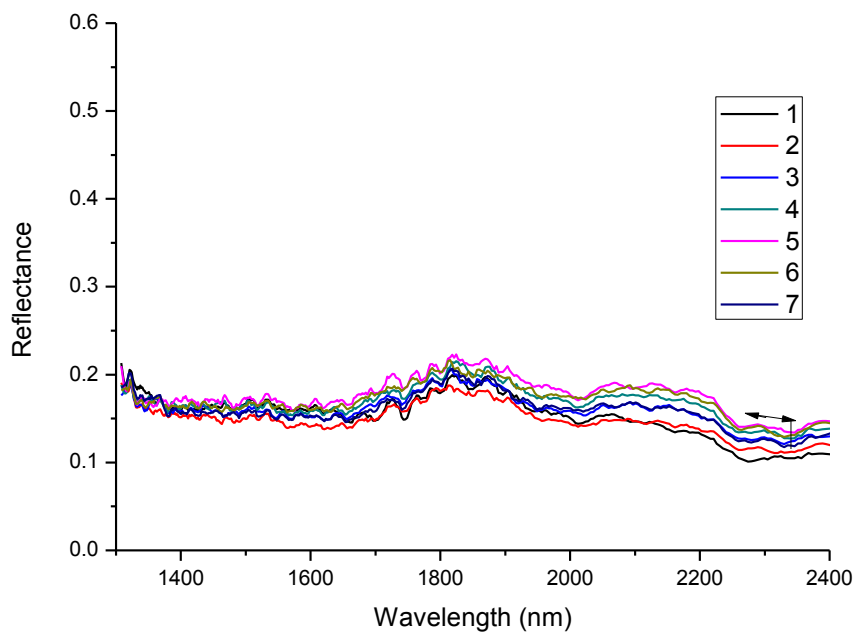


### Sample 37 sector A

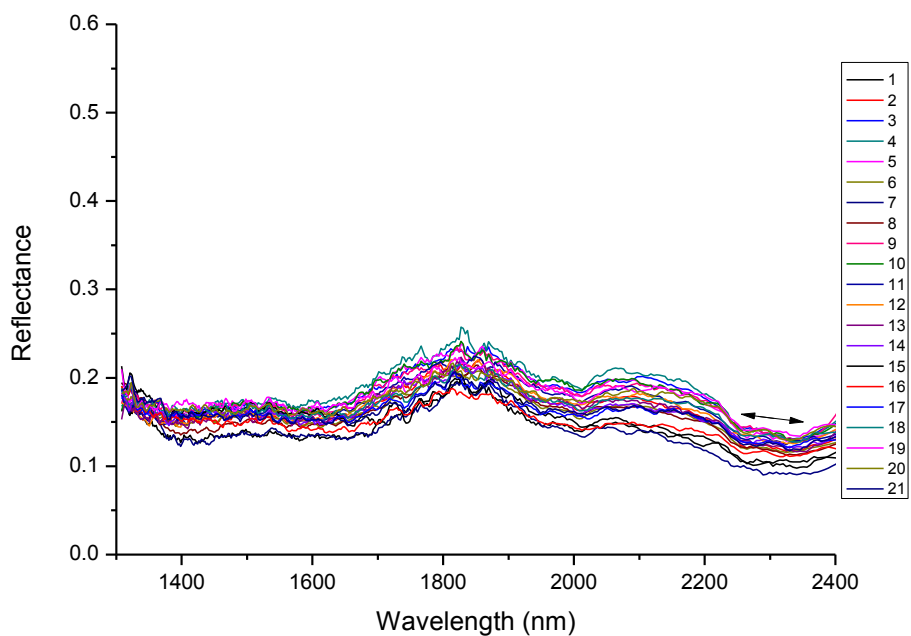


### Sample 37 sector B

### Sample 37

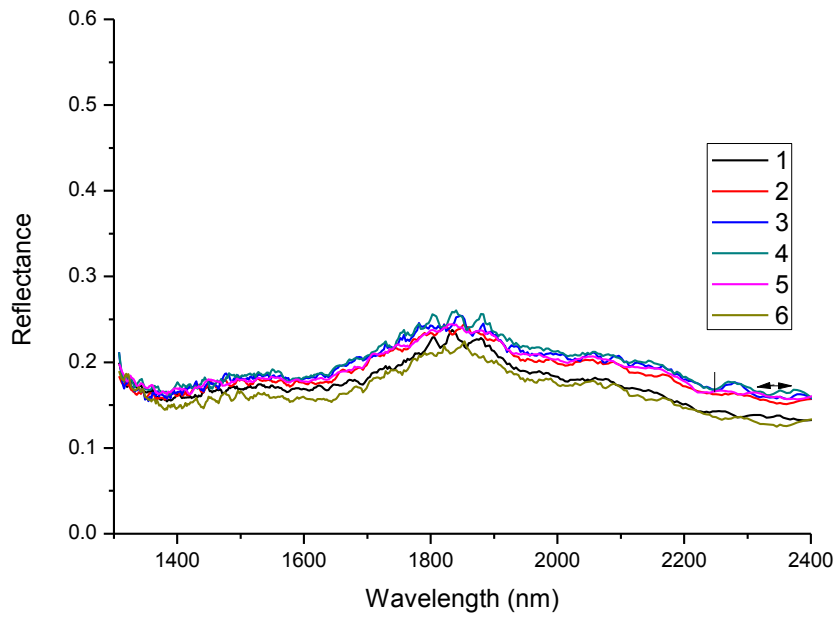


### Sample 37 sector C

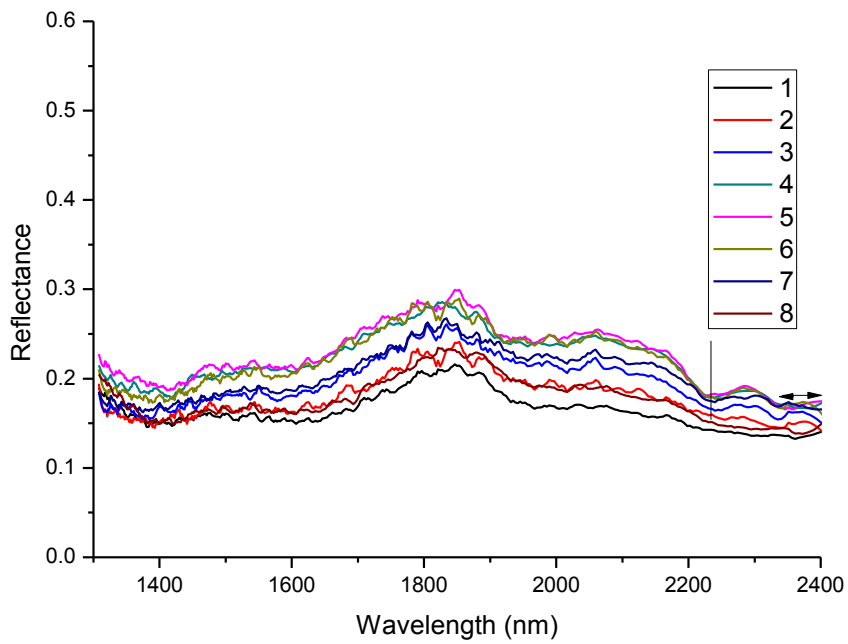


### Sample 37 COMBINED

### Sample 38

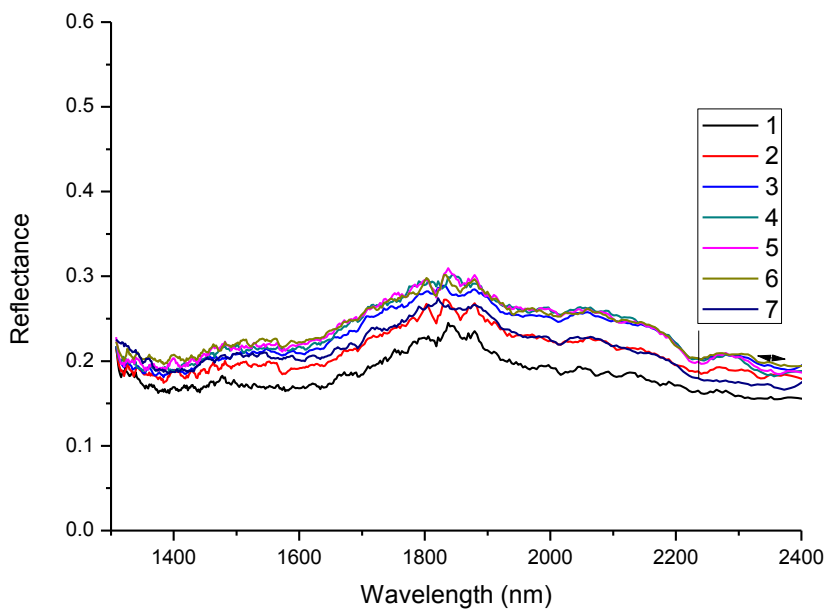


### Sample 38 sector A

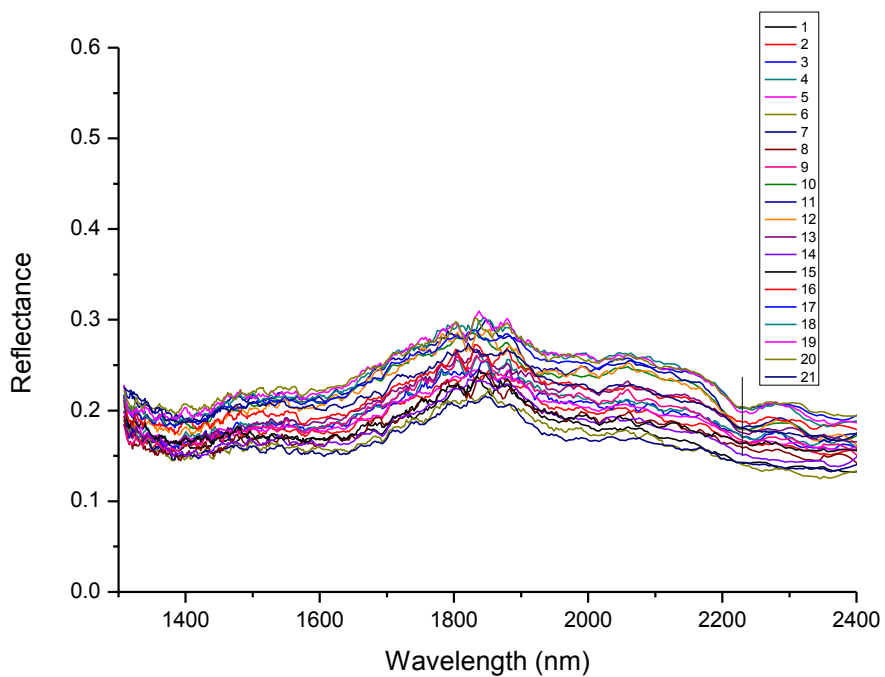


### Sample 38 sector B

### Sample 38

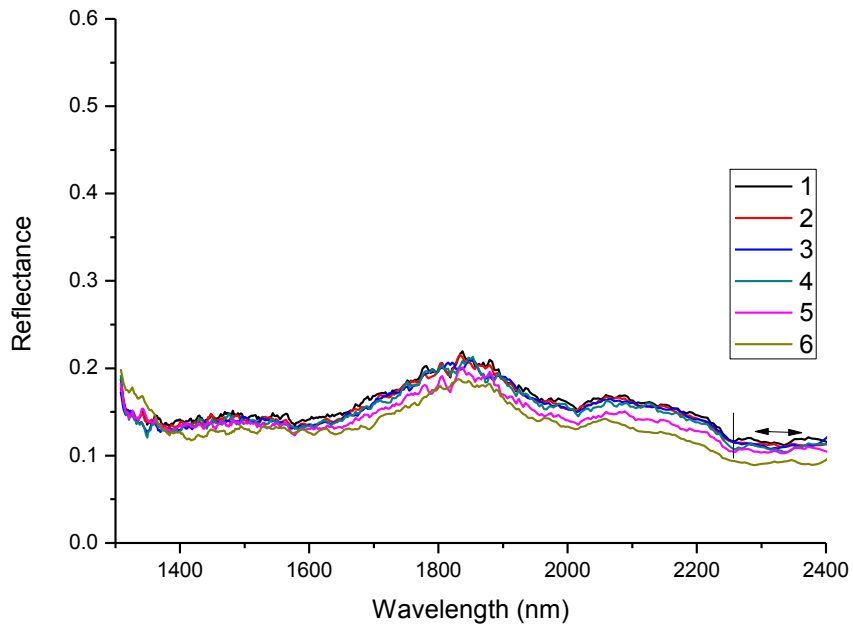


### Sample 38 sector C

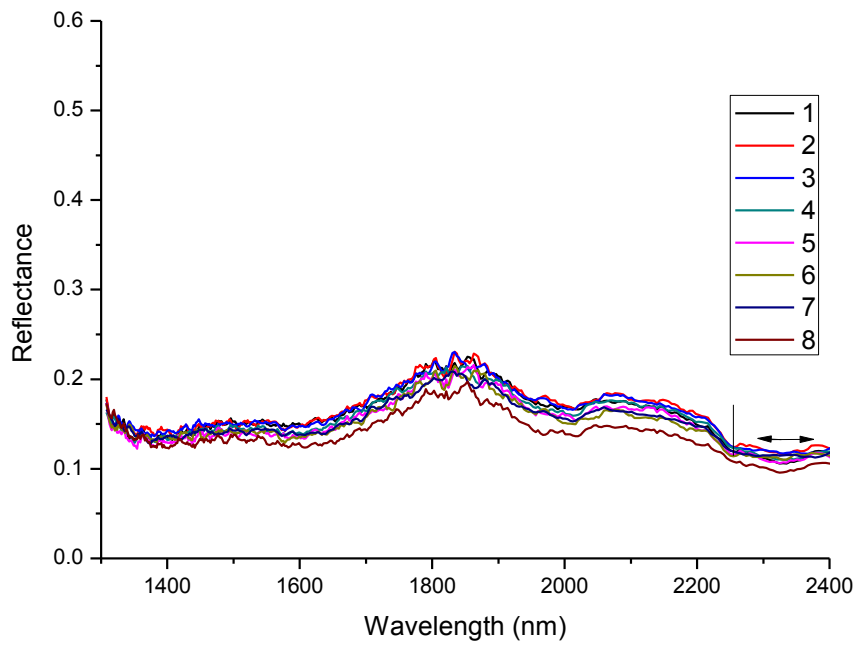


### Sample 38 COMBINED

### Sample 39

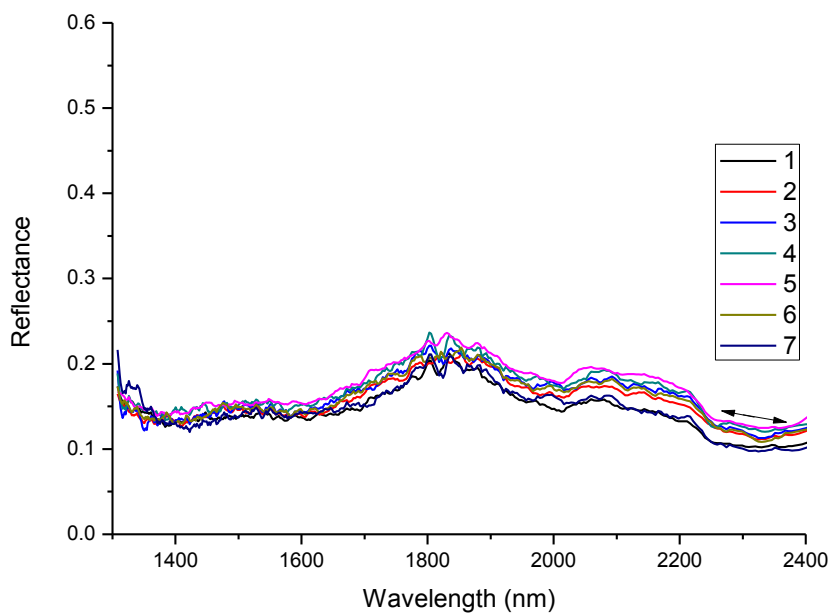


### Sample 39 sector A

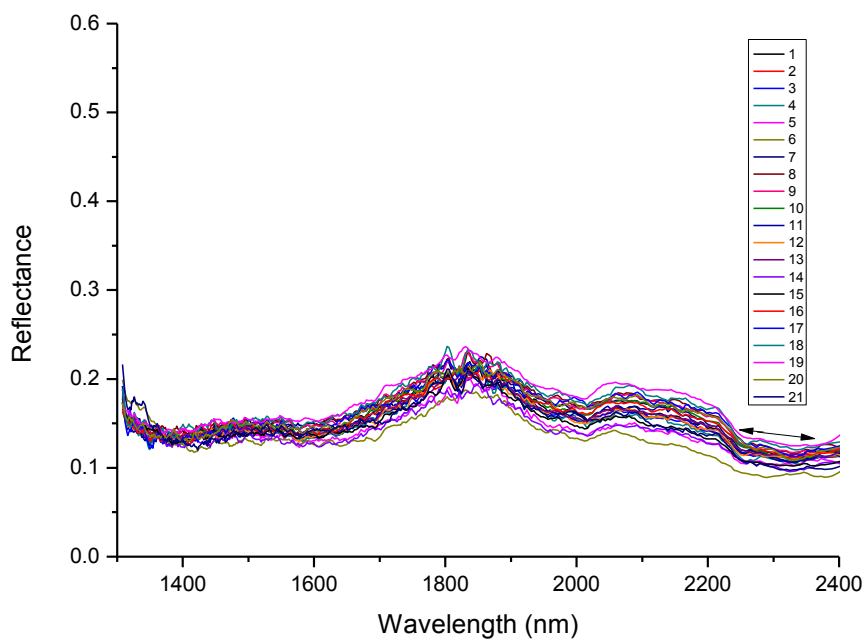


### Sample 39 sector B

### Sample 39

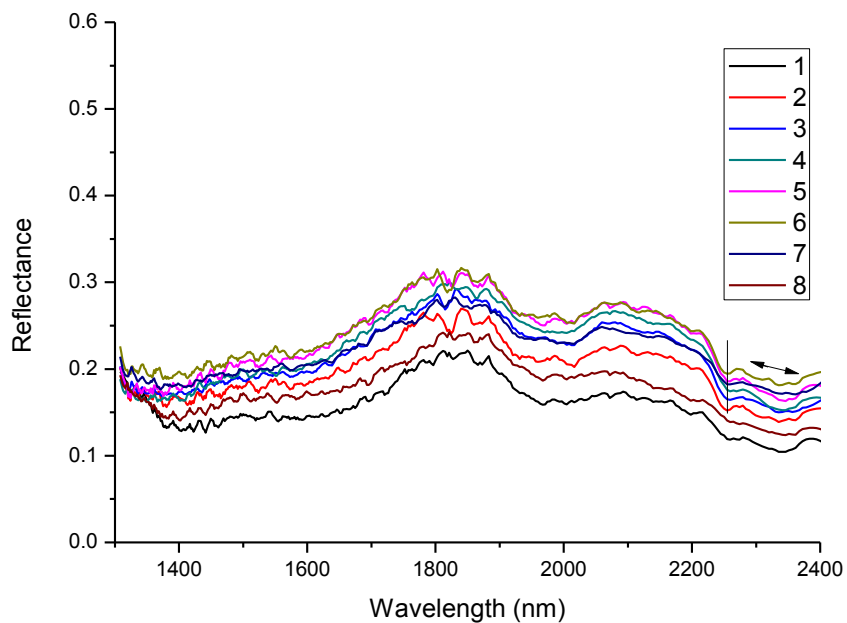


### Sample 39 sector C

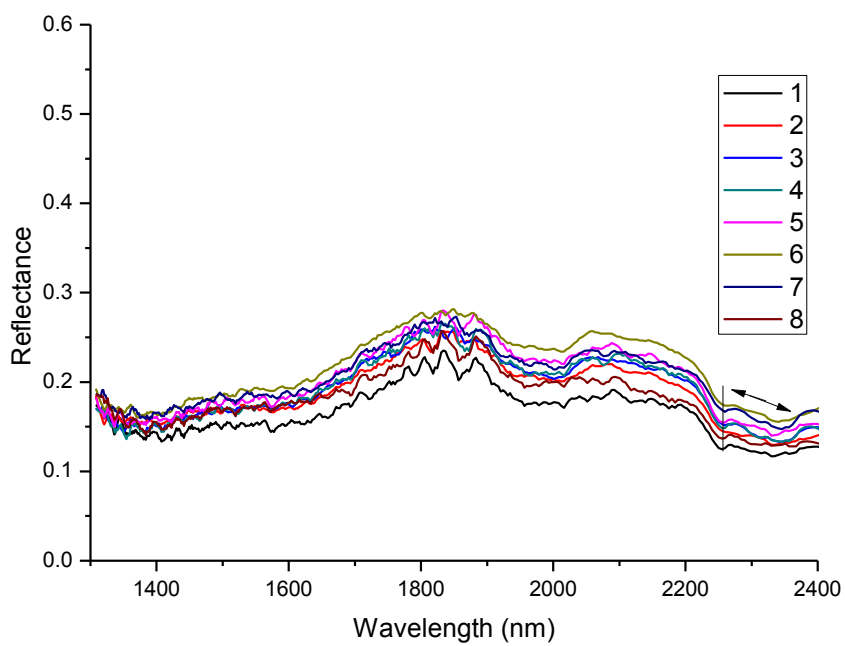


### Sample 39 COMBINED

### Sample 40



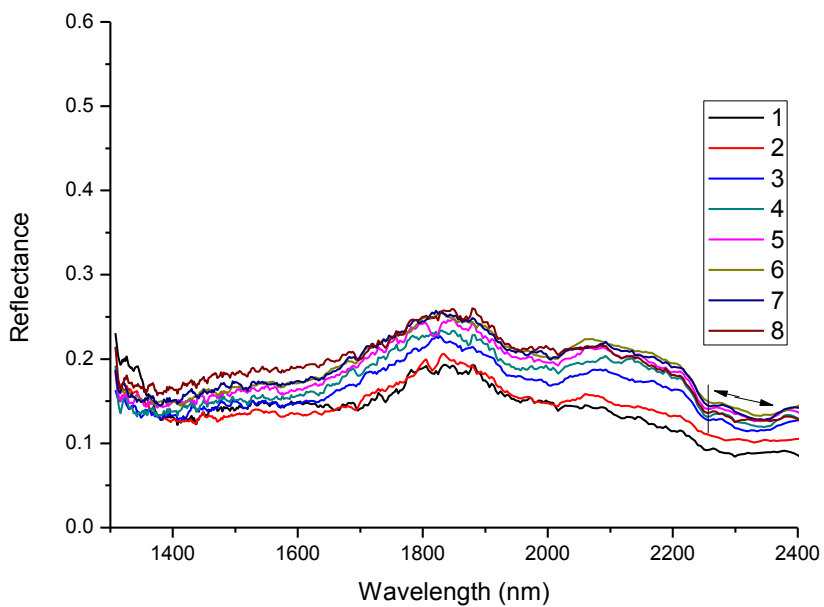
### Sample 40 sector A



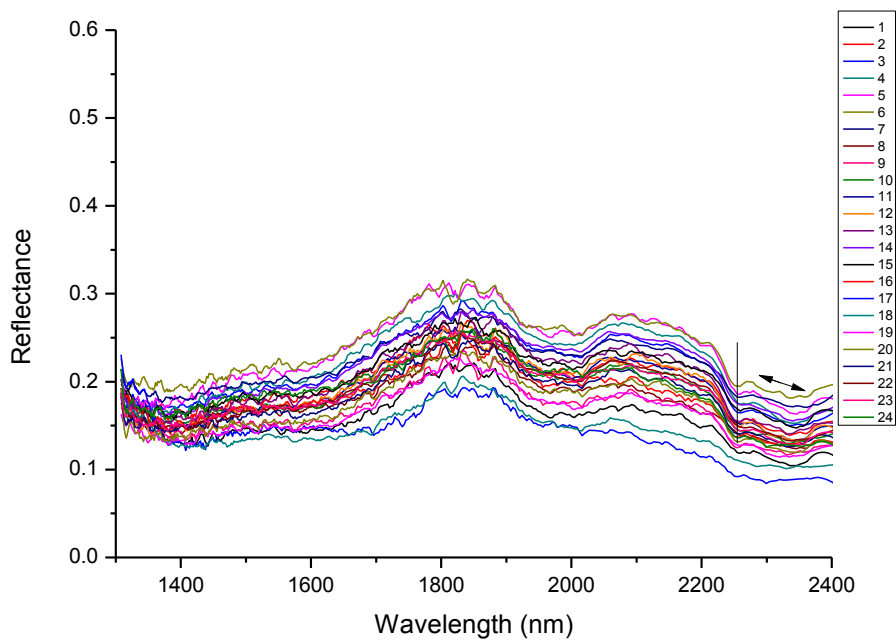
### Sample 40 sector B



### Sample 40

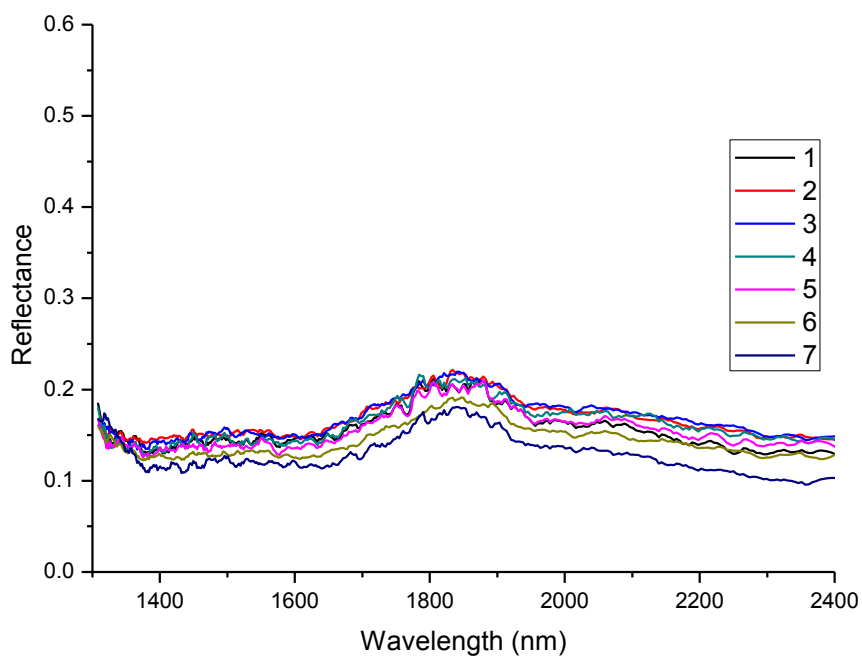


### Sample 40 sector C

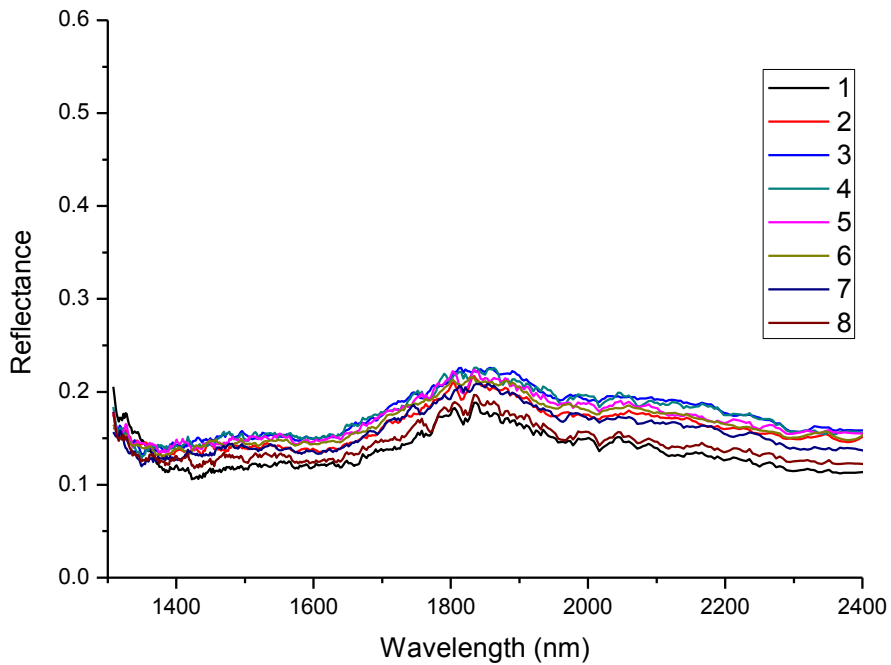


### Sample 40 COMBINED

### Sample 41

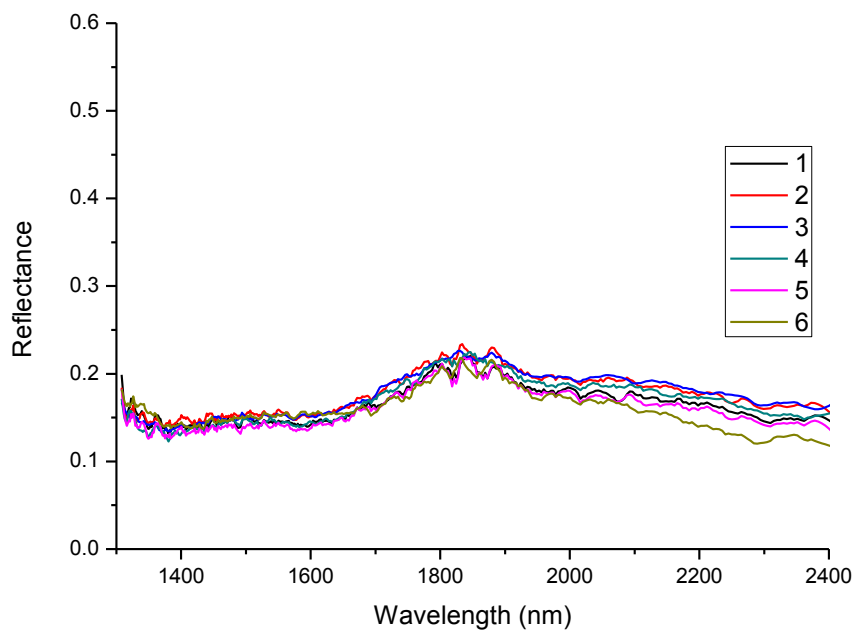


### Sample 41 sector A

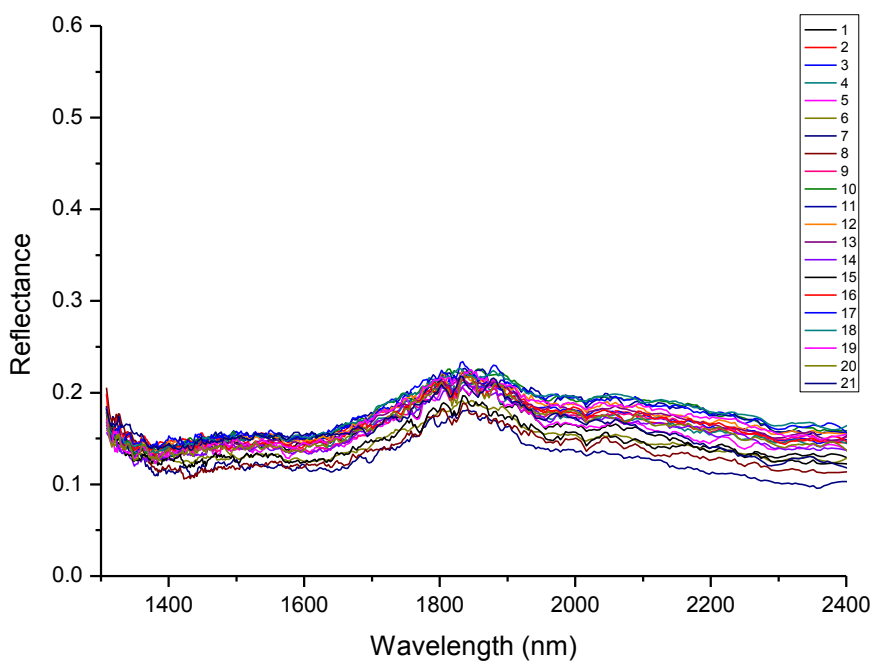


### Sample 41 sector B

### Sample 41

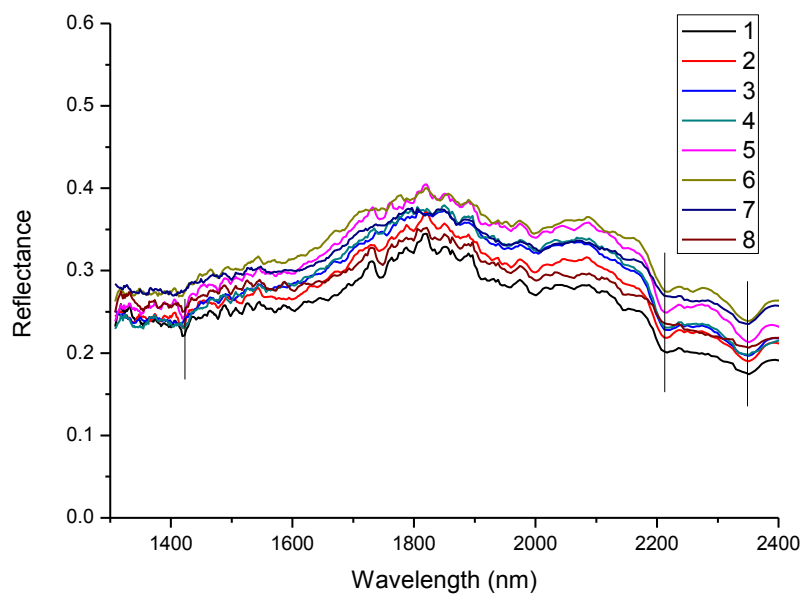


### Sample 41 sector C

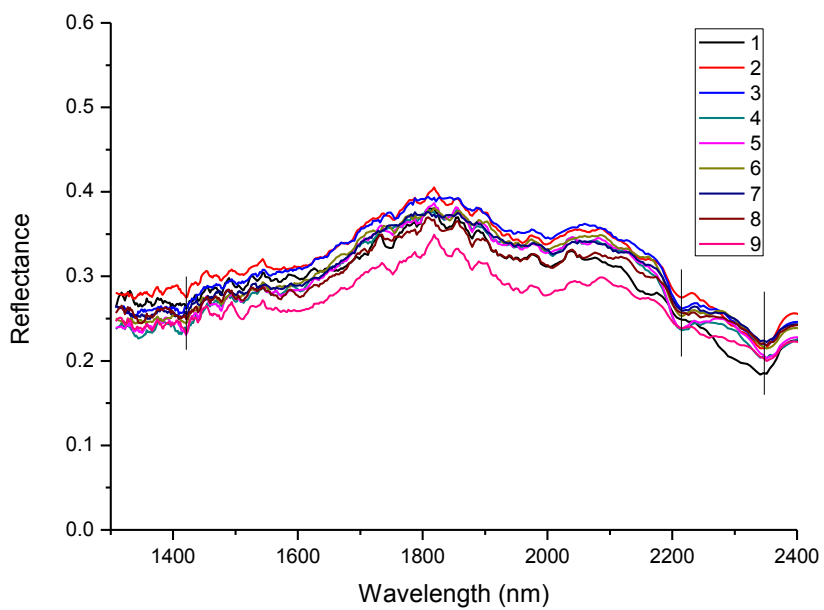


### Sample 41 COMBINED

### Sample 42

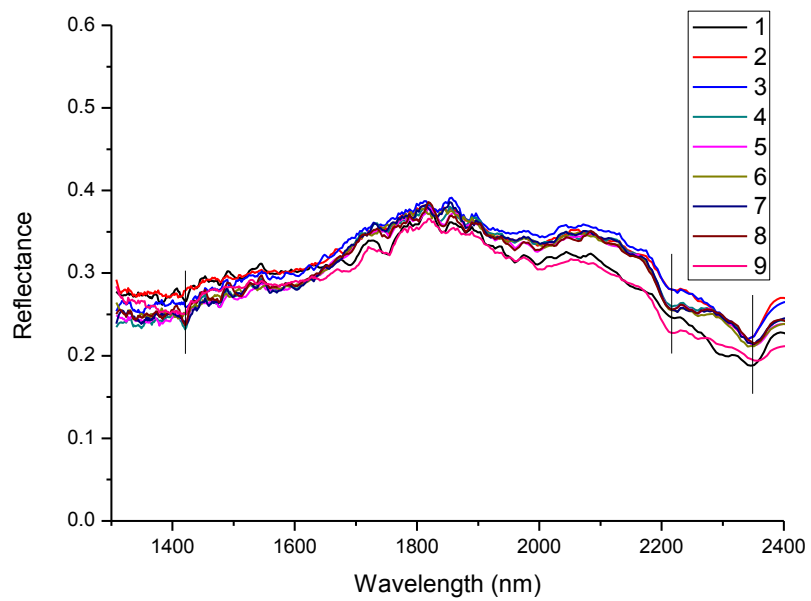


### Sample 42 sector A

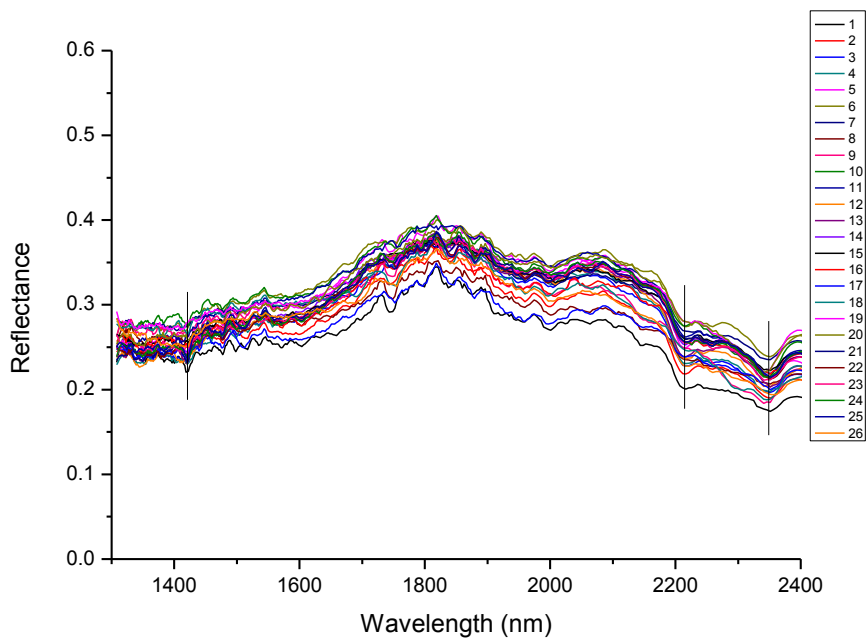


### Sample 42 sector B

### Sample 42

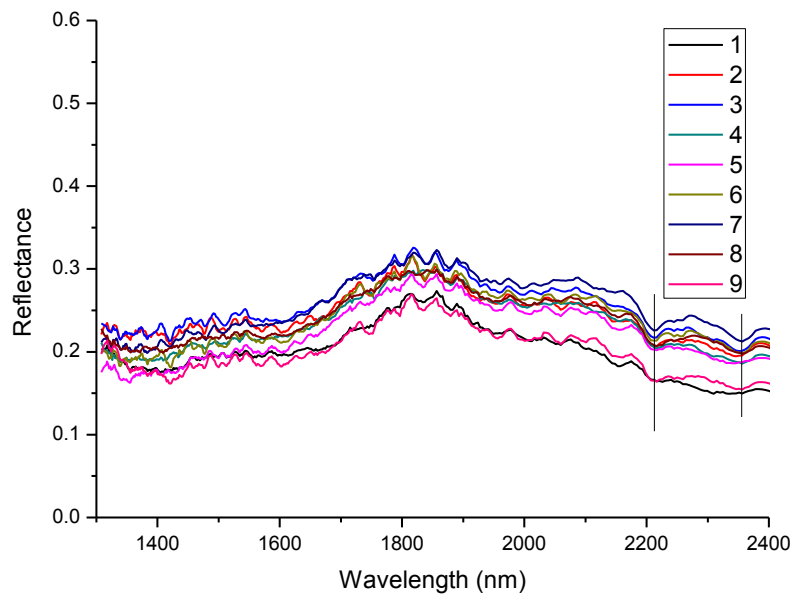


### Sample 42 sector C

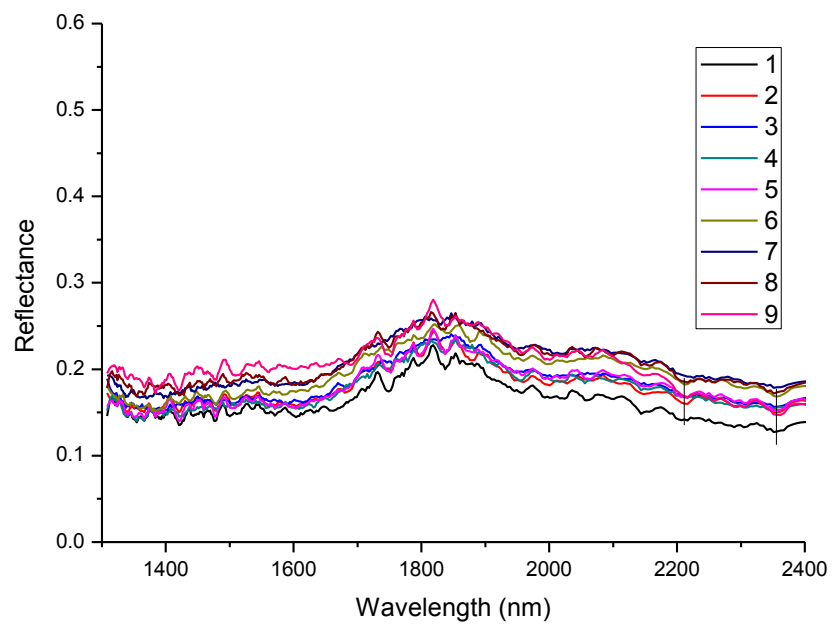


### Sample 42 COMBINED

### Sample 43

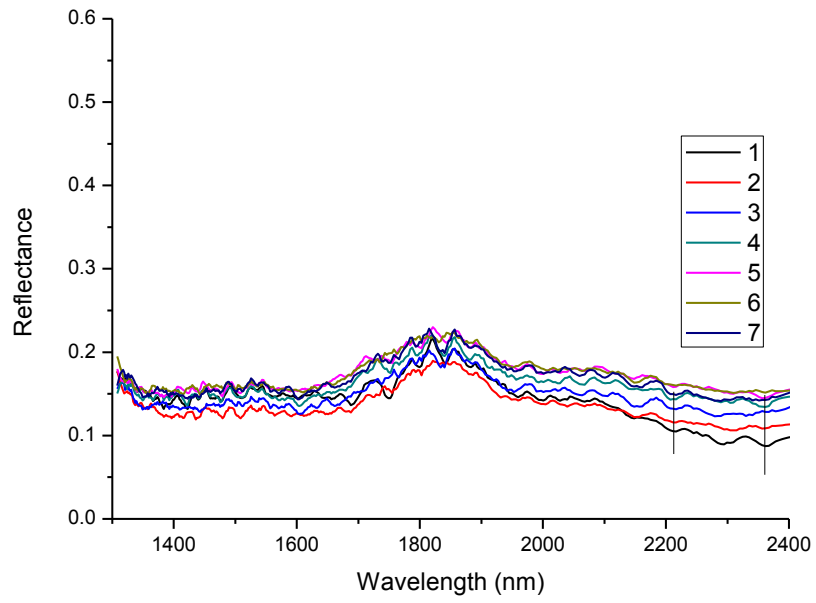


### Sample 43 sector A

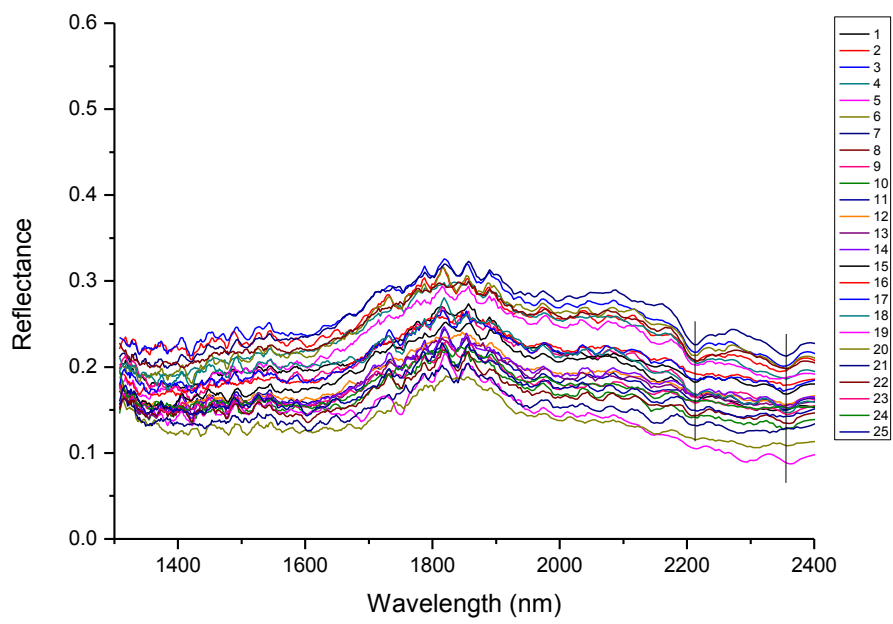


### Sample 43 sector B

### Sample 43

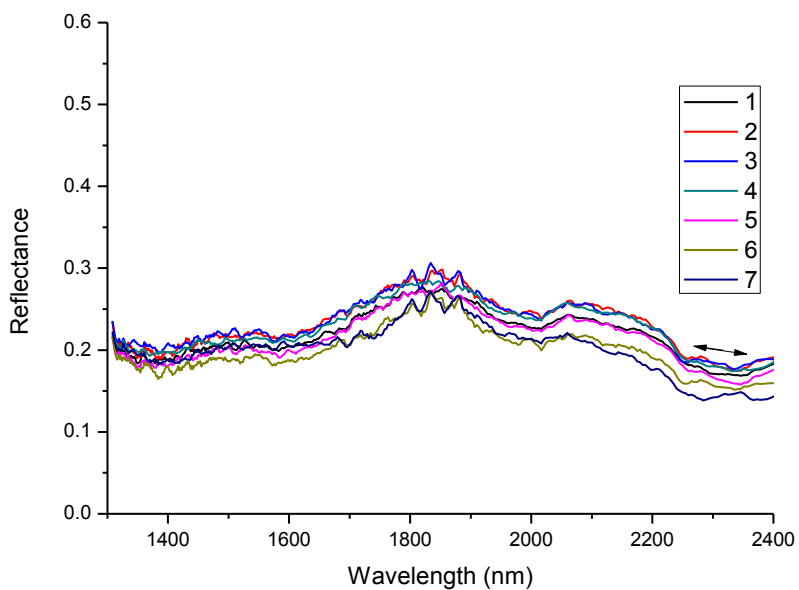


### Sample 43 sector C

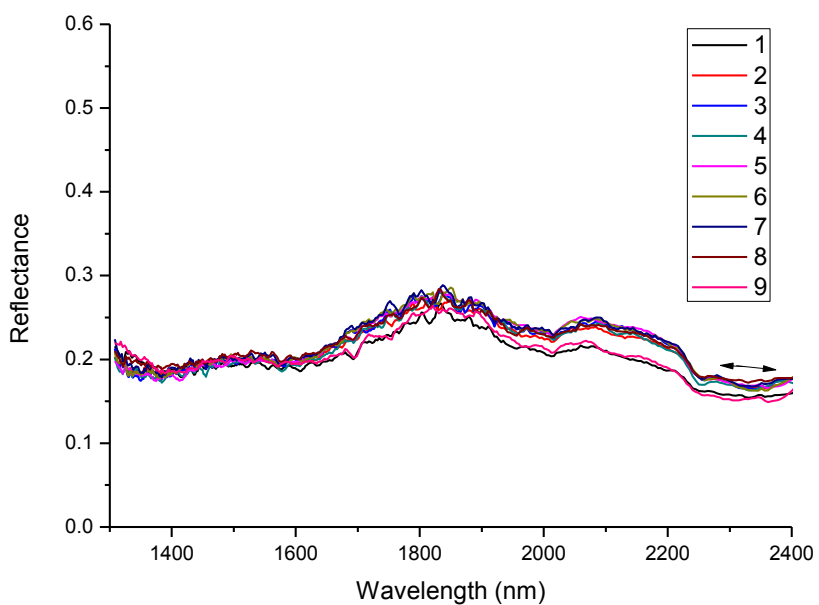


### Sample 43 COMBINED

### Sample 44



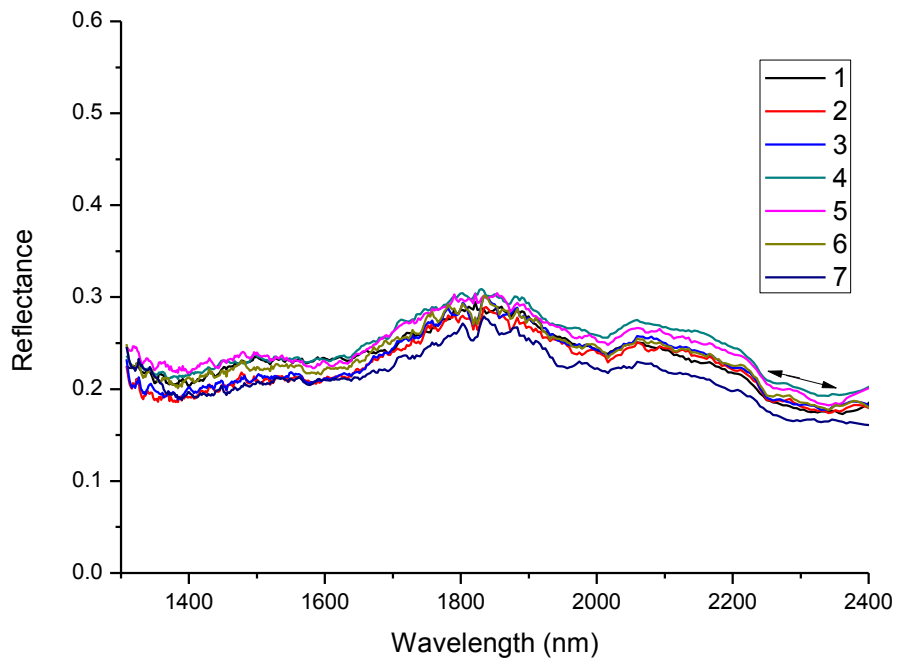
### Sample 44 sector A



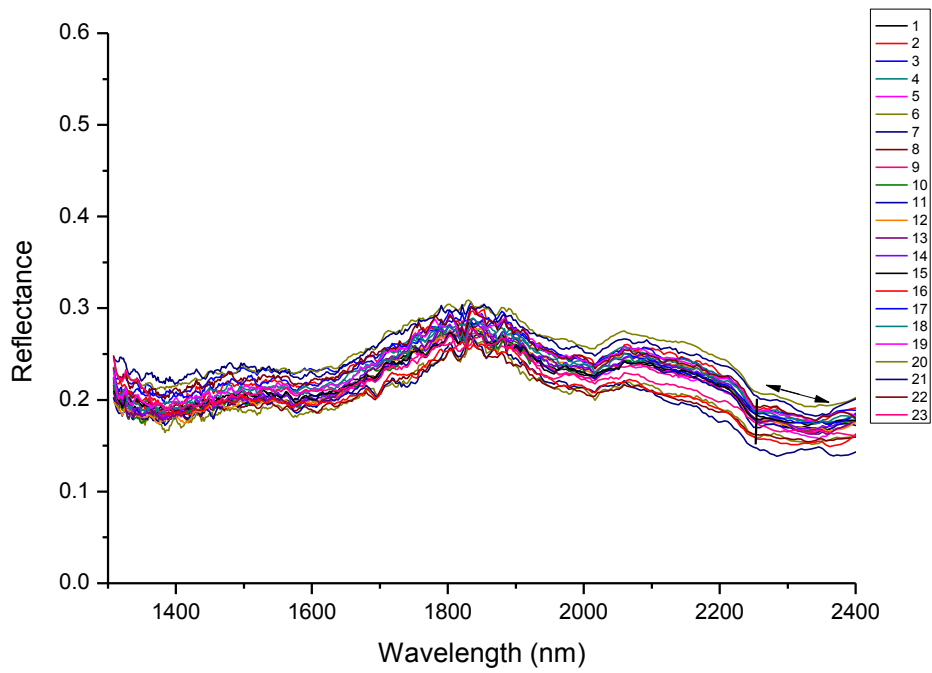
### Sample 44 sector B



### Sample 44

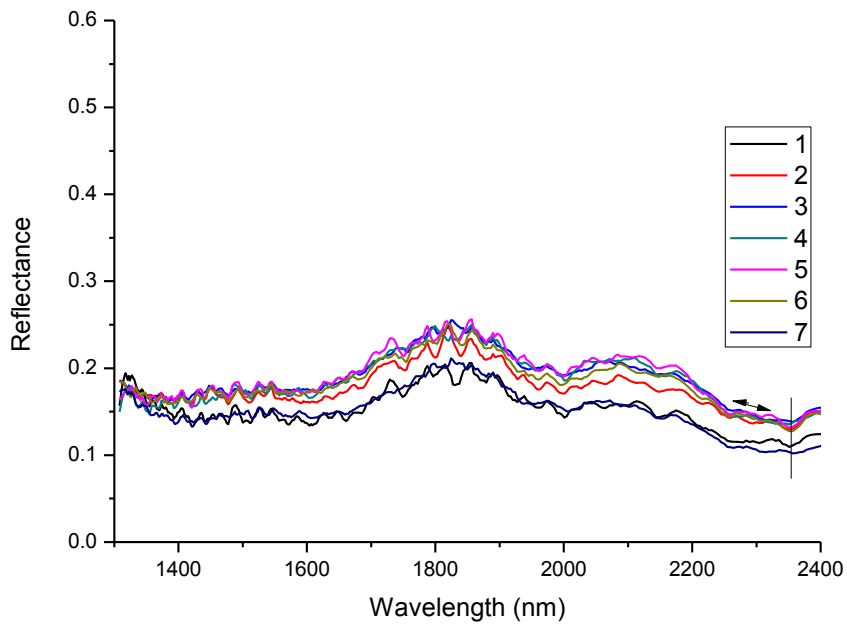


### Sample 44 sector C

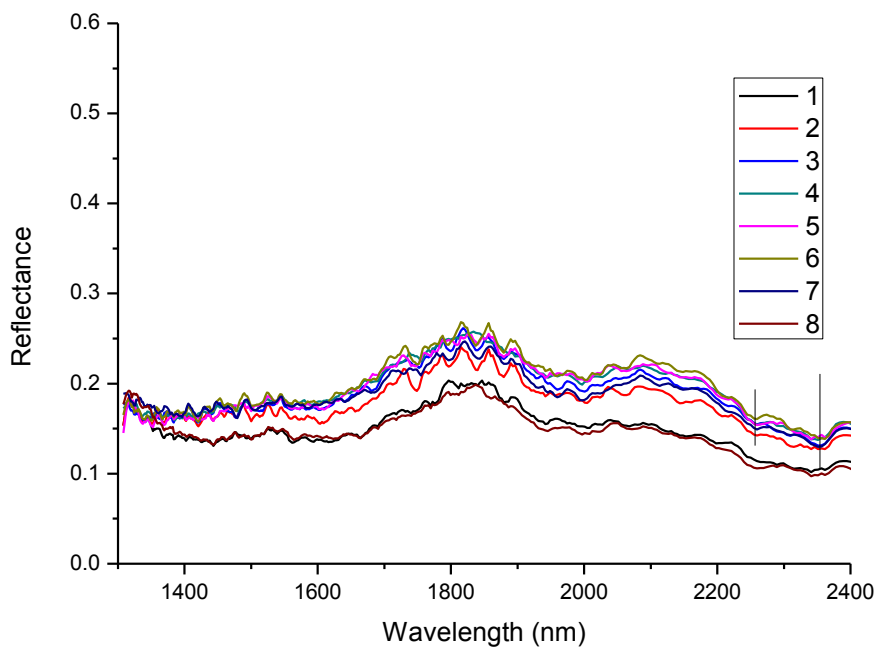


### Sample 44 COMBINED

### Sample 45

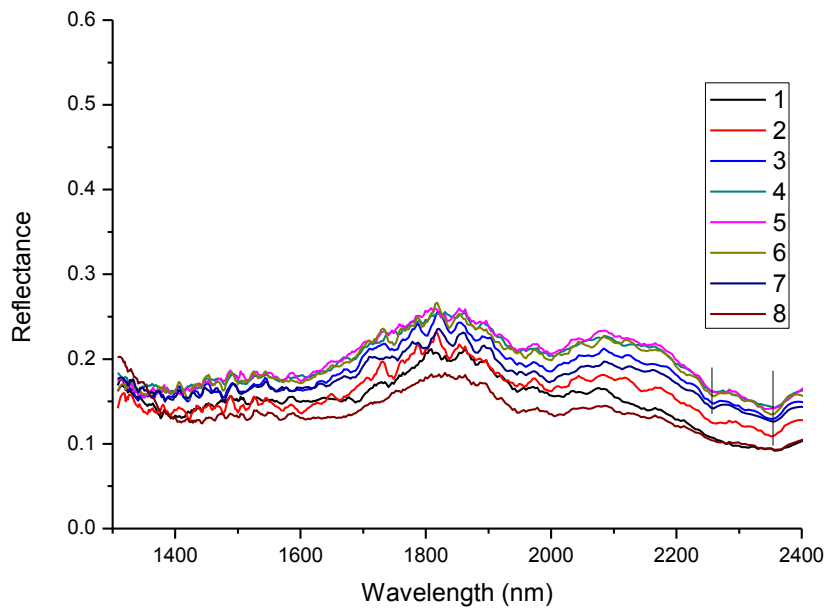


### Sample 45 sector A

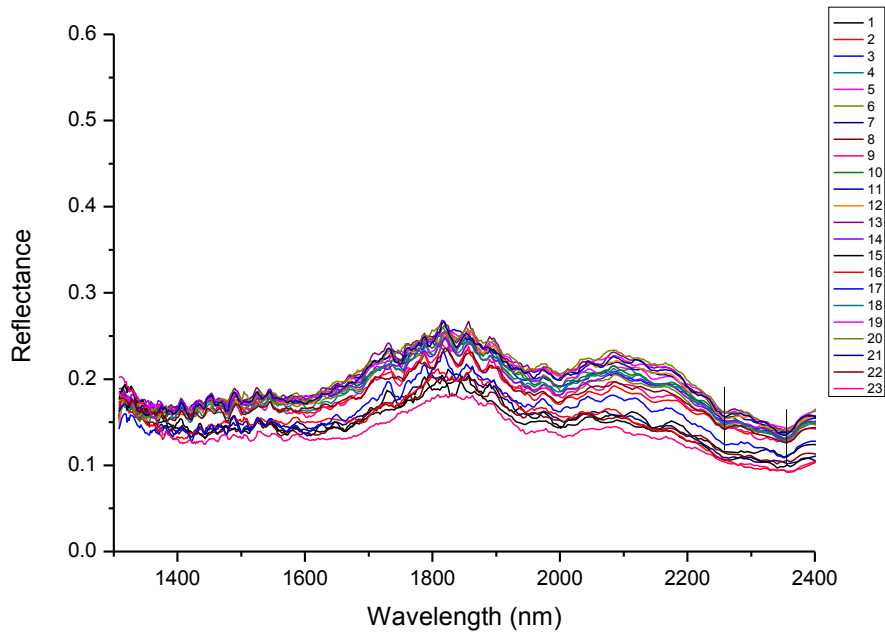


### Sample 45 sector B

### Sample 45

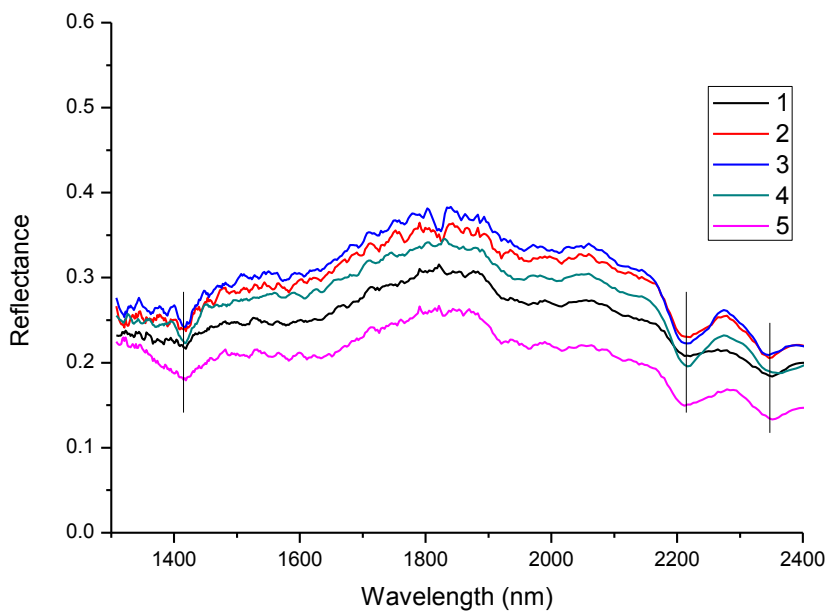


### Sample 45 sector C

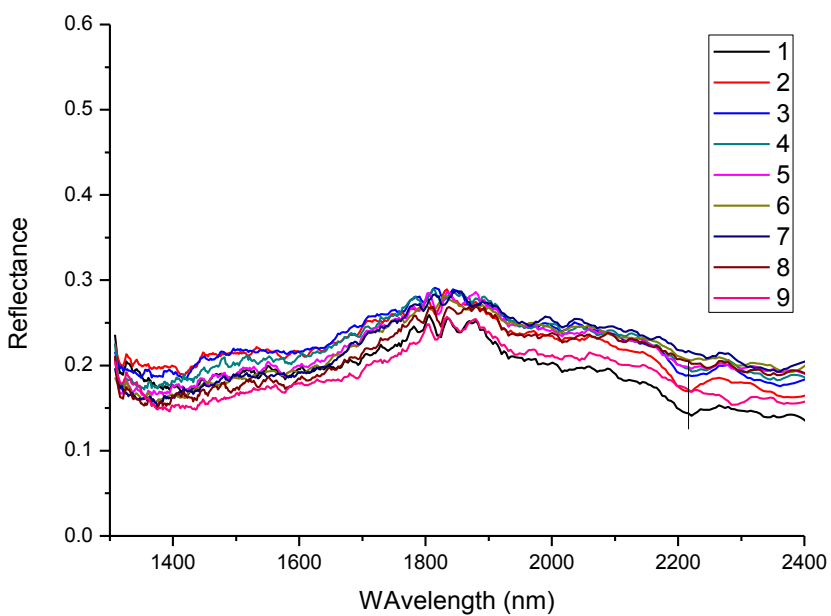


### Sample 45 COMBINED

### Sample 46

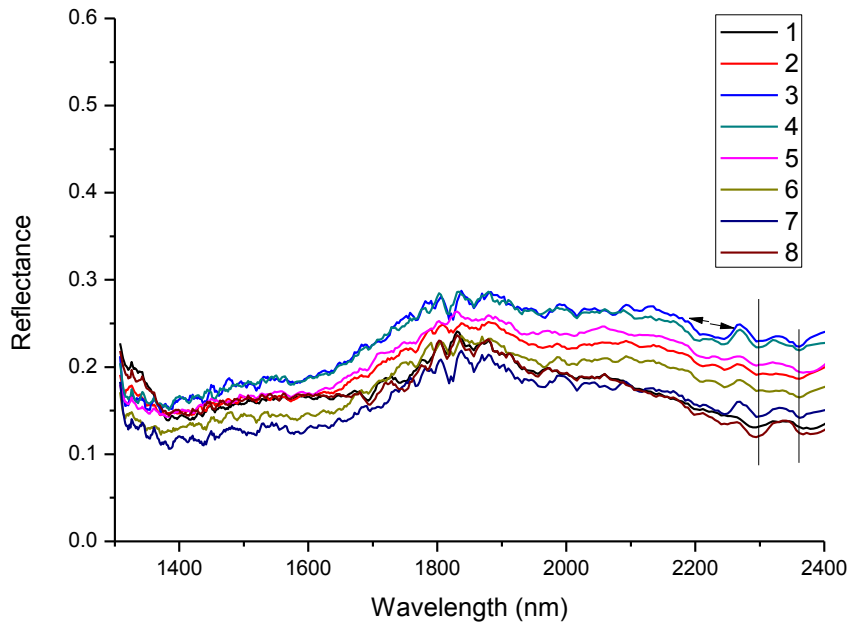


### Sample 46 sector A

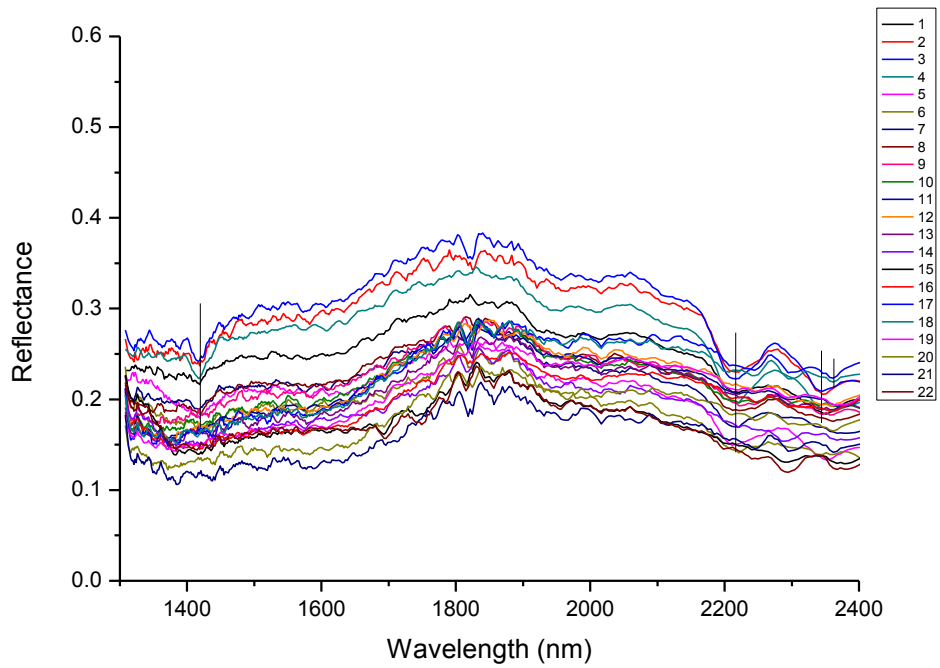


### Sample 46 sector B

### Sample 46

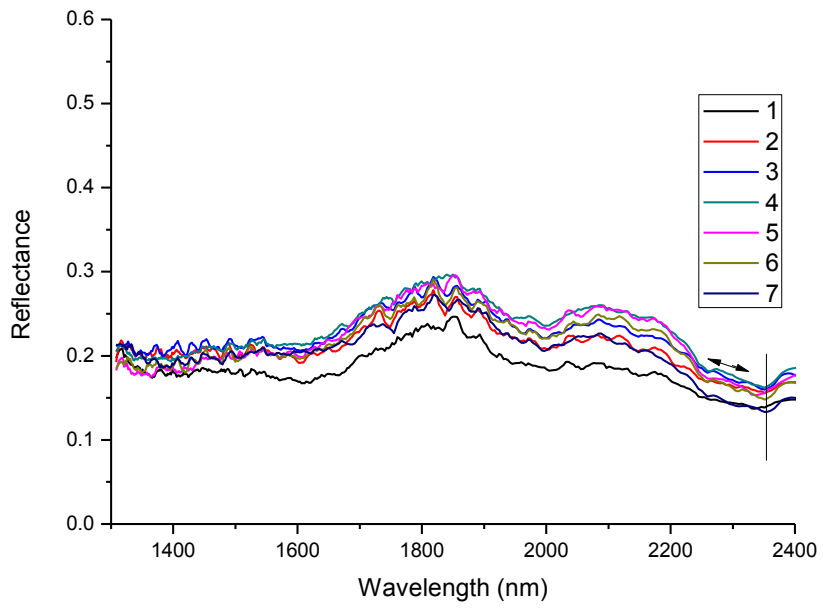


### Sample 46 sector C

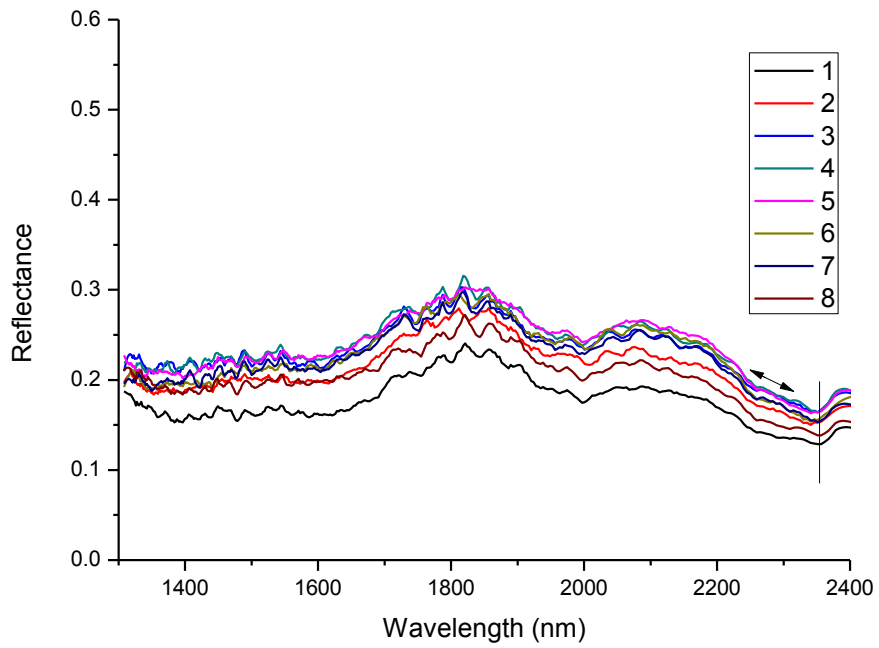


### Sample 46 COMBINED

### Sample 47

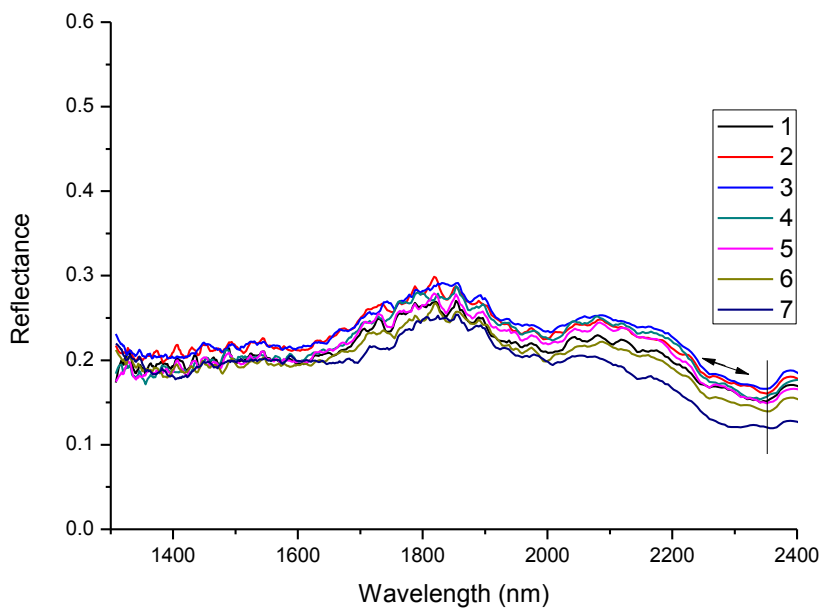


### Sample 47 sector A

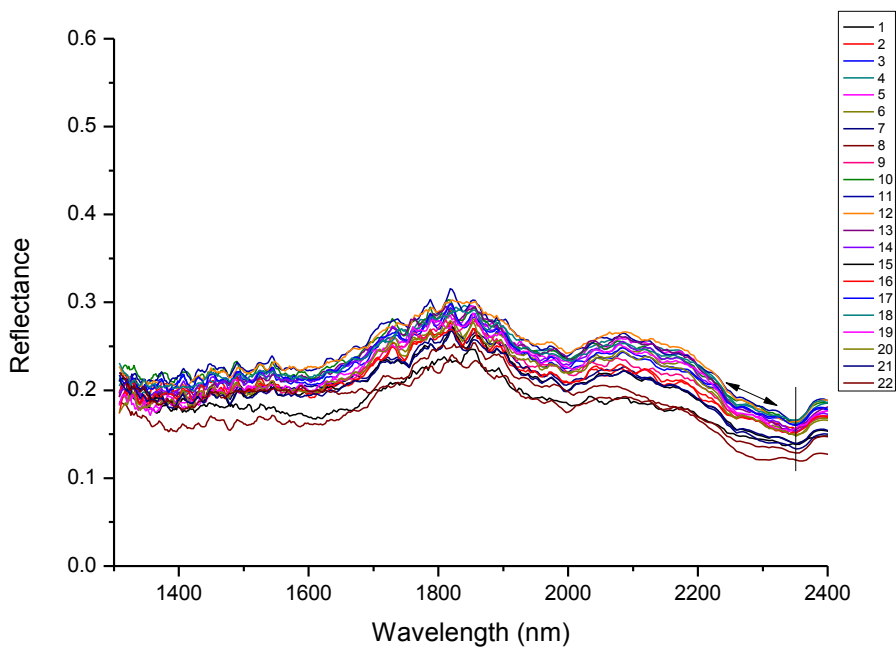


### Sample 47 sector B

### Sample 47

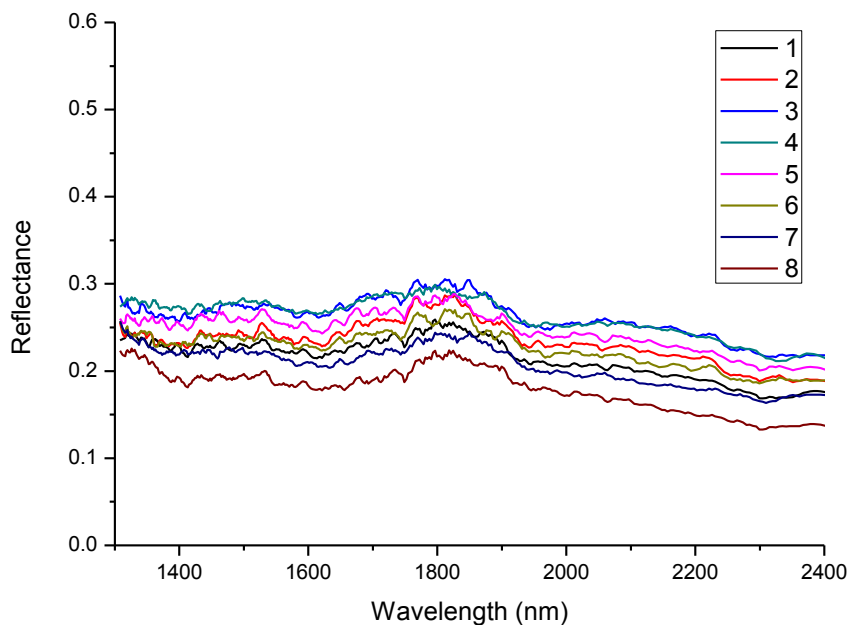


### Sample 47 sector C

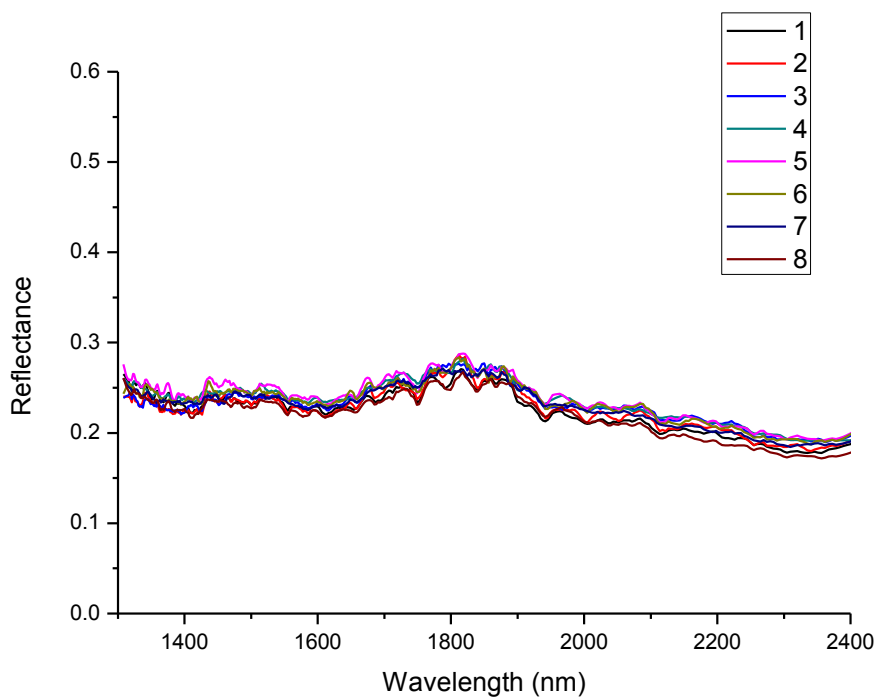


### Sample 47 COMBINED

### Sample 48



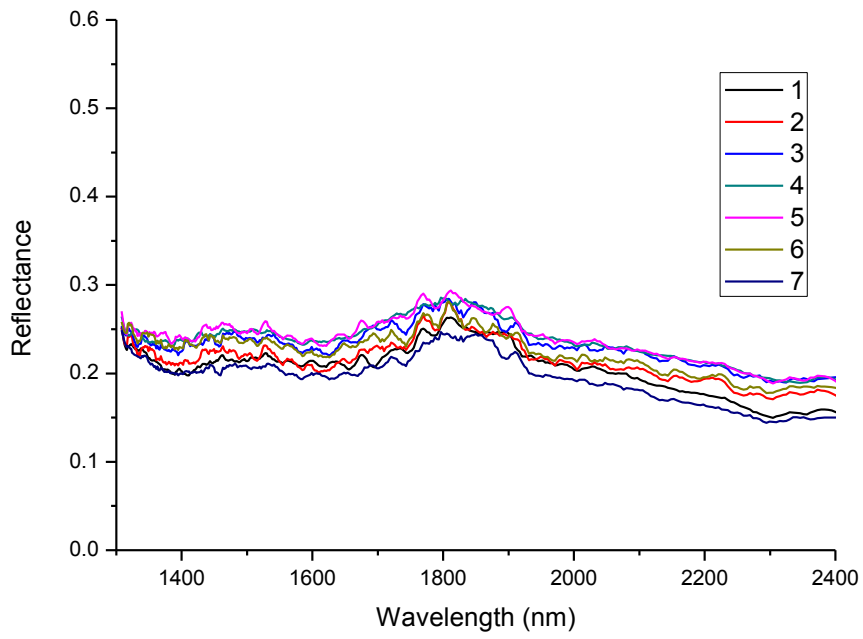
### Sample 48 sector A



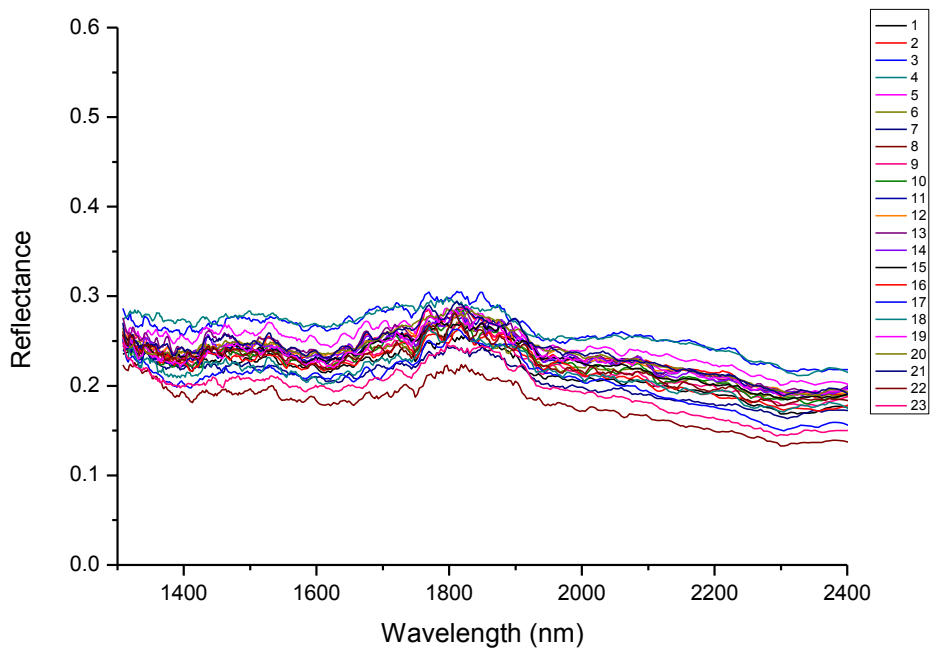
### Sample 48 sector B



### Sample 48

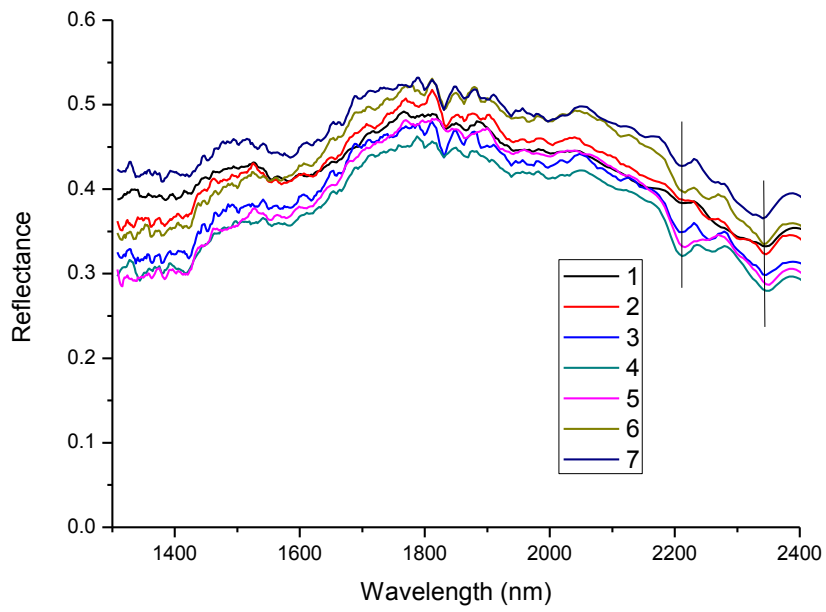


### Sample 48 sector C

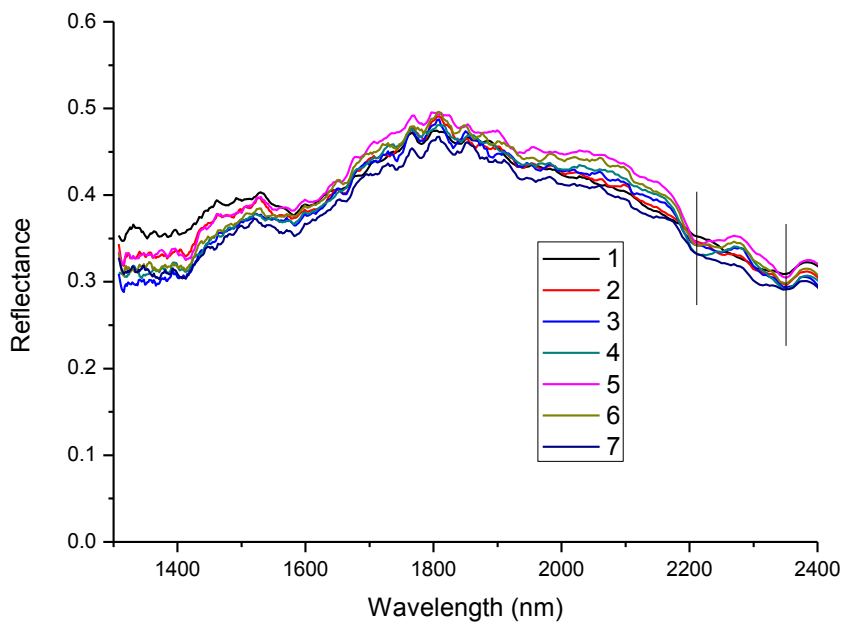


### Sample 48 COMBINED

### Sample 49

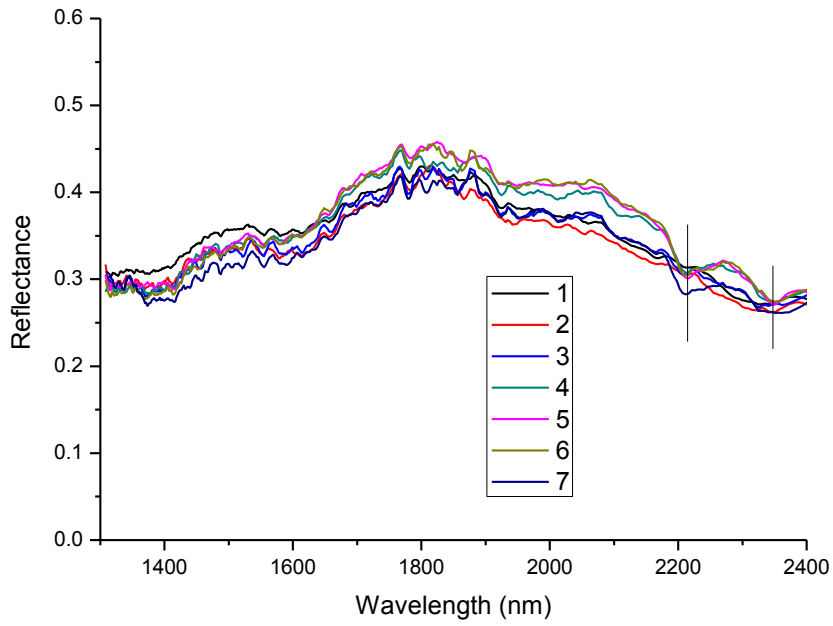


### Sample 49 sector A

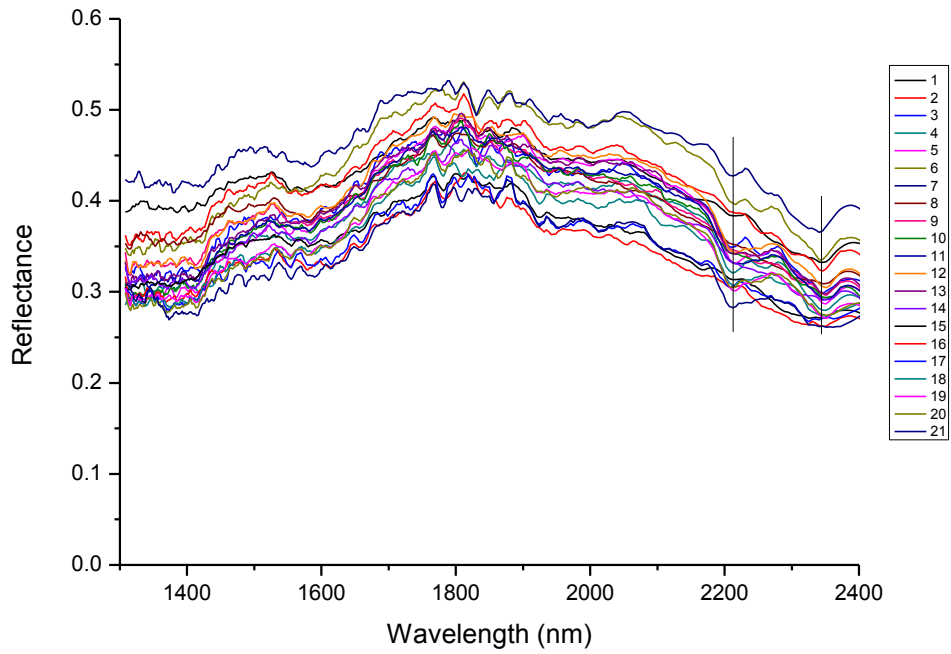


### Sample 49 sector B

### Sample 49

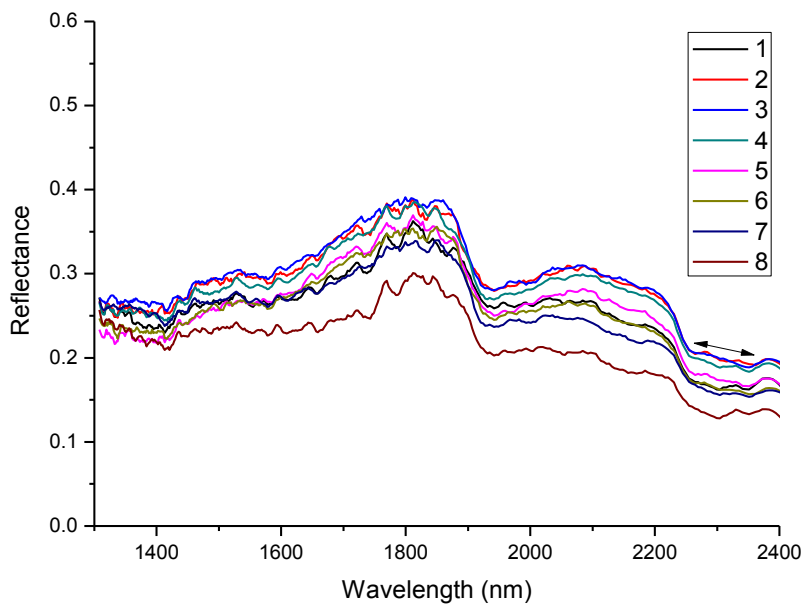


### Sample 49 sector C

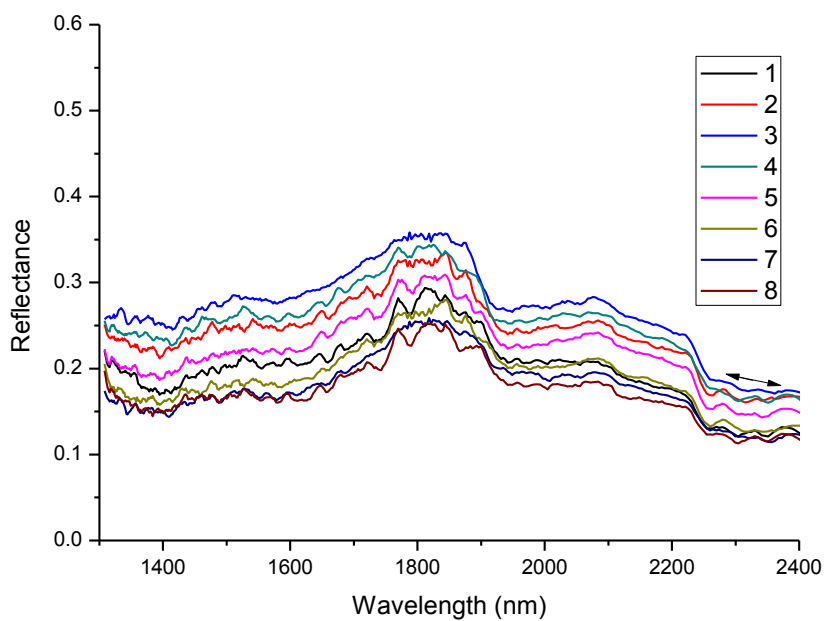


### Sample 49 COMBINED

### Sample 50

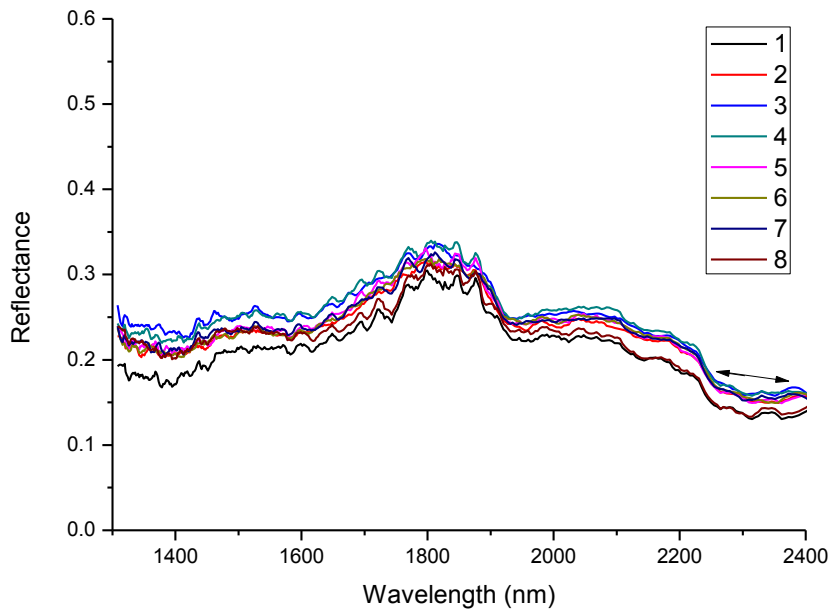


### Sample 50 sector A

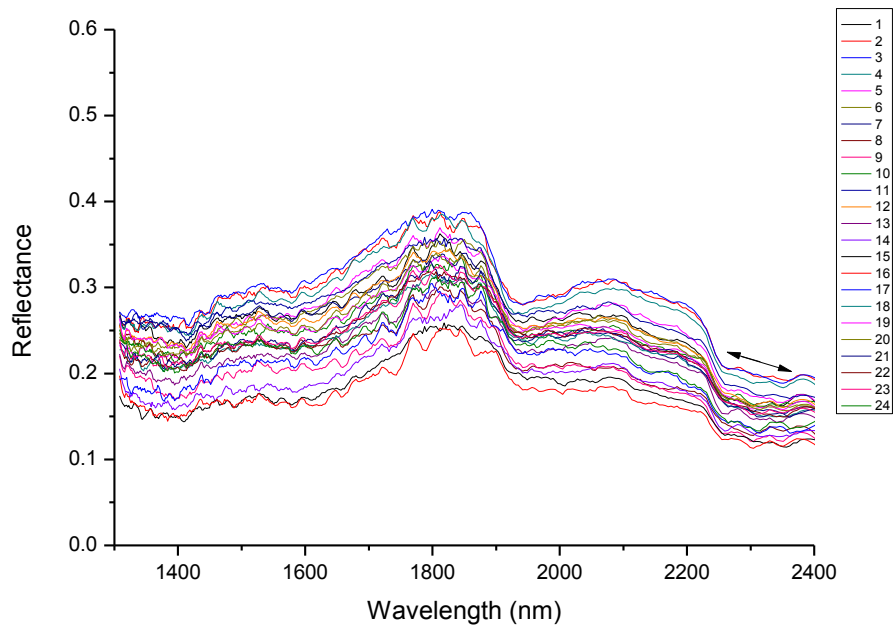


### Sample 50 sector B

### Sample 50

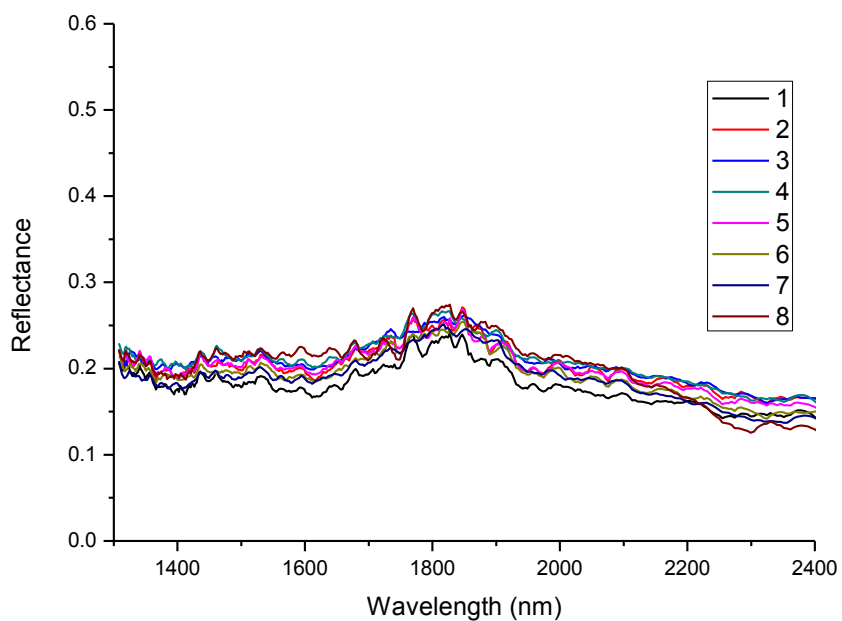


### Sample 50 sector C

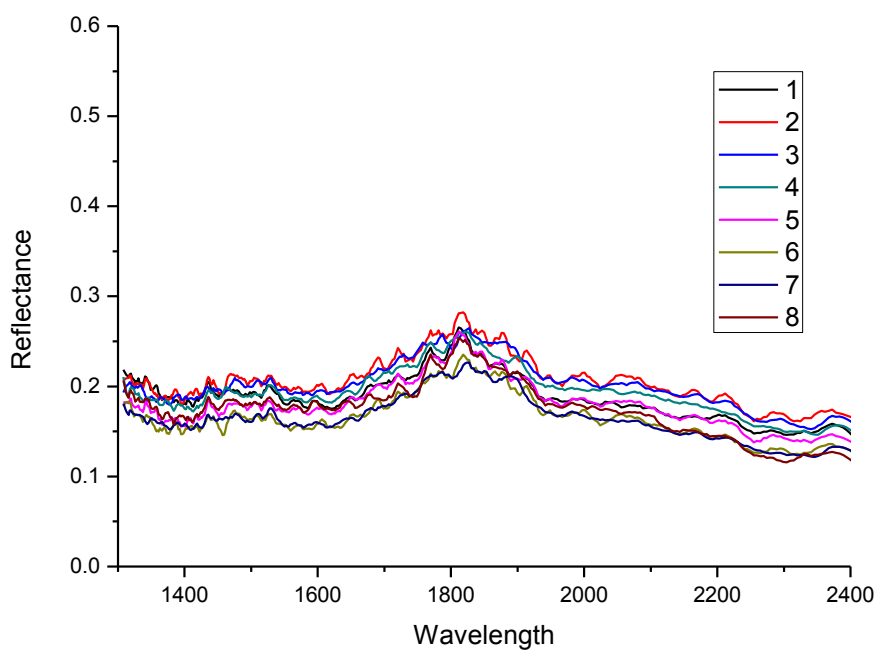


### Sample 50 COMBINED

### Sample 51

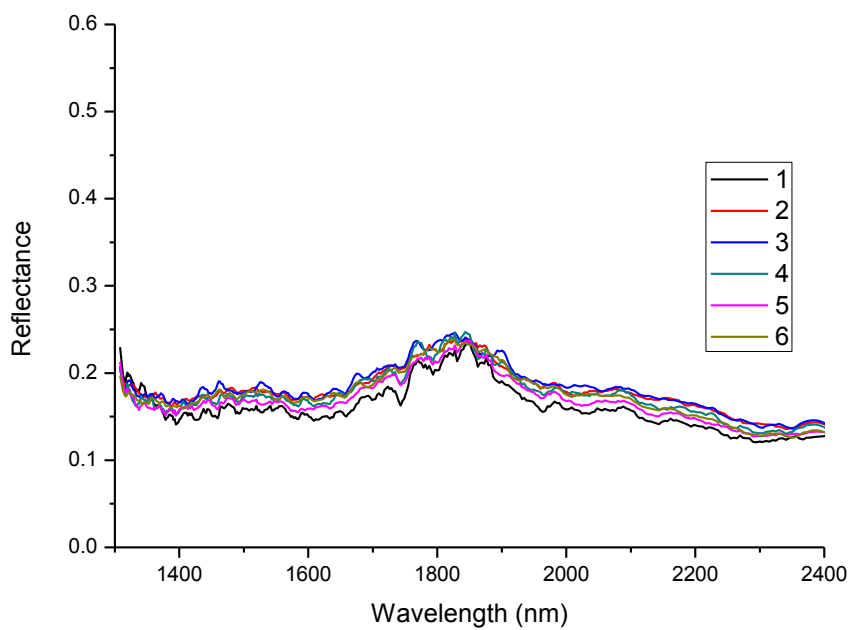


### Sample 51 sector A

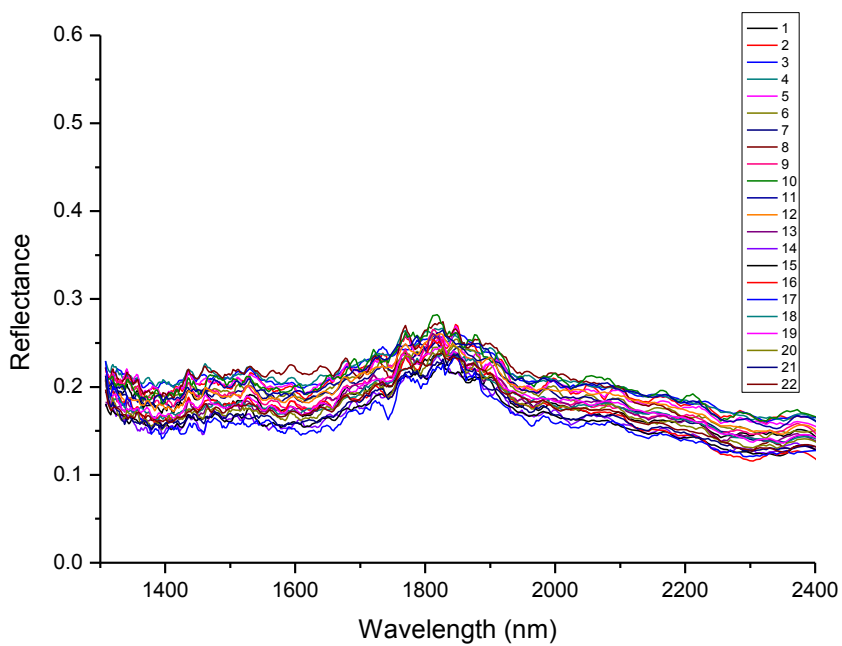


### Sample 51 sector B

### Sample 51

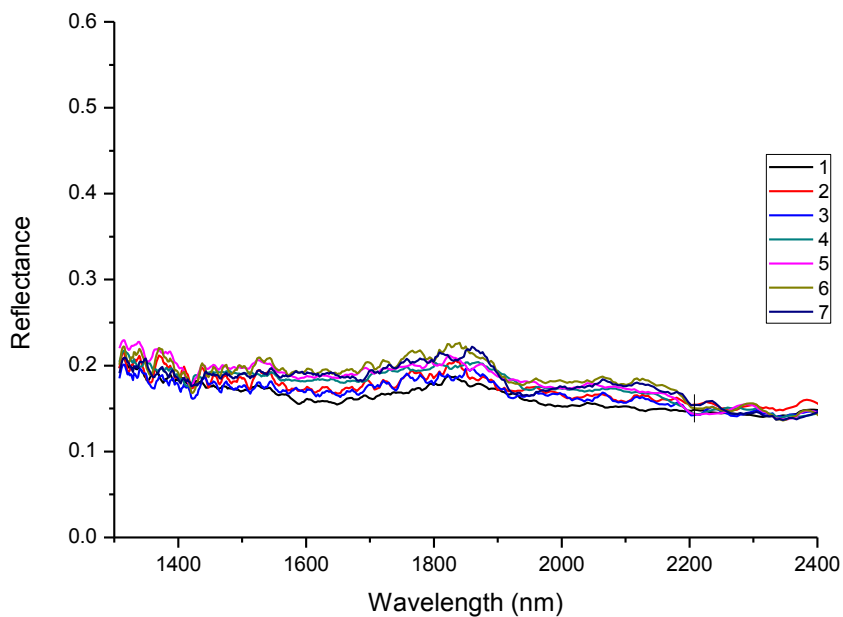


### Sample 51 sector C

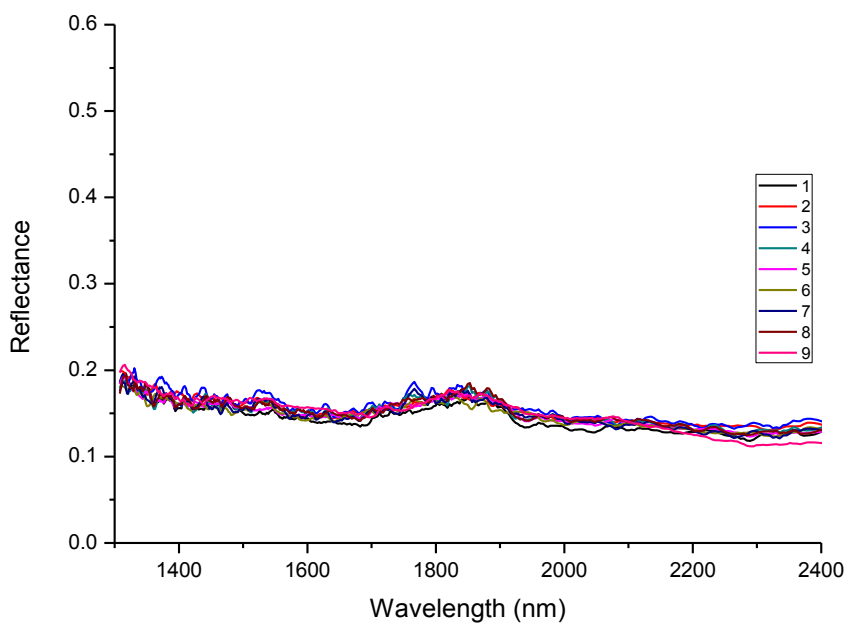


### Sample 51 COMBINED

### Sample 52



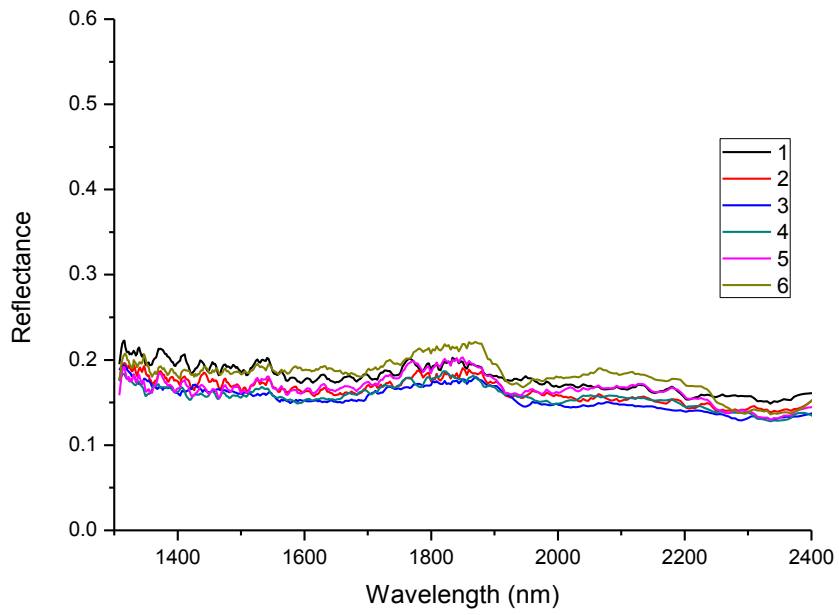
### Sample 52 sector A



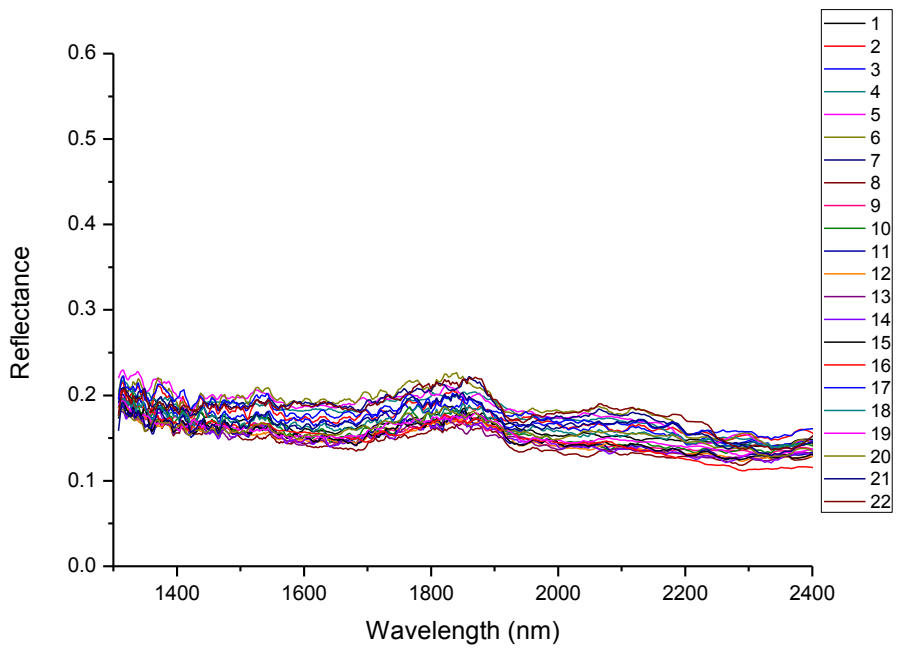
### Sample 52 sector B



### Sample 52

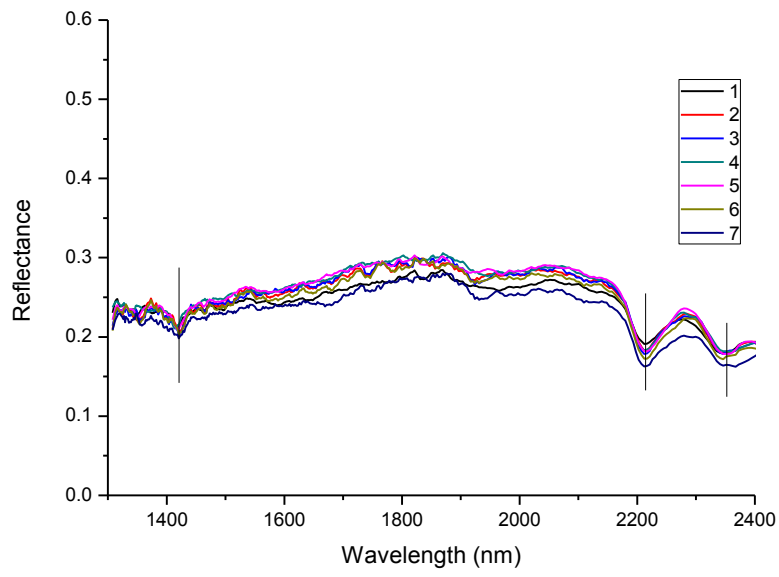


### Sample 52 sector C

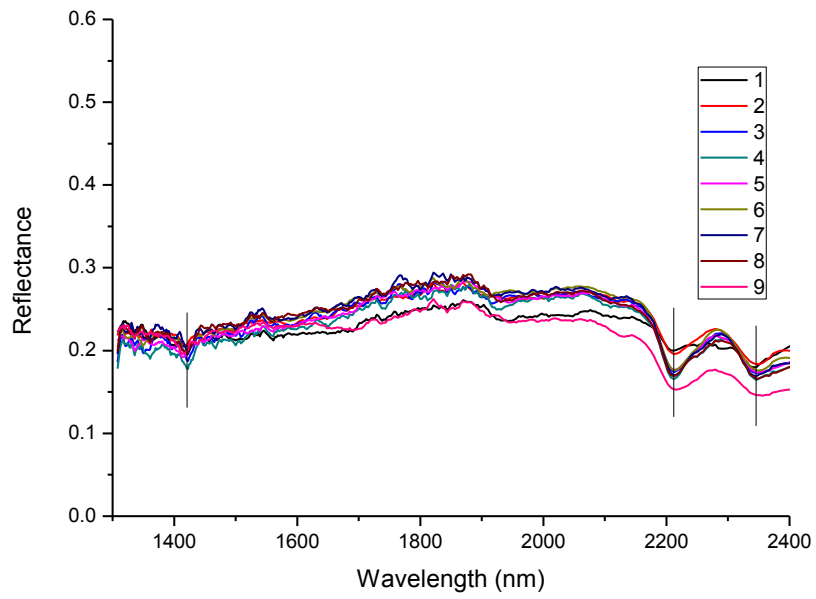


### Sample 52 COMBINED

### Sample 53

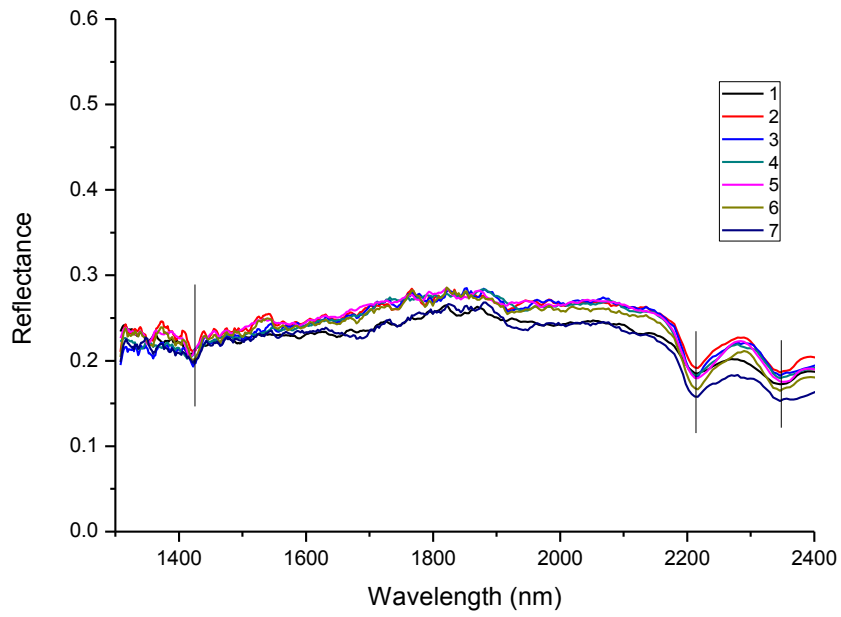


### Sample 53 sector A

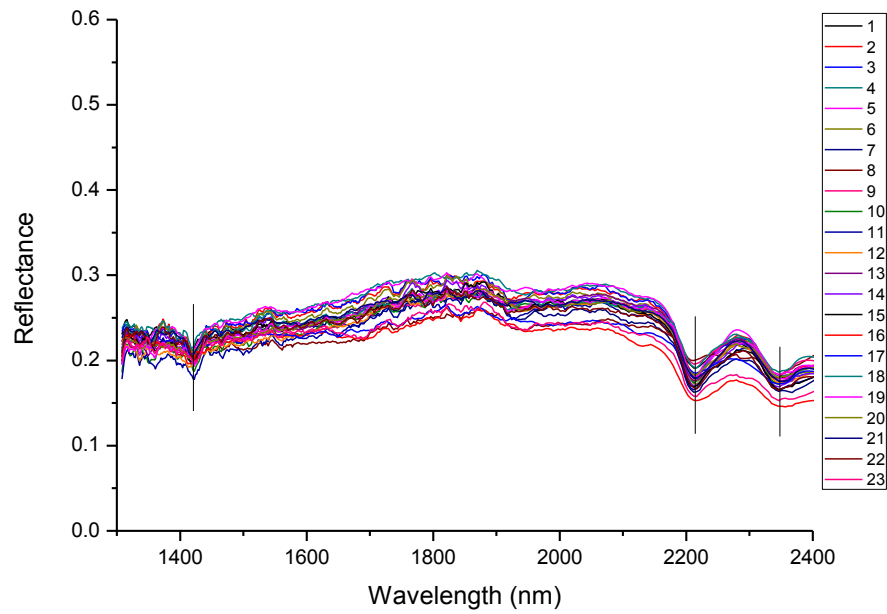


### Sample 53 sector B

### Sample 53

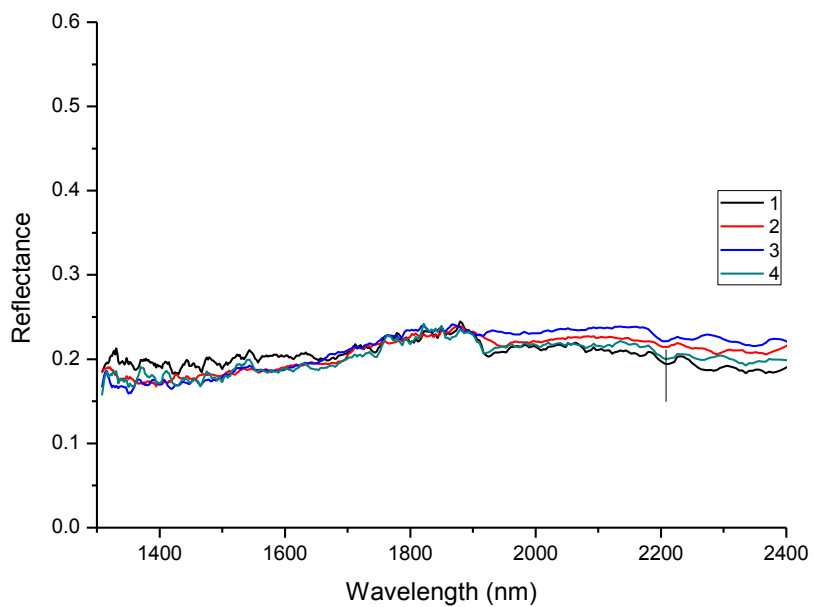


### Sample 53 sector C

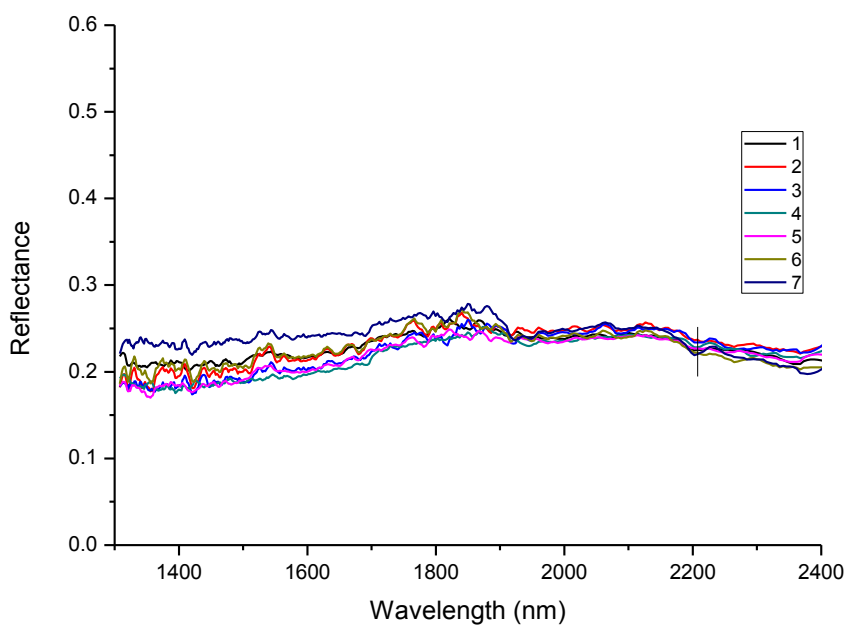


### Sample 53 COMBINED

### Sample 54

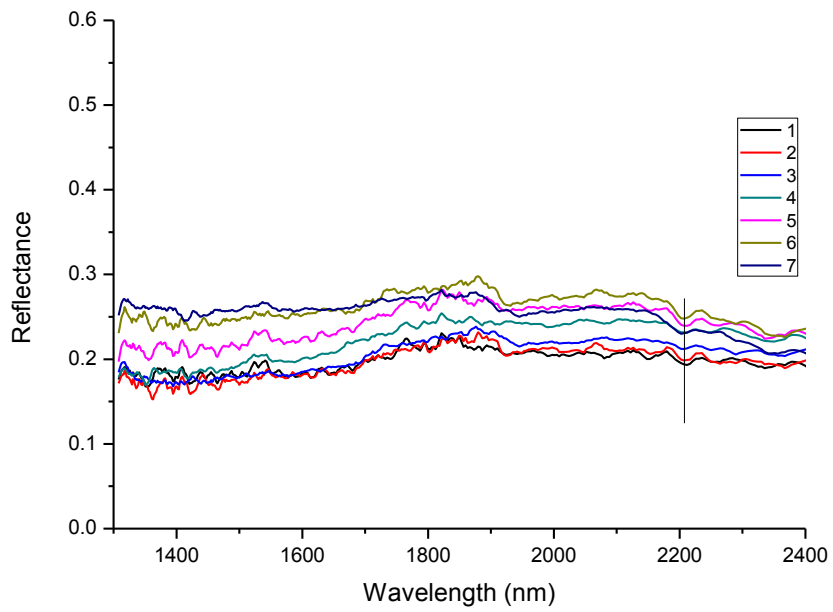


### Sample 54 sector A

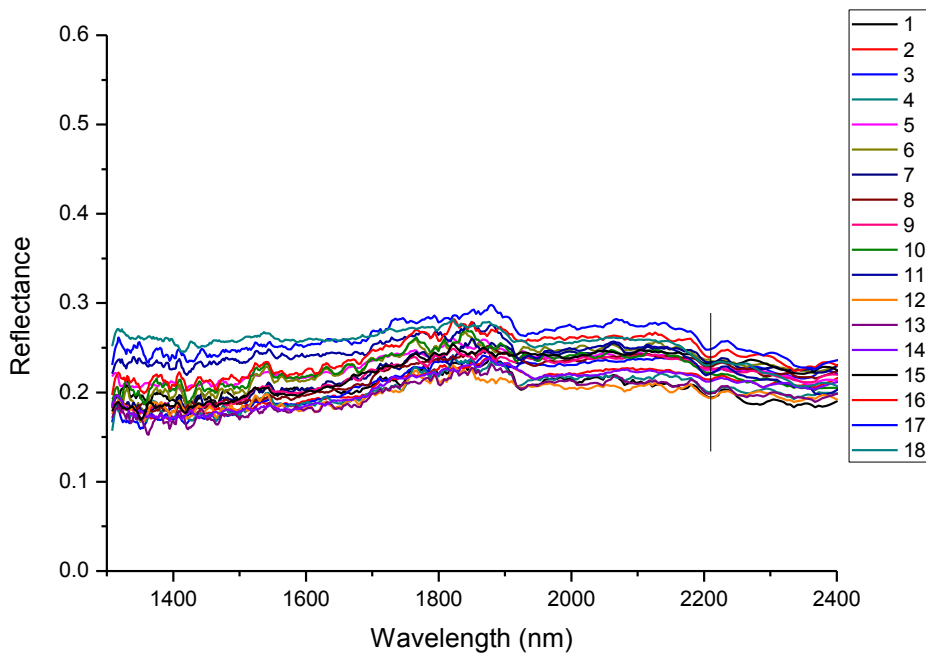


### Sample 54 sector B

### Sample 54

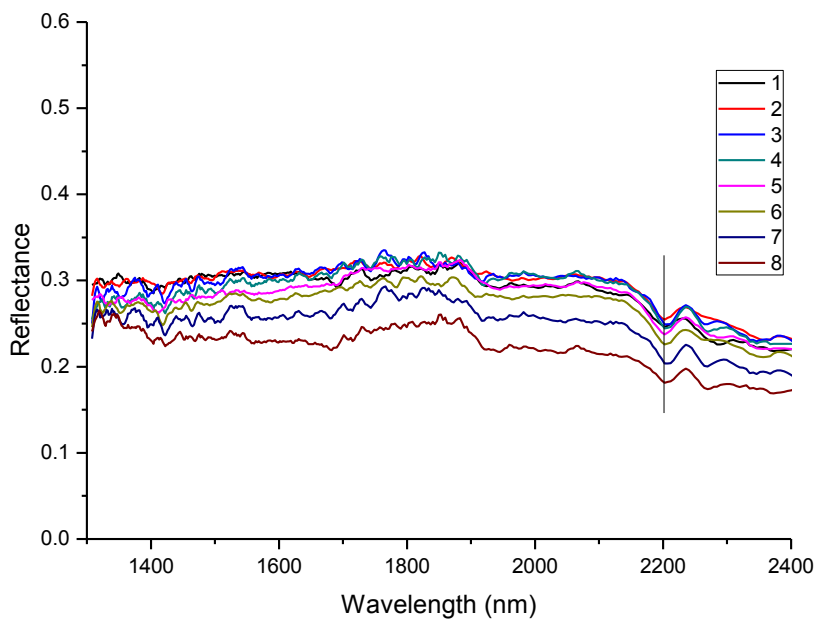


### Sample 54 sector C

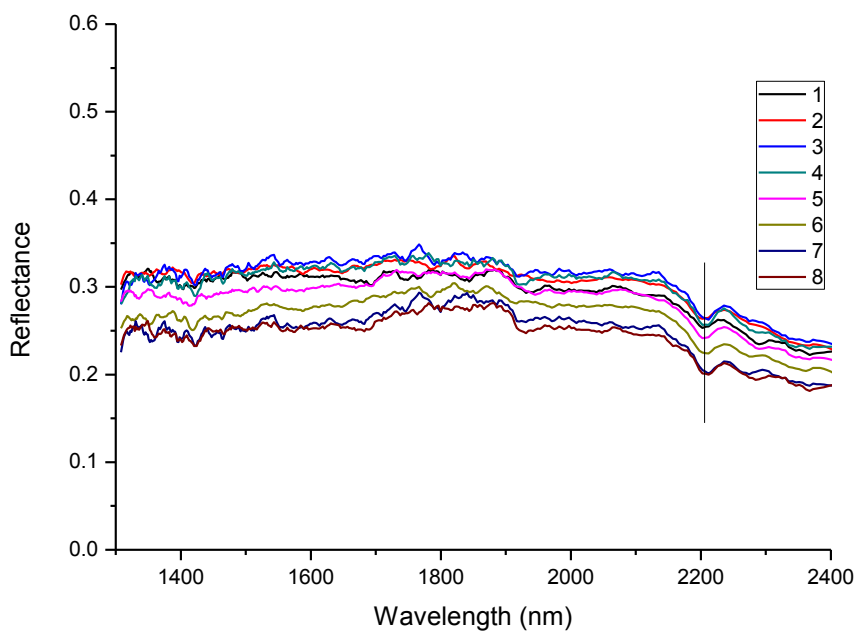


### Sample 54 COMBINED

### Sample 55

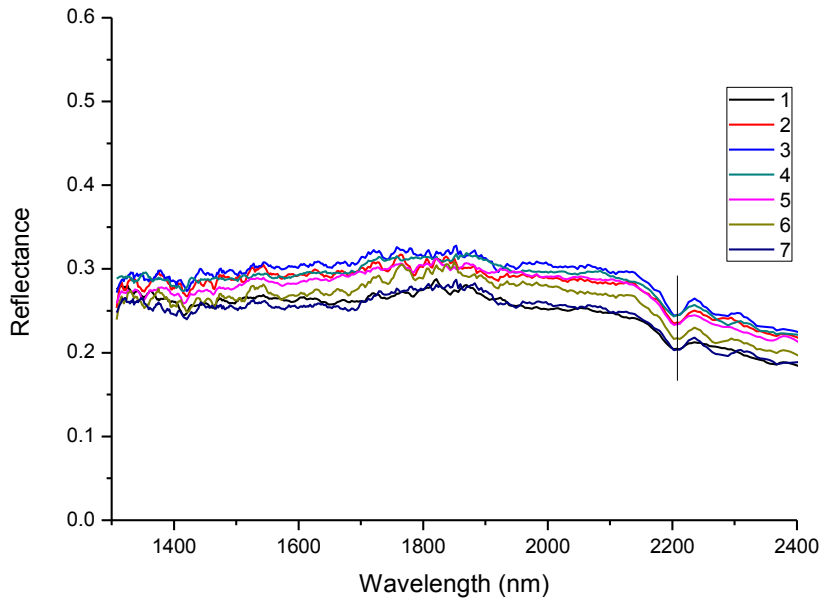


### Sample 55 sector A

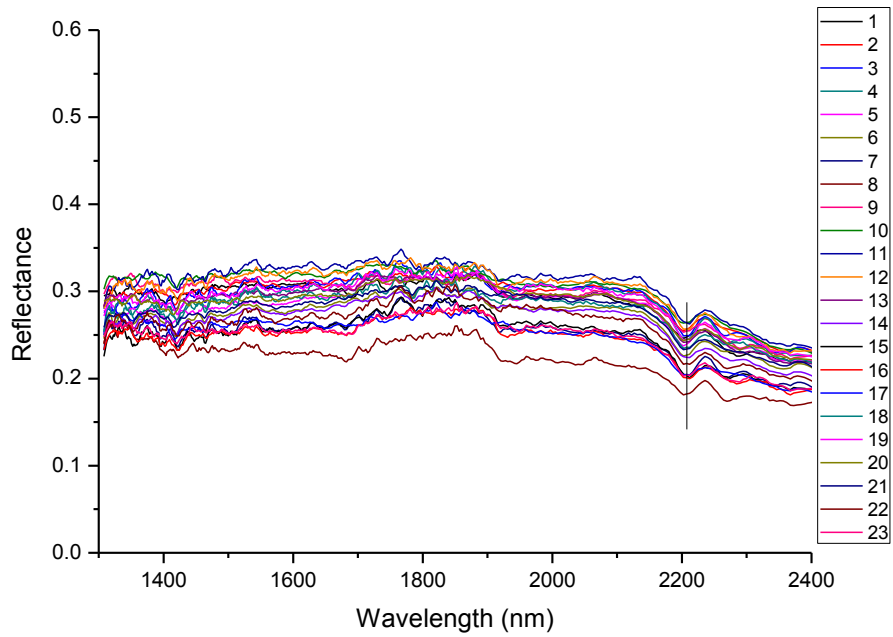


### Sample 55 sector B

### Sample 55

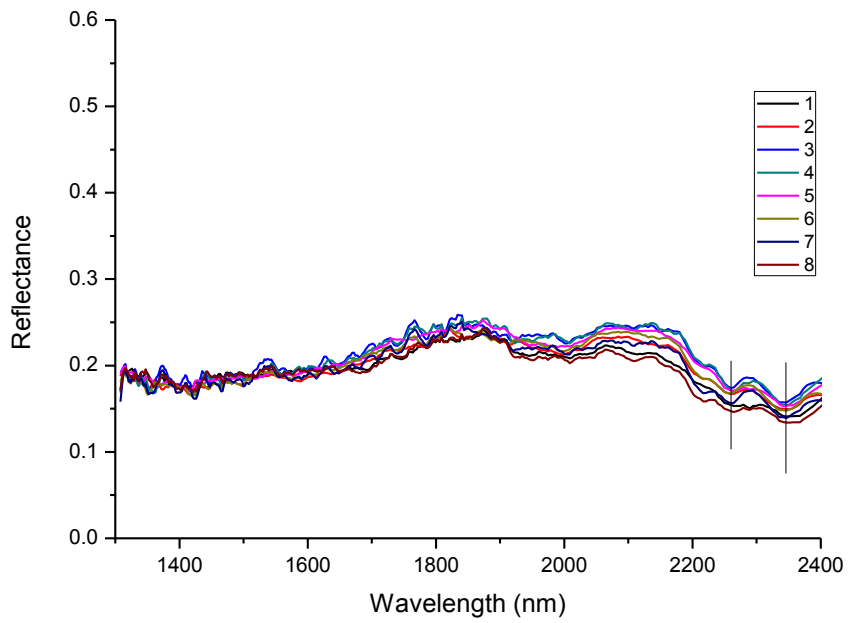


### Sample 55 sector C

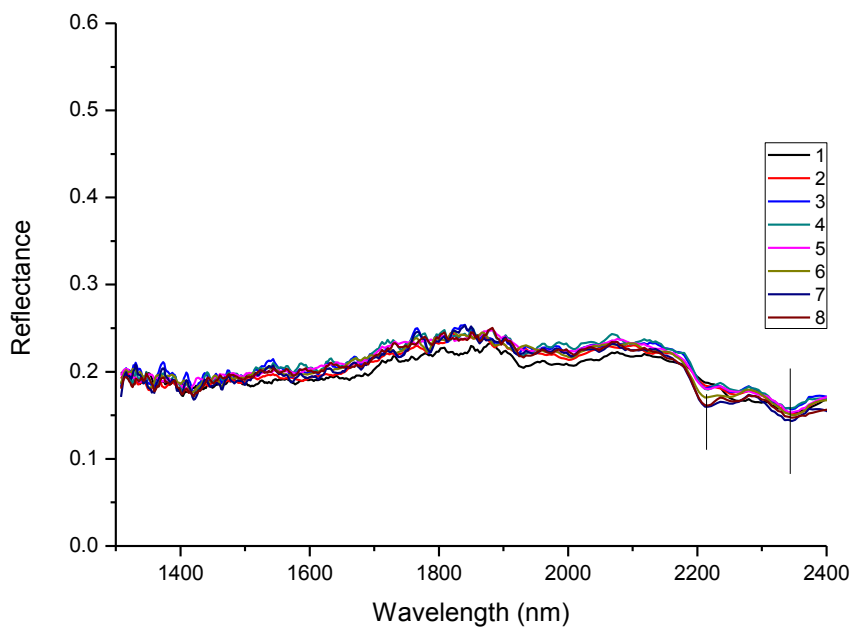


### Sample 55 COMBINED

### Sample 56



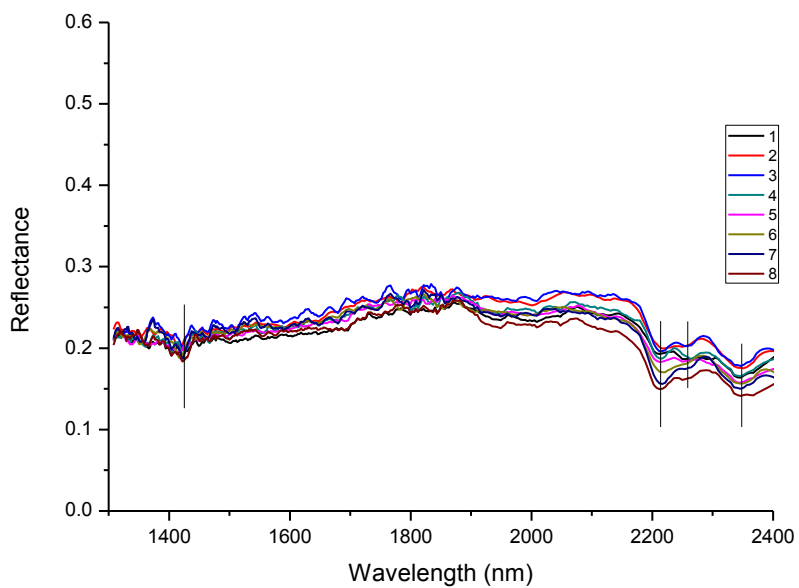
### Sample 56 sector A



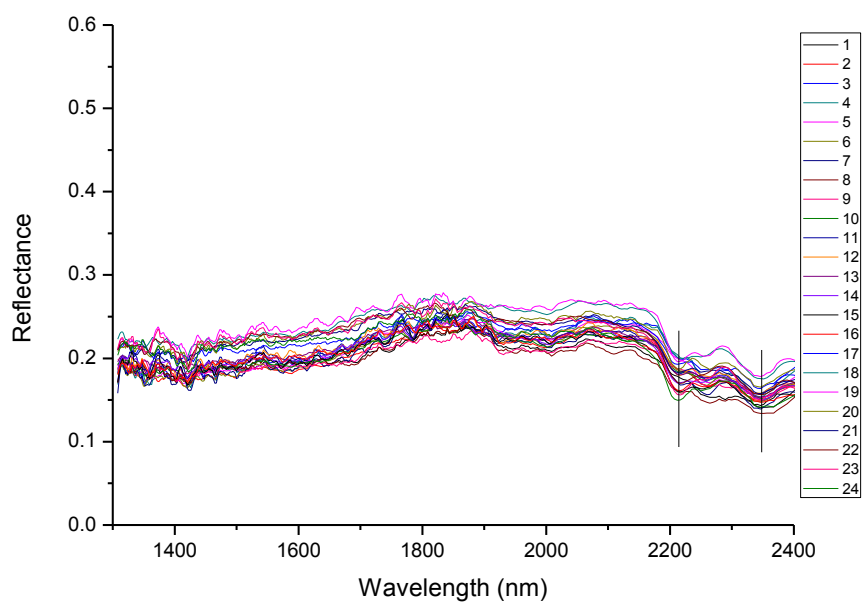
### Sample 56 sector B



### Sample 56

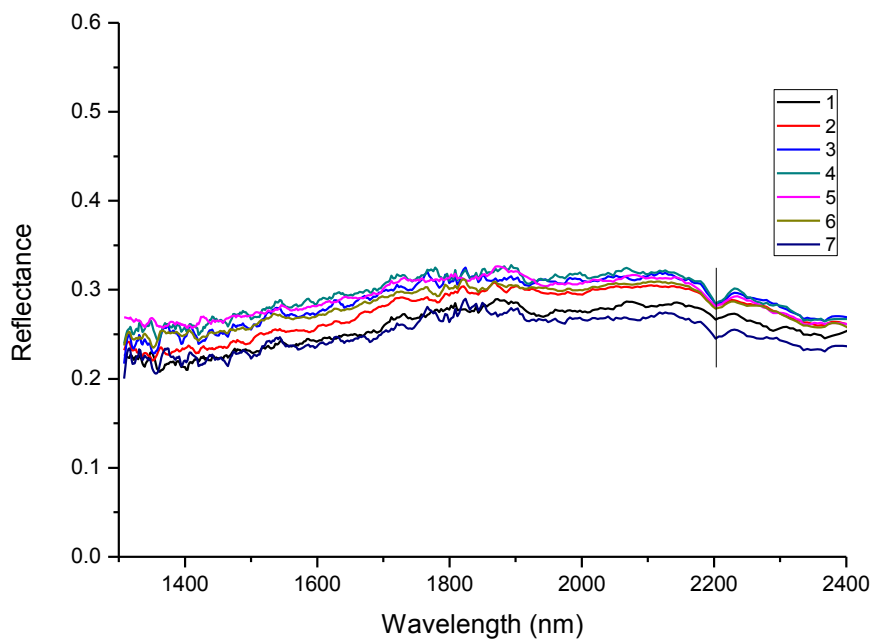


### Sample 56 sector C

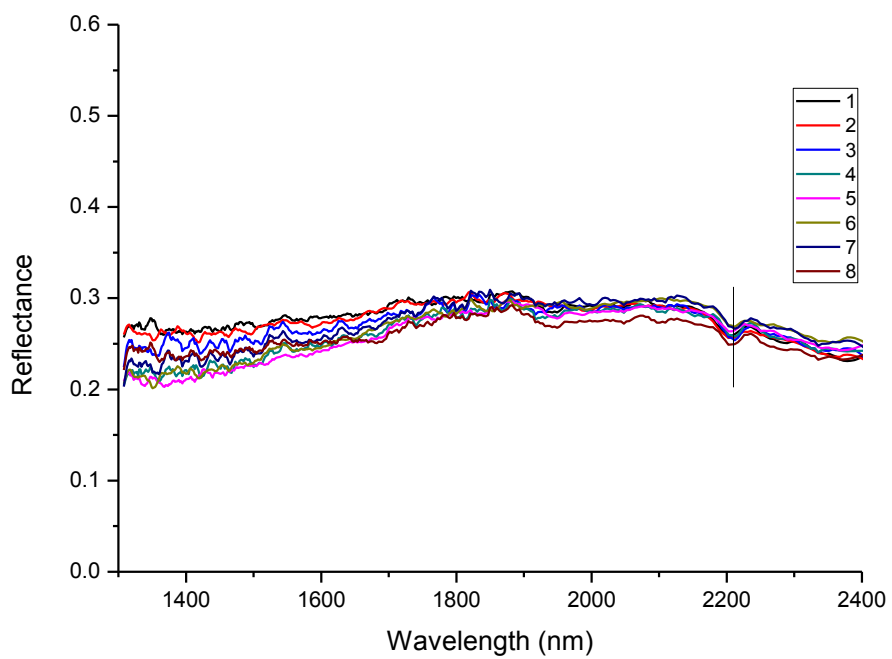


### Sample 56 COMBINED

### Sample 57

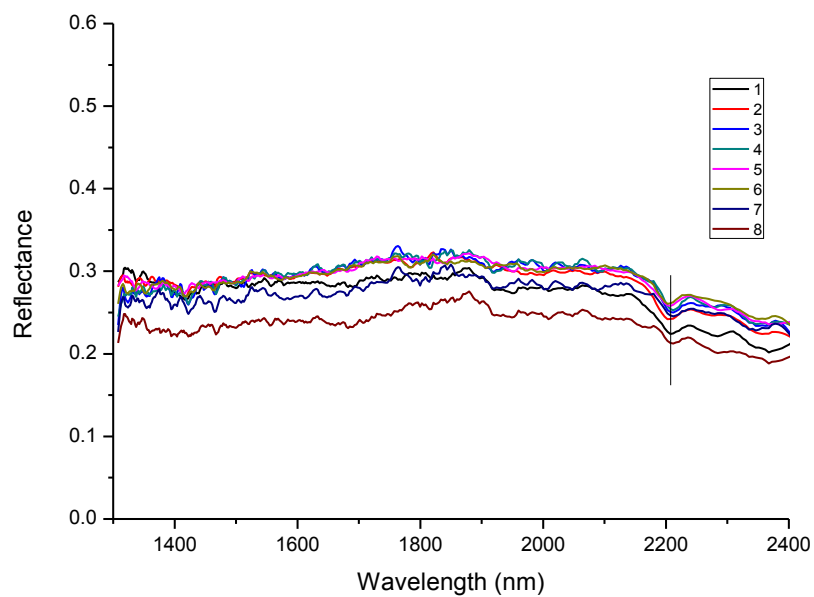


### Sample 57 sector A

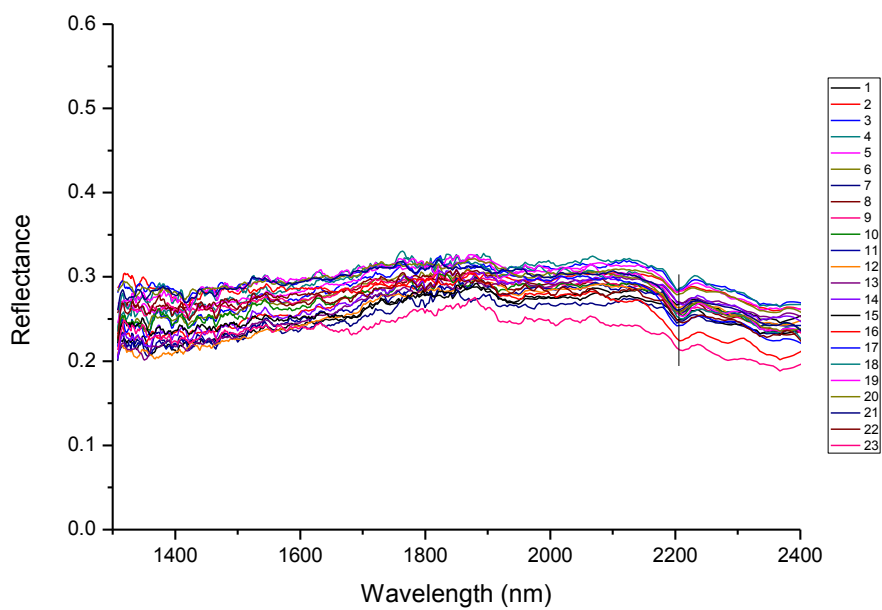


### Sample 57 sector B

### Sample 57

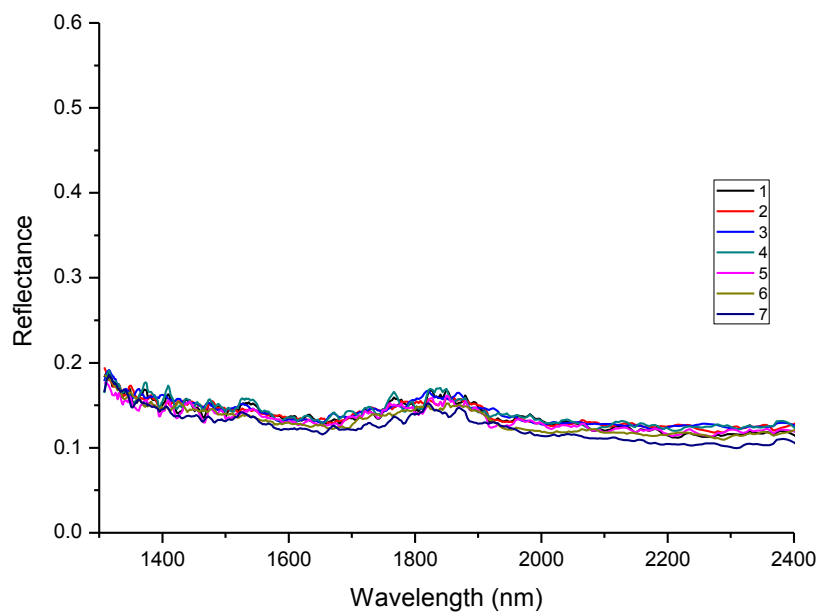


### Sample 57 sector C

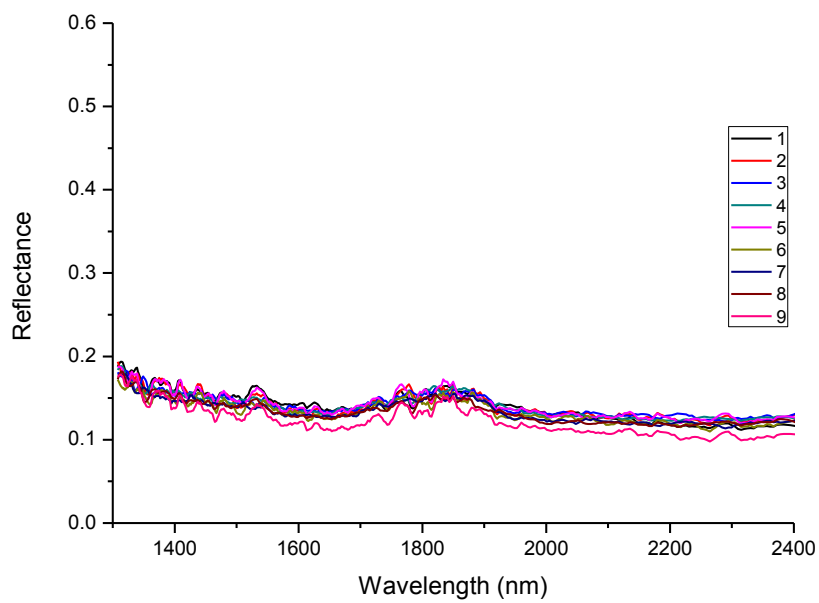


### Sample 57 COMBINED

### Sample 58

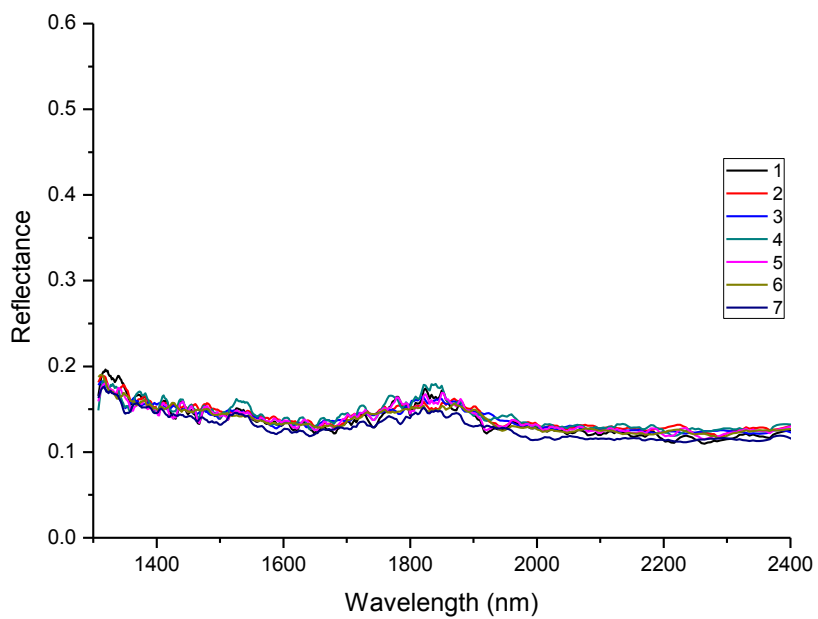


### Sample 58 sector A

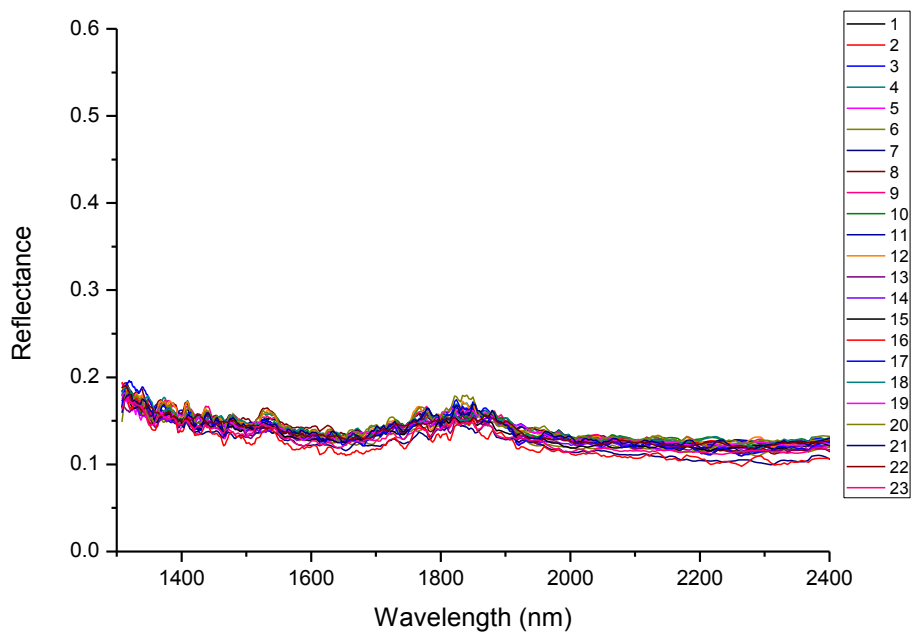


### Sample 58 sector B

### Sample 58

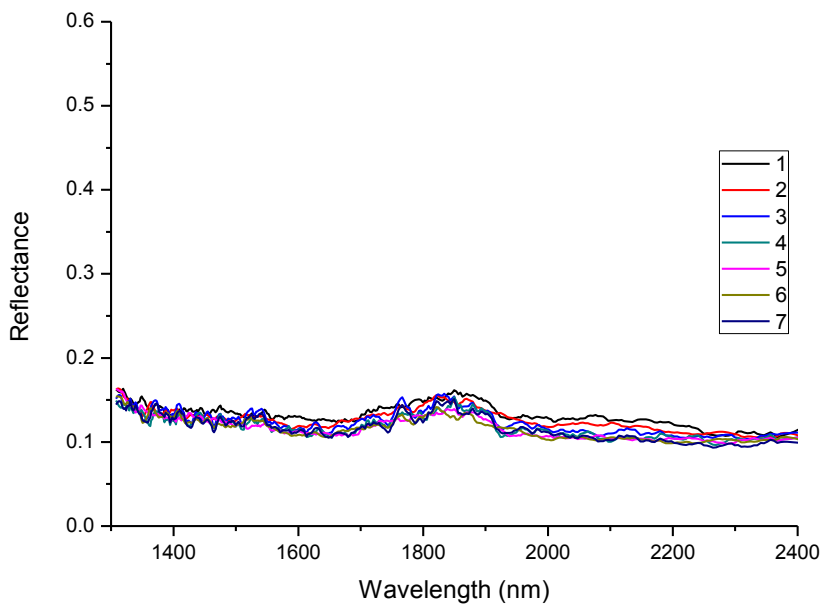


### Sample 58 sector C

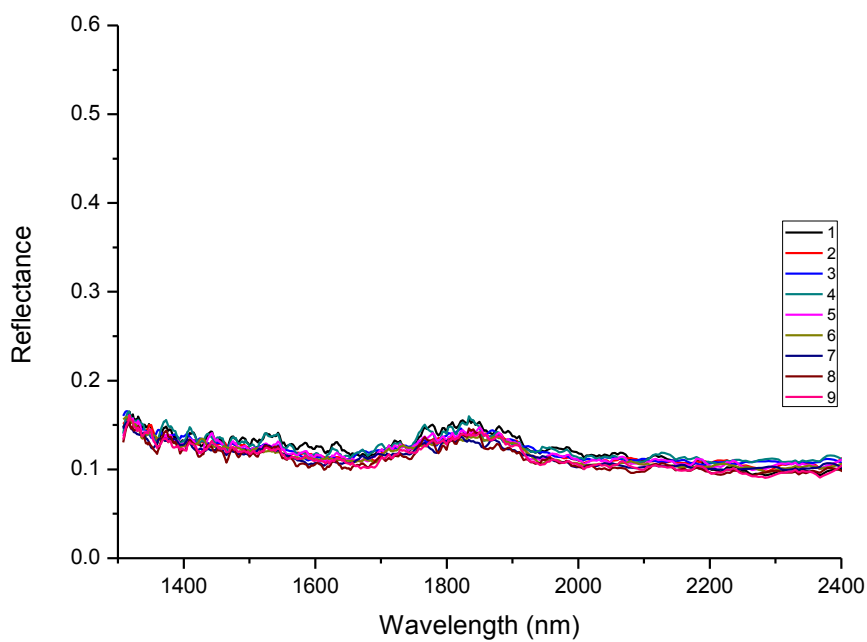


### Sample 58 COMBINED

### Sample 59

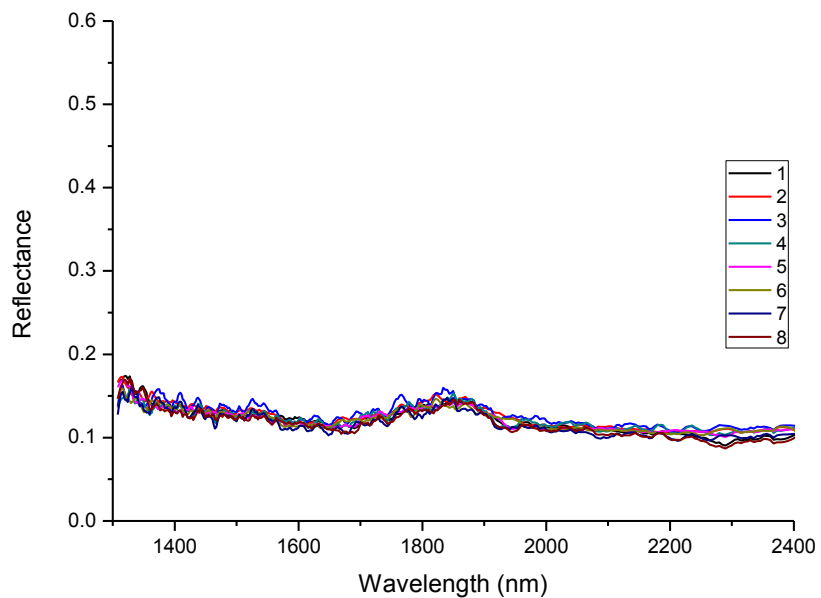


### Sample 59 sector A

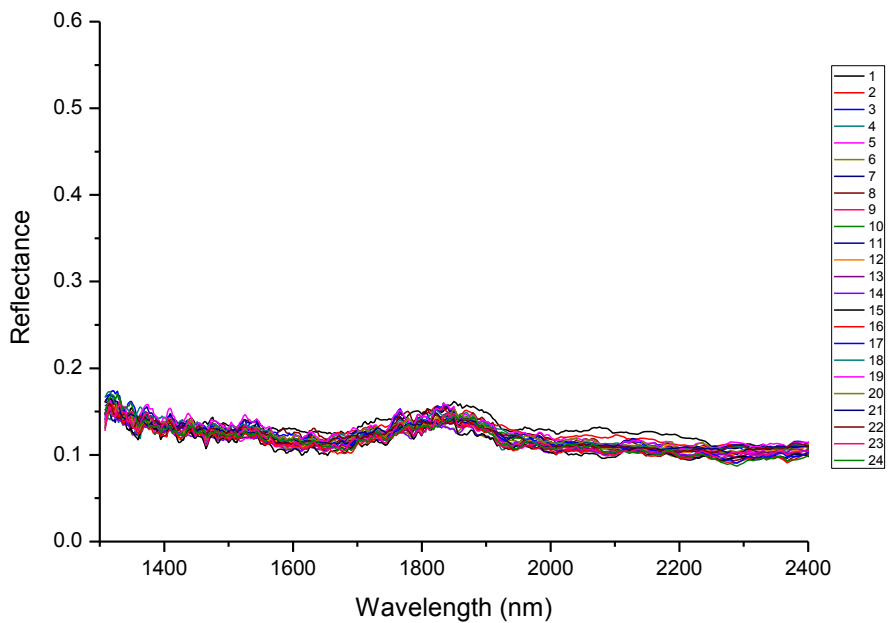


### Sample 59 sector B

### Sample 59

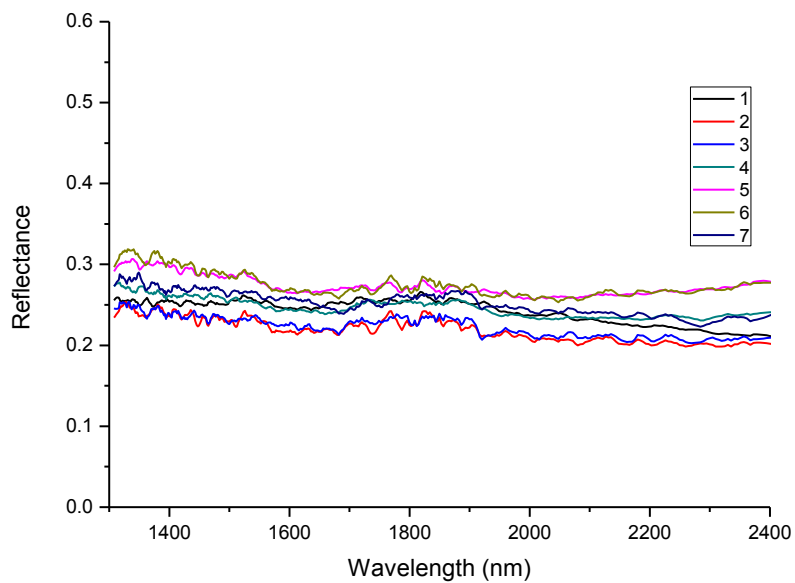


### Sample 59 sector C

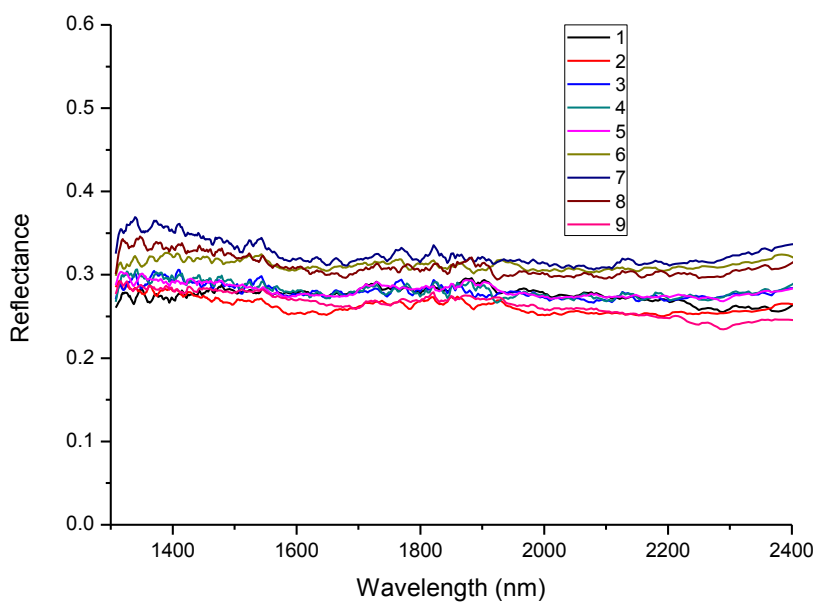


### Sample 59 COMBINED

### Sample 60



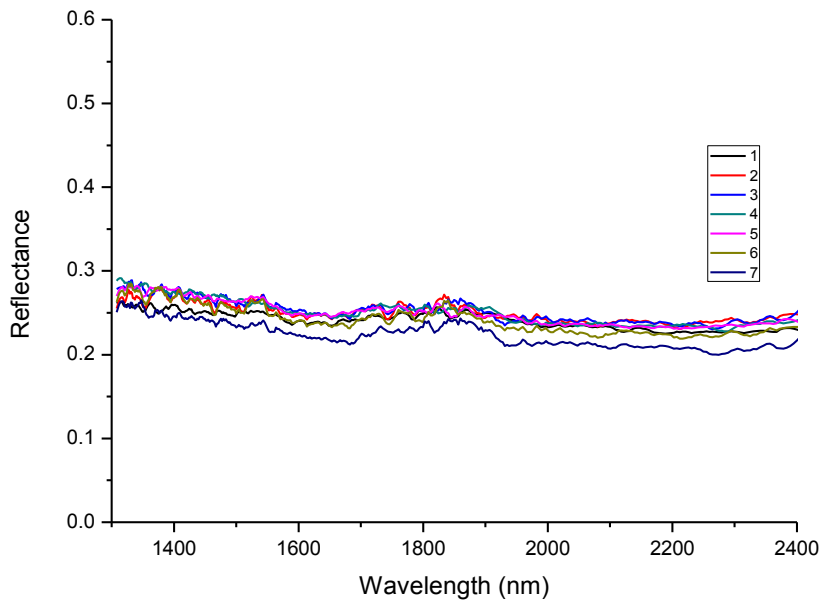
### Sample 60 sector A



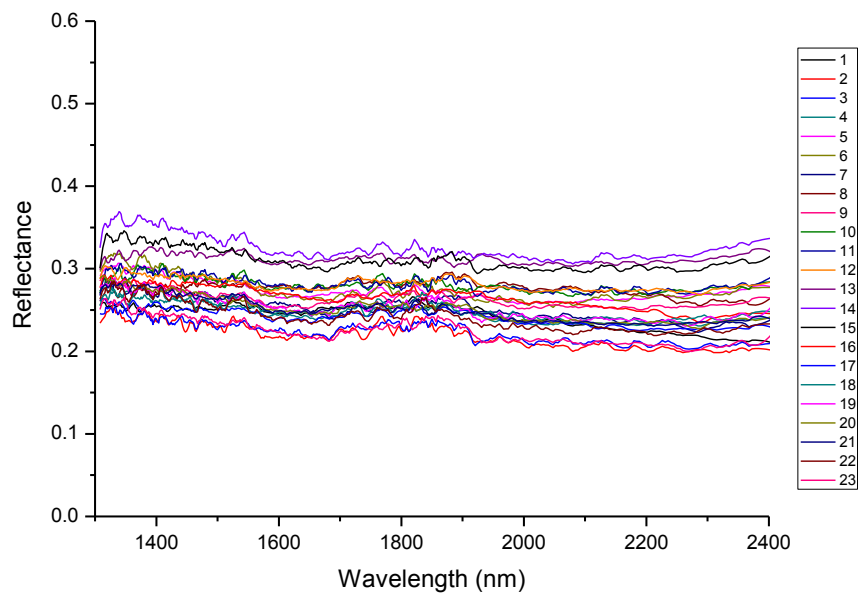
### Sample 60 sector B



### Sample 60

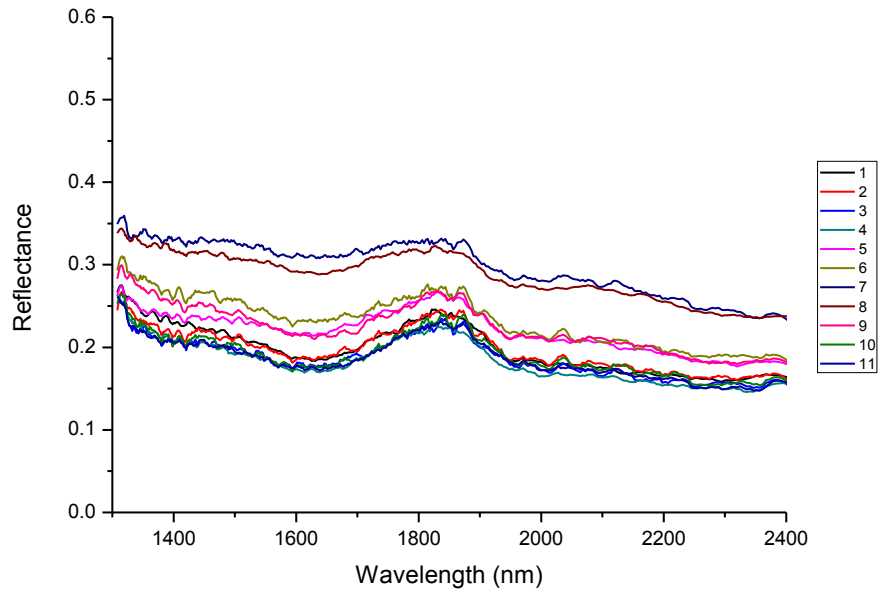


### Sample 60 sector C

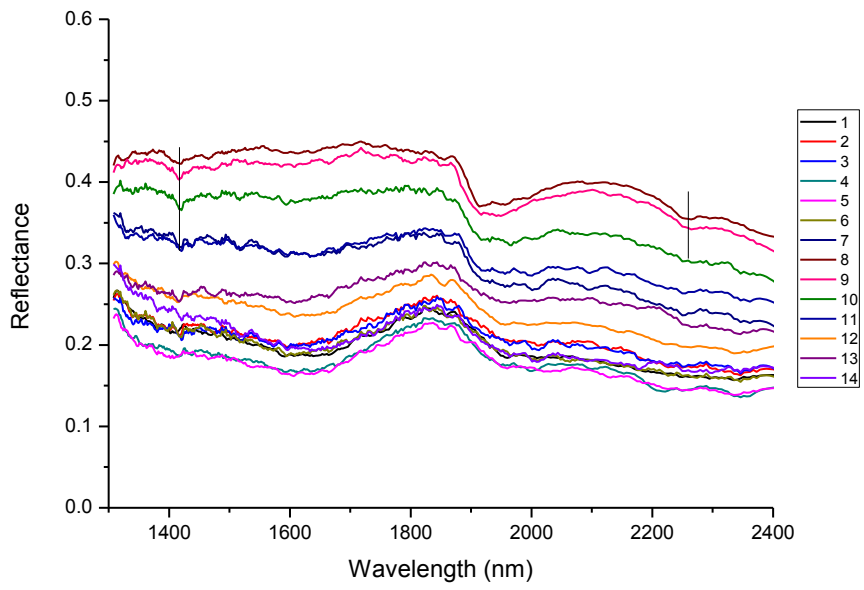


### Sample 60 COMBINED

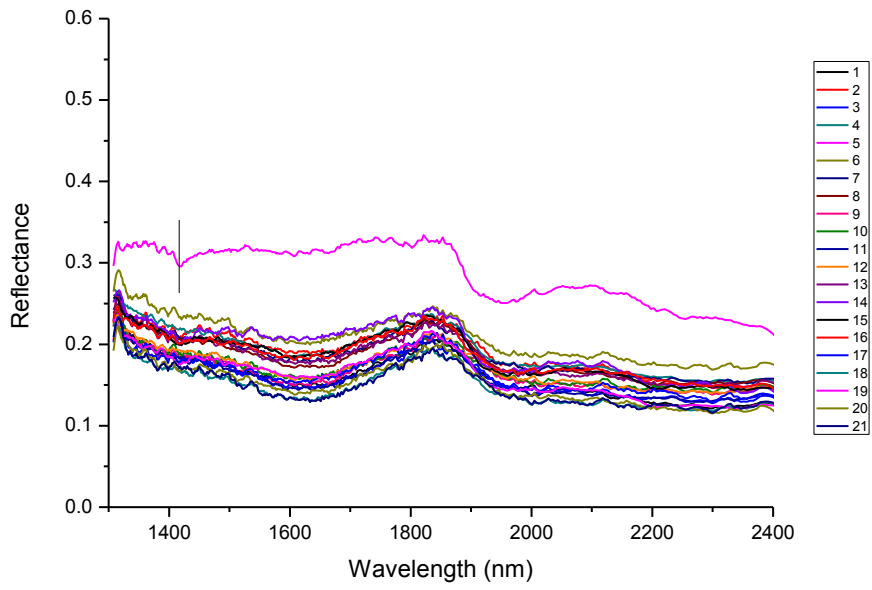
## Appendix 8.1b - NIR spectra of splits B2 samples



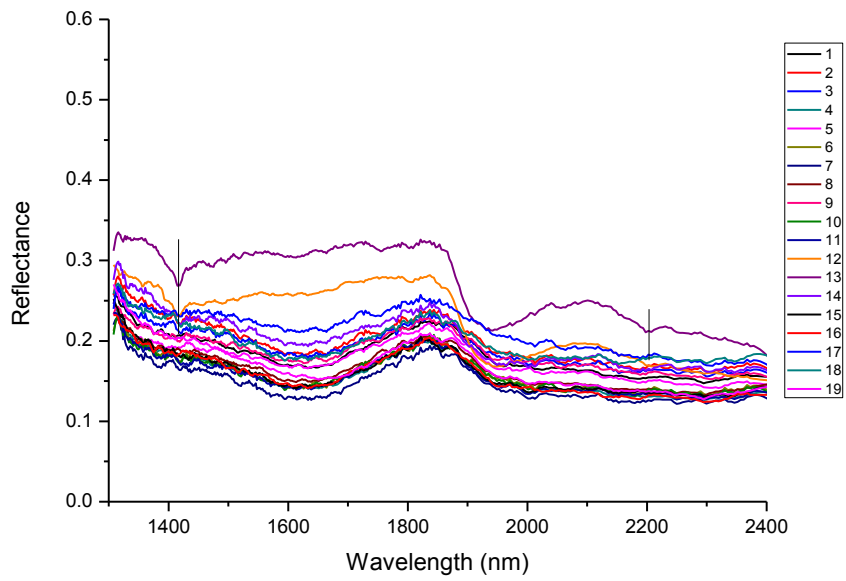
Sample 1



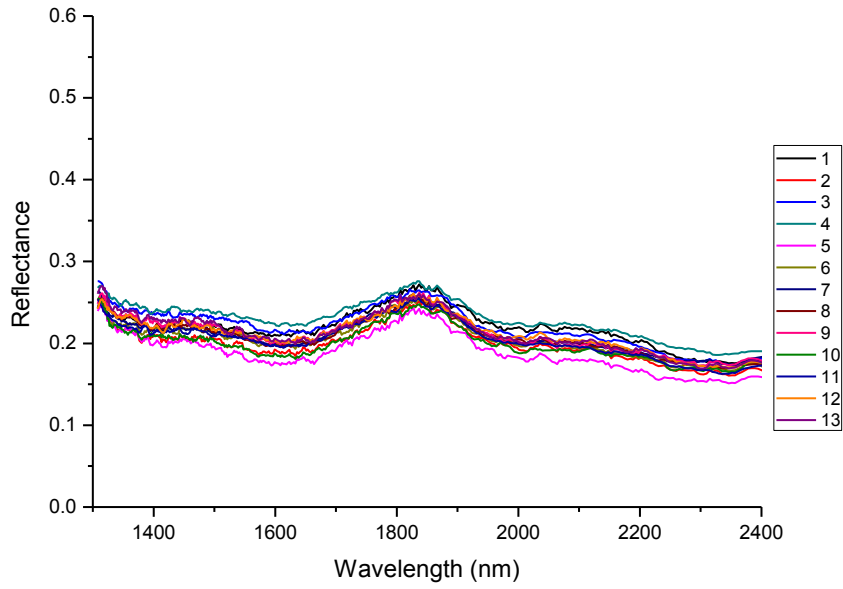
Sample 2



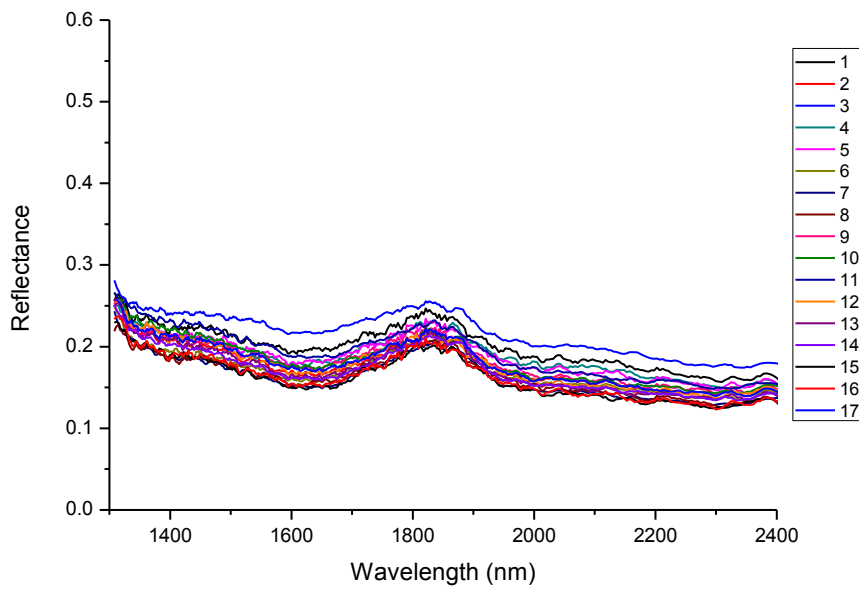
Sample 3



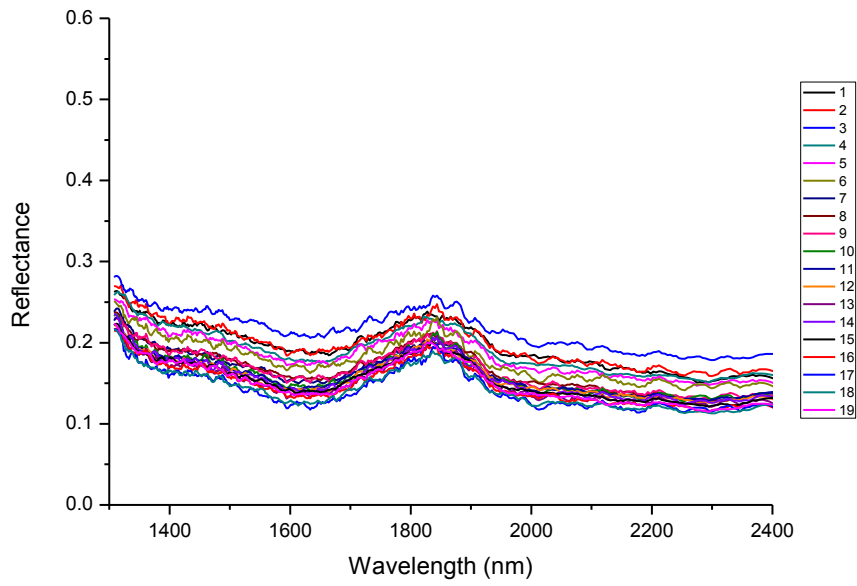
Sample 4



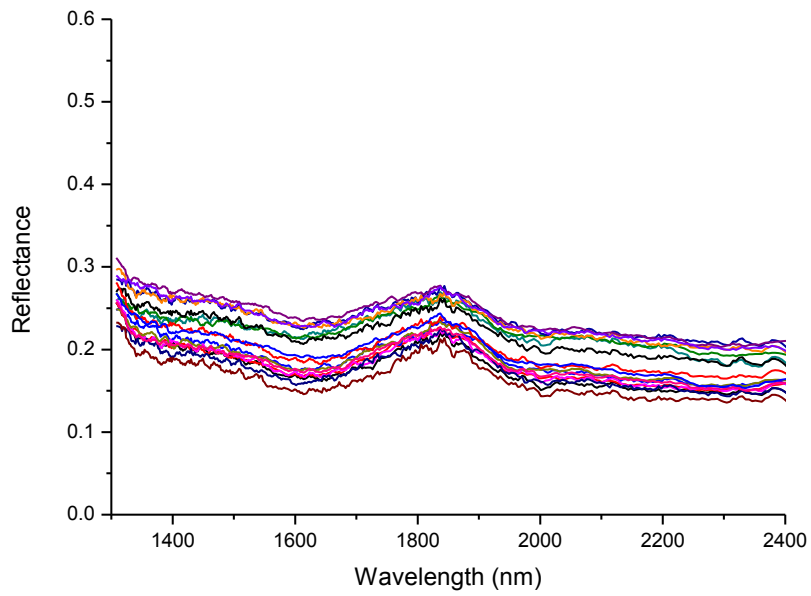
Sample 5



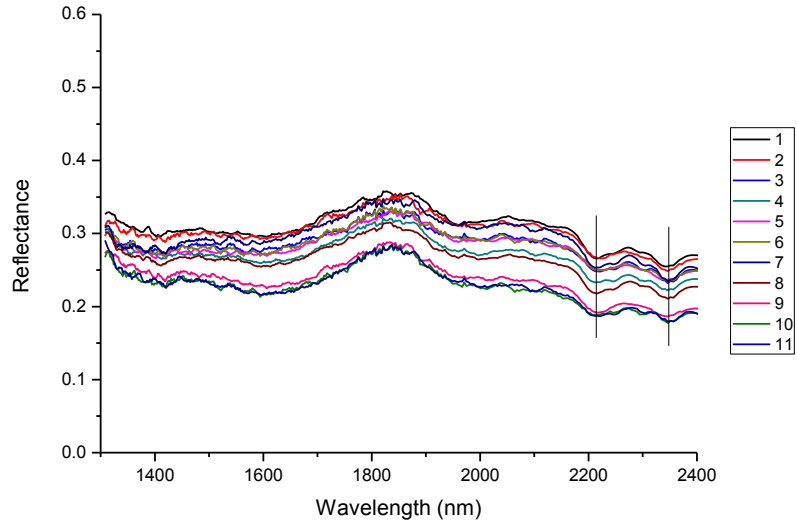
Sample 6



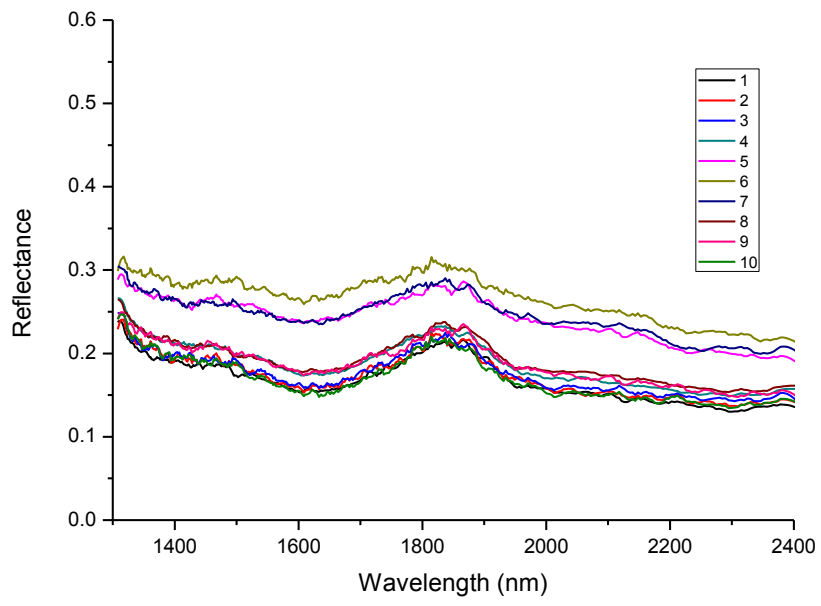
Sample 7



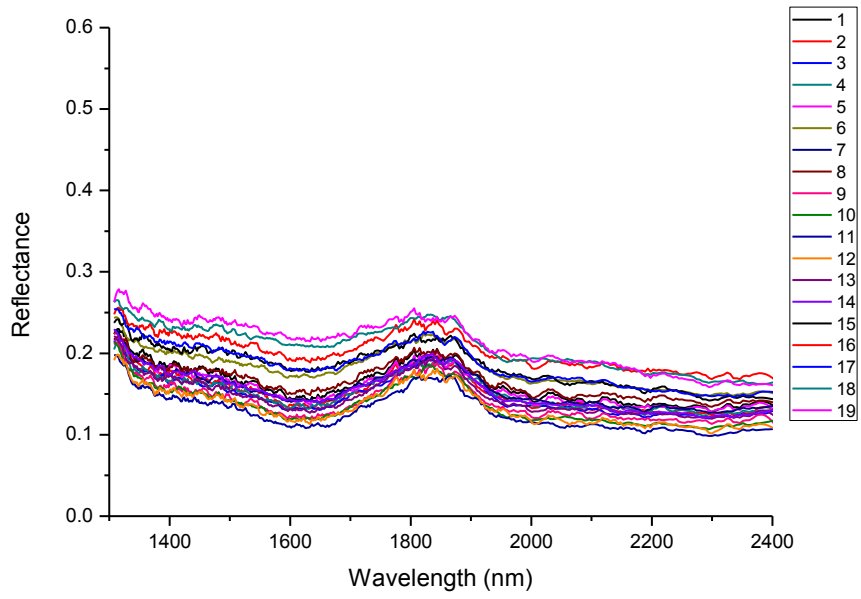
Sample 8



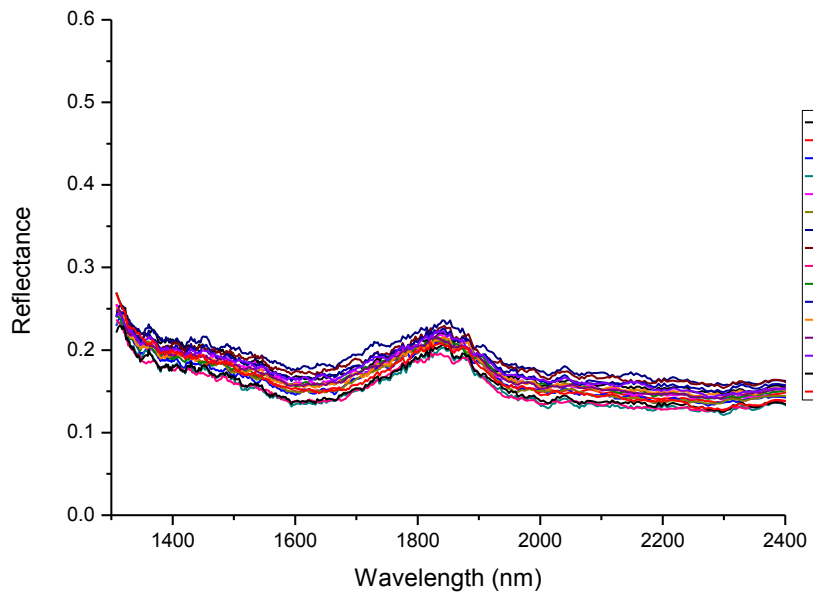
Sample 9



Sample 10

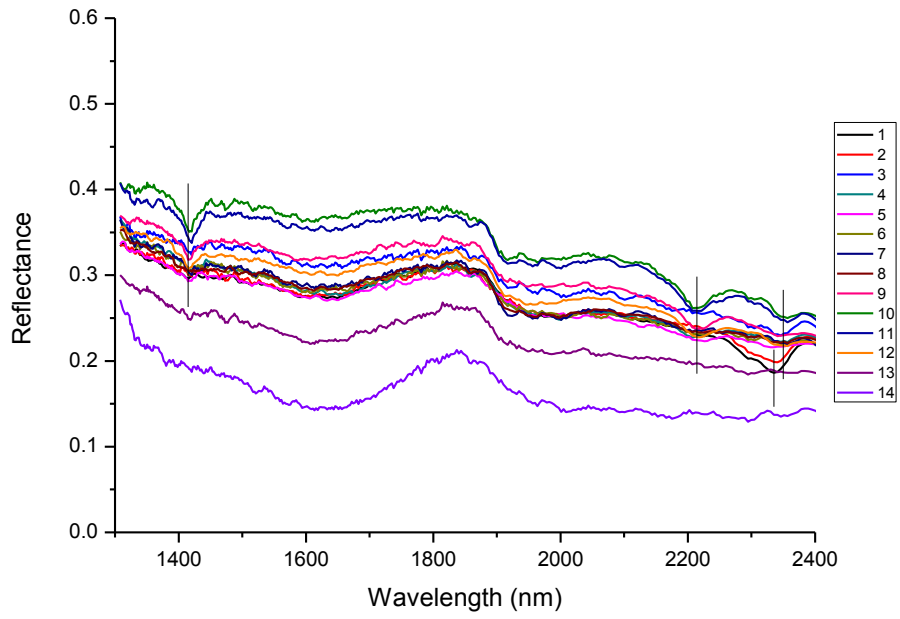


Sample 11

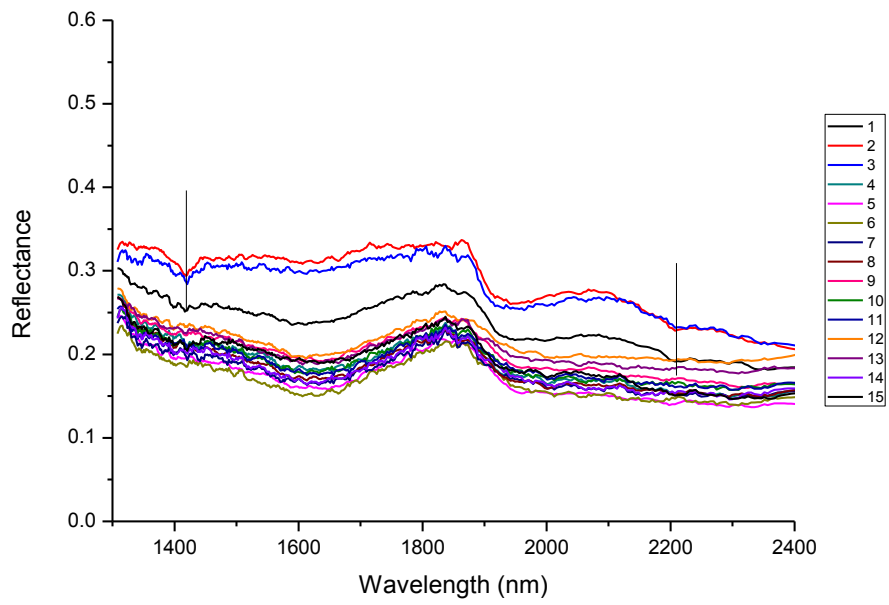


Sample 12

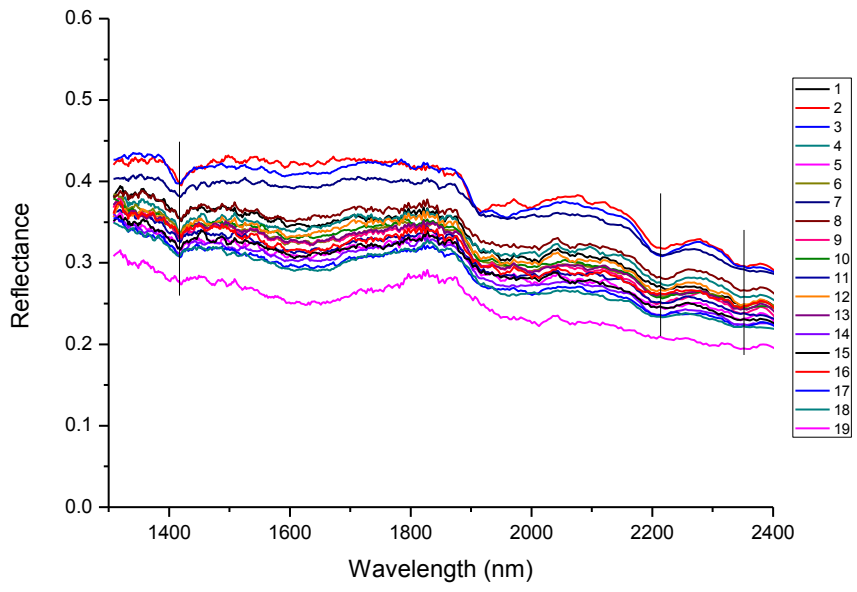




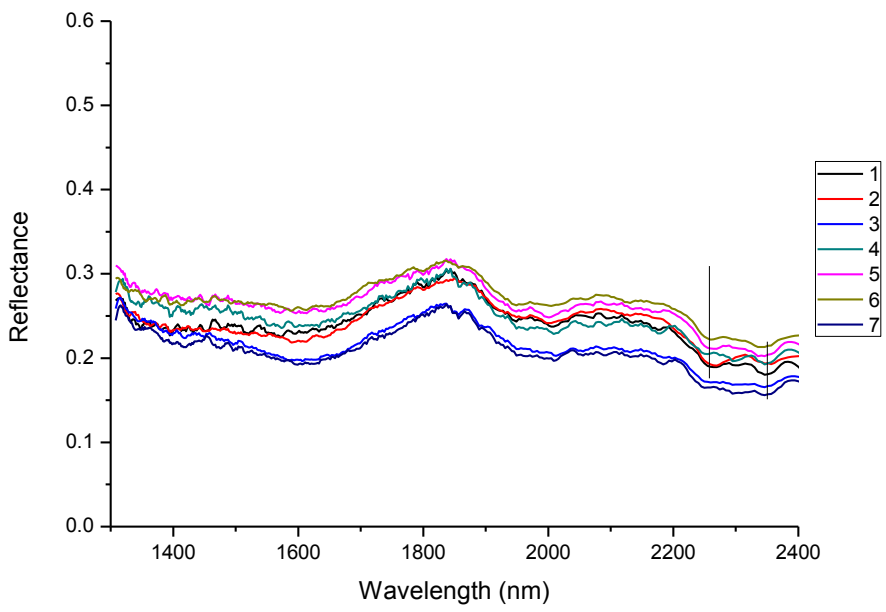
Sample 13



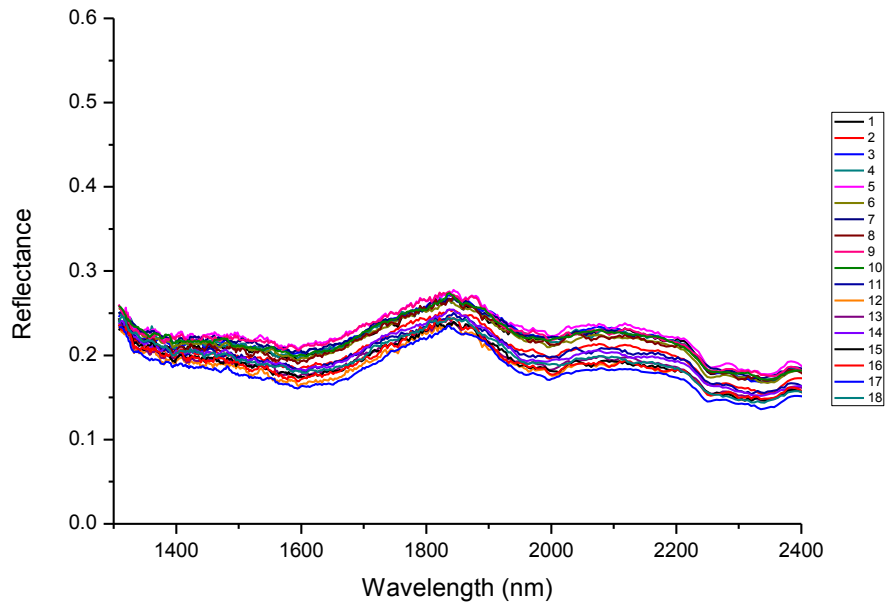
Sample 14



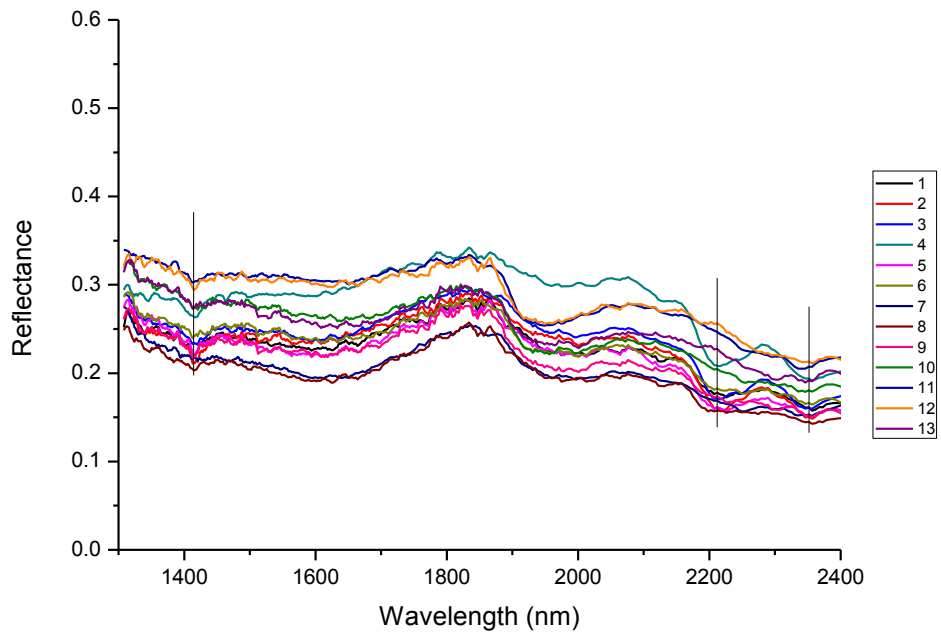
Sample 15



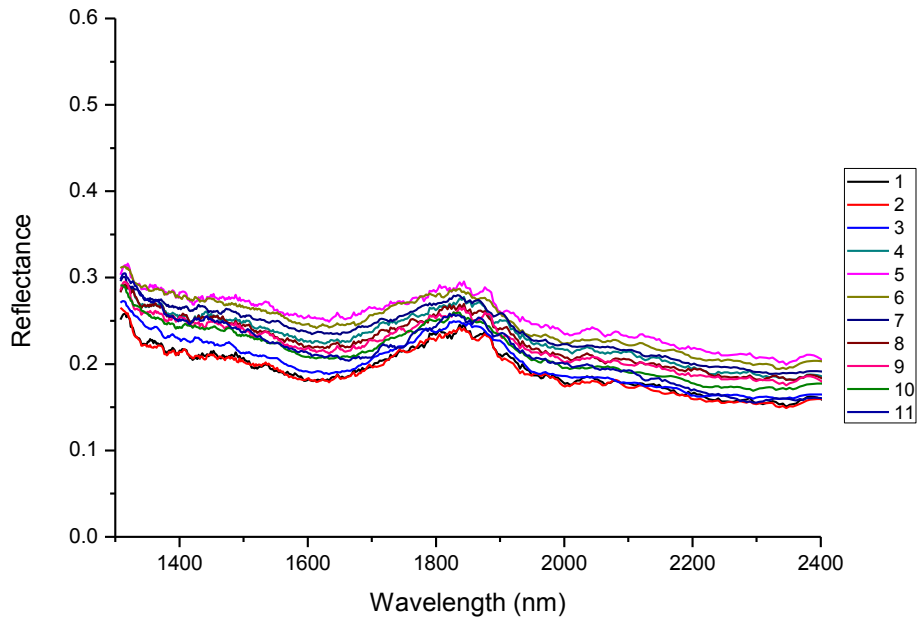
Sample 16



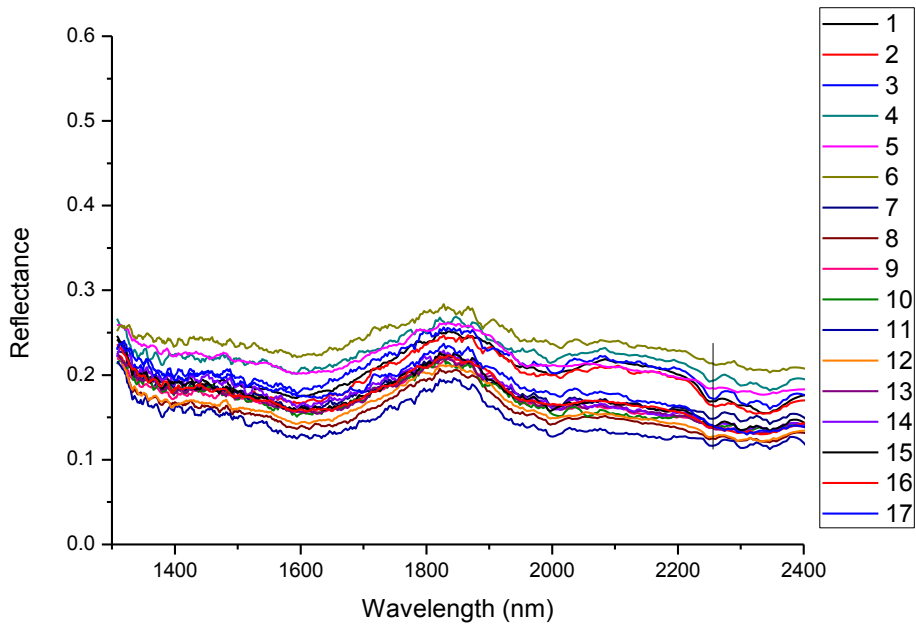
Sample 17



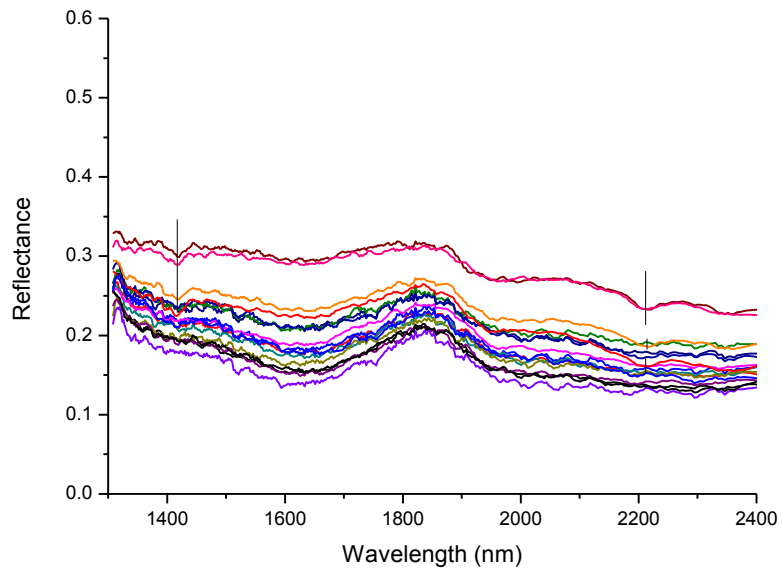
Sample 18



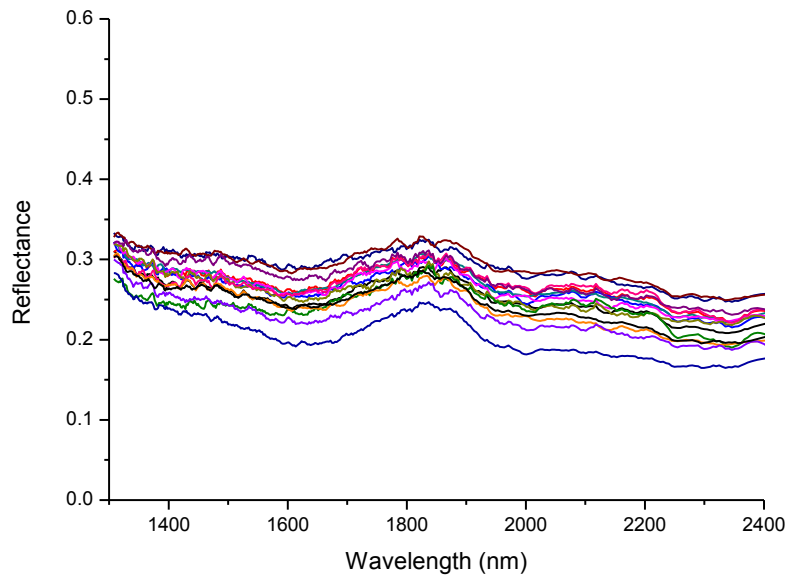
Sample 19



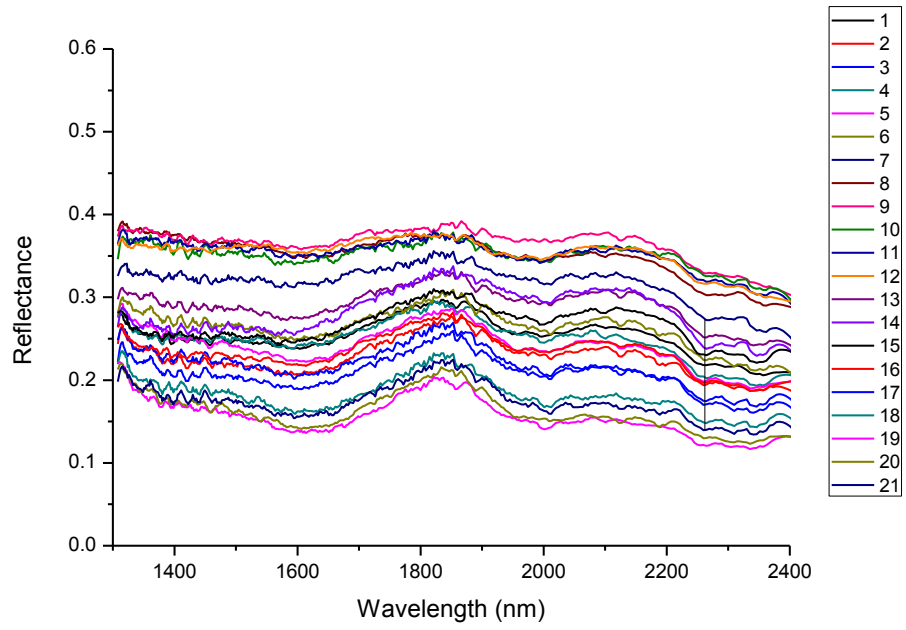
Sample 20



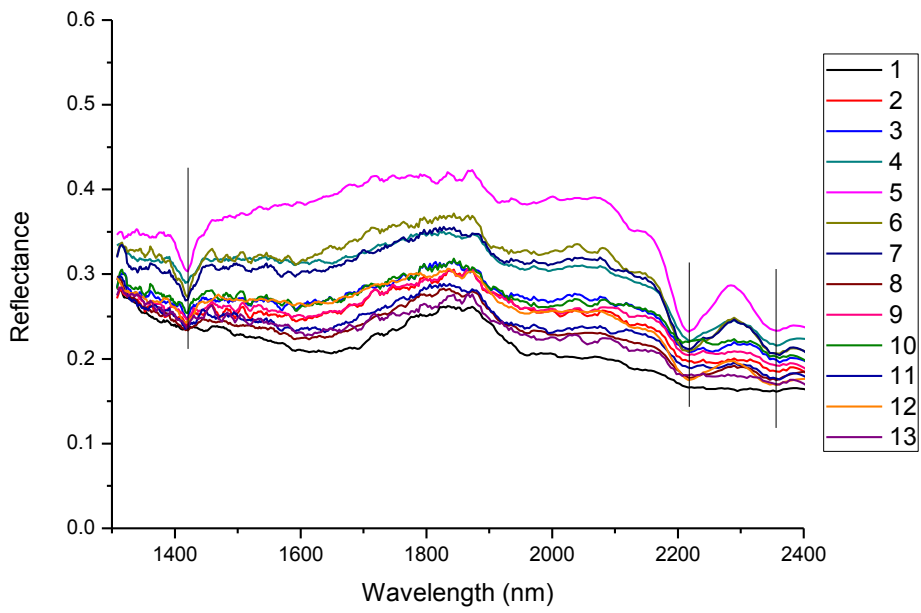
Sample 21



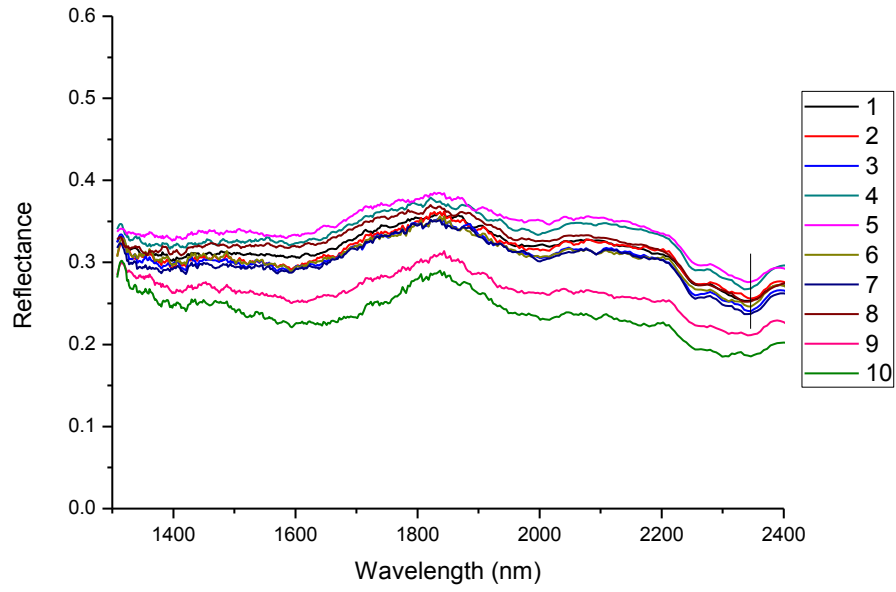
Sample 22



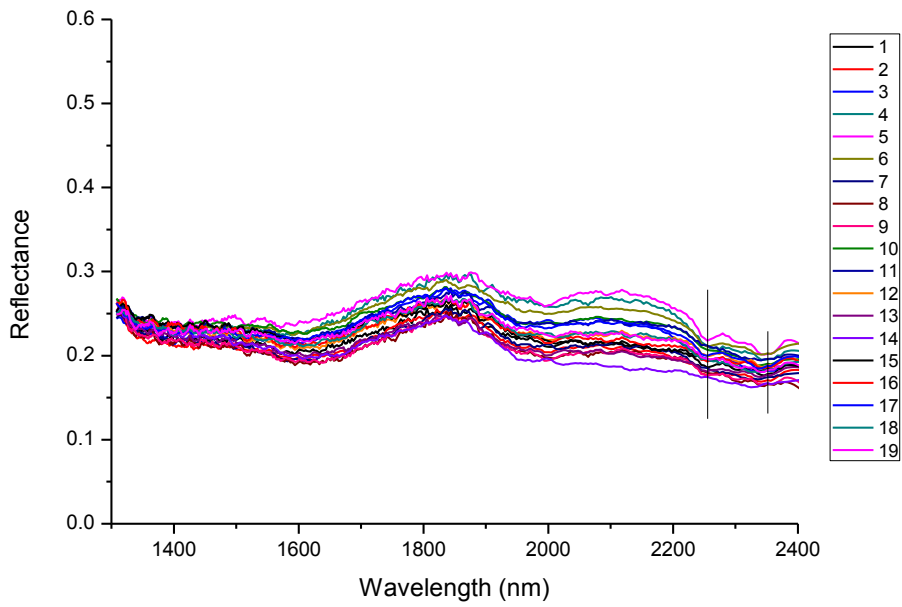
Sample 23



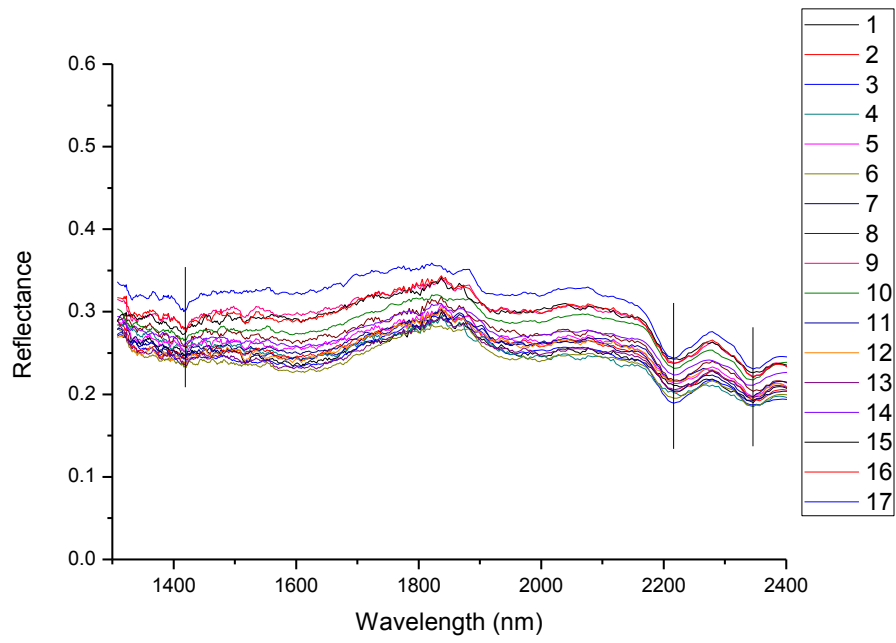
Sample 24



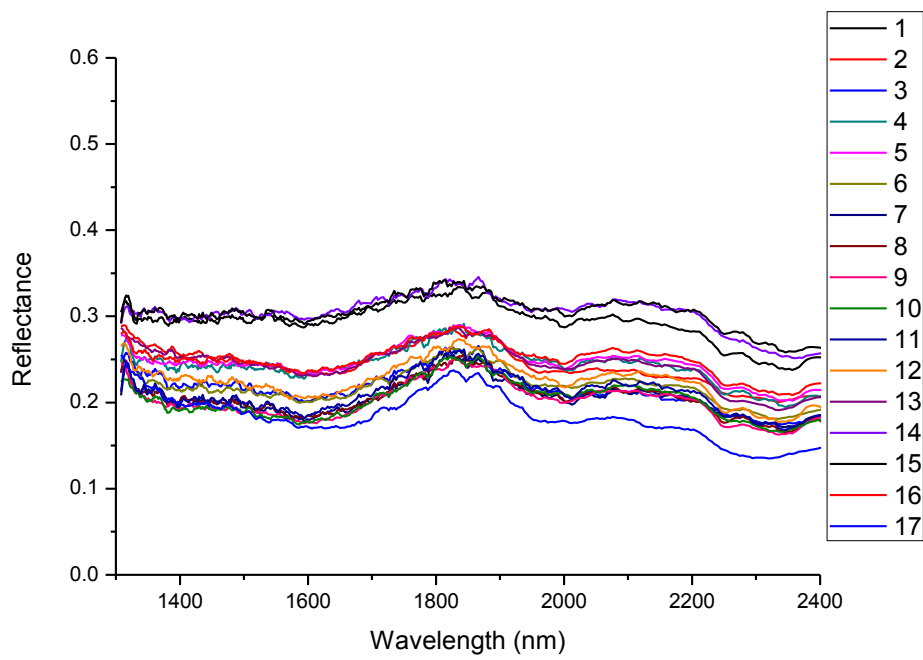
Sample 25



Sample 26

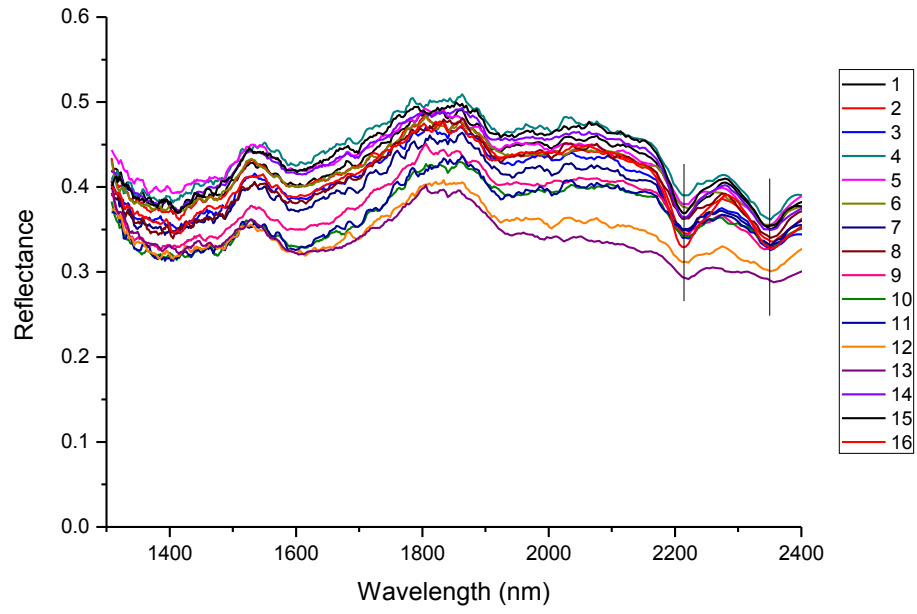


Sample 27

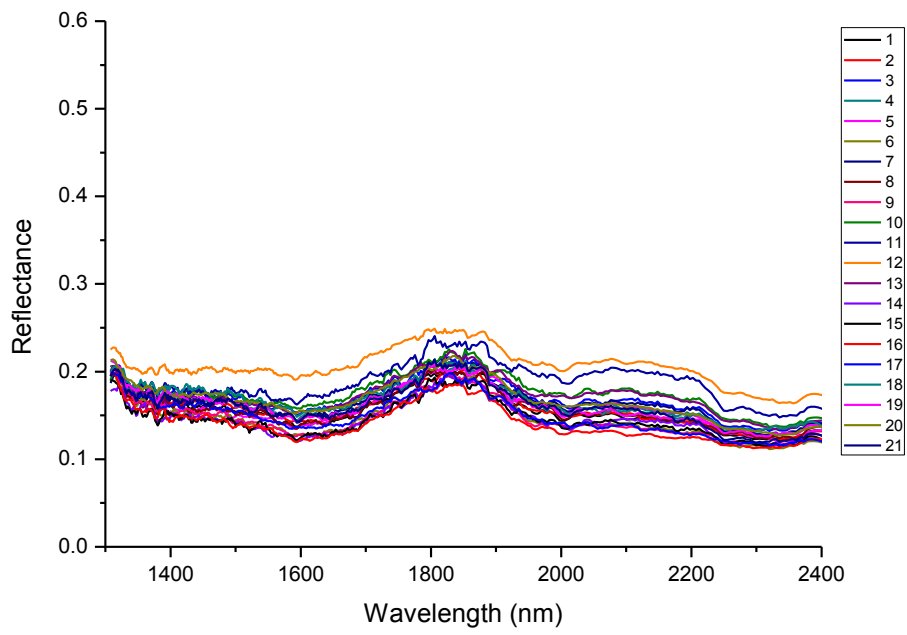


Sample 28

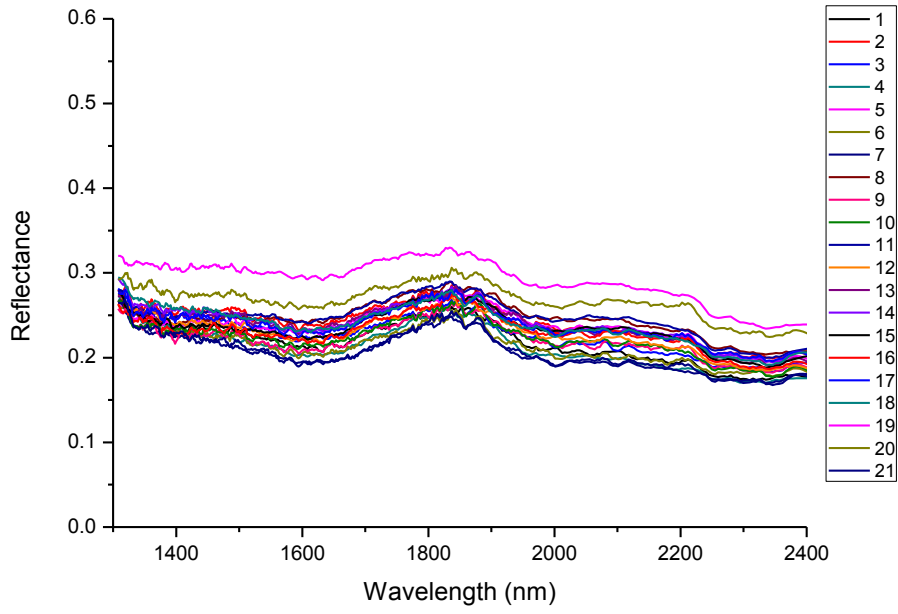




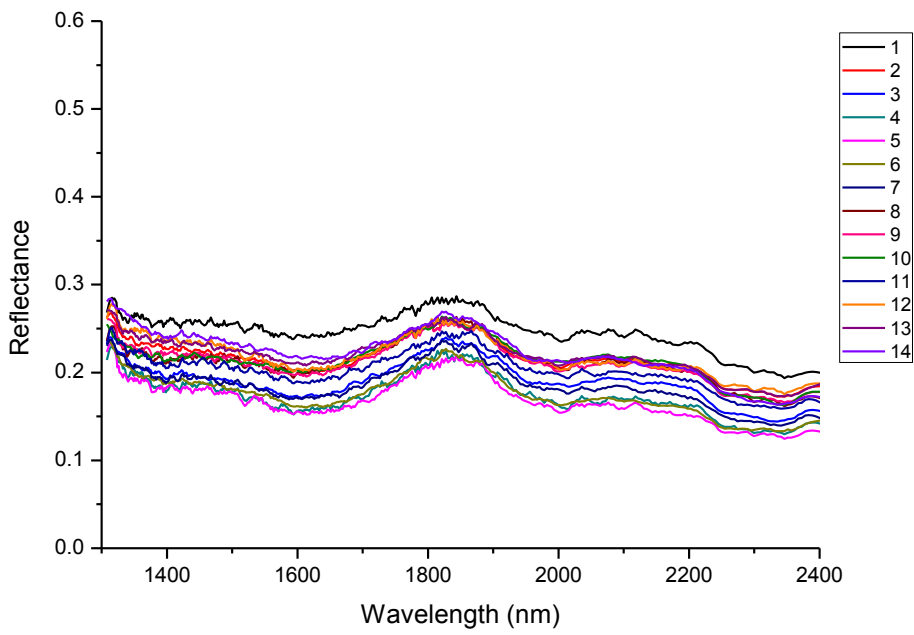
Sample 29



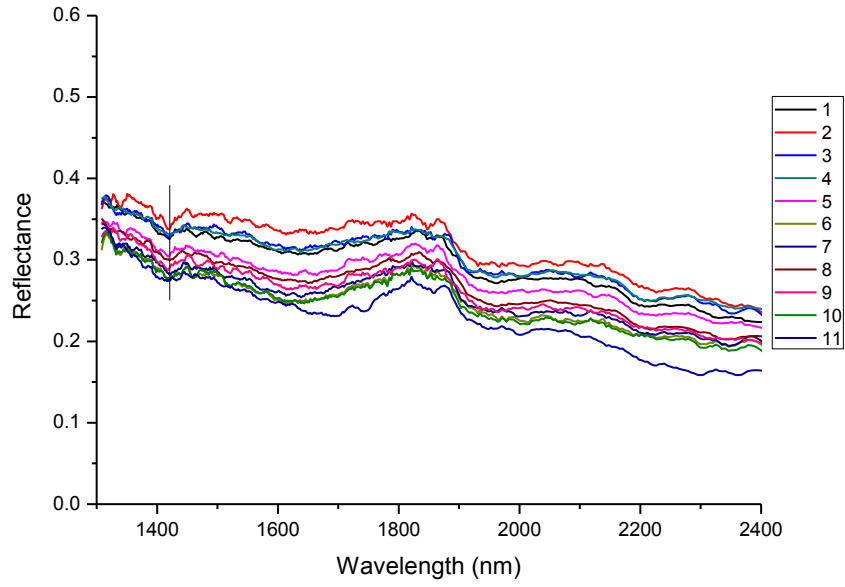
Sample 30



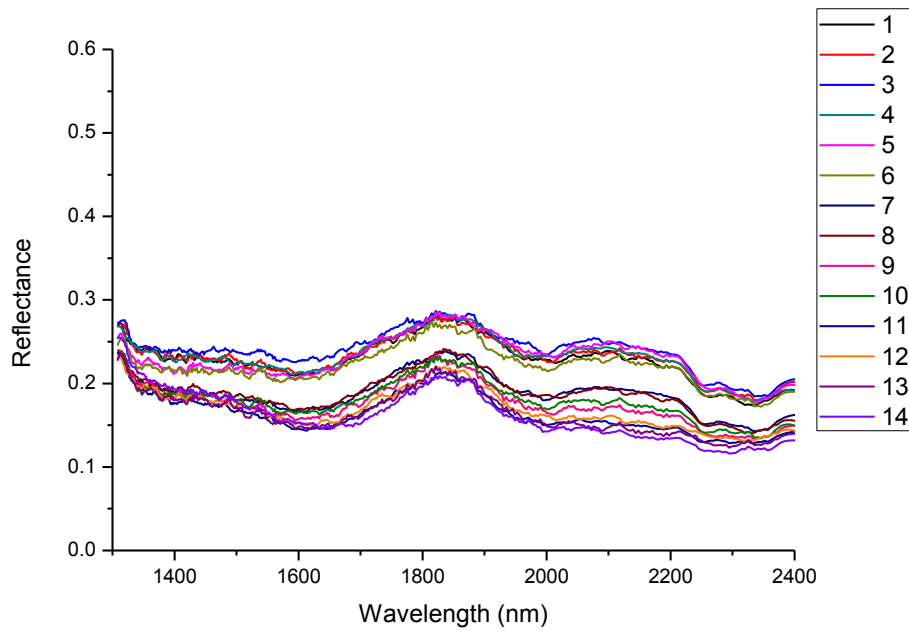
Sample 31



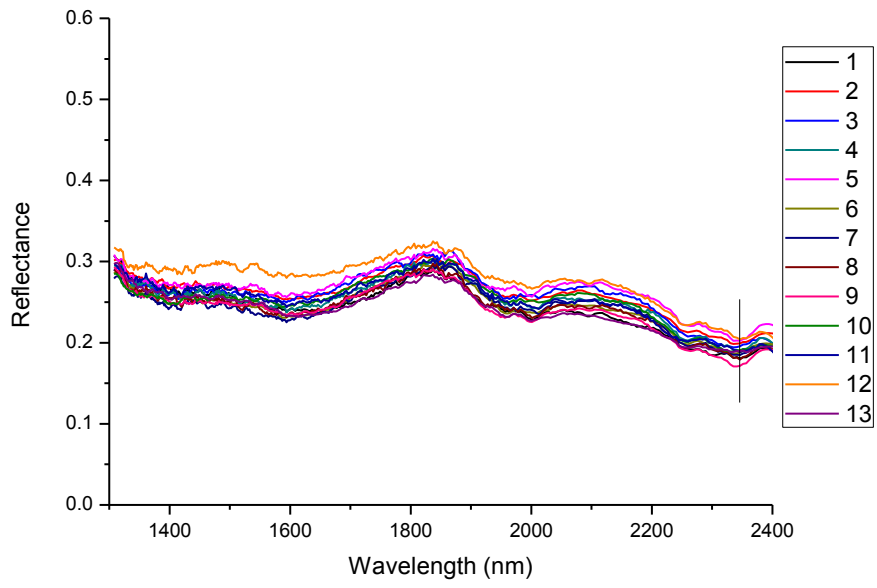
Sample 32



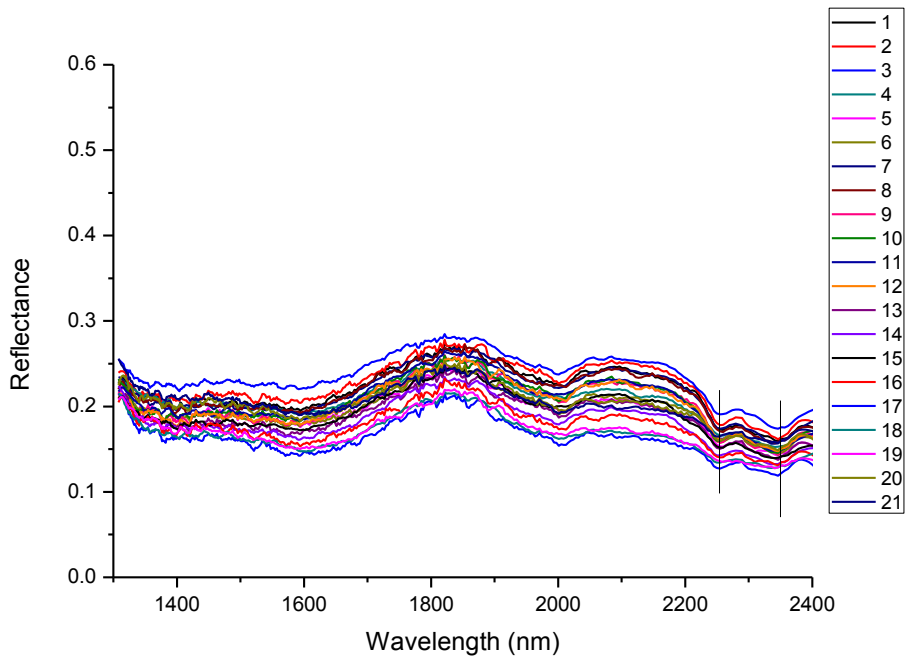
Sample 33



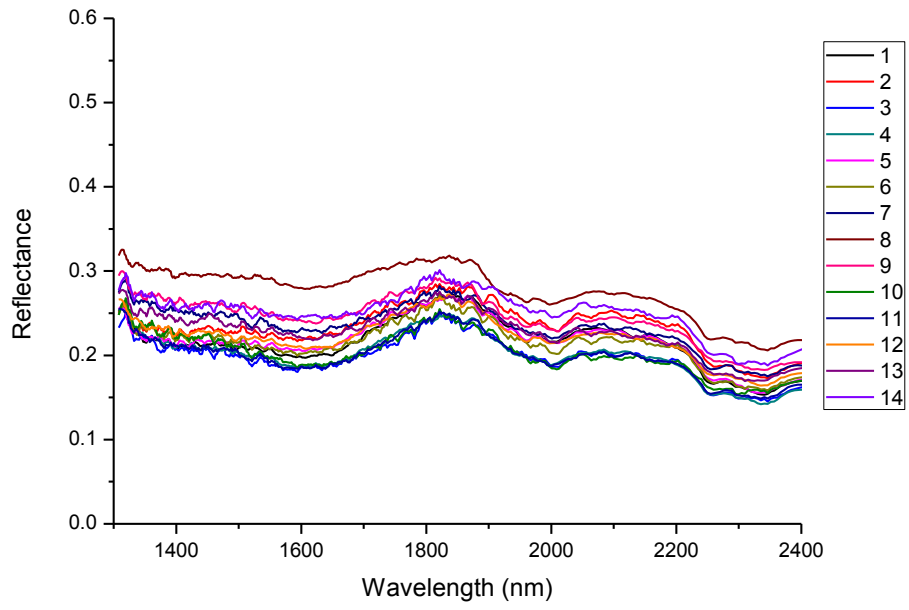
Sample 34



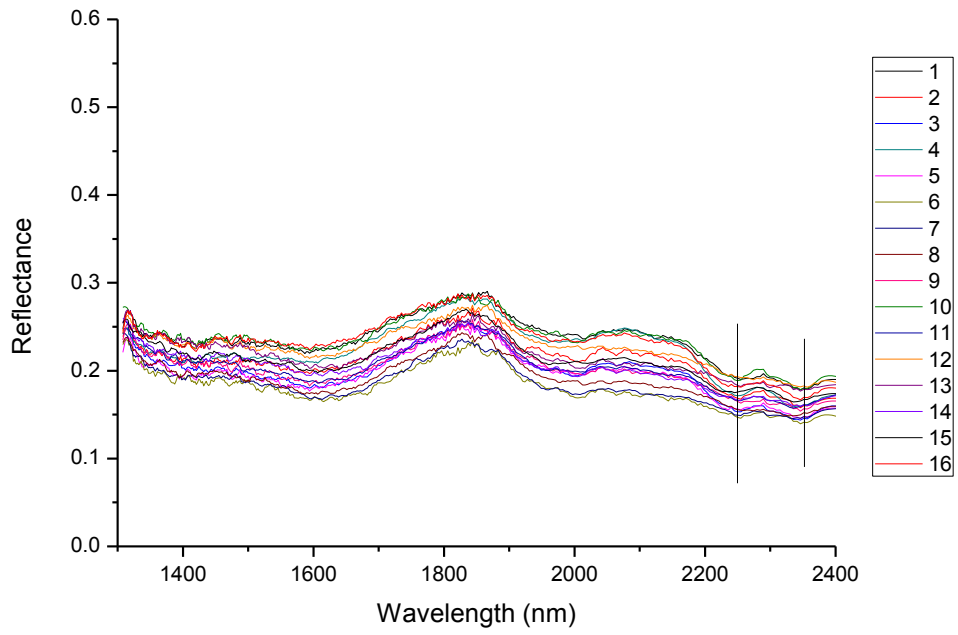
Sample 35



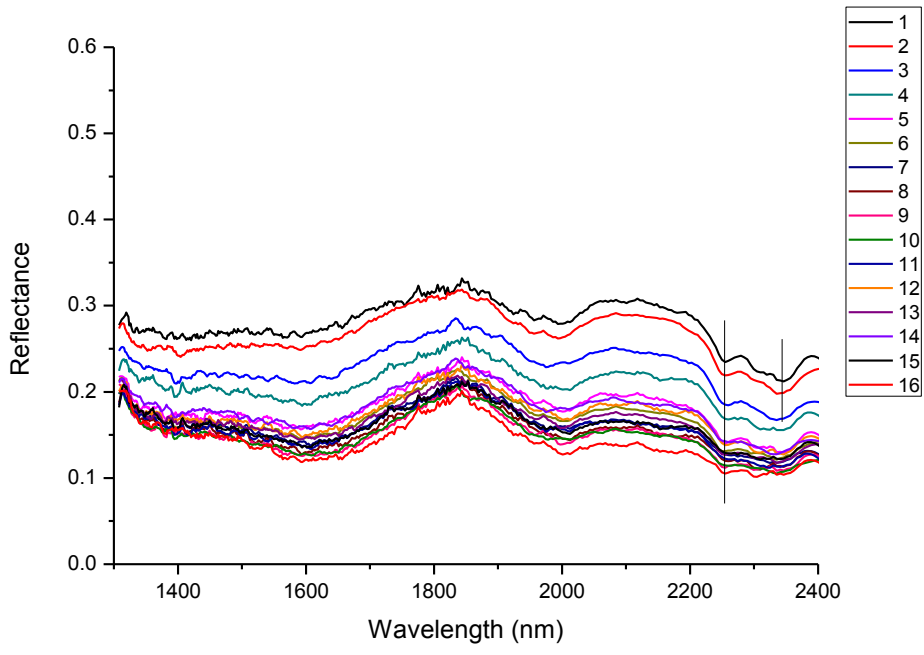
Sample 36



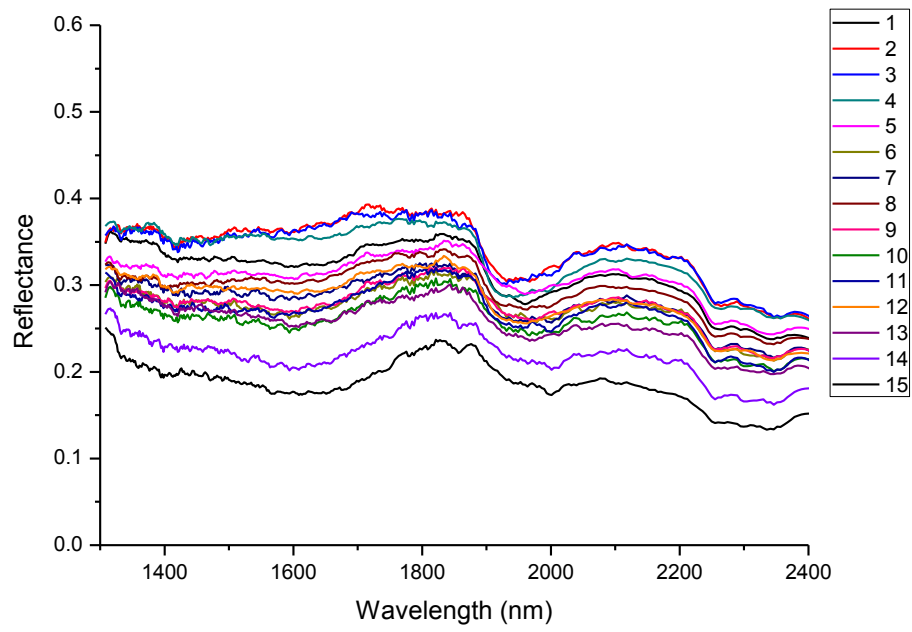
Sample 37



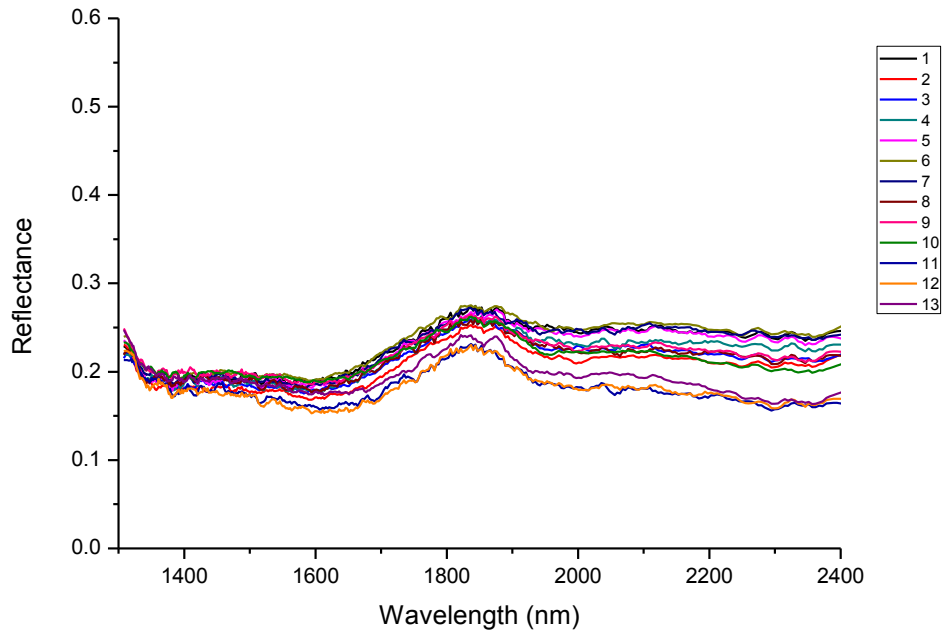
Sample 38



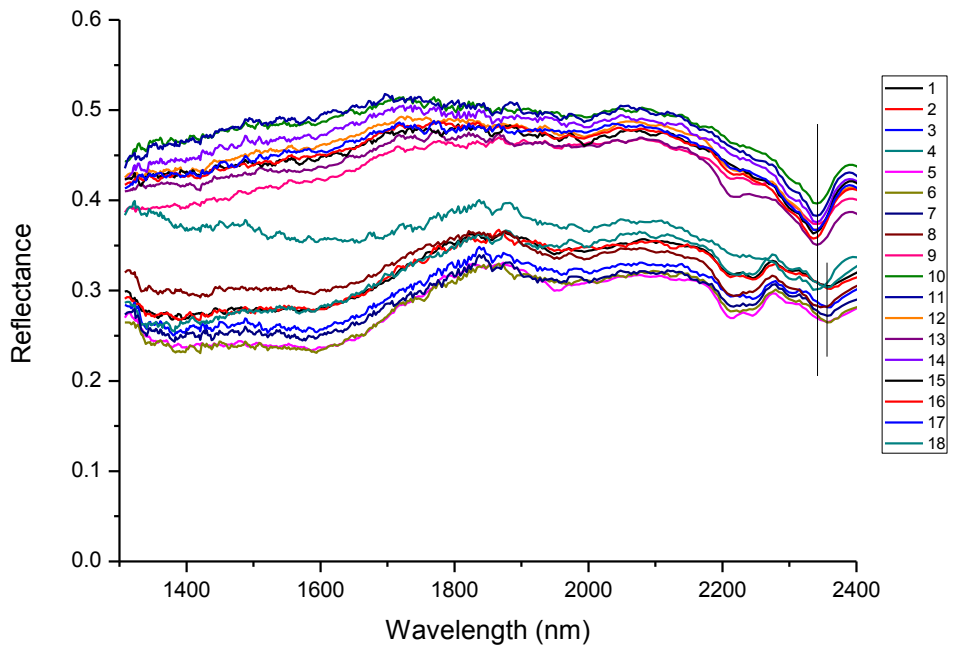
Sample 39



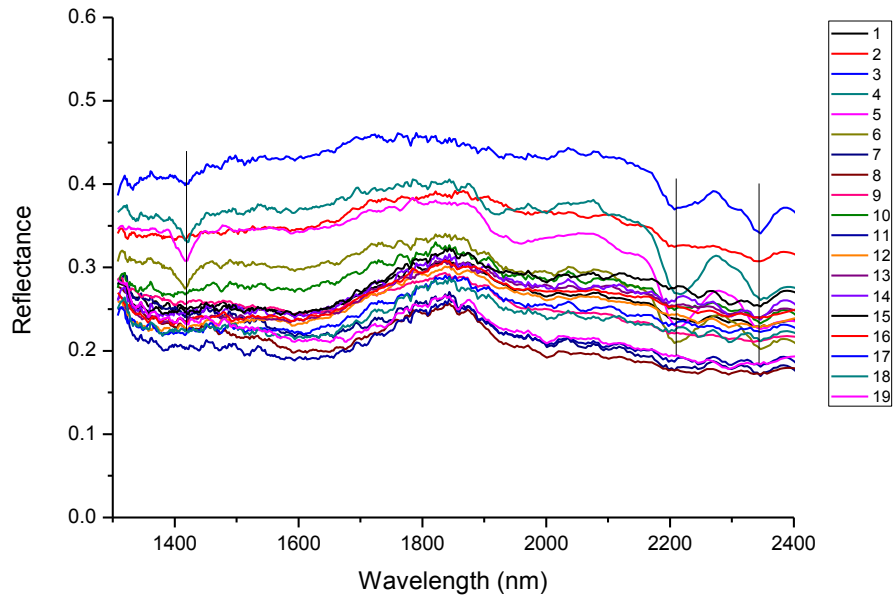
Sample 40



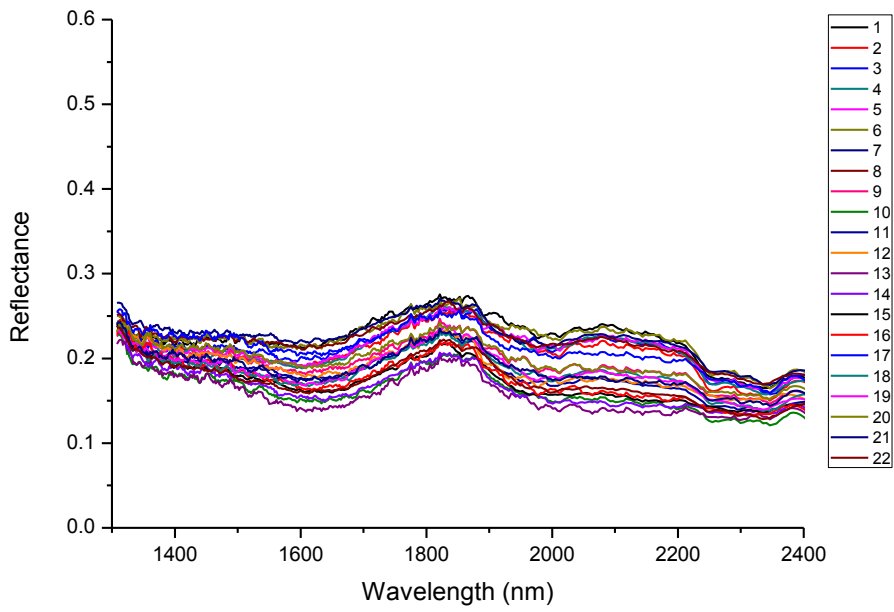
Sample 41



Sample 42

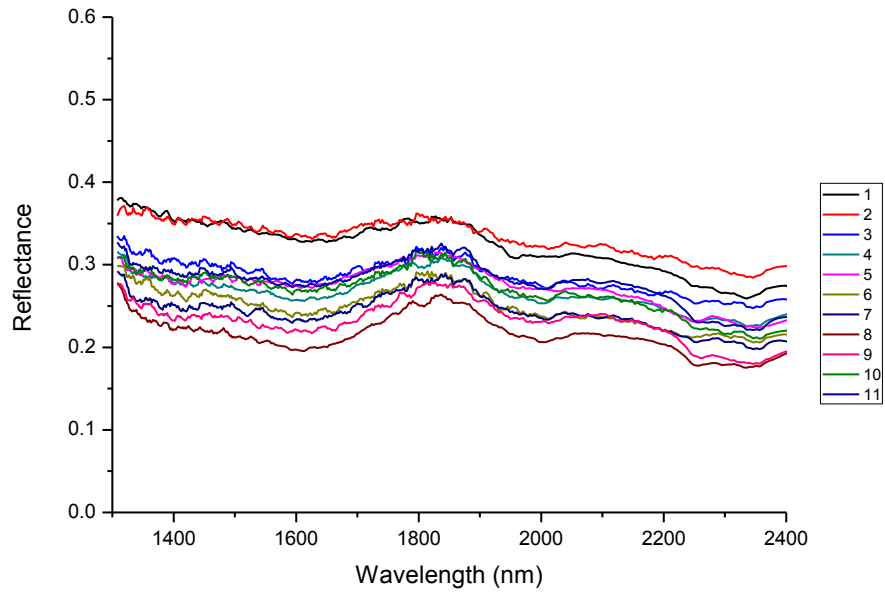


Sample 43

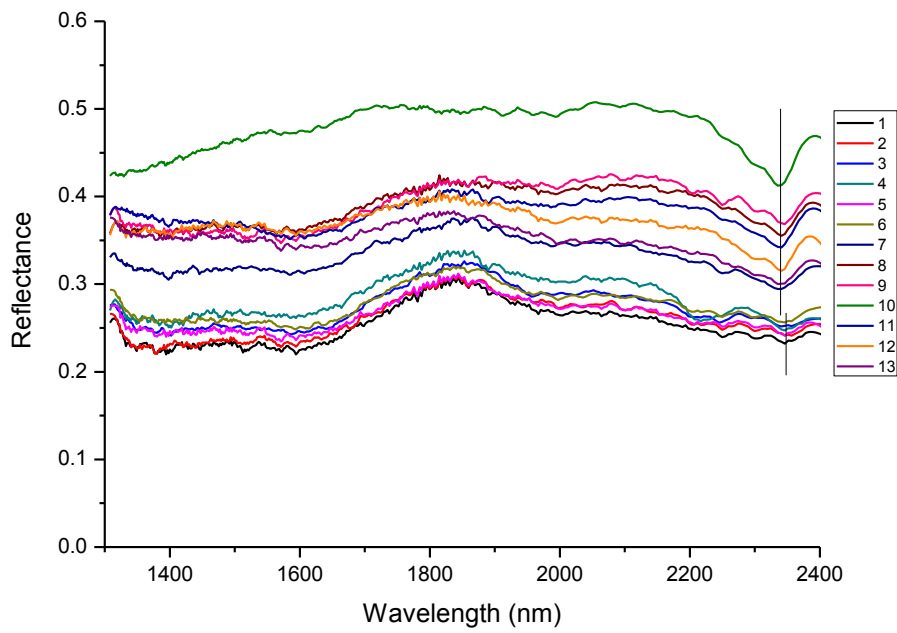


Sample 44

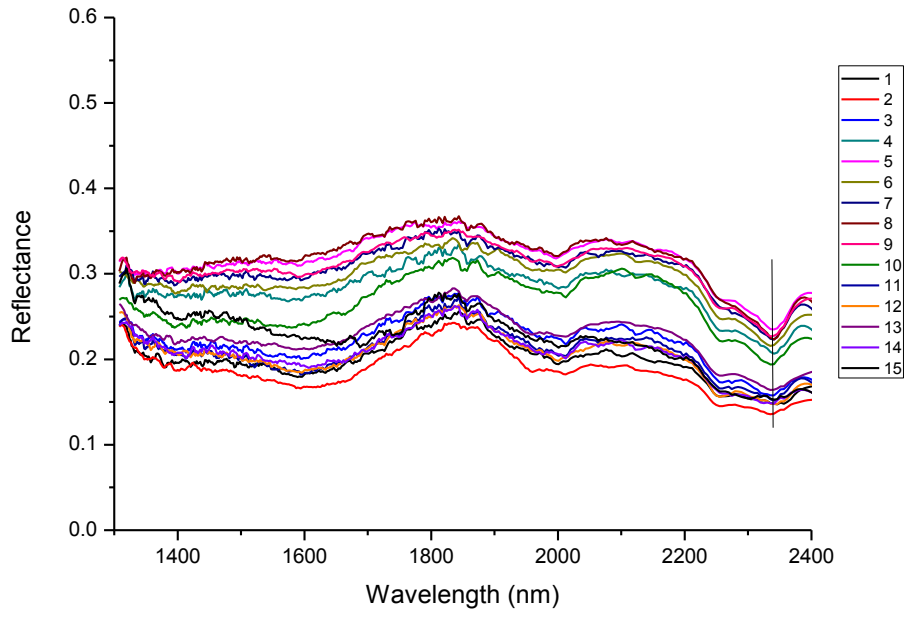




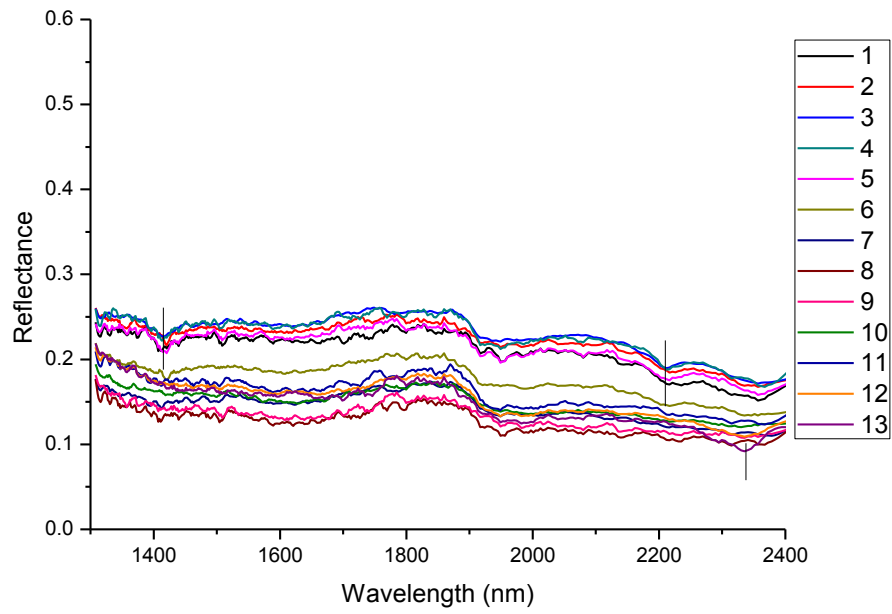
Sample 45



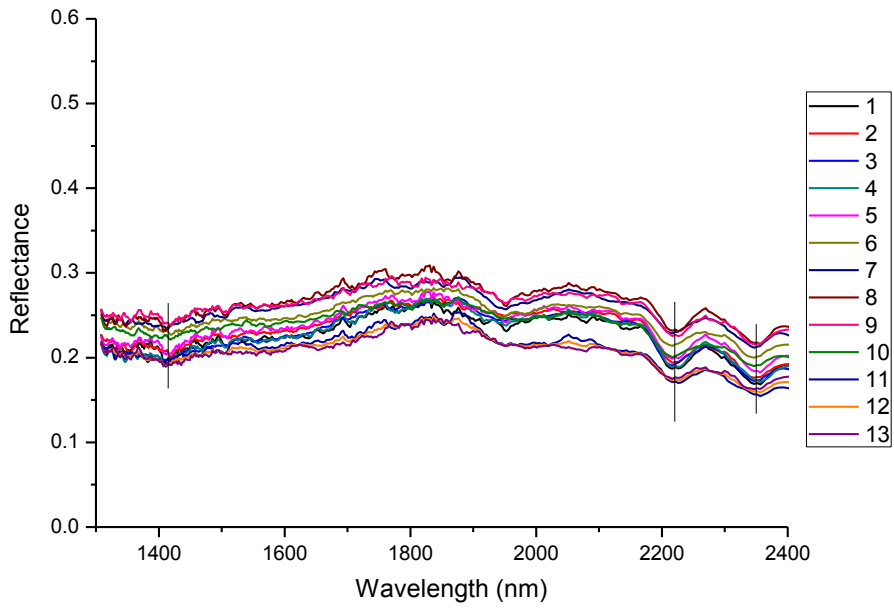
Sample 46



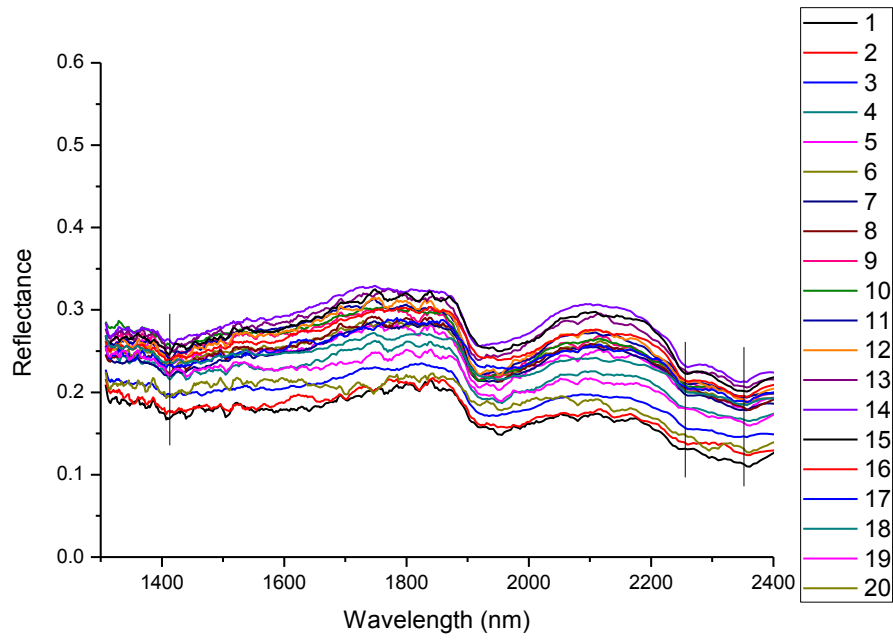
Sample 47



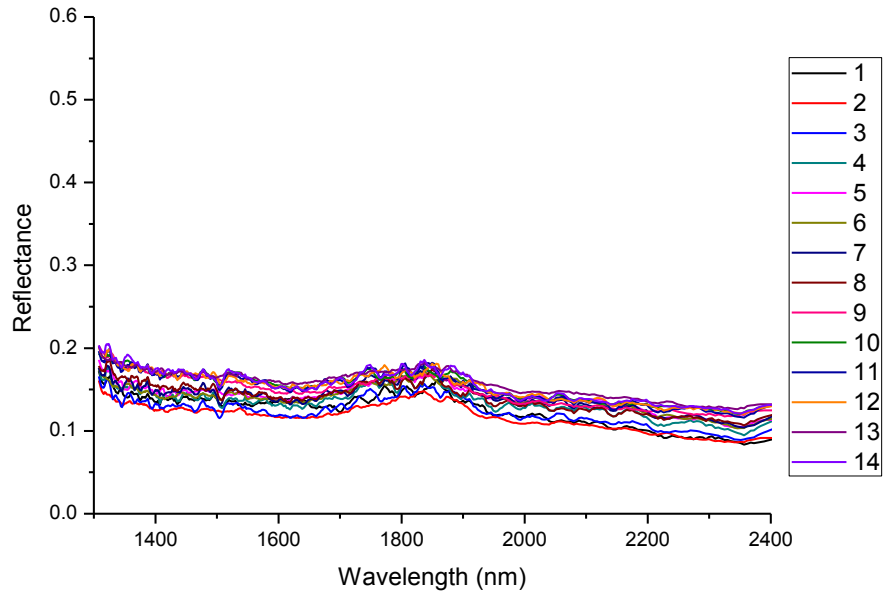
Sample 48



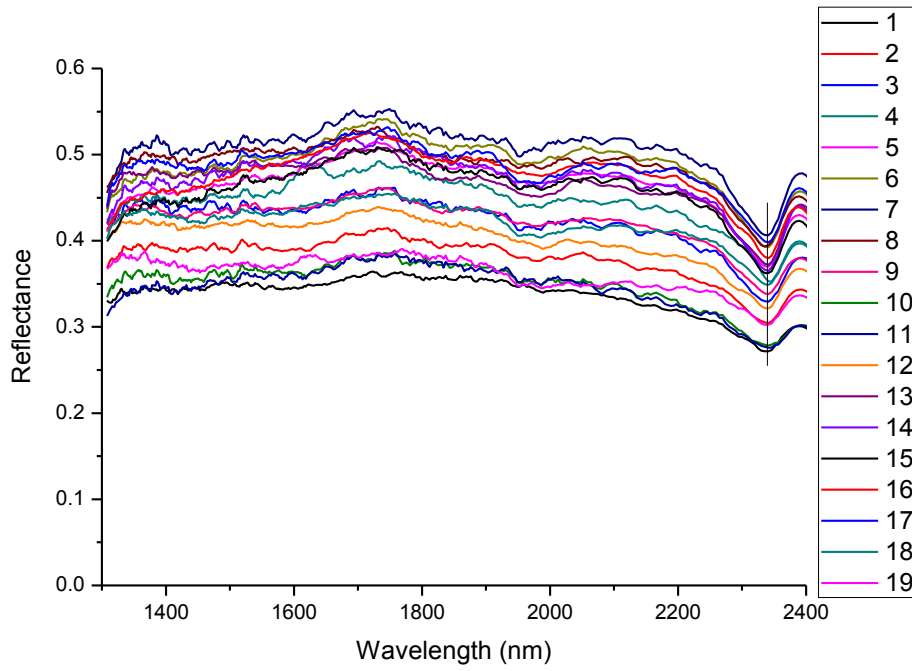
Sample 49



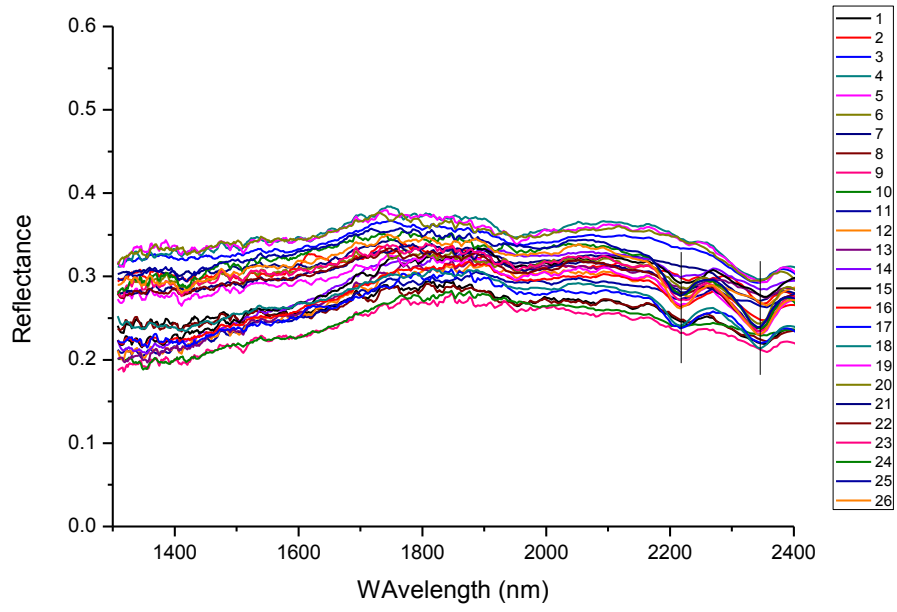
Sample 50



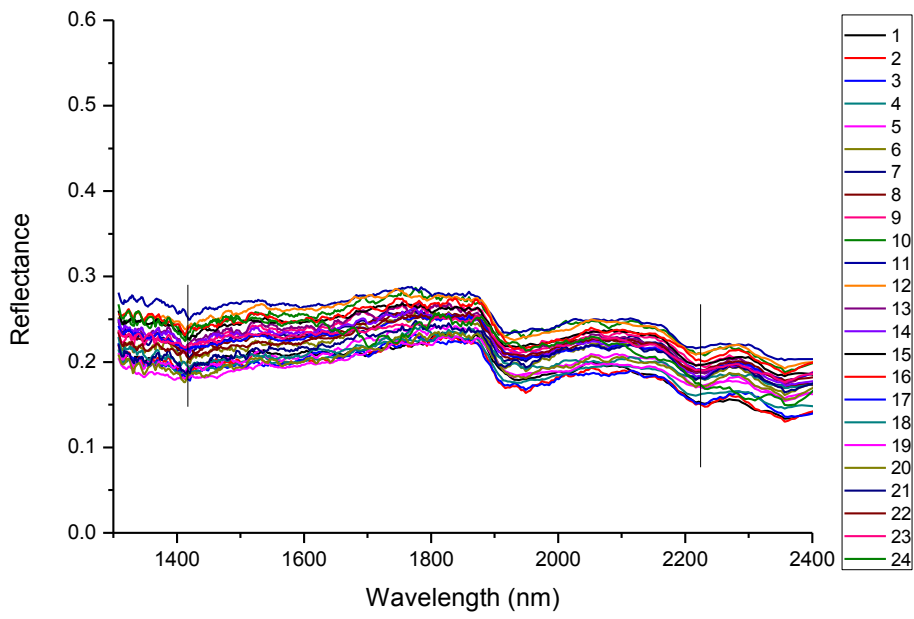
Sample 51



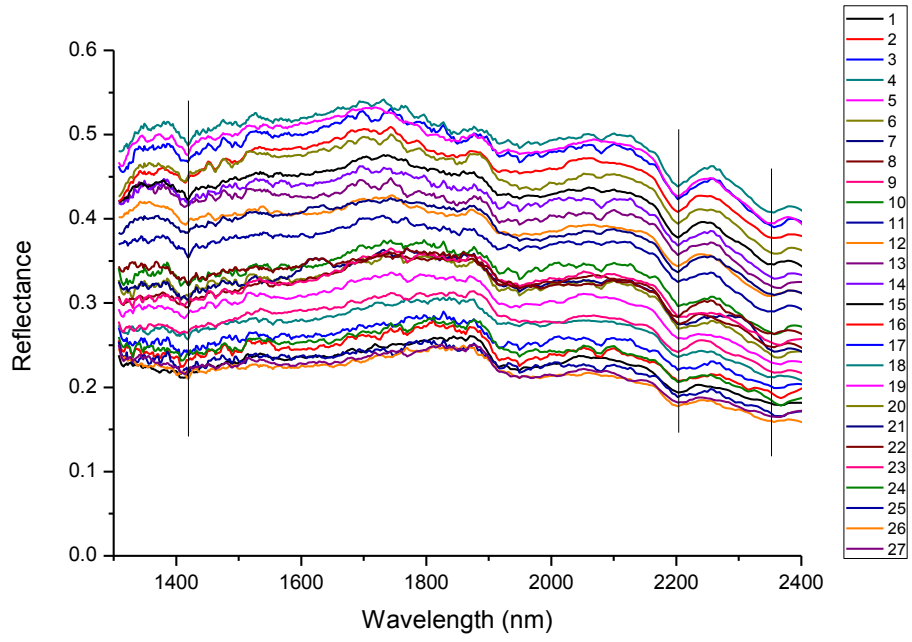
Sample 52



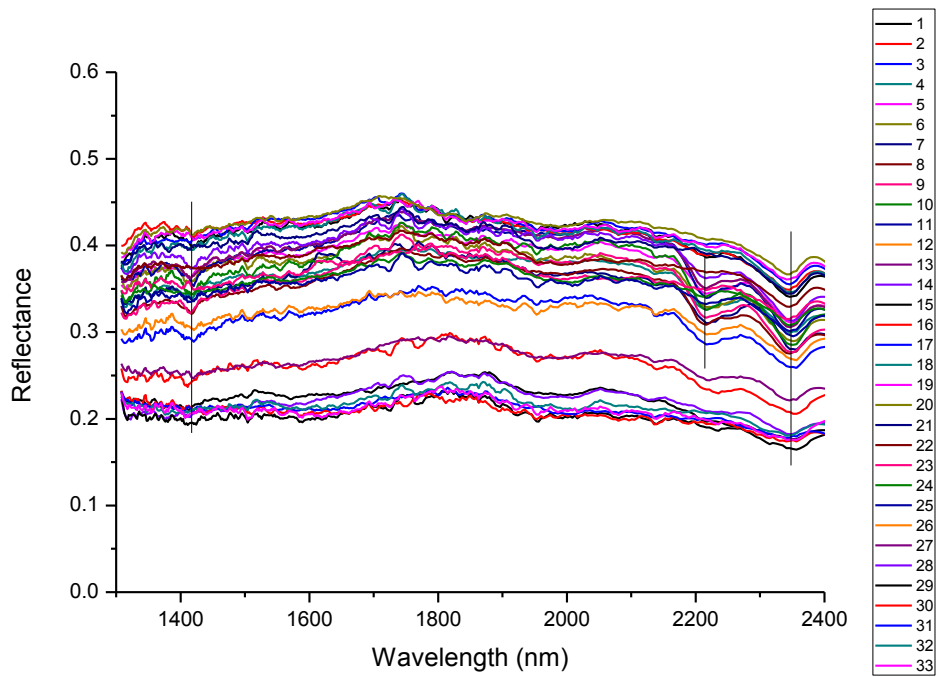
Sample 53



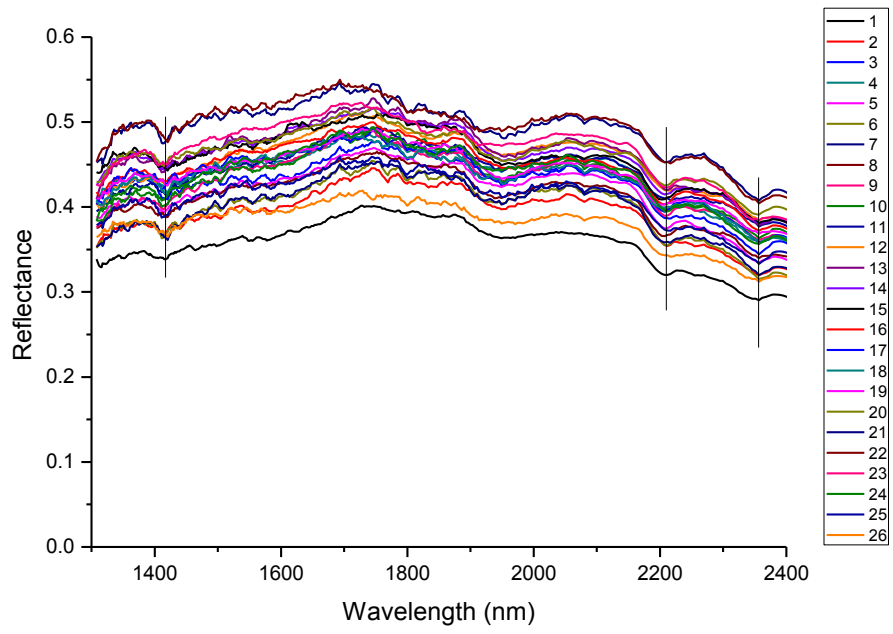
Sample 54



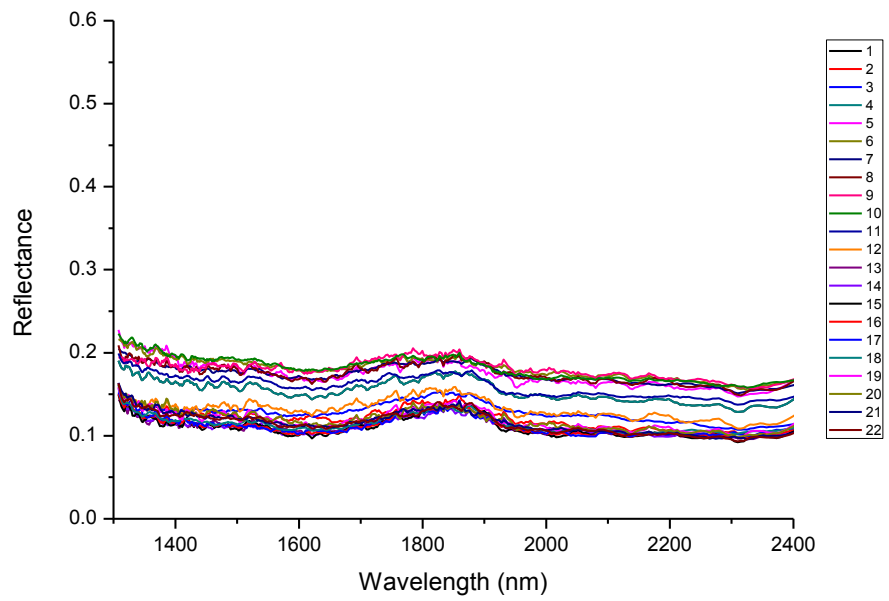
Sample 55



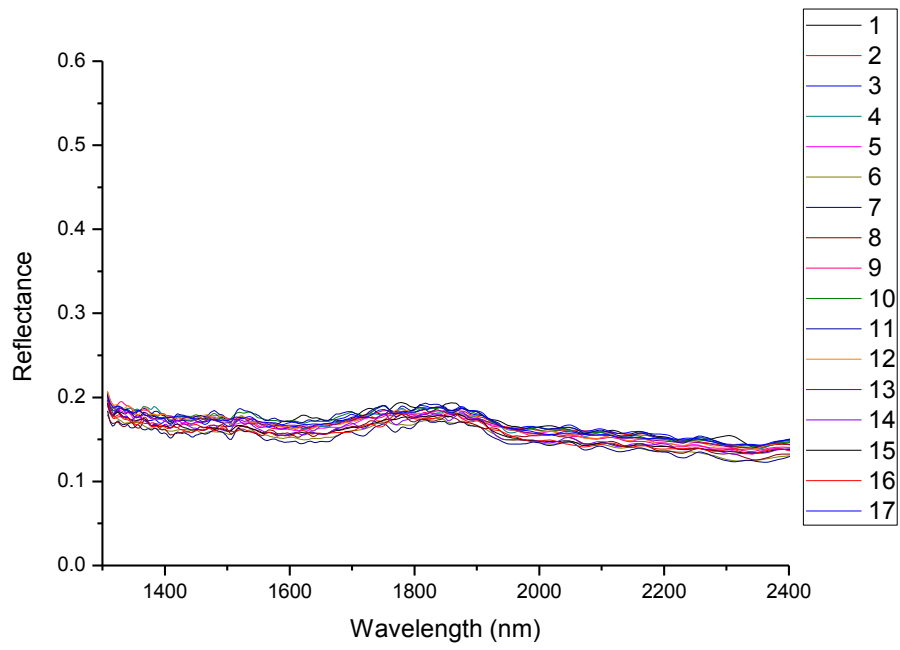
Sample 56



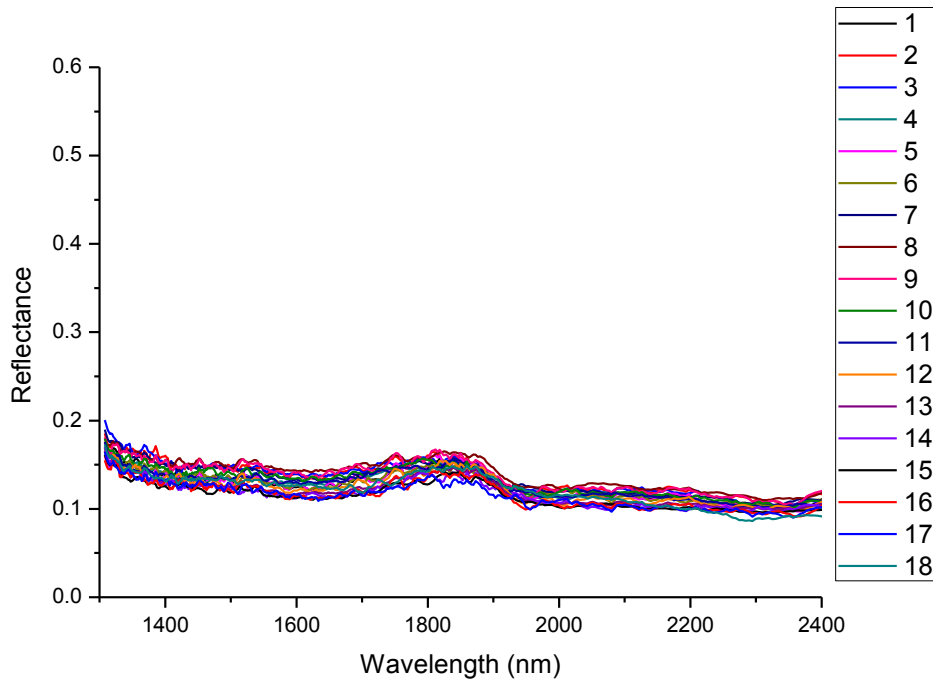
Sample 57



Sample 58



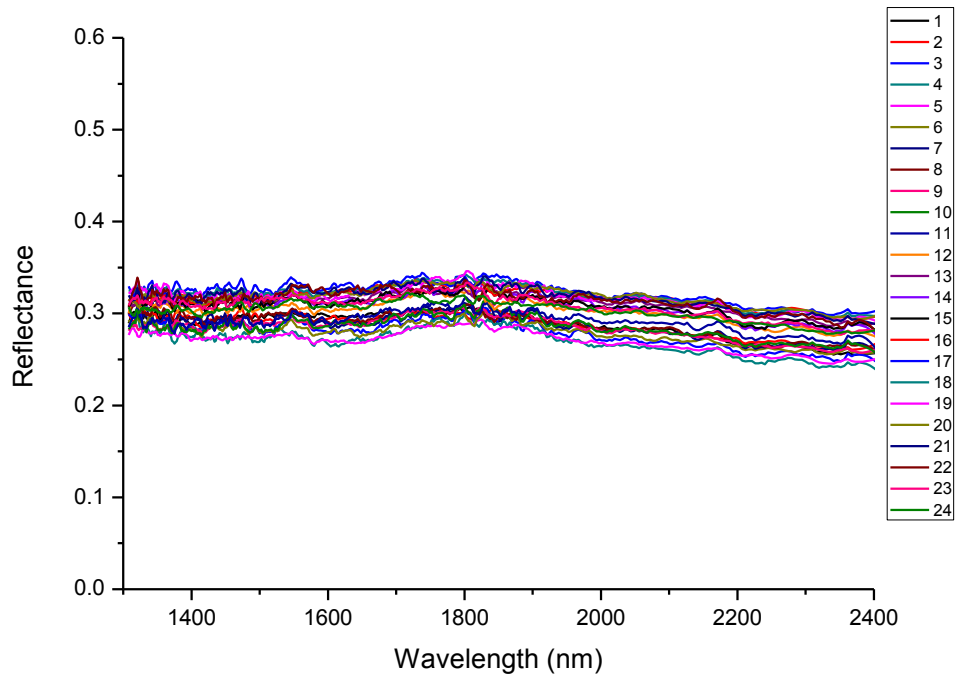
Sample 59



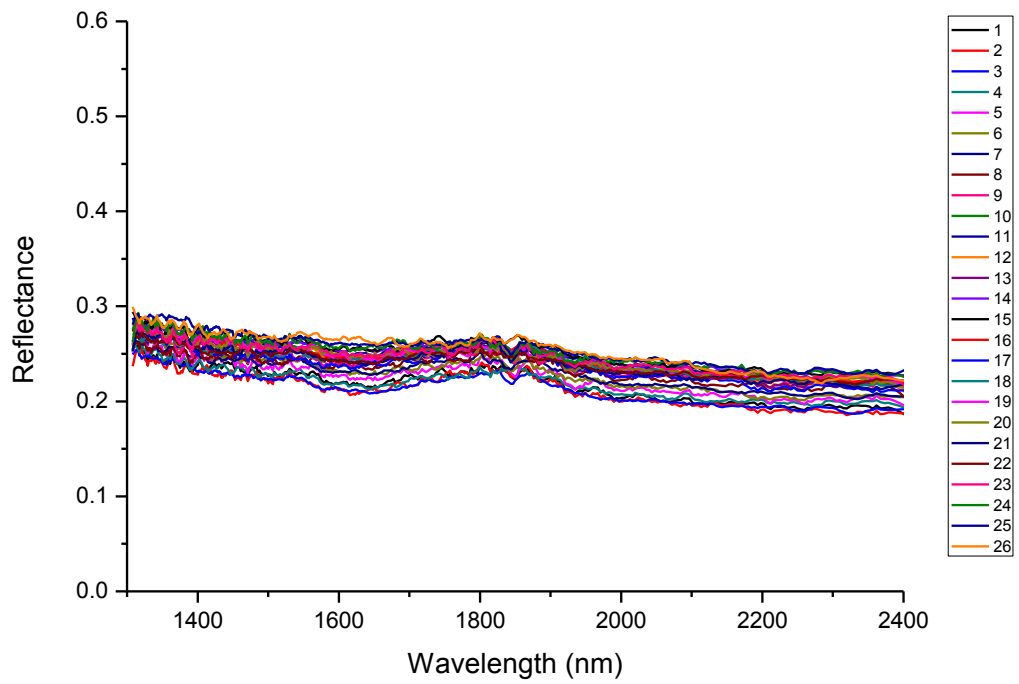
Sample 60



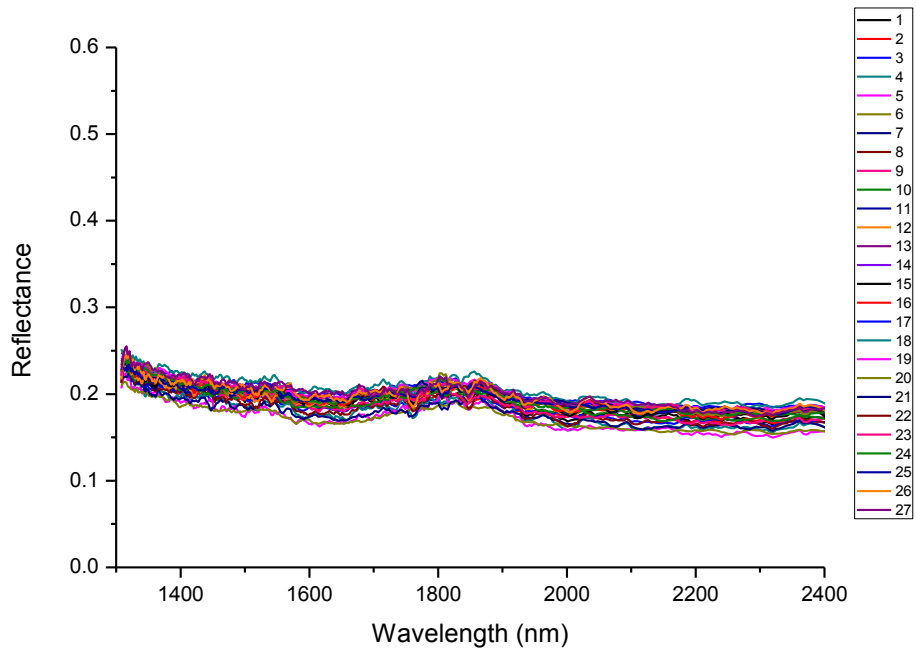
## Appendix 8.1c - NIR spectra of splits A1 samples



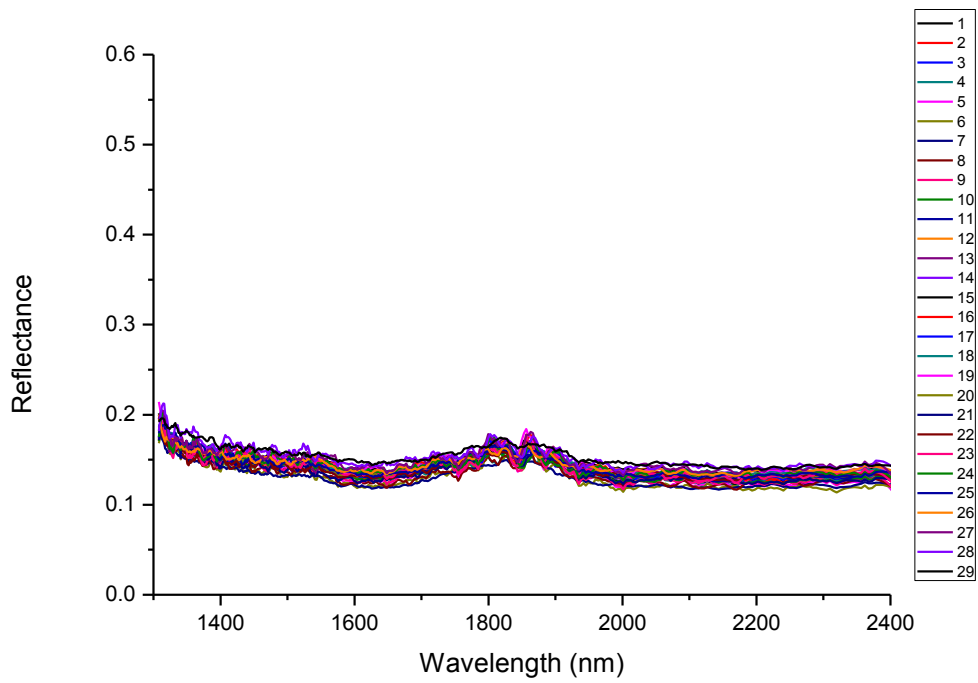
Sample 1



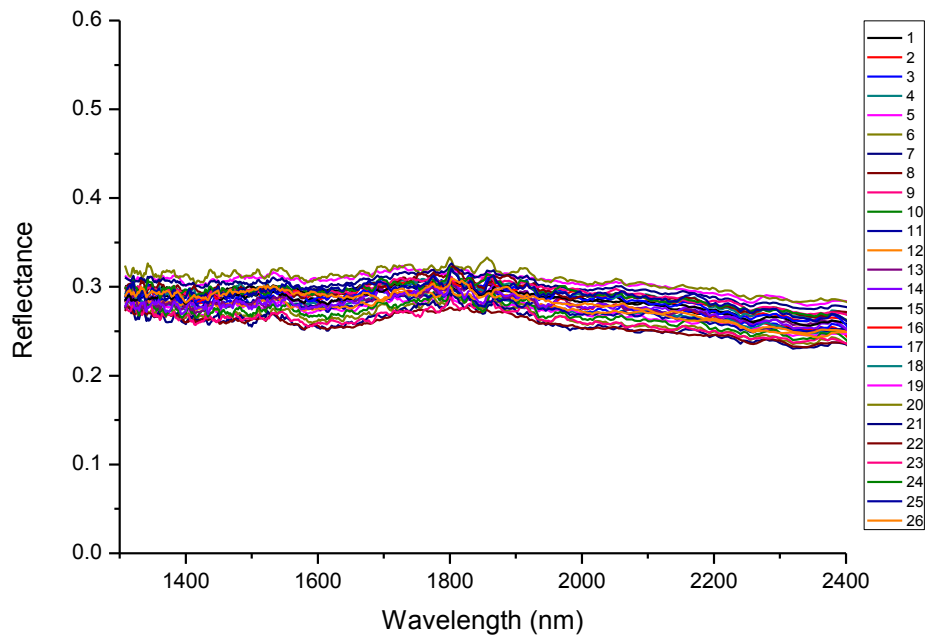
Sample 2



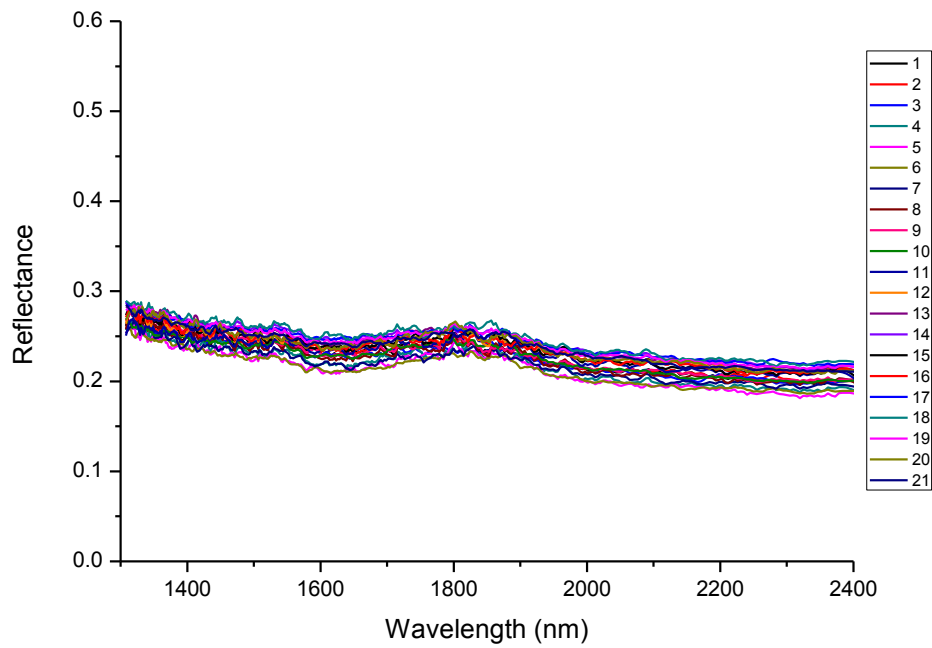
Sample 3



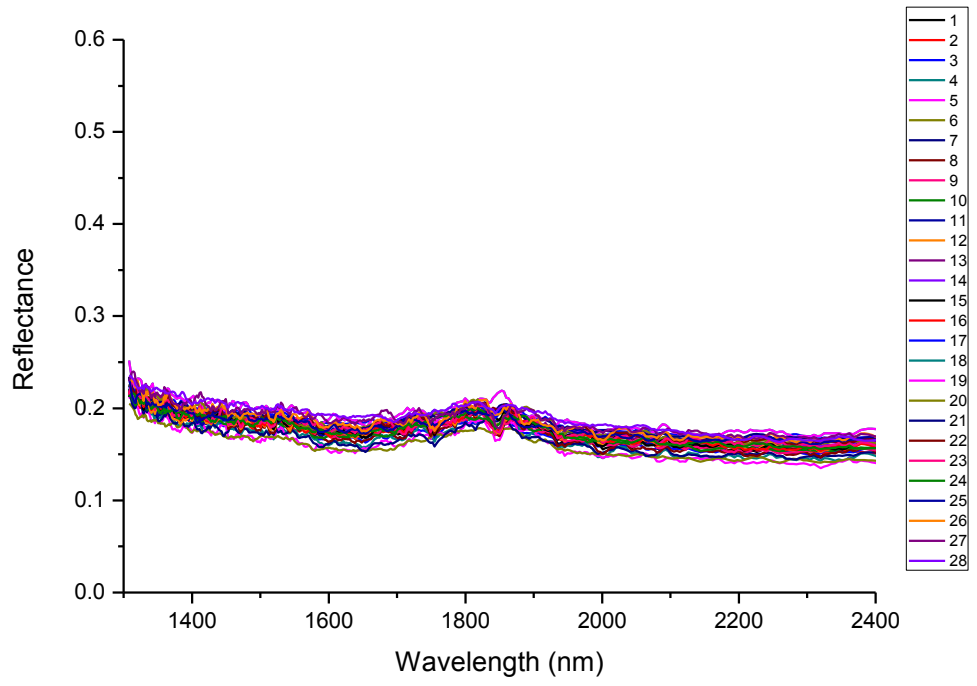
Sample 4



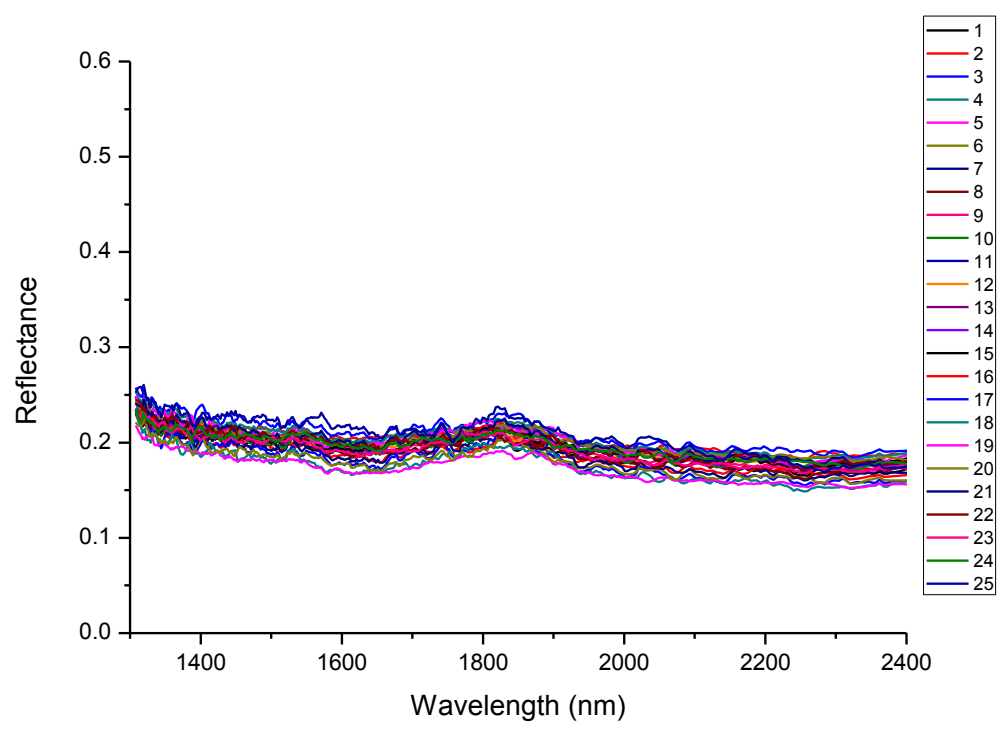
Sample 5



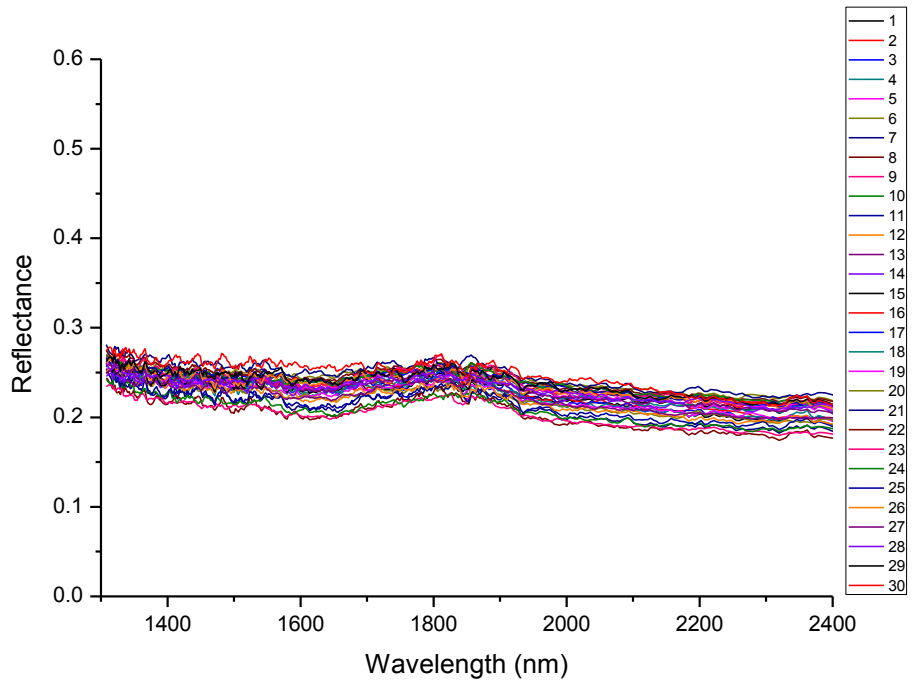
Sample 6



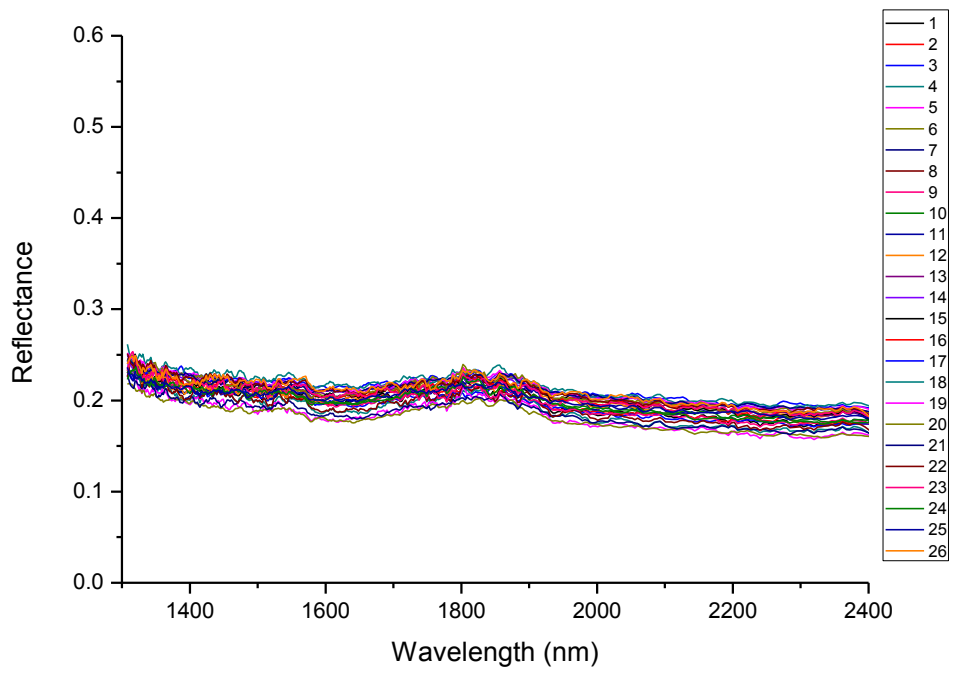
Sample 7



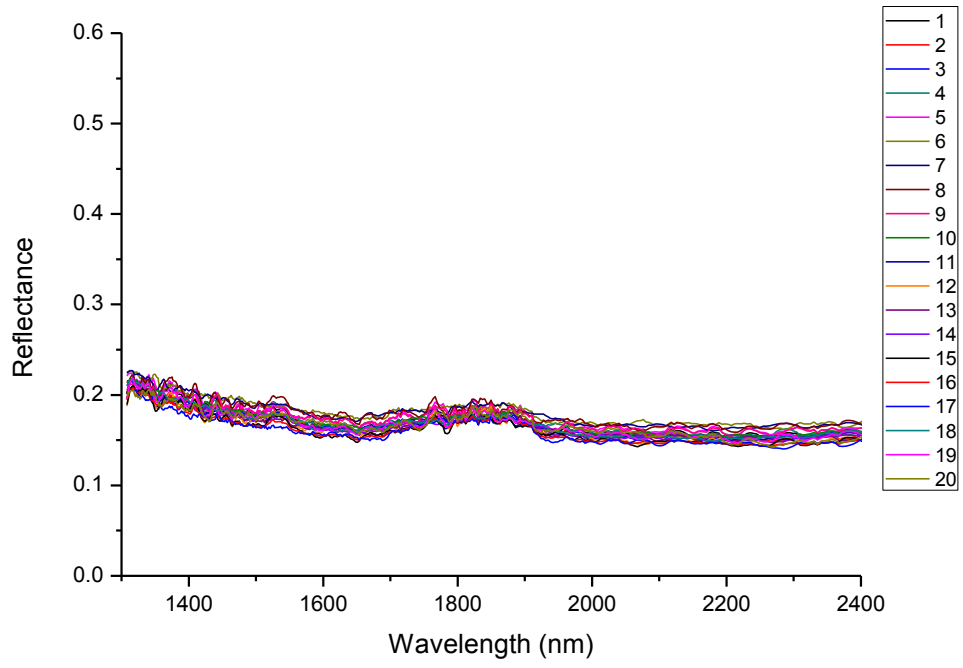
Sample 8



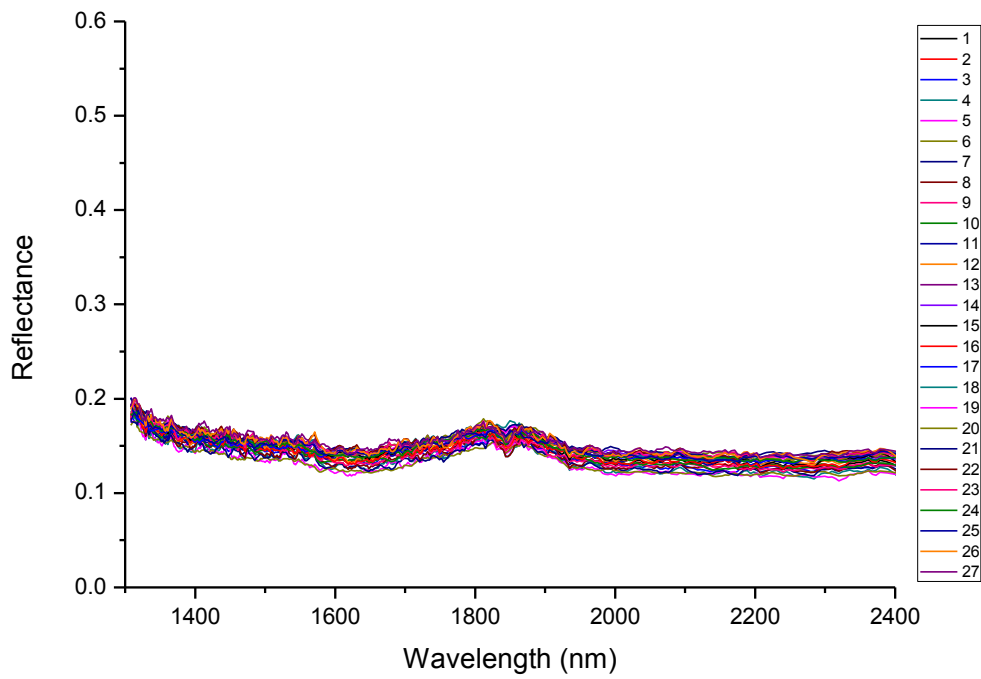
Sample 9



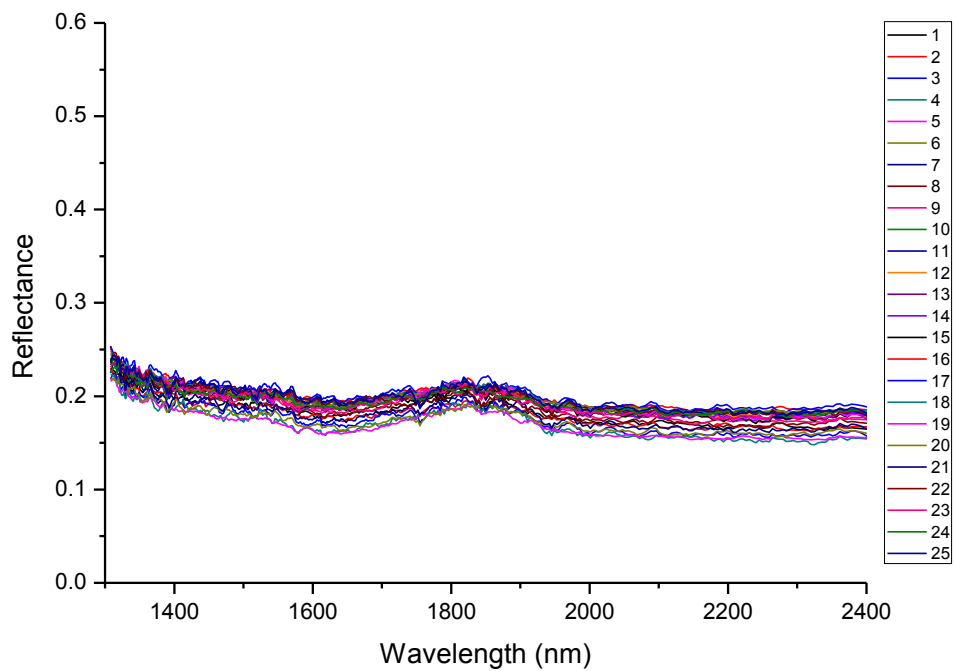
Sample 10



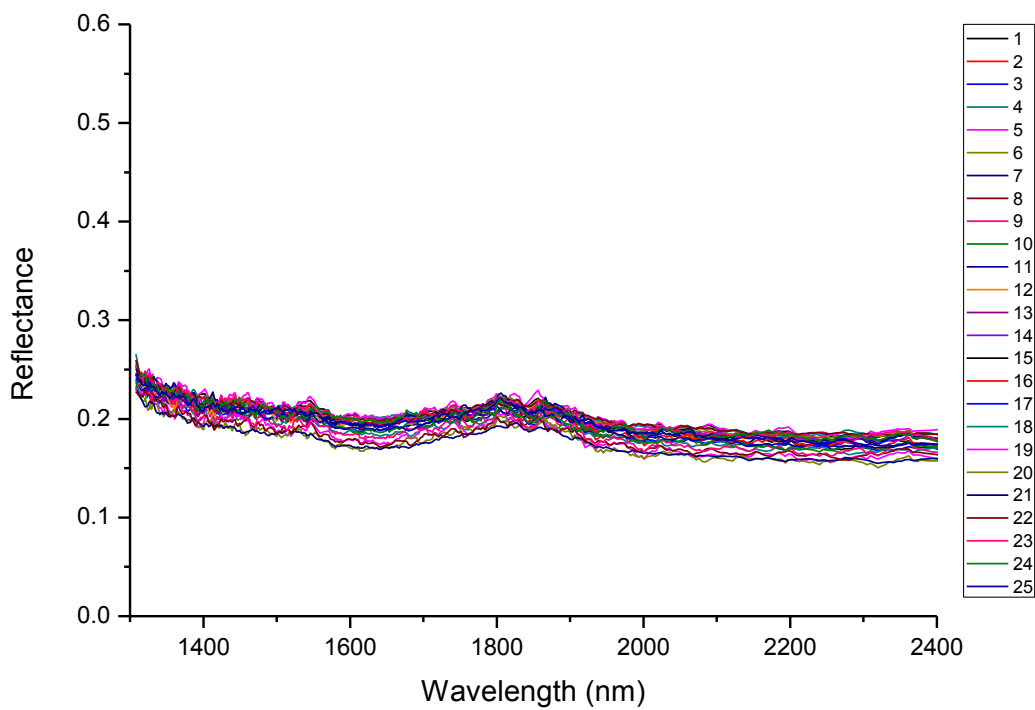
Sample 11



Sample 12

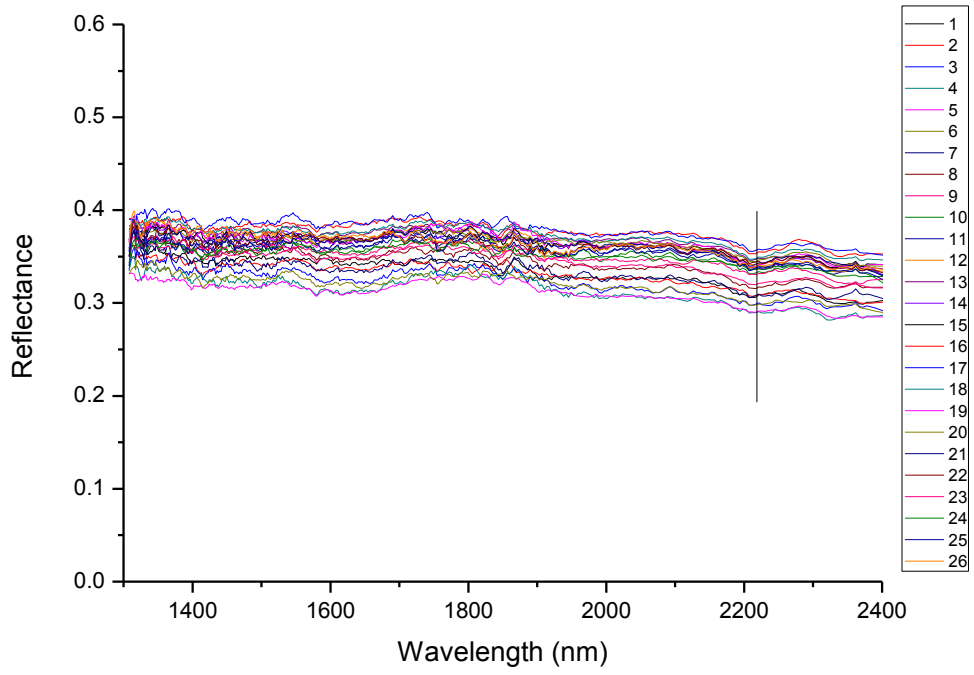


Sample 13

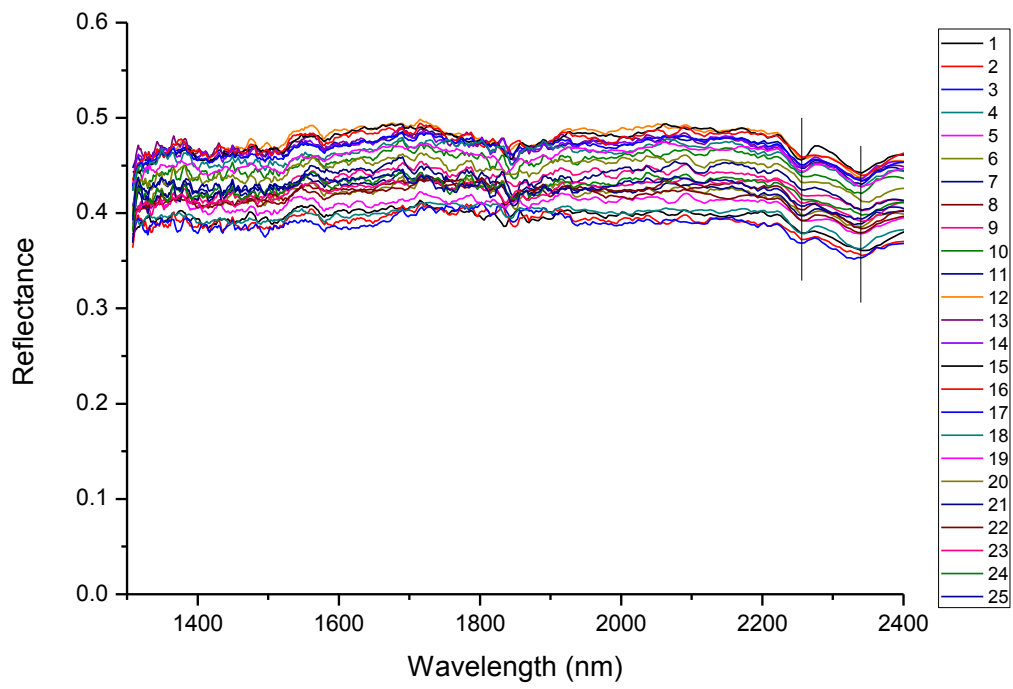


Sample 14

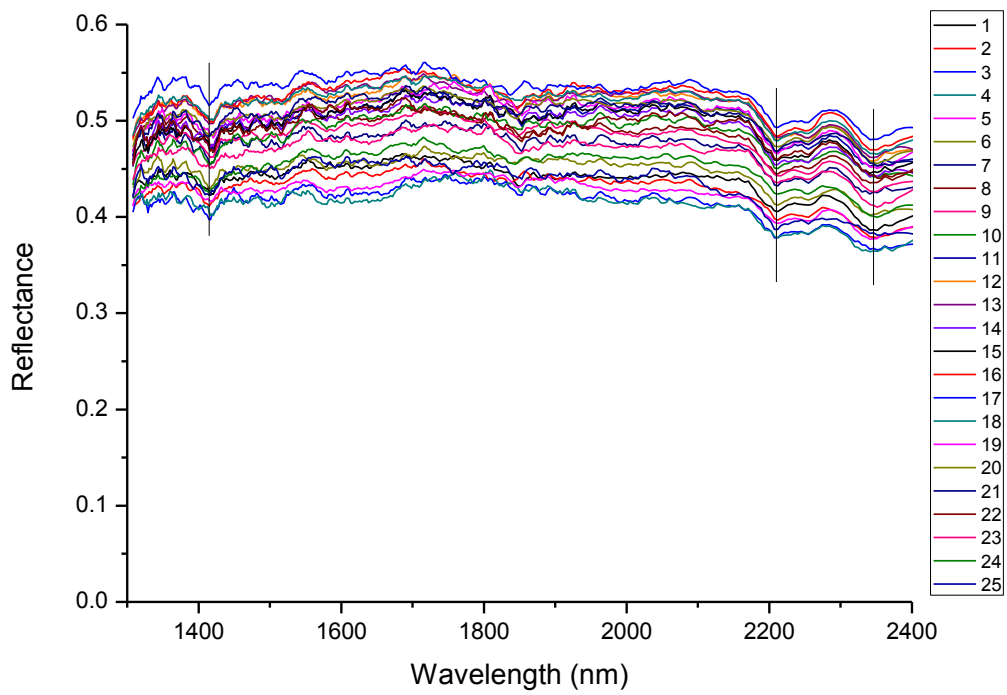
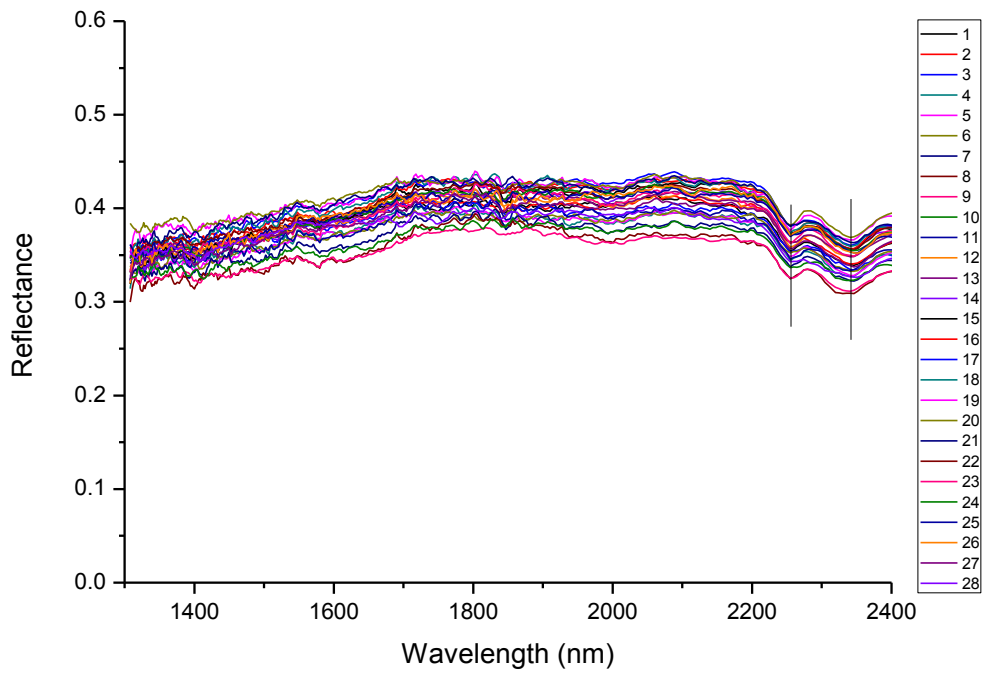


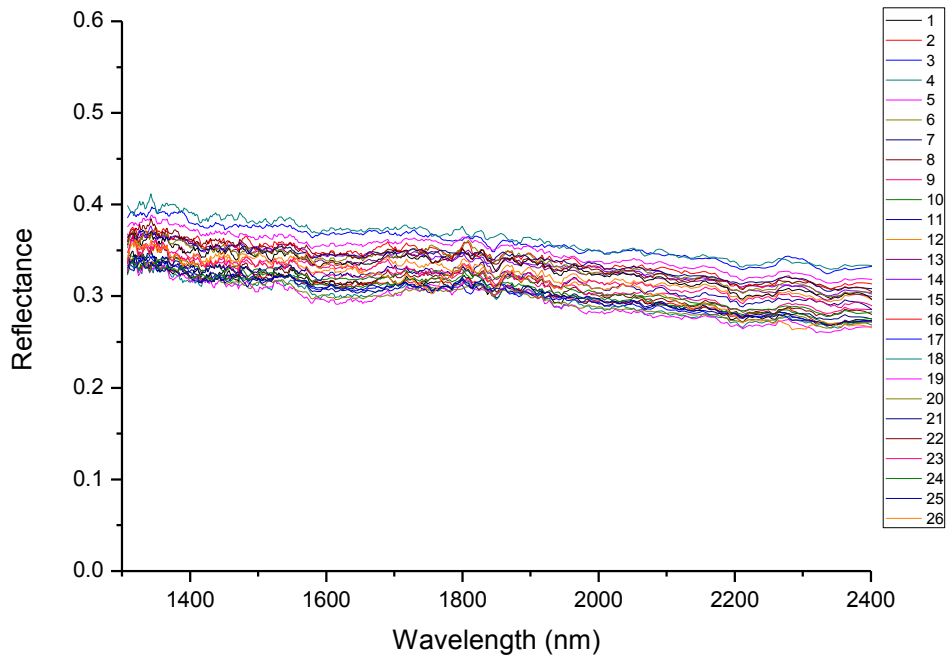


Sample 15

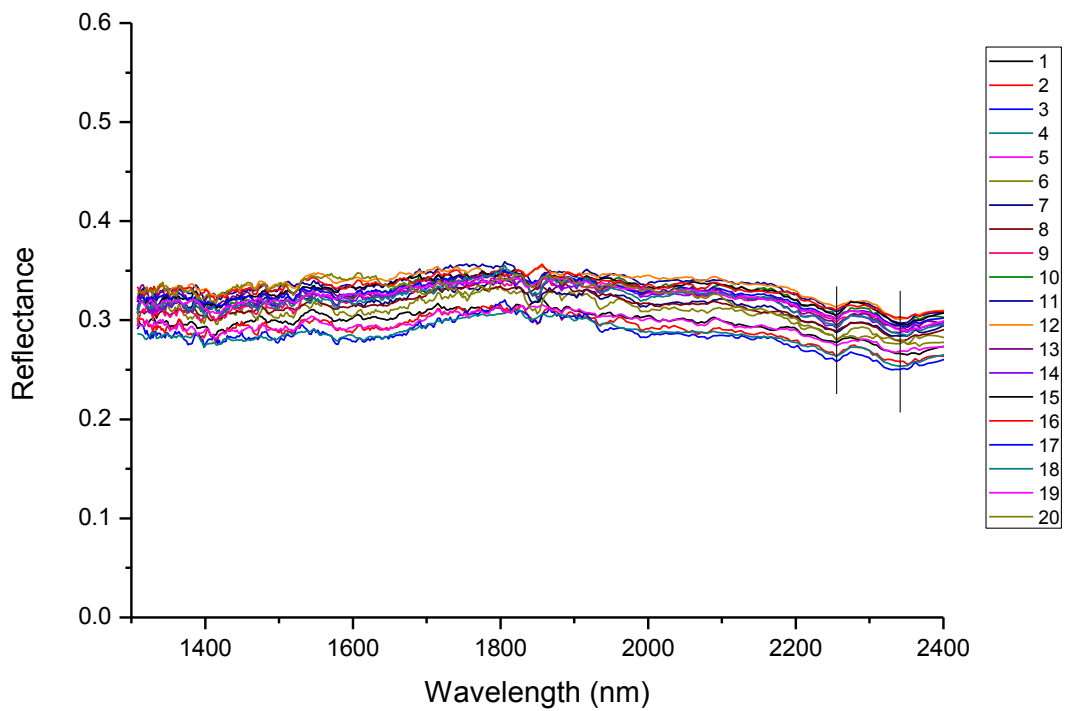


Sample 16

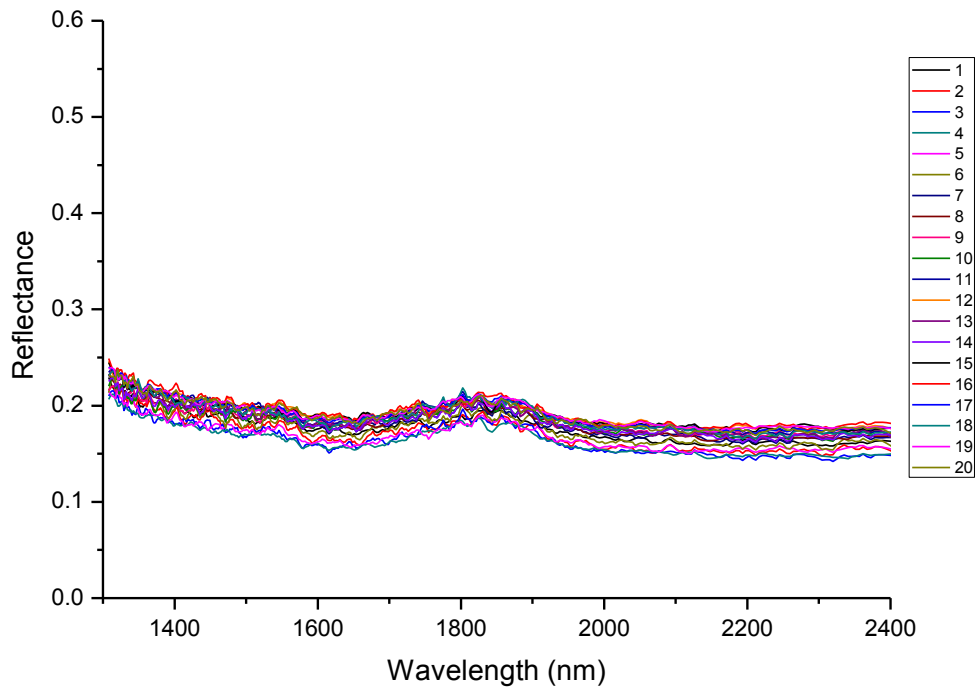




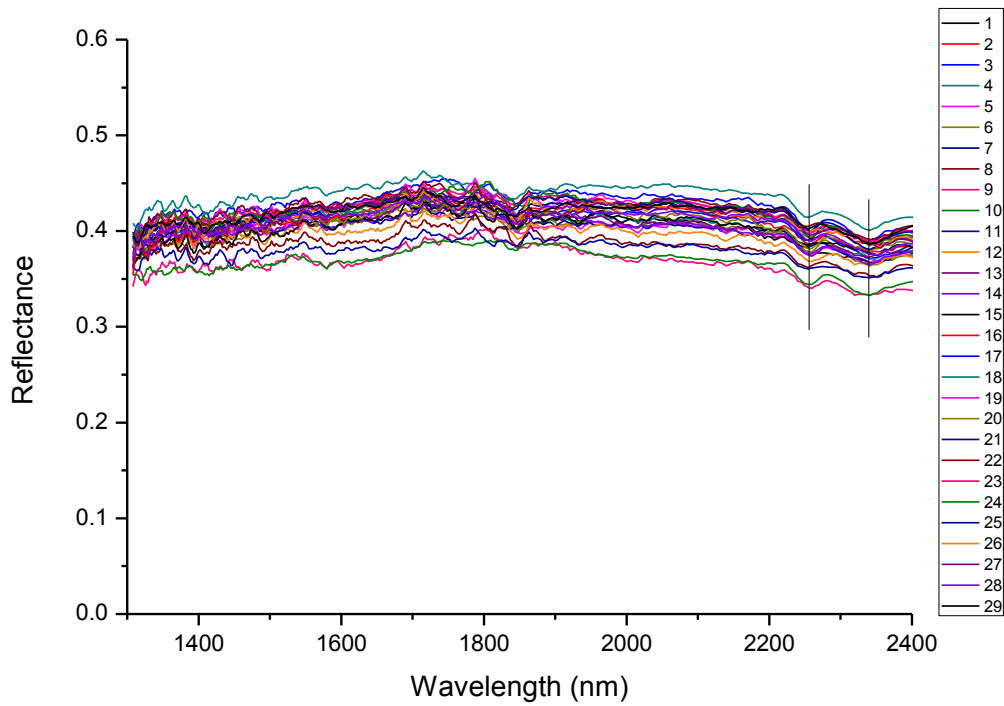
Sample 19



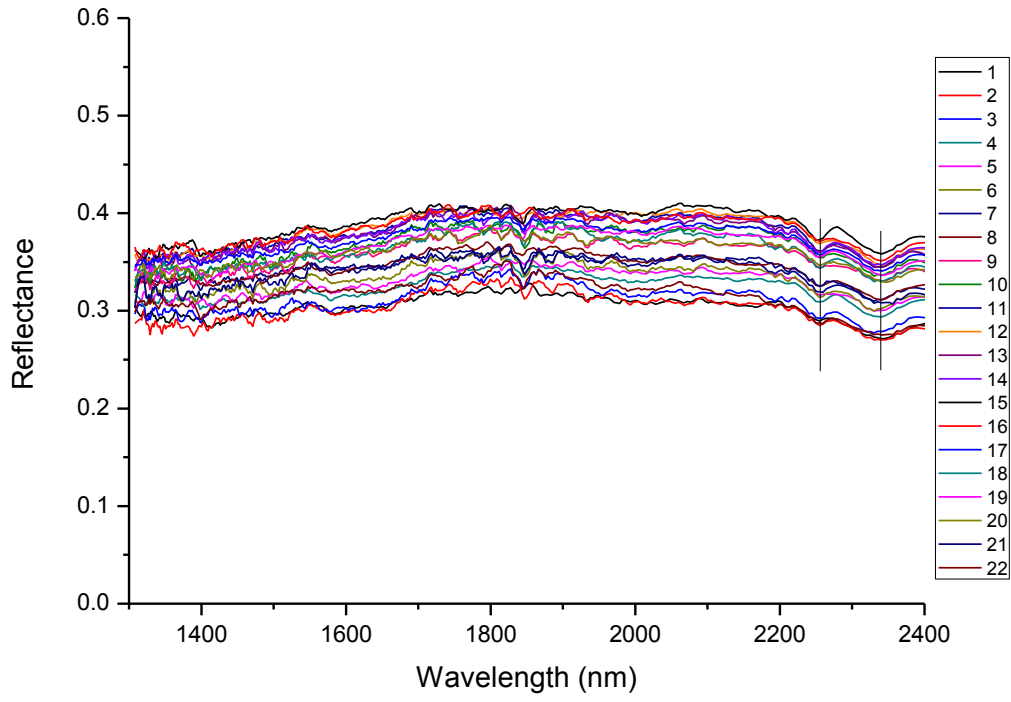
Sample 20



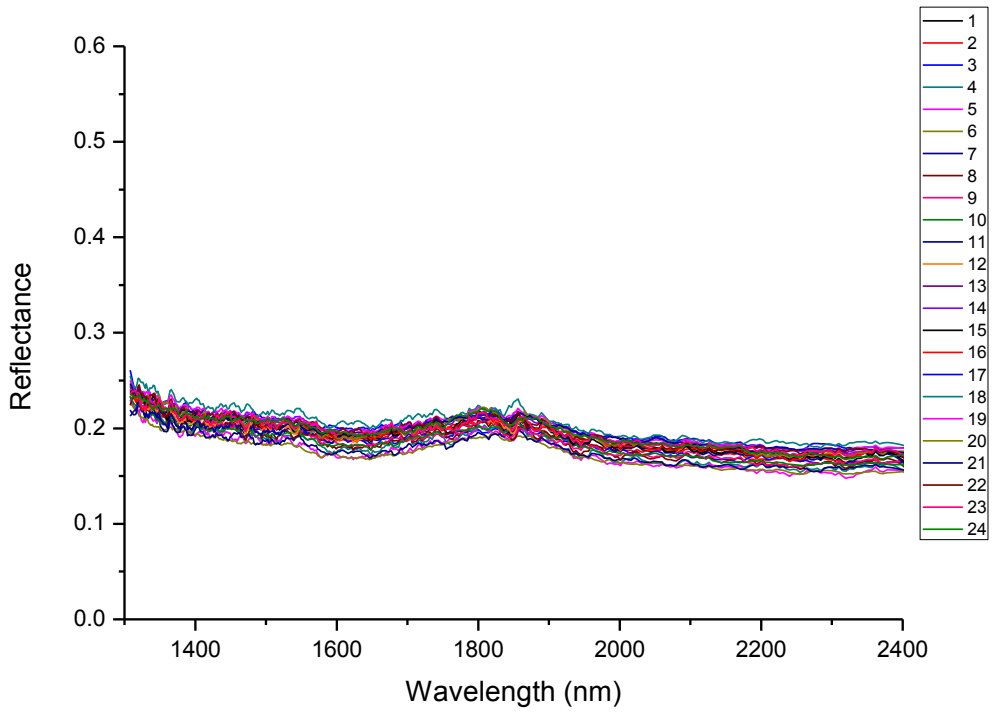
Sample 21



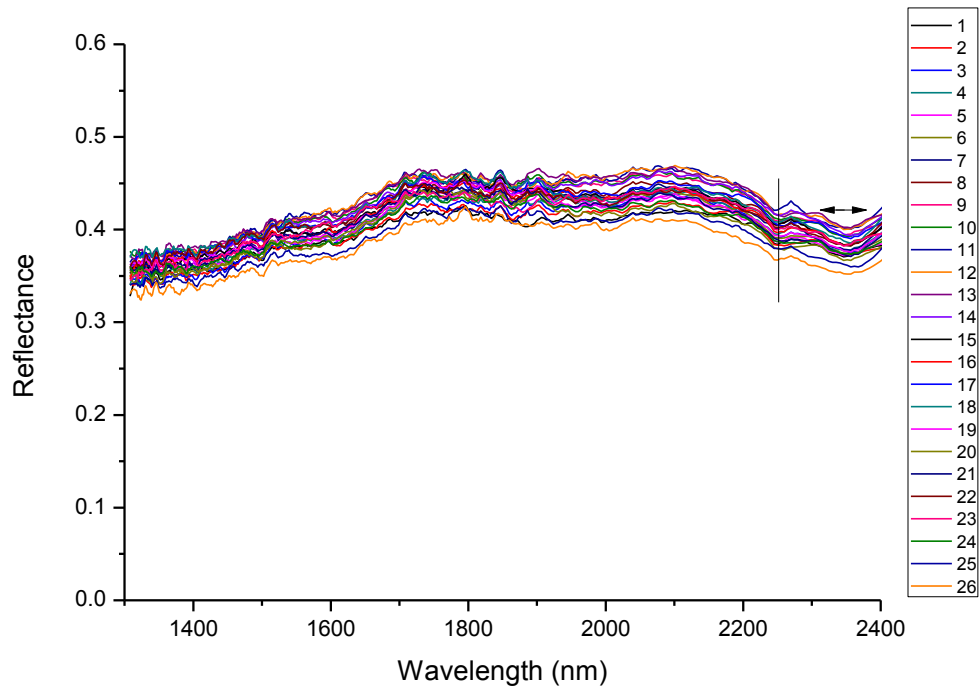
Sample 22



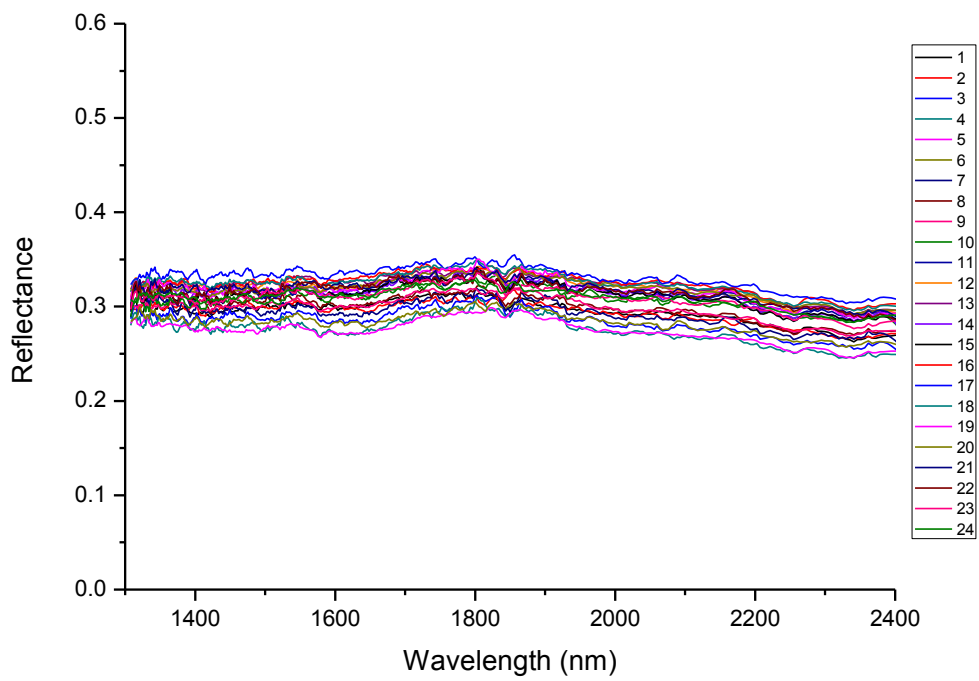
Sample 23



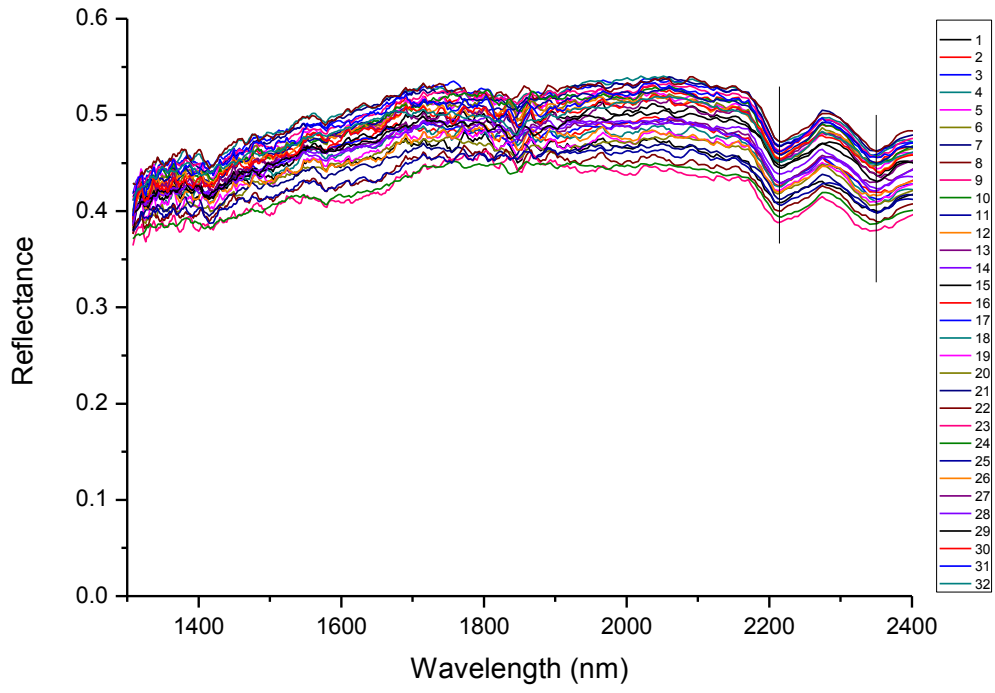
Sample 24



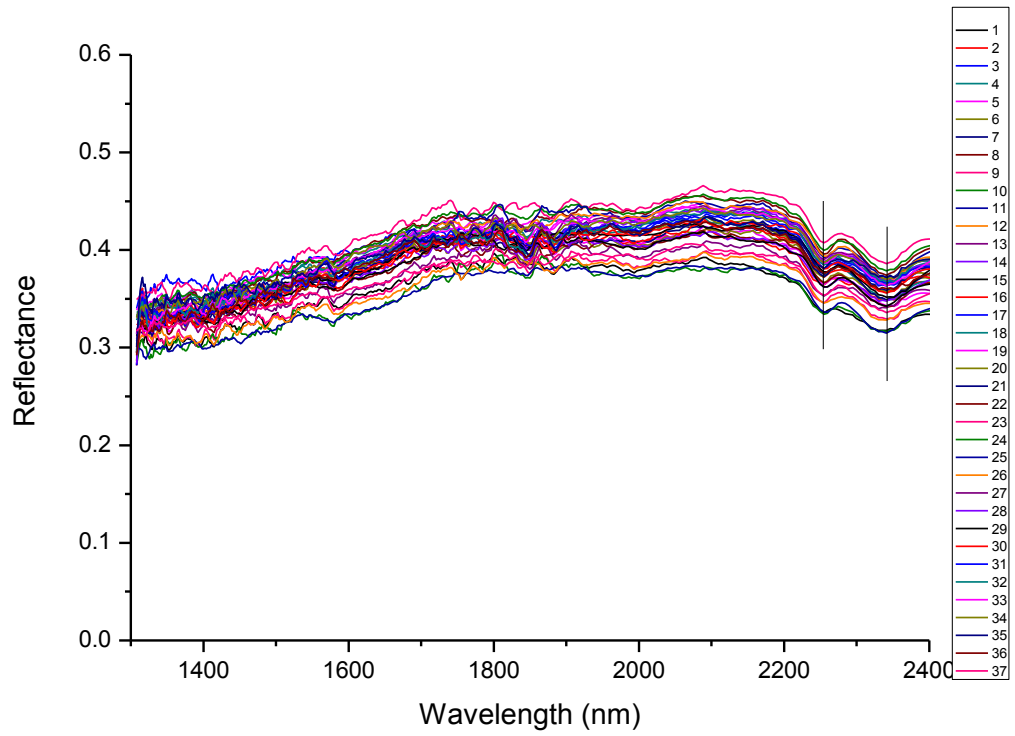
Sample 25



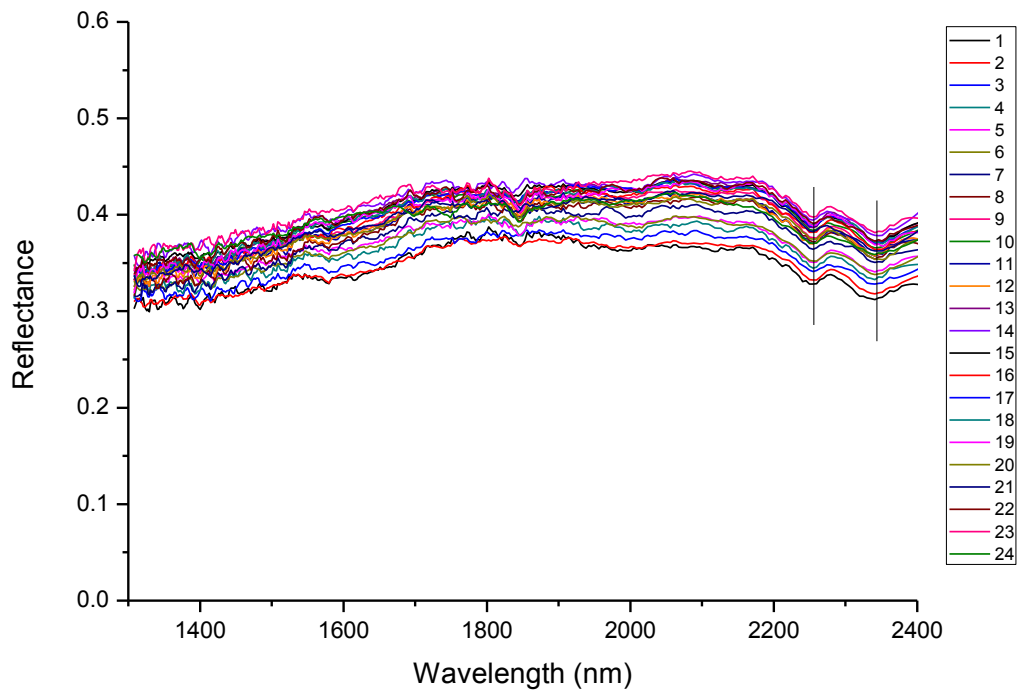
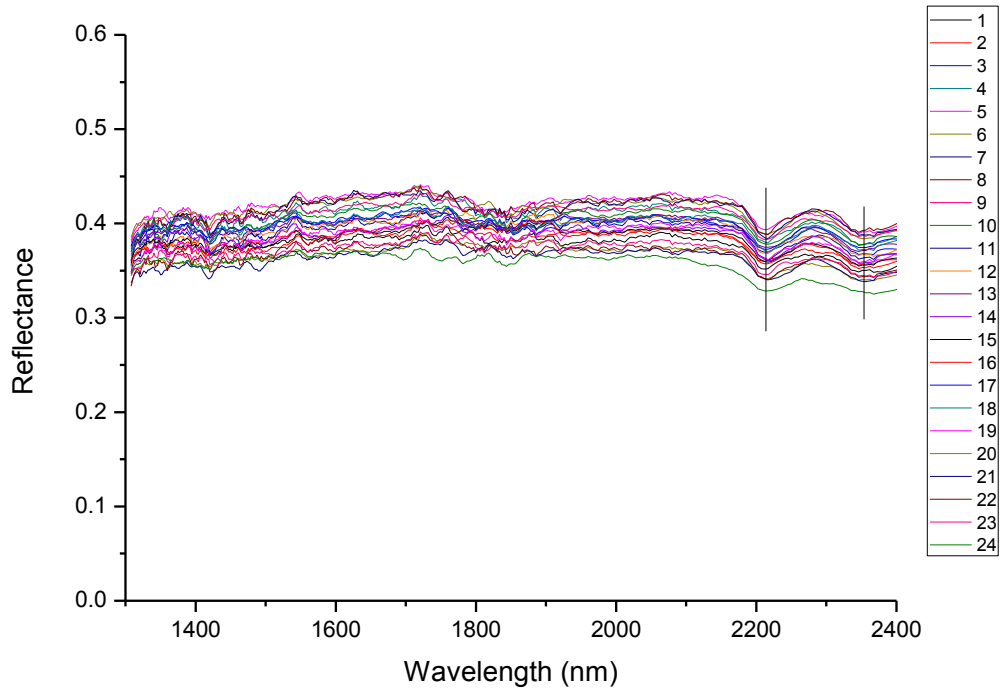
Sample 26



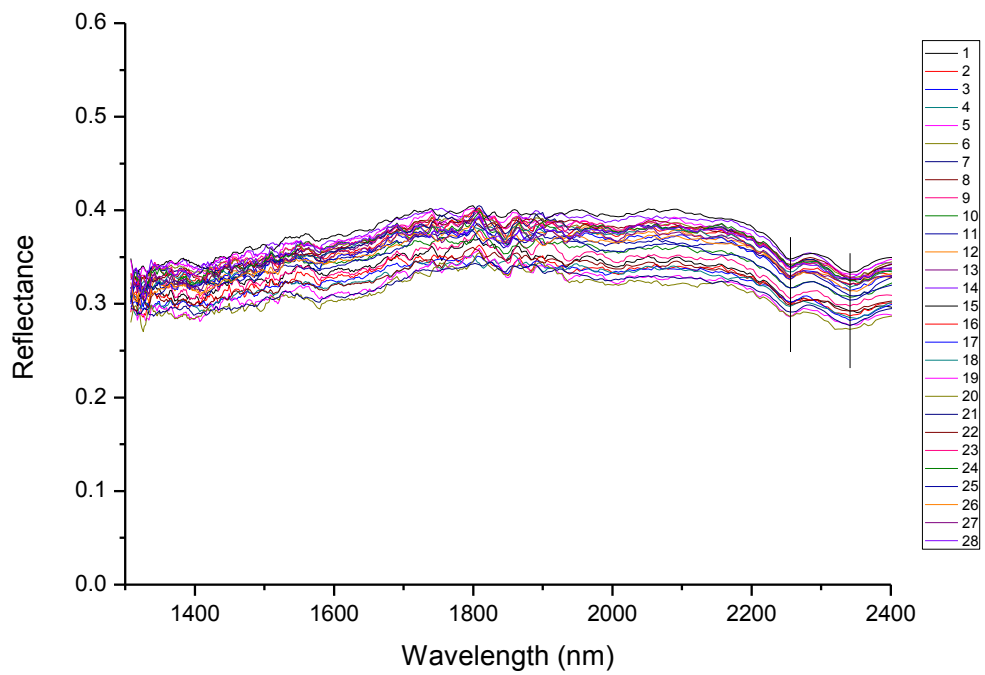
Sample 27



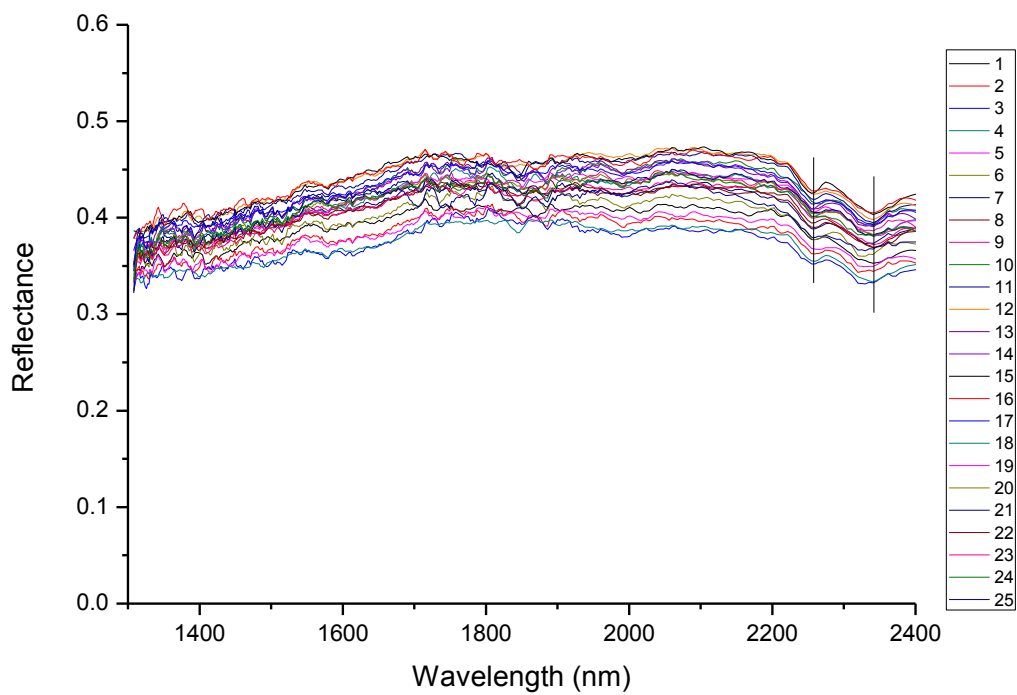
Sample 28



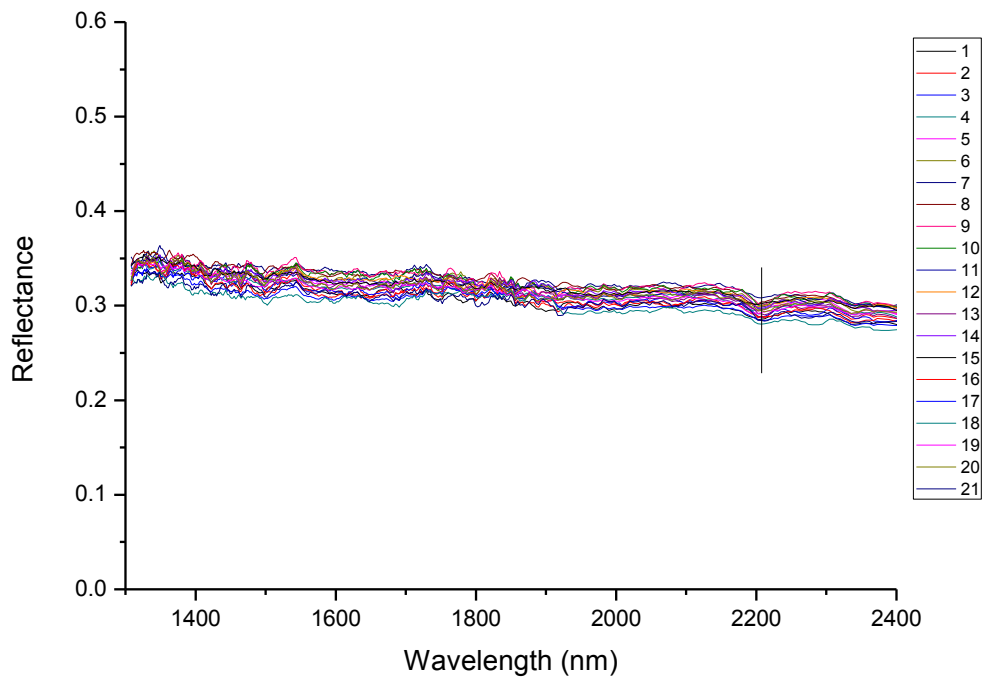




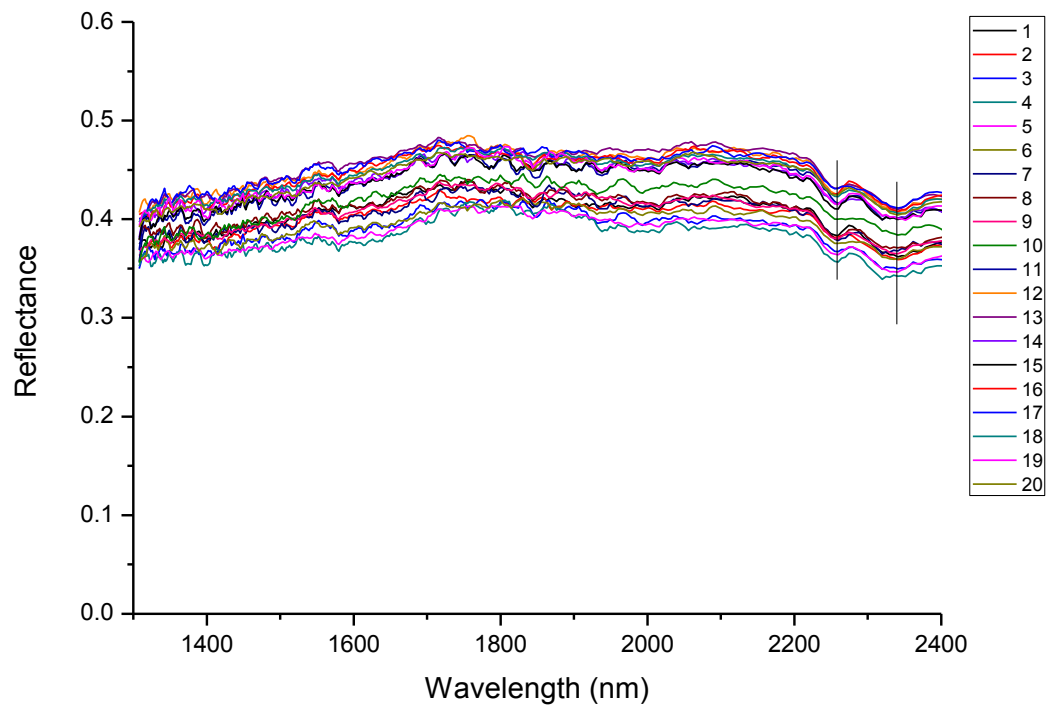
Sample 31



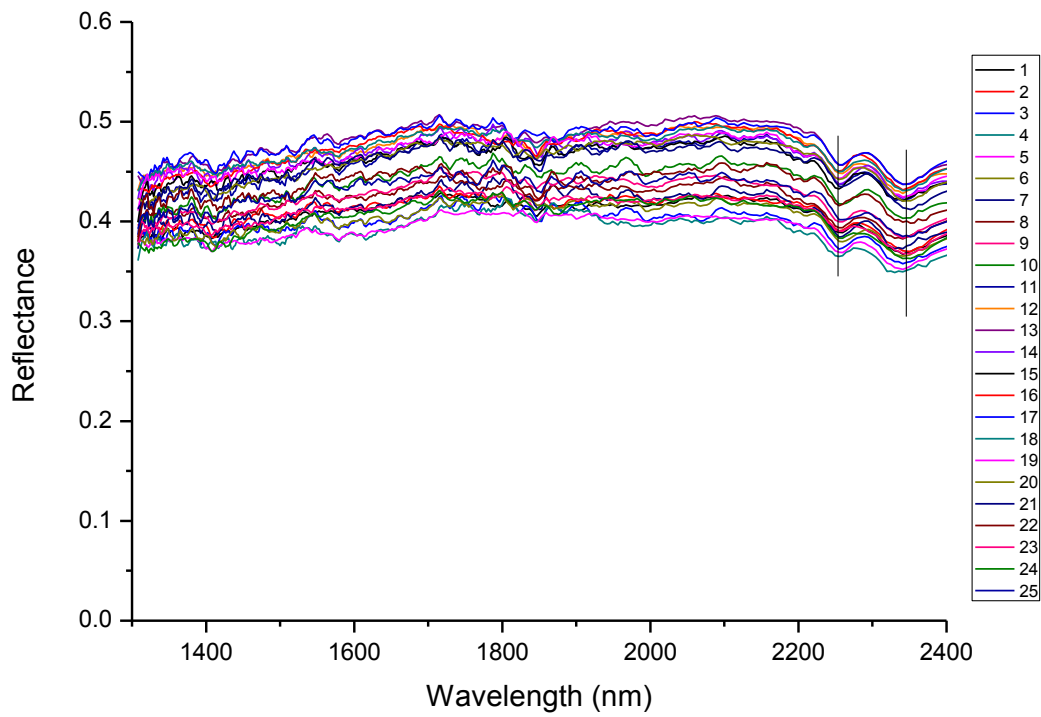
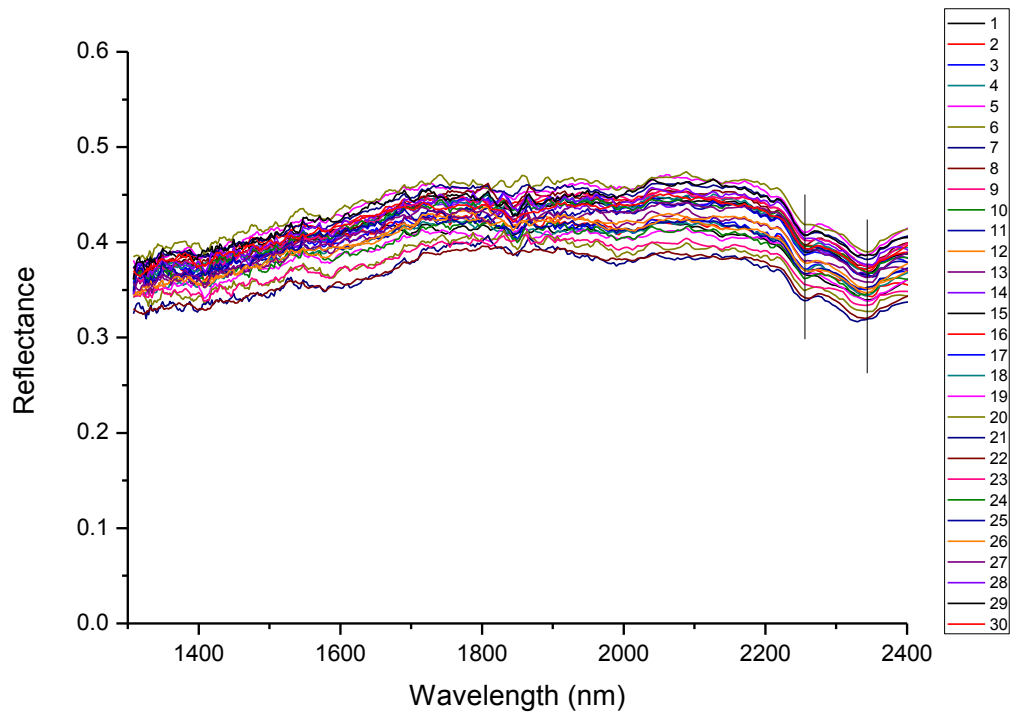
Sample 32

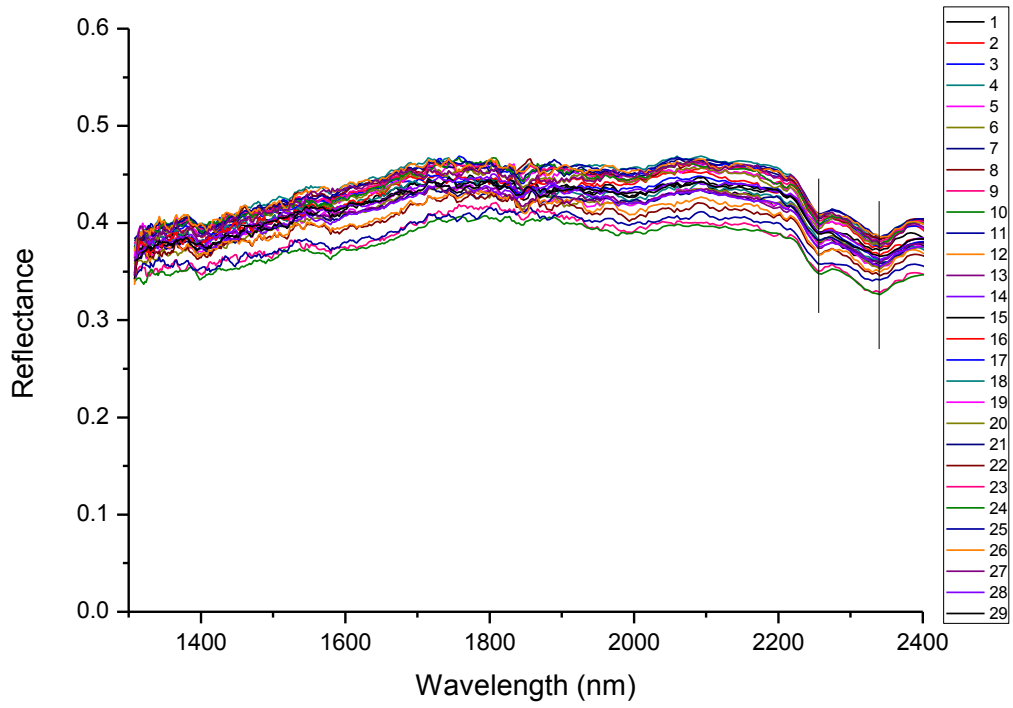


Sample 33

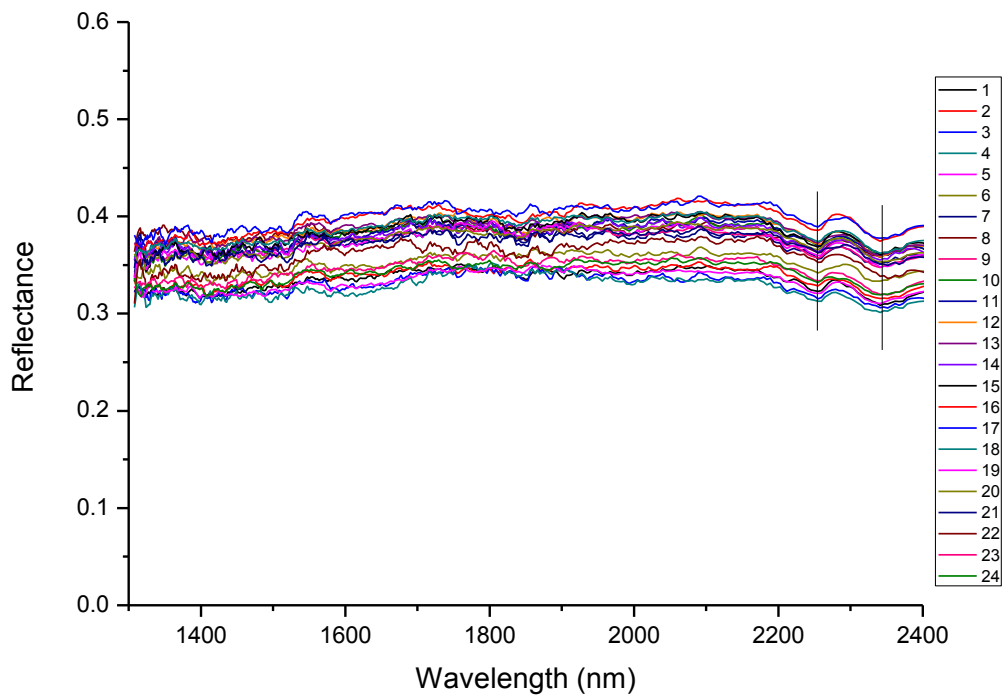


Sample 34

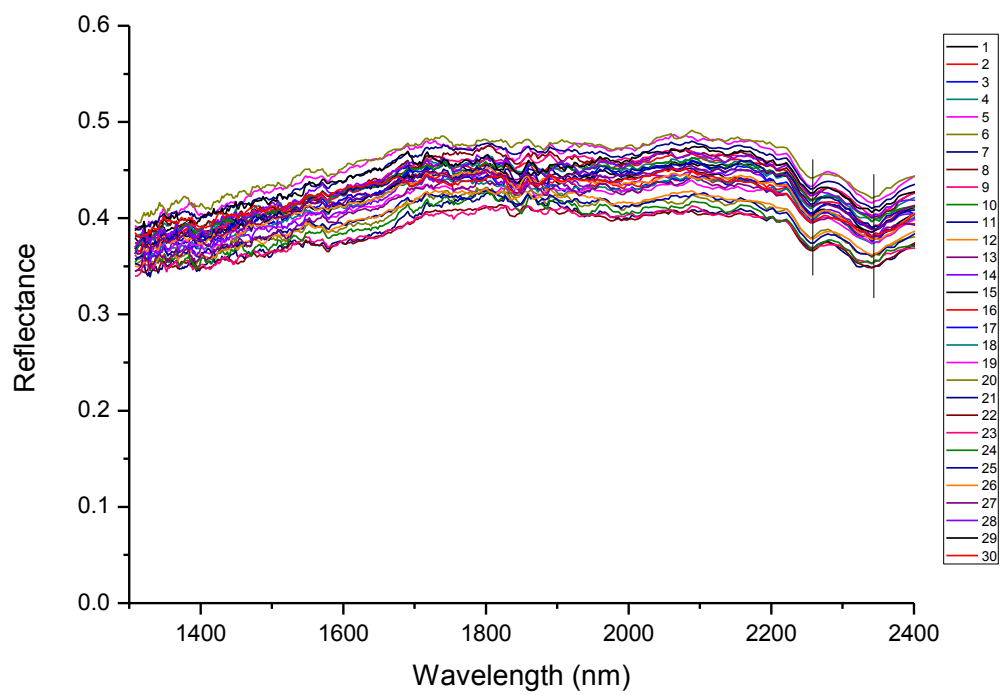
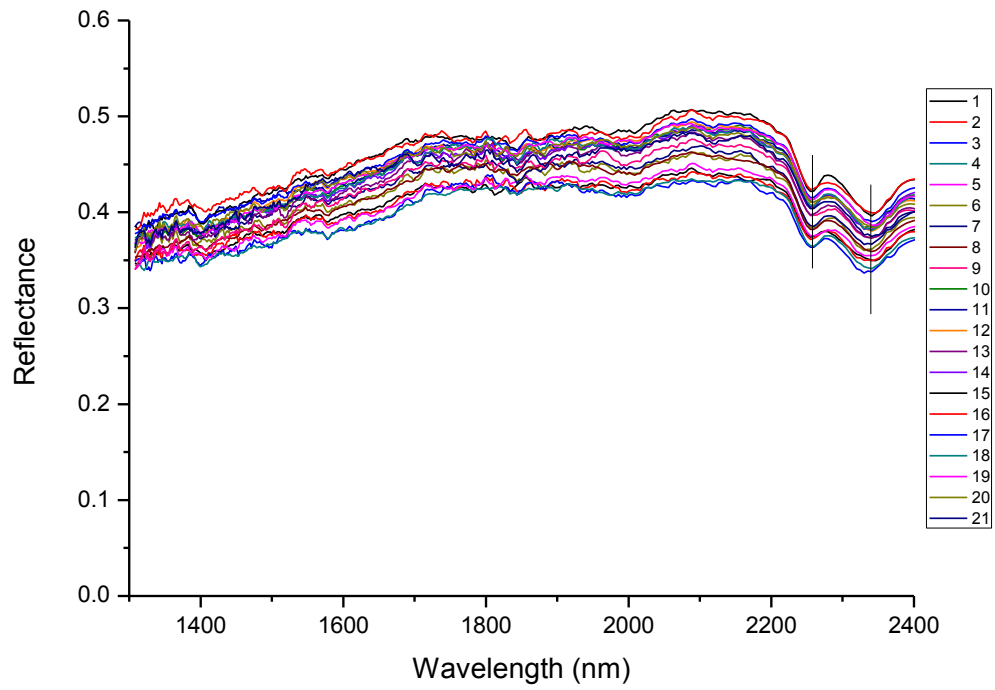


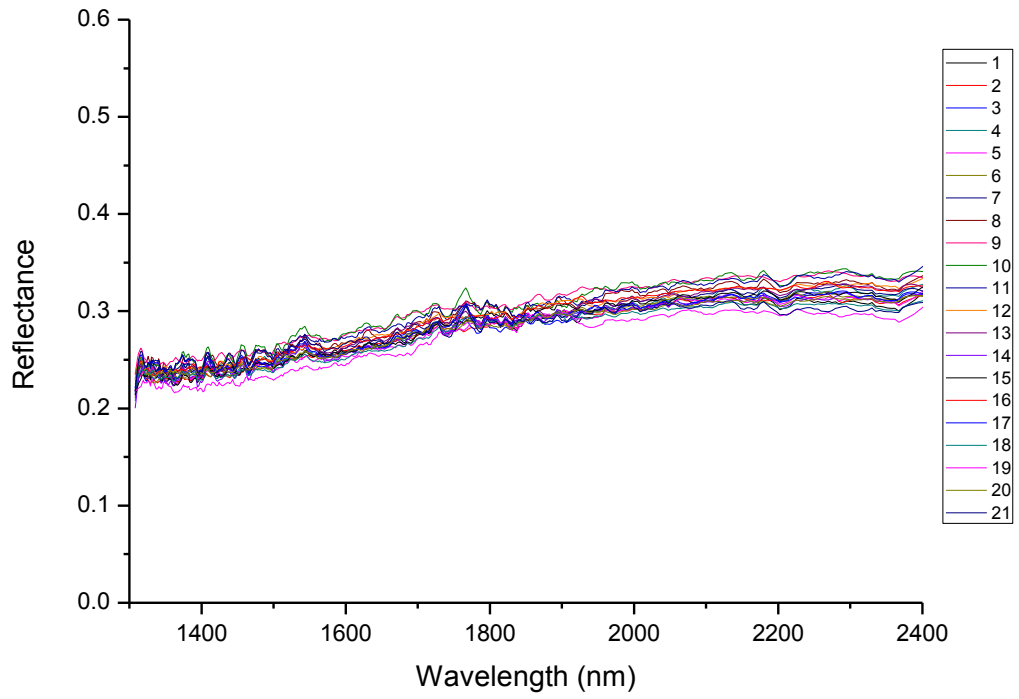


Sample 37

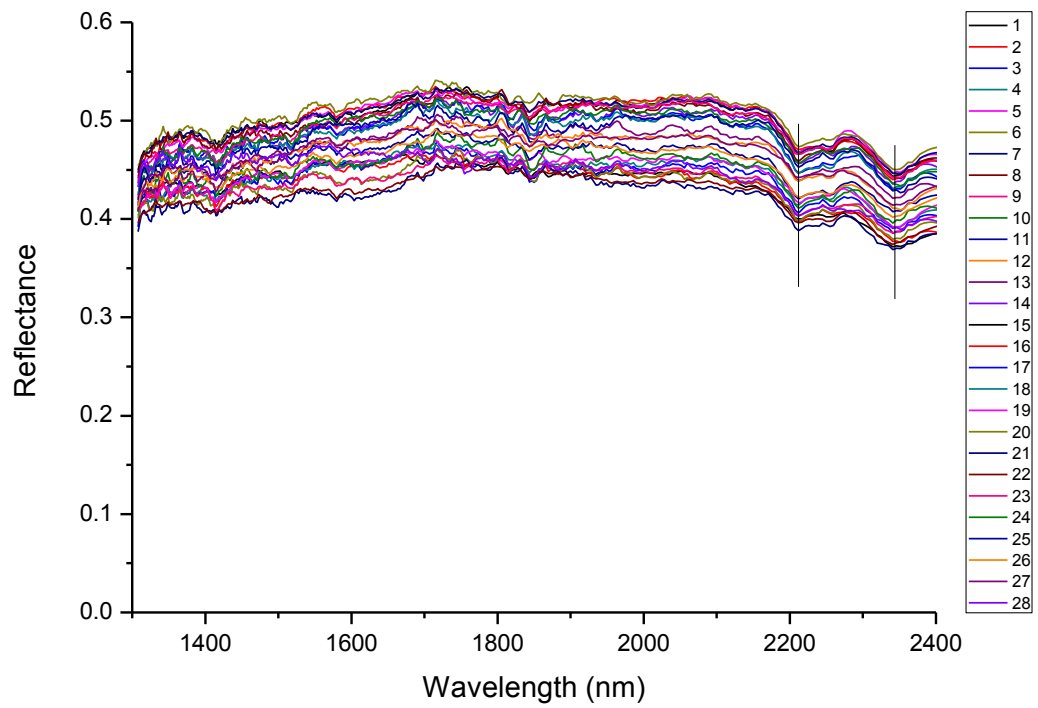


Sample 38

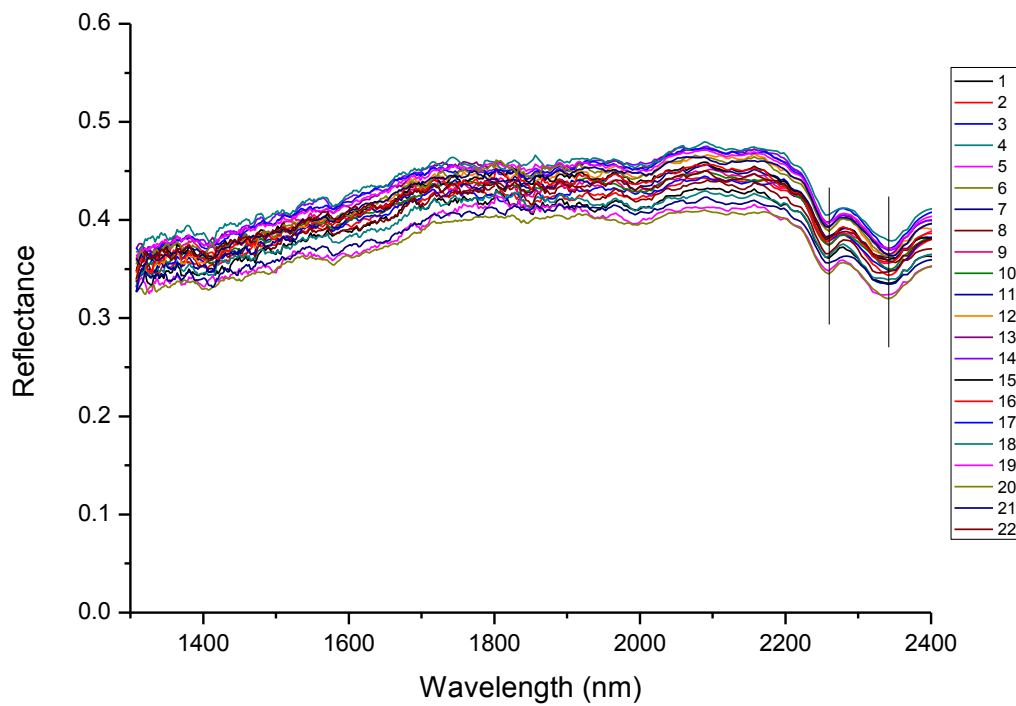
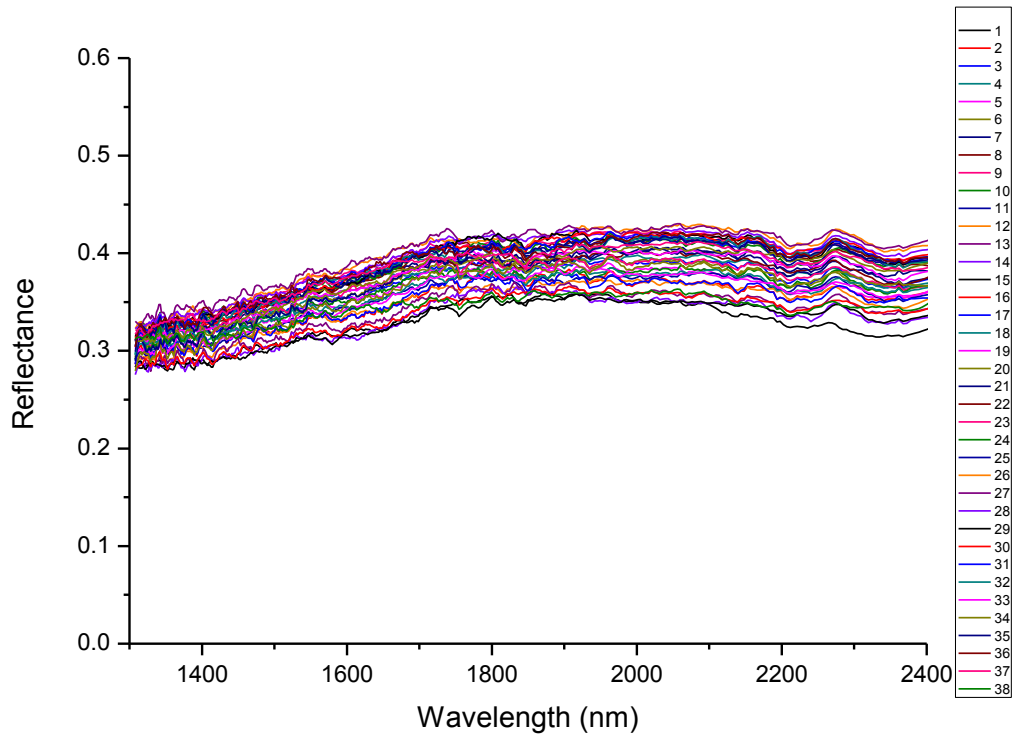


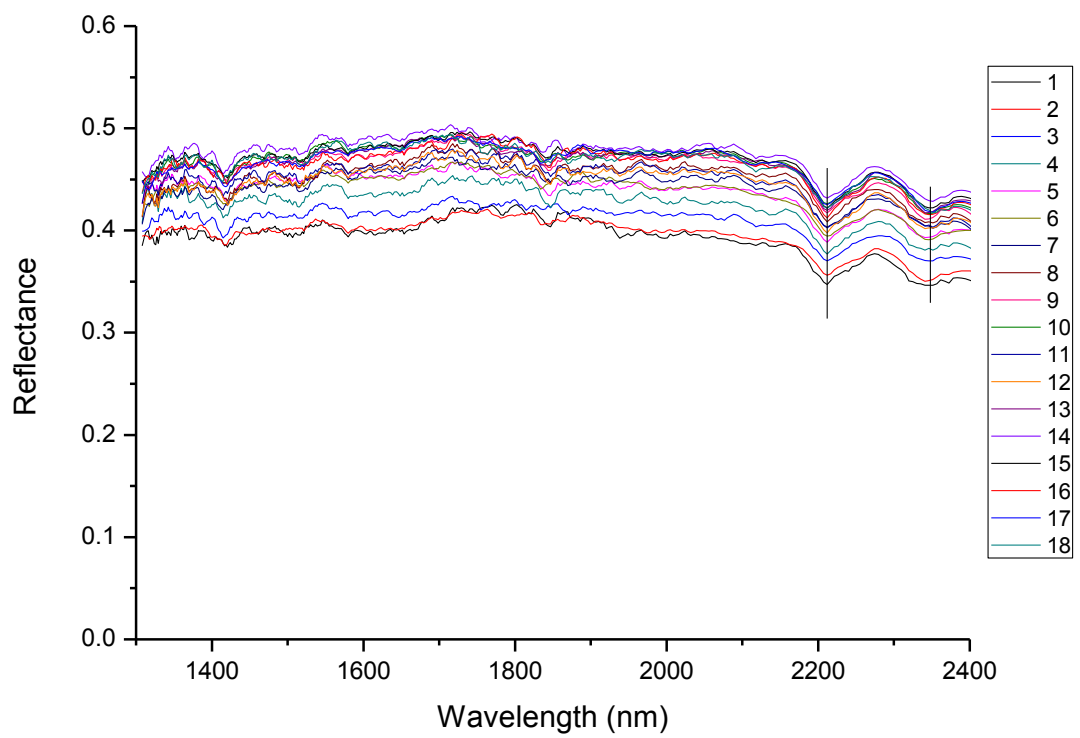
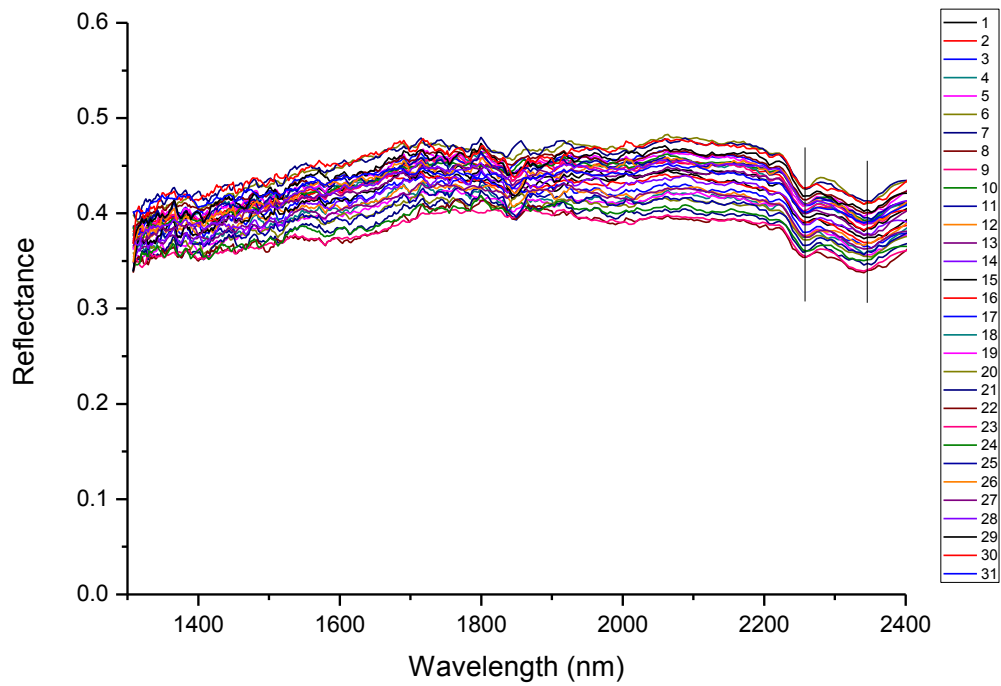


Sample 41

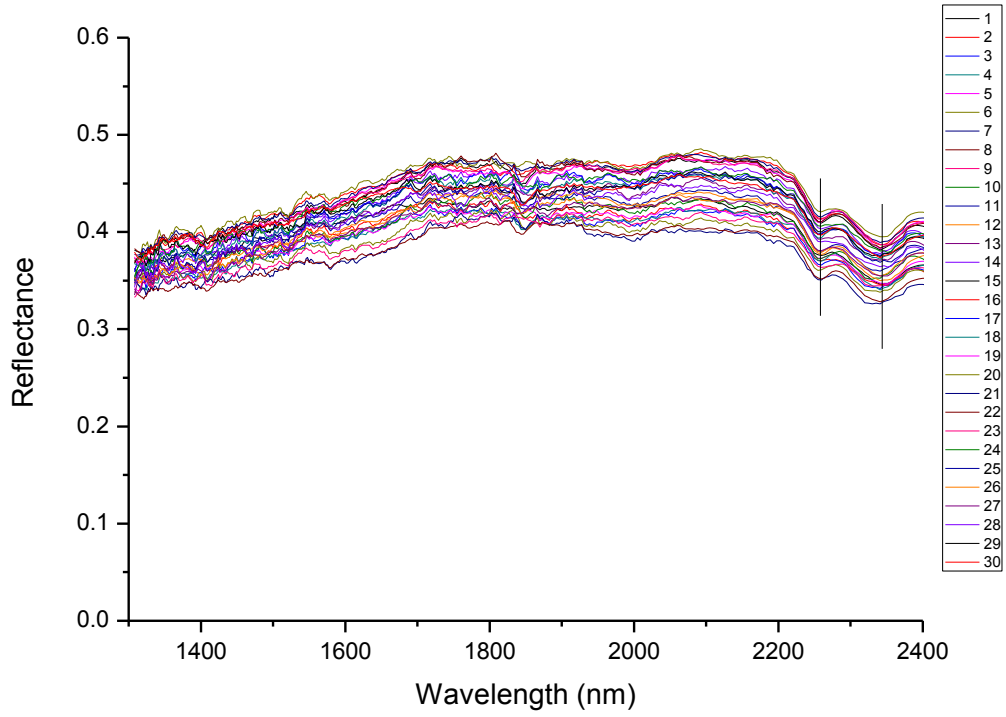


Sample 42

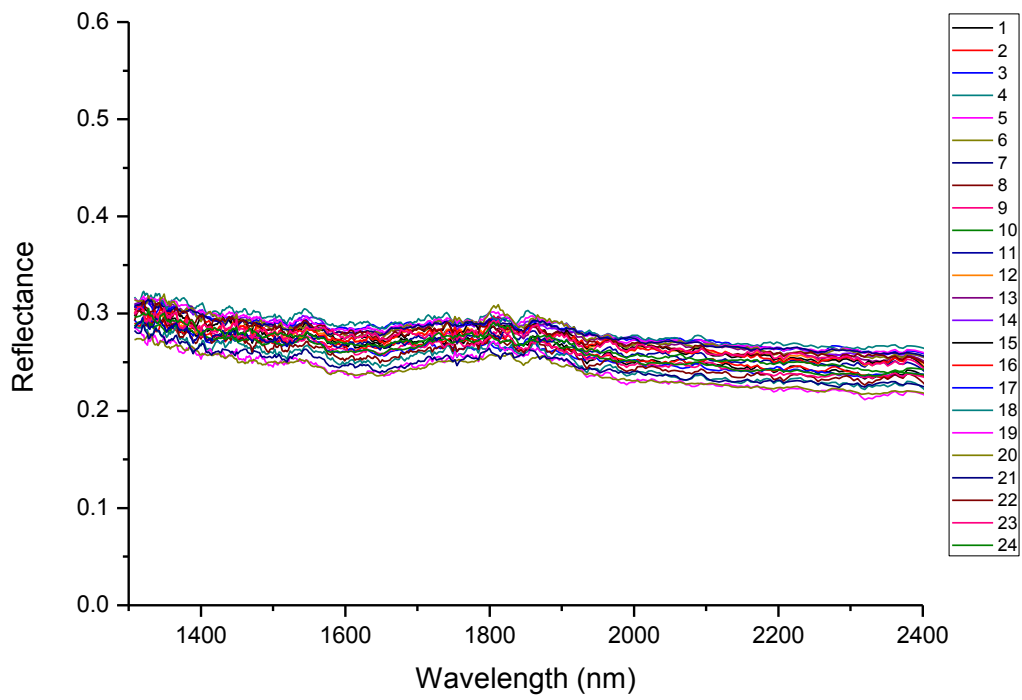




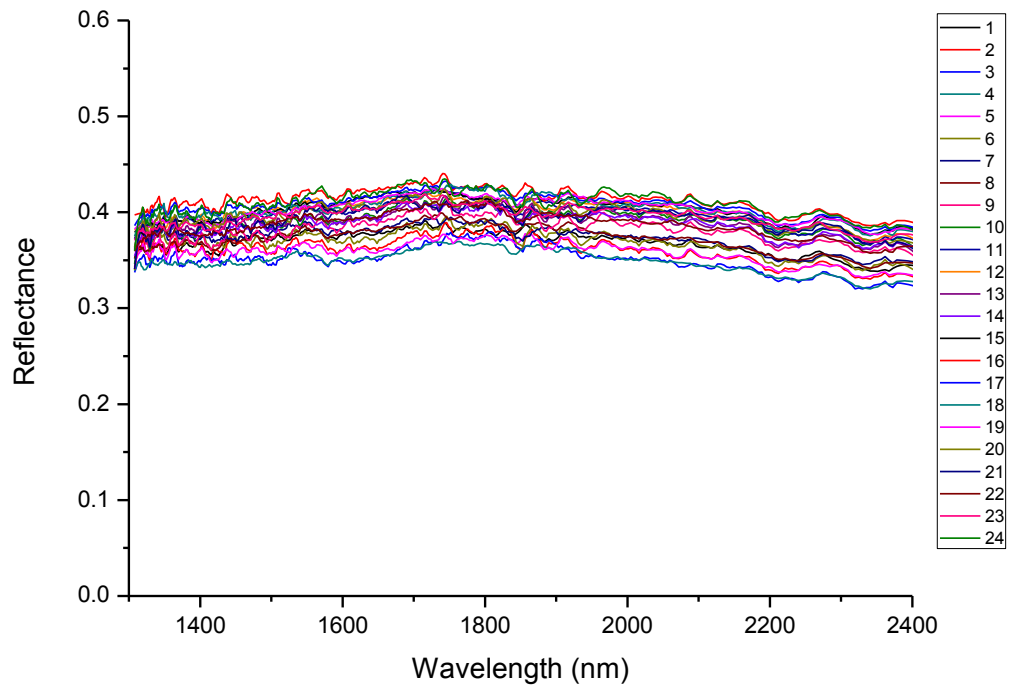




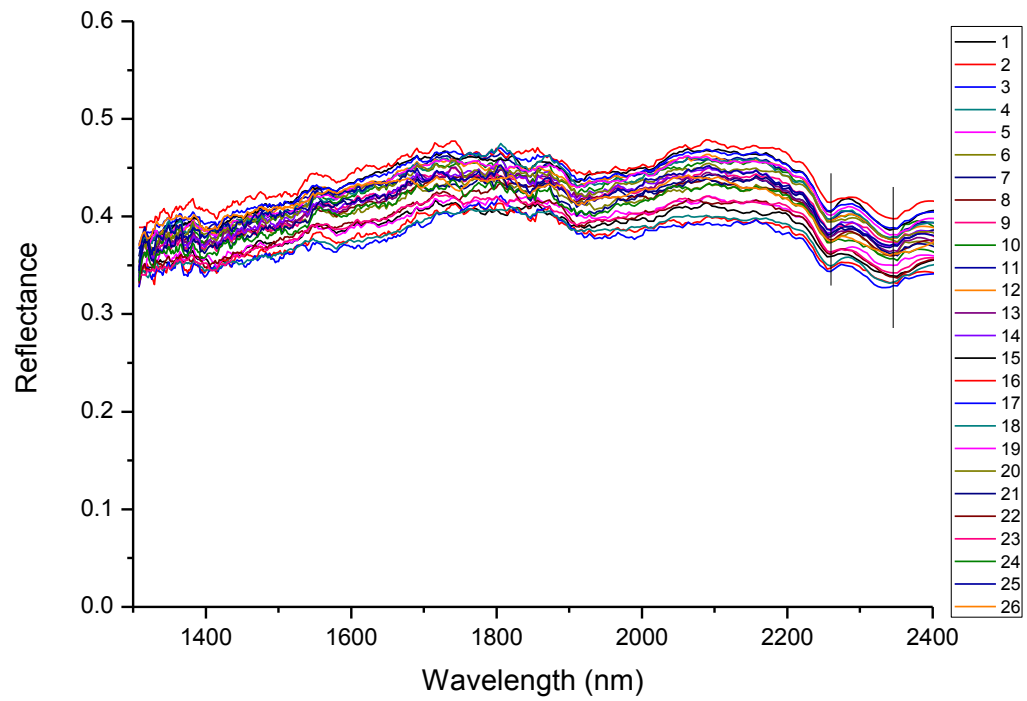
Sample 47



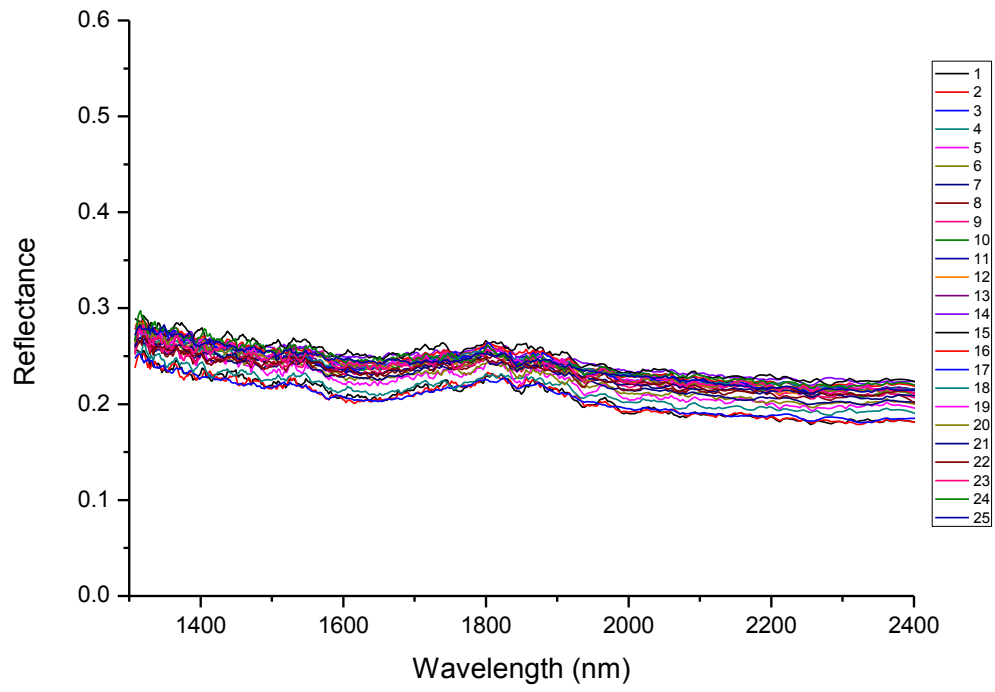
Sample 48



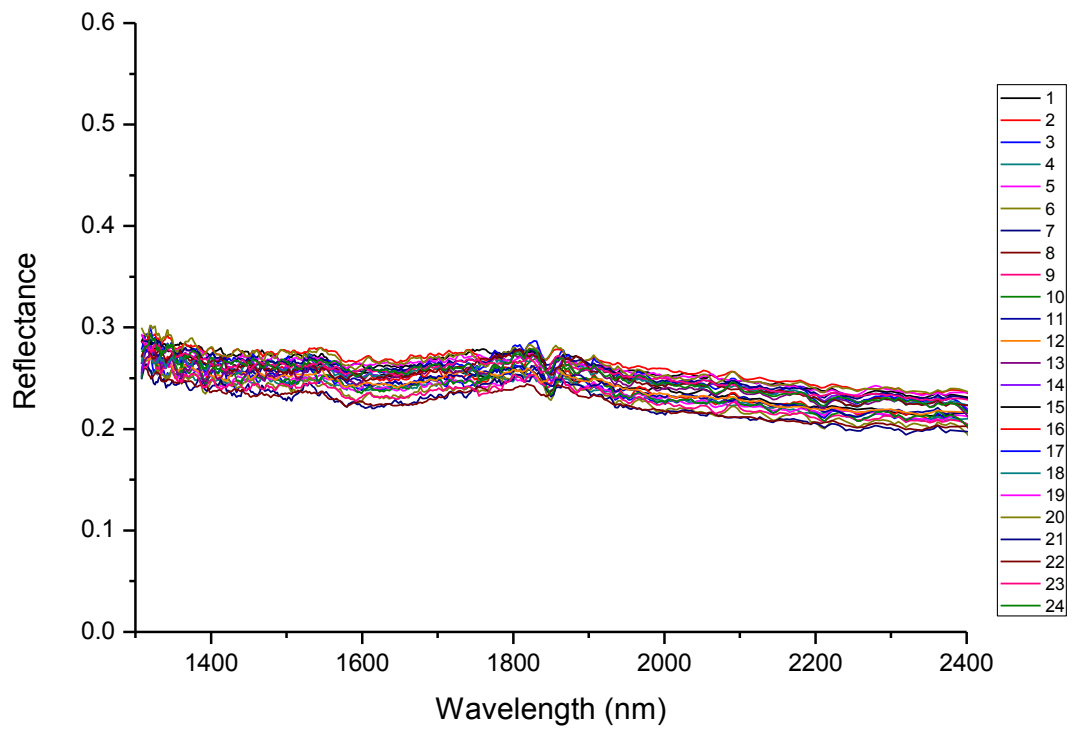
Sample 49



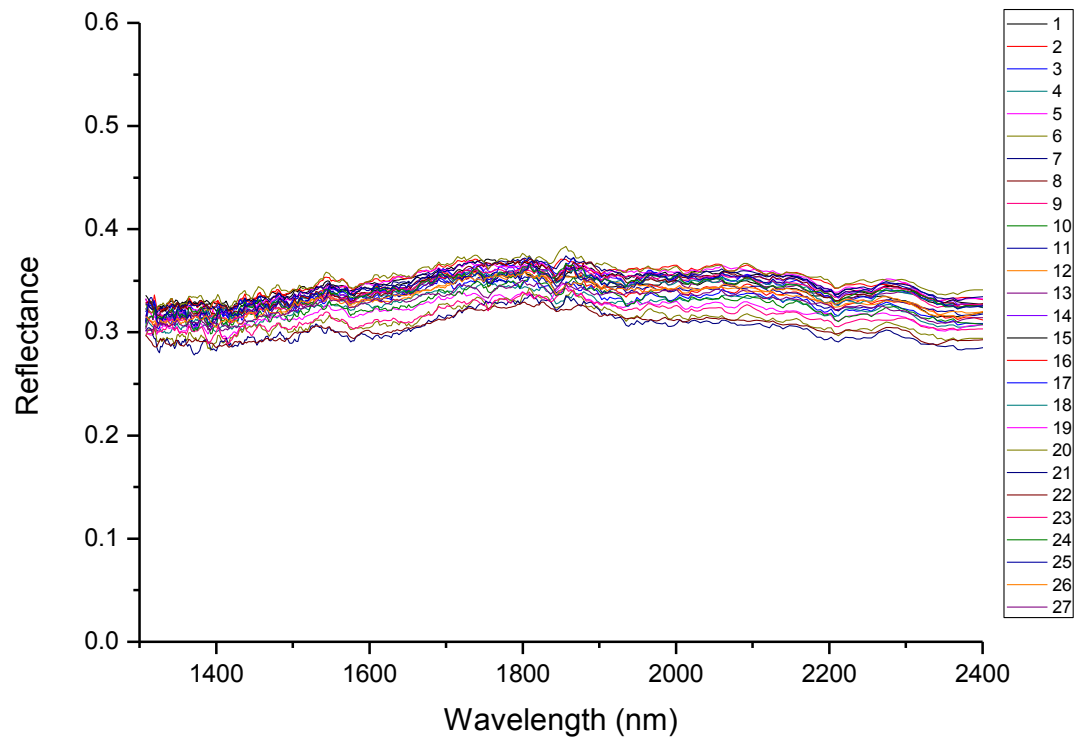
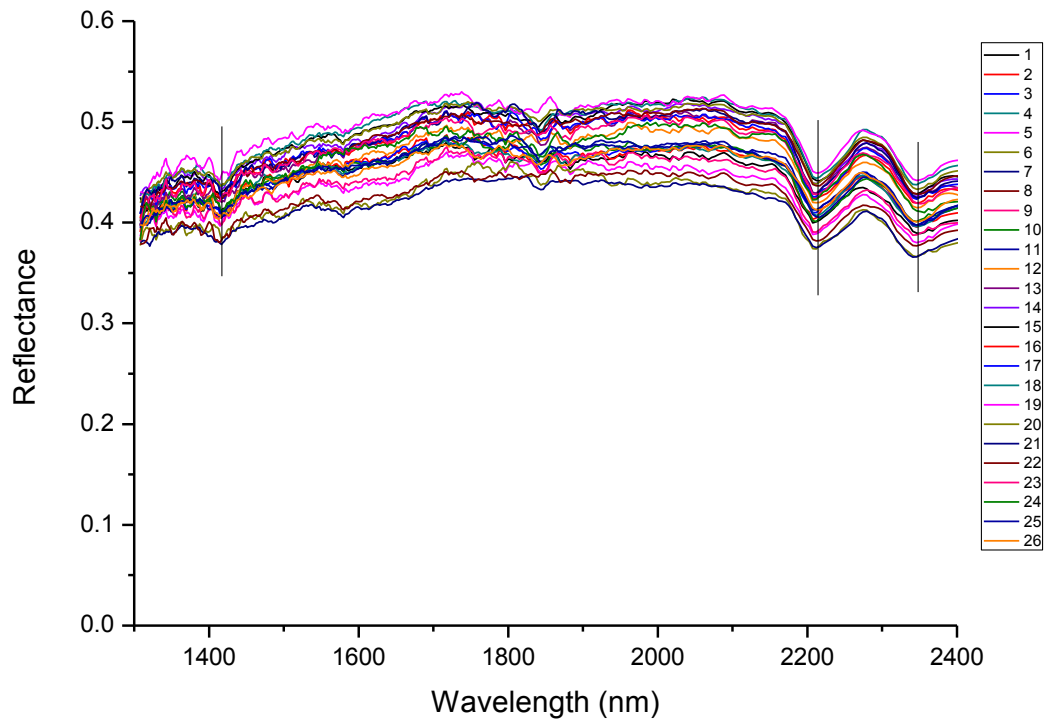
Sample 50

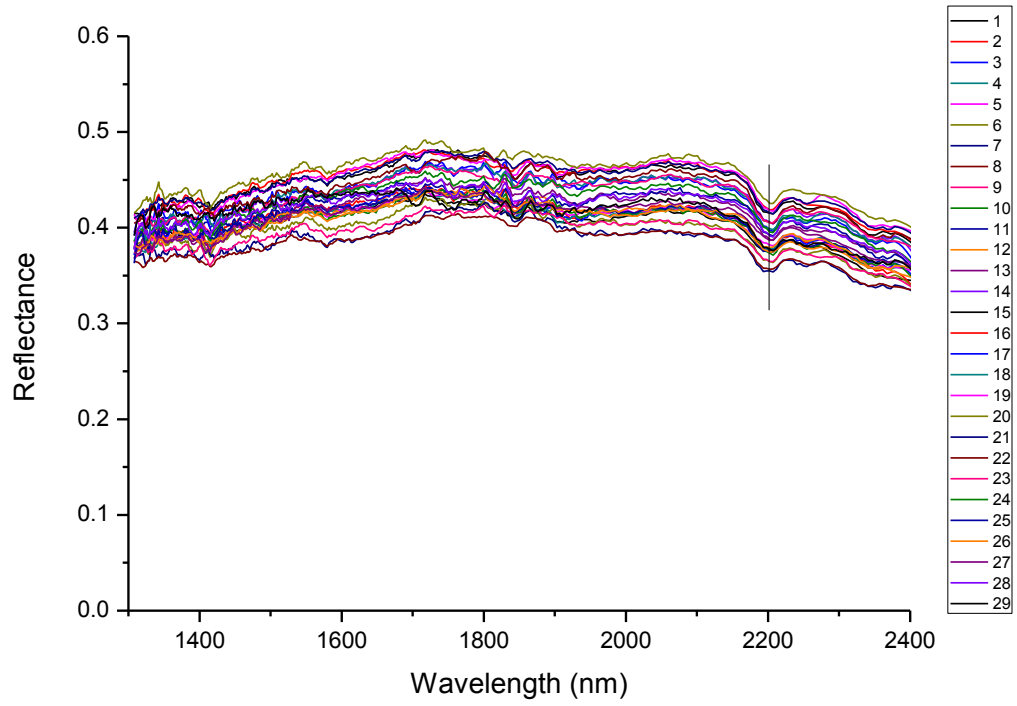


Sample 51

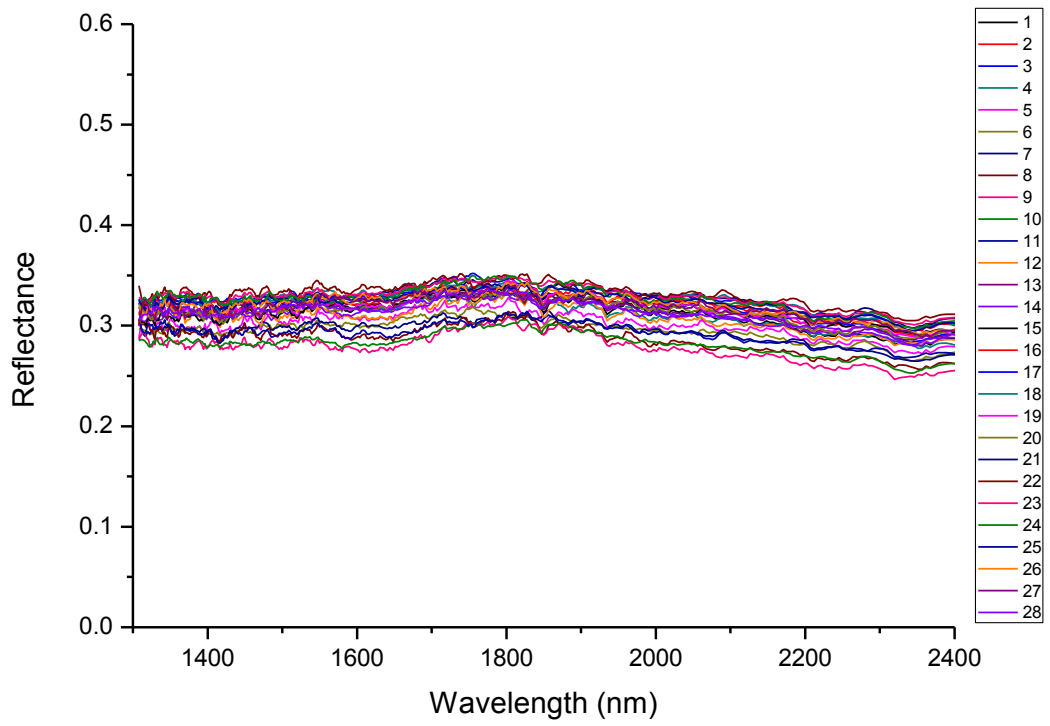


Sample 52

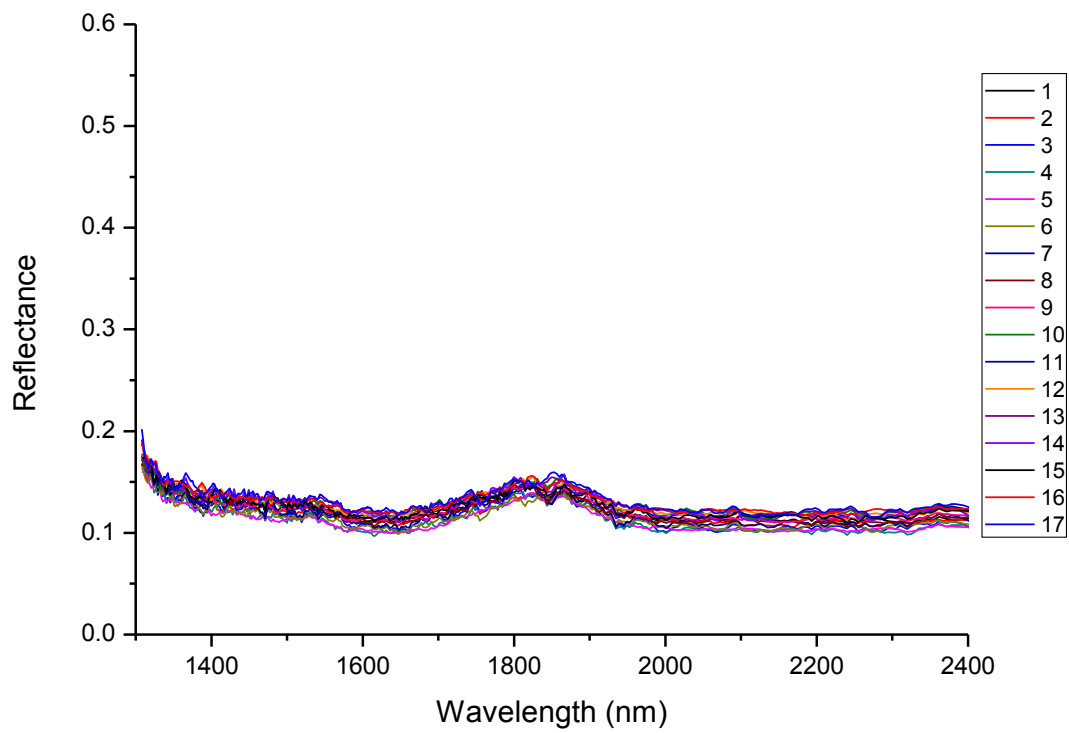
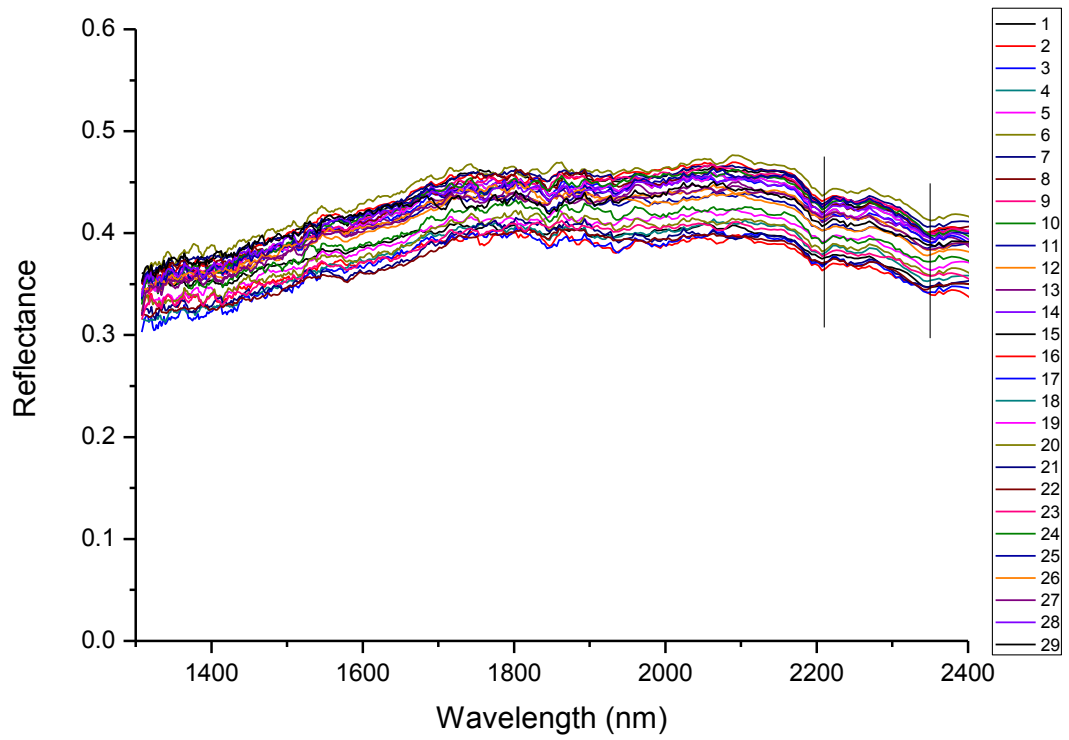


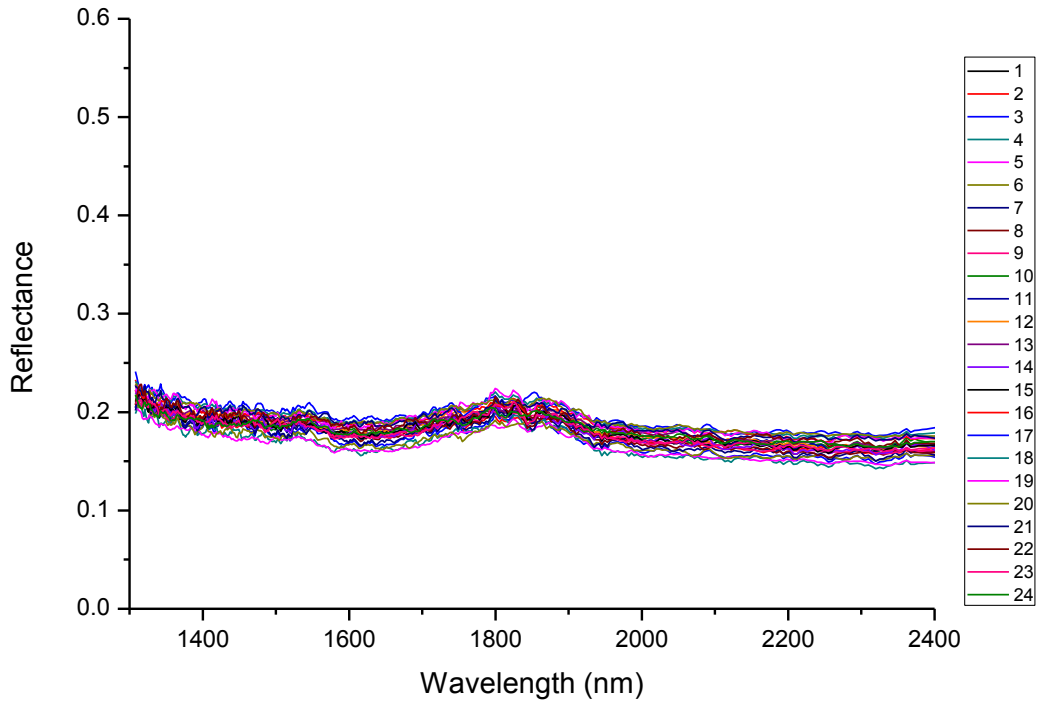


Sample 55

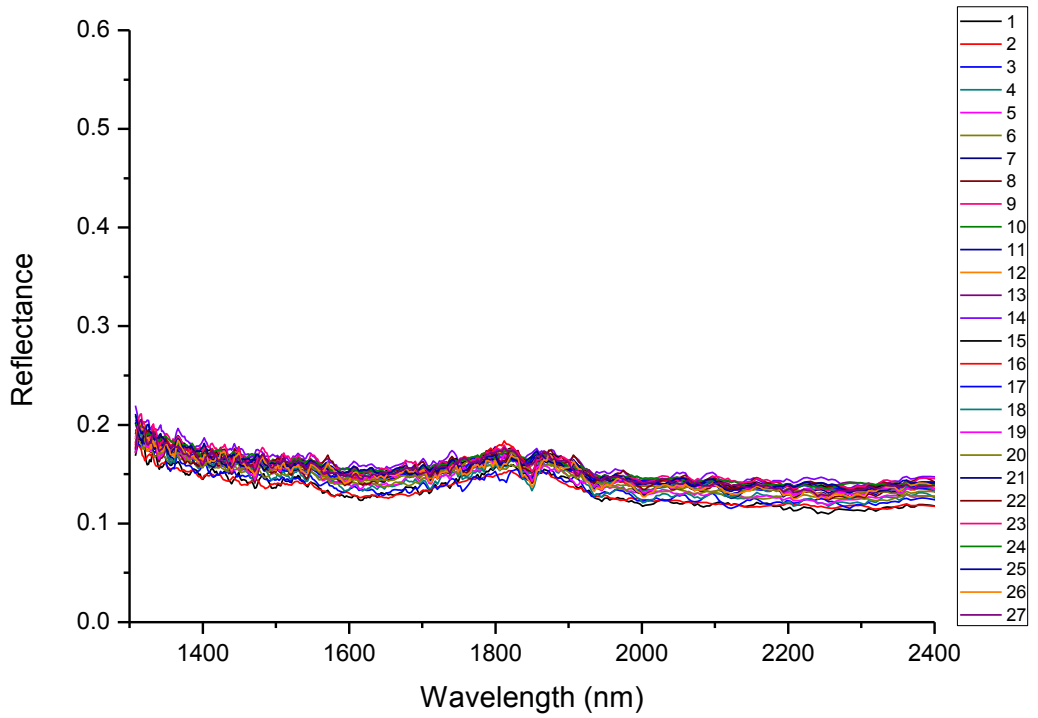


Sample 56





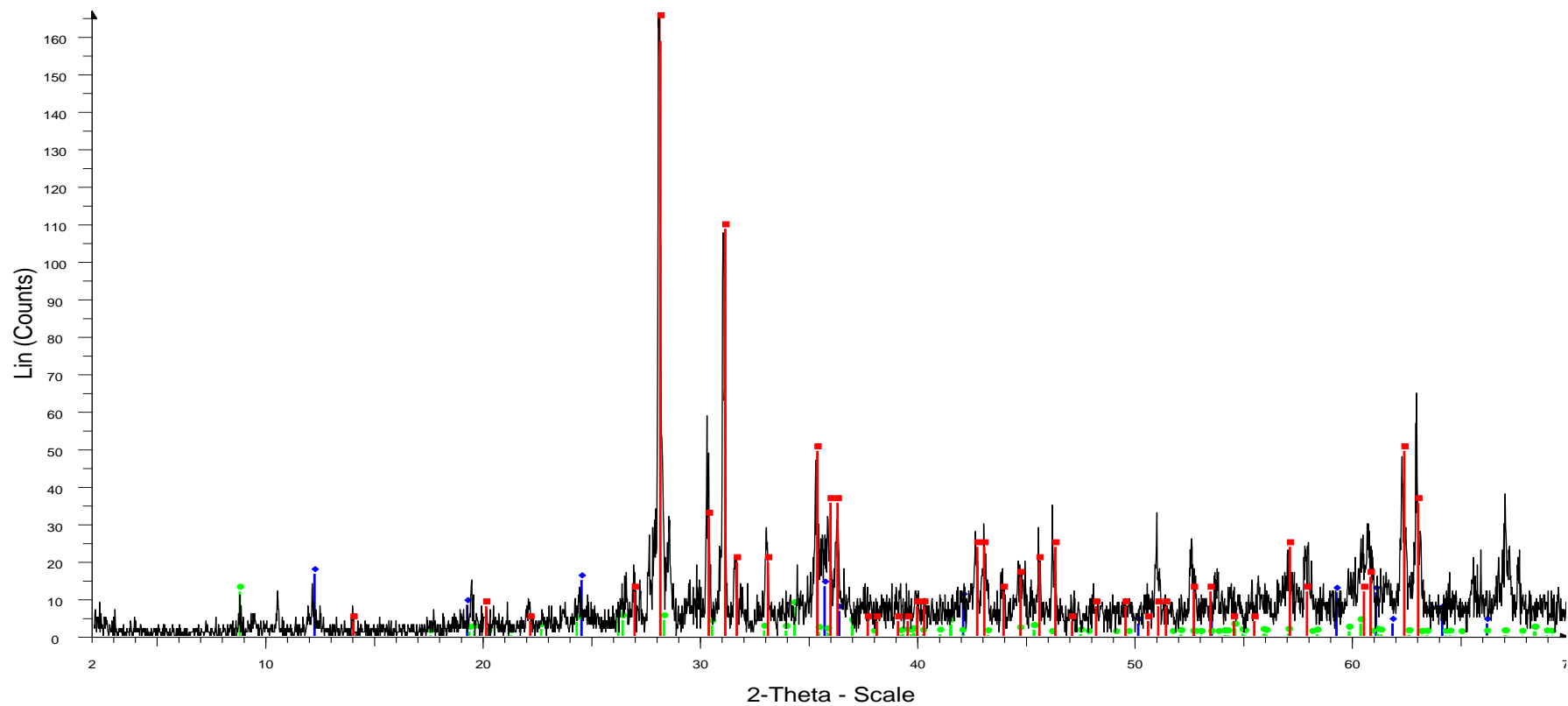
Sample 59



Sample 60

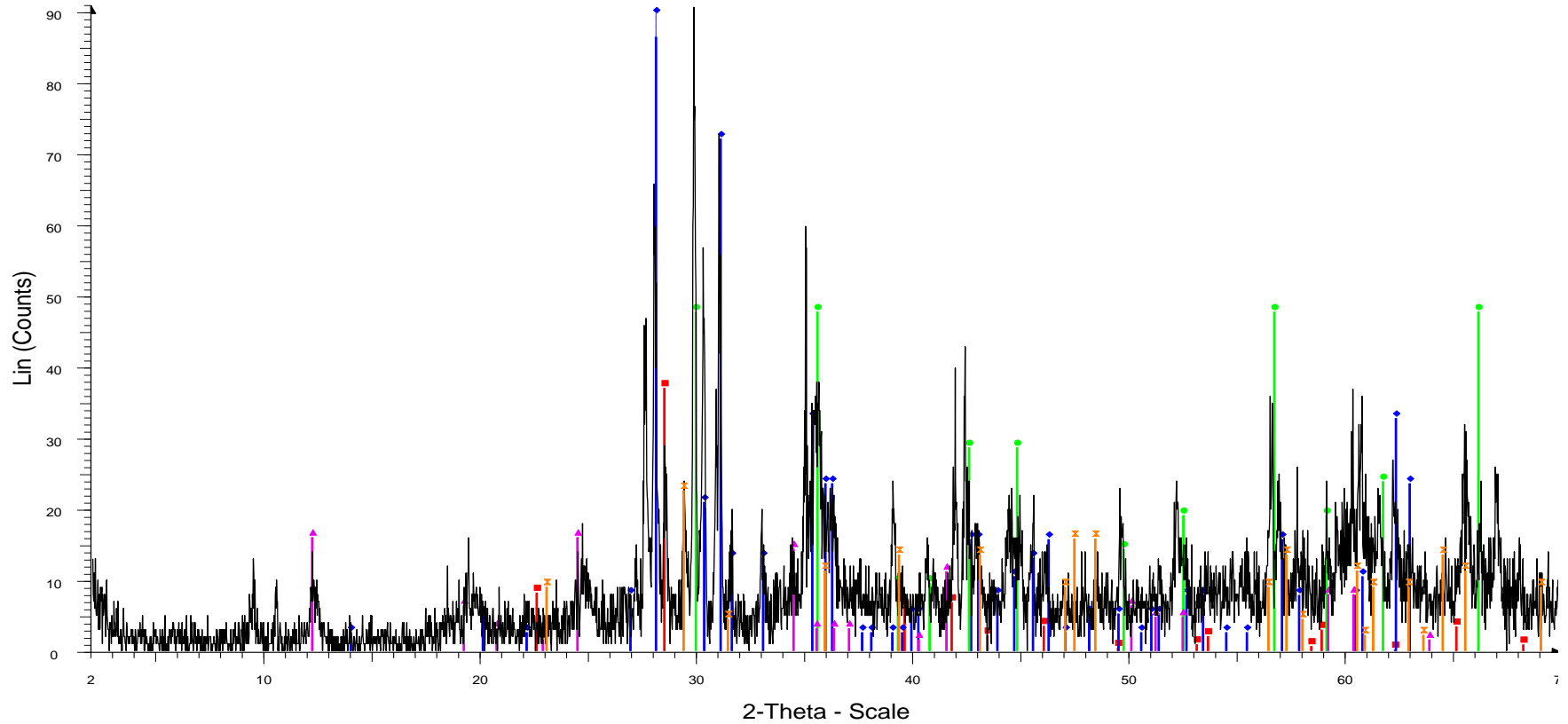
## **Appendix 10.1a – X-Ray diffraction profiles of Mogalakwena Platinum ore samples**





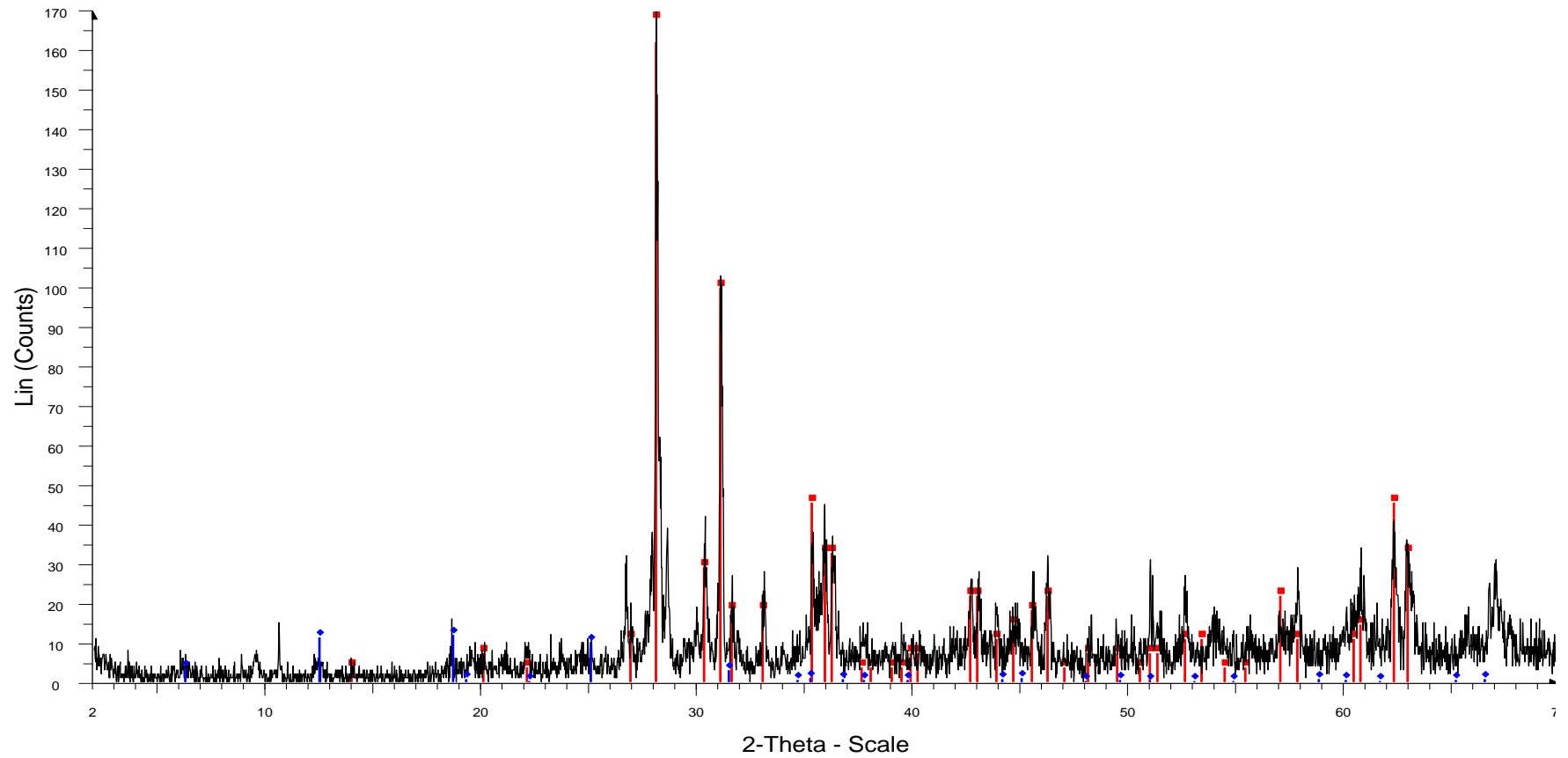
MGSC 1 - File: MGSC 1.raw - Type: 2Th/Th locked - Start: 2.000 ° - End: 70.000 ° - Step: 0.020 ° - Step time: 1. s - Temp.: 25 °C (Room) - Time Started: 17 s - 2-Theta: 2.000 ° - Theta: 1.000 ° - Chi: 0.00 ° - Phi: 0.00  
 Operations: Import  
 00-022-0714 (D) - Enstatite, ordered - MgSiO<sub>3</sub> - Y: 118.77 % - d x by: 1. - WL: 1.5406 - Orthorhombic - a 18.23000 - b 8.84000 - c 5.19000 - alpha 90.000 - beta 90.000 - gamma 90.000 - Primitive - Pbc<sub>a</sub> (61) - 16 - 83  
 00-002-0092 (D) - Antigorite - 3MgO·2SiO<sub>2</sub>·2H<sub>2</sub>O - Y: 9.97 % - d x by: 1. - WL: 1.5406 - Monoclinic - a 5.42000 - b 9.23800 - c 7.27500 - alpha 90.000 - beta 91.670 - gamma 90.000 - Primitive - P (0) - 2 - 364.104 - F  
 01-085-2273 (C) - Phlogopite - KMg<sub>3</sub>Si<sub>3</sub>AlO<sub>10</sub>(F,OH)<sub>2</sub> - Y: 7.13 % - d x by: 1. - WL: 1.5406 - Monoclinic - a 5.30500 - b 9.18900 - c 10.28600 - alpha 90.000 - beta 99.960 - gamma 90.000 - Base-centered - C2/m (12)

Sample 1



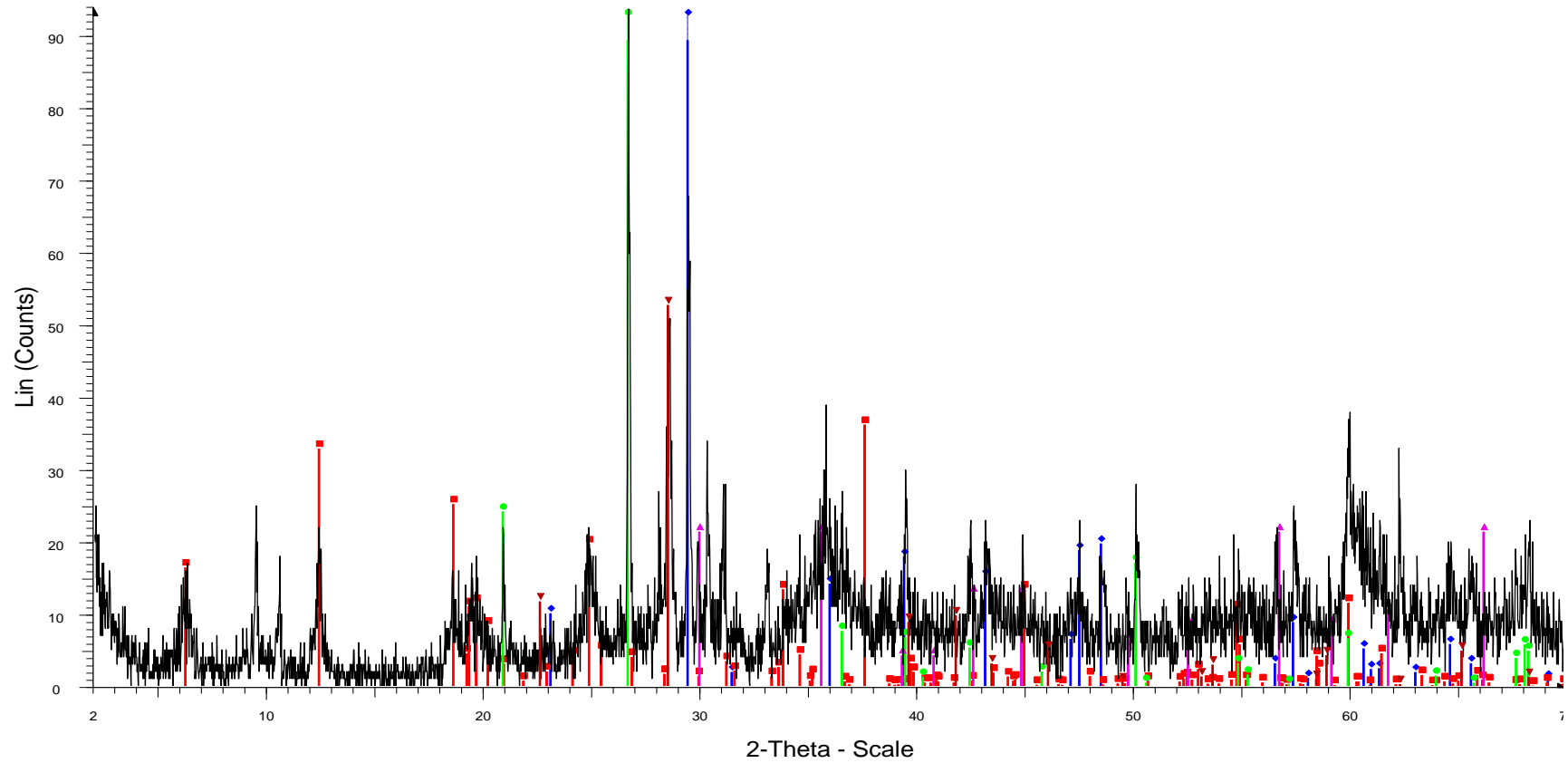
MGSC 4 - File: MGSC 4.raw - Type: 2Th/Th locked - Start: 2.000 ° - End: 70.000 ° - Step: 0.020 ° - Step time: 1. s - Temp.: 25 °C (Room) - Time Started: 17 s - 2-Theta: 2.000 ° - Theta: 1.000 ° - Chi: 0.00 ° - Phi: 0.00  
 Operations: Import  
 ■ 01-070-3318 (C) - Quartz, syn - SiO<sub>2</sub> - Y: 40.86 % - d x by: 1. - WL: 1.5406 - Hexagonal - a 4.54500 - b 4.54500 - c 5.16300 - alpha 90.000 - beta 90.000 - gamma 120.000 - Primitive - P3121 (152) - 3 - 92.3635 - I/Ic  
 ◆ 00-022-0714 (D) - Enstatite, ordered - MgSiO<sub>3</sub> - Y: 144.69 % - d x by: 1. - WL: 1.5406 - Orthorhombic - a 18.23000 - b 8.84000 - c 5.19000 - alpha 90.000 - beta 90.000 - gamma 90.000 - Primitive - Pbc<sub>a</sub> (61) - 16 - 83  
 ● 00-002-0676 (D) - Augite - N(CaO·(Mg,Fe)O·2SiO<sub>2</sub>)·(Al,Fe)<sub>2</sub>O<sub>3</sub> - Y: 52.72 % - d x by: 1. - WL: 1.5406 -  
 ▲ 00-002-0099 (D) - Antigorite - 3MgO·2SiO<sub>2</sub>·2H<sub>2</sub>O - Y: 17.65 % - d x by: 1. - WL: 1.5406 - Monoclinic - a 5.42000 - b 9.23800 - c 7.27500 - alpha 90.000 - beta 91.670 - gamma 90.000 - Primitive - P (0) - 2 - 364.104 -  
 × 00-004-0637 (D) - Calcite - CaCO<sub>3</sub>/CaO·CO<sub>2</sub> - Y: 24.96 % - d x by: 1. - WL: 1.5406 - Rhombo.H.axes - a 4.99500 - b 4.99500 - c 17.06000 - alpha 90.000 - beta 90.000 - gamma 120.000 - Primitive - R-3c (167) - 2 - 3

Sample 4



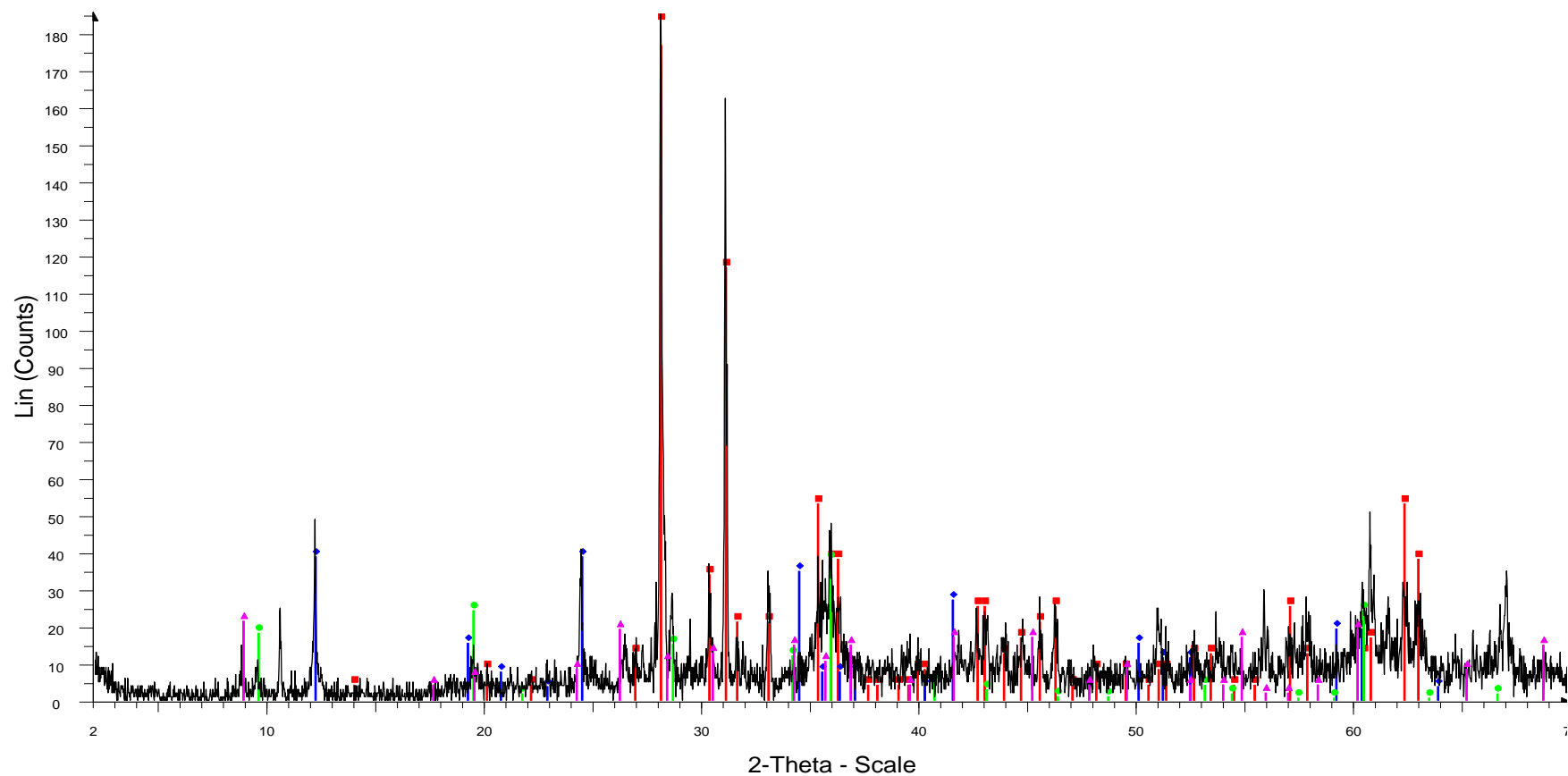
MGSC 5 - File: MGSC 5.raw - Type: 2Th/Th locked - Start: 2.000 ° - End: 70.000 ° - Step: 0.020 ° - Step time: 1. s - Temp.: 25 °C (Room) - Time Started: 17 s - 2-Theta: 2.000 ° - Theta: 1.000 ° - Chi: 0.00 ° - Phi: 0.00  
 Operations: Import  
 00-022-0714 (D) - Enstatite, ordered - MgSiO<sub>3</sub> - Y: 107.01 % - d x by: 1. - WL: 1.5406 - Orthorhombic - a 18.23000 - b 8.84000 - c 5.19000 - alpha 90.000 - beta 90.000 - gamma 90.000 - Primitive - Pbc<sub>a</sub> (61) - 16 - 83  
 00-012-0185 (D) - Clinocllore - (Mg,Fe,Al)<sub>6</sub>(Si,Cr)<sub>4</sub>O<sub>10</sub>(OH)<sub>8</sub> - Y: 7.00 % - d x by: 1. - WL: 1.5406 - Monoclinic - a 5.30000 - b 9.20000 - c 14.30000 - alpha 90.000 - beta 97.000 - gamma 90.000 - 2 - 692.071 - F24=

Sample 5



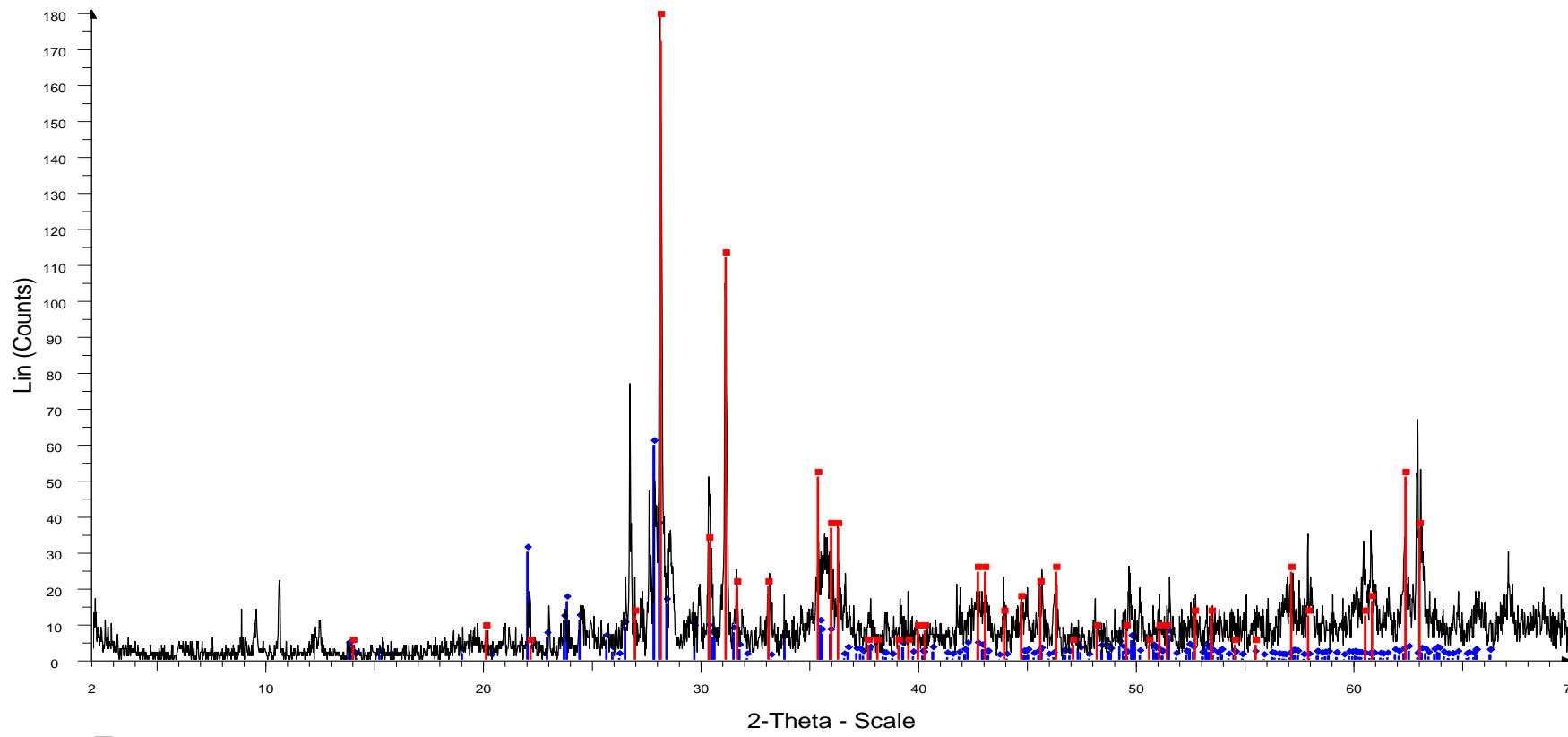
MGSC 6 - File: MGSC 6.raw - Type: 2Th/Th locked - Start: 2.000 ° - End: 70.000 ° - Step: 0.020 ° - Step time: 1. s - Temp.: 25 °C (Room) - Time Started: 17 s - 2-Theta: 2.000 ° - Theta: 1.000 ° - Chi: 0.00 ° - Phi: 0.00  
 Operations: Import  
 01-083-0577 (A) - Calcite - Ca(CO<sub>3</sub>) - Y: 108.51 % - d x by: 1. - WL: 1.5406 - Rhombo.H.axes - a 4.98870 - b 4.98870 - c 17.05290 - alpha 90.000 - beta 90.000 - gamma 120.000 - Primitive - R-3c (167) - 6 - 367.539 -  
 01-072-1385 (C) - Clinocllore, chromian 1Mla-4 - Mg<sub>5</sub>AlH<sub>1.2</sub>Si<sub>3</sub>Cr<sub>7</sub>O<sub>10</sub>(OH)<sub>8</sub> - Y: 38.59 % - d x by: 1. - WL: 1.5406 - Triclinic - a 5.33800 - b 9.24700 - c 14.43500 - alpha 90.000 - beta 97.080 - gamma 90.000 - Bas  
 03-065-0466 (C) - Quartz low, syn - SiO<sub>2</sub> - Y: 153.35 % - d x by: 1. - WL: 1.5406 - Hexagonal - a 4.91410 - b 4.91410 - c 5.40600 - alpha 90.000 - beta 90.000 - gamma 120.000 - Primitive - P3221 (154) - 3 - 113.056 -  
 00-002-0676 (D) - Augite - N(CaO-(Mg,Fe)O-2SiO<sub>2</sub>)-(Al,Fe)2O<sub>3</sub> - Y: 22.80 % - d x by: 1. - WL: 1.5406 -  
 01-070-3318 (C) - Quartz, syn - SiO<sub>2</sub> - Y: 56.28 % - d x by: 1. - WL: 1.5406 - Hexagonal - a 4.54500 - b 4.54500 - c 5.16300 - alpha 90.000 - beta 90.000 - gamma 120.000 - Primitive - P3121 (152) - 3 - 92.3635 - I/c

Sample 6



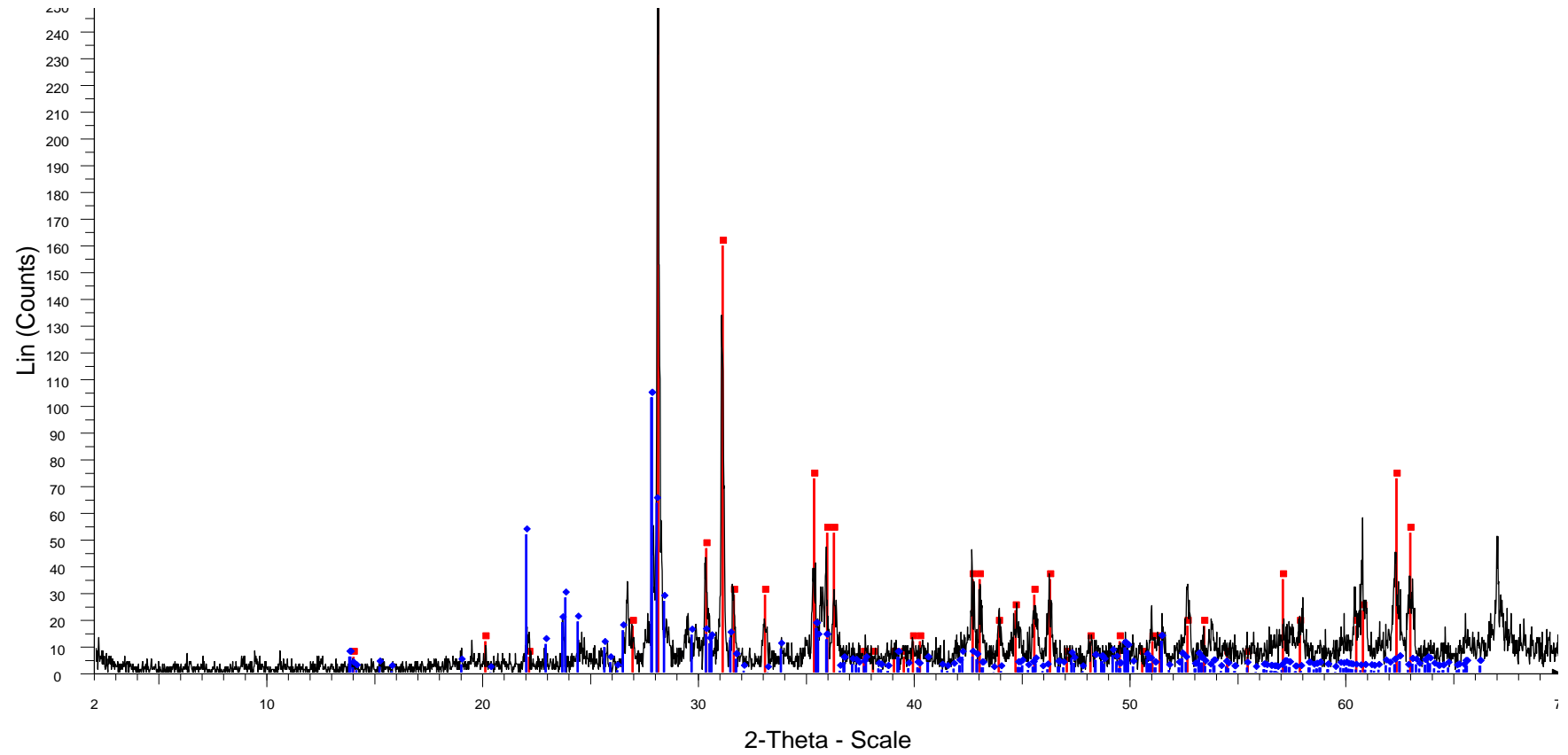
MGSC 7 - File: MGSC 7.raw - Type: 2Th/Th locked - Start: 2.000 ° - End: 70.000 ° - Step: 0.020 ° - Step time: 1. s - Temp.: 25 °C (Room) - Time Started: 17 s - 2-Theta: 2.000 ° - Theta: 1.000 ° - Chi: 0.00 ° - Phi: 0.00  
 Operations: Import  
 ■ 00-022-0714 (D) - Enstatite, ordered - MgSiO<sub>3</sub> - Y: 114.68 % - d x by: 1. - WL: 1.5406 - Orthorhombic - a 18.23000 - b 8.84000 - c 5.19000 - alpha 90.000 - beta 90.000 - gamma 90.000 - Primitive - Pbc<sub>a</sub> (61) - 16 - 83  
 ◆ 00-002-0099 (D) - Antigorite - 3MgO·2SiO<sub>2</sub>·2H<sub>2</sub>O - Y: 20.97 % - d x by: 1. - WL: 1.5406 - Monoclinic - a 5.42000 - b 9.23800 - c 7.27500 - alpha 90.000 - beta 91.670 - gamma 90.000 - Primitive - P (0) - 2 - 364.104 -  
 ● 00-003-0881 (D) - Talc - Mg<sub>3</sub>Si<sub>4</sub>O<sub>10</sub>(OH)<sub>2</sub> - Y: 20.52 % - d x by: 1. - WL: 1.5406 - Monoclinic - a 5.27000 - b 9.12000 - c 18.85000 - alpha 90.000 - beta 100.400 - gamma 90.000 - Base-centered - C<sub>2</sub>/c (15) - 4 - 891.  
 ▲ 00-002-0053 (D) - Phlogopite - KMg<sub>3</sub>(AlSi<sub>3</sub>O<sub>10</sub>)(OH)<sub>2</sub> - Y: 11.60 % - d x by: 1. - WL: 1.5406 - Monoclinic - a 5.32000 - b 9.21000 - c 10.24000 - alpha 90.000 - beta 100.330 - gamma 90.000 - Base-centered - C<sub>2</sub>/c (15)

Sample 7



MGSC 9 - File: MGSC 9.raw - Type: 2Th/Th locked - Start: 2.000 ° - End: 70.000 ° - Step: 0.020 ° - Step time: 1. s - Temp.: 25 °C (Room) - Time Started: 17 s - 2-Theta: 2.000 ° - Theta: 1.000 ° - Chi: 0.00 ° - Phi: 0.00  
 Operations: Import  
 00-022-0714 (D) - Enstatite, ordered - MgSiO<sub>3</sub> - Y: 112.85 % - d x by: 1. - WL: 1.5406 - Orthorhombic - a 18.23000 - b 8.84000 - c 5.19000 - alpha 90.000 - beta 90.000 - gamma 90.000 - Primitive - Pbc<sub>a</sub> (61) - 16 - 83  
 01-078-0433 (C) - Labradorite - Na<sub>0.45</sub>Ca<sub>0.55</sub>Al<sub>1.55</sub>Si<sub>2.45</sub>O<sub>8</sub> - Y: 33.09 % - d x by: 1. - WL: 1.5406 - Triclinic - a 8.17000 - b 12.86000 - c 7.11000 - alpha 93.600 - beta 116.300 - gamma 89.800 - Base-centered - C1

Sample 9



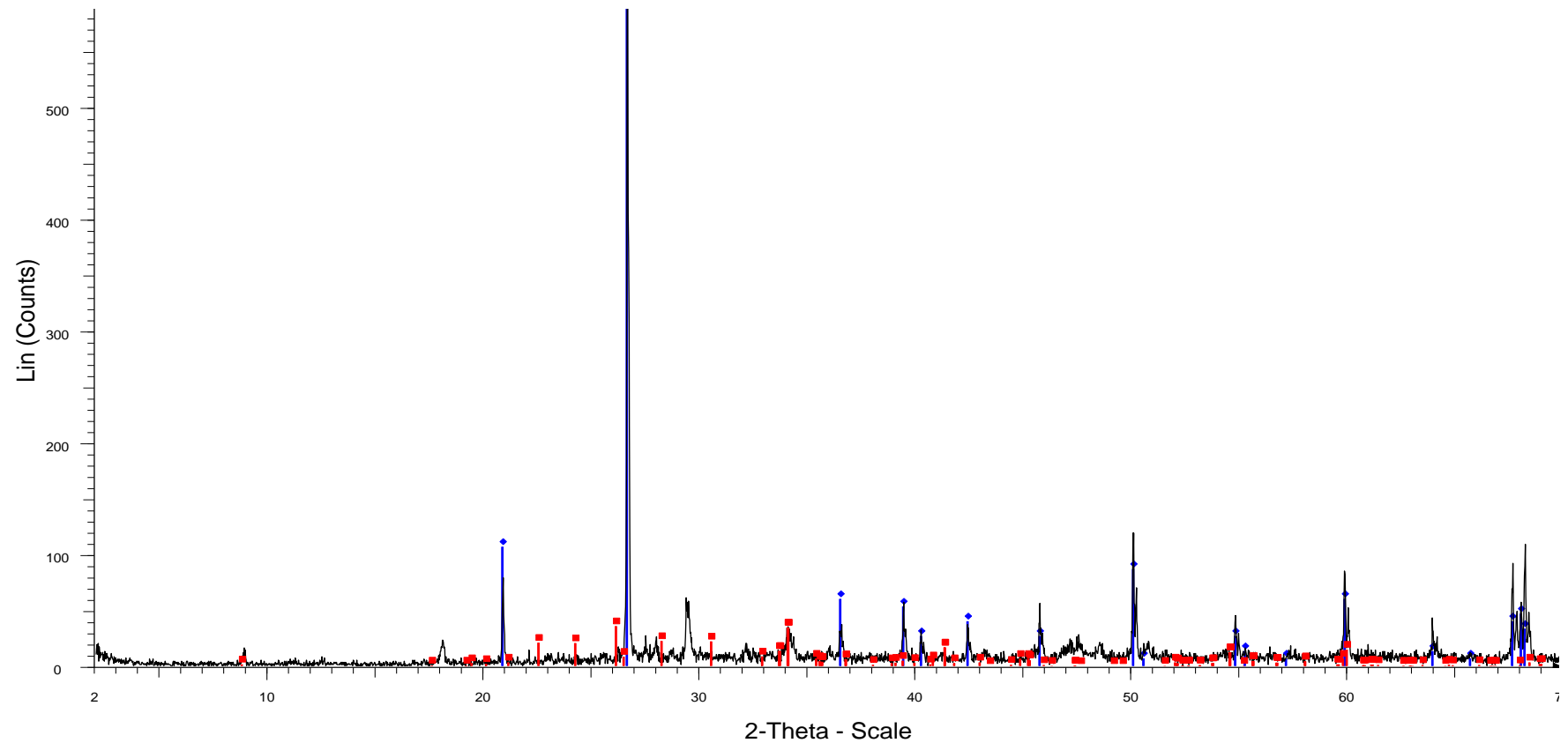
MGSC 10 - File: MGSC 10.raw - Type: 2Th/Th locked - Start: 2.000 ° - End: 70.000 ° - Step: 0.020 ° - Step time: 1. s - Temp.: 25 °C (Room) - Time Started: 17 s - 2-Theta: 2.000 ° - Theta: 1.000 ° - Chi: 0.00 ° - Phi: 0.0

Operations: Import

00-022-0714 (D) - Enstatite, ordered - MgSiO<sub>3</sub> - Y: 107.51 % - d x by: 1. - WL: 1.5406 - Orthorhombic - a 18.23000 - b 8.84000 - c 5.19000 - alpha 90.000 - beta 90.000 - gamma 90.000 - Primitive - Pbc<sub>a</sub> (61) - 16 - 83

01-078-0433 (C) - Labradorite - Na<sub>0.45</sub>Ca<sub>0.55</sub>Al<sub>1.55</sub>Si<sub>2.45</sub>O<sub>8</sub> - Y: 38.08 % - d x by: 1. - WL: 1.5406 - Triclinic - a 8.17000 - b 12.86000 - c 7.11000 - alpha 93.600 - beta 116.300 - gamma 89.800 - Base-centered - C1

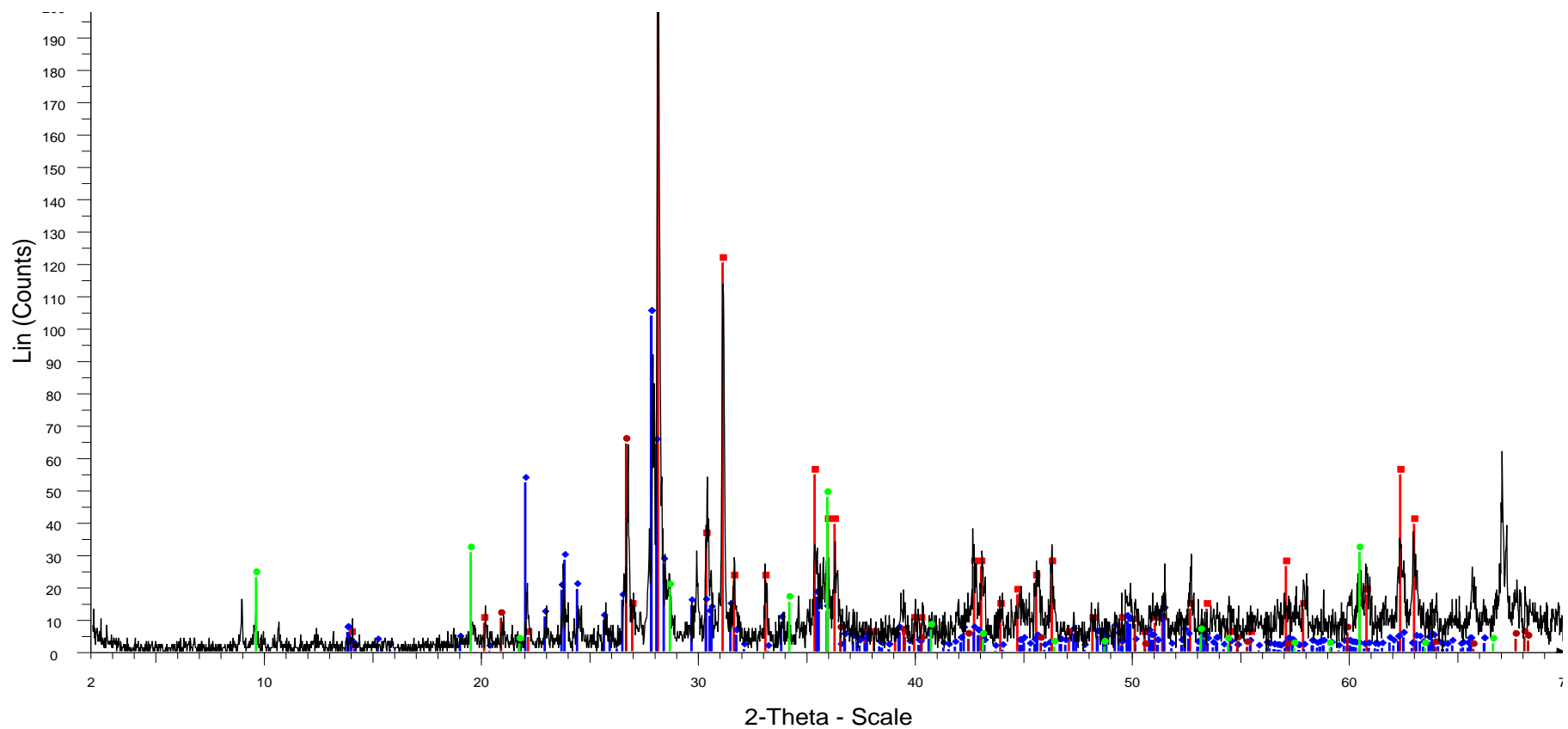
Sample 10



MGSC 12 - File: MGSC 12.raw - Type: 2Th/Th locked - Start: 2.000 ° - End: 70.000 ° - Step: 0.020 ° - Step time: 1. s - Temp.: 25 °C (Room) - Time Started: 17 s - 2-Theta: 2.000 ° - Theta: 1.000 ° - Chi: 0.00 ° - Phi: 0.0  
 Operations: Import  
 00-046-1045 (\*) - Quartz, syn - SiO<sub>2</sub> - Y: 107.92 % - d x by: 1. - WL: 1.5406 - Hexagonal - a 4.91344 - b 4.91344 - c 5.40524 - alpha 90.000 - beta 90.000 - gamma 120.000 - Primitive - P3221 (154) - 3 - 113.010 - I/c  
 01-088-0715 (C) - Phlogopite, manganoan, barian - (Mg,Mn,Al)2(K,Ba,Na)(Si,Al)4(O,OH,F)12 - Y: 5.75 % - d x by: 1. - WL: 1.5406 - Monoclinic - a 5.33000 - b 9.24500 - c 10.24000 - alpha 90.000 - beta 99.920 - gam

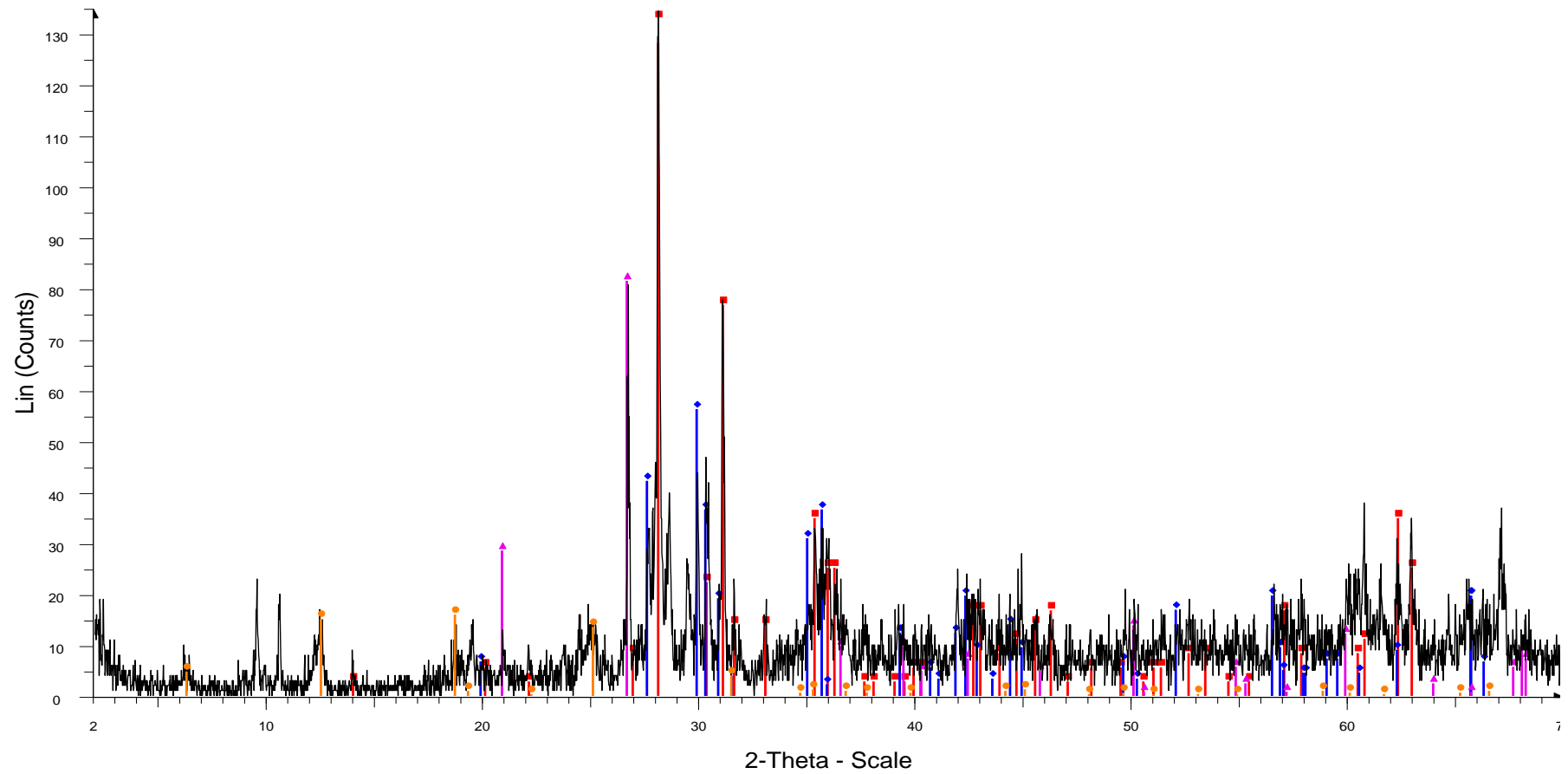
Sample 12





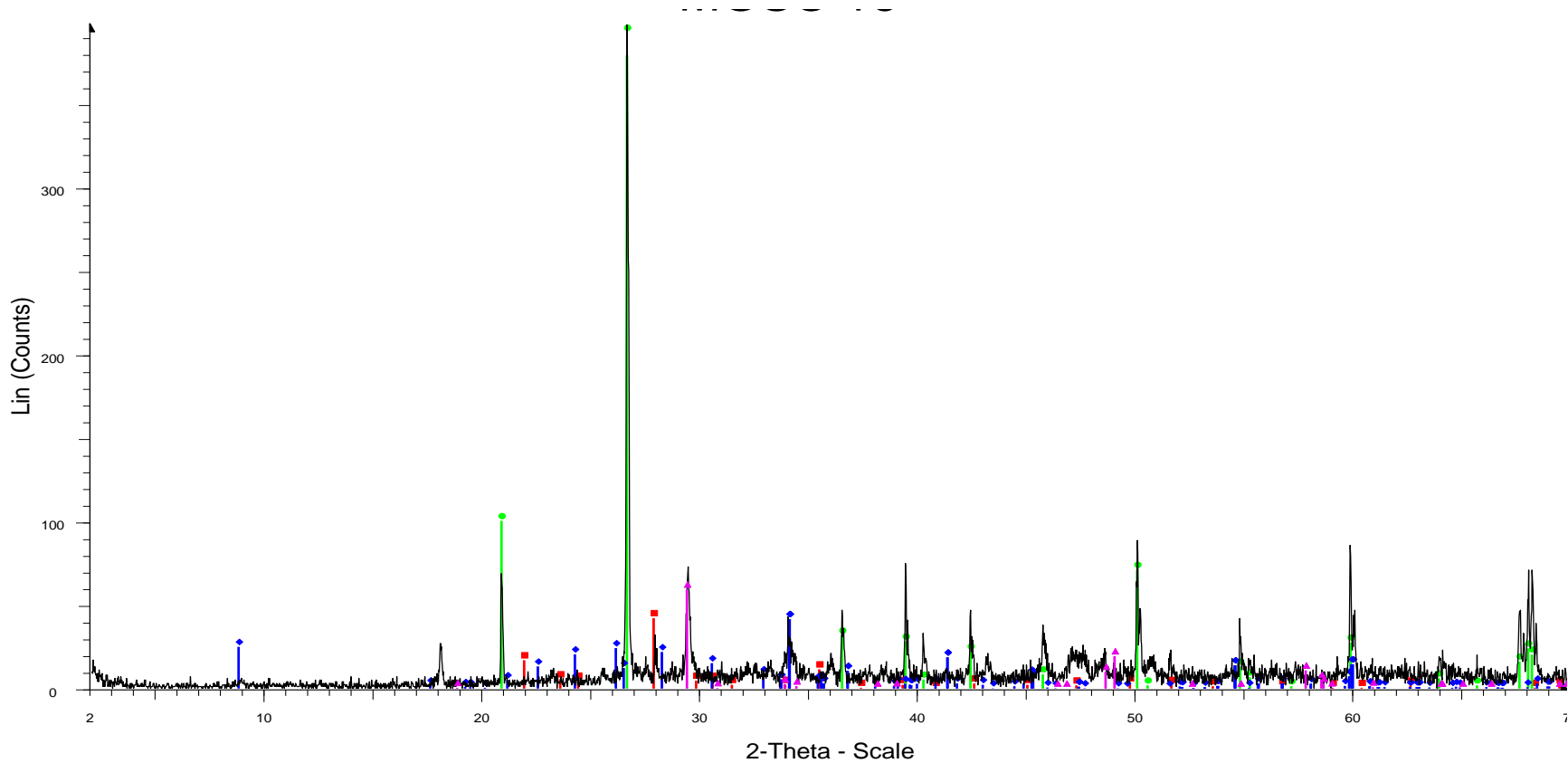
MGSC 13 - File: MGSC 13.raw - Type: 2Th/Th locked - Start: 2.000 ° - End: 70.000 ° - Step: 0.020 ° - Step time: 1. s - Temp.: 25 °C (Room) - Time Started: 17 s - 2-Theta: 2.000 ° - Theta: 1.000 ° - Chi: 0.00 ° - Phi: 0.0  
 Operations: Import  
 00-022-0714 (D) - Enstatite, ordered - MgSiO<sub>3</sub> - Y: 101.10 % - d x by: 1. - WL: 1.5406 - Orthorhombic - a 18.23000 - b 8.84000 - c 5.19000 - alpha 90.000 - beta 90.000 - gamma 90.000 - Primitive - Pbca (61) - 16 - 83  
 01-078-0433 (C) - Labradorite - Na<sub>0.45</sub>Ca<sub>0.55</sub>Al<sub>1.55</sub>Si<sub>2.45</sub>O<sub>8</sub> - Y: 48.04 % - d x by: 1. - WL: 1.5406 - Triclinic - a 8.17000 - b 12.86000 - c 7.11000 - alpha 93.600 - beta 116.300 - gamma 89.800 - Base-centered - C1  
 00-046-1045 (\*) - Quartz, syn - SiO<sub>2</sub> - Y: 29.70 % - d x by: 1. - WL: 1.5406 - Hexagonal - a 4.91344 - b 4.91344 - c 5.40524 - alpha 90.000 - beta 90.000 - gamma 120.000 - Primitive - P3221 (154) - 3 - 113.010 - I/c P  
 00-003-0881 (D) - Talc - Mg<sub>3</sub>Si<sub>4</sub>O<sub>10</sub>(OH)<sub>2</sub> - Y: 22.09 % - d x by: 1. - WL: 1.5406 - Monoclinic - a 5.27000 - b 9.12000 - c 18.85000 - alpha 90.000 - beta 100.400 - gamma 90.000 - Base-centered - C2/c (15) - 4 - 891.

Sample 13



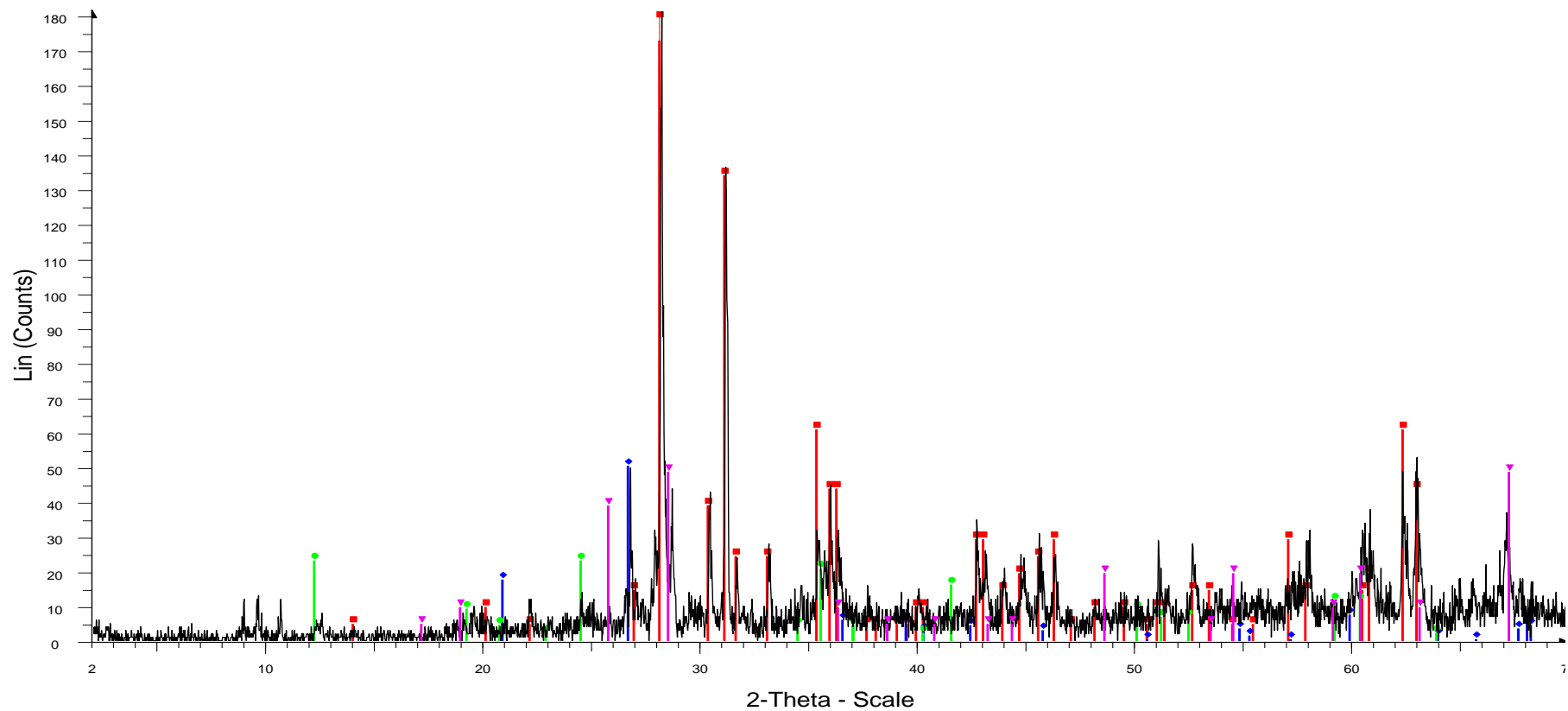
MGSC 15 - File: MGSC 15.raw - Type: 2Th/Th locked - Start: 2.000 ° - End: 70.000 ° - Step: 0.020 ° - Step time: 1. s - Temp.: 25 °C (Room) - Time Started: 17 s - 2-Theta: 2.000 ° - Theta: 1.000 ° - Chi: 0.00 ° - Phi: 0.0  
 Operations: Import  
 00-022-0714 (D) - Enstatite, ordered - MgSiO<sub>3</sub> - Y: 103.81 % - d x by: 1. - WL: 1.5406 - Orthorhombic - a 18.23000 - b 8.84000 - c 5.19000 - alpha 90.000 - beta 90.000 - gamma 90.000 - Primitive - Pbc<sub>a</sub> (61) - 16 - 83  
 00-024-0203 (I) - Augite - Ca(Mg,Fe)Si<sub>2</sub>O<sub>6</sub> - Y: 41.87 % - d x by: 1. - WL: 1.5406 - Monoclinic - a 9.75500 - b 8.92800 - c 5.20400 - alpha 90.000 - beta 106.110 - gamma 90.000 - Base-centered - C2/c (15) - 4 - 435.4  
 00-005-0490 (D) - Quartz, low - alpha-SiO<sub>2</sub> - Y: 60.61 % - d x by: 1. - WL: 1.5406 - Hexagonal - a 4.91300 - b 4.91300 - c 5.40500 - alpha 90.000 - beta 90.000 - gamma 120.000 - Primitive - P3121 (152) - 3 - 112.985  
 00-012-0185 (D) - Clinochlore - (Mg,Fe,Al)<sub>6</sub>(Si,Cr)<sub>4</sub>O<sub>10</sub>(OH)<sub>8</sub> - Y: 11.85 % - d x by: 1. - WL: 1.5406 - Monoclinic - a 5.30000 - b 9.20000 - c 14.30000 - alpha 90.000 - beta 97.000 - gamma 90.000 - 2 - 692.071 - F24=

Sample 15



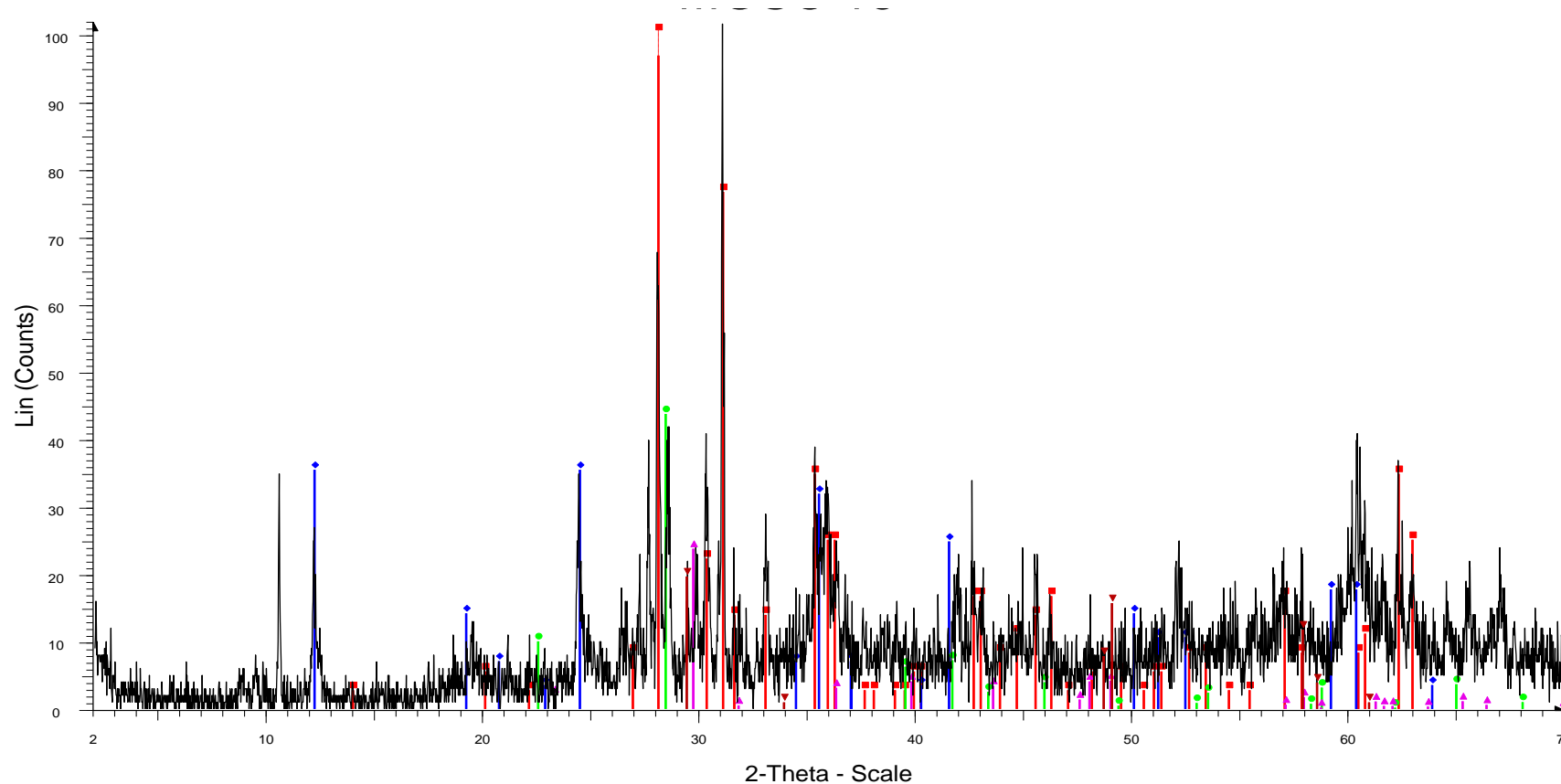
MGSC 16 - File: MGSC 16.raw - Type: 2Th/Th locked - Start: 2.000 ° - End: 70.000 ° - Step: 0.020 ° - Step time: 1. s - Temp.: 25 °C (Room) - Time Started: 33 s - 2-Theta: 2.000 ° - Theta: 1.000 ° - Chi: 0.00 ° - Phi: 0.0  
 Operations: Import  
 00-003-0499 (D) - Labradorite -  $(\text{Na}_{0.4}\text{Ca}_{0.6})\text{Al}_1.6\text{Si}_2.4\text{O}_8$  - Y: 10.59 % - d x by: 1. - WL: 1.5406 - Triclinic - a 8.21000 - b 12.95000 - c 14.16000 - alpha 93.520 - beta 116.050 - gamma 89.920 - 1349.44 - F22= 2(0.0  
 03-065-0466 (C) - Quartz low, syn -  $\text{SiO}_2$  - Y: 150.16 % - d x by: 1. - WL: 1.5406 - Hexagonal - a 4.91410 - b 4.91410 - c 5.40600 - alpha 90.000 - beta 90.000 - gamma 120.000 - Primitive - P3221 (154) - 3 - 113.056 -  
 01-088-0712 (C) - Phlogopite, manganian, barian -  $(\text{Mg},\text{Mn},\text{Al},\text{Fe})_3(\text{K},\text{Ba},\text{Na})(\text{Si},\text{Al},\text{Ti})_4(\text{O},\text{OH},\text{F})_{12}$  - Y: 10.46 % - d x by: 1. - WL: 1.5406 - Monoclinic - a 5.33000 - b 9.24500 - c 10.24000 - alpha 90.000 - beta 99.920  
 01-083-0983 (C) - Chalcopyrite -  $\text{CuFeS}_2$  - Y: 14.91 % - d x by: 1. - WL: 1.5406 - Tetragonal - a 5.28640 - b 5.28640 - c 10.41020 - alpha 90.000 - beta 90.000 - gamma 90.000 - Body-centered - I-42d (122) - 4 - 290.9

Sample 16



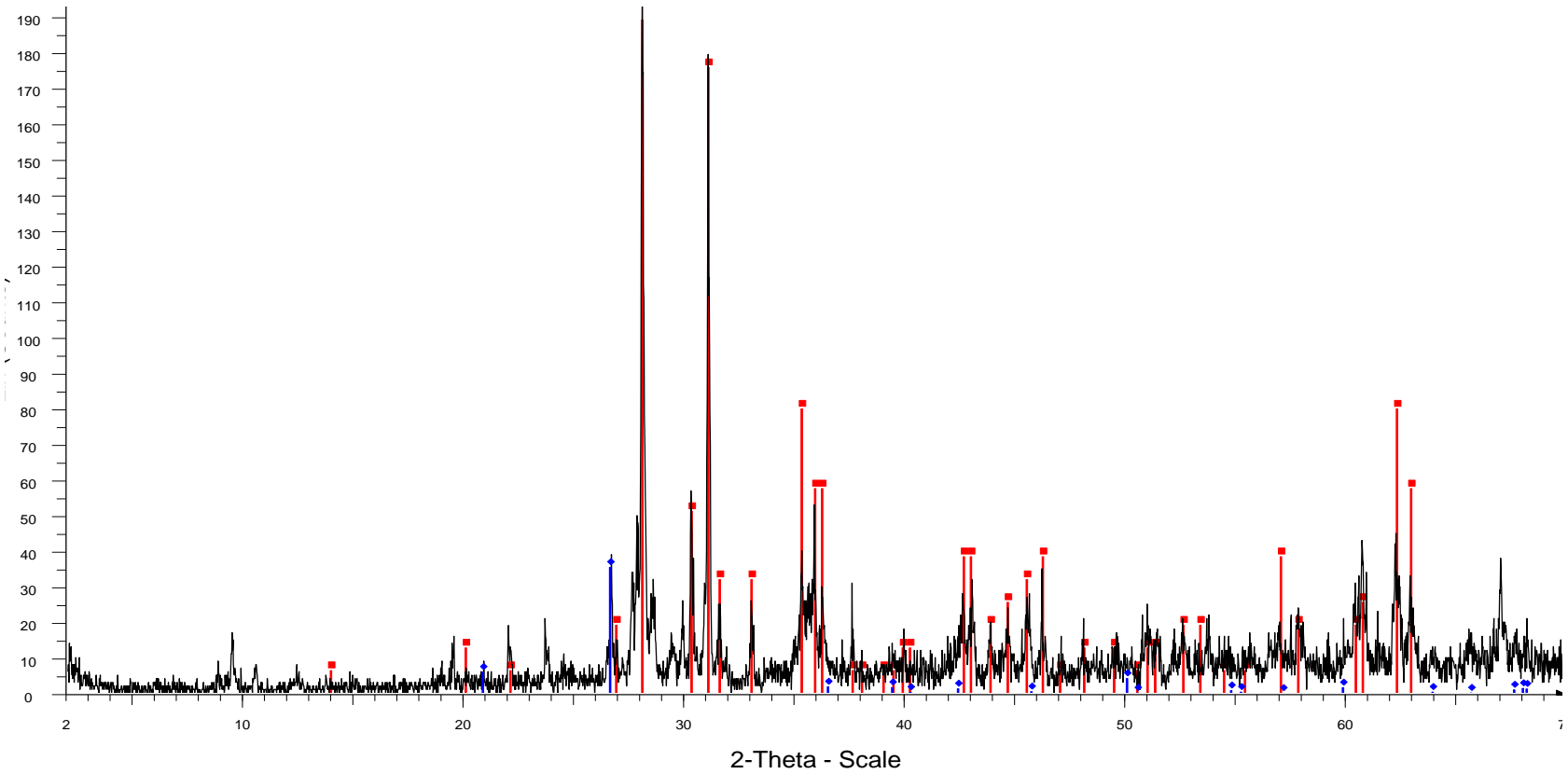
MGSC 17 - File: MGSC 17.raw - Type: 2Th/Th locked - Start: 2.000 ° - End: 70.000 ° - Step: 0.020 ° - Step time: 1. s - Temp.: 25 °C (Room) - Time Started: 17 s - 2-Theta: 2.000 ° - Theta: 1.000 ° - Chi: 0.00 ° - Phi: 0.0  
 Operations: Import  
 ■ 00-022-0714 (D) - Enstatite, ordered - MgSiO<sub>3</sub> - Y: 134.51 % - d x by: 1. - WL: 1.5406 - Orthorhombic - a 18.23000 - b 8.84000 - c 5.19000 - alpha 90.000 - beta 90.000 - gamma 90.000 - Primitive - Pbc<sub>a</sub> (61) - 16 - 83  
 ◆ 00-005-0490 (D) - Quartz, low - alpha-SiO<sub>2</sub> - Y: 27.82 % - d x by: 1. - WL: 1.5406 - Hexagonal - a 4.91300 - b 4.91300 - c 5.40500 - alpha 90.000 - beta 90.000 - gamma 120.000 - Primitive - P3121 (152) - 3 - 112.985  
 ● 00-002-0100 (D) - Antigorite - 3MgO·2SiO<sub>2</sub>·2H<sub>2</sub>O - Y: 12.76 % - d x by: 1. - WL: 1.5406 - Monoclinic - a 5.42000 - b 9.23800 - c 7.27500 - alpha 90.000 - beta 91.670 - gamma 90.000 - Primitive - P (0) - 2 - 364.104 -  
 ▼ 00-003-0535 (D) - Talc - 4MgO·5SiO<sub>2</sub>·H<sub>2</sub>O - Y: 26.85 % - d x by: 1. - WL: 1.5406 -

Sample 17



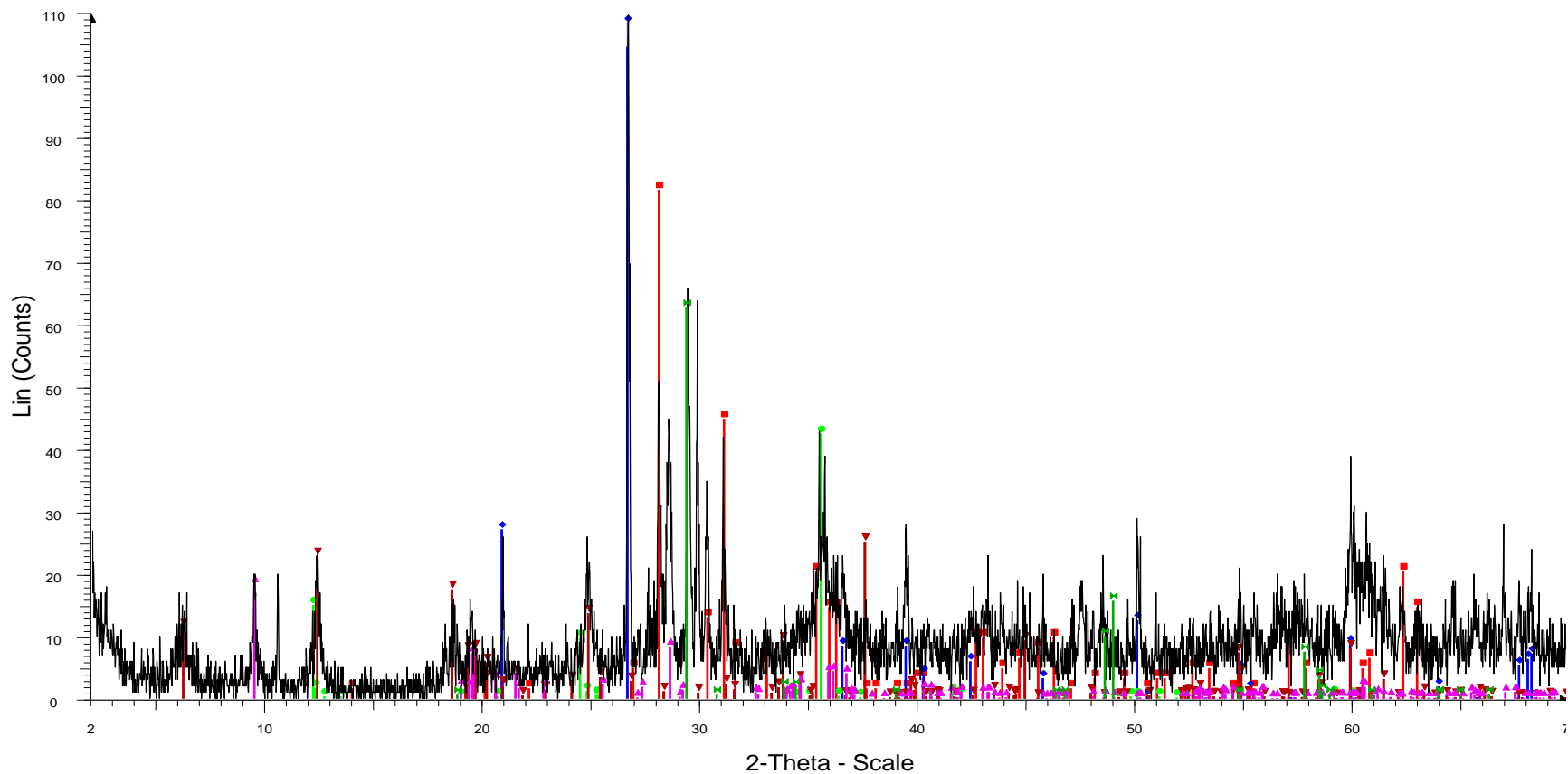
MGSC 18 - File: MGSC 18.raw - Type: 2Th/Th locked - Start: 2.000 ° - End: 70.000 ° - Step: 0.020 ° - Step time: 1. s - Temp.: 25 °C (Room) - Time Started: 17 s - 2-Theta: 2.000 ° - Theta: 1.000 ° - Chi: 0.00 ° - Phi: 0.0  
 Operations: Import  
 ■ 00-022-0714 (D) - Enstatite, ordered - MgSiO<sub>3</sub> - Y: 137.28 % - d x by: 1. - WL: 1.5406 - Orthorhombic - a 18.23000 - b 8.84000 - c 5.19000 - alpha 90.000 - beta 90.000 - gamma 90.000 - Primitive - Pbc<sub>a</sub> (61) - 16 - 83  
 ◆ 00-002-0100 (D) - Antigorite - 3MgO·2SiO<sub>2</sub>·2H<sub>2</sub>O - Y: 34.92 % - d x by: 1. - WL: 1.5406 - Monoclinic - a 5.42000 - b 9.23800 - c 7.27500 - alpha 90.000 - beta 91.670 - gamma 90.000 - Primitive - P (0) - 2 - 364.104 -  
 ● 01-070-3316 (C) - Quartz, syn - SiO<sub>2</sub> - Y: 43.07 % - d x by: 1. - WL: 1.5406 - Hexagonal - a 4.55300 - b 4.55300 - c 5.17500 - alpha 90.000 - beta 90.000 - gamma 120.000 - Primitive - P3121 (152) - 3 - 92.9044 - I/c  
 ▲ 01-071-1663 (C) - Calcite, magnesian - Mg<sub>0.1</sub>Ca<sub>0.9</sub>CO<sub>3</sub> - Y: 23.40 % - d x by: 1. - WL: 1.5406 - Rhombo.H.axes - a 4.94100 - b 4.94100 - c 16.86400 - alpha 90.000 - beta 90.000 - gamma 120.000 - Primitive - R-3c (  
 ▼ 00-009-0423 (D) - Chalcopyrite - CuFeS<sub>2</sub> - Y: 19.33 % - d x by: 1. - WL: 1.5406 - Tetragonal - a 5.28000 - b 5.28000 - c 10.40900 - alpha 90.000 - beta 90.000 - gamma 90.000 - Body-centered - I-42d (122) - 4 - 290.1

Sample 18



MGSC 20 - File: MGSC 20.raw - Type: 2Th/Th locked - Start: 2.000 ° - End: 70.000 ° - Step: 0.020 ° - Step time: 1. s - Temp.: 25 °C (Room) - Time Started: 18 s - 2-Theta: 2.000 ° - Theta: 1.000 ° - Chi: 0.00 ° - Phi: 0.0  
 Operations: Import  
 00-022-0714 (D) - Enstatite, ordered - MgSiO<sub>3</sub> - Y: 161.23 % - d x by: 1. - WL: 1.5406 - Orthorhombic - a 18.23000 - b 8.84000 - c 5.19000 - alpha 90.000 - beta 90.000 - gamma 90.000 - Primitive - Pbc<sub>a</sub> (61) - 16 - 83  
 03-065-0466 (C) - Quartz low, syn - SiO<sub>2</sub> - Y: 17.88 % - d x by: 1. - WL: 1.5406 - Hexagonal - a 4.91410 - b 4.91410 - c 5.40600 - alpha 90.000 - beta 90.000 - gamma 120.000 - Primitive - P3221 (154) - 3 - 113.056 - I

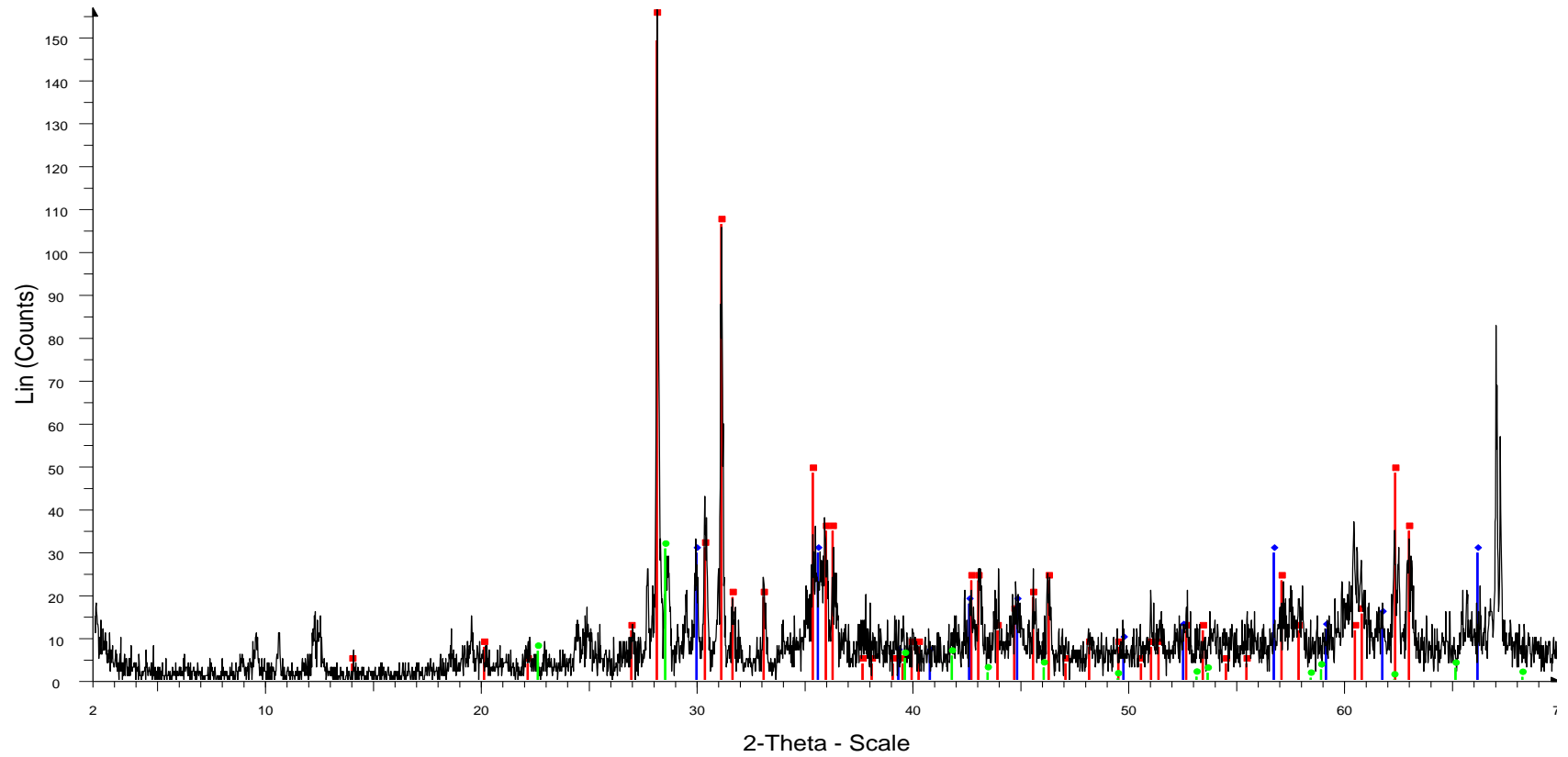
Sample 20



MGSC 22 - File: MGSC 22.raw - Type: 2Th/Th locked - Start: 2.000 ° - End: 70.000 ° - Step: 0.020 ° - Step time: 1. s - Temp.: 25 °C (Room) - Time Started: 17 s - 2-Theta: 2.000 ° - Theta: 1.000 ° - Chi: 0.00 ° - Phi: 0.0  
 Operations: Import

- 00-022-0714 (D) - Enstatite, ordered - MgSiO<sub>3</sub> - Y: 74.44 % - d x by: 1. - WL: 1.5406 - Orthorhombic - a 18.23000 - b 8.84000 - c 5.19000 - alpha 90.000 - beta 90.000 - gamma 90.000 - Primitive - Pbca (61) - 16 - 836
- 01-075-0443 (A) - Quartz - alpha-SiO<sub>2</sub> - Y: 113.47 % - d x by: 1. - WL: 1.5406 - Hexagonal - a 4.91300 - b 4.91300 - c 5.40500 - alpha 90.000 - beta 90.000 - gamma 120.000 - Primitive - P3121 (152) - 3 - 112.985 - I/I
- 00-052-1572 (Q) - Antigorite - Mg<sub>3</sub>Si<sub>2</sub>O<sub>5</sub>(OH)<sub>4</sub> - Y: 38.74 % - d x by: 1. - WL: 1.5406 - Monoclinic - a 5.42400 - b 9.23800 - c 7.27400 - alpha 90.000 - beta 91.320 - gamma 90.000 - Primitive - P (0) - 2 - 364.381 - F24
- 01-072-1385 (C) - Clinocllore, chromian 1Mla-4 - Mg<sub>5</sub>Al<sub>1</sub>2Si<sub>3</sub>Cr<sub>7</sub>O<sub>10</sub>(OH)<sub>8</sub> - Y: 22.95 % - d x by: 1. - WL: 1.5406 - Triclinic - a 5.33800 - b 9.24700 - c 14.43500 - alpha 90.000 - beta 97.080 - gamma 90.000 - Bas
- 01-083-1768 (C) - Talc - Mg<sub>3</sub>(OH)<sub>2</sub>Si<sub>4</sub>O<sub>10</sub> - Y: 16.80 % - d x by: 1. - WL: 1.5406 - Triclinic - a 5.29000 - b 9.17300 - c 9.46000 - alpha 90.460 - beta 98.680 - gamma 90.090 - Base-centered - C-1 (0) - 2 - 453.774 - I/lc
- 00-037-0471 (\*) - Chalcopyrite - CuFeS<sub>2</sub> - Y: 57.24 % - d x by: 1. - WL: 1.5406 - Tetragonal - a 5.28930 - b 5.28930 - c 10.42300 - alpha 90.000 - beta 90.000 - gamma 90.000 - Body-centered - I-42d (122) - 4 - 291.60

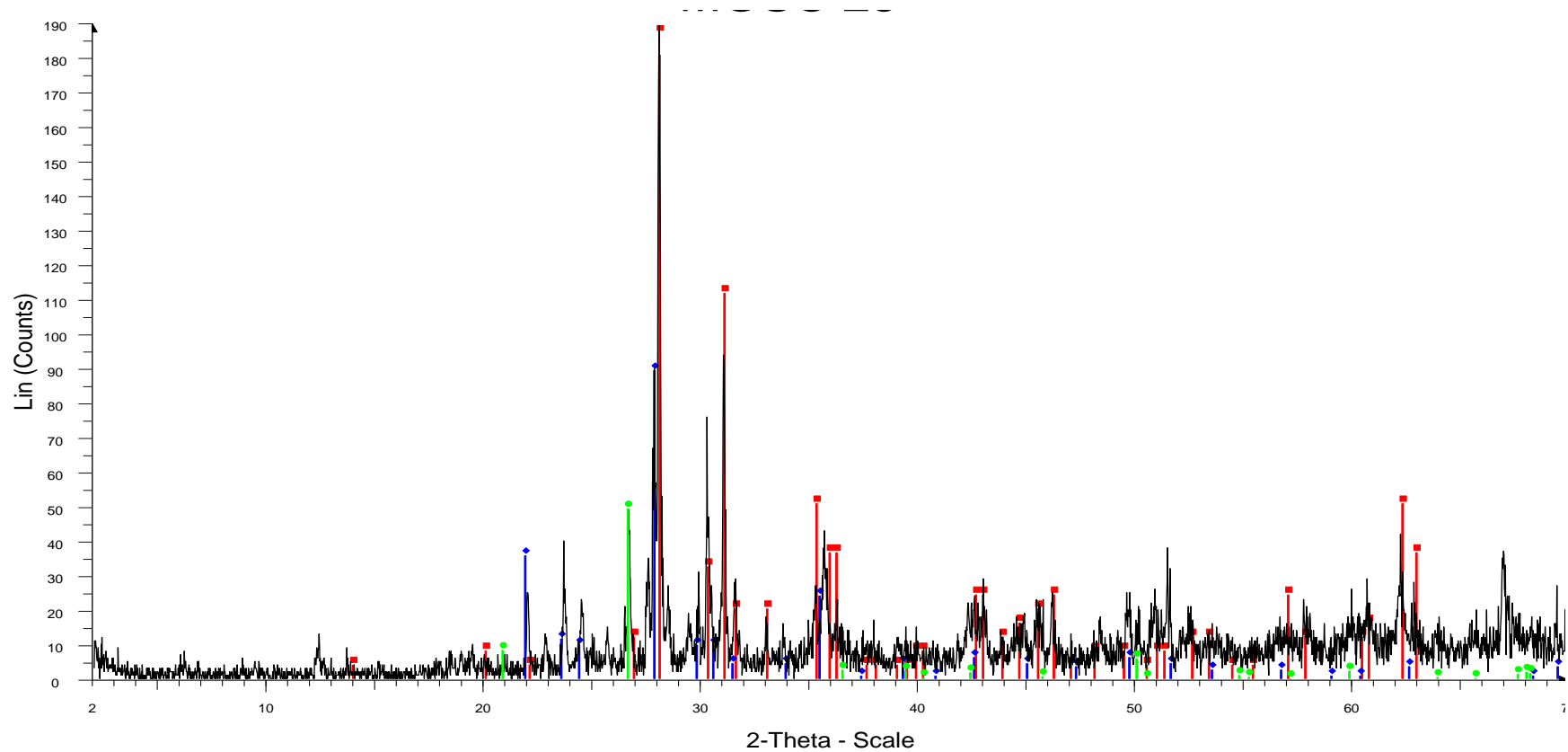
Sample 22



MGSC 24 - File: MGSC 24.raw - Type: 2Th/Th locked - Start: 2.000 ° - End: 70.000 ° - Step: 0.020 ° - Step time: 1. s - Temp.: 25 °C (Room) - Time Started: 17 s - 2-Theta: 2.000 ° - Theta: 1.000 ° - Chi: 0.00 ° - Phi: 0.0  
 Operations: Import  
 00-022-0714 (D) - Enstatite, ordered - MgSiO<sub>3</sub> - Y: 123.72 % - d x by: 1. - WL: 1.5406 - Orthorhombic - a 18.23000 - b 8.84000 - c 5.19000 - alpha 90.000 - beta 90.000 - gamma 90.000 - Primitive - Pbc<sub>a</sub> (61) - 16 - 83  
 00-002-0676 (D) - Augite - N(CaO.(Mg,Fe)O.2SiO<sub>2</sub>).(Al,Fe)<sub>2</sub>O<sub>3</sub> - Y: 18.99 % - d x by: 1. - WL: 1.5406 -  
 01-070-3318 (C) - Quartz, syn - SiO<sub>2</sub> - Y: 19.62 % - d x by: 1. - WL: 1.5406 - Hexagonal - a 4.54500 - b 4.54500 - c 5.16300 - alpha 90.000 - beta 90.000 - gamma 120.000 - Primitive - P3121 (152) - 3 - 92.3635 - I/c

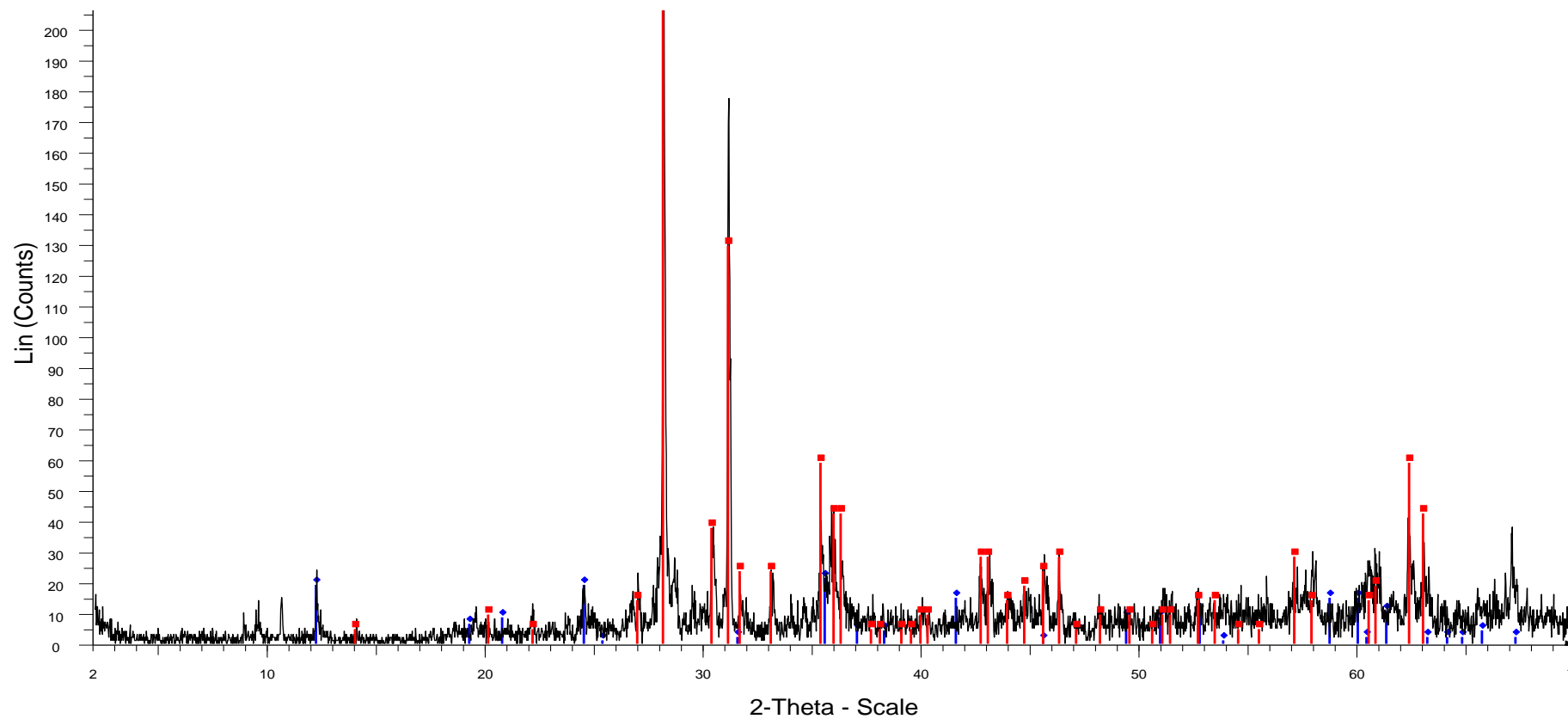
Sample 24





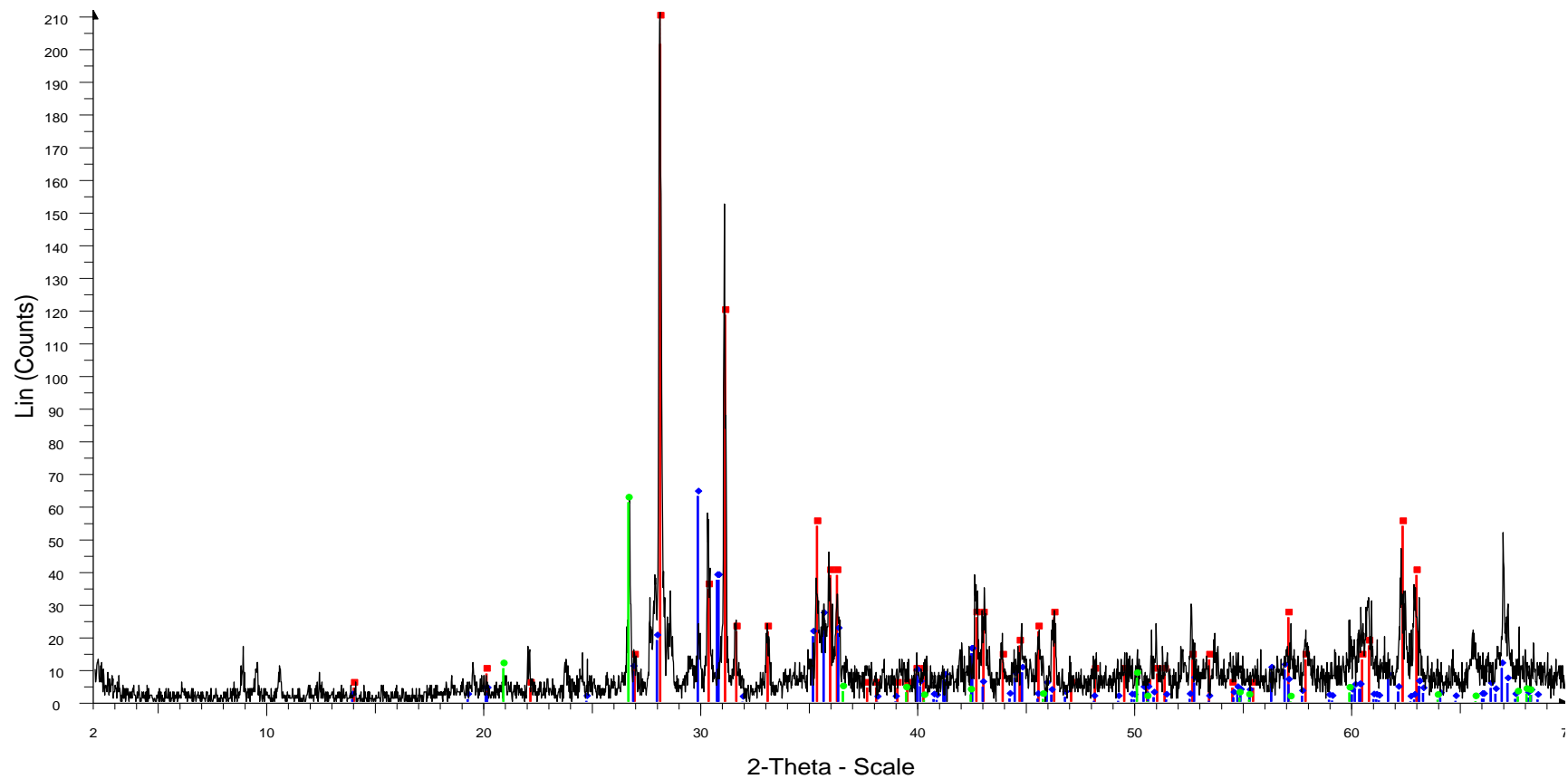
MGSC 25 - File: MGSC 25.raw - Type: 2Th/Th locked - Start: 2.000 ° - End: 70.000 ° - Step: 0.020 ° - Step time: 1. s - Temp.: 25 °C (Room) - Time Started: 17 s - 2-Theta: 2.000 ° - Theta: 1.000 ° - Chi: 0.00 ° - Phi: 0.0  
 Operations: Import  
 00-022-0714 (D) - Enstatite, ordered - MgSiO<sub>3</sub> - Y: 107.27 % - d x by: 1. - WL: 1.5406 - Orthorhombic - a 18.23000 - b 8.84000 - c 5.19000 - alpha 90.000 - beta 90.000 - gamma 90.000 - Primitive - Pbc<sub>a</sub> (61) - 16 - 83  
 00-003-0499 (D) - Labradorite - (Na<sub>0.4</sub>Ca<sub>0.6</sub>)Al<sub>1.6</sub>Si<sub>2.4</sub>O<sub>8</sub> - Y: 47.17 % - d x by: 1. - WL: 1.5406 - Triclinic - a 8.21000 - b 12.95000 - c 14.16000 - alpha 93.520 - beta 116.050 - gamma 89.920 - 1349.44 - F22= 2(0.0  
 03-065-0466 (C) - Quartz low, syn - SiO<sub>2</sub> - Y: 26.05 % - d x by: 1. - WL: 1.5406 - Hexagonal - a 4.91410 - b 4.91410 - c 5.40600 - alpha 90.000 - beta 90.000 - gamma 120.000 - Primitive - P3221 (154) - 3 - 113.056 - I

Sample 25



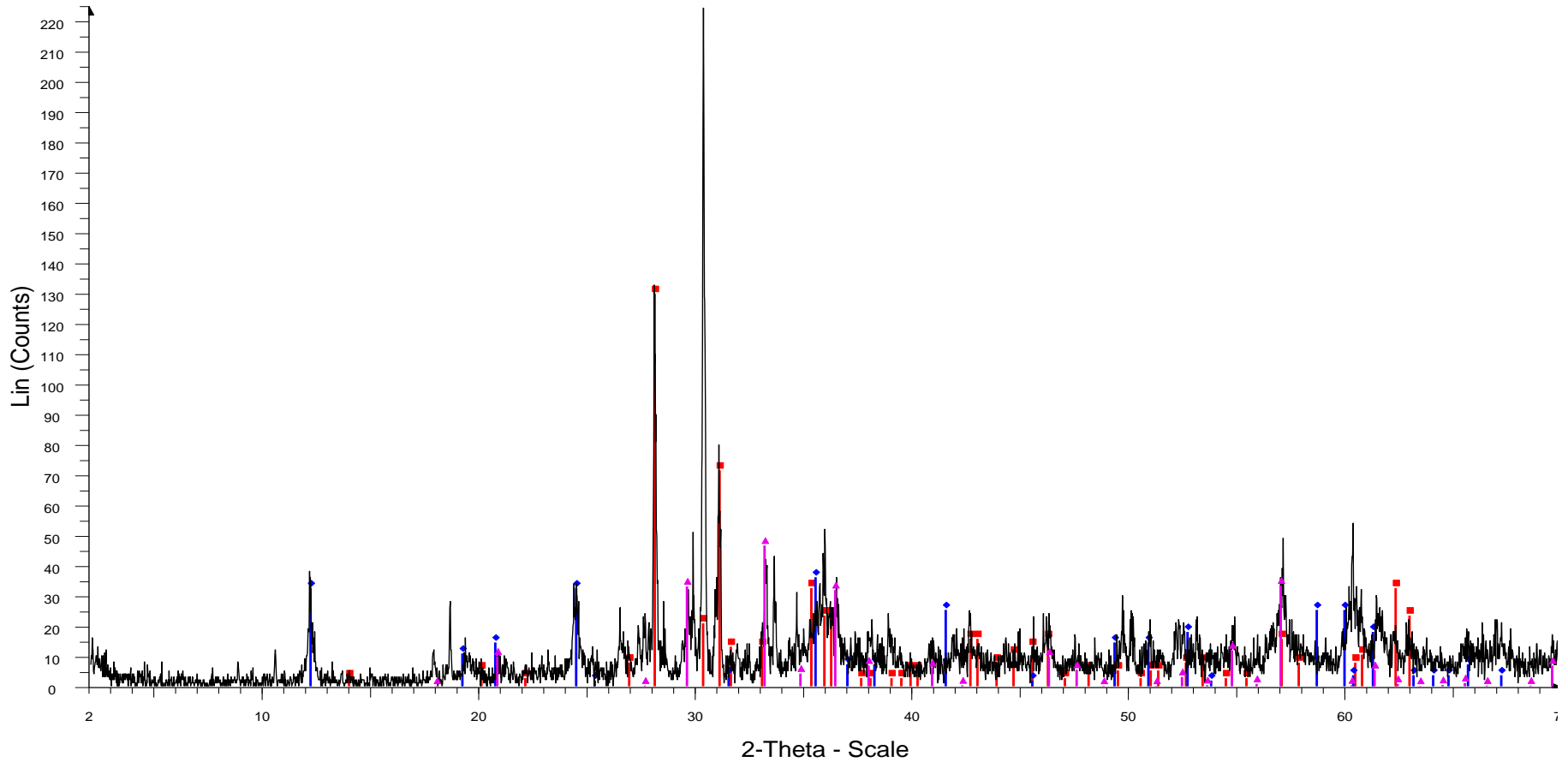
MGSC 27 - File: MGSC 27.raw - Type: 2Th/Th locked - Start: 2.000 ° - End: 70.000 ° - Step: 0.020 ° - Step time: 1. s - Temp.: 25 °C (Room) - Time Started: 17 s - 2-Theta: 2.000 ° - Theta: 1.000 ° - Chi: 0.00 ° - Phi: 0.0  
 Operations: Import  
 00-022-0714 (D) - Enstatite, ordered - MgSiO<sub>3</sub> - Y: 106.42 % - d x by: 1. - WL: 1.5406 - Orthorhombic - a 18.23000 - b 8.84000 - c 5.19000 - alpha 90.000 - beta 90.000 - gamma 90.000 - Primitive - Pbc<sub>a</sub> (61) - 16 - 83  
 00-002-1036 (D) - Antigorite - 3MgO·2SiO<sub>2</sub>·2H<sub>2</sub>O - Y: 9.61 % - d x by: 1. - WL: 1.5406 - Monoclinic - a 5.42000 - b 9.23800 - c 7.27500 - alpha 90.000 - beta 91.670 - gamma 90.000 - Primitive - P (0) - 2 - 364.104 - F

Sample 27



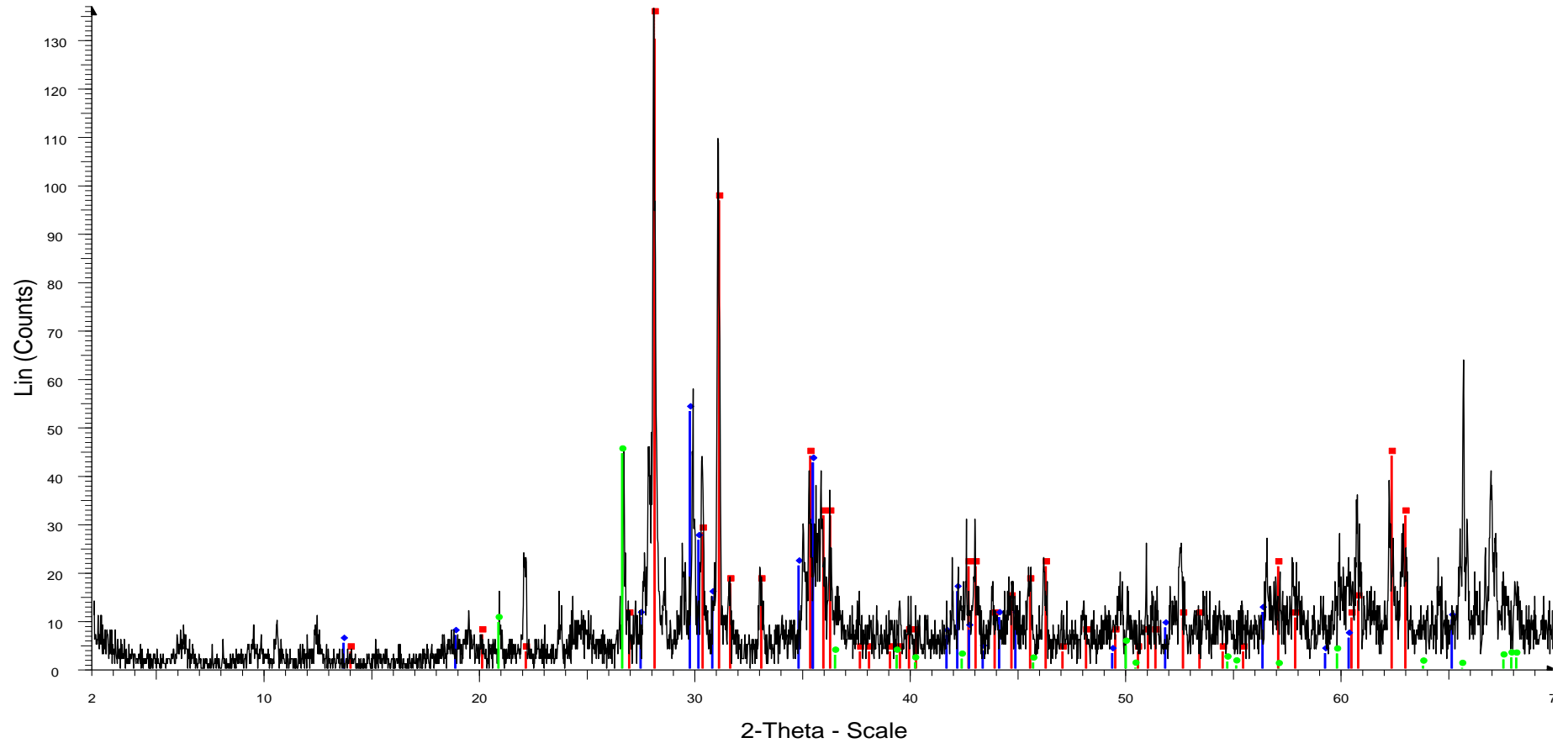
MGSC 30 - File: MGSC 30.raw - Type: 2Th/Th locked - Start: 2.000 ° - End: 70.000 ° - Step: 0.020 ° - Step time: 1. s - Temp.: 25 °C (Room) - Time Started: 17 s - 2-Theta: 2.000 ° - Theta: 1.000 ° - Chi: 0.00 ° - Phi: 0.0  
 Operations: Import  
 ■ 00-022-0714 (D) - Enstatite, ordered - MgSiO<sub>3</sub> - Y: 102.06 % - d x by: 1. - WL: 1.5406 - Orthorhombic - a 18.23000 - b 8.84000 - c 5.19000 - alpha 90.000 - beta 90.000 - gamma 90.000 - Primitive - Pbc<sub>a</sub> (61) - 16 - 83  
 ◆ 01-082-1227 (C) - Augite, syn - (Ca<sub>0.774</sub>Na<sub>0.226</sub>)(Mg<sub>0.901</sub>Fe<sub>0.099</sub>)Fe<sub>0.011</sub>(Si<sub>2</sub>O<sub>6</sub>) - Y: 29.85 % - d x by: 1. - WL: 1.5406 - Monoclinic - a 9.68900 - b 8.82400 - c 5.28000 - alpha 90.000 - beta 107.600 - gamma 90.0  
 ● 03-065-0466 (C) - Quartz low, syn - SiO<sub>2</sub> - Y: 28.94 % - d x by: 1. - WL: 1.5406 - Hexagonal - a 4.91410 - b 4.91410 - c 5.40600 - alpha 90.000 - beta 90.000 - gamma 120.000 - Primitive - P3221 (154) - 3 - 113.056 - I

Sample 30



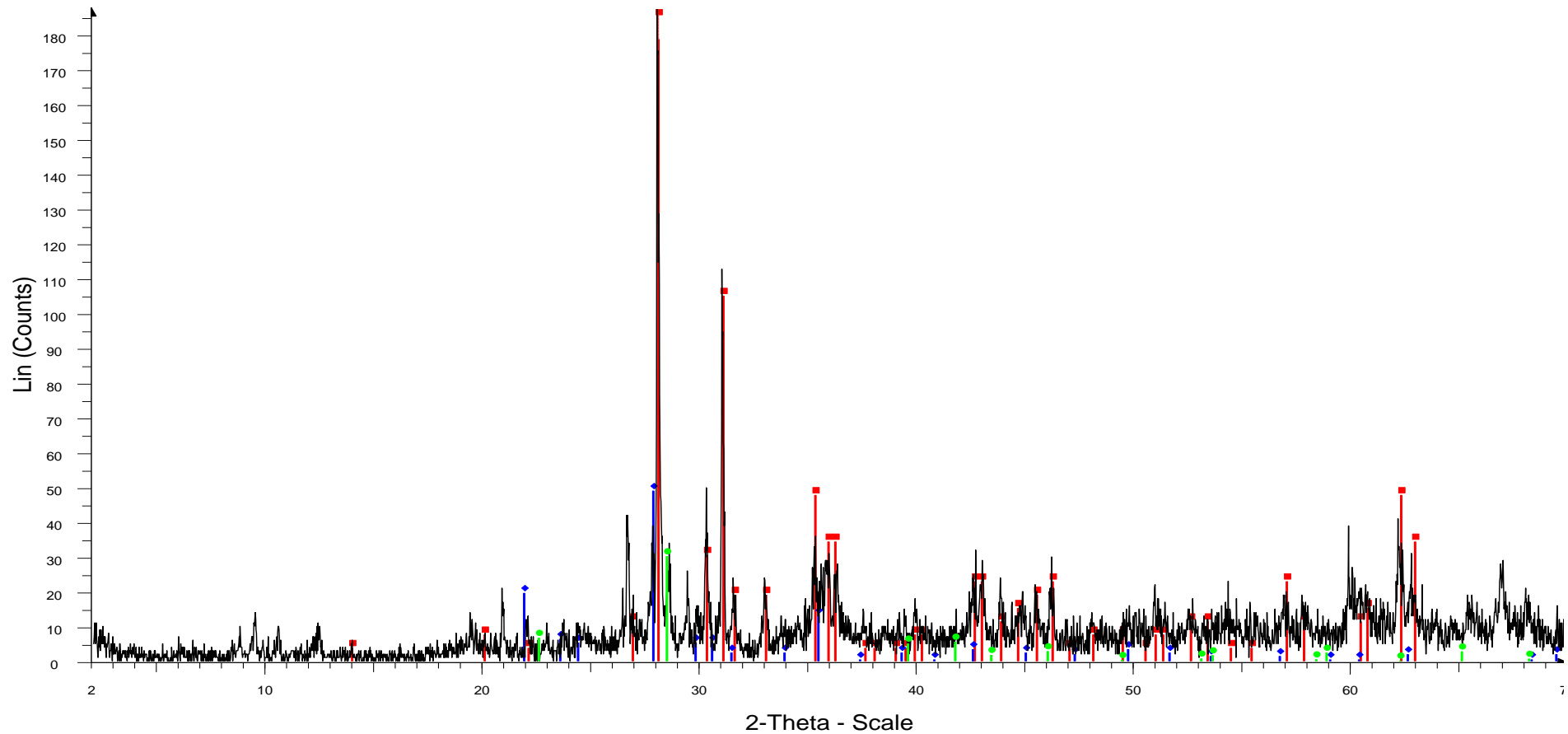
MGSC 32 - File: MGSC 32.raw - Type: 2Th/Th locked - Start: 2.000 ° - End: 70.000 ° - Step: 0.020 ° - Step time: 1. s - Temp.: 25 °C (Room) - Time Started: 18 s - 2-Theta: 2.000 ° - Theta: 1.000 ° - Chi: 0.00 ° - Phi: 0.0  
 Operations: Import  
 ■ 00-022-0714 (D) - Enstatite, ordered - MgSiO<sub>3</sub> - Y: 57.82 % - d x by: 1. - WL: 1.5406 - Orthorhombic - a 18.23000 - b 8.84000 - c 5.19000 - alpha 90.000 - beta 90.000 - gamma 90.000 - Primitive - Pbc<sub>a</sub> (61) - 16 - 836  
 ◆ 00-002-1036 (D) - Antigorite - 3MgO·2SiO<sub>2</sub>·2H<sub>2</sub>O - Y: 16.03 % - d x by: 1. - WL: 1.5406 - Monoclinic - a 5.42000 - b 9.23800 - c 7.27500 - alpha 90.000 - beta 91.670 - gamma 90.000 - Primitive - P (0) - 2 - 364.104 -  
 ▲ 01-084-2160 (A) - Andradite - Ca<sub>3</sub>Fe<sub>2</sub>(SiO<sub>4</sub>)<sub>3</sub> - Y: 20.72 % - d x by: 1. - WL: 1.5406 - Cubic - a 12.06430 - b 12.06430 - c 12.06430 - alpha 90.000 - beta 90.000 - gamma 90.000 - Body-centered - Ia-3d (230) - 8 - 175

Sample 32



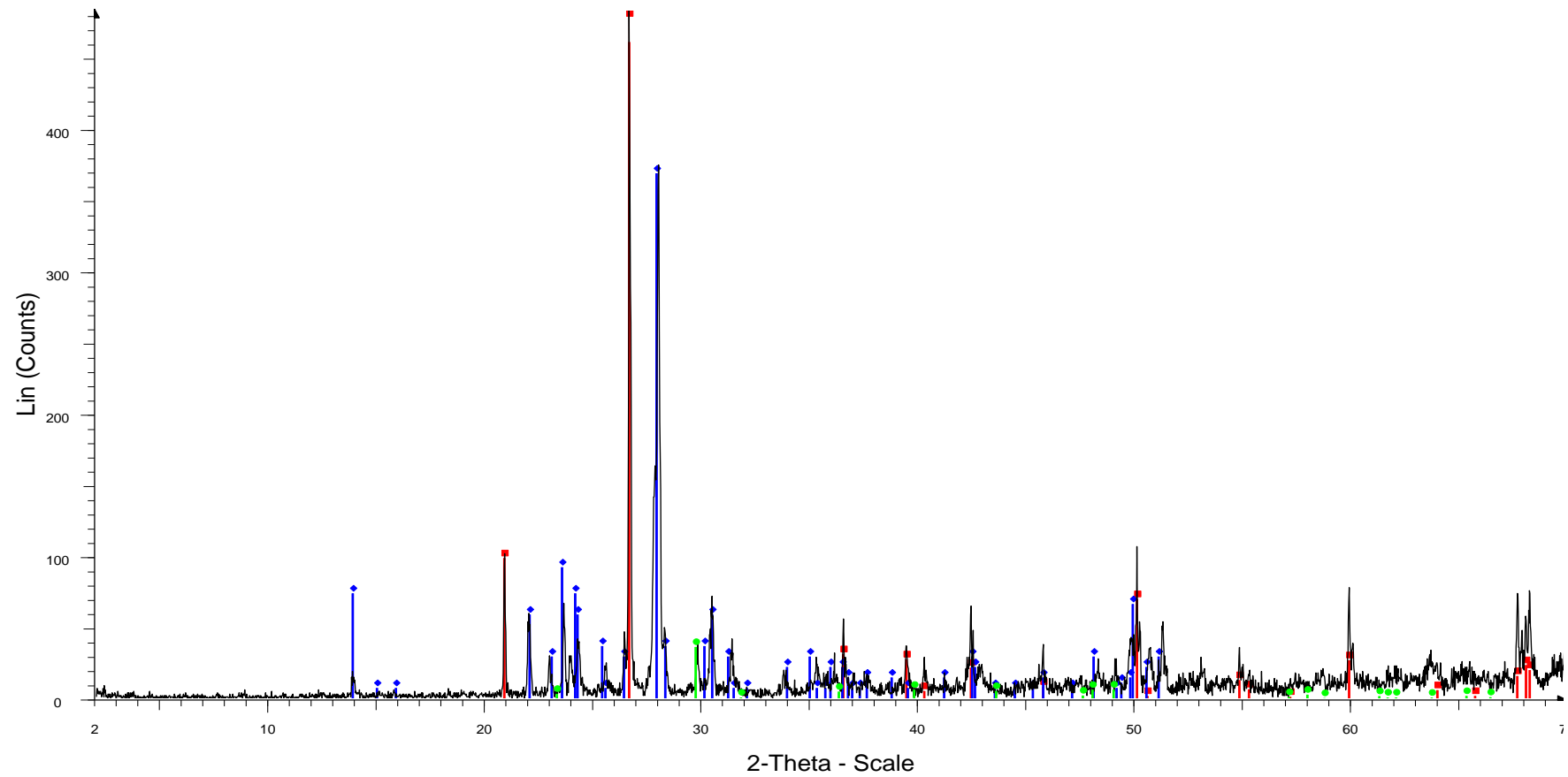
MGSC 33 - File: MGSC 33.raw - Type: 2Th/Th locked - Start: 2.000 ° - End: 70.000 ° - Step: 0.020 ° - Step time: 1. s - Temp.: 25 °C (Room) - Time Started: 17 s - 2-Theta: 2.000 ° - Theta: 1.000 ° - Chi: 0.00 ° - Phi: 0.0  
 Operations: Import  
 ■ 00-022-0714 (D) - Enstatite, ordered - MgSiO<sub>3</sub> - Y: 128.97 % - d x by: 1. - WL: 1.5406 - Orthorhombic - a 18.23000 - b 8.84000 - c 5.19000 - alpha 90.000 - beta 90.000 - gamma 90.000 - Primitive - Pbc<sub>a</sub> (61) - 16 - 83  
 ◆ 00-024-0201 (I) - Augite - Ca(Fe,Mg)Si<sub>2</sub>O<sub>6</sub> - Y: 39.00 % - d x by: 1. - WL: 1.5406 - Monoclinic - a 9.78300 - b 8.96500 - c 5.27200 - alpha 90.000 - beta 105.710 - gamma 90.000 - Base-centered - C2/c (15) - 4 - 445.1  
 ● 01-070-2517 (A) - Quartz low - theoretical - SiO<sub>2</sub> - Y: 32.61 % - d x by: 1. - WL: 1.5406 - Hexagonal - a 4.92000 - b 4.92000 - c 5.42000 - alpha 90.000 - beta 90.000 - gamma 120.000 - Primitive - P3221 (154) - 3 - 113

Sample 33



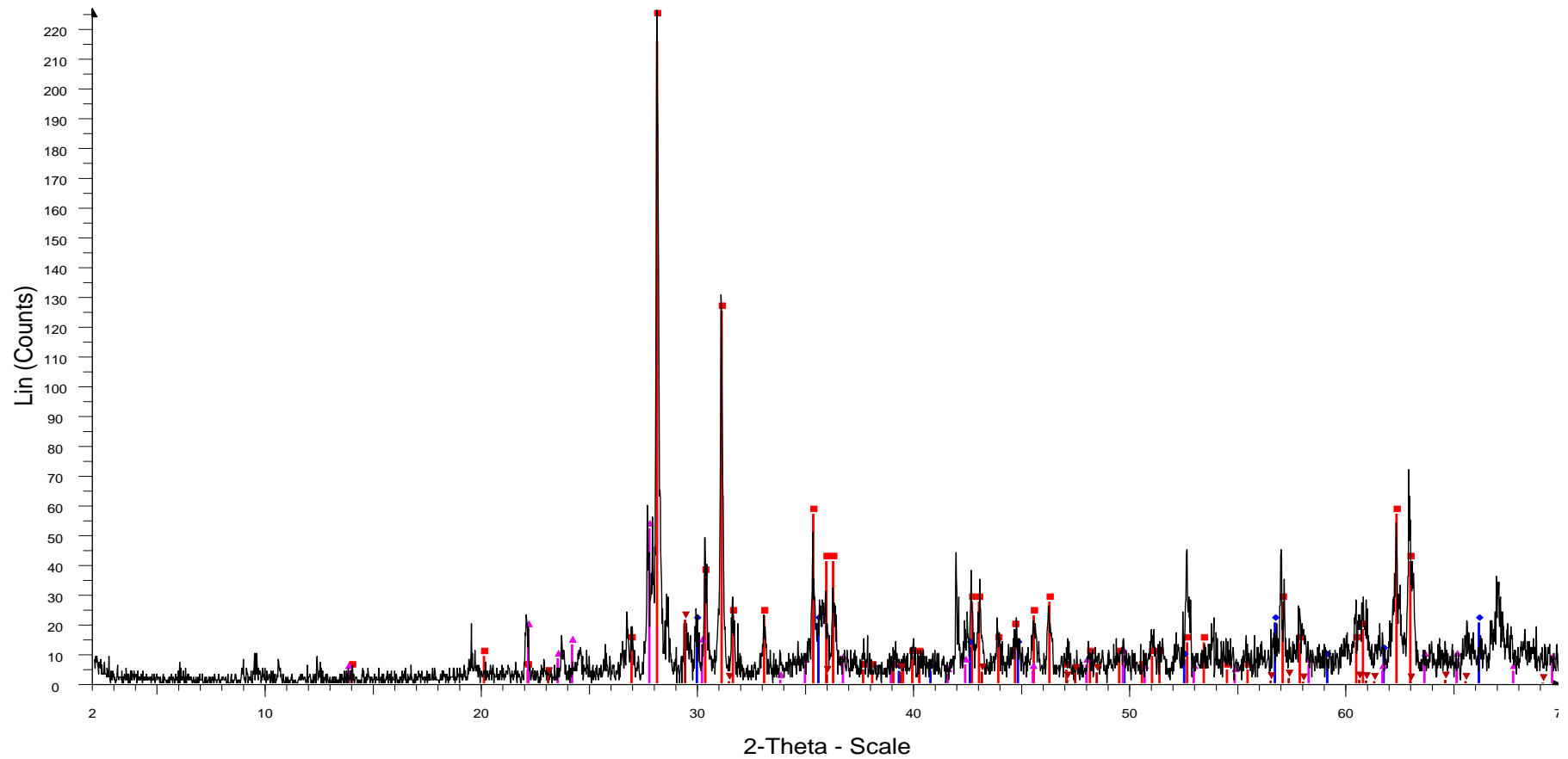
MGSC 34 - File: MGSC 34.raw - Type: 2Th/Th locked - Start: 2.000 ° - End: 70.000 ° - Step: 0.020 ° - Step time: 1. s - Temp.: 25 °C (Room) - Time Started: 17 s - 2-Theta: 2.000 ° - Theta: 1.000 ° - Chi: 0.00 ° - Phi: 0.0  
 Operations: Import  
 00-022-0714 (D) - Enstatite, ordered - MgSiO<sub>3</sub> - Y: 101.95 % - d x by: 1. - WL: 1.5406 - Orthorhombic - a 18.23000 - b 8.84000 - c 5.19000 - alpha 90.000 - beta 90.000 - gamma 90.000 - Primitive - Pbc<sub>a</sub> (61) - 16 - 83  
 00-003-0499 (D) - Labradorite - (Na<sub>0.4</sub>Ca<sub>0.6</sub>)Al<sub>1.6</sub>Si<sub>2.4</sub>O<sub>8</sub> - Y: 26.14 % - d x by: 1. - WL: 1.5406 - Triclinic - a 8.21000 - b 12.95000 - c 14.16000 - alpha 93.520 - beta 116.050 - gamma 89.920 - 1349.44 - F22= 2(0.0  
 01-070-3318 (C) - Quartz, syn - SiO<sub>2</sub> - Y: 16.11 % - d x by: 1. - WL: 1.5406 - Hexagonal - a 4.54500 - b 4.54500 - c 5.16300 - alpha 90.000 - beta 90.000 - gamma 120.000 - Primitive - P3121 (152) - 3 - 92.3635 - I/Ic

Sample 34



MGSC 37 - File: MGSC 37.raw - Type: 2Th/Th locked - Start: 2.000 ° - End: 70.000 ° - Step: 0.020 ° - Step time: 1. s - Temp.: 25 °C (Room) - Time Started: 18 s - 2-Theta: 2.000 ° - Theta: 1.000 ° - Chi: 0.00 ° - Phi: 0.0  
 Operations: Import  
 03-065-0466 (C) - Quartz low, syn - SiO<sub>2</sub> - Y: 121.33 % - d x by: 1. - WL: 1.5406 - Hexagonal - a 4.91410 - b 4.91410 - c 5.40600 - alpha 90.000 - beta 90.000 - gamma 120.000 - Primitive - P3221 (154) - 3 - 113.056 -  
 00-009-0466 (\*) - Albite, ordered - NaAlSi<sub>3</sub>O<sub>8</sub> - Y: 76.34 % - d x by: 1. - WL: 1.5406 - Triclinic - a 8.14400 - b 12.78700 - c 7.16000 - alpha 94.260 - beta 116.600 - gamma 87.670 - Base-centered - C-1 (0) - 4 - 664.83  
 01-071-1663 (C) - Calcite, magnesian - Mg<sub>0.1</sub>Ca<sub>0.9</sub>CO<sub>3</sub> - Y: 7.50 % - d x by: 1. - WL: 1.5406 - Rhombo.H.axes - a 4.94100 - b 4.94100 - c 16.86400 - alpha 90.000 - beta 90.000 - gamma 120.000 - Primitive - R-3c (1)

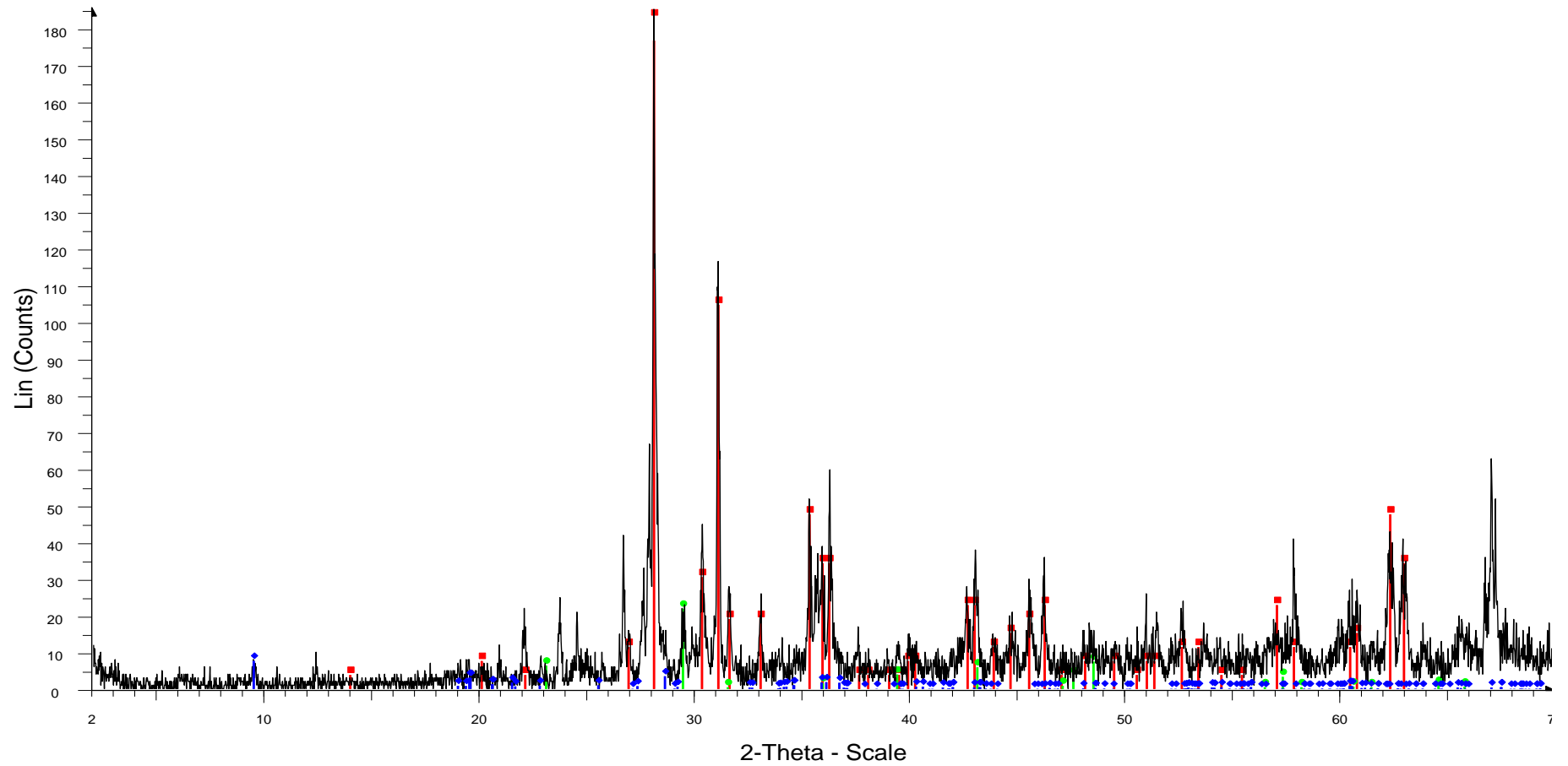
Sample 37



MGSC 39 - File: MGSC 39.raw - Type: 2Th/Th locked - Start: 2.000 ° - End: 70.000 ° - Step: 0.020 ° - Step time: 1. s - Temp.: 25 °C (Room) - Time Started: 17 s - 2-Theta: 2.000 ° - Theta: 1.000 ° - Chi: 0.00 ° - Phi: 0.0  
 Operations: Import  
 ■ 00-022-0714 (D) - Enstatite, ordered - MgSiO<sub>3</sub> - Y: 100.65 % - d x by: 1. - WL: 1.5406 - Orthorhombic - a 18.23000 - b 8.84000 - c 5.19000 - alpha 90.000 - beta 90.000 - gamma 90.000 - Primitive - Pbca (61) - 16 - 83  
 ◆ 00-002-0676 (D) - Augite - N(CaO·(Mg,Fe)O·2SiO<sub>2</sub>)·(Al,Fe)<sub>2</sub>O<sub>3</sub> - Y: 8.99 % - d x by: 1. - WL: 1.5406 -  
 ▲ 00-001-0739 (D) - Albite - NaAlSi<sub>3</sub>O<sub>8</sub> - Y: 23.01 % - d x by: 1. - WL: 1.5406 - Triclinic - a 8.10000 - b 12.90000 - c 7.20000 - alpha 94.000 - beta 116.600 - gamma 88.000 - Base-centered - C-1 (0) - 4 - 671.053 - F30=  
 ▼ 00-005-0586 (\*) - Calcite, syn - CaCO<sub>3</sub> - Y: 9.41 % - d x by: 1. - WL: 1.5406 - Rhombo.H.axes - a 4.98900 - b 4.98900 - c 17.06200 - alpha 90.000 - beta 90.000 - gamma 120.000 - Primitive - R-3c (167) - 6 - 367.780 -

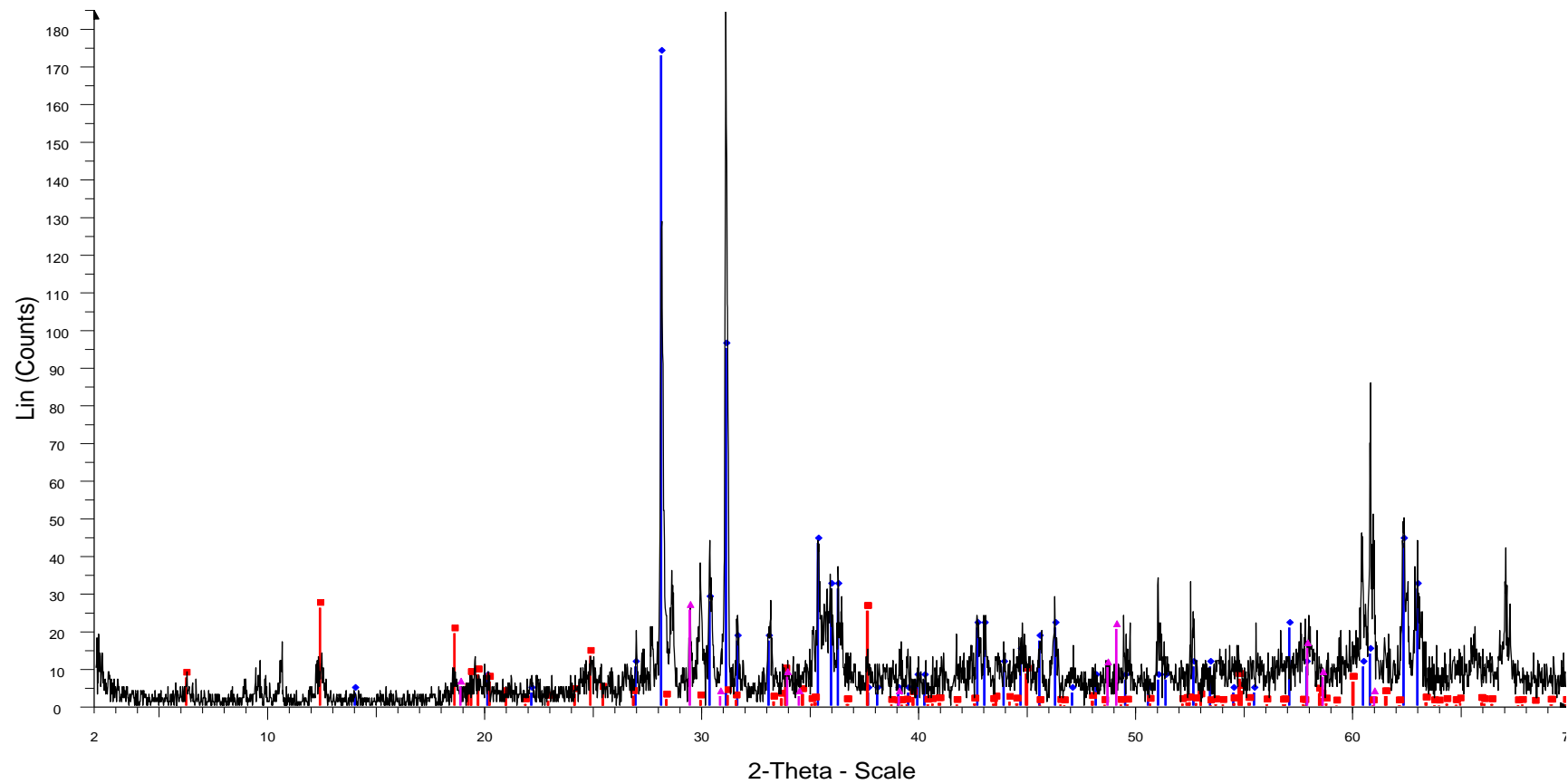
Sample 39





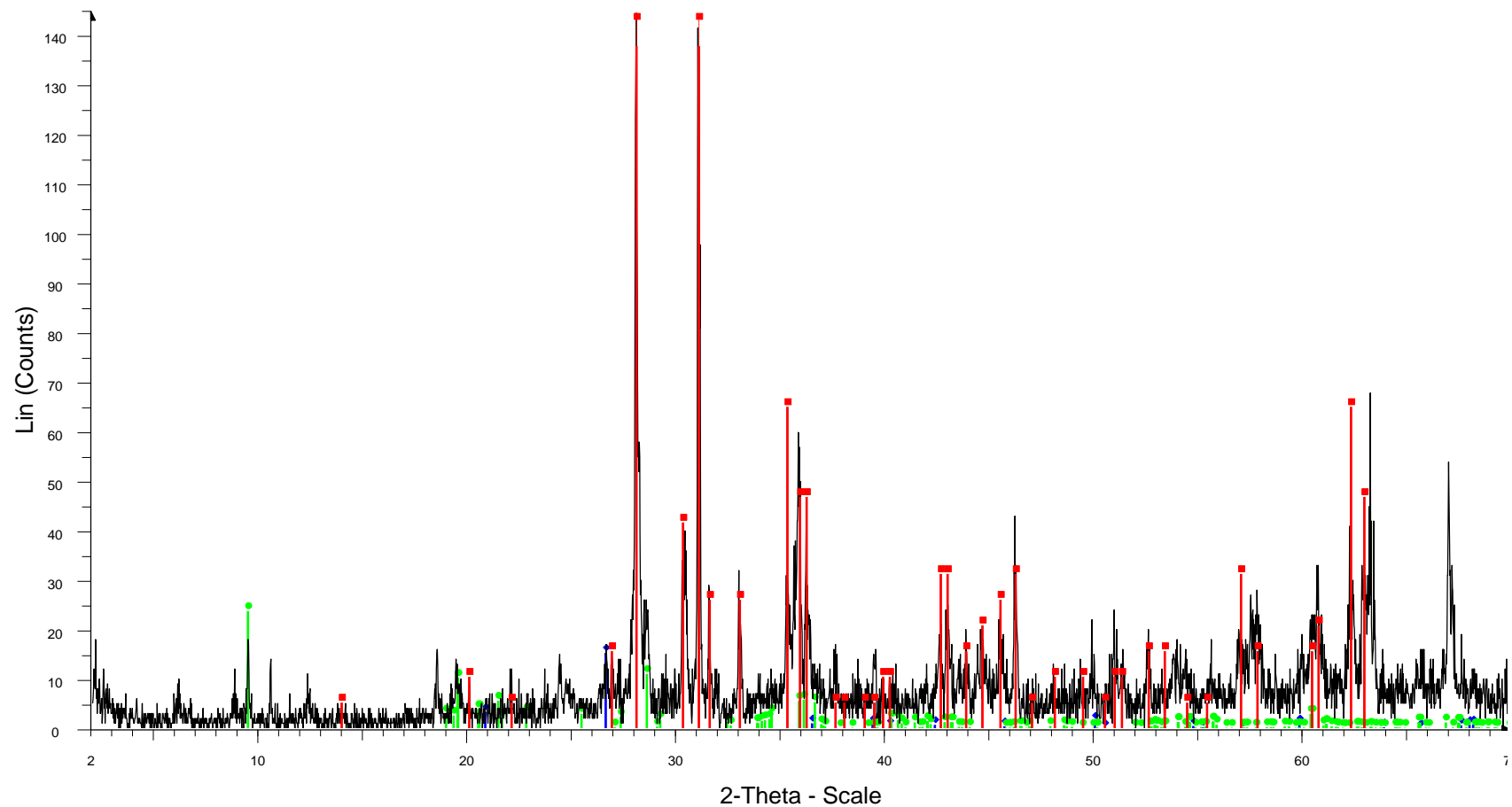
MGSC 42 - File: MGSC 42.raw - Type: 2Th/Th locked - Start: 2.000 ° - End: 70.000 ° - Step: 0.020 ° - Step time: 1. s - Temp.: 25 °C (Room) - Time Started: 17 s - 2-Theta: 2.000 ° - Theta: 1.000 ° - Chi: 0.00 ° - Phi: 0.0  
 Operations: Import  
■ 00-022-0714 (D) - Enstatite, ordered - MgSiO<sub>3</sub> - Y: 102.83 % - d x by: 1. - WL: 1.5406 - Orthorhombic - a 18.23000 - b 8.84000 - c 5.19000 - alpha 90.000 - beta 90.000 - gamma 90.000 - Primitive - Pbc<sub>a</sub> (61) - 16 - 83  
● 00-024-0027 (D) - Calcite - CaCO<sub>3</sub> - Y: 11.82 % - d x by: 1. - WL: 1.5406 - Rhombo.H.axes - a 4.99000 - b 4.99000 - c 17.00200 - alpha 90.000 - beta 90.000 - gamma 120.000 - Primitive - R-3c (167) - 6 - 366.633 - F  
◆ 01-083-1768 (C) - Talc - Mg<sub>3</sub>(OH)<sub>2</sub>Si<sub>4</sub>O<sub>10</sub> - Y: 4.15 % - d x by: 1. - WL: 1.5406 - Triclinic - a 5.29000 - b 9.17300 - c 9.46000 - alpha 90.460 - beta 98.680 - gamma 90.090 - Base-centered - C-1 (0) - 2 - 453.774 - I/lc

Sample 42



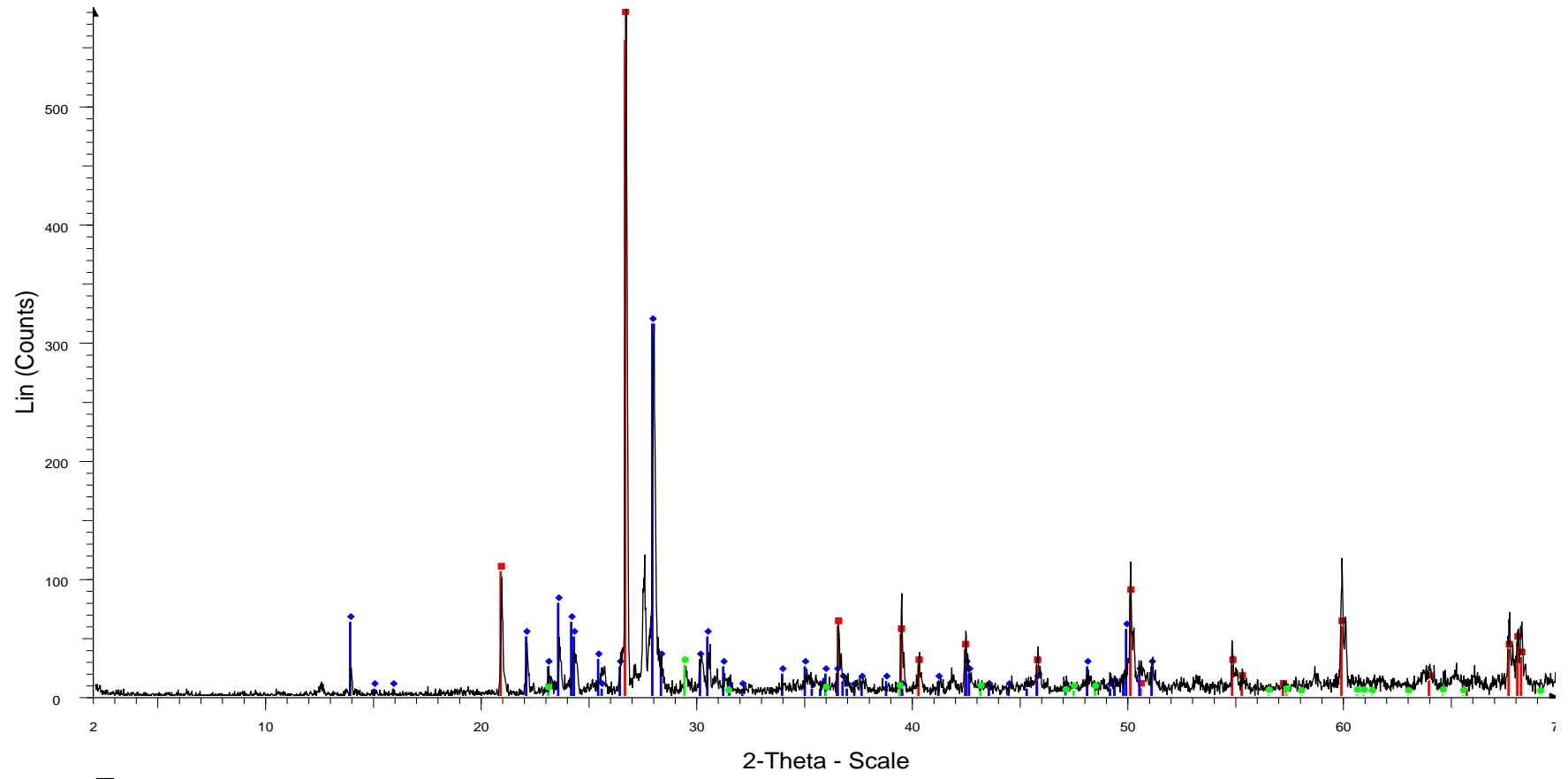
MGSC 43 - File: MGSC 43.raw - Type: 2Th/Th locked - Start: 2.000 ° - End: 70.000 ° - Step: 0.020 ° - Step time: 1. s - Temp.: 25 °C (Room) - Time Started: 17 s - 2-Theta: 2.000 ° - Theta: 1.000 ° - Chi: 0.00 ° - Phi: 0.0  
 Operations: Import  
 00-022-0714 (D) - Enstatite, ordered - MgSiO<sub>3</sub> - Y: 93.69 % - d x by: 1. - WL: 1.5406 - Orthorhombic - a 18.23000 - b 8.84000 - c 5.19000 - alpha 90.000 - beta 90.000 - gamma 90.000 - Primitive - Pbc<sub>a</sub> (61) - 16 - 836  
 01-078-2063 (C) - Clinocllore la chromian - (Mg<sub>5.0</sub>Fe<sub>0.1</sub>Cr<sub>0.7</sub>Al<sub>0.2</sub>)(Si<sub>3</sub>AlO<sub>10</sub>)(OH<sub>0.9875</sub>)<sub>8</sub> - Y: 14.09 % - d x by: 1. - WL: 1.5406 - Triclinic - a 5.32900 - b 9.24600 - c 14.44200 - alpha 90.000 - beta 97.080 - gamma  
 00-025-0288 (D) - Chalcopyrite - CuFeS<sub>2</sub> - Y: 13.82 % - d x by: 1. - WL: 1.5406 - Tetragonal - a 5.28100 - b 5.28100 - c 10.40100 - alpha 90.000 - beta 90.000 - gamma 90.000 - Body-centered - I-42d (122) - 4 - 290.0

Sample 43



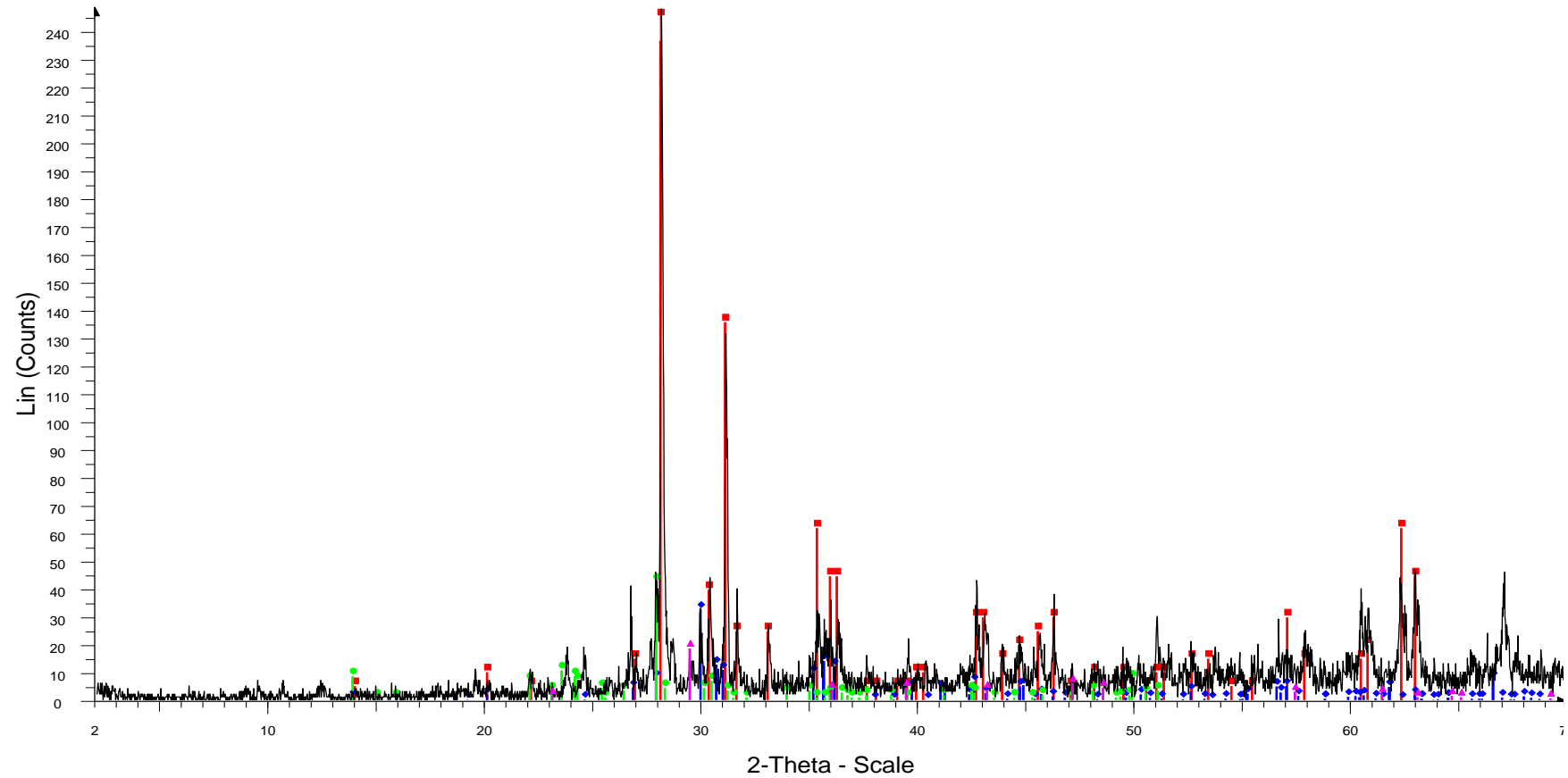
MGSC 44 - File: MGSC 44.raw - Type: 2Th/Th locked - Start: 2.000 ° - End: 70.000 ° - Step: 0.020 ° - Step time: 1. s - Temp.: 25 °C (Room) - Time Started: 17 s - 2-Theta: 2.000 ° - Theta: 1.000 ° - Chi: 0.00 ° - Phi: 0.0  
 Operations: Import  
 00-022-0714 (D) - Enstatite, ordered - MgSiO<sub>3</sub> - Y: 179.87 % - d x by: 1. - WL: 1.5406 - Orthorhombic - a 18.23000 - b 8.84000 - c 5.19000 - alpha 90.000 - beta 90.000 - gamma 90.000 - Primitive - Pbc<sub>a</sub> (61) - 16 - 83  
 01-070-3755 (C) - Quartz - SiO<sub>2</sub> - Y: 10.55 % - d x by: 1. - WL: 1.5406 - Hexagonal - a 4.91600 - b 4.91600 - c 5.40900 - alpha 90.000 - beta 90.000 - gamma 120.000 - Primitive - P3121 (152) - 3 - 113.206 - I/lc PDF  
 01-073-0147 (A) - Talc 1A - Mg<sub>3</sub>(Si<sub>2</sub>O<sub>5</sub>)<sub>2</sub>(OH)<sub>2</sub> - Y: 16.39 % - d x by: 1. - WL: 1.5406 - Triclinic - a 5.29300 - b 9.17900 - c 9.46900 - alpha 90.570 - beta 98.910 - gamma 90.030 - Base-centered - C-1 (0) - 2 - 454.471

Sample 44



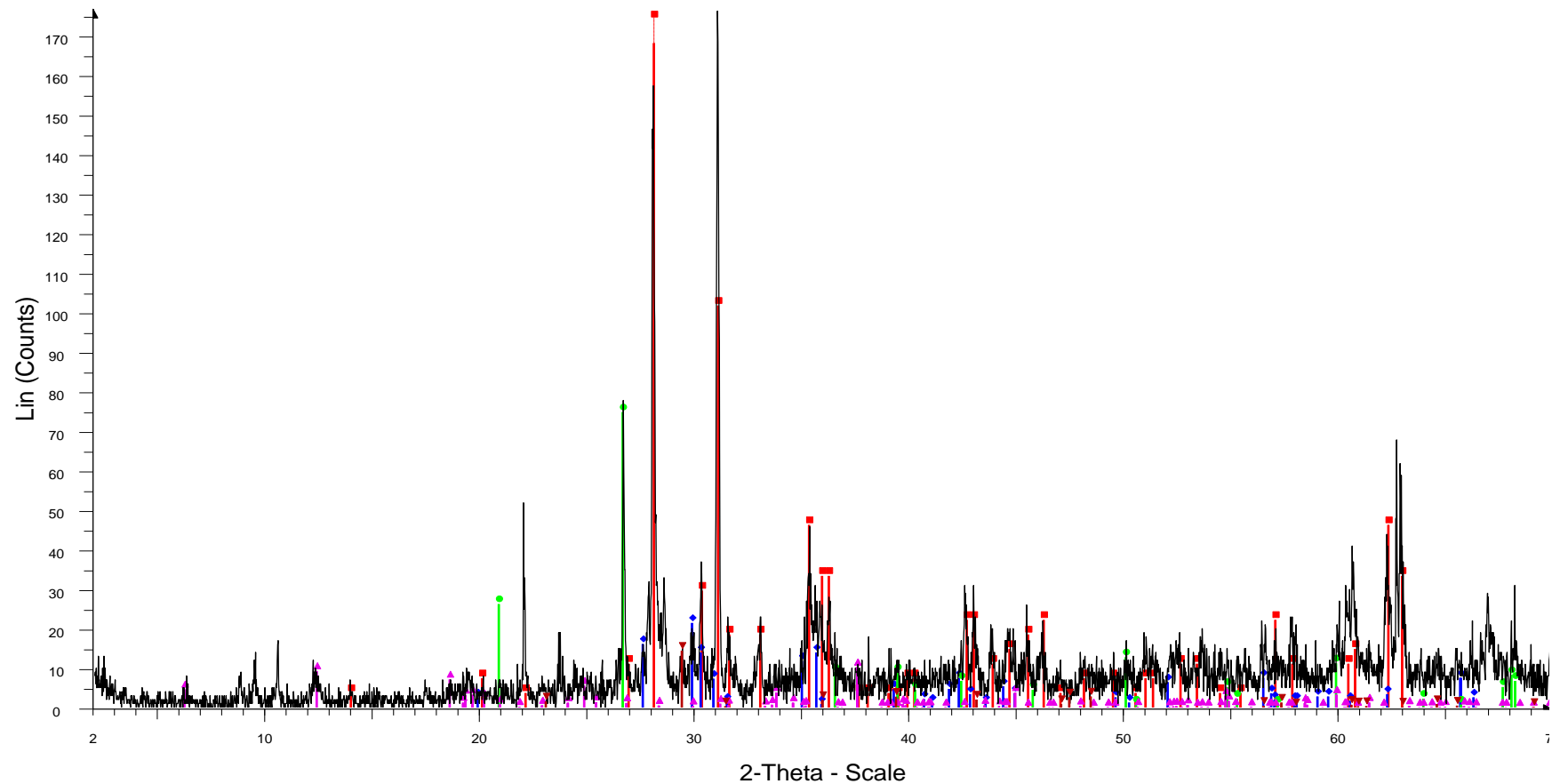
MGSC 48 - File: MGSC 48.raw - Type: 2Th/Th locked - Start: 2.000 ° - End: 70.000 ° - Step: 0.020 ° - Step time: 1. s - Temp.: 25 °C (Room) - Time Started: 34 s - 2-Theta: 2.000 ° - Theta: 1.000 ° - Chi: 0.00 ° - Phi: 0.0  
 Operations: Import  
 00-046-1045 (\*) - Quartz, syn - SiO<sub>2</sub> - Y: 113.40 % - d x by: 1. - WL: 1.5406 - Hexagonal - a 4.91344 - b 4.91344 - c 5.40524 - alpha 90.000 - beta 90.000 - gamma 120.000 - Primitive - P3221 (154) - 3 - 113.010 - I/c  
 00-009-0466 (\*) - Albite, ordered - NaAlSi<sub>3</sub>O<sub>8</sub> - Y: 54.23 % - d x by: 1. - WL: 1.5406 - Triclinic - a 8.14400 - b 12.78700 - c 7.16000 - alpha 94.260 - beta 116.600 - gamma 87.670 - Base-centered - C-1 (0) - 4 - 664.83  
 00-005-0586 (\*) - Calcite, syn - CaCO<sub>3</sub> - Y: 4.55 % - d x by: 1. - WL: 1.5406 - Rhombo.H.axes - a 4.98900 - b 4.98900 - c 17.06200 - alpha 90.000 - beta 90.000 - gamma 120.000 - Primitive - R-3c (167) - 6 - 367.780 -

Sample 48



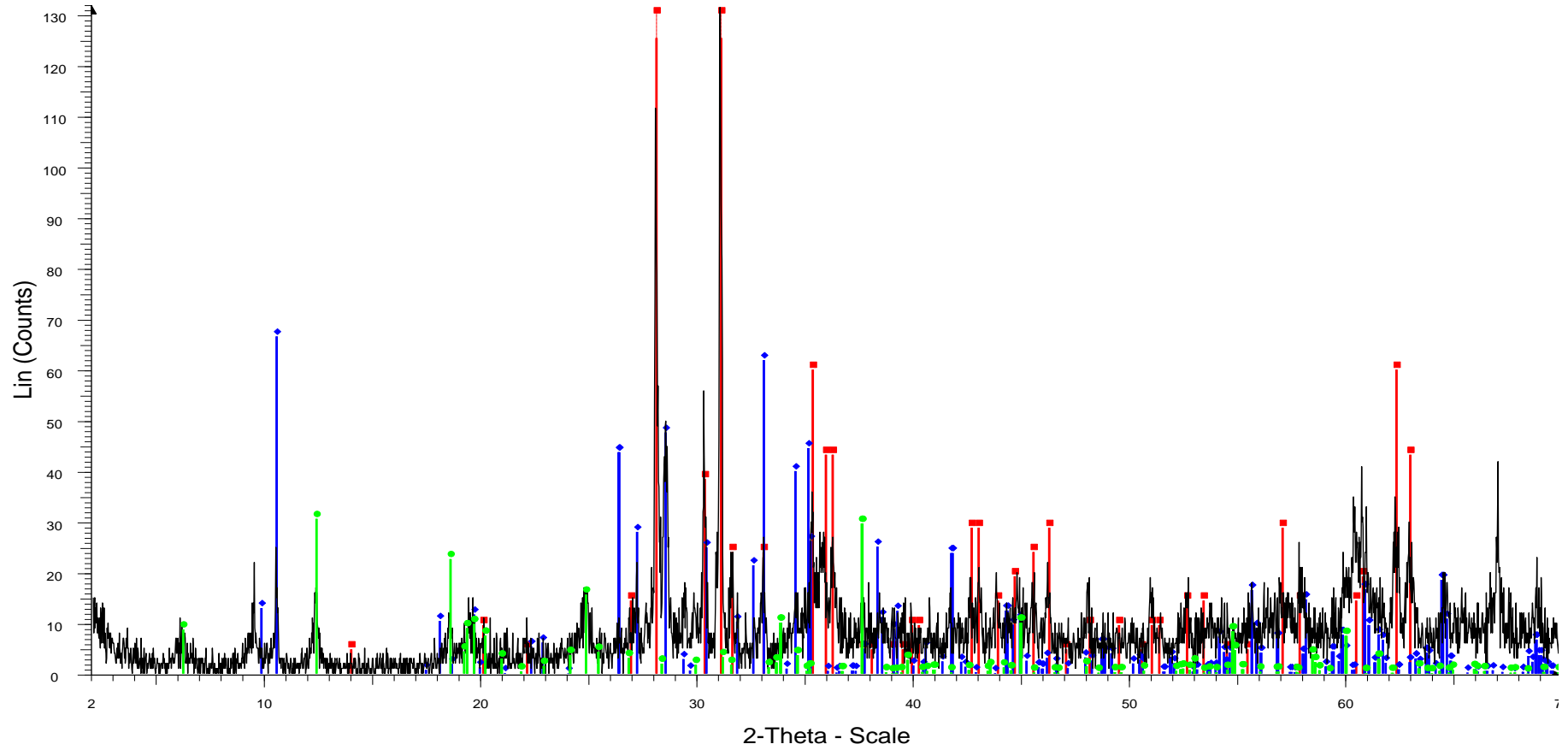
MGSC 49 - File: MGSC 49.raw - Type: 2Th/Th locked - Start: 2.000 ° - End: 70.000 ° - Step: 0.020 ° - Step time: 1. s - Temp.: 25 °C (Room) - Time Started: 18 s - 2-Theta: 2.000 ° - Theta: 1.000 ° - Chi: 0.00 ° - Phi: 0.0  
 Operations: Import  
 00-022-0714 (D) - Enstatite, ordered - MgSiO<sub>3</sub> - Y: 99.42 % - d x by: 1. - WL: 1.5406 - Orthorhombic - a 18.23000 - b 8.84000 - c 5.19000 - alpha 90.000 - beta 90.000 - gamma 90.000 - Primitive - Pbc<sub>a</sub> (61) - 16 - 836  
 01-080-1864 (C) - Augite - (Ca<sub>0.61</sub>Na<sub>0.25</sub>Fe<sub>0.07</sub>Mg<sub>0.07</sub>)(Mg<sub>0.65</sub>Fe<sub>0.10</sub>Fe<sub>0.03</sub>Al<sub>0.22</sub>)(Si<sub>2</sub>O<sub>6</sub>) - Y: 13.05 % - d x by: 1. - WL: 1.5406 - Monoclinic - a 9.66200 - b 8.84100 - c 5.25300 - alpha 90.000 - beta 106.780 - gamma 90.000 - C-1 (0) - 4 - 664.83  
 00-009-0466 (\*) - Albite, ordered - NaAlSi<sub>3</sub>O<sub>8</sub> - Y: 17.11 % - d x by: 1. - WL: 1.5406 - Triclinic - a 8.14400 - b 12.78700 - c 7.16000 - alpha 94.260 - beta 116.600 - gamma 87.670 - Base-centered - C-1 (0) - 4 - 664.83  
 00-001-0837 (D) - Calcite - CaCO<sub>3</sub> - Y: 7.44 % - d x by: 1. - WL: 1.5406 - Rhombo.H.axes - a 4.98300 - b 4.98300 - c 17.01900 - alpha 90.000 - beta 90.000 - gamma 120.000 - Primitive - R-3c (167) - 2 - 365.971 - F1

Sample 49



MGSC 50 - File: MGSC 50.raw - Type: 2Th/Th locked - Start: 2.000 ° - End: 70.000 ° - Step: 0.020 ° - Step time: 1. s - Temp.: 25 °C (Room) - Time Started: 17 s - 2-Theta: 2.000 ° - Theta: 1.000 ° - Chi: 0.00 ° - Phi: 0.0  
 Operations: Import  
 00-022-0714 (D) - Enstatite, ordered - MgSiO<sub>3</sub> - Y: 104.97 % - d x by: 1. - WL: 1.5406 - Orthorhombic - a 18.23000 - b 8.84000 - c 5.19000 - alpha 90.000 - beta 90.000 - gamma 90.000 - Primitive - Pbc<sub>a</sub> (61) - 16 - 83  
 00-024-0203 (I) - Augite - Ca(Mg,Fe)Si<sub>2</sub>O<sub>6</sub> - Y: 12.16 % - d x by: 1. - WL: 1.5406 - Monoclinic - a 9.75500 - b 8.92800 - c 5.20400 - alpha 90.000 - beta 106.110 - gamma 90.000 - Base-centered - C2/c (15) - 4 - 435.4  
 00-005-0490 (D) - Quartz, low - alpha-SiO<sub>2</sub> - Y: 42.44 % - d x by: 1. - WL: 1.5406 - Hexagonal - a 4.91300 - b 4.91300 - c 5.40500 - alpha 90.000 - beta 90.000 - gamma 120.000 - Primitive - P3121 (152) - 3 - 112.985  
 01-072-1385 (C) - Clinocllore, chromian 1Mla-4 - Mg<sub>5</sub>Al<sub>11</sub>Si<sub>3</sub>Cr<sub>7</sub>O<sub>10</sub>(OH)<sub>8</sub> - Y: 5.80 % - d x by: 1. - WL: 1.5406 - Triclinic - a 5.33800 - b 9.24700 - c 14.43500 - alpha 90.000 - beta 97.080 - gamma 90.000 - Base  
 01-072-1214 (A) - Calcite, syn - CaCO<sub>3</sub> - Y: 8.16 % - d x by: 1. - WL: 1.5406 - Rhombo.H.axes - a 4.98900 - b 4.98900 - c 17.06200 - alpha 90.000 - beta 90.000 - gamma 120.000 - Primitive - R-3c (167) - 6 - 367.780

Sample 50

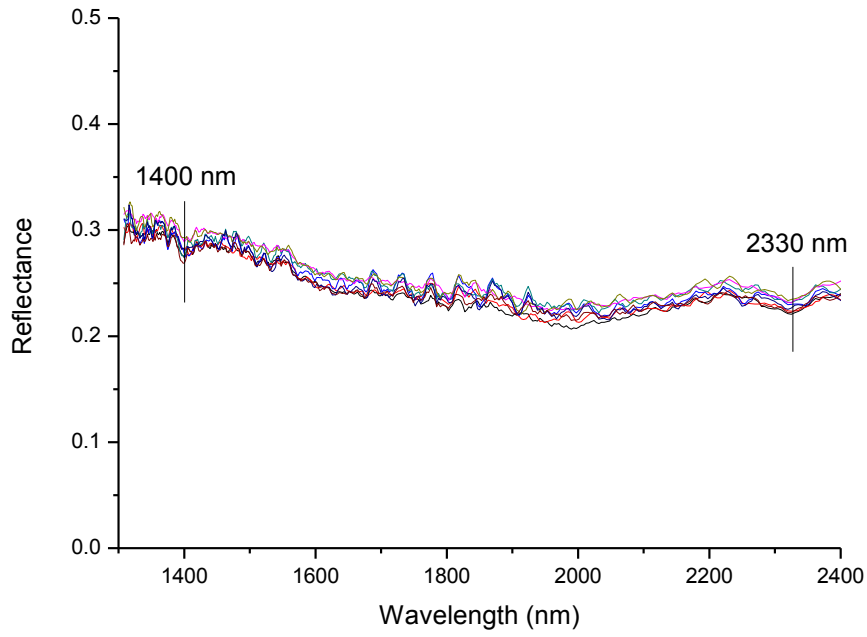


MGSC 51 - File: MGSC 51.raw - Type: 2Th/Th locked - Start: 2.000 ° - End: 70.000 ° - Step: 0.020 ° - Step time: 1. s - Temp.: 25 °C (Room) - Time Started: 18 s - 2-Theta: 2.000 ° - Theta: 1.000 ° - Chi: 0.00 ° - Phi: 0.0  
 Operations: Import  
■ 00-022-0714 (D) - Enstatite, ordered - MgSiO<sub>3</sub> - Y: 182.59 % - d x by: 1. - WL: 1.5406 - Orthorhombic - a 18.23000 - b 8.84000 - c 5.19000 - alpha 90.000 - beta 90.000 - gamma 90.000 - Primitive - Pbc<sub>a</sub> (61) - 16 - 83  
◆ 01-071-1060 (C) - Hornblende - Na<sub>9</sub>K<sub>4</sub>Ca<sub>1.6</sub>Mg<sub>2.8</sub>Fe<sub>1.4</sub>Ti<sub>5</sub>Al<sub>2.4</sub>Si<sub>6</sub>O<sub>23</sub>(OH) - Y: 50.63 % - d x by: 1. - WL: 1.5406 - Monoclinic - a 9.87000 - b 18.05800 - c 5.30700 - alpha 90.000 - beta 105.200 - gamma 90.000 -  
● 01-078-2063 (C) - Clinocllore la chromian - (Mg<sub>5.0</sub>Fe<sub>0.1</sub>Cr<sub>0.7</sub>Al<sub>0.2</sub>)(Si<sub>3</sub>AlO<sub>10</sub>)(OH<sub>0.9875</sub>)<sub>8</sub> - Y: 23.23 % - d x by: 1. - WL: 1.5406 - Triclinic - a 5.32900 - b 9.24600 - c 14.44200 - alpha 90.000 - beta 97.080 - gamma

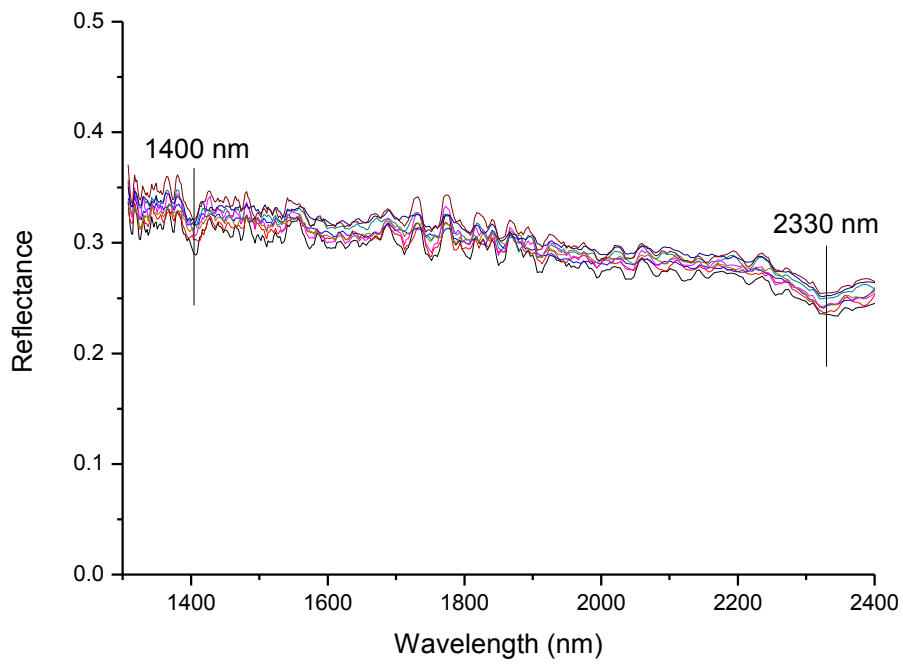
Sample 51

## **APPENDIX 10.1b – NIR spectra of Mogalekwena Platinum samples**

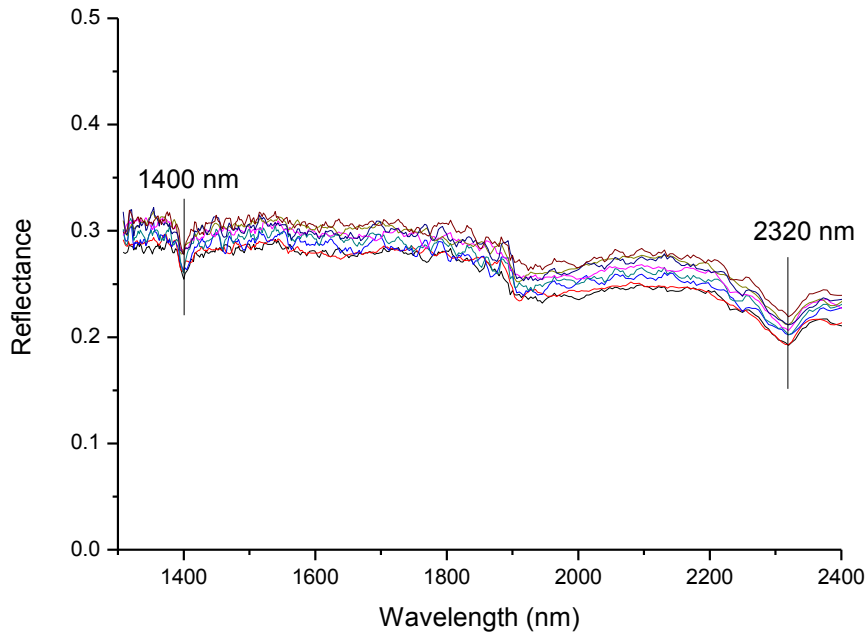




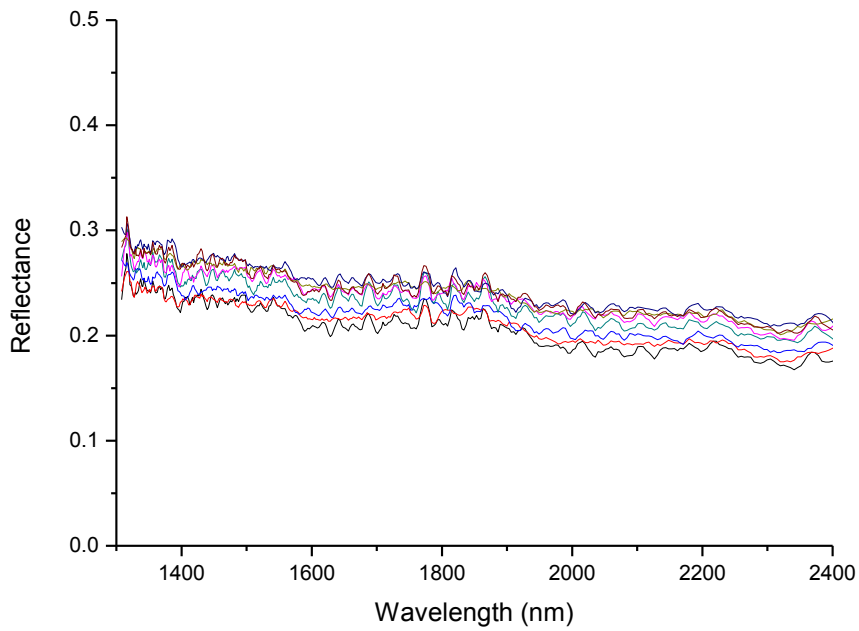
Sample 1 (MSGC10076961)



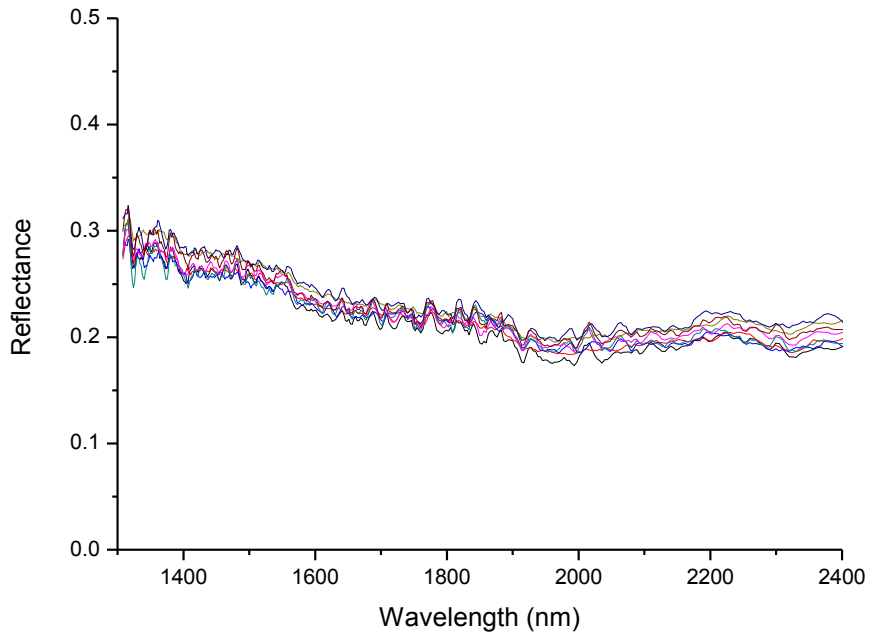
Sample 2 (MSGC10035880)



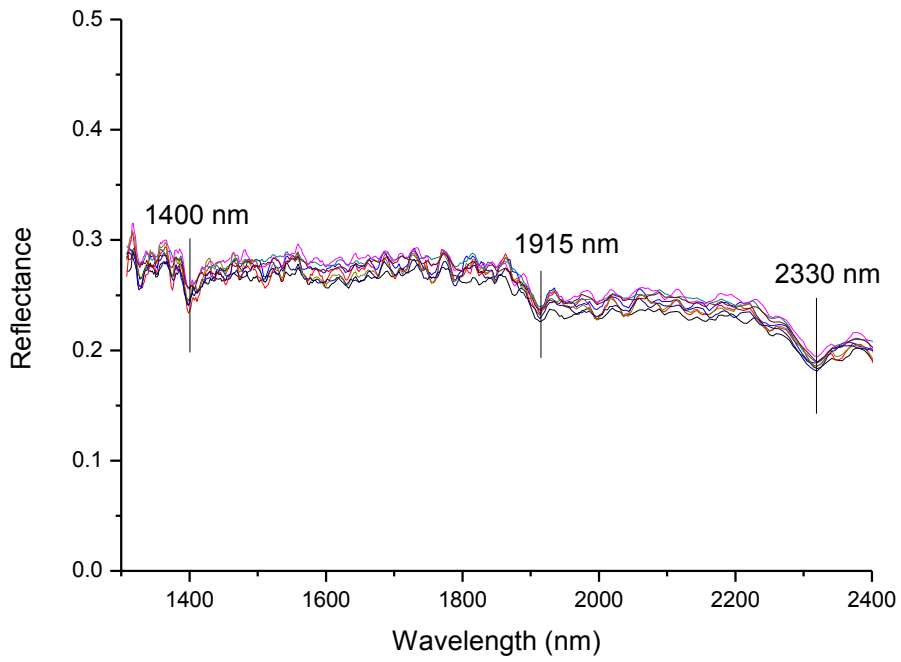
Sample 3 (MSGC10484545)



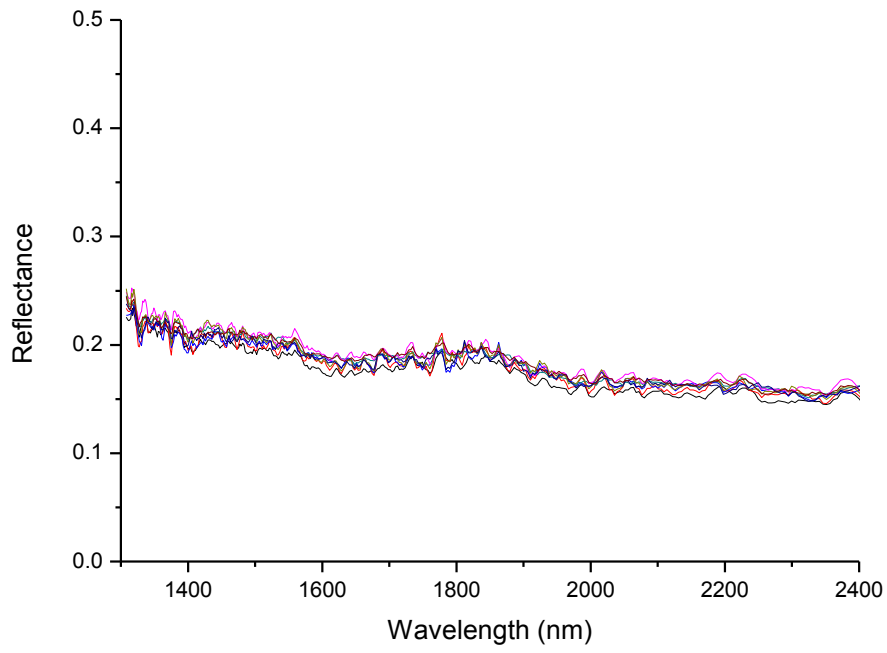
Sample 4 (MSGC10484178)



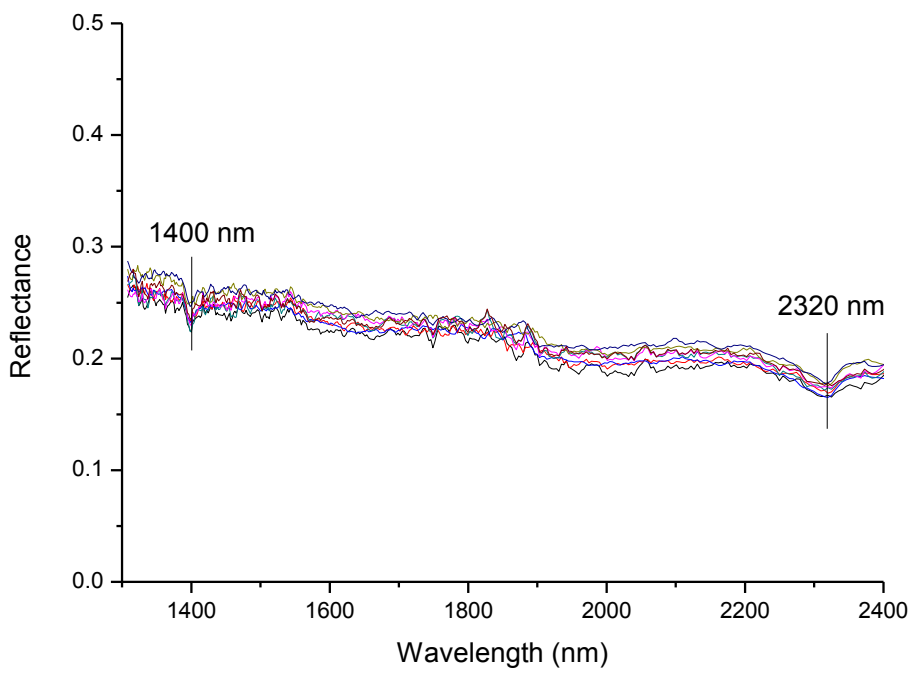
Sample 5 (MSGC10484297)



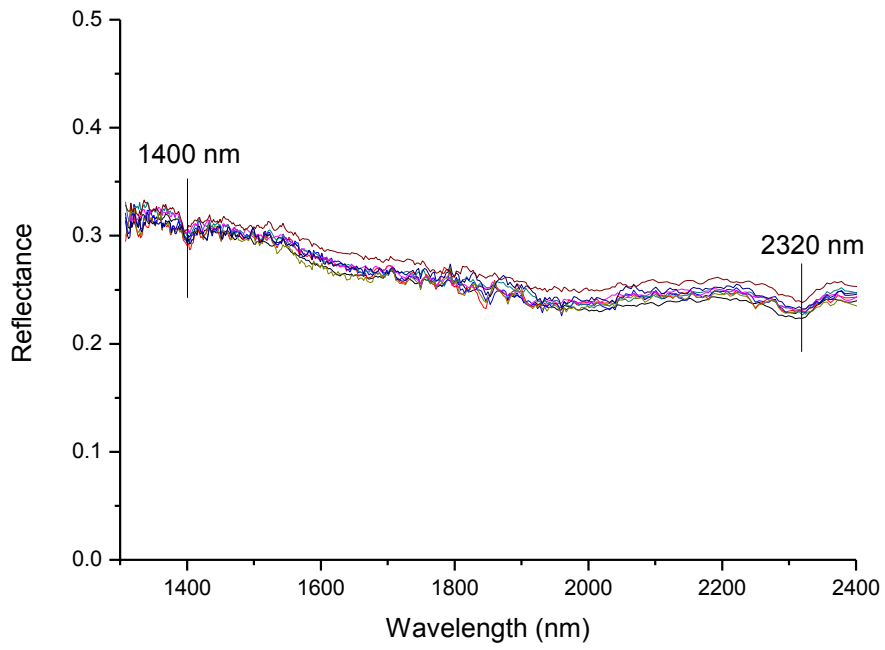
Sample 6 (MSGC10484104)



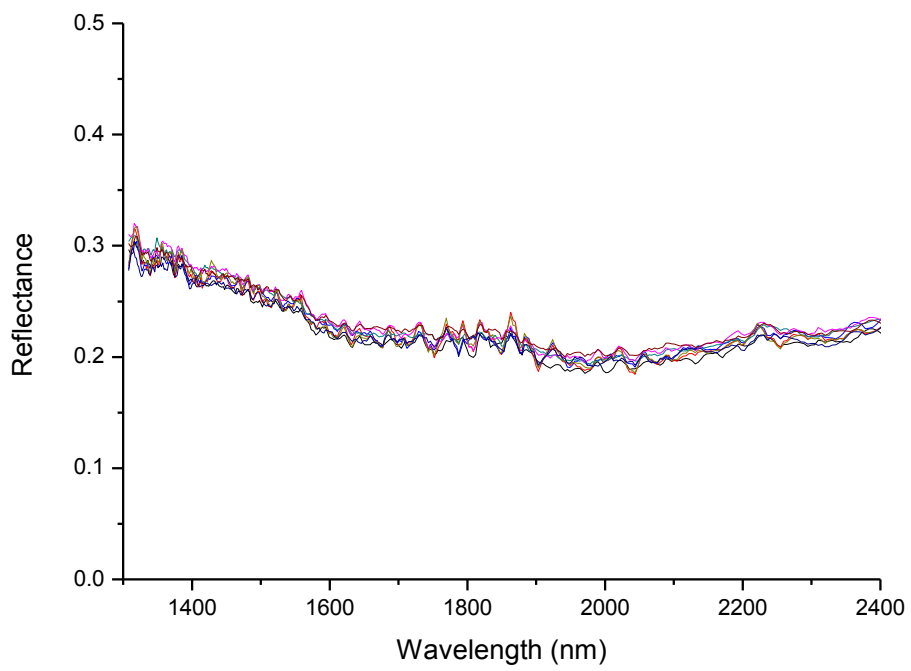
Sample 7 (MSGC10483164)



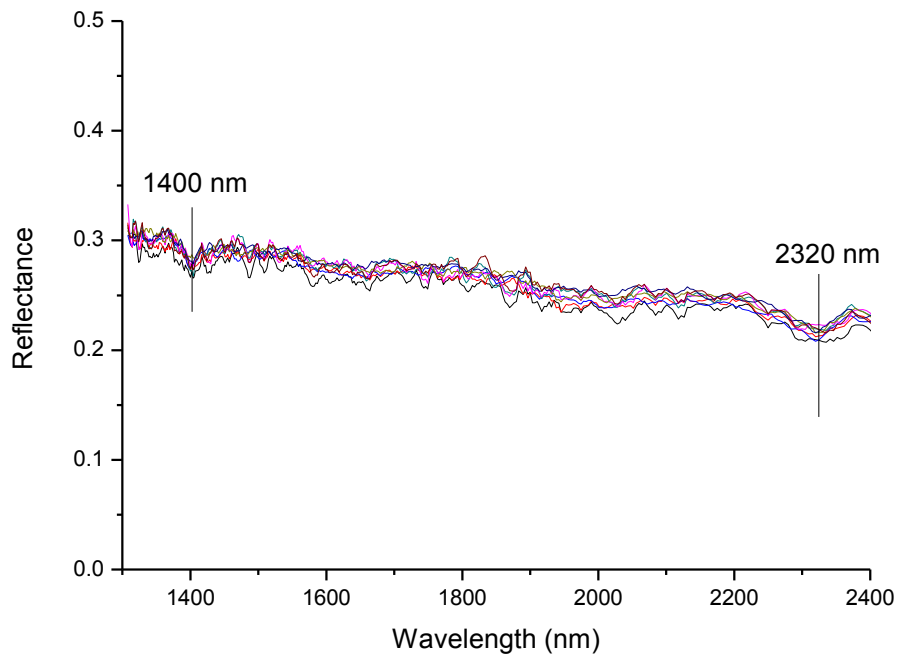
Sample 8 (MSGC10484108)



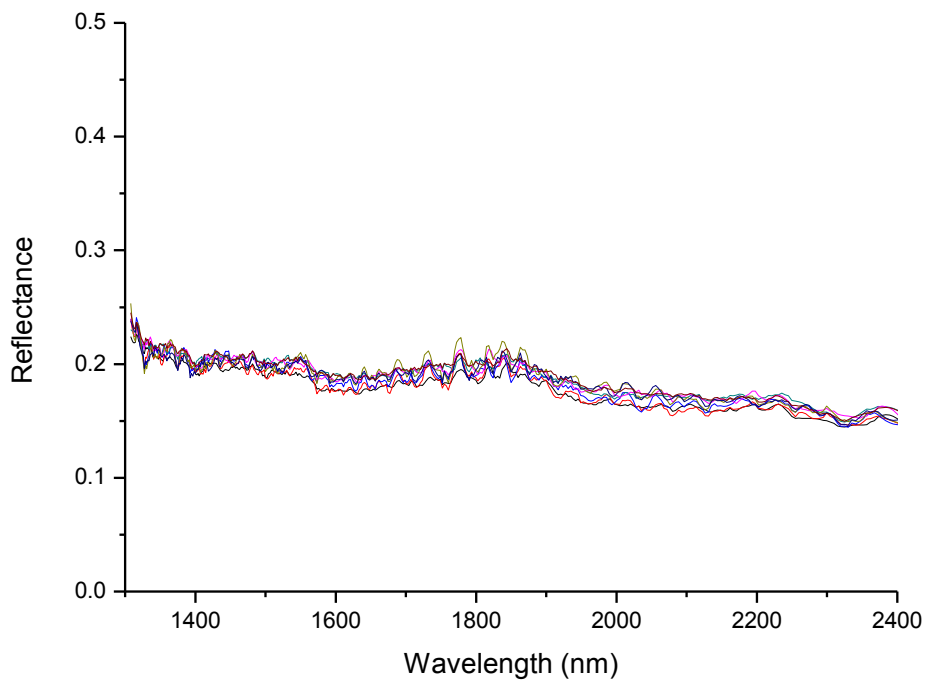
Sample 9 (MSGC10484164)



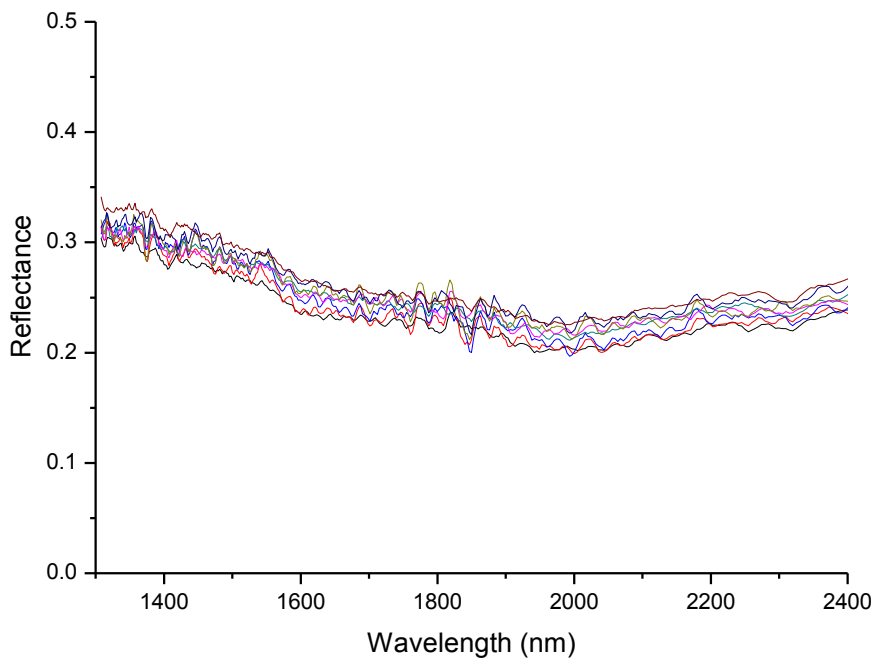
Sample 10 (MSGC10483077)



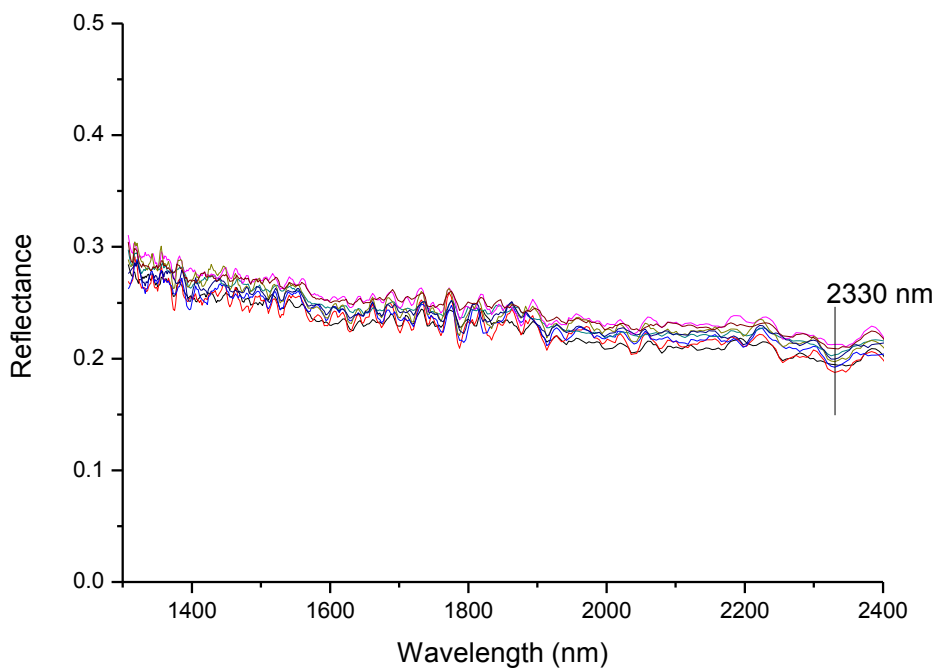
Sample 11 (MSGC10483256)



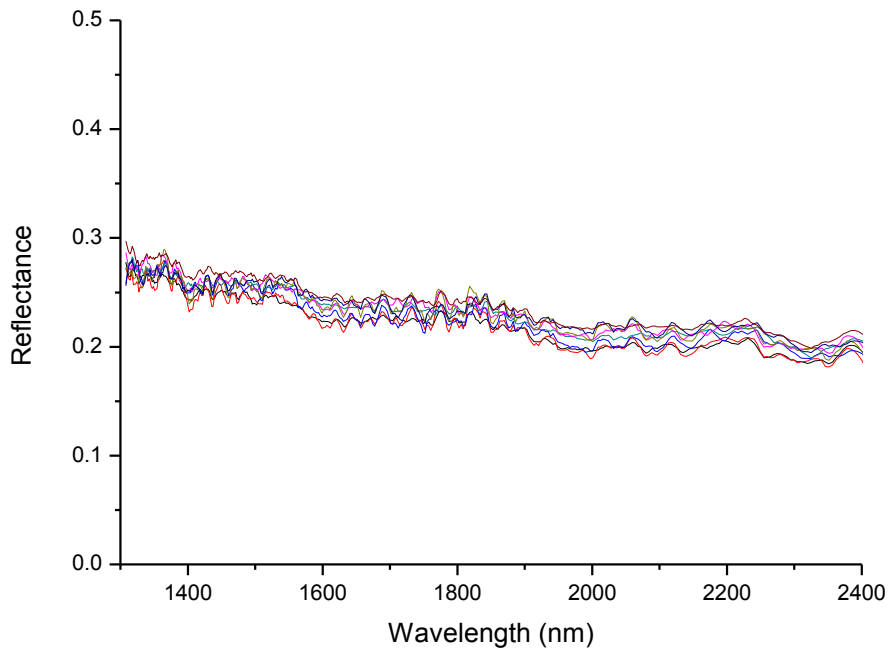
Sample 12 (MSGC10035039)



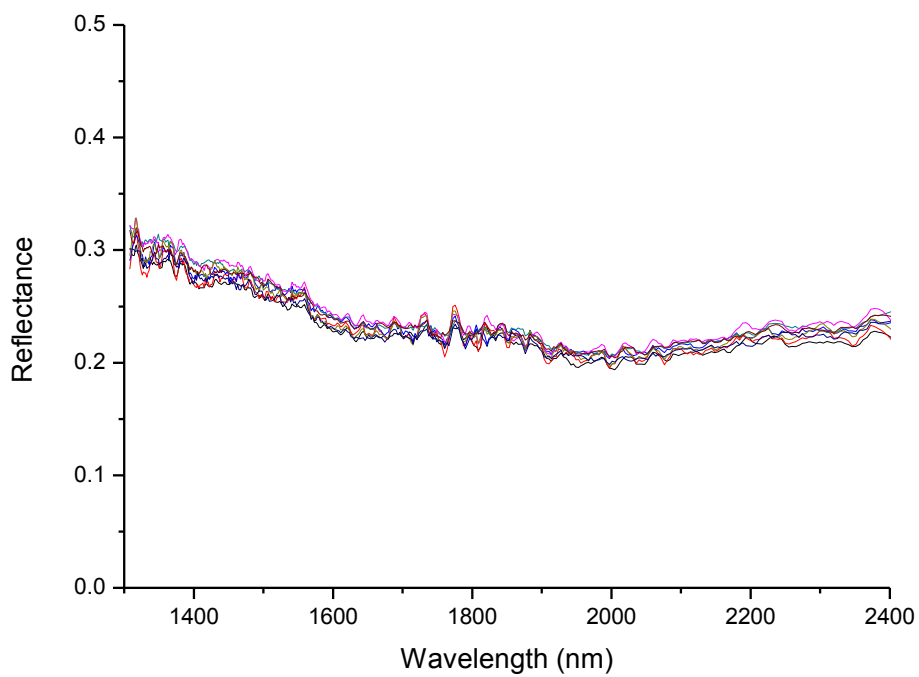
Sample 13 (MSGC10035411)



Sample 14 (MSGC10035682)

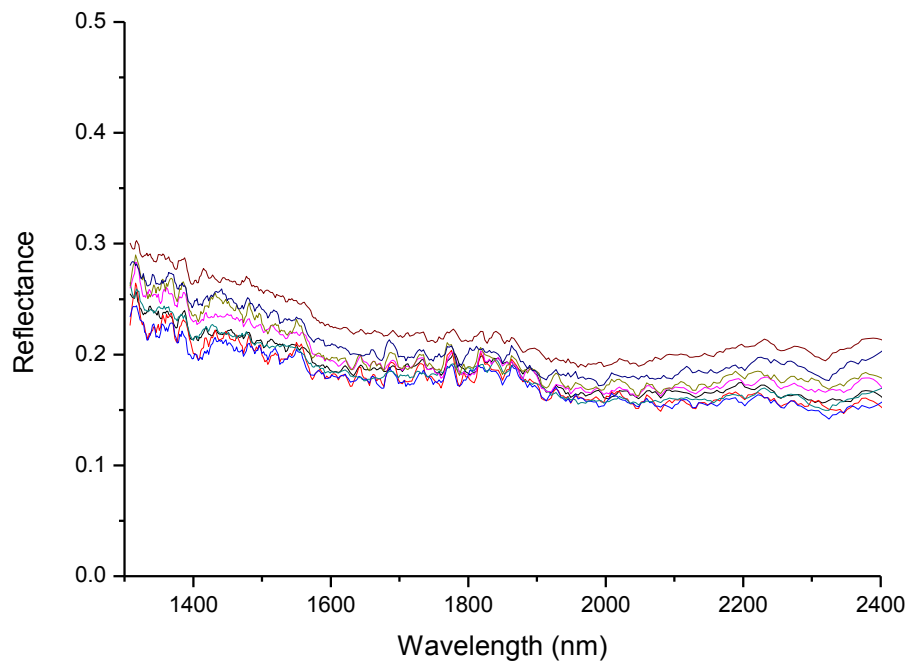


Sample 15 (MSGC10483071)

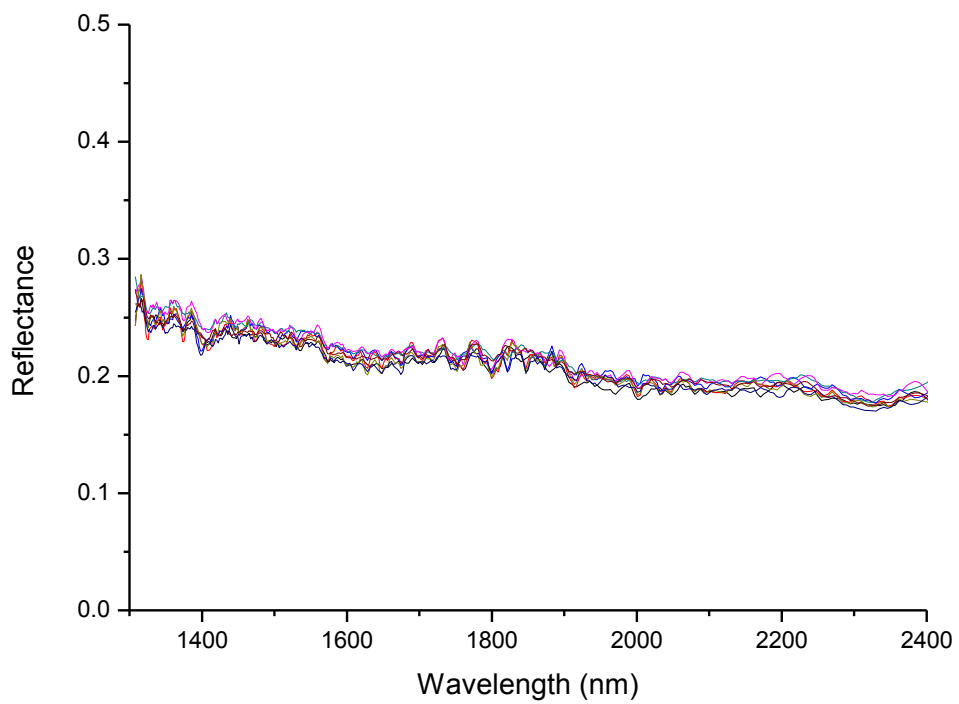


Sample 16 (MSGC10483074)

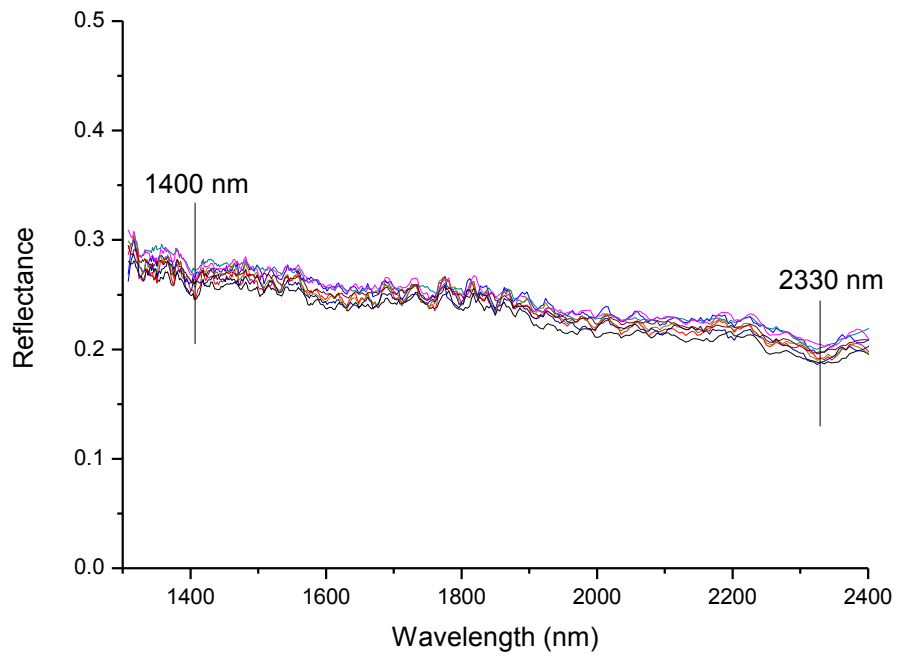




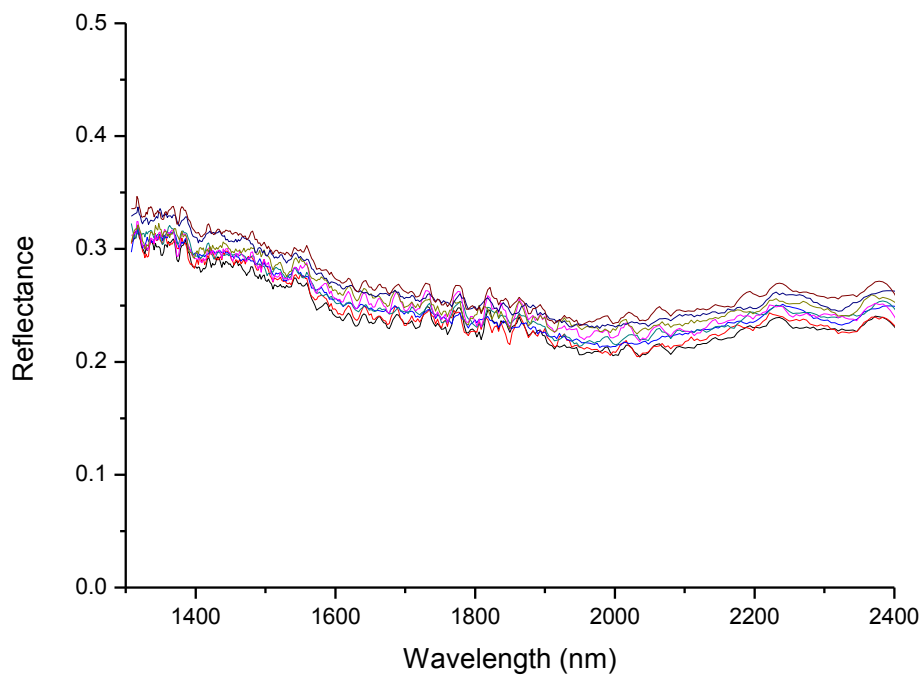
Sample 17 (MSGC10483137)



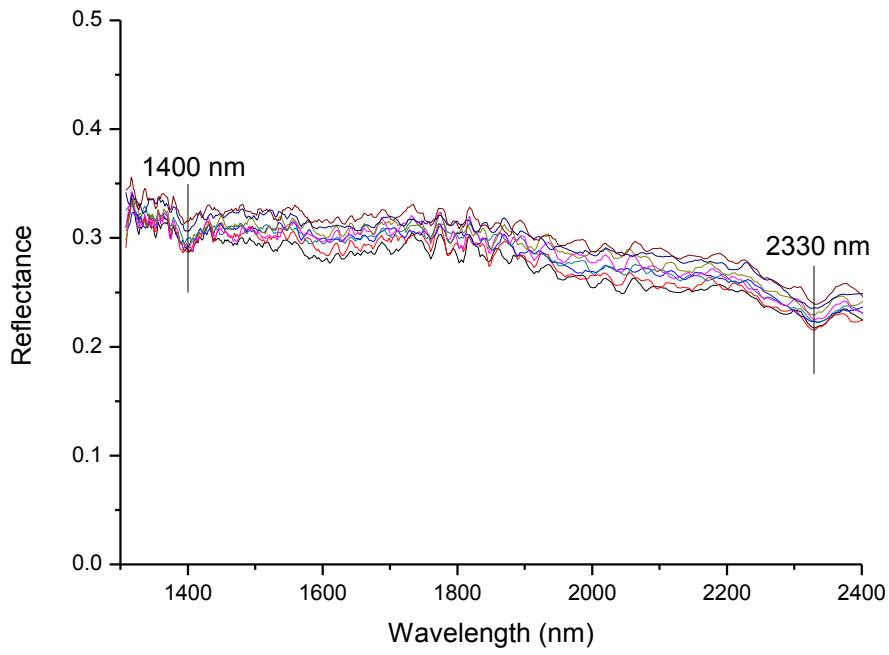
Sample 18 (MSGC10483161)



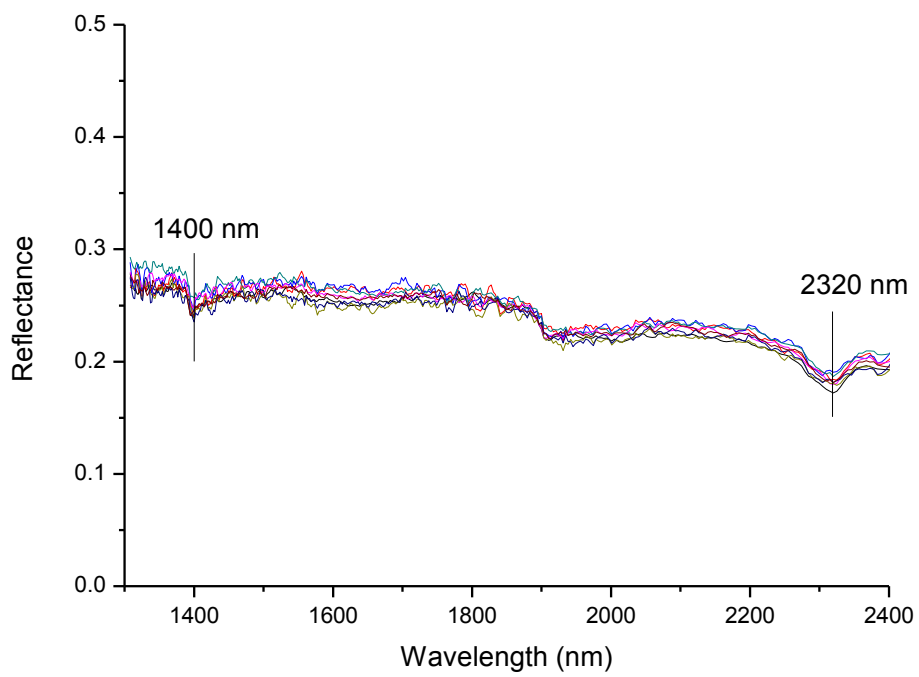
Sample 19 (MSGC10483263)



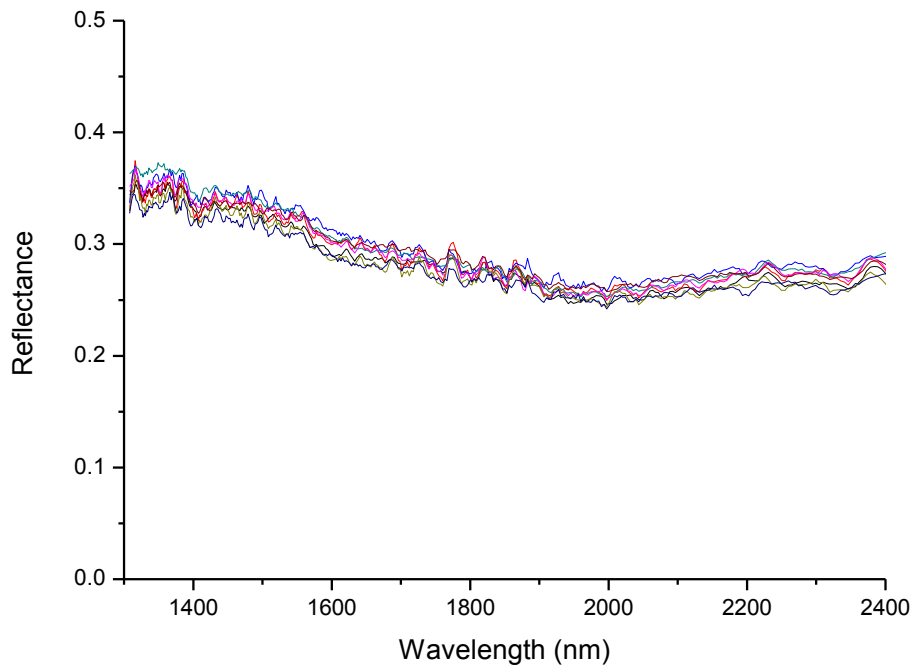
Sample 20 (MSGC10484275)



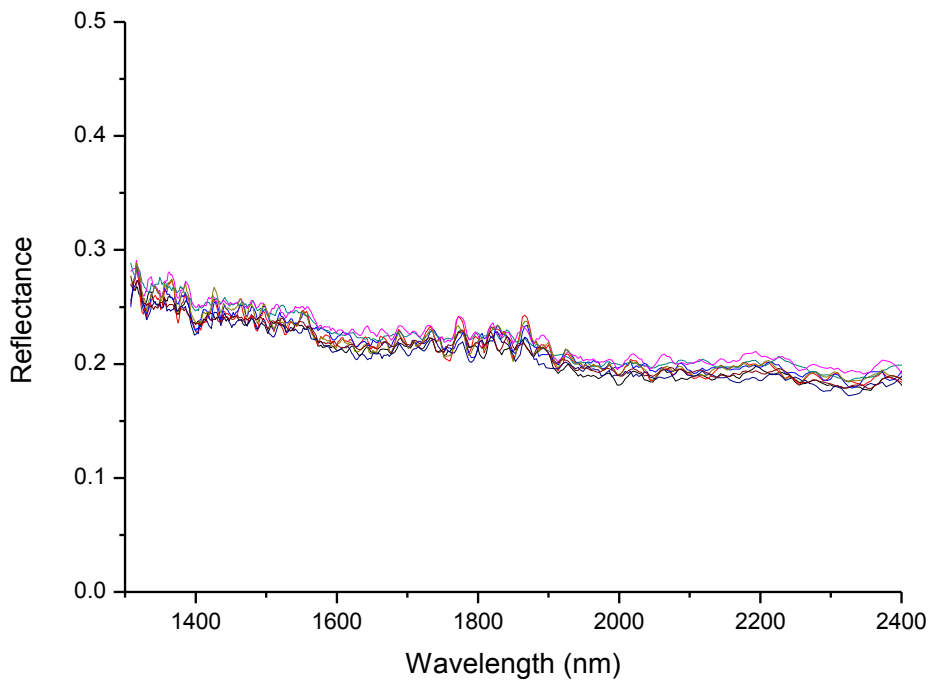
Sample 21 (MSGC10484478)



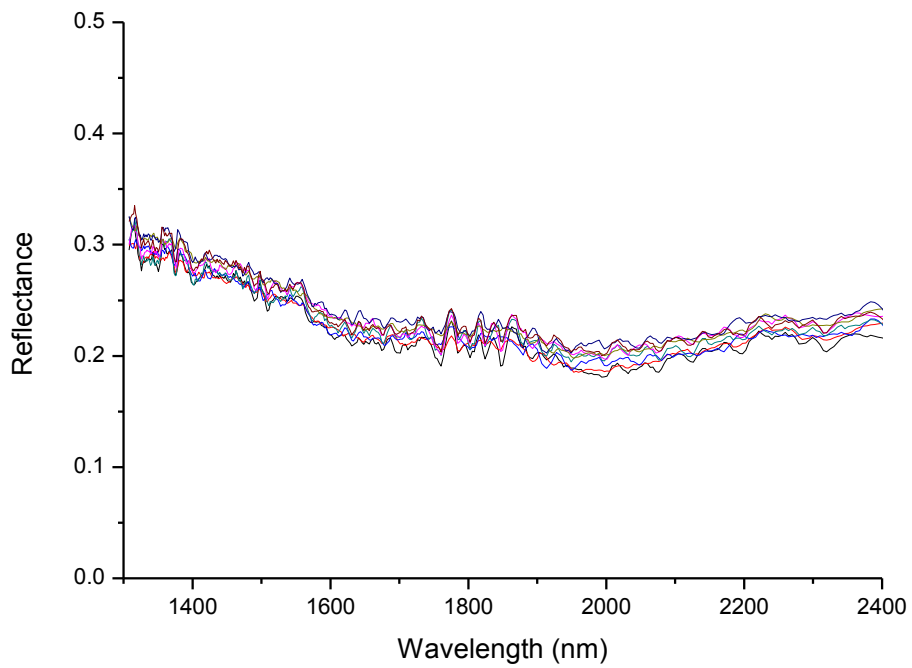
Sample 22 (MSGC10484502)



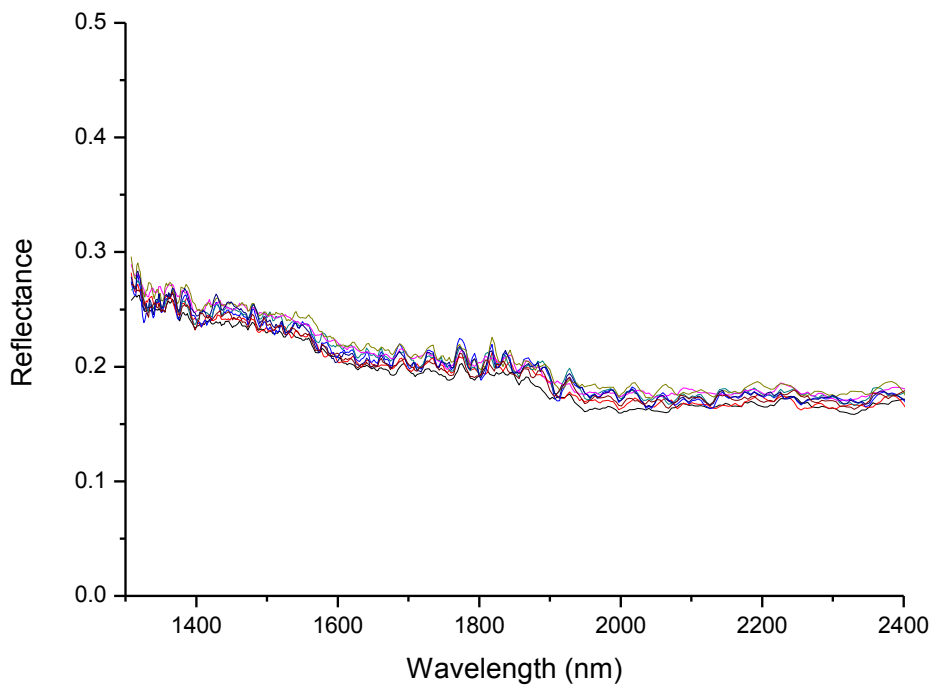
Sample 23 (MSGC10035875)



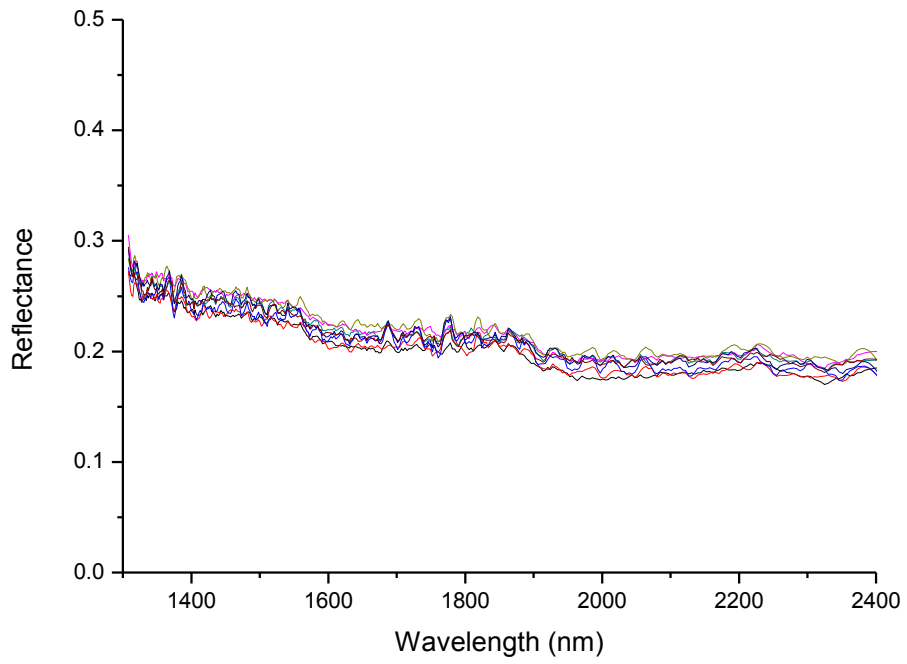
Sample 24 (MSGC10483055)



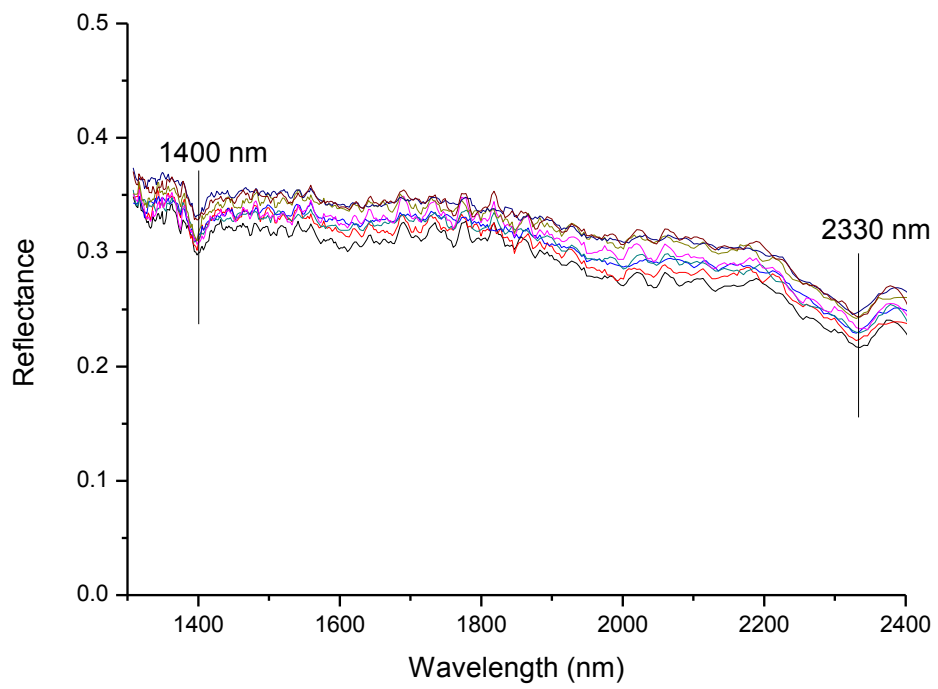
Sample 25 (MSGC10483083)



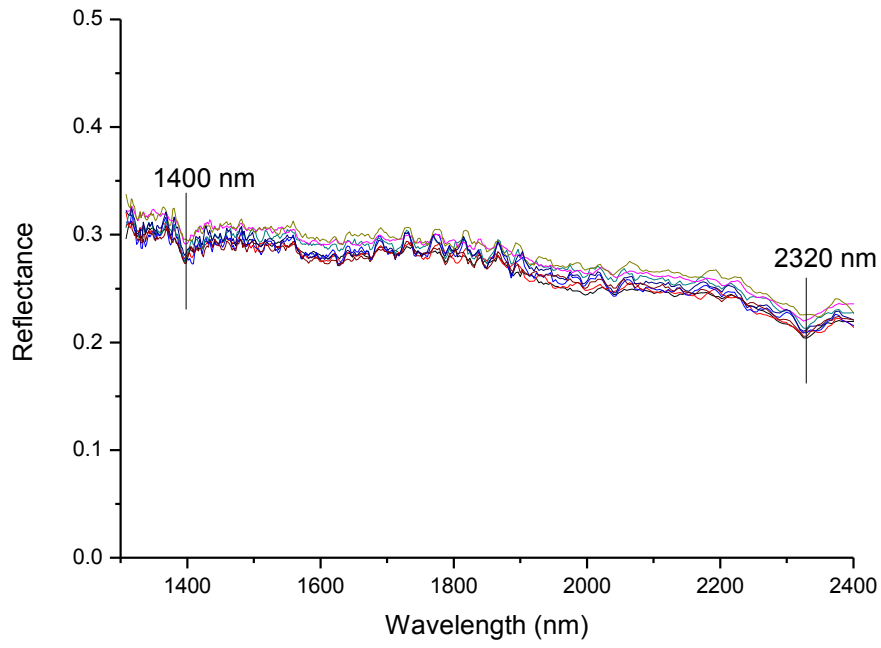
Sample 26 (MSGC10483133)



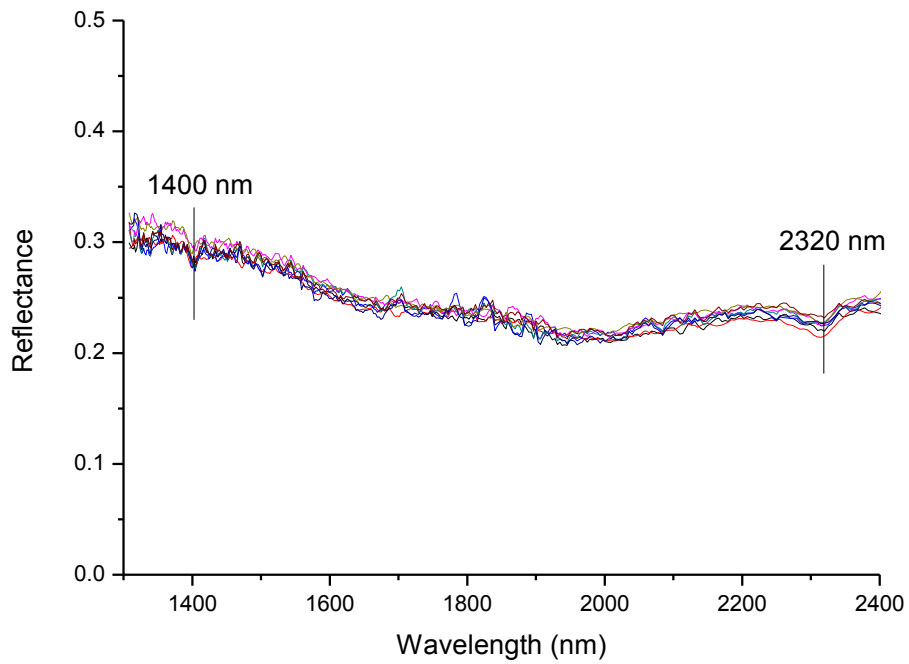
Sample 27 (MSGC10483172)



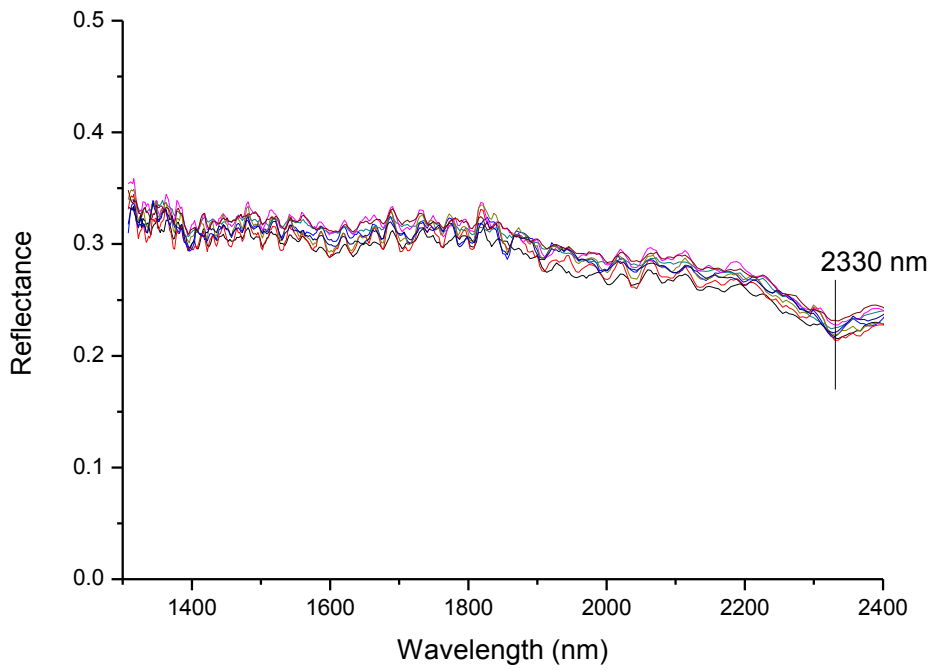
Sample 28 (MSGC10035838)



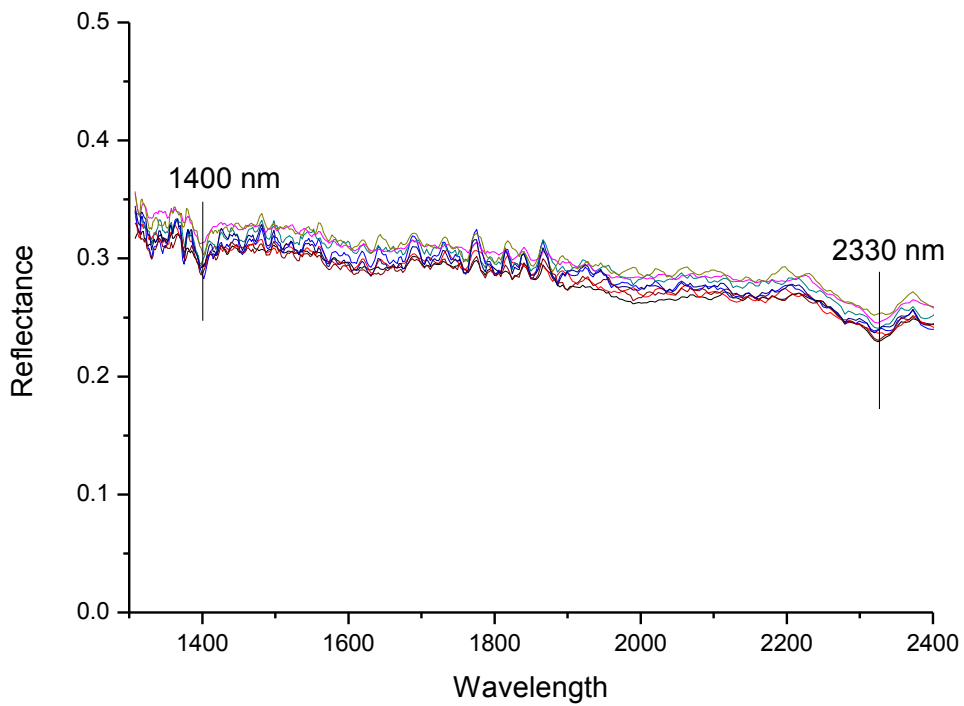
Sample 29 (MSGC10074904)



Sample 30 (MSGC10076956)

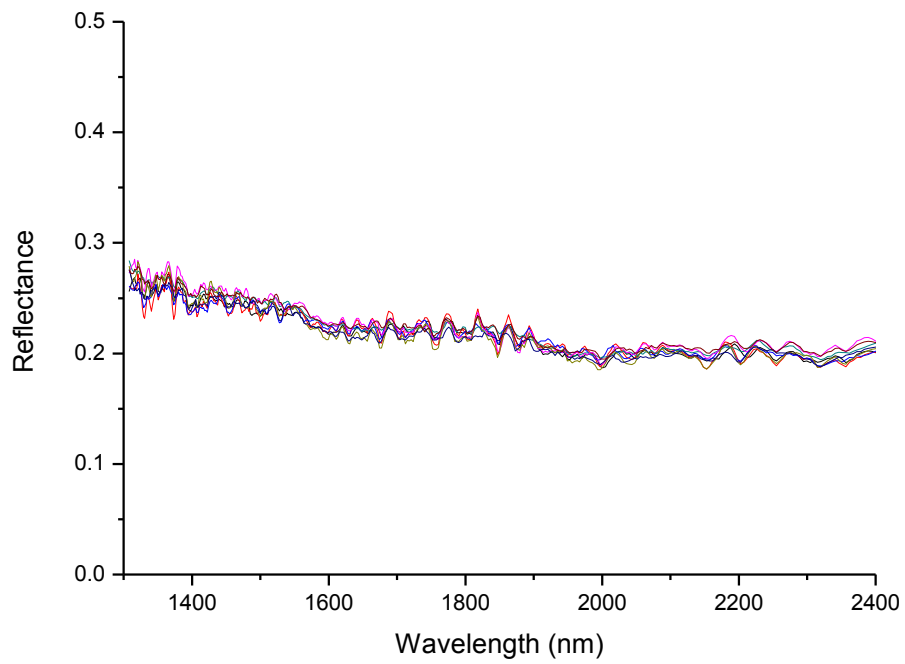


Sample 31 (MSGC10483479)

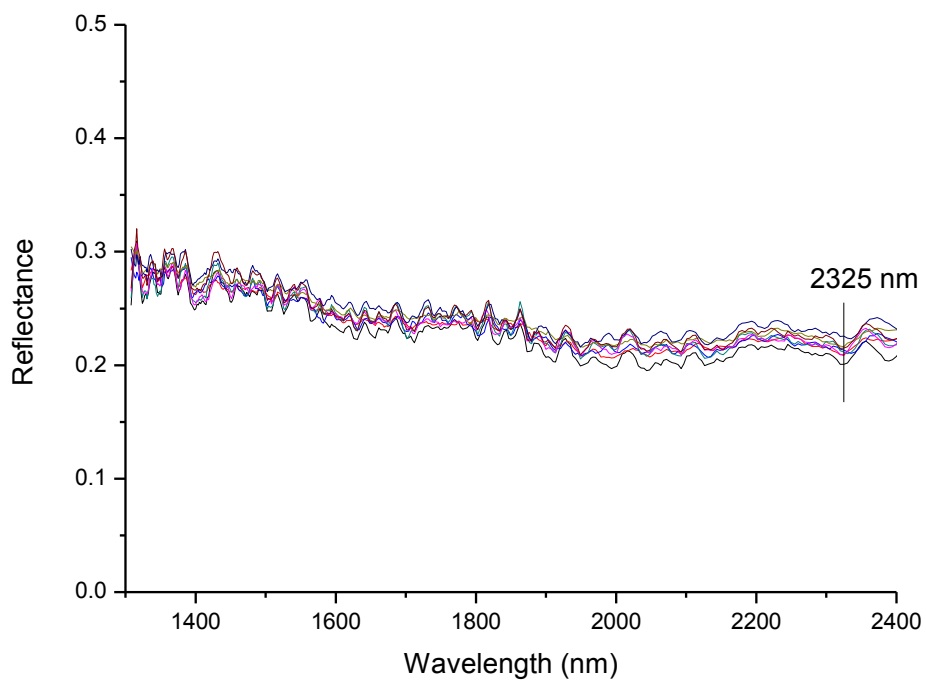


Sample 32 (MSGC10483567)

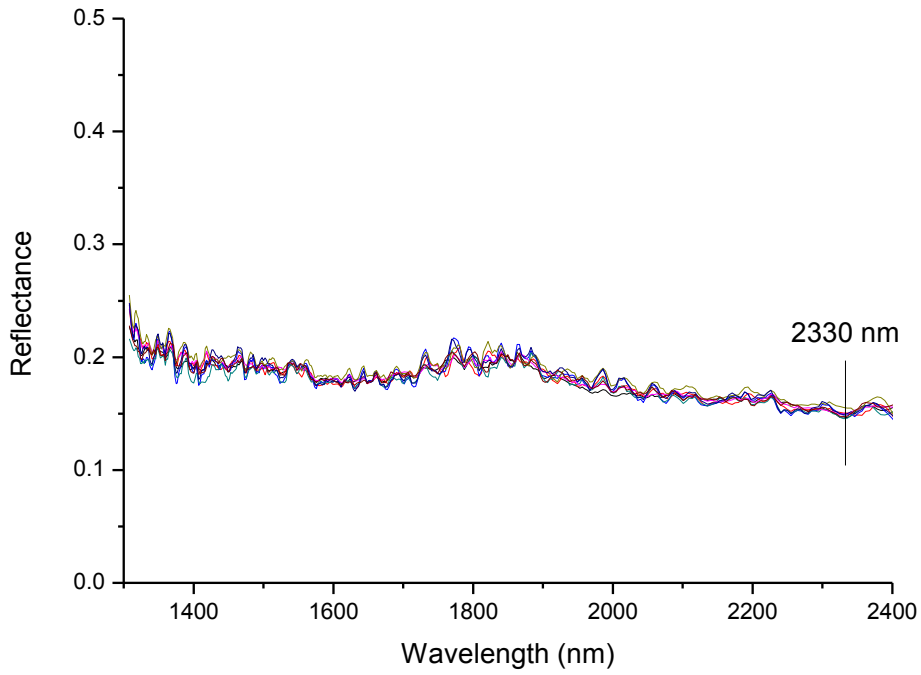




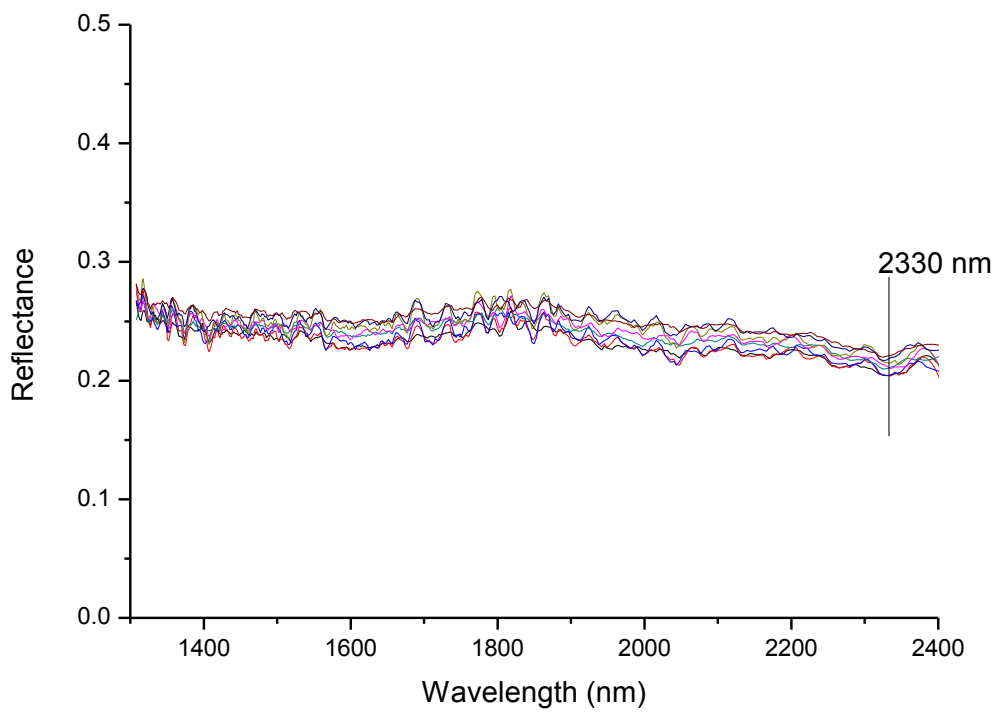
Sample 33 (MSGC10484107)



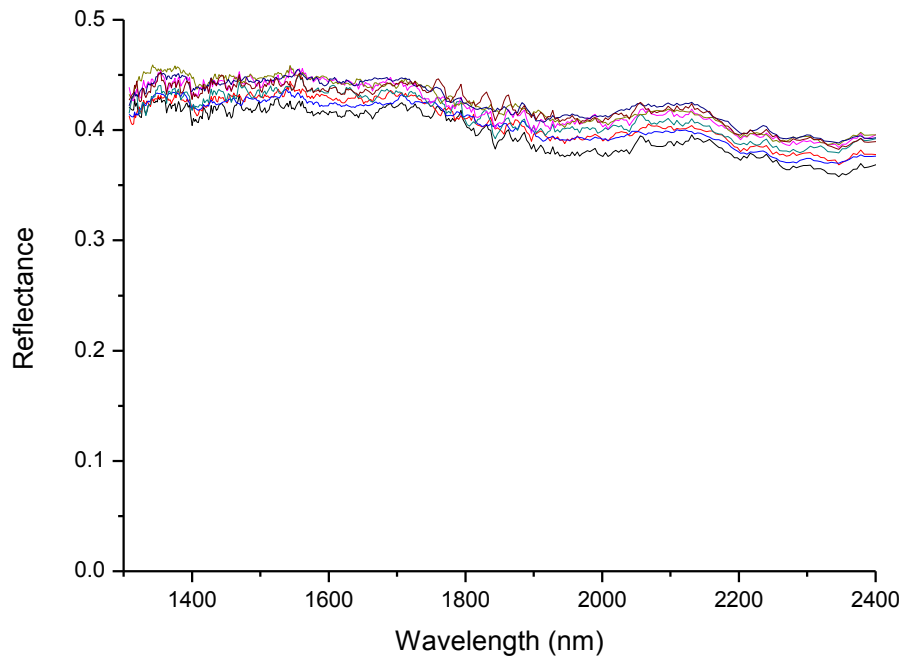
Sample 34 (MSGC10484281)



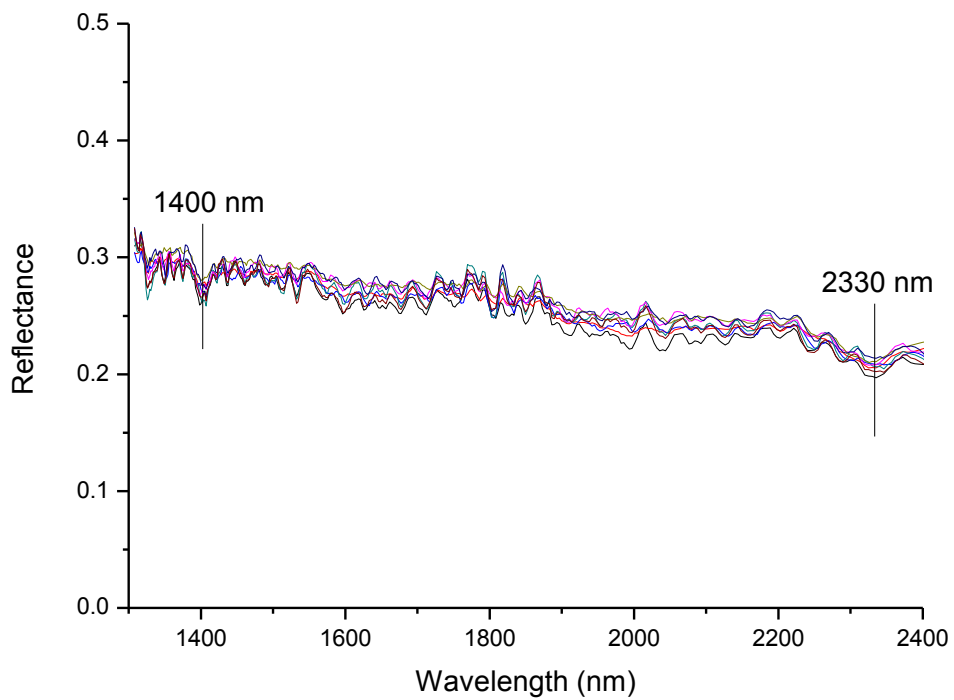
Sample 35 (MSGC10483402)



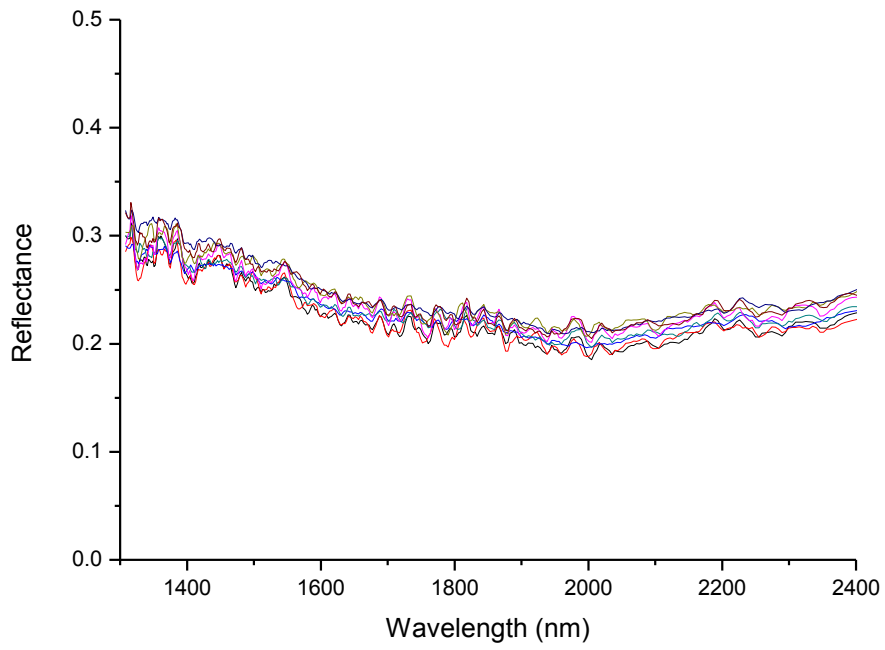
Sample 36 (MSGC10483502)



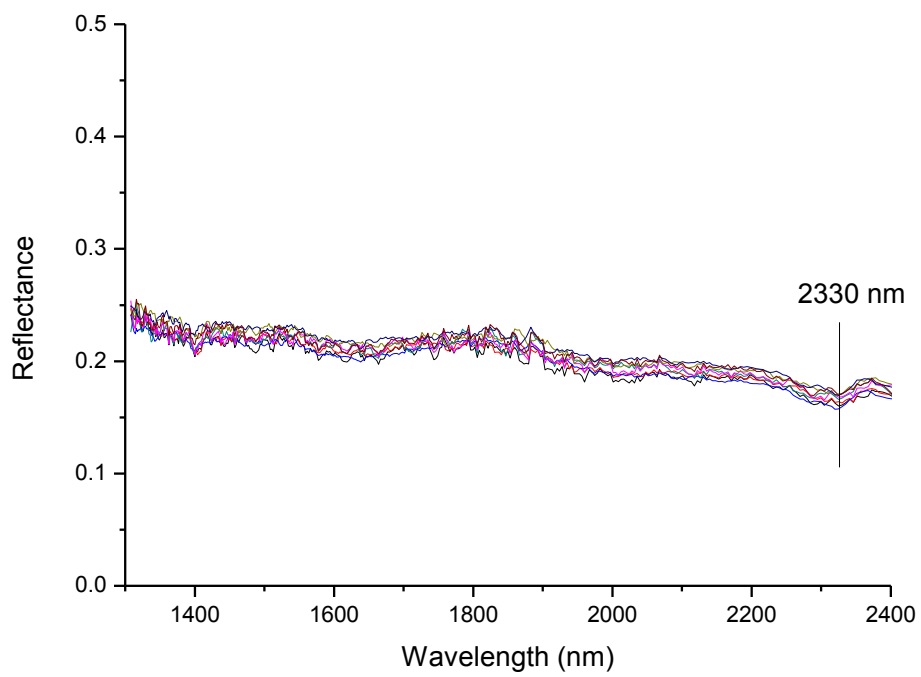
Sample 37 (MSGC10484147)



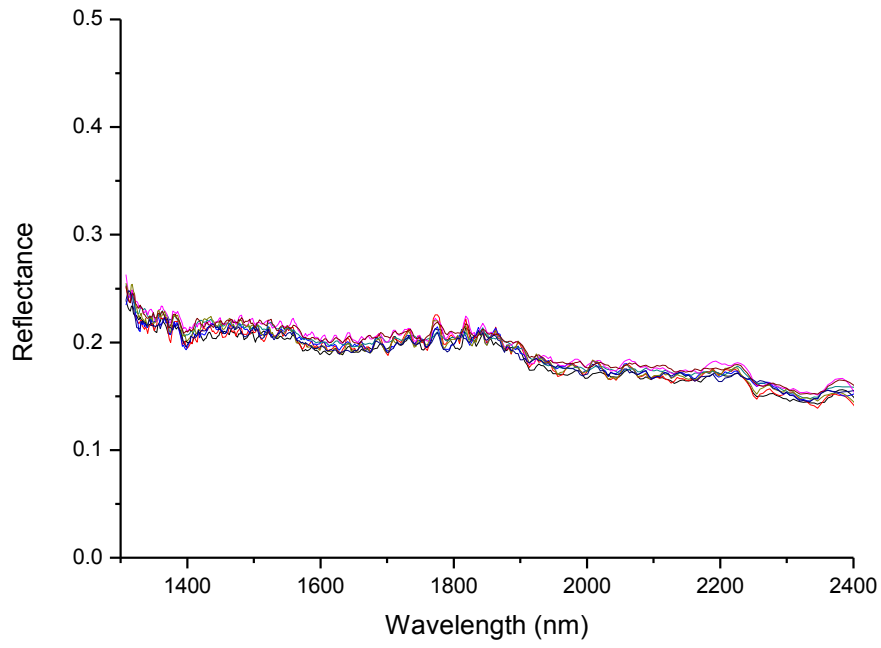
Sample 38 (MSGC10483789)



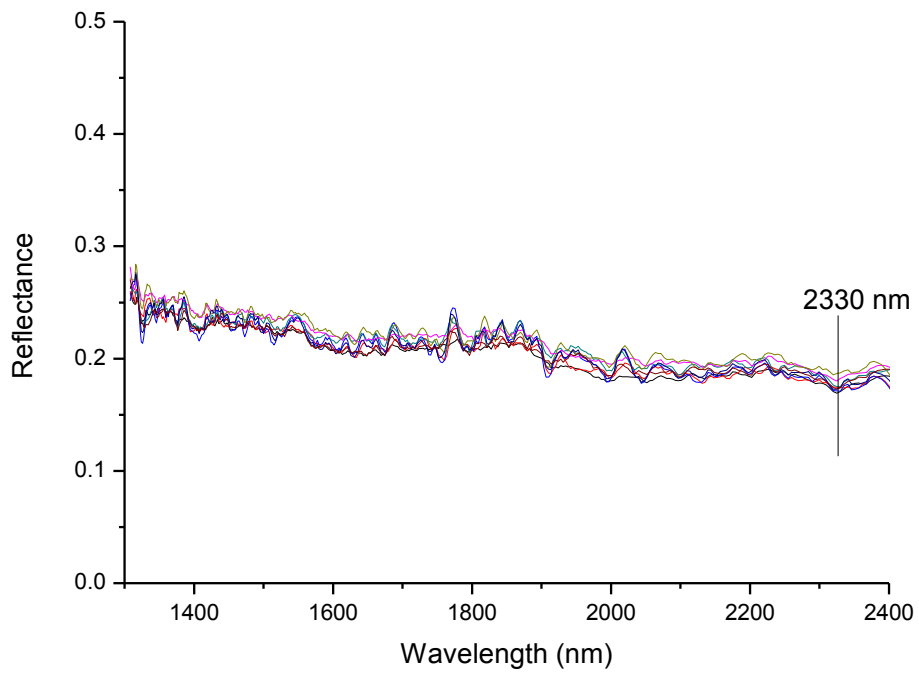
Sample 39 (MSGC10484219)



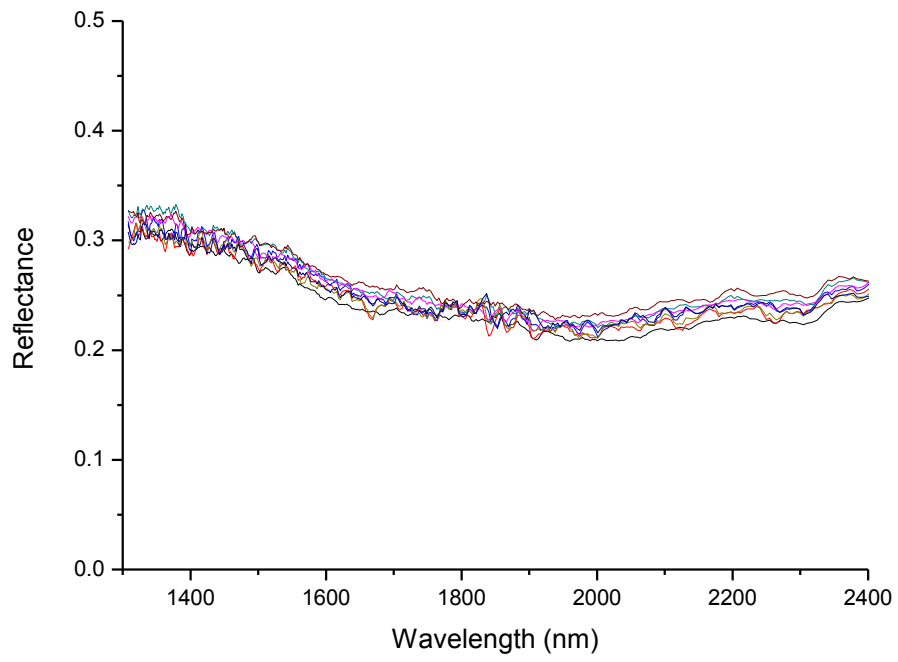
Sample 40 (MSGC10035065)



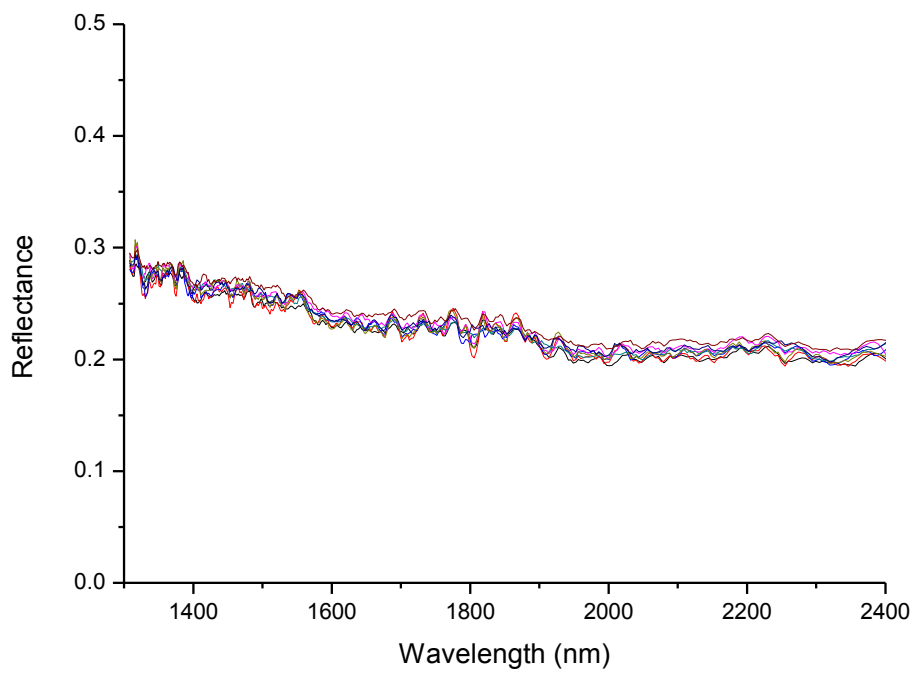
Sample 41 (MSGC10483181)



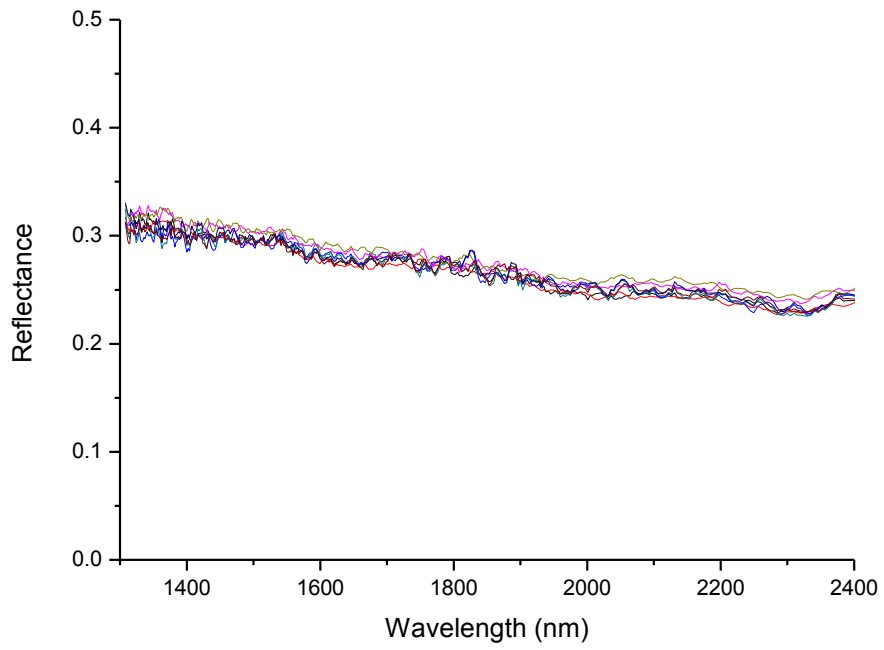
Sample 42 (MSGC10035487)



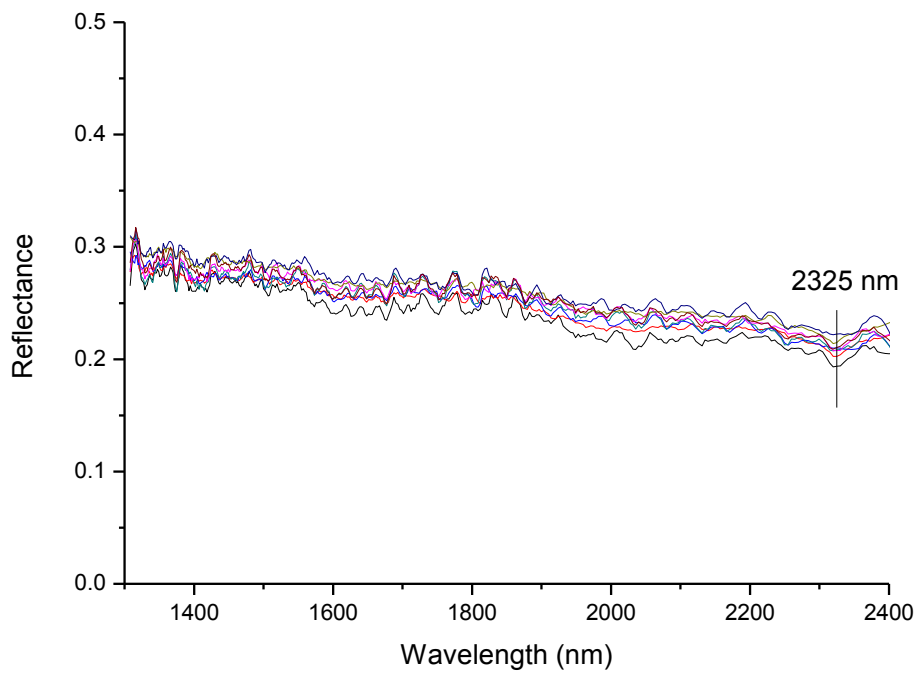
Sample 43 (MSGC10035420)



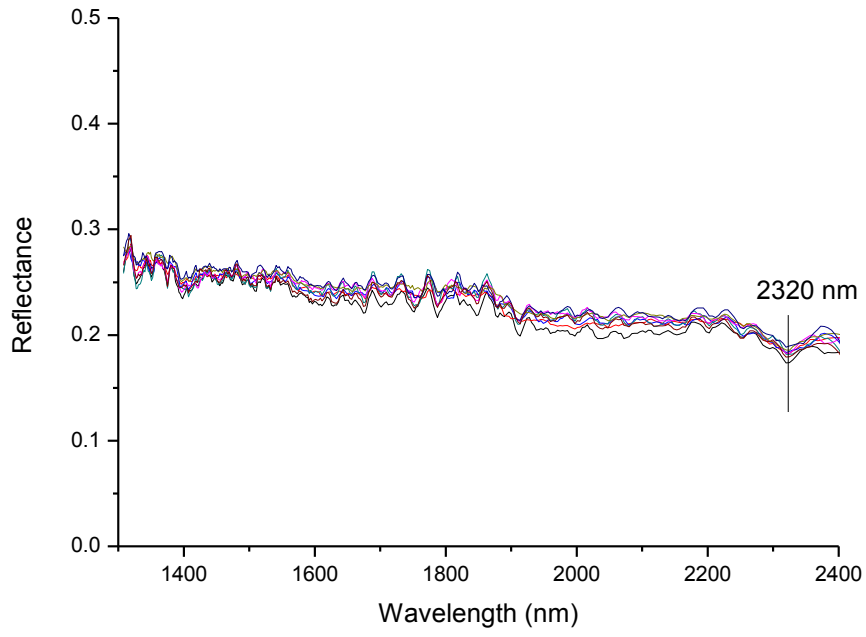
Sample 44 (MSGC10035599)



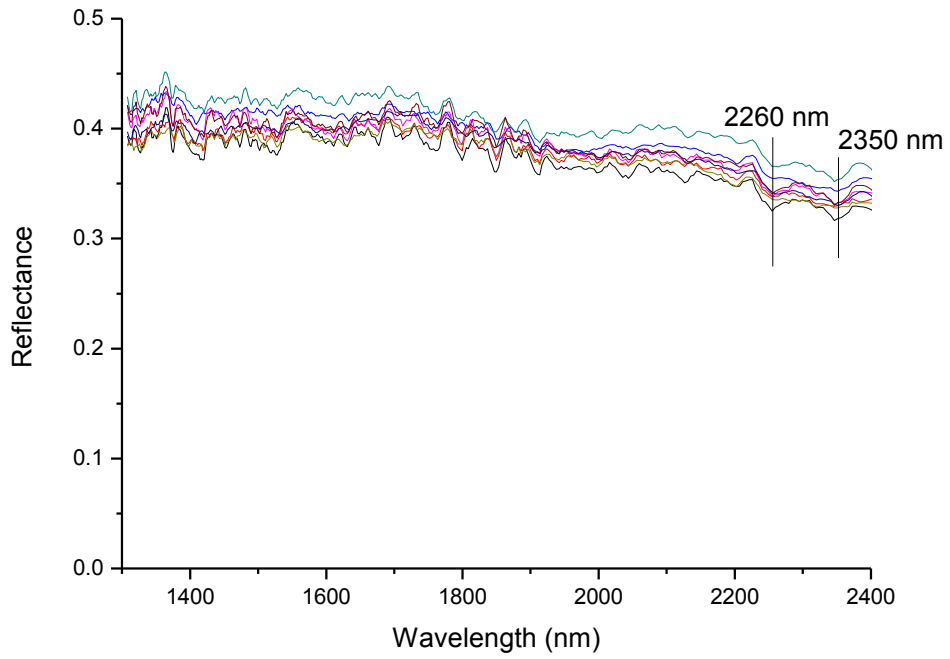
Sample 45 (MSGC10483406)



Sample 46 (MSGC10483490)

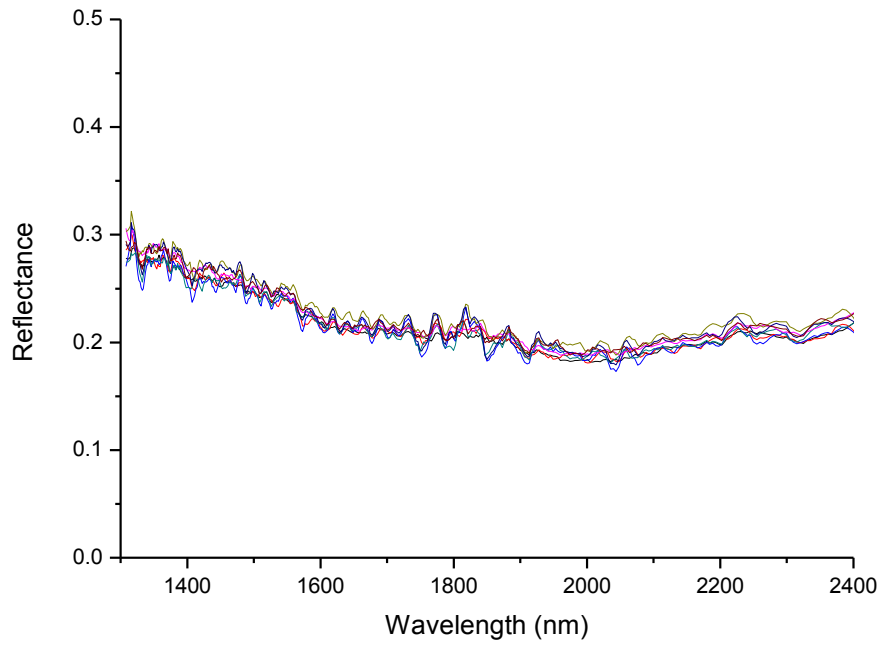


Sample 47 (MSGC10484179)

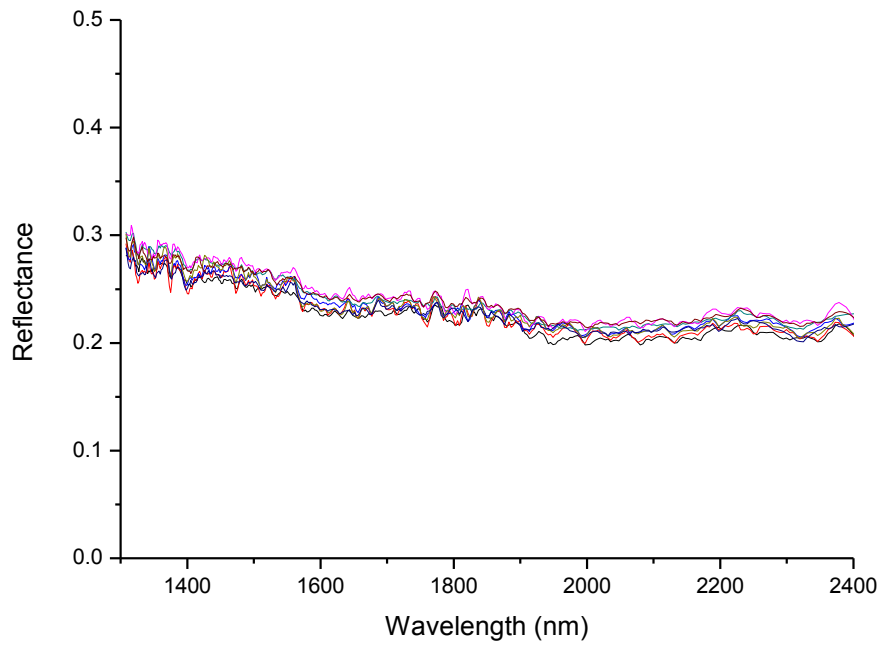


Sample 48 (MSGC10484198)

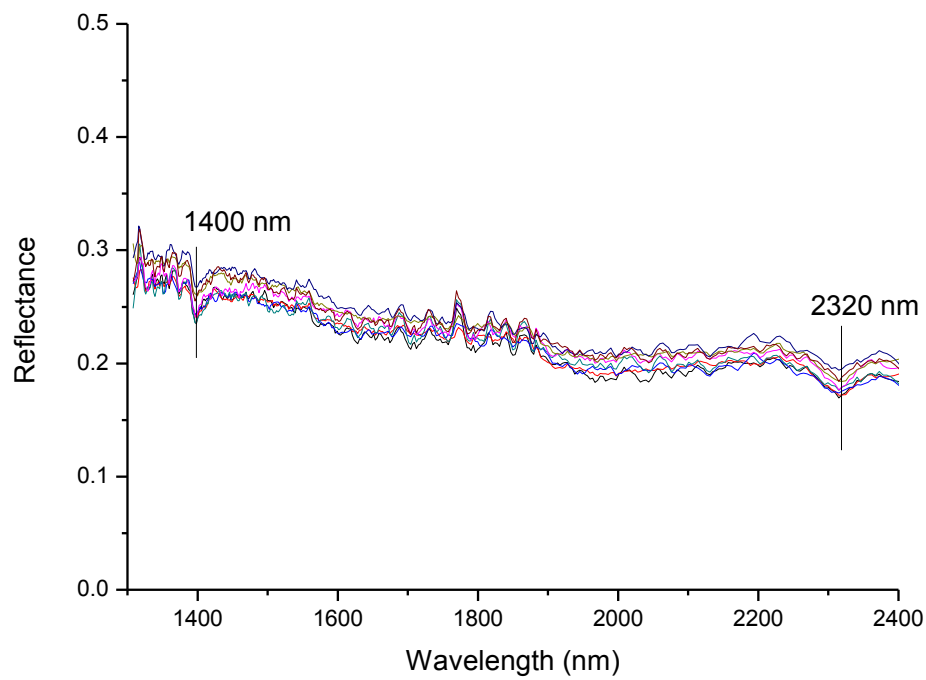




Sample 49 (MSGC10484221)



Sample 50 (MSGC10484280)



Sample 51 (MSGC10484312)